

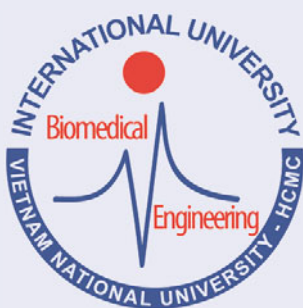
IFMBE Proceedings

Vo Van Toi · Trung Quoc Le ·
Hoan Thanh Ngo · Thi-Hiep Nguyen (Eds.)

Volume 69

7th International Conference on the Development of Biomedical Engineering in Vietnam (BME7)

Translational Health Science and Technology
for Developing Countries



IFMBE Proceedings

Volume 69

Series Editor

Ratko Magjarevic, Faculty of Electrical Engineering and Computing, ZESOI, University of Zagreb, Zagreb, Croatia

Associate Editors

Piotr Ładyżyński, Warsaw, Poland

Fatimah Ibrahim, Department of Biomedical Engineering, Faculty of Engineering, University of Malaya, Kuala Lumpur, Malaysia

Igor Lackovic, Faculty of Electrical Engineering and Computing, University of Zagreb, Zagreb, Croatia

Emilio Sacristan Rock, Mexico DF, Mexico

The IFMBE Proceedings Book Series is an official publication of *the International Federation for Medical and Biological Engineering (IFMBE)*. The series gathers the proceedings of various international conferences, which are either organized or endorsed by the Federation. Books published in this series report on cutting-edge findings and provide an informative survey on the most challenging topics and advances in the fields of medicine, biology, clinical engineering, and biophysics.

The series aims at disseminating high quality scientific information, encouraging both basic and applied research, and promoting world-wide collaboration between researchers and practitioners in the field of Medical and Biological Engineering.

Topics include, but are not limited to:

- Diagnostic Imaging, Image Processing, Biomedical Signal Processing
- Modeling and Simulation, Biomechanics
- Biomaterials, Cellular and Tissue Engineering
- Information and Communication in Medicine, Telemedicine and e-Health
- Instrumentation and Clinical Engineering
- Surgery, Minimal Invasive Interventions, Endoscopy and Image Guided Therapy
- Audiology, Ophthalmology, Emergency and Dental Medicine Applications
- Radiology, Radiation Oncology and Biological Effects of Radiation

IFMBE proceedings are indexed by SCOPUS and EI Compendex. They are also submitted for ISI proceedings indexing.

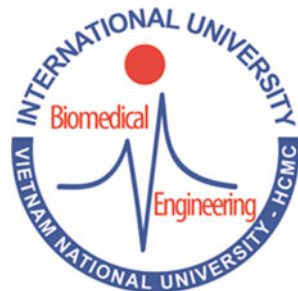
Proposals can be submitted by contacting the Springer responsible editor shown on the series webpage (see "Contacts"), or by getting in touch with the series editor Ratko Magjarevic.

More information about this series at <http://www.springer.com/series/7403>

Vo Van Toi · Trung Quoc Le ·
Hoan Thanh Ngo · Thi-Hiep Nguyen
Editors

7th International Conference on the Development of Biomedical Engineering in Vietnam (BME7)

Translational Health Science and Technology
for Developing Countries



 Springer

Editors

Vo Van Toi
Department of Biomedical Engineering
Ho Chi Minh City International University
Ho Chi Minh, Vietnam

Trung Quoc Le
Department of Biomedical Engineering
Ho Chi Minh City International University
Ho Chi Minh, Vietnam

Hoan Thanh Ngo
Department of Biomedical Engineering
Ho Chi Minh City International University
Ho Chi Minh, Vietnam

Thi-Hiep Nguyen
Department of Biomedical Engineering
Ho Chi Minh City International University
Ho Chi Minh, Vietnam

ISSN 1680-0737 ISSN 1433-9277 (electronic)
IFMBE Proceedings
ISBN 978-981-13-5858-6 ISBN 978-981-13-5859-3 (eBook)
<https://doi.org/10.1007/978-981-13-5859-3>

Library of Congress Control Number: 2019933206

© Springer Nature Singapore Pte Ltd. 2020

This work is subject to copyright. All rights are reserved by the Publisher, whether the whole or part of the material is concerned, specifically the rights of translation, reprinting, reuse of illustrations, recitation, broadcasting, reproduction on microfilms or in any other physical way, and transmission or information storage and retrieval, electronic adaptation, computer software, or by similar or dissimilar methodology now known or hereafter developed.

The use of general descriptive names, registered names, trademarks, service marks, etc. in this publication does not imply, even in the absence of a specific statement, that such names are exempt from the relevant protective laws and regulations and therefore free for general use.

The publisher, the authors and the editors are safe to assume that the advice and information in this book are believed to be true and accurate at the date of publication. Neither the publisher nor the authors or the editors give a warranty, expressed or implied, with respect to the material contained herein or for any errors or omissions that may have been made. The publisher remains neutral with regard to jurisdictional claims in published maps and institutional affiliations.

This Springer imprint is published by the registered company Springer Nature Singapore Pte Ltd.
The registered company address is: 152 Beach Road, #21-01/04 Gateway East, Singapore 189721, Singapore

Organizing Institutions



Vietnam National Universities HCM City (VNU-HCM)



International University of VNU-HCM



Saigon Hi-Tech Park HCM City

Honorary Chairs

Prof. Huỳnh Thành Đạt, President of Vietnam National Universities HCM City
Dr. Trần Tiến Khoa, Rector of International University VNU-HCM

Conference General Chair

Võ Văn Tới, Ph.D.
Professor and Chair of Biomedical Engineering Department
International University—Vietnam National Universities
Quarter 6, Linh Trung, Thu Duc District, Ho Chi Minh City, Vietnam
Tel: (84-28) – 37 24 42 70 Ext. 3236
Fax: (84-28) – 37 24 42 71
Email: bme2018@hcmiu.edu.vn
Website: <http://csc.hcmiu.edu.vn/bme>

Conference General Co-chair

Lê Hoài Quốc, Ph.D.
President of Saigon Hi-Tech Park
Tan Phu, District 9, Ho Chi Minh City, Vietnam
Tel: (84-28) – 37 36 02 93
Fax: (84-28) – 37 36 02 92
Email: lhquoc.shtp@tphcm.gov.vn
Website: <http://www.eng.shtp.hochiminhcity.gov.vn/>

International Organizing Committee

Prof. Beom-Jin Lee, Ajou University, Republic of Korea
Dr. Bui Cong Thanh, Oklahoma University, USA
Dr. Cecile Perrault, University of Sheffield, UK
Dr. Le Chi Hieu, University of Greenwich, UK
Prof. Masahiro Takei, Chiba University, Japan
Prof. Nghiem Doan, University of Queensland, Australia
Prof. Paolo Carloni, German Research School for Simulation Sciences, Germany
Prof. Paul Milgram, University of Toronto, Canada
Prof. Raekil Park, Gwangju Institute of Science and Technology, Republic of Korea
Prof. Tak Shing Ching, National Chung Hsing University, Taiwan R.O.C.
Prof. Walter Lee, Duke University, USA
Prof. Wellington Pham, Vanderbilt University, USA

Local Organizing Committee

Prof. Huỳnh Thành Đạt, Vietnam National University, Ho Chi Minh City, Honorary Chair
Dr. Trần Tiến Khoa, International University, Vietnam National University, Honorary Chair
Prof. Võ Văn Tới, International University-Vietnam National University, Conference General Chair
Prof. Lê Hoài Quốc, Saigon Hi-Tech Park, Vietnam, Conference General Co-Chair
Dr. Lê Quốc Trung, International University-Vietnam National University, Conference Vice Chair
Dr. Nguyễn Lê Thanh An, International University-Vietnam National University
Prof. Nguyễn Thanh Hải, HCM University of Technology Education, Vietnam

Prof. Vũ Duy Hải, Bach Khoa University, Hanoi, Vietnam
Dr. Bùi Thị Hồng Hạnh, International University-Vietnam National University
Dr. Phạm Thị Thu Hiền, International University-Vietnam National University
Dr. Nguyễn Thị Hiệp, International University-Vietnam National University
Dr. Ngô Thanh Hoàn, International University-Vietnam National University
Ms. Nguyễn Tú Khanh, International University-Vietnam National University
Dr. Huỳnh Chấn Khôn, International University-Vietnam National University
Ms. Trần Thị Thanh Lịch, International University-Vietnam National University
Prof. Huỳnh Quang Linh, Bach Khoa University-Vietnam National University
Mr. Nguyễn Phương Nam, International University-Vietnam National University
Dr. Nguyễn Hồng Quang, International University-Vietnam National University
Mr. Nguyễn Thanh Tâm, International University-Vietnam National University
Mr. Đỗ Minh Thái, International University-Vietnam National University
Prof. Võ Văn Thành, Trung Vương Hospital, Vietnam
Dr. Lê Thị Anh Thơ, International University-Vietnam National University
Prof. Nguyễn Văn Thuận, International University-Vietnam National University
Mr. Nguyễn Hoàng Tuấn, International University-Vietnam National University
Dr. Nguyễn Hồng Vân, International University-Vietnam National University
Mr. Nguyễn Lê Ý, International University-Vietnam National University

Secretariat

Ms. Từ Thị Tuyết Nga, International University-Vietnam National University, Vietnam
Ms. Trương Thị Mỹ Tiên, International University-Vietnam National University, Vietnam
Ms. Nguyễn Ngọc Thảo Quyên, International University-Vietnam National University, Vietnam
Ms. Vũ Thiên Ngân, International University-Vietnam National University, Vietnam
Ms. Trần Thị Kim Ngân, International University-Vietnam National University, Vietnam

Preface

Welcome to the 7th International Conference in Vietnam on the Development of Biomedical Engineering

Vietnam is a rapidly developing, socially dynamic country, where interest in biomedical engineering (BME) activities has grown considerably in recent years. The leadership of the Vietnamese government, and of research and educational institutions, are well aware of the importance of this field for the development of the country and have instituted policies to promote its development. The political, economic, and social environment within the country offers unique opportunities for the international community, and this conference was intended to provide a vehicle for the sharing of experiences, development of support and collaboration networks for research, and exchange of ideas on how to improve the educational and entrepreneurial environment to better address the urgent needs of Vietnam. In the following, we would like to share with you our history.

In January 2004, under the sponsorship of the U.S. National Science Foundation, Prof. Vo Van Toi of the BME Department of Tufts University, Medford Massachusetts USA, led a fact-finding U.S. delegation that consisted of BME professors from different universities in the USA, and visited several universities and research institutions in Vietnam from North to South to assess the state of development of this field. This delegation proposed a 5-year plan that was enthusiastically embraced by the international scientific communities to actively develop collaborations with Vietnam.

Within this framework, **in July 2005, the First International Conference** on the Development of BME in Vietnam was held in Ho Chi Minh City. From that conference, a Consortium of Vietnam-International Universities was created to advise and assist the development of BME in Vietnamese universities.

In July 2007, the Second International Conference on the Development of BME in Vietnam was held in Hanoi. During this event, the Vietnamese Association of Biomedical Science and Engineering was endorsed by the Asia-Pacific International Molecular Biology Network (AIMBN), BME Society Singapore (BESS), International Federation for Medical and Biological Engineering (IFMBE), Société Française de Génie Biologique et Médical (SFGBM), and IFMBE Asia-Pacific Working Group.

In March 2009, International University (IU) established its BME Department and the first accredited Engineer in BME degree in Vietnam (code: 52.42.02.04). IU is a member of Vietnam National Universities—Ho Chi Minh City (VNU-HCM), one of the two elite university networks in Vietnam, and is the first public university in Vietnam that teaches all courses in English. It was created as a new model to modernize the higher education in Vietnam. The BME Department at IU has since coordinated with its national and international counterparts to promote the activities of this field in Vietnam.

In January 2010, the Third International Conference on the Development of BME in Vietnam was organized by IU in Ho Chi Minh City. It reflected the steady growth of the activities in this field in Vietnam, and featured the contributions of researchers of 21 countries, including Australia, Belgium, Canada, Denmark, France, India, Japan, Korea, Malaysia, New Zealand, Philippines, Poland, Russia, Singapore, Spain, Switzerland, Taiwan, Thailand, UK,

USA, and Vietnam. The Conference was endorsed by the International Federation for Medical and Biological Engineering (IFMBE). It also hosted the Clinical Engineering Workshop of the IFMBE Asia-Pacific Working Group. The contributed papers were published in the IFMBE Proceedings Series by Springer (ISBN 978-3-642-12019-0).

In **January 2012, the Fourth International Conference** on the Development of BME in Vietnam was organized at IU of VNU-HCM as a Mega-conference. It was kicked off by the Regenerative Medicine Conference (January 8–10, 2012) with the theme “*BUILDING A FACE*” *Using a Regenerative Medicine Approach*, endorsed mainly by the Tissue Engineering and Regenerative Medicine International Society (TERMIS) and co-organized by Prof. Stephen E. Feinberg, University of Michigan Health System, USA, Prof. Anh Le, University of Southern California, USA, and Prof. Vo Van Toi, International University-VNU-HCM, Vietnam. It was followed by the Computational Medicine Conference, endorsed mainly by the Computational Surgery International Network (COSINE) and the Computational Molecular Medicine of German National Funding Agency; and the General BME Conference, endorsed mainly by the International Federation for Medical and Biological Engineering (IFMBE) (January 10–12) and co-organized by Prof. Paolo Carloni, German Research School for Simulation Sciences GmbH, Germany, Prof. Marc Garbey, University of Houston, USA, and Prof. Vo Van Toi, International University-VNU-HCM, Vietnam. It featured the contributions of 435 scientists from 30 countries, including Australia, Austria, Belgium, Canada, China, Finland, France, Germany, Hungary, India, Iran, Italy, Japan, Jordan, Korea, Malaysia, The Netherlands, Pakistan, Poland, Russian Federation, Singapore, Spain, Switzerland, Taiwan, Turkey, Ukraine, UK, USA, Uruguay, and Vietnam. Contributed papers were published in the IFMBE Proceedings series, Vol. 40, Publisher: Springer, ISBN: 978-3-642-32183 in 2013.

The **Fifth International Conference on the Development of BME** was organized by IU of VNU-HCM from June 16 to 18, 2014. Prof. Vo Van Toi of this institution was the Conference General Chair. This **Conference** was a very special event. It officially opened the season for celebration of the 20th Anniversary of VNU-HCM. It also marked the 10th Anniversary of IU and the 5th Anniversary of the BME Department. This Conference featured 231 papers of 532 authors and co-authors from 26 countries including Australia, Bangladesh, Belgium, Canada, China, Croatia, Czech Republic, Denmark, Finland, France, Germany, India, Israel, Italy, Japan, Korea, Malaysia, Norway, Singapore, Slovenia, Switzerland, Taiwan, Turkey, UK, USA, and Vietnam. Almost all Vietnamese institutions have their delegations. Besides Vietnam, the two countries that have the most contributors are the USA and Australia. The plenary session featured the lectures from keynote speakers: (1) Prof. Ratko Magjarevic, President of IFMBE; (2) Dr. Robert A. Lieberman, Vice-President of International Society for Optics and Photonics SPIE; (3) Prof. Vo-Dinh Tuan, Director of Fitzpatrick Institute for Photonics, Duke University, USA; (4) Prof. Christian Griesinger, Director of Max Planck Institute for Biophysical Chemistry, Germany; (5) Prof. Anja Boisen, Director of VKR Centre of Excellence ‘NAMEC’, Denmark; (6) Prof. Yin Xiao, Director of Australia-China Centre for Tissue Engineering and Regenerative Medicine, Queensland University of Technology, Australia; (7) Prof. Yukio Nagasaki, Department of Materials Science and Medical Sciences, University of Tsukuba, Japan; and (8) Prof. Fong-Chin Su, President of Taiwanese Society of BME, Director, Medical Device Innovation Center, National Cheng Kung University, Taiwan. The contributed papers were published in the IFMBE Proceedings Series by Springer, Vol. 46, ISBN 978-3-319-11775 in 2015.

The social events were also organized to introduce to the international guests the Vietnamese culture. Sponsors: Vietnam National Universities—HCMC and International University Office of Naval Research Global, Arizona State University, Alberta University, VikoMed, Trung Son (T.S.S.E.), Saigon Instrumentation Joint Stock Company (Saigon ISC), ITS Vietnam, Saigon Scientists, and National Instruments. SPIE (USA), Technical Co-sponsor, gave two awards to student papers in the field of Biophotonics.

The **Sixth International Conference** on the Development of BME in Vietnam was organized from June 27 to 29, 2016 by IU, VNU-HCM and Saigon HiTech Park (SHTP). Prof. Vo Van Toi was the Conference General Chair. The conference theme was *Healthcare Technology for Developing Countries*. 417 authors and co-authors came from 23 countries

including Australia, Canada, China, Finland, France, Germany, Hong Kong, India, Indonesia, Italy, Japan, Korea, Malaysia, Norway, Portugal, Singapore, Spain, Taiwan, Thailand, UK, USA, and Vietnam. Vietnam, Australia, USA, and Korea had the most contributors. Nine distinguished Keynote Speakers gave their talks either in plenary sessions for the general public or in parallel sessions with specific topics: (1) Prof. Jeff Bulte, Professor of Radiology, Oncology, BME and Chemical & Biomolecular Engineering, Director, Cellular Imaging Section, Institute for Cell Engineering, Johns Hopkins University School of Medicine, USA; (2) Prof. Paolo Carloni, German Research School for Simulation Sciences GmbH and Institute for Advanced Simulation (IAS), Germany; (3) Prof. John Huguenard, Director, Neuroscience Graduate Program, Stanford University, Professional Advisory Board, Epilepsy Foundation, USA; (4) Prof. Ryuji Kohno, Director, Medical Information and Communication Technology Center, Yokohama National University, Japan, Distinguished Professor, University of Oulu, Finland; (5) Dr. Sajeda Meghji, Emeritus Reader in Oral Biology, University College London (UCL), UK; (6) Prof. Beom-Jin Lee, Dean of College of Pharmacy, Ajou University, Head of the Pharmaceutical Research and Development Agency, Korean Pharmaceutical Manufacturing Associations, Korea; (7) Prof. Yu-Lung Lo, Distinguished Professor, Head of Department of Mechanical Engineering, National Cheng Kung University, Taiwan; (8) Prof. Yasuhiko Tabata, Chairman, Department of Biomaterials, Institute for Frontier Medical Sciences, Kyoto University, Board of Governors, Tissue Engineering Society International, Japanese Society of Biomaterials, Japanese Tissue Engineering Society, Society for Hard Tissue Regenerative Medicine, Japanese Society of Inflammation and Regeneration, Japan Society of Drug Delivery System, Japanese Regenerative Medicine Society, Japan; and (9) Prof. Christopher Woods, Director of Master of Science in Global Health, Director of Graduate Studies, Duke Global Health Institute, Duke University, Chief, Infectious Diseases Division, Durham VA Medical Center, USA. Furthermore, 44 Invited Speakers gave their talks or tutorial lectures in the parallel sessions including Materials for Biomedical Applications, Biomechanics, Lab-on-a-chip & Point-of-Care Technologies, Mathematical Modeling in Medicine, Biophotonics, Public Health, Pharmaceutical Sciences and Biomedicine, Medical Instrumentations, Healthcare Information Technology and Bioinformatics, Biomedical Signal & Image Processing, Neuroscience and Neuroengineering, Advanced in Stem Cell and Cell Reprogramming, Molecular and Cellular Techniques in Medicine, Ultrasonic Characterization of Bone Tissues, and Advanced Molecular Simulation and Experimental Biophysical Approaches for Drug Design.

In addition, the Vietnam–UK workshop in the BME field which was funded by the Newton Fund Researcher Links of British Council, conjointly organized by Prof. Le Hoai Quoc (SHTP), Dr. Le Chi Hieu (University of Greenwich), and Prof. Vo Van Toi (BME-IU), and coordinated by Dr. Le Quoc Trung (BME-IU). Researchers from 10 UK universities: (1) University of Greenwich, (2) Cardiff University, (3) North Umbria University, (4) Sheffield University, (5) University of Hertfordshire, (6) Newcastle University, (7) Oxford University, (8) London South Bank University, (9) University of Derby, and (10) Aston University, and representatives of British Council participated. The last day of the workshop was devoted to a round-table discussion among 21 Vietnamese and 12 UK researchers. Other activities included a field trip to visit SHTP and a new medical device manufacturer, and social events were also organized to introduce to the international guests Vietnamese culture. The contributed articles were published in the “IFMBE Proceedings Series” by Springer, Vol. 63, ISBN: 978-981-10-4360-4, 2017. Sponsors included VNU-HCM, IU, Office of Naval Research Global, US Army International Technology Center—Pacific, Springer, IFMBE, SHTP, NAFOSTED, Newton Fund, Korea United Pharm. Inc., Global IMD Center, ESTC and others.

This **Seventh International Conference** in Vietnam on the Development of BME from June 27 to 29, 2018 promotes the connections among research, entrepreneurship, and education in BME with the theme *Translational Health Science and Technology for Developing Countries*. It serves as a forum for researchers, educators, entrepreneurs, administrators, and policy-makers to exchange intellectual ideas, discuss current problems, propose translational solutions, and develop collaborative connections on translational research and technologies in health care for developing countries. On behalf of the Organizing Committee, we would like to

welcome all participants. Please peruse this book for useful information. The full-text accepted articles are in the included USB. We wish you three happy and fruitful conference days. We are looking forward to developing with you in-depth collaborations.

Ho Chi Minh, Vietnam

Vo Van Toi
Trung Quoc Le
Hoan Thanh Ngo
Thi-Hiep Nguyen

Editing Team

Huynh Chan Khon
Pham Thi Thu Hien
Nguyen Le Thanh An
Paul Milgram
Le Thi Anh Tho
Nguyen Phuong Nam
Nguyen Thanh Tam
Nguyen Hong Van

Do Minh Thai
Nguyen Hoang Tuan
Nguyen Tu Khanh
Nguyen Le Y
Tu Thi Tuyet Nga
Truong Thi My Tien
Nguyen Ngoc Thao Quyen
Tran Thi Kim Ngan

Acknowledgements

We would like to express our deepest appreciation to the following sponsors:



And to the following reviewers of submitted manuscripts:

Alex Vitkin
Bich Thuy Vu
Bui Cong Thanh
Bui Thi Cuc
Bui Thi Hanh Duyen
Caroline Cao
Cecile Perrault
Chu Thi Xuan
Cu Gia Huy
Daipayan Guha
Dang Hoang Phuc
Dang Thanh Tin
Dang Trinh Minh Anh
Do Minh Thai
Do Ngoc Hung
Giang Hoa
Hamed Shourabizadeh
Ho Quoc Minh Huy
Hoang Anh Tien
Hoang Trung Thien
Huynh Chan Khon
Huynh Kim Phat
Karen McCloy
Le Chi Hieu
Le Quang Khai
Le Quoc Trung
Le Thanh Hai
Le Thi Anh Tho
Liisa van Vliet
Lisa Tam
Luong Thu Hien
Nghiem Doan
Ngo Dinh Tri
Ngo Thanh Hoan
Nguyen Anh Tai
Nguyen Bao Quoc
Nguyen Bao Toan
Nguyen Duc Thang
Nguyen Hoai Thuong
Nguyen Hoang Tuan
Nguyen Hong Van
Nguyen Le Thanh An
Nguyen Le Y
Nguyen Ngoc Quang
Nguyen Phuong Nam
Nguyen Thanh Hai
Nguyen Thanh Tam
Nguyen Thi Hiep
Nguyen Thi Le Thuy
Nguyen Thi Minh Huong
Nguyen Thi Phuong Nghi

Nguyen Thi Thu Hoai
Nguyen Thi Thu Thao
Nguyen Thuy Ba Linh
Nguyen Tien Anh
Nguyen Tu Khanh
Nguyen Van Hau
Nguyen Vuong Hoang Long
Nishant Chakravorty
Paul Milgram
Paul Watton
Pham Ngoc Doan Trang
Pham Thanh Thao
Pham Thi Kim Tram
Pham Thi Thu Hien
Pham Trung Kien
Phan Minh Duy
Phan Quoc Huy
Phan Quoc Hung
Pingping Han
Quach Mai Boi
Raman Maiti
Thien Duong
Timothy Chan
Tran Anh Hien
Tran Cam Tu
Tran Hai Ly
Tran Hong Anh
Tran Le Son
Tran Nghia Khanh
Tran Thi Bich Lieu
Tran Thi My Khanh
Tran Truong Dinh Thao
Trinh Nhu Thuy
Truong Dinh Tuan
Truong Phuoc Long
Vo Thi Hong Tuyet
Vong Binh Long
Yang Liu
Yinghong Zhou

About IFMBE

The International Federation for Medical and Biological Engineering (IFMBE) is primarily a federation of national and transnational societies. These professional organizations represent interests in medical and biological engineering. IFMBE is also a Non-Governmental Organization (NGO) for the United Nations and the World Health Organization (WHO), where we are uniquely positioned to influence the delivery of health care to the world through biomedical and clinical engineering.

The IFMBE's objectives are scientific and technological as well as educational and literary. Within the field of medical, biological, and clinical engineering, IFMBE's aims are to encourage research and application of knowledge and to disseminate information and promote collaboration. The ways in which we disseminate information include the following: organizing World Congresses and Regional Conferences, publishing our flagship journal *Medical and Biological Engineering and Computing* (MBEC), our Web-based newsletter—IFMBE News, our Congress and Conference Proceedings, and books. The ways in which we promote collaborations are through networking programs, workshops, and partnerships with other professional groups, e.g., Engineering World Health.

Mission

The mission of IFMBE is to encourage, support, represent, and unify the worldwide medical and biological engineering community in order to promote health and quality of life through the advancement of research, development, application, and management of technology.

Objectives

The objectives of the International Federation for Medical and Biological Engineering shall be scientific, technological, literary, and educational. Within the field of medical, clinical, and biological engineering, its aims shall be to encourage research and the application of knowledge and to disseminate information and promote collaboration.

In pursuit of these aims, the Federation may, in relation to its specific field of interest, engage in any of the following activities: sponsorship of national and international meetings, publication of official journals, cooperation with other societies and organizations, appointment of commissions on special problems, awarding of prizes and distinctions, establishment of professional standards and ethics within the field, or in any other activities which in the opinion of the General Assembly or the Administrative Council would further the cause of medical, clinical, or biological engineering. It may promote the formation of regional, national, international, or specialized societies, groups or boards, the coordination of bibliographic or informational services, and the improvement of standards in terminology, equipment, methods and safety practices, and the delivery of health care.

In general, the Federation shall work to promote improved communication and understanding in the world community of engineering, medicine, and biology.

Contents

Part I Medical Instrumentations

Design of Noninvasive Hemodynamic Monitoring Equipment Using Impedance Cardiography	3
Vu Duy Hai, Lai Huu Phuong Trung, Pham Manh Hung, Dao Viet Hung, Pham Phuc Ngoc, Phan Dang Hung, Chu Quang Dan, and Tran Quoc Vi	
Overview of Our Less Invasive Operation System—Development of Three Dimensional Real-Time MR Image Guided Operation System Using Microwave Devices and Relating Technologies	11
Tohru Tani, Shigeyuki Naka, Atsushi Yamada, Soichiro Tani, Dang Tran Khiem, and Nguyen Quoc Vinh	
Design and Implementation of Loop Shaped Steering Mechanisms for Flexible Needles	15
Atsushi Yamada, Norihisa Nitta, Shigeyuki Naka, Khiem Tran Dang, Shigehiro Morikawa, and Tohru Tani	
Development of an MR-Compatible High-Definition Flexible Endoscope for Real-Time MR Image-Guided Microwave Ablation	21
Atsushi Yamada, Shigeyuki Naka, Khiem Tran Dang, Shigehiro Morikawa, and Tohru Tani	
Development of Bio-signal Acquisition and Processing System and Its Utilization for Educational Purpose	27
Sun I. Kim, Jongshill Lee, Dong Pyo Jang, and In Young Kim	
A Non-contact Human Body Height and Weight Measurement Approach Using Ultrasonic Sensor	31
Minh H. Ly, Nguyen M. Khang, Tran T. Nhi, Tin T. Dang, and Anh Dinh	
Brain Tumor Segmentation Using U-Net Based Deep Neural Networks	39
Hai Thanh Le and Hien Thi-Thu Pham	
Noncontact-Body-Temperature-Measurement	43
N. T. Hang, P. T. N. Thao, Tin T. Dang, and Anh Dinh	
Design, Test and Evaluation of a Dental Fluorescence Camera	51
Thi Hai Mien Pham, Bao Ngoc Tran, Ngoc Minh Thinh Nguyen, Tran Khanh Tran Nguyen, Phu Duong Le, and Quang Linh Huynh	
Application of Near—Infrared Technique in Studying Dental Lesions	57
Thi Hai Mien Pham, Tran Kim Hoang Nguyen, Thuy Ha Nguyen, Tan Thanh Vo, Phu Duong Le, and Quang Linh Huynh	

Building an EMG Receiver System to Control a Peripheral Device	61
Khanh Quoc Huynh, Nga Thi-Hang Vu, Nam Hoang Bui, and Hien Thi-Thu Pham	
Development of a Pulse Oximeter for E-Health Applications	67
Thai M. Do, Nam P. Nguyen, and Vo Van Toi	
Detection of Systole and Diastole Points on Seismocardiogram Using Interpolation Method	77
Loc Luu and Anh Dinh	
Application of Computational Anatomy into Primarily Diagnosing Cardiac Status	81
N. V. T. Kien, T. M. Linh, Tin T. Dang, and Anh Dinh	
Implementation of a Pilot Cyber Medical System with Blood Pressure Devices for Telemedicine in Binh Duong Province (Vietnam)	87
T. N. Viet, D. M. Thai, N. P. Nam, and Vo Van Toi	
A Low Cost High Voltage Power Supply to Use in Electrospinning Machines	95
Thai M. Do, Minh H. Ho, Thien B. T. Do, Nam P. Nguyen, and Vo Van Toi	
Part II Workshop in Medical Instrumentations and Entrepreneurship	
A Cloud-Based System for In-Home Fall Detection and Activity Assessment	103
Quoc T. Huynh, Uyen D. Nguyen, and Binh Q. Tran	
An Accuracy and Reliability Comparison Study of Electronic Uroflowmetry Devices	109
Thinh P. Nguyen, An T. L. Nguyen, Y. L. Nguyen, Vo Van Toi, Thien M. Nguyen, and Hai T. Phan	
Comparative Study of Novel Microwave Coagulation Surgical Instrument and Currently Commercialized Energy Devices in an Animal Model	115
Dang Tran Khiem, Tohru Tani, Shigeyuki Naka, Atsushi Yamada, and Soichiro Tani	
Developing Neural-fuzzy-based Unscented Kalman Filter Algorithm for Atrial Fibrillation Onset Prediction	119
Cuc T. Bui, Phat K. Huynh, Hao T. Phan, Trung Q. Le, and Vo Van Toi	
Modeling of Acoustic Tweezers for the Manipulation in Biological Media	127
Quyen B. Huynh, Huy Q. Pham, Nhung T. Nguyen, Trung Q. Le, and Vo Van Toi	
Part III Biomaterials and 3D Printing	
Decellularization of Bovine Cancellous Bone for Bone Tissue Engineering Application	139
Nam Minh-phuong Tran, Dat Tan Nguyen, Tin Dai Luong, Nghia Hieu Bui, Vo Van Toi, and Thi-Hiep Nguyen	
Investigation of Biphasic Calcium Phosphate on Dentin Occlusion for Dentin Hypersensitivity Treatment	143
Nhi-Thao Ngoc Dang, Hien-Phuong Le, Vo Van Toi, and Thi-Hiep Nguyen	
Diatom Particles: A Promising Osteoinductive Agent of Silk Fibroin-Based Scaffold for Bone Regeneration	147
Thi Duy Hanh Le, Volha Liaudanskaya, Walter Bonani, Claudio Migliaresi, and Antonella Motta	

The Use of 3D Printed Microporous-Strut Polycaprolactone Scaffolds for Targeted Local Delivery of Chemotherapeutic Agent for Breast Cancer Application	153
Hoang Phuc Dang, Dietmar W. Hutmacher, and Phong A. Tran	
Fabrication of Vascular Patch from Porcine Pericardium	159
My Thi Ngoc Nguyen, Tuyet Le, and Ha Tran	
Effect of Magnesium on Mechanical Properties of Binary Zn–Mg Alloys	163
Shiyang Liu, Nghiem Doan, and Gui Wang	
A Suitable Protocol to Prepare Decellularized Porcine Vessel for Cardiovascular	169
Minh Quan To, Quoc Thang Bui, Ngoc Le Van Trinh, Thi Vy Tuyet Le, Quang Tri Le, Tho Tuan Anh Pham, and Le Bao Ha Tran	
A Comparative Study on Hydroxyapatite Derived from Bovine Bones and Synthetic Sources	175
Nhi-Thao Ngoc Dang, Hien-Phuong Le, Vo Van Toi, and Thi-Hiep Nguyen	
Synthesis of N,O-Carboxymethyl Chitosan-Aldehyde Hyaluronic Acid Hydrogel Loading Silver Nanoparticles	179
Tien Ngoc-Thuy Nguyen, Dat Tan Nguyen, Vo Van Toi, and Thi-Hiep Nguyen	
Part IV Nanomedicine and Drug Delivery Systems	
Redox Polymeric Nanoparticle as an Effective Oral Nanotherapeutics for Inflammatory Bowel Disease and Cancer	185
Long Binh Vong and Yukio Nagasaki	
Preparation and Characterization of Redox-Sensitive Pluronic F127-Based Nanogel as Effective Nanocarrier for Drug Delivery	189
Diem Huong Tran Nguyen, Dong Yen Pham Nguyen, Linh Phuong Tran Pham, Thanh Nguyet Nguyen Vo, Dai Hai Nguyen, and Ki Dong Park	
Nanoliposomes as an Efficient Drug Carrier System for Paclitaxel Delivery	193
Ngoc Thuy Trang Le, Yen Nhi Nguyen Thi, Bac Ly Pham Thi, Ngoc Lin Hoang, Cuu Khoa Nguyen, and Dai Hai Nguyen	
Engineering of Hollow Mesoporous Silica Nanoparticles Enhancing Drug-Loading Capacity	197
Ngoc Tram Nguyen Thi, Ngoc Hoang Le, Uyen Vy Vo, Cuu Khoa Nguyen, and Dai Hai Nguyen	
Fabrication of Curcumin/Silver Nanoparticles Loaded Gelatin Scaffold	203
Khanh Loan Ly, Vo Van Toi, and Thi-Hiep Nguyen	
Nanoneedles and Nanostructured Surfaces for Studying Cell Interfacing	209
Stuart G. Higgins, Michele Becce, Hyejeong Seong, and Molly M. Stevens	
From Macroscopic to Microscopic: Experimental and Computational Methods to Investigate Bio-tribology	213
Raman Maiti, Rasmus Wagner, Noe A. Martinez Sanchez, Alejandro Ramirez-Reivich, Peter Ellison, Cecile Perrault, Matt J. Carre, Rob Dwyer-Joyce, Anne Neville, and Roger Lewis	

Part V Biomechanics

Bio-safety and Bio-efficiency of Micro-plasma Exposure to Fibroblast Cells L929	219
Ngo Thi Minh Hien, Nguyen Thi Kim Mai, Vo Hoang Thuc Minh, Nguyen Thi My Anh, Nguyen Ngoc Thang, Vo Duong Van Anh, Do Tuyet Nhi, Nguyen Quoc Duy Nam, and Huynh Quang Linh	
Cost-Effective Design and Development of a Prosthetic Hand	225
M. N. Anh, T. D. Tang, V. T. Trung, L. C. Hieu, N. H. Tu, H. L. Minh, and L. H. Quoc	
Controlling the Wheelchair by Eye Movements Using EEG	231
Van Cam Thi Le, Nhan Thanh Le, Hai Ngoc Nguyen, Dang Cao Le, and Keiji Iramina	
Permittivity Measurement for Thrombus Detecting at Connector Gap in Extracorporeal Blood Circulating System	235
M. Koishi, T. Kiet Anh, J. Li, and M. Takei	
Investigating Dielectric Properties of Hemolysis by Electrical Impedance Spectroscopy	239
Kiet Anh Tran, Jianping Li, Huynh Chan Khon, and Masahiro Takei	
An Electrical Impedance Tomography Sensor with Different Diameter	243
Ryota Yanagisawa, Marlin Ramadhan Baidillah, Al Amin Saichul Iman, Panji Nursetia Darma, Huang Jingshi, and Masahiro Takei	
Effect of Surface Roughness on Friction of CoCrMo-on-UHMWPE Bearing in Total Hip Arthroplasty Under Lubrication of Bovine Serum Albumin	247
Cong-Truyen Duong, Cong-Dat Le, and Duc-Nam Nguyen	

Part VI Recent Computational and Experimental Advances in Molecular Medicine

Replacement of Residue H95 with Charged Amino Acids in the Prion Protein Decreases Prion Conversion Propensity	255
Thanh Hoa Tran and Giuseppe Legname	
Computer Simulations Provide Guidance for Molecular Medicine Through Insights on Dynamics and Mechanisms at the Atomic Scale	261
Marc Baaden	

Part VII Regenerative Medicine and Tissue Engineering

Optimization of High Resolution Melting (HRM) Method for Genotyping and Estimating Frequency of SNP rs4284505 in the Vietnamese Breast Cancer	269
Hoang Mai Le Nguyen, Thi Nga Nguyen, Dien Thanh Giang Nguyen, Thi Ngoc Thanh Nguyen, and Thi Hue Nguyen	
Dental Implant or Dental Transplant: A Two Case Report	277
L. Truong, N. Doan, P. Reher, and Q. T. Duong	

Fabrication of N,O Carboxymethyl Chitosan (NOCC)—Aldehyde Hyaluronic Acid (AHA)—Biphasic Calcium Phosphate (BCP)—Poly (Vinyl Phosphonic Acid) (PVPA) Hydrogel for Bone Regeneration	283
Le Nguyen My An, Nguyen Thanh Truc, Vo Ngoc My Tuyen, Vo Van Toi, and Thi-Hiep Nguyen	
Overcoming Single Dental Implant Failure Using Two Small Implant Support for One Crown: Five Year Retrospective Study	289
N. Doan, L. Truong, J. Doan, and P. Reher	
A Three Year Retrospective Study on the Use of Concentrated Growth Factor (CGF) on Dental Patients Who Undergo Oral Regenerative Treatment	295
J. Doan, L. Truong, P. Reher, and N. Doan	
Composite Nano-fiber Mats Consisting of Biphasic Calcium Phosphate Loaded Polyvinyl Alcohol—Gelatin for Bone Tissue Engineering	301
Linh Thuy Ba Nguyen, Thi-Hiep Nguyen, Chan-Khon Huynh, Byong-Taek Lee, and Hua Ye	
Effect of Polyvinyl Alcohol Concentration on Properties of Polyvinyl Alcohol-Chitosan Hydrogel Loading Silver Nanoparticles	307
Ngoc Thi-thanh Nguyen, Nam Minh-phuong Tran, and Thi-Hiep Nguyen	
Fabrication Drug Loaded Polycaprolactone Microparticles by Electrospraying Method	313
Viet Linh Nguyen-Vu and Dai Phu Huynh	
Observation of Fibroblast Cell Attachment and Proliferation on Different Titanium Surface Textures: Morphology and In Vitro Study	319
Minh Thuy Vo, Thanh Truc Nguyen, Hieu Minh Ho, Loan Khanh Ly, Vo Van Toi, Le Minh Huynh, and Thi-Hiep Nguyen	
Comparison of Nail Polish Meth(Acrylates) (MA) Gel Photoresist and Vinyl Adhesive Paper for Low-Cost Microfluidics Fabrication	323
Ha Thach, Hoang-Tuan Nguyen, Uyen Tong, Tuan Hoang, Tuan-Anh Vuong, Cecile M. Perrault, and Khon Huynh	
 Part VIII Lab-on-a-chip and Point of Care Technologies	
Improvements in DNA Extraction and Loop-Mediated Isothermal Amplification (LAMP) Assist Application of LAMP on Malaria Point-of-Care Diagnostic Devices	333
Han Ly, Thanh-Xuan Le, Hoang-Tuan Nguyen, Vo Van Toi, Thanh-Dong Le, Thuy-Vy Pham-Nguyen, Cécile M. Perrault, and Khon Huynh	
Recent Developments in Continuous Monitoring Diagnostics with Microneedle Arrays	337
Anthony E. G. Cass, Danny O’Hare, and Sanjiv Sharma	
Towards the Digital Hospital: From Implant Design to In-Clinic Bio Fabrication	341
J. Munguia, Zhichao Ma, and Y. Ugurluoglu	
Integration of Microfluidic Sensors for Interactive Remote Wireless Data Transmission	347
Enobong E. Basse and Philip Sallis	

An Electrochemical DNA Sensor Based on Conducting Polymer Electrode	353
Trieu Van Vu Quan, Tran Quang Thinh, Le Binh Duong, Tran Hong Thuy, Chu Thi Xuan, and Mai Anh Tuan	
Part IX Technological Development in Microfluidics, and Point-of-Care	
Microfluidic Droplets and Their Applications: Diagnosis, Drug Screening and the Discovery of Therapeutic Enzymes	361
Liisa D. van Vliet and Florian Hollfelder	
A Microfluidic Device for Nucleic Acid-Based Analysis of <i>Helicobacter pylori</i> and Antibiotic Susceptibility Testing	369
Leah Greenhalgh, Mamun Rashid, Patricia E. Linton, and Kirsty J. Shaw	
Part X Biophotonics	
Coherent Hemodynamics Spectroscopy for Dynamic Measurements of Absolute Cerebral Blood Flow	375
Thao Pham, Kristen Tgavalekos, Angelo Sassaroli, and Sergio Fantini	
Investigation of Cerebral Hemodynamic Changes in Mild Cognitive Impairment Due to Alzheimer’s Disease During a Verbal Fluency Task	379
Minhee Kim, Thien Nguyen, Jeonghwan Gwak, Jang Jae Lee, Kyu Yeong Choi, Kun Ho Lee, and Jae Gwan Kim	
Designing and Building the Vein Finder System Utilizing Near-Infrared Technique	383
Long Thanh Tran and Hien Thi-Thu Pham	
Characterization of Non-melanoma Skin Cancer Utilizing the Optical Polarizing System	389
Dan Linh Le, Trinh Ngoc Huynh, and Thi-Thu-Hien Pham	
Investigating on the Effective Wound Healing Therapy Utilizing Laser Optical System	395
Xuan-Hieu Le, Ngoc-Bao-Tran Nguyen, Minh-Vy Huynh, Thi-Phuong-Trinh Vo, and Thi-Thu-Hien Pham	
Non-invasive Glucose Monitoring System Utilizing Near-Infrared Technology	401
Duc Trinh-Minh Dinh, Viet Anh Truong, An Nhu-Phu Tran, Hieu Xuan Le, and Hien Thi-Thu Pham	
Characterization of Liver Cancer Tissues Utilizing the Optical Polarized System	407
Thao-Vi Nguyen, Chi-Bao Bui, and Thi-Thu-Hien Pham	
Using UVB 311 nm Narrow-Band Medical Lamp for the Treatment of Psoriasis	413
Si-Nguyen Mai, Gia-Phu Pham, Vo Van Toi, Khon Huynh, and Thi-Thu-Hien Pham	
Pyramid Hologram in Projecting Medical Images	421
Minh H. N. Than, Minh M. N. Pham, and Hien Thi-Thu Pham	
Building an Automatic Control System for Measuring the Stokes Parameters	427
Minh Lai-Nhat Phan, Minh Nhat Nguyen, and Hien Thi-Thu Pham	

Part XI Healthcare Informatics

- An Efficient Solution to Secure Embedded Information in DICOM Images for Telemedicine** 435
Tuan T. Nguyen, Luan M. Tran, Ngoc C. Nguyen, and Thuong T. Le
- A Wireless Hemodialysis Blood Oozing Detection and Alarm System** 441
Jia-Huang Zeng and Yuh-Show Tsai

Part XII Biomedical Signal and Image Processing

- Detecting and Counting Eyes Blinking Using Haar Cascade—A Handy Way to Diagnose Dry Eyes Disease** 447
Nguyen D. Nguyen, Nguyen D. Quang, Dang T. Tin, and Anh Dinh
- Edge Detection in Low-Quality Medical Images Based on Augmented Lagrangian Method and B-Spline** 455
Vo Thi Hong Tuyet, Nguyen Thanh Binh, and Nguyen Chi Thanh
- Analysis of the Brain’s Response to Visual Stimulation in Reality and Imaginary** 461
Tran Thanh Huy, Le Quoc Khai, and Huynh Quang Linh
- Real Time 3D Pose Estimation of Both Human Hands via RGB-Depth Camera and Deep Convolutional Neural Networks** 467
Geon Gi, Tae Yeon Kim, Hye Min Park, Jeong Min Park, Dong-Luong Dinh, Soo Yeol Lee, and Tae-Seong Kim
- Automatic Facial Expression Recognition System Using Convolutional Neural Networks** 473
Hung Ngoc Do, Kien Trang, Bao Quoc Vuong, Van-Su Tran, Linh Mai, Minh-Thanh Vo, and Mai Hoang Nguyen
- Design of Classifier for Electrocardiography Classification** 477
Duong Van Binh, Nguyen Thanh Nghia, Nguyen Thanh Hai, and Nguyen Manh Hung
- DWT Algorithm for Iris Recognition** 483
Vien Phuc Nguyen, Hai Thanh Nguyen, and Dat Duc Ngo
- Development of a Fingerprint Singularity Detection Method Based on Moment Invariants for Biometrics and Medical Applications** 489
L. V. Dang, S. S. Makhanov, L. C. Hieu, M. S. Packianather, H. L. Minh, and L. H. Quoc
- Pancreas Segmentation in Medical Images Based on Gaussian Mixture Model in Bandelet Domain** 493
Nguyen Huu The, Vo Thi Hong Tuyet, Nguyen Mong Hien, and Nguyen Thanh Binh
- Elevator Motion States Recognition Using Barometer Support Indoor Positioning System** 499
Duong Van Nguyen, Thanh Van Pham, An Van Tran, Khai NguyenTuan, Hang Duong ThiThuy, Hop Hoang The, and Tan Tran Duc
- Predictive Modelling for Cardiovascular Disease Mortality in Intensive Care Units** 505
Anh Thi Ngoc Vo, Trung Quoc Le, Trieu Nguyen Hai Le, and Vo Van Toi

The Characteristics of the Event-Related Potentials with Visual Stimulus	513
Nguyen Thi Minh Huong, Nguyen Trong Nguyen, and Huynh Quang Linh	
Application of Portable EEG Device in Detection and Classification Drowsiness by Support Vector Machine	521
Thi Tram Anh Pham, Thi Diem Hang Nguyen, Quoc Khai Le, and Quang Linh Huynh	
Effect of Trehalose on Preservation of Mouse Freeze-Dried Spermatozoa at Room Temperature	527
Daiyu Ito, Sayaka Wakayama, Yuko Kamada, Masatoshi Ooga, and Teruhiko Wakayama	
Breast Cancer Histopathological Image Classification Utilizing Convolutional Neural Network	531
Tuan Dinh Truong and Hien Thi-Thu Pham	
Electrooculography Feature Extraction Techniques for Classification of Eye Movements	537
Toan Le, Ngu Bui, and Trung Le	
Feature Extraction Techniques for Automatic Detection of Some Specific Cardiovascular Diseases Using ECG: A Review and Evaluation Study	543
Trieu Hai-Nguyen Le, Triet Minh Le, Trung Q. Le, and Vo Van Toi	
Feature Extraction and Electrophysiological Modeling in Personalized Deep Brain Structure Using Electroencephalography Signal	551
Linh Luu, Phong Pham, and Trung Q. Le	
Part XIII Public Health	
Model of Information Technology in Management of Medical Equipment	559
Men Nguyen Thi, Hang Dang Thuy, Minh Nguyen Hong, and Do Tran Quang	
Establishing a Healthcare Research Network in Vietnam: A Platform for Collaborative Quality Improvement	567
Anh The Bui, Dung Dao Trung, Ky Le Minh, Trung Nguyen, Hung Le Dinh, Lien Tran, Nga Nguyen, Priya Vohra, Keven Seung Yong Ji, Eunice Lee, James Campbell, and Walter T. Lee	
Value Signposts in MedTech Development: An Experience from the Field	571
K. T. Nguyen, P. P. Lee, P. G. Yock, N. C. Tan, H. K. Tan, and W. T. Lee	
Design of a Medical Expert System for Consulting Tuberculosis Diagnosis in Vietnam Rural Areas	577
Thi Ngoc Mai Nguyen, Quang Chung Tran, Tien Dat Duong, and Ngoc Anh Mai	
Oral Impacts on Daily Performances of Children 12 and 15-Year-Old in Can Tho City	585
H. G. Do, K. N. Truong, D. H. Pham, L. T. Quynh Ngo, H. T. Tran, and N. Doan	
An Evaluation on Initial Deficiency of Left Ventricular Systolic Function in Patients with Systemic Hypertension by Speckle Tracking Echocardiography	591
D. T. Nguyen, V. A. Nguyen, L. D. Do, and N. Doan	
Biological Alterations of Lung Carcinoma	597
T. Q. Huynh, D. N. Tran, T. P. Chau, M. T. Nguyen, and N. Doan	

Evaluation of the HBV Genotype, Viral Load and Antivirus Drug Resistance Mutation in Tay Ninh Hospital, Vietnam by Real-Time PCR	605
Thuan Duc Lao, Hung Chi Lieu, Thuy Thanh Thi Ho, and Thuy Ai Huyen Le	
A Meta-Analysis of <i>Apolipoprotein B</i> Gene Mutation in Hypercholesterolemia Based on Previous Studies	611
Phuong Kim Truong, Phuong Mai Thi Nguyen, Thuan Duc Lao, and Thuy Ai Huyen Le	
Part XIV Public Health—Cancer Therapy and Reconstructive Surgery	
An Overview of Immune Checkpoints and Immunotherapy in Cancer	619
T. Q. Huynh, D. N. Tran, T. P. Chau, T. M. Huynh, C. H. Trinh, and N. Doan	
A Molecular Alteration Situations of KRAS, NRAS, BRAF, PIK3C and PTEN Loss in Colorectal Adenocarcinoma at Can Tho Oncology Hospital	627
T. Q. Huynh, P. H. Nguyen, D. N. Tran, M. T. T. Nguyen, T. P. Chau, T. M. Huynh, and N. Doan	
Primarily Surgical Treatment of Cervical Cancers Diagnosed in Stages IA–IIA at Can Tho Oncology Hospital: An Overview of 9 Years’ Experience 2000–2008	633
T. Q. Huynh and N. Doan	
Lymph Node Dissection by Laparoscopic Surgery in Patients Underwent Right Colon Cancer Treatment	641
T. Q. Huynh, H. L. Ho, K. V. Vo, L. T. Huynh, T. P. Chau, and N. Doan	
Part XV Advanced Technologies in Sleep Diagnosis and Sleep Medicine	
Study of the Obstructive Sleep Apnea in the Patients with Cardiovascular Risk	647
Hoang Anh Tien and Nguyen Huu Duc	
Application of Oxygen on Gagging Patients with Sleep Disordered Breathing: Ten Year Retrospective Study	651
L. Truong, J. Doan, P. Reher, and N. Doan	
Sleep Onset Detection using the Low-Cost Emotiv EPOC Neuroheadset	657
Le Quoc Khai, Le Nu Ngoc Thuy, Tran Kien, Pham Thi Tram Anh, Nguyen Thi Diem Hang, and Huynh Quang Linh	
Part XVI Biotechnology	
Interaction Between Fluoro Emulsion and Silane Quaternary Ammonium Salt on Dual Antibacterial and Hydrophobic Fabric of Surgical Gown	663
Tuan-Anh Nguyen and Vu Thuc Oanh Ta	
Combination of sST2 and BNP in Predicting the Mortality of ST-Elevation Myocardial Infarction	669
Hoang Anh Tien, Tran Thi Thanh Truc, and Vo Thanh Nhan	
Effects of Culture Conditions on the Antimicrobial Activity of <i>Streptomyces</i> spp. LTB08	677
Ngoc Thuy Linh Do, Quynh Ngan Tran, Trong Thuc Nguyen, Ngoc Phuc Chau Do, and Thi Thu Hoai Nguyen	

Optimizing Conditions for <i>Vibrio Parahaemolyticus</i> Culture and Preservation	681
Thi Lan Anh Pham, Quy Khang Le, Trong Thuc Nguyen, Ngoc Phuc Chau Do, and Thi Thu Hoai Nguyen	
A High M1/M2 Ratio Is Associated with Better Survival in Neuroblastoma	685
Chi Hoang Linh Pham and Chi-Bao Bui	
Part XVII Molecular and Cellular Biology in Medicine	
Design and Development of a Novel Anticancer Peptide from Human Gut Microbiome by Using Recombinant Protein Engineering	693
Thi Kim Cuc Nguyen, Thu Thuy Pham, Thi Bich Mai Huynh, Thanh Hoang Tran, Michael Packianather, Chi Hieu Le, and Van Duy Nguyen	
A Label-Free Electrochemical Immunosensor for Detection of Newcastle Disease Virus	699
Tran Quang Thinh, Trieu Van Vu Quan, Le Binh Duong, Tran Hong Thuy, Chu Thi Xuan, and Mai Anh Tuan	
Part XVIII Miscellaneous	
Determine the Presence of Pathogens on Ticks in the Mekong Delta Region	707
Le Thanh Dong, and Doan Binh Minh	
Integrating Video Recording and Self-reflection to Enhance Communication Skills Training for Dental Students	715
V. Reher, G. Rehbein, and P. Reher	
A Systematic Study of Electronic Structure for Anti-cancer Drug Molecule 5-Fluorouracil Within Various Solvents from First-Principles Calculations	721
Linh Gia Hoang, Trang Thuy Nguyen, Toan The Nguyen, Tan Le Hoang Doan, and Duc Nguyen Manh	
Author Index	727

About the Editors

Prof. Vo Van Toi obtained his Ph.D. degree in Micro-Engineering at the Swiss Federal Institute of Technology in Lausanne (EPFL), Switzerland in 1983. From 1983–1984, he was a Postdoctoral Fellow at the Health Science and Technology Division, a joint program of Harvard and MIT (USA). From 1984 to 2009, he was a faculty of the School of Engineering at Tufts University (USA). During his tenure at Tufts, from 1991 to 1992 he was a Visiting Professor at the Scheie Eye Research Institute of University of Pennsylvania (USA), from 1992 to 1994 he helped create and was the Vice-Director of the Eye Research Institute in Sion (Switzerland), in 2003 he helped establish the Biomedical Engineering (BME) Department at Tufts, and from 2004 to 2009 he was a member of the Board of Directors then Executive Director of the Vietnam Education Foundation (VEF), a U.S. federal agency. In 2009, he went back to Vietnam to establish the BME Department at International University of Vietnam National Universities in Ho Chi Minh City and was its Chair until 2018. Currently, he is the Vice-Provost for Life and Health Science, Engineering and Technology Development at International University. His research interests include Design and Applications of Medical Devices, Human Visual System, Ophthalmology, and Telemedicine. He is the (co)author of many scientific articles, books, and patents of invention.

Dr. Le Quoc Trung is a faculty member of the Biomedical Engineering Department at International University of Vietnam National Universities in Ho Chi Minh City. He received his Ph.D. degree from Oklahoma State University. He was a Postdoctoral Research Associate of Industrial Systems Engineering and a Research Scientist of Biomedical Engineering at Texas A&M University. He collaborates closely with cardiologists, sleep physician, health scientists, and researchers in biomedical engineering and industrial manufacturing engineering to perform his research in three complementary directions including (1) Data-driven and Sensor-based Modeling, (2) Medical Device Manufacturing and Bio-signal Processing, and (3) Predictive Analytics for Personalized Healthcare. His work was published in *IEEE Transaction of Biomedical Engineering*, *IISE Transactions*, *Medical Engineering and Physics*, *IEEE Journal of Translational Engineering in Health and Medicine*, and *PLOS One*. His works have led to several US and International patent applications.

Dr. Ngo Thanh Hoan did his undergraduate in Mechatronics at Bach Khoa University of Vietnam National Universities in Ho Chi Minh City. After graduation, he went abroad to South Korea for a 2-year Master's program in Control and Instrumentation. He then returned to Vietnam to teach for undergraduate students at International University and helped Dr. Toi Van Vo, an Emeritus Professor of Tufts University (MA, USA) and former Executive Director of Vietnam Education Foundation, to set up the first undergraduate Biomedical Engineering (BME) program in Vietnam at International University in early 2009. In 2011, he went to Duke University in the US for Ph.D. study in BME, with specialization in Biophotonics. Under supervision of Dr. Tuan Vo-Dinh, he conducted doctoral research on development of novel nanobiosensors and integrated devices for molecular diagnosis of infectious diseases and cancer. He then did postdoctoral training with Dr. Joseph Izatt at Duke BME and Dr. Cynthia Toth at Duke Eye Center on Optical Coherence Tomography (OCT) for

ophthalmology. His research interest is concerned with the development of technologies and systems for precision medical diagnosis and treatment by leveraging advances in Biophotonics, Molecular Diagnostics, Nanobiosensors, Point-of-Care Diagnostics, Lab-on-a-chip, and Artificial Intelligence. His works have been published on Scientific Reports (Nature Publishing Group), Biosensors and Bioelectronics, Nanoscale, Analytical Chemistry... Currently, he is the Head of the Clinical Engineering Laboratory and Vice Chair of the Biomedical Engineering Department at International University, Vietnam National Universities in Ho Chi Minh City.

Dr. Nguyen Thi-Hiep graduated from Department of Chemistry, University of Science of Vietnam National Universities—Ho Chi Minh City (VNU-HCMC). In 2012, she successfully defended her Ph.D. thesis from the Department of Biomaterials and Tissue Engineering at Soonchunghyang University and had published 13 ISI papers. Shortly after graduation, she returned to Vietnam to develop Tissue Engineering and Regenerative Medicines at the Biomedical Engineering Department at International University and continued following her research interests above. Until now, she has published 42 articles in ISI and Scopus system and 10 domestic papers, attended 60 international conferences in addition to 3 granted patents and over 6 papers in progress. Her interdisciplinary research brings together the fields of polymer chemistry, pharmaceutical science, biology, and basic and clinical medicines, and focuses on the design and preparation of biomaterials for their biological, medical, and pharmaceutical applications. Especially, she received many Awards and Prizes from different agents such as National fellowship award from the L'Oréal UNESCO for Women Science (2016), the winner of the ASEAN-US Science Prize for Women Science (2017), and the International Rising Talent of the L'Oréal UNESCO for Women Science (2018). Currently, she is Co-manager of four Tissue Engineering and Regenerative Medicines laboratories and the Chair of the Biomedical Engineering Department at International University, VNU-HCMC.

Part I

Medical Instrumentations

Design of Noninvasive Hemodynamic Monitoring Equipment Using Impedance Cardiography

Vu Duy Hai, Lai Huu Phuong Trung, Pham Manh Hung,
Dao Viet Hung, Pham Phuc Ngoc, Phan Dang Hung, Chu Quang Dan,
and Tran Quoc Vi

Abstract

Hemodynamic parameters play a very important role in supporting physicians to diagnose and treat cardiovascular diseases. This paper presents the results of the study on designing of noninvasive hemodynamic monitoring equipment using impedance cardiography (ICG). This is a measurement method that shows many advantages and is interested in the present. The equipment has ability of measurement and monitoring hemodynamic parameters include: heart rate HR; thoracic fluid content TFC; left ventricular ejection time LVET; stroke volume SV; cardiac output CO and ICG waveform. Results of measurement between the research equipment BK-NICO and the standard equipment of NICCOMO for 104 patients show that the hemodynamic parameters measured by the two equipments are quite small difference. Specifically, the average deviation of the parameters obtained, HR is 0.16 bpm, TFC is 0.73 1/k Ω , LVET is 5.95 ms, SV is 0.17 ml, CO is 0.01 lpm. With the results of the research, the device is fully capable of deploying the application into practice in the hospitals to replace the current invasive measurement method.

Keywords

Noninvasive hemodynamic monitor • Impedance cardiography • Stroke volume • Cardiac output • Thoracic fluid content • Left ventricular ejection time

1 Introduction

To assist with the diagnosis and intensive treatment of existing cardiovascular diseases, hemodynamic parameters such as heart rate HR; stroke volume SV; total fluid content TFC; left ventricular ejection time LVET; cardiac output CO and thoracic impedance cardiography waveform play a very important role. Hemodynamic parameters will support doctors in classifying the specific cause of a cardiovascular disease, particularly those resulting from ischemia, blood pressure disorders or heart attack. The continuous measurement and monitoring of hemodynamic parameters will also greatly assist the physician in emergency situation or rehabilitation therapy to patients. For example, when the patient is suffering from heart failure or low cardiac output symptom, the physician will not be able to perform the surgery immediately due to the loss of blood, the weakened heart will become weaker [1].

Currently, there are two methods to measure hemodynamic parameters including invasive and non-invasive technique. Invasive techniques include: Fick's method; Dye-dilution; Thermodilution; and PiCCO. Non-invasive techniques include: Doppler ultrasound; magnetic resonance imaging; and impedance cardiography. Invasive techniques have a lot of limitations such as causing pain for patients, complicated manipulation, high risk of blood loss and infection, inability for continuously monitoring, and high-cost expenses. Non-invasive techniques have fundamentally overcome these limitations, but the accuracy of their measuring results is low compared to invasive class. Ultrasound or magnetic resonance imaging techniques cannot be used to continuously monitor hemodynamic indices in addition with high expense. In the meanwhile, ICG technique uses the same type of electrodes as ECG technique. Indeed, impedance cardiography is a non-invasive, simple, low-cost technique in accompany with ability to monitor cardiac output continuously without demanding highly skilled examiner [2].

V. D. Hai (✉) · L. H. P. Trung · P. M. Hung · D. V. Hung
P. P. Ngoc · P. D. Hung · C. Q. Dan
Biomedical Electronics Center, Hanoi University of Science
and Technology, Hanoi, Vietnam
e-mail: hai.vuduy@hust.edu.vn

T. Q. Vi
Vinh Phuc General Hospital, Vinh Phuc, Vietnam

ICG technique has been developed based on the principle of blood flow circulating in human heart during the operation of the circulatory system. Basically, blood is considered as an electrical conductor with a certain resistivity for each person. When the left ventricle pumps, the amount of this blood flows out of the thoracic region to other parts of the body. This operation leads to the change in the overall impedance of thorax. According to bioelectricity, in order to measure the patient's thoracic impedance, the device will inject a constant amplitude current through the thorax and obtain the output voltage adhere to Ohm's law:

$$U = I.R \quad (1)$$

Thus, by applying constant amplitude current I , the voltage drop across the thorax is proportional to the thoracic impedance change. This sensed voltage U is then processed in order to obtain impedance cardiography signal ICG. The thoracic impedance is divided into two components: (1) fixed impedance component Z_o (base impedance) and (2) variable impedance component ΔZ . The base impedance Z_o consists of the impedance of the fatty tissues, muscles, bones, blood stored in the cells.... They are components that have negligible movements during the blood pumping process of the heart. Hence, the impedance of these components can be considered to be invariable. The rest of thoracic impedance is variable impedance ΔZ caused by the circulation of blood through the thorax—which is represented as variable impedance curve. Hence, the overall impedance of thoracic region $Z(t)$ is:

$$Z(t) = Z_o - \Delta Z \quad (2)$$

To calculate hemodynamic parameters, people particularly concern about the rate of thoracic impedance change dZ/dt (first derivative of ΔZ signal), which is called impedance cardiography ICG. ICG over time is a graph related to the heart's activity events; therefore, it will be foundation for calculating hemodynamic indices, especially SV and CO indices [3].

Some researchers have proposed several formula for calculating stroke volume SV parameter based on the ICG waveform, in which Atzler and Lehman were the first people to propose the theory of the correlation between the change in thoracic impedance and the blood volume pumped by the left ventricle during an operating cycle of human's heart. Nyboer developed this theory and introduced a formula for calculating the blood volume variation in any parts of the body based on its impedance changes as follow [4, 5]:

$$\Delta V = \rho L_o^2 Z_o^{-2} \Delta Z \quad (3)$$

where, ΔV is changes of the blood volume of the body segment (cm^3); ρ is blood resistivity (Ωcm); L_o is distance between receiving electrodes (cm); Z_o is base impedance of

the body segment limited by receiving electrodes (Ω); ΔZ is changes of the impedance of the segment limited by receiving electrodes (Ω). This formula (3) is generally accepted to calculate ΔV . However, it is unable to specifically calculate stroke volume SV value of thorax.

Kubicek improved the formula (3) to become a formula particular for chest region by replacing $\Delta Z = dZ/dt_{\max}LVET$ and $\Delta V = SV$, then:

$$SV = \rho L_o^2 Z_o^{-2} dZ/dt_{\max}LVET \quad (4)$$

where, SV is stroke volume (ml per beat); dZ/dt_{\max} is the maximum of the first derivative of the impedance signal (Ω/s); LVET is left ventricular ejection time (s). Kubicek formula was used to be generally accepted to calculate SV value.

Sramek proposed another method of calculating stroke volume using 3 components: volume of electrically participating tissues (VEPT which is a function of patient's gender, height and weight), ventricular ejection time (VET), which has the similar meaning as LVET or ET in Kubicek formula and the ejection phase contractility index (EPCI), which is a product of maximal amplitude of the dZ/dt signal dZ/dt_{\max} and TFC (which is Z_o^{-1}). His idea was to show in the formula that SV is directly proportional to the physical size of a patient (i.e., to VEPT body habitus scaling constant), directly proportional to duration of delivery of blood into the aorta (i.e., to VET), and (SV is directly proportional to the peak aortic blood flow (i.e., to EPCI). This lead to the formula:

$$SV = VEPT.VET.ECPI \quad (5)$$

When substituting the above symbols by the expression used in the Kubicek formula it gives:

$$SV = \frac{(0.17H)^3}{4.25Z_o} dZ/dt_{\max}LVET \quad (6)$$

where, H is the height of the patient in (cm). In comparison with Kubicek formula, distance between receiving electrodes is replaced by 0.17H. However, the Sramek formula is not used frequently because it presents greater error and less flexibility than Kubicek formula.

Sramek–Bernstein also proposed another formula to calculate SV as follow:

$$SV = \delta \frac{(0.17H)^3}{4.25Z_o} dZ/dt_{\max}LVET \quad (7)$$

where, $\delta = IBW/ABW$, is a correction factor relating ideal weight (IBW) and actual weight (ABW) of the patient. For male, $IBW = 50(\text{kg}) + 2.3[H/2.54(\text{cm}) - 60]$; for female, $IBW = 45.5(\text{kg}) + 2.3[H/2.54(\text{cm}) - 60]$. Currently, Sramek–Bernstein's formula (7) is being evaluated as the most accurate formula in calculating the SV value.

2 Design of Equipment

2.1 Design Hardware

Based on the measuring principle, the block diagram of the device's hardware was designed as Fig. 1. Accordingly, the diagram consists of two main blocks as follows: (1) Analog signal processing unit includes: 4 mA/100 kHz constant amplitude current source circuit, amplifier circuit, 80–120 kHz band pass filter, squared circuit, 350 Hz low-pass filter, 2nd order arithmetic circuit (demodulator). The signal is then split into two branches for processing. Put into 0.15 Hz high-pass filter circuit, amplifier circuit, and 1 V subtractor circuit to extract ΔZ signal. Put into 0.2 Hz low-pass filter, 16/5 voltage divider to extract Z_o signal, which is used to calculate the base impedance Z_o . (2) Digital signal processing unit consists of: ADC circuit, central processing circuit to calculate the hemodynamic parameters and display results.

As described above, two critical signals received from analog signal processing unit are ΔZ and Z_o , after digitalizing will be fed on the digital signal processing unit to calculate the parameters. The following section will discuss these algorithms. The ΔZ signal, after digitalizing, will be

differential (dZ/dt) to evaluate the rate of change of the thorax impedance, which is called the ICG signal. The ICG signal has the shape shown in Fig. 2 in accompany with some important points used to calculate the hemodynamic parameters [4, 6].

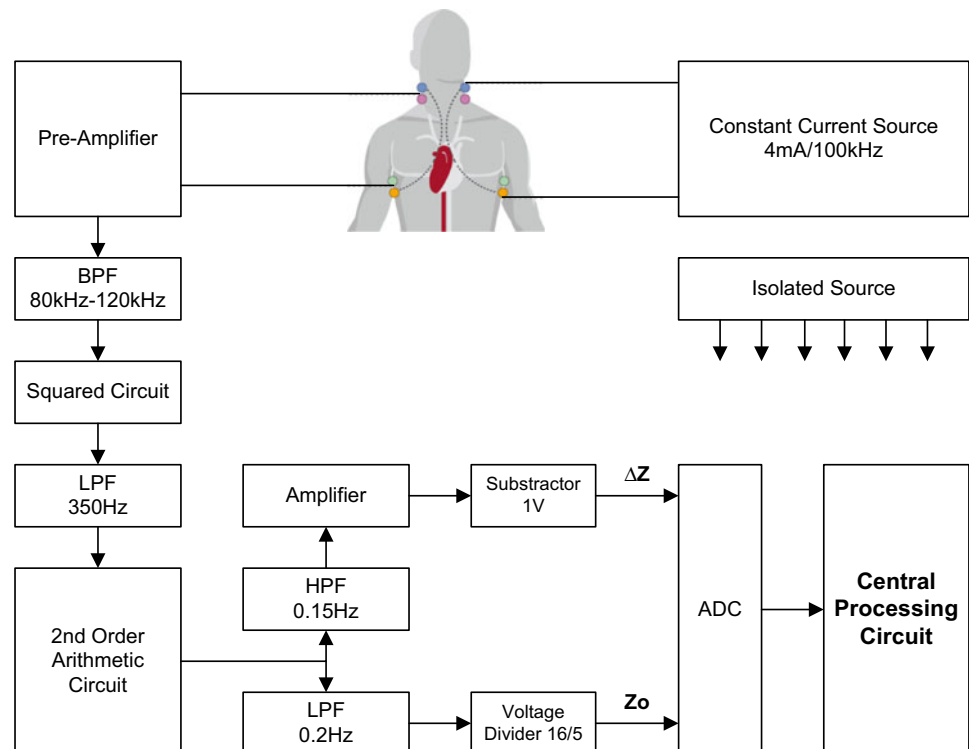
Point B: This point corresponds to the aortic valve opening. This is the starting point for the upward curve of the ICG signal before the value dZ/dt_{\max} . B point can be defined as the zero crossing of ICG signal. Determination of B point is very important in calculating SV, LVET and CO parameters.

Point C: This point is the maximum point of ICG signal each cycle representing the fastest rate of change in thoracic impedance. The value dZ/dt_{\max} is the amplitude from point B to point C.

Point X: This point corresponds to the closure of the aortic valve. Thus, left ventricular ejection LVET is the time interval from the occurrence of point B to the occurrence of point X.

Point O: This point is associated with changing of the volume during the diastolic phase of the cycle and opening snap of the mitral valve. The high value of the O wave (similar to E) might be the symptom of the bicuspid valve malfunction or the heart inefficiency during heart acute ischemia.

Fig. 1 Block diagram of device's hardware design



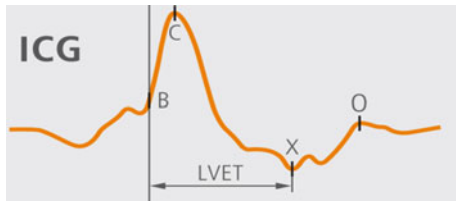


Fig. 2 ICG signal and characteristic points

2.2 Build Software

Develop algorithm to determine C point

During a cycle of ICG signal, point C is the peak with the greatest amplitude, representing the maximum change in thoracic impedance. The most common way to find this point is being used is the thresholding method. To find the peak C, an initial threshold should be initialized based on the first two cycles of the signal. Selecting two signal cycles with a sampling frequency of 1.000 samples/s ensures that at least one point C is present even in low heart rate situation. The first highest amplitude point is taken as the initial threshold. Then the two new thresholds are set as high threshold TH and low threshold TL with amplitude of 70 and 50% the one of initial threshold respectively. Two threshold are set up to warrant no missing in finding C points occur in case of base-line drift in ICG signal. After two first cycles of signal, the elements of signal data array are compared with the thresholds to find the C point. The point with amplitude higher than TH is marked as C point, and then new thresholds are updated. In case of absence of exceeding point, the algorithm will reverse to check whether there are any points exceeding TL. If this point exists, it will be considered as a C point, then new thresholds are updated [7, 8].

Develop algorithm to determine B point

Locating point C in one cycle is the reference for finding B point in ICG signal. This point corresponds to the opening of the aortic valve, or the beginning of blood ejection by the left ventricle. It is the beginning of the ascending phase of ICG trace before dZ/dt_{\max} value. Hence, B point can be defined as the local minimum just before the C point. The algorithm to detect B points can be divided into 2 steps. Step 1: Detect all local minimums in 2 cycles of signal (2.000 samples). Step 2: Locate the C point as the reference to determine the position of B point, which is the local minimum just before point C. In step 1, we use the first order derivative to locate all local minimums. Assume that the function $y = f(x)$ has derivative on the domain D, x_o is the local minimal point if $f'(x_o) = 0$ and the sign of $f'(x)$ changes

from negative to positive when it across x_o . In step 2, after finding the point C, compare positions of local minimums with the C point in a signal segment, the local minimal point just before the C point is defined B point [9, 10].

Develop algorithm to determine X point

Point X is defined as a lowest point of ICG signal on the right of point C in a cardiac cycle corresponding to the closing of the aortic valve. The point X is located within the interval of 1/3 of signal cycle for low heart rate case and 1/2 of signal cycle for high heart rate case with taking C point as the start of signal cycle. After determining C point as marker and signal segment containing X point, the algorithm performs comparisons to find the smallest amplitude point in that segment to identify the X point [11].

Calculate hemodynamic parameters

After determining the characteristic points B, C, X of the ICG signal according to the algorithms presented above, the hemodynamic parameters are calculated as follows: dZ/dt_{\max} : This is the amplitude of the peak C with point B. Left ventricular ejection: $LVET = \text{time interval between 2 adjacent points B and X}$. Heart rate: $HR = 60/T_{C-C}$ with T_{C-C} is the time interval between two consecutive C points. Base impedance Z_o . Total fluid content $TFC = 1/Z_o$. Stroke volume SV is calculated by formula (6). Cardiac output: $CO = SV.HR$.

3 Testing and Evaluation

3.1 Designing Results

The device was designed according to schematic diagram and algorithms presented above. Hardware designing, software developing, and the complete device are illustrated as Fig. 3.

3.2 Testing and Evaluating Results

Testing objectives

Measurement results of hemodynamic parameters obtained by designed BK-NICO device was assessed by using a standard equipment of NICCOMO. This is a device that has been licensed for use in Europe and USA. The method of evaluation is to compare the measurement results of parameters from two equipments simultaneously on the same patient.

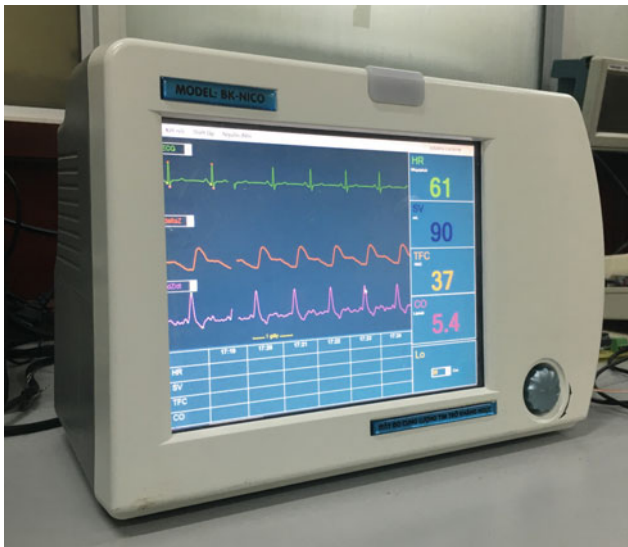


Fig. 3 Completely designed equipment BK-NICO

Testing results

Designed equipment was commissioned for evaluating the operation in 02 health facilities for 104 patients as illustrated in Fig. 4.

Simultaneous measurement results from two equipments of the most important hemodynamic indices including heart rate HR, total fluid content TFC, left ventricular ejection time LVET, stroke volume SV, and cardiac output CO are illustrated as Figs. 5, 6, 7, 8 and 9.

Accordingly, the hemodynamic parameters measured on the two devices are highly correlated with small deviations between them. Specifically for HR, the mean deviation between the two devices was 0.16 bpm, equivalent to 0.24%, with a mean squared error of 2.34 bpm. For TFC, the average deviation between the two devices is 0.73 l/kΩ, equivalent to 2.5%, the mean squared error is 2.59 l/kΩ. For LVET, the average deviation between the two devices is 5.95 ms, or 2.69%, the squared error is 22.29 ms. For SV, the average deviation between the two devices is 0.17 ml, equivalent to 0.24%, the mean squared error is 2.56 ml. CO, the average deviation between the two devices is 0.01 l per minute, equivalent to 0.04%, the mean squared error is 0.21 l per minute. In addition, the recorded signals included ICG signal, signal ΔZ and ECG signal are accurate, clear and stable.



Fig. 4 Experiment at hospitals

4 Conclusions

According to the above results, the equipment has achieved the same accuracy and stability as the standard equipment of NICCOMO. However, in some cases, there is a significant difference between the two measurement results of the two devices. Causes of these major deviations are determined as: Some patients have abnormal spasms in the chest muscles

Fig. 5 Results of HR measurement on 2 devices for 104 patients

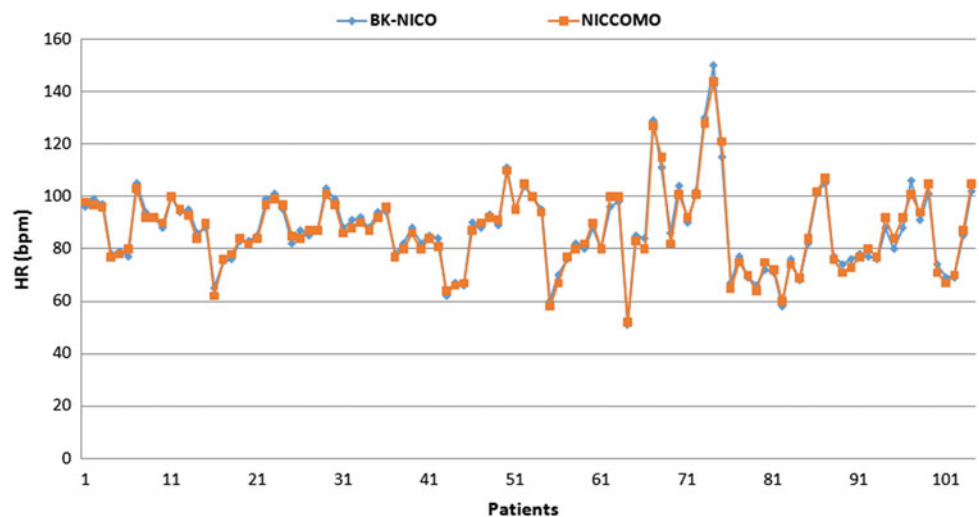


Fig. 6 Results of TFC measurement on 2 devices for 104 patients

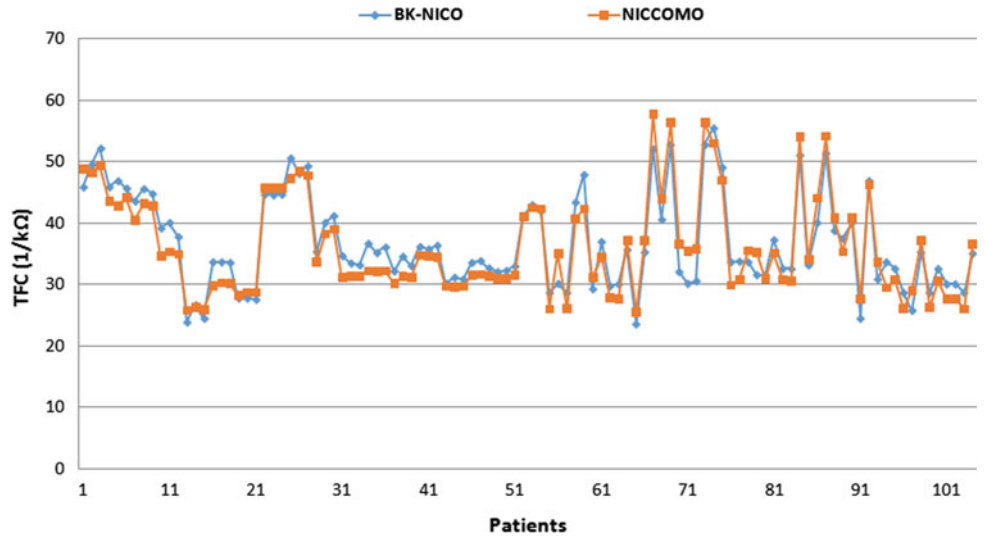


Fig. 7 Results of LVET measurement on 2 devices for 104 patients

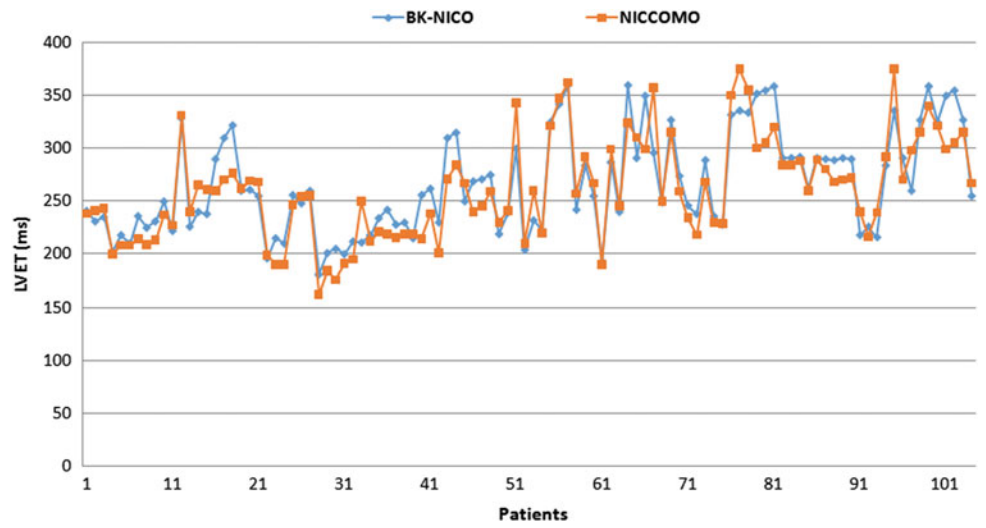


Fig. 8 Results of SV measurement on 2 devices for 104 patients

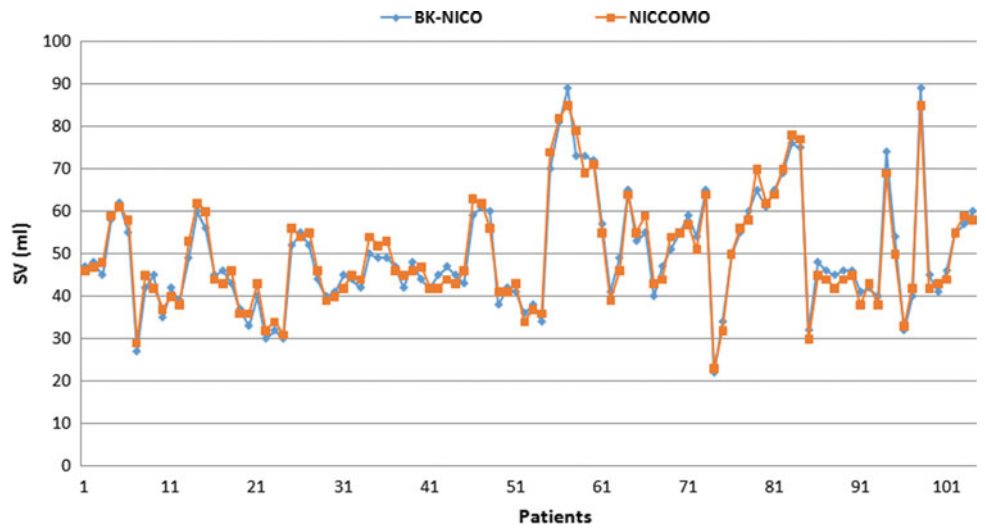
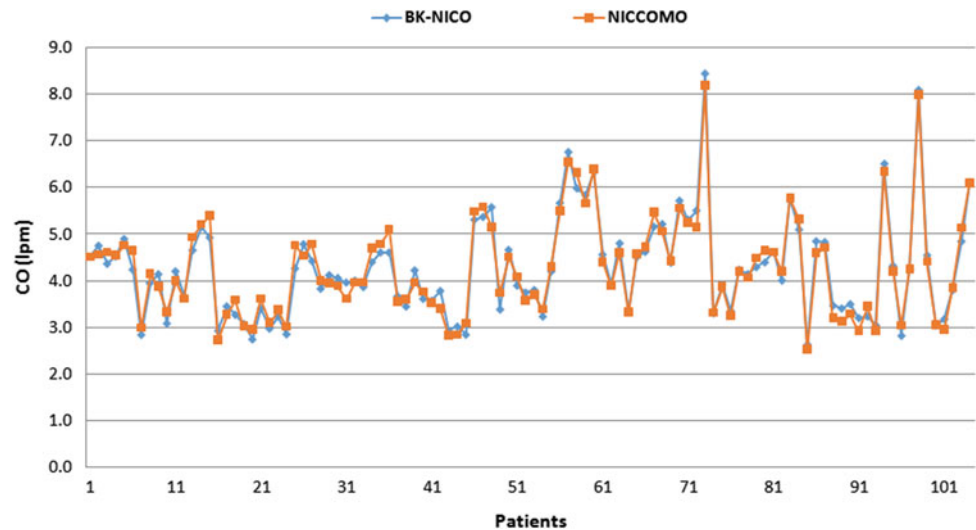


Fig. 9 Results of CO measurement on 2 devices for 104 patients



due to the use of artificial respiration equipment. This contraction causes the body to vibrate, affecting the impedance of the thorax and the connection of electrodes. These vibrations have resulted in great errors in measured hemodynamic parameters. In some cases, the patient must be accompanied by other supporting devices (ventilator, drainage tube, monitor...). This overlaps the standard positions for ICG electrodes placement. We have no choice but place electrodes at other locations nearest to the standard one. However, this has also caused great errors in the measured results. In other cases, patients were taken medications or certain fluids into the blood. This will change the blood resistivity contributing errors in the measurement of the cardiac output. We are continuing the study to eliminate these effects on the results of the measurements.

Acknowledgements We would like to thank the Ministry of Science and Technology (MOST), Hanoi University of Science and Technology (HUST), Viet Duc hospital, Hanoi Heart hospital for their support and encouragement. The system was designed and developed by the faculties and students at the Biomedical Electronics Center (BMEC).

Conflict of Interest The authors declare that they have no conflict of interest.

References

1. Cybulski, G.: Ambulatory Impedance Cardiography—The Systems and Their Applications. Springer, New York (2011)

2. Cybulski, G., Strasz, A., Niewiadomski, W., Gasiorowska, A.: Impedance cardiography: recent advancements. *Cardiol J* **19**(5), 550–556 (2012)
3. Webster, J.G.: Medical Instrumentation: Application and Design: Measurement of Flow and Volume of Blood. Wiley, New York (2010)
4. Ipate, M.C., Dobre, A.A., Morega, A.M.: The stroke volume and the cardiac output by the impedance cardiography. *U.P.B. Sci. Bull.* **74**(3) (2012)
5. Geerts, B.F., Aarts, L.P., Jansen, J.R.: Methods in pharmacology: measurement of cardiac output. *Br. J. Clin. Pharmacol.* **71**(3), 316–330 (2011)
6. Lavdaniti, M.: Invasive and non-invasive methods for cardiac output measurement. *Int. J. Caring Sci.* **1**(3), 112–117 (2008)
7. Horster, S., Stemmler, H.J., Strecker, N., Brettner, F., Hausmann, A., Cnossen, J., Parhofer, K.G., Nickel, T., Geiger, S.: Cardiac output measurements in septic patients: comparing the accuracy of USCOM and PiCCO. *Crit. Care Res. Pract.* (2012)
8. Jain, S., Vafa, A., Margulies, D.R., Liu, W., Wilson, M.T., Allins, A.D.: Non-invasive Doppler ultrasonography for assessing cardiac function: can it replace the Swan-Ganz catheter? *Am. J. Surg.* **196**(6), 961–967 (2008)
9. Cybulski, G.: Ambulatory: Impedance Cardiography—The Systems and Their Applications. Springer, New York (2011)
10. Carvalho, P., Paiva, R.P., Henriques, J., Antunes, M., Quintal, I., Muehlsteff, J.: Robust characteristic points for ICG: definition and comparative analysis. In: Proceedings of the International Conference on Bio-inspired Systems and Signal Processing, Rome, Italy (2011)
11. Vincent, J.-L.: Understanding cardiac output. *Crit. Care* **12**(4), 174 (2008)

Overview of Our Less Invasive Operation System—Development of Three Dimensional Real-Time MR Image Guided Operation System Using Microwave Devices and Relating Technologies

Tohru Tani, Shigeyuki Naka, Atsushi Yamada, Soichiro Tani, Dang Tran Khiem, and Nguyen Quoc Vinh

Abstract

Our concept of “Less invasive treatment” is for both patient and medical staffs. We have invented three dimensional real-time MR image guided endoscopic surgical system using microwave devices which does not emit X-ray. This study aims to establish a less invasive operation system mentioned above. Developed Materials are as follows: (1) software for driving system, imaging of 3T MR scanner and integration of them. (2) MR compatible endoscope with position-direction sensor. (3) microwave energy devices for flexible endoscope. (4) new bending mechanism for catheter and guidewire. For (1) and (2), MR compatible flexible endoscope was invented which could be applied to the operation under 3T MR scanner. Its position and direction of tip is able to be timely reflected on the MR image. For (3), microwave energy was selected by the reason why this frequency band does not interfere with MR imaging. Microwave devices were developed not only MR compatible forceps for endoscope but also devices for open surgery. Open surgery microwave devices, “Acrosurg”, are already commercialized in Japan. For (4), new bending mechanism for catheter has been invented. The prototype catheter 0.58 mm in diameter could be bent with this mechanism. This mechanism is applied to endoscopic forceps, catheter for vessels and intestine. We

evaluated the system integrated with developed technologies (1)–(3) using 5 mini pigs under general anesthesia. Laparoscopic liver ablation was performed with 3D real-time MR image guided. Now, we succeeded in a laparoscopic ablation of virtual liver cancer with microwave needle under this system.

Keywords

Microwave • Laparoscopic surgery • Flexible endoscope • MR image • MR compatible

1 Introduction

The greatest innovation of surgical field in 20th century is thought the invention of endoscopic surgical system [1]. We had performed percutaneous needle ablation of liver cancer guided with real-time MR image at early 21st century. This therapy was applied firstly in the world using the double donuts type MR scanner [2]. 300 cases of liver cancer using microwave ablation were treated. Five years survival rate was 20% higher than those of other institutes [3]. According to this result, information of inner structure, real-time monitoring and 3-dimensional image were noticed to be the essential technologies for the safe, precise and appropriate surgery. MR scanner does not emit X-ray exposure, that guarantees safety of both patient and medical staffs. Consequently, three dimensional real-time MR image guided system is able to realize our concept of “Less invasiveness” as a new operation system with above conditions [4].

So we have started to development MR image guided endoscopic surgical system since 2000. This system composes of a system driving software as a brain (1), 3-dimensional real-time MR image monitor as an eye, newly invented bending mechanism (4) and MR compatible endoscopy as an arm (2), and microwave energy-based surgical device as a hand (3). We have invented all of (1)–(4)

T. Tani (✉) · A. Yamada · D. T. Khiem
Department of Research and Development for Innovative Medical Devices and Systems, Shiga University of Medical Science, Otsu, Shiga 520-2192, Japan
e-mail: tan@belle.shiga-med.ac.jp

S. Naka · S. Tani
Department of Surgery, Shiga University of Medical Science, Shiga, Japan

S. Naka
Department of Surgery, Hino Memorial Hospital, Gamo-gun, Shiga, 529-1642, Japan

N. Q. Vinh
Cho Ray Hospital, Ho Chi Minh City, Viet Nam

for new system and each invention has been developed respectively. In this paper, I would like to overview our inventions relating new operation system.

2 Materials and Methods

2.1 Software for System Driving, Imaging of 3T MR Scanner and Integration of Them

MR scanner is 3T wide bore (Verio 3T MRI: Siemens Germany). Software for integration of images in workstation connects with driving software of MR scanner, visual information from endoscopy and information of location sensor installed in an endoscope, and for integration those information. Initially, modified 3D Slicer has been adapted. Nowadays our own software has been installed. MR image scanning speed is 0.21 s. It actually is real-time monitoring as a movie. Those image information are re-constructed as 3D image with position and direction of endoscope tip. Operator is able to observe all images with a large monitoring panel in the MR scanner room during operation.

2.2 MR Compatible Endoscope with Location Sensor

This endoscope connected with fiber cable can be applied under strong magnetic field and is inserted in the inflamed abdominal cavity via port site. The length of endoscope is 120 cm is sufficient for the 120 cm length of MR scanner bore. Endoscope has the position and direction sensor [5] at the tip, 4 working channels, light guide and water nozzle. Operation are performed with microwave based forceps via flexible endoscope. Endoscopic image is the same level as high-vision using CMOS image sensor 700×700 pixels.

2.3 Microwave Energy Devices for Flexible Endoscopic Surgery

Microwave does not interfere with the frequency of MR image, and emits less smoke and no mist, and shows strong hemostasis power. Needle type and forceps type were developed for the operation under MR image. Animal study for total system evaluation was performed with the needle type device. On the other hand, microwave devices have been developed for ordinary operation, and devices for open surgery have been sold by Nikkiso Ltd. as Acrosurg since summer of 2017. Microwave devices will be presented two other papers.

2.4 New Bending Mechanism for Catheter and Guidewire

Bending mechanism of long channel has depended on wire traction or gear. Dr. Yamada has invented new mechanism [6] which a doubled up tape is inserted in the cannula. When tape was slipped each other, cannula bent. This mechanism realized to double up the thinnest catheter 0.58 mm in diameter in the world. Application of this mechanism should be extended to the guide wire and robot hand.

2.5 Animal Study

Five mini pigs, weight is 42–58 kg. They were intubated under general anesthesia. Port site was made on the center of abdomen. After pig was put in the MR bore, MR compatible flexible endoscope was inserted into the abdominal cavity via port site. Control MR image was scanned before ablation. We have studied animal examination at 5 times until now. Finally, all ablation manipulations under MR image guided system were synthetically performed in a series.

3 Results

In the ultimate studies, liver ablation using microwave needle type forceps was succeeded under real-time MR image.

- (1) Motion of endoscope could be traced in real-time 3D MR image. Ablation process could be monitored by endoscopy. Ablation area were within 2 cm in diameter, and this area could be detected by MR movie image.
- (2) MR compatible endoscope did not show artifact in MR image during activation. The tissue change of liver surface due to ablation could be inspected. The position and direction of endoscope was real timely linked with MR image.
- (3) Microwave device and ablation with this device did not show noise or artifact in the MR monitoring image, and ablated liver sufficiently.
- (4) The prototype of thin bending catheter and needle were achieved [6]. Ultimately, this bending mechanism might contribute to realize bending at all direction and change of bending site in the thin catheter or soft tube.

4 Discussion

Laparoscopic surgical system has been a representative technology of less invasive surgery [1], but cannot supply visual information of inner body structure and its 3D image. Robotic surgery is also the same. We have developed 3D real-time MR image guided operation system which is correspondent to our concept, “less invasive medical treatment”. Four representative technologies composed of this system were also invented (1)–(4). This prototype system was evaluated by animal model. Actually, endoscopic ablation process could be monitored with endoscopic view and 3D MR image without X-ray exposure. Safe and accuracy of operation are secured with 3D image and real-time monitor. And visualization of tissue ablation change realizes appropriate surgery. Microwave devices well coagulated without MR image interfere. Development of microwave devices should bring more surgical strategies under this system [7]. New bending mechanism also brings advanced interventional medical treatments. Now, operation using MR scanner is required long flexible endoscope. But in future, this system might evolve to the new robotic surgery which can monitor not only surface image but also an inner vision.


Conflict of Interest Microwave Coagulation Surgical Instruments have been invented by Tohru Tani and Shigeyuki Naka as a preclinical

model. Nikkiso Co. Ltd. (Tokyo, Japan) was granted the license from which they manufactured “Acrosurg.”—a clinical model. Tohru Tani and Shigeyuki Naka declare that they have the conflict of interest with Nikkiso Co. Ltd. The other authors declare that they have no conflict of interest.

References

1. Himal, H.S.: Minimally invasive (laparoscopic) surgery. *Surg. Endosc.* **16**, 1647–1652 (2002)
2. Schenck, J.F., Jolesz, F.A., Roemer, P.B., et al.: Configuration MR, imaging system for image-guided therapy. *Radiology* **195**, 805–814 (1995)
3. Shigeyuki, N., Yoshimasa, K., Tomoharu, S., et al.: Tumor ablation with MRI navigation,—a novel method coagulation therapy for hepatic tumor. *Jpn. J. Cancer Chemother* **28**, 1591–1594 (2001)
4. Yoshimasa, K., Shigehiro, M., Shigeyuki, N., et al.: Robotic surgery for cancer. *New Perspect. Cancer Res. Therapy* 59–70 (2005)
5. Atsushi, Y., Shigeyuki, N., Tohru, T., et al.: A real-time MR image-guided surgical system for a MR compatible high definition flexible endoscope. In: *ACCAS 2016* (2016)
6. Atsushi, Y., Shigeyuki, N., Norihisa, N., et al.: A loop-shaped flexible mechanism for robotic needle steering. *IEEE Robot. Autom. Lett.* **3**(2), 648–655 (2018)
7. Katsushi, T., Hisanori, S., Shigeyuki, N., et al.: Utility of a microwave surgical instrument in sealing lymphatic vessels. *Am. J. Surg.* **206**, 229–233 (2013)

Design and Implementation of Loop Shaped Steering Mechanisms for Flexible Needles

Atsushi Yamada , Norihisa Nitta, Shigeyuki Naka, Khiem Tran Dang, Shigehiro Morikawa, and Tohru Tani

Abstract

The aim of this study was to develop steerable needle variations based on a simple loop shaped steering mechanism and assess steering performances using a tissue mimicking phantom. Two steerable needle types were developed based on the proposed loop shaped flexible mechanism, called Active Sheath. Each needle consisted of a loop shaped stylet with a conical tip made of superelastic metal alloy Beta-titanium inserted into a fluororesin flexible cannula of a percutaneous transhepatic cholangiodrainage (PTCD) tube with 1.3 mm outer diameter. Push and pull inputs applied to one of the proximal stylet ends can bend the needle right or left. Stylet (A) was homogeneous whereas stylet (B) was thinned around the tip. A robotic steerable system was developed to ensure accurate and precise inputs. The designs were implemented in agar phantom using two input patterns: (1) push and (2) push and pull sequentially. Needle paths with input pattern (1) could be curved depending on input magnitude from 0–0.5 mm at 0.1 mm intervals. Lateral distance for stylet (B) curved path with

0.4 mm input was 35.9 mm from the standard straight path and 16.9% longer than that for stylet (A). Compared with stainless steel and flexible bevel tip needles, stylet (B) distances were 3.1 times longer and 8.5% shorter, respectively. The proposed steerable needles could follow S shaped paths using input (2), and stylet (B) lateral distances were 1.9 times those for stylet (A). Thus, the proposed needles will enable physicians to plan curved paths and extend the target range depending on path shape flexibility.

Keywords

Steerable needles • Loop shaped mechanisms • Flexible mechanisms

1 Introduction

Medical needles enable minimally invasive procedures to reach target lesions through a few skin entry points with small diameters, reducing patient trauma. Several steerable needles and procedures have been developed in medical engineering and robotic fields to avoid deviation from the desired trajectory during needle insertion and/or follow curved paths to avoid organs and tissues sensitive to injury. These steering mechanisms can be classified into passive and active. Passive mechanisms include a flexible needle with a bevel tip made of a superelastic material [1], flexible bevel-tip needles with a flexure joint [2], or a sliding thin part [3] to effectively deflect reaction forces. Programmable bevel tips [4, 5] and combinations of concentric bevel tips [6] to modulate bevel tip angles during insertion are also considered passive mechanisms. Generally, bent-tip needles create largest bending curvature paths [7]. However, passive mechanisms require needle-tissue interaction to control needle path curvature.

In contrast, active mechanisms do not require needle-tissue interaction, and hence can create curved paths

A. Yamada (✉) · K. T. Dang · T. Tani
Department of Research and Development for Innovative Medical Devices and Systems, Shiga University of Medical Science, Otsu, Shiga, 520-2192, Japan
e-mail: ayamada@belle.shiga-med.ac.jp

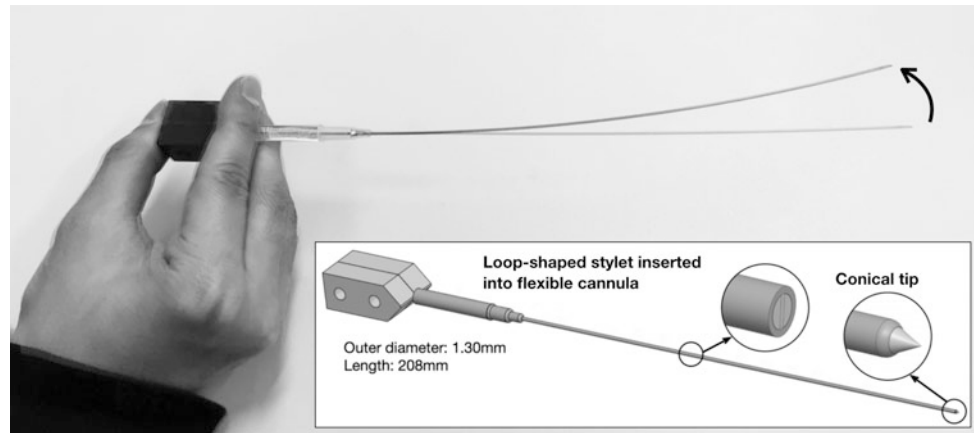
N. Nitta
Department of Radiology, Shiga University of Medical Science, Otsu, Shiga, Japan

S. Naka
Department of Surgery, Shiga University of Medical Science, Otsu, Shiga, Japan

S. Naka
Department of Surgery, Hino Memorial Hospital, Gamo-gun, Shiga, 529-1642, Japan

S. Morikawa
Molecular Neuroscience Research Center, Shiga University of Medical Science, Otsu, Shiga, Japan

Fig. 1 Proposed steerable needle based on Active Sheath mechanism



adaptively during needle insertion even in inhomogeneous tissues. Active mechanisms include pre-curved stylets [8], multiple pre-curved concentric tubes [9, 10], and tendon-driven cannulas [11–13]. Active needles with articulated joints [14], i.e., tendon-driven mechanisms comprising cables, cannula with grooves to align the cables, and a ball joint connected by the cables at the distal end of the stylet, provide adaptive bent-tip needles. However, mechanical robustness is inferior to passive mechanisms due to the small mechanical components and their complicated integration. The authors of this current study previously proposed a loop shaped flexible mechanism called Active Sheath [15–17] to bend a flexible tube from the inside and applied the proposed mechanism to develop an active steerable needle comprising a flexible loop shaped stylet with homogeneous cross section and flexible cannula (Fig. 1) [16, 17].

The objective of this paper was to design an alternative active bent-tip needle based on Active Sheath by introducing a flexible loop shaped stylet with inhomogeneous cross section and develop a steerable needle prototype. Needle prototype steering performances in a tissue mimicking phantom were assessed using a robotic steering manipulator. The technical contribution of the proposed mechanism

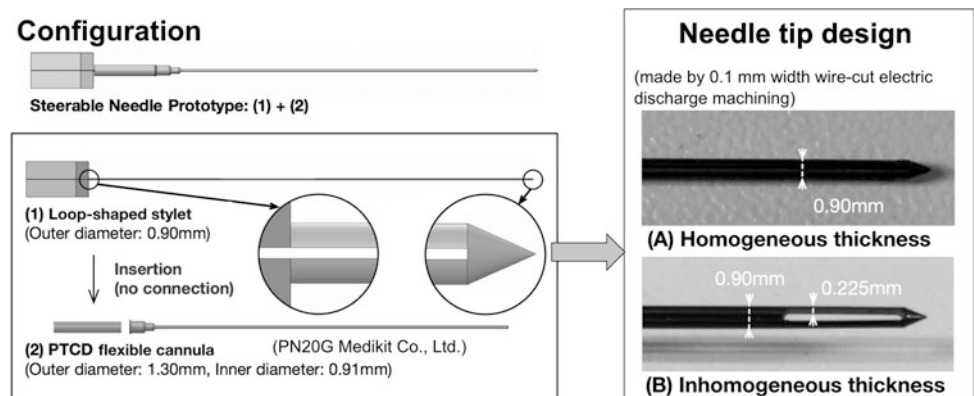
confirms tip-bendable needle fabrication without mechanical complexity or articulated joint that provides a potential viable solution for surgical use.

2 Materials and Methods

2.1 Needle Prototypes Using Sheath Mechanism

Two steerable needle types were developed using Active Sheath [17], as shown in Fig. 2. Each steerable needle consisted of a flexible cannula and a loop shaped flexible stylet. The stylet comprised two flexible columns connected at their distal ends, with a conical tip. Column proximal ends were connected with a pair of rigid segments to allow manually manipulating the loop shaped stylet. The needle can be assembled by simply inserting the loop-shaped stylet into the flexible cannula without fixing or connecting the stylet to the cannula. The loop shaped stylet acts as a flexible backbone [17] to enhance shape stability and a drive mechanism to transmit displacement motions to the distal end as bending force. The pair of rigid segments provides two-degrees-of-freedom (DOF) motion patterns to bend the cannula from the inside, in other words, translational and

Fig. 2 Proposed needle prototypes with two tip designs



rotational motions. Along one DOF, bending motion occurs on a plane by pushing or pulling each rigid segment. Along the other DOF, rotational motion occurs around the axial direction of the cannula by rotating the two rigid segments together, which can change the bending plane of the cannula.

The flexible cannula was composed of the fluororesin tube part of a percutaneous transhepatic cholangiodrainage (PTCD) needle kit (PN 20G, Medikit Co., Ltd., Tokyo, Japan). Cannula outer and inner diameters were 1.3 and 0.94 mm, respectively. The loop shaped stylet was composed of beta-titanium alloy (JIS80 Ti-22V-4AL, Daido Steel Co., Ltd., Aichi, Japan) with Young's modulus = 85 GPa; fabricated by cutting a beta-titanium wire with 0.1 mm wide electric discharge machining except around the distal end. Rigid segments were composed of pure titanium alloy. Stylet outer diameter = 0.9 mm, length = 208 mm, and conical tip angle = 55°. Stylet (A) type had columns with homogeneous thickness = 0.37 mm, whereas stylet (B) had columns with the same thickness but thinner parts (0.225 mm) around the distal ends of each column (5.0 mm long), providing a virtual articulated rotational joint.

2.2 Steering Manipulator

We used a previously developed robotic steering manipulator [17] to push and pull the distal end of the loop shaped stylet, hence precisely and accurately bending and pushing the needle prototype. The manipulator components are described elsewhere [17], and it provided push and pull motions to the left rigid segment of the loop shaped stylet.

2.3 Tissue-Mimicking Phantom

A tissue mimicking phantom was created using 2% agar (010–15815 agar powder, Wako Pure Chemical Industries, Ltd., Osaka, Japan) in an acrylic box (175 mm × 318 mm × 173 mm (width × depth × height)). The acrylic box had 2 mm diameter holes at 10 mm intervals on one side panel for needle insertion.

2.4 Comparative Needle

We compared steering performance for the two proposed Active Sheath type needles with a flexible needle with bevel tip (C) and a conventional stainless-steel needle with bevel tip (D). Needle (C) was composed of beta-titanium alloy with 30° bevel tip, 0.90 mm outer diameter and 200 mm long. Needle (D) was the conventional needle component of the usual PTCD kit, with 20° bevel tip, 0.91 mm outer

diameter, and 200 mm long. Both needles were inserted into the same flexible cannula used for the prototype needles for needle insertions to ensure trial geometrical conditions were as fair as possible.

2.5 Steering Performance

The steering performances were assessed from the path shapes in the agar phantom, using feature points labeled on the flexible cannula (black dots at 10 mm intervals). Path shapes were recorded using a 3.3-megapixel camera (HDR-CX 130, Sony Corporation of America, Inc., NY, USA). The robotic manipulator for the steerable needle prototypes and the agar phantom box were connected to separate lab jacks (LJA-16223, OptoSigma Co., Ltd., CA, USA) to adjust their relative heights and locations. The manipulator was 100 mm from the phantom box, i.e., the needles needed to be pushed 42 mm to encounter the agar phantom through the holes on the side panel.

We employed two input protocols.

1. Needle insertions were performed applying one input. The needle was pushed 100 mm without the input and stopped. Then pushing input was applied at this position, chosen sequentially from 0.0 to 0.5 mm at 0.1 mm intervals for each trial. Finally, the needle was pushed a further 100 mm under the applied input. All 4 needles were inserted the same total distance. Each needle insertion was repeated five times for each input.
2. Needle insertions were performed applying two inputs. The needle was pushed 100 mm with 0.5 mm pulling input and stopped. Then, 1.0 mm pushing input was applied at this position. Finally, the needle was pushed further 100 mm under the applied input. Two comparative needles were pushed 100 mm, respectively. Then, these needles were rotated 180° around their long axes to change bevel tip directions and pushed 100 mm. Each needle insertion was repeated five times.

After each full needle insertion, the cannula dot positions were recorded and plotted on an XY plane.

3 Results and Discussion

Figure 3 shows needle paths obtained using protocol (1). The needle paths curved depending on the pulling input magnitude. Lateral distance for prototype (B) with 0.4 mm input = 35.9 mm from the standard straight path, 16.9 and 310% larger, and 8.5% smaller than for prototype (A), and needles (D) and (C), respectively. Figure 4 shows needle paths obtained using protocol (2). Prototypes (A) and

Fig. 3 Protocol 1 needle insertion paths for **a** prototype (A), comparative needles (C) and (D), and **b** prototype (B)

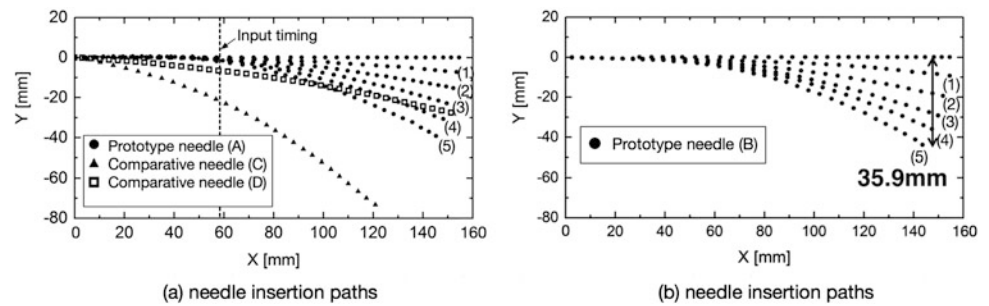
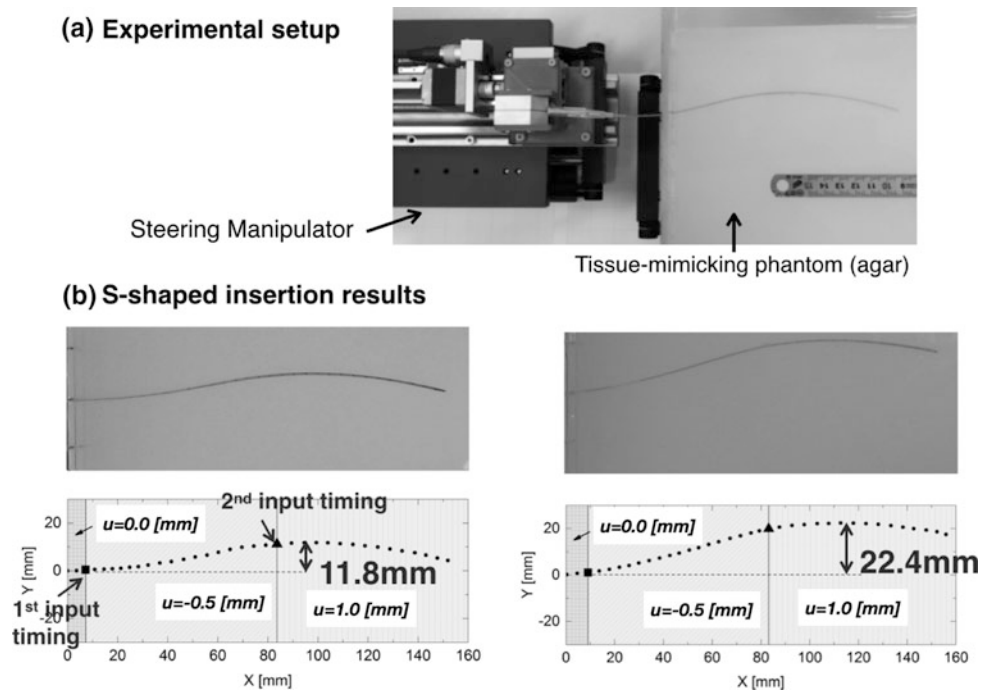


Fig. 4 Protocol 2 **a** experimental setup and **b** needle insertion paths. Left figures show prototype (A) and right figures show prototype (B)



(B) followed S shaped paths, with prototype (B) lateral distance 190% larger than prototype (A).

The prototype steerable needle (B) using the loop shaped stylet with inhomogeneous cross sections succeeded in bending the needle better than the needle (A). This result implied that the thin part of the loop shaped stylet functioned as a bent-tip needle with an acute angle by applying the input. This result showed that the steerable needle based on Active Sheath would be a potential solution to realize active bent-tip needles with simple structures, which can create curved needle paths adaptively during needle insertions.

targeting range depending on planned path shape flexibility. In the assessment study using the input protocol 2, the bending directions were switched in a fixed bending plane. However, when rotating the bending plane by rotating the stylet, the ideal needle paths require the rotational accuracy. The assessment of the rotational accuracy is a potential future work direction.

Acknowledgements This work was supported in part by JSPS KAKENHI Grant Number 18H01408.

Conflict of Interest The authors declare that they have no conflict of interest.

4 Conclusion

This study aimed to develop steerable needles based on Active Sheath, a flexible loop shaped steering mechanism. Experimental results verified that the proposed needles could enable physicians to plan curved paths and extend the

References

1. Webster, R.J., Kim, J.S., Cowan, N.J., Chirikjan, G.S., Okamura, A.M.: Nonholonomic modeling of needle steering. *Int. J. Robot. Res.* **25**(5), 509–525 (2006)

2. Swaney, P.J., Burgner, J., Gilbert, H.B., Webster, R.J.: A flexure-based steerable needle: high curvature with reduced tissue damage. *IEEE Trans. Biomed. Eng.* **60**(4), 906–909 (2013)
3. Bui, V.K., Park, S., Park, J.-O., Ko, S.Y.: A novel curvature-controllable steerable needle for percutaneous intervention. *Inst. Mech. Eng. Part H Proc.* **230**(8), 727–738 (2016)
4. Ko, S.Y., Frasson, L., Baena, F.R.: Closed-loop planar motion control of a steerable probe with a programmable bevel inspired by nature. *IEEE Trans. Rob.* **27**(5), 970–983 (2011)
5. Ko, S.Y., Baena, R.Y.: Towards a miniaturized needle steering system with path planning for obstacle avoidance. *IEEE Trans. Biomed. Eng.* **60**(4), 910–917 (2012)
6. Scali, M., Pusch, T.P., Breedveld, P., Dodou, D.: Needle-like instrument for steering through solid organs: a review of the scientific and patent literature. *Inst. Mech. Eng. Part H Proc.* **231**(3), 250–265 (2017)
7. Majewicz, A., Marra, S.P., van Vledder, M.G., Lin, M., Choti, M. A., Song, D.Y., Okamura, A.M.: Behavior of tip-steerable needles in ex vivo and in vivo tissue. *IEEE Trans. Biomed. Eng.* **59**(10), 2705–2715 (2012)
8. Okazawa, S., Ebrahimi, R., Chuang, J.C., Salcudean, S.E., Rohling, R.: Hand-held steerable needle device. *IEEE/ASME Trans. Mechatron.* **10**(3), 285–296 (2005)
9. Webster, R.J., Okamura, A.M., Cowan, N.J.: Toward active cannulas: miniature snake-like surgical robots. In: *IROS2006 IEEE/RSJ International Conference on Intelligent Robots and Systems Proceedings*, pp. 2857–2863. Beijing, China (2006)
10. Sears, P., Dupont, P.E.: A steerable needle technology using curved concentric tubes. In: *IROS2006 IEEE/RSJ International Conference on Intelligent Robots and Systems Proceedings*, pp. 2850–2856. Beijing, China (2006)
11. Mathis, M. et al.: Steerable device for accessing a target site and methods. U.S. Patent 200601674416, 27 Jul 2006
12. Osseon: <http://www.osseon.com/osseoflex-sn-steerable-needle/>. Last accessed 1 June 2017
13. AprioMed: <http://apriomed.com/products/morrison-steerable-needle/9292/>. Last accessed 1 June 2017
14. Adebar, T.K., Greer, J.D., Laeseke, P.F., Hwang, G.L., Okamura, A.M.: Methods for improving the curvature of steerable needles in biological tissue. *IEEE Trans. Biomed. Eng.* **63**(6), 1167–1177 (2016)
15. Yamada, A., Naka, S., Morikawa, S., Tani, T.: MR compatible continuum robot based on closed elastica with bending and twisting. In: *IROS2014 IEEE/RSJ International Conference on Intelligent Robots and Systems Proceedings*, pp. 3187–3192. Chicago, Illinois (2014)
16. Yamada, A., Naka, S., Nitta, N., Morikawa, S., Tani, S., Tani, T.: An adaptive steerable needle based on a loop-shaped flexible arm. In: *CARS 2017 Computer Assisted Radiology and Surgery Proceedings*, LE-276, NH Collection Constanza Hotel, Barcelona, Spain (2017)
17. Yamada, A., Naka, S., Nitta, N., Morikawa, S., Tani, T.: A loop-shaped flexible mechanism for robotic needle steering. *IEEE Robot. Autom. Lett.* **3**(2), 648–655 (2018)

Development of an MR-Compatible High-Definition Flexible Endoscope for Real-Time MR Image-Guided Microwave Ablation

Atsushi Yamada[✉], Shigeyuki Naka, Khiem Tran Dang, Shigehiro Morikawa, and Tohru Tani

Abstract

This study aims to develop a magnetic resonance (MR)-compatible flexible endoscope for minimally invasive real-time MR image-guided microwave ablation as proposed by the author with a widely available 3-Tesla close-bore MR scanner and to assess the feasibility of including a position tracking sensor. A unique MR-compatible high-definition (HD) endoscope was developed to access a target organ from outside the scanner bore by obtaining endoscope optical camera and scan images simultaneously. The camera unit consists of a CMOS image sensor with 400×400 pixels. The camera head and the lens barrel are made of phosphor bronze and a Pebax elastomer sheath with a 2.1 mm diameter shielded by tin-plated copper wires. The image resolution was up-converted to 700×700 pixels using a high-resolution image processing technique. The endoscope had two working channels (2.0 mm in each outer diameter) and two sensor ports (2.5 mm in each outer diameter). One port had a gradient-magnetic-based tracking sensor to identify the tip position and orientation; the outer diameter and length of the endoscope were 11 and 1200 mm. A pig was scanned as a pre-procedural MR image and the result was used as navigation images to assess the endoscope's feasibility. The camera image

quality was sufficient to identify organs without critical noise during scanning, and its resolution was 295 times that of the conventional MR-compatible fiber endoscope we developed. The refresh rates of the sensor position and orientation were <0.5 s, which includes data transmission from the scanner to the navigation software. The verification study showed that the proposed MR-compatible endoscope has the potential to enable a surgeon to access target organs from the outside bore while simultaneously obtaining optical and scanned images.

Keywords

Magnetic resonance compatibility • Flexible endoscope • Navigation system

1 Introduction

Needle-based treatments such as cryotherapy, radiofrequency, and microwave ablation are widely performed as minimally invasive procedures. These ablations require pre-procedural and intra-procedural images to plan the ideal needle paths to targets and monitor needle artifacts for targeting because, in practice, targets may reside deep within patients' bodies and be adjacent to organs and tissues that are sensitive to injury. Intra-operative magnetic resonance imaging (MRI) is helpful for delineating soft tissue structures with needle artifacts and can be further enhanced in open-configuration MRI scanners because physicians can access the patient on the scanner bed during imaging. A real-time MR image-guided navigation system dedicated for needle insertions with a vertical open-configuration MRI scanner (Signa SP2, GE Healthcare, Waukesha, WI, USA) was developed to allow physicians to review two perpendicular MR images that are updated continuously and always display vertical cross-sections of a needle during needle insertion. These intra-procedural real-time MR images could be obtained by controlling the scan planes during scanning

A. Yamada (✉) · K. T. Dang · T. Tani
Department of Research and Development for Innovative Medical Devices and Systems, Shiga University of Medical Science, Otsu, Shiga, 520-2192, Japan
e-mail: ayamada@belle.shiga-med.ac.jp

S. Naka
Department of Surgery, Shiga University of Medical Science, Otsu, Shiga, Japan

S. Naka
Department of Surgery, Hino Memorial Hospital, Gamo-gun, Shiga, 529-1642, Japan

S. Morikawa
Molecular Neuroscience Research Center, Shiga University of Medical Science, Otsu, Shiga, Japan

based on the orientation of a unique passive needle locator [1, 2] that guides the needle. This navigation system was applied in real-time MR image-guided microwave needle-ablations of liver tumors [1–4] that were performed successfully in the hospitals to which the authors belong between 2000–2016 for more than 300 clinical cases, including thoracoscopy-assisted coagulations [5, 6] and laparoscopy-assisted coagulations [7].

Although the success of the clinical studies is encouraging, applying the developed image-guided system to widely available closed-bore MRI scanners was challenging because inside the closed-bore scanner, inserting needles manually into a liver obviously requires a shorter and wider scanner bore or long assistive devices to access the patient from outside the bore. This clinical challenge motivated us to develop an MR-compatible high-definition (HD) flexible endoscope and a dedicated viewer system for the endoscope as a potential solution. The developed system's feasibility was assessed in an animal study. The contribution of this study was to show a potential of microwave needle ablations for a patient abdomen in an MRI bore by using an MR-compatible HD flexible endoscope [8] and a flexible microwave probe, and MR-compatible in-room monitor.

2 Materials and Methods

This section provides the proposed MR-compatible flexible endoscope and the viewer system to allow physicians to review endoscope camera images in a magnet room. The viewer system consists of a wide closed-bore 3-Tesla

(T) MRI scanner (MAGNETOM Verio dot 3T, Siemens Healthcare GmbH, Erlangen, Germany), an MR-compatible flexible endoscope, MR-compatible in-room monitors, a flexible microwave probe, a gradient-magnetic-field-based tracking system (EndoScout II, RobinMedical Inc., Baltimore, MD, USA) with a catheter-type sensor, and a navigation console running custom-made navigation software. The magnet room of the scanner has radiofrequency (RF)-filtered penetration panels (Riken Electromagnetic Compatibility Inc., Fukuoka, Japan) with waveguides of length 250 mm and inner and outer diameters respectively of 57.2 and 60.5 mm to provide power for the in-room monitors and signal communication between the magnet room and operation room.

2.1 MR-Compatible Flexible Endoscope

The MR-compatible HD flexible endoscope was originally developed for use inside the scanner bore during scanning or outside the bore before and after scanning [8] (Fig. 1). The endoscope employed an MR-compatible housing the outer diameter and length of which were 11.0 and 1200 mm, respectively. The distal end of the endoscope could be bent controllably up to 100° in four directions using a conventional tendon-driven mechanism. The endoscope has two working channels (2.0 mm in each inner diameter) and two sensor ports (2.5 mm in each inner diameter). A light guide was wired through the center of the endoscope's vertical section and this was connected to an optical source (RX-3300, Machida Endoscope Co., Ltd., Chiba, Japan).

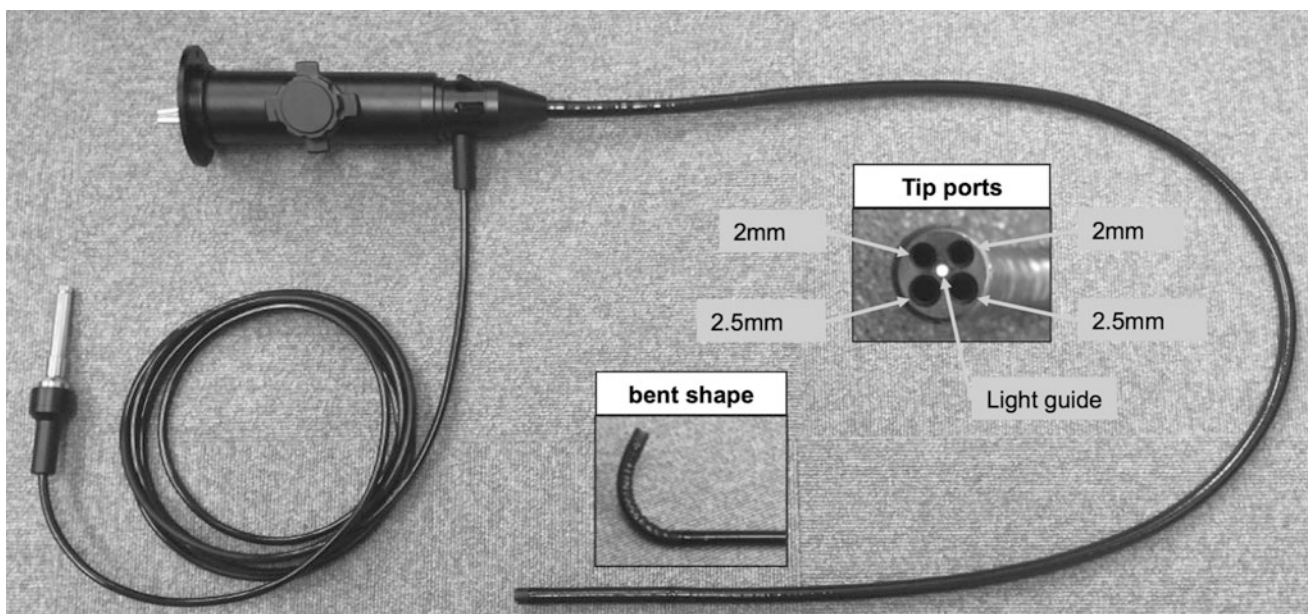


Fig. 1 MR-compatible high-definition (HD) flexible endoscope prototype

One sensor port included an installed camera unit that consisted of an analog complementary metal oxide semiconductor (CMOS) image sensor with 400×400 pixel resolution, a camera head and lens barrel made of phosphor bronze, and a Pebax elastomer sheath of diameter 2.1 mm shielded by tin-plated soft copper wires. The image resolution was up-converted to 700×700 pixels using super high-resolution image processing. The catheter-type tracking sensor was installed in the other sensor port [9, 10], the outer diameter of which was approximately 2.1 mm. The tracking sensor could work during scanning by using a specific pulse sequence that includes excitation pulses dedicated for the sensor.

2.2 MR-Compatible in-Room Monitors

MR-compatible in-room monitors (Prototype, Takashima Prototype Engineering, Tokyo, Japan) were developed that consist of two liquid-crystal flat-panel displays arranged vertically and attached to an aluminum trolley with two imaging-signal-converter boxes. This dual display system uses two commercially available 32-inch light-emitting diode (LED) color television systems (32LB6500, LG Electronics Inc., Seoul, Korea) to display navigation images including the endoscope camera image, a pre-procedural MR image set, and a tracker model to represent the catheter sensor location from a bird's-eye view. The MR compatibility of the dual displays was developed by replacing the original bezel and frames with custom aluminum bezel and frames that are placed close to the MRI scanner in the magnet room. Each imaging-signal-converter box has an HDMI-cable output port to connect to one of the displays and an optical-fiber-cable input port to transmit navigation images. The optical fiber cable inserted into the input port was connected to another signal converter placed in the control room to relay navigation images from the endoscope console workstation through the waveguide. A power supply for the in-room monitors was placed in the control room and connected through the penetration panel.

2.3 Flexible Microwave Probe

The flexible microwave probe prototype was originally based on a coaxial cable structure to ablate targets through an MR-compatible flexible endoscope. The outer diameter and length are respectively 1.7 and 1820 mm, and the length of the probe tip—which is the hard part—was 20 mm. The probe prototype was installed into one of the endoscope's working channels. The distal end of the probe prototype was

placed outside of the magnet room through the RF-filtered penetration panel and connected to a microwave generator (Microtaze HSD-20M, Alfresa Pharma Corp., Osaka, Japan) that operated at 2.45 GHz.

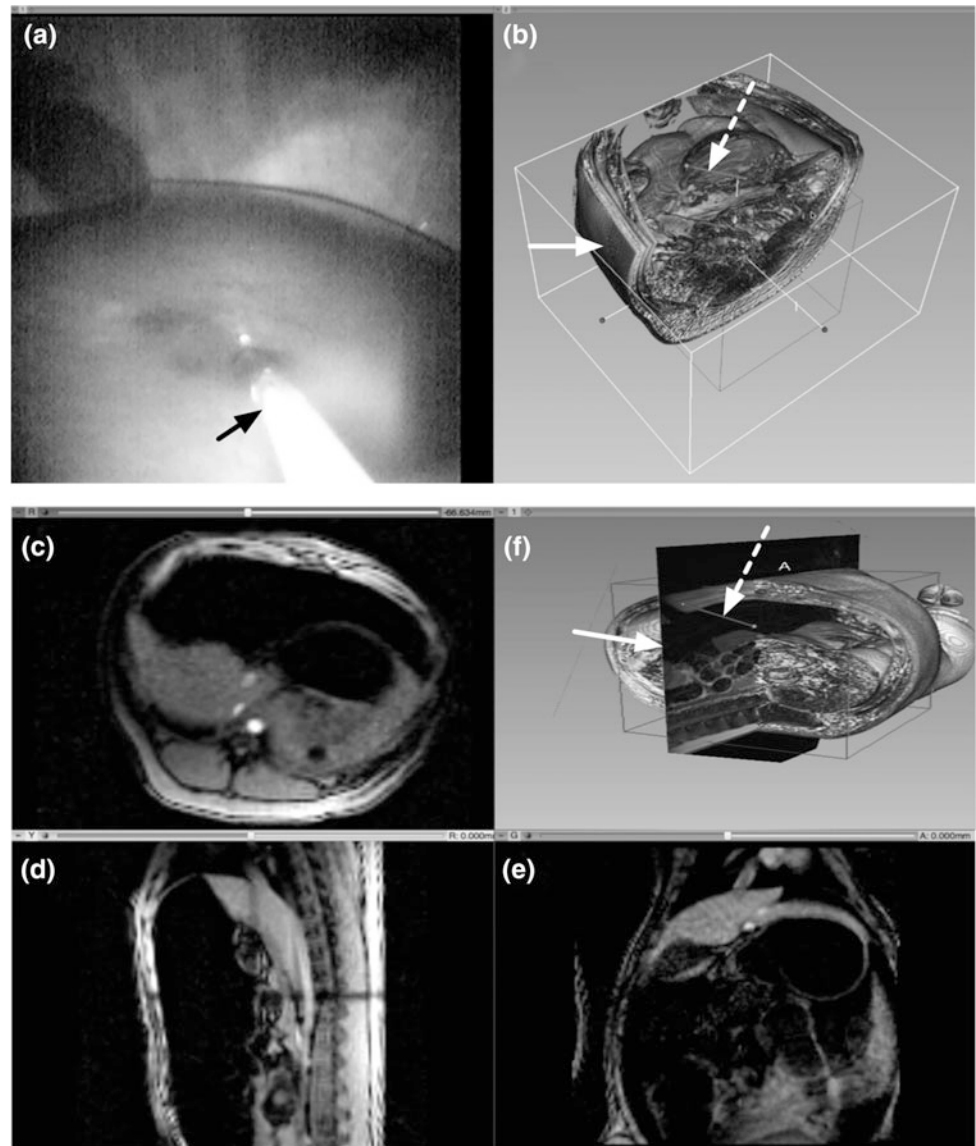
2.4 Navigation Software Configuration

Navigation software was developed based on 3D Slicer; free open-source medical imaging software (3D Slicer release 4.4.0, SVN revision #23971) [11–13]. It consists of a module of a 3D Slicer termed “EndoscopeConsole,” which uses a free open-source computer vision library (OpenCV 2.4.8, Intel Corporation, Santa Clara, CA, USA) with FFmpeg library to continually process the captured camera images. The navigation software was executed on the navigation console (Mac Pro, 3 GHz 8-core Intel Xeon E5 processor, 64 GB 1866 MHz DDR3 ECC RAM, AMD FirePro D700 6144 MB, Apple Inc., Cupertino, CA, USA) with a signal converter (DVI2USB 3.0, Epiphan Systems, Ottawa, Canada) to capture the camera image. The signal converter was connected to a camera control box that was dedicated for the endoscope camera unit by an HDMI cable that runs through the penetration panel. The navigation user interface (UI) was displayed on the MR-compatible in-room monitors to allow physicians to observe the magnet room.

The user interface was displayed on the in-room monitors as shown in Fig. 2. For the top monitor, the user interface displayed the endoscope camera image (a) and a bird's-eye view (b) including a volume rendering model which was reconstructed from the pre-procedural image set, an endoscope model that represents the distal end location of the endoscope. In the bottom monitor, the user interface displayed three perpendicular planes (c–e) and another bird's-eye view (f). The reconstructed plane in the pane (f) represents the pre-procedural MR image plane shown in (d) which was reconstructed following the endoscope tip orientation. In the pane (f), the reconstructed MR image plane (d) enables surgeon to understand the endoscope orientation and where the image plane (d) located in the animal abdomen. Both panes (b) and (f) indicate bird's eye views but viewpoints are different from each other. Furthermore, only the pane (f) has the reconstructed MR image plane. Therefore, the pane (b) is used for identifying the endoscope location and surrounded tissues and organs by the volume rendering model. The pane (f) is used to identify where the pane (c–e) are located, which allows physicians to understand the orientation of the endoscope. Figure 2 shows a pig abdomen which was used in an animal study in Sect. 2.5.

The pre-procedural MR image set was scanned by the imaging protocol of the T1-weighted dynamic images

Fig. 2 Navigation software user interface on MR-compatible in-room monitors. **a** Endoscope camera image and **b** virtual bird's-eye view for the top monitor. The image pane **(a)** displays a flexible microwave probe (solid arrow). The bird's-eye pane **(b)** displays a volume rendering model (solid arrow) and an endoscope model (dotted arrow). **c–e** Display three orthogonal planes of pre-procedural MRI reconstructed according to a sensor location. **f** Displays bird's-eye view with a reconstructed plane (solid arrow) and the endoscope model (dotted arrow)



acquired with a three-dimensional (3D) fast-acquisition low-flip-angle spoiled gradient echo sequence (TR/TE:4.77/2.46 ms; matrix size 256×256 with 9.0° flip angle; 1.5 mm section thickness; and 380 mm field of view) using the spine matrix coil and 4ch large flex coil. The obtained image set was transferred from the scanner console to the navigation console through Orthanc, which is open-source Picture Archiving and Communication System (PACS) software, on a PACS server (Amphis bz SV5100, 3.1 GHz 4-core Intel Xeon E3-1220V2 Processor, 16 GB 1333 MHz DDR3 ECC RAM, UNIT.COM Inc., Osaka, Japan) that was running the FreeBSD 11.1-RELEASE operating system.

2.5 Feasibility Study of the Proposed System

An animal experiment was performed with the approval of the committee on animal care of Shiga University of Medical Science. A female pig that weighed 57.2 kg was involved in this study. General anesthesia was administered to the pig and a pre-procedural image set for the pig abdomen was scanned and loaded on the navigation console. The volume rendering model was generated by reconstructing the image set and the navigation software displayed the endoscope camera image.

One of this paper's co-authors who is a surgeon and has been involved in real-time MR image-guided microwave

ablations performed in our hospital 2000–2016 inserted the endoscope into the pig pneumoperitoneum through a trocar, manipulated the endoscope, and then decided upon three virtual targets in the liver. For these targets, the surgeon performed microwave ablations while observing the navigation UI. During the procedure, two types of verification were performed as follows: the navigation interface was subjectively assessed by the surgeon combining the camera view and the virtual bird's-eye view. In the first verification, a specific scan sequence including excitation pulses dedicated for the sensor was used to update the model position and orientation so that the model was synchronized with the camera image. The second was used to assess the potential of obtaining continuous real-time imaging [9] with sufficient quality to identify the target organ and adjacent structures for microwave probe insertions and ablations; this was performed by the same surgeon. The second verification used a BEAT-IRT sequence that was dedicated for the SIEMENS scanner.

3 Results and Discussion

The verification studies were performed successfully as shown in Fig. 3. On the specification, the obtained image resolution of the developed MR-compatible flexible endoscope was 295 times that of an MR-compatible fiberscope

that the authors had previously developed [9]. In the first verification, the endoscope camera image was of sufficient quality to observe organs including the liver thanks to the super high-resolution image processing and lack of critical noise for the endoscope camera. The in-room monitors also worked to display the navigation UI. The sensor location refresh rate was <0.5 s and the sensor accuracy was high enough that the surgeon could identify the endoscope location from the camera image and the bird's-eye view model simultaneously. In the second verification, there was no critical noise on the real-time images during the ablation that could have obscured the target areas and the real-time image's refresh rate was <1.5 s/slice.

In the studies, the sequence including the sensor excitation pulses was different from BEAT-IRT for real-time MR imaging and therefore, the three perpendicular planes of the navigation UI in the first verification displayed the planes of the reconstructed pre-procedural MRI according to the sensor location. However, if the sensor excitation pulses could be combined with the real-time MR imaging sequence, the scan planes could be controlled according to the sensor location [8, 14].

The working channels of the endoscope could not only install the passive device as a microwave flexible probe but also active flexible devices including steerable needles [15] to adaptively control the needle paths. These active devices require extended scan plane control so that the real-time MR



Fig. 3 Experimental setup and trials using the developed MR-compatible endoscope, the navigation software displayed on the MR-compatible in-room monitors, and a 3T MRI scanner

images always display needle artifacts since the sensor was not installed in the needle tip but instead in endoscope's distal end.

4 Conclusion

This study demonstrated the basic performance of the developed MR-compatible flexible endoscope and the dedicated navigation software for the endoscope. The MR-compatible HD flexible endoscope had the potential to provide simultaneous imaging acquisition between the endoscope camera view and real-time images with widely available closed-bore 3T high-magnetic-field MRI as a novel option for safe and seamless minimally invasive surgeries.

Acknowledgements This work was supported in part by JSPS KAKENHI Grant Number 18H01408.

Conflicts of Interest The authors declare that they have no conflict of interest.

References

- Morikawa, S., Inubushi, T., Kurumi, Y., Naka, S., Sato, K., Tani, T., Haque H. A., Tokuda, J., Hata, N.: New Assistive devices for MR-guided microwave thermocoagulation of liver tumors. *Acad. Radiol.* **10**(2), 180–188 (2003)
- Kurumi, Y., Tani, T., Naka, S., Shiomi, H., Shimizu, T., Abe, H., Endo, Y., Morikawa, S.: MR-guided microwave ablation for malignancies. *Int. J. Clin. Oncol.* **12**(2), 85–93 (2007)
- Morikawa, S., Inubushi, T., Kurumi, Y., Naka, S., Sato, K., Demura, K., Tani, T., Haque, H.A., Tokuda, J., Hata, N.: Advanced computer assistance for magnetic resonance-guided microwave thermocoagulation of liver tumors. *Acad. Radiol.* **10**(12), 1442–1449 (2003)
- Morikawa, S., Inubushi, T., Kurumi, Y., Naka, S., Sato, K., Tani, T., Yamamoto, I., Fujimura, M.: MR-guided microwave thermocoagulation therapy of liver tumors: Initial clinical experiences using a 0.5 T open MR system. *J. Magn. Reson. Imaging* **16**(5), 576–583 (2002)
- Shiomi, H., Naka, S., Sato, K., Demura, K., Murakami, K., Shimizu, T., Morikawa, S., Kurumi, Y., Tani, T.: Thoracoscopy-assisted magnetic resonance guided microwave coagulation therapy for hepatic tumors. *Am. J. Surg.* **195**(6), 854–860 (2008)
- Sonoda, H., Shimizu, T., Takebayashi, K., Ohta, H., Murakami, K., Shiomi, H., Naka, S., Hanaoka, J., Tani, T.: Minimally invasive surgery using the open magnetic resonance imaging system combined with video-assisted thoracoscopic surgery for synchronous hepatic and pulmonary metastases from colorectal cancer: report of four cases. *Surg. Today* **45**(5), 652–658 (2014)
- Murakami, K., Naka, S., Shiomi, H., Akabori, H., Kurumi, Y., Morikawa, S., Tani, T.: Initial experiences with MR Image-guided laparoscopic microwave coagulation therapy for hepatic tumors. *Surg. Today* **45**(9), 1173–1178 (2014)
- Yamada, A., Naka, S., Morikawa, S., Tani, T.: A real-time MR image-guided surgical navigation system for a MR-compatible high definition flexible endoscope. In: ACCAS2016 the 12th Asian Conference on Computer Aided Surgery, pp. 94–95. DCC, Daejeon, Korea (2016)
- Haque, H.A., Morikawa, S., Naka, S., Kurumi, Y., Murayama, H., Tani, T.: Simultaneous endoscopy and MRI acquisition. In: Kahn, T., Busse, H. (eds.) *Interventional magnetic resonance imaging. Medical radiology. Interventional magnetic resonance imaging*, pp. 471–479. Springer, Berlin, Heidelberg (2012)
- Wang, W.: MR guided active catheter tracking. *Magn. Reson. Imaging Clin. N. Am.* **23**(4), 579–589 (2015)
- 3D Slicer: <https://www.slicer.org>. Last accessed 29 Mar 2018
- Kikinis, R., Pieper, S.D., Vosburgh, K.: 3D Slicer: a platform for subject-specific image analysis, visualization, and clinical support. In: Jolesz, F.A. (eds.) *Intraoperative imaging image-guided therapy*, pp. 277–289 (2014)
- Fedorov, A., Beichel, R., Kalpathy-Cramer, J., Finet, J., Fillion-Robin, J.-C., Pujol, S., Bauer, C., Jennings, D., Fennessy, F.M., Sonka, M., Buatti, J., Aylward, S.R., Miller, J.V., Pieper, S., Kikinis, R.: 3D Slicer as an image computing platform for the quantitative imaging network. *Magn. Reson. Imaging* **30**(9), 1323–1341 (2012)
- Qing, K., Pan, L., Fetics, B., Wacker, F.K., Valdeig, S., Philip, M., Roth, A., Nevo, E., Kraitchman, D.L., van der Kouwe, A.J., Lorenz, C.H.: A multi-slice interactive real-time sequence integrated with the EndoScout tracking system for interventional MR guidance. In: ISMRM2010 Proceedings (2010)
- Yamada, A., Naka, S., Nitta, N., Morikawa, S., Tani, T.: A loop-shaped flexible mechanism for robotic needle steering. *IEEE Robot. Autom. Lett.* **3**(2), 648–655 (2018)

Development of Bio-signal Acquisition and Processing System and Its Utilization for Educational Purpose

Sun I. Kim, Jongshill Lee, Dong Pyo Jang, and In Young Kim

Abstract

There are many biological signal measurement systems such as BIOPAC and evaluation boards for specific signals. However, most of these boards and systems are manufactured for research, not for educational purpose. There are many limitations in adding or modifying circuits directly. Therefore, we developed a bio-signal acquisition and processing system (BMDAQ) that is highly utilized in educational purpose. The BMDAQ board consists of an analog board, a digital board and PC application programs, as well as teaching materials of educational lectures. We designed an analog board using three Op-Amps instrumentation amplifiers instead of a single chip for electrocardiogram (ECG). The digital board is designed to convert the signal coming from the analog board into digital and transmit the data to the PC through serial communication. The application program provides real-time filtering of biomedical signal and display of original and filtered signal. BMDAQ board and textbook were designed and produced for educational purpose and have been used as teaching materials.

Keywords

Biological signal measurement • BMDAQ • Electrocardiogram

1 Introduction to BMDAQ

There are many systems and devices that acquire bio-signal, such as Biopac (BIOPAC Systems Inc., USA) [1] and evaluation boards for specific signals. These devices have limitations in terms of education because it is difficult to modify and add modules. Therefore, we developed a

S. I. Kim (✉) · J. Lee · D. P. Jang · I. Y. Kim
 Department of Biomedical Engineering, Hanyang University,
 Seoul, South Korea
 e-mail: sunkim7114@gmail.com

biological measurement and processing system for educational purpose.

As shown in Fig. 1, the BMDAQ system consists of analog, digital boards, board-to-PC interface and PC application software. We designed an analog board using three Op-Amps instrumentation amplifiers instead of a single chip for electrocardiogram (ECG) which is one of the most important bio-signals, and also included several analog filters. This analog board is designed as a removable expansion type for several other applications and is manufactured so that students can do soldering for themselves. The digital board is designed to convert the analog signal coming from the analog board into digital and perform several signal processing before transmit the data to the PC through serial communication.

The microcontroller used in the digital board is MSP430 (Texas Instruments Inc., USA) and we basically used the 12-bit ADC built in the microcontroller. In addition, an external 24-bit ADC was used to acquire a bio-signal with high resolution. Also the BMDAQ is designed to isolate the signal and power from the human body for safety which is the most important factor in medical devices.

Communication between BMDAQ and PC is performed by UART communication via USB serial port. The application program provides real-time filtering of biomedical signal and display of original and filtered signal. We provide the source code for the real-time filtering method including the QRS complex detecting algorithm to students. The textbook presents a method of designing a digital filter using MATLAB and provides a method to implement the designed filter to be driven in real time.

2 Characteristics of BMDAQ

2.1 BMDAQ

Figure 2a, b show an assembled BMDAQ and its block diagram respectively. Dimension of the BMDAQ board is

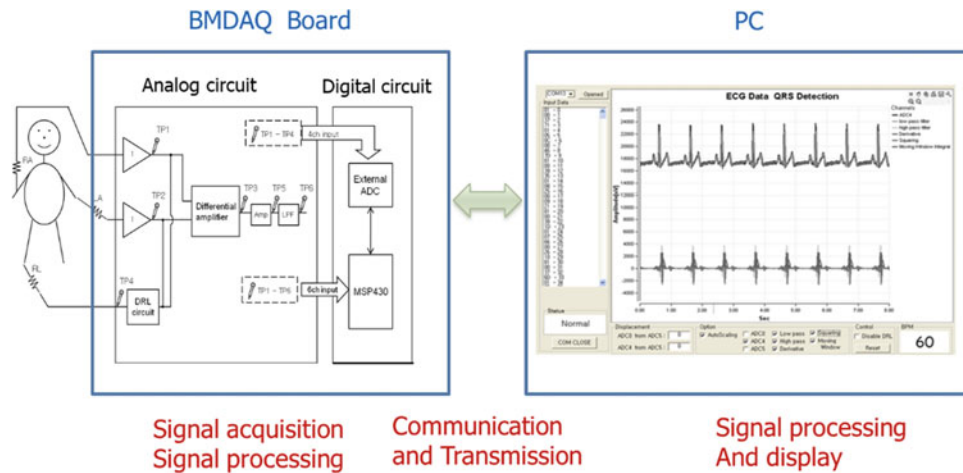


Fig. 1 Overall diagram of the BMDAQ system. BMDAQ system consists of analog and digital boards and PC application software

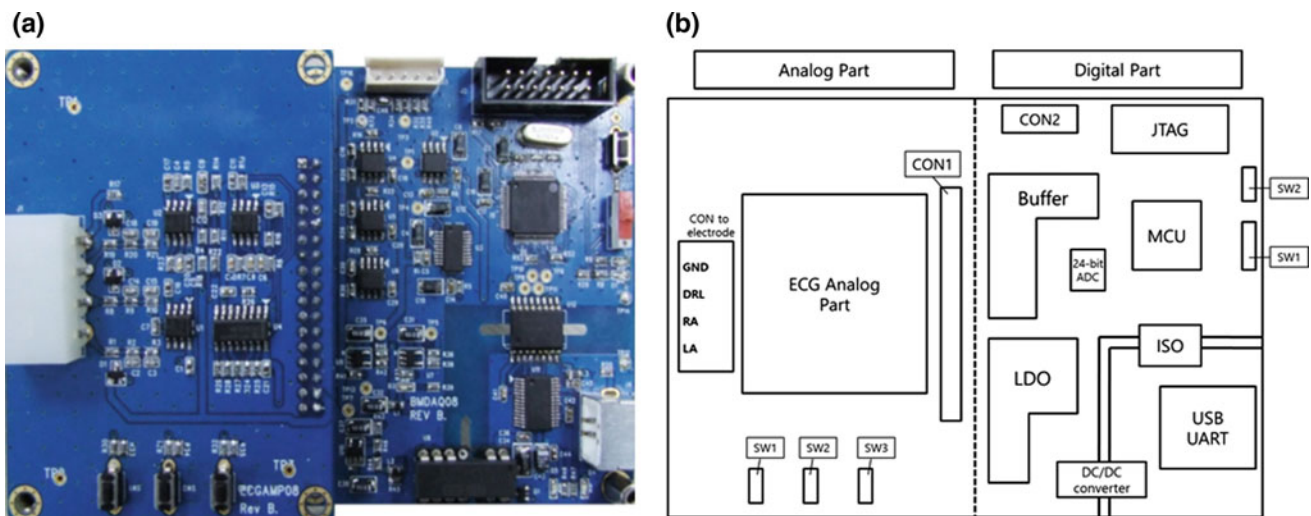


Fig. 2 Board and block diagram for BMDAQ. **a** Assembled Analog and digital board, **b** block diagram for BMDAQ

12 cm × 8 cm and consist of two-layer, double-sided PCB. The board is divided into a mounted analog and digital part, which are connected to each other by connector (CON1) and can be removable.

The analog part amplifies and filters the electrocardiogram signal coming through the electrode and sends it to the digital part, and the switches are programmable switches that can be used by the user. The power source uses the 5 V supplied from the USB of the PC, and the microcontroller used in the digital part is the MSP430 (Texas Instruments Inc., USA).

The 24-bit ADC on the digital board is an external high-resolution analog-to-digital converter which is used to convert a weak electrical signal to a digital signal, which is not amplified in the analog part and has an amplitude in the

order of microvolts to millivolts. The analog-to-digital conversion is implemented through serial peripheral interface (SPI) communication between the microcontroller and the ADC chip.

The DC/DC converter converts the USB 5V voltage to the required voltage from the BMDAQ board and isolates the circuit from the power supply with an ISO (isolator).

The main features of BMDAQ are as follows.

- Use the popular microcontroller MSP430
- USB power supply (DC 5V)
- Firmware download and debug using JTAG
- Firmware download using serial port
- Separation design of power unit considering safety (optical and electrical)

- Input range of analog electric signal: ± 4.5 V
- MCU internal 12-bit 6-channel ADC and 24-bit 4-channel ADC through SPI
- Easy to expand other analog module.

2.2 Analog Circuits for Electrocardiogram

We designed an analog board using three Op-Amps instrumentation amplifiers [2] instead of a single chip for electrocardiogram (ECG) to help students understand analog circuits.

Figure 3 shows the circuits of the analog board and is divided into 8 functions. The input stage has a protection circuit and a filter to reduce noise, and then passes through a buffer to reduce the load effects of the input signal.

The common mode component of the signal passed through the buffer is removed through the differential

amplifier. For the signal with the common mode component removed, a high-pass filter is used to eliminate the signal with a very low frequency component including DC. Then the signal is largely amplified. Finally, it passes through a second-order low-pass filter to remove high-frequency components.

To summarize the characteristics of this circuits, amplification is performed 4.7 times in the differential amplifier and 220 times in the amplifier, amplifying 1000 times in total, and has a pass band of 0.5–150 Hz.

3 Conclusion

BMDAQ board and textbook were designed and produced for educational purpose and have been used as teaching materials and laboratory equipment in biomedical/electronic related engineering department of many universities in Korea for 10 years. We plan to upgrade BMDAQ to reflect

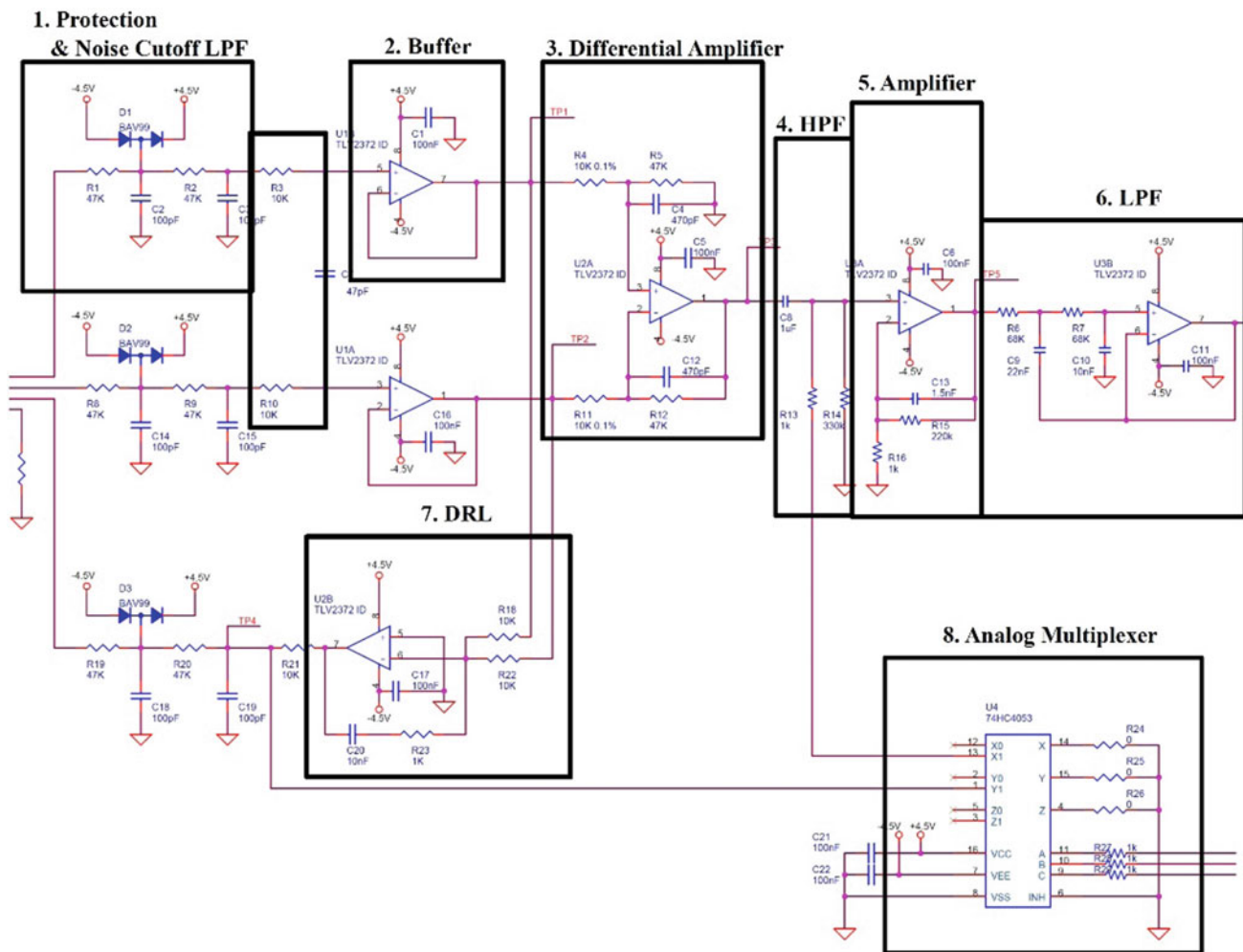


Fig. 3 Circuits for analog board

new trends in these days, and will add new modules such as pulse oximeter, EEG and IMU (Inertia Measurements Units). We plan to publish 2nd edition containing new contents in an international version (English).

Conflict of Interest The authors declare that they have no conflict of interest.

References

1. BIOPAC Systems Inc. Homepage: <https://www.biopac.com>. Last accessed 25 Mar 2018
2. Wester, J.G.: Medical Instrumentation: Application and Design, 4th edn. Wiley, USA (2009)

A Non-contact Human Body Height and Weight Measurement Approach Using Ultrasonic Sensor

Minh H. Ly, Nguyen M. Khang, Tran T. Nhi, Tin T. Dang, and Anh Dinh

Abstract

Human body height and weight are the key factors for personal health monitoring and many works have been conducted to accurately and conveniently measure these two physiology parameters. However, in many conditions such as in the outer space, measuring human body weight becomes impossible for traditional approaches such as using weight scale. In this paper, we present a medical instrument, called the Ultrasonic Measurer to measure human body height and weight using a non-contact approach. This is a low-cost, efficient device to estimate human body sizes using an ultrasonic sensor, the SRF04. This sensor provides good measurements in close distance over a range up to 300 cm. Moreover, we present a convenient approach to estimate human body weight from the measured sizes using the close relationship between a human body's weight and its sizes, despite the variation in shapes. The measurements and estimations were implemented on a set of 50 men and women with different body shapes. The proposed method proved to give good results as the sizes are estimated with the average error of less than 0.3% and weight is estimated with the average error of less than 2.8%. The module is currently designed to be used as a standalone device. In the future, the module is equipped with the Internet of Things (IoT) for various remote health monitoring applications.

Keywords

Non-contact human body measurements • Ultrasonic sensor • Medical instrumentation • Health monitoring

1 Introduction

Human body parameters convey a lot of valuable information about an individual's physical status, shape, size, physique, and body composition [1]. Non-contact human body measurement is playing an increasingly vital role in physical healthcare, surveillance [2] and the demand for determining these indexes is inevitable. Over the centuries, people use a weight scale and a measuring tape to measure the human weight and height. However, accuracy still stands as a problem of these traditional methods. Although the advance in technology such as digital measurement techniques can minimize the error, there still exist many practical circumstances that need a specific tool. For instance, when an astronaut is in space, which is nearly weightless, he/she cannot use a scale to measure his/her weight.

Systematic attempts to characterize and estimate the main anatomical and compartmental components of the human body weight have been proposed and reviewed for a long time [3]. Sendroy and Collison, in [4], determined the human body volume from height and weight and then constructed a diagram for the relationship of V/S (Volume/Surface area) to W_E/H (Weight/Height) for male and female body and the most acceptable relationship between V and S, W_E and H. This approach gives an estimation of human body volume from height and weight and proposes an idea of some relationship between the human body's dimensions and its weight, which is critical for the human body weight estimation without using a weight scale. In the last decades, researchers have begun to measure body parameters indirectly using modern devices and methods.

M. H. Ly · N. M. Khang · T. T. Nhi · T. T. Dang (✉)
Faculty of Electrical and Electronics Engineering, Ho Chi Minh
City University of Technology, Ho Chi Minh City, Vietnam
e-mail: dtin@hcmut.edu.vn

A. Dinh
Department of Electrical and Computer Engineering, University
of Saskatchewan, Saskatoon, Canada

Recently, marker-less multi-view systems have become proficient at obtaining human body models but these solutions usually require large space and the measurements are difficult to set up [2]. Some other devices such as laser or Kinect camera [2] can present a convenient way to estimate human body volume; however, these methods are quite expensive since a three-dimensional laser scanner may cost from \$40,000 to \$150,000 US dollar [2]; the Microsoft's Kinect sensor V2 costs more than \$300. In addition to high investment cost, the above system requires complicated algorithm running on a computer to provide the measurements. Choosing the ultra-sound transducers can solve this problem because they are small, lightweight and cheap, making them suitable for placing the sensors on several human body segments [5], thus proposes a natural way to determine the volume of an object. This paper describes the development of a fairly accurate, cheap, and standalone human body height and weight measuring using a system of ultrasonic sensors SRF04 and the Arduino microcontroller. The algorithm to calculate weight based on the study of the relationship between a human body's volume and its weight is presented in the following sections.

The paper is organized into five sections. After the introduction, Sect. 2 depicts the method to implement an effective algorithm in a low-cost hardware. Section 3 shows the results and the corresponding error rate. Section 4 presents the advantages and drawbacks of the work and then propose further improvements. Finally, Sect. 5 contains conclusion and scope for the future investigations.

2 Method and Material

2.1 Ultrasonic Sensor SRF04

This ultrasonic sensor is a product of Devantech Limited company where SRF stands for ultraSonic Range Finder. The ultrasonic range sensor SRF04 has 2 heads, one for ultrasonic wave emission and the other for wave receiving. The unit pinouts are connected to the microcontroller unit, the Arduino Uno R3 in this case. These pins are responsible for triggering and measuring the time-of-flight of the echo [6]. The emission head emits ultrasonic wave whenever it is triggered by a triggering pulse. The frequency of the ping wave is 40 kHz [7]. The wave will reflect upon hitting an obstacle along its transmission path and the other head captures this reflection wave. The integrated timing circuit looks for a 40 kHz return signal to identify it as an echo [7]. The distance between the sensor and the obstacle is calculated based on the time-of-flight and the velocity of the ultrasonic wave. The sensor provides good measurements in close distance over a range of [3, 300 cm] with approximately 99% accuracy [8] (Fig. 1).

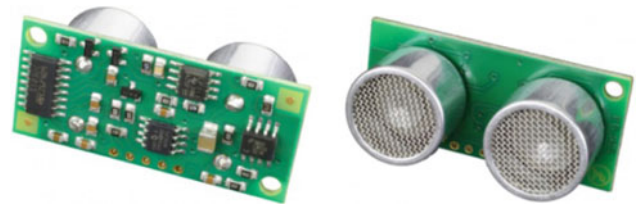


Fig. 1 Ultrasonic range sensor SRF04 [8]

2.2 The Integrated Circuit

The main circuit was designed as shown in Fig. 2. In addition to the SRF04 sensor, one resistor, one microcontroller Arduino Uno R3 and a LCD (liquid crystal display) screen are required. The sizes are first calculated by the ultrasonic sensor and then the information is sent to the Arduino microcontroller to calculate the weight based on the volume information and the density of a human body. Eventually, the weight and height are visually displayed on the LCD.

2.3 Algorithm

Figure 3 shows the algorithm to estimate the human body's dimensions (i.e., height, frontage, and width). These values are then used to calculate the volume and subsequently, weight of a human body. The measured height and weight results are then displayed on the LCD screen.

The dimension Height (H), Width (W), Frontage (F) of a human are defined as illustrated in Fig. 4.

Height, Frontage and Width measurement. All of the dimensions (height, frontage, width) are measured using one common principle. For example, W (width) of a human body equals the distance between the sensor and the reference point, b , subtracts the distance between the sensor and the body, a , provided that the human is standing just beside the reference point:

$$W = b - a \quad (1)$$

The principle is illustrated in Fig. 5. In order to have an accurate result, the distance between the sensor and the reference point is made unaltered. In other words, b is a constant. Moreover, the body being measured needs to stand right in the transmission path of the ultrasonic wave. As illustrated in Fig. 6, the width W is measured many times across the upper part of the body and the mean of these values is calculated to get the estimated W value. Taking the mean value would help reduce the error caused by the instability of the body parameters because when human takes breath, the parameter of the waist will increase while the parameters of other parts will hardly change. To further

Fig. 2 Schematic of the designed circuit

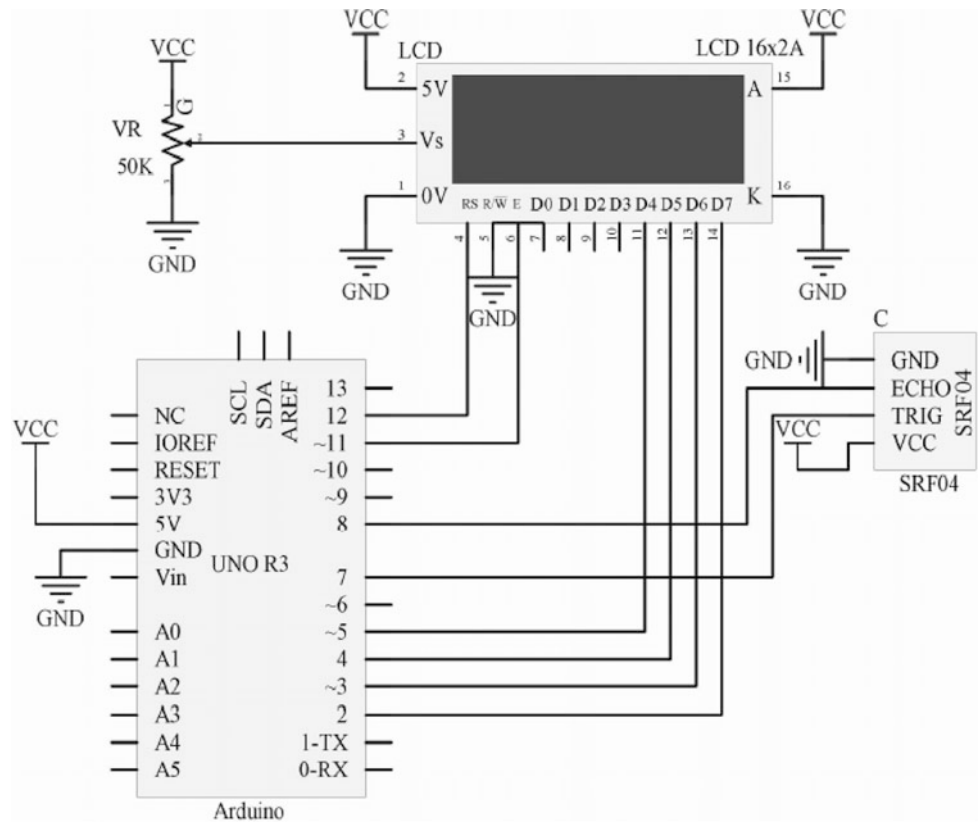
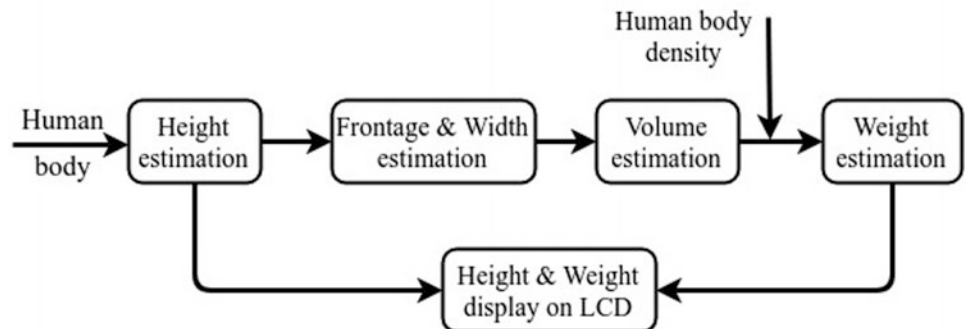


Fig. 3 Structure of the proposed algorithm for weight and height estimation



increase the accuracy of the measurement, the beam width should be narrowed by installing a paper tube around both heads of the sensor [8].

Volume estimation. Volume V of a human body is estimated as a first-order function of 3 independent parameters:

$$V = H.F.W.\alpha \tag{2}$$

where α is the compact coefficient. We have determined the value of this coefficient by measuring the body parameters (height, weight, frontage) and the true value of the human body volume (measured by water displacement technique [3]) of a set of 50 men and women with the ages between 15 and 60 and infer the value of α from these measured values.

The estimated α value of the sampled human bodies is 0.385 and this value is used to estimate the volume of Vietnamese human bodies since Asian population demonstrates significantly small variation in key body measures within population [9]. This value is critical for an accurate estimation of the human body volume. Experimental measurements show that although the value of α varies with the physical shape of the body of interest, from person to person as well as from men to women, the value lies in the range of [0.37; 0.41].

Weight estimation. After having an estimated value of human body volume, we can easily get a quite accurate estimation of human body weight (W_E) using the formula:

$$W_E = V.B \tag{3}$$

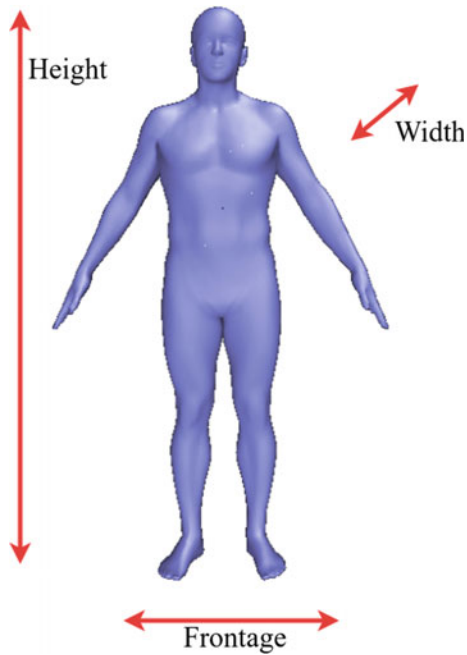


Fig. 4 Defined dimensions of a human body

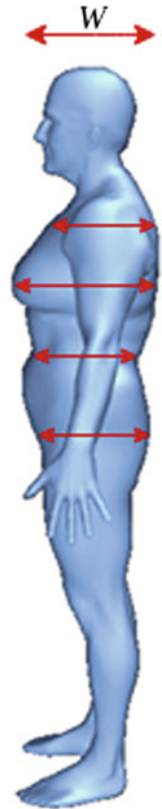


Fig. 6 Estimated W value is the mean of the measured values

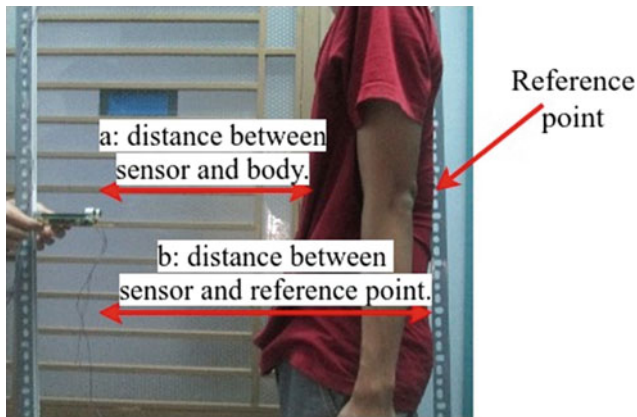


Fig. 5 Dimension Width (W) estimation using sensor

where Weight is calculated in kg, Volume is calculated in m^3 and B is human body density whose average value is approximately 985 kg/m^3 , according to [3].

3 Experimental Result

Figure 7 is a photograph of the implemented circuit board which contains 3 components: the Arduino microcontroller, the ultrasonic sensor SRF04 and the LCD screen. The measurements were conducted on 12 distinct individuals, (6 men, 6 women with the ages between 15 and 60). Each subject was measured 3 times. The α value being used is 0.385. Tables 1 and 2 show the results of the experiments.

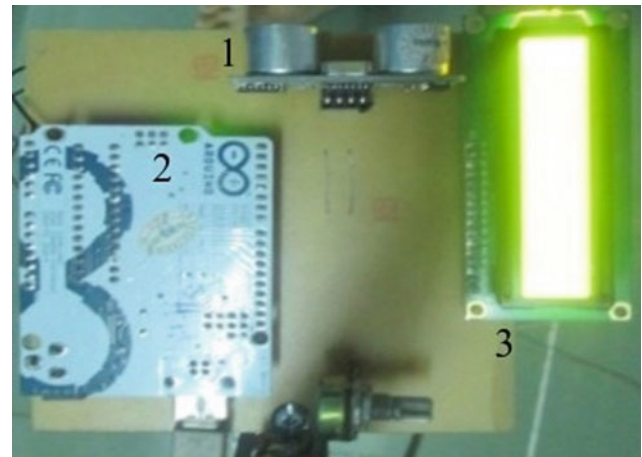


Fig. 7 The implemented board for the measurements with 1—the ultrasonic sensor, 2—the Arduino Uno R3 and 3—the LCD screen

One can see that while the variance of the measured height values is quite small and neglectable, the variance of the measured weight values is quite high compared to other electronic devices. This is due to the inaccuracy of the dimension estimations (i.e., frontage estimation and width estimation) when the individual who is under the test takes in a breath and thus changes his/her overall body volume. Height measurement is, in some senses, a simple measurement compared to the weight measurement.

Table 1 Measured heights and weights

Person	Measured heights (cm)			Measured weights (kg)		
	1st	2nd	3rd	1st	2nd	3rd
1	174	175	175	57.74	59.93	61.32
2	174	173	172	78.92	67.84	75.01
3	171	169	172	57.87	54.67	56.13
4	157	160	159	64.78	63.23	62.76
5	173	176	174	60.24	64.97	65.61
6	165	168	169	59.67	66.83	65.55
7	175	176	177	52.51	55.43	55.56
8	164	167	168	76.71	75.03	88.96
9	169	171	171	65.45	67.16	71.33
10	180	181	181	70.12	71.35	72.06
11	185	185	184	75.55	76.72	74.42
12	192	193	192	78.82	77.58	79.05
<i>Average variance</i>			<i>1.13</i>			<i>7.48</i>

Table 2 Errors in the measurements

Person	Average height	Real height	Error (%)	Average weight	Real weight	Error (%)
1	174.67	175	0.1	59.66	57	4.67
2	173.00	174	0.5	73.92	75	1.44
3	170.67	170	0.3	56.22	55	2.22
4	158.67	159	0.2	63.59	61	4.25
5	174.33	175	0.3	63.61	62	2.59
6	167.33	168	0.3	64.02	63	1.61
7	176.00	177	0.5	54.50	52	4.50
8	166.33	166	0.2	80.23	83	3.30
9	170.33	170	0.2	67.98	70	2.90
10	180.67	181	0.18	71.18	70	1.69
11	184.67	185	0.18	75.56	77	1.88
12	192.33	192	0.17	78.48	80	1.90
<i>Average error</i>			<i>0.26</i>			<i>2.75</i>

Table 2 shows the errors in the height and weight measurements, which depend on the inaccuracy of the sensor, the value of α (compact coefficient) and the value of B (human body density). A comprehensive inspection of the value of α and B can help reduce the error to less than 2.3%.

4 Discussion

In this paper, we described the design and implementation of a device which can estimate the human body height and weight through a non-contact approach using the ultrasonic

sensor. This method of measuring human body weight and height does not outperform traditional methods (with less than 0.1% lower accuracy in the height measurement and less than 1.5% lower accuracy in the weight measurement). However, this method overcomes one major drawback of traditional weight measurement method (using weight scale) is that the output measured weight changes with altitude due to the change of the gravitational acceleration value with altitude. When compared to other products to measure human body's height and weight such as the infrared laser of Microsoft's Kinect camera, our product cost is much lower. The system cost will reduce drastically if it is in mass

production. One of the ways to reduce the cost of the product is to replace the Arduino microcontroller with specific ICs (Integrated circuit), which are equivalent to the Arduino microcontroller with a lower price. Although accuracy is not one of the advantages of the product, we strongly believe that we can improve its quality and accuracy in the future. The following subsections discuss the advantages, drawbacks and the ways to improve the accuracy of the system.

4.1 Advantages

Our product provides a simple approach for measuring human body height and weight that differs from other traditional methods when the body weight is estimated through its dimensions/sizes. It helps to:

- Overcomes one major drawback of traditional weight measurement using weight scale: the output measured weight changes with altitude due to the change of the gravitational acceleration value with altitude.
- Integrate height measurement and weight measurement in one measurement device.
- Measure human body parameters without any limitation to the height and weight value range of the body being measured.

It is easy to increase the range of the measurement by switching to a better ultrasonic sensor.

4.2 Drawbacks

There still exists some shortcomings in the projects, some major imperfections are:

- In order to have a reasonable result, the person needs to stand just beside the reference point.
- His/her clothes should fit tightly to his/her body so that the volume estimation step would give a reasonable result.

4.3 Improvements

In the future, to improve the product's performance, we suggest some solutions:

- Setting costume requirements for human body measurement. People should wear tight clothes to reduce error in estimations.
- Improving the accuracy of the sensor by replacing the SRF04 sensor with a better, more advanced sensing technologies such as laser, infrared or magnetic sensor.
- Improving the accuracy of the volume estimation by providing a more accurate value of α and human body density B using statistical analysis method.
- Programming the device to automatically taking measurements and sending the measured data to the user using IoT technology.

5 Conclusion

Using a system of ultrasonic sensor and Arduino development platform, we can measure the height, the width and the frontage of the human body, then calculate its volume and subsequently, its weight based on the human body's density information. While the measured height is very close to the real height with less than 0.3% error, in the weight measurement operation, there are still some substantial errors. It is understandable since the depth of a human body changes when the person breaths. Breathing leads to the change in the human body's volume and subsequently, to the error in the weight measurement. Moreover, clothing is one of the elements that make the results inaccurate. Therefore, we recommend that people should hold their breath and wear tight clothes during the measurements.

Conflict of Interest The authors declare that they have no conflict of interest.

References

1. Singh, S.P., Mehta, P.: Human Body Measurements: Concepts and Applications, 1st edn. Prentice Hall of India, India (2009)
2. Xu, H., Yu, Y., Zhou, Y., et al.: Measuring accurate body parameters of dressed humans with large-scale motion using a kinect sensor. *J. Sens.* **13**, 11362–11384 (2013)
3. Krzywicki, H.J., Chinn, K.S.K.: Human body density and fat of an adult male population as measured by water displacement. *Am. J. Clin. Nutr.* **20**(4), 305–310 (1967)
4. Sendroy, J., Collison, H.: Determination of human body volume from height and weight. *J. Appl. Physiol.* **21**(1), 167–172 (1966)

5. Weenk, D., van Beijnum, B.J.F., Roetenberg, D., et al.: Ambulatory estimation of relative foot positions by fusing ultrasound and inertial sensor data. *IEEE Trans. Neural Syst. Rehabil. Eng.* **23**, 817–826 (2015)
6. Dang, T.T., Nguyen Tran, K.Q., Le, H.M., et al.: A tool using ultrasonic sensor for measuring breathing rate. In: *The 6th International Conference on the Development of Biomedical Engineering in Vietnam (IFMBE)*, pp. 139–143 (2016)
7. University of Utah: Ultrasonic sensors lab exercise. <http://www.mech.utah.edu/~me3200/labs/sonar.pdf>. Last accessed 13 May 2018
8. Devantech Limited Company: Ultrasonic sensor datasheet. http://www.robot-electronics.co.uk/htm/sonar_faq.htm. Last accessed 13 May 2018
9. Webster, J., Cornolo, J.: Comparison of European and Asian morphology. In: *The 4th International Conference on 3D Body Scanning Technologies*, pp. 238–242 (2013)

Brain Tumor Segmentation Using U-Net Based Deep Neural Networks

Hai Thanh Le and Hien Thi-Thu Pham

Abstract

Treatment planning plays an important role in improving the quality of life of patients, especially in brain tumor disease. Magnetic resonance imaging (MRI) is a widely used imaging technique to assess these tumors, but the large of data obtained by MRI makes manual segmentation in time-consuming, less precise quantitative measurements in the clinical practice. We present an automatic brain tumor segmentation method based on a deep neural network with U-Net architecture to classify tumorous tissues into four classes for necrosis, edema, non-enhancing and enhancing tumor. Our network was trained and validated on the Brain Tumor Segmentation Challenge 2013 (BRATS 2013) dataset. Our method obtained the high performance score with the metric values Dice = 0.83 and sensitivity = 0.85. These results were compared to the similar methods.

Keywords

Brain tumor • Deep neural networks • Segmentation • U-Net

1 Introduction

Accurate brain tumor segmentation plays a key role in cancer diagnosis, treatment planning, and treatment evaluation. Since manual segmentation of brain tumors is laborious, the development of semi-automatic or automatic brain tumor

segmentation methods makes enormous demands on researchers [1]. Ultrasound, computed tomography (CT) and magnetic resonance imaging (MRI) acquisition protocols are standard image modalities used clinically. Many previous studies have shown that the multimodal MRI protocols can be used to identified brain tumors for treatment strategy because the different image contrasts of these MRI protocols can use to extract important complementary information. The multimodal MRI protocols include T2-weighted fluid-attenuated inversion recovery (FLAIR), T1-weighted (T1), T1-weighted contrast-enhanced (T1c), and T2-weighted (T2).

In recent years, an annual workshop and challenge, called Multimodal Brain Tumor Image Segmentation (BRATS), is held for different benchmark methods that developed to segment the brain tumor [2]. Our previous method [3] trained ExtraTrees classifier for brain tumor segmentation based on a region of interest (ROI) of tumor in FLAIR sequence. This method obtained 0.9 Dice score of the complete tumor but remained the low score of enhancing and core tumor with BRATS 2013 dataset [2].

Various deep learning methods have achieved the high score in BRATS challenges [4–6]. A detailed review of various medical image classification, segmentation and registration methods can be found in [7]. Biomedical images have many patterns of the object such as a tumor, and their intensities are usually variable. Ronneberger et al. [8] developed the U-Net based fully convolutional networks (FCNs), which consisted of a down-sampling (encoding) pathway and an up-sampling (decoding) pathway with residual connections between the two that concatenate feature maps at different spatial scales, to segment the cell cancer. Based on the original U-Net architecture, some groups [9, 10] proposed a method for brain tumor segmentation and achieved the competitive performance of those built models with BRATS datasets.

In this study, we present a novel 2D segmentation method that uses the fully convolutional neural networks (FCNNs)

H. T. Le (✉)
HCMC University of Technology, VNU HCMC, Ho Chi Minh
City, Vietnam
e-mail: lthai@hcmut.edu.vn

H. T.-T. Pham
International University, VNU HCMC, Ho Chi Minh City,
Vietnam

by U-Net architecture [8] to detect and segment tumorous tissues in the brain. The proposed network has been evaluated on BRATS 2013 dataset acquired for both LGG and HGG patients.

2 Method

2.1 Dataset

The proposed method is trained and validated on the BRATS 2013 dataset [2] which consists of 30 patient MRI scans of which are 20 HGG and 10 LGG. Each patient has four MRI sequences including FLAIR, T1, T1c, and T2 as shown in Fig. 1. This dataset with multimodal MRI data that has been already skull-stripped, registered into the T1c scan and interpolated into $1 \times 1 \times 1 \text{ mm}^3$ with a sequence size of $240 \times 240 \times 155$. In addition, the ground truth images of dataset were manually labeled into four types of intra-tumoral classes (labels): 1-necrosis (red), 2-edema (green), 3-non-enhancing (blue) and 4-enhancing tumor (yellow) and the others are 0-normal (healthy) tissue (black). The ground truth data have been used in two steps, model training, and final segmentation performance evaluation.

However, in this study we build a segmentation network using three MRI modalities with FLAIR, T1c and T2 to reduce the memory and training time but it still achieves competitive performance as proved by Zhao et al. [11].

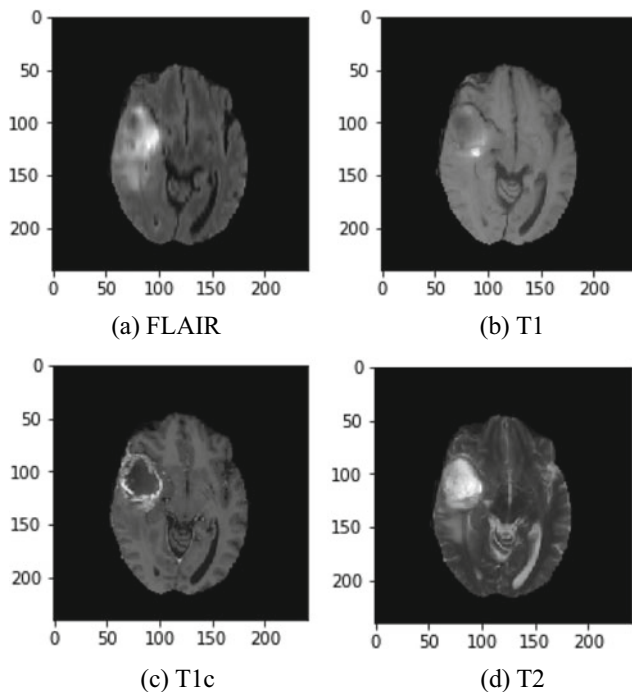


Fig. 1 Four MRI modalities in imaging data from HGG patient 0001

2.2 Preprocessing

In this study, we applied the N4ITK method [12] to reduce inhomogeneity in MR images. A histogram normalization method [13] was then employed to address data heterogeneity caused by multi-scanners acquisitions of MR images. Finally, the intensities of each MRI sequence are normalized by subtracting the average of intensities of each sequence and dividing by its standard deviation.

2.3 U-Net Based Deep Convolutional Neural Networks

Our network is similar in spirit to the U-Net [9] which is different from the original U-Net [8]. The U-Net architecture [9] as shown in Fig. 2, uses deconvolution operator instead of an up-sampling operator in the decoding path and applies zero padding to keep the same resolution of output images as the input images. Therefore, the network does not require a cropping operator of the border regions. Our network is then added the batch normalization [14] layer after each convolutional layer for regularization purposes. On the other hand, our model also has a slight difference from [9] for inputting the full slices of three modalities of BRATS dataset with a size $240 \times 240 \times 3$.

For batch optimization, we use the stochastic gradient descent (SGD) algorithm to update the parameters at each iteration. The SGD simply gets rid of the expectation in the parameter update and calculates the gradient of the parameters using only a few training examples that help to reduce the variance in the update and get more stable convergence. The parameters of our SGD optimizer are set as: learning rate = 0.0001, decay = 0.01 and the maximum number of epochs = 100.

2.4 Training Set and Test Set

From BRATS 2013 dataset, we used the first half of HGG and LGG cases with three MRI modalities (FLAIR, T1c, T2) for the training set and the second half of dataset including 10 HGG and 5 LGG cases are used to validate the performance of our method. In this study, the HGG and LGG training sets are combined, trained and cross-validated together.

2.5 Performance Evaluation

The final step of segmentation is an evaluation of the obtained results. In this study, we evaluate the tumor segmentation on three sub-tumoral regions followed [2] as the enhancing tumor, the core (necrosis + non-enhancing

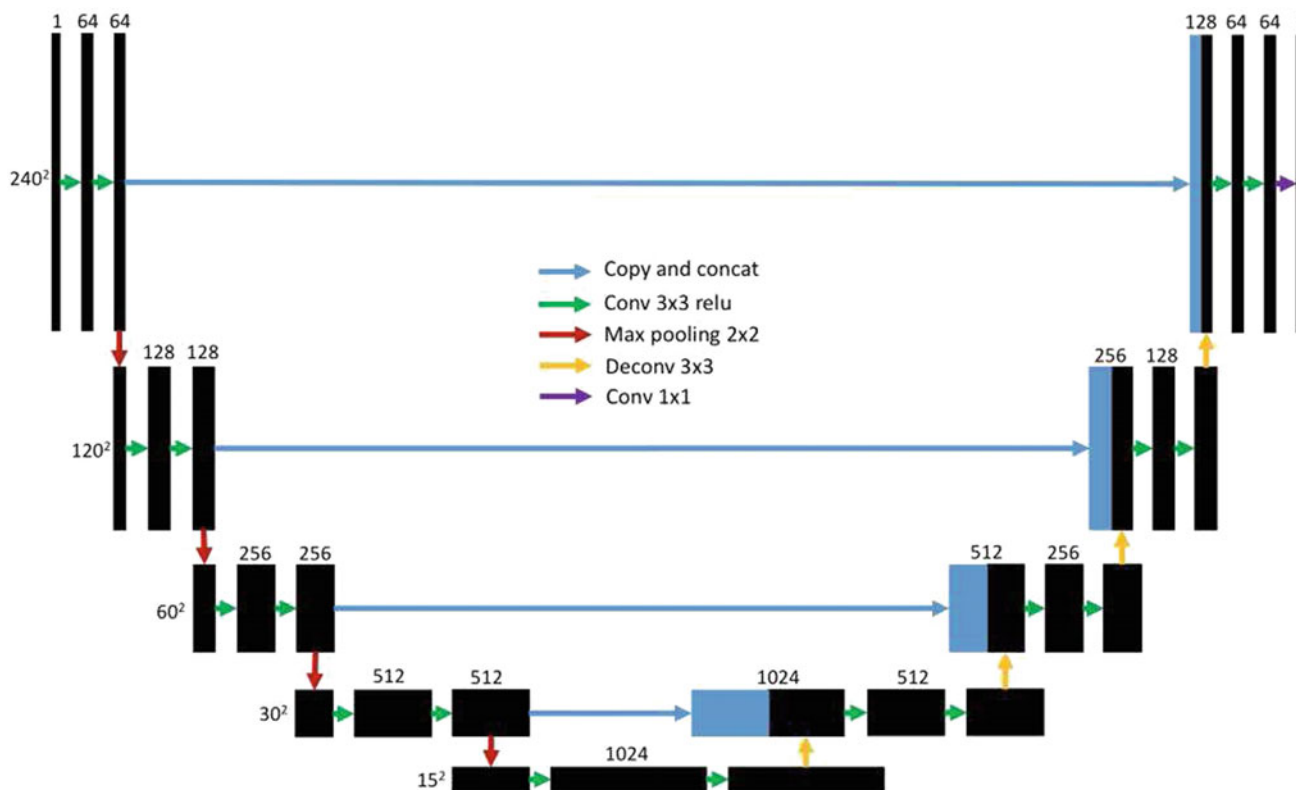


Fig. 2 U-Net architecture [9]

tumor + enhancing tumor), and the complete tumor (all classes combined) by the measurements of Dice coefficient and Sensitivity as described in [15].

3 Results and Discussion

In this study, we proposed the 2D segmentation model based fully convolutional neural networks using U-Net architecture with three MRI modalities for solving the brain tumor segmentation challenge. For HGG and LGG training sets, the images were selected from each MRI sequence that depended on their ground truth's energy with a threshold value of HGG greater than LGG. Therefore, this step helped to reduce the number of images which are put into U-Net model to extract features for training data.

Our U-Net model was implemented in Keras [16] with a TensorFlow [17] backend. The most advantage of our proposed method is that the training time is only around one hour, but for the prediction, the computation time is about $2 \div 3$ min per case. Compared to some studies, our computational time is less than [5, 6] and longer than [9].

The results of our proposed method which is applied on BRATS 2013 dataset and the recent the state-of-the-art methods validates on the same dataset are shown in Table 1. Table 1 shows that our method achieves the promising results in Dice score and performs slightly better in sensitivity measurement for all types of brain tumor with the smaller data for learning.

Figure 3 shows some examples of our qualitative overlaid segmentation results for both HGG and LGG patients on FLAIR MR images compared to the ground truth images. The segmented results are colored as described in Dataset

Table 1 Dice and sensitivity scores of our proposed method compared to the results from other groups recently published ExtraTrees and U-Net based methods for BRATS 2013 dataset

Method	Dice score			Sensitivity		
	Complete	Core	Enhancing	Complete	Core	Enhancing
Proposed	0.83	0.81	0.72	0.85	0.83	0.75
Our previous [3]	0.90	0.63	0.61	0.87	0.72	0.65
Dong [9]	0.86	0.86	0.81	0.88	0.90	0.78

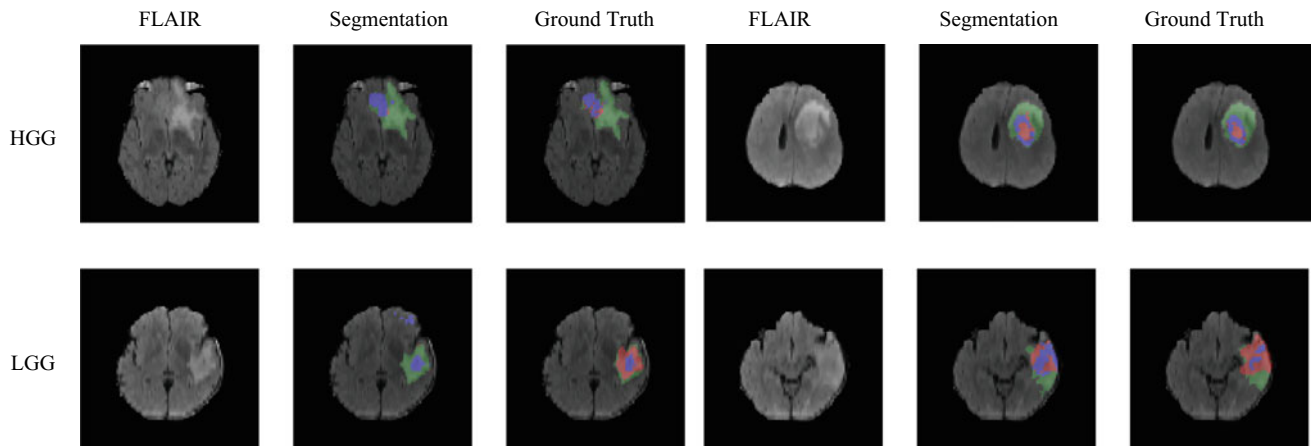


Fig. 3 Segmentation results for the HGG and LGG patients compared to their ground truth

section. Due to the limitation of resource, our model is only trained and evaluated on the BRATS 2013 dataset, which contains much less HGG and LGG patient cases than the BRATS 2015 dataset. Besides, our model segmenting the enhancing tumor for LGG cases is less successful than for HGG cases because there are fewer LGG cases than HGG cases and in most of LGG cases rarely have regions of enhancing tumor.

4 Conclusion

In this paper, we developed a learning-based automatic method for brain tumor segmentation in three MRI modalities (FLAIR, T1c, T2). This method uses the U-Net based deep convolutional networks to segment the brain tumor. Based on the experiment results on the BRATS 2013 dataset, our model can obtain robust segmentation with efficient memory and training time compared to the manual ground truth. Furthermore, in comparing to other state-of-the-art methods, we demonstrated that our approach could achieve comparable results with average Dice scores of 0.83, 0.81, 0.72 for whole tumor, tumor core and enhancing tumor core, respectively.

Conflict of Interest The authors declare that they have no conflict of interest.

References

- Bauer, S., Wiest, R., Nolte, L.P., Reyes, M.: A survey of MRI-based medical image analysis for brain tumor studies. *Phys. Med. Biol.* **58**, 97–129 (2013)
- Menze, B.H., et al.: The multimodal brain tumor image segmentation benchmark (BRATS). *IEEE Trans. Med. Imaging* **34**(10), 1993–2024 (2015)
- Le, H.T., Pham, H.T.T.: Automatic brain tumor segmentation using extremely randomized trees. *J. Sci. Technol. (Tech. Univ.)* (accepted)
- Pereira, S., Pinto, A., Alves, V., Silva, C.A.: Brain tumor segmentation using convolutional neural networks in MRI images. *IEEE Trans. Med. Imaging* **35**, 1240–1251 (2016)
- Havaei, M., et al.: Brain tumor segmentation with deep neural networks. *Med. Image Anal.* **35**, 18–31 (2017)
- Kamnitsas, K., et al.: Efficient multi-scale 3D CNN with fully connected CRF for accurate brain lesion segmentation. *Med. Image Anal.* **36**, 61–78 (2017)
- Litjens, G., Kooi, T., Bejnordi, B.E., Setio, A.A., Ciompi, F., Ghafoorian, M., van der Laak, J.A.W.M., Ginneken, B.V., Sanchez, C.I.: A survey on deep learning in medical image analysis. *Med. Image Anal.* **42**, 60–88 (2017)
- Ronneberger, O., Fischer, P., Brox, T.: U-Net: convolutional networks for biomedical image segmentation. *Med. Image Comput. Comput.-Assist. Interv.* 234–241 (2015)
- Dong, H., Yang, G., Liu, F., Mo, Y., Guo, Y.: Automatic brain tumor detection and segmentation using U-Net based fully convolutional networks. *arXiv preprint arXiv:1705.03820v3* (2017)
- Beers, A., et al.: Sequential 3D U-Nets for biologically-informed brain tumor segmentation. *arXiv preprint arXiv:1709.02967v1* (2017)
- Zhao, X., Wu, Y., Song, G., Li, Z., Zhang, Y., Fan, Y.: A deep learning model integrating FCNNs and CRFs for brain tumor segmentation. *Med. Image Anal.* **43**, 98–111 (2018)
- Tustison, N.J., et al.: N4ITK: improved N3 bias correction. *IEEE Trans. Med. Imaging* **29**(6), 1310–1320 (2010)
- Loizou, C.P., Pantziaris, M., Pattichis, C.S., Seimenis, I.: Brain MR image normalization in texture analysis of multiple sclerosis. *J. Biomed. Graph. Comput.* **3**(1), 20–34 (2013)
- Ioffe, S., Szegedy, C.: Batch normalization: accelerating deep network training by reducing internal covariate shift. In: *Proceedings of the 32nd International Conference on Machine Learning*, vol. 37, pp. 448–456, Lille, France (2015)
- Powers, D.M.: Evaluation: from precision, recall and F-measure to ROC, informedness, markedness and correlation. *J. Mach. Learn. Technol.* **2**(1), 37–63 (2011)
- Keras Homepage: <https://github.com/keras-team/keras>. Last accessed 15 May 2017
- Tensorflow Homepage: <https://www.tensorflow.org/>. Last accessed 15 May 2017

Noncontact-Body-Temperature-Measurement

N. T. Hang, P. T. N. Thao, Tin T. Dang, and Anh Dinh

Abstract

Our study aims to design the prototype system, which includes the non-contact temperature sensor, embedded system, and database. Using a specialized mechanical fixture and a simple calibration technique, preliminary results show desirable temperature measurement performance. To reduce the inconvenience caused during direct measurement to the users such as having the thermometer clamped to one part of the body (mouth, armpit, or rectum) and kept fixed for a certain period, our device provides a new measuring method without the need for contact and quickly displays results with high accuracy compare with other devices. Moreover, our purpose is to use this device for making the timely diagnosis of malaria through the human temperature in households, schools, and hospitals.

Keywords

Non-contact • Infrared thermal • Temperature • Microcontroller • Reducing noise

1 Introduction

The temperature of the human body is one of four main vital signs which must be observed daily to ensure safe, effective care and is being applied in all healthcare environments [1]. Consequently, recent years have seen increased attention being given to automatic temperature monitoring technology. In comparison with traditional techniques including the Digital Axillary Thermometer (DAT), the automatic

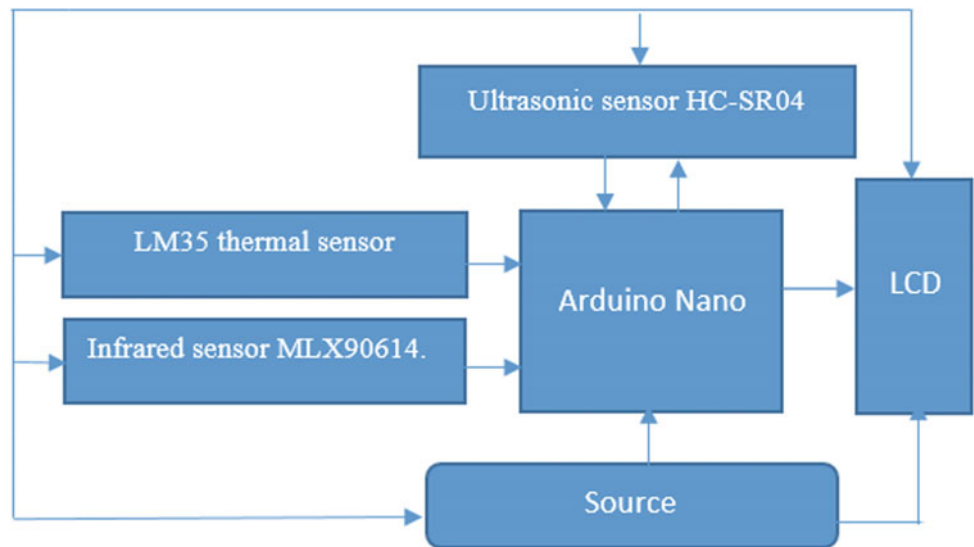
thermometer can reduce the labor cost and capture continuous, reliable and rapid recording.

This paper deals with non-contact measurement methods, using the infrared sensor. Everything emits infrared light. Infrared sensor detects infrared light and microcontroller analyze them to get the temperature. Non-contact thermometers use infrared thermal allow measure body's temperature with minimal (tympanic membrane) or no (Non-contact Infrared thermometer NCIT) contact with the body [2]. Moreover, allowing for easier and faster use when monitoring huge numbers of individuals like in school, in hospital, in airports or in border crossings (limit the disinfection of the thermometer process), apply widespread following the SARS(Severe Acute Respiratory Syndrome) infection, and particularly during the pandemic H1N1 outbreak [3]. In a similar situation when the outbreak of the disease in Hong Kong, the student was required to measure their body temperature at the entrance of the school. The design of an automatic and rapid measuring device is an urgent demand. However, the accuracy of the device is a matter to be considered and it also causes a lot of discomfort when users wear the device like a forehead mask [4]. In the researching process, we found that infrared sensors give inaccurate results due to the effect of external factors such as ambient temperature and distance from the sensor to the object.

Consequently, in our paper, we find an approximately function to reduce noise. Besides the infrared sensor MLX90614 [5] for non-contact temperature measurement, we use (SONAR) sensor [6] to measure distance and the thermal sensor LM35 [7] to capture the environment temperature. The approximation functions based on the distance, environment temperature and body temperature will be calculated by excel. Then, we applied them to the Arduino IDE's program to gain the exact temperature for each circumstance and display in the LCD [8]. By taking into account the influence of environmental factors, the approximation gives a more realistic result, respond flexibly to

N. T. Hang · P. T. N.Thao · T. T. Dang (✉)
Faculty of Electrical and Electronics Engineering, Ho Chi Minh
City University of Technology, Ho Chi Minh City, Vietnam
e-mail: dtin@hcmut.edu.vn

A. Dinh
Department of Electrical and Computer Engineering, University of
Saskatchewan, Saskatoon, Canada

Fig. 1 Operational principle

changes in the environment and contributes to simplifying the measurement process.

2 Hardware Design and Operating Principle

2.1 Hardware Design

According to the method described above, the components on the board are divided into four main units:

- *Receiver, transmitter, data processor*: LM35 thermal sensor, ultrasonic sensor HC-SR04, infrared sensor MLX90614.
- *Control Device*: Arduino Nano [9], LCD Contrast Ratio Switch, On/Off Switch.
- *Display Device*: LCD.
- *Independent DC power supply*: source 9 V DC.

The relationship between the components is shown in the diagram. We use the power 9 V to power all the devices in our system. The environmental temperature is measured by the LM35 sensor. To determine the human temperature, we use the Infrared sensor. The other essential data is the distance between the human and the sensor which is measured by the ultrasonic sensor. All data is transmitted to the Arduino Nano, which will combine, process, output the result to the user. When all data is processed, we use LCD to display the result (Fig. 1).

Arduino with LCD: The Arduino Nano is complete, small, board-friendly board base on the ATmega328 (Arduino Nano 3.0) or ATmega168 (Arduino Nano 2.x), in this product, we use Arduino 3.0. This board is easy to use

and programming (using Arduino IDE software based on C programming language) and connected to LCD through 12, 11, 5, 4, 3, 2 pins. We use LCD 16×2 , with 2 rows on the screen, each row has a maximum of 16 characters. During measurement, the LCD shows the distance, ambient temperature, and temperature from the IR sensor. After calculating the influence of environment, the value of the MLX is replaced by the body temperature (Fig. 2).

Thermal sensor LM35: LM35 [7] is an analog, linear temperature sensor. The voltage output of the LM35 increases 10 mV per degree Celsius rise in temperature. The accuracy is high and depends on the temperature range, at a temperature of 25 °C, the error is ± 1 °C, the room temperature accuracy is 0.25 and the error between -55 and 150 is ± 1.5 °C. We can calculate the temperature:

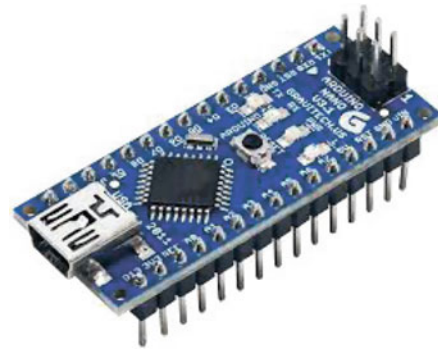
$$U = t * k \quad (1)$$

$$t = U/k = 1.1/1024/0.01 = 0.10742188 \text{ } ^\circ\text{C} \quad (2)$$

where U is the value read from the analog-Read function and U = 1.1 is the maximum value of the reference voltage, connected to Arduino via A0 pin and k = 0.01. This means that it will map input voltages between 0 and 1.1 volts into integer values between 0 and 1023. This yields a resolution between readings of 1.1 volts/1024 units or 0.0010742188 volts (1.0742 mV) per unit. So, the temperature is 1.0742/10 equal to 0.10742188 per unit.

Infrared sensor: Infrared sensor MLX90614 [5] uses I2C interface. It has a compact design, high precision thermal sensor. This sensor calibrated in wide range: -40 to 125 °C for sensor temperature and -70 to 380 °C for the object temperature, high accuracy of 0.5 °C within the range of 0–50 °C for both T ambient and T object. This sensor can

Fig. 2 Arduino nano [9] and LCD 16x2 [8]



(a) Arduino nano.



(b) LCD 16x2.

transmit continuously the measured object temperature for an object temperature range of -20 to 120 °C with an output resolution of 0.14 °C by the 10-bit PWM. Supported by the Adafruit-library Master [10] and is communicated with Arduino by two pins A4 and A5. Follow is the image of MLX90614 sensor (Fig. 3).

Ultrasonic (SONAR): Module Ultrasonic sensor HC-SR04 [6] is able to measure the range from 2 to 400 cm, precision 3 mm and effectual angle is smaller than 15° . The working principle of the ultrasonic sensor is as follows: the high-level signal is sent at least $10 \mu\text{s}$ by using IO Trigger. The module sends eight 40 kHz signal automatically and then detects whether a pulse is received or not. If the signal is received, through high level, time of high duration is the time gap between sending and receiving the signal.

$$\text{Distance} = (\text{Time} \times \text{Speed of Sound} \in \text{Air}) / 2 \quad (3)$$

In the circuit connections, “TRIGGER” an “ECHO” pins are connected to pin (A4) and (A5) of Arduino. This sensor



Fig. 4 Ultrasonic sensor [6]

measures precisely the distance without actual contact and used at several places like water level measurement, small distance measurement (Fig. 4).

2.2 Operating Principle

Figure 5 is the flow chart which talks about the method that we can define and calculate the approximating function. At first, we have to measure the body temperature in twelve times by the IR sensor, so we create a counter begins at 1 and finish at 12, the initial distance is 10 cm (measured by the Ultrasonic sensor). Then, the LM35 sensor is used to measure the ambient temperature, each time the value of T_a and T is saved, we calculate ΔT with $\Delta T = T - T_a$, increase the distance to about 20 cm, and increase the counter to 1, while the counter is smaller than 12, we continue to measure and collect the data from the device. If the variable counts to the last value, we perform the function approximation by excel. Typically, this function is a quadratic or a fifth polynomial of the variable that is the distance between the device and the meter. The accuracy of this function will be checked by comparing the error with 3%. We have to do this process until found the logical result. On the contrary, saving the function. We divide the ambient temperature into a variety of gap, from 23 to 34, increase one degree for one



Fig. 3 MLX90614 sensor [5]

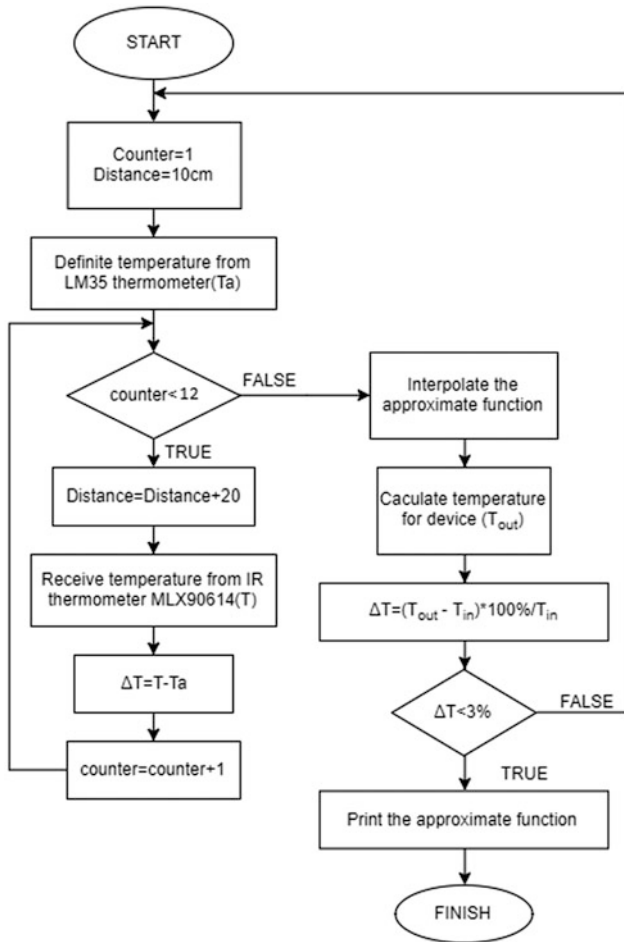


Fig. 5 Operating system algorithm

step, so we have an approximating function corresponding with each T_a . So, the final result quite exactly with the error is smaller than 3%, this rate is the optimal value that we chose from the experimental process. Our final product is shown in Fig. 6.

Body temperature measurement by the infrared sensor (IR sensor) depends on factors such as angle of measurement, vibration, ambient light, ambient temperature. Thus, the result we get is not accurate. In order to have good results, we have to reduce the noise, we made a small tube at the head of infrared sensor to allow transfer directly to the infrared sensor. This tube is presented in Fig. 3b. Next, we remove noise caused by environmental distance and temperature by set function ΔT with L varies at different ambient temperature ranges.

$$\Delta T = T_r - T \quad (4)$$

- T_r ($^{\circ}\text{C}$) is the body temperature measured with a mercury thermometer.
- T ($^{\circ}\text{C}$) is the temperature measured by the LMX90614 sensor.
- L (cm) is the distance from the device to the object defined by the Ultrasonic.
- The ambient temperature is determined by LM35.

Table 1 shows the temperature of the hand measured by 2 devices at an ambient temperature of 28.36°C , where L is the distance from the device to the object, T is the temperature obtained from IR sensor MLX90614, T_r is the temperature measured from the mercury thermometer.

Before reducing noise, the result is far from with the reality, which the average is approximately 19.7%. So, we calculate the function by the distance and environmental factors to minimize the error. Table 2 is the list of ΔT functions at different ranges of ambient temperature.

Figure 7 that is the flow chart, represents the operation of the device. At first, we measure the ambient temperature T_a , if $23 < T_a < 34$, we continue to measure the distance L and receive the temperature from the IR sensor which named T . Then, calculating $T_r = f_{T_a}(T, \Delta T) = T + \Delta T$, which the approximating function ΔT corresponding with T_a and L . Finally, presenting T_r to the LCD. If not, we print $T_r = 0$ into the LCD screen and finish this process.

3 Experimental Results

Figure 8 shows that the hand temperature measured by this device is 35°C , the result is not much different from the actual temperature. T_a is the environmental temperature, T is the body temperature from our product and L is the distance from the user to the equipment.

Table 3 shows the results after eliminating the noise. The correct operating range of device is at an ambient temperature from 23 to 28°C , an error rate from 1 to 3%. IN this table, the error 1 is the error of REFCO LP-79 which is one of the IR thermometer in the market and the error 2 is the error of our product. So, in this case, the result is precise with the small error-approximately 0.9%.

4 Discussion

4.1 Advantage

Non-contact temperature measuring methods are used to overcome the limitations of mercury and electronic

Fig. 6 The final package



(a) The front side of package.



(b) The back side of package with small tube around the IR sensor.

Table 1 The temperature of the hand is measured by IR sensor at 28.36 °C (with noise)

L (cm)	T	T _r	Error
10.13	29.85	35.8	16.62011173
20	29.19	35.8	18.46368715
30.03	28.91	35.8	19.24581006
39.97	28.63	35.8	20.02793296
50.03	28.63	35.8	20.02793296
60.1	28.51	35.8	20.36312849
70.19	28.51	35.8	20.36312849
80	28.57	35.8	20.19553073
89.53	28.59	35.8	20.1396648
99.78	28.53	35.8	20.30726257
110.61	28.53	35.8	20.30726257
120.37	28.59	35.8	20.1396648
Average error			19.68342644

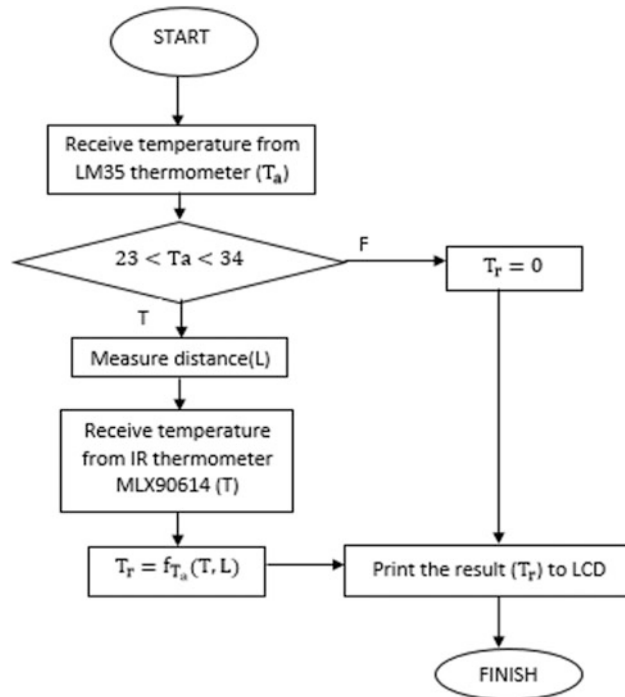


Fig. 7 Operation of device



Fig. 8 Temperature measuring device

Table 2 The approximating function ΔT at different ambient temperature (T_a)

T_a (°C)	ΔT
23–24	$-6E-05L^5 + 2E-07L^4 - 2E-05L^3 + 0.0005 L^2 - 0.0127L + 5.824$
24–25	$-3E-10L^5 + 9E-08L^4 - 7E-06L^3 - 0.0002L^2 + 0.0359L + 5.6334$
25–26	$2E-06L^3 - 0.0006L^2 + 0.0478L + 3.8664$
26–27	$-2E-08L^4 + 7E-06L^3 - 0.0009L^2 + 0.0512L + 3.8116$
27–28	$-3E-09L^5 + 9E-07L^4 - 9E-05L^3 + 0.0038 L^2 - 0.0279L + 6.1046$
28–29	$-3E-08L^4 + 1E-05L^3 - 0.0012L^2 + 0.0796L + 4.9914$
29–30.5	$-4E-08L^4 + 1E-05L^3 - 0.0014 L^2 + 0.081L + 4.8359$
30.5–32	$-3E-08L^4 + 9E-06L^3 - 0.001L^2 + 0.0531L + 3.7695$
32–34	$1E-07L^4 + 3E-06L^3 - 0.002L^2 + 0.1423L + 1.2785$

Table 3 Experimental result after noise cancellation

Ta	L (cm)	Electronic thermometer	REFCO LP-79	Error 1	Device	Error 2
23.85	80.46	32	31	3.125	31.27	2.335
24.17	68.59	32	29	9.375	31.92	0.251
25.89	60.34	32	31	3.125	31.68	1.01
26.43	56.83	32	32	0	31.8	0.629
27.61	64.07	36	32	11.111	36.1	0.277
28.36	68.68	36.1	32	11.357	35.88	0.613
28.47	97.83	36.1	32	11.357	36.48	1.042
28.57	36.89	36.1	32	11.357	35.63	1.319
<i>Average error</i>				7.601	<i>Average error</i>	0.934

thermometers. They could avoid cross-contamination because it is non-contact with the object and also have shorter measuring time. In this product, we concentrate on the noise reduce and bring the convenience to the user. Our product obtains certain enhancements such as, it can measure in longer distance with limiting the effect of some environmental factors (ambient temperature and distance) to the result from the sensors, and its cost is lower than the Infrared thermometer on the market.

4.2 Disadvantage

Our product has some shortcoming, such as, the professional infrared sensor hasn't been used because of its shortage in Vietnam market, the range of temperature is still small.

5 Conclusion and Future Work

Nowadays, there are some better IR sensors such as the medical version and new thermometer sensors which the fresh technique, thus, the results will be more accurate. Moreover, the precision can be improved by increasing the number of sampling times. With industrial scale, we can reduce the size as well as the price of this product.

Conflict of Interest The authors declare that they have no conflict of interest.

References

1. John Hopkins Medicine: https://www.hopkinsmedicine.org/healthylibrary/vital_signs. Last accessed 15 May 2018
2. PubMed Health Homepage: Non-contact Thermometers for Detecting Fever: A Review of Clinical Effectiveness. Canadian Agency for Drugs and Technologies in Health, Ottawa (2014)
3. Ring, E.F.J., Mcevoy, H., Jung, A., Zuber, J., Machin, G.: New standards for devices used for the measurement of human body temperature. *J Med Eng Technol* (2010)
4. Tang, H.-F., Hung, K.: Design of a non-contact body temperature measurement system for smart campus. In: ICCE-China (2016)
5. MLX90614 Datasheet: p. 1, p. 2, p. 26. <http://www.datasheetlib.com/datasheet>. Last accessed 15 May 2018
6. Morgan, E.J., HC-SR04 ultrasonic sensor. <http://centmesh.csc.ncsu.edu>. Nov. 16 2014. Last accessed 15 May 2018
7. LM35 Datasheet: LM35 precision centigrade temperature sensors. Texas Instrument, SNIS 159H-August 1999, revised December 2017
8. LCD 16×2 Datasheet: Specifications of LCD module. Module no: ADM1602 K-NSW-FBS/3.3V, Xiamen Amotec Display co, LTD, 29/10/2008
9. AVRCHIP.COM: Arduino Namo Datasheet and tutorial. <http://avrchip.com/arduino-nano-datasheet-and-tutorial/>. Last accessed 15 May 2018
10. Ladyada: Using Melexis MLX90614 Non-contact Sensors. Adrafruit Learning System. Last update 28 Feb 2014, Last accessed 15 May 2018

Design, Test and Evaluation of a Dental Fluorescence Camera

Thi Hai Mien Pham, Bao Ngoc Tran, Ngoc Minh Thinh Nguyen, Tran Khanh Tran Nguyen, Phu Duong Le, and Quang Linh Huynh

Abstract

Dental diseases are ranked the third disaster after cancer and cardiovascular by World Health Organization. The early diagnosis of decay is important for children and adults to treat and prevent diseases. In this study, a fluorescence device was designed and manufactured for this purpose. Device used a 380-nm LED, which stimulates the luminescence of porphyrins—a product of *Streptococcus Mutans* bacteria in plaque or caries. This equipment was included camera which can record images in real time as well as the fluorescence image was processed by a designed software. The test results showed that the fluorescence camera can detect numerous types of the carious lesions including dental plaque, dental caries, hidden caries and the early stage of caries. In this research, a statistic software was applied for this research in order to show the device's sensitivity and specificity.

Keywords

Camera • Dental caries • Diagnosis • Fluorescence

1 Introduction

Nowadays, in many countries, the knowledge of the oral health is not still concerned properly. Specially, decay is one of the most popular dental diseases. Moreover, it is impor-

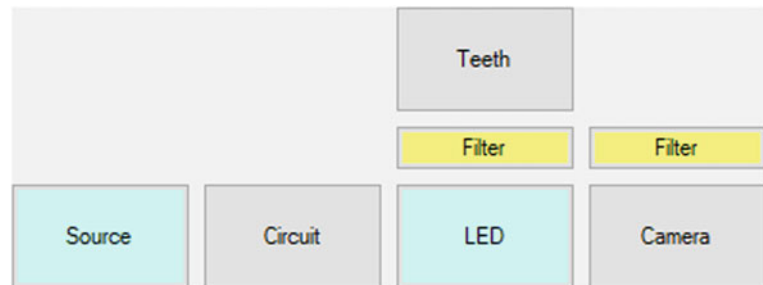
tant to detect the early stage of the carious lesions and still a big challenge for dentist at this moment.

Currently, there are a lot of common diagnostic methods for detecting dental problems such as: clinical inspection, X-rays, optical methods, etc. Traditional method which is the most widespread is the clinical examination; however, this method is not sensitive enough, especially for early lesions and those affecting the proximal tooth surfaces. Bitewing radiographs have also been used for a long time for the detection of proximal lesions, but they are not reliable for occlusal defects, especially when only the enamel is involved [1]. Moreover, the effect on pediatric and pregnant women's health is still existed in X-rays methods. In summarize, a great challenge is being asked to study a new method for detecting dental caries in the early stage that is more accurate and not harmful to patients. As the technology developments, some new diagnostic tools are constantly being researched and developed. One of the new developed diagnostic procedures employs fluorescence diagnostics. Many investigators have shown that under UVA light (near ultraviolet), such as 380 nm, sound teeth emit blue-green color, while caries teeth emit the red fluorescence [2–10]. Based on the difference in the color of the teeth fluorescence caries lesions can be detected.

The fluorescence technique using 380 nm LED is non-destructive, non-invasive, and non-ionizing radiation. Furthermore, this method also showed high sensitivity in the detection of the early demineralization and early dental caries. In this study, a fluorescence camera with 380-nm LED was designed and tested, database was created as well as the sample for ROC curve in order to evaluate the diagnostic capabilities of the device in a medical manner. Last but not least, a software was designed and built to enhance the image's fluorescence contrast and quality by Matlab. Especially, recording and processing image in real time was also supported to observe and evaluate by a designed software.

T. H. M. Pham (✉) · N. M. T. Nguyen · T. K. T. Nguyen · P. D. Le · Q. L. Huynh
Ho Chi Minh City University of Technology, VNU – HCM,
Ho Chi Minh City, Vietnam
e-mail: phamhaimien@hcmut.edu.vn

B. N. Tran
Pham Ngoc Thach University of Medicine,
Ho Chi Minh City, Vietnam

Fig. 1 Device diagram

2 Materials and Methods

2.1 Materials for Device

The device for detecting dental caries is a system that consists of a light source, optical filters, camera, power source and stable voltage circuit, as shown schematically in Fig. 1.

LED. The wavelength and power of light play an important role in stimulating fluorescence. The device used 3W-SMD-LED emitting 380 nm wavelength with 3 W power for exciting teeth fluorescence. The field of view of 380-nm LED had to provide the full overview of the oral cavity in the inspection process. Besides, the device was ensured that device temperature was low to avoid destroying LED.

In addition, the device should be had a radiator because LED was usually operated with high temperature ($\sim 100^\circ\text{C}$). The temperature does not affect the course of the survey and the quality of fluorescence images but shortens the life span of LEDs. A 10 mm-thickness bronze plate combined with thermal compound was set up to the backside of LED. With using this radiator, the temperature was down quickly.

Filters. The light emitted from the 380 nm LED is not monochromatic with a spectrum from 370 to 390 nm. Besides that, the edge of the LED spectrum in the visible region causes the overlap with the fluorescence spectrum of teeth. In this case, one band-pass filter (UG-1, Edmund Optics) was used for passing only wavelengths shorter than 400 nm and eliminating unwanted visible light from the LED.

The 380-nm LED was arranged close to the camera so the LED light can scatter and decrease the quality of fluorescence images recorded by camera. Therefore, a JB490 filter was placed in front of the camera to block the scattered light from LED and pass the fluorescence signals from teeth into camera.

Camera. The fluorescence images of the teeth can be directly observed with the naked eye or through the camera. Due to the poorness of the light and space condition in the oral cavity, the camera should have a short focal length and high sensitive for recording fluorescence image. ORC-03 camera was connected to computer by USB cable 2.0. The distance between camera and teeth is about 1–2 cm for obtaining images with high quality.

Source and stable voltage circuit. LED is provided with 3.3 V-DC-power from batteries or USB port of the computer through a stable voltage circuit and source selector switch. The power of LED is controlled by hand in a flexible manner. The stable voltage circuit receives input from 3.7 to 4.2 V and the output voltage is 3.3 V and makes sure the direct current 280 mA to match the performance parameters of the LED. The used battery was Lipo 1 cell 1000 mAh that can be used for 3 h (Fig. 2).

2.2 Design of Device

The aim of this study was to design a portable fluorescence camera for observation in the oral cavity. Therefore, the device must be easy to use: the camera header is small for comfortable manipulation in the visual inspection, the body of device should be light and fit for hand, and the LED controller in a convenient location for controlling LED intensity. Solidworks software and 3D printing technique were used to manufacture the device body. The body color was black to decrease the scattering from LED light.

2.3 Image Processing

One part of this research is image processing due to the poorness of the light in oral cavity, so that the image quality

Fig. 2 Full device
(length \times width \times height =
233 \times 35 \times 29)



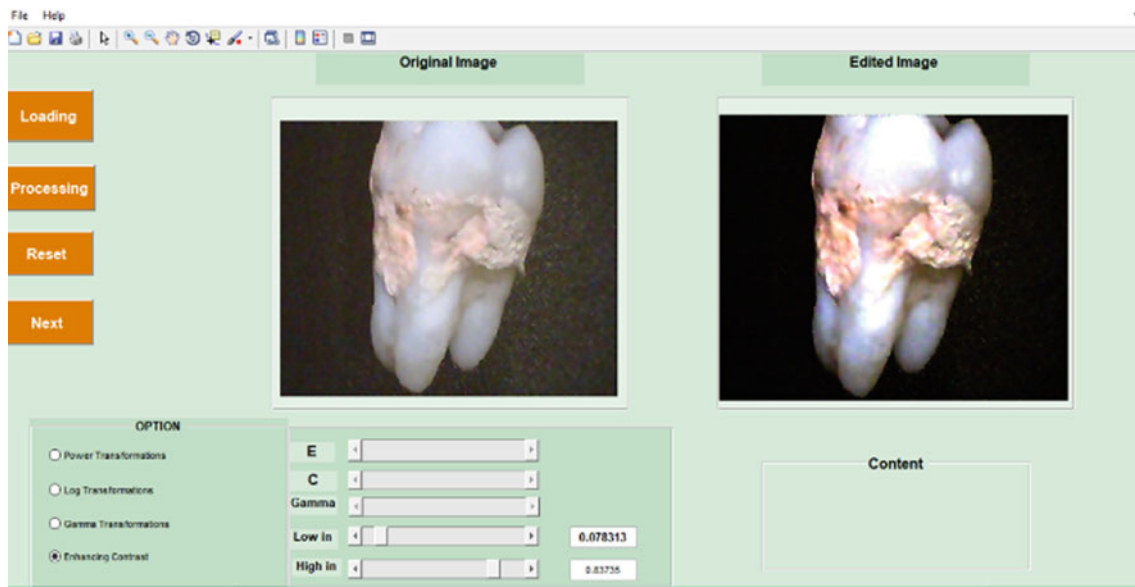


Fig. 3 Default image (left) and processed image (right)

is not high. Thus, the software was designed to enhance the image quality. It was designed by Matlab and can adjust image contrast; segment separately one tooth from others in fluorescence image and record real-time video. By using real-time video, we can observe decay teeth immediately without capturing by camera.

Firstly, we should adjust the contrast image. Matlab has a function that can adjust image intensity values or colormap. This function is *imadjust*, it has structure $s=imadjust(image, [low_in, high_in], [low_out, high_out])$ [11], *image* is matrix picture elements, $low_in=0$ and $high_in=1$, we will input *low_out* and *high_out* to adjust contrast of picture (Fig. 3).

Secondly, when an image was captured in mouth, it could have several teeth in an image. If we want to focus on only one carious tooth for more detailed observation or saving medical record, we will cut this area from whole image. We have 2 choices to cut the image: automatic or by hand. In automatic segmentation, it depends on threshold from Otsu's method [12]. But this way is unusually to use because if 2 teeth were side by side, that method cannot separate them. Thus, we have another choice to segment. By hand, we use computer mouse to cut this area by *imcrop* function in Matlab.

Finally, the last advantage of our device is real time video. Camera was used to capture continuously picture and combine them to create a video. In Matlab, we have a function *snapshot* to do it. Besides, video could be adjusted immediately by using *imadjust* function.

3 Experimental Results and Discussion

All samples, without dental restorations to ensure the presence of questionable occlusal caries, were classified according to the visual criteria of the International Caries Detection and Assessment System (ICDAS).

In the first case, Fig. 4 shows a sound teeth specimen. Under UVA excitation, as can be seen in Fig. 4b, this sample emitted the blue-green color on a white background. As known that the healthy teeth emit blue or green fluorescence when irradiated with near ultraviolet or violet-blue light, respectively [9]. For many years,

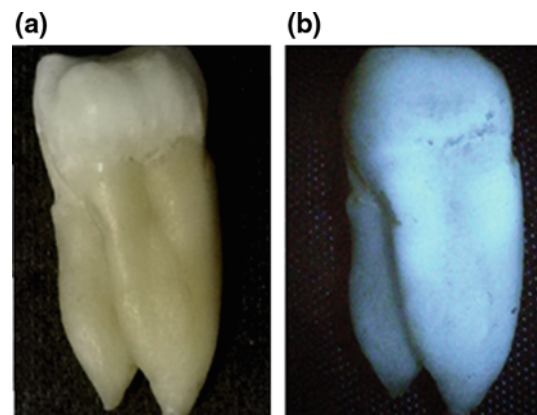


Fig. 4 Sound tooth: white light image (a), fluorescence image (b)

researchers have studied the origin of natural fluorescence in dental hard tissue. Thus, the determination of fluorophores emitting blue–green color in sound teeth requires further investigation.

In the second case, Fig. 5 displays a carious tooth that absorbed energy from LED then emitted spectrum in visible region, including blue and red color. Basically, the higher density of carious bacterium, the stronger red fluorescence. To explain “Why do we see blue-white or red colors on teeth”, we should answer the question “Where is this caries cavity from”? Note that the enamel layer (thickness 1–3 mm) is a filtering membrane allowing the transit of substances from the exterior to the interior, and vice versa. These zones allow the flow of acids from bacterial plaque, giving rise to disintegration of the organic material and posteriorly conditioning demineralization of the inorganic component—thus supporting the proteolysis-chelation theory of dental caries. Thus, these teeth will appear *Streptococcus mutans* bacterium and *Lactobacilli* bacterium which are main reasons why our teeth were destroyed. The mouth contains a wide variety of oral bacteria, but only a few specific species of bacteria are believed to cause dental caries: *Streptococcus mutans* and *Lactobacillus* species among them. The difference of them is *Streptococcus mutans* bacterium producing special substance called Porphyrin, but *Lactobacilli* bacterium is not.

Next, we will answer the question “Why do we see blue-white or red colors on teeth”: it depends on teeth substance. In lesions, *Streptococcus mutans* bacterium produces special substance called Porphyrin which increasing strongly in our plaque and tartar. Porphyrins are the native fluorophores that strongly emits red light under UVA excitation. This fluorescence is detected in some studies [1, 2, 9]. When these areas were stimulated and absorbed by 380 nm LED, these emit longer wavelength in visible region, from 630 to 740 nm wavelength. If density of these areas is high, teeth will clearly show red color. In sound teeth, there are no porphyrin so the healthy teeth emits blue or green fluorescence when irradiated with near ultraviolet or violet-blue light, respectively [7].

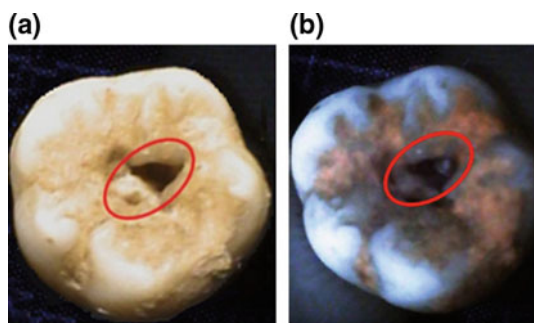


Fig. 5 Carious tooth: white light image (a), fluorescence image (b)

In the last case, Fig. 6 illustrates that red color didn't appear on lesions when stimulated by 380 nm LED. Decay teeth by *Lactobacilli* bacterium also have demineralization but doesn't produce Porphyrin so teeth are not red color. *Lactobacilli* is a saprophylic bacteria, it lives in saprophytic plants and animal's product (example: milk). It can absorb acid, if absorbable time is longer, bacterium will convert more sugar into acid. It leads to lose mineral on teeth's surface but not producing porphyrin. Besides, in experimental process the porphyrin density was lost due to that these teeth maybe were preserved not very well. ROC—Receiver operating characteristic. ROC is a figure that shows sensitivity and specificity. In this study it was used for evaluating efficiency of diagnostic device in detecting dental caries. It is based on a curve line, sensitivity and specificity have value from 0 to 1. If the ROC line is above 45°—line and closed to top and left edges of figure, it means our device is effective. Otherwise, if ROC line is near by 45°—line, it means our device is not effective. An area under the curve line approximate 1 value that means our tests are exact and not exact if 0.5 value.

In our research, we used SPSS software (Statistical Package for the Social Sciences) to draw curve line. SPSS is a statistic software, it helps us to draw ROC line and evaluate the results. In the first step, we should create a dental sample database which included 30 samples. The sample included 13 sound teeth and 17 carious teeth that were evaluated by a dentist (Table 1).

Sensitivity and specificity mean diagnostic probability of caries and diagnostic probability of sound teeth, respectively. In the second step, we used SPSS software to draw ROC line with 3 variables: number, caries and emitting red color. Number is a value from 1 to 30 that help us to mark on teeth. Caries is 0 value for healthy teeth and 1 value for

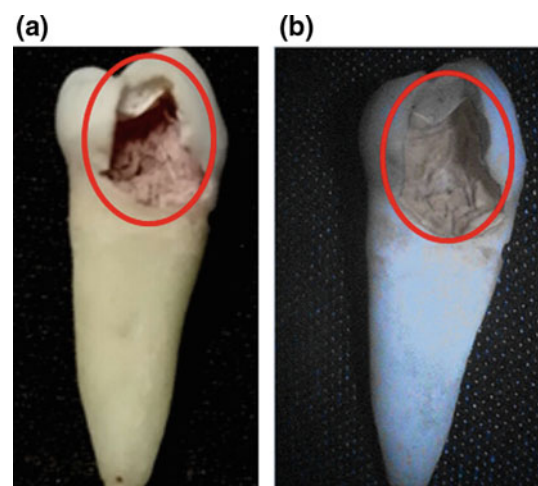


Fig. 6 Carious tooth but not emitting red color: white light image (a), fluorescence image (b)

Table 1 Sensitivity and specificity of device

Fluorescence property	Dental status		Total
	Dental sample		
	Cariou	Not cariou	
Red color fluorescence	15	6	21
Not red color fluorescence	2	7	9
Total	17	13	30

Sensitivity = $15/17 = 0.882$, specificity = $7/13 = 0.538$

decay teeth. Emitting red color is 0 value if tooth did not emit red color and 1 value if it emitted. After entering the data table to SPSS software, this program will analyze the data and draw ROC curve line.

This study shows value of Area under curve (AUC). According to AUC classification, value from 0.9 to 1 show excellent, 0.8–0.9 show good, 0.7–0.8 show medium, 0.6–0.7 show poor and 0.5–0.6 show insignificant value. Our AUC result is 0.71 that shows medium. Software shows the value of sensitivity, specificity and evaluation. The sensitivity value is 0.882 corresponding with 15 teeth emitting red color on 17 carious teeth, the specificity is 0.538 corresponding with 7 healthy teeth not emitting red color on 13 sound teeth.

4 Conclusion

In conclusion, the aim of this research is manufacturing the fluorescence device that supports to diagnose tooth lesions; design the image processing software; and appreciation of experimental results. Firstly, device was designed and manufactured by using 380 nm LED to stimulate teeth, using camera to capture and record image or video from excited teeth. Secondly, image processing software was designed to enhance the image quality. The software has 3 functions: adjusting image contrast, segmenting image by hand and automatic; recording real-time image processing that we can adjust contrast immediately. Besides, experimental results

were applied on 30 teeth including sound and decayed. The fluorescence images had good quality at normal condition: sound teeth emitted blue-white fluorescent image and high intensity while carious teeth emitted red color.

Acknowledgements This research is funded by Vietnam National University HoChiMinh City (VNU-HCM) under grant number **C2018-20-04**.

Conflict of Interest Statement The authors declare that they have no conflict of interest.

References

1. Takorova, M.M., et al.: Effectiveness of near-infrared transillumination in early caries diagnosis. *Biotechnol Biotechnol. Equip.* **30** (6), 1207–1211 (2016)
2. Jenkins, G.N. *The Physiology and Biochemistry of the Mouth*, pp. 54–112. Blackwell Scientific, Oxford, UK (1978)
3. Sukhinina, A.V., Gonchukov, S.A., Bakhmutov, D.N.: Fluorescence Diagnostics of Periodontitis, vol. 37, pp. 175–176. *Bulletin of the Lebedev Physics Institute* (2010)
4. Iulian, I.: Early diagnosis of tooth decay using fluorescence and polarized Raman spectroscopy. *Optoelectron. Adv. Mater.–Rapid Commun.* **3**, 1122–1126 (2009)
5. Laird, W.R.E., Grant, A.A.: Dental bacterial plaque. *Int. J. Biochem.* **15**, 1095–1102 (1983)
6. Uzunov, T.S., Uzunov, T., Grozdanova, R., Kosturkov, D.: Diagnosis of dentin caries—ultraviolet fluorescence, *Acta Medica Bulgarica* **41**, 55–60 (2014)
7. Walsh, L.J., et al.: Ultraviolet-induced fluorescence: Shedding new light on dental biofilms and dental caries. *Aust. Dent. Pract.* **18**(6), 56–60 (2007)
8. Laurence, J.W., et al.: Ultraviolet-induced fluorescence: shedding new light on dental biofilms and dental caries. *Aust. Dent. Pract.* **18**(6), 56–60 (2007)
9. Sinyaeva, M.L., et al.: Fluorescence diagnostics in dentistry. *Laser Phys.* **14**(8), 1132–1140 (2004)
10. Lutskaya, I.K., et al.: Fluorescence of dental hard tissue and restorative materials. *Int. Dent. Afr. Ed.* **2**(5), 162–168 (2012)
11. Mattsson, M.O.: Health effects of artificial light. *Emerging and newly identified health risks*, Brussels. 15–78 (2012)
12. Otsu, N.: A threshold selection method from gray-level histograms. *IEEE Trans. Syst. Man Cybern.* **9**(1), 62–66 (1979)

Application of Near—Infrared Technique in Studying Dental Lesions

Thi Hai Mien Pham, Tran Kim Hoang Nguyen, Thuy Ha Nguyen, Tan Thanh Vo, Phu Duong Le, and Quang Linh Huynh

Abstract

NIR technique depends on scattering and absorption of sound enamel, dentin and damaged tissues in NIR wavelengths. Several researches have indicated that the optical properties of sound and demineralized enamel-dentin in NIR wavelengths are so different. In this study, two optical systems consisting of the transillumination and scattering methods were built to observe the approximal and occlusal of teeth in that order by 850 nm. The NIR images detected from these systems have high contrast. The areas suspected to be the demineralized enamel are distinctly distinguished from the stain and pigmentation because the demineralization areas are a lot darker than the surrounding areas in NIR images. In the clinical examination by using visible light, the early tooth lesions will be difficult to detect if they do not appear on the surface of the tooth. But under NIR illumination, the early tooth lesions are observed clearly in NIR images.

Keywords

Demineralization • Dental • Near-infrared

1 Introduction

Dental lesions are one of the most popular diseases affecting all ages on over the world, especially for children. Dental lesions are formed from a shift in the ecology and metabolic activity of the biofilm, whereby causes an ecological

imbalance in the physiological equilibrium between tooth minerals and oral microbial biofilms by increasing acid concentration ($\text{pH} < 5$) [1]. Some dental lesions like lesions on occlusal surfaces (proximal, buccal and lingual surfaces; cavitation) [2]. Nowadays, the diagnosis for damaged structure of tooth in general and early dental caries in particular are still a challenge for dentistry. Failure to detect dental lesions may leave the clinician with no option but restorative treatment rather than the application of non-invasive measures to reverse or arrest the lesion. Some diagnostic methods of dental lesions including X-rays, clinical visual inspection, caries indicator dyes, fluorescent methods, electrical conductance measurements (ECM), etc., are available.

The visual method is based on the combination of light, mirror, and the probe for detailed examination of every tooth surface, is by far the most commonly applied method in general practice worldwide [3]. With low sensitivity and high specificity, it may be possible to detect noncavitated enamel lesions on the free smooth surfaces (buccal and lingual), most anterior proximal surfaces, and the opening of some fissures [3]. However, this method is not sensitive enough, especially for early lesions and those affecting the proximal tooth surfaces [4].

X-rays is one of the most common diagnostic tool in dentistry. When X-rays pass through the oral cavity, much of the X-rays are absorbed by hard tissues like teeth and bones [3]. The absorbed X-rays will pass through the film or a digital sensor, creation a radiographic image of the tooth. This method makes to observe structure of hard tissue and surrounding soft tissues that cannot be observed by clinical examination methods, for example proximal tooth surfaces. However, this method also produces many adverse effects especially for children and pregnant women by the use of ionizing radiation.

Today, near-infrared method is new research, that is being investigated for the detection of early damages without using of ionizing radiation [5, 6]. NIR method shows tooth structure image detected by NIR camera. The created images

T. H. M. Pham (✉) · T. H. Nguyen · T. T. Vo · P. D. Le · Q. L. Huynh
Ho Chi Minh City University of Technology, VNU-HCM,
Ho Chi Minh City, Viet Nam
e-mail: phamhaimien@hcmut.edu.vn

T. K. H. Nguyen
University of Medicine and Pharmacy, Ho Chi Minh City,
Viet Nam

are based on the optical properties of the tooth due to the transmission, absorption and scattering of dental tissues in NIR wavelength. For enamel, the absorption coefficients are very small in visible light and near [7, 8], while scattering is strong in visible light and weak in NIR [9]. Scattering in enamel decreases, this value is only $2\text{--}3\text{ cm}^{-1}$ at wavelengths 1310 and 1550 nm [8, 9]. It is 20–30 times lower than in visible light [9]. For dentin, the absorption is independent on wavelength in between wavelengths 400 and 700 nm [8]. Dentin strongly absorbs the 543–1060 nm wavelengths [8]. This translates to a mean free path of 3.2 mm for 1310 nm photons, indicating that enamel is transparent in the near infrared [10]. Therefore, near infrared method can observe the tooth structure lesions without the use of ionizing radiation (X-rays).

The damaged tooth structure is mostly demineralized enamel in which mineral density is reduced. Demineralization creates gaps scattering strongly in near infrared at the wall of gaps [10]. For demineralization, the scattering coefficient of demineralized enamel increases by 1–2 orders of magnitude at wavelength 1300 nm [11]. Because of the optical properties difference of sound enamel and demineralized enamel, the contrast between sound enamel and demineralized enamel in the near infrared image is high. In X-rays method, the contrast between sound enamel and demineralized enamel isn't clear [6, 10].

The purpose of this study was to build the optical system observing tooth structure in wavelength 850 nm. Many researches have indicated that wavelength 1300 nm is more effective than 850 nm, it's extinction and absorption of water is nearly 0 cm^{-1} but performance is so hard because of the limited equipment (LED and camera). Therefore, the system used wavelength 850 nm whose extinction is lower than 40 cm^{-1} in enamel and absorption of water is negligible [10]. 850-nm LED and NIR camera are available to get with affordable cost. In this study, the transillumination and the scattering NIR optical systems were designed to record the approximal and occlusal images of teeth.

2 Materials and Methods

2.1 The Transillumination System

The transillumination system shown in Fig. 1 consists of a light source, tooth sample and NIR camera. Approximal image of tooth was observed clearly by this system. transillumination method suits for thin teeth such as incisor and canine. Samples were illuminated at visible light and 850 nm wavelength, operated with an illumination source. In the NIR region, the wavelength and power play an important role in providing image quality. In this study, the 850 nm LED with 3 W power was chosen. An oral camera

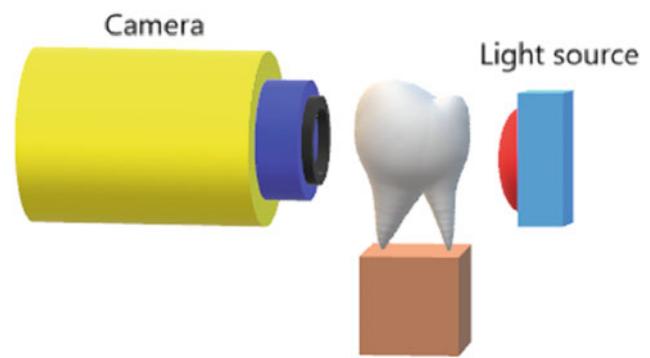


Fig. 1 Schematic diagram of the transillumination system

was used for image acquisition. The camera was connected to computer with USB cable 2.0. The illuminating light intensity and source-to-sample distance ($\sim 1\text{--}1.5\text{ cm}$) were adjusted for each sample to obtain the maximum contrast of images.

2.2 The Scattering System

The optical scattering system is shown schematically in Fig. 2. It consists of light source, specimen and NIR camera. System used two symmetrical light sources on two opposite sides of the sample. Scattering system was used for observing occlusal surface. This method is an effective way to observe molar tooth because of their thickness. Camera was put above the tooth and perpendicularly to the light path. Samples were illuminated in visible and NIR light respectively. The distance between the camera and sample was adjusted to suit each sample. Quality of tooth structure image depends on position of camera, light sources and tooth. Distance between sample and camera is 1–1.5 cm and light sources was located below the gum line of tooth. Power of light sources are also an important factor. If LED power is too high, the recorded images will be overwhelmed by light and no detail of teeth can be seen. For this system, the power of each LEDs was 1.5 W.

3 Results and Discussion

3.1 Tooth Discoloration

Figure 3 shows the result of a caries tooth specimen with dental discoloration (sample 1) taken by the designed systems. Figure 3a–c show a stained defect that is visible over a large portion of the tooth crown. In contrast, the transillumination image at wavelength 850 nm shows the lesion localized in the red circle (Fig. 1b). The appearance of discoloration on the tooth is caused by many factors such as

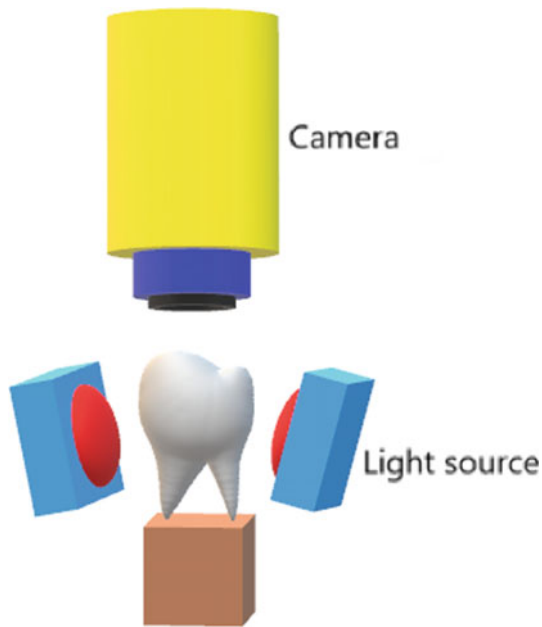


Fig. 2 Schematic diagram of the scattering system

smoking, fluorosis, etc., or demineralization. Smoking or fluorosis origins of stained teeth do not make change in crystal structure of tooth, but demineralization do. Demineralization is the process of removing minerals, in the form of mineral ions, from dental enamel.

As above mentioned, scattering of enamel is strong in visible wavelength region and weak in NIR, thereby increasing the transparency under NIR illuminating. Upon demineralization the scattering coefficient of enamel increases to yield high contrast between sound and demineralized teeth. The more demineralization is, the more scattering is, so the higher contrast between sound and

demineralized teeth is [5]. The images recorded by this method allow differentiating between the various degrees of tooth demineralization because and the contrast in NIR images increases according to the disease evolution.

The similar result of the discolored specimen on the surface is shown in Fig. 4 (sample 2). Inside the enamel, there is a small area showing sign of demineralization. In the clinical visual inspection, the signs of the discolored specimen on the surface are often difficult to be determined due to exogenous factor (cafein, smoking, etc.) or endogenous factors (tetracycline, fluor, demineralization, etc.). This result shows that the NIR method is able to determine exactly the demineralized locations and the early treatment is more effective. The researches show that staining and pigmentation do not interfere with observation in the NIR images, so the demineralization is easily discriminated between stains as well as between pigmentation [6].

3.2 Occlusal Lesions

Figure 5 shows a molar tooth (sample 3) with the occlusal lesion. In the molar tooth, the central and the distal fossae usually are sites that typically accumulate plaque and hence are also sites where caries most often occurs. In general terms, the initiation of occlusal lesion takes place in locations where bacterial accumulations are best protected against functional wear.

In the white light image, it is difficult to locate the position of the demineralization due to the similar color between the sound enamel and the graduation of pigmentation. Under white light (Fig. 5a–c) there is not sign of demineralization. But under NIR, as the red circle in Fig. 5d, a dark area appeared with high contrast that is suspected of the

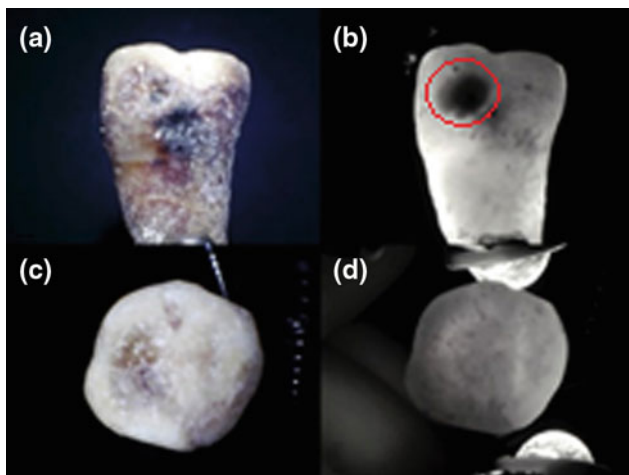


Fig. 3 Sample 1 taken by transillumination system (a–b) and scattering system (c–d) under white (left) and NIR (right) light

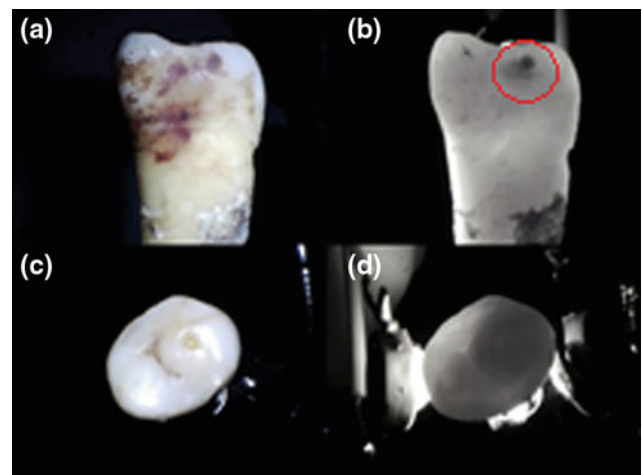


Fig. 4 Sample 2 taken by transillumination system (a–b) and scattering system (c–d) under white (left) and NIR (right) light

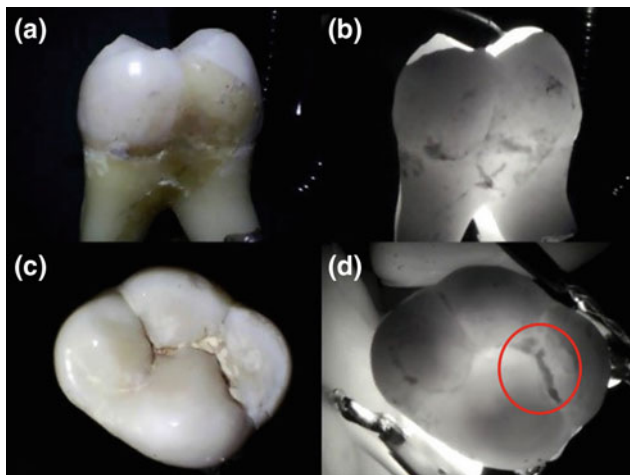


Fig. 5 Sample 3 taken by transillumination system (a–b) and scattering system (c–d) under white (left) and NIR (right) light

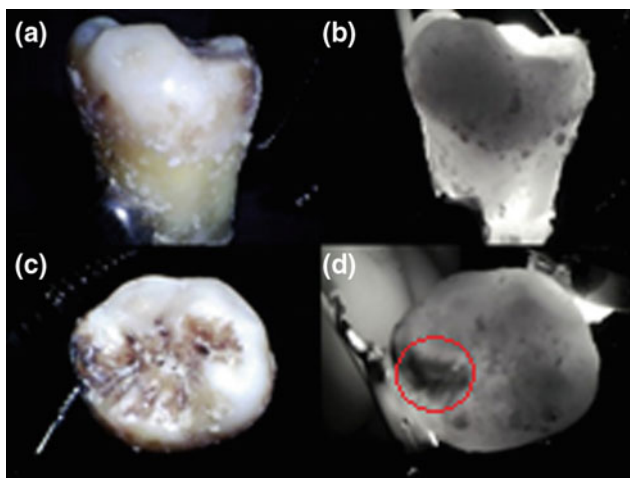


Fig. 6 Sample 4 taken by transillumination system (a–b) and scattering system (c–d) under white (left) and NIR (right) light

demineralization. Demineralization begins at the atomic level at the crystal surface inside the enamel or dentine and can continue unless halted with the end-point being cavitation. There are many possibilities to intervene in this continuing process to arrest or reverse the progress of the lesion. The similar result of the discolored specimen on the surface is shown in Fig. 6 (sample 4).

The radiograph of the tooth is difficult to determine the dental lesions because of the overlapping images of dental tissues in X-rays method [6]. Because enamel is transparent in the near infrared, the occlusal lesions inside the enamel are easily detected without the use of ionizing radiation. NIR method is an effective way to observe entire tooth in general and occlusal surface in particular.

4 Conclusions

This study has designed and built two optical systems with transillumination and scattering techniques using 850 nm LED. These systems were used to observe the approximal and occlusal of teeth and they had the ability to discriminate between the demineralized and discolored tooth. The result shows the possibility to apply NIR technique in the development of a specificity and sensitivity dental screening tool without the use of ionizing radiation. This dental device can support clinician to detect the early dental lesions. In the future, a photo processing software will be built to increase the image quality.

Acknowledgements This research is funded by Vietnam National University Hochiminh City (VNU-HCM) under grant number C2018-20-04.

Conflict of Interest Statement The authors declare that they have no conflict of interest.

References

1. Fejerskov, O., Kidd, E.: *Dental Caries: The Disease and Its Clinical Management*. Blackwell Munksgaard, Oxford (2008)
2. Ferreira, Z.A., Santiago, E., et al.: The natural history of dental caries lesions: a 4-year observational study. *J. Dent. Res.* 841–846 (2012)
3. Booshehry, Z.: Dental caries diagnostic methods. *DJH* 2(1), 1–12 (2010)
4. Marinova-Takorova, M., et al.: Effectiveness of near-infrared transillumination in early caries diagnosis. *Biotechnol. Biotechnol. Equip.* 30, 1207–1211 (2016)
5. Bussaneli, D.G., et al.: Assessment of a new infrared laser transillumination technology (808 nm) for the detection of occlusal caries—an in vitro study. *Lasers Med. Sci.* 30, 1873–1879 (2015)
6. Bühler, C.M.: Imaging of occlusal dental caries (decay) with near-IR light at 1310-nm. *Opt. Express* 13(2), 573–582 (2005)
7. Spitzer, D., et al.: The absorption and scattering of light in bovine and human dental enamel. *Calcif. Tissue Res.* 17, 129–137 (1975)
8. Daniel, F., et al.: Nature of light scattering in dental enamel and dentin at visible and near-infrared wavelengths. *Appl. Opt.* 34(7) 1278–1285 (1995)
9. Jones, R.S., Fried, D.: Attenuation of 1310 and 1550-nm laser light through dental enamel. *Lasers Dent.* VIII, 187–190 (2002)
10. Robert, S.J., et al.: Near-infrared transillumination at 1310-nm for the imaging of early dental decay. *Opt. Express* 11(18), 2258–2265 (2003)
11. Jacob, C.S., et al.: Near-IR transillumination and reflectance imaging at 1300 and 1500–1700 nm for in vivo caries detection. *Lasers Surg. Med.* 48, 828–836 (2016)

Building an EMG Receiver System to Control a Peripheral Device

Khanh Quoc Huynh, Nga Thi-Hang Vu, Nam Hoang Bui,
and Hien Thi-Thu Pham

Abstract

Electromyogram (EMG)—called myoelectric activity—representing the neuromuscular activity measuring electrical currents in the muscle. The current related studies show the potentials in applications of controlling peripheral devices, especially for handicapped people. This paper demonstrates a low-cost and non-invasive EMG acquisition system that collects and amplifies EMG signals from three surface EMG electrodes. The process of the acquired signal consists of 4 stages: amplification, filter, rectification, and low pass filter. The system also has an accelerometer sensor to detect hand movements, which improves the flexibility of control. Next, the processed signal is then analyzed and digitalized by a microcontroller (Arduino) to manipulate the external appliance, which can lead to further researches and studies to perform the application on other devices. For initial results, the system has been tested with 16 male and 15 female volunteers to validate the accuracy of the EMG sensor as well as compared it to EMG sensor in NI Toolkit. The results show both high accuracy and sensitivity of the designed system. The final product contains EMG acquisition system and code source for bio-signal processing and controlling the peripheral device.

Keywords

EMG signals • Bio-signal processing • EMG acquisition system

1 Introduction

1.1 A Subsection Sample

Electromyogram (EMG) is a physiological signal that measures the electrical activity of muscles generated during their contraction. This signal depends on the anatomic and physiologic properties of the muscles. Acquiring the EMG signal and its analysis are widely used in clinical diagnosis and biomedical applications.

In 1666, the development of the electromyogram began with the documentation of Francesco Redi. The document states that electric ray fish particular muscles produce electricity [1]. The publication was written by A. Galvani, named ‘De Viribus Electricitatis in Motu Musculari Commentarius,’ demonstrated that electricity could launch contractions of muscle in 1792 [2]. To treatment of more specific disorders, the clinical utility of surface Electromyogram was started in the 1960s [3]. Surface EMG was utilized by Hardyck and his researchers in 1966 as the first practitioners [3].

Skeletal muscle is composed of thousands of muscle fibers; each fiber is a multi-nucleated cell. The muscle fiber that is supplied by one motor-neuron through its single axon along with branches is called a motor unit, which is the fundamental of generating EMG [4].

When the motor unit is activated, it produces a ‘Motor Unit Action Potential’ (MUAP). The aggregate electric signal generated from all of the MUAPs in a detected area is referred as the myoelectric signal, which is also called electromyogram (EMG) [5]. The amplitude of EMG signals can be ranged from 0 to 1.5 mV (RMS) [6].

There are two favorite products for acquiring EMG currently available on the market those are MyoWare Muscle Sensor and Myo Gesture Control Armband. The former has a small size, low price, and adjustable gain. However, it needs an external power supply and has no other value except receiving EMG signal. The latter has a simple setup,

K. Q. Huynh · N. T.-H. Vu · N. H. Bui · H. T.-T. Pham (✉)
Biomedical Engineering Department, International
University-Vietnam National University HCMC, Ho Chi Minh,
70000, Vietnam
e-mail: ptthien@hcmiu.edu.vn

expandable design, broad compatibility, and fast response. However, it is expensive, and the calibration takes times.

In this study, we improved the peripheral communication of existing systems. We detected and analyzed EMG signal and the angular position of the arm and then transmit signals to control peripheral devices through a Bluetooth connection. We inherit the advantages of both current products: low price, real-time response, and flexibility while improving the wireless connection for an easier way to control the devices.

2 Acquisition System Process Flow

2.1 General System Process Flow

To activate the system, the user bends the arm actively to produce the EMG signal. The system checks the voltage whether it is higher than the pre-set peak value to begin collecting and processing the EMG signal and angular position to control the device. As shown in Fig. 1, the positions of the user's arm directly control the device to move forward, backward, left and right, corresponding with the arm movements. To turn off the system, the user can repeat the procedure that he/she used to activate the system: bending the arm to create enough high voltage to overtake the peak value to turn off the system.

2.2 EMG Signal Acquisition Process

The sensor collects EMG signal from biceps by three electrodes. Two electrodes are placed firmly on the skin of the user dominant hand biceps the other is placed at the elbow.

The first stage is a signal acquisition. In this stage, the body nervous system's electrical impulses used to active muscle fibers are acquired. The collected EMG signal is then amplified with an instrumental amplifier with the gain 100.

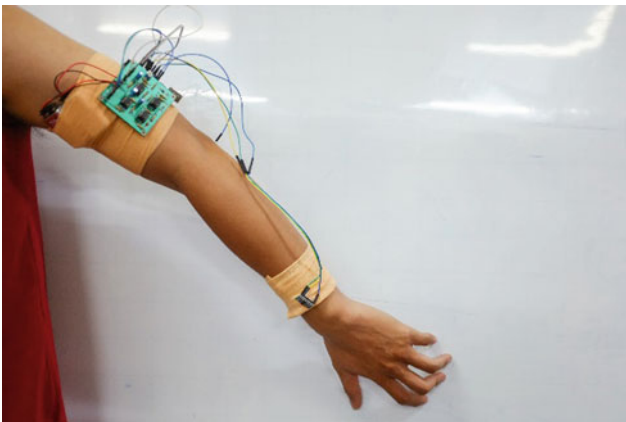


Fig. 1 The whole system implemented on the subject

Because the raw EMG signal is minimal, it is hard to utilize for detection. Thus, the amplification stage for EMG signal with high gain is essential.

Next, the acquired EMG signal goes through two steps of signal processing. The first is inverting amplifier which amplifies and inverts the signal. It has the gain of -15 . In this stage, a capacitor is added to AC couple the signal and remove DC error offset in a signal. DC offset and low-frequency noise are also get rid of by another active high pass filter.

The next step is rectification by using an active full-wave rectifier. The rectifier takes the negative portion of the EMG signal and turns it positive, so the entire signal is in the affirmative voltage region. AC signal into DC voltage is converted by this coupled with a low pass filter.

The final stage is smoothing and amplification. The humps in the EMG signal are filtered by using an active low-pass filter. This stage produces a smooth signal to send to the microcontroller. Since this is an active filter, there is a side effect of inverting the signal. Therefore, the signal needs to be inverted one more time using another inverting amplifier circuit with a trimmer configured as a variable resistor. With this trimmer, the gain can be adjusted for different signal strengths from different subjects.

A three-axis accelerometer gyroscope module is used to sense angular velocity and angular position. For this study, we are only interested in the angular position. Both the EMG signal and hand posture are processed simultaneously in real-time by the microcontroller. Moreover, then the results are used to control peripheral device through a wireless connection.

3 Components of the Acquisition System

3.1 EMG Signal (INA128 and TL072)

Input EMG signal detected is fed into acquisition system with some signal pre-processing component as shown in Fig. 2.

The acquisition system has two main components: instrumental amplifier INA128 and operational amplifier TL072.

The INA128 is a 3 op-amp design, multi-purpose instrumental amplifier. Among the plenty of ICs, we decide to choose the INA128 because of its relative price and design, excellent accuracy and high gain creation (up to 100 times), which is primarily essential to amplify the minimal EMG signal from the human body. Furthermore, it can operate with the power supply up to ± 40 V so that it can work stably in our system without damage.

After being acquired and amplified by the INA128, the EMG signal is sent to the rectification, amplification and smoothing stages, which is operated by 3 operational amplifier TL072. The TL072 JFET operational amplifier can

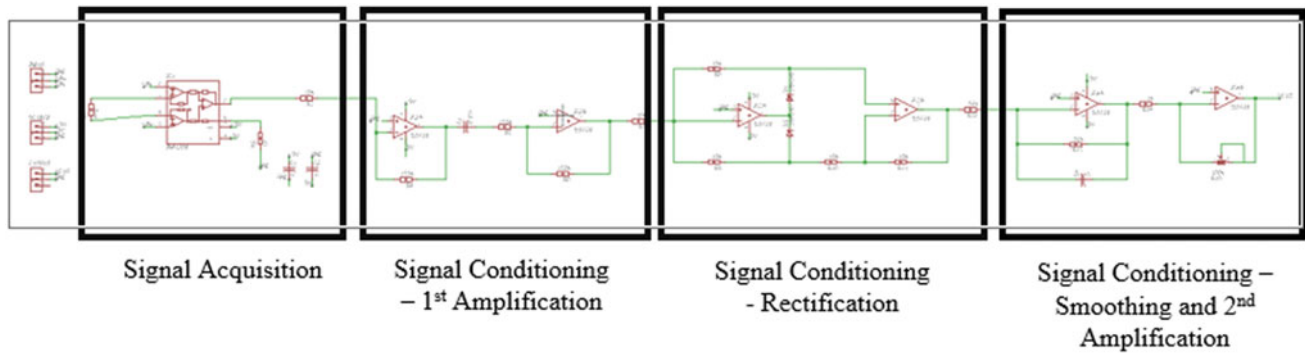


Fig. 2 Circuit diagram EMG acquisition system

undertake with many options. The signal going through the TL072 is acceptably low harmonic distortion. Before the relatively low price, low power supply requirement, multi-tasking ability, and easy-to-operate with another component, we decide to choose this IC as our main filter and rectifier.

The raw EMG signal is collected and enter the amplified system through three electrodes attached to the bicep muscle. In fact, the real EMG signal from the human body is minimal, so amplification and rectification are needed. The amplified system divides into two main parts. The instrument amplifier (INA128) acquires and amplify the raw EMG, with the gain can be set with a single resistor R_G . In this case, the R_G of the INA128 is equal to 470Ω , making the gain of the amplifier:

$$G = 1 + \frac{50 \times 10^3}{470} = 107.38 (\approx 110) \text{ times} \quad (1)$$

Three operational amplifiers (TL072s) amplify and rectify the signal after go through the instrument amplifier. The first TL072, with the gain of -15 (inverting amplifier), amplifies the acquired signal from the INA128. The amplified signal is now rectified by the second TL072, connected with the diodes, to eliminate the negative part of the EMG signal (full-wave rectifier). In this last phase of the circuit assembly, we are using an active low-pass filter to filter out the humps of our signal to produce a smooth signal for our microcontroller. However, since this is an active filter, we need to invert the signal one more time (and have the ability to amplify it more if desired) using another inverting amplifier circuit with a $100 \text{ k}\Omega$ trimmer configured as a variable resistor. The trimmer can control the amplification with gain from 0 to 20. Then, the final signal is sent to the Arduino microcontroller for processing.

3.2 Angular Position (MPU6050)

The MPU6050 has an integrated 3-axis MEMS (Micro Electrical Mechanical Systems) accelerometer and 3-axis MEMS gyroscope. It is a 6 DOF (Degree of Freedom) which give 6 values in the output. Three values of the accelerometer are angular velocity, and three of the gyroscope are the angular position. This module also has embedded algorithms for run-time bias and compass calibration. Thus, it can give highly accurate data but requires no user intervention.

3.3 Microcontroller

Arduino is one of the most popular MCU family that is very easy to use, especially for student's research. In our project, Arduino Uno R3 is used to receive, analyze data and control peripheral devices. The code had already uploaded to the board. Thus, Arduino executes the code automatically once powered up the circuit.

3.4 Wireless Signal Transmission

The HC05 module is an easy to use Bluetooth SPP (Serial Port Protocol) module, designed for transparent wireless connection setup. Serial port Bluetooth module is fully qualified Bluetooth V2.0 + EDR (Enhanced Data Rate) 3 Mbps Modulation with complete 2.4 GHz radio transceiver and baseband. The effective range of connection of HC05 to Arduino is about 10 m or 30 feet. This module is chosen because it has a reasonable price, low power consumption, relative accuracy and high compatible with Arduino and other devices.

4 Controlling Process

The user needs to press a power button to turn the system on. When turned on, the device begins to collect EMG signal and angular position value continuously. To be able to control the device, the user needs to produce EMG signal more significant than the threshold value, which is set to be equal to one-fourth of the maximum EMG signal and can be adjustable using the potentiometer. The purpose of setting the threshold value is to help user avoiding action accidentally while they are relaxing or doing other things which can distort the signal and produce noise, leading to unwanted control (Fig. 3).

At α angle greater than 15° with respect to the ground, the system is able to detect the arm's angular position at four states: forward, backward, left and right (as shown in Fig. 4).

Whether the EMG signal satisfies the controlling condition, the system can divert the remote-controlled car to the corresponding direction. Finally, the user presses the power button again to turn off the system.

5 Results

The system has been developed as shown in Fig. 5. EMG signal is collected from user biceps with three surface EMG electrodes. Two electrodes are placed on the biceps, and the other on the elbow. The gyroscope module is placed on the wrist. The wrist must be parallel to the ground and faced up to make sure it works correctly. At the end of the study, Arduino can control the remote-controlled car with four commands: forward, backward, turn left and right.

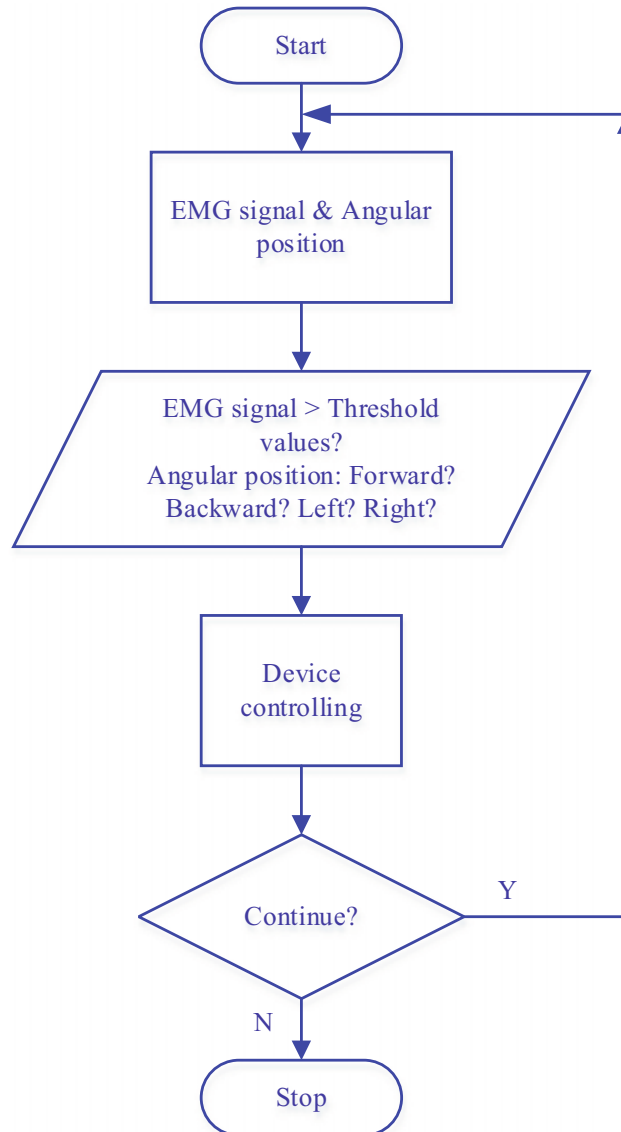


Fig. 3 Control process flowchart

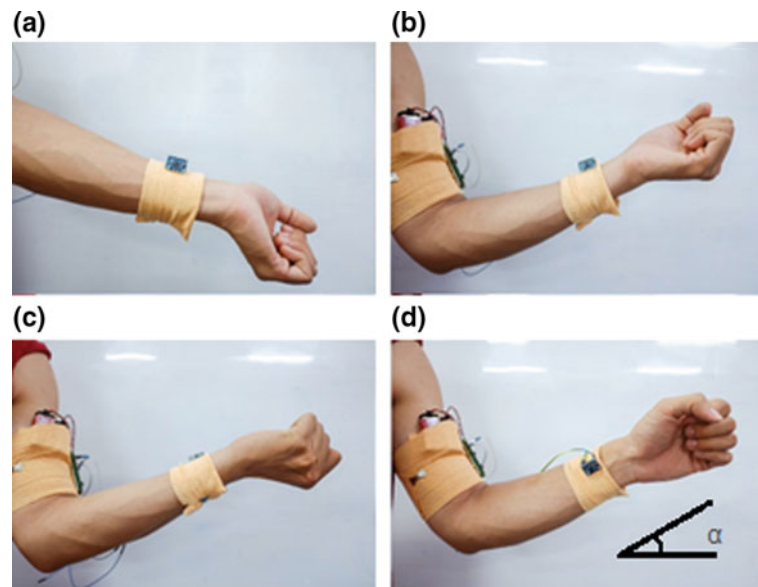


Fig. 4 Hand position to control device. **a** Forward, **b** backward, **c** left, **d** right

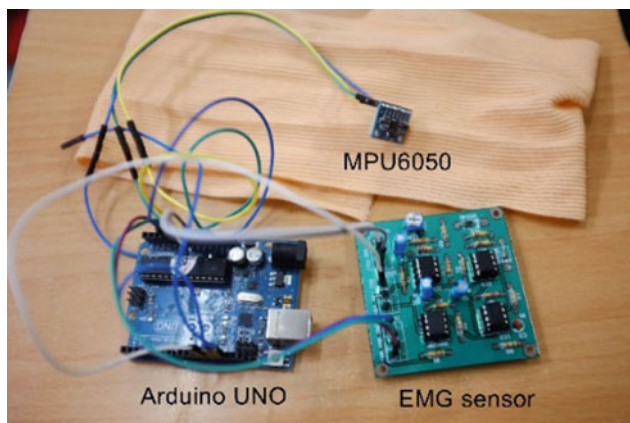


Fig. 5 Schematic view of EMG and angular position acquisition system

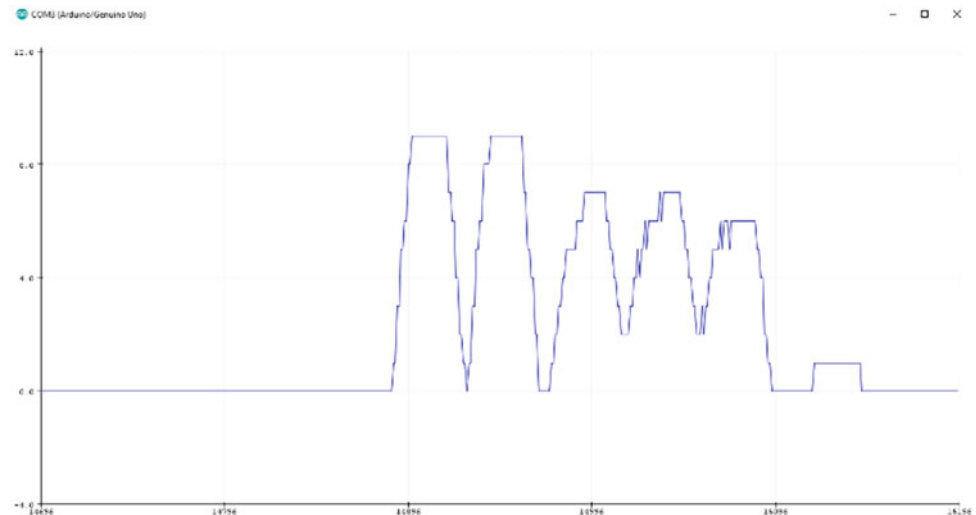
The system has been tested with 31 subjects to have the most suitable calibration.

In the test, subjects were asked to use the system to control a remote-controlled car. Subjects were instructed in advance, and the system was adjusted to be suitable for each before the test. Subjects had to use the system to control the car to go more than twice for each direction. The average duration of the test is about 3 min. The results showed that subjects were able to control the car adequately. There were still a few errors occurred during the testing phase. The possible reasons are their force are too weak so that the system cannot detect signals or the calibration is not suitable for that specific individual. The average threshold value is set to be in ranged from 0.384 to 0.409 V based on the results obtained in Table 1 (Fig. 6).

Table 1 EMG signal acquisition results

	Number of subjects	Mean (V)	Average threshold value	SD
Male subject	16	1.636	0.409	0.04626
Female subject	15	1.535	0.384	0.04565

Fig. 6 EMG signal plotted by Arduino Serial Plotter



6 Conclusion and Discussion

In this study, we have developed a low price, the real-time Bluetooth communication system utilizing EMG signal and angular position. The system has successfully used EMG signal and angular position to control the peripheral device. The system has also addressed the problem of non-use period of usage, by allowing users to put the system into a rest state and activate it by doing specific requirements. It has great potential for the system to develop further by adding more gesture using the velocity angular, which makes the controlling more flexible. With a flexible control, this system can be used to control many other devices through wireless communication.

Although the research has reached our aims, there are still some limitations. First, because of the time limit, the research was conducted only on a small size of the population. Therefore, to generalize the peak value suitable for larger group, the study should have involved more participants at various ages. Second, the system needs to have a portable and stable power supply. Finally, the system also needs to be redesigned to reduce the overall size and enhance the wearing experience.

Acknowledgements This research is funded by International University, VNU-HCM under grant number SV2017-BME-02.

Conflict of Interest The authors declare that they have no conflict of interest.

References

1. Basmajian, J.V., de Luca, C.J.: *Muscles alive—the functions revealed by electromyography*. The Williams & Wilkins Company, Baltimore (1985)
2. Kleissen, R.F.M., Buurke, J.H., Harlaar, J., Zilvold, G.: *Electromyography in the biomechanical analysis of human movement and its clinical application*. *Gait Posture*. **8**(2), 143–158 (1998)
3. Cram, J.R., Kasman, G.S., Holtz, J.: *Introduction to Surface Electromyography*. Aspen Publishers Inc., Gaithersburg, Maryland (1998)
4. Campbell, W.W.: *Essentials of Electrodiagnostic Medicine*. Williams & Wilkins, Baltimore, Maryland (1999)
5. Day, S.: *Important factors in surface EMG measurement*. *Bortec Biomed.* (2008)
6. De Luca, C.J.: *Surface Electromyography: detection and recording* (2008)

Development of a Pulse Oximeter for E-Health Applications

Thai M. Do, Nam P. Nguyen, and Vo Van Toi

Abstract

The oxygen plays crucial role in our life. Especially, the brain and heart have a variety of sensitive with limited oxygen in the blood. If the limited oxygen which is called hypoxia in human body happens in several minutes, the human will be died immediately. Therefore, the pulse oximeter is compulsory for research and development. In this paper, we designed a new pulse oximetry which has a special function called telemedicine and a software program in the server for obtaining results of this device by using HL7 Standard. In this way, the patients can be supported and treated from far a distance. Indeed, it can be called a system of Internet of Thing (IoT) in health cares. By means of calibrating with SpO₂ FLUKE simulator, the Tele-Pulse Oximeter works effectively as our expecting, and the result of patients on the server software is received accurately as well. In the near future, this device has a vast potential in Vietnam E-Health system.

Keywords

Pulse oximeter • Telemedicine • Oxygen saturation

1 Introduction

Telemedicine is the use of telecommunications and information technologies in order to supply clinical health care from a distance. It helps eliminate distance barriers of doctors and patients, and it also can improve access to medical services in distant rural communities [1]. Nowadays, Telemedicine is more captivated by scientists. Due to its efficiency, Telemedicine has been used in huge variety of home health care which is health services delivered to patients'

T. M. Do (✉) · N. P. Nguyen · V. Van Toi
Department of Biomedical Engineering, International
University - VNU HCM, Ho Chi Minh City, Vietnam
e-mail: dmthai@hcmiu.edu.vn

homes in part by telecommunication devices such as smartphone, tablet, and etc. [2]. In additionally, Telemedicine is very useful because it can save lives in critical care and emergency situations [1]. Especially, the government of Viet Nam focuses on improvement of health care ability in Viet Nam's hospitals. With this new method, it can help to reduce the workload of central hospitals, and the doctor can take care of many patients at the same time immediately.

Oxygen is very important in our lives. People always need it to breathe and live. Therefore, the monitoring of saturation oxygen in blood is necessary with the patients concerning with a problem of limited oxygen. In this paper, we introduce a design for Telemedicine of home healthcare for monitoring oxygen saturation in the blood which includes hardware and software of having a capability of transmitting data over the internet. This device allows patients to measure SpO₂ index on their finger at home using a non-invasive technique continuously.

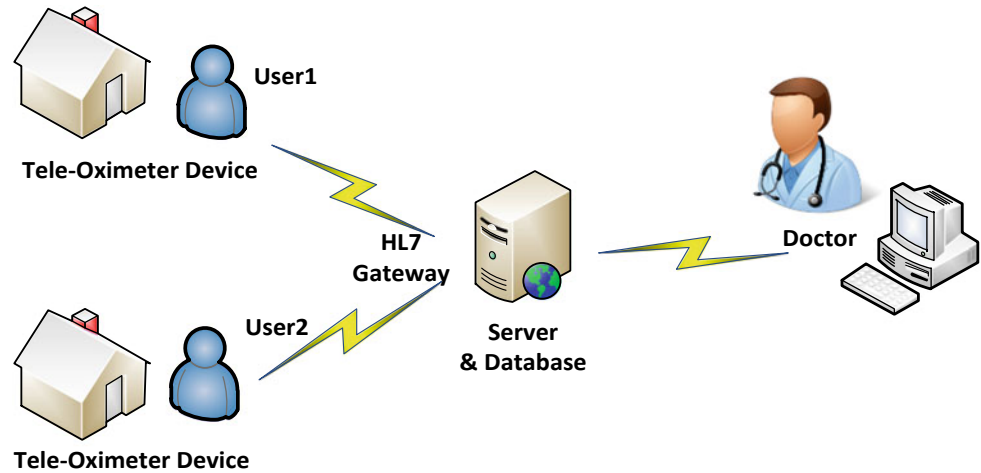
2 Designing of the Tele-Oximeter System

Home Tele-healthcare services for oxygen saturation measurement are based on Client-Server architecture [3]. Therefore, it contains server applications that receive in-coming SpO₂ results from the clients and then storages into database. The device client is responsible in real-time for measuring SpO₂ and heart rate from patients and transmitting them through internet; The data of SpO₂ are packed in HL7 international standard. This system is shown in Fig. 1.

2.1 Implement Hardware of the Tele-Oximeter in Client Side

In the client side, it contains hardware devices of a pulse oximeter having a special function with sending the SpO₂

Fig. 1 Demonstrated a Tele-oximeter system including server and client side



index and heart rate via Wi-Fi communication to a central server. It is called the Tele-Oximeter. The firmware in this device is programmed to measure blood oxygen saturation level (SpO_2) and Pulse rate using of non-invasive method. This approach is based on altering intensity of light of Red and Infrared LED which transmit through tissue. This signal is obtained in arterial blood pulse and it is called photoplethysmography(PPG) [4].

Principal of measuring SpO_2 index.

The SpO_2 index is calculated from monitoring the percentage concentration of hemoglobin saturation with oxygen which is called oxyhaemoglobin, to the total haemoglobin concentration. The pulse oximetry has a foundation of spectrophotometric measurements of alternatives in blood color; oxygenated blood is typically red. In contrast, deoxygenated blood is dark blue coloration. In the visible, the optical property of blood (between 400 and 700 nm) and near-infrared (between 700 and 1000 nm). The special regions concern strongly with the amount of oxygen concentration in the blood [5]. The graph of haemoglobin light absorption is shown in Fig. 2.

In Fig. 2, it is illustrated the absorption process of two light wavelengths transported through blood. This process depends on whether Hb(haemoglobin) is bound to oxygen in blood [4]. The Hb reaches a higher optical absorption coefficient in the red line of spectrum some 660 nm when comparing to HbO_2 . In addition, the region of near-infrared of spectrum is around 940 nm, and the optical absorption of Hb is less than HbO_2 [5].

The light absorbance of haemoglobin solution is determined by the Beer-Lambert's Law, by using the below formula:

$$I_t = I_0 \cdot e^{-\alpha cd} \quad (1)$$

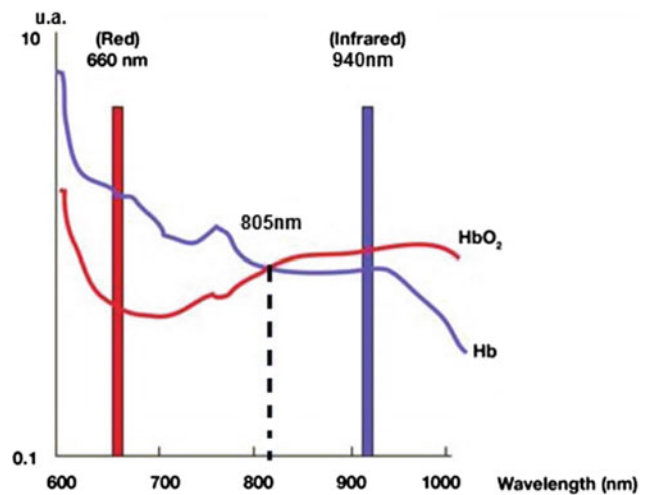


Fig. 2 Oxygenated versus de-oxygenated blood light absorption at different wavelengths [5]

where: I_t is the transmitted light intensity, I_0 is the incident light intensity, α is the specific absorption coefficient of the sample, c is the concentration of the sample, and d is the path length of light transmission.

By using two different wavelengths, Red and infrared, the ratio of absorption of these light wavelengths is made use of determining the fraction of saturated haemoglobin. Because of different optical attenuation at hemoglobin and deoxy-haemoglobin. The pulse oximeter is usually to use the light with wavelengths: 660 nm(R) and 940 nm(IR). The measure of oxygen concentration can be calculated in Eq. (2).

$$SpO_2 = \frac{H_bO_2}{H_bO_2 + Hb} * 100 \quad (2)$$

By means of calculating R/IR, called “ratio of ratios”, It has a concerning with SpO_2 concentration. This ratio is calculated in the following equation:

$$\frac{R}{IR} = \left(\frac{AC_R/DC_R}{AC_{IR}/DC_{IR}} \right) \quad (3)$$

In the Eq. (3), the “AC” component is described the pulsatile part of PPG signal, and the “DC” component is concerned with venous blood, skin, and tissue. Both of signals are shown in Fig. 3.

With normalization for both Red and infrared wavelengths, the component signal due to venous blood and surrounding tissues does not influence to the measurement of SpO₂. Consequently, the ratio of ratios can be concerned with SpO₂ index as shown in Fig. 4.

This algorithm is performed with the help of altering one of the two intensity of transmitter LEDs until the DC components of the red and infrared signals are equal as Fig. 4. The ratio of ratios is simplified in the below formula (4) [6]

$$\frac{R}{IR} = \left(\frac{AC_R}{AC_{IR}} \right) \quad (4)$$

Because of correlation between SpO₂ and SaO₂, the SpO₂ index can calculate by using the relationship of estimation in SaO₂ and Ratio (R/IR). It is shown in the Eq. (5)

$$SaO_2 = A - B.(R/IR) \quad (5)$$

The constants A and B in the Eq. (5) derived practically during calibration by correlation between Ratio of Ratios and SaO₂. This process is demonstrated in Fig. 5.

Hardware Design of the Oximeter device.

In this project, we designed the Tele-oximeter device for keeping track of SpO₂ index and heart rate supporting for hypoxia patients who suffer from limiting oxygen in the

blood. In terms of hardware diagram in this device, the microcontroller with ARM-32 bit architecture is taken advantage of controlling the system of device. With the help of ARM cortex-M3 technology, it has enough performance for calculating the algorithm of SpO₂ index. In Fig. 6, it is illustrated for diagram of hardware design. In detail, the AFE4490 IC is utilized for key solution of SpO₂ measuring. With using SpO₂ Nellcor sensor and DB9 connector, signals in the device become better and calculating of results is more reliable.

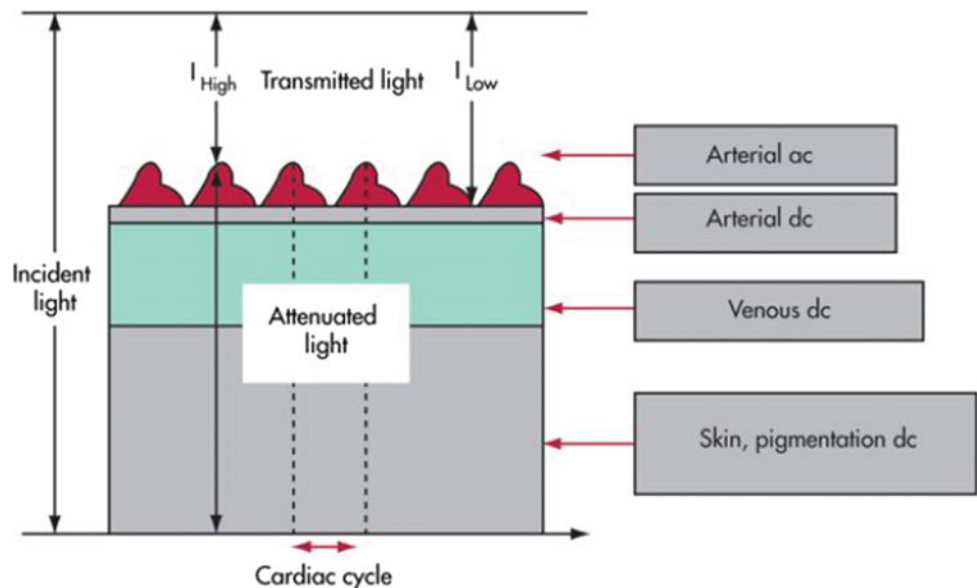
From Fig. 6, There are three data connections in the oximeter device: GPRS, WiFi, and Bluetooth. The SpO₂ index and heart rate after measuring will be sent to a server by using wireless communication as GPRS or WiFi. In terms of configuration for users, the Bluetooth interface is utilized, and it is also used for transferring data of PPG signals into Personal Computer. All information of configuration such as username, user ID, and etc. will be saved in a ROM IC. In regarding to display results, the LCD 20 * 4 is made use of showing these results.

In related to controlling LED (Red and infrared) and receiver (Photodiode), the AFE IC can change LED current by means of an H-bridge configuration capable of driving up to 150 mA. In Fig. 7, the photodiode circuitry in the AFE can amplify currents less than 1uA with resolution 13 bit [5].

Sensor of SpO₂.

In this device, we chose SpO₂ Sensor via a DB9 connector and accompanied by a standard of Nellcor Company. In detail, the rules of connector are named in the pins demonstrated in Fig. 8.

Fig. 3 Variations of light attenuation by tissue [5]



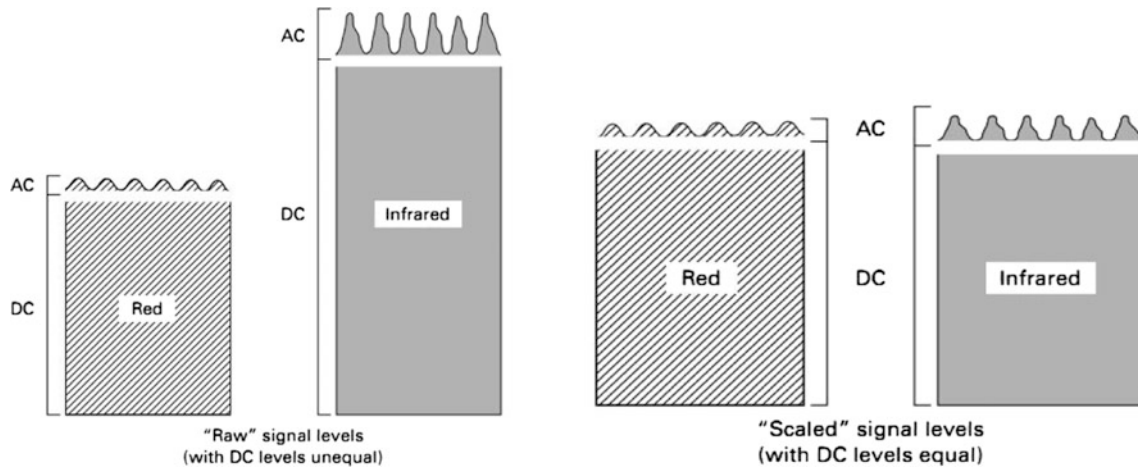


Fig. 4 Normalization of R and IR wavelengths to eliminate the influences of DC components [6]

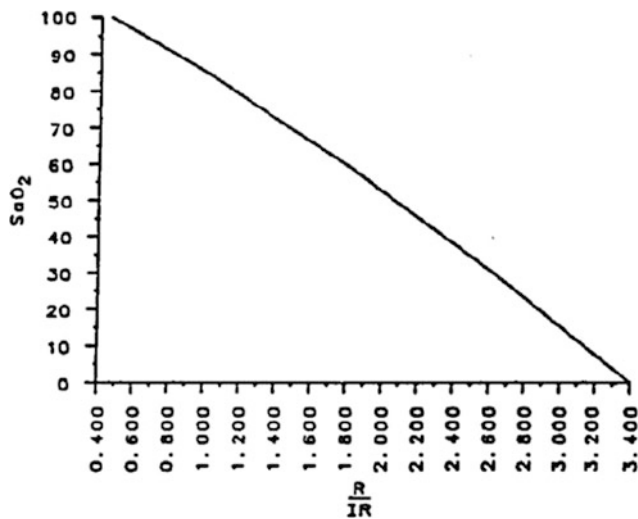


Fig. 5 Empirical relationship between arterial SaO₂ and normalized (R/IR) ratio [5]

Digital signal processing in the SpO₂ device.

Because there is a huge amount of noise in received photodiode signals, the techniques of digital filter are applied to eliminating the noise. The processing data flow is displayed in Fig. 9.

In the acquisition of data, the AFE IC is configured with 1 ms period span of interrupt for collecting data. When time of ADC conversion finishes, ADC_RDY pin of AFE IC have a pulse that indicates the completion of ADC conversion. This pin is connected to an external microcontroller. With external interrupt, the MCU is programmed to read data of PPG signals with 1 ms. Then, these signals are limited with a FIR Filter for removing noise signals, and the IIR Filter is used for eliminating a DC component in the

PPG signal. In order to reducing effect of DC components in calculating Ratio R/IR, an algorithm of DC correction is developed. It means that MCU have to manipulate the intensity of LED in transmitter side until the difference of DC component in Red and infrared is lowest.

2.2 Develop Software Programs for Collecting Directly Data and Central Server Side

The software program in the server will collect all data sent from the Tele-Oximeter and it stores these data in the database of patients. Every physician has an account and password to access this database. In addition, they also view the graph of measured results over time. Because of the access permissions of system, the doctor can only see the results of their tracking. The platform software programs are capable working on Personal Computer, smartphone, and website. With the help of these software programs, the doctor can easily take care of the patient from a distance. Even though, they can also give guidelines related to treatment or diagnosis for the patient.

3 Results of Experiment

We consider designing of the SpO₂ device with high compatibility for customers, because our target is that we want to manufacture mass-production of this device. Therefore, it is mandatory designing with small, comfortable, and reliable. In regards to the calibration, we make use of Simulator Fluke Index 2 for finding the relationship of SpO₂ value and ratio of R/IR. The process of calibration is shown in Fig. 10.

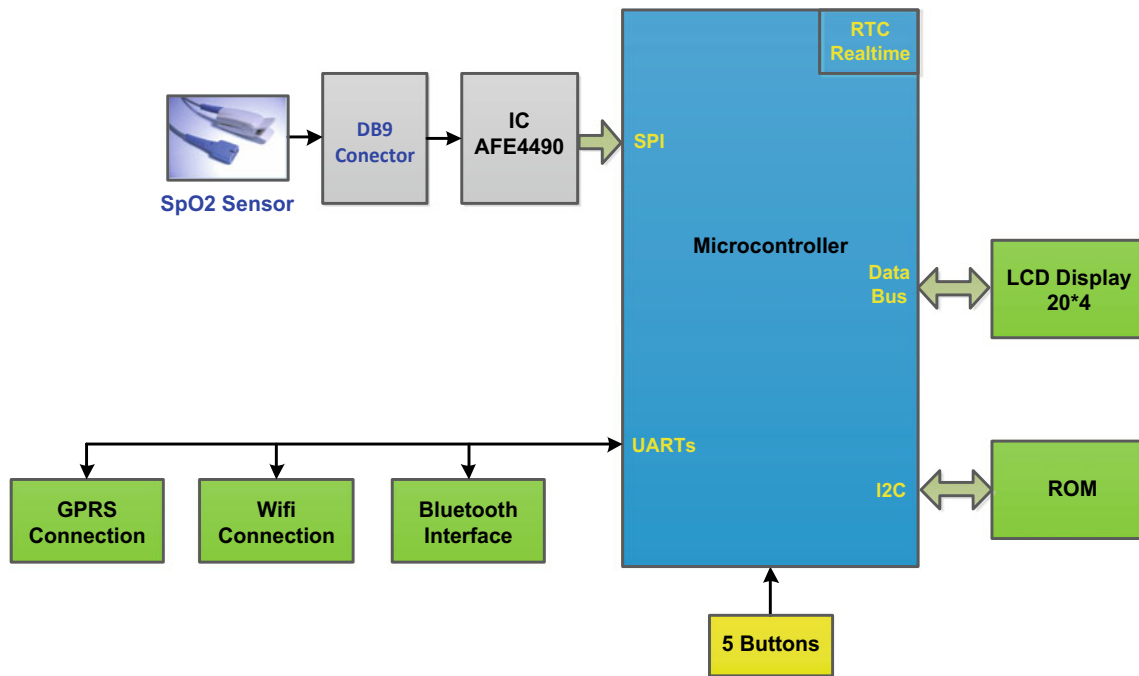
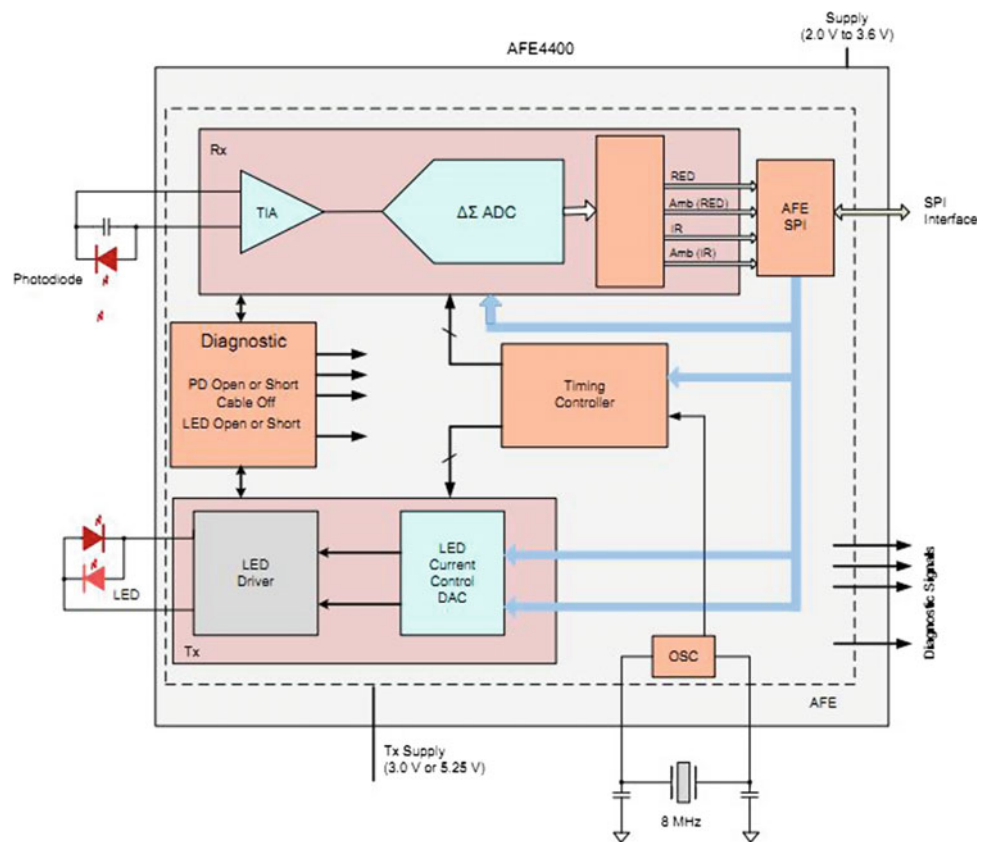


Fig. 6 Diagram of the designed Tele-oximeter device

Fig. 7 Simplified diagram of AFE4490 IC [7]



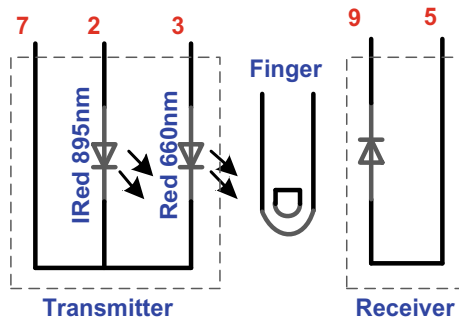


Fig. 8 Insight schematic of SpO₂ Nellcor

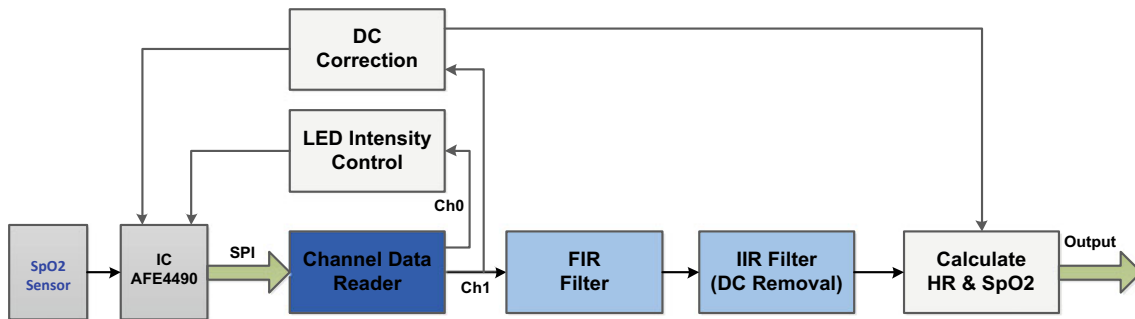


Fig. 9 The data flow and digital processing in the oximeter device

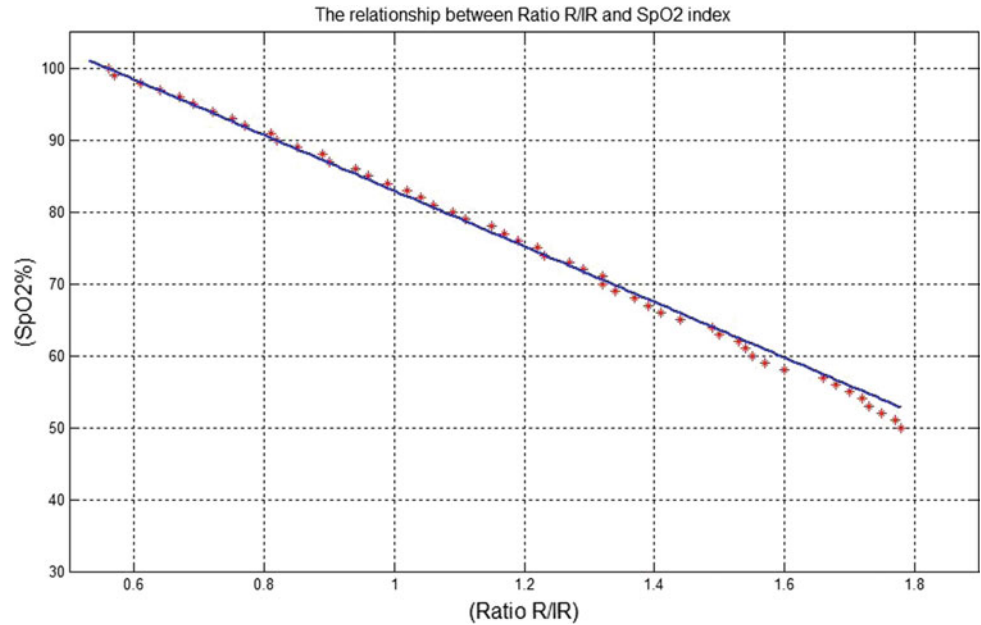
Fig. 10 Calibrated the SpO₂ device with Simulator Fluke Index 2



Because the Simulator of Fuke Index has oxygen simulations with saturation levels from 50 to 100%, and each of steps is with 1%, we investigate this range of SpO₂ value

and calculate ratios of R/IR. Then, the slope of relationship is estimated with a linear function of -38.68 . This function of blue line is displayed in Fig. 11.

Fig. 11 The relationship between ratio R/IR and SpO₂ value



In regarding to comparing with FLUKE Simulation index 2, we utilized the Tele-Oximeter device to measure with the range saturation lever of Simulator. These results are presented in Fig. 12.

As results in Fig. 12, with a range from 100% reducing to 73%, we can easily see that

The error of oxygen saturation is lower than 1%. With the range of 73 and 50%, the error is reached up 2%. Explaining for this result is cause of the first range of relationship between Ratio of R/IR and SpO₂ saturation more linear than the other described in Fig. 11.

Beside the SpO₂ device is implemented and designed for a cyber-medical system, the software program running on PC is also developed for acquiring PPG signals of Red and

IRed; The communication of this transmission is Bluetooth interface. All information as Ratio, heart rate, and etc. are also gained such as Fig. 13.

In Fig. 14, we developed two software program for an e-health system, the first case of a is software on server side by obtaining data from the Tele-oximeter device using HL7 standard and then saving these data into a database. On the other hand, the other software on client side is to access the server to display SpO₂ index and heart rate.

To prove the quality of our device, we carried out an experiment of measuring on human subjects. With comparing with the results of Nonin SpO₂ device in Table 1, we can draw some conclusions that the errors of SpO₂ are pretty precise with $\pm 1\%$ as well as heart rate with around ± 2 bpm.

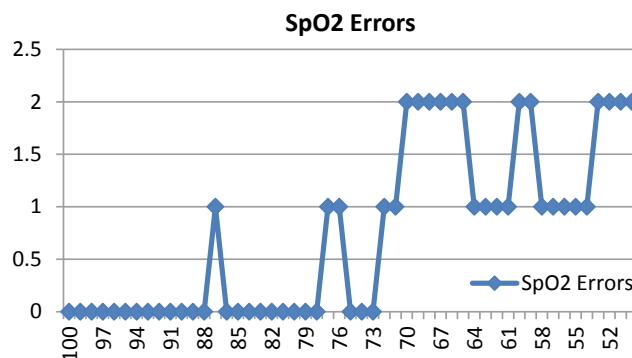


Fig. 12 The errors when calibrating with FLUKE Simulator Index 2

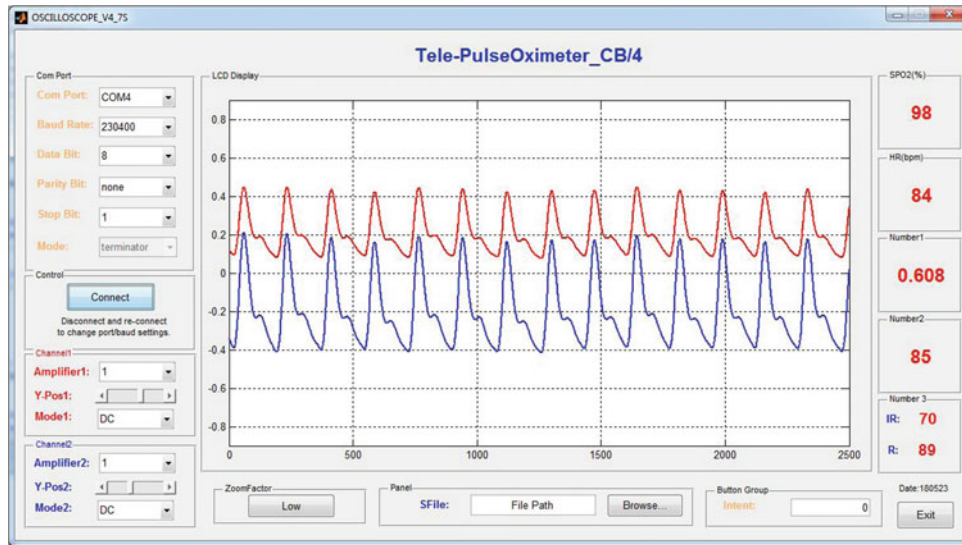


Fig. 13 A software program in order to collect data of PPG signals and SpO₂ results in MATLAB

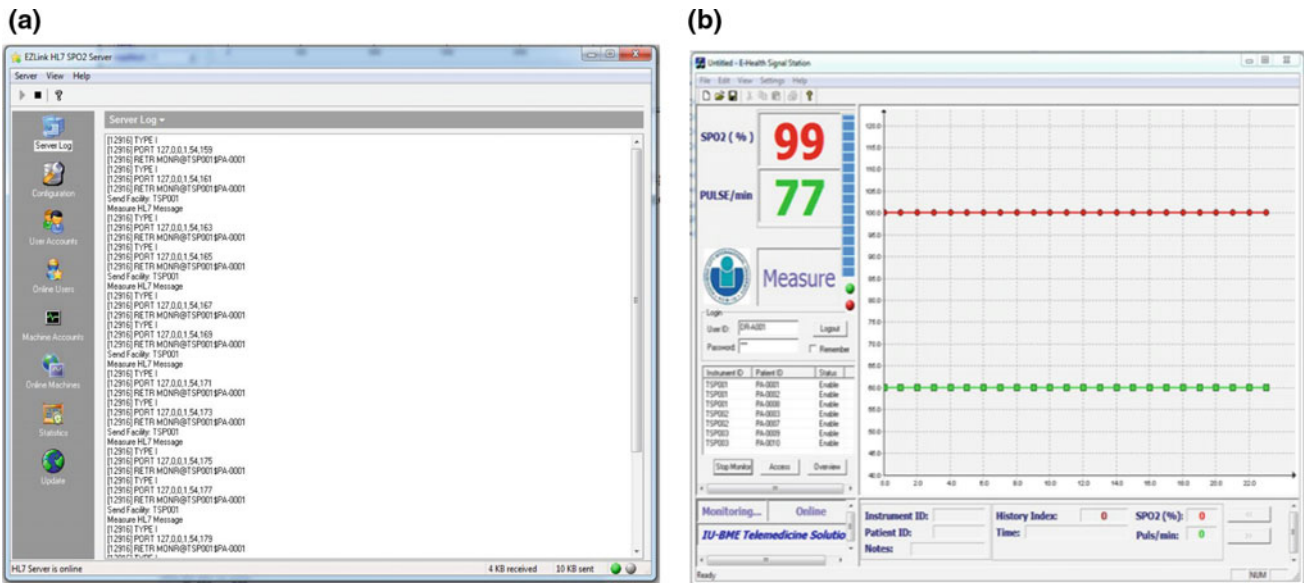


Fig. 14 Administrator and client software program: **a** on server side, **b** on client side

Table 1 Errors of measurement between a Nonin device and the Tele-Oximeter

Person	Nonin SpO ₂ device		The tele-oximeter		Error (%)	Error (bpm)
	SpO ₂ (%)	Heart rate (bpm)	SpO ₂ (%)	Heart rate (bpm)		
1	98	73	99	71	1	2
2	98	78	99	77	1	1
3	98	70	98	72	0	1
4	98	88	99	87	1	1
5	98	75	99	75	1	0
<i>Maximum error</i>					1	2

Because it is difficult for us to find the patients with hypoxia, the range of low SpO₂ saturation not verified effectively in human subject experiments. So, This will be studied in the future.

4 Conclusions

In this paper, we developed a pulse oximeter which is called Tele-Oximeter. This device is compulsory for the people suffered from diseases of hypoxia due to having telemedicine functions. In regarding to software, we developed some programs on server and client side for telemedicine system, and a software program running MATLAB to plot PPG Signals on PC. Consequently, the errors when comparing with simulator Fluke index 2 is less than $\pm 1\%$ in the range 100% down to 73, and $\pm 2\%$ in the range of 73–50%. With respect to performing a human subject experiment, we have just studied on the good healthy subject; the results are pretty accurate with $\pm 1\%$ for SpO₂ saturation and ± 2 bpm for heart rate. Although the number of human subjects is small, we will increase numbers of sample subjects and

testing on real diseases of limiting oxygen saturation in the blood in the future.

Conflict of Interest The authors declare that they have no conflict of interest.

References

1. Wikipedia: Telemedicine. <https://en.wikipedia.org/> (2018)
2. Currell, R., et al.: Telemedicine versus face to face patient care: effects on professional practice and health care outcomes (1469-493X (Electronic))
3. Ning, L.I.U., Li, J.: Design and implementation of embedded medical data transmission platform based on HL7/XML system (2011)
4. Bagha, S., Shaw, L.: A real time analysis of PPG signal for measurement of SpO₂ and pulse rate (2011)
5. Designs, T.R., SpO pulse Ox wrist oximeter reference design (2010)
6. Moyle, J.T.B.: Pulse Oximetry, 2nd edn, p.182. BMJ Books, London (2002). ISBN 0-7279-1740-4
7. Instruments, T.: DataSheet AFE4490 integrated analog front-end for pulse oximeters (2014)

Detection of Systole and Diastole Points on Seismocardiogram Using Interpolation Method

Loc Luu and Anh Dinh

Abstract

Seismocardiogram (SCG) is a cardio-mechanical signal generated by the heart activities. The waveform is obtained by placing an accelerometer on the chest. This work proposes a low complex algorithm to identify the systolic and diastolic regions of the SCG in real time without referencing to the ECG as in the traditional methods. The technique uses the slope, an interpolation threshold, and systolic interval constraint to identify the regions. The method has an average detection error rate of 2.3% for systolic and 7.3% for diastolic on the eight testing subjects. The average processing time is 83.5 ms for one-minute of data which can be implemented in real-time wearable devices.

Keywords

Seismocardiogram • Analysis • Interpolation • Systole • Diastole

1 Introduction

Seismocardiogram (SCG) is obtained from the vibrations picked up by an accelerometer attached to the chest. The waveform contains cardiac activities and their timing. Readers can find the timing relationship between the ECG's components and the SCG's events in [1]. The events happening in the heart are identified on the SCG waveform by collating the manual annotation of the echocardiogram with SCG signal peaks. As shown in [2], the QRS complex corresponds to the valve operations and status of the heart during the systole period. The diastolic phase relates to the

aortic and mitral valves movements for refilling. As long as the systolic and diastolic regions are correctly recognized, the events in the SCG waveform can be identified. In the past, ECG is collecting at the same time with the SCG and is used as a reference for the region identification [2–4]. A recent study detected the regions without the referenced ECG but the technique is complicated due to the use of wavelet transform [5]. In this work, we use the total acceleration of a tri-axial accelerometer to automatically locate systolic and diastolic zones without the aide of the ECG.

2 Methodology

For *Data collection and testing subjects*, a wireless data acquisition system was used to collect the data. Two non-contact ECG sensors—PS25451 (Plessey Semiconductor) were attached horizontally on the subject's chest to capture the modified Lead I ECG for ground truth checking. The SCG sensor is a tri-axis accelerometer with a range of ± 2 gravity. The signals from the sensors were amplified and bandpass filtered (5–50 Hz) using op-amp. The DAQ was designed to simultaneously collect 8 channels at 16-bit resolution and 1 kHz sampling rate. All data were sent wirelessly to Matlab in a laptop for saving and processing. The SCG and ECG were simultaneously recorded. The experimental procedures involving human subjects were approved by the University of Saskatchewan Research Ethics Board. The tests were on eight volunteers who have no previous record relating to heart diseases: age 32.1 ± 4.5 years, weight 78.2 ± 12.7 kg and height 171.1 ± 7.5 cm. The accelerometer was placed at the sternum and each subject performed one minute stationary, one minute walking on a treadmill with a speed around 5 km/h, and one minute running with a speed approximately 8 km/h. Figure 1 illustrates the processing steps of the detection. For *Data pre-processing*, as the tri-axial sensor provides acceleration in three different planes, the total acceleration represents the 3D SCG (which is different from the z-axis only

L. Luu · A. Dinh (✉)

Department of Electrical and Computer Engineering,
University of Saskatchewan, Saskatoon, SK, Canada
e-mail: anh.dinh@usask.ca

L. Luu

e-mail: loc.luu@usask.ca

waveform as in other previous studies). The Total acceleration (TOTAL_ACC) was calculated from all the three axes data using Eq. (1). Because the accelerometer is powered at 3.3 V, the zero acceleration point is at the center (1.65 V) for an equivalent of 1650 in the ADC data.

$$\text{TOTAL_ACC} = \sqrt{(x - 1650)^2 + (y - 1650)^2 + (z - 1650)^2} \quad (1)$$

The *Bandpass filter* was designed to have an effective frequency range from 20 to 50 Hz. This was based on experimental data with signal and noise analysis in addition to the noise frequencies determined from [6, 7]. For *Absolute finding*, the filtered TOTAL_ACC contains high frequency components and distributed mostly in the systolic and diastolic regions. To concentrate all energy of those zones in positive domain, the filtered TOTAL_ACC is taken absolute. The *Low-pass filter* was designed based on the constraints of the heart beat per minute and the systolic and diastolic ratio (S:D) of less than 1.2 claimed in [8]. The FIR low-pass filter was designed by Matlab with configurations of 330 orders, 6 dB cut-off frequency at 6.7 Hz, 60 dB of stopband attenuation, and 1 dB of passband ripple. The signal is also applied zero-phase filtering to maintain the timing. For *Detection*, the process includes interpolation, find minima, and detection of systole and diastole. The SCG signal has a maxima pattern very close to a sinewave as indicated in Fig. 1. Then, interpolation of maxima is taken to

obtain the sine wave pattern. The sample points of interpolation are the maxima of the SCG energy signal, and the coordinates of the query points are the coordinates of the signal. The method to interpolate is spline. All minimum peaks of interpolation waveform are detected using a custom function with condition:

$$y(nT - T) > y(nT) < y(nT + T) \quad \text{for minimum at } y(nT) \quad (2)$$

It was also found that between two minima, there contains one systole which has the highest amplitude among maxima. All the maxima which reside in the range between two minima of interpolation waveform are searched. The largest amplitude peak is marked as systole. The next high level amplitude is ticked as diastole. Figure 2 illustrates the interpolation algorithm with the blue line is the interpolation waveform.

3 Results and Discussion

The location of each systole or diastole of automatic detection method and search backward and forward within an interval (70 ms) called tolerance provides the error rate. If there is one manual annotated systole or diastole inside that range, that detected systole or diastole will be marked as correct; otherwise, it is marked as a fault. To calculate the missing rate, we base on the location of each systole or diastole of manual annotation and look backward and

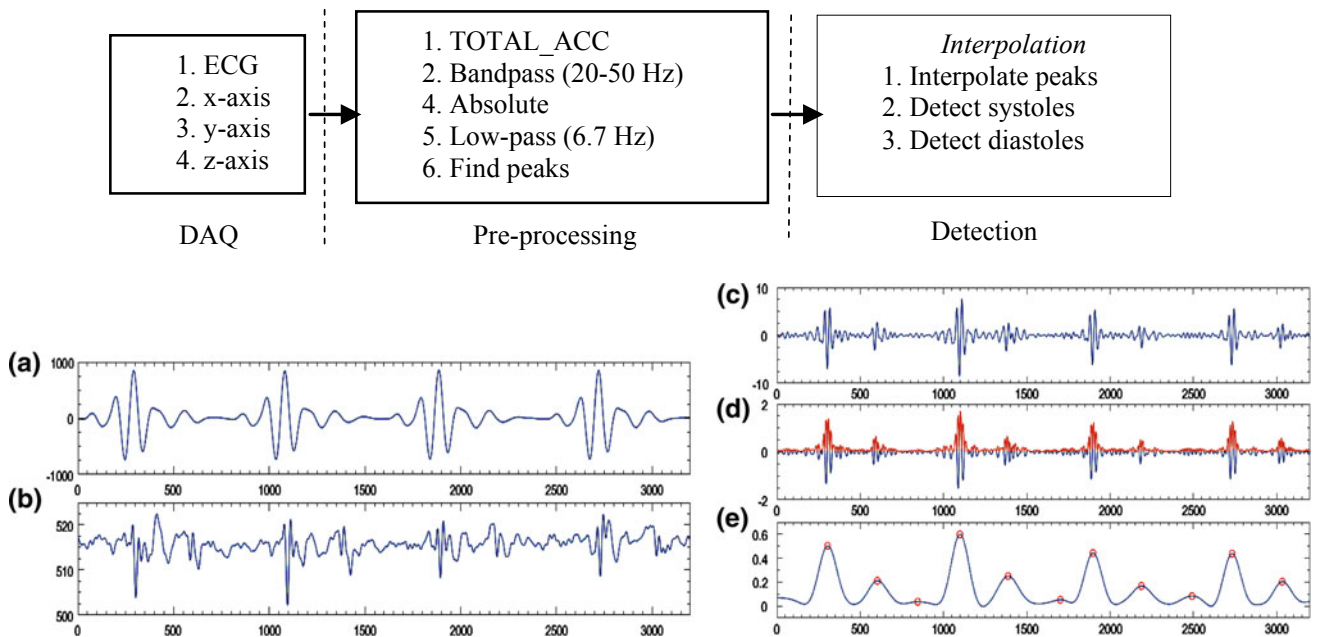


Fig. 1 Top: System and algorithm overview. Bottom: Pre-processing steps: **a** 5–15 Hz Filtered ECG as reference, **b** total acceleration of the SCG, **c** bandpass filtered SCG, **d** absolute, **e** low-pass filtered signal (SCG energy signal) with maxima (red circles)

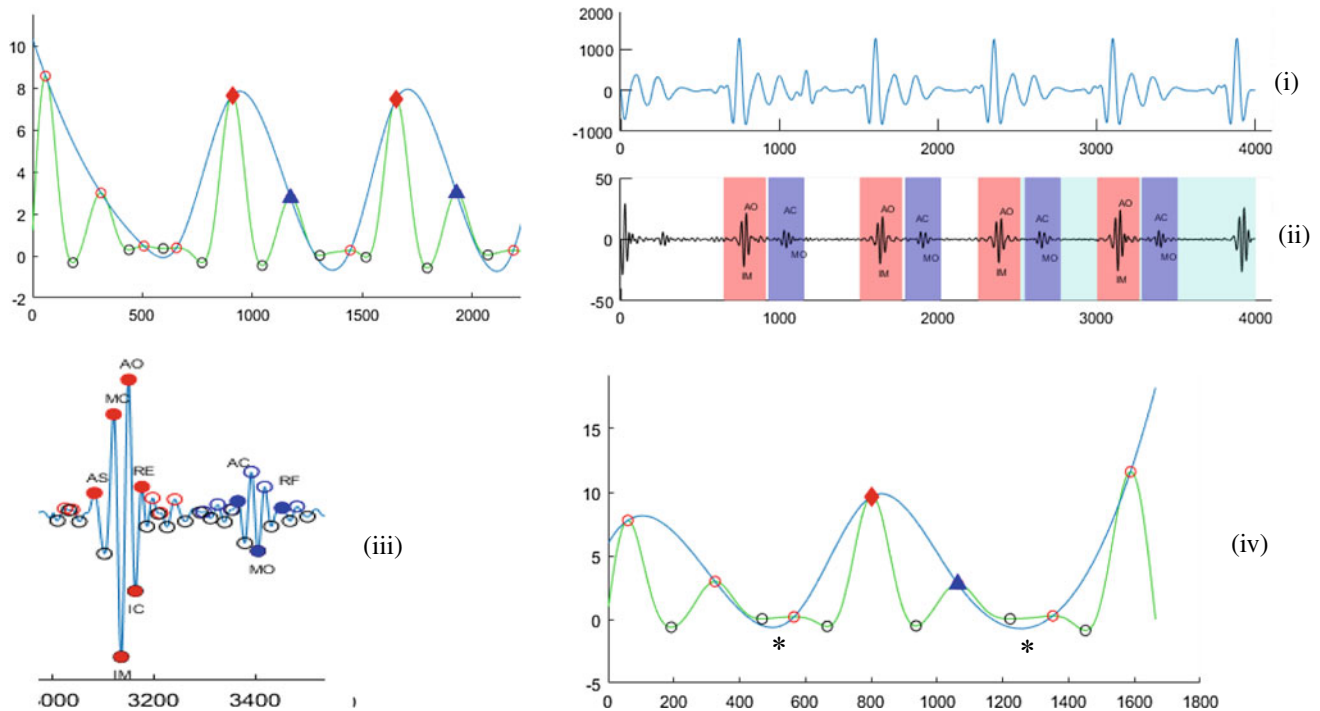


Fig. 2 Detection using interpolation. **a** Detection at the 3rd second. **b** Detection at the 4th second. (i) ECG, (ii) Searching intervals (red = systoles, blue = diastole), detected events and processing buffer (cyan rectangle) in 8-second window view. (iii) Detected events in

processing buffer. (iv) Detected phases using interpolation (Red diamonds = systolic phases, Blue triangles = diastolic phases, Green = SCG energy signal, Red and black circles = maxima and minima of interpolation, Stars = minima of the interpolation)

forward within the same tolerant interval. The total of missing count was compared with the total manual annotated systoles or diastoles to obtain the missing rate. The calculation time is also measured to estimate the performance. Table 1 shows the results of eight subjects including the error rate and the missing rate. The average shows the mean error and missing rates is under 3% for systolic detection and 5% for diastolic detection. The error and missing rate of diastolic detection are higher than systolic detection. The algorithm has an excellent result on subject 1. Subject 8 is a special case who has very weak diastolic signal, so it causes the high error and missing rate of the diastolic detection. The average calculation time of the interpolation algorithm is 83 ms. Because the method is not too complicated, it can be implemented in real-time applications.

4 Conclusions

The method uses total acceleration of the SCG signal to detect the systolic and diastolic regions based on the detection of aortic valve open and mitral valve open peaks. Because both peaks have stiff slope and high amplitude, they can be located by finding the peaks of the SCG energy signal. The recognition of the systole and diastole algorithm is based on the interpolation and the systolic interval constraint. To improve the overall performance, an adaptive systolic interval should be used instead of a fixed interval. A regression line between the heart rate and the systolic interval should be determined. Cut-off frequency of the low-pass filter should also be adaptive to the heart rate to

Table 1 Error and missing rate on 8 subjects (subject #8 has very low diastolic signal)

Subjects	Manual				Interpolation			
	Heart rate	S:D ratio	Total sys.	Total dias.	Systole (%)		Diastole (%)	
					Error	Miss	Error	Miss
1	78.7 ± 2.7	0.50 ± 0.06	84	84	0	1.2	0	1.2
2	88.7 ± 3.8	0.55 ± 0.09	90	90	1.1	3.3	4.4	8.8
3	75.2 ± 2.9	0.57 ± 0.09	76	77	0	1.3	0	2.6
4	98.9 ± 4.3	0.65 ± 0.10	100	100	0	1	5	6
5	76.4 ± 4.3	0.55 ± 0.04	80	79	5	7.5	5	6.3
6	79.7 ± 2.3	0.67 ± 0.10	84	84	4.7	7.1	7.1	9.5
7	70.6 ± 4.5	0.53 ± 0.12	72	73	5.5	0	6.8	2.7
8	102.0 ± 3.2	0.72 ± 0.11	105	106	1.9	4.7	30.1	33.9
Ave. (w/o #8)	83.77	0.59	76.8	77.0	2.3	3.1	4.0	5.0
σ (w/o #8)	11.52	0.07	11.4	11.4	2.6	3.1	2.9	2.9

maximize accuracy. From the regression line, one can also divide the heart rate into small ranges, then each range has a different cut-off frequency.

Conflict of Interest The authors declare that they have no conflict of interest.

References

- Crow, R.S., Hannan, P., Jacob, D., Hedquist, L., Salerno, D.M.: Relationship between seismocardiogram and echocardiogram for events in the cardiac cycle. *Am. J. Noninvasive Cardiol.* **8**, 39–46 (2006)
- Marcus, F.I., He, D.S.: Accelerometer-based method for cardiac function and therapy assessment. United States Patent No. US 2006/0095085 A1. Tucson, United States: United States Patent Office (2006)
- Khosrow-khavar, F., Tavakolian, K., Blaber, A.P., Zanetti, J.M., Fazel-Rezai, R., Menon, C.: Automatic annotation of seismocardiogram with high-frequency precordial accelerations. *IEEE J. Biomed. Health Inform.* **19**, 1428–1434 (2015)
- Shafiq, G., Tatinati, S., Ang, W.T., Veluvolu, K.C.: Automatic identification of systolic time intervals in seismocardiogram. *Sci. Rep.* **6**, 3752 (2016)
- Laurin, A., Khosrow-Khavar, F., Blaber, A.P., Tavakolian, K.: Accurate and consistent automatic seismocardiogram annotation without concurrent ECG. *Physiol. Meas.* **37**(9), 1588–1604 (2016)
- Cooper, S., Cant, R., Sparkes, L.: Respiratory rate records: the repeated rate? *J. Clin. Nurs.* **23**, 1236–1238 (2016)
- Webster, J.G.: *Medical Instrumentation: Application and Design*. Wiley, New York (1998)
- Modal, T., et al.: Prognostic implications of the systolic to diastolic duration ratio in children with idiopathic or familial dilated cardiomyopathy. *Circ. Cardiovasc. Imaging* **7**(5), 773–780 (2014)

Application of Computational Anatomy into Primarily Diagnosing Cardiac Status

N. V. T. Kien, T. M. Linh, Tin T. Dang, and Anh Dinh

Abstract

Computational anatomy refers to the study field of anatomical geometry and the visible scale of the form and structure of organisms. It greatly benefits cardiac experts by exposing the visual structure of the heart: by modelling internal organ in its three-dimension image, general conclusions can be drawn from observing its shape, taking its measurements, calculating its volume, and so on. This method has minimized the time taken as well as the cost needed to diagnose accurately. The goal of this paper is to create a software which allows to construct a 3D cardiac image from patient's CT scan or MRI. Through this model, several data can be extracted and used to make the first-stage deduction whether the heart is in its healthy state. The state is determined by applying computer graphics and data analysis methods for modelling and computing.

Keywords

Cardiac diagnosis through images • 3D model from CT scans • Application of computational anatomy • Healthy heart features • Common properties of a normal heart

1 Introduction

Located at the center of the chest, the heart possesses various significant functions essential for a healthy, living body as its malfunction can create critical, even lethal, effects. As an organ, the heart is also vulnerable to ailments as well as

maladies. According to World Health Organization (WHO), nearly one-third of all deaths worldwide is caused by cardiovascular disease (CVD), which includes cardiac malfunction or structure disorder such as stroke, cardiovascular disease, cardiac valve disease, peripheral artery disease, etc. A recent report [1] from the American Heart Association in 2017 about heart disease and stroke statistics claims that approximately 800,000 strokes take place in the United States yearly. This apparently means nearly every four minutes pass, a person in America dies of a stroke. Globally, stroke becomes the second-leading cause of death after ischemic heart disease.

Nonetheless, 90% of CVD is curable if early detection and timely medication are applied. Since the invention of CT scan, research, diagnosis, and treatment of heart diseases have achieved numerous significant results. CT scan images (DICOM images) provide physicians a better view of the internal parts of a human body, thus allowing them the means to analyse the organs in a more effective and accurate way. To further improve the analysis results, rendering a 3D image is necessary.

This work aims to apply computational methods into visualizing the 3D anatomy of the heart and estimating a number of cardiac data for further determination its healthiness by a professional. The entire process in this report consists of three parts.

First, a number of healthy heart CT scan data are collected and thoroughly analysed. Average values of those sample data are calculated and few of cardiac properties are chosen. One of the easiest calculable properties to state a heart healthy is its volume. Another essential characteristic of the heart can include the roughness index of its surface. The ratio of the inner part of heart should also be mentioned. While there are other criteria to define a well-functioned heart, this paper focuses on presenting those three features: the volume, the surface roughness and the ratio.

Second, based on these mean values from sample data, a 'model' heart is displayed in 3D. To construct this three-dimensional image of the heart, these following steps

N. V. T. Kien · T. M. Linh · T. T. Dang (✉)

Department of Electricals and Electronics Engineering, Ho Chi Minh City University of Technology, Ho Chi Minh City, Vietnam
e-mail: dtin@hcmut.edu.vn

A. Dinh

Department of Electrical and Computer Engineering, University of Saskatchewan, Saskatoon, Canada

must be carried out respectively: Extract part of CT image, which contains cardiac data -> Use Hysteresis threshold to set the chosen parts to binary value -> Extract all blobs from segmented data (Connected-component labelling) -> Find and fill the maxima blob and delete other smaller ones -> Render 3D model.

Third, the CT cardiac scan images from a patient are read. Similar processes are applied on this set of data, as the crucial values (volume, surface roughness index, ratio, etc.) are measured and compared with its sample counterpart to conclude its healthiness. To give out a vividly visual view, a 3D image of this heart is also produced and displayed along with the 'model' ones.

Criteria of a healthy heart depends on many biology factors. Therefore, a 'model' heart with its standard features should only be applied to a determined group of people who bear similar physical traits. In this paper, due to lack of access to authentic cardiac CT data, only one set of data (188 slices) is used to present the final results. Nevertheless, it is believed that the theoretical conclusion should be accurately reached if sufficient data are gathered.

2 Algorithms

2.1 Three Dimensions-Model of the Heart

Normally, CT images that contain data of the heart are the scans of the chest. To be more exact, it is located in the central part of each slice, surrounded by other organs such as ribs and lungs. Distinguishing one organ from the others is possible due to the principle that intensity values are usually similar for each organ but different from their neighbour ones. Primary segmentation is still required, however, since it allows for extracting useful data from the whole slice without mixing with other parts having same intensity values. By manually selecting the necessary area on the slice that shows the largest data, the same operation can be practiced on the rest of the CT set.

The second step of image analysing process strengthens the boundary differences through the threshold. CT scan images are grey-level, thus the threshold can convert them into binary by setting all pixels whose intensity value are above a certain degree to 'one' (or 'zero') and the rest to 'zero' (or 'one'). To give out clearer results, multiple thresholds are used. In this report, Hysteresis Threshold is applied:

1. Determine 2 thresholds T_{low} and T_{high} .
2. For all pixels whose value T is between T_{low} and T_{high} , set T to 1.

3. For all pixels whose value T is lower than T_{low} or higher than T_{high} , set T to 0.

Different thresholds being chosen lead to diverse binary images. Therefore, appropriate parameters should only be reached after various attempts.

Thirdly, extracting blobs [2] is conducted. A blob is defined as a part of the image whose certain properties are constant or nearly constant. All pixels in one blob are considered as the same organ. There are many methods for extracting blob, labelling connected-component (Two-pass) is utilized in this work since the previous step has made the data into '0' and '1'. From relevant input data, a graph is constructed which contains vertices (store information required by the comparison heuristic) and connecting edges (inform about connected 'neighbor'). The algorithm scans the whole graph through each pixel respectively and labels the vertices based on their neighbour's connectivity and relative values.

The next step is to delete the unwanted blobs to retain precisely only the data needed. This is the last step to exclude any other information on CT slice. Calculating every blob's pixel number and comparing them is the fastest way to determine the most significant ones. Then the smaller blobs are omitted, as the largest one's inner part is filled. The output of this step is a set of binary images, in which each slice contains only a single blob illustrated parts of the heart.

Finally, 3D model is constructed by a lot of polygons through the Marching Cubes technique [3], which aims to generate an iso-surface (contour). The Marching Cubes algorithm includes:

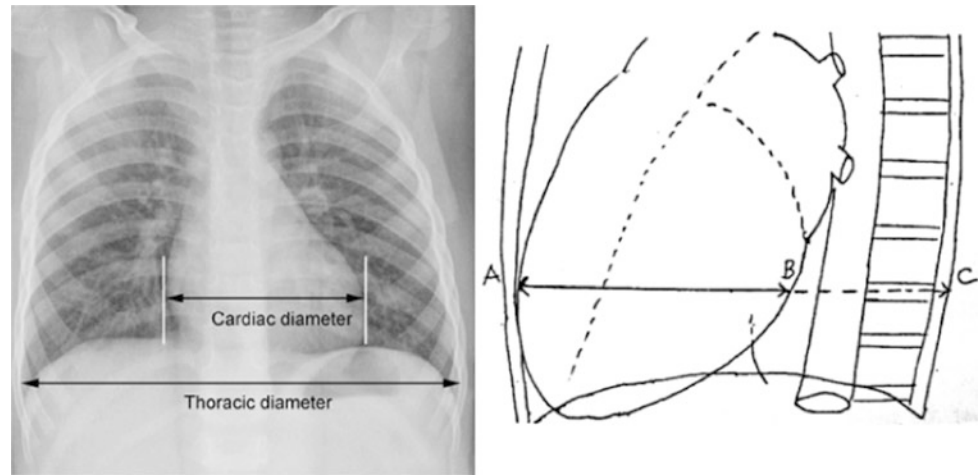
1. A lookup table of iso-surface is prepared.
2. Retrieve iso-surface boundary of every grid cube.
3. Apply linear interpolation to calculate iso-surface vertex coordinates.

2.2 Volume of the Heart

After image analysis process, the volume of the heart can be computed by simple mathematical calculation. Having known the length of gaps between CT slices, a unit cube can be determined with its precise parameters $a \times b \times c$. The description of this step consists of three minor actions:

1. Measure a , b , c .
2. Scan through slices to count the non-background pixels, store in a variable.
3. Multiply the value of that variable with the volume of the determined unit cube.

Fig. 1 Front view of heart [5] (left) and side view of heart from left side [6] (right)



2.3 Surface Roughness of the Heart

Digitalizing the characteristics of surface roughness [4] is the most effective method to compare and diagnose defects or tumours of the heart. Numerous parameters are defined and widely applied to characterize this property of the surface. They are listed in BS EN ISO 4287:2000 British standard, which is based on the mean line (the average height of a surface) system. Three of the most common ones is the arithmetic average of absolute values, the root-mean-squared and the peak-to-valley values.

1. The arithmetic average of absolute value:

$$R_a = \frac{1}{n} \sum_{i=1}^n |y_i| \quad (1)$$

where y_i is the distance from the mean line running across the measurement i , and n describe the number of measurements.

2. The root mean squared:

$$R_{RMS} = \sqrt{\frac{1}{n} \sum_{i=1}^n y_i^2} \quad (2)$$

3. The peak-to-valley values:

$$R_{zd} = \frac{1}{n} \sum_{i=1}^n (R_{pi} - R_{vi}) \quad (3)$$

where R_{pi} and R_{vi} are the maximal distance from the mean line toward directions of up and down relatively for each of n number of measurements.

2.4 The Ratio of a Healthy Heart

Among various ratio to judge the healthiness of the heart, diameter ratio [5] and side ratio [6] comes primarily. Based on these numbers, cardiac examiners can confidently diagnose many cases of abnormality such as boot-shaped heart, egg-on-side appearance, snowman appearance, triangular heart, cascade right heart border, and water-bottle appearance. Therefore, patients can receive timely treatment as the diseases are still in its developing stages.

By comparing the horizontal diameter of the heart with the horizontal diameter of the thoracic cage seen on the frontal of the model constructed from CT images, the approximate value of diameter ratio can be estimated. If this value is less than 50%, the conclusion of 'normal' can be drawn. Side ratio is taken from the side view of the heart. This number is the comparison of AB and AC. As illustrated in Fig. 1, AB is the largest distance traversed through the organ and AC is the straight line extended from AB to the end of the spinal cord (point C). According to [6], any value of this ratio remains less than 42% is acceptable as 'normal'.

3 Result

In the result table (Fig. 2), four features of the patient's heart are computed and shown respectively, along with the preset standard values. The first two features (volume and surface roughness) are calculated based on the 3D model, which indicates that their errors are corresponded to and accumulated from every step of the image processing method. Among those steps, choosing threshold levels is significantly

Feature	Healthy Heart	Patient's heart	Judgement
Volume	~3000000	3054933	Healthy
Roughness	~0.2	0.1762	Healthy
Diameter ratio	≤ 0.5	0.4843	Healthy
Side ratio	≤ 0.42	0.5291	Unhealthy

Fig. 2 Final diagnosis results

contributed to the loss of data. The choice of threshold levels is highly dependent on the quality of input data. It is well-known that different scanners produce varying image qualities, and each set of data has its own optimal threshold levels. Thus, the practical performance of thresholding algorithms such as Adaptive thresholding and Otsu thresholding is inferior to that of the manual technique of choosing threshold levels. This manual technique shows its domination in the case of processing multiple sets of data that are collected from different scanners. Most of the lost data points are then interpolated by filling the image holes and using the gaussian filter technique. The accuracy in image processing can be thoroughly determined by comparing the cross-sectional area of the extracted image with that of the original image. The other two features (diameter ratio and side ratio) have smaller error range as they are determined directly from the CT scan images without any relates to the image processing method. Their precision solely depends on the user's measurement and usually has tolerable error.

The final 3D model can be displayed in both rigid form and polygon mesh form which gives the user a clear vision on the

defects or tumors, by setting the standard heart model in rigid form and the diagnosing heart in the mesh form and displaying both at the same time. It can be seen from the model that the segmentation is at the acceptable level in the middle part. However, the upper part and the lower part still contain flaws such as the discontinued regions. These errors can be reduced in further research by applying other algorithms.

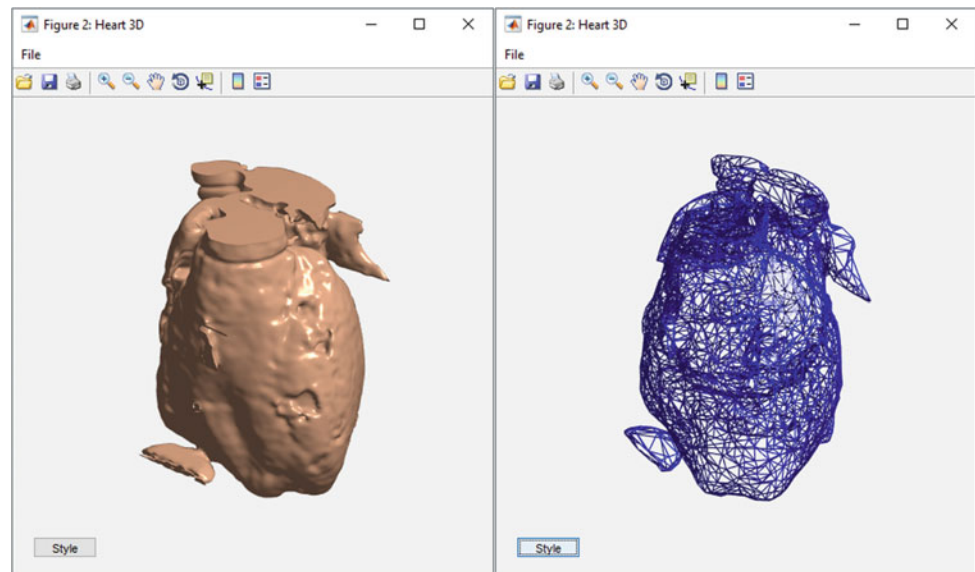
4 Conclusions

The primary diagnosis process of cardiac status through computational anatomy has been simulated in MATLAB. Results have shown that 3D model of hearts are successfully built and four features of healthiness are computed and analyzed. In theory, a large amount of CT sets is used to determine healthy features of heart. In this work, due to the lack of available data, statistic results from medical research are used to define 'normal' instead. However, the display of a patient's heart along with standard one is achievable by demonstrating the former in mesh form and the latter in rigid form (Fig. 3). This technique can be applied to other organs as well.

In further research, the quality of the 3D model can be improved by applying better image processing method. The number of features to prove the healthiness of heart can also increase to draw out more precise diagnosis.

Conflict of Interest The authors declare that they have no conflict of interest.

Fig. 3 Final 3D display (left) and display model in polygon grid (right)



References

1. Benjamin, E.J., Blaha, M.J., Chiuve, S.E., Cushman, M., et al.: Heart Disease and Stroke Statistics. The American Heart Association (2017)
2. Connected-component labeling. Wikipedia. https://en.wikipedia.org/wiki/Connected-component_labeling. Accessed 27 Mar 2017
3. Volume rendering and marching cubes. <http://teaching.csse.uwa.edu.au/units/CITS4241/Handouts/ppt/Lect05-06-VolumeRendering-MarchingCubes.pdf>. Accessed 08 Mar 2018
4. Adams, T., Grant, C., Watson, H.: A simple algorithm to relate measured surface roughness to equivalent sand-grain roughness. *Int. J. Mech. Eng. Mechatron.* **1.2**(2012) (2008)
5. Heart size, overall configuration, and specific chamber enlargement. *Radiology Key*. <https://radiologykey.com/heart-size-overall-configuration-and-specific-chamber-enlargement/>. (2016). Accessed 06 Apr 2017
6. Khoang, N.: Chẩn đoán hình ảnh Hệ tim mạch. *Hình ảnh y khoa* <https://hinhanhkyhoa.com/video-y-khoa/video-sieu-am-tim-mach/chan-doan-hinh-anh-tim-mach-bs-nguyen-quy-khoang.html> (2017). Accessed 30 May 2017

Implementation of a Pilot Cyber Medical System with Blood Pressure Devices for Telemedicine in Binh Duong Province (Vietnam)

T. N. Viet, D. M. Thai, N. P. Nam, and Vo Van Toi

Abstract

In this project, we implemented a pilot cyber medical system which consists of 100 devices to measure blood pressures and heart rate, and a core software to collect and manage obtained data. We developed a special Manufacturing and Quality Test System to test and control the device's quality during their manufacturing. The final products were tested for precision and reliability against a mercury device and a simulator. We developed a core software based on the Cloud Telemedicine Information System. It runs on personal computer and/or smartphone to provide considerable utilities for physicians to monitor patient's blood pressures online. The healthcare providers will take care of patients from distance and intervene immediately, if necessary. Each patient has his/her own website. This allows patients to get access to their measurement history and exchange messages with the doctors when needed. The healthcare providers have also their own website to monitor their patients. To protect the confidentiality all data were coded using Advanced Encryption Standard 128 bit. This cyber medical system was implemented in Binh Duong province (in Vietnam) to test its efficacy. To this end, 100 patients will use the device and another 100 will not use it (control group). Both groups will be monitored by the same healthcare providers. The obtained results will be compared using paired t-test.

Keywords

Telemedicine • Blood pressure • Heart rate

1 Introduction

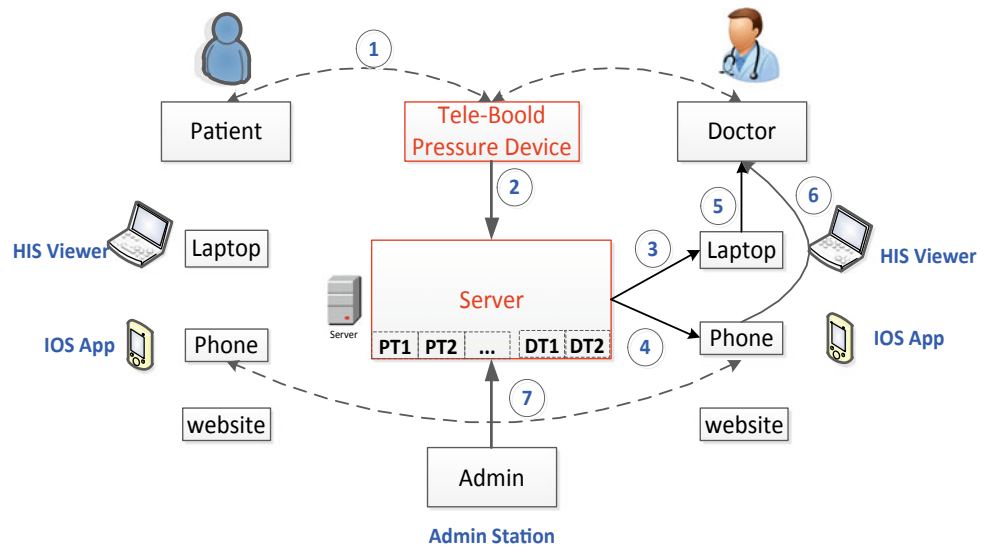
Diseases related to blood pressure such as hypertension and hypotension have become a great burden in either economy or sociality, they are also the leading cause of human death in the world. The World Health Organization (WHO) has recorded 7.5 million cases of death, which accounted 12.8% of the cases of total death in 2008 [1]. In Viet Nam, there are more than 90 million people and a large part of them live in remote areas where the healthcare services are quite limited. According to official statistics from the Vietnam Cardiovascular National Institute the rate of high blood pressure among adult population increases rapidly from 1.5% in 1960 to more than 10% in 1970, 16% in 2000 and 25% in 2012 [2]. An important aspect is that most of them do not realize that they have high blood pressure.

The reasons for this situation are lack of adequate healthcare establishments, lack of competent health care providers and lack of appropriate medical devices. Because high quality telecommunication covers the whole country, the aforementioned lacks would not be so severe if there is a system that links together healthcare establishments, healthcare providers by means of appropriate medical devices. Therefore, we proposed to develop a cyber-physical system for healthcare for Binh Duong province (Vietnam) and this model can be expanded to other third world countries.

Figure 1 illustrates the basic cyber medical system in Binh Duong province. In the first process, the patients use the tele-blood pressure devices to measure their blood pressure results, with the help of internet accessing of the device, this result will be sent and stored in a central server for long-term observation of patients and doctors in the second process. In cases of having any problem concerning with patient's hypertension, the server system will automatically send an alert to the doctor who has responsibility to take care of that patient. This alarm process is displayed by means of laptop (process 3, 4) or smartphone (process 4, 6). Then, the doctor can recognize and give a soon diagnosis by using cell phone

T. N. Viet (✉) · D. M. Thai · N. P. Nam · V. Van Toi
Department of Biomedical Engineering, International
University—VNU, HCM, Ho Chi Minh City, Vietnam
e-mail: tranngocviet93@gmail.com

Fig. 1 The cyber medical system is performed in Binh Duong province



showed in process 7. Evidences show that effects of hypertension can be prevented by soon diagnosis, prognosis and proper treatment. Therefore, monitoring of patient’s blood pressure result is mandatory to eliminated diseases with respect to cardiovascular.

2 Designing of the Cyber Medical Healthcare System

2.1 Design and Manufacture Tele-Blood Pressure Device

We design a Tele-Blood Pressure device with characteristics that fit in the environment of developing countries such as affordable, sturdy, fixable, durable, reliable, easy to use, and

energy efficient. Because the device will be mass produced therefore its design will take into account the human factors, cost-effectiveness and local capacity of production. The diagram of hardware design is displayed in Fig. 2, the STM32 is chosen to design for microcontroller, with the aid of ARM cortex- M3 insight in MCU, this IC can calculate the algorithm of measuring blood pressure by oscillometric method. In addition, we designed analog filter circuits to remove noise signals from a cuff.

Specially, the Tele-blood pressure has three data connection: GPRS, WiFi, and USB. The result of blood pressure will be sent to a central server via wireless connection as GPRS or Wifi. The direct connection of USB is used for configuration of the device via particular software. And all information config is saved in ROM IC. In regarding to display indexes as Systolic, Diastolic, and Heart rate, the

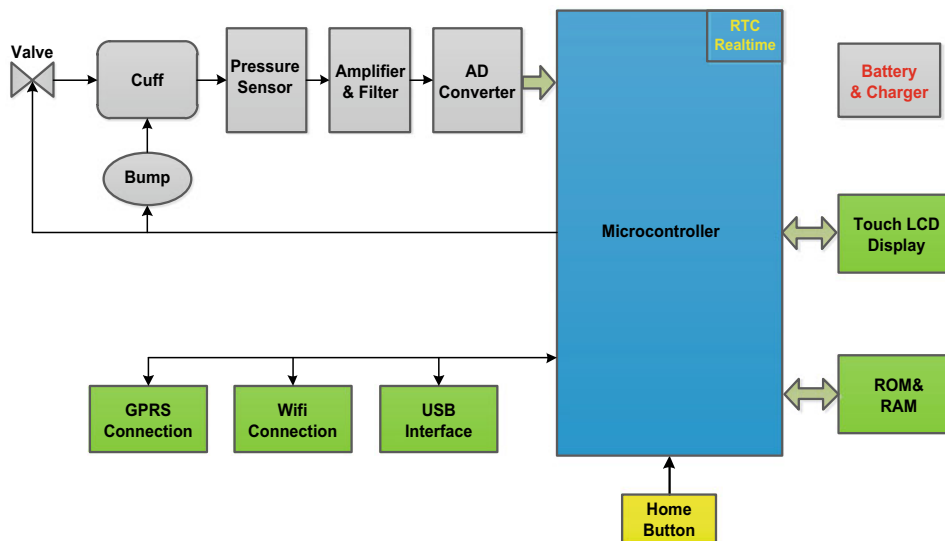


Fig. 2 Diagram of tele-blood pressure device



Fig. 3 The LCD with 320×240 in tele-blood pressure

touch LCD with 320×240 resolutions is used to show that results. This LCD is illustrated in Fig. 3.

Implement of MQTS Tester for manufacturing

The production will follow the Manufacturing and Quality Test System (MQTS). We carry out the tester illustrated in Fig. 4 to manipulate factors of PCB main board manufactured by a factory for instances: cut frequency of analog filter block, LCD display, battery charger, and etc. To ensure the quality of the circuit and the accuracy of the specification, the final product will be applied for public using permission. As this is a standard non-invasive device, we foresee there will be no issue.

Calibration process of the blood pressure device

The product will be tested for accuracy and reliability following a standard test protocol e.g., European Society of Hypertension International Protocol, with the standard mercury sphygmomanometer. In addition, it is difficult to calibrate follow in this protocol; we have proposed the new procedure demonstrated in Fig. 5 for calibrating Tele-blood pressure device.

In Fig. 5, the acoustic signal in cuff is recorded by analyzing software in PC. At the same time, we also acquire the

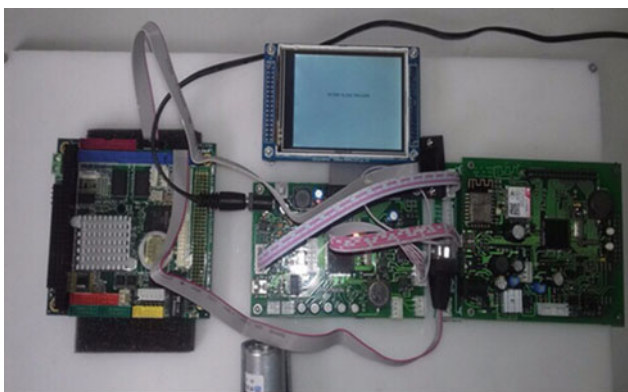


Fig. 4 Demonstrated the tester system is performed

pressure signal in sphygmomanometer. The results in the blood pressure device are compared to the result of calculating by Korotkoff sound in the audio signal on analyzing software. In terms of Simulator, we use FLUKE Pump2 to calibrate the quality of the devices. We will apply standard tests to make our system reliable and compatible with other systems and to be developed devices. It allows connecting to systems in developed countries to benefit their latest progress.

2.2 Build a Cloud Telemedicine Information System—CTIS

CTIS is a core of infrastructure platform capable of implementing Tele-healthcare applications for hospitals, doctors and patients. It includes:

- **CTIS Server:** based on cloud computing, it allows the Tele-blood Pressure Device to measure blood pressure of patients at home or anywhere, connect and send results via the Internet. It also saves the results in a database system helping doctors to diagnose and treat patients from distance using HL7 international standard. This system is shown in Fig. 6.
- **Application software development:** The software connects doctors and patients, and allows them to communicate together in real time. Each patient has a personal and protected website displaying results history in charts, patient and doctor information and communications, and patient medical history. Each doctor has his/her own website to manage the current state of patients for immediate intervention, if necessary. Patient records will be processed, protected, stored and retrieved. Efforts will be made to protect confidentiality and avoid hacking, errors and loss of data. We also developed software running on smartphone or tablet of Android/iOS with data transferring based on GPRS or Wifi technology. It will allow the doctors to access easily the internet to receive notifications of abnormal results from their patients for immediate intervention. The technology used in this system has become more and more accessible, popular and affordable.

2.3 Establish a Network of Patients in Binh Duong and Healthcare Providers in Well-Established Hospitals to Test the Efficiency of the System

This system will support diagnosing and monitoring and take care of hypertension patients remotely. So, our subjects

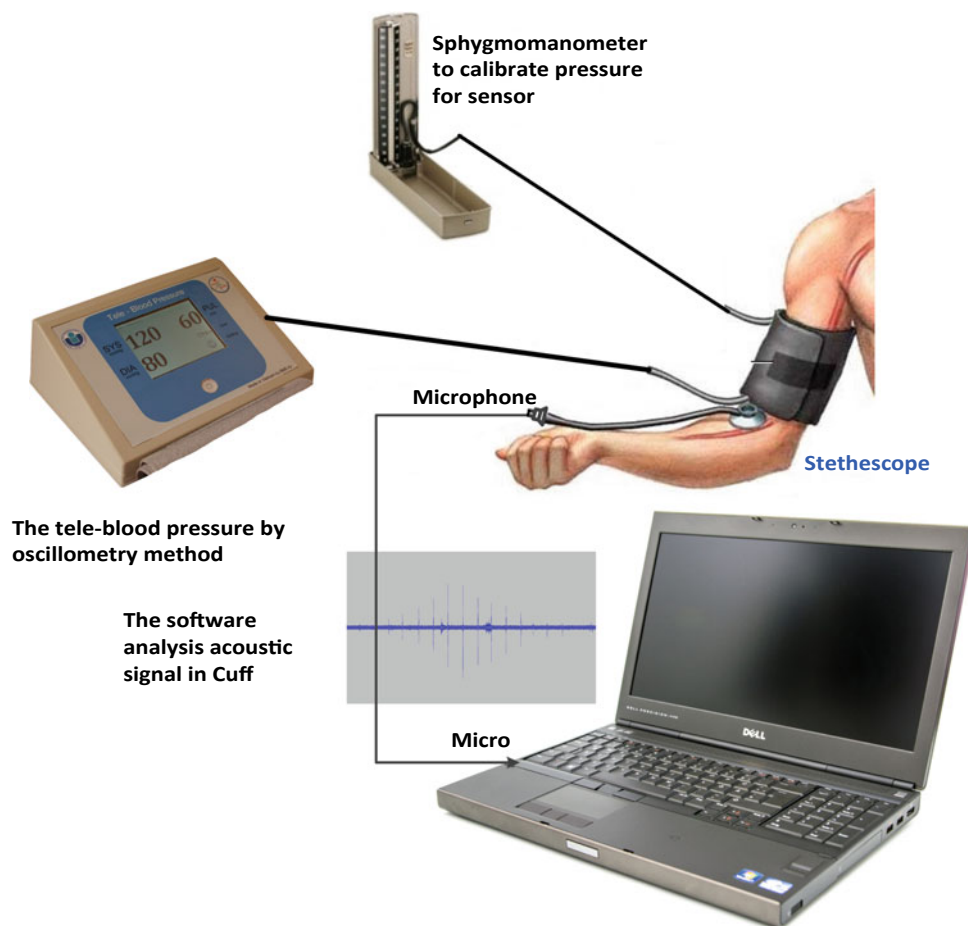


Fig. 5 The method of calibration between sphygmomanometer and our devices

are 100 patients suffering from cardiovascular disease at Binh Duong. In addition, the system will also connect doctors of Board of Health Care for Binh Duong Leader and outpatients in order to remote keep tracking. In difficult treatment cases, it allows that the doctor of the Binh Duong Hospital needed to hold a consultation or remote diagnosing from the central hospital.

Total of research time is 12 months, and randomized controlled clinical trial (RCT) method is used for estimate two groups pretest and posttest randomized experiment design. Therefore, this research is performed in 2 parts of 2 patient groups:

- Part 1: before intervention, in 6 months, when the Tele-medicine is developed, two patient groups will be kept track and treatment using traditional method at clinical rooms in order to estimate the condition of patients.
- Part 2: in the next 6 months, the Tele-Health is already to implement in practice, the intervention group will be

monitor by using the Tele-Blood Pressure Device while the other group is still used normal method of treatment.

The innovation of this project is application of new technologies in medical device design in order to increase their value in treatment and diagnose patients remotely, transferring the Technology to companies, and training of technical person. Regarding to statistics, all data of patient will be processed according to t-test model.

3 Result of Experiment

We designed Tele-Blood Pressure device with high compatibility to customers, because our purpose is that we will create industrial mold completely with small, comfortable, and reliable. In additional, PCBs of the device are optimized for mass production by using by using our MQTS Tester. We also develop firmware of blood pressure device suitable

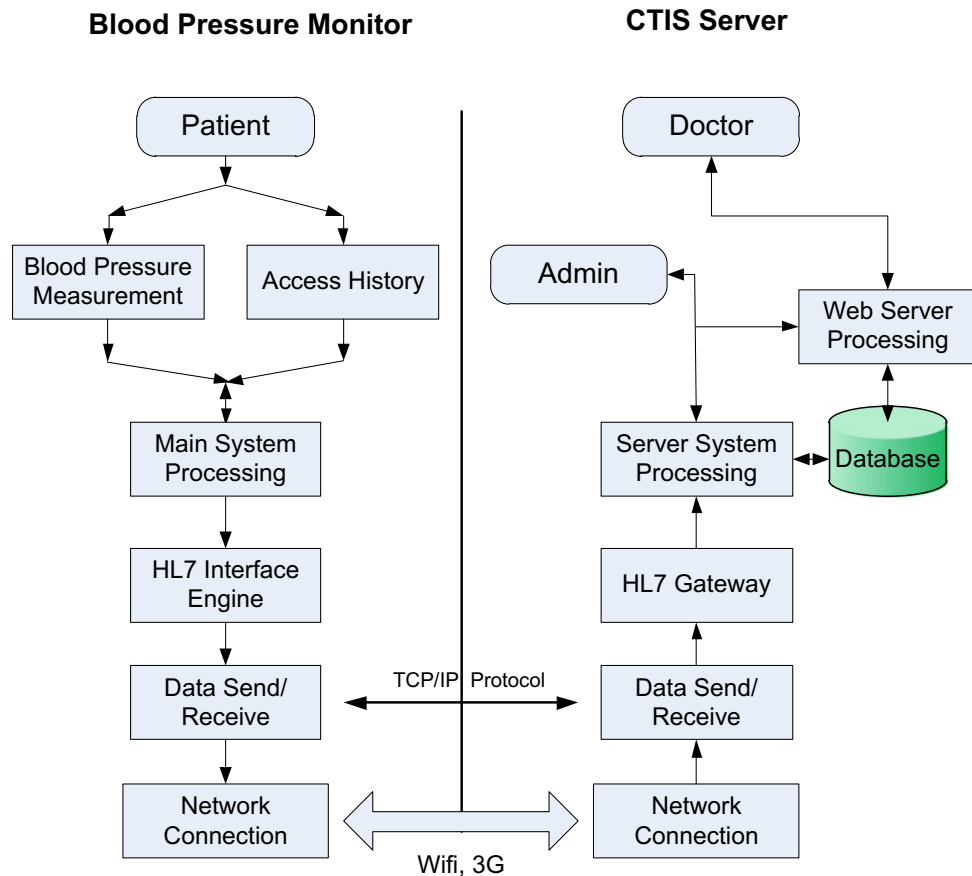


Fig. 6 The data flow of blood pressure from patient to CTIS server and doctor



Fig. 7 The tele-blood pressure after assembly successfully

to our CTIS System. Consequently, we manufactured 100 Tele-Blood pressure devices uniformly quality successfully, and this device is shown in Fig. 7.

In related to comparing with BP pump2 FLUKE Simulation, we use a random device of blood pressure to measure with the simulator. These results are displayed in Fig. 8.

Form results presented in Fig. 8, with a range from 80/40 mmHg (Systolic/Diastolic) to 150/110 mmHg, we can

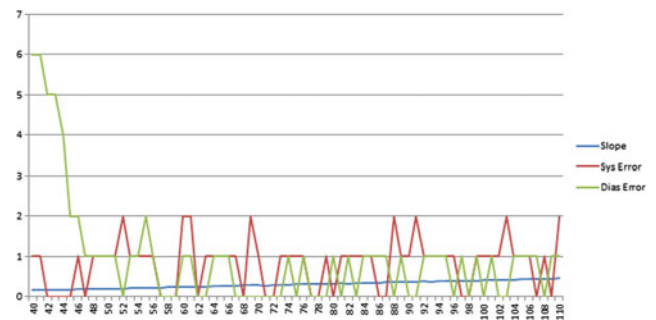


Fig. 8 The errors when calibrating with FLUKE Pump2 Simulator

see that if the pressure of systolic in the simulator is greater than 46 mmHg, the total errors of systolic and diastolic is smaller or equal than 2 mmHg. This error is acceptable in manufacturing digital blood pressure devices.

In terms of CTIS system, we developed amounts of software for tracking and monitoring the patients' data of blood pressure. There are three main software systems: CTIS AppServer, CTIS AdminStation, and CTIS HISViewer. More importantly, the Graphic User Interface (GUI) and functions of aforementioned software programs adequate the

requirements of initial design target. These GUIs are demonstrated in Figs. 9, 10 and 11.

The admin software showed in Fig. 10 is used by Administrator, an account having the highest level control in the system. It can enable or disable any user account and accessing and monitoring all data in the system.

Bellowing the accounts of administrator and super moderator in the CTIS system, there are numbers of accounts of doctor and user-patient. Every doctor account is divided to take care of patients by above accounts of admin and mod. The GUI of HISViewer is illustrated in Fig. 11.

Because of developing of portable connected device, we also performed a software for iOS on Apple Device such as iPhone, iPad, and iPod in Fig. 12. This software is programmed in Swift language of Apple. Basically, this software is similar to PC software in Fig. 11. This software can monitor data for instances: systolic with red line, diastolic with blue line, and heart rate with green line. Indeed, it can run on iOS operating system, the convenient of the system is

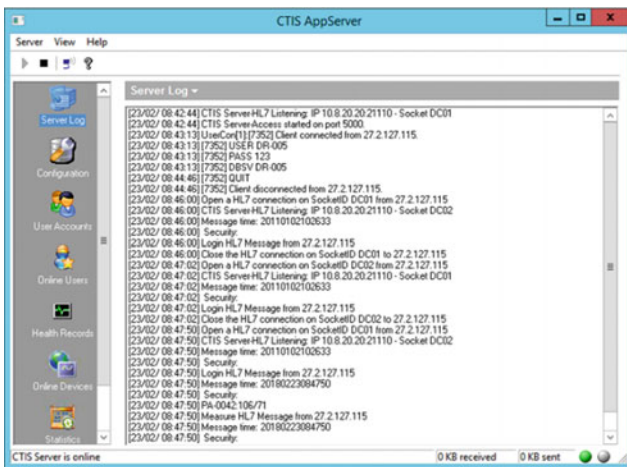


Fig. 9 A core system software of CTIS AppServer

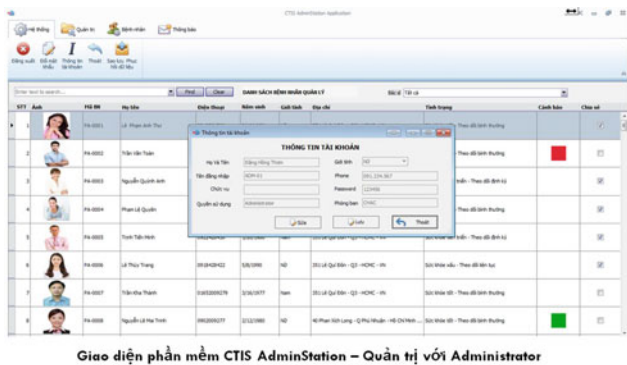


Fig. 10 A administrator software for CTIS system

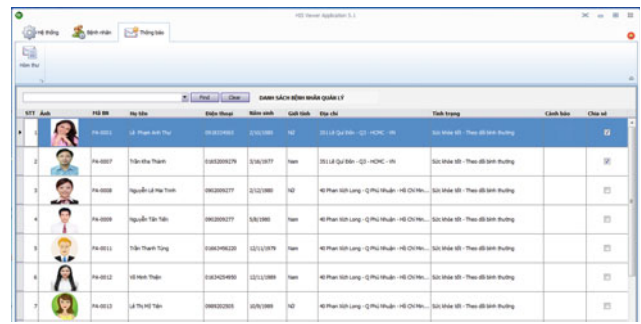


Fig. 11 A HISViewer software for doctor in CTIS system

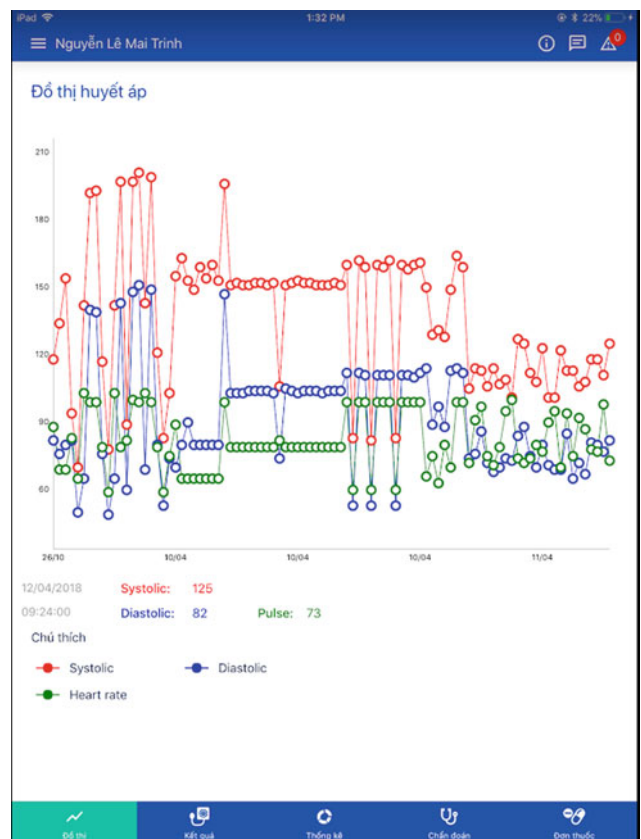


Fig. 12 Illustrated HISViewer software for Apple devices

expanded considerably, because the doctor can use their phone to look after of the patient anywhere.

The CTIS system can store the patient’s blood pressure from a distance, improve their health and save their time. Therefore, the long-term data storage can help the doctor pre-diagnosis the patient’s problem by the soon alert in the health indicators sent from the device. The system also helps doctors share experience of treatment methods, the use of medicine with each other.

4 Conclusions

In this paper, we developed a cyber-medical system which is telemedicine system for Binh Duong province for pilot research. If it success, this model can be extended to third world country to eliminate some health care problems. Basically, this system contains implementing hardware of Tele-blood pressure devices, developing of software programs for CTIS system, and establishing a network between patients and healthcare providers. As a result, with the aid of designing MQTS Tester, we measured a number of factor related to quality of PCB board, and manufactured 100 blood pressure devices with uniformity quality successfully. With respect to calibration, we use two methods: the first one is calibration with BP pump2 FLUKE Simulator, and the other is checked by comparison with a standard of blood pressure, a sphygmomanometer. In implement of CTIS system, we developed a huge numbers of software programs

on many infrastructures for instances: computer, Apple devices, and etc. Concerning with establishing the network to test performance of our system, we will divide two groups of patients: traditional group and controlled group. All data of these groups will analyze by using t-test model in statistic.

Acknowledgements This research is funded by Department of Science and Technology of Binh Duong under grant number 02/HĐ-SKHCHN.

Conflict of Interest The authors declare that they have no conflict of interest.

References

1. WHO, World Health Organization: A global brief on hypertension (2013)
2. VCNI, Vietnam Cardiovascular National Institute (2016)

A Low Cost High Voltage Power Supply to Use in Electrospinning Machines

Thai M. Do, Minh H. Ho, Thien B. T. Do,
Nam P. Nguyen, and Vo Van Toi

Abstract

Nowadays, Researching in the electrospinning field has expanded significantly because electrospinning can create nanofiber scaffolds for the flourish of tissue engineering. The scaffold is essential a platform that supports the migration, proliferation of cells and formation of tissues for wound healing applications. Therefore, the developing of electrospinning is also mandatory for spreading of tissue engineering field at Vietnam. In electrospinning machines, the main components include a high voltage DC source, a syringe pump and a grounded collector. In this study, we designed a low-cost high voltage power for electrospinning process by using a Zero Cross Voltage Switching (ZVS) driver circuit and a flyback transformer. As a result, the power worked effectively and stably as well as we expected. To prove its advantage quality, we do an experiment and investigation to examining the high voltage in an electrospinning system; we found out a set of parameters in our conditions that give a good membrane of structure morphology at 15% (w/v) PCL, 1 ml/h, 17 KVDC, and 20 cm in distance between needle tip and collector.

Keywords

High voltage power supply • Electrospinning • Flyback transformer

1 Introduction

Because the material on the nano-size has a great deal of potential in huge applications such as biology, engineering disciplines and space applications, the scientists are interested in researching and developing nanotechnology [1]. One of the more popular processes to create nanofibers, a form of nanotechnology, is through electrospinning. Electrospinning is used to create nanofibers by means of application of a very high electric field [2]. The nanofibers of electrospinning have an essential role because of the similarities of the properties of the extracellular matrix within tissue human [1].

1.1 Some Methods to Treat Wound Healing

For the treatment of skin lesions, there are some methods to be studied extensively, such as the application of “auto-grafts”, a method of implantation of the patient’s own tissue on their wound; or “allograft”, implanting the raw tissue of the donor on the wound of the patient. Although these methods have solved most of the problems concerning with skin lesions, the results of autografts are costly, painful, limited by surgical tasking, and localized tissue grafts. The treatments can result in blood infections and hematoma. Similarly, the allograft method also has serious limitations, as the problem of finding a donor, risk of rejection by the immune system of patients and disease from the donor [3].

With the help of advances in tissue technology, the manufacture and research of synthetic cellular by scaffolds, created by biocompatible materials that support wound healing. It is a good way for effective skin regeneration [4]. The scaffold is essentially a scaffold that supports the formation of tissues and usually implanted with high growth factor. The new tissue of scaffold is rapidly replaced a huge of venerable tissue. Therefore, the scaffold of implant cells can be used to synthesize tissues, and then it be injected

T. M. Do (✉) · M. H. Ho · T. B. T. Do · N. P. Nguyen · V. Van Toi
Department of Biomedical Engineering, International University—VNU HCM, Ho Chi Minh City, Vietnam
e-mail: dmthai@hcmiu.edu.vn

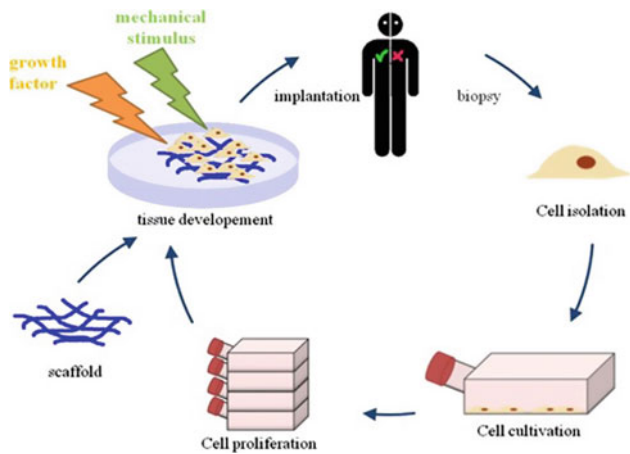


Fig. 1 Illustrated the process of artificial skin formation on the scaffold [4]

in vitro to remove loss tissues in particular. The implantation is directly into the wound by means of the patient's tissue to self-regenerate the lost tissue [4]. This process is demonstrated in Fig. 1.

1.2 Basic Components of Electrospinning Machines

The main components of an electrospinning system content a high voltage DC supply, a syringe pump system and a collector connected to ground of the DC source. This system is illustrated in Fig. 2. In regarding to research of the electrospinning machine, it has been very successful in over the word. However, in Vietnam, there is a few research related to developing electrospinning machines.

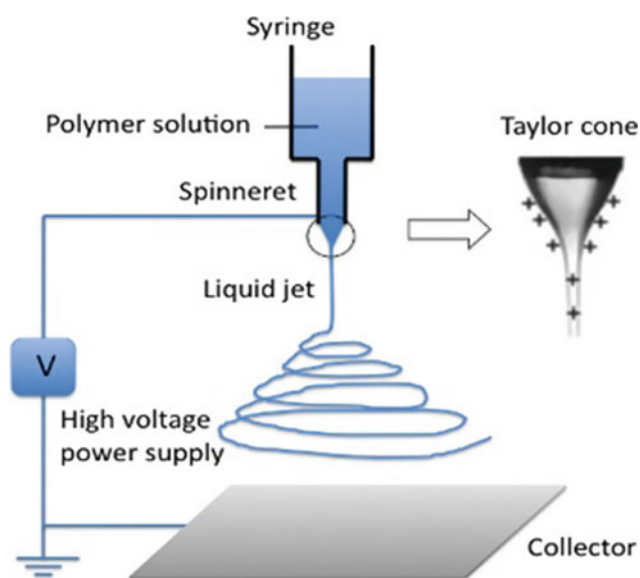


Fig. 2 Principles of operation of electrospinning machines [5]

In this situation, this machine that we want to create is obligatory for Vietnam, and it will play an important role and considerably affects to make a break through in Vietnam's tissue engineering field.

2 Designing of the High Voltage Power Supply for the Electrospinning Machine

2.1 Design High Voltage Power

In Fig. 3, the 220 V AC RMS source is converted to 26 V AC RMS source by using a transformer with 240 W. Then, this 26 V AC RMS source will be rectified to 33 VDC source. This power is continuously used to supply the boost circuit to creating the high voltage power with 0–40 KVDC, 2 mA for electrospinning.

Regulator circuit with adjustment output.

This is a basic circuit that as the main source of power for flyback transformer and its driver. The XL406 IC is selected to make buck circuit, because the requirement of this block is converted from 33VDC to the adjustment output with 0 → 32 VDC, 8A [6]. By using the variable resistor of R10 in Fig. 4, the output voltage of the regulator can be changed.

ZVS Driver and Flyback transformer.

ZVS (Zero Cross Voltage Switching) Driver is a mazilli oscillator—a basic circuit that can oscillate a various of power with 90% efficiency. For explanation of the oscillator, a simplified version of the mazilli oscillator is demonstrated in Fig. 5.

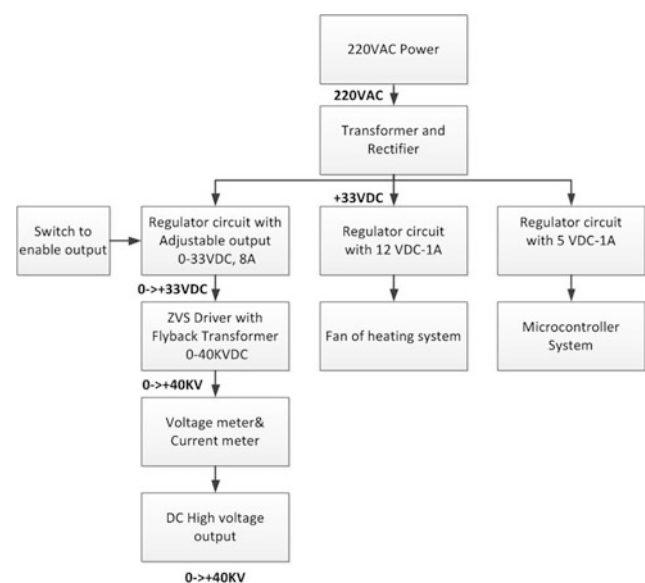


Fig. 3 Diagram of the designed DC high voltage power

Fig. 4 XL4016 typical application circuit (VIN = 33VDC, VOUT = 0–32 V/8A)

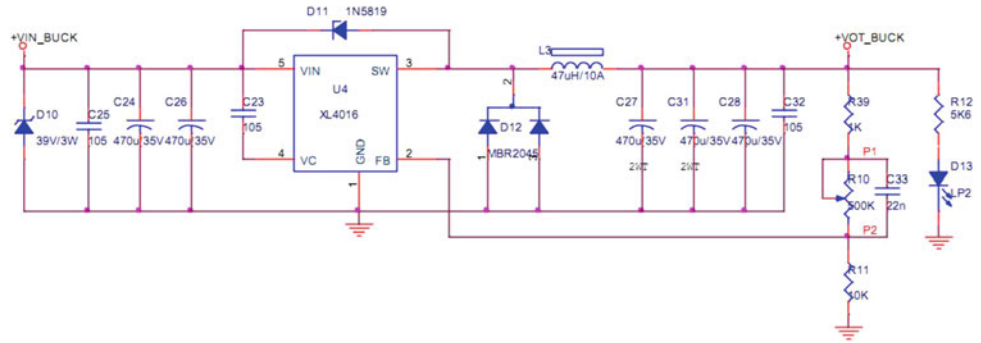
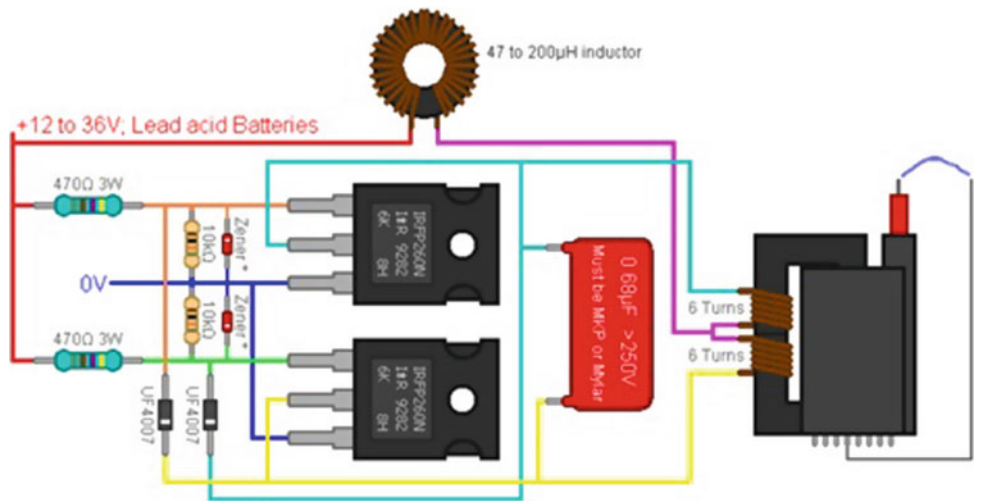


Fig. 5 The easy schematic of demonstration for ZVS driver and flyback transformer [7]



$$f = \frac{1}{2\pi\sqrt{LC}} \quad (1)$$

where: f is the frequency in Hertz, L is the inductance of the primary in Henries, C is the capacitance of the capacitor in Farads.

Because flyback transformers are high frequency transformers, it is very useful to generate high output voltages at relatively low currents. The essential applications are in televisions, monitors, and high voltage power supplies. For this reason, we decided to choose the flyback transformer for this project. It is possible to get high voltage with low cost.

ADC of Microcontroller system.

With the help of internal ADC in the MCU, the voltages of circuits will be recorded; this family has one ADC in-sight with 10-bit resolutions. Because MCU can multiplex between ADC channels, we designed four voltage dividers

with buffer opamp s to monitor the operation of power. The circuits of the voltage divider are described in Fig. 6.

Voltage and current meter.

In relation to voltage indicator, we used the 44C2 m with 100 kV/100 μA to display the high voltage output of the power. Because the internal wire resistance is too small, we must use a shunt resistor for this indicator. To enlarge the scale of the voltmeter, this resistor is connected to the indicator in serial. This circuit is demonstrated in Fig. 7.

$$R_{shunt} = \frac{U_s}{I_{fs}} - R_m = \frac{100 \text{ kV}}{100 \mu\text{A}} = 1000 \text{ M}\Omega - 1 \text{ K}\Omega \approx 1000 \text{ M}\Omega \quad (2)$$

In this case, we choose two high voltage resistors of glaze film technology with 10 W. Each of resistors is 500 MJ–30 kV. When they are connected in serial, the maximum of voltage is 60 kV more than 40 kV which is required in this

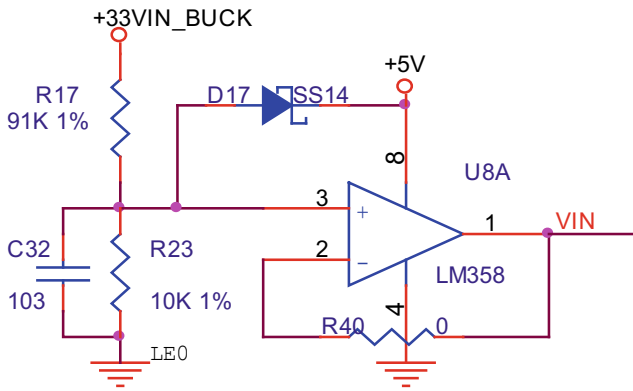


Fig. 6 The divider is used for measuring high voltage in STM8’s ADC

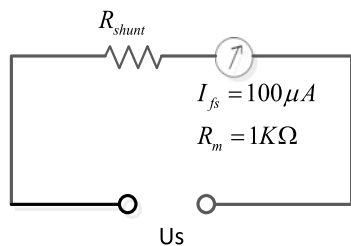


Fig. 7 By using a shunt resistor to expand the measured voltage

project. The PCB main board after soldering all components is displayed in Fig. 8.

Firmware design.

This flow chart in Fig. 9 shows the program in the STM8F003S. In the first processes, MCU is programmed to initial some basic tasks such as input or output for GPIOs, turn on some mandatory timers, and choice an operation mode of ADC. Because of limiting a number of GPIOs in MCU with 32 pins, we must design 7-segment LED circuit with scanning technique. There are three 7-segment LEDs on the PCB, so we can program to display all mode of the high voltage power.

The power after resembling all components: the main PCB of high voltage supply, voltage and current meter, and etc. is described in Fig. 10.

2.2 Implement of an Electrospinning Machine

To prove working of our electrospinning effectively, we set up a system with the high voltage power, a syringe pump, and a rum collector described in Fig. 11. We conduct some experiments with PCLs and acetone solvents.

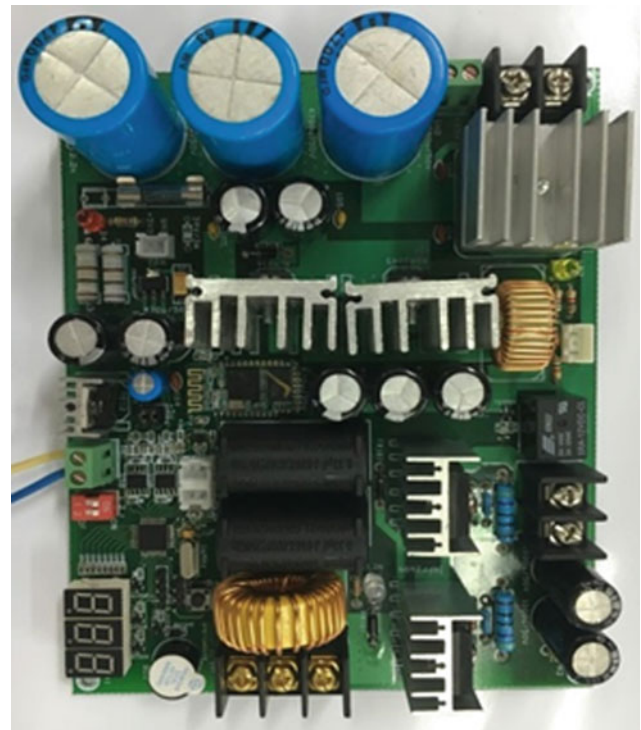


Fig. 8 The PCB main board after soldering all components

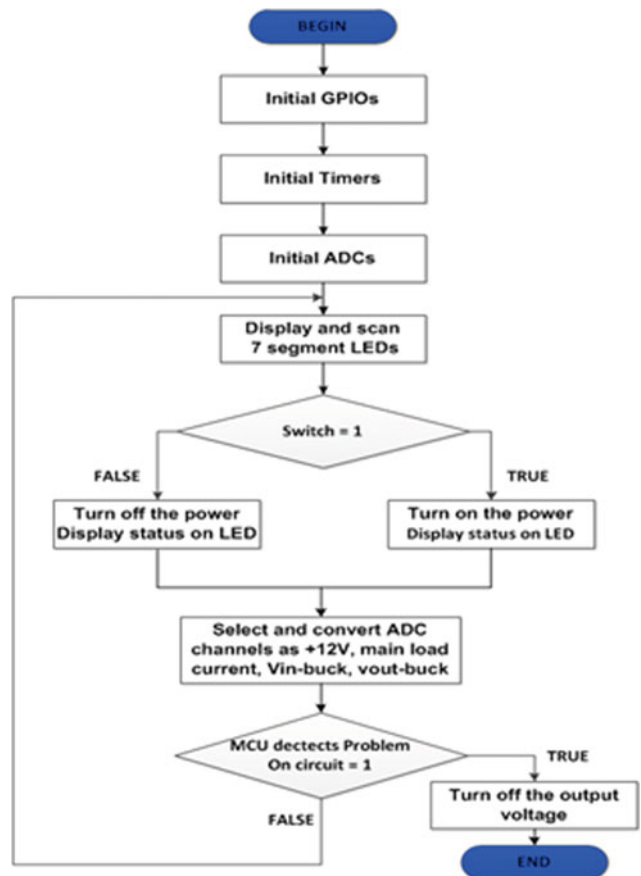


Fig. 9 Flowchart of the program in the MCU



Fig. 10 The high voltage power source after finishing

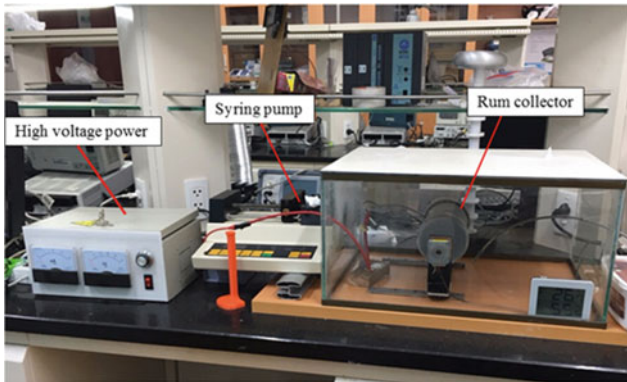
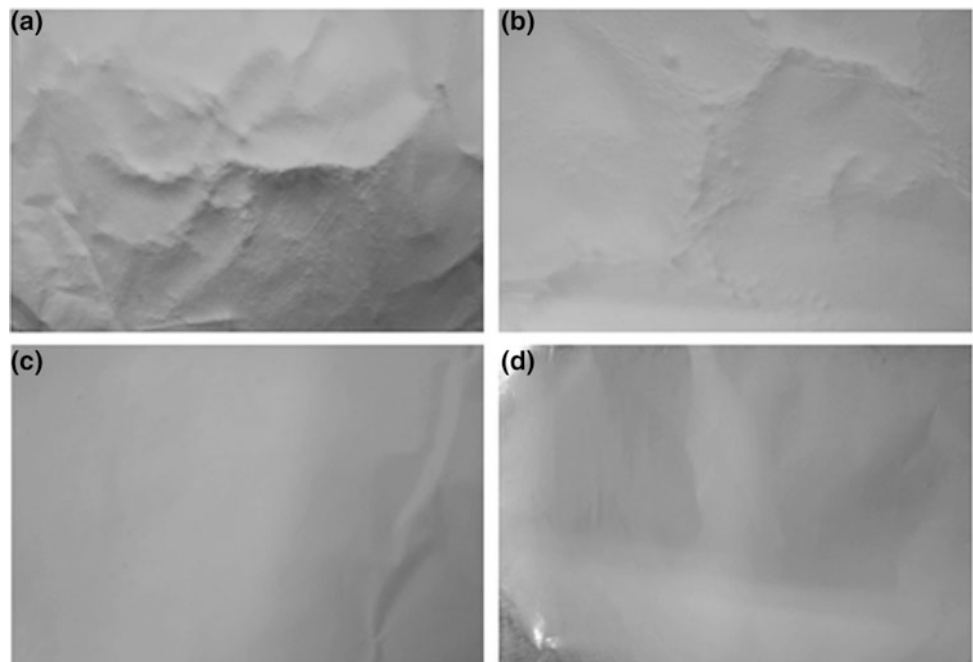


Fig. 11 Designing the electrospinning machine by using our power supply

Fig. 12 Photographs of EsPCL membrane at different flow rates. **a** 8, **b** 5, **c** 2 and **d** 1 ml/h (with the other conditions: 17 kV, 15%, and 20 cm)



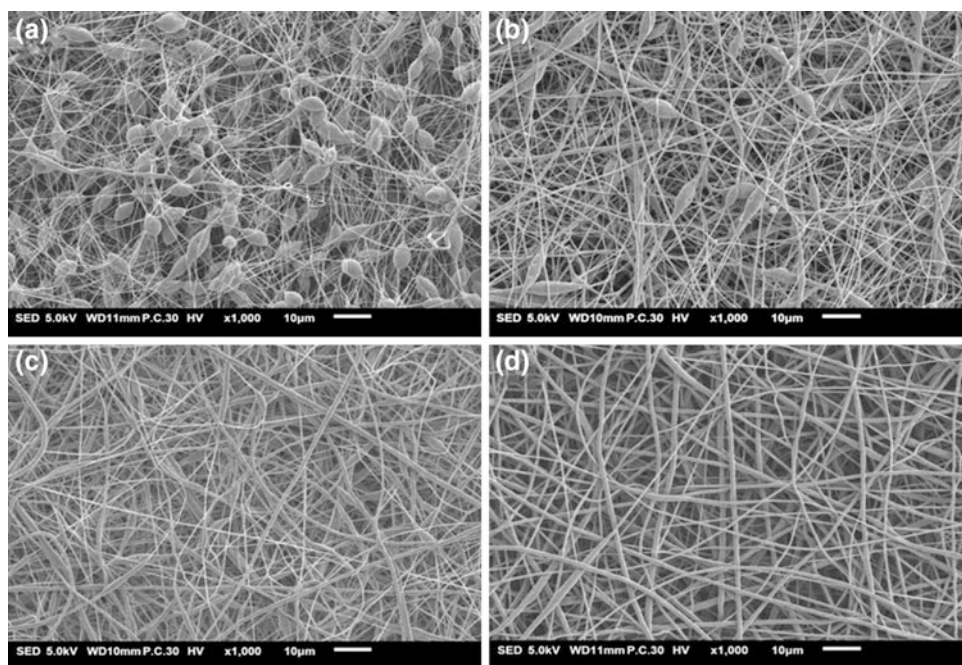
3 Result of Experiment

Because each laboratory conditions and environmental factors are different, in the future we will re-investigated how to get required fibers's morphology. In this experiment, we chose Polycaprolactone (PCL) to use as polymer solution for the investigation. Then, the scanning electron microscopy (SEM) is applied to study the nano-fibers' structure, morphology and diameter size.

In Fig. 12, after electrospinning process, photos of PCL membrane on aluminum foil at different flow rates of syringe pump are taken. It is easy to observe that at very fast flow rates as 8 and 5 ml/h the PCL membrane looks rough too much. When the flow rate is reduced at 2 and 1 ml/h, the surface of PCL membrane become smoother. Consequently, because PCL polymer solutions have enough time for polarization in lower flow rate cases, the fibers of membrane will be smoother and eliminated beads.

Form Fig. 13, we can see that concentrations of polymer solution play an essential role in the fiber of the membrane while the electrospinning process. At the low concentration 8% and 10%, there are greatly numbers of mixture of beads in the membrane. When increasing a little higher amount of concentration as 12% and 15%, smoother nanofibers can be obtained. As a result, the concentration with 15% is rather than suitable for this electrospinning process.

Fig. 13 SEM morphology of EsPCL fibers at different concentrations. **a** 8%, **b** 10%, **c** 12% and **d** 15% (17 kV, 1 ml/h, 20 cm) at 1000 \times



4 Conclusions

In this study, the high voltage source is developed to use in the electrospinning system. The main principle contents converting 220 VAC to low 26 VAC by a step-down transformer, this low AC energy is rectified and filtered to generate +33 VDC. From the +33 VDC, the buck circuit with high current is offered to get the adjust voltage output 0 \rightarrow +33 VDC. With the help of ZVS Driver and Flyback transformer, it can transfer from the low voltage and high current to the high voltage and low current. This power is a low-cost power for research and study of electrospinning machine effectively.

Continuously, not only did we design the high voltage power but also implemented the electrospinning machine. When decreasing flow rate of PCL solution in syringe pump, the membrane of fiber is smoother. Thank to using 15% PCL solution, 1 ml slow rate, 17 kV, and 20 m in distance, this machine gives a good result of structure morphology membrane.

Acknowledgements This research is funded by International University—VNUHCM under grant number T2016-04-BME.

Conflict of Interest The authors declare that they have no conflict of interest.

References

1. Call, C.C.: The study of electrospun nanofibers and the application of electrospinning in engineering education, in mechanical engineering. Texas A&M University (2008)
2. Boudriot, U., et al.: Electrospinning approaches toward scaffold engineering—a brief overview. *Artif. Organs* **30**(10), 785–792 (2006)
3. Atala, A.: Tissue engineering and regenerative medicine: concepts for clinical application. *Rejuvenation Res.* **7**(1), 15–31 (2004)
4. Killian, M.L., et al.: Recent advances in shoulder research. *Arthritis Res. Therapy* **14**(3), 214 (2012)
5. Sapountzi, E., et al.: One-step fabrication of electrospun photo-cross-linkable polymer nanofibers incorporating multiwall carbon nanotubes and enzyme for biosensing. *J. Electrochem. Soc.* **162**(10), B275–B281 (2015)
6. XLSEMI, Datasheet XL4016 (2016)
7. Munich, A.: ZVS (Mazilli) Driver. <http://adammunich.com/zvs-driver/> (2017)

Part II

**Workshop in Medical Instrumentations and
Entrepreneurship**

A Cloud-Based System for In-Home Fall Detection and Activity Assessment

Quoc T. Huynh, Uyen D. Nguyen, and Binh Q. Tran

Abstract

Falls are a major global health problem that may result in long-term health issues, disabilities, and even death (~650,000 fatalities each year). Each year approximately 37.3 million elderly worldwide experience a fall event that is severe enough to require medical attention. This research proposes a system for activity assessment and fall detection intended for in-home applications using the Internet of Things (IoT) for real-time detection of falls events and potentially fall prevention using a low-cost, wearable sensor system. While the proposed system uses an integrated MEMS sensor (i.e. accelerometer, gyroscope) for biomechanical monitoring and event detection, the developed algorithms can also be deployed onto other smart devices. The system communicates periodically with a cloud server system for uploading, archiving, and analyzing sensor data. Data is transferred to the cloud. Once data is received, the cloud server can provide alerts (i.e. automated calls, SMS, EMAIL) to formal and informal caregivers as well as emergency services when falls or other emergencies occur. Additionally, individuals and their caregivers can access and review personalized activity information to assess health, wellness and independence. Preliminary tests using healthy subjects performing Activity Daily Living (ADL) is quite promising, with specificity to detect fall of 100% in about 200 h normal activities in real-world setting. This research will also present practical challenges to deployment of the proposed system in real-world settings including usability, performance, and feedback from end-users.

Keywords

Fall detection • ADL • IoT • AWS • LoRa

1 Introduction

According to World Health Organization (WHO) statistics [1], there are about 37.3 million elderly individuals aged 65 and over worldwide experience a fall event severe enough to require medical attention. Of these fall events, 80% of these incidents occur in low and middle-income countries with limited resources [2]. Falls are a major global health problem that may result in long-term health issues, disabilities, and even death (~650,000 fatalities each year). In 2015, the Centers for Disease Control and Prevention (CDC) estimated that total medical costs of fall events totaled more than \$50 billion in US [3]. However, it is estimated that timely response to detected fall events can dramatically decrease risk of hospitalization by 26% and fatalities by 80% [4]. Technological innovation such as mobile health, wearable sensors, and smart environments may potentially provide a cost-effective solution to the problem of falls in the elderly if a highly accurate and robust (i.e. high sensitivity and high specificity) fall detection device with communications capabilities can be developed to contact caregivers, providers and emergency services, as warranted. Research by Bertera et al. [5] have shown that the elderly are interested in new technologies to support their health, independence, and safety, especially as it supports their desire to age-in-place.

This paper presents a cloud based system for activity assessment and fall detection using a low-cost, wearable sensor or other low-power network strategies such as LoRa networks and cloud computing server. The proposed system can be used for timely detection and alerting in the case of residential fall events and potentially can potentially be used in combination with other fall prevention strategies.

Q. T. Huynh (✉) · B. Q. Tran
Catholic University of America, Washington, DC 20064, USA
e-mail: Quochuynhtan@gmail.com

U. D. Nguyen
International University—Vietnam National University, Ho Chi Minh City, Vietnam

2 Related Work

Recent advances in micro-electromechanical systems (MEMS) have opened up great opportunities for the implementation of smart environments, especially in the healthcare area. Many studies already use of the biomechanical sensors (accelerometer and gyroscope) for fall detection and daily activity monitoring. They have achieved high accuracy in detecting falls in the lab with test subjects performing prescribed activities [4, 6–8]. We have demonstrated wearable sensors systems using a combination accelerometer and gyroscope for fall detection can achieve 96.3% sensitivity and 96.2% specificity in the lab. However, there is a lack of studies validating accuracy of these systems in the real-world over long time frames in which activities are unscripted and experience much more variability and activity noise (i.e. bumping). In this study, we validate the accuracy of a wearable fall detection system while test subjects performed daily activities in real-world settings. Accuracy and efficacy of a hierarchical neural network algorithm [9] for classification of daily activity is also tested on collected data.

Currently, health care systems store and analyze data either on a local device or computer in an user's residence. However, trends such as the Internet of Things (IoT), cloud computing, and artificial intelligence can potentially provide alternate and/or additional solutions for a wide range of health applications and services. Luo et al. [10] have developed a platform to manage and monitor medical health information and behavioral state information of patients of hypertension and other diseases such as stroke, heart disease, kidney disease, chronic lung disease, disorders of consciousness, etc. Doukas and Maglogiannis [11] implemented a smartphone system for collecting motion and heartbeat data via Bluetooth and cloud-based store-and-forward

strategies for subsequent analysis. These systems show potential applications of novel and emerging technologies for supporting health and wellness in at-home elderly populations.

3 System Architecture Overview

In this work, we further advance and propose a technological architecture for fall detection and notification of caregivers. Figure 1 provides an illustration of the proposed architecture. This system consists mainly of two parts: the activity data collection unit and cloud server computing part.

3.1 Activity Data Collection Component

The activity data collection unit is developed to continuously measure biomechanical and physiological data while users are performing daily activities. The device can detect and immediately send alerts to a cloud server when a fall event is detected following our optimized fall detection algorithm [12]. The algorithm uses a combined accelerometer and gyroscope sensor strategy for robust fall detection. While the accelerometer provides valuable information regarding body inertial changes due to impact, the gyroscope provides unique information regarding the body's rotational velocity during a fall event. A fall event produces both high acceleration and angular velocity, the combination of which is not observed during normal daily activities. Table 1 [13] shows summary data of acceleration and angular velocity for various daily activities and fall events. Using an optimization approach, critical thresholds (lower and upper fall threshold of acceleration, and upper fall threshold of angular velocity)

Fig. 1 Architecture of residential fall detection system with local activity data collection component (left) and cloud-based computing and services component (right)

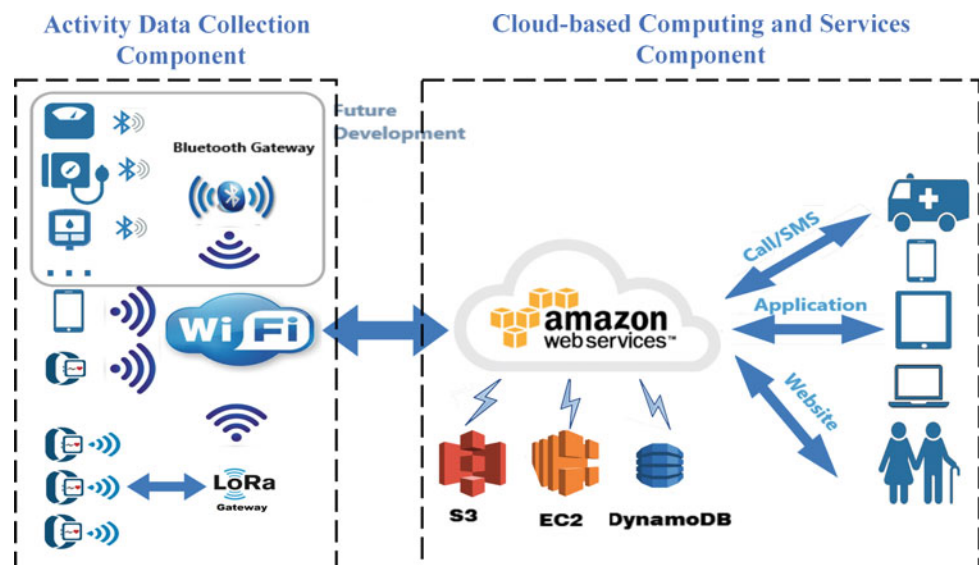


Table 1 Summary of acceleration and angular velocity of ADLs and fall

Activities	Negative peak acceleration (g)	Positive peak acceleration (g)	Peak angular velocity ($^{\circ}/s$)
Standing	0.98	1	0
Walking	0.55–0.66	1.5–1.9	10–20
Sitting down/standing up	0.47–0.58	1.6–2.1	50–170
Lying down/sitting up	0.6–0.85	1.3–1.4	130–260
Stepping	0.3–0.45	1.8–2.3	40–80
Running	0.2–0.34	2.3–2.8	60–120
Falling	0.15–0.35	2.5–5.4	200–320

were empirically determined from experimental data. When both of signals exceed these thresholds, a fall event is detected. The optimized fall algorithm is illustrated in Fig. 2. It was able to detect falls with high sensitivity (96.3%) and specificity (96.2%) compared to prior strategies by other researchers who were able to achieve either high sensitivity or high specificity, but not both. In addition, information features of daily activities from sensor data are extracted and

uploaded to a cloud server periodically for later analysis and daily activities classification. In our system, a wearable device (i.e. smartwatch, sensor unit) or smart phone can flexibly serve as the activity data collection unit.

Wearable device shown in Fig. 3, is a small device (3.2 cm \times 3.4 cm) designed to be worn continuously while users perform regular daily activities. It can be wristworn (i.e. watchlike) or clipped on the waist (i.e. pedometer-like). The sensor device uses a motion processing unit (MPU-9250; Invensense, San Jose, CA) to measure 3-axes of acceleration and angular velocity to classify ADLs and detect fall events. The unit also uses an ultra low-power STM32L microcontroller (STMicroelectronics; Geneva, Switzerland). Depending on the demand and the user's environment, either a Wi-Fi module or LoRa module is integrated into with the wearable device for data communications.

Currently, Wi-Fi is a popular choice for IoT connectivity because its coverage is almost ubiquitous in a typical home. A wearable device using Wi-Fi can be easily setup and deployed. However, Wi-Fi has some drawbacks and is not always the appropriate choice. These drawbacks include the short-range connectivity between device and access point (AP), limitations to possible number of devices connected to an AP, and, most prominently, low efficiency and high battery consumption. These last limitations are particularly relevant for this intended fall detection application for usability and effectiveness reasons. LoRa technology is a new trend for building IoT networks which is already widely available in European countries and increasingly used in the United States. The advantage of LoRa networks is its combination long-range capabilities and low-power consumption that is especially useful with IoT. A wearable device can operate between 2 and 10 km from a LoRa base station with optimized device battery life lasting week between charging. This LoRa base station would then need to be initially connected to the Internet in order to forward data to a cloud-based server.

The wearable fall detection device communicates with the cloud server by utilizing established techniques for IoT communication directly via Wi-Fi or forwarded to the Internet via the LoRa network. The device has a small

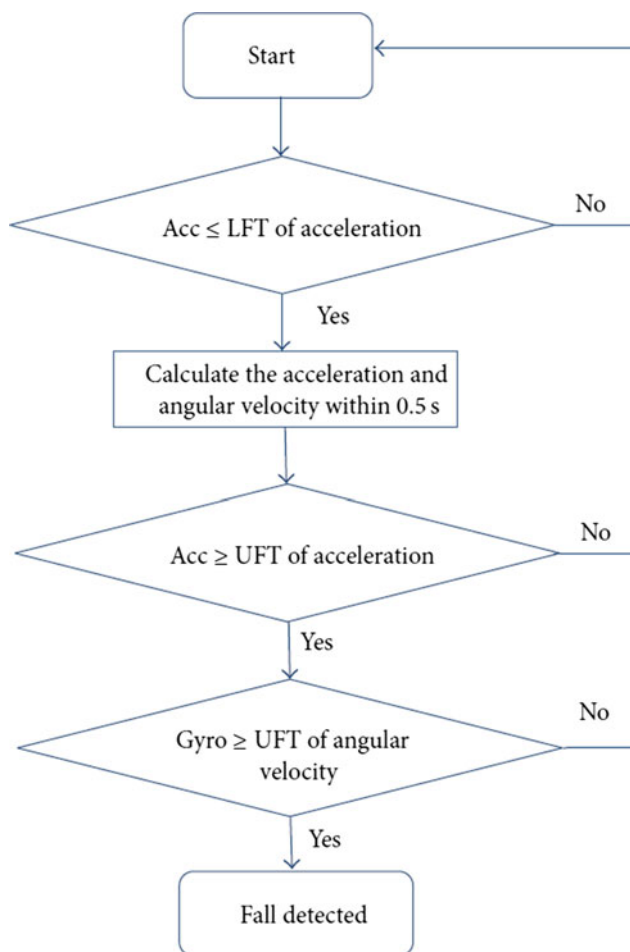
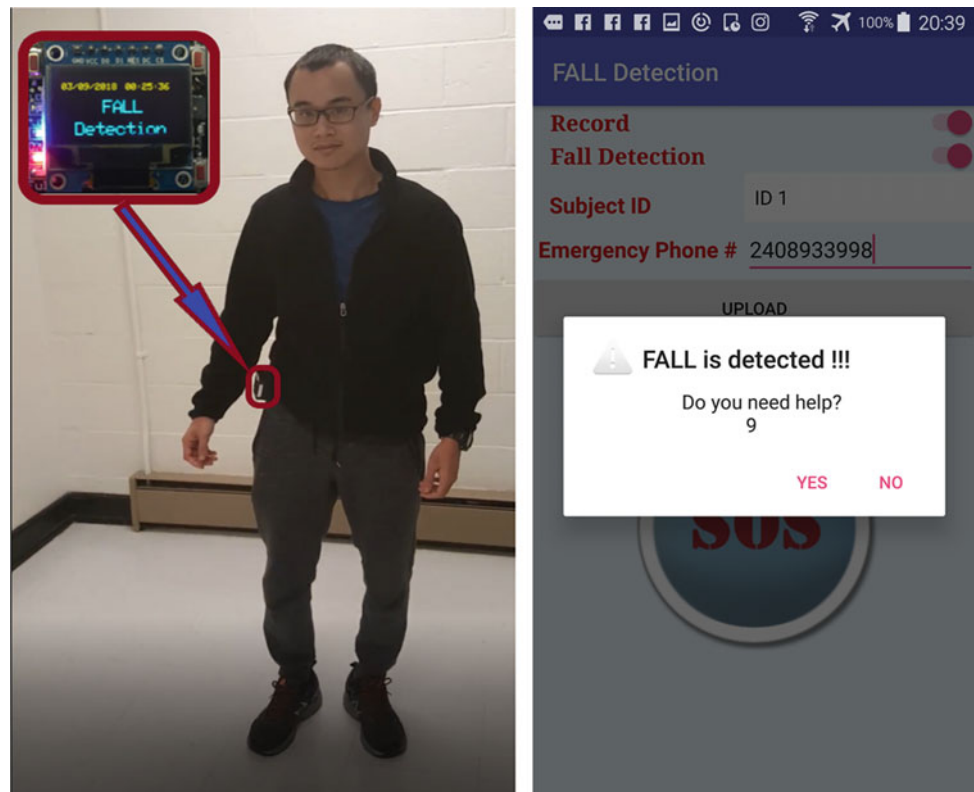
**Fig. 2** The optimized fall detection algorithm

Fig. 3 Wearable sensor device electronics unit with imbedded fall detection algorithms (left) and graphical user interface for fall detection app using built-in sensors with a smartphone (right)



OLED screen for displaying information directly to the end-user and a SOS button for user-activated, immediate call to a response center in case of emergency. In addition, wireless charging is integrated in the device for ease-of-use.

Smartphone: The use of smartphones among elderly populations with numerous built-in sensors such as accelerometer, gyroscope, etc. is growing at a remarkable rate [14]. As with the general population, smartphones will become an increasingly familiar tool for the elderly population for managing their daily needs, including health and wellness information, communications, and scheduling. For this project, a fall detection and activity assessment application was developed on the Android platform. Taking advantage of the built-in smartphone sensors, we implement the algorithms previously developed in our lab for fall detection and activity classification. Figure 3 (right) shows a graphical user interface for the fall detection application.

3.2 Cloud-Based Computing and Services Component

Our cloud service component was developed using Amazon Web Services (AWS), a platform that allows researchers to perform large-scale storage, management, and analysis of remotely collected data. Figure 1 (right) illustrates our cloud service component. For this application, standard

infrastructure services, such as Amazon DynamoDB, S3 and EC2 are used.

First, Amazon DynamoDB is a fast and flexible SQL database service for all applications. It stores key user information, device ID and contact information for caregivers (i.e. neighbor, family member, friends, etc.). Second, Amazon S3 (Simple Storage Service) is flexible cloud storage. All of raw daily activity's data are easily and quickly uploaded to S3 from devices using Wi-Fi or LoRa for later analysis by the research team. Finally, Amazon EC2 (Elastic Compute Cloud) is central part of cloud service that can be utilized for data processing and alert management. It is used to issue alarm and notification via SMS, automated call and/or Email to caregivers, prior to initiating a call for emergency services when emergent events such as a fall is detected. Additionally, EC2 is used for analysis and classification of daily activities based upon key data features extracted and upload from the sensor device or smartphone app. This cloud-based analysis strategy can reduce the local computing burden of analyzing non-essential, real-time data, thereby extending battery life of the wearable device or smartphone. EC2 also provides a website interface to facilitate fast setup of user accounts, devices, and caregiver contact information. The users and their caregivers can access and review personalized activity information to assess health, wellness and independence (like history of emergency case, location, activity status, etc.).

4 Real-World Experimental Setup

In this study, the IoT fall detection system is validated in real-world. Following an institutional review board (IRB) approved protocol; ten (10) healthy, adult subjects (18–50 years old) wore the fall sensor device while performing normal daily activities. The device was worn at the waist and continuously collected activity data in real-time. In the event the wearable device detects a fall event, an immediate alert was sent over Wi-Fi or LoRa to AWS for alert notification. For normal activities, all sensor data and information are sent periodically (every 30 min) to AWS for storage and analysis. Each subject was provided a notecard and asked to log and record timing related to rigorous activities or critical events including falls and near falls. These logs were used to validate and confirm falls detected by the algorithm. In the event falls were detected, subjects were contacted and interviewed further relating to the time of detected event.

For this study, approximately 200 h of activities of daily living were recorded in all subjects. No subjects reported having experienced a fall. No fall events were detected from the wearable device after 190 h normal activities and 7 h of rigorous (exercise) activities. However, our system showed no false positive detection of fall event (specificity 100%) during 342,000 windows of normal daily activities (time duration each window is 2 s). With high rigorous activities i.e. walking up stair, down stair, run, workout in gym, etc., five (5) false positives were identified from 12,545 event windows. These incidents were validated against activities reported by subjects on note cards. Subjects were further contacted and interviewed regarding detected events. However, they can be eliminated by incorporating posture detection with our algorithm. It showed high accuracy and robustness of our system and its ability to accurately generate alert notification in the event of a fall.

5 Discussion and Conclusion

The primary advantage of this IoT enabled fall event monitoring system is its focus on the targeted end-user, elderly individuals, and usability in the home environment. The system is flexible in incorporating stand-alone wearable sensors with embedded fall detection algorithms or integration with existing smartphone platforms running the fall detection app in order to collect biomechanical data for detection of fall events and daily activities. Because of the ubiquity of smartphones in today's society and its on-board communications capabilities, there are strategic advantages

to its use for continuous fall monitoring. This work demonstrates the feasibility of deployment of an integrated IoT solution for fall detection and activity assessment using wearable sensors, cloud-based services using AWS to collect, store, analyze and provide alert notification in the event a fall is detected. Real-time alert notification to caregivers and emergency service providers, as appropriate, is particularly important in this application as long-lies resulting from falls have been directly associated with hospitalization risk and fatalities [4], as well as increased cost.

Performance testing of the system in real-world settings provide valuable information regarding the efficacy of fall detection systems and potential barriers to adoption of the technology. Data collected from ~200 h of field testing reveals the robustness and specificity (i.e. low false positives) of the fall detection system.

Technological and usability issues remain challenges to future implementation and adoption of in-home fall detection systems. For example, variability of sensor placement may affect accuracy of fall detection algorithms. Wrist-worn and waist-worn sensor devices ensure consistent placement and orientation of sensors and are directly related to biomechanical motion during performance of daily activities. While waist or chest worn sensors remain the best locations for fall detection, wrist-worn devices may be the most convenient and acceptable by end-users who are used to wearing watchlike devices or activity sensors (i.e. FitBit). However, signals from wrist-worn sensors may exhibit extra noise due to arm swing during gait and activity or occasional bumping during daily activity. Further testing in real-world settings is warranted.

Another key challenge for consumer adoption is battery life and frequency of charging devices. Fall monitoring and activity assessment requires the sensor to be "always on" for 24/7 fall surveillance as falls can happen at any time, day or night. This utilization results in continuous battery consumption by the sensor unit (i.e. stand-alone device or smartphone) and therefore frequent re-charging. When the sensor device is charging, it is not available for fall monitoring and therefore may miss fall events. Further, when an user removes a device for charging, there is increased potential to forget to wear the device again after it is fully charged. Thus, strategies for reducing battery consumption for extended use between charges is critically essential for this application.

In our system, this is done in hardware using low-power electronics as well through the use of more advanced strategies such as LoRa and cloud-based analysis of non-emergent data. Using the proposed strategies mentioned, the wearable device is designed to be lightweight,

small and low cost (<\$50). The battery can last for more than a week to a month with continuous monitoring and data transmission using LoRa. We have also implemented the fall detection algorithm on a commercially available smartwatch. However, battery life remains a critical problem lasting only 3–5 h between charge.

Cloud server AWS had shown performance efficiency, reliability and cost-effectively.

It can reduce burden of computing and storage data on the device that can extend battery life.

The last aspect of the system relates to presentation a utilization of the collected data to enhance health and wellness. Users and their caregivers can easily access and review personalized activity information using developed website or applications. Gamification to motivate increased activity, exercise, and healthy behaviors may enhance strength, endurance, and cognitive function as evidenced in the literature. Further, through machine learning and artificial intelligence strategies, there is potential for IoT based activity monitoring to enable sensitive measures of longitudinal declines in activity levels and changes resulting from chronic illness and disease. This area requires further study and development as more sensors are deployed in real-world settings.

In conclusion, the work proposes an IoT-based architecture for fall monitoring and alert notification that can be used to assess health and independence of at-home elderly individuals. Based on IoT functional principles and design, it allows communication of wearable sensor devices with a cloud server for data collection, storage and advance analytics. The architecture can be extended to incorporate periodic measurements from Bluetooth enabled devices (i.e. blood pressure, weight scale, glucometers, etc.) for monitoring and management of chronic illnesses.

Conflict of Interest The authors declare that they have no conflict of interest.

References

1. World Health Organization: <http://www.who.int/mediacentre/factsheets/fs344/en/> (2018)
2. Centers for Disease Control and Prevention: <https://www.cdc.gov/media/releases/2016/p0922-older-adult-falls.html> (2016)
3. Centers for Disease Control and Prevention: <https://www.cdc.gov/homeandrecreationalafety/falls/fallcost.html> (2016)
4. Noury, N., Rumeau, P., Bourke, A.K., ÓLaighin, G., Lundy, J.E.: A proposal for the classification and evaluation of fall detectors. *Innov. Res. BioMed. Eng.* 340–349 (2008)
5. Bertera, E.M., Tran, B.Q., Wuertz, E.M., Bonner, A.: A study of the receptivity to telecare technology in a community-based elderly minority population. *J. Telemed. Telecare* 13(7) (2007)
6. Nyan, M.N., Tay, F.E.H., Tan, A.W.Y., Seah, K.H.: Distinguishing fall activities from normal activities by angular rate characteristics and high-speed camera characterization. *Med. Eng. Phys.* 28 (2006)
7. Zhang, T., Wang, J., Xu, L., Liu, P.: Fall detection by wearable sensor and one-class SVM. In: Proceedings of the 26th Annual International Conference of the IEEE EMBS, pp. 2204–2207 (2004)
8. Zhang, T., Wang, J., Liu, P., Hou, J.: Fall detection by embedding an accelerometer in cellphone and using KDF algorithm. *Int. J. Comput. Sci. Netw. Secur.* 6(10)
9. Huynh, Q.T., Nguyen, U.D., Walsh, T., Tran, B.Q.: Hierarchical neural network algorithm for classification of normal daily activity using wearable sensors. In: Northeast Bioengineering Conference. New Jersey (2017)
10. Luo, S., Cheng, L., Ren, B.: Medical monitoring and managing application of the information service cloud system based on internet of things. *J. Softw.* 9(7), 1802–1809 (2014)
11. Doukas, C., Maglogiannis, I.: Managing wearable sensor data through cloud computing. In: IEEE Third International Conference on Cloud Computing Technology and Science. Athens (2011)
12. Huynh, Q.T., Nguyen, U.D., Irazabal, L.B., Ghassemian, N., Tran, B.Q.: Optimization of an accelerometer and gyroscope-based fall detection algorithm. *Abstract* 2015, 8 (2015)
13. Huynh, Q.T., Nguyen, U.D., Liem, K.T., Tran, B.Q.: Detection of activities daily living and falls using combination accelerometer and gyroscope. In: IFMBE Proceedings (2015)
14. Li, Q., Stankovic, J.A., Hanson, M.A., Barth, A.T., Lach, J., Zhou, G.: Accurate, fast fall detection using gyroscopes and accelerometer-derived posture information. In: International Workshop on Wearable and Implantable Body Sensor Networks. Berkeley (2009)

An Accuracy and Reliability Comparison Study of Electronic Uroflowmetry Devices

Thinh P. Nguyen, An T. L. Nguyen, Y. L. Nguyen, Vo Van Toi, Thien M. Nguyen, and Hai T. Phan

Abstract

Uroflowmetry is a simple test measuring the volume of voided urine in a period of time. Being the only non-invasive test among urodynamic methods, it is most commonly ordered by urologists to evaluate the urination of patients, especially in males over 50 years old with lower urinary tract symptoms (LUTS). In Vietnam, however, the test is only available in urology department in large hospitals or medical diagnostic centers as it is relatively new in the field and the cost of a uroflowmeter device is still very high. Aiming to make the device more affordable to urologists and clinics and thus increase accessibility of Vietnamese patients to the test, the engineers from Biomedical Engineering Department, Ho Chi Minh International University have developed IUROF, an electronic uroflowmeter. This device allows patients to perform the uroflowmetry at home; the results and data are collected in a memory card and sent to physicians. The objective of this study is to evaluate the accuracy and reliability of IUROF by comparing it with the Andromeda Helix, a commercialized uroflowmeter device currently used in hospitals. The study was conducted at MEDIC Healthcare Center (Vietnam) in three months. A total of 40 males (57.6 ± 10.1 years of age) with LUTS were eligible and agreed to participate in the study. After signing the informed consent, the patients took turn to urinate into the IUROF and Andromeda Helix. The order of testing by the two devices altered across patients. As a result, the mean difference of Q_{\max} was 0.05 ml/s, Q_{ave} was 0.6 ml/s, V_{void} was 0.9 ml, and t_{void} was 0.2 s between the two devices. All of these differences were not statistically significant ($p > 0.05$).

The Intra-class Correlation Coefficient (ICC) of Q_{\max} was 0.891, showing the high level of reliability of the IUROF as compared to the Andromeda Helix. The results show that the IUROF is technically comparable to the Andromeda Helix. This has an important implication for a product developed in a university laboratory to be commercialized in the market.

Keywords

Uroflowmetry • LUTS • IUROF

1 Introduction

Uroflowmetry is a useful urodynamic tool for the assessment of intravesical obstruction and is helpful in the decision-making process and management of benign prostatic hyperplasia (BPH) and other urinary disorders [1]. Uroflowmetry provides physicians a simple and non-invasive way to evaluate the urination of patients by detecting flowrate parameters.

The electronic uroflowmeters based upon the gravimetric method are widely developed and used in clinics and hospitals. However, the price of those devices is pretty high, thus, the accessibility of uroflowmeter is limited for the clinics and district hospitals in Vietnam, although uroflowmetry is an essential test for Lower Tract Urinary Symptoms (LUTS) patients.

IUROF (International University Uroflowmeter) is an ATmega328 MCU-based device using the gravimetric method of the load cell. It is specifically designed to monitor micturition parameters including maximum flow rate and voided volume. When the process of data logging initiates, the volume change is continuously detected and stored into the volume break; at the end of micturition process, the microcontroller-based device is programmed to determine the desired parameters which are related to urinary flow.

T. P. Nguyen (✉) · A. T. L. Nguyen · Y. L. Nguyen · V. Van Toi
Department of Biomedical Engineering, Ho Chi Minh
International University, Vietnam National University, Ho Chi
Minh City, Vietnam
e-mail: thinhputin1803@gmail.com

T. M. Nguyen · H. T. Phan
Medic (Hoa Hao) Healthcare Center, Ho Chi Minh City, Vietnam

These parameters are used to determine whether or not the patient is emptying their bladder normally [2].

In this study, the IUROF uroflowmeter is tested in the clinical setting, and its accuracy and reliability are evaluated by comparing with the already commercialized device—Andromeda Helix used in MEDIC Healthcare Center (Vietnam).

2 Methodology

The cross-sectional study was designed and conducted by the Biomedical Engineering Department, International University, Vietnam. The project was approved by The Institutional Review Board (IRB) established by the collaboration with Hoa Hao (MEDIC) Healthcare Center, Vietnam.

A total of 43 male patients with LUTS were enrolled in the study after they signed the consent form. The uroflowmetry data of patients were collected from two different devices within the same day. The Andromeda Helix and IUROF were alternatively used. The order of using Andromeda or IUROF was changed patient to patient to avoid bias. Three participants were excluded as the voided volume was under the standard of International Continence Society (ICS) for uroflowmetry test (which must be ≥ 150 ml) [3–5]. The parameters to be compared were voided volume (V_{void}), maximum flowrate (Q_{max}), average flowrate (Q_{ave}), and voiding time (t_{void}). The difference among the results of Andromeda Helix and IUROF device were evaluated by Paired t-test method. The reliability of IUROF was calculated using the Intra-class Correlation Coefficient (ICC) and its 95% confidence interval [The coefficient has the range from 0 to 1; therein 1 shows the absolute reliability of the test with no error in measurement, and 0 gives a complete unreliability]. The statistical software IBM SPSS V22 was employed to analyze and test the parameters.

The results were also used to diagnose whether the patients had Bladder Outlet Obstruction (BOO) or not. The

agreement in BOO diagnosis by IUROF and Andromeda Helix results is also explored to evaluate the graph quality produced by the IUROF.

3 Results

There were 40 out of 43 male patients eligible for the analysis. The mean age was 57.6, ranging from 27 to 73. There were 25 patients (62.5%) reported to have the LUTS, and 15 (37.5%) men were diagnosed with Benign Prostatic Hyperplasia (BPH).

Table 1 reports the values of uroflow parameters by IUROF and Andromeda Helix. The mean Q_{max} values were 15.1 ± 6.06 ml/s and 15.0 ± 5.17 ml/s, respectively. The corresponding mean of Q_{ave} were 7.2 ± 3.22 ml/s and 7.8 ± 3.36 ml/s. The mean volume (V_{void}) and time of urination collected in IUROF were 58.5 s and 366.5 ml; in Andromeda Helix were 58.3 s and 365.6 ml.

In comparison using Paired sample t-test, the results showed in Table 2 indicated the mean Q_{max} of IUROF was 0.05 ml/s higher than the one in Andromeda Helix, V_{void} of IUROF was higher 0.9 m, and t_{void} was higher 0.2 s. With the 5% significant differences, those disparities were not statistically significant ($p = 0.931$, $p = 0.957$, and $p = 0.960$). Similarly, the difference in the average flowrate measured in both devices was not statistically significant although the results in Andromeda Helix was 0.6 ml/s greater than IUROF.

Additionally, the order measurement of patients was also recorded for further specific analysis in Table 3. The results showed that there was no significant difference between devices though patients urinated into the IUROF first or Andromeda Helix first.

The reliability evaluation of the IUROF by the Intra-class Correlation Coefficient (ICC with Two-way mixed, absolute agreement, single rater) was described in Table 4. To the Q_{max} , Q_{ave} , V_{void} , the ICC was pretty high with the 95% confidence interval [0.793; 0.942], [0.768; 0.936]; [0.790; 0.941],

Table 1 Parameters of uroflowmetry in IUROF and Andromeda Helix

	Q_{max} (ml/s)		Q_{ave} (ml/s)		V_{void} (ml)		t_{void} (s)	
	IU	Andro	IU	Andro	IU	Andro	IU	Andro
N	40	40	40	40	40	40	40	40
Mean	15.1	15.0	7.2	7.8	366.5	365.6	58.5	58.3
Median	14.6	13.8	5.7	6.7	311.5	344.0	55.9	54.7
s.d.	6.06	5.17	3.22	3.36	169.77	151.65	21.30	20.78
s.e.	0.96	0.82	0.51	0.53	26.84	23.98	3.37	3.29
Min	5.9	7.1	3.0	2.7	151.4	151.0	24.1	20.1
Max	31.1	25.9	16.7	17.0	742.4	655.0	104.9	107.8

Table 2 The difference between IUROF and Andromeda Helix in general

	Mean	s.d.	s.e.	95% CI of the difference		p-value
				Lower	Upper	
Q _{max} (ml/s)	0.05	3.57	0.56	-1.1	1.2	0.931
Q _{ave} (ml/s)	-0.6	2.12	0.33	-1.3	0.1	0.073
V _{void} (ml)	0.9	102.69	16.24	-31.9	33.7	0.957
t _{void} (s)	0.2	22.71	3.59	-7.1	7.4	0.960

Table 3 The difference between IUROF and Andromeda Helix in measurement order

		Mean	s.d.	s.e.	95% CI of the difference		p-value
					Lower	Upper	
Andromeda—IUROF <i>Sub1</i> (N = 22)	Q _{max} (ml/s)	-0.5	3.31	0.71	-2.0	0.95	0.468
	Q _{ave} (ml/s)	-1.4	1.81	0.39	-2.2	-0.6	0.002
	V _{void} (ml)	-3.0	90.13	19.22	-42.9	37.0	0.878
	t _{void} (s)	4.5	20.04	4.27	-4.4	13.4	0.304
IU-ROF—Andromeda <i>Sub2</i> (N = 18)	Q _{max} (ml/s)	0.75	3.85	0.91	-1.2	2.7	0.422
	Q _{ave} (ml/s)	0.3	2.11	0.50	-0.7	1.4	0.504
	V _{void} (ml)	5.6	118.80	28.00	-53.4	64.7	0.843
	t _{void} (s)	-5.1	25.16	5.93	-17.6	7.4	0.402

Table 4 Intra-class correlation coefficient between IUROF and Andromeda Helix

	Intra-class correlation	95% confidence interval		F test with true value 0			
		Lower bound	Upper bound	Value	df1	df2	sig.
Q _{max}	0.891	0.793	0.942	8.944	39	39	0.000
Q _{ave}	0.878	0.768	0.936	8.643	39	39	0.000
V _{void}	0.889	0.790	0.941	8.828	39	39	0.000
t _{void}	0.595	0.228	0.787	2.435	39	39	0.003

respectively. This proved the reliability was in range from good to excellent. However, ICC of urination time was moderate with 0.595 and in the 95% confident interval from 0.228 to 0.787.

The agreement on BOO diagnostic between two devices was also explored. We found that most of the results give the same diagnosis (70.8% with BOO, and 81.3% without BOO). Furthermore, in the cases where BOO diagnoses are different between devices, we noted that the mean difference of uroflow parameters was high as compared to the mean difference of the whole sample (Table 5).

This indicated that the difference of Q_{max}, Q_{ave}, V_{void}, V_{void}, t_{void} among measurements strongly affect to result of a patient. The BOO diagnostic value based only on one measurement was not precise due to the moderate sensitivity, and specificity of uroflowmetry. Particularly, in a research of Reynard et al. the sensitivity and specificity of

Table 5 The mean difference of cases that are different in BOO diagnosis

Parameters	Difference between two measurements	Difference of whole sample
Q _{max}	1.01 ml/s	0.05 ml/s
Q _{ave}	0.04 ml/s	0.6 ml/s
Q _{void}	10.5 ml	0.9 ml
t _{void}	2.4 s	0.2 s

BOO were 47 and 70% within the threshold value of Q_{max} of 10 ml/s; and 82 and 38% within the threshold Q_{max} = 15 ml/s, respectively. Therefore, the developing of home devices to collect multi-result uroflowmetry in normal routine will have a huge impact on improving the diagnosis of this simple and non-invasive method.

4 Discussion

In this study, the statistical testing method proved there was no difference between two devices regarding uroflow parameters. Ozgur et al. investigated the effect of repeating uroflowmetry test on 79 male patients and noted no significant change in measured results except the micturition time (t_{void}). To our study, we also found no statistical difference between two measurements, except the Q_{ave} when using the Andromeda Helix in the first measurement. Ozgur also identified the need for a large clinical multicenter trial for the evaluation of multiple uroflowmetry tests and the impact factors for the probable changes [6]. Thus, the process of sequent performing two uroflowmetries on patients was not the factor that affected the difference between IUROF and Andromeda Helix. However, for further evaluation studies to firm the accuracy and reliability of IU-ROF, the consideration to enlarge the scale and clinic-base of research is essential.

Recently, many researchers found that the environmental factors affected the result of uroflowmetry such as the finding suitable venue, spending enough time on each test, psychological factors. The devices that can be used at home were invented to reduce the artifacts of clinical measurement. The changes in the results of home uroflow tests were proved. Particularly, it was shown that Q_{max} varies typically by up to 10 ml/s in an individual by home uroflowmetry studies [6]. Sonke et al. analyzed the Q_{max} and V_{void} results by collecting multiple home flows and found them to differ considerably among individuals. It was shown that one way to determine a single measurement of Q_{max} is to calculate the standard deviation (s.d.) of multiple reading [7]. In many home following-up studies of uroflowmetry have found that the s.d. of multiple measurements of Q_{max} in an individual range up to 6.0 ml/s [8]. In our results, the s.d. of the Q_{max} was less than 4 ml/s for twice urinations. In combination with the information collected in previous researches, we could anticipate the difference upon comparing the clinic and home uroflowmetry in future.

The changes of different uroflowmetry parameters have been evaluated by many authors. Golomb et al. indicated the variability of uroflowmetry in the patient with BPH [9]. In their study samples, the uroflow parameters fluctuated more in men with BPH than in healthy controls. In our study, although the medical records of patients were collected (37.5% with BPH), we could not conclude more effect on any group of patients since we did not group our patients based on BPH. Porru et al. found significant circadian differences in multiple measurements of Q_{max} at home in more than a hundred patients with LUTS [10]. Our patients were invited to conduct the test consecutively in the most

comfortable time for them of the same day, and we could not conclude about the circadian changes since exact time for testing varied (all the test was performed between 8 am and 4 pm). Many other factors affecting the variabilities have been mentioned by different authors. Significant systematic variability in Q_{max} was found in the clinic with voiding position (e.g., sitting versus standing), ambient light, and temperature [8, 11]. Our study lasted four months (from April to August 2017) and the temperature of the testing room was stable at 27 °C. All of the joined patients were accustomed to voiding in standing position. However, our study does not focus on the variations in temperature or voiding position. In another study that supports the idea of changing of uroflowmetric test, Caffarel et al. invited 22 patients to perform two uroflow and record home uroflows for two weeks and concluded considerable variation between the two clinic readings meanwhile the comparison of average Q_{max} from multiple home flow recordings showed little variation [12].

The increase of Q_{max} , when measured at clinics, was reported in several studies [13, 14]. The reason was proved that the patients got familiar with the environment of examination [15]. Feneley invited 147 patients voided twice on two separate clinic visits. The average reading from the second void was statistically higher than the first on both visit, with a difference of approximately 0.5 ml/s [13]. Reynard observed the same experiment in larger scale, where the mean Q_{max} of voids one to four clinic voids in 165 men with LUTS rose progressively from 10.2 to 14.9 ml/s [14].

To avoid the psychological effects, in our study, the clinic's condition remained unchanged, and we recruited the patients to urinate with the sequentially changing order of the devices using. However, patients who experienced uroflowmetry before joining our study was not differentiated; thus, this is also a drawback that we must control in future research.

As discussed above, most of the previous studies relied on Q_{max} in the results and ignored all the other parameters. However, the interpretation of Q_{ave} , V_{void} , voiding time, flow time, time to start voiding are all crucial parameters and should be discussed [16]. In our study, those parameters were identified with no difference between two devices. The clinical meaning of those index should be investigated and examined to enhance the accuracy and reliability of the uroflow test.

The further limitations of our study must be considered. Since we focused on the male volunteers, the results cannot be generalized to the female ones. Additionally, the present study had a small sample size in only one venue. These two issues should be addressed in the further study.

5 Conclusion

Through this comparison study, we found no difference between the two uroflowmetry findings (Q_{\max} , Q_{ave} , V_{void} , t_{void}) between IU-ROF and Andromeda Helix device. The ICC showed the reliability of Q_{\max} , Q_{ave} , V_{void} of IUROF were high (0.891, 0.878, 0.889), and the ICC of t_{void} was intermediate (0.595). The agreement on the BOO diagnosis between devices is greater than 70%. Our low cost device is proved to be comparable with a commercialized device, although a larger clinical multicenter and home use studies for the evaluation of multiple uroflowmetry may be more desirable.

Conflict of Interest The authors declare that they have no conflict of interest.

References

- De La Rosette, J.J., Witjes, W.P., Debruyne, F.M., Kersten, P.L., Wijkstra, H.: Improved reliability of uroflowmetry investigations: results of a portable home-based uroflowmetry study. *Br. J. Urol.* **78**(3), 385–390 (1996)
- Le, Y.: Design, construction and clinical test of a homecare uroflowmeter (2017)
- Goldman, H.B., et al.: International continence society good urodynamic practices and terms 2016 : urodynamics, uroflowmetry, cystometry, and pressure-flow study, pp. 1–18. May 2016
- Rosier, P.F.W.M., et al.: International continence society standard good urodynamic practices and terms 2015. Urodynamics, uroflowmetry, cystometry and pressure-flow study, pp. 1–37 (2015)
- Gammie, A. et al.: International continence society guidelines on urodynamic equipment performance. November 2013, 2014
- Ozgun, B.C., Sarici, H.C., Yuceturk, N., Karakan, T., Eroglu, M.: How many times should the uroflowmetry be repeated before making a treatment decision in the elderly males? pp. 252–255
- Sonke, G.S., Kiemeny, L.A.L.M., Verbeek, L.M.: Low reproducibility of maximum urinary flow rate determined by portable flowmetry. **191**, 183–191 (1999)
- Mizuno, T., et al.: Variation in urinary flow according to voiding position in. 2–3 (1999)
- Golomb, J., Lindner, A., Siegel, Y., Korczak, D.: Variability and circadian changes in home uroflowmetry to normal controls. *J. Urol.* **147**(4), 1044–1047 (1992)
- Porru, C.R.D., Scarpa, R.M., Prezioso, D., Bertaccini, A.: Home and office uroflowmetry for evaluation of LUTS from benign prostatic enlargement. *Prostate Cancer Prostatic Dis.* **8**, 45–49 (2005)
- Watanabe, T., et al.: Seasonal changes in symptom score and uroflowmetry in patients with lower urinary tract symptoms (2007)
- Caffarel, J., et al.: Home uroflow device : basic but more accurate than standard in- clinic uroflowmetry? 285(163), 2–3
- Fenely, M.R., Pearce, J., Dunsmuir, W.D.: Reproducibility of uroflow measurement: experience during double-blind, placebo-controlled study of doxazosin in benign prostatic hyperplasia. *Adult Urol.* **4295**(96) (1996)
- Reynard, J.M., Donovan, J., Yang, Q.: The ICS- ‘BPH’ study : uroflowmetry, lower urinary tract symptoms and bladder outlet obstruction. *Br. J. Urol.* **82**, 619–623 (1998)
- Bray, A., Griffiths, C., Drinnan, M., Pickard, R.: Methods and value of home uroflowmetry in the assessment of men with lower urinary tract symptoms : a literature review. **12**(February 2011), 7–12 (2012)
- Chung, J.Y., Lee S.E.: Uroflowmetry in the normal males: Relationship between volume voided and flowrate. *Korean J. Urol.* **25**, 679–684 (1984)

Comparative Study of Novel Microwave Coagulation Surgical Instrument and Currently Commercialized Energy Devices in an Animal Model

Dang Tran Khiem, Tohru Tani, Shigeyuki Naka, Atsushi Yamada, and Soichiro Tani

Abstract

Background The concept of a multitasking surgical device used microwave energy has been developed over a decade. Then, a microwave scissor-shaped surgical instrument (Acrosurg.[®]) has been invented and employed for pre-clinical experiments. **Methods** An animal study using specific pathogen-free pigs was conducted to compare surgical functions of newly developed microwave coagulation surgical instrument (Acrosurg.[®]) with current electro-surgical devices such as the electric current-based LigaSure[™] Small Jaw Sealer (LS) and the ultrasound-based Harmonic Focus[®] Shears (HF). The Acrosurg.[®] was tested on 5 mm vessels with regard to seal time, burst pressure (BP), lateral thermal injury (LTI), cutting time for hepatectomy and mesenterectomy. **Results** In the Acrosurg.[®]'s group, the seal time for 5 mm vessels was shorter and LTI was narrower in comparison with the outcomes in the LigaSure[™]'s group. Although BP in the Acrosurg.[®]'s group was lower than BP in the LigaSure[™]'s group, it reached approximately 900 mmHg. Cutting time for hepatectomy was not different in both groups (Acrosurg.[®] and Harmonic Focus[®]) but time consumption for mesenterectomy in the Acrosurg.[®]'s group was significantly shorter. There were some bleedings existing in both groups but achieving complete hemostasis. **Conclusion** Novel microwave

coagulation surgical instrument has the same effectiveness as compared to other commercialized energy devices. Moreover, it is more advantageous to some specific tissues and could be considered on clinical trial.

Keywords

Electrosurgical device • Microwave • High frequency • Ultrasound • Microwave coagulation surgical instrument

1 Introduction

In modern surgery, electro-surgical instruments gradually play an important role. Beside traditional sources of energy which have been applied throughout a long era such as high frequency electric current, radio frequency and ultrasound, microwave is recognized as a notable source which can be broadly used for surgical devices. From the 1970s, microwave tissue coagulator had been used to perform hepatectomy and to ablate liver tumors with positive results [1–3]. Over a decade, a concept of multitasking surgical device powered by microwave energy has been developed under a general name Microwave Coagulation Surgical Instrument [4]. Henceforth, some prototypes have been invented consisting of a scissor-shaped device (Acrosurg.[®]'s prototype) which is focused on cutting and dissecting tissues. Based on their unique mechanism and impact on various tissues, microwave devices are considered to succeed other electro-surgical devices in the future surgery. In order to evaluate their surgical functions including coagulation ability, vascular sealing and tissue resection speed, an example of novel microwave devices, Acrosurg.[®] (Nikkiso Co., Ltd., Tokyo, Japan), was employed to a comparative experiment with other current energy devices that are widely being used in routine operations: Harmonic Focus[®] Shears and LigaSure[™] Small Jaw Sealer.

D. T. Khiem · T. Tani (✉) · A. Yamada
Department of Research and Development for Innovative Medical Devices and Systems, Shiga University of Medical Science, Seta-Tsukinowa, Otsu, Shiga, Japan
e-mail: tan@belle.shiga-med.ac.jp

S. Tani
Department of Surgery, Shiga University of Medical Science, Otsu, Shiga, Japan

S. Naka
Hino Memorial Hospital, Hino, Shiga, Japan

D. T. Khiem
Department of Surgery, University of Medicine and Pharmacy at Ho Chi Minh City, Ho Chi Minh City, Vietnam

2 Materials and Methods

The protocol of this experiment was reviewed and approved by the Ethical Research Committee for Animal Life Science at Shiga University of Medical Science (SUMS).

2.1 Instruments

A scissor-shaped device (Acrosurg.[®]) powered by microwave energy were used for this experiment. It is developed from the last generation of the so-called Microwave Coagulation Surgical Instrument invented by Tani's team at Shiga University of Medical Science [4]. Nikkiso Co., Ltd. (Tokyo, Japan) has manufactured and commercialized this product within Japan market from June, 2017. The device was connected via a coaxial flexible cable to a generator which radiated microwaves at a frequency of 2450 MHz (12 cm wavelength) (Fig. 1). The power output is adjustable from 10 to 100 W. The other commercialized energy devices used as comparative groups were the bipolar electric current-based LigaSure[™] Small Jaw Sealer (LS; Covidien, USA) and the ultrasound-based Harmonic Focus[®] Shears (HF; Ethicon Endo-Surgery Inc., USA). In this experiment, power output was set at 60 W for Acrosurg.[®]. The energy level was set at 3 for LS and at 5 for HF according to each manufacturer's manual.

2.2 Animals

Six domestic pigs weighed from 38 to 42 kg were raised in a pathogen-free environment in the Research Center for Animal Life Science of SUMS for this experiment. The pigs were anesthetized with an intramuscular injection of ketamine hydrochloride (10 mg/kg) and medetomidine chloride (20 µg/kg). Anesthesia was maintained by inhaled isoflurane 5% through a facemask.

2.3 Procedure

Under general anesthesia, the pig was placed in a supine position. Laparotomy was performed to expose the

abdominal cavity. The liver was cut through 2 cm from the free edge by Acrosurg.[®] and HF to evaluate the cutting time. Similarly, the mesentery was exhibited and cut for each 10 cm long segment by Acrosurg.[®] and HF, respectively. Cutting time, bleeding cases and hemostasis time were measured for each group. The pig was then sacrificed to harvest the iliac arteries, aorta and carotid arteries which were measured the diameter at the simulated physiologic blood pressure. The 5 mm arteries were used for ex vivo experiments. The 5 mm group was subsequently sealed by Acrosurg.[®] and LS. Intraluminal pressure was created by an electric pump using physiologic saline 0.9% via a small catheter which was introduced into the open lumen of the vessel. The BP measured by the KDJ20 manometer (KD Scientific, Inc. Holliston, MA, USA) was defined as the intraluminal pressure at the leaking point. Sealed samples were collected and underwent Hematoxylin-eosin stain. LTI was measured from the sealed edge to the closest margin of the intact tissue under a light microscopy. We conducted the comparative studies as follow: Acrosurg.[®] versus LS in 5 mm artery group; Acrosurg.[®] versus HF in the liver resection group and Acrosurg.[®] versus HF in the mesenterectomy group.

2.4 Statistics

Quantitative variables were presented as mean \pm SD. Student t-test was used to compare the difference of the means between the two groups. The results were recognized as statistical significance if p value was less than 0.05.

3 Results

In the 5 mm artery group, Acrosurg.[®] need shorter time for complete coagulation than LigaSure[™] (5.1 ± 0.4 vs. 5.9 ± 4.0 s, $p < 0.05$). Although burst pressure (BP) at the sealed edges created by LigaSure[™] was significantly higher (1000 mmHg), BP in the Acrosurg.[®]'s group reached approximately 900 mmHg (882.6 ± 165.9 mmHg). The LTI affected by Acrosurg.[®] was also statistically narrower (2.8 ± 0.5 vs. 3.3 ± 0.4 mm, $p < 0.05$) (Table 1).

Fig. 1 Microwave device (Acrosurg.[®]) and its generator



Table 1 Functional comparison of Acrosurg.[®] with currently-used LigaSure[™] Sealer in 5 mm artery group

Device	No. of sample	Mean seal time (s)	Burst pressure (mmHg)	LTI (mm)
<i>5 mm artery group</i>				
Acrosurg. [®]	5	5.1 ± 0.4	882.6 ± 165.9	2.8 ± 0.5
LigaSure [™]	5	5.9 ± 4.0	1000 ± 0.0	3.3 ± 0.4
		p < 0.05	p < 0.05	p < 0.05

LTI: Laterall Thermal Injury (area)

Table 2 Summary of comparative studies between Acrosurg.[®] and widely-used Harmonic Focus[®] Shears on tissue resection

Device	No. of sample	Mean cutting time (s)	Mean no. of vessels	Bleeding case	Hemostasis time (s)
<i>Mesentery (10-cm-long segment each)</i>					
Acrosurg. [®]	9	21.3 ± 4.9	17.1	1/154 (0.7%)	1.7
Harmonic focus [®]	9	29.0 ± 5.6	18.8	2/169 (1.2%)	1.9
		p < 0.05		NC	NC
<i>Liver resection</i>					
Acrosurg. [®]	9	40.1 ± 6.9	–	1/9	19.2
Harmonic focus [®]	9	41.2 ± 6.2	–	1/9	2.4
		NS		NC	NC

NS: not significant, NC: not comparative

To perform mesenterectomy in a 10 cm long segment (each segment contains about 17–18 vasa recta), the Acrosurg.[®] cut faster than HF (21.3 ± 4.9 vs. 29.0 ± 5.6 s, p < 0.05). Meanwhile, when applying for liver resection, both Acrosurg.[®] and HF did not show any statistical difference in cutting time (40.1 ± 6.9 vs. 41.2 ± 6.2 s, not significant) (Table 2).

Regarding mesenterectomy, the number of bleeding cases out of total vasa recta in Acrosurg.[®]'s group and in HF's group were 1/154 (0.7%) and 2/169 (1.2%), respectively. Acrosurg.[®] took about 1.7 s while HF took about 1.9 s for hemostasis. Each group had one of 9 cases bled during liver resection and the new Acrosurg.[®] device needed more time for hemostasis than Harmonic Focus[®] (19.2 vs. 2.4 s) (Table 2). Because of the very low quantity of bleeding and hemostasis cases in both groups, case reports were conducted instead of statistical comparison.

4 Discussion

LigaSure[™] Small Jaw Sealer (LS) and Harmonic Focus[®] Shears (HF) are two most commonly used electrosurgical devices in recent years. They are widely accepted in many surgical procedures because of their easy-to-use handling. The notable features of both devices are quick dissection with stable hemostasis and safe vessel control even in moderate-to-large size arteries. In previous studies,

Harold KL et al. (2003) demonstrated that the mean burst pressure of electrothermal bipolar vessel sealer (a type of LigaSure's family) was statistically higher than the burst pressure created by ultrasonic coagulating shears at 4 or 5 mm arteries [5]. Newcomb et al. (2008) showed the same result in a later study. Currently, LS reaches the peak pressure of 1261 mmHg on 5 mm vessels and is considered as a reliable device for arteries up to 7 mm [5–7]. Therefore, we conducted the comparative study between the Acrosurg.[®] and LS but not HS when testing vascular sealing function. In our study, BP by LS also achieved a record of 1000 mmHg and it tended to decrease with vessel size elevation whereas the Acrosurg.[®], a device tailored to resection, could also approach a burst pressure of 882 mmHg. The pressure at the vascular sealed edge was definitely higher than any maximal physiologic blood pressure. Such an endurance could secure any in vivo sealed vessel. Moreover, the scissor-shaped design helped microwave device resect tissues faster with less thermal injury. When applying for mesenterectomy, the Acrosurg.[®] expressed a significant performance not only in cutting speed but also in bleeding control. Besides, both Acrosurg.[®] and HF resulted in the same outcome in liver resection. In case of bleeding after liver resection, Acrosurg.[®] spent longer time for hemostasis. Nevertheless, because there was only one bleeding case out of total series for each group, it is impossible to attribute the longer hemostasis time to any reasonable factor. A larger sample size would be needed for statistical comparison. In fact, the

microwave devices impact on tissues quite differently in comparison with other electrosurgical devices which transmit mechanical vibration (HF) or electric current (LS) directly to the tissue surface. Like electric oven, they provide electromagnetic energy to agitate water molecules inside, then heat the surrounding tissues and all portions of the given organ, therefore, will be coagulated at the same level concomitantly [8]. In the previous study, the microwave scissor-shaped prototypes were proved to be equivalent to LS and HF for lymphatic vessel sealing [9]. They also created effective coagulation and limited thermal spread in a rat hepatectomy [10]. Combined with relevant outcomes from this study, it is undeniable that microwave device can replace current electrosurgical products in many surgical procedures.

5 Conclusion

Microwave scissors (Acrosurg.®) achieved faster resection and similar coagulation in various types of tissue. Especially, it seems to be more effective on some specific tissues like the bowel mesentery when compared with one of the most secure surgical devices Harmonic Focus®. Therefore, microwave device can be a potential candidate for clinical trial.

Acknowledgements The authors express high gratitude to the doctors and technicians from the Department of Surgery, Shiga University of Medical Science for their supports. This research received financial support from Nikkiso Co., Ltd. (Tokyo, Japan).

Conflict of Interest Microwave Coagulation Surgical Instruments have been invented by Tohru Tani and Shigeyuki Naka as a preclinical model. Nikkiso Co. Ltd. (Tokyo, Japan) was granted the license from which they manufactured “Acrosurg.®”—a clinical model—A part of results from animal experiments which were conducted with the support of Nikkiso Co. Ltd. was used to draft the manuscript. D. T. Khiem (first author) and the other co-authors performed these animal experiments. Tohru Tani and Shigeyuki Naka declare that they have the

conflict of interest with Nikkiso Co. Ltd. The other authors declare that they have no conflict of interest.

References

1. Tabuse, K., Katsumi, M., Kobayashi, Y., Noguchi, H., Egawa, H., Aoyama, O., Kim, H., Nagai, Y., Yamaue, H., Mori, K., Azuma, Y., Tsuji, T.: Microwave surgery: hepatectomy using a microwave tissue coagulator. *World J. Surg.* **9**, 136–143 (1985)
2. Ryu, M., Watanabe, K., Yamamoto, H.: Hepatectomy with microwave tissue coagulator for hepatocellular carcinoma. *J. Hep. Bil. Pancr. Surg.* **5**, 184–191 (1998)
3. Strickland, A.D., Clegg, P.J., Cronin, N.J., Swift, B., Festing, M., West, K.P., Robertson, G.S., Lloyd, D.M.: Experimental study of large-volume microwave ablation in the liver. *Br. J. Surg.* **89**, 1003–1007 (2002). <https://doi.org/10.1046/j.1365-2168.2002.02155.x>
4. Tani, T., Kurumi, Y., Naka, S., Morikawa, S., Demura, K.: A new evolution of the microwave surgery: Development of a new surgical device using microwave and its application. *J. Microwave Surg.* **25**, 31–36 (2007)
5. Harold, K.L., Pollinger, H., Matthews, B.D., Kercher, K.W., Sing, R.F., Heniford, B.T.: Comparison of ultrasonic energy, bipolar thermal energy, and vascular clips for the hemostasis of small-, medium-, and large-sized arteries. *Surg. Endosc.* **17**, 1228–1230 (2003). <https://doi.org/10.1007/s00464-002-8833-7>
6. Newcomb, W.L., Hope, W.W., Schmelzer, T.M., Heath, J.J., Norton, H.J., Lincourt, A.E., Heniford, B.T., Iannitti, D.A.: Comparison of blood vessel sealing among new electrosurgical and ultrasonic devices. *Surg. Endosc.* **23**, 90–96 (2008). <https://doi.org/10.1007/s00464-008-9932-x>
7. Mishra, V.: Comparative study between harmonic scalpel and ligasure vessel sealing system: in open and laparoscopic surgery. *World J. Laparosc. Surg.* **6**(2), 74–76 (2013)
8. Simon, C., Dupuy, D.E., Mayo-Smith, W.W.: Microwave ablations: principles and applications. *RadioGraphics* **25**, 69–83 (2005)
9. Takebayashi, K., Shiomi, H., Naka, S., Murayama, H., Murakami, K., Akabori, H., Yamaguchi, T., Shimizu, T., Murata, S., Yamamoto, H., Kurumi, Y., Tani, T.: Utility of a microwave surgical instrument in sealing lymphatic vessels. *Am. J. Surg.* **206**, 229–233 (2013)
10. Nguyen, Q.V., Tani, T., Naka, S., Yamada, A., Murakami, K.: Thermal tissue change induced by a microwave surgical instrument in a rat hepatectomy model. *Am. J. Surg.* **211**, 189–196 (2016)

Developing Neural-fuzzy-based Unscented Kalman Filter Algorithm for Atrial Fibrillation Onset Prediction

Cuc T. Bui, Phat K. Huynh, Hao T. Phan, Trung Q. Le, and Vo Van Toi

Abstract

Atrial fibrillation is the most common arrhythmia, which substantially increases the risk of stroke and other heart-related complications. Hence, forecasting the onset of paroxysmal atrial fibrillation (PAF) has become increasingly paramount and influential in AF managements and preventive treatments. Previous studies mainly focused on utilizing the morphological-temporal or time-frequency features from the surface electrocardiogram (ECG) to heighten the accuracy of PAF classification but not truly yielded onset predictions. To address this issue, this paper proposes a model that deploys the adaptive neuro-fuzzy inference system (ANFIS) and Unscented Kalman Filter to approximate the nonlinear-system state distribution for PAF onset prediction. The model is based on a combination of Kalman filter algorithm and a neural fuzzy network to predict PAF onset in 70 patients. Initially, we extracted the feature AWSUM to quantify the accumulation of extrasystolic beats within 30-min ECG recordings prior to the PAF onset of 24 patients. The extracted features then were utilized to reconstruct the dynamic-system state space, on which neural fuzzy based UKF algorithm were performed. The forecasting results highlighted low-level prediction errors averaged over 24 patients, by which RMSE = 0.42 ± 0.24 for the training data and RMSE = 0.34 ± 0.46 for the testing data; the

testing-error had large variance due to the interpatient variabilities and abrupt changes in the system.

Keywords

Unscented Kalman filter • Paroxysmal atrial fibrillation • Adaptive neuro-fuzzy inference system • Onset prediction • Predictive modeling

1 Introduction

Atrial fibrillation (AF) is the most prevalent sustained type of tachyarrhythmia, which delineates shivering or irregular heartbeat that may result in stroke and other heart-related complications. In the United States, AF is diagnosed in 2.2 million individuals with a large proportion of middle-aged and senior patients [1]. Based on the duration of manifestation, AF is classified into two major types: paroxysmal AF and chronic AF [2]. Paroxysmal AFs (PAFs) are AF attacks enduring from 2 min to less than 7 days, while chronic AFs are pathological episodes that have the duration of 7 days or even longer. Chronic AFs may be the consequence of PAF development in almost 30% of the group of PAF patients [3].

In short-term forecasting, time-series forecasting and analysis techniques [4] have been successfully employed to serve cardiovascular disease diagnostics, prognostics, and preventive treatments. In those techniques, future values of random variables are estimated using mathematical and statistical models based on the past observations and prior knowledge under certain assumptions about data probability distributions, noise behaviors, and stochastic processes. Short-term forecasting is divided into two main branches, namely mathematical modeling and physiological-based modeling. Mathematical models include dynamical systems, statistical models, and differential equations; whereas physiological-based models represent a human body system of interest with the consideration into various

C. T. Bui · V. Van Toi
Department of Biomedical Engineering, International University - Vietnam National University, Ho Chi Minh City, Vietnam

H. T. Phan
Pham Ngoc Thach University of Medicine, Ho Chi Minh City, Vietnam

P. K. Huynh · T. Q. Le (✉)
North Dakota State University, Fargo, North Dakota, USA
e-mail: trung.q.le@ndsu.edu

P. K. Huynh
e-mail: phat.huynh@ndsu.edu

physiological factors, which govern complex behaviors in the system.

Researchers have extensively employed the mathematical models to representing the system dynamics of cardiovascular diseases. Those models utilized the input data from Electrocardiography (ECG) and other bio-signals (namely blood pressure, pulse rate, and respiration) to capturing the behaviors of the complex system [5, 6]. However, multiple mismatches between the realistic system and the modeled system were discovered due to the hardly-captured nonlinear dynamics and non-stationary physiological processes of cardiac activities. Several methods [7, 8] have attempted to adjust their techniques to derive a more plausible physiological-based model, which accounts for the coupling effects provoked from various biological processes and causal temporal dependencies, but their current solutions were inconsistent in model performance, which produced significant error difference between the training and testing set.

Therefore, in this paper, we seek to address this challenge by proposing neural-fuzzy-based UKF framework for PAF onset k-step forecasting that combines the adaptive neuro-fuzzy inference system (ANFIS) and the UKF statistical model, to optimizing the process of state-measurement estimation under the assumptions of statistical Gaussian noise and monitoring the transient dynamics while the system undergoes different phases.

2 Literature Review and Background

In the literature, various approaches have been proposed to address the challenge of predicting PAF onset, which can be categorized into premature atrial complexes (PAC) investigations and heart rate variability (HRV) analysis. Zong et al. [9] investigated the number and timing of PACs in the ECG episodes. Thong et al. [5] conducted a systematic study using the number of isolated PACs followed by a regular RR interval, runs of atrial bigeminy and trigeminy. In addition, Lynn and Chiang [6] analyzed non-linear features estimated from return map and difference map of HRV signal. In 2009, Maryam and Hassan [7] together developed novel HRV features including spectrum features, bispectrum features, and non-linear features to predict the occurrence PAF attacks. Shumway [8] presented a predictive method through dynamic modeling of the PR interval of ECG signals with the utilization of a artificial neural network. Despite the fruitful achievements, “prediction” term, for those studies particularly, is referred to as yielding PAF classification results between close-onset and distant-onset cases on new data not literally performing the onset forecasting [10, 11].

Being successfully applied concept in time series forecasting and analysis, Kalman filtering (KF—linear quadratic estimation) [12] is a set of recursive equations for determining the estimates of unknown variables given a series of measurements observed over time. Yet, the main drawback of the KF algorithm is that it is only applied for linear systems, which limits the plausibility of applications on the nonlinear system. One possibility is to linearize dynamic equations, which presented in the Extended Kalman Filter (EKF) [13]. This approximation, however, can induce large errors in the true posterior mean and covariance of the state variables leading to the divergence in the estimation process. Hence, the Unscented Kalman Filter (UKF) [13, 14] was introduced to address the approximation issues of the EKF, where the states’ probability distribution is defined over a set of Gaussian Random Variables (GRVs) [15], but instead of performing solely mean estimation the GRVs’ mean and covariance are determined using a minimal set of carefully chosen sample points called Sigma points.

Adaptive Neuro-Fuzzy Inference System (ANFIS) [16, 17] is an algorithm developed in the early 1990s originating from Takagi-Sugeno fuzzy inference system. Since it incorporates both the neural network and the fuzzy logic principles into a single framework, its inference system that is comprised of a set of fuzzy If-Then rules empowers the learning capability to constructing the nonlinear mapping functions, which makes ANFIS become a universal estimator. When combined with the UKF algorithm, statistics of the GRVs (the mean and covariance) are estimated through ANFIS after performing a nonlinear transformation on the GRVs. Our method presents a novel algorithm, which is a fusion of UKF framework and ANFIS to investigate about the behaviors of PAF before the onset and derive predictions correspondingly.

The outline of the paper is as follows. The first and second section gives a brief overview of PAF, the relevant background, and various proposed methods that addressed prediction challenge of PAF onsets. Section 3- Methodology elaborates on the mathematical problem formulation and the neuro-fuzzy-based UKF framework. Section 4 consists of detailed implementations of the established model and statistical preliminary results. Section 5 concludes with the justification of unexpected results and the highlights of the contributions and future work of this paper.

3 Methods

The block diagram of our method is illustrated in Fig. 1 comprising of four steps: (1) PAF database of ECG recordings selection from Physionet.org website, (2) Phase space reconstruction step generated a state space using the extracted feature AWSUM from ECG signal, (3) ANFIS

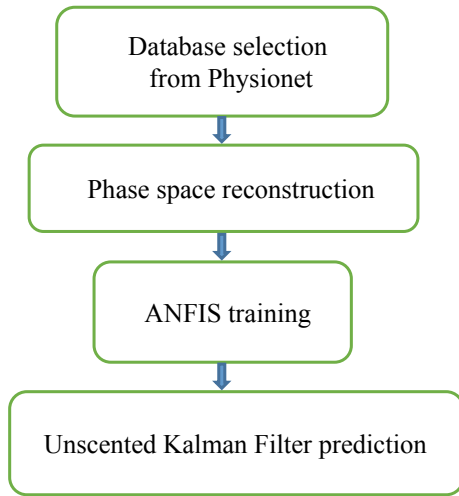


Fig. 1 Block diagram of the proposed algorithm

training, which estimated the hyperparameters of ANFIS and parameters of neuro-fuzzy rules deriving from the AWSUM-feature reconstructed state space, (4) Unscented Kalman Filter prediction step performed state-measurement estimations and state predictions iteratively from which k-step forecastings were obtained. In continue, each block is described in more details.

3.1 Database Description

We selected the PAF Prediction Challenge [18] to be the benchmark database to performing comparative validation with other methods. This two-channel ECG database was established for the Computers in Cardiology Challenge in 2001 with the intention of developing automated methodologies for predicting PAF. The database is further divided into a learning set (sufficiently provided the onset annotations) and a test set without annotations. Therefore, the learning set was used to train and validate our model, which contains 24 sets of PAF-patient ECG records. Each set is further partitioned into two 30-minute records, by which one record is precisely 30 minutes prior to the PAF onset (abnormal episode), while the other record is distant from the onset (normal episode).

3.2 Prediction Model

State-space Reconstruction

The features AWSUM, which was extracted from the PAF-patient ECG recordings of the Physionet database above, was considered as a state variable evolving over

time represented by a time-series for each 30-min episode preceding the PAF onset. For a window of size w , the proposed AWSUM feature is expressed as:

$$AWSUM(t) = \sum_i^n [\exp(t_i/\eta) - \exp((t_i - t_{i-1})/\sigma)] u(t - t_i + w) \quad (1)$$

Where $u(t)$ is the unit step function, t ($t > 0$) is the current time, $t_i \in [0, t]$ denotes the time of the i th detected Premature Atrial Complexes (PACs) [5, 9] with respect to t , which are clinical indicator of PAF onset, n is the total number of detected PAC beats within the sliding window, and σ, η are free scale parameters. The first term $\exp\left(\frac{t_i}{\eta}\right)$ accounts for the exponential increase of the feature AWSUM as the time of detected PACs t_i approaches the current time t , whereas the latter term $\exp\left(\frac{t_i - t_{i-1}}{\sigma}\right)$ penalizes the large distance between successive detected PAC peaks. The feature aims to quantify the behaviors of the system during that time, but insufficiently capture the intrinsic dynamics of it. Therefore, we applied time-delay reconstruction [19] on the time series AWSUM (t) containing K data points with a pre-specified pair of embedding dimension M and time delay τ resulting in K M -dimensional state vectors $S(K, M)$.

ANFIS: Adaptive Neuro-Fuzzy Inference System

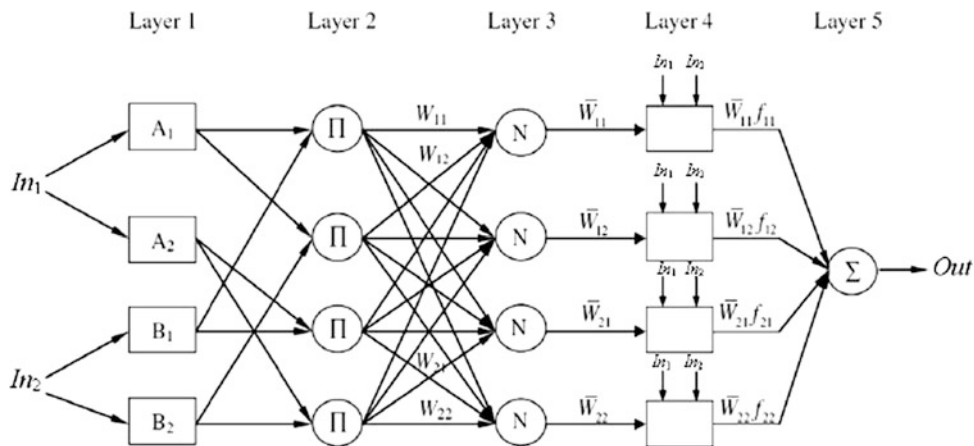
The number of inputs to the network is equal to the number of state variables, i.e. the chosen dimension M of the reconstructed phase space, then the corresponding mapping function f between two consecutive states is obtained after propagating inputs through all layers in the ANFIS network. To estimate the membership functions and linear parameters, the ANFIS was trained using $K-1$ input-output pairs of $2M$ -tuples, where the first M values are the state vector values of the previous time step as opposed to that of the current step for the latter M values. For simplicity, we assumed that there are two inputs ($m = 2$) $In1$ and $In2$ and one integrated output f from two fuzzy rules $f1$ and $f2$. Two rules were used in the method of “If-Then” for Takagi–Sugeno model, as follows:

$$\begin{aligned} \text{Rule 1} &= \text{If } In1 \text{ is } A1 \text{ and } In2 \text{ is } B1 \text{ Then } f1 = p1 * In1 + q1 * In2 + r1 \\ \text{Rule 2} &= \text{If } In1 \text{ is } A2 \text{ and } In2 \text{ is } B2 \text{ Then } f2 = p2 * In1 + q2 * In2 + r2 \end{aligned}$$

Where $A1, A2$ and $B1, B2$ are the membership functions of each input $In1$ and $In2$ (part of the premises), while $p1, q1, r1$ and $p2, q2, r2$ are linear parameters in part-Then (consequent part) of Takagi–Sugeno fuzzy inference model. Subsequently, all those hyperparameters and parameters were learned through the reconstructed state vectors $S(K, M)$.

ANFIS architecture consists of five layers. An adaptive node is integrated in the first and fourth layer, while the other

Fig. 2 The graphical representation of ANFIS architecture consisting of five layers



layers contain a stationary node. A brief description of each layer illustrated in Fig. 2 is as follows:

The ANFIS network established a set of rules to approximate the feature AWSUM progression according to fuzzy logics. When combined with ANN, the fuzzy rules are effectively deduced through a fuzzy inference system (FIS), which is able to adaptively learn, adjust the membership functions (Mfs), and reduce the percentage of errors in the specification of rules in fuzzy logic. This unique characteristic conforms neatly to the temporal state-measurement estimation process in the UKF framework.

The Unscented Kalman filter (UKF)

To elaborate on our performance, the basic framework of mathematics is expressed for a general discrete-time nonlinear dynamic system as follows:

$$x_{k+1} = \mathbf{F}(x_k, v_k, u_k, w)$$

$$y_k = \mathbf{H}(x_k, n_k, w)$$

Where \$x_k\$ represents the unobserved state at time k, \$u_k\$ is a known exogenous input (control input), and \$y_k\$ denotes the observed measurement signal. The process noise \$v_k\$ governs the dynamic system, whereas the observation noise \$n_k\$ accounts for the noise variance within the

measurement system. \mathbf{F} and \mathbf{H} are dynamic models to derive the next state and the measurement signal respectively through nonlinear functions, which are assumed to be known. The set of parameters \$w\$ is simultaneously estimated from the observed noisy signal \$y_k\$. A visualization of a discrete time nonlinear dynamic system is shown in Fig. 3.

Regarding our system, each time-delay embedding variable in the reconstructed phase space served as a state variable under statistical noise \$v_k\$, which was assumed to be the Gaussian white noise. The control input \$u_k\$ was omitted, as there existed no external input in the system. To explicitly specify \mathbf{F} , ANFIS generated a nonlinear function of M-dimensional state vector \$x_k\$, which enabled for a candid representation in terms of fuzzy rules rendering the relationship between the current state and the next one. Thus, \$w\$ fundamentally consisted of the required parameters of ANFIS, namely the membership function types, the number of membership functions, and the training set size; and UKF parameters (parameters control the spread of sigma points and the state distribution). \mathbf{H} was set to be the identity function associated with the Gaussian noise \$n_k\$. The means and covariances of process noise \$v_k\$ and measurement noise \$n_k\$ were adjusted based on the estimation residuals derived from the ANFIS algorithm.

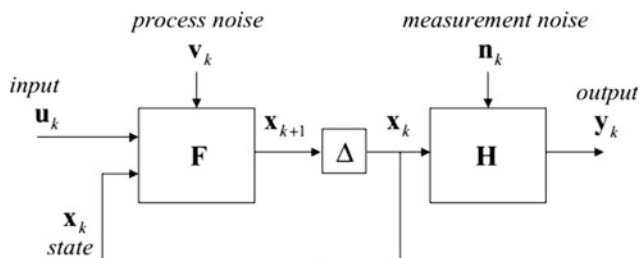


Fig. 3 Discrete-time nonlinear dynamic system diagram

4 Implementations and Results

4.1 ANFIS System

Parameter tuning

The Sugeno fuzzy inference system were implemented using the built-in toolbox ANFIS of MATLAB 8.0, the main function to train the ANFIS required the selection of a set of hyperparameters (arguments). Table 1 below represents the empirically chosen values of the hyperparameters and the diagram in Fig. 4 demonstrates the diagram of the inference system being used.

The function displays a representative high-level diagram of a fuzzy inference system trained by the feature AWSUM of an arbitrarily selected PAF patient, to which the time-delay embedding inputs are propagated. However, the sample membership functions shown in the boxes do not explicitly depict the actual shapes of the membership functions. There were totally 27 fuzzy rules being learned from the ANFIS system to characterize the relationship between successive states.

Output surface of the system

To visualize the linear dependence of each rule on the input variables, we examined the output surface of the system. Figure 5 below illustrates a surface plot, which generates a

3-D surface from two input variables and the output of a FIS (Fuzzy Inference System).

The output surface appeared to be uniformly linear with the slope of the surface as increasing toward the upper left corner. As seen, the shape of the surface revealed a positive linear mapping between the current state and the next state, but the elevation of the surface was more likely accounted for by the second variable dim2 as comparing the steepness between two input variables with respect to the output variable.

4.2 Unscented Kalman Filter

The Neural-fuzzy-based UKF was implemented to perform 1-step prediction for the AWSUM time series corrupted by additive Gaussian white noise. Figure 6 shows the results of our algorithm applied on one representative patient data with 100 training data points, and the remaining 106 points were used for testing.

The forecasting results exhibited low-level prediction errors averaged over 24 patients, in which $RMSE = 0.42 \pm 0.24$ for the re-evaluation process, which performed 1-step prediction on the training data, and the testing data error reduced to $RMSE = 0.34 \pm 0.46$ but possessed higher

Table 1 The list of ANFIS hyperparameters and their corresponding assignments

Hyperparameters	Optimal values
Number of epochs	300
Number of membership functions	3
Number of training data points (L)	L/2
Input membership functions type	Gbellmf (Generalized bell-shaped membership function)
Output membership function type	Linear

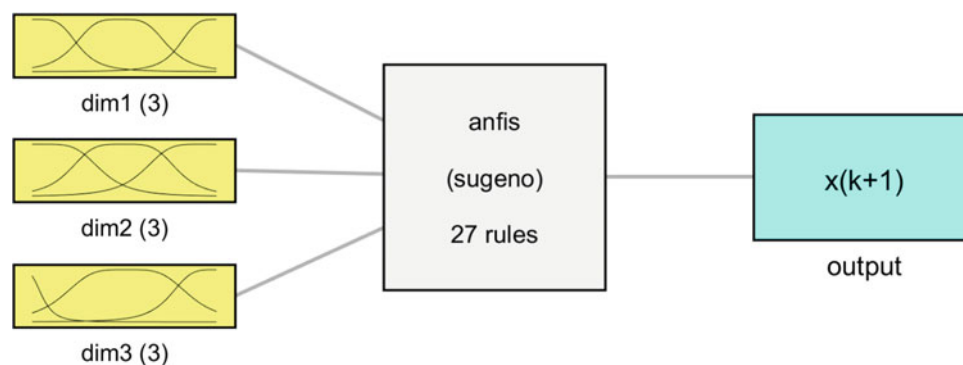


Fig. 4 The diagram of the fuzzy inference system of a representative patient after the training process with the names of the input variables on the left (dim1, dim2, dim3), which obtained from the 3-dimensional state vector at time t, and the output variable of the next state vector x

(k + 1) on the right. For each input variable, three Gbellmf membership functions' parameters were tuned in response to the training data influencing their shapes as shown in the green boxes. The next state vector $x(k+1)$ was determined using 27 learned rules of ANFIS

Fig. 5 The surface view of the constructed rule base

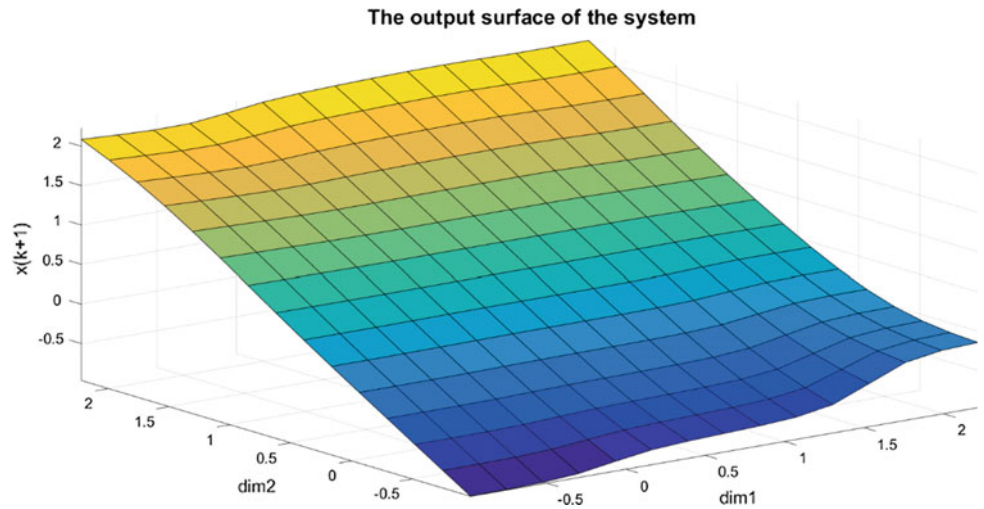
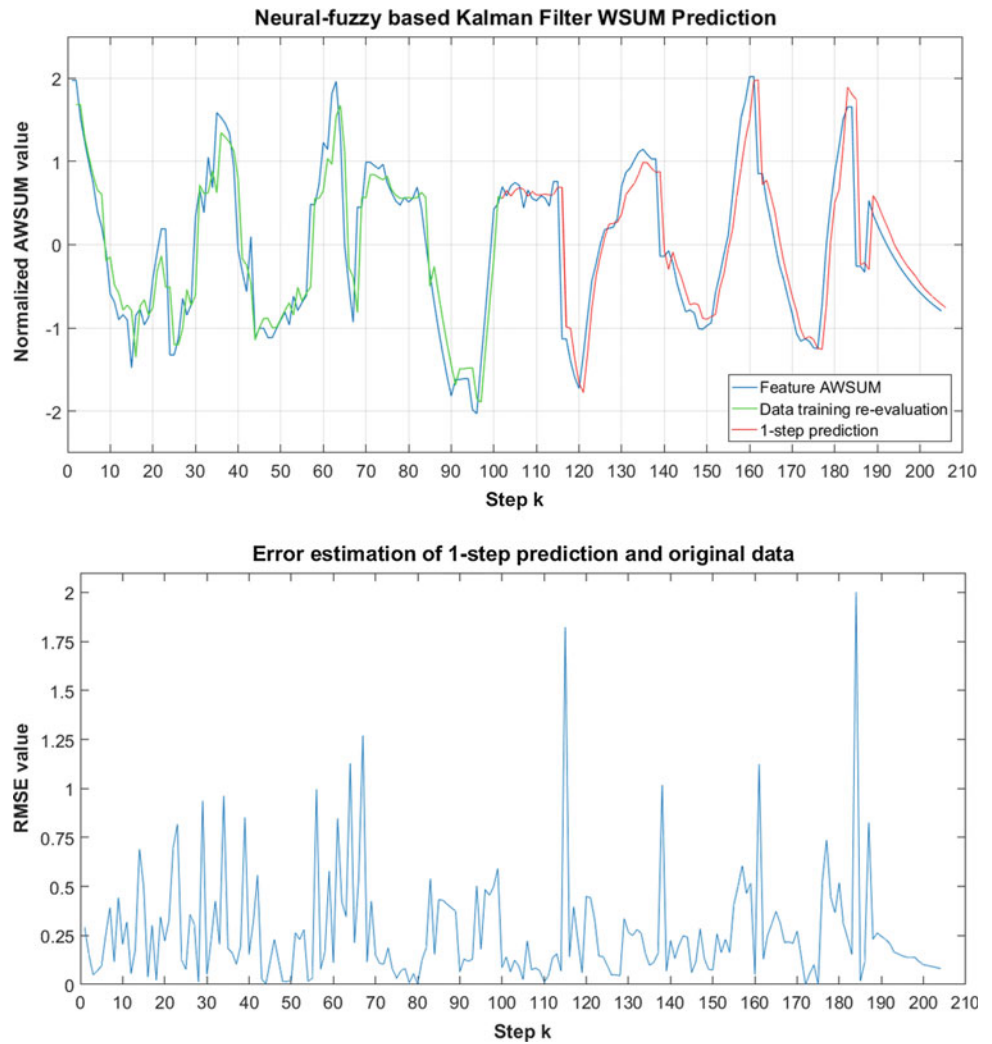


Fig. 6 Neural-fuzzy based Unscented Kalman filter 1-step prediction of the AWSUM time series of one representative specific patient was represented in the first figure, in which blue line is one dimension of the state vector AWSUM, green line and red line are the predicted values on the training set and testing set respectively. The bottom graph shows the RMSE estimation of 1-step prediction and the original data



variance; this might be due to the variabilities among patients and abrupt changes (shown by the overshootings) in the system.

5 Conclusion

In this study, we aim to develop a short-term forecasting method, in which we integrate the principles of Neuro-fuzzy logic inference system and Unscented Kalman Filter. The method assists physicians in making clinical decisions for the accurate PAF interventions and preventive treatments. Furthermore, it attempts to confirm the hypothesis proposed in a vast PAF clinical population and established a robust and reliable framework of prediction method depending on the aforementioned-extracted feature. With previous work on the localization to myocardial infarction [20], the present findings have important implications for understanding the dynamic rules in the cardiovascular system under PAF inferred from ANFIS system, and track the nonlinearity variations associated with noise through UKF. However, there are potential shortcomings need to be considered, namely the generalization of the model and the justification of the underlying assumptions. Future studies should target to address this emerging challenge.

Conflict of Interest The authors declare that they have no conflict of interest.

References

1. Feinberg, W.M., et al.: Prevalence, age distribution, and gender. *Arch. Intern. Med.* **155**, 469–473 (1995)
2. Levy, S.: *Atrial fibrillation: old and new classifications*, p. 107–113, Futura Publishing, Armonk, NY (1998)
3. Takahashi, N., et al.: Clinical features of paroxysmal atrial fibrillation. *Jpn. Heart J.* **22**(2), 143–149 (1981)
4. Das, S.: *Time series analysis*. Princeton University Press, Princeton, NJ (1994)
5. Thong, T., et al.: Prediction of paroxysmal atrial fibrillation by analysis of atrial premature complexes. *IEEE Trans. Biomed. Eng.* **51**(4), 561–569 (2004)
6. Lynn, K., Chiang, H.: A two-stage solution algorithm for paroxysmal atrial fibrillation prediction. In: *Computers in Cardiology 2001*, IEEE (2001)
7. Mohebbi, M., Ghassemian, H.: Prediction of paroxysmal atrial fibrillation based on non-linear analysis and spectrum and bispectrum features of the heart rate variability signal. *Comput. Methods Programs Biomed.* **105**(1), 40–49 (2012)
8. Shumway, R.H., Stoffer, D.S.: State-Space models. In: *Time Series Analysis and its Applications*, p. 319–404. Springer (2011)
9. Zong, W., Mukkamala, R., Mark, R.: A methodology for predicting paroxysmal atrial fibrillation based on ECG arrhythmia feature analysis. In: *Computers in Cardiology 2001*, IEEE (2001)
10. Bui, C., et al.: Time series forecasting for healthcare diagnosis and prognostics with the focus on cardiovascular diseases. In: *The 6th International Conference on the Development of Biomedical Engineering in Vietnam, IFMBE Proceedings*, vol. 63, pp. 809–818. Springer (2017)
11. Cheng, C., et al.: Time series forecasting for nonlinear and nonstationary processes: a review and comparative study. *IIE Trans.* **47**(10):1053–1071 (2015)
12. Zarchan, P.: Progress in astronautics and aeronautics: fundamentals of Kalman filtering: a practical approach. In: *Aiaa*, vol. 208 (2005)
13. Julier, S.J., Uhlmann, J.K.: New extension of the Kalman filter to nonlinear systems. In *Signal processing, sensor fusion, and target recognition VI*, International Society for Optics and Photonics (1997)
14. Julier, S.J., Uhlmann, J.K.: Unscented filtering and nonlinear estimation. *Proc. IEEE* **92**(3), 401–422 (2004)
15. Grinstead, C.M., Snell J.L.: *Introduction to Probability*, American Mathematical Soc (2012)
16. Jang, J.-S.: ANFIS: adaptive-network-based fuzzy inference system. *IEEE Trans. Syst. Man Cybern.* **23**(3), 665–685 (1993)
17. Jang, J.-S.R. Fuzzy modeling using generalized neural networks and Kalman filter algorithm. In *AAAI*. (1991)
18. Moody, G., et al.: Predicting the onset of paroxysmal atrial fibrillation: The Computers in Cardiology Challenge 2001. In: *Computers in Cardiology 2001*. IEEE (2001)
19. Casdagli, M., et al.: State space reconstruction in the presence of noise. *Physica D: Nonlinear Phenomena* **51**(1–3), 52–98 (1991)
20. Le, T.Q., et al.: Topology and random-walk network representation of cardiac dynamics for localization of myocardial infarction. *IEEE Trans. Biomed. Eng.* 2325–2331 (2013)

Modeling of Acoustic Tweezers for the Manipulation in Biological Media

Quyen B. Huynh, Huy Q. Pham, Nhung T. Nguyen, Trung Q. Le,
and Vo Van Toi

Abstract

Acoustic waves can hover and manipulate particles by the trapping effect. Since this energy has good penetration through the human tissues, acoustic manipulation have potential prospects for in vivo environments. However, previous attempts are constrained to the common physical host fluids like air, water or oil. In this paper, we delineate the generation of acoustic traps to levitate a particle in a single and composite biological layer. Furthermore, we also provide a thorough analysis of the behavior of the acoustic traps subjecting to the increase of frequency for the single medium case. The formation of acoustic traps in human-imitating fluids plays a major role for non-invasive treatment, target-drug delivery, and in vivo translation.

Keywords

Acoustic waves • Hover and manipulation •
Biological • In vivo

1 Introduction

Acoustic manipulation has been received with considerable interest during the last decades. Many studies have been conducted towards sound's capabilities of levitating and manipulating various targets without physical contact. The rapid development of this technology has resulted in various

applications such as crystallography [1], microfluidic fabrication [2], cell manipulation and separation [3], material transportation [4–6], biomaterials [7], and levitation of small living organisms [8]. Additionally, due to acoustic's good penetration and safety properties, in vivo operations are prospectively executable. This is of paramount importance for biomedical applications, namely controlling capsules to specified organs or treating diseases by non-invasive tackling the disease-causing agent, etc. Despite this unlimited potential, previous studies have only focused on manipulating targets immersed in ex vivo medium (air, water or oil). Therefore, demonstrating the acoustic manipulation process in an in vivo condition is highly desirable.

Traditionally, hovering and translating microscopic particles require the generation of the complex energetic fields (referred to as “tweezers”) to trap them. The energies used to cause trapping effect historically originates from optics and magnetics [9, 10]. It is until the past decade that acoustics tweezers have emerged and popularly practiced. Among the earliest acoustic levitating system is of the dual-beam configuration. Dual opposite transducers (or transducer arrays) generate standing-wave field whose nodes behave as traps to maintain the particles in suspended positions [1, 5, 11, 12]. Later studies have witnessed single-beam acoustic tweezers [13, 14], which are preferable due to its simple design and promising prospects for maneuvering applications. Single-beam systems configured as one single transducer or an ultrasonic phased-array generate acoustic tweezers that share similar characteristics with the optical tweezers [13]. Diverse single-beam acoustic tweezers have been reported. References [15, 16] demonstrated the capability of trapping particles through a single-focused acoustic beam utilizing a highly-focused ultrasonic emitter. Reference [13, 17] illustrated using a phased-array to form a vortex-based trap characterized by a helicoidal pattern and constituted by gradual phase change from 0 to 2π along the center axis; the x-y plane of this trap shows a high amplitude well surrounding a null-core where particles are trapped. Due to twister trap's nature of exerting angular momentum, the

Q. B. Huynh · N. T. Nguyen · V. Van Toi
Department of Biomedical Engineering, International University -
Vietnam National University, Ho Chi Minh City, Vietnam
e-mail: huynhquyen.dvtv@gmail.com

H. Q. Pham · T. Q. Le (✉)
Industrial and Manufacturing Engineering, North Dakota State
University, 1340 Administration Ave, Fargo, ND 58105, North
Dakota, USA
e-mail: trung.q.le@ndsu.edu

H. Q. Pham
e-mail: huy.pham@ndsu.edu

trapped particle spins around its own axis. Reference [13] discussed the generation of a twin trap utilizing various phased-array configurations. This trap, characterized by opposite phases between two halves of the array, is composed of two cylindrical fields of high amplitude that exposes tweezing force on the trapped expanded-polystyrene (EPS) spheres in the x-direction. Trapped particles under the twin trap's complex field can be rotated by adjusting its corresponding so-called signature.

Based on these achievements, we generalized acoustic manipulation process in different biological host fluids using single-beam tweezers. In detail, we model the complex fields of these acoustic traps in surrounding artificial media imitating human biological environments, namely blood (for single-medium), and fat-muscle complex (for dual-layered media). We also varied the driving frequency to investigate its effect on the morphology of the acoustic traps, potential energy and the radiation force on the same size particle. Moreover, we generate acoustic traps in idealized two-layered media of fat-muscle divided by a planar interface. This study provides insight into the creation of acoustic traps in the various biological media settings and suggest promising in vivo acoustic trapping and manipulation utilizing the single-beam acoustic traps.

2 Methods

2.1 Determination of Phase Delays Characteristic Acoustic Tweezers

To create these single-beam acoustic tweezers, estimating appropriate phase inputs to drive an ultrasonic phased-array is of special importance. The phase modulation to drive the ultrasonic array emitting the acoustic traps are estimated as follows. The transmitting time from the individual loudspeaker to the focal point is calculated and referenced with a standard to derive the corresponding time-delay; separate sources then radiate the time-delay wavefronts to form the focused beam. This technique ensures that the compressional or shear bulk waves to arrive instantaneously at the desired focal point. The focal structure is subsequently added with the so-called trap signatures identifying the morphology of the corresponding traps. Here, we select two most preferred traps, namely twin trap and vortex trap. These traps have been reported experimentally to lure expanded polystyrene (EPS) particles stably thus serve as a foundation for acoustic manipulation process [13, 14]. Twin trap's signature is characterized by opposite phase modulation between two halves of the array and shown to enforce rotation motion on the trapped particle. The signature of vortex trap is defined by a helicoidal phase alteration around the center axis, resulting in the particle's spinning action due to momentum

exertion. By adding the phase values forming the focused beam with those representing the trap signatures, the combined phase modulation that shapes the steady acoustic traps are computed. Determining the phase modulation for dual-layered media is based on the same principle but necessitates the incident point positions at the interface, which can be computed by using an algebraic manipulation equation of the Snell's Law equation with a 3-D coordinate transformation technique [18].

2.2 Theory of Potential Energy and Acoustic Radiation Force

The simulation models justify the acoustic radiation force on the particles. Originally, particles suspended in the acoustic fields exhibit the so-called potential energy. Though several theories on this energy were discussed very early in the work of [19, 20], it is until Gor'kov that the theory is more approachable thus widely practiced for manipulation applications. Bruus then once again explained the theory clearly with a complete demonstration of the underlying equations of the phenomenon [21]. The potential energy generated by a particle under the expectation of complex acoustic field is expressed as [13, 14]:

$$U = 2C_1(|p|^2) - 2C_2(|p_x|^2 + |p_y|^2 + |p_z|^2) \quad (1)$$

where p and p_x, p_y, p_z denote the incident pressure and its first order spatial derivatives at the location of the particle; C_1, C_2 are two physical constants and expressed as:

$$C_1 = \frac{1}{4} V_p \left(\frac{1}{c_f^2 \rho_f} - \frac{1}{c_p^2 \rho_p} \right) \quad (2a)$$

$$C_2 = \frac{3}{4} V_p \left(\frac{\rho_f - \rho_p}{(\rho_f + 2\rho_p)\omega^2 \rho_f} \right) \quad (2b)$$

where V_p represents the volume of the object; ρ_f, c_f demonstrate the density and the speed of sound in fluid, respectively; ρ_p and c_p represent the density of the particle and its compressional speed of sound. The volume and the difference in acoustic properties between the particle and the surrounding fluid contribute to decide the magnitude and sign of the potential energy. This implies that particles varied in size and properties under the same acoustics field behave distinctly [17].

The radiation force emerges because of the interference between the incident and the scattered waves. This force impacting on the spherical object equals to the negative gradient of the potential, which is denoted by:

Table 1 Acoustic characteristics of the media in the models

Medium	Density (kg/m ³)	Speed of sound (m/s)
Blood	1042.8	1570
Fat	909.4	1450
Muscle	1060	1585

$$F_i = -\nabla U \quad (3)$$

For our simulations, the conditional parameters are demonstrated as follows. Biological-imitating host fluids are selected as blood (for single medium) and fat-muscle aggregate (for dual-layered media). The acoustic characteristics of these media are summarized in Table 1.

These media are assumed to be ideal without resorting to the viscosity effect, energy absorption, and drag force. To simplify the discussion, we choose the particles with the radiuses significantly smaller than the driving wavelength (i.e.: the Rayleigh regime). Hence, cellulose particles of 0.56 mm diameter with density 1400 kg/m³ and speed of sound 2973 m/s are chosen for these simulations.

2.3 Finite Element Analysis

The acoustics fields are determined and visualized using finite element method (COMSOL Multiphysics 5.2). We use “Pressure Acoustics” interface to solve for the pressure

defined in the Helmholtz equation. The array of 8 × 8 loudspeakers (9.9 mm diameter each) are positioned side-by-side without distance and operated with a frequency of 40 kHz. “Plane wave” boundary condition is used to define each loudspeaker with fixed pressure value over its surface area. The loudspeakers are defined with constant pressure amplitude and different phase delay. “Perfectly matched layer” is used to model the non-reflecting effect of acoustic waves. For the case of dual-layered media, the continuity condition of acoustic pressure and velocity are automatically enforced when waves pass through the refractive interface.

3 Results

3.1 Acoustic Manipulation in Single Biological Medium-Blood

Acoustic manipulation originates from the creation of the acoustic tweezers that act as traps to hold the particles. Generation of the typical acoustic traps has been demonstrated in [13, 14]. The focused beam can theoretically trap the particles; however, tends to push out dense particles. The capabilities of twin trap and vortex trap for levitating and manipulating particles were discussed and share similar characteristics with their optical counterparts. Figure 1 shows the three acoustic structures generated in blood as host fluid.

Fig. 1 Generation of acoustic traps **a, b** Focus beam. **c, d** Twin trap. **e, f** Vortex trap in blood

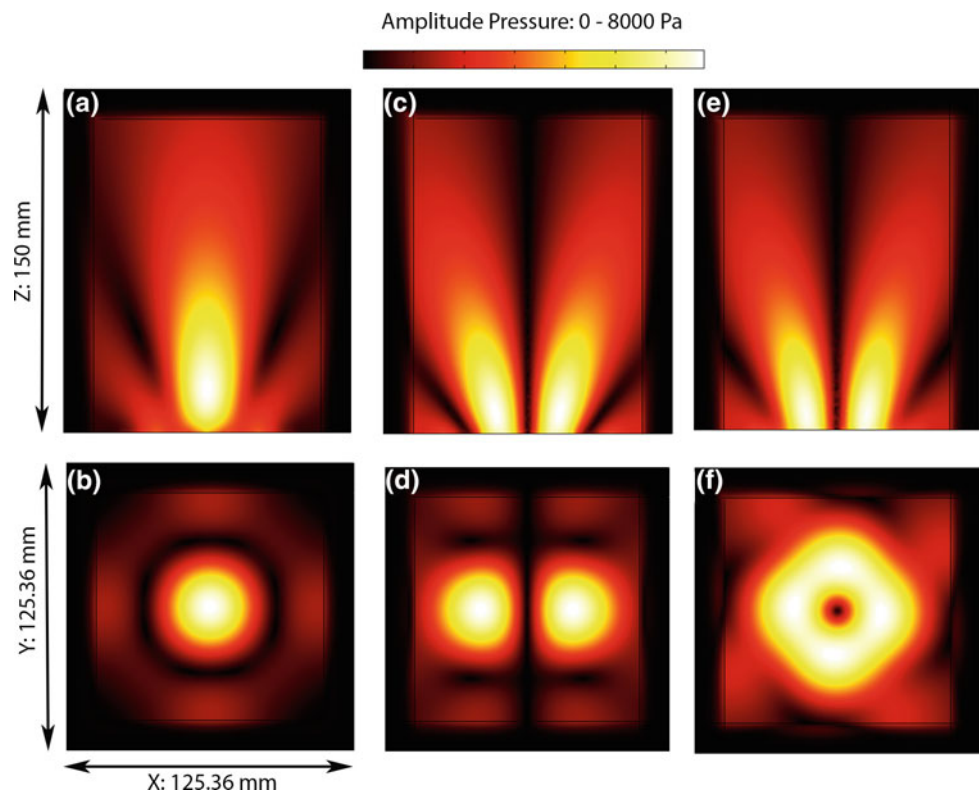


Fig. 2 Acoustic radiation force acting on the 0.56 diameter cellulose particles of **a, b** Focus beam. **c, d** Twin trap and **e, f** Vortex trap at $z = 40$ mm. Force contours illustrate the magnitude of the force and the arrows indicate the forces directions

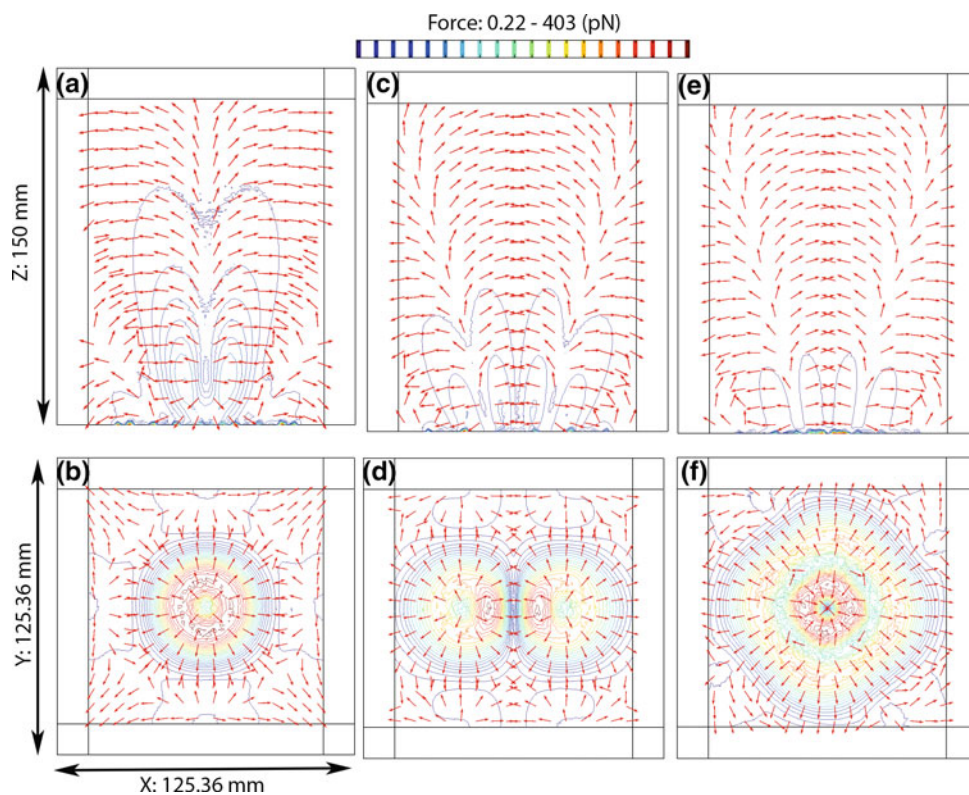


Fig. 3 The cross-sectional view at the x-y plane at $z = 40$ mm of twin trap subjected to increment of the driving frequency: **a** 60 kHz, **b** 80 kHz, **c** 100 kHz and **d** 120 kHz

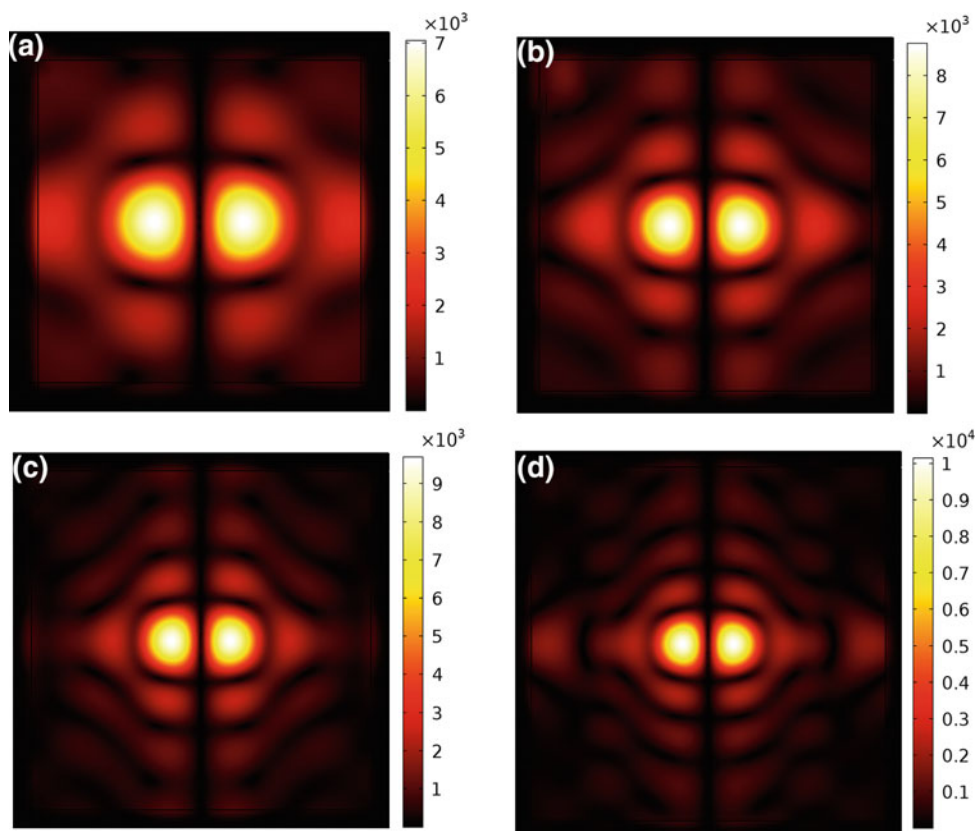
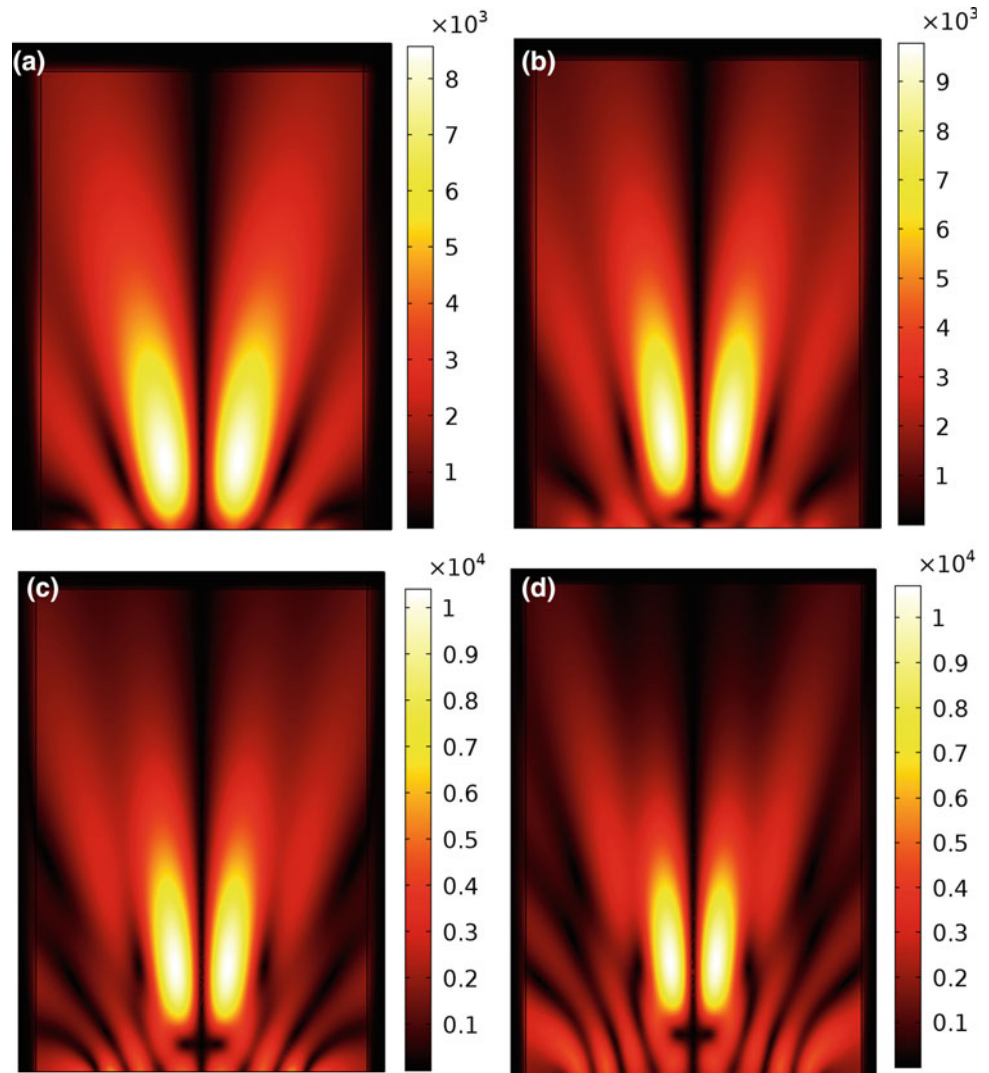


Fig. 4 The x-z plane view of twin trap at $y = 0$ subjected to increment of the driving frequency: **a** 60 kHz, **b** 80 kHz, **c** 100 kHz and **d** 120 kHz



The existence of particles in the acoustic fields creates the potential energy (Gor'kov potential). The cellulose particles tend to be attracted to the points where this energy is smallest. When the potential energy varies, the acoustic radiation force is formed and considered as the underlying force for levitation and manipulation phenomenon. Figure 2 shows the trend of the cellulose particles to move to the center of the twin trap and vortex trap.

Here, we increase the frequency to 120 kHz with a step number of 20 kHz to investigate what parameters are affected and how these changes correlate with the force acting on the cellulose particles. As can be seen from Figs. 3, 4, 5 and 6, with the increase of the driving frequency from 60 to 120 kHz with a step number of 20 kHz, the structures of acoustic traps (twin trap and vortex trap) tends to be smaller and more concentrating to the levitation point.

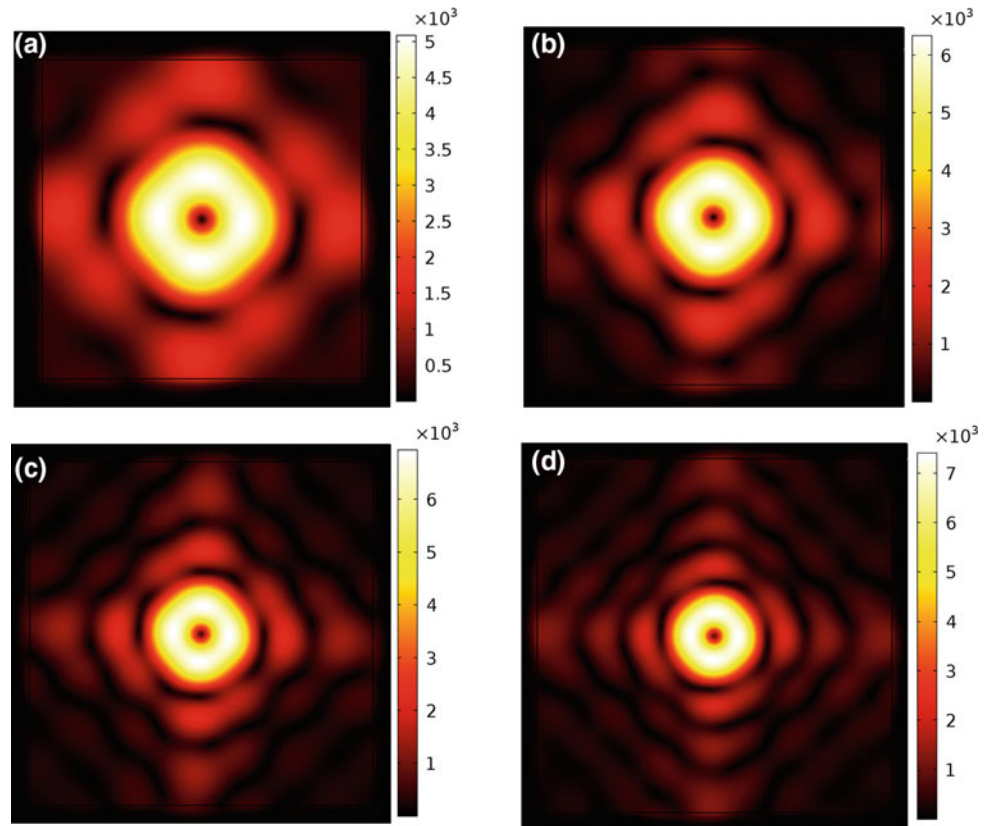
Additionally, the overall amplitude pressure also increases proportionally with the frequency rise.

The Gor'kov potential and total radiation force also rises with the frequency increment. These are expressed clearly in Tables 2 and 3. This trend shows that a suitable driving frequency is required to accomplish the desired radiation force. This is extremely necessary when the user clearly knows his wanting force and can alter the frequency parameter.

3.2 Acoustic Manipulation in Idealized Dual Biological Layers—Fat and Muscle

To levitate the cellulose particles in the idealized dual-layered media consisting of fat and muscle, we utilize

Fig. 5 The cross-sectional view at the x-y plane at $z = 40$ mm of vortex trap gets smaller subjecting to the increase of the driving frequency: **a** 60 kHz, **b** 80 kHz, **c** 100 kHz and **d** 120 kHz



the Focal Law for an ultrasonic phased-array but accounting the Snell's Law of refraction to precisely represent the ray paths from the sources to the focal point (levitation point). Figure 7 demonstrates the travelling pathway of each acoustic source to the focal point. As can be seen, the rays are bent due to the refraction effect.

The phase retardation represent the acoustic traps are calculated based on the information of these incident points. As a result, the acoustic traps in the two immiscible tissues of fat and muscle are formed (Fig. 8).

The magnitude and morphology of the acoustic traps generated in the fat-muscle complex media are nearly the same with the blood fluid because the phase retardation driving the loudspeakers for these two cases are rather similar. It is noted that to estimate the phase delays requires the information of the acoustic properties (density and speed

of sound) of the surrounding fluids. These parameters almost equal for blood, fat, and muscle and thus the computed phase delays for both cases are likely to be close to each other. The fact that insignificant refraction effect between fat-muscle is also another reason for the slight consistency in phase delays between two cases.

4 Discussion and Conclusion

In this paper, we provide a thorough description on the acoustic manipulation procedures in various biological human tissues: a single blood medium and dual-layered media of fat-muscle. Additionally, we also demonstrate the effects of driving frequency on the behaviour of acoustic traps in a homogeneous medium. Our study suggests that

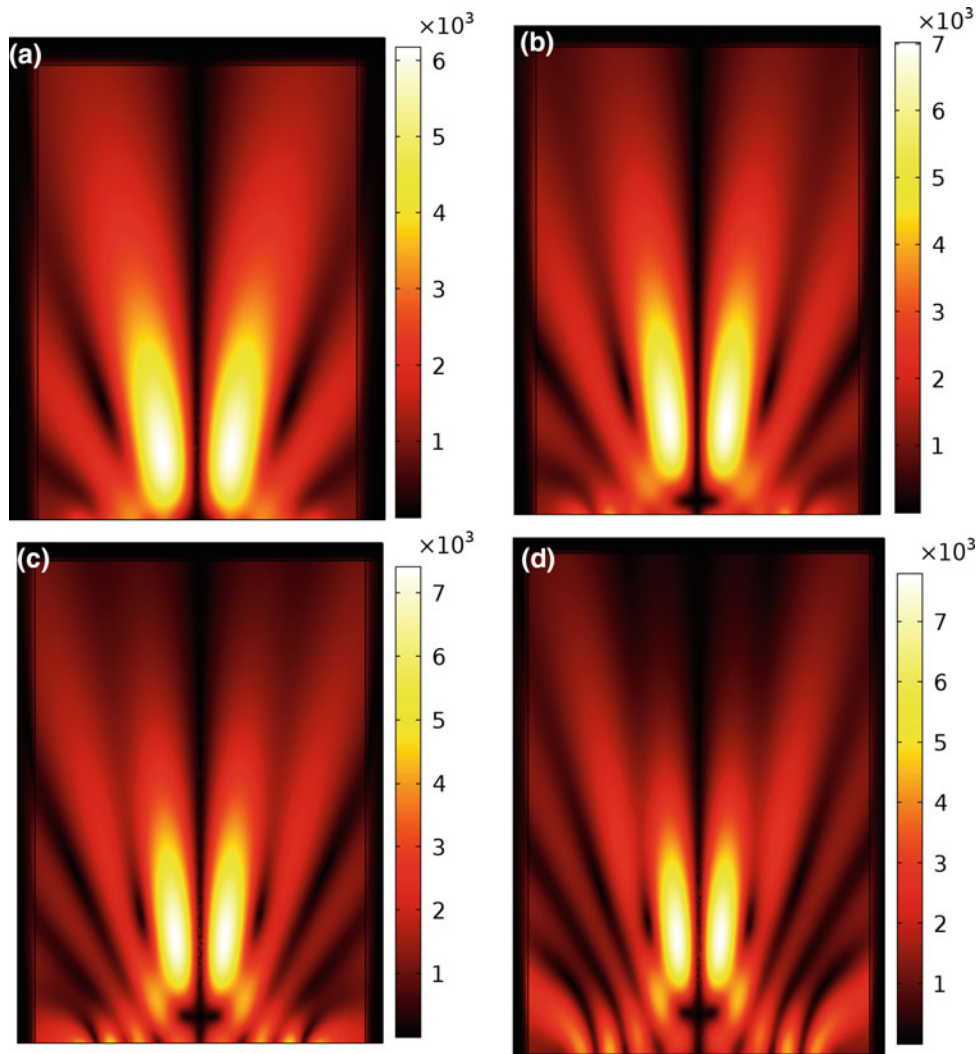


Fig. 6 The x-z plane view of vortex trap at $y = 0$ subjected to increment of the driving frequency: **a** 60 kHz. **b** 80 kHz. **c** 100 kHz and **d** 120 kHz

Table 2 Change in Gor'kov potential and force (twin trap)

Frequency (kHz)	Parameters	
	Gor'kov potential (pJ)	Force (pN)
40	0.014	0.784
60	0.031	0.499
80	0.044	1.055
100	0.052	6.536
120	0.058	10.906

Table 3 Change in Gor'kov potential and force (vortex trap)

Frequency (kHz)	Parameters	
	Gor'kov potential (pJ)	Force (pN)
40	0.016626	0.72017
60	0.034174	1.3166
80	0.050769	1.6375
100	0.059991	7.4414
120	0.068499	12.531

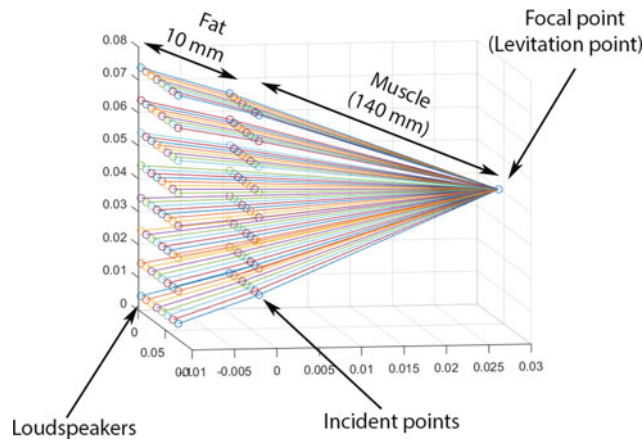
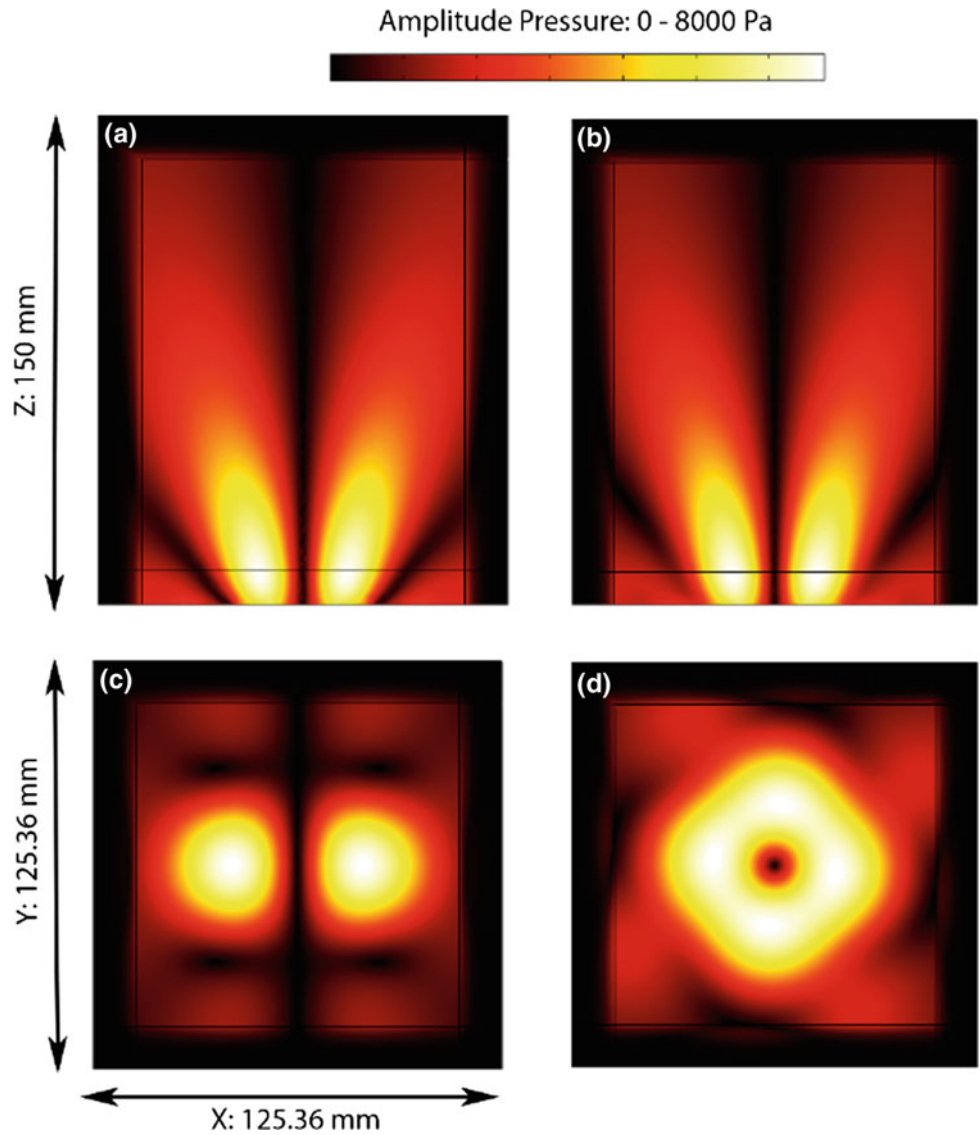


Fig. 7 A demonstration on the travelling pathway from each source through its respective incident point to the focal point for a planar interface

Fig. 8 Generation of acoustic traps in dual-biological layered media composed of fat and muscle



in vivo acoustic manipulation can be theoretically executable, provide potential prospects for biomedical applications. However, there are still several factors that must be considered for appropriate clinical use. Factors like energy absorption and attenuation; existence of many contributing forces like drag force due to acoustic streaming, frictional force between the particles and the fluid etc.; and the conversion from sound to heat energy leading to tissue destruction.

Conflict of Interests The authors declare that there are no conflicts of interest regarding the publication of this paper.

References

- Hong, Z., Xie, W., Wei, B.: Acoustic levitation with self-adaptive flexible reflectors. *Rev. Sci. Instrum.* **82**(7), 074904 (2011)
- Ding, X., Lin, S.-C.S., Kiraly, B., Yue, H., Li, S., Chiang, I.-K., Shi, J., Benkovic, S.J., Huang, T.J.: On-chip manipulation of single microparticles, cells, and organisms using surface acoustic waves. *Proc. Natl. Acad. Sci.* **109**(28), 11105–11109 (2012)
- Laurell, T., Petersson, F., Nilsson, A.: Chip integrated strategies for acoustic separation and manipulation of cells and particles. *Chem. Soc. Rev.* **36**(3), 492–506 (2007)
- Foresti, D., Poulidakos, D.: Acoustophoretic contactless elevation, orbital transport and spinning of matter in air. *Phys. Rev. Lett.* **112**(2), 024301 (2014)
- Whymark, R.: Acoustic field positioning for containerless processing. *Ultrasonics* **13**(6), 251–261 (1975)
- Vasileiou, T., Foresti, D., Bayram, A., Poulidakos, D., Ferrari, A.: Toward contactless biology: Acoustophoretic DNA transfection. *Scientific reports* **6** (2016)
- Weber, R.J., Benmore, C.J., Tumber, S.K., Taylor, A.N., Rey, C. A., Taylor, L.S., Byrn, S.R.: Acoustic levitation: recent developments and emerging opportunities in biomaterials research. *Eur. Biophys. J.* **41**(4), 397–403 (2012)
- Xie, W., Cao, C., Lü, Y., Hong, Z., Wei, B.: Acoustic method for levitation of small living animals. *Appl. Phys. Lett.* **89**(21), 214102 (2006)
- Grier, D.G.: A revolution in optical manipulation. *Nature* **424**(6950), 810 (2003)
- Simon, M.D., Heflinger, L.O., Ridgway, S.: Spin stabilized magnetic levitation. *Am. J. Phys.* **65**(4), 286–292 (1997)
- Foresti, D., Nabavi, M., Klingauf, M., Ferrari, A., Poulidakos, D.: Acoustophoretic contactless transport and handling of matter in air. *Proc. Natl. Acad. Sci.* **110**(31), 12549–12554 (2013)
- Glynn-Jones, P., Demore, C.E., Ye, C., Qiu, Y., Cochran, S., Hill, M.: Array-controlled ultrasonic manipulation of particles in planar acoustic resonator. *IEEE Trans. Ultrason. Ferroelectr. Freq. Control* **59**(6), 1258–1266 (2012)
- Marzo, A., Seah, S.A., Drinkwater, B.W., Sahoo, D.R., Long, B., Subramanian, S.: Holographic acoustic elements for manipulation of levitated objects. *Nat. Commun.* **6** (2015)
- Marzo, A., Corkett, T., Drinkwater, B.W.: Ultraino: an open phased-array system for narrowband airborne ultrasound transmission. *IEEE Trans. Ultrason. Ferroelectr. Freq. Control* **65**(1), 102–111 (2018)
- Lee, J., Shung, K.K.: Radiation forces exerted on arbitrarily located sphere by acoustic tweezer. *J. Acoust. Soc. Am.* **120**(2), 1084–1094 (2006)
- Lee, J., Ha, K., Shung, K.K.: A theoretical study of the feasibility of acoustical tweezers: ray acoustics approach. *J. Acoust. Soc. Am.* **117**(5), 3273–3280 (2005)
- Kang, S.-T., Yeh, C.-K.: Potential-well model in acoustic tweezers. *IEEE Trans. Ultrason. Ferroelectr. Freq. Control* **57**(6) (2010)
- Dziewierz, J., Gachagan, A.: Correspondence: Computationally efficient solution of snell's law of refraction. *IEEE Trans. Ultrason. Ferroelectr. Freq. Control* **60**(6), 1256–1259 (2013)
- Yosioka, K., Kawasima, Y.: Acoustic radiation pressure on a compressible sphere. *Acta Acustica united with Acustica* **5**(3), 167–173 (1955)
- King, L.V.: On the acoustic radiation pressure on spheres. *Proc. R. Soc. Lond. A* **147**(861), 212–240 (1934)
- Bruus, H.: Acoustofluidics 7: The acoustic radiation force on small particles. *Lab Chip* **12**(6), 1014–1021 (2012)

Part III
Biomaterials and 3D Printing

Decellularization of Bovine Cancellous Bone for Bone Tissue Engineering Application

Nam Minh-phuong Tran[✉], Dat Tan Nguyen, Tin Dai Luong, Nghia Hieu Bui, Vo Van Toi, and Thi-Hiep Nguyen[✉]

Abstract

Cancellous bovine bone represents an inexhaustible source of material for bone tissue engineering. However, its natural marrow-filled structure can greatly limit the efficacy and prolong the duration of the decellularization procedure. Here this research formulates an efficient, shorten decellularization protocol for cancellous bovine bone with an initial delipidation step to improve the effect of following methods. The samples were then treated with a series of physical and chemical treatments including thermal shock and detergent wash. The samples acquired from this protocol have shown effective removal of cellular materials and fat while maintaining the essential bone extracellular matrix, which was confirmed through scanning electron microscopy observation and histological staining results. The decellularized bone showed potential to be further investigated, developed and combined with other material to create biocompatible scaffold for bone tissue engineering application.

Keywords

Decellularization • Bovine bone • Xenograft • Delipidation

1 Introduction

In many cases of bone loss due to diseases or injuries, adjunctive measures to fill the defect site and stimulate bone-healing are required. Thus, bone grafting is introduced and become an usual surgical procedure to serve these purposes [1, 2]. With roughly two million bone grafting performed worldwide every year [3], interest in finding the ideal material for the procedure is still continuously growing. An ideal bone graft needs to (1) replace the missing bone, (2) accelerate bone regeneration as an osteoconductive scaffold and (3) provide osteogenic and osteoinductive molecules [4].

Even though autograft is still considered the “gold standard” for bone grafting material, the use of xenogeneic bone for human bone reconstruction is rising with advancement in biomaterials research [5]. Cancellous bone, although lack of mechanical strength, is more osteogenic than cortical bone thanks to its porous structure and the large surface area [6]. Thus, materials derived from this type of bone are mostly preferred as a space filler where neo-osteogenesis is emphasized [7].

With an appropriate process to eliminate the risk of immunological and inflammatory host reactions, grafting made from xenogeneic cancellous bone promise an unlimited, accessible and inexpensive supply of material [8]. Among proposed procedure, decellularization, which aims to completely remove the cellular component of the native tissue, while preserving the original extracellular matrix (ECM) at most, is considered advantageous. Since the ECM and its osteoinductive molecules are maintained, decellularized bone would be more beneficial than synthesized bone graft in terms of osteoconduction and osteoinduction [9]. However, the native cancellous bone structure is filled with fat and red bone marrow. These obstructing substances might block the pathway of detergents used in the decellularization process and subside their effect. If these matters are not removed completely during the procedure, they form

Nam Minh-phuong Tran and Dat Tan Nguyen—Contributed equally.

N. M. Tran (✉) · D. T. Nguyen · T. D. Luong · N. H. Bui
V. Van Toi · T.-H. Nguyen
Department of Biomedical Engineering, International University,
Vietnam National University-Ho Chi Minh City (VNU-HCMC),
HCMC, 700000, Vietnam
e-mail: tmpnambme@gmail.com

T.-H. Nguyen
e-mail: nthiep@hcmiu.edu.vn

a barrier which limits cell invasion and reduce the osseointegration of the graft [10]. The risk of bone resorption and encapsulating fibrosis caused by triggered giant cells reaction is also present when fat remained in bone graft [11]. Thus, delipidation at the beginning of the decellularization procedure is essential to reduce the required amount of used chemicals and processing time as well as to yield an osseointegration material.

Therefore, this study conceived a combination of physical and chemical methods with an initial delipidation step using absolute ethanol to create an acellular scaffold for bone tissue engineering application. Morphological and histological analyses had been conducted to investigate the structural features of the material.

2 Materials and Methods

2.1 Materials

Fresh bovine femurs were collected from local slaughterhouse. The cylindrical bone blocks (thickness of 1 cm, diameter of 1 cm) were then harvested from the epiphysis and stored at -80°C until use.

Triton-X100 was purchased from Sigma (USA). Mayer's Hematoxylin solution and Eosin solution were bought from Sigma-Aldrich (USA). Absolute ethanol was obtained from Xilong Chemicals (China). All other chemicals used were analytic grade without further purification.

2.2 Methods

Cancellous bovine bone decellularization. The extracted bovine cancellous bones were processed as previously described in the literature with modification [12]. Decellularization of bovine bone blocks started with a wash in PBS. Then, the bones were immersed and shaken in absolute EtOH until the lipid was mostly removed. Then, four cycles of thermal shock, each comprising a step at 121°C for 20 min, followed by freezing in liquid nitrogen (-196°C) for 8 h, were carried out. During these passages, bone blocks were immersed in distilled water (DW); the solution was changed after every cycle. After the thermal shock cycle, the bone blocks were washed with the following procedure. Cellular debris was removed by washing bone blocks in 1% Triton X-100 for 8 h, followed by a second wash in 0.1% Triton X-100 for 16 h. Triton X-100 was dissolved in DW. To remove residual detergent, bone samples were washed in DW for 24 h. Finally, the samples were dehydrated by a graded ethanol series with 2 h for each step (50, 70, 96 and

100%) before being stored in vacuum oven at room temperature.

Scanning electron microscopy observation. The surface structure of the decellularized bone and native bone was examined using a scanning electron microscopy (SEM, JSM-IT100, JEOL, Japan). The bone was sputter-coated with gold. An accelerating voltage of 10 kV was used to acquire the SEM images.

Hematoxylin & Eosin and Masson's Trichrome staining. The decellularized bones were decalcified by immersed in 10% (v/v) acetic acid for 48 h. The decalcification solution is 5 times the volume of the bone specimens and it was changed after 24 h. After the decalcification was completed, the bones are rinsed in running tap water thoroughly for 2 h.

The samples were objected to serial sectioning of 4–6 μm thickness using a cryotome (ThermoFisher). The sections were stained with Hematoxylin and Eosin (H&E) and Masson's Trichrome stain before images of tissue sections were captured using an inverted microscope (Nikon, Japan).

3 Results and Discussion

3.1 Morphology Observation

After the combination of treatments, the decellularized bones were tested to examine the efficacy of the proposed protocol. As shown in Fig. 1, fat and red bone marrow located in the space between the cancellous bone structure had been removed to expose the porous morphology.

To further examine the surface of the processed samples, SEM images of the bones were captured at high magnification. Figure 2a, b showed the native bones at $5000\times$ and $1000\times$, respectively. The underneath bone structures were covered completely by a layer of fat. In contrast, the bare surface of decellularized bone can be seen clearly in Fig. 2c, d. The bone ECM (composed mainly of hydroxyapatite crystals and long collagen chains) and the lacuna (indicated by the arrows) were exposed as the lipid has been eliminated efficiently. Even though no bone cells were found, few unidentified debris were observed on the exterior of the bone in Fig. 2c. Overall, the results initially suggested that this protocol removed fat and cells, while preserving successfully the microscopic structure of the ECM as well as the organic components of the bone, which is critical to the osteoconductivity and osteoinductivity of the processed bone. Such result suggested that the use of absolute ethanol could be a convenient and accessible alternative delipidation treatment. The treatment also left no toxic residues in the graft and did not required expensive equipment.

Fig. 1 Images of bone blocks **a** before and **b** after decellularization

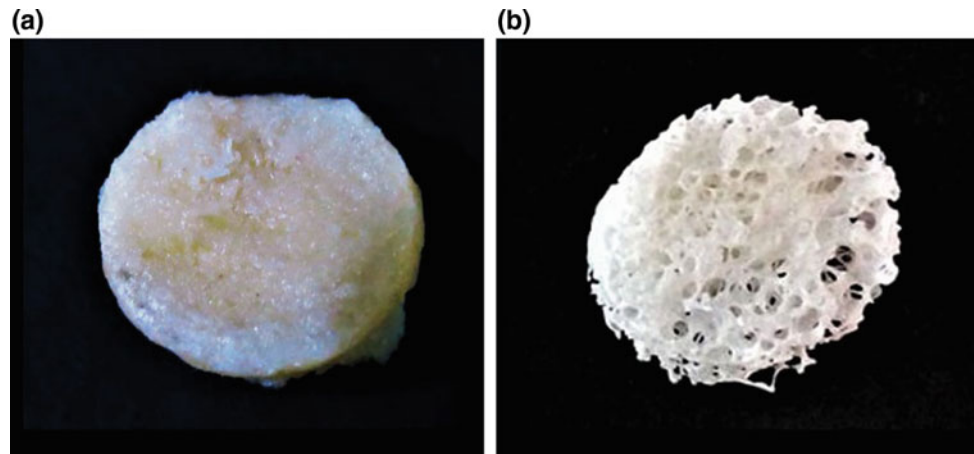
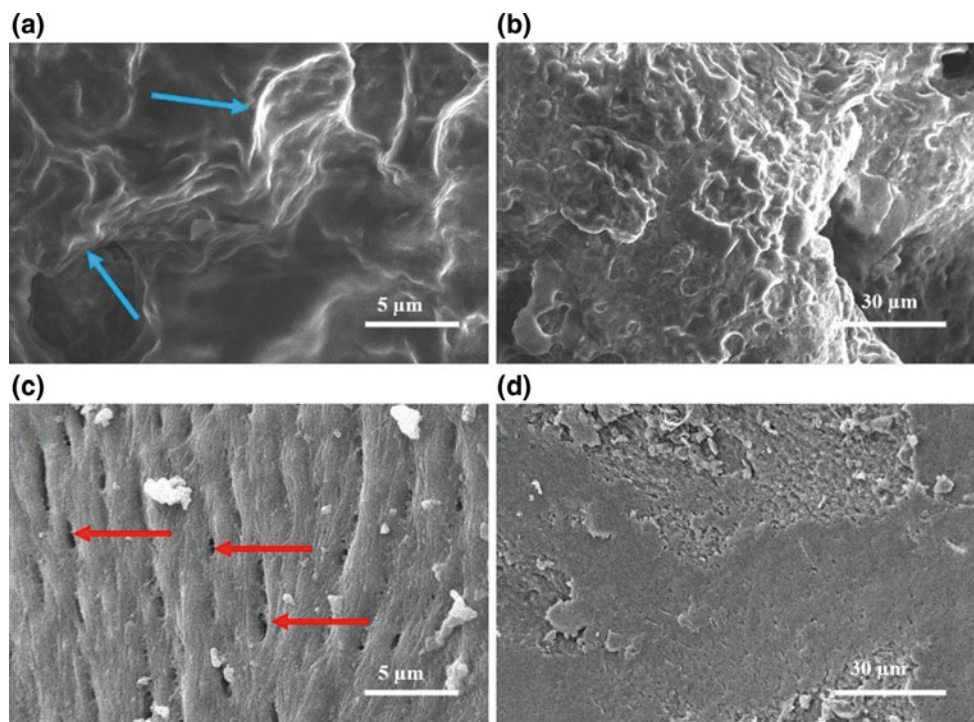


Fig. 2 SEM images of native bovine cancellous bone at **a** 5000 \times , **b** 1000 \times and decellularized bone at **c** 5000 \times , **d** 1000 \times



3.2 Histological Analysis

Histological staining was used to provide deeper evaluation of the decellularized bone. Both the Masson's Trichrome stained and H&E stained sections revealed normal, preserved bone ECM with well-observed lacunae. In addition, the lacunae (empty holes situated inside the bone structure) were found empty with no observable osteocyte inside as well as no detectable osteoblasts or osteoclast around the periphery

of the bones. The Masson's Trichrome section (Fig. 3a) also showed that the cytoplasm was eliminated as no red-hue region was seen while the collagen (blue stained) were kept well. As foreign cells and cellular materials are the main factors that trigger immune response in clinical application [13], this excellent removal is promising in terms of creating biocompatible material for bone substitute application. Also, the preserved ECM might provide an advantageous osteoconductivity and osteoinductivity to this material.

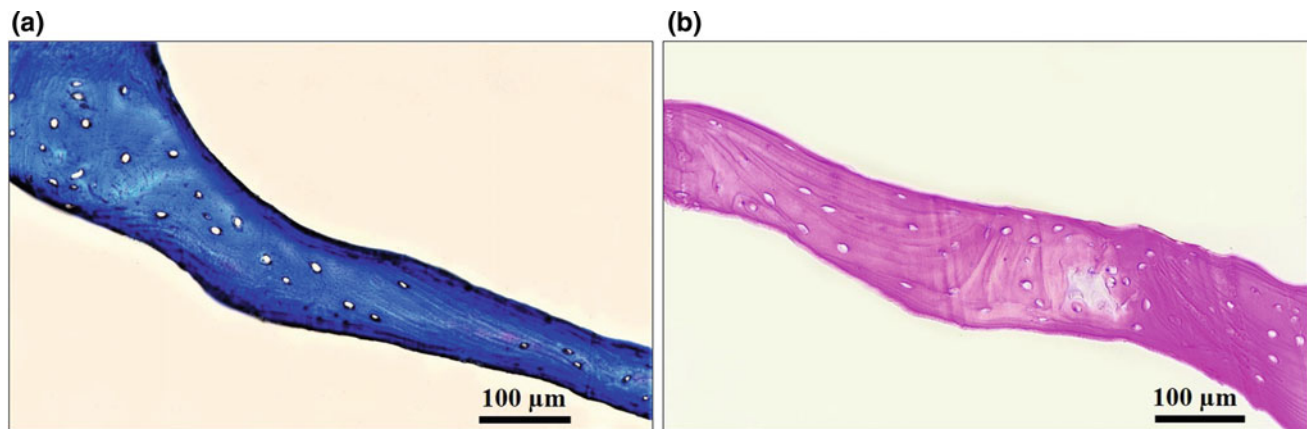


Fig. 3 Histological observation of decellularized bovine bone. **a** Masson's Trichrome staining; **b** H&E staining. The lacunae (white holes) were found empty with no visibly-stained nucleus of osteocytes

4 Conclusion

The study initially developed a bone substitute from bovine bone using multiple treatments including delipidation by ethanol, thermal shock cycles and detergent wash. The findings demonstrated high efficiency in terms of cellular materials removal and ECM preservation. Positive results suggested that ethanol would be an efficient, non-toxic and cost-effective defat reagent. Thus, the processed sample is appropriate for further investigations and developments to examine and enhance its biocompatibility *in vitro* and *in vivo* as well as its clinical practicability.

Acknowledgements This research is funded by International University, Vietnam National University Ho Chi Minh City under grant number: 03-BME-2017/HDSV-QLKH

Conflict of Interest The authors declare that they have no conflict of interest.

References

1. Thi Hiep, N., Chan Khon, H., Dai Hai, N., Byong-Taek, L., Van Toi, V., Thanh Hung, L.: Biocompatibility of PCL/PLGA-BCP porous scaffold for bone tissue engineering applications. *J. Biomater. Sci. Polym. Ed.* **28**(9), 864–878 (2017)
2. Nguyen, T.-H., Bao, T.Q., Park, I., Lee, B.-T.: A novel fibrous scaffold composed of electrospun porous poly (ϵ -caprolactone) fibers for bone tissue engineering. *J. Biomater. Appl.* **28**(4), 514–528 (2013)
3. Campana, V., Milano, G., Pagano, E., Barba, M., Cicione, C., Salonna, G., Lattanzi, W., Logroscino, G.: Bone substitutes in orthopaedic surgery: from basic science to clinical practice. *J. Mater. Sci. Mater. Med.* **25**(10), 2445–2461 (2014)
4. Nguyen, T.H., Lee, B.T.: *In vitro* and *in vivo* studies of rhBMP2-coated PS/PCL fibrous scaffolds for bone regeneration. *J. Biomed. Mater. Res. Part A* **101**(3), 797–808 (2013)
5. Zhang, N., Zhou, M., Zhang, Y., Wang, X., Ma, S., Dong, L., Yang, T., Ma, L., Li, B.: Porcine bone grafts defatted by lipase: efficacy of defatting and assessment of cytocompatibility. *Cell Tissue Banking* **15**(3), 357–367 (2014)
6. Khan, S.N., Cammisa Jr., F.P., Sandhu, H.S., Diwan, A.D., Girardi, F.P., Lane, J.M.: The biology of bone grafting. *JAAOS-J. Am. Acad. Orthop. Surg.* **13**(1), 77–86 (2005)
7. Elsalanty, M.E., Genecov, D.G.: Bone grafts in craniofacial surgery. *Craniofacial Trauma Reconstr.* **2**(03), 125–134 (2009)
8. Katz, J., Mukherjee, N., Cobb, R.R., Bursac, P., York-Ely, A.: Incorporation and immunogenicity of cleaned bovine bone in a sheep model. *J. Biomater. Appl.* **24**(2), 159–174 (2009)
9. Badylak, S.F., Taylor, D., Uygun, K.: Whole-organ tissue engineering: decellularization and recellularization of three-dimensional matrix scaffolds. *Annu. Rev. Biomed. Eng.* **13**, 27–53 (2011)
10. Chappard, D., Fressonnet, C., Genty, C., Baslé, M.-F., Rebel, A.: Fat in bone xenografts: importance of the purification procedures on cleanliness, wettability and biocompatibility. *Biomaterials* **14**(7), 507–512 (1993)
11. Moreau, M.F., Gallois, Y., Baslé, M.-F., Chappard, D.: Gamma irradiation of human bone allografts alters medullary lipids and releases toxic compounds for osteoblast-like cells. *Biomaterials* **21**(4), 369–376 (2000)
12. Gardin, C., Ricci, S., Ferroni, L., Guazzo, R., Sbricoli, L., De Benedictis, G., Finotti, L., Isola, M., Bressan, E., Zavan, B.: Decellularization and delipidation protocols of bovine bone and pericardium for bone grafting and guided bone regeneration procedures. *PLoS ONE* **10**(7), e0132344 (2015). <https://doi.org/10.1371/journal.pone.0132344>
13. Anderson, J.M., Rodriguez, A., Chang, D.T.: Foreign body reaction to biomaterials. In: *Seminars in Immunology*, vol. 2, pp. 86–100. Elsevier (2008)

Investigation of Biphasic Calcium Phosphate on Dentin Occlusion for Dentin Hypersensitivity Treatment

Nhi-Thao Ngoc Dang , Hien-Phuong Le, Vo Van Toi, and Thi-Hiep Nguyen 

Abstract

Dentin hypersensitivity, a common and painful dental condition, can be treated by the promotion of dentin tubule occlusion. The objective of this study is to evaluate tubule occlusion capacity of Biphasic calcium phosphate (BCP) with the available hydroxyapatite/ β -tricalcium phosphate (HA/ β -TCP) content ratios comprising of 80/20, 40/60 and 20/80. The experimental BCP samples were daily brushed on the demineralized bovine dentin for 7 days. Then, the dentin surface was observed by SEM. These results show that a decrease in the number of exposed dentin tubules varied according to different HA/ β -TCP ratios in BCP powders.

Keywords

Dentin hypersensitivity • Biphasic calcium phosphate • Demineralization

1 Introduction

Dentin, a calcified tissue, has a numerical density of tubules which are usually covered by enamel in the crown surface and by a thin layer of cementum in the root surface of the tooth [1]. In dental problems, the loss of these overlying layer by attrition, abrasion, erosion, or gingival recession increases the risks of several common dental diseases such as dentin hypersensitivity, a transient pain resulted from nerve ending activation by oral chemical, thermal tactile or osmotic stimuli when the dentinal surfaces were exposed [2, 3]. Therefore, blocking the open dentin orifices is one of the strategies for preventing irritant invasion, reducing dentin

tubule permeability, and subsequently preventing from other dental diseases like tooth decay and pulp inflammation [4]. It is preferable to develop biomimetic barriers by similar mineral components of dentin, calcium phosphates (CaP) substances, to infiltrate into the tubular orifices without irritating the pulp and provide tubule occlusion in dentin.

Among the CaP ceramics, hydroxyapatite (HA) and β -tricalcium phosphate (β -TCP) are both bioactive, non-toxic materials and frequently used in many medical and dental applications [5, 6]. HA with its chemical formula of $\text{Ca}_{10}(\text{PO}_4)_6(\text{OH})_2$ and Ca/P ratio of 1.67, is an abundant mineral component in hard tissues comprising 60–70% of bone and 98% of dental enamel [7, 8]. HA is the most stable phase in the body fluid, it provides mechanical bone strength and has bioactive property to form direct chemical bonding to native bone [9, 10]. About β -TCP, it possesses the chemical formula of $\beta\text{-Ca}_3(\text{PO}_4)_2$ and the Ca/P ratio of 1.52 [11]. In contrast with HA, β -TCP is a bioabsorbable material and permits bone ingrowth on their surface, into pores, channels, or pipes [12]. In clinical trials of dental health, the HA containing dentifrice was demonstrated its effectiveness in reducing dentin tubule occlusion [13] while the addition of functionalized TCP to a dentifrice enhances the ability of dentifrice fluoride in reducing dentine sensitivity [14]. Therefore, BCP in this study, which contains both HA and β -TCP, is considered to have a potential of occluding the exposed dentin tubules. Consequently, the purpose of this research was to evaluate tubule occlusion capacity of BCP with three available HA/ β -TCP ratios by using the fully demineralized bovine dentin models. BCP powders were topically applied to the bovine dentin specimens three times per day and the specimens then were examined with a scanning electron microscope (SEM) after 7 days.

N.-T. N. Dang (✉) · H.-P. Le · V. Van Toi · T.-H. Nguyen
Department of Biomedical Engineering, International University,
Vietnam National University-Ho Chi Minh City (VNU-HCMC),
HCMC, 700000, Vietnam
e-mail: dangntnhi@gmail.com

2 Materials and Methods

2.1 Materials

The calcium nitrate tetrahydrate [$\text{Ca}(\text{NO}_3)_2 \cdot 4\text{H}_2\text{O}$] (GuanghuaSci-tech, China) and diammonium phosphate [$(\text{NH}_4)_2\text{HPO}_4$] (GuanghuaSci-tech, China) were used as the starting materials. Sodium hydroxide (NaOH), sodium hypochlorite (NaOCl) and acid phosphoric (H_3PO_4) were purchased from GuanghuaSci-Tech Company (China).

2.2 Methods

BCP powders synthesis. Three BCP samples (BCP9, BCP7 and BCP6) with respective ratios of HA/ β -TCP (80/20, 40/60 and 20/80) were synthesized by following previous study [15]. Besides, the powder properties had been completely analyzed by X-Ray Diffraction (XRD) and Fourier Transform Infrared Spectroscopy (FT-IR) in that earlier study. In this research, the particle size and agglomeration of BCP particles were investigated by SEM (JEOL, JSM-IT100, Japan).

The preparation of bovine dentin specimens. The bovine incisors were obtained from a local slaughterhouse. Root segments of 15 mm in 1 mm-thick slices were prepared by a diamond disc. The dentin specimens were then immersed in a solution containing 37% H_3PO_4 for 2 min to mimic dentin hypersensitivity and remove the smear plugs. After that, they were rinsed in running water and sonicated for 15 min to eliminate the excess acidic. The distribution of dentin tubules and their size were observed by SEM observation.

Dentine specimens treated BCP. To evaluate tubule occlusion ability of different BCP samples, the treatment was performed by directly applying three synthesized BCP powders on the specimen surfaces in triplicate for each powder. These were mixed with distilled water to make

slurry and brushed over the surface using a spatula lab spoon for a minute and three times per day. The specimens were then rinsed in distilled water after each brushing session to remove weakly adsorbed materials and stored in a closed container containing artificial saliva (AS) which was refreshed every day. After a 7 day treatment, the specimens were examined for the tubule occlusion capacity by using SEM.

3 Results and Discussion

In Fig. 1, the SEM micrographs show the particle sizes of the synthesized BCP powders at the magnification of $\times 10,000$. Overall, the agglomeration of powder particles was observed in all BCP samples after calcination. The particle diameters of BCP9 ranged from 0.5 to 1.0 μm while those of BCP7 varied between 1.0 and 2.0 μm . BCP6 powders clearly had the highest degree of particle agglomeration with the diameters of clusters varying between 2.0 to 4.0 μm . It was, therefore, difficult to distinguish separate grain, and the size of BCP6 particles could not be estimated by SEM.

Figure 2 presents the SEM of the root canal dentin surface at coronal, middle, and apical levels at $\times 500$ of magnification. These results illustrated that debris and the smear layer were absent and dentin tubules were highly visible on dentin surface. During the root preparation by instrumentation, it was inevitable to form a smear layer composed dentin debris, organic materials and microorganisms on the dentin wall [16]. In this study, as the smear layer acted as a loosely adherent structure which temporarily blocked the dentin tubules and limited the penetration of CaP particles, it should be completely removed from the surface of the root canal wall. In terms of the diameters of dentin orifices at different levels, they ranged from 2.0 to 5.0 μm . The dentin tubules were oriented parallel to each other and radially from the

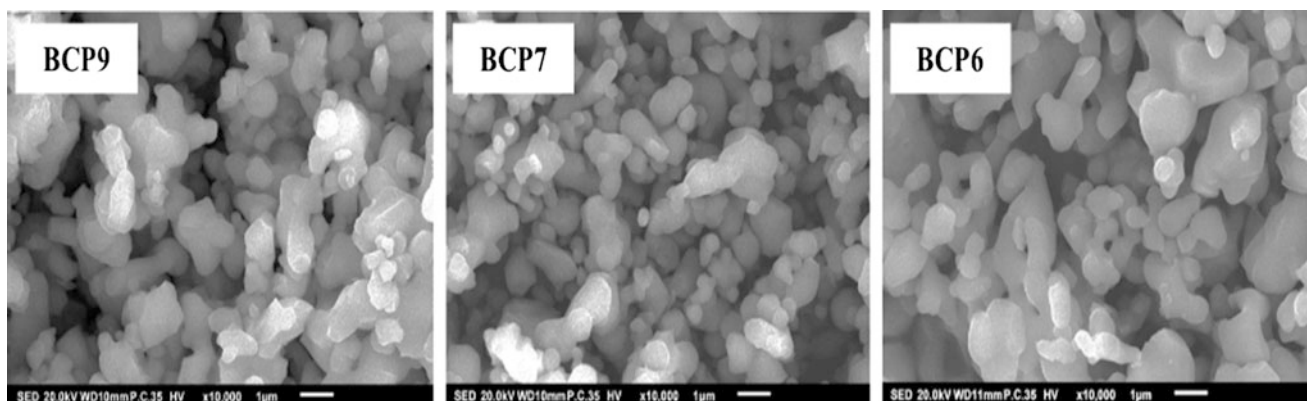


Fig. 1 SEM image of BCP particles at $\times 10,000$ of magnification

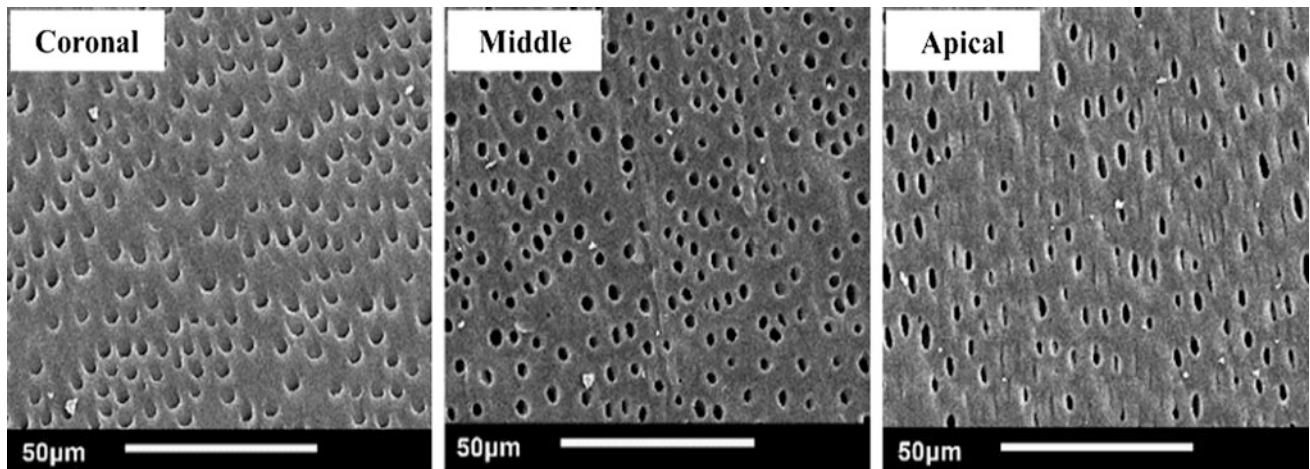


Fig. 2 The SEM of bovine dentin surface in coronal, middle, and apical position at $\times 500$ of magnification

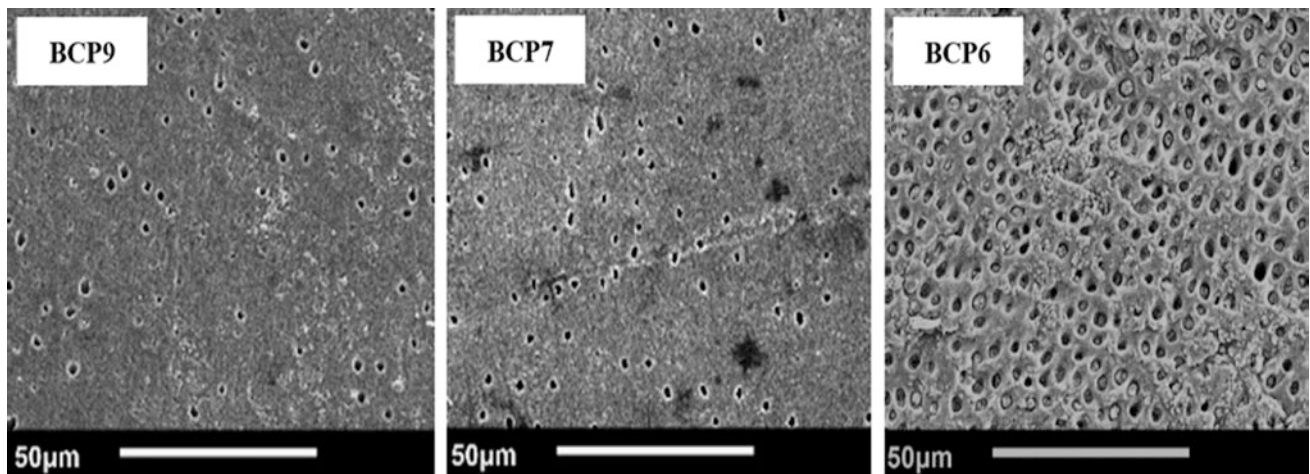


Fig. 3 SEM of the bovine dentine after BCP treatment for 7 days

pulp toward the dentin-enamel junction. Therefore, as observed in cross-section, the round orifices of tubules appeared in the middle and apical area while oblique ones were found on the fractured surface of coronal.

The dentin surfaces after 7 days of BCP treatment were illustrated in Fig. 3. SEM examination showed a decrease in the number of visible dentin orifices after BCP treatment, which confirmed that all BCP samples had the ability to promote the blocking of open tubules. To be more specific, the root surfaces treated with BCP6, containing the highest rate of β -TCP content, were still noticeably observed the almost peritubular dentin with the obvious infiltration of particles into the tubules, comparing to the others by BCP9 and BCP7. Besides, many prominent parts located between the two adjacent dentine tubules, the inter-tubular dentin, were still highly detected in specimens treated with BCP6 while the majority of those were partially disappeared in specimens treated with BCP9 and BCP7. It was, therefore,

induced that there formed a new mineral protective layers covering the dentin surfaces treated with BCP9 and BCP7, which contain 80/20 and 40/60 of HA/ β -TCP in turn. However, there have been required the further analysis to figure out the unique characteristics of blocking dentin tubule by these BCP samples.

In dentistry field, the regeneration of damaged enamel/dentin by HA containing in dentifrices to reduce hypersensitivity has been studied in the recent years. As the results, the present study showed that effective tubule occlusion by BCP powder containing 80% of HA in composition could have possibly occurred. However, a new outcome of the current research was the effect of BCP on occlusion of dentin tubules by the steady increase of β -TCP content rather than HA only. These results can serve as the primary evaluation that the extent of coverage onto or the degree of occlusion into the dentin tubules varied among the BCP samples with different ratios of HA/ β -TCP. This shows

the potential affinity and the enhancement new biological apatite of by the combination of HA and β -TCP particles as the dental repairing agents.

4 Conclusion

In conclusion, the ability of BCP for blocking dentinal tubules varied with different HA/ β -TCP. The SEM observations in 20/80 of HA/ β -TCP ratio (BCP6) clearly showed the particle infiltration into dentine tubule orifices while the surface micrographs of the specimens treated with 80/20 of HA/ β -TCP ratio (BCP9) and 40/60 of HA/ β -TCP ratio (BCP7) suggested a new crystalline layer firmly attaching to the root surface. This strategy may have prospective applications in dentistry as it offers an easy but effective method to compensate for the mineral loss by reconstructing tooth protective barrier. Further investigations should be conducted in order to evaluate the dental restoring capacity corresponding to HA/ β -TCP ratio.

Acknowledgements This research is funded by International University—VNUHCM under grant number T2017-03-BME.

Conflict of Interest The authors declare that they have no conflict of interest.

References

- Goldberg, M., et al.: Dentin: Structure, Composition and Mineralization: The role of dentin ECM in dentin formation and mineralization. *Front. Biosci.* **E3**, 711 (2011)
- Davari, A., Ataei, E., Assarzadeh, H.: Dentin hypersensitivity: etiology, diagnosis and treatment; a literature review. *J. Dent. (Shiraz, Iran)* **14**(3), 136–45 (2013)
- West, N.X., Lussi, A., Seong, J., Hellwig, E.: Dentin hypersensitivity: pain mechanisms and aetiology of exposed cervical dentin. *Clin. Oral Investig.* **17**(1), 9–19 (2013)
- Dentin, I.: A new method of treatment for dentin hypersensitivity precipitation of calcium phosphate in situ by Yohji IMAI and Takahiro AKIMOTO Institute for Medical and Dental Engineering. Tokyo Medical and Dental University, 2-3-10 Kanda. Received on July 26, 19, **9**(2), 167–172 (1990)
- Hiep, N.T., Khon, H.C., Hai, N.D., Taek, L.: Fabrication of PCL/PLGA-BCP porous scaffold for bone tissue engineering applications. *J. Biomater. Sci. Polym. Ed. Taylor & Francis engineering applications*, **5063**(March), 0–1 (2017)
- Jang, D.W., Nguyen, T.H., Sarkar, S. K., Lee, B.T.: Microwave sintering and in vitro study of defect-free stable porous multilayered HAp–ZrO₂ artificial bone scaffold. *Sci. Technol. Adv. Mater.* **13**(3) (2012)
- Palmer, L.C., et al.: Biomimetic systems for hydroxyapatite mineralization inspired by bone and enamel. *Chem. Rev.* **108** (11), 4754–4783 (2008)
- Kim, H., Camata, R.P., Vohra, Y.K., Lacefield, W.R.: Control of phase composition in hydroxyapatite/tetracalcium phosphate biphasic thin coatings for biomedical applications. *J. Mater. Sci. Mater. Med.* **16**(10), 961–966 (2005)
- Amera, A., et al.: Synthesis and characterization of porous biphasic calcium phosphate scaffold from different porogens for possible bone tissue engineering applications. **43**, 183–192 (2011)
- Manjubala, I., Sivakumar, M.: In-situ synthesis of biphasic calcium phosphate ceramics using microwave irradiation. *Mater. Chem. Phys.* **71**(3), 272–278 (2001)
- Rameshbabu, N., Rao, K.P.: Microwave synthesis, characterization and in-vitro evaluation of nanostructured biphasic calcium phosphates. *Curr. Appl. Phys.* **9**(1), S29–S31 (2009)
- Wagner, D.E., Jones, A.D., Zhou, H., Bhaduri, S.B.: Cytocompatibility evaluation of microwave sintered biphasic calcium phosphate scaffolds synthesized using pH control. *Mater. Sci. Eng. C* **33**(3), 1710–1719 (2013)
- Gopinath, N.M., et al.: Evaluation of dentifrice containing nano-hydroxyapatite for dentinal hypersensitivity: a randomized controlled trial. *J Int Oral Health: JIOH* **7**(8), 118 (2015)
- Naoum, S.J., et al.: Enhancing fluoride mediated dentine sensitivity relief through functionalised tricalcium phosphate activity. *Int. Scholarly Res. Not.* (2015)
- Ngoc, T.N.D., et al.: Preparation and characterization of nano-sized biphasic calcium phosphate (BCP) for demineralized dentin infiltration in hypersensitivity treatment. In: *International Conference on the Development of Biomedical Engineering in Vietnam*. Springer, Singapore (2017)
- Menezes, A.C.S.C.D., Zanet, C.G., Valera, M.C.: Smear layer removal capacity of disinfectant solutions used with and without EDTA for the irrigation of canals: a SEM study. *Pesquisa Odontológica Brasileira* **17**(4), 349–355 (2003)

Diatom Particles: A Promising Osteoinductive Agent of Silk Fibroin-Based Scaffold for Bone Regeneration

Thi Duy Hanh Le, Volha Liaudanskaya, Walter Bonani, Claudio Migliaresi, and Antonella Motta

Abstract

The regeneration of bone tissue via tissue engineering procedures is a challenging task that requires the selection of materials/scaffolds, with tailored biological and physical properties, and possibly the use of osteogenic additives that can stimulate cells to produce and mineralize collagen. Apart from growth factors, whose use is restricted by their high cost, inorganic compounds, such as calcium phosphates or silicates, have demonstrated intrinsic ability to facilitate the collagen mineralization and to address the differentiation of cells towards osteoblast lineage. Silicon, in particular, is considered to have a great relevance in the early stages of bone formation. In the past, we investigated the use of silk fibroin scaffolds, in form of sponges or gels, for bone tissue engineering. In this paper we have combined silk fibroin with diatoms, that are silica-based organisms, and we have evaluated the biological response of human mesenchymal stem cells (hMSCs) cultured on diatom loaded fibroin sponges. We found proofs of the improved osteogenic activity of the diatoms loaded scaffolds in the increase of alkaline phosphatase activity (ALP) and in the early fibronectin and collagen type I formation.

Keywords

Diatom particles • Osteoinduction • Bone loss • Bone regeneration

1 Introduction

Tissue engineering combines principles of engineering and life sciences to create tissue substitutes that can facilitate tissue regeneration and repair. Bone tissue engineering (BTE) field achieved a great success in the last decades, from complete repair of non-union bone fractures to the recovery of bone mass in the case of large-size bone defects. In order to facilitate bone regeneration, BTE relies on three main components, including scaffold, cells and bioactive factors [1]. In the last decades, a large attention was paid to the development of ideal materials for bone repair with osteoconductive and osteoinductive potential, in order to support cells differentiation and bone tissue growth [2, 3].

Silk fibroin was shown to be an excellent candidate for BTE applications due to its biocompatibility, biodegradability, tunable mechanical properties, and osteoconductive characteristics [4, 5]. However, silk alone did not show osteoinductive properties that are crucial for bone regrowth [6]. So, inorganic fillers, such as silicate nanoclay, hydroxyapatite, calcium phosphate [7], and biomaterials containing silica can be used as additives to improve SF osteoinductive properties [8]. In the previous study, we demonstrated that the incorporation of diatom particles, as a source of silica, into SF scaffold improves both bioactivity and early bone specific markers expression of human osteosarcoma cell lines MG-63 [9]; however, the effect of composite silk/diatom particles scaffolds on the bioactivity of osteoprogenitor cells has never been studied.

For bone graft application, the induction of osteogenesis is considered as a critical point for a successful bone healing process [10]. Hence, the aim of this study was to investigate osteoinductive properties of the composite silk/diatom

T. D. H. Le (✉)

Department of Chemical Technology, Ho Chi Minh City of Technology and Education, Ho Chi Minh City, Viet Nam
e-mail: duyhanhle@hcmute.edu.vn

T. D. H. Le · V. Liaudanskaya · W. Bonani · C. Migliaresi
A. Motta

Department of Industrial Engineering, BIOTech Research Center and European Institute of Excellence on Tissue Engineering and Regenerative Medicine, University of Trento, Trento, Italy

V. Liaudanskaya

Presently at Department of Biomedical Engineering, Tufts University, Medford, MA, USA

particles scaffolds. Here scaffold systems were studied with human mesenchymal stem cells (hMSC); moreover, scaffold osteoinductive ability were assessed through fibronectin, collagen type I and ALP markers expression.

2 Materials and Methods

2.1 Materials and Scaffold Fabrication

Reagents including phosphate buffer solution (PBS), sodium hydroxide (NaOH), hydrochloric acid (HCl), lithium bromide (LiBr), Triton X-100, sodium chloride (NaCl), formalin, bovine serum albumin (BSA), 4-6 diamidino-2-phenylindole, dilactate (DAPI), polyethylene glycol (PEG) and ethanol were purchased from Sigma-Aldrich (St. Louis, MO, USA).

Diatom particles, including both diatom microparticles (DMPs) and diatom nanoparticles (DNPs), were obtained following Le et al. [11]. Silk fibroin solution and scaffold fabrication have been prepared following Le et al. [9]. In this work, two groups of porous scaffolds were fabricated by solvent casting-particulate leaching method, as described in reference Le et al. [9]. Names and compositions of the scaffolds were given in Table 1.

After fabrication, scaffolds were cut into cylinders 2×6 mm of height versus diameter, and autoclaved at 1 bar, 121 °C for 45 min before use.

2.2 In Vitro Experiment

Human mesenchymal stem cells (hMSCs) were subcultured in 175 mm² culture flask coated with collagen in Dulbecco's Modified Eagle Medium (DMEM) supplemented with 20% of fetal bovine serum (FBS) and 1% of penicillin/Streptomycin (P/S). The cells were then incubated at 37 °C with 5% CO₂ until cells reached around 80% of confluency. Medium was changed every three days.

Scaffolds were fully immersed in the medium for 30 min and then dried into hood for 1.5 h before seeding cells. Subsequently, scaffolds were placed into a 48-well-plate and aliquots of media (30 µl) containing 10⁵ cells were seeded on the top of each scaffold with the addition of 400 µl of medium. Seeded scaffolds were transferred into a new plate

after 24 h of incubation and added the medium. Medium was replaced every 3 days until the testing points.

Cell proliferation

Cell proliferation in the seeded scaffolds was determined with DNA quantification by using Quant-iTPicoGreen® dsDNA Assay Kit (Invitrogen, Molecular Probes, Oregon, USA). At selected time points, scaffolds were washed in PBS and then total DNA content was collected with 0.5 ml of Triton-X 0.05%. All the DNA samples were stored at -20 °C before quantification. Prior assay, all samples were thawed at room temperature (RT) and sonicated for 20 s. Afterwards PicoGreen was used to quantify DNA content measured in 96-well black plates with a fluorescent plate reader (Safire, Tecan, Austria). To calculate DNA concentration, a calibration curve was built up by using the DNA standard provided with the kit to correlate with the studied samples.

Immunocytochemistry

Immunocytochemistry against fibronectin and collagen I were used to evaluate the capacity of hMSCs differentiation. Seeded scaffolds were collected at every tested time points. The scaffolds were washed with PBS (without Ca²⁺ and Mg²⁺) and then fixed with 4% of formalin for 30 min at room temperature (RT). Subsequently, the samples were incubated in blocking and permeabilizing buffer containing 1% of BSA and 0.3% of Triton-X in PBS for 1 h at RT, then stained with the diluted primary antibody against collagen type I (1:200, Meridian Life Science, Saco, ME, USA) and fibronectin (ab23751—abcam, Cambridge, UK) overnight at 4 °C. After washing with PBS, the samples were incubated with secondary antibodies (1: 500, anti-rabbit Alexa Fluor 568, Molecular Probes, Grand Island, NY) for both fibronectin and collagen type I for 1 h. The stained scaffolds were washed again in PBS. Afterwards, the samples were incubated with DAPI solution (1:1000) for 10 min at RT. After final rinses with PBS, samples were visualized with the confocal microscope (A1, Nikon Instruments, Amsterdam, the Netherlands).

Alkaline phosphatase quantification

The alkaline phosphatase (ALP) activity was measured on the cell lysates. At each time point, cell culture medium was removed, followed by washing with PBS. Then, 500 µl of Triton X—0.05% was added into per well and incubated for 30 min at RT. Samples were frozen at -20 °C. Before measurement, samples were thawed and sonicated on ice for 20 s with a Virsonic ultrasonic cell disrupter (Virtis,

Table 1 Type and content of porous scaffold

Scaffold name	DNPs, %wt.	DMPs, %wt.
SF	0	0
SF-(N+M)3.2	1.6	1.6

Warminster, PA). The ALP activity was tested following the manufacturer's instructions (ab83371 ALP assay Fluorometric, Cambridge, UK). Fluorescence intensity was measured with a Tecan (Austria) microplate reader.

Statistical analysis

All *in vitro* assays were performed on three biological replicates with triple technical replicates. Data are expressed as mean \pm standard error. To determine the statistical significant difference among two scaffold groups, Two Way of variance (ANOVA, origin Pro 8.5.1) was used. A significance was defined at *p* value less than 0.05.

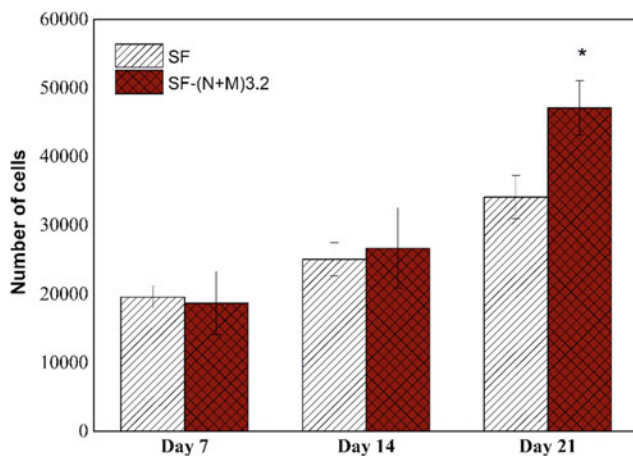


Fig. 1 Cell proliferation up to 21 days of culture of two scaffold groups: pure silk fibroin (SF) and SF-(N+M)3.2 silk fibroin loading 3.2% of diatom particles *: *p* < 0.05

3 Results and Discussion

3.1 Cell Proliferation

Proliferation of human mesenchymal stem cells presents in Fig. 1. No difference in hMSCs proliferation was observed during the first 14 days between SF-(N+M)3.2 scaffolds and control group. Generally, small increase in cell number was detected for both groups; however, by 21 day of growth, proliferation rate of hMSCs in composite scaffolds was significantly higher compared to the control group (pure silk fibroin).

An increased growth rate of hMSCs in SF-(N+M)3.2 scaffolds can be explained by the effect of silicon released from composite scaffolds in media, as previous literature reported [12].

3.2 Immunocytochemistry

Fibronectin

Fibronectin is one of the proteins that composes extracellular matrix (ECM) together with collagen, elastin and laminin. Fibronectin is considered to be the key factor inducing bone cell differentiation and one of the earliest proteins synthesized by osteoblasts [13].

Figure 2 summarizes FN production in both SF-(N+M)3.2 and the control groups. At day7 SF-(N+M)3.2 group showed significantly higher expression of fibronectin comparing to the control group. By third week of cell

Fig. 2 Fibronectin (green) synthesized: after day 7, 14 and 21 of hMSCs culture and DAPI for nuclei (blue) of SF-silk fibroin, and SF-(N+M)3.2—silk fibroin loading 3.2% of diatom particles (scale bar = 50 μ m)

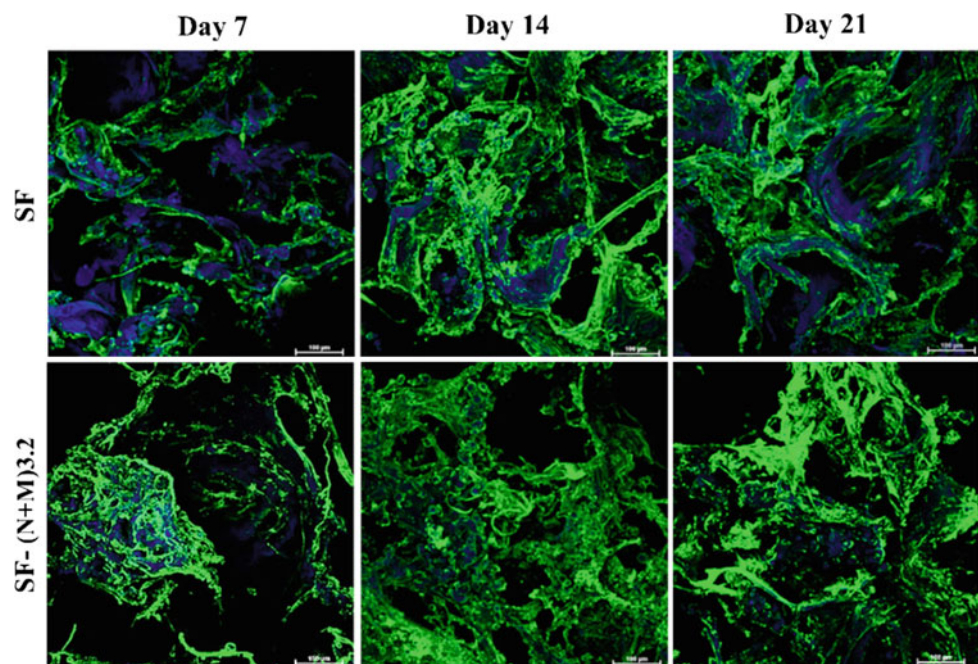
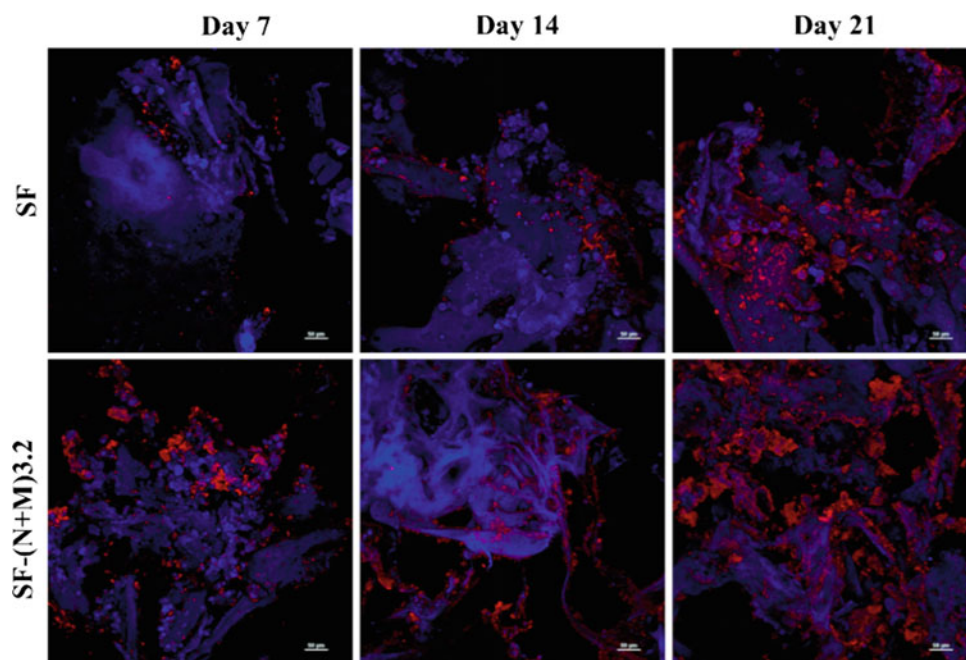


Fig. 3 Confocal scanning laser microscopy images of collagen type I (red) observation of hMSCs culture after day 7, 14 and 21 of incubation and DAPI for nuclei (blue): SF—pure silk fibroin, and SF-(N+M)3.2—silk fibroin loading 3.2% of diatom particle (scale bar = 50 μ m)



growth, significant increase in FN expression was observed in both groups. Differences of FN in two scaffold groups seemed to flatten at day 14 as well as day 21 of culture.

Early FN expression may enhance ECM proteins expression and deposition by hMSCs culture in silk/diatom particles scaffold; eventually, supporting osteogenic commitment of hMSCs [14]. The presence of insoluble FN may facilitate physiological processes of bone healing including angiogenesis, thrombosis and inflammation [15].

Collagen type 1

Type I collagen is a major component of bone ECM, accounting for 80% of total bone protein content. Type I collagen is also an important bone marker due to involvement in many critical processes for healthy bone development and functionality [16].

The obtained results (Fig. 3) showed a general increase of collagen I synthesis in both groups; however, SF-(N+M)3.2 group presented significantly higher level of collagen type I secretion at all experimental time points.

As already demonstrated by previous studies, the increase of fibronectin and collagen type I synthesis can explain the osteogenic commitment of hMSCs⁸.

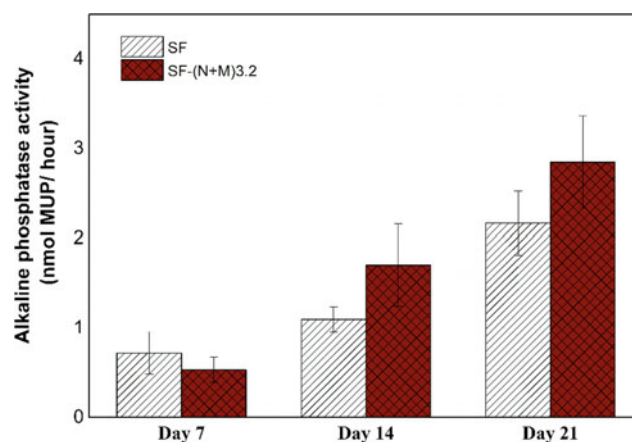


Fig. 4 Alkaline phosphatase activity induced by hMSCs seeded into pure silk fibroin (SF) and silk fibroin loading 3.2% of diatom particles (SF-(N+M)3.2) up to 21 days

3.3 Alkaline Phosphatase Quantification

Alkaline phosphatase (ALP) plays an important role on osteogenesis, and commonly used to predict bone maturation and mineralization in *in vitro* studies [15].

ALP production steadily upregulated during experimental time points of cell growth (Fig. 4). As anticipated, the

amount of ALP produced in the composite scaffold was generally higher than in the control group (silk only scaffold) after three weeks of culture; however, no statistical significance was observed.

We hypothesize that the release of silicon from DPs dissolution may contribute to the ALP production, as the previous reported in the case of osteoblasts [17].

4 Conclusion

This pilot study demonstrated that the silk fibroin loaded with diatom particles could be used as osteogenic enhancer for hMSCs differentiation. Increased early production of fibronectin and collagen type I together with elevated ALP production in composite scaffolds supported the original hypothesis of silica critical contribution to osteogenic differentiation.

The conducted study could provide early evidence for diatom particles application as promising osteoinductive additives for bone healing.

Acknowledgements The authors would like thank Erasmus Mundus - One More Step project for financial support.

Conflict of Interest Statements The authors declare that there is no conflict of interest.

References

1. Khan, W. S., Rayan, F., Dhinsa, B. S., Marsh, D.: An osteoconductive, osteoinductive, and osteogenic tissue-engineered product for trauma and orthopaedic surgery: how far are we? *Stem Cells Int.* **2012** (2012)
2. Dimitriou, R., Jones, E., McGonagle, D., Giannoudis, P.V.: Bone regeneration: current concepts and future directions. *BMC Med.* **9**, 66 (2011)
3. Stevens, M.M.: Biomaterials for bone tissue engineering. *Mater. Today* **11**, 18–25 (2008)
4. Mandal, B.B., Kundu, S.C.: Cell proliferation and migration in silk fibroin 3D scaffolds. *Biomaterials* **30**, 2956–2965 (2009)
5. Elliott, W.H., et al.: Silk hydrogels of tunable structure and viscoelastic properties using different chronological orders of genipin and physical cross-linking. *ACS Appl. Mater. Interfaces.* **7**, 12099–12108 (2015)
6. Kim, J.H., et al.: Osteoinductive silk fibroin/titanium dioxide/hydroxyapatite hybrid scaffold for bone tissue engineering. *Int. J. Biol. Macromol.* **82**, 160–167 (2016)
7. Gaharwar, A.K., et al.: Bioactive silicate nanoplatelets for osteogenic differentiation of human mesenchymal stem cells. *Adv. Mater.* **25**, 3329–3336 (2013)
8. Reffitt, D.M., et al.: Orthosilicic acid stimulates collagen type I synthesis and osteoblastic differentiation in human osteoblast-like cells in vitro. *Bone* **32**, 127–135 (2003)
9. Le, T.D.H., Liaudanskaya, V., Bonani, W., Migliaresi, C., Motta, A.: Enhancing bioactive properties of silk fibroin with diatom particles for bone tissue engineering applications. *J. Tissue Eng. Regen. Med.* **12**, 89–97 (2018)
10. Albrektsson, T., Johansson, C.: Osteoinduction, osteoconduction and osseointegration. *Eur. Spine J.* **10**, 96–101 (2001)
11. Le, T.D.H., et al.: Processing and characterization of diatom nanoparticles and microparticles as potential source of silicon for bone tissue engineering. *Mater. Sci. Eng. C* **59**, 471–479 (2016)
12. Reis, S., Castro, A., Fernandes, M.H.: Bone anabolic effects of soluble Si : in vitro studies with human mesenchymal stem cells and CD14 + Osteoclast Precursors (2015)
13. Weiss, R.E., Reddi, A.H.: Appearance of fibronectin during the differentiation of cartilage, bone, and bone marrow. *J. Cell Biol.* **88**, 630–636 (1981)
14. Di Benedetto, A., et al.: Osteogenic differentiation of mesenchymal stem cells from dental bud: Role of integrins and cadherins. *Stem Cell Res.* **15**, 618–628 (2015)
15. Prins, H.-J., et al.: In vitro induction of alkaline phosphatase levels predicts in vivo bone forming capacity of human bone marrow stromal cells. *Stem Cell Res.* **12**, 428–440 (2014)
16. Niyibizi, C., Eyre, D.R.: Structural characteristics of cross-linking sites in type V collagen of bone. Chain specificities and heterotypic links to type I collagen. *Eur. J. Biochem.* **224**, 943–950 (1994)
17. Kim, E.-J., Bu, S.-Y., Sung, M.-K., Choi, M.-K.: Effects of Silicon on Osteoblast Activity and Bone Mineralization of MC3T3-E1 Cells. *Biol. Trace Elem. Res.* **152**, 105–112 (2013)

The Use of 3D Printed Microporous-Strut Polycaprolactone Scaffolds for Targeted Local Delivery of Chemotherapeutic Agent for Breast Cancer Application

Hoang Phuc Dang, Dietmar W. Hutmacher, and Phong A. Tran

Abstract

Local recurrent cancer remains a challenge for breast cancer patients receiving implants after mastectomy or lumpectomy. The use of radiotherapy and/or systemic administration of chemotherapeutic agents post-surgery can be beneficial yet they also kill healthy cells and introduce systemic side effects. In this study, a new method was introduced to utilize 3D printed microporous polycaprolactone (PCL) scaffolds as a multifunctional device—an implant and a drug delivery vehicle for targeted local delivery. Their microporous structure was characterized by scanning electron microscopy (SEM) and atomic force microscopy (AFM). The dependence of release profiles of Doxorubicin (DOX) loaded scaffolds on pH and ionic strength of the environment was demonstrated. Lastly, their chemotherapeutic effect was characterized by *in vitro*. Overall, the results demonstrated the utility of the microporosity and surface charge of PCL scaffolds to immobilize DOX for local, targeted drug delivery.

Keywords

Local delivery • Doxorubicin • Breast cancer • 3D printing • FDM

1 Introduction

The concept of drug encapsulation in polymer system has been developed for long time with the initial use of microsphere or polymer conjugating combined with local injection [1, 2]. Other methods include DOX loaded silk film [3] and modified hydrogels for pH and photo triggered release [4]. Though the results are promising, the systems are only limited to simple structure and the use of patient-customized scaffolds in drug delivery is mainly for bone regeneration [5]. 3D printed scaffolds if can be used as a breast implant and a local delivery method will give breast cancer patients a better choice to regain their body images and prevent recurrent cancer.

In this study, a new method was proposed to fabricate 3D scaffold with microporous struts for both breast reconstruction and chemotherapy drug delivery. The scaffolds were characterized by SEM and AFM. DOX loaded scaffolds were used to study the release profile in different pH and ionic strength conditions. Lastly, chemotherapeutic effect of DOX loaded scaffolds was evaluated *in vitro*.

2 Methodology

2.1 Scaffold Fabrication and Surface Characterization

PCL (PURASORB® PC12) was mixed with porogen (38- μm PBS particles) in chloroform at the weight ratio of 5:0 (nonporous, nPCL) and 5:4 (microporous, pPCL), casted into films, dried out at room temperature, fed into a Dual BioExtruder and printed at 100 °C with 6 layers of 40 × 40 mm², bar diameter of 0.3 mm, bar distance of 1 mm and 0–90° orientation. The porogen was leached in NaOH 0.01 M for 14 days.

Surface and liquid nitrogen fractured crosssection of PCL scaffolds were gold coated, imaged using a Zeiss FESEM

H. P. Dang (✉) · D. W. Hutmacher · P. A. Tran
ARC Centre in Additive Biomaterials, Queensland
University of Technology, Brisbane, Australia
e-mail: hoangphuc.dang@hdr.qut.edu.au

D. W. Hutmacher
e-mail: dietmar.hutmacher@qut.edu.au

P. A. Tran
e-mail: phong.tran@qut.edu.au

H. P. Dang · D. W. Hutmacher · P. A. Tran
Queensland University of Technology (QUT), Brisbane,
Queensland, Australia

(Zeiss, Germany) and analyzed using ImageJ (NIH, US). Surface roughness of struts was characterized scanning areas of $20 \times 20 \mu\text{m}^2$ using a NT-MDT Solver SPM apparatus with Ted Pella Tap300-G cantilevers (US).

2.2 Drug Loading and Release

$2 \times 1 \times 1.5 \text{ mm}^3$ scaffolds were sterilized by ethanol 70% in Eppendorf tubes, immersed in DOX (doxorubicin hydrochloride, Sigma-Aldrich, US) solutions according to 2 doses: 0.4 and 2 μg DOX/mg PCL (low dose (LD) and high dose (HD), respectively) and left dried out overnight. DOX loaded scaffolds were transferred to new tubes and the drug lost amounts in the previous tubes were dissolved by methanol 60% for measurement at 480 nm using an xMark microplate absorbance spectrophotometer (Bio-Rad, US). Drug loading efficacy was calculated following Eq. (1), where E is loading efficacy, I is initial drug amount and L is drug lost amount.

$$E(\%) = \frac{I - L}{I} \times 100\% \quad (1)$$

DOX loaded scaffolds were imaged using a Nikon SMZ25 stereomicroscope (Japan) and their crosssection were imaged using a Leica TCS SP5 confocal fluorescent microscope (US). Their release profiles in PBS solution with pH 7.4 and 5.5 and simulated body fluid (SBF) solution with pH 7.4 were performed at 37 °C in shaking incubator at 200 rpm. The solutions were completely collected (200 μL) and refreshed at each timepoint. The collected solutions were measured as previously described.

2.3 In Vitro Cell Proliferation Assay

MDA-MB-231 cells were seeded in 24-well plate at 15×10^3 cells/well and cultured in DMEM supplemented with 10% FBS and 1% penicillin/streptomycin overnight. Samples were placed into each well containing cells and 1 mL of fresh full culture media and incubated at 37 °C for 2 days. Then the culture medium and scaffolds were removed and the plates were frozen at $-80 \text{ }^\circ\text{C}$ for 48 h. After that, proteinase K was added (300 μL /well) and cultured overnight at 37 °C. Then, the cell-proteinase suspensions were transferred into Eppendorf tubes and incubated at 56 °C for 8 h. The samples were then diluted in PBE buffer and transferred into black 96-well plates. picogreen 1X (Sigma-Aldrich, US) was added at 1:1 volume ratio, the plates were wrapped with aluminum foil and incubated for 10 min at room temperature before reading using a POLARstar Optima plate-reader (BMG Labtech, Germany) at excitation and emission wavelengths of 480 and 520 nm, respectively.

3 Results

3.1 Scaffold Fabrication and Surface Characterization

SEM micrographs confirmed complete leach out of porogen. The Results showed surfaces of pPCL had similar porosity, yet with smaller pores than that of nPCL (Fig. 1a). pPCL pores was produced from empty space of leached porogen whereas pores on surface of nPCL were produced from the arrangement of PCL grains. In pPCL, the crosssection porosity ($16.0 \pm 1.2\%$) was more than 10 times higher than that of the surface ($1.3 \pm 1.1\%$), of which 63% of pores were less than 200 μm^2 and few pores with area larger than 500 μm^2 due to porogen aggregation (Fig. 1b). AFM results showed similar root-mean-square (RMS) surface roughness between 2 groups (Fig. 1c).

3.2 Drug Loading and Release

The results of drug loading efficacy showed microporous structure significantly increased the efficacy from $86 \pm 2\%$ to $97 \pm 1\%$. Stereomicroscopy images illustrated DOX was distributed evenly in both nPCL and pPCL scaffolds (Fig. 2a). Besides, confocal images indicated the even distribution of DOX on the surface of bars of nPCL scaffolds whereas in pPCL scaffolds, DOX was also distributed on surface and into the inner porous structure of pPCL struts (Fig. 2b).

The effects of pH and ionic strength on the release profile of DOX were characterized. Results after 2 weeks indicated pH had stronger effect on release profile of pPCL than that of nPCL (Fig. 3a). In pPCL group, the release amount was significantly increased when the pH decrease in all doses. For nPCL, they also showed the same trend of increasing in the amount released when the pH decreased, however the increase was much lower as compared to pPCL.

About burst release properties, thanks to the microporous structure, the burst releases of pPCL were minimized and significantly lower than that of nPCL. Besides reducing burst release, microporous structure also gave sustain release profile for pPCL. After burst release, pPCL was sustainably release until day 5 and then started to significantly slow down; whereas, nPCL only showed the small increase in the first 3 days and then significantly dropped in the releasing rate.

Then, the drug release results in different ionic strength conditions indicated the stronger the ionic strength, which mean higher ion concentration, the higher the release amount of DOX from scaffolds (Fig. 3b). After 14 days, there was a significant increase in the amount released in SBF as

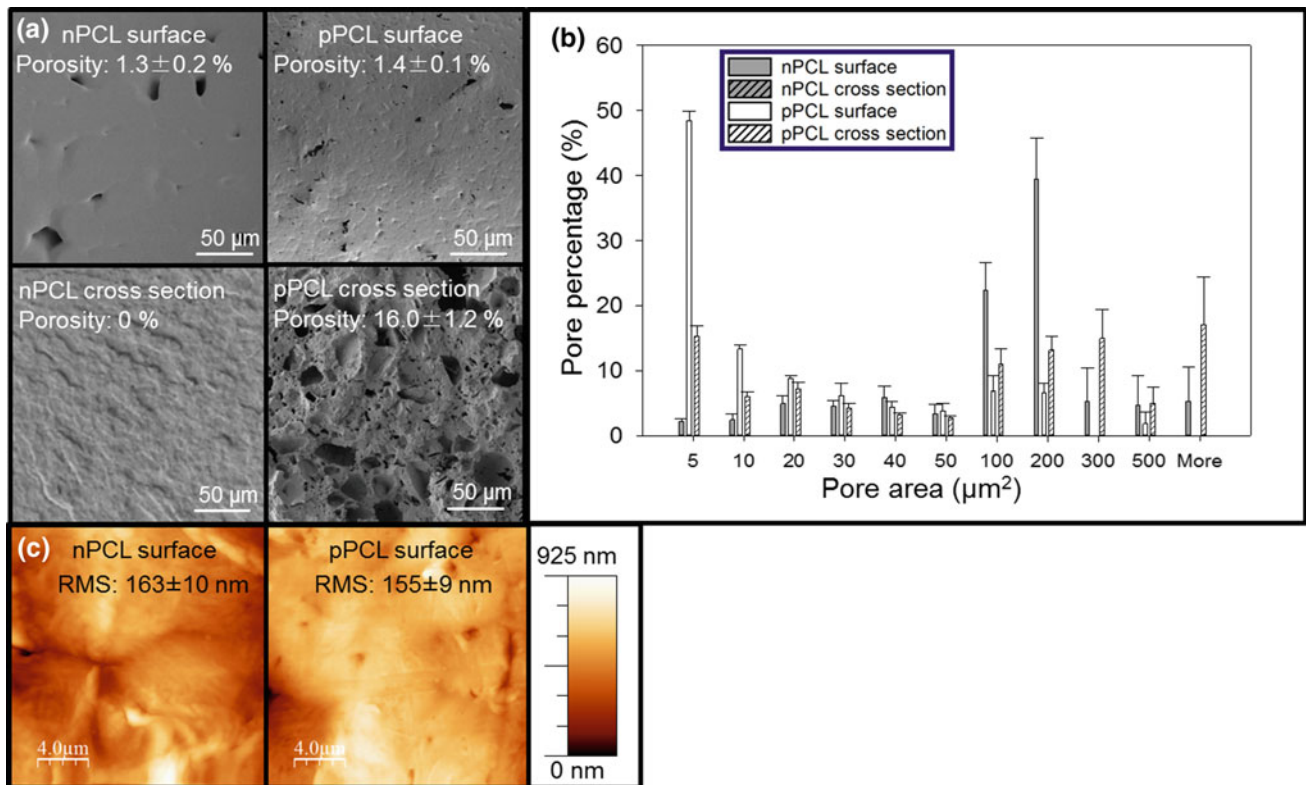
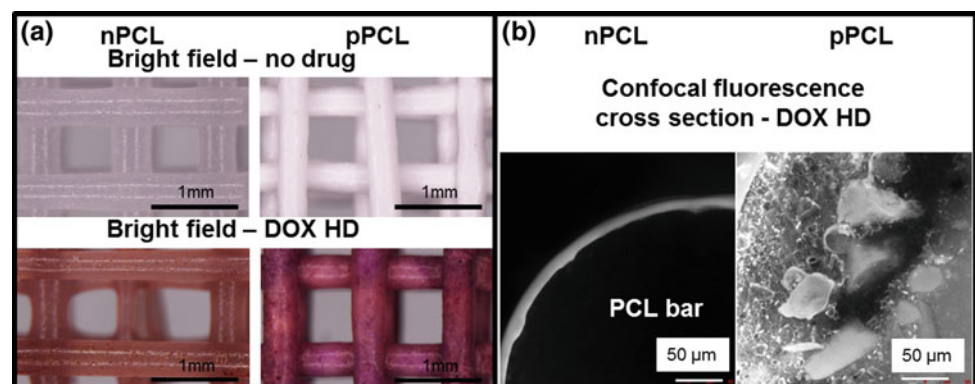


Fig. 1 a SEM micrographs of surface and cross-section of nPCL and pPCL struts and their porosity b Pore size distribution of surface and cross-section of nPCL and pPCL analyzed using image processing

software imageJ c Data are expressed as mean ± SEM (n = 8). AFM micrographs of nPCL and pPCL surfaces and their RMS surface roughness (RMS). Data are expressed as mean ± SEM (n = 6)

Fig. 2 a Bright field images of nPCL and pPCL with/without DOX loading and b fluorescence images of nPCL and pPCL loaded with DOX



compared to that of PBS solution. Comparing the burst release, pPCL showed lower burst release as compared with nPCL. Last but not least, SBF strongly enhance the sustainable release of pPCL from 5 days in PBS up to 14 days. All in all, it can be said that the porous structure helped reduced the burst release and increase the sustainability for PCL scaffolds and low pH and high ionic strength could enhance the release of DOX.

3.3 In Vitro Cell Proliferation Assay

The results from PicoGreen DNA quantification showed a strong dependence of cell proliferation on DOX concentration (Fig. 4). As DOX concentration increased, DNA amount per μg DOX significantly decreased. Compared between nPCL and pPCL, PicoGreen results showed DOX loaded pPCL still maintained chemotherapeutic effect

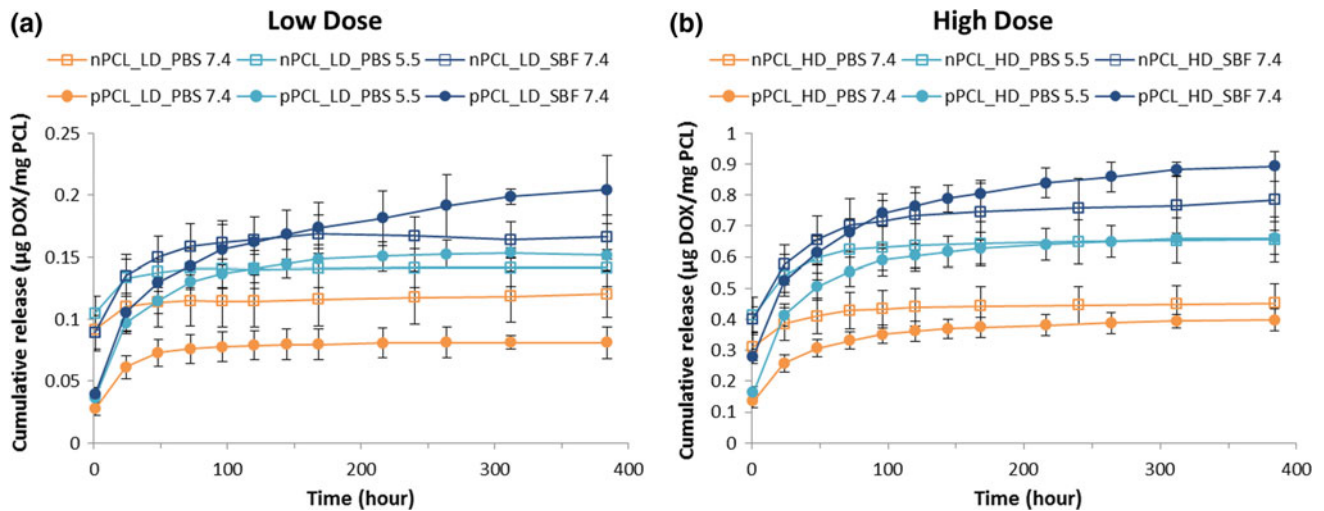


Fig. 3 Drug release of DOX loaded scaffolds in PBS pH 7.4, pH 5.5 and SBF pH7.4. Data are expressed as mean \pm SEM (n = 6)

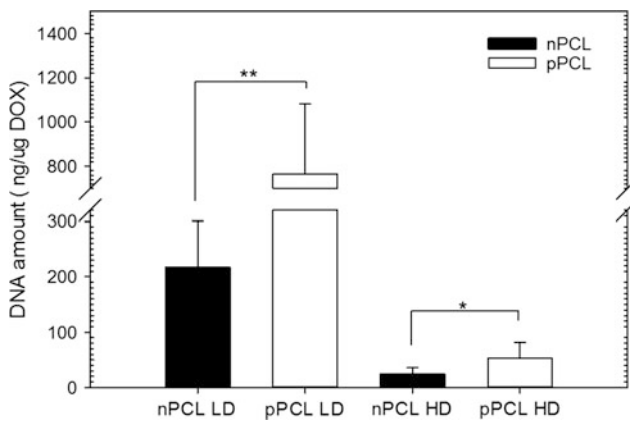


Fig. 4 PicoGreen results. DNA amount of MDA-MB-231 cells cultured with PCL construct with and DOX for 2. Data = mean \pm SEM (n = 4). * is $p < 0.05$; ** is $p < 0.01$

against MDA-MB-231 cells, yet less than DOX loaded nPCL thanks to the reduction of initial burst release.

4 Discussion

The purpose of this research was to introduce a new method to fabricate and characterize 3D printed scaffolds with microporous struts for breast reconstruction and chemotherapy drug delivery applications. PCL, an FDA approved biocompatible polymer with low melting temperature, which makes it easy to be customized, was chosen as an input material. The SEM micrograph and PBS turbidity confirmed the validity of this method to generate microporous structure by the completion of porogen leached out and even distribution of micropores throughout the strut structure. Results

from DOX loading showed microporous structures can improve drug loading efficacy up to 97%. Besides, pPCL also had higher interaction with DOX thanks to the increase in surface area generated from the microporous structure. DOX are macromolecules positively charged by their amine groups and are expected to form ionic interaction with carboxyl group of PCL molecules [6, 7]. The interaction makes DOX loaded pPCL more sensitive to pH, which is very beneficial to target the micro environment of tumour, which has low pH down to 5.5. Moreover, under complex ionic condition in SBF, pPCL also had a better release profiles with the substantial release up to 14 days whereas the release of DOX from nPCL was significantly slowed down after 4–5 days. In PBS pH 7.4, the ionic strength in the solution was not strong enough to breakdown DOX-PCL interaction on surface of strut and also pores' surface; therefore, pPCL, which had higher surface area thanks to the porous structure, release less as compared to nPCL. Low burst release and long substantial release were strong advantages of pPCL as they could prolong the DOX concentration in the effective range. Lastly, the cell proliferation results indicated DOX loaded pPCL could maintain chemotherapeutic effect and reduce cytotoxicity. Though rapid anticancer effect would be more favorable, other factors including cell viability of normal cell and maximum tolerate dose should also be considered when choosing the doses.

5 Conclusion

Local drug delivery for postmastectomy patients with breast reconstruction remains a challenge due to the lack of local drug delivery systems, the systemic cytotoxic of

chemotherapeutic drugs and the risk of cancer recurrence which may require implant removal. By using the implant as the drug carrier, it can solve the problem of local delivery, decrease the systemic side effects and prevent recurrent cancer. In this study, 3D printed scaffolds with microporous struts were fabricated and characterized as a drug carrier for DOX. The microporous scaffolds were sufficiently fabricated and their surface roughness was not altered. The drug release profiles indicated pPCL had potential for local targeted drug delivery application. However, further study need to be done to determine the optimum doses that would have sufficient chemotherapeutic effects with minimum cytotoxic to healthy cells.

Acknowledgements This work was enabled by use of the Central Analytical Research Facility hosted by the Institute for Future Environment at QUT.

Conflict of Interest Statement All of the authors confirmed no conflict of interest with regard to this work.

References

1. Saltzman, W.M., Fung, L.K.: Polymeric implants for cancer chemotherapy. *Adv. Drug Deliv. Rev.* **26**(2–3), 209–230 (1997)
2. De Souza, R., et al.: Polymeric drug delivery systems for localized cancer chemotherapy. *Drug Deliv.* **17**(6), 365–375 (2010)
3. Seib, F.P., Kaplan, D.L.: Doxorubicin-loaded silk films: drug-silk interactions and in vivo performance in human orthotopic breast cancer. *Biomaterials* **33**(33), 8442–8450 (2012)
4. Norouzi, M., Nazari, B., Miller, D.W.: Injectable hydrogel-based drug delivery systems for local cancer therapy. *Drug Discov. Today* **21**(11), 1835–1849 (2016)
5. Bose, S., Vahabzadeh, S., Bandyopadhyay, A.: Bone tissue engineering using 3D printing. *Mater. Today* **16**(12), 496–504 (2013)
6. Manocha, B., Margaritis, A.: Controlled release of doxorubicin from doxorubicin/ γ -polyglutamic acid ionic complex. *J. Nanomaterials* **2010**, 1–9 (2010)
7. Cacicedo, M.L., et al.: Modified bacterial cellulose scaffolds for localized doxorubicin release in human colorectal HT-29 cells. *Colloids Surf. B Biointerfaces* **140**, 421–429 (2016)

Fabrication of Vascular Patch from Porcine Pericardium

My Thi Ngoc Nguyen, Tuyet Le, and Ha Tran

Abstract

Pericardial tissues have been studied and applied in biomedicine, especially in the cardiovascular field as vascular grafts for their advantages of availability, excellent biocompatibility, and low rate of infection. Porcine pericardial tissues with similar adequate biological and mechanical properties have also recently been in great interest for cardiovascular transplantation. Our study focused on the fabrication of vascular patch from acellular porcine pericardium. Porcine pericardium was collected and decellularized, which were then undergone the treatment in glutaraldehyde for sterilization and cross-linking. The results demonstrated that glutaraldehyde presented a great effectiveness in sterilization and increase the tensile strength of pericardium, which was also confirmed by the degradation resistance in plasma and collagenase solution. MTT assay confirmed liquid extracts from the glutaraldehyde treated pericardium caused no cytotoxicity towards human fibroblasts. Additionally, SEM image indicated that the treated pericardium can support an appropriate attachment of human endothelial progenitor cells. Taken together, our results demonstrated the glutaraldehyde treated pericardium to be a suitable patch material for further application in cardiovascular field as vascular grafts.

Keywords

Pericardium • Decellularization • Patch • Cardiovascular

1 Introduction

Cardiovascular diseases remain the leading cause of death for both men and women in the world, such diseases killed approximately 17.5 million people in 2012, that is 3 in every 10 deaths [1]. For patients, taking medication can help alleviate symptoms, but there are several possible side effects associated with the medicine. Based on the fact that it is more beneficial to treat the root cause by repairing injured tissues, there has been much study aiming at determining a new patch material with potential advantages for the heart and blood vessels repair. In terms of cardiovascular patching, animal originated pericardium with advantage of ready availability, excellent biocompatibility, and a low rate of infection, has been developed and tested in preclinical and clinical studies [2–4]. Porcine pericardial tissues were demonstrated for adequate biological and mechanical properties [5], and also represented a great interest for cardiovascular transplantation recently. Previous reports of Gauvin et al. (2013) suggested that due to their structure and cross-linking of the collagen bundles, the porcine pericardium might be regarded as a suitable alternative for cardiovascular disease treatments [5]. In the present study, we focus on developing an efficient procedure for vascular patch preparation from porcine pericardium.

2 Materials & Methods

2.1 Preparation of Glutaraldehyde Treated Acellular Porcine Pericardium

Porcine pericardium samples were harvested and decellularized according to our previous publication [6]. Briefly, pericardium samples were washed thoroughly with PBS, followed by the decellularization in 10 mM Tris-HCl (Merck, USA) for 8 h, and 0.1% SDS (Sigma, USA) for 12 h. Finally, all specimens were rinsed for 90 min in PBS to

M. T. N. Nguyen (✉) · T. Le · H. Tran
Department of Physiology and Animal Biotechnology, University of Science, Ho Chi Minh City, Vietnam
e-mail: ntnmy@hcmus.edu.vn

remove residual chemicals and cellular remnants. The acellular pericardium samples were then treated in 0.05% glutaraldehyde for 24 h for the vascular patch (porcine pericardium derived vascular patch—PPVP) preparation, which was followed by washing in NH_4Cl and PBS for 24 h.

2.2 Mechanical Testing

5 × 2 cm PPVP strips were mounted into holders and mechanically examined for response to stress relaxation and fracture behavior by extending to fracture at an extension rate of 50 mm/min as described previously (Sung et al. 1999). The mechanical testing was conducted in an EZ50 universal testing machine (Lloyd Instruments, UK) equipped with NEXYGENPlus material test and data analysis software. The native pericardium tissues were used as the control group.

2.3 In Vitro Enzyme Degradation Resistance

PPVP samples were freeze-dried and incubated in collagenase solution (Sigma, USA) (100 mg of dried sample per 1 ml of collagenase solution), at 37 °C for 24 h, followed by washing in PBS and the 2nd freeze-dried to determine the percentage of losing mass. Additionally, PPVP samples were tested for enzyme resistance in an in vivo mimicking environment by incubating in human plasma at 37 °C for up to 14 days. Mechanical properties of the incubated samples were recorded to evaluate enzyme degradation resistance.

2.4 MTT Assay

Liquid extract was prepared by incubating PPVP in culture medium (6 cm² per ml) at 37 °C for 24 h according to ISO 10993/12. Meanwhile, human fibroblasts were seeded into 96 well-plate with 4 × 10³ cell per well, and cultured for 24 h. Liquid extract was harvested and added as test group. Culture medium as used as a blank group, and liquid extract from Latex gloves was used as positive group which caused cytotoxic towards cells. After incubation for 24 h, the liquids were replaced by culture medium containing 0.5 mg/ml MTT (Sigma, USA), and cultured for another 4 h. Medium was removed, 100 μl DMSO (Sigma, USA) was added into each well. The absorbance at 575 nm was determined using a spectrophotometer (Perkin, USA). Relative growth rate (RGR) was calculated upon OD₅₇₅ values according to ISO 10993/5 protocol as $\text{RGR} (\%) = (\text{OD}_{\text{test}}$

$\text{group}/\text{OD}_{\text{blank group}}) \times 100$). If RGR value as reduced more than 30%, liquid extract would be considered to cause cytotoxic effect (ISO 10993/5).

2.5 Evaluation of Cell Attachment and Proliferation on the Membrane

Human endothelial progenitor cells (hEPCs) were seeded at a density of 10⁴ cells/cm² on PPVP. The attachment and morphology of hEPCs on the PPVP were observed at 24 h by scanning electron microscope (SEM). Furthermore, hEPCs proliferation on PPVP was monitored by MTT assay.

3 Results

3.1 Properties of Porcine Pericardium Derived Vascular Patch (PPVP)

Acellular porcine pericardium was prepared by our previous protocol, and was demonstrated to be cell-free which indicated via the absence of nuclei remnants in Hematoxylin and Eosin section, and a extremely low DNA content (which must be less than 50 ng DNA per mg dried weight of sample) (Data not shown). The use of Glutaraldehyde represented a great effect on sterilization of porcine pericardium. There was no bacterial colonies presenting surrounding 0.05% glutaraldehyde treated porcine pericardium, which was found with a great amount in native samples (see Fig. 1a). Mechanical properties of PPVP (strain in percentage) was significant increased in comparison with native tissue (see Fig. 1b).

3.2 In Vitro Enzyme Degradation Resistance

The native pericardium samples were completely degraded in collagenase solution (see Fig. 2a), whereas, PPVP remained the intact appearance and more that 85% dried mass after 24 h incubation in collagenase (see Fig. 2b). PPVP also preserved its mechanical properties in plasma solution, which was indicated by a limitation in strain change after 14 days of plasma incubation (see Fig. 2c).

3.3 In Vitro Cytotoxicity

Liquid extract of PPVP had no effect on cell viability indicated by normal cell morphology after incubation for 24 h

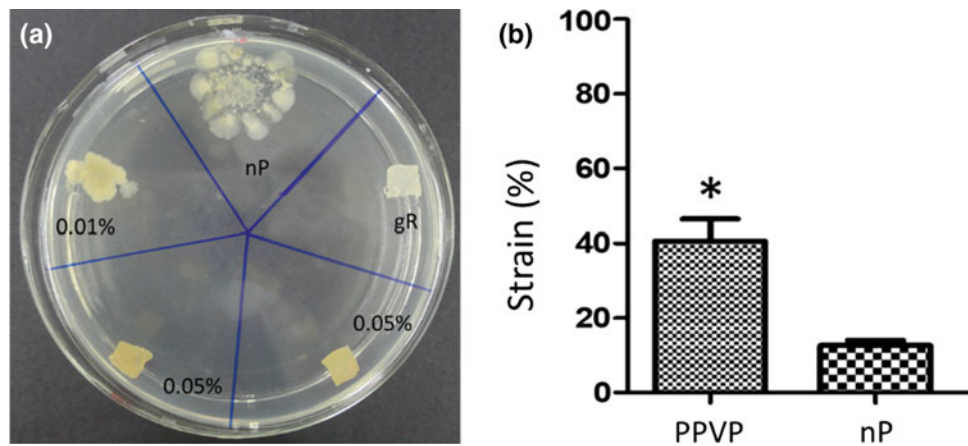


Fig. 1 Properties of porcine pericardium derived vascular patch (PPVP). **a** Sterilization testing on bacterial culture agar. **b** Mechanical testing. nP: native pericardium. 0.01%: 0.01% glutaraldehyde treated

porcine pericardium. 0.05%: 0.05% glutaraldehyde treated porcine pericardium. gR: gamma irradiated pericardium as control

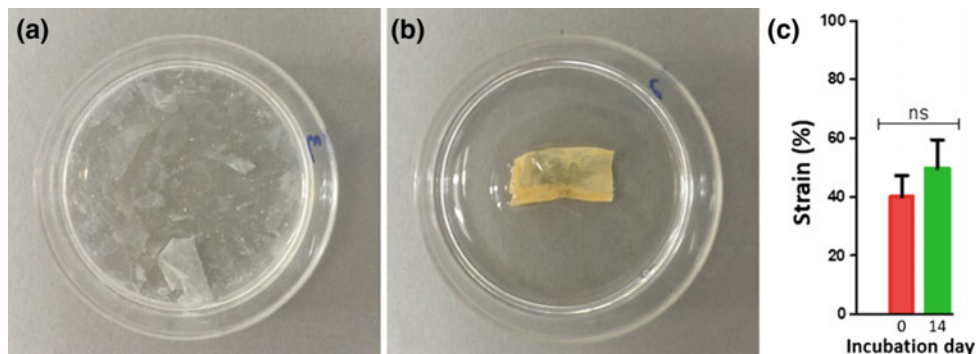


Fig. 2 In vitro degradation of PPVP. **a** Native pericardium incubated in collagenase. **b** PPVP incubated in collagenase. **c** Strain (%) of PPVP at day 0 and day 14 incubation in plasma

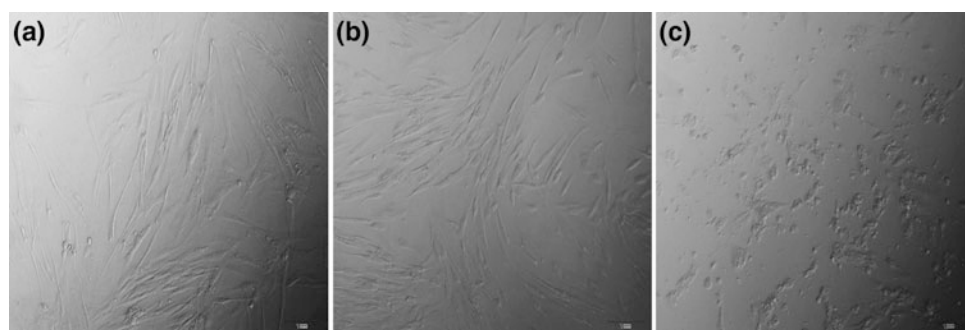


Fig. 3 In vitro cytotoxicity assay. **a** Human fibroblast in culture medium. **b** Human fibroblast in liquid extract from PPVP. **c** Human fibroblast in liquid extract from Latex as positive control

(see Fig. 3a, b), and RGR value which was found to be as high as RGR value of group treated with culture medium (see Table 1). On the other hand, liquid extract from latex gloves as positive control expectedly caused cytotoxic to cells after incubation for 24 h (see Fig. 3c).

3.4 hEPC Attachment and Proliferation on PPVP

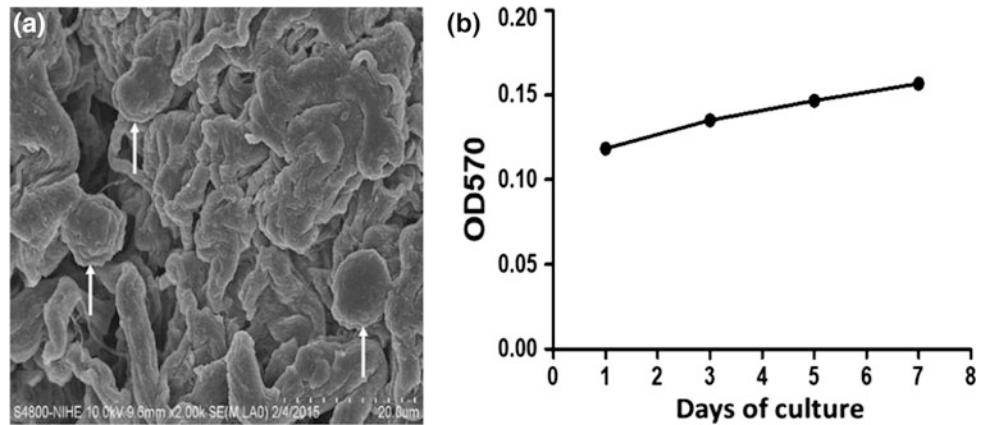
hEPCs were used to examine cell attachment support of PPVP. EPCs were seeded onto PPVP samples and visualized by SEM. SEM images revealed EPCs morphology on

Table 1 Relative growth rate (RGR - %) evaluation of human fibroblasts incubated in tested liquid extracts

	Liquid extract samples		
	Blank	PPVP	Latex
OD 575 nm	0.412	0.518	0.087
	0.502	0.346	0.053
	0.517	0.521	0.054
%RGR	100%	94.99 ± 11.90	13.31 ± 2.298
In vitro cytotoxicity		No	Yes

Blank – Culture medium; PPVP – Porcine pericardium derived vascular patch

Fig. 4 hEPC cultured on PPVP. **a** SEM image of hEPCs on PPVP. **b** hEPC proliferation on PPVP



PPVP. EPCs attached onto pericardial matrix and spreaded into polygonal-rounded appearance after culturing for 48 h (see Fig. 4. A white arrow). EPCs were demonstrated to proliferate on PPVP which was shown in the increase OD value from day 1 to 7 by MTT assay (see Fig. 4b).

Conflict of Interest The authors declare that they have no conflict of interest.

References

1. Roger, V.L., et al.: Heart disease and stroke statistics–2012 update: a report from the American Heart Association. *Circulation* **125**(1), e2–e220 (2012)
2. Biasi, G.M., et al.: Nine-year experience of bovine pericardium patch angioplasty during carotid endarterectomy. *J. Vasc. Surg.* **36**(2), 271–277 (2002)
3. Kim, J.H., et al.: Ten-year comparative analysis of bovine pericardium and autogenous vein for patch angioplasty in patients undergoing carotid endarterectomy. *Ann. Vasc. Surg.* **26**(3), 353–358 (2012)
4. Pires, A.C., et al.: Bovine pericardium used as a cardiovascular patch. *Heart Surg. Forum.* **2**(1), 60–69 (1999)
5. Gauvin, R., et al.: A comparative study of bovine and porcine pericardium to highlight their potential advantages to manufacture percutaneous cardiovascular implants. *J. Biomater. Appl.* **28**(4), 552–565 (2013)
6. Tran, H.L.B., et al.: Preparation and characterization of acellular porcine pericardium for cardiovascular surgery. *Turk. J. Biol.* **40**(6), 1243–1250 (2016)

Effect of Magnesium on Mechanical Properties of Binary Zn–Mg Alloys

Shiyang Liu, Nghiem Doan, and Gui Wang

Abstract

Zinc based alloys possess a number of attractive characteristics that make alloys potential candidates to use as implants for load bearing applications in the medical industry due to its good biocompatibility and biodegradability. In this current work, a number of binary Zn–Mg alloys were investigated in term of phase constitutions, microstructure, and mechanical properties. Magnesium was selected to tune mechanical properties of pure Zn. The microstructures of alloys were inspected by an optical metallographic microscope and SEM equipped with EDS analyser. Mechanical properties were tested using standard tensile testing instruments. While the Zn alloys with different wt% Mg are shown here, the influence of different content of Mg elements on mechanical properties also will present here.

Keywords

Implant • Mechanical properties • Microstructure • Zinc alloy

1 Introduction

Biomaterials are intended to be implanted in the human body as constituents of devices to perform certain biological functions by substituting or repairing tissues [1]. The adverse effects of the conventional permanent implant materials, such as migration, mechanical mismatches between bone and implant, chronic inflammation or infection of body tissue caused by the toxic corrosion products and wear debris effects on a cellular level often accompany the use of the implant materials [2]. To mitigate the long-term side effects associated with permanent implants, a new generation of

biodegradable metal implants are currently being developed [3, 4]. The concept of this kind of biodegradable metals is providing a temporary support for the healing process of diseased tissue and progressively degrades thereafter [2–4]. Implants made from biodegradable metals possess three distinguishing features including (1) temporary support; (2) degradation and (3) positive interaction (bioactive). They offer many advantages in load-bearing applications compared to the nondegradable ones including the elimination of a second removal surgery that could be required otherwise, facilitation of tissue regeneration and healing by providing temporary mechanical support as diseased tissues restore their functions or new cells gradually replace the defects produced through biodegradation. Investigations in this field are ongoing as researchers strive for optimized materials that can fulfil clinical requirements, including controllable degradation rates, prolonged mechanical stability, and excellent biocompatibility.

Zn and Zn-based alloys have been recognized as highly promising biodegradable materials for clinical applications, for example, orthopedic implants and cardiovascular stents due to their proved biocompatibility and proper degradable behaviours [3, 5–10]. Bowen et al. [3, 5] conducted an animal trial by implanting Zn wire in rat abdominal aorta for up to 6 months and found that it remains intact for 4 months, degradation accelerated after 4 months thus ensuring timely degradation of the implant. Drelich et al. [6] characterised a 20 months surveillance of zinc implant in the murine artery, and found that zinc wires implanted in the murine artery exhibit steady corrosion without local toxicity for up to at least 20 months post-implantation. Another recent research [7] on the degradation mechanism of pure zinc stent has shown that the pure zinc stent remained its mechanical integrity for 6 months and degraded $42 \pm 30\%$ of stent volume after 12 months implantation. The degradation of pure zinc stent showed an excellent biocompatibility with no severe inflammation, platelet aggregation, thrombosis formation or obvious intimal hyperplasia. With these favorable

S. Liu · N. Doan · G. Wang (✉)
Centre for Advanced Materials Processing and Manufacturing,
The University of Queensland, St Lucia, QLD 4072, Australia
e-mail: gui.wang@uq.edu.au

physiological degradation behaviours, it is believed that zinc has a great potential for developing biodegradable stents.

The major drawback of the pure Zn as a structural material for biodegradable implant application is its low mechanical properties. Developing high strength and ductility zinc with sufficient hardness, while retaining its biocompatibility, is one of the main goals of metallurgical engineering. A considerable number of researches have been conducted in order to achieve the desired mechanical properties through alloying chemistry and thermomechanical processing [8–12]. Mechanical properties and in vitro biodegradation behaviours of as-cast Zn–Mg alloys with Mg ranging from 0.5 to 3 wt% have been investigated by Vojtech et al. [9]. It was found that degradation rate of Zn–Mg alloy in the BSF did not change significantly with various Mg percentages, and through Mg alloying chemistry, the strength and elongation reached around 190 MPa and 1.8% in the as cast condition. Li et al. [10] have investigated the Zn–1X binary alloys with nutrient alloying elements Mg, Ca and Sr. their experimental study showed adding Mg, Ca and Sr, the UTS and elongation of as-cast Zn–1X binary alloys are significantly improved to 185 MPa and 1.82% (Zn–1 Mg); 165 MPa and 2.1% (Zn–1Ca); and 171 MPa and 2.03% (Zn–1Sr). After hot rolling or hot extrusion, the YS, UTS and elongation of Zn–1X binary alloys are further improved. Gong et al. [11] compared in vitro biodegradation behavior, mechanical properties, and cytotoxicity of biodegradable Zn–1 Mg alloy, revealed that as-cast Zn–1 Mg suffered from significant nonuniform microgalvanic corrosion and extruded Zn–1 Mg alloy with homogenous microstructure, uniform and slow biodegradation, improved mechanical properties and good biocompatibility is a suitable candidate material for load-bearing biodegradable implant application. Kafri et al. [12] have investigated as-cast Zn–1.3% Fe alloy to identify the corrosion rate affected by adding Fe elements and found the corrosion rate of Zn–1.3%Fe nearly doubled in vitro and vivo conditions since the formation of Delta phase ($Zn_{11}Fe$) generates the microgalvanic effect. Sikora-Jasinska et al. [13] indicate that Ag has a positive influence on mechanical properties, antibacterial properties and biocompatibility of Zn matrix.

In this research, we sought to systematically investigate the suitability of as-cast and as rolled Zn–Mg alloys as a biodegradable implant material in terms of mechanical properties. Zn–Mg alloys with addition of Mg from 0.1–0.8% were selected due to their good mechanical properties as shown in the previous study.

2 Materials and Methods

Pure Zn (99.99%) and a Zn–30 Mg master alloy were melted in an induction furnace to make designed alloys of pure Zn, Zn–0.1 Mg, Zn–0.2 Mg, Zn–0.3 Mg, Zn–0.4 Mg, Zn–

0.5 Mg, and Zn–0.8 Mg. The alloyed melt was casted in a steel mould to make Zn–Mg alloy plate with a dimension of 150 mm (Length) \times 100 mm (Height) \times 20 mm (Depth). The selected cast plates for pure Zn, Zn–0.4 Mg alloy and Zn–0.8 Mg alloy were hot rolled to 1 mm thick sheet through multiple rolling passes at 250 °C. Tensile test specimens were cut using EDM wire method according to ASTM-E8-04. The tensile tests were performed on an Instron single axis servo-hydraulic testing system with a load rate of 0.1 mm/min. Fracture morphology was observed using a desktop SEM (Hitachi TM3030) equipped with energy-dispersive X-ray spectrometers. Specimens for metallographic inspection were ground by silicon carbide abrasive papers with successive grades from 400 to 2000 and polished with 0.5 μ m diamond suspension. Micrographs were obtained by a Leica Polyvar microscope with polarized light after anodizing using a 4.6% HBF₄ solution for about 25 s at 15 V.

3 Results and Discussions

3.1 Microstructure

Macrostructure and microstructure of as cast pure zinc as shown in Fig. 1 consists of very coarse grain structures with the average grain size of $3094.96 \pm 841.44 \mu\text{m}$.

With the addition of the 0.1% of Mg, grain size of the Zn–Mg alloy was significantly refined to around 180 μm as shown in Fig. 2a, grain size was further reduced to 160, 100, 80, 70 and 65 μm with the further increase the Mg content to 0.2, 0.3, 0.4 and 0.5%. At the same time, the increase volume ratio of the eutectic phase at grain boundary can be observed because the solid solubility of Mg in Zn is lower than 0.1 wt% (Fig. 2b–e). With the addition of the 0.8%Mg, grain size was increased to about 100 μm as shown in Fig. 2f, a typical hypoeutectic microstructure consisting of primary Zn dendrites and a eutectic mixture was observed.

Figure 3 showed the microstructure of the as hot rolled pure Zn, Zn–0.4 Mg alloy and Zn–0.8 Mg alloy. After hot rolled, the grain structure became more homogeneous and smaller compared with their as-cast counterparts, and large dendritic grains of as-cast Zn–Mg disappeared and uniform small equiaxial grains formed. At the same time, eutectic phase transformed into smaller precipitates due to high shear stress generated during the rolling process and recrystallization at high temperature.

3.2 Mechanical Properties and Fracture Morphology

Figure 4a shows the effect of Mg addition on tensile properties of the as-cast Zn–Mg alloys, and the tensile properties

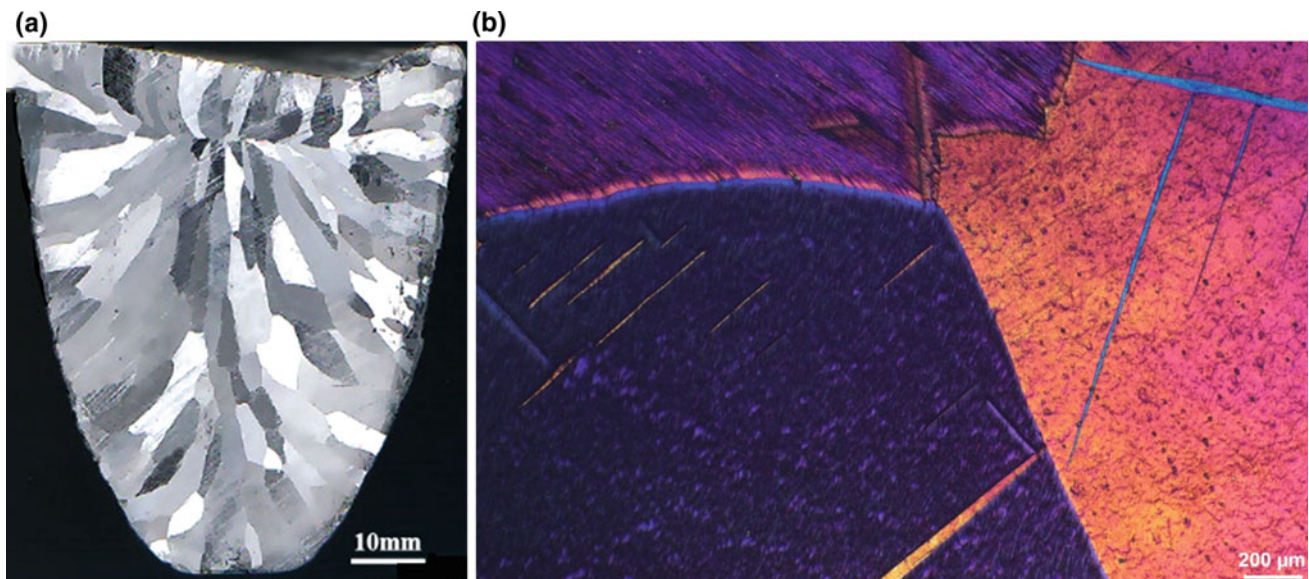


Fig. 1 a Macro- and b Micro- structure of pure zinc

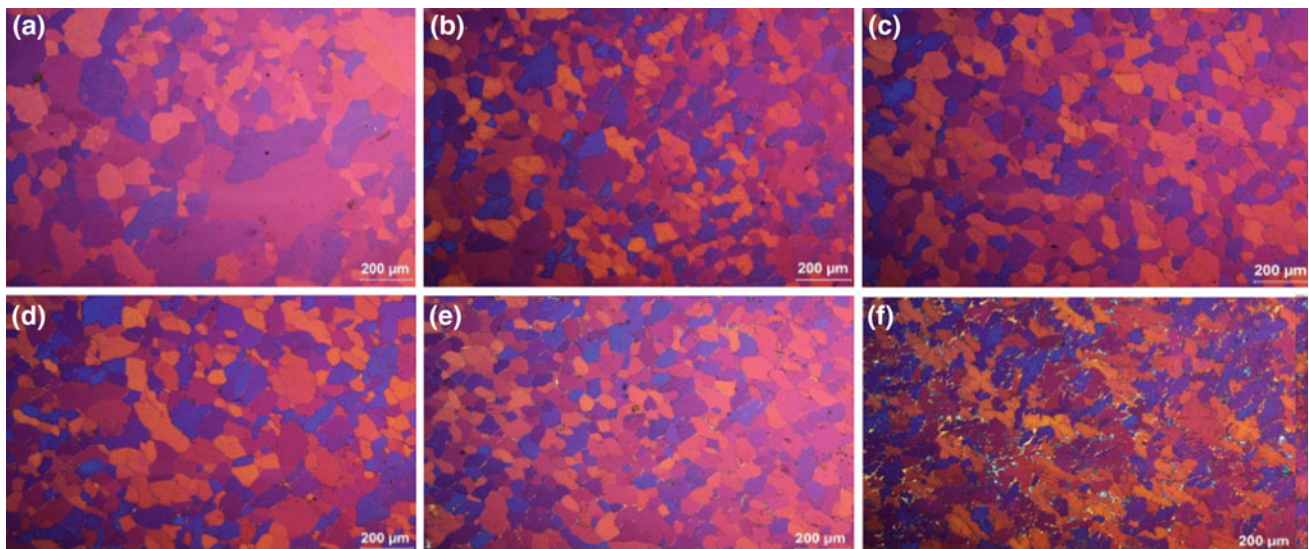


Fig. 2 Microstructure of the as cast Zn-Mg alloys, a Zn–0.1 Mg, b Zn–0.2 Mg, c Zn–0.3 Mg, d Zn–0.4 Mg, e Zn–0.5 Mg and f Zn–0.8 Mg

of the as-cast pure Zn are very low with ultimate tensile strength (UTS) 29.7 MPa, yield strength (YS) 27.5 MPa, and elongation of 0.62%, respectively. With the addition of the alloying elements Mg, the UTS and YS of the as-cast Zn alloy samples were significantly improved, for instance, the UTS and YS of the as-cast Zn–0.1 Mg alloy were increased to 81.5 and 72 MPa. With the addition of 0.8% Mg, the UTS and YS of the as-cast Zn–Mg alloy were reached to 120 and 112 MPa. On the other hand, no noticeable improvement to the elongation of the Zn–Mg alloys can be observed with the increase of Mg addition.

Tensile strain-stress curves of the as-rolled pure Zn, Zn–0.4 Mg and Zn–0.8 Mg alloy samples were shown in Fig. 4b. After hot rolling, the YS, UTS and elongation of Zn-based ternary alloy samples are remarkably improved. UTS, YS and elongation for unalloyed pure Zn were reached to 118, 85 MPa and 26.8%, which represented 4.0, 3.1, and 48.7 times improvement respectively compared to the as cast unalloyed pure Zn. For both Zn–0.4 Mg and Zn–0.8 Mg alloys, the UTS, YS, and elongation in the as hot rolled condition were reached to 230, 225 MPa, 23%; and 268, 260 MPa, and 7.2%, which were also increased significantly.

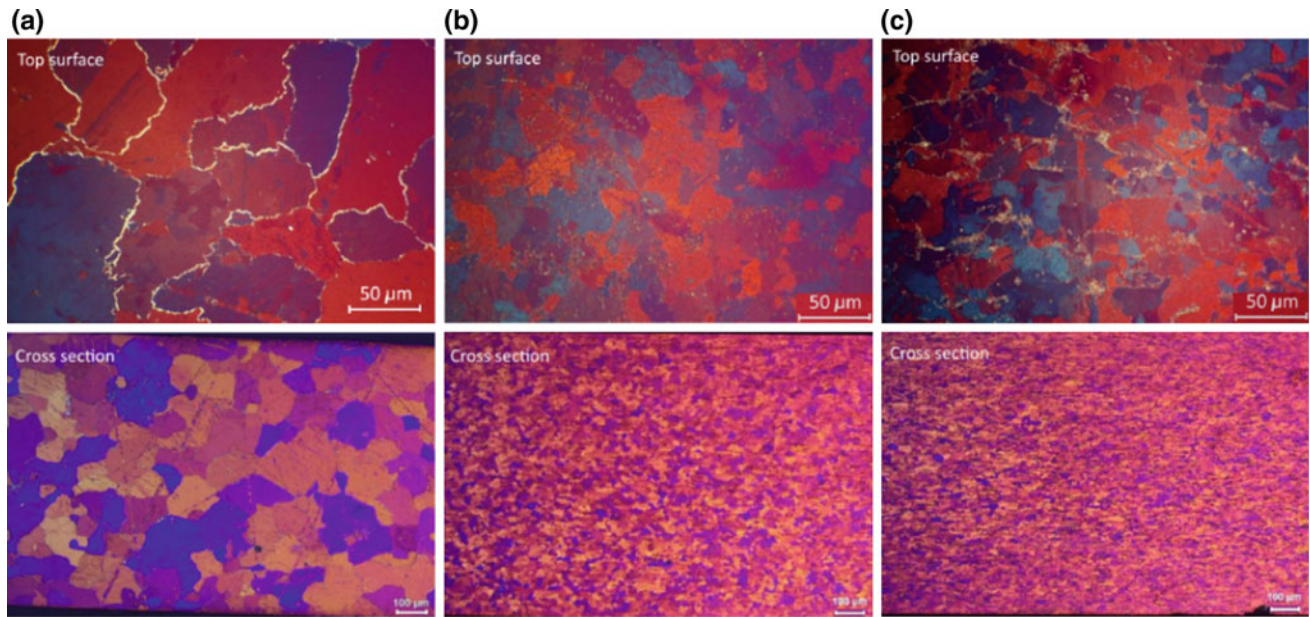


Fig. 3 Microstructure of as hot rolled **a** pure Zn **b** Zn-0.4 Mg and **c** Zn-0.8 Mg

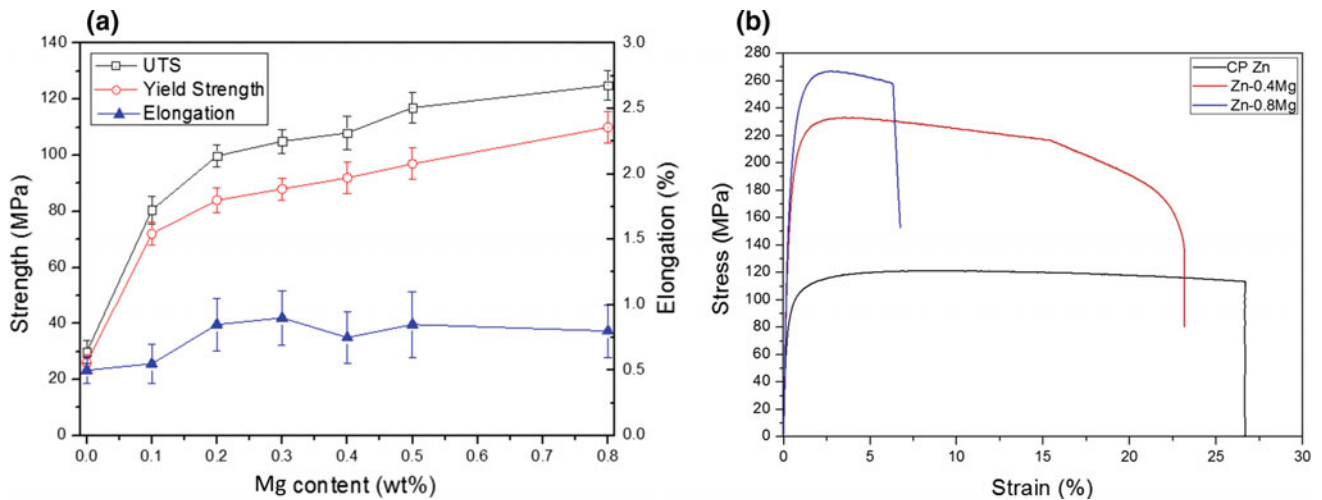


Fig. 4 **a** The effect of the Mg addition on tensile properties of the as-cast Zn-Mg alloys and **b** Tensile strain-stress curves of the as-rolled pure Zn, Zn-0.4 Mg and Zn-0.8 Mg alloy

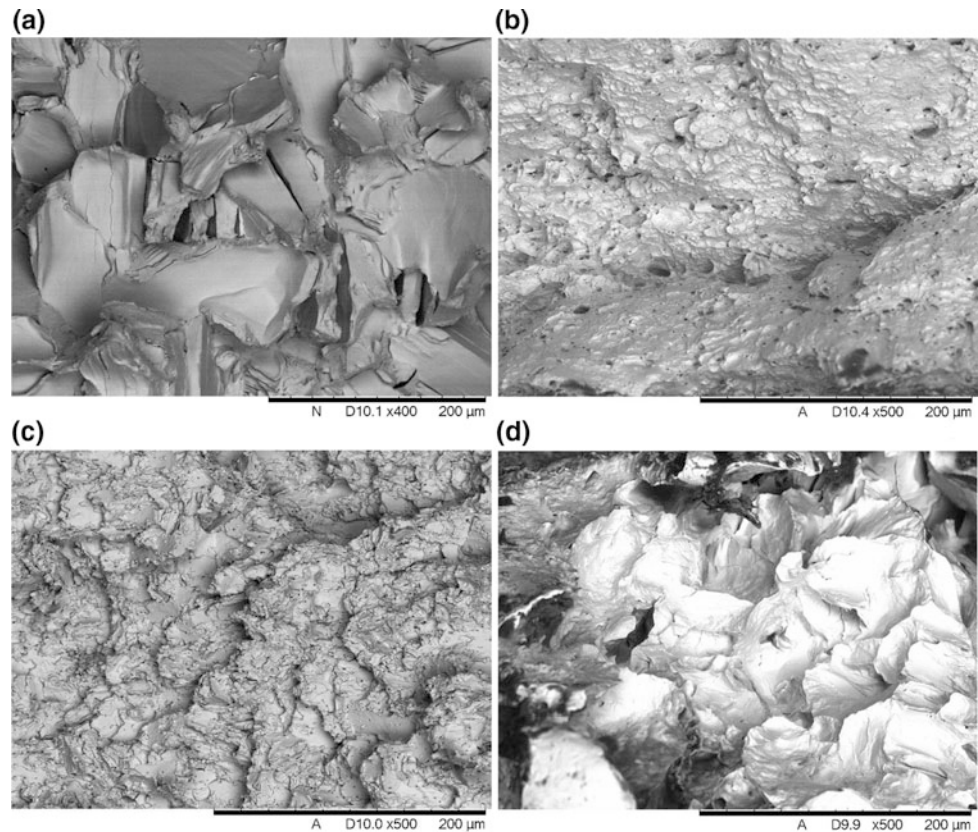
However the reduction of the elongation of the as rolled Zn-Mg alloys were noticeable with the increase of the Mg addition.

Figure 5 shows the tensile fracture surface of (a) as cast Zn-0.4 Mg alloy, as-rolled (b) pure Zn, (c) Zn-0.4 Mg alloy, and (d) Zn-0.8 Mg alloy samples. The fracture surface of the as cast Zn-0.4 Mg alloy (Fig. 5a) showed a typical brittle features characterised transgranular fracture with faceted texture and relatively smooth with some tiny voids, the fracture surface shown little or no plastic deformation prior to failure. As rolled pure Zn exhibited typical dimple fracture features, and this is consistent with its excellent elongation performance (Fig. 5b). Tearing edges can be evidently

observed on the fracture surface of the pure Zn. Small and uniform dimples can be obviously observed on the fracture surface. Figure 5 The fracture morphology of as rolled Zn-0.4 Mg and Zn-0.8 Mg was the quasi-cleavage fracture, a mixture of brittle and ductile fracture (Fig. 5c, d).

Figure 5b indicated that the thermomechanical processing such as hot rolled significantly improve the microstructure and mechanical properties of the Zn-Mg binary alloys. This is mainly attributed to (1) thermal deformation process results in a great reduction of the grain size through work hardening, dynamic recovery and recrystallization; (2) elimination of the cast void defects; and (3) homogeneous of the grain structure.

Fig. 5 SEM fracture surface for tensile specimens of **a** the as cast Zn–0.4 Mg alloy, the as rolled **b** pure Zn, **c** Zn–0.4 Mg alloy and **d** Zn–0.8 Mg alloy



3.3 Discussions

The implants are used to substitute for the human tissue, and their mechanical performance play an incredible role in order to support a damaged biological structure, or enhance an existing biological structure. As the 4th most common metal in use, Zn is most commonly used as an anti-corrosion agent rather than structure application. Only structure application of the Zn alloys is under the name of Zamak, the Zn alloying with Al, Cu and Mg. Even the YS of these alloys is in the range of 200–360 MPa, their low ductility at around 2% and the addition of about 4 wt% Al make them unsuitable for the implant applications. Therefore there is emergent requirement to develop new alloy system for medical application.

Pure zinc has a lattice structure of Hexagonal Close Packed (HCP), with the Lattice c/a ratio of 1.856, higher than the ideal HCP ratio of 1.633, and very low basal critical resolved shear stresses (CRSS) of 0.2 MPa [14]. Therefore pure Zn presents a low yield strength. Mg has been considered as a potential alloying element to improve the mechanical properties of Zn and also to tailor the degradable rate and profile for various implant applications. According to Zn–Mg phase diagram, the Zn–Mg alloys are in a eutectic system with the eutectic point corresponding to about 3 wt% of Mg, and the solid solubility of Mg in Zinc is in less than 0.1 wt%. Such low solid solubility of Mg in Zinc means a

very limited solid solution strengthening can be achieved in the alloy system.

The enhanced constitute phase for the hypoeutectic Zn–Mg alloys is the intermetallic compound Mg_2Zn_{11} . The hardness of the Mg_2Zn_{11} is 4.7 time of the pure Zn, and Young's modules is 42% higher than pure Zn [15]. The increase of Mg_2Zn_{11} will improve the strength the Zn alloy, as revealed in Fig. 5 Mg alloying exhibited effective strengthening effect for Zn alloy. The significantly refined and dimple-like morphologies are shown on Pure Zn and Zn–0.4 Mg, which are holes made around the hard and brittle Mg_2Zn_{11} -intermetallic particles, and the well-developed plastic Zn phase surround these holes. The highly improved elongation of pure Zn and Zn–0.4 Mg attributed to the plastic zone.

However, with the low eutectic point of 3% Mg, the window for enhancement of the Zn–Mg alloy is relatively small. As concluded by Vojtech et al. Mg concentration must be lower than 3 wt%, otherwise Zn–Mg alloy will mainly contain brittle eutectic phase [9].

Mg has a very high growth restriction factor in Zn, therefore Mg refines the as cast grain structure of Zn effectively. As demonstrated in Figs. 1 and 2, even with as low as 0.1% Mg concentration, it can still refine the grain structure from around 3000 to 160 μm . based on the Hall Petch relation, the yield strength has an inverse square root relation

with grain size. The strengthening of the refined grain is associated to the fact of more grain boundaries, more barriers to slip. The other problem for the as cast Zn–Mg alloys is their low ductility with less than 1% elongation, the addition of Mg has almost no effect on the ductility, this is probably due to the cast defect, residual stress, etc. So it is obvious that the unsatisfactory mechanical properties of the as cast Zn–Mg alloys need further modification in order to meet the requirement of the various biomedical applications, for example develop more complicated alloy system.

4 Conclusion

The mechanical properties and microstructure of casted Zn with the low content of Mg have been investigated, the results of the experiment demonstrated:

1. The formation of intermetallic compound Mg_2Zn_{11} played an important role in the improvement of mechanical properties of Zn alloys. The hardness and Young's modules of Mg_2Zn_{11} are significantly better than pure Zn, so the increase of Mg_2Zn_{11} will enhance the strength of Zn alloy.
2. As cast grain structure of Zn has refined by Mg effectively, since the high growth restriction factor of Mg in Zn.

Therefore, the Zn–0.4 Mg alloy has profoundly modified the mechanical properties and biodegradability of pure Zn. The alloy showed a good potential for use in a new generation of biodegradable implants.

Conflict of Interest The authors declare that they have no conflict of interest.

References

1. Navarro, M., Michiardi, A., Castano, O., Planell, J.A.: Biomaterials in orthopaedics. *J. R. Soc. Interface* **5**, 1137–1158 (2008)

2. Hallab, N.J.: A review of the biologic effects of spine implant debris: Fact from fiction. *Int. J. Spine Surg.* **3**, 143–160 (2009)
3. Hermawan, H.: Biodegradable metals from concept to applications. Springer, Heidelberg, New York, Dordrecht, London. <https://doi.org/10.1007/978-3-642-31170-3> (2012)
4. Bowen, P.K., Shearier, E.R., Zhao, S., Guillory, R.J., Zhao, F., Goldman, J., Drelich, J.W.: Biodegradable metals for cardiovascular stents: from clinical concerns to recent Zn–alloys. *Adv. Healthc. Mater.* **5**, 1121–1140 (2016)
5. Bowen, P.K., Drelich, J., Goldman, J.: Zinc exhibits ideal physiological corrosion behavior for bioabsorbable stents. *Adv. Mater.* **25**, 2577–2582 (2013)
6. Drelich, A.J., Zhao, S., Guillory, R.J., Drelich, J.W., Goldman, J.: Long-term surveillance of zinc implant in murine artery: Surprisingly steady biocorrosion rate. *Acta Biomater.* **58**, 539–549 (2017)
7. Yang, H., Wang, C., et al.: Evolution of the degradation mechanism of pure zinc stent in the one year study of rabbit abdominal aorta model. *Biomaterials* **145**, 92–105 (2017)
8. Levy, G.K., Goldman, J., Aghion, E.: The prospects of zinc as a structural material for biodegradable implants—a review paper. *Metals* **7**, 402 (2017). <https://doi.org/10.3390/met7100402>
9. Vojtech, D., Kubasek, J., Serak, J., Novak, P.: Mechanical and corrosion properties of newly developed biodegradable Zn-based alloys for bone fixation. *Acta Biomater.* **7**(2011), 3515–3522
10. Li, H.F., Xie, X.H., Zheng, Y.F., et al.: Development of biodegradable Zn–1X binary alloys with nutrient alloying elements Mg, Ca and Sr. *Sci. Rep.* **5**. <https://doi.org/10.1038/srep12190>
11. Gong, H., Wang, K., Strich, R., Zhou, J.G.: In vitro biodegradation behavior, mechanical properties, and cytotoxicity of biodegradable Zn–Mg alloy. *J. Biomed. Mater. Res. B* **103**, 1632–1640 (2015). <https://doi.org/10.1002/jbm.b.33341>
12. Kafri, A., Ovadia, S., Goldman, J., Drelich, J., Aghion, E.: The suitability of Zn–1.3%Fe alloy as a biodegradable implant material. *Metals* **8**, 153 <https://doi.org/10.3390/met8030153> (2018)
13. Sikora-Jasinska, M., Mostaed, E., Mostaed, A., Beanland, R., Mantovani, D., Vedani, M.: Fabrication, mechanical properties and in vitro degradation behavior of newly developed Zn–Ag alloys for degradable implant applications. *Mater. Sci. Eng. C* **77**, 1170–1181 (2017)
14. Britton, T.B., Dunne, F.P.E., Wilkinson, A.J.: On the mechanistic basis of deformation at the microscale in hexagonal close-packed metals. *Proc. R. Soc. A* **471**, 20140881 (2015). <https://doi.org/10.1098/rspa.2014.0881>
15. Kammerer, C.C., Behdad, S., Zhou, L., Betancor, F., Gonzalez, M., Boesl, B., Sohn, Y.H.: Diffusion kinetics, mechanical properties, and crystallographic characterization of intermetallic compounds in the Mg–Zn binary system. *Intermetallics* **67** 145–155 (2015)

A Suitable Protocol to Prepare Decellularized Porcine Vessel for Cardiovascular

Minh Quan To, Quoc Thang Bui, Ngoc Le Van Trinh, Thi Vy Tuyet Le, Quang Tri Le, Tho Tuan Anh Pham, and Le Bao Ha Tran

Abstract

Although autologous and artificial grafts are commonly used to solve cardiovascular disease or trauma, decellularized vessels scaffolds are recent promising materials for vascular transplantation. The purpose of this study was to introduce a simple and effective protocol to prepare decellularized porcine vessels. Porcine carotid arteries (pCA) were decellularized by 4 methods including 3 commonly protocols: SDS 0.5% for 24 h or distilled water for 24 h or Triton X100 0.1% for 24 h and our protocol, combination of SDS 0.5% 24 h and distilled water for 24 h. After removing the cells, structure and collagen were determined by Heamatoxylin/Eosin (HE) and Trichrome staining. In vitro cytotoxicity test on fibroblasts was performed according to ISO 10993-5. Additionally, mesenchymal stem cells (MSCs) were seeded on the acellular porcine carotid arteries (aCA) pieces to examine their attachment and growth for 11 days. To investigate in vivo behaviors, aCA were implanted subcutaneously into mouse dorsal skin (Dacron grafts were used as control) and grafts were then isolated and stained with HE after 7, 14, 28 days. The results showed that our protocol removed all cells and maximally preserve extracellular matrix (ECM) comparing to other basis methods. aCA are non-toxic to fibroblast (level 0) and evoked weak inflammation in vivo which was absent in week 4 (similar to Dacron grafts). MSCs attached and

grow successfully on the lumen of aCA. Conclusion: Our research may provide a promising protocol to prepare a potential vascular graft with its quality is suitable for cardiovascular surgery.

Keywords

Porcine carotid • Decellularization • Vascular grafts • Dacron • Xenogenic/allogenic transplantation

1 Introduction

Extracellular matrix (ECM) is composed of extracellular molecules secreted by resident cells of each tissue, organ. Decellularization is a process to obtain ECM of tissues/organs by removing all native cells [1, 2]. Removal of cellular components can reduce immunogenicity of tissues/organs; component and structure of ECM (decellularized tissues/organs) is similar to its native [3]. So, this process is commonly used in allogeneic and xenogeneic tissues/organs and ECM can be used as biological scaffold in regenerative medicine for replacement of damaged tissues/organs. Thus, decellularization is a useful method to face the greatest challenge of organ transplantation, deficiency of donated organs/tissues. Some commercial products are AlloDerm®, Oasis®, CopiOs®....

In vascular tissue engineering, carotids are suitable arteries for decellularization because of their size and mechanical resistance [4, 5]. Decellularized carotids can be used in bypass surgery or used as vascular patches for healing leaky blood vessels. Some common decellularizing reagents such as sodium dodecyl sulfate (SDS), Triton X100, distilled water... are intended to alter ultra structure and composition of carotids. The intent of decellularizing protocols is to combine many different reagents to retain maximally ECM. In this study, we aim to make a simple and effective decellularization protocol for porcine carotids (pCA).

M. Q. To · N. L. V. Trinh · T. V. T. Le · L. B. H. Tran
University of Science, Vietnam National University
Ho Chi Minh City, Ho Chi Minh City, Vietnam

Q. T. Bui (✉) · T. T. A. Pham
Pediatric Cardiovascular Surgery Department,
Cho Ray Hospital, Ho Chi Minh City, Vietnam
e-mail: buiquocthang.vn@gmail.com

Q. T. Bui
Department of Cardiovascular Surgery,
University of Tsukuba, Tsukuba, Japan

Q. T. Le
7A Military Hospital, Ho Chi Minh City, Vietnam

2 Method

Decellularization methods: pCA were obtained from a local slaughter house and transferred to laboratory in cold phosphate buffer saline (PBS). Adjacent tissues such were removed carefully. pCA were shaken in one of these methods (5 arteries/method): SDS (Sigma) 0.5% (in PBS) for 24 h at room temperature (RT), distilled water for 24 h, Triton X100 (Sigma) 0.1% (in PBS) for 24 h at RT, and combination of SDS 0.5% (in PBS) 24 h with then distilled water for 24 h at RT. Efficiency was evaluated by Hematoxylin/Eosin (HE) and Trichrome staining.

In vitro cytotoxicity test was performed according to ISO 10993-5. Fibroblast cells were seeded into 10 wells of 4-well plate with concentration of 3×10^4 cells/well and incubated at 37 °C, 5% CO₂ for 1 day. After 1 day, these wells were divided to 2 groups: sample group included five pieces (3×3 mm²) of acellular pCA (aCA) were placed on the fibroblast layer of 5 wells; and second group for control in other 10 wells which contained only fibroblast layer. 1 day after, cell appearance and viability were observed by microscope and performed by MTT assay (MTT 5 mg/ml was added into wells of both groups (10 µl/well) and incubated in dark, 37 °C for 4 h) at wave length of 495 nm. Then, formazan crystals were dissolved in absolute DMSO for 4 h and optical density (OD) was measured at wavelength of 495 nm.

Adipose—derived stem cells (ADSC) were cultured in DMEM//F12 containing 10% FBS (fetal bovine serum). ADSC were isolated by Trypsin/EDTA and adjusted to 2×10^5 cells/ml, then seeded onto lumen of aCA pieces (10 µl/piece) and incubated in 37 °C for 2 h. After that, these pieces were cultured in 37 °C, 5% CO₂ through experimental period. On the 1st, 3rd, 5th, 7th, and 9th days, MTT assay was performed with 5 aCA pieces with ADSC-seeded and 5 aCA pieces without ADSC for control.

In vivo cytotoxicity test was performed by using one piece of aCA (3×3 mm²), which was implanted subcutaneously into one side of mouse dorsal skin, other side was implanted by Dacron graft (control group). On the 7th, 14th and 28th days, grafts were isolated and tested by HE staining (3 mouse per day).

3 Result

Decellularization: HE and Trichrome staining of treated pCA were shown in Fig. 1. The results showed that native pCA composed of 3 layers contained extensively cellular components. When using separately, SDS 0.5% (24 h), Triton X100 0.1% (24 h), distilled water (2 h) removed cellular components and retained 3 layer structure of ECM with different levels and none of these methods removed all

resident cells. When combining together, 2-step protocol (Fig. 1i, j) including SDS 0.5% (24 h) and distilled water (2 h) completely removed native cells and retained structure integrity and collagen of ECM. This method was used to create aCA for next examination.

In vitro cytotoxicity test: The results showed: in sample group, few fibroblast cells were dead or detached from dish, most of cultured cells hold elongated appearance similar to cells in control group. MTT assay showed that OD rate of sample (0.226) and positive control (0.235) was 96% (level 0). According to ISO 10993-5, cytotoxicity of aCA is 0. Thus, aCA are non-toxic in vitro (Fig. 2).

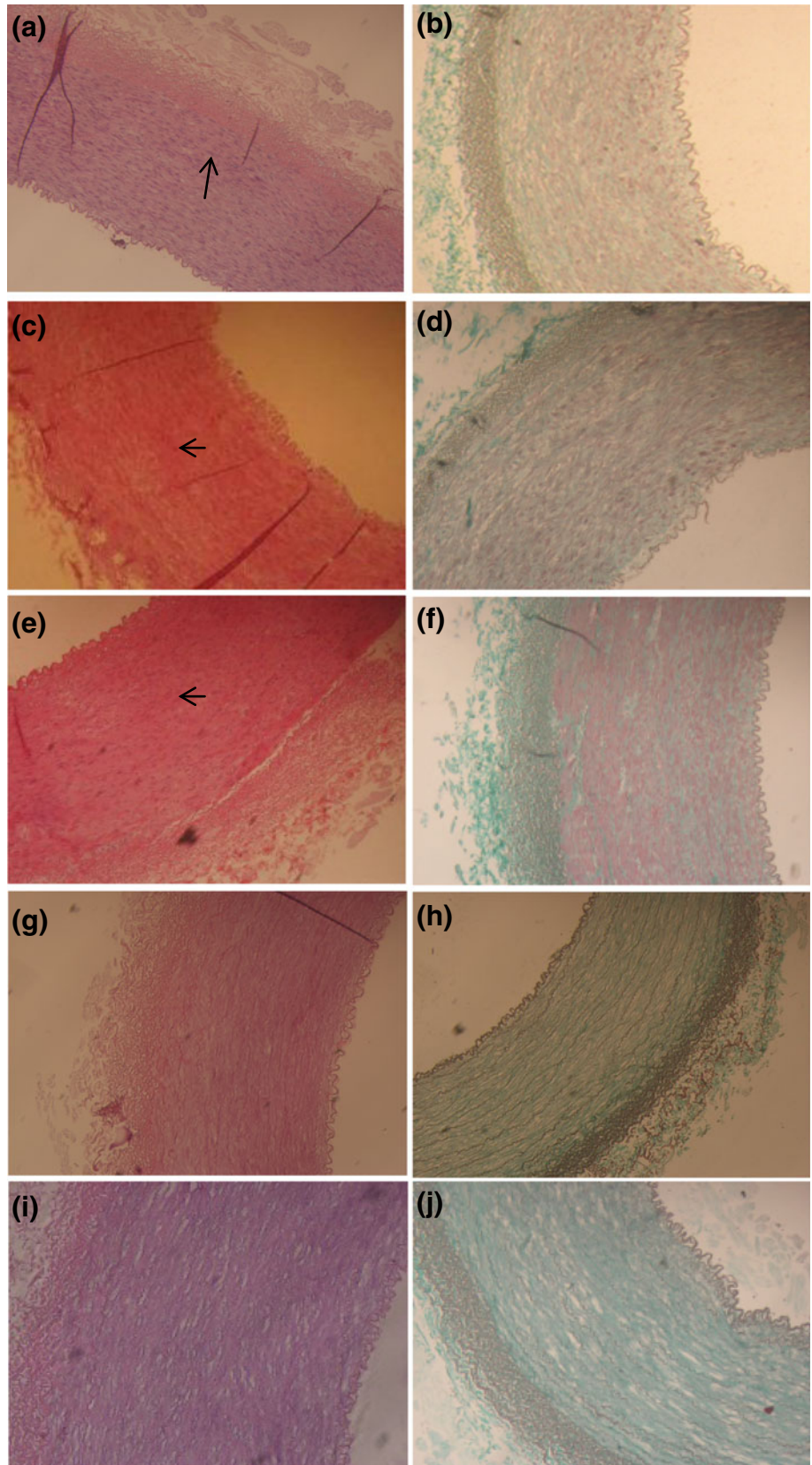
ADSCs growth: HE staining and MTT assay showed that cells were attached to aCA on day 1, grew from day 1st to 7th, declined from day 7th to 9th (Fig. 3).

In vivo cytotoxicity: After implanting, suture was healed after 4–5 days, some inflammation signs such as swelling, redness didn't appear after 28 days. HE staining showed that inflammation evoked by aCA was similar to Dacron grafts during a period of 28 days. On day 7, hemorrhage, lymphocytes (T and B) and fibrous connective tissue appeared around the grafts (both aCA and Dacron). On day 28, lymphocyte was absent, hemorrhages went away and fibrous connective tissue invaded more deeply to aCA and Dacron grafts (Fig. 4).

4 Discussion

More 116,000 people around the world are on national waiting list until August 2017. In 2016, only 33,611 transplants were performed all over the world and 20 people pass away every day while waiting a suitable organ [6]. Decellularization can create biological scaffolds composed of ECM to overcome the challenge of organ shortage for transplantation. In vascular tissue engineering, in 2017, over 600,000 coronary arterial bypass grafting were performed. About 1/3 patients don't have suitable blood vessels for grafting [6, 7]. So, vascular tissue engineering play an important role in regenerative medicine to make artificial blood vessels for artery bypass grafting and for leaky blood vessels. Nowadays, to make acellular artery composed of ECM is one of many main trend in vascular tissue engineering. In this study, we used 3 common decellularizing agents such as SDS, Triton X100 and distilled water to remove porcine carotids' cells. SDS is an ion detergent, Triton X100 is a non-ion detergent and distilled water is a hypotonic agent. We aimed to find out a simple and efficient protocol for decellularization of pCA by combining these reagents. First, pCA were decellularized by SDS 0.5% for 24 h or Triton X100 0.1% for 24 h or distilled water for 24 h at RT to examine decellularization efficiency of each reagent. Histological results showed that none of these

Fig. 1 HE and Trichrome staining of treated CAs ($\times 100$). **a, c, e, i** HE staining. **b, d, f, j** Trichrome staining. **a, b** control. **c, d** Triton X100 0.1% (24 h). **e, f** Distilled water (24 h). **g, h**: SDS 0.5% (24 h). **i, j** SDS 0.5% (24 h) + distilled water (24 h). Arrow: cells



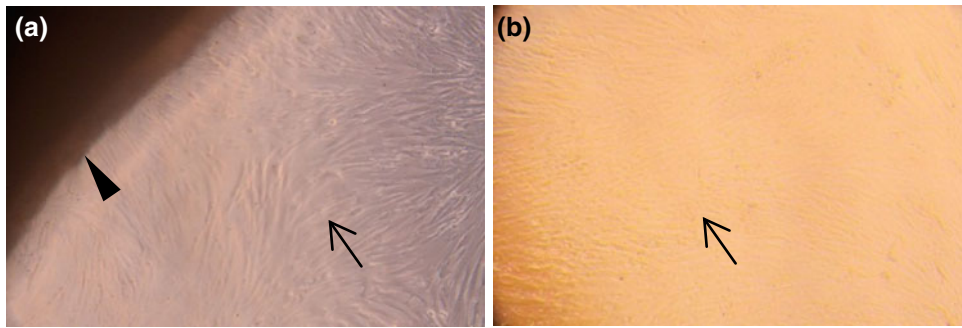


Fig. 2 Cell appearance in cytotoxicity in vitro test (x100). **a** aCA. **b** control (cells in culture medium). Arrow: cell, arrowhead: aCA

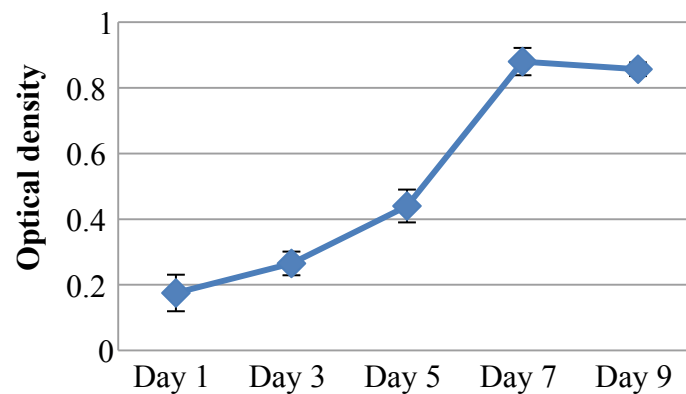
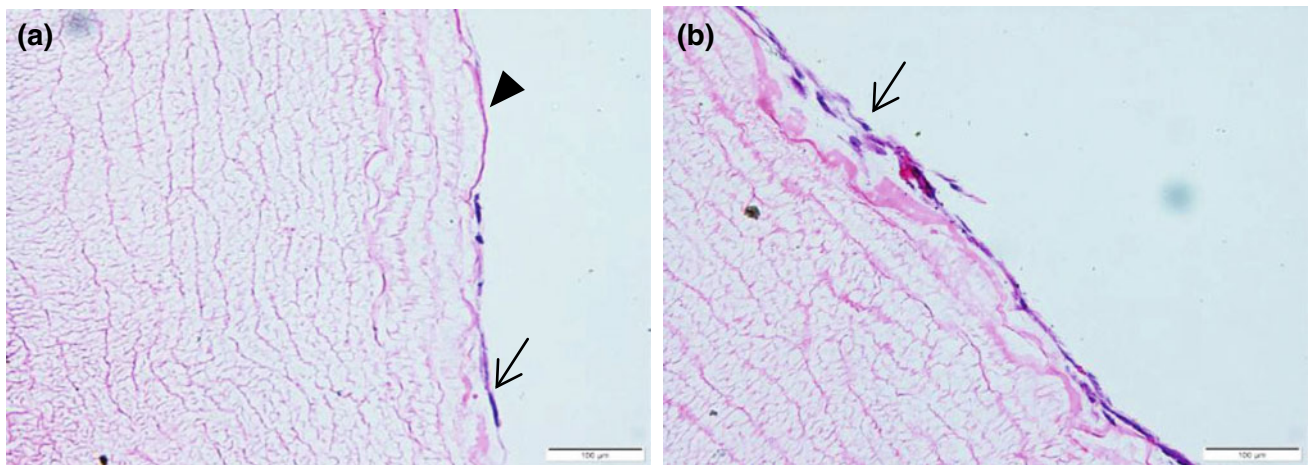


Fig. 3 Growth of MSC on aCAs. **a, b** HE staining (x200). **a** Day 1. **b** Day 7. Chart: growth curve Arrow: ADSC, arrowhead: aCAs

methods removed all native cell of pCA, SDS is the strongest decellularizing reagent and distilled water is the weakest. HE and Trichrome staining are convenient and required methods to examine decellularization efficiency. They show the structure, cell component and collagen in carotids before and after treatment. Based on these results, we made a combination method including SDS 0.5% for 24 h and distilled water for 24 h. This process removed all cells and maximally preserved ECM. The next results showed that aCA is non-toxic for cells and is an appropriate substrate for the growth of MSC in vitro. In vascular tissue engineering,

endothelial and smooth muscle cells are important cell lines. EC can make an antithrombotic layer and SMC enhance mechanical properties of vascular grafts but the disadvantages of these cells are the limited number of autologous cell and proliferation capacity [8]. Mesenchymal stem cells have higher proliferation capacity and ability to differentiate to EC and SMC in vitro, so application of MSC in vascular tissue engineering is increasing rapidly [9, 10]. When grafting subcutaneously into mouse skin, aCA evoke inflammatory responses similar to Dacron grafts (biocompatible commercial grafts in bypass surgery) throughout the experimental

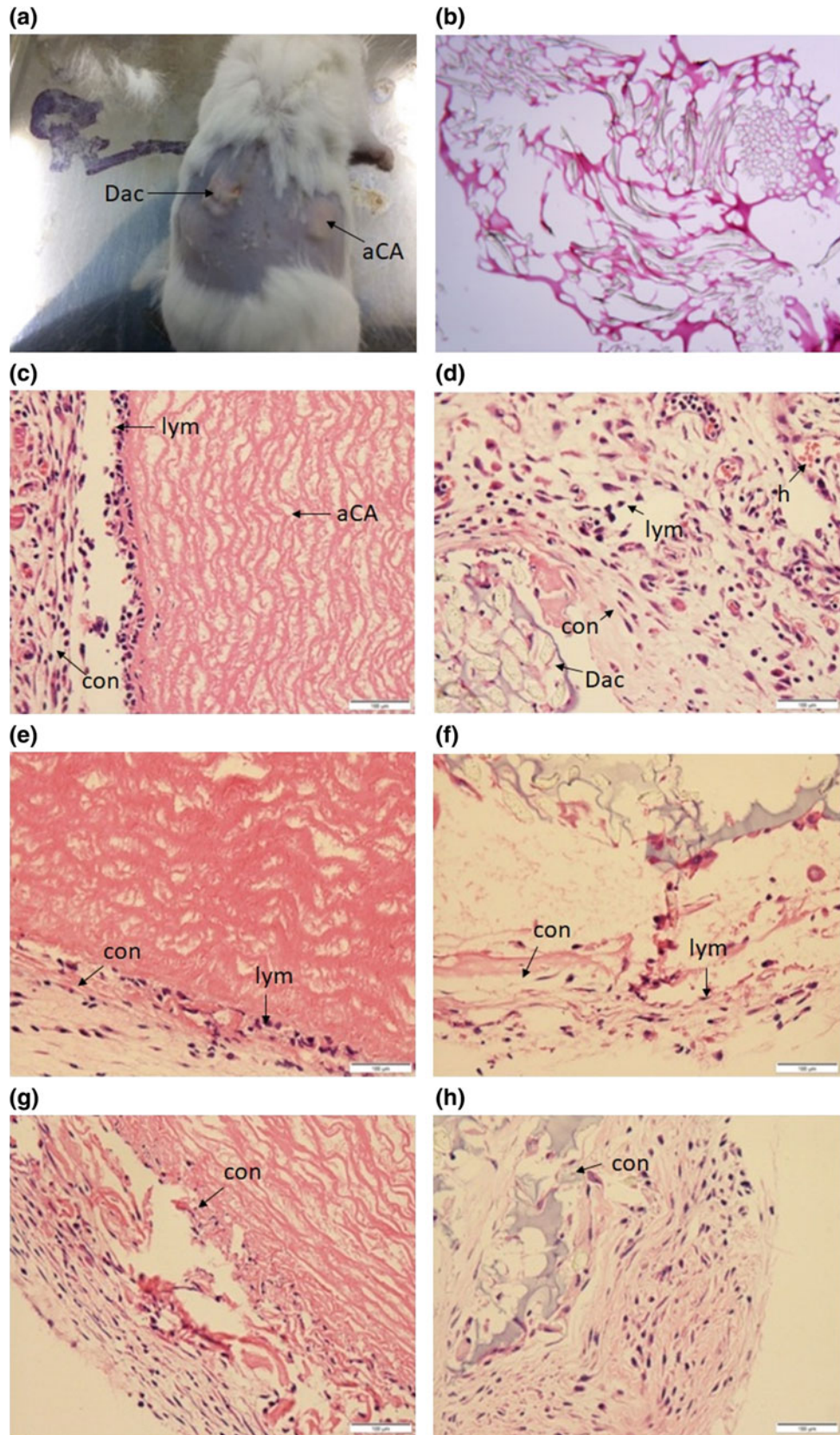


Fig. 4 Results of in vivo cytotoxicity test. **a** aCA and Dacron in a mouse. **b** Histological result of Dacron (200x). **c, e, g** histological results of implanted aCA (200x). **d, f, h** histological results of

implanted Dacron (200x). **c, d** day 7. **e, f** day 14. **g, h** day 28. **h**: heamorage, **con**: connective tissue, **lym**: lymphocyte

period. Although this study has some limitations: residual DNA in treated pCA should be quantified, other proteins of ECM such as elastin should be determined, some inflammatory cytokines in mouse should be measured ..., this study provides initial results of decellularization of pCA. The final protocol uses only cheap and common chemicals including SDS, distilled water and phosphor buffer saline. This protocol is composed of 3 steps: shaking in SDS 0.5% for 24 h, rinsing in PBS 36 h and shaking in distilled water for 24 h. Cycle time is relatively short (84 h) compared to other authors such as Boer's cycle time (86 h) or Daug's cycle time (several days) [4, 5].

5 Conclusion

The simple and effective decellularization method was successfully created for porcine carotids.

Acknowledgements This research is funded by The Youth Scientific and Technological Promotion Center (TST), The Ho Chi Minh Communist youth union of Ho Chi Minh city, with contract of "09/2017/HD – KHCHN – VU" (Mas. To Minh Quan).

Conflicts of Interest The authors declare that there are no conflicts of interests.

References

1. Gilbert, T.W.: Decellularization of tissues and organs. *Biomaterials* **27**, 3675–3683 (2006)
2. Lehr, E.J.: Decellularization reduces immunogenicity of sheep pulmonary artery vascular patches. *J. Thorac. Cardiovasc. Surg.* **141**, 1056–1062 (2011)
3. Crapo, P.M.: An overview of tissue and whole organ decellularization processes. *Biomaterials* **32**, 3233–3243 (2011)
4. Daus, A.: Detergent-based decellularization of bovine carotid arteries for vascular tissue engineering. *Ann. Biomed. Eng.* **45**, 2683–2692 (2017)
5. Boer, U.: Effect of intensified decellularization of equine carotid arteries on scaffold biomechanics and cytotoxicity. *Ann. Biomed. Eng.* **43**, 2630–2641 (2015)
6. Chang, W.G.: A short discourse on vascular tissue engineering. *NPJ Regenerative Med.* **2**, (2017)
7. Mao, Z.: Predictors associated with stroke after coronary artery bypass grafting: a systematic review. *J. Neurol. Sci.* **357**, 1–7 (2015)
8. Huang, N.F.: Mesenchymal stem cells for vascular regeneration. *Regenerative Med.* **3**, 877–892 (2008)
9. Salem, H.K.: Mesenchymal stromal cells: current understanding and clinical status. *Stem Cells (Dayton, Ohio)* **28**, 585–596 (2010)
10. Planat-Benard, V.: Plasticity of human adipose lineage cells toward endothelial cells: physiological and therapeutic perspectives. *Circulation* **109**, 656–663 (2004)

A Comparative Study on Hydroxyapatite Derived from Bovine Bones and Synthetic Sources

Nhi-Thao Ngoc Dang , Hien-Phuong Le,
Vo Van Toi, and Thi-Hiep Nguyen 

Abstract

Hydroxyapatite (HA), a mineral component of bones and teeth, has been widely studied for various medical applications. The purpose of this research is to compare the HA from diverse bovine sources and chemical synthetic in the respectively physical and chemical powder properties such as grain size, morphology, crystallinity, phase stability and chemical functional groups. Bovine HA (B-HA) were extracted from the fresh femur bones of adult bovine, calf and bovine bone bio-waste. Synthesized HA (S-HA) were prepared by chemical precipitation method with the pH 6.0 and 12.0 of mother liquor. All of HA samples then were calcined at 800 °C. The TEM observation illustrated that particle shapes and sizes of HA differed depending on their bovine sources. In addition, XRD and FT-IR results implied that pure HA have been successfully obtained in B-HA group while S-HA with high pH value of 12.0 occurred the phase transformation after thermal treatment.

Keywords

Hydroxyapatite • Chemical reaction • Bovine bone

1 Introduction

HA is an abundant mineral part of human hard tissue with its chemical formula of $\text{Ca}_5(\text{PO}_4)_3(\text{OH})_2$ and molar ratio Ca/P of 1.67 [1, 2]. HA can directly bond with native bone without formation of collagen interface layer, which usually appear in cases of many bio-inert material implantations [3]. Due to these properties, HA has been used for decades as an

alternative biomaterial for bone grafting [4, 5]. In fact, HA can either be synthesized from the chemical reactions or derived from the natural sources [6]. The laboratory synthesized HA can be obtained by using precipitation [7], ultrasonic [8], spray drying [9], sol-gel [10], multiple emulsion [11] and microwave assistant [12]. It is worth noting that the structural and the mechanical properties of synthetic HA can be modified by varying the processing method. However, these synthesis procedures might be complicated because of dependence on many factors such as the starting chemicals, concentration of the initial solution, pH maintenance and synthetic method. About the natural HA, it can be directly taken from common bio-waste sources such as eggshell [13], porcine [14], bovine [15], fish bone [16] by the one of the following methods as thermal decomposition [17], subcritical water process [18] or alkaline hydrolysis [19]. Besides, HA extracted from animal bone could be a non-stoichiometric material due to the presence of other calcium phosphate (CaP) phases or the trace ions such as Na, Mg, and Zn [20, 21].

Therefore, the manufacturing stage of HA from diverse sources and its final powder properties have been investigated as crucial factors to produce the desired biomaterials. There was some evidence that demonstrated the powder properties of nature HA corresponding to the different strains of animals. However, the factors influencing animal physique such as age have not been considered. Consequently, the primary purpose of this research is to compare the HA from different bovine sources in the respective physical and chemical properties such as grain size, morphology, crystallinity, phase stability, and chemical functional groups. The natural HA powders were obtained from fresh femur bones of adult bovine (HA-A), calf (HA-C) and bovine bones bio-waste (HA-W). In addition, the synthetic HA group with influencing factor of varying pH value at 6.0 and 12.0 were also prepared for the comparison.”

N.-T. N. Dang (✉) · H.-P. Le · V. Van Toi · T.-H. Nguyen
Department of Biomedical Engineering, International University,
Vietnam National University- Ho Chi Minh City (VNU-HCMC),
700000 Ho Chi Minh City, Vietnam
e-mail: dangntnhi@gmail.com

2 Materials and Methods

2.1 Materials

Calcium hydroxide ($\text{Ca}(\text{OH})_2$, 98%) and phosphoric acid (H_3PO_4 , 85–87%) was purchased from GuangDong GuangHua Sci-Tech Co., Ltd, China. The fresh femur bones of adult bovine (2–3 years old) and calf (10–12 months old) were collected from a slaughterhouse while the bovine bone bio-waste was from a local animal boneyard

2.2 Methods

Hydroxyapatite synthesized by chemical reaction. S-HA samples were obtained from chemical substances through a 4-step process included stirring, pH adjustment, microwave irradiation and calcination. Firstly, $\text{Ca}(\text{OH})_2$ was mixed with H_3PO_4 at 1.67 of Ca/P ratio to produce a precursor precipitation. Throughout the mixing process for 2 h, the pH of the system was maintained at pH 6.0 and 12.0. After that, these mixtures were placed in a micro-wave at the power of 750 W for 25 min and then calcined at 800 °C for 3 h under ambient condition.

Hydroxyapatite derived from bovine bone. HA was extracted from bovine bone by the same method in the previous research [22]. Briefly, the fresh femur bones were washed and went to the 5-h boiling process in ambient condition and then 2-h boiling process under pressure. The boiling procedure was repeated three times. After that, they

were calcined at 800°C for 3 h. The HA obtained from femur of adult bovine, calf, and waste bone was labeled as HA-A, HA-C, HA-W in turn.

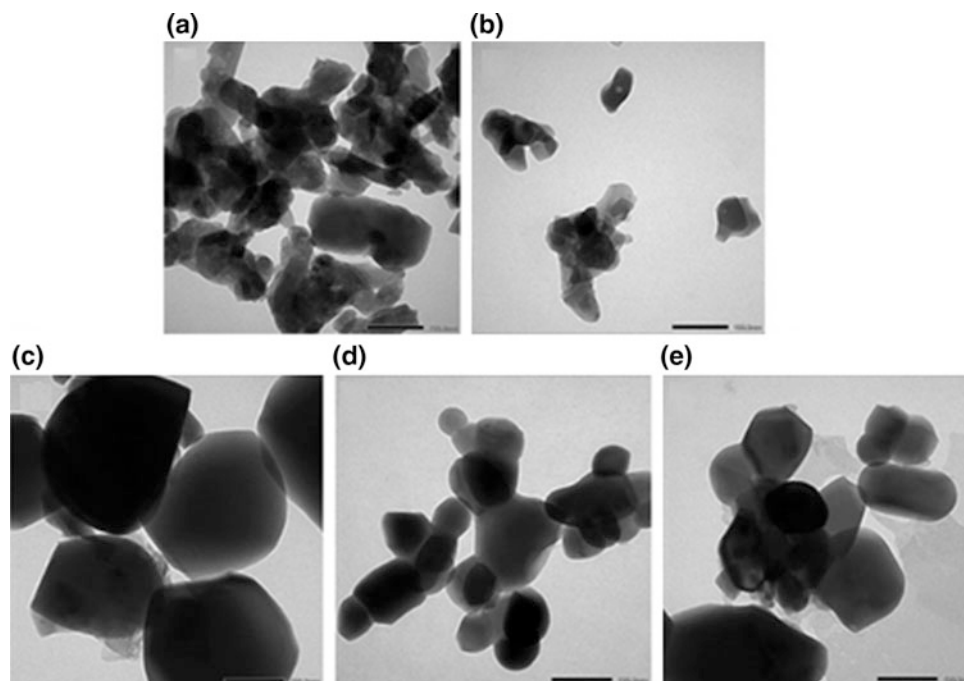
Characterization. Firstly, the morphology and particle size of HA samples were analyzed by transmission electron microscopy (TEM) observation. Then, the crystal structure of each sample was characterized by X-ray diffractometer (XRD). Data were collected over the diffraction angles (2θ) from 20° to 80° with scanning speed of 2°/min. Fourier transform infrared (FT-IR) spectra of the samples were obtained with wave number from 4000 to 400 cm^{-1} .

3 Results and Discussion

In the Fig. 1, the TEM images show the size and morphology of HA particles with the magnification of 50.0 k times. HA at pH 6.0 and 12.0 had non-uniform shape distribution with early high agglomeration by forming neck between HA particles, bonding them together. It was, therefore, difficult to distinguish separate grain and the size of S-HA particles could not temporarily be estimated. In contrast with S-HA group, HA particles in B-HA groups had uniform spherical shape with their diameters varied according to the different bovine sources. In specific, the particle diameters of HA-A, HA-C and HA-W were approximately 200, 100, and 170 nm, respectively.

From these results, they suggested that S-HA would be easy to achieve the interconnection in microstructure under the thermal treatment. About the B-HA, the bovine sources

Fig. 1 TEM images of HA with **a** pH 6.0, **b** pH 12.0, **c** HA-D, **d** HA-C and **e** HA-W at the magnification of 50.0 k times with scale bar of 100.0 nm



clearly had an impact on the calcination behavior such as the grain sizes of HA particles, which required for further investigations. Besides, the uniform spherical shape of HA particles, along with particle size, could be one of the important effect on their interactions with live cells [23].

The successful synthesis of HA from chemical reaction and bovine bone was confirmed by XRD and FT-IR analysis. In Fig. 2, the XRD patterns of all HA samples calcined at 800 °C exhibited in sharp diffraction peaks, indicating a high crystallinity, and well matched with standard peaks of HA (JCDs File No.9-432) [24]. Briefly, the peaks of pure HA at diffraction angles as 2θ of 21°, 25°, 28°, 29°, 31°, 32°, 35°, 36°, 37°, 39°, 40°, 42°, 43°, 45°, 46°, 48°, and 49° were fully showed in the spectra in both S-HA and B-HA. However, those of HA with pH 12.0 appeared strange peaks at the diffraction angle 2θ of 29.2°, 43°, 47.3°, and 48.3°, which suggested the generation of tri-calcium phosphate (TCP) as by-product after the calcination.

In Fig. 3, B-HA presents the FT-IR spectra of chemical functional groups in HA structure, which consists of hydroxyl (OH^-) and phosphate (PO_4^{3-}) band. For the (OH^-) band, two peaks at 3572 cm^{-1} and 631 cm^{-1} represented for hydroxyl stretching mode and vibrational mode (ν_1), respectively. Next, for the PO_4^{3-} group consists of four vibrational modes ν_1 , ν_2 , ν_3 , and ν_4 . In detail, a peak at 954 cm^{-1} represented for ν_1 vibration, a weak peak at 471 cm^{-1} represented for ν_2 vibration, two peaks at 1087 and 1046 cm^{-1} represented for ν_3 vibration, and a set of peaks at 638, 599, and 574 cm^{-1} represented for ν_4 vibration. In addition, the carbonate (CO_3^{2-}) group can also be seen in the infrared spectrum. For ν_2 and ν_3 vibrations of CO_3^{2-} group, a peak at 875 cm^{-1} indicated for ν_2 vibration and two peaks at 1650 and 1300 cm^{-1} indicated for ν_3 vibration [25]. The peak for ν_4 vibration of this group had very low intensity and hence it was not able to be seen.

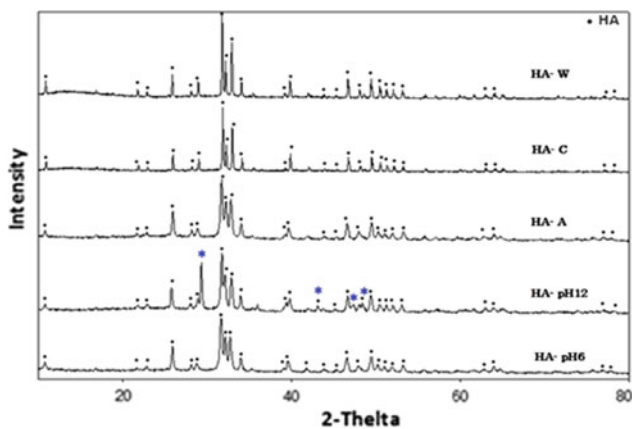


Fig. 2 XRD results of all HA samples. Blue asterisks indicate not HA peaks at the 2θ angles of 29.2°, 43°, 47.3°, and 48.3°

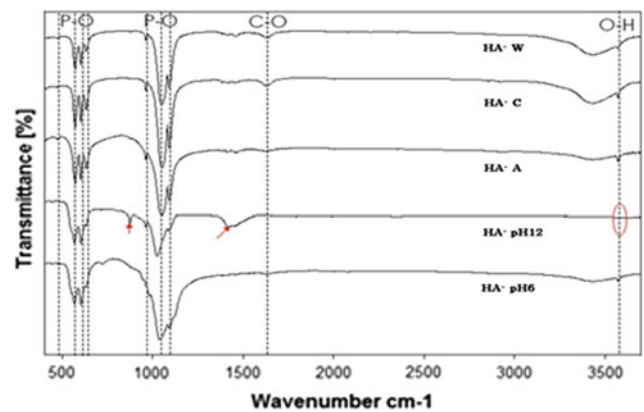


Fig. 3 FTIR results of all HA samples. The red ellipse indicates the lack of hydroxyl band in the spectrum of HA with pH 12.0

Beside the peaks of the main structure of HA but lack of (OH^-) peak at 3572 cm^{-1} as indicated by the red ellipse, the spectrum of HA with pH 12.0 noticeably presented the bands of PO_4^{3-} stretch ν_1 at 960 cm^{-1} and PO_4^{3-} bend ν_3 at 1122 cm^{-1} corresponding to TCP [26].

From the XRD and the FT-IR results, HA derived from bovine bones had no signs of HA phase decomposition into secondary phases such as α -TCP, β -TCP, TTCP or CaO after calcination. In opposition to S-HA, although the temperature of 800 °C had been carefully chosen to transform the precursor precipitation into HA and prevent the appearances of other calcium phosphate (CaP) phases, these results indicated that decomposition into other CaP phrases in S-HA group has still considerably occurred. Thus, this was not in agreement with some reports those had mentioned the decomposition of HA into secondary phases proceeded above 1100 °C [27], thereby suggesting that HA synthesized with high pH is thermodynamically less stable than bovine HA.

4 Conclusion

In this study, the different routes of HA was a critical factor influencing grain size, formation of microstructure and phase stability. Under the heat treatment, TEM images illustrated that S-HA group was accessible to achieve the microstructure by the grain interconnection while HA particles in B-HA group varied their uniform spherical shape according to the different bovine sources. XRD and FI-IR demonstrated that B-HA was beneficial in producing thermally stable phase of stoichiometric HA whereas the phrase decomposition took place in S-HA after calcination below 1000 °C. Thus, these primary results in this study suggest that the unique characterizations of natural and synthetic HA must be significantly considered to achieve the desired HA

properties and the suitable stability sources for biomedical applications.

Acknowledgements This research is funded by International University, Vietnam National University Ho Chi Minh under grant number SV2017-BME-08.

Conflict of Interest The authors declare that they have no conflict of interest.

References

- Suchanek, W., Yoshimura, M.: Processing and properties of hydroxyapatite-based biomaterials for use as hard tissue replacement implants. *J. Mater. Res.* **13**(1), 94–117 (1998)
- Ferraz, M.P., Monteiro, F.J., Manuel, C.M.: Hydroxyapatite nanoparticles: a review of preparation methodologies. *J. Appl. Biomater. Biomech.* **2**(2), 74–80 (2004)
- Ducheyne, P., Radin, S., King, L.: The effect of calcium phosphate ceramic composition and structure on in vitro behavior. *I. Dissolution J. Biomed. Mater. Res. Part A* **27**(1), 25–34 (1993)
- Damien, C.J., Parsons, J.R.: Bone graft and bone graft substitutes: a review of current technology and applications. *J. Appl. Biomater.* **2**(3), 187–208 (1991)
- Suneelkumar, C., Datta, K., Srinivasan, M.R., Kumar, S.T.: Biphasic calcium phosphate in periapical surgery. *J. Conservative Dent. JCD* **11**(2), 92 (2008)
- Sánchez-Salcedo, S., Vila, M., Diaz, A., Acosta, C., Barton, I., Escobar, A., Vallet-Regí, M.: Synthesis of HA/ β -TCP bioceramic foams from natural products. *J. Sol-Gel. Sci. Technol.* **79**(1), 160–166 (2016)
- Mobasherpour, I., Heshajin, M.S., Kazemzadeh, A., Zakeri, M.: Synthesis of nanocrystalline hydroxyapatite by using precipitation method. *J. Alloy. Compd.* **430**(1–2), 330–333 (2007)
- Cao, L.Y., Zhang, C.B., Huang, J.F.: Synthesis of hydroxyapatite nanoparticles in ultrasonic precipitation. *Ceram. Int.* **31**(8), 1041–1044 (2005)
- Bastan, F.E., Erdogan, G., Moskalewicz, T., Ustel, F.: Spray drying of hydroxyapatite powders: The effect of spray drying parameters and heat treatment on the particle size and morphology. *J. Alloy. Compd.* **724**, 586–596 (2017)
- Padmanabhan, S.K., Balakrishnan, A., Chu, M.C., Lee, Y.J., Kim, T.N., Cho, S.J.: Sol-gel synthesis and characterization of hydroxyapatite nanorods. *Particuology* **7**(6), 466–470 (2009)
- Kimura, I.: Synthesis of hydroxyapatite by interfacial reaction in a multiple emulsion. *Adv. Mater. Sci. Eng.* (2007)
- Hassan, M.N., Mahmoud, M.M., El-Fattah, A.A., Kandil, S.: Microwave-assisted preparation of Nano-hydroxyapatite for bone substitutes. *Ceram. Int.* **42**(3), 3725–3744 (2016)
- Sah, M.K., Rath, S.N.: Soluble eggshell membrane: A natural protein to improve the properties of biomaterials used for tissue engineering applications. *Mater. Sci. Eng. C* **67**, 807–821 (2016)
- Qiao, W., Liu, Q., Li, Z., Zhang, H., Chen, Z.: Changes in physicochemical and biological properties of porcine bone derived hydroxyapatite induced by the incorporation of fluoride. *Sci. Technol. Adv. Mater.* **18**(1), 110–121 (2017)
- Niakan, A., Ramesh, S., Ganesan, P., Tan, C.Y., Purbolaksono, J., Chandran, H., Teng, W.D.: Sintering behaviour of natural porous hydroxyapatite derived from bovine bone. *Ceram. Int.* **41**(2), 3024–3029 (2015)
- Sunil, B.R., Jagannatham, M.: Producing hydroxyapatite from fish bones by heat treatment. *Mater. Lett.* **185**, 411–414 (2016)
- Hosseinzadeh, E., Davarpanah, M., Nemati, N. H., Tavakoli, S.A.: Fabrication of a hard tissue replacement using natural hydroxyapatite derived from bovine bones by thermal decomposition method. *Int. J. Org. Transplant. Med.* **5**(1), 23 (2014)
- Barakat, N.A., Khil, M.S., Omran, A.M., Sheikh, F.A., Kim, H.Y.: Extraction of pure natural hydroxyapatite from the bovine bones bio waste by three different methods. *J. Mater. Process. Technol.* **209**(7), 3408–3415 (2009)
- Venkatesan, J., Lowe, B., Manivasagan, P., Kang, K.H., Chalisserry, E.P., Anil, S., Kim, S.K.: Isolation and characterization of nano-hydroxyapatite from salmon fish bone. *Materials* **8**(8), 5426–5439 (2015)
- Akram, M., Ahmed, R., Shakir, I., Ibrahim, W.A.W., Hussain, R.: Extracting hydroxyapatite and its precursors from natural resources. *J. Mater. Sci.* **49**(4), 1461–1475 (2014)
- Rey, C., Combes, C., Drouet, C., Glimcher, M.J.: Bone mineral: update on chemical composition and structure. *Osteoporos. Int.* **20**(6), 1013–1021 (2009)
- Tram, B.N.T., Nguyen, T.H., Van Toi, V.: Synthesis and characterization of hydroxyapatite biomaterials from bio wastes. In: 5th International Conference on Biomedical Engineering in Vietnam pp. 336–338. Springer, Cham (2015)
- Shang, L., Nienhaus, K., Nienhaus, G.U.: Engineered nanoparticles interacting with cells: size matters. *J. Nanobiotechnol.* **12**(5), b26 (2014)
- Rahavi, S.S., Ghaderi, O., Monshi, A., Fathi, M.H.: A comparative study on physicochemical properties of hydroxyapatite powders derived from natural and synthetic sources. *Russ. J. Non-Ferrous Met.* **58**(3), 276–286 (2017)
- Rehman, I., Bonfield, W.: Characterization of hydroxyapatite and carbonated apatite by photo acoustic FTIR spectroscopy. *J. Mater. Sci. - Mater. Med.* **8**(1), 1–4 (1997)
- White, J.M., Goodis, H.: In vitro evaluation of an hydroxyapatite root canal system filling material. *J. Endod.* **17**(11), 561–566 (1991)
- Ramesh, S., Tan, C.Y., Tolouei, R., Amiriyan, M., Purbolaksono, J., Sopyan, I., Teng, W.D.: Sintering behavior of hydroxyapatite prepared from different routes. *Mater. Des.* **34**, 148–154 (2012)

Synthesis of N,O-Carboxymethyl Chitosan-Aldehyde Hyaluronic Acid Hydrogel Loading Silver Nanoparticles

Tien Ngoc-Thuy Nguyen, Dat Tan Nguyen, Vo Van Toi, and Thi-Hiep Nguyen

Abstract

The enormous potential of a hydrogel from Aldehyde Hyaluronic Acid (AHA)—a modification of Hyaluronan, and N,O-Carboxymethyl Chitosan (NOCC)—a polymer derived from Chitosan, has been discussed in our previous study. This research presents two approaches to combine silver nanoparticles (AgNPs) with the hydrogel in order to yield a biogel with higher antimicrobial property. The first one utilized the reaction between reactive aldehyde groups in D-glucuronic acid units of the AHA molecular chain and Tollens' reagent, which is known as silver mirror reaction, while the latter attempted to synthesize NOCC-AHA hydrogel loading AgNPs through thermal decomposition of silver nitrate (AgNO_3) with NOCC and AHA respectively. From primary results, heating a mixture of AgNO_3 -NOCC appeared to attain the best hydrogel in terms of gelation time and elasticity, broadening the application of the hydrogels in the medical field.

Keywords

Chitosan • Hyaluronan • Hydrogel • Silver nanoparticles

1 Introduction

Antibiotic resistance has always been one of the most significant health threats. The reason is apparent as microbes “adapt” to existing antibiotics too fast while the development of new antibiotics takes decades. This problem, however,

has stimulated the attention for metallic drugs, which were used to treat infections before the total dominance of antibiotics [1]. Consequently, many researchers conducted experiments to study thoroughly not only the properties of those metals such as silver (Ag), copper (Cu), zinc (Zn), and magnesium (Mg), but also the application of them in current treatments. Recently, antimicrobial metallic studies have been associated with the term nanoparticles [2–4]. Nanoparticles are defined as particulate dispersions or solid particles that can still have the same properties and transport as the whole entity. Although their sizes range from 1 to 1000 nm, the 1–100 nm scale is preferable with regard to biological interfaces [5]. Silver nanoparticles (AgNPs) are among the most widely investigated nanoparticles in biomedical field because of their antimicrobial activity and therapeutic potential [6, 7]. AgNPs protect the wound and facilitate healing process by promoting the proliferation and migration of keratinocytes, decreasing the collagen formed by fibroblasts, regulating cytokines generation, and effectively preventing fungi and virus [8]. However, like any other drugs, AgNPs only express effectively when there is a loading system stabilizing the structure and controlling the release of AgNPs.

Hydrogel has been considered as one of the major methods to synthesize scaffold for application in wound healing [9]. Excluding the properties of materials used, hydrogel form has many advantages such as the extracellular matrix (ECM) resembling structure and composition, filling properties, and even being able to act as a physical loading system. In our previous study, synthesis of the hydrogel from Hyaluronic Acid (HA) and Chitosan (Cs) has been introduced [10]. HA, a major component of the skin ECM, possesses essential position in wound reconstruction and various medical applications [11]. Chitosan, the deacetylated derivative of chitin, has the properties of biocompatibility, biodegradability and antibacterial activity which are widely used in drug delivery, gene therapy, as well as tissue engineering [12]. However, HA exhibits rapid erosion and degradation whereas Cs displays poor solubility in

T. N.-T. Nguyen · D. T. Nguyen · V. Van Toi · T.-H. Nguyen (✉)

Department of Biomedical Engineering, International University, Vietnam National University - Ho Chi Minh City (VNU-HCMC), Ho Chi Minh City, 700000, Vietnam
e-mail: nthiep1981@gmail.com

T. N.-T. Nguyen
e-mail: nnt0001@gmail.com

physiological solvents. By introducing carboxymethyl groups to the N, O-position of chitosan (NOCC) to solubilize it, and by cleaving carbon-carbon bonds of the cisdiol group of HA to create aldehyde groups (AHA), a hydrogel can be formed via Schiff's base linkage between the amino groups in NOCC solution and aldehyde groups in AHA solution [10]. On the other hand, Cs and HA are proven to be both stabilizers of the silver colloidal solution and reducing agents [13–21], which means that the hydrogel is a potential loading system of AgNPs.

Chemical reduction is the most common way to synthesize AgNPs [22]. Tollens' reagent, which consists of silver nitrate (AgNO_3) and ammonia solution (NH_3), was an oxidizing agent well known for its silver mirror reaction with aldehyde groups. It is shown in previous studies that this reagent can be utilized to synthesize AgNPs [22–25]. The reactive aldehyde groups in D-glucuronic acid units of the AHA reduce Ag^+ ion to form AgNPs. However, these aldehyde groups also greatly contribute to the formation of hydrogel. Therefore, in this experiment, AHA with the highest theoretical oxidation rate (50%) available in the laboratory was used. Furthermore, NOCC and AHA are expected to maintain their origins' critical properties in high temperature. Therefore, thermal decomposition of AgNO_3 is considered a possible method.

In brief, the combination of AgNPs and the NOCC–AHA hydrogel probably yields a more suitable biomaterial with desirable properties for wound healing application. This study demonstrates two methods that were attempted to synthesize NOCC–AHA hydrogel loading AgNPs and their results, including evaluation of the gelation time and its elasticity.

2 Materials and Method

2.1 Materials

Chitosan (>75% deacetylated), hyaluronan and silver nitrate (99%) were obtained from Sigma (USA). Dialysis membrane (Spectra/Por 4, Standard RC Tubing, WCO: 12–14 kDa) was from Spectrum Laboratories, Inc., United States.

Chloroacetic acid was bought from HiMedia Laboratories Pvt. Ltd., India. Sodium periodate, ethylene glycol, isopropyl alcohol, ethanol, sodium hydroxide, hydrochloric acid, ammonia solution (25%) were from Xilong Chemical Co., Ltd., China.

2.2 Synthesis of AHA and NOCC

AHA was synthesized with trivial modifications from our previous research [10]. HA 1% was prepared by adding

0.4 g HA into 40 mL distilled. Then, 0.084 and 0.105 g NaIO_4 in 2 mL distilled water were added dropwise to HA solution respectively to create 40 (AHA40) and 50 (AHA50) oxidation degrees. After 2 h, 0.2 mL ethylene glycol was added and the mixture was stirred for another hour before being dialyzed using dialysis bag (MWCO 10,000) against distilled water for 3 days. The water was changed 3 times per day. The solution was then kept at -80°C overnight before being freeze dried to obtain the final product.

NOCC was synthesized with slight changes. First, Cs was dissolved in 10 mL isopropanol and 10 mL of NaOH 13 M was added. The mixture was kept stirring for 1 h before being supplemented with 5.2 g chloroacetic acid in 10 mL isopropanol. The mixture was stirred for 3 h at 60°C . The obtained solid was rinsed 3 times with 80% (v/v) ethanol/water and dissolved in 67 mL distilled water to form a homogenous solution. Later, pH value of the solution was slowly adjusted by HCl 2.5 M until it reached 7.5. The resulting solution was undergone dialysis process using dialysis bag (MWCO 10,000) against distilled water for 3 days. The water was changed 3 times per day. The solution was kept at -80°C overnight before being freeze-dried to obtain the final product.

AHA samples were stored at -20°C , while NOCC samples were placed in vacuum at room temperature.

2.3 Synthesis of AHA/Ag by Silver Mirror Reaction

First, 50 mg of AHA50 was dissolved in 5 mL of distilled water. Then, 66.67 μL of AgNO_3 0.1% solution was mixed carefully with 50 μL of NH_3 25% solution in 5 min before adding to the prepared AHA solution. The final solution was stirred for another 5 min and let stand afterward. After 24 h, the solution turned into a light yellow color which marks the existence of AgNPs. It was then stored at -80°C to prepare for the lyophilization. After lyophilization, the residual NH_3 was completely removed and the sample was stored in vacuum oven at room temperature.

2.4 Synthesis of AHA/Ag and NOCC/Ag by Thermal Decomposition

For AHA/Ag synthesis, first 66.67 μL of AgNO_3 0.1% solution was added into 5 mL of AHA (10 mg/mL) solution. The solution was vigorously stirred in the dark for 30 min at room temperature, then it was kept stirring at 60°C for 30 min.

For NOCC/Ag synthesis, briefly, 133.34 μL of AgNO_3 0.1% was added into 10 mL of NOCC (10 mg/mL). The solution was vigorously stirred in the dark for 30 min in

room temperature, then, it was divided into two parts: (1) 56 μL of NaOH 0.028% was added into the solution and (2) nothing was added into the solution. After that, the temperature of both samples was raised to 60 $^{\circ}\text{C}$ and kept stirring for 8 h. The control solution was the mixture of 5 mL of distilled water and 66.67 μL of AgNO_3 0.1%.

3 Results and Discussion

The color of AHA/Ag solution after the silver mirror reaction became light yellow, which proves that there was a reaction (Fig. 1). Noticeably, when AHA/Ag was dissolved in distilled water, the solution was opaque and light yellow, however, when it was dissolved in normal saline, the solution was cloudy. This is because the AgNPs were unstable in normal saline and they aggregate together. The instability of AgNPs causing by the presence of electrolytes is one major obstacle needing to avoid [14]. The AHA/Ag sample solution was stirred with 0.5 mL of NOCC solution to form hydrogel. However, the hydrogels were more like a cloudy viscous solution with darker yellow color. This may be due to the lack of aldehyde groups in AHA/Ag making the Schiff's base linkage in the hydrogels weaker.

For thermal decomposition experiment, the AHA/Ag solution changed from crystal clear color to muddy form with no sign of yellow color at the end of the process. This suggests that the molecular weight of AHA may have decreased and its properties may have changed with respect to its origin HA, which is the main reason led to the failure of silver reduction.

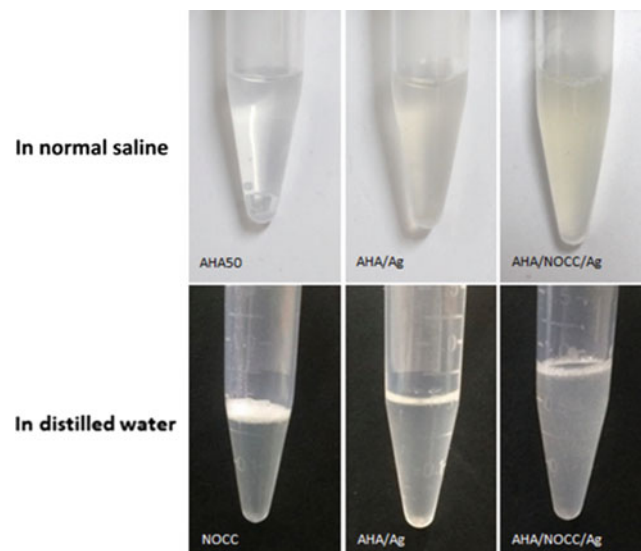


Fig. 1 The difference between samples while they were dissolved in normal saline and in distilled water

NaOH was used as a reagent as a factor to make sure that AgNO_3 reacted thoroughly with NOCC. Because the original NOCC solution has light yellow color, reaction indication needs a control to compare. Hence, a solution of distilled water and AgNO_3 served as a control. After the reaction, both NOCC/Ag samples were muddy light yellow, while the indicator solutions turned into light transparent yellow with tiny small yellow dust on their surface. This again proves the role of NOCC as a stabilizer for AgNPs and as a reducing agent in the reaction. After being freeze-dried, the samples showed no difference in color or texture, which could be observed in Fig. 2. The samples were then dissolved in 0.5 mL normal saline with concentration 30 mg/mL, and finally mixed with AHA40 and AHA50 solution (30 mg/mL with normal saline as a solvent) to form hydrogel with volume ratio 1:1 (Fig. 3.).

The properties of the hydrogels were summarized in Table 1. The desired hydrogel requires clear color, low gelation time and a soft to little hard texture, therefore, the sample AHA50/NOCC/Ag(2) appeared to be the best out of the four samples.

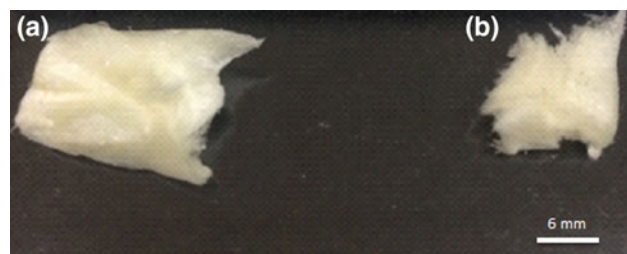


Fig. 2 Samples after being freeze-dried: a NOCC/Ag with NaOH and b NOCC/Ag without NaOH

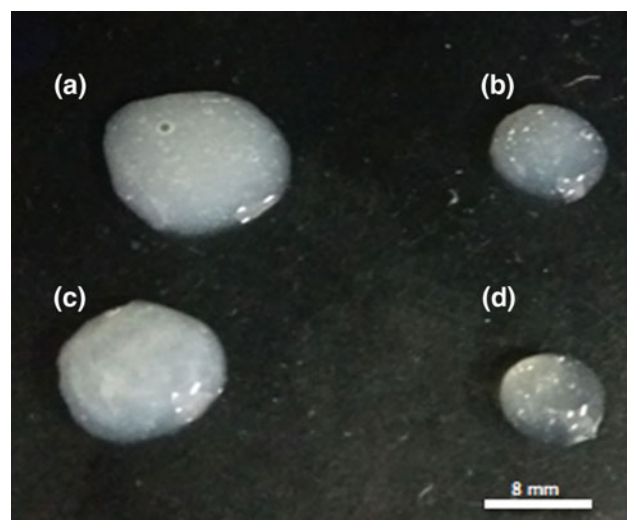


Fig. 3 Hydrogels made from AHA and NOCC/Ag samples: a AHA40/NOCC/Ag(1). b AHA40/NOCC/Ag(2). c AHA50/NOCC/Ag(1). d AHA50/NOCC/Ag(2)

Table 1 Properties of the hydrogels from NOCC/Ag samples

Samples	Gelation time (s)	Elasticity
AHA40/NOCC/Ag(1)	47	Too low
AHA40/NOCC/Ag(2)	41	Moderate
AHA50/NOCC/Ag(1)	74	Low
AHA50/NOCC/Ag(2)	42	Moderate

4 Conclusion

The study introduced two approaches to combine NOCC/AHA hydrogel and AgNPs: the first one was via Tollens' reagent and the other employed thermal decomposition. Early results showed succession in merging the two materials, which opened up a path for an application of AgNPs and NOCC/AHA hydrogel in wound healing applications.

Acknowledgements This research is funded by Vietnam National University HoChiMinh City (VNU-HCM) under grant number C2018-28-02.

Conflict of Interest The authors declare that they have no conflict of interest.

References

- Zheng, K., et al.: Antimicrobial silver nanomaterials. *Coord. Chem. Rev.* **357**, 1–17 (2018)
- Nhi, T.T., et al.: Fabrication of electrospun polycaprolactone coated with chitosan-silver nanoparticles membranes for wound dressing applications. *J. Mater. Sci. Mater. Med.* **27**(10), 156 (2016)
- Nguyen, T.-H., Lee, K.-H., Lee, B.-T.: Fabrication of Ag nanoparticles dispersed in PVA nanowire mats by microwave irradiation and electro-spinning. *Mater. Sci. Eng. C* **30**(7), 944–950 (2010)
- Nguyen, T.H., et al.: Nano Ag loaded PVA nano-fibrous mats for skin applications. *J. Biomed. Mater. Res. B Appl. Biomater.* **96**(2), 225–233 (2011)
- Shah, J.N., Shah, A.P., Shah, H.J., Vijaykumar B. Sutariya.: *Biointeractions of Nanomaterials*, p. 73 (2014)
- Wei, L., et al.: Silver nanoparticles: synthesis, properties, and therapeutic applications. *Drug Discovery Today* **20**(5), 595–601 (2015)
- Caruso, G., Merlo, L., Caffo, M.: Nanoparticles potential: types, mechanisms of action, actual in vitro and animal studies, recent patents. pp. 53–150 (2014)
- Naidu Krishna, S., Govender, P., Adam, J.K.: Nano silver particles in biomedical and clinical applications. (2015)
- Naahidi, S., et al.: Biocompatibility of hydrogel-based scaffolds for tissue engineering applications. *Biotechnol. Adv.* **35**(5), 530–544 (2017)
- Nguyen, N.T.-P., et al.: Synthesis of Cross-Linking Chitosan-Hyaluronic Acid Based Hydrogels for Tissue Engineering Applications. **63**, 671–675 (2018)
- Ferguson, E.L., et al.: Evaluation of the physical and biological properties of hyaluronan and hyaluronan fragments. *Int. J. Pharm.* **420**(1), 84–92 (2011)
- Mohandas, A., et al.: Chitosan-hyaluronic acid/VEGF loaded fibrin nanoparticles composite sponges for enhancing angiogenesis in wounds. *Colloids Surf. B Biointerfaces* **127**, 105–113 (2015)
- Khachatryan, G., et al.: Formation and properties of hyaluronan/nano Ag and hyaluronan-lecithin/nano Ag films. *Carbohydr. Polym.* **151**, 452–457 (2016)
- Kemp, M.M., et al.: Hyaluronan- and heparin-reduced silver nanoparticles with antimicrobial properties. *Nanomedicine (Lond)* **4**(4), 421–429 (2009)
- Abdel-Mohsen, A.M., et al.: A novel in situ silver/hyaluronan bio-nanocomposite fabrics for wound and chronic ulcer dressing: in vitro and in vivo evaluations. *Int. J. Pharm.* **520**(1–2), 241–253 (2017)
- Abdel-Mohsen, A.M., et al.: Green synthesis of hyaluronan fibers with silver nanoparticles. *Carbohydr. Polym.* **89**(2), 411–422 (2012)
- Xia, N., et al.: Green synthesis of silver nanoparticles by chemical reduction with hyaluronan. *Carbohydr. Polym.* **86**(2), 956–961 (2011)
- Khalil, A.M., et al.: Synthesis, Characterization, and Evaluation of Antimicrobial Activities of Chitosan and Carboxymethyl Chitosan Schiff-Base/Silver Nanoparticles. *J. Chem.* **2017**, 1–11 (2017)
- Modrzejewska, Z., Zarzycki, R., Sielski, J.: Synthesis of silver nanoparticles in a chitosan solution. *Prog. Chem. Appl. chitin* **15**, 63–72 (2010)
- Abdelgawad, A.M., Hudson, S.M., Rojas, O.J.: Antimicrobial wound dressing nanofiber mats from multicomponent (chitosan/silver-NPs/polyvinyl alcohol) systems. *Carbohydr. Polym.* **100**, 166–178 (2014)
- Lu, B., et al.: In situ reduction of silver nanoparticles by chitosan-l-glutamic acid/hyaluronic acid: Enhancing antimicrobial and wound-healing activity. *Carbohydr. Polym.* **173**, 556–565 (2017)
- Iravani, S., et al.: Synthesis of silver nanoparticles: chemical, physical and biological methods. *Res. Pharm. Sci.* **9**(6), 385 (2014)
- Kienskaya, K.I., et al.: Synthesis of silver metal nanodispersions using tollens reagent. *Colloid J.* **73**(2), 294–295 (2011)
- Li, X., et al.: Facile synthesis of silver nanoparticles with high concentration via a CTAB-induced silver mirror reaction. *Colloids Surf. A* **400**, 73–79 (2012)
- Al-Muhanna, M.K.A., et al.: Preparation of stable sols of silver nanoparticles in aqueous pectin solutions and properties of the sols. *Colloid J.* **77**(6), 677–684 (2015)

Part IV

Nanomedicine and Drug Delivery Systems

Redox Polymeric Nanoparticle as an Effective Oral Nanotherapeutics for Inflammatory Bowel Disease and Cancer

Long Binh Vong and Yukio Nagasaki

Abstract

Excess generation of reactive oxygen species (ROS) in colonic mucosa of patients with ulcerative colitis (UC), a type of inflammatory bowel disease, causes the inflammation, risk of colitis-associated colon cancer (CAC), and drug resistance. Oral administration is more convenient for patients; however, current medications for UC are not effective due to instability in the gastrointestinal (GI) tract, non-specific distribution, and adverse effects. To address these issues, we have developed novel oral redox nanoparticles (RNP), which was prepared by self-assembly of an amphiphilic block copolymer with stable nitroxide radicals, ROS scavengers, in a hydrophobic segment as a side chain via an ether linkage. After oral administration, RNP highly accumulated in colon region, and specifically diffused into colonic mucosa of inflamed sites. Orally administered RNP effectively scavenged overproduced ROS in the inflamed colon, resulting in suppression of inflammation in mice model of colitis. Interestingly, when anticancer drug irinotecan (Iri) was administered in combination with RNP, a remarkable suppression of tumor growth was observed in CAC model mice treated with combination compared to mice treated with Iri alone. Iri-induced adverse effects, such as diarrhea and GI inflammation, were remarkably reduced by RNP treatment. Toxicity evaluation on

zebrafish embryos showed that TEMPOL induces severe mitochondrial dysfunction, leading to the death of all zebrafish embryos while RNP did not cause mitochondrial dysfunction in zebrafish embryos, and no zebrafish death was observed, indicating that RNP did not disturb intracellular redox balance. RNP is a promising nanotherapeutics for treatment of UC and other ROS-related diseases.

Keywords

Redox nanoparticles • Oral drug delivery • Ulcerative colitis • Reactive oxygen species

1 Introduction

Excessive generation of reactive oxygen species (ROS) is strongly related to gastrointestinal (GI) disorders including inflammatory bowel disease (IBD) and cancer [1]. In fact, oxidative stress has been proposed as a critical mechanism underlying pathophysiology of IBD and number of antioxidants/free radical scavengers have been studied exhibiting therapeutic efficacies in animal models of IBD to some extent [2, 3]. Although oral drug administration route is preferable for patients, the use of low-molecular-weight (LMW) drugs is limited due to low stability, non-specific distribution in GI tract, and causing undesired adverse effects. Nanomedicine has recently developed as promising drug carriers; however, these nanocarriers themselves often cause toxic adverse effects. In this study, we have developed a novel redox nanoparticle (RNP) prepared by self-assembly of an amphiphilic block copolymer possessing stable nitroxide radical TEMPO, an ROS scavenger (Fig. 1), as an oral nanotherapeutics for treatment of GI disorders [4, 5].

L. B. Vong (✉) · Y. Nagasaki
Department of Biochemistry, Faculty of Biology and Biotechnology, University of Science, Vietnam National University Ho Chi Minh city (VNU-HCM), Ho Chi Minh, Vietnam
e-mail: vblong@hcmus.edu.vn

L. B. Vong
Department of Materials Science, Graduate School of Pure and Applied Sciences, University of Tsukuba, Tsukuba, Japan

Present Address:

L. B. Vong · Y. Nagasaki
Department of Biomedical Engineering, International University, Vietnam National University Ho Chi Minh City, Ho Chi Minh, Vietnam

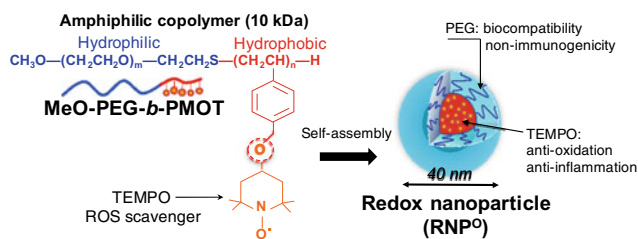


Fig. 1 Design of redox nanoparticles (RNP). (Adopted by Ref. 7)

2 Methods

RNP was prepared by self-assembly of methoxy-poly(ethylene glycol)-*b*-poly(4-[2,2,6,6-tetramethylpiperidine-1-oxyl]oxymethylstyrene) (MeO-PEG-*b*-PMOT), which is an amphiphilic block copolymer with stable nitroxide radicals in a hydrophobic segment as a side chain via an ether linkage (Fig. 1). Cellular uptake of RNP *in vitro/in vivo* and its accumulation in colon were determined using rhodamine-labeled RNP by fluorescent microscope and electron spin resonance. Therapeutic efficacy of RNP was evaluated using dextran sodium sulfate (DSS)-induced colitis and azoxymethane (AOM) combining DSS-induced CAC model in mice.

3 Results and Discussion

The size of RNP is approximately 40 nm in diameter with high colloidal stability owing to the poly(ethylene glycol) (PEG) shell layer maintaining the micelle form and ROS scavenging activity under physiological and GI environments without their aggregation. To evaluate the accumulation of nanoparticles in colon, we firstly investigated the size-dependent character using different sizes of commercially available polystyrene latex particles and found the size-dependent accumulation in colon, in which polystyrene latex particles with 40 and 100 nm in size accumulated higher than large-sized particles (0.5 and 1 μm) [5]. Interestingly, a considerable high accumulation of RNP in colon was observed, as compared to TEMPOL and polystyrene latex particles, even though the same size (40 nm) due to high stability of RNP in GI tract (Fig. 2). Importantly, we did not observe the uptake of RNP into the bloodstream, preventing the side effects of nitroxide radical to entire body. Since orally administered RNP remarkably accumulated in the colonic mucosa of mice and was not absorbed into the bloodstream, it is anticipated to be an ideal nanomedicine for treatment of ulcerative colitis (UC), which is well-known as main type of IBD. Alternatively, we found that orally administered RNP tended to accumulate in inflamed colon of

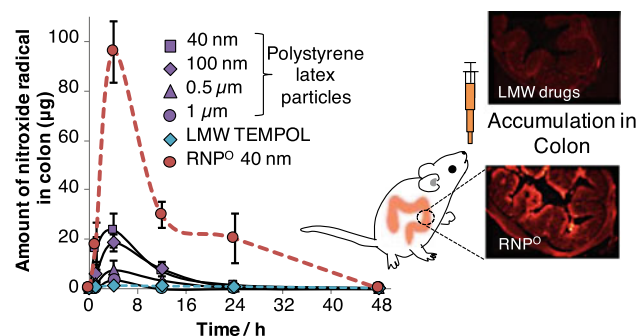


Fig. 2 Accumulation of RNP and polystyrene latex particles with different sizes in colon mucosa after oral administration. (Adopted by Ref. 5)

DSS-induced colitis mice, resulting in an effective ROS scavenging in colonic mucosa of colitis mice. As compared to LMW TEMPOL and mesalamine, a commercially available drug for UC treatment, the mice treated with RNP significantly suppressed the pro-inflammatory mediators in the colon and improved survival rate in colitis mice [5, 6].

We next confirmed the efficacy of RNP on colon cancer model mice chemically induced by AOM and DSS. Although anticancer efficacy was not observed at low dose treatments (1 and 2 mg/mL of free drinking), the mice given higher dose of RNP (5 mg/mL) for a month had slightly reduced tumor scores compared to AOM/DSS-treated mice. Since overproduced ROS is reported to induce anticancer drug resistance and RNP clearly suppressed ROS/inflammation around tumor microenvironment, a combination treatment with RNP and conventional cancer drugs is a robust strategy. Therefore, when an anticancer drug Irinotecan (Iri) was administered in combination with free drinking RNP, a remarkable suppression of tumor growth was observed in mice treated with combination compared to mice treated with Iri alone (Fig. 3) [7]. It should be noticed that the Iri-induced adverse effects, such as diarrhea and GI toxicity, were remarkably reduced in RNP-treated mice (Fig. 3). These results indicate that oral administration of RNP^o not only significantly enhances the anticancer efficacy

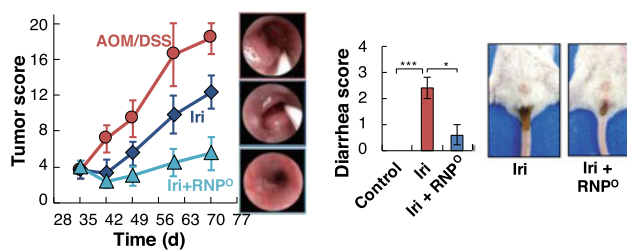


Fig. 3 Combination therapy of RNP and Irinotecan in colitis-associated colon cancer mice. (Adopted by Ref. 7)

of Iri against colon cancer development, but also effectively suppresses the severe adverse effects of Iri. In another study, combinative therapy of RNP and conventional drug, Doxorubicin (Dox) showed that RNP enhanced the uptake of Dox in the cancer cells, significantly improved chemotherapeutic effect of Dox and suppressing the Dox-induced cardiotoxicity in the colon cancer model mice [8].

Eventually, the adequate assessment of toxicity and safety of our nanotherapeutics must be addressed for pre-clinical and clinical applications. In fact, there were no noticeable toxicities in tissues from the GI tract, hematology and other organs, even in mice treated with a high concentration (5 mg/mL) of free drinking RNP for a month [7]. On the other hand, orally administered RNP did not change the population of intestinal microbiota [9]. Alternatively, the zebrafish (*Danio rerio*) has been widely utilized as a correlative and predictive model for evaluation of nanoparticle toxicity for the past decades. Therefore, we also utilized this zebrafish embryo model to confirm the toxicity of RNP and compared to LMW TEMPOL and control polymeric nanoparticle without ROS scavenging character. The results showed that all zebrafish was died after few days treatment with TEMPOL (3 mM dose) or control polymeric nanoparticle, while no zebrafish death was observed by treatment with RNP under even high concentrations (30 mM), indicating an extremely low toxicity of RNP [10]. It is important to note that almost all mitochondria were damaged for the LMW TEMPOL treatment, while no damage was observed for RNP treatment, indicating a protection of healthy mitochondria is one of important mechanism for our nanoparticle antioxidant [10].

4 Conclusions

In summary, in this study we have developed an oral redox nanotherapeutics to specifically scavenge ROS in diseased tissues, particularly in inflamed and cancer tissues in GI tract. Based on the obtained results, RNP is a promising and

safe nanomedicine for treating not only GI disorders but also other ROS-related diseases.

Acknowledgements Author would like to express his sincere appreciation to Prof. Nagasaki Yukio (University of Tsukuba) and all collaborators for their supports and valuable advices, and funding from Japan Society for the Promotion of Science (JSPS) for Young Scientist. This work was also partly supported by Vietnam National Foundation for Science and Technology Development (NAFOSTED under Grant number 108.05-2017.327 to L.B. Vong). **Conflict of Interest** The authors declare that they have no conflict of interest.

References

1. Khor, B., Gardet, A., Xavier, R.J.: Genetics and pathogenesis of inflammatory bowel disease. *Nature* **474**, 307–317 (2011)
2. Coussens, L.M., Werb, Z.: Inflammation and cancer. *Nature* **420**, 860–867 (2002)
3. Cui, X., Jin, Y., Hofseth, A.B., Pena, E., et al.: Resveratrol suppresses colitis and colon cancer associated with colitis. *Cancer Prev. Res.* **3**, 549–559 (2010)
4. Yoshitomi, T., Hirayama, A., Nagasaki, Y.: The ROS scavenging and renal protective effects of pH-responsive nitroxide radical-containing nanoparticles. *Biomaterials* **32**, 8021–8028 (2011)
5. Vong, L.B., Tomita, T., Yoshitomi, T., Matsui, H., Nagasaki, Y.: An orally administered redox nanoparticle that accumulates in the colonic mucosa and reduces colitis in mice. *Gastroenterology* **143**, 1027–1036 (2012)
6. Vong, L.B., Mo, J., Abrahamsson, B., Nagasaki, Y.: Specific accumulation of orally administered redox nanotherapeutics in the inflamed colon reducing inflammation with dose-response efficacy. *J. Controlled Release* **201**, 19–25 (2015)
7. Vong, L.B., Yoshitomi, T., Matsui, H., Nagasaki, Y.: Development of an oral nanotherapeutics using redox nanoparticles for treatment of colitis-associated colon cancer. *Biomaterials* **55**, 54–63 (2015)
8. Vong, L.B., Nagasaki, Y.: Combination treatment of murine colon cancer with doxorubicin and redox nanoparticles. *Mol. Pharm.* **13**, 449–455 (2016)
9. Vong, L.B., Yoshitomi, T., Morikawa, K., Saito, S., et al.: Oral nanotherapeutics: Effect of redox nanoparticle on microflora in mice with dextran sodium sulfate-induced colitis. *J. Gastroenterol.* **49**, 806–813 (2014)
10. Vong, L.B., Kobayashi, M., Nagasaki, Y.: Evaluation of the toxicity and antioxidant activity of redox nanoparticles in zebrafish (*Danio rerio*) embryos. *Mol. Pharm.* **13**, 3091–3097 (2016)

Preparation and Characterization of Redox-Sensitive Pluronic F127-Based Nanogel as Effective Nanocarrier for Drug Delivery

Diem Huong Tran Nguyen, Dong Yen Pham Nguyen, Linh Phuong Tran Pham, Thanh Nguyet Nguyen Vo, Dai Hai Nguyen, and Ki Dong Park

Abstract

An emerging approach in development of nanocarriers for the delivery of hydrophobic anticancer drugs has recently been paid much attention. In this study, a redox-sensitive Heparin-ss-Pluronic F127 (Hep-ss-Plu127) nanogel was fabricated for paclitaxel (PTX) delivery. In the synthetic process, Plu127 was mono-activated by 4-Nitrophenyl chloroformate (NPC) and conjugated with Hep via redox-sensitive disulfide bond of cystamine. The chemical structure of the resulting product was characterized by fourier transform infrared (FTIR) and proton nuclear magnetic resonance ($^1\text{H-NMR}$) spectroscopy. The PTX-loaded Hep-ss-Plu127 nanogels were formed by solvent dialysis method and showed the hydrodynamic diameter of 91.4 ± 0.3 nm, determined by dynamic light scattering (DLS) instrument. Size and morphology of PTX-loaded Hep-ss-Plu127 nanogels were shown to be 104 nm and spherical in shape by transmission electron microscopy (TEM). In addition, PTX was effectively encapsulated into Hep-ss-Plu127 nanogels, which was around $66.2 \pm 4.7\%$ for drug loading efficiency and $13.2 \pm 0.9\%$ for drug loading content, determined by

high performance liquid chromatography (HPLC). Overall, the redox-sensitive Pluronic F127-based nanogel was successfully synthesized and could be an effective nanocarrier that holds a great potential to enhance the redox responsiveness and efficacy for the delivery of PTX in cancer treatment.

Keywords

Pluronic F127 • Heparin • Redox-sensitive nanogel • Paclitaxel • Delivery system

1 Introduction

Paclitaxel (PTX) is one of the most outstanding chemotherapeutic drugs having been extensively used to treat a broad range of tumor types including breast, ovarian, lung, colon cancer, etc. [1, 2]. However, its use in cancer treatment is restricted due to its poor water solubility and low therapeutic index. Many adverse effects such as hair loss, nausea, neurotoxicity, nephrotoxicity, ocular toxicity, and hemolysis have been observed in clinic when using currently commercial PTX formulation [3]. Thus, the development of drug delivery systems (DDSs) with the ability to overcome these limitations is necessary.

Among various nanosized-DDSs, nanogels are promising carriers for hydrophobic therapeutic agent delivery, such as PTX, thanks to their low toxicity and ability to improve the solubility and therapeutic index of the loaded drug. These advantages of nanogels are based on the relatively high drug loading capacity, great colloidal stability, high cellular uptake efficiency, and the ability to escape the entrapment of reticuloendothelial system [4, 5]. Moreover, their size range is also suitable for intracellular delivery and cancer chemotherapy by facilitating the passive accumulation of drug within tumor site through enhanced permeation and retention (EPR) effect, hence reduces side effects of drug [6, 7].

D. H. T. Nguyen · D. Y. P. Nguyen · D. H. Nguyen (✉)
Institute of Applied Materials Science, Vietnam Academy of Science and Technology, Ho Chi Minh City, Vietnam
e-mail: nguyendaihai0511@gmail.com

D. Y. P. Nguyen · D. H. Nguyen
Vietnam Academy of Science and Technology, Graduate University of Science and Technology, Hanoi, Vietnam

K. D. Park
Department of Molecular Science and Technology, Ajou University, 5 Woncheon, Yeoungtong, Suwon, Korea
e-mail: kdp@ajou.ac.kr

D. H. T. Nguyen · L. P. T. Pham
Department of Biotechnology, International University-Vietnam National University, Ho Chi Minh City, Vietnam

T. N. N. Vo
Faculty of Applied Sciences, Ton Duc Thang University, Ho Chi Minh City, Vietnam

Pluronic F127, an amphiphilic tri-block copolymer of polyethylene oxide (PEO) and polypropylene oxide (PPO), has been well-utilized as formulated material for DDSs. The hydrophobic PPO is capable of incorporating hydrophobic drugs and protecting them from degradation while the hydrophilic PEO benefits their solubilizing capacity to better stabilize and improve the retention time of drug in the circulatory system [4]. Besides, heparin is known for the ability to self-assemble into nanoparticles for the effective delivery of anticancer drugs. It is able to improve the drug bioactivity via intra- and extra-cellular interaction and prolong the circulation time by hindering complement activation and suppressing phagocytosis [6, 8].

In present work, redox-sensitive Hep-ss-Plu127 nanogels, in which Pluronic F127 was mono-activated and then grafted onto heparin via redox-sensitive disulfide bond of cystamine, were developed for effective PTX delivery. Notably, disulfide linkages are selectively cleaved under the reductive condition of cytoplasm, which contains higher concentration of a reducing agent called glutathione (GSH) [9, 10]. Therefore, disulfide linkage-containing nanogels would facilitate the site-specific delivery of anticancer drugs only when the drugs are uptaken by tumor cells. The characteristics of Hep-ss-Plu127 nanogels including chemical structure, size, morphology, redox sensitivity, and drug loading efficacy were examined in this study.

2 Materials and Methods

2.1 Materials

Pluronic F127 (Plu127) and cystamine (Cys) were purchased from Sigma (USA). Heparin (Hep) was purchased from TCI (Japan). 4-Nitrophenyl chloroformate (NPC), 3-amino-1-propanol, and ethyl-3-(3-dimethylaminopropyl) carbodiimide (EDC) were purchased from Acros Organics (Belgium). Tetrahydrofuran (THF) and triethylamine (TEA) were obtained from Scharlau (Sentmenat, Spain). Diethyl ether was received from Fisher Scientific (Houston, TX). Dimethyl sulfoxide (DMSO) was purchased from VWR (USA). Paclitaxel was received from Samyang Corporation (Korea). All reagents and solvents were used as received without further purification.

2.2 Preparation of Hep-Ss-Plu127

Hep-ss-Plu127 was prepared through three steps, in which Plu127 was mono-activating using NPC and then was conjugated with Cys to obtain Plu127-Cys (Plu-Cys), followed by the coupling of carboxyl groups of Hep with amino groups of Plu-Cys. Briefly, a mixture of Plu127 (5 g) and

NPC (0.18 g), in a three-necked flask, was molten and stirred at 65 °C for 5 h under nitrogen atmosphere with HCl entrapment equipment. To solubilize the mixture, 10 ml of THF was added after the mixture was cooled out to 40 °C. The reaction was maintained overnight at room temperature. After that, 30 µL of 3-amino-1-propanol was added; then the reaction mixture was stirred for another 5 h. The resulting solution was precipitated by diethyl ether, filtered and dried under vacuum to obtain the powdery mono-activated Plu127.

To obtain Plu-Cys conjugate, Cys (0.1 g) and TEA (130 µL) was dissolved completely in DMSO at room temperature and mixed with the mono-activated Plu127 (5 g) solution. The mixture was kept under stirring for 24 h, then precipitated in diethyl ether and dried under vacuum to give Plu-Cys.

For the preparation of Hep-ss-Plu127, 0.1 g of Hep was prepared in distilled water, followed by immediate addition of 0.02 g EDC. Thereafter, Plu-Cys solution was added to Hep solution in drop-wise manner. The reaction was carried out at room temperature for 24 h under constant stirring. Then, the solution was dialyzed against distilled water with dialysis membrane (MWCO 12–14 kDa, Spectrum Laboratories, Inc., USA) before freeze-drying to obtain Hep-ss-Plu127 copolymer.

2.3 Preparation of PTX-Loaded Hep-Ss-Plu127 Nanogels

To Hep-ss-Plu127 (50 mg) dissolved in deH₂O, PTX (10 mg) dissolved in methanol was added. Subsequently, the mixture was stirred and dialyzed (dialysis membrane MWCO 3.5 kDa) to remove un-loaded PTX, then lyophilized to obtain PTX-loaded Hep-ss-Plu127 nanogels. Drug loading efficiency (DLE) and drug loading content (DLC) were measured using HPLC system (PerkinElmer, US) and presented by the following equations:

$$\text{DLE}(\%) = \frac{\text{weight of drug in particles}}{\text{weight of drug feed initially}} \times 100 \quad (1)$$

$$\text{DLC}(\%) = \frac{\text{weight of drug in particles}}{\text{weight of particles and drug}} \times 100 \quad (2)$$

2.4 Characterization

Synthesized copolymer was characterized by ¹H-NMR (Bruker Avance, USA) and FTIR (PerkinElmer, USA). Size and morphology of PTX-loaded Hep-ss-Plu127 were evaluated by TEM (JEOL, Japan) at an accelerating voltage

of 100 kV. The hydrodynamic diameter was determined using DLS (Horiba, Japan). The stability of PTX-loaded nanogels was examined by DLS under reductive environment by treating samples with GSH (10 mM).

3 Results and Discussion

The chemical structure of Hep-ss-Plu127 was determined by $^1\text{H-NMR}$. As shown in Fig. 1, signals at 3.40–3.65 ppm and 1.24 ppm are assigned to the PEO and PPO blocks of Plu127. Signals at 3.27 ppm and 4.23 ppm are attributed to $\text{CH-CH}_2\text{-O}$ and NH-SO_3 from Hep. Particularly, signals at 2.1, 2.98, and 3.14 ppm, respectively assigned to NH , S-CH_2 , and N-CH_2 , confirming the successful conjugation of Hep-Plu127 via redox-sensitive disulfide linkage of Cys. Additionally, FTIR was carried out to further confirm the structure of synthesized polymers. The characteristic band of C=O stretching appeared at 1630 cm^{-1} in the Hep-ss-Plu127 spectrum, are not observed in other spectra, indicating the amide formation between Hep and Plu-Cys. Moreover, typical bands of C-O-C and $\text{-SO}_2\text{-O-}$ at 1110 and 1245 cm^{-1} indicate the presence of both Plu127 and Hep, respectively, in the conjugate.

The size and morphology of PTX-loaded Hep-ss-Plu127 nanogels were analyzed by TEM and DLS (Fig. 2). From the TEM image, it is clear that the nanogels are well separated

and spherical in shape with the average diameter of 104 nm. As reported by previous studies, nanoparticles that are ranging from 10 to 200 nm in size can be easily entrapped by endosome during endocytosis, thus facilitate the passive targeting of nanoparticles to tumor cells through the EPR effect and reduce toxicity to healthy tissues [11, 12]. Therefore, the obtained PTX-loaded Hep-ss-Plu127 nanogels have a high potential to be delivered more effectively to tumor cells. In DLS, the hydrodynamic size of the nanogels is $91.4 \pm 0.3\text{ nm}$. The difference between the size obtained from TEM and DLS is due to the difference in processing, in which DLS analysis is performed in aqueous solution whereas TEM is performed on dried sample.

The redox sensitivity of PTX-loaded Hep-ss-Plu127 nanogels was confirmed by examining the particle size under the reductive environment. Result revealed that the size of nanogels is quickly reduced to $88.4 \pm 0.8\text{ nm}$ after 60-min treatment of GSH, demonstrating the redox-sensitive dissociation of disulfide-containing nanogels in intracellular environment. Thus, Hep-ss-Plu127 nanogels can enhance the redox responsiveness for the selective intracellular delivery of PTX in cancer treatment.

Regarding DDSs, DLE is a critical factor influencing their therapeutic efficacy. In this study, the amounts of loaded-PTX in Hep-ss-Plu127 nanogels were quantified by HPLC; and the DLE (%) as well as DLC (%) were found to be $66.2\% \pm 4.7\%$ and $13.2\% \pm 0.9\%$, respectively.

Fig. 1 $^1\text{H-NMR}$ spectrum of Hep-ss-Plu127 (left) and FTIR spectra of **a** Plu127. **b** Hep and **c** Hep-ss-Plu127 (right)

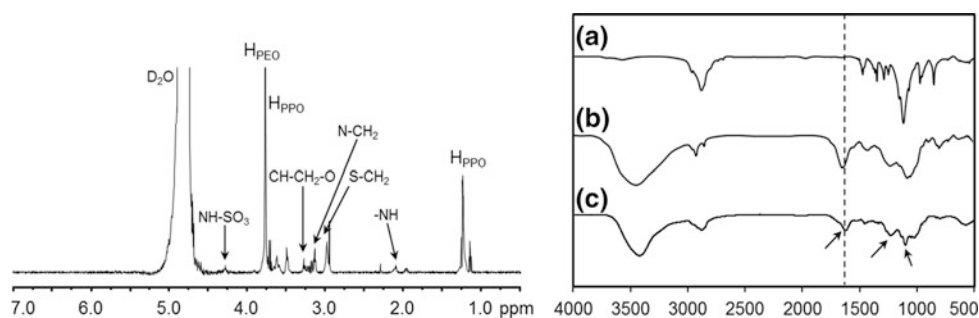
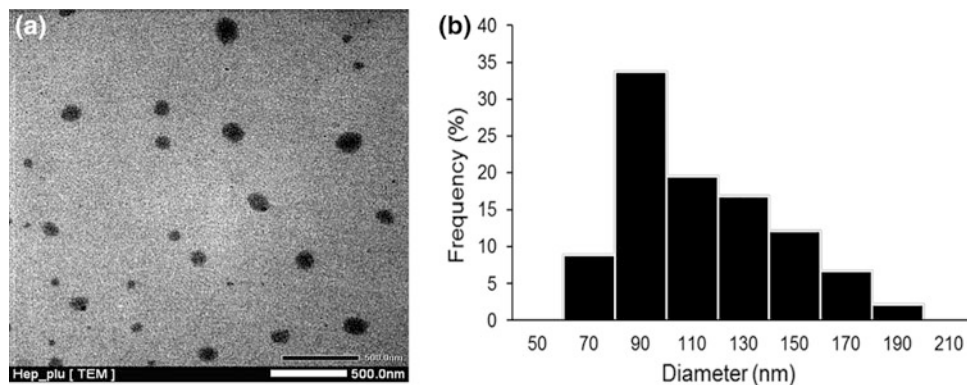


Fig. 2 **a** TEM image and **b** size distribution of PTX-loaded Hep-ss-Plu127 nanogels



Meanwhile, in a prior study where Hep-Plu nanogels were prepared by straightly coupling of carboxylated Plu127 onto Hep backbone, DLE was shown to be around 10% after PTX loading [3]. Therefore, Hep-ss-Plu127 nanogels with high loading efficiency could possibly enhance the therapeutic efficacy of PTX delivery.

4 Conclusion

Redox-sensitive Plu127-based nanogel was successfully prepared and characterized for the delivery of water-insoluble PTX, with a suitable size range, spherical shape, and high loading capacity (up to $66.2 \pm 4.7\%$ for DLE). Furthermore, disulfide bonds benefit these nanogels in terms of site-specific drug delivery, resulting in enhanced therapeutic index. These obtained results give insights into the potential of redox-sensitive Hep-ss-Plu127 nanogels as an efficient nanocarrier for PTX delivery.

Declaration of Conflicting Interests The authors declare that there is no conflict of interest.

References

1. Thu, H.P., Nam, N.H., Quang, B.T., Son, H.A., Toan, N.L., Quang, D.T.: In vitro and in vivo targeting effect of folate decorated paclitaxel loaded PLA-TPGS nanoparticles. *Saudi Pharmaceutical J.* **23**(6), 683–688 (2015)
2. Zou, H., Li, L., Carcedo, I.G., Xu, Z.P., Monteiro, M., Gu, W.: Synergistic inhibition of colon cancer cell growth with nanoemulsion-loaded paclitaxel and PI3 K/mTOR dual inhibitor BEZ235 through apoptosis. *Int. J. Nanomed.* **11**, 1947 (2016)
3. Joung, Y.K., Jang, J.Y., Choi, J.H., Han, D.K., Park, K.D.: Heparin-conjugated pluronic nanogels as multi-drug nanocarriers for combination chemotherapy. *Mol. Pharm.* **10**(2), 685–693 (2012)
4. Choi, J.H., Joung, Y.K., Bae, J.W., Choi, J.W., Quyen, T.N., Park, K.D.: Self-assembled nanogel of pluronic-conjugated heparin as a versatile drug nanocarrier. *Macromol. Res.* **19**(2), 180–188 (2011)
5. Wani, T.U., Rashid, M., Kumar, M., Chaudhary, S., Kumar, P., Mishra, N.: Targeting aspects of nanogels: an overview. *Int. J. Pharmaceutical Sci. Nanotechnol.* **7**(4), 2612–2630 (2014)
6. Nguyen, D.H., Choi, J.H., Joung, Y.K., Park, K.D.: Disulfide-crosslinked heparin-pluronic nanogels as a redox-sensitive nanocarrier for intracellular protein delivery. *J. Bioact. Compatible Polym.* **26**(3), 287–300 (2011)
7. Nguyen, D.H., Lee, J.S., Choi, J.H., Lee, Y., Son, J.Y., Bae, J.W., Lee, K., Park, K.D.: Heparin nanogel-containing liposomes for intracellular RNase delivery. *Macromol. Res.* **23**(8), 765–769 (2015)
8. Gu, Z., Rolfe, B.E., Thomas, A., Campbell, J.H., Lu, G., Xu, Z.: Heparin-related nanomaterials. In: *Heparin, Properties, Uses and Side Effects*. Nova Publisher, pp. 159–178 (2012)
9. Nguyen, A.K., Nguyen, T.H., Bao, B.Q., Bach, L.G., Nguyen, D. H.: Efficient Self-Assembly of mPEG End-Capped Porous Silica as a Redox-Sensitive Nanocarrier for Controlled Doxorubicin Delivery. *Int. J. Biomater.* **2018** (2018)
10. Nguyen, D.H., Joung, Y.K., Choi, J.H., Moon, H.T., Park, K.D.: Targeting ligand-functionalized and redox-sensitive heparin-Pluronic nanogels for intracellular protein delivery. *Biomed. Mater.* **6**(5), 055004 (2011)
11. Nguyen, D.H.: Potential 5-Fluorouracil encapsulated mPEG-Chitosan nanogels for controlling drug release. *J. Adv. Med. Pharmaceutical Sci.* **12**(4), 32493 (2017)
12. Thi, T.T.N., Tran, T.V., Tran, N.Q., Nguyen, C.K., Nguyen, D.H.: Hierarchical self-assembly of heparin-PEG end-capped porous silica as a redox sensitive nanocarrier for doxorubicin delivery. *Mater. Sci. Eng. C* **70**, 947–954 (2017)

Nanoliposomes as an Efficient Drug Carrier System for Paclitaxel Delivery

Ngoc Thuy Trang Le, Yen Nhi Nguyen Thi, Bac Ly Pham Thi, Ngoc Lin Hoang, Cuu Khoa Nguyen, and Dai Hai Nguyen

Abstract

Paclitaxel (PTX), a compound extracted from the Pacific yew tree (*Taxus brevifolia*), is widely used as a natural-source cancer drug in the treatment of ovarian, breast and lung cancers. Previous studies showed that PTX had obvious effects on cancer cells, it blocks the cell cycle in its G1 or M phases by stabilizing the microtubules and preventing depolymerization. However, the use of PTX is inconvenient and associated with significant and poorly predictable side effects, due to its low bioavailability and poor water solubility. The aim of this study was to develop PTX-loaded soy lecithin nanoliposomes (PTX-LP) to improve its bioavailability. In this study, PTX-LP was prepared by thin film hydration method. The average size, polydispersity index (PDI), zeta potential and encapsulation efficiency (EE) of the PTX-LP were characterized. Results indicated that PTX-LP was able to loaded with suitable encapsulation efficiency values, nanometric particle size (100–200 nm), low polydispersity (less than 0.5), negative zeta potential, and slowly released up to 96 h. Therefore, the study expected that PTX-LP developed herein would serve as a potent drug carrier system for PTX in cancer therapy.

Keywords

Paclitaxel • Soy lecithin • Nanoliposome • Drug carrier system

1 Introduction

Cancer is one of the hardest problem to understand and solve in the medical field. To against this disease, different healing methods are exercised depending on the cancer stage and the recidivism risks. Among these choices, chemotherapy is the most exploited for advanced cancers [1]. However, cancer chemotherapeutics need a high pharmacokinetic volume of distribution and a rapid elimination rates, requiring more frequent and high dose administration, causing unacceptable damage to normal tissue [1]. In order to overcome this drawback, soybean lecithin-based liposomes (LP) have been developed. LP are spherical vesicles with a one or two phospholipid bilayer, biocompatible and presenting a low toxicity to the human body. The rigidity/fluidity and the charge of the bilayer depend on the characteristics of the bilayer components [2]. They are mostly saturated or non-saturated phospholipids such as soybean lecithin. Indeed Soy Lecithin, a phospholipid extracted from soybeans, facilitates large-scale industrial production because of the production costs as compared with saturated phospholipids and they don't present any problem owing to their toxicity in the human body [3]. Thus, liposomes will be used to overcome cancer chemotherapeutic drawbacks and also target to the tumor area.

Herein, our study aimed to develop a paclitaxel-loaded soy lecithin nanoliposome system (PTX-LP), which could enhance the delivery of PTX. PTX-LP was prepared by thin film hydration method and characterized by dynamic light scattering (DLS) and transmission electron microscopy (TEM). Moreover, high performance liquid chromatography (HPLC) evaluated the drug loading content, the drug loading efficiency and the release behavior of the PTX-LP. This

N. T. T. Le · C. K. Nguyen · D. H. Nguyen (✉)
Graduate University of Science and Technology,
Vietnam Academy of Science and Technology,
Ha Noi, Vietnam
e-mail: nguyendaihai0511@gmail.com

N. T. T. Le · Y. N. Nguyen Thi · B. L. Pham Thi · C. K. Nguyen ·
D. H. Nguyen
Institute of Applied Materials Science, Vietnam Academy
of Science and Technology, Ho Chi Minh City, Vietnam

Y. N. Nguyen Thi · B. L. Pham Thi
Faculty of Applied Sciences, Ton Duc Thang University,
Ho Chi Minh City, Vietnam

N. L. Hoang
Mientrung Institute for Scientific Research, Hue, Vietnam

study tends to demonstrate the stability of a drug soy lecithin nanoliposome for a safety and efficacy of chemotherapy and their ability to improve PTX delivery in cancer therapy.

2 Materials and Method

PTX was purchased from Samyang Corporation (Seoul, Korea). Lecithin from soybean and Tween 80 (Polyoxyethylene sorbitan monooleate) were procured from TCI Co., LTD (Tokyo, Japan). Cholesterol and Mannitol were purchased from Sigma-Aldrich (St Louis, MO, USA). Cetyltrimethylammonium bromide (CTAB) was obtained from Merck (Darmstadt, Germany). All chemicals and solvents were either highest analytical grade or the best possible pharma grade and were used as supplied.

2.1 Preparation of PTX-Loaded Liposomes (PTX-LP)

Liposomes (LP) were prepared by thin film hydration method with using soy lecithin, cholesterol, CTAB and Tween 80. Firstly, soy lecithin and cholesterol (9:1) and CTAB were dissolved using chloroform-methanol (2:1, v/v) at room temperature. Then, the mixture was dried to a thin film at 45 °C by using a rotary evaporator (Büchi Rotavapor R-114, Essen, Germany) and maintained overnight under vacuum condition to remove trace of solvents. The obtained film was hydrated with deionized water (deH₂O) containing Tween 80 (0.5%, v/v) by stirring at 60 °C until the lipid film was completely hydrated. Afterwards, five techniques (sonicated, extruded, homogenized, sonicated and extruded or sonicated and homogenized) for narrowing down the particle size distribution were tested. Method resulted in a significant decrease in particle size distribution was chosen as the size reducing technique in the PTX-LP preparation.

PTX, soybean lecithin, cholesterol and CTAB were dissolved in chloroform-methanol, dried in a rotary evaporator, and then reduced particle size distribution by size reducing method for the preparation of PTX-LP. Unencapsulated PTX was removed from the liposome dispersion by centrifuging at 16,000 rpm for 30 min and filtered through 0.1 µm filter. The PTX-LP sample was then lyophilized in distilled water containing mannitol (mannitol:lipid = 1:2) and freeze-dried. The PTX-LP powders were stored at 2–8 °C.

2.2 Characterization

The particle size, polydispersity index (PDI) and zeta potential of liposomal dispersions were analyzed by DLS. The samples were diluted with distilled water (1 mg/mL) and measured by Nanosizer (SZ-100, Horiba Ltd., Japan) with a detection angle and the temperature were 90 and 25 °C, respectively. The morphology of the PTX-LP sample was examined (TEM; JEM-1400, Jeol, Tokyo, Japan) at an accelerating voltage of 300 kV.

2.3 Determination of Encapsulation Efficiency of PTX

Briefly, 1 mL of LP dispersions diluted to 11 mL by deH₂O were centrifuged at 16,000 rpm for 30 min and filtered through 0.1 µm filter to remove unencapsulated PTX. After removing the unencapsulated PTX by filtration, the PTX-LP was then dissolved with 6 mL mobile phase (HPLC). The total amount of PTX in LP was measured by 1 mL of LP dispersion was dissolved with the same mobile phase (6 mL). The drug loading content (DL) and encapsulation efficiency (EE) was calculated according to the equation:

$$EE(\%) = \frac{\text{weight of PTX encapsulated in LP}}{\text{weight of PTX in LP dispersion}} \times 100$$

$$DL(\%) = \frac{\text{weight of PTX encapsulated in LP}}{\text{weight of freeze - dried PTX - LP}}$$

2.4 In Vitro Drug Release

The release studies of free PTX and PTX-LP was assessed by using HPLC system and the rate of PTX releasing was obtained following the standard curve. The in vitro drug release experiments were performed in Phosphate buffer pH 7.4 at 37 °C using dialysis membrane method. Briefly, a dialysis membrane (MWCO 6–8 kDa) which was filled with an amount of PTX suspended in PBS including 2% Tween 80 was immersed into 20 mL of the release environment in vial. The vial was assembled on a magnetic stirrer and the medium was equilibrated at 37 °C. At several time intervals, 2 mL of the release medium was gathered and an equal volume of fresh buffer medium was added. The withdrawn samples were filtered through 0.2 µm filter before high

performance liquid chromatography analysis. Finally, cumulative percentage drug release was calculated by absorbance values.

3 Results and Discussion

3.1 Effect of Different Techniques Used for Nanosizing LP

Results in Table 1 showed that LP prepared by sonication followed by homogenization techniques was found to be the most efficient in reducing LP size, followed by sonication followed by extrusion, homogenization, extrusion and sonication. The average particle size was approximately 135.6 ± 3.9 nm with a uniform size distribution (PDI = 0.398 ± 0.028) and zeta potential was -64.3 ± 2.6 mV, whereas LP before treatment with size reducing techniques (control) was 2311.0 ± 183.4 nm (PDI = 1491 ± 0.120) and -81.5 ± 0.9 mV, respectively. The size of extruded liposomes was found to be influenced by the extrusion flow rate and membrane pore size. This indicates the flow rate reduced the size of LP.

3.2 Characterization of LP and PTX-LP

The particle size of LP and PTX-LP and their particle size distribution were 136.2 ± 7.9 and 127.3 ± 0.7 nm, whereas the polydispersity index values were 0.297 ± 0.04 and

0.285 ± 0.30 , respectively. These results indicated that the particle sizes of LP and PTX-LP were in a close interval measurement. Otherwise, zeta potential of LP was -61.5 ± 2.9 mV and pointed out an decrease in the surface intensity in accordance with the encapsulation of PTX where the zeta potential was -55.5 ± 2.4 mV but still negative and enable PTX-LP was stable (Fig. 1).

According to morphological evaluation analysis, TEM images showed spherically-shaped LP and confirmed an average size beneath 200 nm. Thus, PTX-LP might serve as stable spherical nanocarriers with longterm circulation in the bloodstream.

3.3 Drug Loading and Encapsulation Efficiency

Herein, the amount of PTX encapsulated in LP and the total amount of PTX in LP were calculated according to the standard curve for PTX. Using the EE (%) and DL (%) formula, the results demonstrated that the percent was 98.14% and 3.06% for EE and DL, respectively. These results showed a satisfying encapsulation rate for PTX.

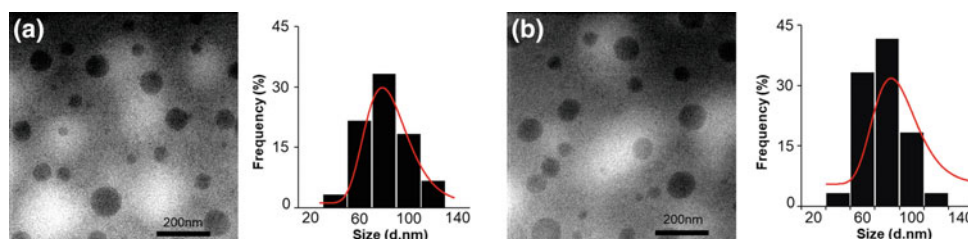
3.4 In Vitro Drug Release

PTX solubility in a medium containing a surfactant such as Tween 80 is reported to be much higher. In this study, in vitro release profiles of free PTX and PTX from PTX-LP were evaluated in PBS (pH 7.4) containing 2% Tween 80.

Table 1 Physical characterization of liposomes after treatment with size reduction techniques

Sample	Particle size (nm)	PDI	Zeta potential (mV)
Control	2311.0 ± 183.4	1.491 ± 0.120	-81.5 ± 0.9
Sonication	196.5 ± 4.9	0.622 ± 0.024	-73.1 ± 0.8
Extrusion	166.7 ± 2.2	0.332 ± 0.011	-74.0 ± 2.2
Homogenization	164.9 ± 8.4	0.339 ± 0.020	-76.8 ± 0.9
Sonication followed by extrusion	146.5 ± 0.4	0.376 ± 0.043	-68.1 ± 0.7
Sonication followed by homogenization	135.6 ± 3.9	0.398 ± 0.028	-64.3 ± 2.6

Fig. 1 a TEM images of LP and b PTX-LP



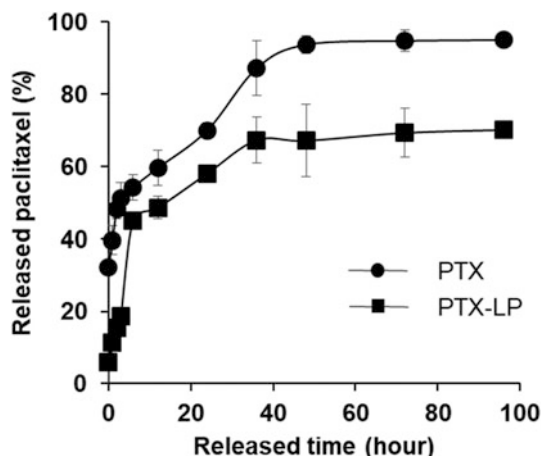


Fig. 2 In vitro release profiles of free PTX and PTX from PTX-LP in PBS buffer (pH 7.4; 2% Tween 80) at 37 °C up to 96 h

As seen in Fig. 2, PTX exhibited a distinct and sequential release pattern, with free PTX released faster than PTX-LP. Approximately 60% of PTX was released within 24 h, whereas less than <50% of PTX was released during the same period. By 96 h, nearly 95% of PTX was released, compared to 70% of PTX from PTX-LP. Our results are then compared to the results of previous studies. Similar findings were noted previously by Thi Lan Nguyen et al. reported that the initial release of PTX from the targeting PTX-loaded soy lecithin liposome prepared by thin film method and narrowed down the particle size distribution by high pressure homogenizer was less than 60% in 96 h [4]. In other words, the releasing of drug-loaded LP is significantly slower than free drug. Therefore, drug-LP can keep the drug stable, prolong drug inside body and increase drug accumulation into tumor sites as an efficient drug delivery system.

4 Conclusions

LP from soy lecithin has been successfully fabricated for PTX loading by thin film method and narrowed down the particle size distribution by sonication followed by homogenization. The physical properties of PTX-LP were of ideal range, with spherical shapes, particle size around 127.3 nm and surface charge around -55.5 mV, which would be suitable in vivo drug delivery. The EE calculation as well as a sustained release profile of around 70% after 96 h suggest that LP formulation from soy lecithin is a promising candidate for a safe, biocompatible and stable delivery system for PTX as an anticancer agent.

Acknowledgements This work was supported by the Development of Science and Technology (DOST) under grant no. 69/2016, dated 18 July, 2016. **Conflict of Interests** The authors declare that there is no conflict of interests.

References

1. Thi, T.T.N., Tran, T.V., Tran, N.Q., et al.: Hierarchical self-assembly of heparin-PEG end-capped porous silica as a redox sensitive nanocarrier for doxorubicin delivery. *Mater. Sci. Eng. C* **70**, 947–954 (2017)
2. Pagano, A., Honoré, S., Estève, M.A., et al.: Nanodrug potential in cancer therapy: efficacy/toxicity studies in cancer cells. *Int. J. Nanotechnol.* **9**, 502–516 (2012)
3. Mohan, A., McClements, D.J., Udenigwe, C.C.: Encapsulation of bioactive whey peptides in soy lecithin-derived nanoliposomes: influence of peptide molecular weight. *Food Chem.* **213**, 143–148 (2016)
4. Nguyen, T.L., Nguyen, T.H., Nguyen, D.H.: Development and in vitro evaluation of liposomes using soy lecithin to encapsulate paclitaxel. *Int. J. Biomater.* **2017**(2017)

Engineering of Hollow Mesoporous Silica Nanoparticles Enhancing Drug-Loading Capacity

Ngoc Tram Nguyen Thi, Ngoc Hoang Le, Uyen Vy Vo, Cuu Khoa Nguyen, and Dai Hai Nguyen

Abstract

Hollow mesoporous silica nanoparticle (HMSN) has been recognized as an outstanding candidate for improving the drug loading capacity of silica nanoplateforms. This study reports the synthesis of hollow mesoporous silica nanoparticles (HMSN) as a potential bioactive to improve the drug loading capacity of the nanoparticles delivery systems. Herein, HMSN was successfully synthesized by using tetraethyl orthosilicate (TEOS) and cetyltrimethyl ammonium bromide (CTAB). The prepared HMSN nanocarriers were characterized by X-ray diffraction (XRD), transmission electron microscopy (TEM), nitrogen absorption-desorption isotherms, dynamic light scattering (DLS), thermogravimetric analysis (TGA), and fourier transform infrared (FTIR). In aqueous solution, HMSN existed as nanoparticles with morphology, spherical shape and the diameter range of 180–200 nm. Especially, RhB was effectively encapsulated into HMSN nanoparticles to form RhB-loaded nanocarriers (RhB/HMSN) with high loading efficiency. These results demonstrated that this prepared HMSN nanocarrier may serve as a promising nanocarrier with high drug loading capacity for its potential applications in drug delivery.

Keywords

Rhodamine B • Hollow mesoporous silica • High drug loading capacity • Nanoparticles • Drug delivery system

1 Introduction

Silica nanoparticles have received growing attention as a promising nanocarrier for drug delivery applications due to its large surface areas, high pore volume, good chemical and thermal stability, excellent biocompatibility, and easy surface functionalization [1]. Hollow mesoporous silica nanoparticle (HMSN), with a large of cavity inside each original mesoporous silica nanoparticle, provides a promising approach to address the challenge. In this regard, solid SiO₂ core (sSiO₂) is initially prepared as hard templates using a modified Stöber method. Thus, as-prepared sSiO₂ spheres are coated by controllable PNS layer, which is formed through sol-gel process of tetraethylorthosilicate (TEOs) catalyzed by acid or base in the presence of hexa-decyltrimethylammonium bromide (CTAB). Finally, the silica cores were removed via Na₂CO₃-etching process at elevated temperature or selective etching in an appropriate solvent. Liu et al. grafted 3-(3, 4-dihydroxyphenyl) propionic acid (DHPA)-functionalized beta-cyclodextrin (b-CD) onto the surface of HMSNs to form HMSNs-b-CD nanocarrier and further anchored polyethylene glycol (PEG)-conjugated adamantane (Ada) on HMSNs-b-CD via host-guest interaction for doxorubicin (DOX) delivery. The TGA result of this study indicated that around 10 wt% of DOX was encapsulated into HMSNs-b-CD/Ada-PEG system, which was higher than that of PNSs (approximately 5 wt%) with similar dimensions, mainly due to the hollow cavity structure of HMSNs [2]. Zhao et al. grafted positively charged CD_{PEI} nanoparticles on the pore openings of HMSN through disulfide bonds, which was later loaded with DOX and grafted with hyaluronic acid (HA) to form a more

N. T. N. Thi · U. V. Vo · C. K. Nguyen · D. H. Nguyen (✉)
Graduate University of Science and Technology, Vietnam,
Academy of Science and Technology, Hanoi, Vietnam
e-mail: nguyendaihai0511@gmail.com

N. T. N. Thi · N. H. Le · U. V. Vo · C. K. Nguyen · D. H. Nguyen
Institute of Applied Materials Science, Vietnam Academy
of Science and Technology, 01 TL29, District 12,
Ho Chi Minh City, 700000, Vietnam

N. T. N. Thi
Tra Vinh University, No. 126, Nguyen Thien Thanh Ward 5,
Tra Vinh City, Tra Vinh Province 940000, Vietnam

N. H. Le
Ton Duc Thang University, 19 Nguyen Huu Tho Street,
Tan Phong Ward, District 7, Ho Chi Minh City, 700000, Vietnam

U. V. Vo
Industrial University of Ho Chi Minh City, Ho Chi Minh City,
700000, Vietnam

complex structure DOX/HMSN-SS-CD_{PEI}@HA. The result of drug loading capacity of DOX showed that the loading efficiency of DOX/HMSN-SS-CD_{PEI}@HA was 30.5%, which was significant larger than that of DOX loaded in the PNS nanocarrier (12.5%). This phenomenon was attributed to the high specific surface area, mesoporous structure, and especially the hollow cavity of the prepared HMNS nanoparticle [3]. More importantly, the prepared HMSN-SS-CD_{PEI}@HA nanoparticles exhibited excellent biocompatibility. Consequently, the use of HMSN can indeed be valuable tool for developing nanocarriers with high drug loading [4].

Herein, we report the synthesis process of HMSN nanocarriers and its applications in Rhodamine (RhB) loading. In order to evaluate the successful preparation and the drug loading properties of HMSN nanocarriers, X-ray diffraction (XRD), transmission electron microscopy (TEM), nitrogen adsorption-desorption isotherms, dynamic light scattering (DLS), thermogravimetric analysis (TGA), and Fourier transform infrared (FTIR) were used.

2 Experimental

2.1 Materials

Tetraethyl orthosilicate (TEOS, 98%) was purchased from Sigma-Aldrich (St. Louis, MO, USA). Cetyltrimethylammonium bromide (CTAB, 99%) was purchased from Merck (USA). Ammonia solution (NH₃ (aq), 28%), ethanol, Rhodamine B was purchased from HiMedia (India). All chemicals were of reagent grade and used without further purification.

2.2 Preparation of HMSN

HMSN was synthesized using the protocol reported in the literature with minor modification [5]. The synthesis included three main steps: (1) sSiO₂ spheres were prepared as hard templates using a modified Stöber method (2) Thickness-controllable PNS layer was coated on each sSiO₂ using CTAB as the soft templates to form a core@-shell structure sSiO₂/PNS@CTAB. (3) As-synthesized sSiO₂@PNS(CTAB) together with free CTAB in the solution was mixed with aqueous Na₂CO₃ solution for 9 h at 50 °C. The mixture was later freeze-dried to obtain HMSN spheres, which were washed several times to remove the CTAB template.

2.3 Characterization

XRD measurement was performed using a Bruker D2 Phaser diffractometer. Morphology and size of sSiO₂, sSiO₂/PNS@CTAB and HMSN were imaged by TEM. N₂ adsorption-desorption isotherms were measured using a TRISTAR 3000 apparatus. The surface charge of HMSN were measured at 37 °C using a Zetasizer Nano ZS and the loading content of HMSN with RhB was determined by UV-Vis spectroscopy with a wavelength of 544 nm.

2.4 Preparation of RhB/HMSN

RhB was loaded in HMSN using equilibrium dialysis method as reported earlier. Initially, 16 mg of HMSN was separately added into RhB solution (10 µg/mL), and thus these solution were stirred, sonicated and centrifuged to remove non-encapsulated RhB. The amount of unloaded RhB (W_{U-RhB}) in dialysis solution was determined using UV-Vis absorbance method. Briefly, fresh RhB was dissolved in deH₂O to obtain a series of known concentration solutions (0–5 µg/mL), which were used as standard samples. Absorbance of the standard and dialysis solution samples was recorded at 544 nm using a UV/Vis spectrophotometer (Shimadzu, Japan). The concentration of RhB in the samples was calculated using a standard curve, which was established based on the relationship between RhB concentrations and absorbance of standard solutions. RhB loading efficiency (LE) was calculated by $LE (\%) = (100 - W_{U-RhB}) / 100 * 100$. The RhB loading capacity (LC) was also calculated using the equation, $LC (\%) = (100 - W_{U-RhB}) / (W_{HMSN} + 100 - W_{U-RhB}) * 100$, in which 100 (mg) is the initial amount of RhB for loading experiment, W_{U-RhB} is the total amount of unloaded RhB in the dialysis solution, and W_{HMSN} is the dried weight of HMSN nanocarriers.

3 Result and Discussion

3.1 Characterization of HMSN

HMSN was synthesized following the literature procedures with minor modification, as shown in Fig. 1. In this regard, the preparation of HMSN was carried out in three main steps, preparing of sSiO₂ core, porous shell (sSiO₂@PNS (CTAB)) and hollow core (HMSN), as described in Fig. 1b. The morphology and size of these prepared nanoparticles were further examined using TEM (Fig. 1). We obtained

average sSiO_2 (114 ± 13.11 nm) in Fig. 1a. and HMSN nanoparticles possessed spherical shape with 191.12 ± 15.94 nm for HMSN (Fig. 1c). Thus, the selective etching solid silica core and protecting the integrity of silica shell were our first two priorities of the synthesis of HMSN. During the etching process, positively charged CTAB (CTAB^+) would absorb to the surface of $\text{sSiO}_2@\text{PNS}$ (CTAB) via electronic attraction, leaving behind the shell

intact. Subsequently, this process started and would be accelerated in the presence of Na_2CO_3 in the solution, CTAB in the porous shell, and free CTAB in the media. After the etching process, acid acetic/ethanol (1:1, v/v) solution was used to remove CTAB in mesopore.

As shown in Fig. 2, the broad XRD patterns reflection peaks of HMSN ($2\theta = 23.0^\circ$) indicate the amorphous nature of silica nanoparticles. Furthermore, HMSN has a

Fig. 1 a, a' TEM images and particle size distribution of sSiO_2 . b, b' $\text{sSiO}_2@\text{PNS}(\text{CTAB})$ and c, c' HMSN respectively

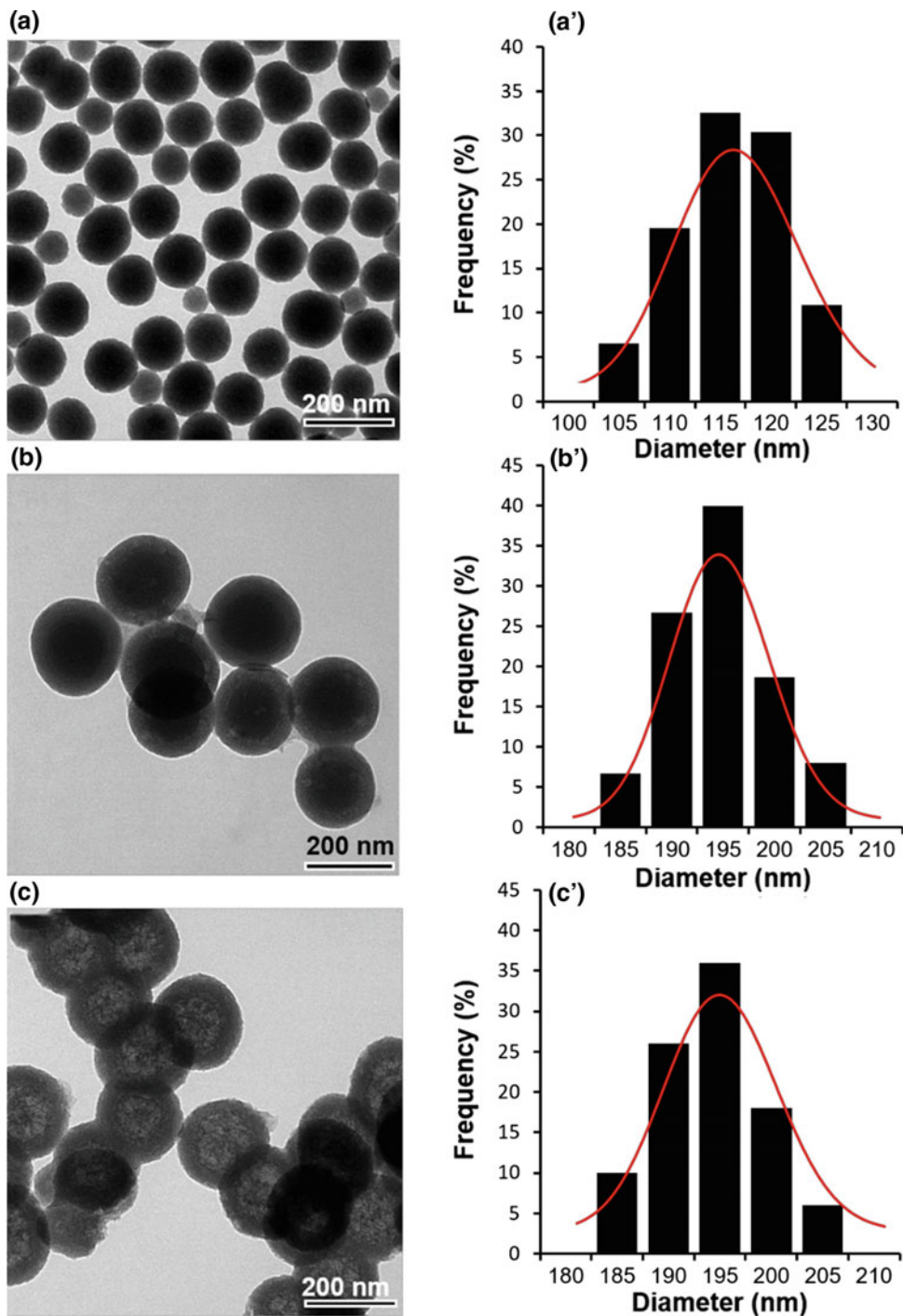


Fig. 2 a XRD patterns and b NO₂ adsorption–desorption isotherms of HMSN

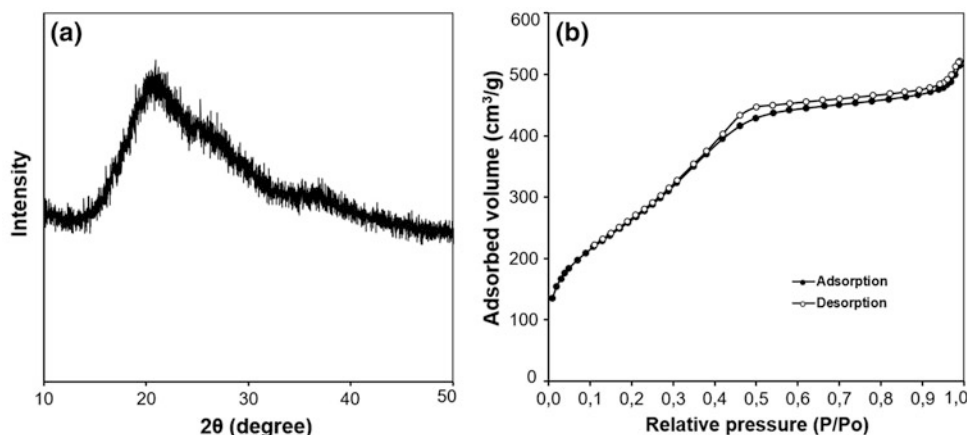
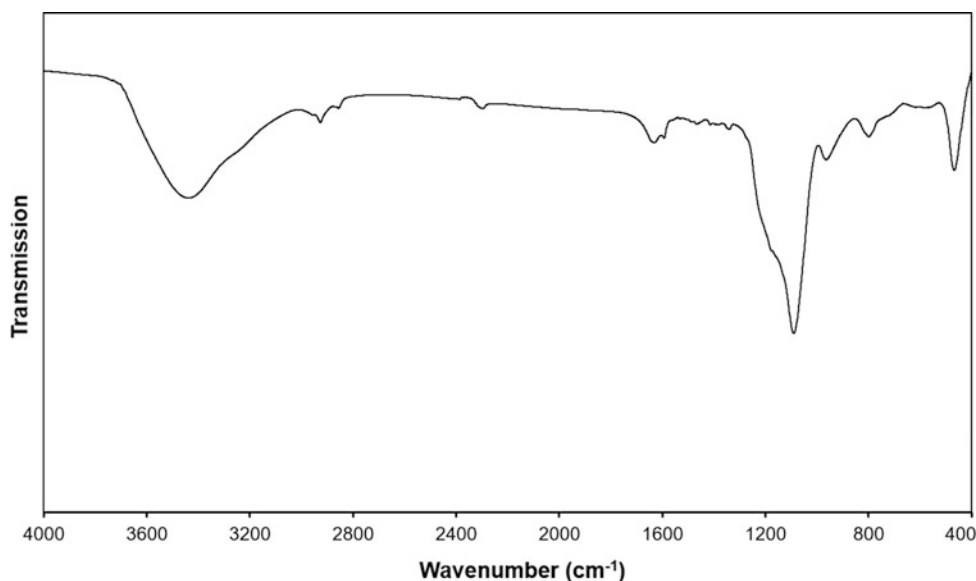


Fig. 3 The FTIR spectra HMSN



specific area of 983.7 m²/g and pore volume of 2.33 cm³/g. These results indicate that the synthesized HMSN with larger surface area and high pore volume. In this report, the surface charge of the sSiO₂ was found to be -43.3 ± 0.87 mV, and sSiO₂/PNS@CTAB increased dramatically to 32.5 ± 0.66 mV. By contrast, the zeta potential of HMSN was -25.45 ± 0.07 mV, as compared with sSiO₂/PNS (CTAB). The TGA curve of HMSN displayed the following mass loss of HMSN was only 13%.

The FTIR spectra HMSN are shown in Fig. 3, a band at 1640 cm⁻¹ was attributed to the OH stretching vibration of water molecules present in HMSN. The strong peaks appeared at around 1089, 973 and 836 cm⁻¹ were assigned to the stretching vibration of Si–O–Si, Si–OH and Si–O, respectively [1], which are typical infrared characteristic peaks of the silica nanoparticles. Besides, the broad band observed at around 3444 cm⁻¹ was associated with OH stretching frequency for the silanol group. Similarly, these peaks were also observed in the FTIR spectrum of HMSN.

3.2 Drug Loading Capacity Analysis

The RhB/HMSN was prepared by using equilibrium dialysis method. The LE was calculated indirectly from the amount of non-encapsulated RhB. The LE, LC of HMSN was $51.67 \pm 0.11\%$ and $10.44 \pm 0.02\%$, respectively. These results showed that introducing hollow form resulted in high LE and LC of nanoparticles, which may also help to enhance tumor-targeted delivery of loaded drug from RhB/HMSN nanocarriers.

4 Conclusion

In this study, HMSN nanoparticles has been successfully prepared via sol-gel method in spherical shape with average particle size of 191.12 ± 15.94 nm and acted as potential nanocarriers for effectively loading of anticancer drugs. RhB was effectively encapsulated into the HMSN nanoparticles

with 51.67% of LE. The developed HMSN nanoparticles could be a promising candidate for control the release of anticancer drug with high drug loading efficiency.

Acknowledgements This research was funded by Vietnam National Foundation for Science and Technology Development (NAFOSTED) under grant no. 104.02-2014.83.

Conflict of Interest The authors declare that they have no conflict of interest.

References

1. Nguyen, A.K., Nguyen, T.H., Bao, B.Q., Bach, L.G., Nguyen, D. H.: Efficient self-assembly of mPEG end-capped porous silica as a redox-sensitive nanocarrier for controlled doxorubicin delivery. *Int. J. Biomater.* **2018** (2018)
2. Liu, J., Luo, Z., Zhang, J., Luo, T., Zhou, J., Zhao, X., Cai, K.: Hollow mesoporous silica nanoparticles facilitated drug delivery via cascade pH stimuli in tumor microenvironment for tumor therapy. *Biomaterials* **83**, 51–65 (2016)
3. Zhao, Q., Wang, S., Yang, Y., Li, X., Di, D., Zhang, C., Jiang, T., Wang, S.: Hyaluronic acid and carbon dots-gated hollow mesoporous silica for redox and enzyme-triggered targeted drug delivery and bioimaging. *Mater. Sci. Eng. C* **78**, 475–484 (2017)
4. Chen, F., Hong, H., Shi, S., Goel, S., Valdovinos, H.F., Hernandez, R., Theuer, C.P., Barnhart, T.E., Cai, W.: Engineering of hollow mesoporous silica nanoparticles for remarkably enhanced tumor active targeting efficacy. *Sci. Rep.* **4** (2014)
5. Ghasemi, S., Farsangi, Z.J., Beitollahi, A., Mirkazemi, M., Rezayat, S., Sarkar, S.: Synthesis of hollow mesoporous silica (HMS) nanoparticles as a candidate for sulfasalazine drug loading. *Ceram. Int.* (2017)

Fabrication of Curcumin/Silver Nanoparticles Loaded Gelatin Scaffold

Khanh Loan Ly[✉], Vo Van Toi, and Thi-Hiep Nguyen[✉]

Abstract

In this study, a scaffold comprising of curcumin (Cur) and silver nanoparticles (AgNPs) with gelatin (Gel) as carrier matrix was fabricated to develop a novel system potential of antibacterial, anti-inflammatory, and antioxidant properties to aid in wound healing process. UV irradiation was employed in the synthesis of GelAg matrix, followed by the utilization of sonoprecipitation method to encapsulate Cur into GelAg matrix. Since Gel is a polyelectrolyte which possesses different charge when varying pH of solution, the interaction of Gel and AgNPs strongly affects to characteristics of fabricated scaffold. This study aims to investigate the effect of this interaction on morphology of GelAgCur scaffold by varying the amount of AgNPs. The results suggested that at AgNPs equaled to 75 ppm, the system obtained the most potential topography with highly porous structure and even distribution of pores and interconnected pores.

Keywords

Gelatin (Gel) • Curcumin (Cur) • Silver nanoparticles (AgNPs) • Morphology observation

1 Introduction

Wound healing is a dynamic and complex process of tissue regeneration and growth progress through four different phases. During inflammatory phase, abundant neutrophil infiltration at the wounded site and through respiratory burst

activity, these cells release proteases, oxygen free-radicals and inflammatory mediators. These radicals contribute to oxidative stress, which has been recognized as a significant feature in the pathogenesis of chronic non-healing wounds [1, 2]. Meanwhile, perpetuation of inflammation subsequently damages the growing tissue at the repair site, finally resulting in the non-healing state [3]. Furthermore, antimicrobial property is another crucial factor to prevent wound from microorganism for a long healing process [4]. This leads to a need of a distinctive composite which possesses great antibacterial, anti-inflammatory, and antioxidant properties with a controlled release rate specialized for certain applications to fight against microorganisms and stimulate skin regeneration within wounded site.

Silver is one of the most prevalent metallic materials to tackle infectious problems owing to its strong bactericidal effects and a broad spectrum antimicrobial activity [5]. The antibacterial activity of silver nanoparticles (AgNPs) is associated with the release of Ag ions, in which small silver ions released from AgNPs carry positive charges can easily attracted to negatively charged cell membrane of bacteria, then entrap, penetrate into the bacteria, disrupt respiratory processes and cause bacterial death [6, 7]. In order to control the release of antibacterial agents, AgNPs loaded on cross-linked Gel fiber mats to control the release by varying the immersing time in cross-linker can be a potential approach [8]. Curcumin (Cur) has been widely used in the topical treatment due to its biological potential of anticancer, antioxidant, anti-inflammatory, antibacterial, and supportive wound healing properties [9–11]. However, the therapeutic efficacy of curcumin is limited due to its low solubility, short half-life, poor bioavailability hydrophobic, light-sensitive and practically instable in alkaline and in vivo environment [12].

In order to control release of AgNPs and overcome the disadvantages of Cur, Gelatin (Gel) which is a natural protein obtained from the hydrolysis of collagen and widely known its biodegradability, biocompatibility, and non-toxicity, has emerged as a potential carrier matrix [8].

K. L. Ly · V. Van Toi · T.-H. Nguyen (✉)
Department of Biomedical Engineering, International University,
Vietnam National University- Ho Chi Minh City (VNU-HCMC),
Ho Chi Minh City, 700000, Vietnam
e-mail: nthiep@hcmiu.edu.vn

K. L. Ly
e-mail: llkhanh2303@gmail.com

The diverse in functional groups in Gel structure offers many benefits for chemical modification and covalent drug attachment [8]. When drug is encapsulated in gelatin, not only can the drug possess site-specific delivery but also increase drug stability and control drug release effectively. In this study, GelAg complex was prepared using green synthesis approach involving the use of UV irradiation. Subsequently, Cur was incorporated into GelAg complex using sonoprecipitation method. The particle characteristics including size, stability and scaffold morphology were investigated among different GelCurAg formulations to obtain the most potential system for further research.

2 Materials and Methods

2.1 Materials

Curcumin powders were supplied by Shanghai Zhanyun Chemical Co. Ltd. Silver nitrate ($\text{AgNO}_3 \geq 99\%$), and methanol (CH_3OH) were purchased from Xilong chemical Co., Ltd (China). Gelatin (porcine skin, type A), Glutaraldehyde 25% (GA), and poloxamer 407 (POX 407) were obtained from Sigma-Aldrich Co., St Louis, MO (USA). All other chemicals used in this study were purchased from major suppliers. Ultraviolet light source came from fluorescent lighting fixture (FLF-48, 40w–220v, 50–60 Hz).

2.2 Methods

Fabrication of gelatin loaded silver nanoparticles matrix.

The process of synthesis AgNPs using Gel as green stabilizer and employing UV light was described in previous research [13]. Briefly, Gel solution 1 wt% was stirred at 40 °C for 1 h until obtaining transparent solution. After that, different amount of AgNO_3 1 wt% were added into Gel solutions and stirred at room temperature for 10 min. Then Gel– AgNO_3 mixtures were exposed under ultraviolet light using fluorescent lighting fixture for 6 h to synthesize Gel loaded AgNPs (GelAg) solutions.

Encapsulation of curcumin using gelatin loaded silver particles. Transparent solution containing Cur and POX 407 in 5 ml methanol was prepared and quickly wise-dropped into 20 ml of prepared GelAg solution while stirring. The mixture was sonicated for 20 min using probe sonication (QSONICA, USA) with amplitude of 30 and temperature was kept at 25 ± 1 °C in an ice-water bath. Then, 30 μl of

glutaraldehyde (GA) 5% was added into the mixture and left stirring for 2 h. After that, the mixture was centrifuged at 1000 rpm for 30 min. Finally, the supernatant was collected and lyophilized at -50 °C for 24 h.

UV-Visible absorbance. In order to confirm the presence of AgNPs within GelAg complex, Multi-plate reader (Varioskan™ LUX multimode microplate reader) was employed for spectrum absorbance measurement.

Particle size and zeta potential. The particle size and zeta potential of GelCurAg system were analyzed by Zetasizer Nano Series (Malvern Instrument Limited, UK) ($n = 3$).

Morphological observation. A scanning electron microscope (SEM, JEOL JSM-IT100) was employed to observe the morphology of GelCurAg scaffold at 7 and 14 kV. Before SEM observation, the samples were coated with platinum using the coating machine (Cressington Sputter Coater 108 auto).

3 Results and Discussion

3.1 UV-Visible Absorbance

Figure 1 displays the change in color of GelAg solution, in which the color of GelAg solution changed from colorless to yellowish due to the excitation of surface plasmon resonance, a characteristic feature of synthesized AgNPs [14]. The more the amount of AgNPs resided in solution, the darker the color of GelAg solution is.

Figure 2 illustrates the UV-Visible spectrum of GelAg complex. The absorption peak was recorded at around 430–450 nm in the UV-Visible spectrum confirming the formation of AgNPs [13]. Aquatic solution containing AgNO_3 and Gel under the effect of UV irradiation can produce solvated electrons which in turn reduce the metallic cations to the metallic atoms and finally coalesce to form agglomerates [15]. Then AgNPs are stabilized by the amine pendant groups on the gelatin backbone, ultimately leading to the formation of gelatin-stabilized AgNPs. After the synthesis of GelAg complex, Cur was loaded into this system using sonoprecipitation method. Cur and POX 407 were dissolved in methanol and to form solvent phase, which was then dropwised into anti-solvent phase (GelAg complex) to form an oil-in-water emulsion. Then, POX 407 with a hydrophobic portion and a hydrophilic one was employed as emulsifier to stabilize this system.

Fig. 1 Fabricated GelAg solution with different AgNPs concentration **a** 30. **b** 45. **c** 60. **d** 75 and **e** 150 ppm

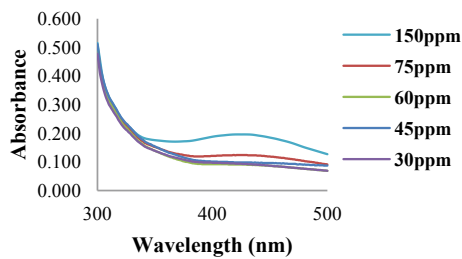
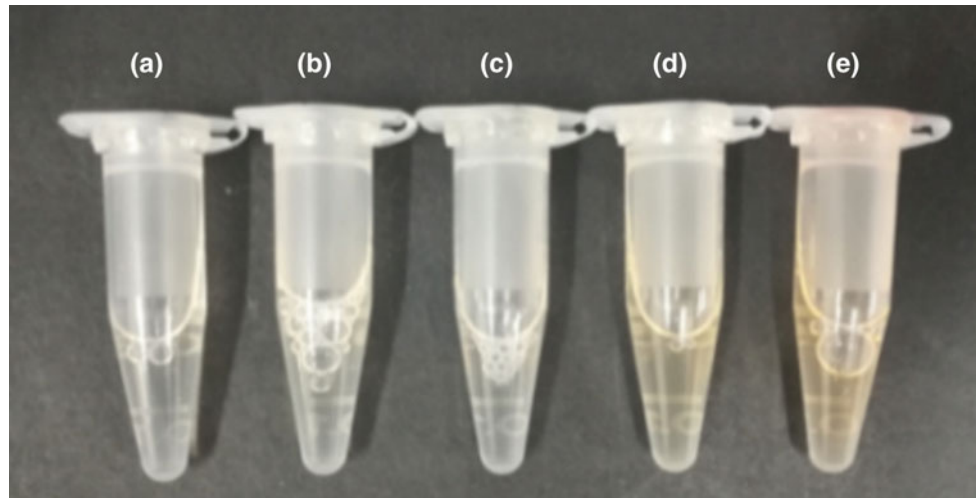


Fig. 2 Corresponding UV-visible spectrums of GelAg complexes

Table 1 Zeta sizer analytical results of different formulations GelCurAg scaffold (n = 3)

Code	Particle size (nm)	PdI	Zeta potential (mV)
GelCur	217.0 ± 16.4	0.21 ± 0.06	29.1 ± 0.5
GelCurAg ₁₅₀	207.5 ± 47.8	0.31 ± 0.03	25.7 ± 0.7
GelCurAg ₇₅	238.9 ± 40.8	0.13 ± 0.07	32.9 ± 1.9
GelCurAg ₆₀	230.2 ± 39.8	0.11 ± 0.06	33.5 ± 0.8
GelCurAg ₄₅	262.5 ± 71.8	0.14 ± 0.09	27.1 ± 0.6
GelCurAg ₃₀	387.7 ± 67.4	0.18 ± 0.13	32.9 ± 0.9

3.2 Particle Size and Zeta Potential Analysis

Shown in Table 1 are various analyzed parameters obtained by Zeta sizer. The presence of AgNPs inside the system slightly increased the size of GelCurAgNPs, except for GelCurAg₃₀, while there was no significant difference in stability among different formulations. The formation of AgNPs did not alter the size of the NPs significantly and the nano-suspension remained stable for two weeks before the

oil-in-water emulsion collapsing, leading to the separation of oil and water phase. However, since the gel strength of Gel type A used was high, ~300 g Bloom, the system was more in the gel form and could be utilized for topical treatment (Fig. 3).

3.3 Morphology Observation

SEM was employed to observe the differences in morphology of GelCurAg scaffold of different formulations. Polymeric scaffolds are substrates for the implanted cells with good physical support to control the tissue restoration or improve the functional tissue regeneration. The 3D polymeric scaffolds with highly porous and well-interconnected open pore structure can also support cell adhesion, migration, proliferation, and differentiation. Gel loaded Cur alone obtained the largest pore size and when AgNPs were loaded, the pore size of GelCurAg became smaller due to the interaction between AgNPs and Gel backbone. While at 150 ppm, the GelAg interaction created a disoriented structure due to the dominance in negative charge of AgNPs. After reducing the amount of AgNPs the system became more even in distribution of smaller size pores and interconnected pores. When decreasing AgNPs loaded to 45 ppm, the system became disorient again and larger pores 3D structure was observed, this might due to the lack of AgNPs leading to the unbalance in solution electrolyte charge and altered the topography of GelCurAg scaffold. Based on SEM observation, GelCurAg₇₅ seems to possess the most promising structure with the pore size ranging from 100 to 200 μm, which is suitable to support cells to migrate and adhere (Table 2).

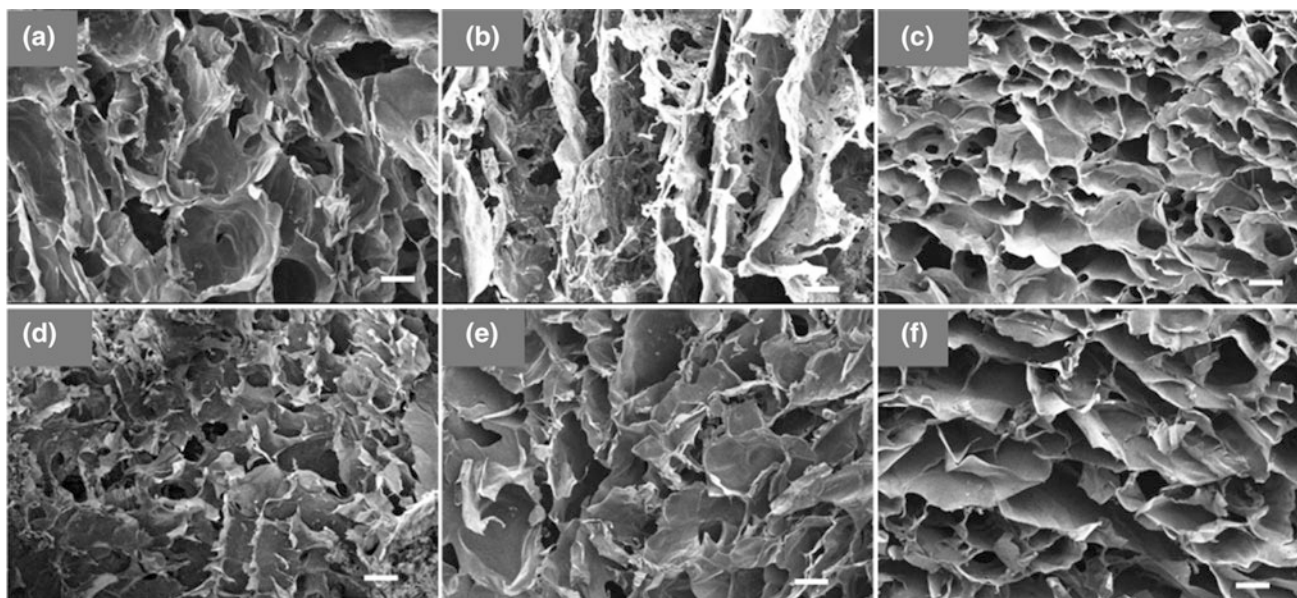


Fig. 3 SEM morphology of fabricated GelCurAg scaffold at different AgNPs: **a** 0. **b** 150. **c** 75. **d** 60. **e** 45. **f** 30 ppm. Scale bar: 100 μ m

Table 2 Formulation compositions (weight basis) for the preparation of GelCurAg scaffold

Code	UV time	Ag ⁺
GelCur	–	–
GelCurAg ₁₅₀	6 h	150 ppm
GelCurAg ₇₅	6 h	75 ppm
GelCurAg ₆₀	6 h	60 ppm
GelCurAg ₄₅	6 h	45 ppm
GelCurAg ₃₀	6 h	30 ppm

4 Conclusion

In this initial study, GelAg complex was utilized to encapsulate Cur to achieve a novel system which is anticipated to possess outstanding antibacterial property and aim to stimulate wound healing capacity. The results suggest that at AgNPs equaled to 75 ppm, the system obtained the most potential topography due to highly porous structure and even distribution of pores and interconnected pores. Thus, the processed sample is appropriate for further investigations and developments to examine and enhance its characteristics and in vitro performance to achieve the most optimal formulation.

Acknowledgements This research is funded by Vietnam National University HoChiMinh City (VNU-HCM) under grant number C2018-28-02.

Conflict of Interest The authors declare that they have no conflict of interest.

References

1. Olczyk, P., Mencner, L., ukasz, Komosinska-Vassev, K.: The role of the extracellular matrix components in cutaneous wound healing. *BioMed Res. Int.* **2014**, 8 (2014). <https://doi.org/10.1155/2014/747584>
2. Mohanty, C., Sahoo, S.K.: Curcumin and its topical formulations for wound healing applications. *Drug Discov. Today* **22**(10), 1582–1592 (2017). <https://doi.org/10.1016/j.drudis.2017.07.001>
3. Mohanty, C., Das, M., Sahoo, S.K.: Emerging role of nanocarriers to increase the solubility and bioavailability of curcumin. *Expert Opin. Drug Deliv.* **9**(11), 1347–1364 (2012). <https://doi.org/10.1517/17425247.2012.724676>
4. Kramer, A., Maassen, A.: Wound dressings from a hygienic point of view using the example of sorbion sachet S. *GMS Krankenhhyg Interdiszip* **4**(2), Doc11 (2009). <https://doi.org/10.3205/dgkh000136>

5. Nguyen, T.H., Kim, Y.H., Song, H.Y., Lee, B.T.: Nano Ag loaded PVA nano-fibrous mats for skin applications. *J. Biomed. Mater. Res. B, Appl. Biomater.* **96**(2), 225–233 (2011). <https://doi.org/10.1002/jbm.b.31756>
6. Hiep, N.T., Khon, H.C., Niem, V.V.T., Toi, V.V., Ngoc Quyen, T., Hai, N.D., Ngoc Tuan Anh, M.: Microwave-assisted synthesis of chitosan/polyvinyl alcohol silver nanoparticles gel for wound dressing applications. *Int. J. Polym. Sci.* **2016**, 11 (2016). <https://doi.org/10.1155/2016/1584046>
7. Nhi, T.T., Khon, H.C., Hoai, N.T.T., Bao, B.C., Quyen, T.N., Van Toi, V., Hiep, N.T.: Fabrication of electrospun polycaprolactone coated with chitosan-silver nanoparticles membranes for wound dressing applications. *J. Mater. Sci. Mater. Med.* **27**(10), 156 (2016). <https://doi.org/10.1007/s10856-016-5768-4>
8. Nguyen, T.-H., Lee, B.-T.: Fabrication and characterization of cross-linked gelatin electro-spun nano-fibers. *J. Biomed. Sci Eng.* **03**(12), 8 (2010). <https://doi.org/10.4236/jbise.2010.312145>
9. Gopinath, D., Ahmed, M.R., Gomathi, K., Chitra, K., Sehgal, P. K., Jayakumar, R.: Dermal wound healing processes with curcumin incorporated collagen films. *Biomaterials* **25**(10), 1911–1917 (2004)
10. Basnet, P., Skalko-Basnet, N.: Curcumin: an anti-inflammatory molecule from a curry spice on the path to cancer treatment. *Molecules (Basel, Switzerland)* **16**(6), 4567–4598 (2011). <https://doi.org/10.3390/molecules16064567>
11. Yang, M., Wu, Y., Li, J., Zhou, H., Wang, X.: Binding of curcumin with bovine serum albumin in the presence of iota-carrageenan and implications on the stability and antioxidant activity of curcumin. *J. Agric. Food Chem.* **61**(29), 7150–7155 (2013). <https://doi.org/10.1021/jf401827x>
12. Kumar, A., Dogra, S., Prakash, A.: Protective effect of curcumin (*Curcuma longa*), against aluminium toxicity: Possible behavioral and biochemical alterations in rats. *Behav. Brain Res.* **205**(2), 384–390 (2009). <https://doi.org/10.1016/j.bbr.2009.07.012>
13. Darroudi, M., Ahmad, M.B., Zak, A.K., Zamiri, R., Hakimi, M.: Fabrication and Characterization of Gelatin Stabilized Silver Nanoparticles under UV-Light. *Int. J. Mol. Sci.* **12**(9), 6346–6356 (2011). <https://doi.org/10.3390/ijms12096346>
14. Nguyen, T.-H., Lee, K.-H., Lee, B.-T.: Fabrication of Ag nanoparticles dispersed in PVA nanowire mats by microwave irradiation and electro-spinning. *Mater. Sci. Eng. C* **30**(7), 944–950 (2010). <https://doi.org/10.1016/j.msec.2010.04.012>
15. Marignier, J.L., Belloni, J., Delcourt, M.O., Chevalier, J.P.: Microaggregates of non-noble metals and bimetallic alloys prepared by radiation-induced reduction. *Nature* **317**, 344 (1985). <https://doi.org/10.1038/317344a0>

Nanoneedles and Nanostructured Surfaces for Studying Cell Interfacing

Stuart G. Higgins[✉], Michele Becce[✉], Hyejeong Seong[✉],
and Molly M. Stevens[✉]

Abstract

Nanoneedles are a materials platform that facilitates intimate tissue- and cell-interfacing, and drug and nanoparticle delivery. Engineering silicon needles, with <100 nm sharpened tips, allows the response of cells to be studied when the cell membrane and nucleus is placed under extreme curvature. Different cell types respond differently, and are influenced by the geometry of the nanostructures. Topography, material mechanical properties, and surface chemistry all play important roles—with the challenge understanding the impact of each. Here, we briefly review the use of nanoneedles in multiple applications within the Stevens Group, and present the fabrication method used to create biologically relevant nanostructured surfaces. We also discuss the current challenges and future opportunities for nanoneedles.

Keywords

Nanoneedles • Cell interfacing • Microfabrication

1 Biological Applications for Nanoneedles

1.1 Introduction to Nanoneedles

Nanoneedles are high-aspect-ratio nanostructures, patterned on flat surfaces, with typical heights of one to ten micrometres [1–3]. They are conical in nature, and tapered to a sharp point less than 100 nm in radius of curvature (see Fig. 1). This sharp point is the defining feature of a nanoneedle, differentiating it from blunter high-aspect-ratio structures such as nanopillars [4]. In the literature, nanoneedles are often referred to by the synonym nanowires, which is used somewhat interchangeably, and often to refer to less conical, vertically-aligned needles with sharp tips [5].

Silicon is a common material choice for nanoneedles. It offers several advantages: silicon processing is well-established thanks to the extensive investment in tools to fabricate silicon-based microprocessors; silicon is readily available as near-atomically flat wafers, providing a smooth surface which helps yield uniform nanoneedles; crystalline silicon can be converted into porous silicon, dramatically altering the material properties, and enabling biodegradable nanoneedles. While other material systems, such as carbon fibres and quartz have been explored [4, 6], silicon remains the most-widely used.

Nanoneedles and other nanostructured materials have been developed for a wide-range of research activities. In the case of biological interfacing, the research impetus has been to stimulate biological responses and access to the intracellular environment. The most common areas are: delivery of biorelevant cargoes into cells [2, 5, 7]; sensing of the biochemical intracellular environment [2, 8, 9]; providing topographical cues to guide cell expression [10]; sensing and stimulating the electrophysiological cellular environment [11]; and, in the case of prokaryotic cells, acting as an anti-bacterial surface [12].

S. G. Higgins (✉) · M. Becce · H. Seong · M. M. Stevens
Department of Materials, Imperial College London, London, SW7
2AZ, UK
e-mail: stuart.higgins@imperial.ac.uk

M. M. Stevens
e-mail: m.stevens@imperial.ac.uk

S. G. Higgins · H. Seong · M. M. Stevens
Department of Bioengineering, Imperial College London, London,
SW7 2AZ, UK

M. M. Stevens
Institute of Biomedical Engineering, Imperial College London,
London, SW7 2AZ, UK

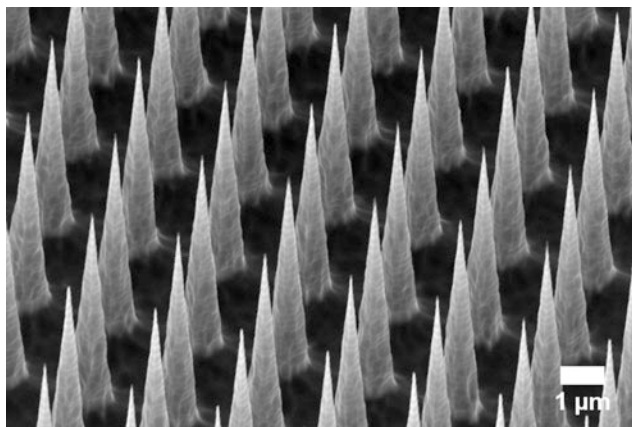


Fig. 1 A scanning-electron microscopy micrograph showing an array of 2 μm spaced silicon nanoneedles. Sample prepared by S.G. Higgins, Stevens Group

1.2 Nanoneedles for Studying Cellular and Nuclear Mechnotransduction

Cells are highly sensitive to their environment, and susceptible to mechanical and physical cues. In the case of pluripotent and multipotent stem cells, understanding and controlling this behaviour is an area of great interest, aiding the development of new regenerative therapies and disease models [13]. Microstructured topographical surfaces have been explored extensively: microgrooved and microcontact printed substrates can guide stem cell fate [14, 15]; the formation of focal adhesions between the cell membrane and surrounding material can be modified by patterning regions of different material stiffness [16].

The sharpness of nanoneedles presents an opportunity to probe cellular mechanotransduction with even greater precision. Recent studies have suggested that membrane curvature is intimately linked to fundamental processes such as endocytosis [17], where modulating curvature may influence endocytotic behaviour. Nanoneedles are the ideal platform for probing this type of behaviour, as surfaces can be readily tailored using microfabrication processes to yield a range of geometries and test structures.

1.3 A Materials Platform for Delivery

Nanoneedles have been demonstrated as an effective technology for delivering a wide variety of cargoes into cells. Different biorelevant molecules can be physisorbed onto the needle surface. Typically, the surface is prepared using an oxygen plasma treatment and/or treatment with an amino-silane self-assembled monolayer, both of which

promote binding. This approach has been used to attach nucleic acids, nanoparticles, proteins and peptides to the surface of silicon nanoneedles [1, 2, 5, 8]. Diced silicon chips of nanoneedles are immersed in a solution or suspension of the target molecule, and incubated. Cell interfacing is achieved either by seeding cells directly onto loaded nanoneedles, or by placing the inverted chip onto a cell culture. In the latter case, penetration can be enhanced by centrifuging the chip in situ on top of the cells.

Within the Stevens Group, Gopal, Hansel and Chiappini et al. have used this approach to demonstrate how nanoneedles modulate endocytotic machinery [22], inhibit membrane focal adhesion maturation [23], and deliver hydrophilic cadmium telluride quantum dots into HeLa cells [2]; quantum dots were dispersed throughout the cytosol in less than one hour after interfacing. Nanoneedles can also deliver molecules in vivo; nanoneedles loaded with a human VEGF165 plasmid DNA transfected muscle cells in a mouse model, inducing neovascularisation in the tissue [1]. This behaviour was more pronounced than a direct injection of the same plasmid. Such approaches could help deliver relevant factors to aid wound-healing, and for encouraging tissue to graft to implanted structures.

1.4 A Materials Platform for Sensing

Nanoneedles can sense the intracellular environment. By covalently binding a pH-sensitive fluorophore (fluorescein isothiocyanate) and a reference fluorophore (AlexaFluor 633), the ratio of the two fluorescent signals can be used to map the intracellular pH in different cell-culture regions [2]. Two cell lines were investigated: the cancerous esophageal adenocarcinoma cell line OE33 and a healthy esophageal cell line HET-1A. The more acidic cytosolic environment of the cancerous cells was sensed as a quenching of the fluorescence of the fluorescein isothiocyanate marker, and corresponding shift in the ratiometric fluorescence.

Enzymatic activity can also be sensed by conjugating a fluorescently-tagged peptide to the surface of a nanoneedle array [8]. This peptide can be cleaved by Cathepsin B, a cysteine protease, releasing the fluorescent marker into the cytosol. Cathepsin B is upregulated under several circumstances, including in cancerous tissues, and is used as a biomarker for some solid tumours. This approach showed that seeding both healthy and cancerous esophageal cell lines onto labelled needles, allows enzymatic activity to be mapped using fluorescent microscopy. This approach could be used to develop a sensor capable of assisting with esophageal cancer diagnoses.

2 Manufacturing Approach for Silicon Nanoneedles

2.1 Microfabrication Technique

Within the Stevens Group, a p-type boron-doped silicon wafer is first coated with a layer of low-stress silicon nitride using low-pressure-vapor deposition. Use of a low-stress layer is particularly important for providing a continuous, hard-etch mask, chemically resistant to subsequent wet etching. An array of disks, nominally of ~ 600 nm diameter is patterned onto the surface using photolithography. The array dimensions are a function of the patterning mask design; commonly, $2\ \mu\text{m}$ spaced nanoneedles provide a good needle-to-cell ratio for the average eukaryotic cell size, although the precise relationship between spacing and cell response is still under study.

The disk pattern is transferred into the silicon nitride etch mask using reactive-ion etching, by exposing the substrate to a directed CF_4 plasma. After transfer, the photoresist is removed and a descum step carried out.

The negative of the flat disk pattern is etched into the substrate to form three-dimensional cylinders. While this step can be performed by a variety of techniques, a wet etching process known as metal-assisted chemical etching (MACE) allows the formation of biodegradable nanoneedles. Metallic silver nanoparticles are coated onto the patterned surface using electroless deposition. The metal-coated substrate is then immersed in a bath of hydrofluoric acid and hydrogen peroxide. The silver catalyses the etching of silicon by the hydrofluoric acid, preferentially increasing the etch rate on flat silicon areas. As the surface is slowly eroded, the exposed sidewalls of the silicon pillars are not coated with silver and therefore etch slower. This makes the process highly anisotropic. By using an appropriately conductive silicon wafer, and by tuning the concentration of hydrogen peroxide, the remaining material is converted from solid into porous silicon. This gives the nanoneedles their biodegradable nature. Upon exposure to aqueous conditions, porous silicon reacts to form orthosilicic acid, a product found natively in the body, and readily excreted [18].

After wet-etching, the remaining silver metal is chemically removed, and the substrate exposed to another reactive-ion-etching plasma, SF_6 . This step: removes the silicon nitride etch mask, tapers the cylinders into sharpened needles, and strips very thin residual silicon structures left between nanoneedles by the MACE process. The silicon wafer is diced into the desired size, and oxygen plasma cleaned before use (Fig. 2).

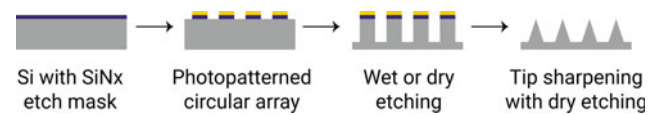


Fig. 2 Illustration of the microfabrication process of silicon nanoneedles

3 Future Challenges for Nanoneedles

3.1 Understanding the Mechanism of the Cell-Material Interface

The interfacing behavior of nanoneedles has been a topic of much discussion. Nanoneedle tips are an order of magnitude smaller than most eukaryotic cells. As needles are interfaced with the cell, the cell membrane is contorted by the sharp tip. Whether the nanoneedle penetrates the cell, or merely convolutes the membrane, has been a topic of much discussion throughout the literature [1, 3, 7, 19]. As well as being highly dependent upon nanoneedle geometry, most reports of penetration require that cells be electroporated before intracellular access is observed. For example: nanoneedle electrodes show a reduction in the electrical resistance between electrode and cell after electroporation [11], and cells on hollow nanoneedles similarly show greater delivery of a fluorescently-tagged marker after electroporation [20]. Studies using focussed ion-beam milling scanning electron microscopy (FIB-SEM) have suggest that in the absence of electroporation the membrane is strongly perturbed, but not penetrated [21]. Recently, we have shown using a combination of electron- and scanning-ion-conductance microscopy that porous silicon nanoneedles stimulate endocytotic pathways in cells, resulting in an increase in cellular uptake [22].

3.2 Impact of Geometry and Material Choices

Another area for further investigation is developing a clearer understanding of the impact of nanoneedle geometry on cell response. While studies have shown that the deformation of the cell membrane of fibroblast cells (NIH-3T3) to nanopillars is strongly dependent upon pitch spacing and nanopillar radius [4], it is unclear if the same behaviour applies to sharp nanoneedles. Cells mechanically interact with their environment through the formation of focal adhesions, protein complexes embedded in the cell membrane, which form a direct mechanical contact between the extracellular environment and internal actin cytoskeleton. Different cell types also exhibit different responses, adding a

further complication. Investigating a wider range of needle geometries and cell types will provide better insight into the underlying mechanisms.

To date, the majority of nanoneedles have focussed on the use of silicon and other mechanically-hard inorganic materials such as quartz or alumina, for practical processing reasons. Although technically challenging, developing systems from softer materials, such as organic polymers, present an opportunity to explore the impact of both the topographical nanoneedle cues, and material properties. This would also have implications for the practical application and adoption of nanoneedles as a delivery and sensing system in the clinical environment.

3.3 Summary

Nanoneedles are an exciting technology platform that enable a wide-range of sensing, delivery applications, as well as providing a means to study fundamental cellular behaviours. Within the Stevens Group, we have already demonstrated the value of nanoneedles by transfecting tissue *in vivo*, delivering quantum dots to cells, and sensing intracellular pH and enzyme activity. Moving forward, questions remain over the precise impact of nanoneedle geometry and material cues, providing a new set of research challenges.

Acknowledgements SGH and MMS acknowledge support from the ERC Seventh Framework Programme Consolidator grant 'Naturale CG' (616417). MB acknowledges support from Rosetrees Trust.

Conflict of Interest The authors declare that they have no conflict of interest.

References

- Chiappini, C., De Rosa, E., Martinez, J.O., et al.: Biodegradable silicon nanoneedles delivering nucleic acids intracellularly induce localized *in vivo* neovascularization. *Nat. Mater.* **14**, 6–13 (2015). <https://doi.org/10.1038/nmat4249>
- Chiappini, C., Martinez, J.O., De Rosa, E., et al.: Biodegradable nanoneedles for localized delivery of nanoparticles *in vivo*: exploring the biointerface. *ACS Nano* **9**, 5500–5509 (2015). <https://doi.org/10.1021/acs.nano.5b01490>
- Robinson, J.T., Jorgolli, M., Shalek, A.K., et al.: Vertical nanowire electrode arrays as a scalable platform for intracellular interfacing to neuronal circuits. *Nat. Nanotechnol.* **7**, 180–184 (2012). <https://doi.org/10.1038/nnano.2011.249>
- Hanson, L., Zhao, W., Lou, H.-Y., et al.: Vertical nanopillars for *in situ* probing of nuclear mechanics in adherent cells. *Nat. Nanotechnol.* **10**, 554–562 (2015). <https://doi.org/10.1038/nnano.2015.88>
- Shalek, A.K., Robinson, J.T., Karp, E.S., et al.: Vertical silicon nanowires as a universal platform for delivering biomolecules into living cells. *Proc. Natl. Acad. Sci.* **107**, 1870–1875 (2010). <https://doi.org/10.1073/pnas.0909350107>
- Rawson, F.J., Cole, M.T., Hicks, J.M., et al.: Electrochemical communication with the inside of cells using micro-patterned vertical carbon nanofibre electrodes. *Sci. Rep.* **6**, 37672 (2016). <https://doi.org/10.1038/srep37672>
- Vandersarl, J.J., Xu, A.M., Melosh, N.A.: Nanostraws for direct fluidic intracellular access. *Nano Lett.* **12**, 3881–3886 (2012). <https://doi.org/10.1021/nl204051v>
- Chiappini, C., Campagnolo, P., Almeida, C.S., et al.: Mapping local cytosolic enzymatic activity in human esophageal mucosa with porous silicon nanoneedles. *Adv. Mater.* **27**, 5147–5152 (2015). <https://doi.org/10.1002/adma.201501304>
- Higgins, S.G., Stevens, M.M.: Extracting the contents of living cells. *Science* **356**(80), 379–380 (2017). <https://doi.org/10.1126/science.aan0228>
- Bonde, S., Buch-Månson, N., Rostgaard, K.R., et al.: Exploring arrays of vertical one-dimensional nanostructures for cellular investigations. *Nanotechnology* **25** (2014). <https://doi.org/10.1088/0957-4484/25/36/362001>
- Abbott, J., Ye, T., Qin, L., et al.: CMOS nanoelectrode array for all-electrical intracellular electrophysiological imaging. *Nat. Nanotechnol.* **1–8** (2017). <https://doi.org/10.1038/nnano.2017.3>
- Tripathy, A., Sen, P., Su, B., Briscoe, W.H.: Natural and bioinspired nanostructured bactericidal surfaces. *Adv. Colloid Interface Sci.* **248**, 85–104 (2017). <https://doi.org/10.1016/j.cis.2017.07.030>
- Crowder, S.W., Leonardo, V., Whittaker, T., et al.: Material cues as potent regulators of epigenetics and stem cell function. *Cell Stem. Cell* **18**, 39–52 (2016). <https://doi.org/10.1016/j.stem.2015.12.012>
- Downing, T.L., Soto, J., Morez, C., et al.: Biophysical regulation of epigenetic state and cell reprogramming. *Nat. Mater.* **12**, 1154–1162 (2013). <https://doi.org/10.1038/nmat3777>
- von Erlach, T.C., Bertazzo, S., Wozniak, M.A., et al.: Cell-geometry-dependent changes in plasma membrane order direct stem cell signalling and fate. *Nat. Mater.* (2018). <https://doi.org/10.1038/s41563-017-0014-0>
- Biggs, M.J.P., Fernandez, M., Thomas, D., et al.: The functional response of mesenchymal stem cells to electron-beam patterned elastomeric surfaces presenting micrometer to nanoscale heterogeneous rigidity. *Adv. Mater.* **1702119**, 1–13 (2017). <https://doi.org/10.1002/adma.201702119>
- Zhao, W., Hanson, L., Lou, H.-Y., et al.: Nanoscale manipulation of membrane curvature for probing endocytosis in live cells. *Nat. Nanotechnol.* **12**, 750–756 (2017). <https://doi.org/10.1038/nnano.2017.98>
- Anderson, S.H.C., Elliott, H., Wallis, D.J., et al.: Dissolution of different forms of partially porous silicon wafers under simulated physiological conditions. *Phys. Status Solidi Appl. Res.* **197**, 331–335 (2003). <https://doi.org/10.1002/pssa.200306519>
- Jahed, Z., Zareian, R., Chau, Y.Y., et al.: Differential collective- and single-cell behaviors on silicon micropillar arrays. *ACS Appl. Mater. Interfaces* **8**, 23604–23613 (2016). <https://doi.org/10.1021/acsami.6b08668>
- Cao, Y., Hjort, M., Chen, H., et al.: Nondestructive nanostraw intracellular sampling for longitudinal cell monitoring. *Proc. Natl. Acad. Sci.* **114**, E1866–E1874 (2017). <https://doi.org/10.1073/pnas.1615375114>
- Santoro, F., Zhao, W., Joubert, L.M., et al.: Revealing the cell-material interface with nanometer resolution by focused ion beam/scanning electron microscopy. *ACS Nano* **11**, 8320–8328 (2017). <https://doi.org/10.1021/acs.nano.7b03494>
- Gopal, S., Chiappini, C., Penders, J., et al.: Porous silicon nanoneedles modulate endocytosis to deliver biological payloads. *Adv Mater* **1806788**, (2019). <https://doi.org/10.1002/adma.201806788>
- Hansel, C.S., Crowder, S.W., Cooper, S., et al.: Nanoneedle-mediated stimulation of cell mechanotransduction machinery. *ACS Nano* (2019). <https://doi.org/10.1021/acs.nano.8b06998>



From Macroscopic to Microscopic: Experimental and Computational Methods to Investigate Bio-tribology

Raman Maiti, Rasmus Wagner, Noe A. Martinez Sanchez,
Alejandro Ramirez-Reivich, Peter Ellison, Cecile Perrault, Matt J. Carre,
Rob Dwyer-Joyce, Anne Neville, and Roger Lewis

Abstract

Tribology is an important factor (among other factors) during biological interactions of devices and tissues. The paper discusses how new computational and experimental methods can be used to understand and improve the design and development of medical devices at macro and micro scales to sustain life beyond 50 years. We have used pre-clinical experiments and computational methods to understand interactions between orthopaedic implants at the macro scale. The computational model has been validated with experiments. Now this computational model can predict damage in implants for different patients. One such application was successfully tried and tested in collaboration with University National Autonomous Mexico. This methodology can be used in future to design patient specific, affordable (using 3D printing) and robust implants which will be useful for developing countries like Vietnam, India and Mexico. Improvement of catheter designs is important to reduce damage to the internal tissues while being used for cardiovascular problems. We are developing new experimental techniques (in micro scale) that can be used to understand the interaction of cells with the catheter material. These will help reduce the hospital costs incurred during longer stay of the patients admitted for cardiovascular related problems.

Keywords

Friction • Wear • Patella femoral joint • Endothelial cells • Catheter

1 Introduction

Experimental work is robust, however, it is time consuming and costly [1, 2]. The experimental investigations of kinematics for artificial patella femoral joint replacements for new samples and samples after 15 million cycles took more than 15 months to complete [3]. On the other hand, computational modelling is not costly and explain quasi-static conditions of any interactions, however, requires validation with the experiments [3]. The same kinematics generated using multi-body dynamic simulations took 2 h. The kinematics generated using the multi-body dynamic simulations were validated with experimental methods [3]. This paper outlines the two methods (namely computational and experimental) for understanding surface to surface interactions at macro and micro scales. These methods are useful in conditions where great in-depth knowledge is required for design and development of medical devices. The paper is divided into two studies. The first study compares the damage/contact maps generated by experimental, computational and retrieval studies of artificial patella femoral joint replacements at the macro scale. The second study highlights a frictional study between a glass bead (representing a catheter tip) against a fibronectin layer on a glass plate (representing tissues without the endothelial cells). Computational studies have been planned in future. However, the micro cellular interactions will be beneficial to understand tribology at the micro level.

R. Maiti (✉) · R. Wagner · C. Perrault · M. J. Carre ·
R. Dwyer-Joyce · R. Lewis
University of Sheffield, Sheffield, UK
e-mail: R.Maiti@Sheffield.ac.uk

N. A. Martinez Sanchez · A. Ramirez-Reivich
National University Autonomous Mexico,
Mexico City, Mexico

P. Ellison
University of Bergen, Bergen, Norway

A. Neville
University of Leeds, Leeds, UK

2 Materials and Methods

2.1 Experimental and Computational Tribological Studies at the Macroscopic Scale

For the studies at the macroscopic scale, artificial patella femoral joint components (38 mm dome moderately linked ultra-high molecular weight polyethylene patella and Cobalt Chrome Molybdenum size 3 right femoral) were acquired from DePuy International. Experimental tests were carried out in Knee Sim I (Leeds) at gait cycle [1, 2] for 12 million cycles. The damage maps generated due the tribological interactions were compared with retrievals [4]. More details on the kinematics associated with the gait cycle, lubrication used during the pre-clinical testing are reported elsewhere [1].

A computational study was carried out using Multi-body Dynamic Simulations (MBDS) platform namely, MSC ADAMS (Siemens Inc., USA). The model was generated by importing the computer aided design (in STL formats). More details on the design and development of the model is reported elsewhere [3]. The tracks generated by any elements of femoral component were mapped on the patella component. Joining the highest superior and lowest inferior points of the tracks resulted in generation of a contact map. The contact map generated was validated against experimental and retrieval studies.

2.2 Experimental and Computational Tribological Studies at the Microscopic Scale

The experimental studies were carried out using a Universal Material tester (UMT-2). An interaction of engineered tissue with endothelial cells and a catheter tip. Hence, the first step to understand the complete tribological interaction between catheter and engineered tissue was to investigate the effect on fibronectin. A glass bead of 1000 μm diameter was slid (0.20 mm/s) against HiLyte FluorTM 488 Fibronectin (Cytoskeleton Inc., USA) coated on a glass petri dish to generate a contact pressure of 350 kPa. The tribological interaction was submerged in PBS solution. Images of the fibronectin layer before and after the interaction with the glass bead were captured using inverted microscopy (Nikon Eclipse Ti, Amsterdam). Due to the complexity in the tissue being poroelastic and viscoelastic, a computational model will be developed in the future.

3 Results and Discussion

3.1 Experimental and Computational Tribological Studies at the Macroscopic Scale

Good correlation between the experimental damage and MBDS contact maps were achieved (see Fig. 1). The damage and contact maps were covering 40% of the total surface area. However, the contact map was stretched towards the inferior side and the damage map was stretched towards the medial lateral side. This is due to the presence of limited medial lateral patellar motion (<1 mm) in the MBDS.

Further studies to include medial lateral motion (up to 6 mm) will be conducted in future. The sensitivity analysis show that the medial lateral motion and flexion extension angles are important parameters influencing the size of contact maps generated by the MBDS computational model. These studies will help be helpful to design right implant for right patients for developing countries like Vietnam, India and Mexico.

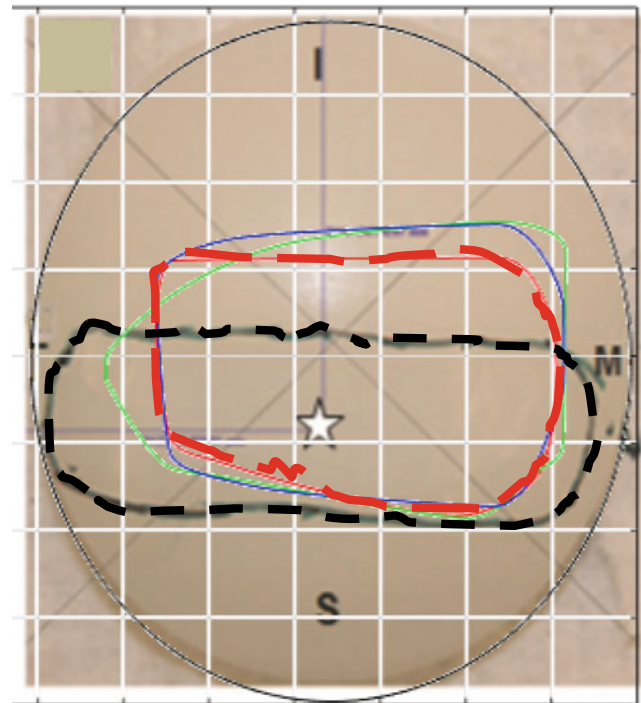
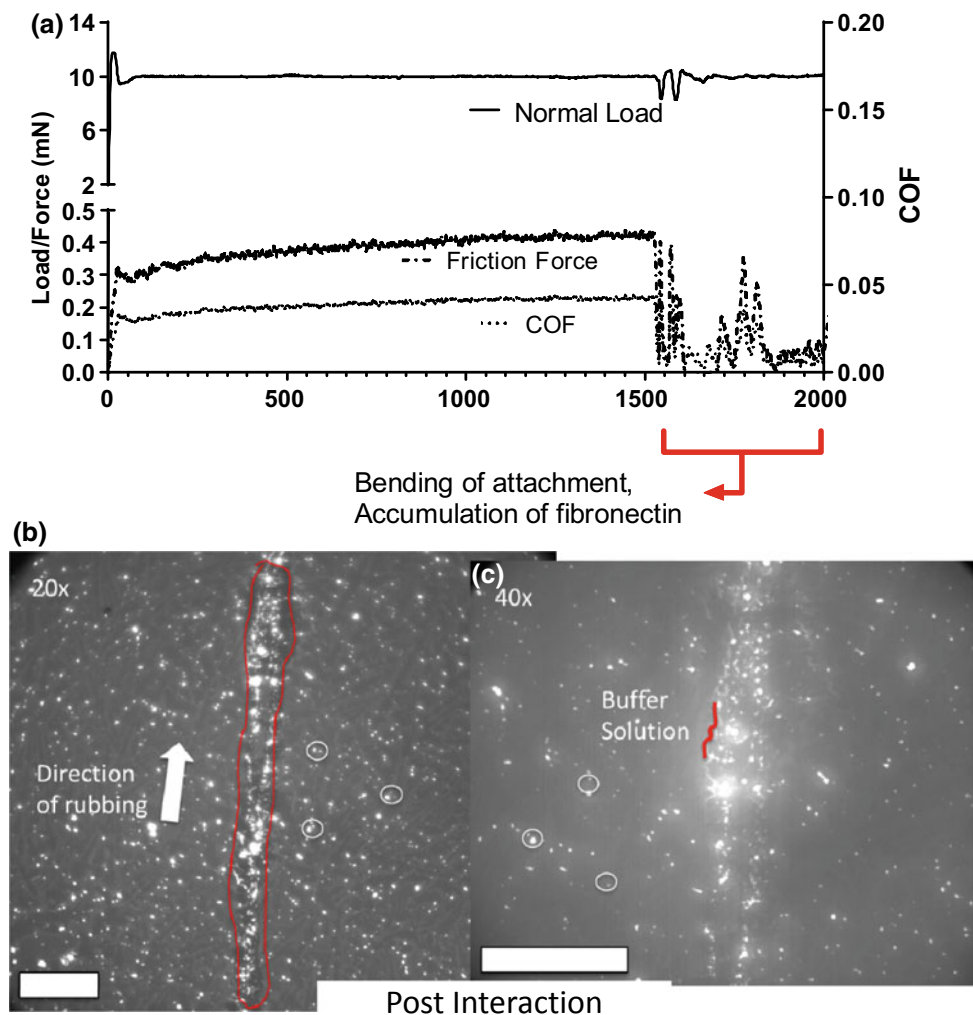


Fig. 1 Comparison of experimental damage map (in black short dash) and computational contact map (in red long dash). Sensitivity analysis of the contact maps with change in kinematics are presented in solid green and solid blue. The star represents the centroid of the damage map. S: Superior, I: Inferior, M: Medial and L: Lateral side of the patella component

Fig. 2 a Frictional graph of interaction between fibronectin and glass bead, microscopic image of fibronectin layer post interaction at, b 20x and c 40x. The arrow represents the direction of sliding and red line represents the boundary of the scratch. The circle represents the fibronectin on the glass petri dish



3.2 Experimental Tribological Studies in Microscopic Scale

The tribological interaction of a glass bead on a fibronectin layer generated a frictional graph as shown in Fig. 2a. The coefficient of friction is constant at 0.2 for most of the interaction. After a certain point, there is a drop in coefficient friction. This is due to the accumulation of fibronectin between the contacts resulting in lubrication and decrease in the coefficient friction as shown in Fig. 2b, c. Due to the presence of PBS and buffer solution, the scratch boundaries can be easily located at 40x scale.

Frictional studies with hydrogel will be conducted in future to assess the effect of hydrogel on the tribological properties. The computational studies will be conducted and validated in parallel to understand the catheter tissue interaction. We predict the changes in catheter design in future based on the studies which will save a lot of money for developing countries in terms of number of days a patient takes to recover after the surgery in a hospital.

4 Conclusion

Experimental and computational methods are useful for understanding the interaction between two interacting surfaces in macro and micro scales. The paper describes two such studies: artificial patella femoral joint replacements and catheter tissue interactions. These studies will generate substantial knowledge to improve design and development of medical devices in future.

Acknowledgements This research was supported by Engineering and Physical Sciences Research Council (grant number EP/R001766/1) as a part of 'Friction: The Tribology Enigma' (www.friction.org.uk), a collaborative Programme Grant between the universities of Leeds and Sheffield, Royal Academy of Engineering Newton Fund (grant number NRC1617/6/181) between University of Sheffield and University National Autonomous Mexico, and Peter Jost Travel Award. Dr Raman Maiti would also like to thank Institute of Medical and Biological Engineering, University of Leeds and DePuy Synthesis for the assistance offered while conducting experimental studies of artificial patella femoral joint replacements during his Ph.D. **Conflict of Interest** The authors declare that they have no conflict of interest.

References

1. Maiti, R., Fisher, J., Jennings, L.M.: The influence of kinematic conditions and design on the wear of patella-femoral replacements. *Proc. Inst. Mech. Eng. H* **228**(2), 175–181 (2014)
2. Maiti, R., Cowie, R.M., Fisher, J., Jennings, L.M.: The influence of malalignment and ageing following sterilisation by gamma irradiation in an inert atmosphere on the wear of ultra-high-molecular-weight polyethylene in patellofemoral replacements. *Proc. Inst. Mech. Eng. H* **1**(7), 634–642 (2017)
3. Maiti, R.: Computational modelling of patella femoral kinematics during gait cycle and experimental validation. *J. Inst. Eng. India Ser. C* **99**(3), 271–276 (2018)
4. Ellison, P., Fisher, J.: Assessment of the damage in retrieved patellar components. *J. Long Term Eff. Med. Implants* **20**(1), 57–72 (2010)

Part V
Biomechanics

Bio-safety and Bio-efficiency of Micro-plasma Exposure to Fibroblast Cells L929

Ngo Thi Minh Hien, Nguyen Thi Kim Mai, Vo Hoang Thuc Minh, Nguyen Thi My Anh, Nguyen Ngoc Thang, Vo Duong Van Anh, Do Tuyet Nhi, Nguyen Quoc Duy Nam, and Huynh Quang Linh

Abstract

In recent years, there has been a wide range of studies about demonstration of micro-plasma safety on cells. This study emphasizes micro-plasma effects on cells, especially proliferation and migration, by using Western Blot technique and Image J analysis software determines the relative density of protein γ -H2AX (the protein marks a deoxyribonucleic acid—DNA breaks) in groups of muscle cell of mice (L929) treated by N₂/Ar micro-plasma in different exposure time (0, 5, 10 and 15 s) with capacity 17 W. Analysis of results aims to evaluate and compare micro-plasma safety in various exposure time. In conclusion, by those results lead to confirm the safety of micro-plasma at the molecular level in terms of cell viability, proliferation and migration. Thanks to micro-plasma effects on cell, micro-plasma is used in wound healing, sterilization, and can even be used to kill cancer cells.

Keywords

N₂/Ar micro-plasma • Cell proliferation • Cell migration • Western blot • Protein γ -H2AX

1 Introduction

The term plasma in physics refers to a partially ionized medium, usually gas. Importantly, plasma not only produces electrons and various ions, but also neutral (uncharged)

atoms and molecules, such as free radicals and electronically excited atoms having high chemical reactivity and the capability to emit UV [1]. Plasma-based electrosurgical devices have long been employed for tissue coagulation, cutting, desiccation, and cauterizing [2]. Recently, there have been significant developments in cold atmospheric pressure plasma science and engineering. New sources of cold atmospheric pressure plasma with well-controlled temperatures below 40 °C have been designed, permitting safe plasma application on animal and human bodies [3]. In the last decade, a new innovative field, often referred to as plasma medicine, which combines plasma physics, life science, and clinical medicine has emerged. This field aims to exploit effects of plasma by controlling the interactions between plasma components (and other secondary species that can be formed from these components) with specific structural elements and functionalities of living cells [4].

Micro-plasma is a cold atmospheric pressure plasma. The size of micro-plasma depends on the distance between the two electrodes, ranging from tens, hundreds, even thousands of micrometers. In micro-plasma, gas can be maintained close to room temperature [5]. By virtue of outstanding features such as reactive oxygen nitrogen species production at the atmospheric pressure and room temperature conditions, micro-plasma becomes the best choice for wound healing, sterilization, blood coagulation, Studies on the application of micro-plasma for cells and animals have determined that a certain amount of plasma can promote wound healing, cell proliferation and migration, etc.

However, detailed mechanisms at the cellular and molecular level are not yet fully understood. Is it really safe to use micro-plasma for treatment on cells, animals and humans? This study will test the safety of micro-plasma effects on L929 mouse skin fibroblasts through the determination of γ -H2AX protein content (the protein marks a DNA breaks) by Western Blot technique. From there, reaffirmed the safety of micro-plasma in the stimulation of cell proliferation and migration.

N. T. M. Hien (✉)

Department of Biomedical Engineering-Faculty of Applied Science, Ho Chi Minh City University of Technology, Ly Thuong Kiet, Ho Chi Minh City, Vietnam
e-mail: nmhien@hcmut.edu.vn

N. T. K. Mai · V. H. T. Minh · N. T. M. Anh · N. N. Thang · V. D. Van Anh · D. T. Nhi · N. Q. D. Nam · H. Q. Linh
Department of Biomedical Engineering-Faculty of Applied Science, Ho Chi Minh City University of Technology, Ho Chi Minh City, Vietnam

2 Materials and Methods

2.1 Fibroblast Cell (L929) Culture

Fibroblast cells derived from an immortalized mouse fibroblast cell line were preserved in alpha modified Eagle's medium (a-MEM) with 10% horse serum (Gibco, Invitrogen, CA, USA) and 10 ml 10,000-U ml⁻¹ penicillin—10,000 mgml⁻¹ streptomycin (Sigma, St. Louis, MO). Before the experiments, fibroblast cells were washed with phosphate buffered saline (PBS), and detached with trypsin (Gibco, Invitrogen). In the cell coverage model, fibroblast cells were placed consistently in a 24-well plate (Nunc, Thermal Scientific), with 7.5×10^5 cells/ml in a complete medium, and maintained at 37 °C under 5% CO₂ for 24 h. Fibroblast cells with two different cell densities were prepared for the various experiments, and these are denoted as “the test cells”.

2.2 Protein γ -H2AX

In recent years, a new biomarker, the phosphorylated histone H2AX, has become a powerful tool to monitor DNA breaks. When DNA damage, whether it is endogenous or exogenous, forms double stranded breaks (DSBs) or single stranded breaks (SSBs) which are in chromatin. They promptly initiate the phosphorylation of the histone H2A variant, H2AX, at Serine 139 to generate γ -H2AX [6]. This newly phosphorylated protein, γ -H2AX, is the first step in recruiting and localizing DNA repair proteins. DNA breaks can be induced by mechanisms such as ionizing radiation or cytotoxic agents and subsequently, γ -H2AX foci quickly form. These foci represent the DNA breaks in a 1:1 manner and can be used as a biomarker for damage.

Given the nexus between DNA breaks and the γ -H2AX response, as well as the allowable conditions of the study, we used the Western Blot technique to obtain γ -H2AX protein density to determine DNA breaks.

2.3 Micro-plasma System

A custom-made micro-plasma jet source was driven by a radio-frequency power supply of 13.56 MHz (ENI ACG-3B, MKS Instruments Inc., Rochester, New York, USA) with a matching device (ACG-3B, ENI Corp., Rochester, USA). This jet source was a capillary electrode through which the additive N₂. The micro-plasma device used in this work contained a quartz tube as the gas channel and a dielectric layer with an outer diameter of 2 mm. At the center of the quartz tube, a stainless steel capillary tube (with a diameter

of 0.2 mm, fixed by a perforated Teflon fitting) was used as the inner electrode as well as the N₂ or O₂ feeding tube. A copper chip was used as the outer electrode, and this was connected to a generator (Fig. 1).

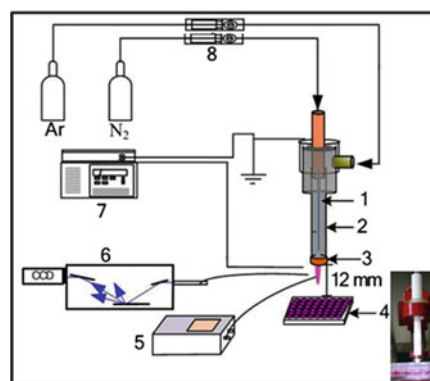
2.4 Temperature Measuring

Plasma plume temperature was estimated using a fiber optic thermometer. The distance from the fiber to micro-plasma jet nozzle was about 4 mm. The temperature was measured in a range of applied powers from 13 to 17 W with a flow rate of 5 standard litre per minute (slm) Ar. To produce N-containing radicals in an excited phase, 0.1, 0.5, and 1% (2.5, 12.5, and 50 sccm) of N₂ were poured into Ar plasma in the capillary tube.

For a given supplied power, an increase in N₂ content significantly decreased the average temperature, in particular for the cases with relatively high supplied powers. In the following studies, a supplied power of 13 W and a distance of about 4 mm between the target substance and micro-plasma jet nozzle were used in order to maintain the desired temperature (Fig. 2).

2.5 Ultraviolet Detection

Plasma UVA and UVB were estimated using a UV sensor. Micro-plasma device was placed on an X-Y coordinated



1. Hollow inner electrode.
2. Dielectric quartz tube.
3. Outer copper electrode.
4. 48-well plate
5. Fiber optic thermometer.
6. Optical Emission Spectroscopy-OES system.
7. RF power supply with matching network.
8. Mass flow control.

Fig. 1 Illustration of non-thermal atmospheric N₂/Ar micro-plasma applied for the stimulation of fibroblast cells in medium

Fig. 2 The apparent plasma plume temperatures were measured as a function of the supplied power with the addition of N₂

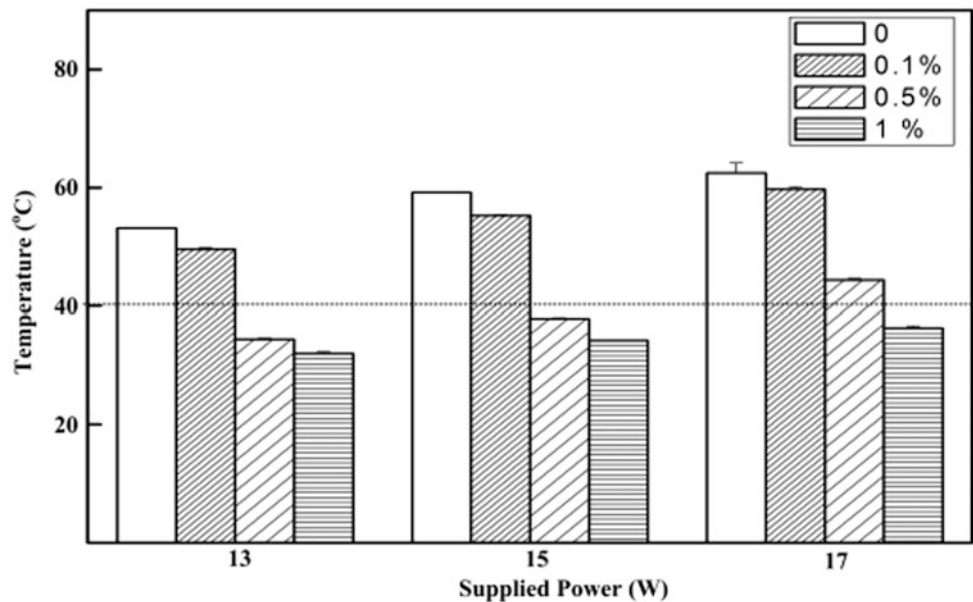


table and the distance from micro-plasma jet nozzle to the UV sensor was varied from 3 to 9 mm. The UV intensity was measured in applied powers from 13 W with a flow rate of 5 slm Ar. To produce N-containing radicals in an excited phase, 0.1, 0.3, and 0.5% of N₂ were poured into Ar plasma in the capillary tube.

UVA and UVB intensity were significantly decreased with the different distance from the plasma jet to UV sensor. The result of the UVA and UVB in the case of 0.5% N₂/Ar micro-plasma, the UV intensity with the distance vary from 3 to 9 mm also smaller than the UV standard (1000 J/cm²), therefore this result is confirm the bio-safety of micro-plasma device for biomedical applications (Fig. 3).

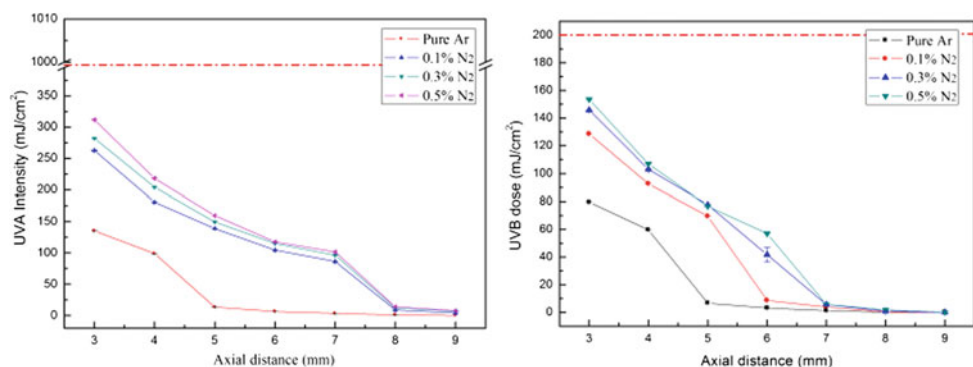
2.6 Cell Proliferation and Cell Coverage Tests

The test-cell viability with and without plasma exposure was assessed via MTS assay (CellTiter 96 Aqueous One

Solution proliferation, Promega). In the experiments, plasma-exposed cells were cultured for 24 or 48 h (two groups). The reagent Aqueous One solution (≈60 μl) was directly added to the culture wells containing both groups of cells. After 3 h incubation at 37 °C under 5% CO₂, the solution (≈100 μl) in each culture well was transferred to 96-well plates (Nunc, Thermal Scientific). The absorbance at 492 nm for the solution in 96-well plates as measured with a standard microplate reader (Multiskan EX Labsystems, Finland). The quantity of formazan product in association with the intensity of absorbance was directly proportional to the number of cultured living cells. The migration ability of the plasma-exposed cells was assessed.

The test cells were first exposed to N₂/Ar micro-plasma for 5, 10, or 15 s. The gaps filled by the test cells and plasma-exposed cells were observed using an optical microscope and evaluated with the WIMASIS image analysis software. Cell coverage tests were carried out every 3 h until the gaps were fully covered.

Fig. 3 The UVA and UVB vary with the addition of N₂ (0.1, 0.3, and 0.5%, respectively) to the Ar micro-plasma



2.7 Analysis of H2AX Phosphorylation by Western Blot

Protein extraction and quantification:

Wash cells with cold PBS and then lyse with ice cold RIPA buffer for 45 min at 4 °C. Centrifuge the extracts at 12,000 g for 15 min at 4 °C. Collect the supernatant containing total extracted proteins. BCA protein assay kit (Pierce Scientific Ltd.) will be used for protein quantification.

SDS-PAGE and Western blot:

- Load samples (30–50 µg protein) on a polyacrylamid gel (4.0% stacking gel and 15% running gel).
- Run gel at 100 V (Bio-Rad Mini-Protean gel electrophoresis system will be used).
- Transfer proteins from the gel to the membrane.
- Equilibrate gel in transfer buffer for 15 min.
- During equilibration, cut nitrocellulose to the size of the gel; wet in water and soak in transfer buffer.
- For each gel, cut 2 pieces of 3 mm paper to size of gel and soak in transfer buffer.
- Wet pads with transfer buffer.
- Assemble transfer unit as outlined below: (Red) pos. pole—clear plate—pad—3 mm—nitrocellulose—gel—3 mm—pad—black plate—neg. pole (Black). Make sure no bubbles are trapped.
- Close the sandwich board and dunk into partially filled transfer chamber.
- Put in “BioIce” and fill chamber to top, but do not over fill.
- Run transfer at 30 V overnight in a cold room.
- Verify transfer by staining with Ponceau S dye.
- Block membrane for 1 h at room temperature on an orbital shaker using 5% (w/v) non-fat milk in TBST.
- Incubate with primary antibody diluted in TBST (1:1000-Phospho-Histone H2A.X (Ser139) (20E3) Rabbit mAb#9718 Cell Signaling) overnight at 4 °C on an orbital shaker.
- Pour off primary antibody solution and wash 3 × 10 min in TBST at room temperature.
- Incubate with secondary antibody (Anti-rabbit IgG, HRP-linked Antibody #7074—Cell Signaling) diluted (1:2000) in 5% milk in TBST for 1 h at room temperature on an orbital shaker.
- Pour off secondary antibody solution and wash 3 × 10 min in TBST at room temperature.
- ECL chemi-luminescence [Amersham Biosciences (GE)] will be used to detect protein bands. Manual band quantification will be carried out using Image J.

3 Results

3.1 Stimulation of Fibroblast Cell Proliferation

Figure 4a shows images taken during the cell coverage tests for the plasma-exposed cells after incubation for 6 or 12 h. Figure 4b further examines the cells coverage rates in association with the cell migration ability. Significant increases in cell migration were found for the plasma exposed cells (5, 10, or 15 s) after incubation for 6 or 12 h ($p < 0.05$ or 0.01), as compared with the untreated ones.

For example, there was ≈80% increase in the cell coverage rate (≈60% increase for the untreated cells) for the cells after 10 s plasma exposure and 6 h incubation. For a similar plasma exposure time and 12 h incubation, ≈98% increase of cells coverage rate (≈87% increase for the untreated cells) was estimated.

3.2 The Relative Density (γ -H2AX/ α -Tubulin) Corresponds to Proliferation and Cell Migration from the Results in Sect. 3.1

Based on the results of the γ -H2AX protein concentration obtained, the DNA breakages at different dose times are different (Fig. 5).

In this primary result, the amount of DNA breakage in the groups is not too large. Correspondingly, the relative density of the γ -H2AX protein of the cell group which is exposed for 5 s, is 0.5. It is 0.1 unit lower than the cell group not exposed by micro-plasma. It is the same with the cell group exposed to micro-plasma for 10 s, the relative density of the γ -H2AX protein was 0.52. It is 0.12 unit lower comparing to the untreated group. This proves that the rate of DNA breakages in the 5-s and 10-s groups are lower than in the untreated group. There might be cell deaths exit due to the effects of ROS on DNA fragmentation, but the amount is not significant. Essentially, the amount of DNA that breaks down is still within the DNA repair range. The amount of cells observed during these periods proliferate, due to the mechanism of action of RNS. The reasonable dose time (5 and 10 s) can be considered reasonable for cell proliferation with the power of 0.5% N_2/Ar at 13 W.

At 15-s duration, the relative density of the γ -H2AX protein increases by 0.1 compared to the untreated cell group. This may be due to DNA repair does not respond fast enough to DNA damage, resulting in cell death in the form of apoptosis but there is no signs of necrosis.

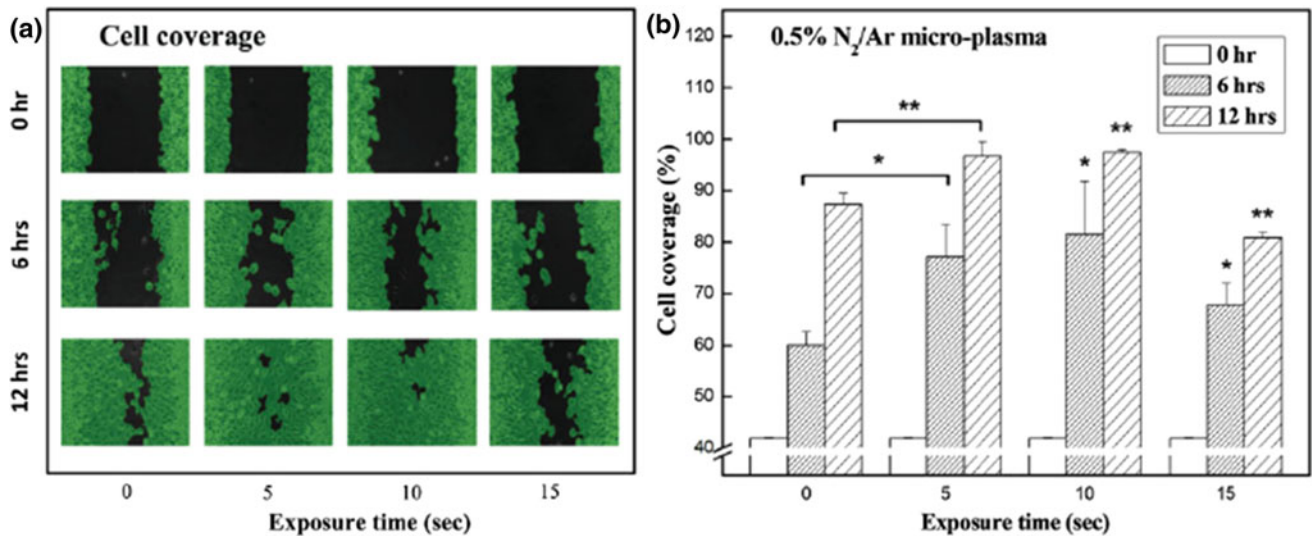


Fig. 4 a The progression of cell coverage, 6 and 12 h after plasma exposure times of 5, 10, and 15 s, were recorded with an optical microscope and b plotted for statistical analyses. Error bars indicate the standard error of the mean for $n = 6$ independent experiments

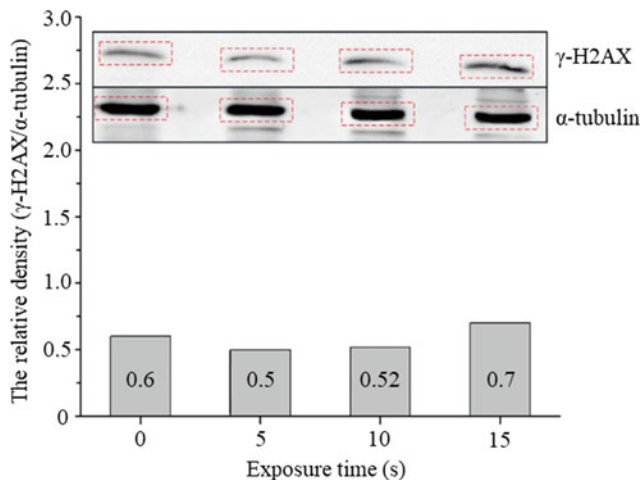


Fig. 5 The graph showing the relative density of the γ -H2AX protein derived from L929 cell samples treated by 0.5% N₂/Ar micro-plasma at different exposure times

4 Conclusions

From the results of the experiment, the level of safety of the micro-plasma is confirmed again. It is possible to see that the effective time of cell exposure micro plasma to stimulate cell proliferation is from 5 to 10 s with 13 W capacity. The reason is that many components of micro-plasma interact with cells, especially ROS/RNS concentration generated from micro-plasma is enough to stimulate proliferates cells.

Evidence is that the number of cells observed under the microscope increases and that the relative density obtained is very low. Without a DNA repair mechanism, DNA breakage will cause cell death.

When the dosage of micro-plasma exceeds the allowable safety threshold (high power, long exposure time), the number of DNA breaks increases (due to excessive ROS oxidative stress, high levels of ultraviolet rays, etc.). As can be seen in the results with a 15-s exposed-time, the number of cells decreases significantly and the relative density increases. This primary result demonstrates that with a low dosage, micro plasma can minimize DNA damage, restore cells, proliferate cells (heals wounds), but with a higher dose level, micro-plasma can cause cell death in the form of apoptosis. As a consequence, it can be said that micro-plasma is safe for cells with low dosage.

Acknowledgements This result is funded by Ho Chi Minh City University of Technology-VNU-HCM under grant number SVCQ-2017-KHUD-98.

Conflict of Interest Statement The authors declare that they have no conflict of interest.

References

1. Smith, H.M.: History of plasma. *Nature* **233**(5316), 219 (1971)
2. Soffels, E., et al.: Cold atmospheric plasma: charged species and their interactions with cells and tissues. *Plasma Sci.* **26**(4), 1441–1457 (2008)

3. Chu, P.K., Lu, X.P.: *Low Temperature Plasma Technology: Methods and Applications*. Chemical Rubber Company Press (2013)
4. Winter, J., et al.: Atmospheric pressure plasma jets: an overview of devices and new directions. *Plasma Sour. Sci. Technol.* **5**(24), 1–19 (2015)
5. Hong, Y.C., Uhm, H.S.: Micro-plasma jet at atmospheric pressure. *Appl. Phys. Lett.* **27**(36), 89–93 (2006)
6. Linda, J.K., et al.: γ -H2AX—a novel biomarker for DNA double-strand breaks. *Mol. Cell* **10**(22), 305–310 (2008)

Cost-Effective Design and Development of a Prosthetic Hand

M. N. Anh, T. D. Tang, V. T. Trung, L. C. Hieu, N. H. Tu, H. L. Minh, and L. H. Quoc

Abstract

The prosthetic hand is used to replace a missing part of a hand, which may be lost through trauma, disease, or congenital conditions in order to restore the normal functions of the hand. The state of the art design and development of prosthetic hands has been well studied and documented. The modern prosthetic hands which are computer-controlled via the means of electromyogram (EMG) signals are very helpful for amputees; however, they are expensive, not always available for low-income populations. This study presents a cost-effective solution for innovative design and development of a prosthetic hand for a patient who lost both hands due to the work accident. Design concepts of the prosthetic hand were successfully developed and tested. Different strategies for cost-effective design and development of the high-value added prosthetic hand are also discussed, including mass-customization and design for additive manufacturing.

Keywords

Prosthetic arm • Rehabilitation • Reverse engineering • Design

1 Introduction

A prosthetic hand is an artificial device that replaces a missing part of a hand, which may be lost through trauma, disease, or congenital conditions, in order to restore the normal functions of the hand. The prosthetic hands can be divided into cosmetic hand, body-powered hand and electromyogram (EMG) prosthetic hand or bionic prosthetic hand [1, 2]. There has been a lot of effort working on design and development of the smart prosthetic hand which is computer-controlled by the means of EMG surface electrodes [1–5].

The EMG technology allows the amputees to conveniently control and use the prosthetic hand for the daily activities. However, most of the EMG prosthetic hands are expensive for the low-income populations. In addition, the use and maintenance issues of the prosthetic hands need to be taken into account, especially for cases where amputees have to work and use the prosthetic hands in different working environments and weather conditions.

In this study, cost-effective solutions for innovative design and development of a prosthetic hand for a patient who lost both hands due to the work accident are presented and discussed, with the focus on the meeting well the daily need of a patient, and the use of the state of the art design and product development to obtain the added-values.

The rest of the paper is organized as follows. Section 2 presents materials and methods used for cost-effective and innovative design and development of a prosthetic hand. Section 3 presents the main results and discussions about the design analysis and test of a developed prosthesis hand. Finally, Sect. 4 presents summaries, conclusions and suggestions for further studies.

M. N. Anh (✉) · V. T. Trung
Centre of Advanced Technology, Le Quy Don Technical
University, Hanoi, Vietnam
e-mail: maingocanh.atc@mta.edu.vn

T. D. Tang
Faculty of Aerospace Engineering, Le Quy Don Technical
University, Hanoi, Vietnam

L. C. Hieu
Faculty of Engineering and Science, University of Greenwich,
Kent, UK

N. H. Tu
Vietnam Young Physician Association, Ministry of Health,
Hanoi, Vietnam

H. L. Minh · L. H. Quoc
Department of S&T Management, Saigon Hi-Tech Park,
Ho Chi Minh, Vietnam

2 Materials and Methods

2.1 Data Collection and Identifications of Need and Technical Requirements

Figure 1 presents a patient who lost both hands due to the accident with the common daily activities, including driving a bike or motorcycle (a, d, h), using the computer (b), preparing the food and cooking (e), drinking and eating (c, f), and writing (g).

Both the RE and CT scanning techniques were used for the patient data collection to be sure that the obtained 3D models of anatomical parts are reconstructed with the required accuracies. The full 3D body model is used as the reference and direct inputs for designing assistive components such as Velcro straps for attachment of the prosthetic arm to the body.

The main requirement is to develop prosthetic hands used to mainly assist the daily basic activities of a patient with the reasonable price, easy use and maintenance. Both forearms were partly missing in which only the right forearm and elbow is able to move and pro-actively assist the daily work. First of all, in order to fully develop the prosthetic hand that meet well the clinical and technical requirements, the patient data in the form of 3D models of the forearm, elbow, arm and shoulder needs to be collected and reconstructed. In this study, the non-contact Reverse Engineering (RE) techniques are used with the use of RE scanner and CT/MRI images [6, 7] as shown in Fig. 2.

2.2 Concept Design, Embodiment and Detail Design

Figure 3 presents a method for innovative design and development of a prosthetic hand. Based on the identified

need of a patient and technical requirements, different design concepts are proposed, taking into account the prioritized daily activities to meet well the customer need. In order to obtain the cost-effectiveness and proposed functions of a product, within the scope of this study, the selected design concept for embodiment and detailed design is the manually-controlled prosthetic hand, not the bionic EMG one which will be further developed in the next versions of the product.

State of the art design methods were applied for the design, including modular design, mass-customization [8], design for assembly, disassembly and design for manufacturability (3D printing and Additive Manufacturing). The basic design tasks are normally divided into three main groups: (i) Connection of hand-forearm- upper arm parts; (ii) Control of the hand for getting skillful jobs; and (iii) Diversification of functions of hand kits. Figure 4 presents the fully developed 3D CAD assembly of the first design concept of a body-powered prosthetic hand. This first design concept is able to allow the user do the most commonly daily activities such as picking-up and carrying objects (a) and using the computer (b) mouse via two different end-effector (action units).

3 Results and Discussions

Figure 5 presents the successfully developed prototypes of the first design concept of a body-powered prosthetic hand, evaluation and test of using a prosthetic hand to do the common daily activities.

This first design concept is used mainly to meet the basic daily requirements of a patient, especially it is used for detailed evaluations of the clinical need for further development of the next version of a product, including the bionic

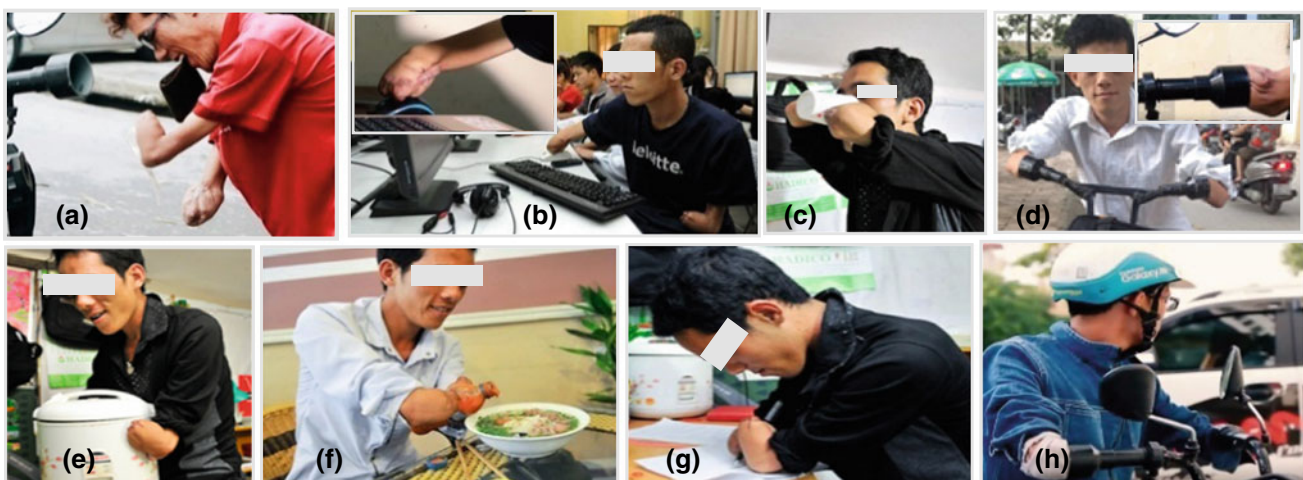


Fig. 1 Daily activities of a patient who lost both hands due to the accidents

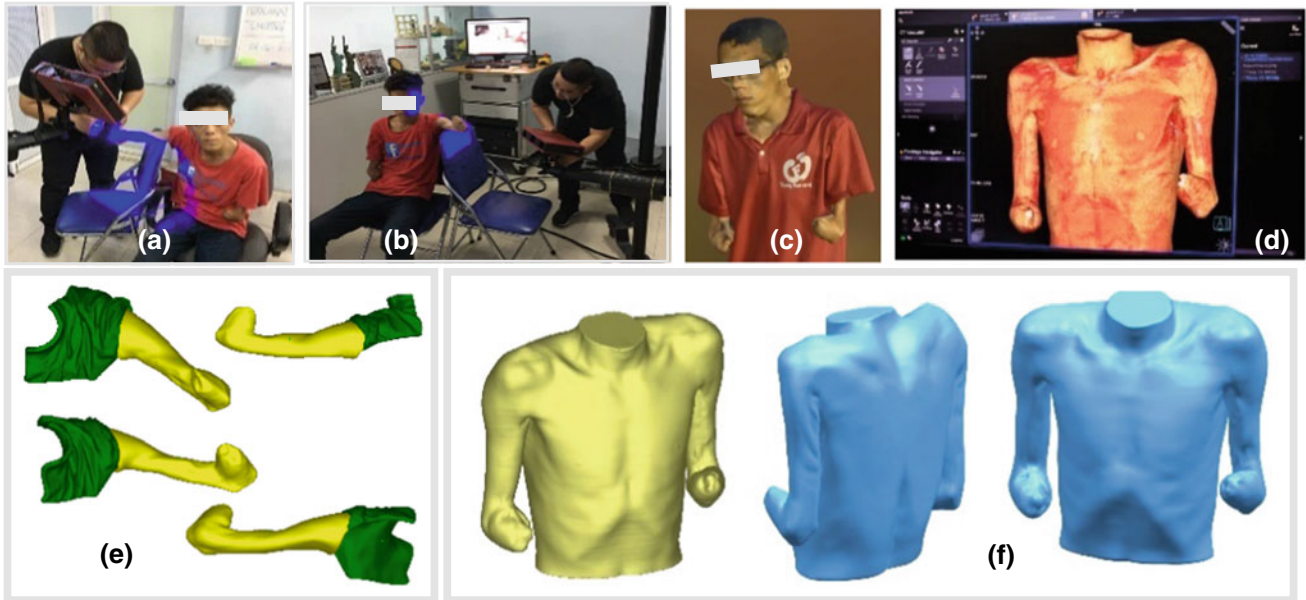


Fig. 2 Data collection and 3D modeling of the body parts for design activities. **a, b** RE scanning. **c, e** 3D models constructed from scanned point data. **d, f** 3D models constructed from CT images

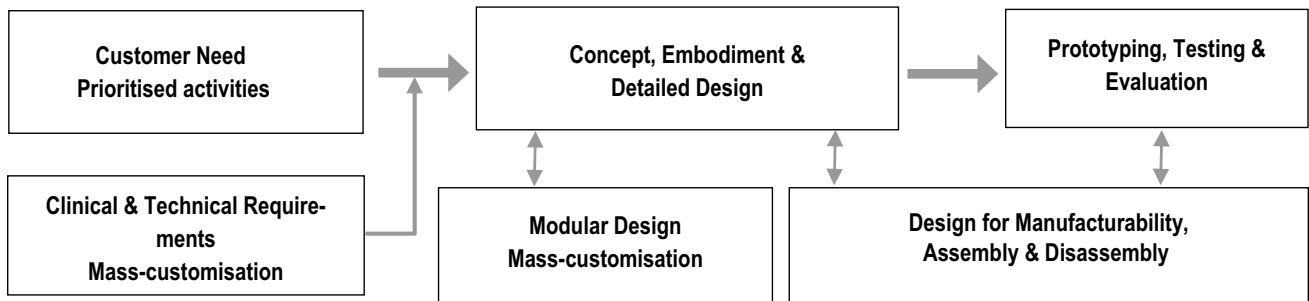
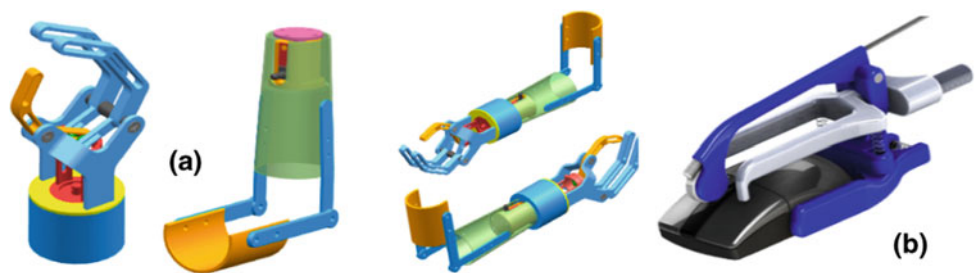


Fig. 3 A method for innovative design and development of a prosthetic hand

Fig. 4 A fully developed 3D CAD assembly of the first design concept of a prosthetic hand



EMG one, with the focus on Design for Additive Manufacturing and Design for Mass-customization.

For the technical aspects, the following are the most important specification and important points taken into account during the design: (i) Light weight, (ii) Mechanical strength, (iii) Grasping load and stability, (iv) Functionality, (v) Ease of assembly and disassembly, and (iv) Size and personalized design feature for a device to be well fitted with

the forearm. In order to obtain the light weight, the forearm tube, hand, and fingers, the light materials are used such as plastic, silicon, rubber or aluminum. For the next version, the topology optimization and design for additive manufacturing will be applied to achieve both lightweight and mechanical strengths as well as personalized design [6–8].

In order to control well the grasping load and to obtain the stability when using the prosthetic hand, it is required to



Fig. 5 a–f Successfully developed prototypes of a body-powered prosthetic hand. g–k Evaluation and testing of using a prosthetic hand for the common daily activities

use at least 3 fingers including a thumb and two others [9]. This property enables the fingers to be accurate in holding and grasping. Different functional kits for the end-effector (action unit) are used in order to obtain the multifunction (Figs. 4 and 5), with the ease of changes (assemblies and disassembly).

Based on the 3D CAD models of the arm and forearm (Fig. 2), the part for fixation of the prosthetic hand to the forearm and arm was optimally designed with the personalized features. The innovative features of the design are shown in the design of the wrist connector with a mechanical trigger. The wrist connector plays the important role of a mechanical interface to make the forearm easy to combine with different functional kits, to allow the user to manually change (assembly and disassemble) the functional kits by simply pulling the mechanical trigger. The wrist connector runs as a plug and play device and allows the user to carry

out one-touch action of assembly and disassembly. Finally, the holding belt with a curved sickle shape like a crescent moon was integrated in the design to allow the prosthetic hand fixed to the forearm and arm of the user tightly and comfortably with the ease of use. Moreover, the design was simplified by the use of connection bars between the upper and low fixation parts which function as the elbow; this reduces the weight of the prosthetic hand, with reduced frictions.

In order to work on the detailed analysis and evaluation of the clinical need for further development of the next version of a product, including the bionic EMG one, the design evaluation and practical tests were implemented with the use of different functional kits for the end-effector, in which the main objective is to evaluate the performance of the comfortableness, stiffness, and accuracy as well as the functionality of the developed prosthetic hand, aimed to meet well the

need of a patient (user). In this way, the following are the questionnaire and the raised issues for a feedback from a patient after the test: (a) Ease of assembly and disassembly of the functional kits and wearability without the help of others, (b) The weight of a prosthetic hand, (c) Ease of use and control and (d) Performance of the daily activities with and without the use of the prosthetic hand.

The test procedure consists of four groups as follows. The first one is to self-wear the prosthetic hand with the several times (Fig. 5g). With the short training and guide, a patient can self-wear the prosthetic hand in less than a minute. The second one is to wear the prosthetic hand as long as possible with the position shown in Fig. 5h, in order to assess the comfortability of wearing a device. The average time of wearing comfortably is about 19 min. The third one is to hold and grasp objects (Fig. 5i). The patient said that he was able to control the fingers to hold cylinder objects easily. However, the weight and the diameter of objects should not be over 5 kg and 10 cm respectively. The fourth one is to use the computer mouse (Fig. 5d, e, k). The patient was able to use the computer mouse by clicking on the right and left buttons, and easily move the mouse. However, if he needs to click a button longer than a 5 s, it is a bit challenging. A patient was happy with the proposed functions and the issues related to the safety and noise during the use of a device were well-controlled.

4 Conclusion

In this study, the cost-effective solutions for innovative design and development of a prosthetic hand for a patient who lost both hands due to the work accident are presented and discussed, with the focus on the simple design concepts to meet the basic daily requirements of a patient. Basic design concepts of the prosthetic hand with different functional kits were successfully developed and tested, and it allows a patient to do the most common daily activities. The successfully developed prototype is also used for detailed analysis and evaluation of the clinical need for further development of the next version of a product, including the bionic EMG one.

The successfully developed prototypes meet the key technical requirements and basic need of a patient. The next

versions of a product will be developed with the better functionality, cost-effectiveness and the ease of use, especially the following ones: (1) To apply the emerging design methods, including topology optimization, design for additive manufacturing, mass-customization and personalized design [6–8], in order to minimize the weight and to obtain a better wearability and functionality as well as added values for a device, and (2) To work on personalized design and cost-effective development of the EMG prosthetic hand or bionic prosthetic hand [1–5].

Acknowledgements British Council and Newton Fund are acknowledged for their support.

Conflict of Interest The authors declare that they have no conflict of interest.

References

1. Nianfeng, W., et al.: Design and myoelectric control of an anthropomorphic prosthetic hand. *J. Bionic Eng.* **14**(1), 47–59 (2017)
2. Mahmoud, T., et al.: Single channel surface EMG control of advanced prosthetic hands: a simple, low cost and efficient approach. *Expert Syst. Appl.* **79**(15), 322–332 (2017)
3. Ivan, I.B., et al.: Prototyping of EMG-controlled prosthetic hand with sensory system. *IFAC-PapersOnLine* **50**(1), 16027–16031 (2017)
4. Clement, R.G.E., et al.: Bionic prosthetic hands: a review of present technology and future aspirations. *Surgeon* **9**(6), 336–340 (2011)
5. Pilar, A., et al.: Quantitative functional evaluation of a 3D-printed silicone-embedded prosthesis for partial hand amputation: a case report. *J. Hand Ther.* **31**(1), 129–136 (2018)
6. Chi Hieu, L., et al.: Medical rapid prototyping applications and methods. *Assembly Autom* **25**(4), 284–292 (2005)
7. Chi Hieu, L., et al.: Medical reverse engineering application and methods. *Rom. Rev. Precis. Mech. Opt. Mechatron.* **37**, 19–29 (2010)
8. Chi Hieu, L., et al.: Customer driven mass-customization and innovative product development with parametric design & generative modeling. In: *Proceedings of the 15th International Conference on Manufacturing Research—ICMR 2017, London* (in press) (2017)
9. Yu, W.S., et al.: Thumb and finger forces produced by motor units in the long flexor of the human thumb. *J. Physiol.* **583**(3), 1145–1154 (2007)

Controlling the Wheelchair by Eye Movements Using EEG

Van Cam Thi Le, Nhan Thanh Le, Hai Ngoc Nguyen, Dang Cao Le, and Keiji Iramina

Abstract

In this study, we propose a method to control the wheelchair by eye movement using Electroencephalography (EEG). Firstly, we collect EEG signal by five types of eye movement: Blink, Double blink, look at Right, look at Left and Relax. These movements correspond to five directions of wheelchair motion: Go forward, Go backward, Turn right, Turn left and Stop. After that, the offline EEG signal is analyzed using MATLAB to find out the classified threshold of the signal amplitude in Alpha band and Delta band. Finally, an effective algorithm is built allowing us to identify the type of eye movement and control the external device—the powered wheelchair. As the result, the average accuracy for five motion directions (Go forward, Go backward, Turn right, Turn left and Stop) are 92.333, 93, 81.667, 86.667 and 83% respectively. With this study, we expect it can give people the help they need and be applied to many fields in the near future.

Keywords

Brainwave control algorithm • Wheelchair • Eye movement • EEG

1 Introduction

Nowadays, Electroencephalography (EEG) has become the most versatile and powerful tools not only in medical to diagnose the mental diseases or brain injury but also in

technology to help disabled people who got the severe disabilities to engage with their surroundings and live more comfortable.

In many cases, the severe disabilities affect the patient's daily life, including activities of self-care and movement, causing major changes in the quality of life. Besides the physical therapy, many types of technique were applied for disabled people to help them live more comfortable. With brain control technique, they can use their own physiological signal such as EEG signal, eye movement signal to interact with external environment by the supported equipment such as wheelchair.

This study proposes a cheap and effective method to control the wheelchair with a commercially low-cost EEG headset—Emotiv EPOC Headset. This headset is easy to use with the 14 channels fixed on the scalp to collect the EEG signal and the software development kit (SDK) to process and interpret the signals [1]. In this study, the main issue is to identify the types of eye movement in EEG signal in order to control the wheelchairs. We use MATLAB language to analyze raw offline data and calculate the amplitude threshold value for each eye movement type. Thus we can use these threshold value for wheelchair application.

2 Method

Subject: One healthy female, 23 years old.

Requirements for the subject: Because the aim of this study is total paralysis patients so when we collect the data, she must do not move the body except her eyes.

EEG equipment: EPOC Emotiv headset and its packet tools.

By observing the actual experiments, we choose five types of eye movement to be the controlling commands: Blink eye (B) as Go Forward command; fast Double blink eye (D) as Go Backward command; look at Left (L) as Turn left command; look at Right (R) as Turn right command and relax or closed eye (X) such as Stop command. We collected

V. C. T. Le (✉) · K. Iramina
Graduate School of Systems Life Sciences, Kyushu University,
Fukuoka, Japan
e-mail: lethicamvan273@gmail.com

N. T. Le · H. N. Nguyen · D. C. Le
BME Laboratory, Faculty of Applied Science, Ho Chi Minh City
University of Technology, Ho Chi Minh City, Vietnam

the EEG data by EPOC Emotiv headset in total 661 samples from four channels: AF3 (Fp1), AF4 (Fp2), F7 and F8 in 5 s [2]. In every 5 s sample, the subject does only one type of eye movements such as Blink, Double Blink, look at Right, look at Left or Closed eye. The data then are analyzed offline by MATLAB. After doing pre-processing by the Notch and band-pass filters to extract the desired frequencies, we use Fast Fourier Transform method to compute the power spectral density ratio (R-value).

$$R_i = \frac{P_i}{\sum P_i} \quad (1)$$

where:

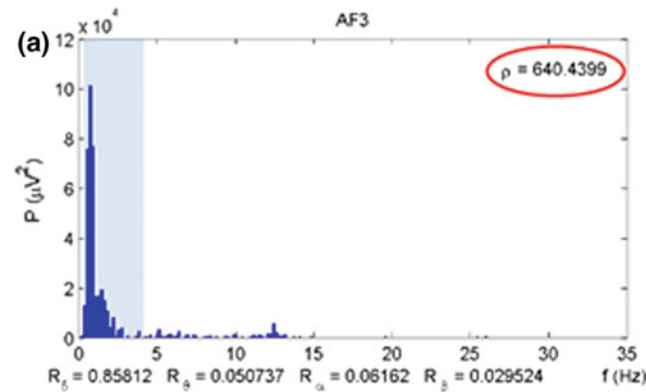
- R is power spectral density ratio
- P (μV^2) is power spectral density
- i sequentially is δ , θ , α and β band

In this study, we only give the attention on two frequency regions δ and α which have the significant change in amplitude for the eye movement behaviors.

Identify X signal

As we know, when we're relaxing, the alpha wave of our brain will increase. In this case, the R-value in the alpha region of the X signal is significantly higher than the other four signals B, D, L, and R in the same region. At the same time, the R-value in the delta region of X signal is smaller than the R-value in the same region of the other four signals. Therefore, we got the sign to recognize the X signal as follow:

$$\begin{cases} \{R_{\alpha X}\} > \{R_{\alpha B}; R_{\alpha D}; R_{\alpha L}; R_{\alpha R}\} \\ \{R_{\delta X}\} < \{R_{\delta B}; R_{\delta D}; R_{\delta L}; R_{\delta R}\} \end{cases}$$



Identify Blink eye (B) and Double blink eye (D) signal

Looking at Fig. 1 that shows the power spectrum of two groups B signal and D signal, we observe in the same frequency range [0.5; 4 Hz], the power spectrum of group B is gathered in one part, whereas the power spectrum of group D is tended to be divided into two distinct parts. For the sake of identification, we argue and compute a coefficient to distinguish B signal and D signal. It is ρ -value and computed by the following equation:

$$\rho = \frac{P_{[0.5 \text{ Hz}; 1.5 \text{ Hz}]} \cdot P_{[0.5 \text{ Hz}; 3 \text{ Hz}]}{P_{[1.5 \text{ Hz}; 4 \text{ Hz}]} \cdot P_{[3 \text{ Hz}; 4 \text{ Hz}]} \quad (2)$$

With: $P_{[a; b]}$ is the power spectral density which is limited to the frequency segment [a; b] (Hz).

The value of $\rho_B \gg \rho_D$ in most samples. So we use this coefficient to distinguish B signal and D signal.

Identify look at Left (L) and look at Right (R) signal

The Correlation Coefficient is the powerful index that indicates the strength of the linear relationship between two random variables. To distinguish L signal and R signal, we calculate 6 correlation coefficients of 6 pairs of channel: (AF3,F7); (AF3,F8); (AF3,AF4); (F7,F8); (F7,AF4); (F8,AF4).

By calculating the correlation coefficients between the pairs of channels according to behaviors B, D, L or R, we have the distribution of correlation coefficients as Fig. 2.

From Fig. 2, we can deduce the trend of correlation coefficient as Table 1 using for the identification algorithm.

From Table 1, we divided four behaviors B, D, L and R into two groups using the correlation coefficient $cr(F7,F8)$ and $cr(F7,AF4)$. The first group includes B and D behaviors

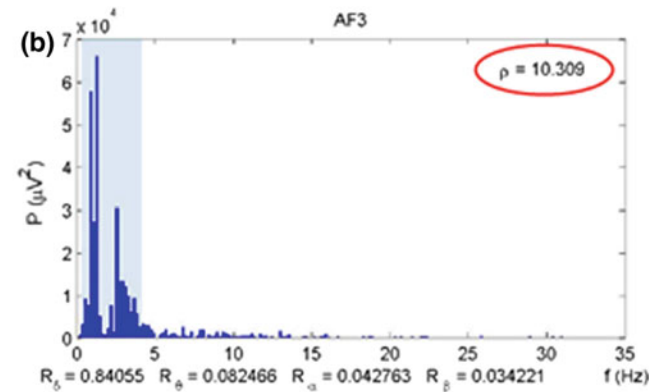


Fig. 1 ρ values of B signal (a) and D signal (b)

Fig. 2 The graph that distribute the correlation coefficients between the pairs of channels according to behaviors B, D, L or R

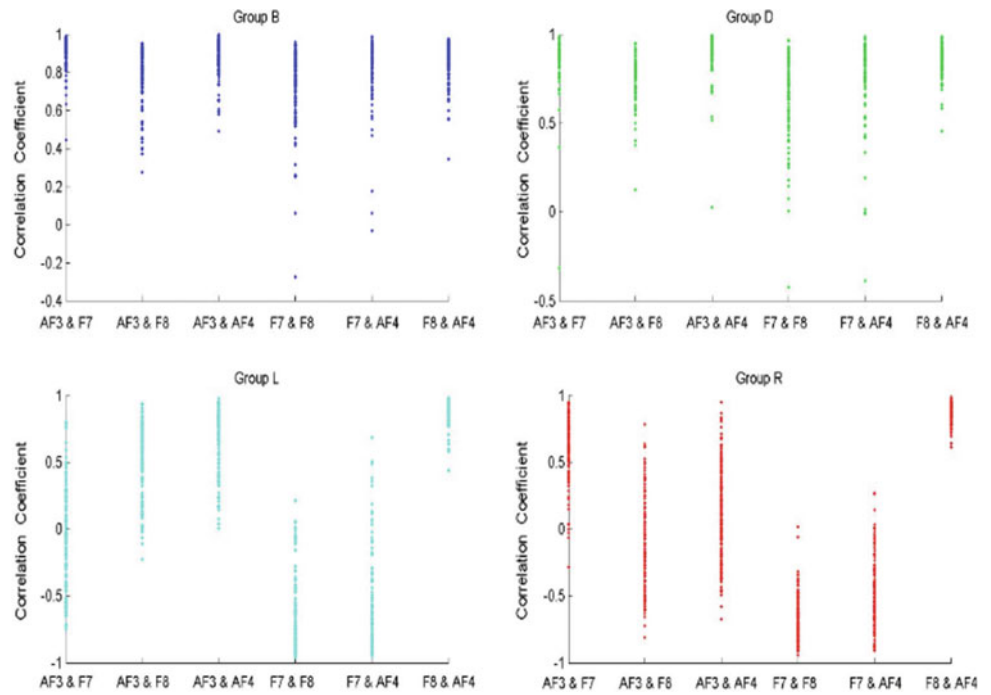


Table 1 The trend of correlation coefficients

Correlation coefficients pairs	B	D	L	R
cr(AF3,F7)	+	+	-	+
cr(AF3,F8)	+	+	+	-
cr(AF3,AF4)	+	+	+	-
cr(F7,F8)	+	+	-	-
cr(F7,AF4)	+	+	-	-
cr(F8,AF4)	+	+	+	+

because they had a positive coefficient while L and R behavior had a negative coefficient. In addition, based on the opposite trend of the correlation coefficient $cr(AF3,F7)$, $cr(AF3,F8)$ and $cr(AF3,AF4)$, we can distinguish the L and R signals.

Threshold statistic

Threshold statistic is the method we built to define the threshold value of the data set R_α , R_δ , ρ and correlation coefficients. The R_α value and R_δ value are used to recognise $\{X\}$ signal from $\{B, D, L, R\}$, ρ value is use to identify group $\{B\}$ and $\{D\}$ while correlation coefficients are used to distinguish $\{L\}$ and $\{R\}$ signal. In every set, there always is the opposite distribution of the data between two groups in the same value domain that we call Upper Domain (UD) and Lower Domain (LD). In particular, for the set of R_α , UD is the $R_{\alpha\{X\}}$ and LD is $R_{\alpha\{B,D,L,R\}}$, while in R_δ set, UD is $R_{\delta\{B,$

$D,L,R\}$ and LD is $R_{\delta\{X\}}$. Similar, in the set of ρ value, UD is $\rho_{\{B\}}$ and LD is $\rho_{\{D\}}$. For correlation coefficients, UD are $cr(F7, AF4)$ and $cr(F7, F8)$ of group $\{B, D\}$; $cr(AF3, AF4)$ and $cr(AF3,F8)$ of $\{L\}$ signal; and $cr(AF3, F7)$ of $\{R\}$ signal. From that distribution, we compute the a specific value as the boundary between two domain sets, called the intersection value μ , defined by the formula below:

$$\mu = \frac{\sum_{j=1, m}^i i = \frac{1, n}{n} \left(\frac{min_{UD_i} + max_{LD_j}}{2} \right)}{m.n} \tag{3}$$

With:

- min_{UD_i} the smallest value of each subsets of the upper domain.
- max_{LD_j} the biggest value of each subsets of the lower domain.

Table 2 The performance of the algorithm after every test

Type of signal and command	B	D	L	R	X
	Go forward (%)	Go backward (%)	Turn left (%)	Turn right (%)	Stop (%)
The 2nd test	89	86	60	78	71
The 3rd test	88	93	92	87	93
The 4th test	100	100	93	95	85
Average	92.333	93	81.667	86.667	83

Note The first test was rejected since the mechanical problems of the wheelchair so we didn't mention it here

- n The number of subsets is in the upper domain.
 m The number of subsets is in the lower domain.

3 Results

The threshold values of R_{α} , R_{δ} , ρ and 6 correlation coefficients of 6 pairs of channel are calculated by statistic to identify each type of signal. Whereas the online collecting data program and control program are built on LabVIEW so that we can do the performance test for our algorithm. After every test, the performance of the algorithm is better. However, this result was dependent on every subject and the training session.

The International University in Vietnam also did the project about “An EEG-Controlled Wheelchair Using Eye Movements” using the number of blinks to control the wheelchair with the Biosemi Active Two system [3–6]. In our study, we use the direction of eye movement to be the control signal. With Epoc Emotiv headset, the subject feels more comfortable to do the test for a long time and it also saves our time with a wearable device and fixed channels. In Table 2, the performance of group B and D are almost absolute since there is a big difference of ρ -value with the ratio of ρ_B/ρ_D is always more than 10 times. After several adjustments for threshold value, the performance of Turn left and Turn right signals were improved significantly. Besides, the Stop signal is still stable. This study also gives us the effective performance with the accuracy of five motion directions (Go forward, Go backward, Turn right, Turn left and Stop) are 92.333, 93, 81.667, 86.667 and 83% respectively in indoor environment.

4 Conclusion

This current study adds an other high-productive method to help disable people control the wheelchair by eye movement via their EEG signal with five commands: Go forward, Go

backward, Turn right, Turn left and Stop. The wearable EEG equipment that we use in this study—EPOC EMOTIV—brings more convenient for the subject and easy to conduct the experiment because of its light weight and quick response. In near future, we hope this algorithm will have the potential application and not only be used for motion controlling but also can expand to many equipments in other fields.

Conflict of Interest The authors declare that they have no conflict of interest.

References

1. Epoc, E.: EMOTIV EPOC & TESTBENCH™ specifications. Brain Computer Interface & Scientific Contextual EEG (2014)
2. Gupta, S.S., Soman, S., Raj, P.G., Prakash, R., Sailaja, S.D., Borgohain, R.: Detecting eye movements in EEG for controlling devices. In: IEEE International Conference on Computational Intelligence and Cybernetics (CyberneticsCom), 2012
3. Tran, H.T., Nguyen, H.T., Phan, H.V., Van, Toi, V., Ngo, T.V., Bui-Thu, C.: An EEG-Controlled wheelchair using eye movements. In: Toi, V., Lien Phuong, T. (eds.) 5th International Conference on Biomedical Engineering in Vietnam, IFMBE Proceedings vol. 46 (2015). Springer, Cham
4. Hai, N., Trung, N., Toi, V.: Mean threshold and ARNN algorithms for identification of eye commands in an EEG-Controlled wheelchair. *Engineering*, 5, 284–291 (2013). <https://doi.org/10.4236/eng.2013.510B059>
5. Nguyen, H.T., Trung, N., Toi, V., Tran, V.: An autoregressive neural network for recognition of eye commands in an EEG-controlled wheelchair. In International Conference on Advanced Technologies for Communications (ATC 2013), Ho Chi Minh City pp. 333–338 (2013). <https://doi.org/10.1109/ATC.2013.6698132>
6. Nguyen T., Nguyen T.H., Truong K.Q.D., Van Vo, T.: A mean threshold algorithm for human eye blinking detection using EEG. In: Toi, V., Toan, N., Dang Khoa, T., Lien Phuong, T. (eds.) 4th International Conference on Biomedical Engineering in Vietnam. IFMBE Proceedings, vol. 49 (2013). Springer, Berlin, Heidelberg

Permittivity Measurement for Thrombus Detecting at Connector Gap in Extracorporeal Blood Circulating System

M. Koishi, T. Kiet Anh, J. Li, and M. Takei

Abstract

Background Connector gap, a gap between connector and tube, is where very easily to occur thrombus formation in extracorporeal blood circulating system. **Objective** The aim of this study is to develop a system to detect thrombus formed at the connector gap in an extracorporeal blood circulating system and evaluate it. **Method** The bio-mate flow path incorporating the connector electrode is filled with fresh porcine blood and circulated by a centrifugal pump. Calcium chloride and sodium citrate are added to the circulating system to adjust ACT (Activated clotting time) to be around 160 s. In the case that the thrombus formation detected by permittivity measurement, heparin is added to stop the coagulation reaction, and the measurement is terminated. **Results** Thrombus parameter is not affected by ACT change or drug addition and it increased to 20% at the end of the experiment, which confirms the feasibility of the proposed thrombus detecting sensor. As thrombus is not confirmed in extracorporeal blood circulating system besides the connector gap, it is considered to be the early stage of thrombus formation. Since thrombus formation is made on the end face b and large regardless of the position of the electrode, the promotion of thrombus formation by electrical measurement is not observed.

Keywords

Thrombus detection • Artificial organs • Electrical spectroscopy

1 Introduction

Recent years, a number of the patients with cardiovascular diseases receive efficient therapies to support their life with artificial organs [1]. However, thrombus formation within artificial organs is a serious problem and it can be a cause of thrombosis. Activated clotting time (ACT) and Thromboelastography (TEG) are used for examination of coagulability, however, it is not to assay the thrombus formation directly.

Currently electrical measurement has applied to monitor the blood, and it is known that permittivity measurement is effective in the thrombus formation process in the stationary field [2]. Detecting the thrombus formation directly, we focused on a connector gap, a gap between connector and tube, where thrombus formation very easily occur in an extracorporeal blood circulating system. In this study, we proposed a new sensor and a parameter and evaluated them through thrombus formation experiment in blood circulating flow path.

2 Material and Method

2.1 Blood Sample and Experimental Setup

Porcine blood which has similar hematological and biochemical properties to human blood was used in this experiment. After the blood sample was withdrawn from the swine subject, the tri-sodium citrate solution (0.011 M; Shibaura Zouki K.K., Japan) was added (blood: tri-sodium citrate solution = 9:1) to prevent natural thrombus formation. As shown in Fig. 1, the experimental setup consisted of a centrifuge pump (Gyro pump SE; Kyocera corporation, Japan), a flow meter, a pressure sensor, a circulation tube, a reservoir, a thermostat bath and a connector sensor. The connector sensor was made of an acrylic pipe attached two stainless tapes, connected with a tube along the flow direction. An impedance analyzer (IM7581; Hioki E.E.

M. Koishi (✉) · T. Kiet Anh · J. Li · M. Takei
Graduate School of Science and Technology, Chiba University,
1-33 Yayoi, Inage, Chiba, 263-8522, Japan
e-mail: s41012mk@chiba-u.jp

J. Li
e-mail: li.jp@chiba-u.jp

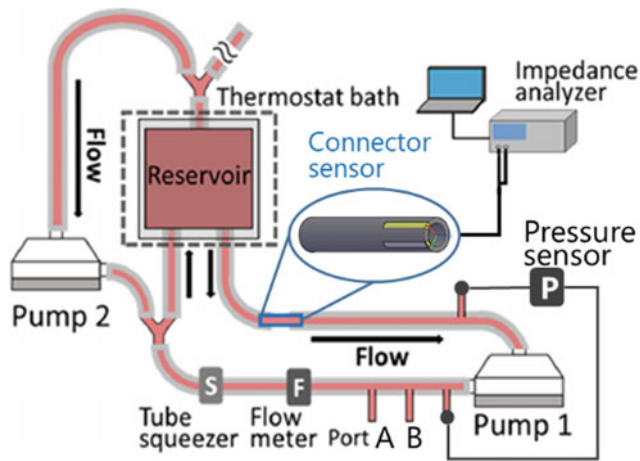


Fig. 1 Experimental setup

Corporation, Japan) was connected with the connector part. The connector sensor only focused on connector part.

2.2 Method and Experimental Condition

The circulation shown in Fig. 1 was filled with 800 ml porcine whole blood. During the experiment, the blood samples were withdrawn from a port on the circulation tube to measure Activated Clotting Time (ACT) with Sonoclot Analyzer (Model SC1, Sienco, Inc., America) to evaluate coagulability. The blood was circulated by using the centrifuge pump at a constant flow rate $Q = 2.0$ L/min at all times. The reservoir was put in the thermostatic bath that always maintained the circulating blood's temperature at 37 °C. In order to adjust ACT value around 120–160 s, CaCl_2 solution and tri-sodium citrate solution were appropriately used.

Electrical measurement was carried out with the connector sensor and its measurement frequency was 100 kHz–300 MHz. Then, when thrombus formation was detected by electrical measurement, sodium heparin was injected into the circuit to prevent thrombus formation anymore and the measurement was ended. After that, the circulation was washed with saline and observed the thrombus in the circuit besides the connector sensor.

2.3 Thrombus Parameter α

In order to determine the thrombus parameter, we measured permittivity in a stationary field where unintended change did not occur. In this report, thrombus parameter α was defined as percentage of thrombus occupied in measurement range. Addition to measurement of the thrombus formation process, we measured the hematocrit change β which has a

large influence on the permittivity. We assumed that relationship between permittivity change and the blood state change (thrombus formation process or hematocrit variation) were linear. Getting the slope of lines from the experiments at 1 and 10 MHz, we made a simultaneous equation and solve it for α . Obtained α is shown below:

$$\alpha = 4.34\Delta\varepsilon_{1\text{MHz}} - 4.18\Delta\varepsilon_{10\text{MHz}} \quad (1)$$

where, $\Delta\varepsilon_{1\text{MHz}}$ and $\Delta\varepsilon_{10\text{MHz}}$ are the change in dielectric constant from the start of experiment at 1 and 10 MHz.

3 Result and Discussion

Figure 2 shows time course of thrombus parameter α (solid line) and ACT (broken line) during the experiment. Looking at the time course of the thrombus parameter α reached 10% at $t = 90$ min, and then it reached 20% in about five minutes thereafter. From this transition of the thrombus parameter α , it is assumed that a thrombus was formed quickly on the end face of the connector sensor after $t = 90$ min. When thrombus parameter α reached 20% was, heparin was added and the measurement was completed.

ACT firstly decreased by CaCl_2 and it was recovered by sodium citrate added in the latter half of the experiment, thrombus parameter α continued to increase. This might be because the measurement range of the connector electrode is focused on the thrombus attached to the connector part. Figure 3 is a photo of thrombus formed on the end face of the connector sensor after the measurement and its color tone has been adjusted. The thrombus was formed not only on the electrode but on the entire end face. So promotion of thrombus formation by the electrical measurement was not observed. In addition, thrombus formation was could not be confirmed in the circulation flow path except the connector sensor. It can be said that the whole system was an early stage of thrombus formation.

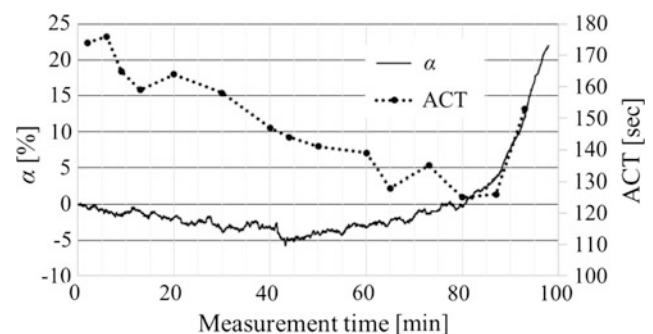


Fig. 2 Time course of thrombus parameter α (solid line) and ACT (broken line)

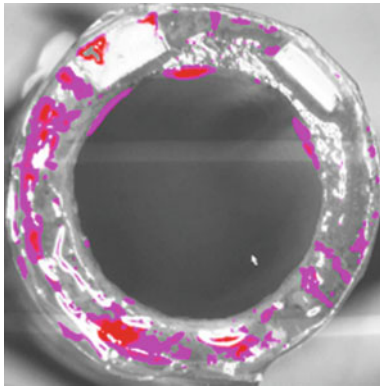


Fig. 3 Thrombus formed on the end face of the connector sensor

- (1) Since thrombus formed on the entire end face of the connector sensor regardless of the position of the electrode, promotion of thrombus formation by electric measurement was not observed.
- (2) Thrombus parameter α increased to 20% without being affected by ACT change and drug addiction. As thrombus was not confirmed in the circulation flow path, it may be considered to be the early stage of thrombus formation.

Acknowledgements The author wishes to acknowledge the financial support by JSPS KAKENHI Grant Number JP16H02312. There are no conflict of interest.

4 Conclusion

In this study, the thrombus formation experiment was conducted in the circulation flow path and measured capacitance of the blood with connector sensor. As a result, the following findings were obtained:

References

1. Jhun, C.S., Cysyk, J.P.: Ventricular contractility and compliance measured during axial flow blood pump support: in vitro study. *Artif. Organs* **38**(4), 309–315 (2014)
2. Hayashi, Y., Brun, M.A., Machida, K., Nagasawa, M.: Principles of dielectric blood coagulometry as a comprehensive coagulation test. *Anal. Chem.* **87**(19), 10072–10079 (2015)

Investigating Dielectric Properties of Hemolysis by Electrical Impedance Spectroscopy

Kiet Anh Tran, Jianping Li, Huynh Chan Khon, and Masahiro Takei

Abstract

This paper presents a study toward the investigation of electrical properties of static bovine blood samples during hemolysis by electrochemical impedance spectroscopy (EIS). RBC hemolysis was induced by adding different volume fractions of distilled water into static bovine blood samples that causes cell membrane breakage and release of cytoplasm into blood plasma. EIS measurements were conducted with frequency range between $f = 100$ kHz and $f = 300$ MHz. Our data show that changes in electrical properties indicating hemolysis are observed under high frequency conditions. Moreover, the impedance increase related to the release of cytoplasm into plasma and increment of hemoglobin's amount. The highest resistance of second semi-circle (Z') shows a linear relationship with the hemoglobin concentration (H_b). This relationship is described by the equation $Z' = 0.7932H_b + 15.788$, with correlation coefficient of 0.9978.

Keywords

Hemolysis • Electrical impedance spectroscopy • Red blood cells

1 Introduction

Hemolysis is characterized as the release of hemoglobin (H_b) and other intracellular components, including metabolites (structural proteins, lipids, and carbohydrates) and enzymes, from red blood cell (RBC) to the surrounding extracellular fluid following damages of the cell membrane or its disruption [1]. Hemolysis is correlated with several diseases such as sickle-cell disease [2], hereditary spherocytosis [3], malaria [4], hemolytic anemia, and mechanical heart valve induced anemia. Moreover, hemolysis occurs during blood collection, processing, handling, storage within the transfusion service [5], and during transport to the patients [6]. Detecting excessive hemolysis is vital in reducing complications in patients due to that transfusion of elevated potassium levels, free H_b and bacteria contaminate RBC units [7, 8]. However, hemolysis RBC analyzers are huge and expensive devices, which need to be operated by skilled technicians. Furthermore, access to this equipment is an issue in developing countries, where less reliable equipment and evaluation techniques are available. These different factors push towards the development of point-of-care (PoC) hemolysis detecting devices that provide an easy to use, reliable and economic test for patients.

Fricke et al. concluded that increment of permittivity is attributable to the increase in erythrocyte size or membrane capacity [9]. Analyzing by the Pauly-Schwan's theory based on the assumption that erythrocytes are spherical which is not suitable for hemolysis, in fact, shape the RBCs after hemolysis lose their standard biconcave shape into unpredictable form. Jyoti et al. examined low-frequency impedance spectroscopy to monitored hemolysis at various temperatures from -200 to -140 °C and times domain to point out frequency increases with the impedance decreases [10]. Although these studies did show the physical relationship of hemolysis and impedance signal, and are much simpler than traditional methods, the signal conditioning

K. A. Tran (✉) · J. Li · M. Takei
Graduate School of Mechanical Engineering, Division of Artificial System Science, Chiba University, 1-33 Yayoi, Inage, Chiba, 263-8522, Japan
e-mail: anhkietbme@gmail.com

H. C. Khon
Department of Biomedical Engineering, International University, Vietnam National University-Ho Chi Minh City (VNU-HCM), Quarter 6, Linh Trung Ward, Thu Duc District, Ho Chi Minh City, 70000, Vietnam

circuit cannot be applied for RBC hemolysis, which possess shapes other than spherical or ellipsoidal.

2 Materials and Methodology

2.1 Sample Preparation

The bovine blood samples (Shibauro Zouki K. K., Japan) were prepared by following the procedure shown in Fig. 1. First, the RBCs were separated from the whole blood by centrifuging (CN-1040; Hsiang Tai, Taiwan) under 2000 rpm for 10 min. Second, distilled water was added to the RBCs before another instance of centrifuging. After these two steps, different concentrations of hemoglobin H_b concentration were obtained (Table 1).

2.2 Experimental Setup

Figure 1 displayed the experimental setup, which includes one equilateral cubic as blood container, one impedance analyzer, and one personal computer (PC). The electro-poration cuvette had a 2 mm gap (Nepa Gene) and two electrodes (length \times width \times thickness: 10 \times 20 \times 0.15 mm) attached to the two symmetric inner surfaces of the

container. The impedance analyzer data were obtained using the Hioki IM7581 impedance analyzer (Hioki E.E. Corporation, Japan and personal computer (PC). These electrodes were connected to the impedance analyzer by a coaxial cable (Four-terminal probe L2000: Hioki E.E. Corporation, Japan).

The impedance analyzer data such as impedance (Z), phase angle (θ), resistance (Z') and reactance (Z'') were obtained. The Z' and Z'' were measured at various frequencies f (201 values between $f = 100$ kHz and $f = 300$ MHz). All experiments were conducted at room temperature ($T = 25$ °C).

The supernatant hemoglobin (H_b) concentration was measured by the commercial HemoCue system. The absorbance was measured at two separate wavelengths ($\lambda = 570$ and $\lambda = 800$ nm) to determine the H_b concentration and compensation for turbidity in each sample.

3 Results

Figure 2 shows the influence of hemolysis red blood cells. The comparison of the same phenomena with the decrement of RBCs in both hematocrit and hemolysis is shown in Fig. 2a. In Fig. 2a the Nyquist plots comprise two semi-circles. In the case of HTC, the tread of two

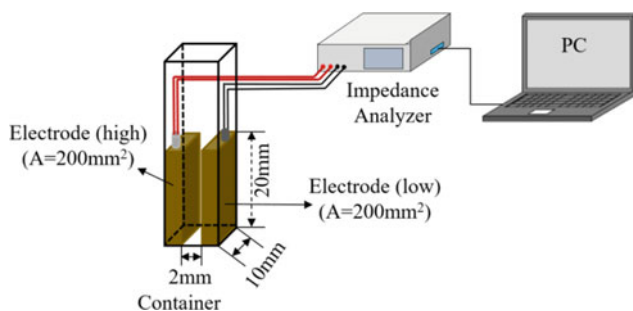


Fig. 1 Experimental setup for electrical impedance spectroscopy measurement

Table 1 Experimental samples prepared from various concentrations of RBCs and RBC hemolysis [11]

		φ_p	φ_c	φ_r	$V_w(\mu\text{L})$	$H_b(\text{g/L})$
HCT	HCT 10%	0.6	–	0.4	–	0.04
	HCT 20%	0.7	–	0.3	–	0.04
	HCT 30%	0.8	–	0.2	–	0.04
	HCT 40%	0.9	–	0.1	–	0.04
RBC hemolysis	HCT 40% + 0.55% dH ₂ O	0.6	–	0.4	20	1.4
	HCT 40% + 0.55% dH ₂ O	0.6	–	0.4	40	2.2
	HCT 40% + 0.55% dH ₂ O	0.6	–	0.4	60	3.1

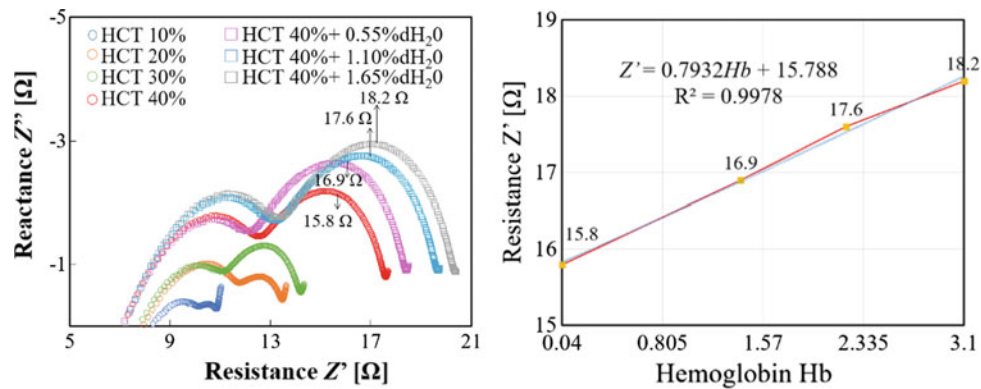


Fig. 2 Nyquist plot of RBC hemolysis, and relationship between resistances Z' with hemoglobin H_b

semi-circles decreases the concentration of the RBCs while the diameter of the two semi-circles in case of RBC hemolysis ascends regardless the descending of RBCs with the occurring of RBC hemolysis. The Nyquist plots of blood with different hematocrit decreased while it is opposite in the case of RBC hemolysis. The effect of cytoplasm produced by the rupture of RBCs on impedance is much greater than that of RBC concentration. From analyzing the data, the highest resistance of second semi-circle (Z') shows a linear relationship with the hemoglobin concentration (H_b). This relationship is described by the equation $Z' = 0.7932Hb + 15.788$, with correlation coefficient of 0.9978.

4 Conclusion

This study demonstrates for the first time EIS measurements of RBC hemolysis that show a strong relationship between impedance changes and the release of cellular hemoglobin. Our experiments on blood samples with different RBCs concentration in hematocrit and different added water volume fractions indicate that the effect of cytoplasm produced by the rupture of RBCs on impedance is much greater than that of RBC concentration.

Acknowledgements The author wishes to acknowledge the financial support by JSPS KAKENHI grant Number JP16H02312.

Conflict of Interest The authors declare that they have no conflict of interest.

References

- Jacob, H.S., Ingbar, S.H., Jandl, J.H.: Oxidative hemolysis and erythrocyte metabolism in hereditary acatalasia. *J. Clin. Inv.* **44**(7), 1187 (1965)
- Reiter, C.D., et al.: Cell-free hemoglobin limits nitric oxide bioavailability in sickle-cell disease. *Nat. Med.* **8**(12), 1383 (2002), December
- Emerson, C.P., et al.: Studies on the destruction of red blood cells: IX. Quantitative methods for determining the osmotic and mechanical fragility of red cells in the peripheral blood and splenic pulp; the mechanism of increased hemolysis in hereditary spherocytosis (Congenital Hemolytic Jaundice) as related to the functions of the spleen. *AMA Arch. Intern. Med.* **97**(1) (1956), 1-38 LNCs Homepage, <http://www.springer.com/lncs>. Last Accessed 2016/11/21
- Clark, I.A., Hunt, N.H.: Evidence for reactive oxygen intermediates causing hemolysis and parasite death in Malaria. *Infect. Immun.* **39**(1), 1-6 (1983)
- Linden, J.V., et al.: Transfusion errors in New York State: an analysis of 10 years' experience. *Transfusion* **40**(10), 1207-1213 (2000)
- Vercaemst, L.: Hemolysis in cardiac surgery patients undergoing cardiopulmonary bypass: a review in search of a treatment algorithm. *J. Extra-corporeal Technol.* **40**(4), 257 (2008)
- Neter, E.: Bacterial hemagglutination and hemolysis. *Bacteriol. Rev.* **20**(3), 166 (1956)
- Reiter, C.D., et al.: Cell-free hemoglobin limits nitric oxide bioavailability in sickle-cell disease. *Nat. Med.* **8**(12) (2002)
- Fricke, H., Curtis, H.J.: The electric impedance of hemolyzed suspensions of mammalian erythrocytes. *J. Gen. Physiol.* **18**(6), 821-836 (1935)
- Srivastava, J., Khade, S.: Assessment of physical damage of cryopreserved RBCs during thawing by impedance spectroscopy. *Int. J. Med. Sci. Public Health.* **4**(8), 1121-1125 (2015)
- Tran, A.K., et al.: Linear relationship between cytoplasm resistance and hemoglobin in red blood cell hemolysis by electrical impedance spectroscopy & eightparameter equivalent circuit. *Biosensors and Bioelectronics.* **119**, 103-109 (2018). <https://www.sciencedirect.com/science/article/pii/S0956566318306006>. 15 Nov

An Electrical Impedance Tomography Sensor with Different Diameter

Ryota Yanagisawa, Marlin Ramadhan Baidillah, Al Amin Saichul Iman, Panji Nursetia Darma, Huang Jingshi, and Masahiro Takei

Abstract

Electrical Impedance Tomography (EIT) has been proposed to assess the adipose tissue distribution in the upper arm of patients with different arm diameters. The aim of this study is to develop an adjustable EIT sensor, whose diameter can be adjusted within a certain range by changing the electrode-to-gap ratio (EGR) of the EIT sensor. In order to improve the reconstructed image quality and stability, investigation of the effect of changing the diameter of EIT sensor is needed. A prototype EIT sensor with an adjustable diameter and consisting of 32 electrodes was manufactured and evaluated through experimental studies. The experimental results show that the EIT sensor with the adjustable diameter can provide similar reconstructed images just as the traditional EIT sensor which has a fixed sensor diameter. The adjustable EIT sensor can therefore adapt the EIT to the changing diameters of the upper arm of different patients during the adipose tissue assessment.

Keywords

Adjustable EIT sensor • Adipose tissue assessment • Different diameter • Electrode-to-gap ratio

1 Introduction

Lymphedema is a sequelae of gynecological cancer that develops by the accumulation fluid in the adipose tissue of the upper arm limb [1]. Lymphedema diagnostic tries to

detect the accumulation of fluid in the interstitium such as adipose tissue in upper arm or upper leg limbs due to the blockage of lymph vessel after surgery. When the Lymphedema condition is getting worse, the limbs become enlarged and difficult to be recovered.

Electrical Impedance Tomography (EIT) has a potential capability to visualize the cross section of the upper arm limb in terms of the electrical properties distribution that related to the accumulation of fluid in the interstitium. This method is easier to be miniaturized and be manufactured inexpensively as compared to X-ray CT or MRI.

The reconstructed image accuracy of EIT depends on the location of electrodes attached in the periphery of limbs. The location of electrodes should be known prior to the image reconstruction. In the conventional EIT sensor, the geometry of sensor is fixed with a regular shape such as circle [2]. However, the diameters of upper arm are different depending on the individual body conditions which causes to reconstruction process and lymphedema diagnostic are difficult. Therefore, it is needed to modify the new design of electrodes location to overcome the different diameter of upper arm.

In order to overcome this issue, in this study, a prototype EIT sensor with adjustable diameter, consisting of 32 electrodes is developed. The quality and stability of reconstructed image based on manufactured adjustable sensor is investigated under changing the diameter with saline agar phantom.

2 Materials and Method

2.1 Adjustable EIT Sensor

The appearance and diagram of the adjustable EIT sensor is shown in Fig. 1. It consists of an electrode-attached chuck (inside part) and a multi-electrode switching system (outside circuit parts). The electrode-attached chuck is an electrode sensor designed to cope with the change in the diameter of

R. Yanagisawa · M. R. Baidillah (✉) · A. A. S. Iman · P. N. Darma · H. Jingshi · M. Takei
Graduate School of Science and Engineering, Division of Fundamental Engineering, Chiba University, Chiba, 263-8522, Japan
e-mail: mr.baidillah@c-techlabs.com

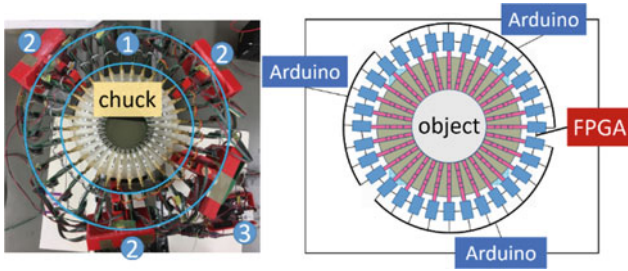


Fig. 1 The appearance and diagram of the adjustable EIT sensor

the measured object, and is a mechanism similar to the scroll chuck of the lathe. Multi-electrode switching system is mainly made up of three parts, ① Switch circuit, ② Arduino and ③ FPGA.

2.2 Image Reconstruction of EIT

A schematic diagram of image reconstruction EIT is shown in Fig. 2. A constant AC current I is injected between the two electrodes (Hc to Lc), and the potential V between the other electrodes (Hp to Lp) is measured. By switching pairs of the current injecting electrodes and the voltage measuring electrodes, the conductivity change distribution σ (S/m) on the cross section of the upper arm can be created.

The basic equation of EIT is expressed as follows.

$$U = J\sigma \tag{1}$$

$$J = \begin{pmatrix} \frac{\partial U_1}{\partial \sigma_1} & \dots & \frac{\partial U_1}{\partial \sigma_m} \\ \vdots & \ddots & \vdots \\ \frac{\partial U_n}{\partial \sigma_1} & \dots & \frac{\partial U_n}{\partial \sigma_m} \end{pmatrix} \tag{2}$$

U is the measurement voltage matrix, J is the sensitivity matrix, and σ (S/m) is the conductivity change distribution. Since the measurement voltage U and the sensitivity matrix J are known, meanwhile the sensitivity matrix J does not have an inverse matrix and has no unique solution, thus it is necessary to obtain an approximate solution by an appropriate algorithm.

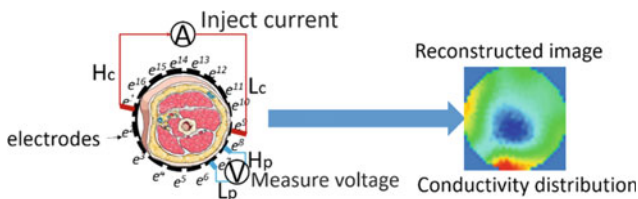


Fig. 2 The schematic diagram of image reconstruction EIT

2.3 Experimental Condition

Appearance of the phantoms condition is shown in Fig. 3. In this experimental studies, we compared the reconstructed images with three diameter diameters ($D = 70, 80, 90$ mm) so that the electrode-to-gap ratio (EGR) is changed. The conductivity of the inclusion area A was $\sigma_A = 0.7$ S/m and the conductivity of the background area B was $\sigma_B = 0.2$ S/m. The three object phantoms are made so that their cross sections are similar ($D : d : a = 70 : 14 : 1$) to each other in order to confirm the influence of change in diameter. The measurement frequency was $f = 20, 50, 100$ kHz, and injected current was $I = 1$ mA.

3 Results and Discussion

The experimental results are shown in Fig. 4 which are the conductivity change distribution obtained by image reconstruction of each phantom for each frequency. The inclusion area with higher conductivity was detected with blue color.

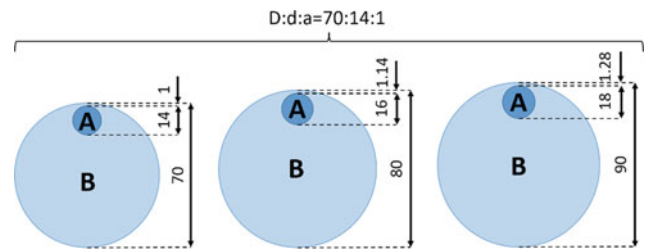


Fig. 3 Phantoms conditions for experimental studies

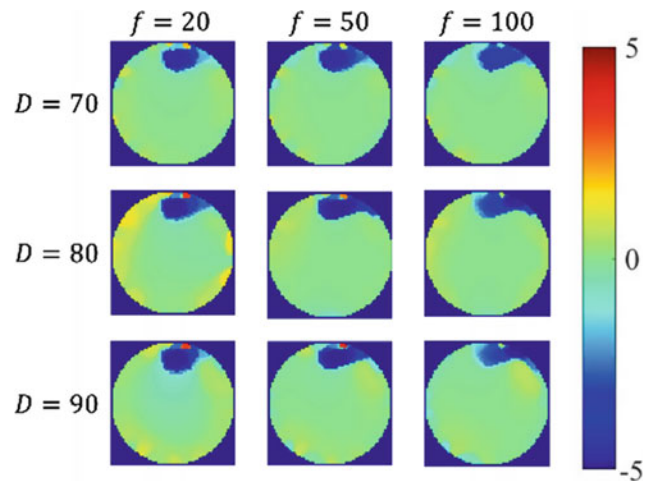


Fig. 4 Conductivity change distribution σ (S/m)

In the measured frequency ranges, almost no image change due to change in diameter or the electrode-to-gap ratio (EGR) was observed. The blue part appears to be distorted to the right. This seems to be caused by a slight deviation of the distance between the electrodes of the adjustable EIT sensor. It seems that the blue color of the high conductivity part seems to be thin due to the increase of frequency. This is thought to be due to (1) change in conductivity due to frequency characteristics and (2) decrease in signal-to-noise SN ratio in the high frequency measurements.

4 Conclusion

In this study, an adjustable EIT sensor has been manufactured and proposed to overcome the technical problem of Lymphedema diagnostic with EIT. The technical problem of Lymphedema diagnostic with EIT arose due to the different diameter of individual body conditions. In order to

investigate the influence of the changing the diameter, experimental studies using phantom was carried out. The following results is clarified: that the manufactured adjustable EIT sensor provides similar reconstructed images in the case of different diameter or changing electrode-to-gap ratio (EGR).

Acknowledgements The author wishes to acknowledge the financial support by JSPS KAKENHI Grant Number JP16H02312. **Conflict of Interest** The authors declare that they have no conflict of interest.

References

1. Akita, S., et al.: Early diagnosis and risk factors for lymphedema following lymph node dissection for gynecologic cancer. *Plast. Reconstr. Surg.* **131**(2), 283–290 (2013)
2. Baidillah, M.R., Iman, A.-A.S., Sun, Y., Takei, M.: Electrical impedance spectro-tomography based on dielectric relaxation model. *IEEE Sens. J.* **17**(24) (2017)

Effect of Surface Roughness on Friction of CoCrMo-on-UHMWPE Bearing in Total Hip Arthroplasty Under Lubrication of Bovine Serum Albumin

Cong-Truyen Duong, Cong-Dat Le, and Duc-Nam Nguyen

Abstract

The study aims to examine the effect of surface roughness as well as lubricant and normal load on frictional response of CoCrMo-on-UHMWPE bearing using a custom friction-measuring device. A cylindrical CoCrMo pin with surface roughness of $0.25\ \mu\text{m}$ was prepared. Ten UHMWPE discs with different surface roughness of 2.5 and $0.25\ \mu\text{m}$ were machined. BSA at concentration of $25\ \text{mg/ml}$ was prepared by dissolving in PBS. A custom pin-on-disc friction-measuring device was designed to measure the coefficient of friction (μ). The normal loads were varied in two values of 4 and $16\ \text{N}$ at sliding velocity of $28\ \text{mm/s}$. The mean μ values were taken in $3600\ \text{s}$. Results demonstrated that BSA $25\ \text{mg/ml}$ improved the frictional properties between CoCrMo-on-UHMWPE bearing ($p < 0.0001$) and the μ values were increase with the increase of the surface roughness as well as with the increase of the normal loads ($p < 0.0001$). These results suggest that BSA plays an important role in improving the lubricating ability of CoCrMo-on-UHMWPE bearing and the frictional response between CoCrMo-on-UHMWPE depend on the surface roughness as well as the normal load.

Keywords

Surface roughness • Coefficient of friction • CoCrMo • UHMWPE • BSA • Lubrication

1 Introduction

One of the most commonly used material combination in arthroplasty is metal-on-UHMWPE. Despite the good mechanical and frictional properties of this bearing,

C.-T. Duong (✉) · C.-D. Le · D.-N. Nguyen
 Industrial University of Ho Chi Minh City, Ho Chi Minh City,
 Vietnam
 e-mail: truyencd@gmail.com

problems related to friction and wear lead to failure of the prosthesis. Therefore, most studies on artificial joint materials, such as CoCrMo and UHMWPE, were related to the mechanism of friction, wear and lubrication between implant materials [1–4]. Such studies will lead to a better understanding of the lubricating mechanisms and to the development of new materials that show better lubricating characteristics in synovial fluid.

The frictional characteristics of a material combination not only depend on the type of materials used and on their surface properties but also on the lubricant. Several studies have been reported on the effect of synovial fluid components on friction and wear with different conclusions [5–10]. Mazzucco et al. examined the effect of synovial fluid components on the friction between CoCrMo and UHMWPE and they concluded that albumin, gamma-globulin, phospholipids and hyaluronic acid do not act as boundary lubricants [5]. In contrast, Gispert et al. observed the friction between CoCrMo and UHMWPE and showed that albumin and hyaluronic acid improve the frictional response of implant [6].

Therefore, the aim of this study is to investigate the effect of surface roughness as well as lubricant and normal load on frictional response of CoCrMo-on-UHMWPE bearing using a custom friction-measuring device.

2 Materials and Methods

2.1 Pin and Disc Samples Preparation

A cylindrical CoCrMo pin (diameter \times length of $10\ \text{mm} \times 15\ \text{mm}$) was provided by Denken Highdental, Japan; then the pin surface roughness of $R_a = 0.25 \pm 0.05\ \mu\text{m}$ was prepared using a grinding machine. UHMWPE (Ultra high molecular weight polyethylene) was provided by Wefapress, Germany and ten UHMWPE discs (diameter \times thickness of $90\ \text{mm} \times 5.2\ \text{mm}$) with different surface roughness of $R_a = 2.5 \pm 0.5\ \mu\text{m}$ and $R_a = 0.25 \pm 0.05\ \mu\text{m}$ were

machined by CNC machining method. The surface roughness of CoCrMo pin and UHMWPE discs were measured using a Mitutoyo portable surface roughness tester (SJ-310) (Fig. 1).

2.2 Lubricant Preparation

The phosphate buffered saline (PBS) powder was provided by Bomei, Taiwan. Then the PBS solution at concentration of 10 mg/ml was prepared by dissolving in distilled water. Finally, the bovine serum albumin (BSA) at concentration of 25 mg/ml was prepared by dissolving the BSA powder (Bomei, Taiwan) in PBS solution. The BSA concentration was chosen based on the total protein concentration of human synovial fluid, ranging from 15 to 50 mg/ml [11] (Fig. 2).

2.3 Macroscale Frictional Measurements

A custom pin-on-disc friction-measuring device (Fig. 3) was designed to measure the macroscale coefficient of friction between CoCrMo-on-UHMWPE under without lubricant condition and under lubrication of BSA 25 mg/ml. The normal loads (F_N) were varied in two values of 4 and 16 N at

sliding velocity of 28 mm/s. The sliding velocity was chosen based on the movement velocity of human hip joint ranging from 0 to 50 mm/s [6]. During the measurements, the voltage signal of frictional force was measured by loadcell and it was then converted to the frictional force (F_{FMS}) value. The coefficient of friction (μ) between CoCrMo pin and UHMWPE disc is calculated by dividing the frictional force to the normal load. The mean values of μ were taken in 3600 s. The experimental parameters were summarized in Table 1.

2.4 Statistical Analyses

A one-way analysis of variance (ANOVA) was used to detect the significant differences in coefficient of friction of the CoCrMo-on-UHMWPE bearing between different UHMWPE surface roughness, lubricants and normal loads with $p < 0.05$ considered significant.

3 Results and Discussion

The current study reports the effect of the surface roughness, lubricant and normal load on the coefficient of friction of the CoCrMo-on-UHMWPE bearing. The variations of the

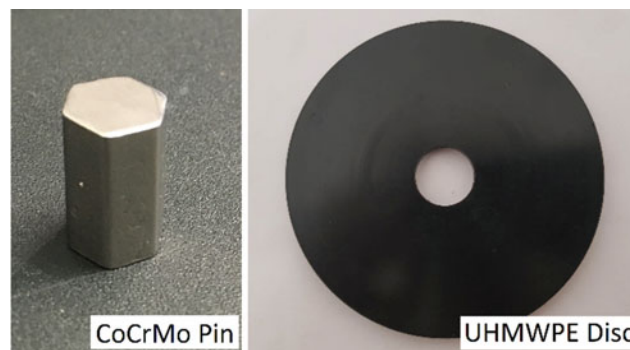


Fig. 1 Typical CoCrMo pin and UHMWPE disc samples were used for the experiments



Fig. 2 PBS and BSA lubricants were used for the experiments

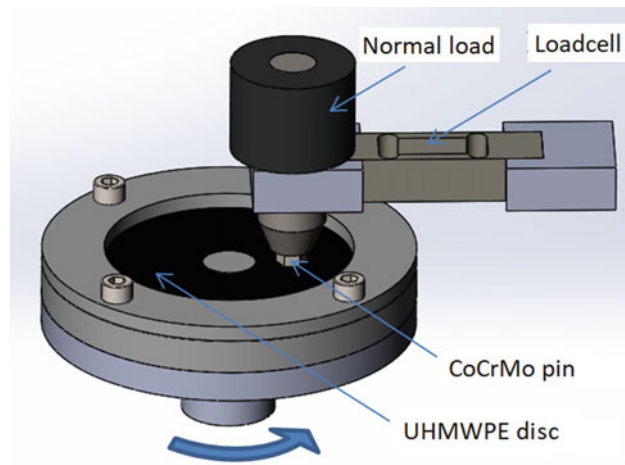


Fig. 3 A custom pin-on-disc friction-measuring device was designed for the experiments

Table 1 Parameters were used for the experiments

Experimental parameters	Values
Time (t)	3600 s
Sliding velocity (v)	28 mm/s
Normal load (F_N)	4 and 16 N
Surface roughness of CoCrMo pin (R_a)	$0.25 \pm 0.05 \mu\text{m}$
Surface roughness of UHMWPE disc (R_a)	$0.25 \pm 0.05 \mu\text{m}$ and $2.5 \pm 0.5 \mu\text{m}$

coefficient of friction (μ) during the measuring time of 3600 s were showed in Fig. 4, indicating that the μ increases with the increase of the UHMWPE surface roughness (R_a) as well as with the increase of the normal loads (F_N). Lubricant of BSA with the concentration of 25 mg/ml improves the lubricating ability of the CoCrMo-on-UHMWPE bearing due to the adsorption of BSA molecules on the bearing surface. The mean \pm standard deviation values of μ were summarized in Table 2. The one-way ANOVA revealed that there were statistically significant differences in μ of the CoCrMo-on-UHMWPE bearing between UHMWPE surface roughness of $2.5 \pm 0.5 \mu\text{m}$ and $0.25 \pm 0.05 \mu\text{m}$ ($p < 0.0001$). Similarly, there were statistically significant differences in μ between the normal load of 4 and 16 N as well as between without lubricant and lubrication with BSA 25 mg/ml ($p < 0.0001$) (Fig. 5). The μ values measured

with BSA 25 mg/ml ranging from 0.017 ± 0.005 to 0.069 ± 0.007 and measured without lubricant ranging from 0.028 ± 0.007 to 0.079 ± 0.004 are consistent with those reported in the literature [1, 2, 6]. The dependences of the frictional response of the CoCrMo-on-UHMWPE bearing on BSA and normal load are also consistent with previous friction study [6, 8, 10].

4 Conclusions

The main result of the study is that the frictional response of the CoCrMo-on-UHMWPE bearing depends on the surface roughness, lubricant and normal load. The coefficient of friction increased with the increase of the UHMWPE surface roughness. BSA 25 mg/ml improved the lubricating ability

Fig. 4 Variation of coefficient of friction between CoCrMo-on-UHMWPE surfaces during the measurement time of 3600 s

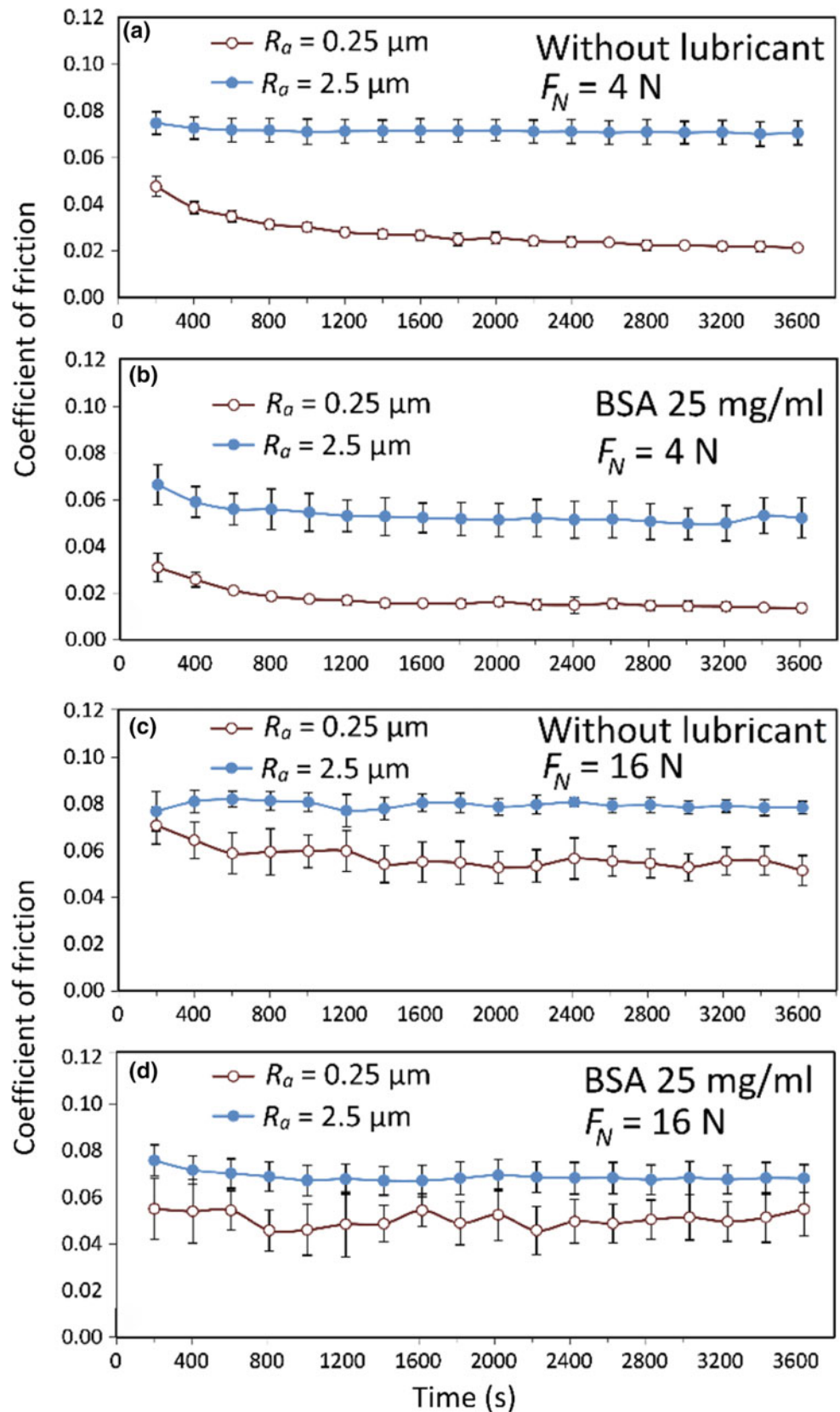
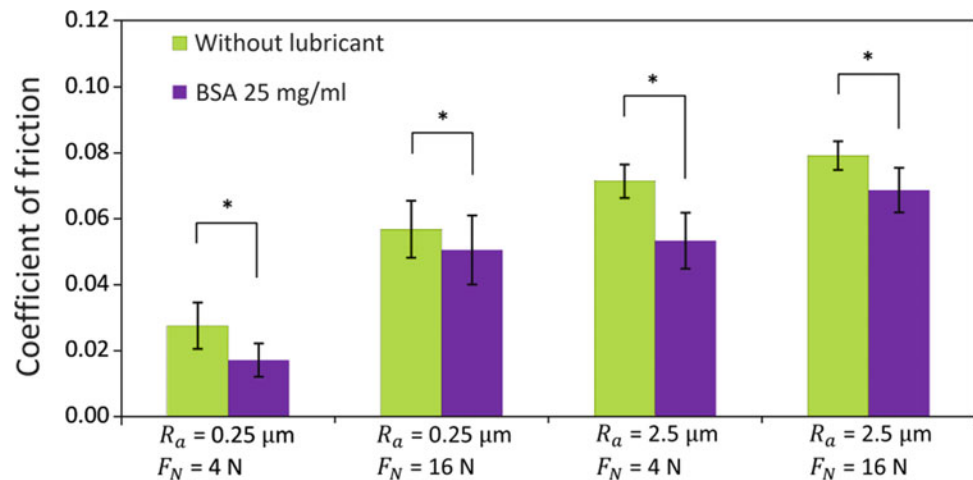


Table 2 Mean \pm standard deviation values of μ between CoCrMo-on-UHMWPE surfaces measured during 3600 s

Experimental conditions	Coefficient of friction \pm standard deviation		p value
	$R_a = 0.25 \pm 0.05 \mu\text{m}$	$R_a = 2.5 \pm 0.5 \mu\text{m}$	
Without lubricant, $F_N = 4 \text{ N}$	0.028 ± 0.007	0.071 ± 0.005	<0.0001
Without lubricant, $F_N = 16 \text{ N}$	0.057 ± 0.009	0.079 ± 0.004	<0.0001
BSA 25 mg/ml, $F_N = 4 \text{ N}$	0.017 ± 0.005	0.053 ± 0.008	<0.0001
BSA 25 mg/ml, $F_N = 16 \text{ N}$	0.051 ± 0.010	0.069 ± 0.007	<0.0001

Fig. 5 Mean μ values of CoCrMo-on-UHMWPE bearing measured in BSA 25 mg/ml with different values of UHMWPE surface roughness and of normal loads (*: $p < 0.0001$)

of the CoCrMo-on-UHMWPE bearing and the increase of the normal load led to the decrease of the frictional response of the CoCrMo-on-UHMWPE bearing.

Acknowledgements This research was funded by the Industrial University of Ho Chi Minh City, Vietnam through the University Research Foundation (No. 28/2018/HĐ-ĐHCN). **Conflict of Interest** The authors declare that they have no conflict of interest.

References

- Jin, Z.M., Stone, M., Ingham, E., Fisher, J.: Biotribology. *Curr. Orthop.* **20**(1), 32–40 (2006)
- Puccio, F.D., Mattei, L.: Biotribology of artificial hip joints. *World J. Orthop.* **6**(1), 77–94 (2015)
- Zivic, F., Babic, M., Adamovic, S., Pelemis, S.: Friction coefficient of UHMWPE during dry. *Tribol. Ind.* **36**(3), 281–286 (2014)
- Linn, F.: Lubrication of animal joints. II. The mechanism. *J. Biomech.* **1**(3), 193–205 (1968)
- Mazzucco, D., Spector, M.: The role of joint fluid in the tribology of total joint arthroplasty. In: *Hip-Society Meeting*, pp. 17–32. Lippincott Williams & Wilkins, San Francisco (2004)
- Gispert, M.P., Serro, A.P., Colaco, R., Saramago, B.: Friction and wear mechanisms in hip prosthesis: comparison of joint materials behaviour in several lubricants. *Wear* **260**(1–2), 149–158 (2006)
- Mishina, H., Kojima, M.: Changes in human serum albumin on arthroplasty frictional surfaces. *Wear* **265**(5–6), 655–663 (2008)
- Saikko, V.: Effect of lubricant protein concentration on the wear of ultra-high molecular weight polyethylene sliding against a CoCr counterface. *J. Tribol-T ASME* **125**(3), 638–642 (2003)
- Sawae, Y., Murakami, T., Chen, J.: Effect of synovia constituents on friction and wear of ultra-high molecular weight polyethylene sliding against prosthetic joint materials. *Wear* **216**(2), 213–219 (1998)
- Wang, A., Essner, A., Schmidig, G.: The effects of lubricant composition on in vitro wear testing of polymeric acetabular components. *J. Biomed. Mater. Res. B* **68**(1), 45–52 (2004)
- McPherson, R.A., Pincus, M.R.: *Henry's Clinical Diagnosis and Management by Laboratory Methods*, 23rd edn. Elsevier, Philadelphia (2017)

Part VI

**Recent Computational and Experimental Advances
in Molecular Medicine**



Replacement of Residue H95 with Charged Amino Acids in the Prion Protein Decreases Prion Conversion Propensity

Thanh Hoa Tran and Giuseppe Legname

Abstract

Transmissible spongiform encephalopathies (TSEs) or prion diseases are fatal neurodegenerative disorders caused by a change in conformation of the prion protein from the normal cellular form (PrP^C) to a misfolded form (PrP^{Sc}). Prion diseases have been widely studied, but despite many great leaps in our knowledge many gaps in our knowledge are still unknown, especially in prion conformational conversion mechanism. In this work, we perform an amino acid scan at histidine (H)95, a key regulator residue within proposed prion conversion of the fifth copper-binding site. We created a series of mutant PrP by replacing H95 with every other common amino acid and compared the prion conversion propensity by ScN2a assay. The results are remarkable with the residues with electrically-charged side chains (H95D, H95E, H95K and H95R) decreasing prion conversion by about 50–75%, compared to wild-type (wt) PrP. We next analyze the localization, trafficking and biochemical features of PrP H95E, the most promising mutant for reducing conversion, in N2aPrP^{-/-} cells stably transfected with the mutant PrP. The only difference observed was relative to the endosomal recycling compartments, with mutant PrP H95E showing less co-localization compared to WT PrP. This is in agreement with other work that links the endosomal recycling compartments with prion conversion. We conclude that the replacement of PrP H95 with electrically charged side chains decreases the prion conversion propensity, and this is likely due to reduced co-localization with the endosomal recycling compartments.

Keywords

Prion • Transmissible spongiform encephalopathies • Copper binding site

1 Introduction

Prion diseases in human and animals are a group of fatal neurodegenerative diseases that are also referred to as transmissible spongiform encephalopathies (TSEs). They have a common feature in aberrant metabolism of the prion protein (PrP) [1]. During the pathogenesis of these diseases, the cellular isoform of the prion protein (PrP^C) adopts a pathogenic conformation denoted as prion (PrP^{Sc}), which accumulates in cells and causes the disease. Although there have been numerous studies, the mechanism of prion conversion and replication remains elusive.

Most point mutations linked to inherited prion diseases are clustered in the C-terminal globular domain of PrP. These mutations may affect secondary structure elements and structure flexibility of the globular domain [2] and also accelerate the misfolding process in vitro [3]. Several structural studies on this globular domain proposed a role of the $\beta 2$ – $\alpha 2$ loop as dynamic “switch” that is able to modulate the PrP^C-PrP^{Sc} conversion [4, 5]. Interestingly, some point mutations are located in the unstructured N-terminal domain. These mutations cause the disease without affecting the kinetics of fibril formation in vitro [6]. Moreover, there is little evidence for a direct molecular effect of the mutations in the N-terminus on the globular structure of PrP^C [2]. This suggests that N-terminal mutations might affect to the PrP^{Sc} formation in different way, indicating the potential critical impact of the N-terminal domain on prion conversion.

The N-terminal domain of PrP has been shown to have high affinity binding to copper ions [7], with four copper binding sites at octapeptide region (OR) and the fifth copper binding site at non-octapeptide region (non-OR). The fifth copper binding site locates in the protease-resistant core of

T. H. Tran (✉) · G. Legname
Prion Biology Laboratory, Neuroscience Area, Scuola
Internazionale Superiore di Studi Avanzati (SISSA), Trieste, Italy
e-mail: thtran@sissa.it

PrP^{Sc} and is adjacent to the hydrophobic region that contained the palindromic motif sequence AGAAAAGA involving in structural changes during the early stage of prion conversion [8]. In our previous study, we showed that this copper binding site has a critical role in prion conversion and the substitute histidine by tyrosine at H95 promoted prion conversion in ScN2a cells [9]. Here, to further investigate the role of the fifth copper-binding site, we performed an amino acid scan at H95, replacing histidine with every other amino acid. By using ScN2a assay, we found that the substitution of histidine by charged amino acid at H95 showed a negative influence on prion formation.

2 Results

H95 substituted with amino acids containing charged side chains reduces prion conversion in vitro

To investigate the effect of H95 on prion conversion, we completed an amino acid scan of H95, replacing the histidine with other amino acid and measuring the prion conversion propensity by prion conversion assay. We transiently transfected ScN2a cells with our PrP constructs, collected the cell lysates 72 h later and analyzed by PK digestion and immunoblot. The 3F4 tag, a human-specific epitope, was added to all constructs to discriminate between endogenous and transfected PrP.

The results showed that there are marked changes in the prion conversion propensity among the constructs. When H95 was substituted with neutral or small amino acids (A, G, C, S, T, N, Q, P), the PrP^{Sc} levels were comparable to WT PrP. However, when H95 was replaced by hydrophobic amino acids (F, Y, L, M, V, W, I), the PrP^{Sc} levels were dramatically increased. On the other extreme, substitutions

with the charged amino acid residues (D, E, K, R) had a low rate of PrP^{Sc} conversion, about 50–75% when compared to WT PrP. This suggested that substitutions H95 by charge amino acids somehow dissuade prion conversion. For further studies of this inhibitory effect, we chose to focus the PrP mutation with the lowest prion conversion propensity: H95E (Fig. 1).

PrP H95E shares similar biochemical properties with wild-type PrP

To study the biochemical features of the H95E mutant, we employed the mouse neuroblastoma cell line in which the PrP gene was knocked out. We created two stable cell lines: WT PrP N2aPrP^{-/-} and PrP H95E N2aPrP^{-/-}. In these cell lines, WT PrP or PrP H95E was reintroduced to N2aPrP^{-/-} cells, therefore without the need of epitope tagging. First, we analyzed the glycosylation patterns of these PrP constructs. The Western blotting result showed that PrP H95E and WT PrP all share the same glycosylation patterns (Fig. 2b, untreated lanes), migrating with the classical three bands composed of the diglycosylated, monoglycosylated and unglycosylated PrP.

To monitor physiological processing of the posttranslational modification of PrP H95E and WT PrP, we treated cell lysates to Endo H or PNGase F digestion. Endo H is a highly specific endoglycosidase, which cleaves asparagine-linked mannose-rich oligosaccharides, but not highly processed complex oligosaccharides from glycoproteins. Therefore, Endo H is used to monitor posttranslational modification in the Golgi apparatus. Because glycoproteins acquire Endo H resistance upon transport to the Golgi compartments, Endo H sensitivity is considered a sign of protein immaturity [10]. Meanwhile, PNGase F is able to remove N-glycans and used to detect glycoproteins. We found that both PrP H95E and WT PrP were resistant to Endo H digestion and showed

Fig. 1 Effect of amino acid substitutions at H95 on prion conversion

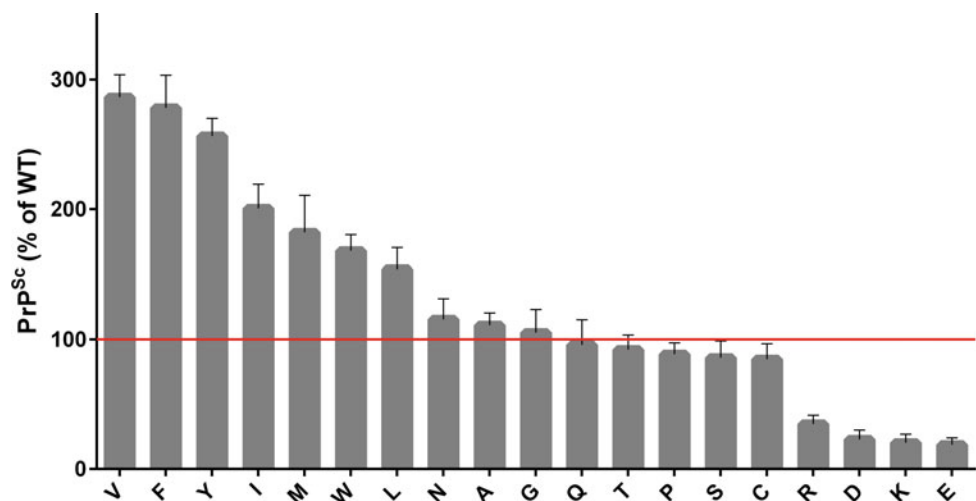
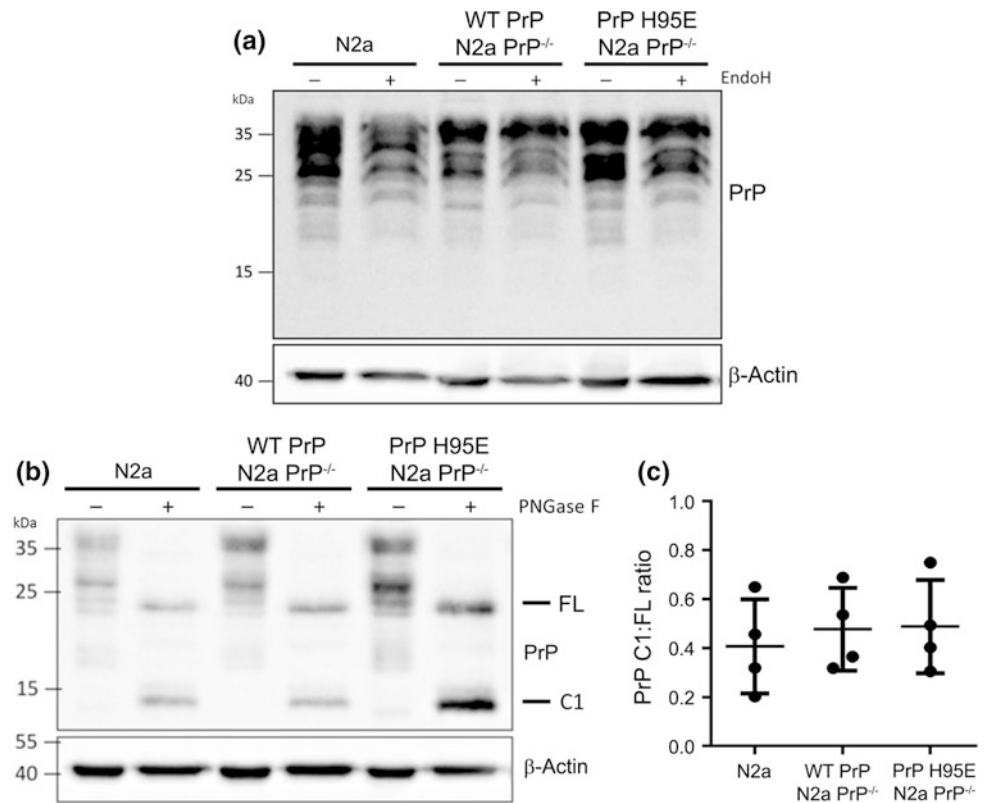


Fig. 2 Biochemical properties of WT PrP and PrP H95E. **a** Cell lysates was treated or untreated with Endo H or **b** PNGase F. The full-length PrP (FL) and C1 fragment (C1) are indicated. PrPs were detected by anti-PrP W226 antibody and β -actin was used as an internal loading control. **c** Quantitative analysis of the ratio of C1:FL after PNGase F digestion



no differences between them (Fig. 2a). Also, treatment with PNGase F in all cases resulted in only two bands, the unglycosylated full-length PrP (FL) and the C1 fragment of PrP (C1), with bands with higher molecular weight (35–45 kDa) corresponding to mono and diglycosylated PrP^C undetected. Taken together, these data suggested that PrP H95E were successfully processed through ER and Golgi compartments during their maturation. Also, PNGase F assay showed there were no statistically significant differences of the proportions of C1:FL between the cell lines (Fig. 2c). These results indicate that the substitution of histidine by glutamic acid at H95 did not affect the proteolytic processing of PrP.

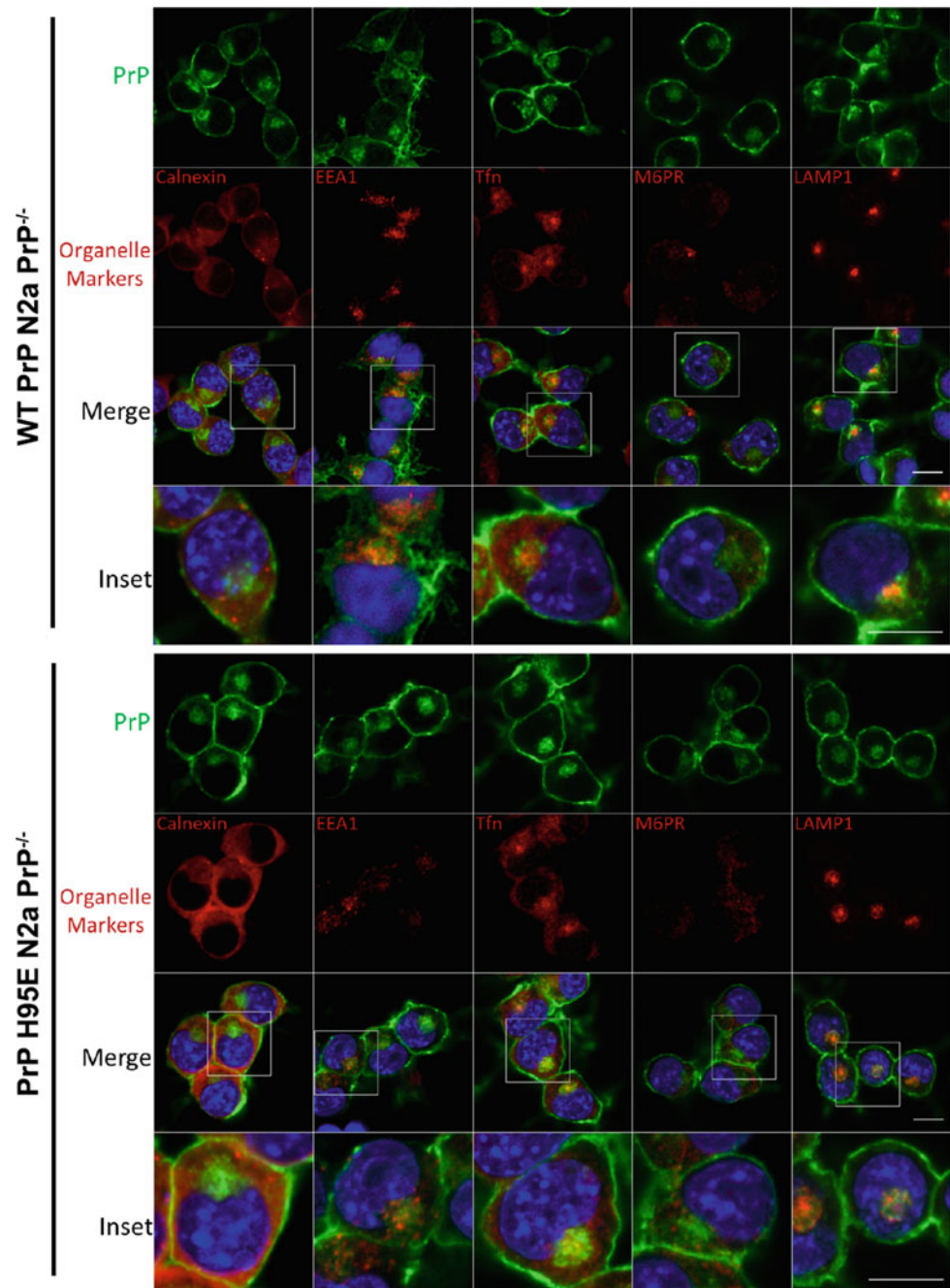
PrP H95E displays altered localization pattern in recycling endosomes

Because the subcellular and trafficking of PrP may have an impact on prion formation, we next analyzed the localization pattern of PrP H95E. Compared to WT PrP, PrP H95E showed similar PrP distribution with predominantly localization at the cell surface. These cell lines WT PrP N2a PrP^{-/-} and PrP H95E N2a PrP^{-/-} also shared the same

co-localization patterns with several organelle markers, except for the endosomal recycling compartment marker. WT PrP exhibited clearly co-localization with Tfn, a marker of recycling endosomes. In contrast, cells expressing the PrP H95E showed that only a very small proportion of PrP co-localized with Tfn.

Endosomal compartments have been known as acidic compartments [11]. This acidic pH has been suggested as a critical condition for changes in PrP conformation [12]. Previous studies have shown that the transition of PrP from its native state to soluble oligomers is a pH-dependent process [13] and the acidic condition is favor for the existence of soluble PrP oligomers [14]. Additionally, various studies demonstrated that PrP^{Sc} is detected throughout endosomal compartments, being particularly abundant in recycling endosome and the endosomal recycling compartment was identified as the likely site of prion conversion [15]. Therefore, the lesser accumulation of H95E in recycling endosomes, a proposed suitable environment for PrP^{Sc} formation, might be an appropriate explanation for inhibitory effect on prion conversion of PrP constructs with charged amino acid at the fifth copper-binding site (Fig. 3).

Fig. 3 PrP localization in WT PrP N2a PrP^{-/-} and PrP H95E N2a PrP^{-/-}. PrPs were detected by anti-PrP W226 antibody (green), nuclei were labeled with DAPI (blue) and organelle markers were labeled in red: Calnexin (ER marker), EEA1 (early endosome marker), Tfn (endosomal recycling compartment marker), M6PR (late endosome marker) and LAMP1 (lysosome marker). Insets show a magnification of the merged panels from white boxed areas. Scale bar: 10 μ m



3 Conclusions

By performing amino acid scanning at fifth copper-binding site H95, we found that the substitution of histidine by charged amino acids results in the decline of prion conversion propensity. Among these substitutions, mutant PrP H95E showed the highest inhibitory effect on PrP^C-PrP^{Sc}

conversion process. Based on our data, this inhibitory effect relates to the co-localization of PrP with the endosomal recycling compartment, and the degree of PrP accumulation in recycling endosomes seems to be directly correlated with prion conversion.

Conflict of Interest The authors declare that there are no conflict of interests.

References

1. Prusiner, S.B.: The prion diseases. *Brain Pathol.* **8**, 499–513 (1998)
2. Van Der Kamp, M.W., Daggett, V.: The consequences of pathogenic mutations to the human prion protein. *Protein Eng. Des. Sel.* **22**, 461–468 (2009)
3. Apetri, A.C., Surewicz, K., Surewicz, W.K.: The effect of disease-associated mutations on the folding pathway of human prion protein. *J. Biol. Chem.* **279**, 18008–18014 (2004)
4. Sigurdson, C.J., Nilsson, K.P.R., Hornemann, S., et al.: A molecular switch controls interspecies prion disease transmission in mice. *J. Clin. Invest.* **120**, 2590–2599 (2010)
5. Kurt, T.D., Bett, C., Fernández-Borges, N., et al.: Prion transmission prevented by modifying the $\beta 2$ - $\alpha 2$ loop structure of host PrP^C. *J. Neurosci.* **34**, 1022–1027 (2014)
6. Jones, E.M., Surewicz, K., Surewicz, W.K.: Role of N-terminal familial mutations in prion protein fibrillization and prion amyloid propagation in vitro. *J. Biol. Chem.* **281**, 8190–8196 (2006)
7. Aronoff-Spencer, E., Burns, C.S., Avdievich, N.I., et al.: Identification of the Cu²⁺ binding sites in the N-terminal domain of the prion protein by EPR and CD spectroscopy. *Biochemistry* **39**, 13760–13771 (2000)
8. Abskharon, R.N.N., Giachin, G., Wohlkonig, A., et al.: Probing the N-terminal β -sheet conversion in the crystal structure of the human prion protein bound to a nanobody. *J. Am. Chem. Soc.* **136**, 937–944 (2014)
9. Giachin, G., Mai, P.T., Tran, T.H., et al.: The non-octarepeat copper binding site of the prion protein is a key regulator of prion conversion. *Sci. Rep.* **5**, 1–14 (2015)
10. Maley, F., Trimble, R.B., Tarentino, A.L., Plummer, T.H.: Characterization of glycoproteins and their associated oligosaccharides through the use of endoglycosidases. *Anal. Biochem.* **180**, 195–204 (1989)
11. Gagescu, R., Demarex, N., Parton, R.G., et al.: The recycling endosome of Madin-Darby canine kidney cells is a mildly acidic compartment rich in raft components. *Mol. Biol. Cell* **11**, 2775–2791 (2000)
12. Hornemann, S., Glockshuber, R.: A scrapie-like unfolding intermediate of the prion protein domain PrP(121-231) induced by acidic pH. *Proc. Natl. Acad. Sci.* **95**, 6010–6014 (1998)
13. Gerber, R., Tahiri-Alaoui, A., Hore, P.J., James, W.: Conformational pH dependence of intermediate states during oligomerization of the human prion protein. *Protein Sci.* **17**, 537–544 (2008)
14. Baskakov, I.V., Legname, G., Baldwin, M.A., et al.: Pathway complexity of prion protein assembly into amyloid. *J. Biol. Chem.* **277**, 21140–21148 (2002)
15. Marijanovic, Z., Caputo, A., Campana, V., Zurzolo, C.: Identification of an intracellular site of prion conversion. *PLoS Pathog.* **5** (2009)

Computer Simulations Provide Guidance for Molecular Medicine Through Insights on Dynamics and Mechanisms at the Atomic Scale

Marc Baaden 

Abstract

Computer simulations provide crucial insights and rationales for the design of molecular approaches in medicine. Several case studies illustrate how molecular model building and molecular dynamics simulations of complex molecular assemblies such as membrane proteins help in that process. Important aspects relate to build relevant molecular models with and without a crystal structure, to model membrane aggregates, then to link (dynamic) models to function, and finally to understand key disease-triggering phenomena such as aggregation. Through selected examples—including key signaling pathways in neurotransmission—the links between a molecular-level understanding of biological mechanisms and original approaches to treat disease conditions will be illuminated. Such treatments may be symptomatic, e.g. by better understanding the function and pharmacology of macromolecular key players, or curative, e.g. through molecular inhibition of disease-inducing molecular processes.

Keywords

Molecular dynamics • Model building • Molecular mechanisms of disease

1 Introduction

Models at the molecular level play a crucial role for the field of medicine, or more generally-speaking biology. Their importance goes back well before the use of computational approaches: for instance Watson and Crick used a mechanical model fabricated in a workshop to gain insight into

DNA structure. Such modeling approaches are nowadays carried out on the computer, be it with a laptop or at a supercomputer centre. They are very useful, from trying to understand the key properties of molecular building blocks such as metabolites, sugars, lipids and macromolecular fragments to rationalizing the effect of mutations, identifying specific regions of interest, for instance aggregation-prone ones, characterizing the dynamics of biological and medical processes, and to gain insight into fundamental mechanisms governing disease.

Beyond such qualitative observations, the quantitative implementation of the modeling process in relation to verifiable experimental measures represents one of the key challenges. There are a few direct points of comparison, for example distances in a model can be linked to FRET experiments, which are of interest for the validation of the models, but not for medical purposes. Free energies and binding affinities may provide quantitative information on the effect of mutations or the potency of drug molecules, yet a direct prediction leading from the molecular level to a measurable impact on disease conditions is nowadays clearly out of scope. Such a goal would at the very least require to anticipate the complex interrelationships in metabolic networks—where the actors examined by molecular modeling are interconnected through a web of other macromolecules—by linking the molecular level with a systems biology representation. An overall scheme is provided in Fig. 1.

In this contribution, we focus on the atomic scale aspects using several case studies. It is illustrated how computational approaches, in particular molecular model building and molecular dynamics simulations of complex molecular assemblies such as membrane proteins help in understanding these molecular processes. The examples comprise important aspects related to building medically relevant molecular models with and without a crystal structure, to model aggregates, then to link (dynamic) models to function, and finally to understand key disease-triggering phenomena such as aggregation. In each case, the links between a molecular-level understanding of biological mechanisms and original

M. Baaden (✉)
Laboratoire de Biochimie Théorique, CNRS, UPR9080,
Université Paris Diderot, Sorbonne Paris Cité, PSL Research
University, 13 rue Pierre et Marie Curie, Paris, 75005, France
e-mail: baaden@smplinux.de

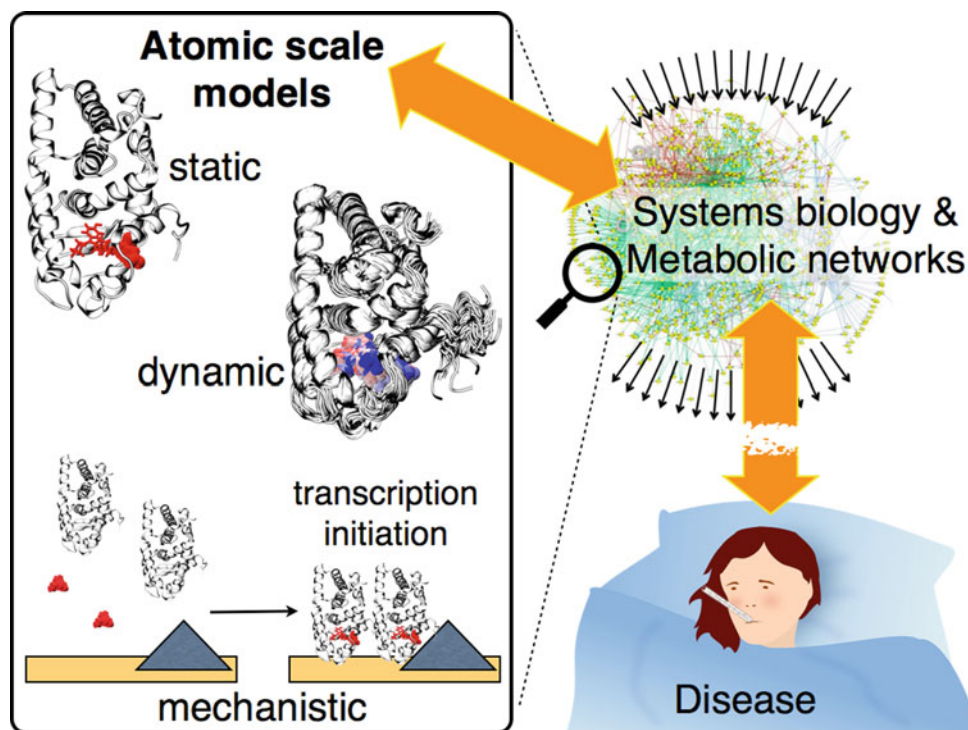


Fig. 1 Schematic view of the connections between atomic scale models, representing a zoom of complex interrelated metabolic networks, and disease, as a consequence of a network perturbation. Atomic scale models are illustrated with the estrogen receptor based on simulations described in [1], showing a static model with a key mutation and a drug molecule highlighted in red. A dynamic picture is

provided as the next level of interpretation, here drug and mutation are colored from blue to red as a function of timestep. Then, these computational models need to fit into a mechanistic picture, here of estrogen receptor assembly, initiated by an estrogen signal and leading to the initiation of transcription

approaches to treat disease conditions will be briefly illuminated. Such treatments may be symptomatic through a better understanding of the function and pharmacology of macromolecular key players, or curative, through molecular inhibition of disease-inducing molecular processes, for instance. The manuscript ends with an overview of upcoming new tools that are likely to further improve the power of computational approaches in the near future.

2 Linking Computer Simulations to Disease

The key challenge for computer simulations to be of relevance for molecular medicine is to establish a clear link between the insight gained at the atomic scale and a given disease. This aspect is explored from three directions, (i) the value of static, three-dimensional molecular models, (ii) adding dynamic information to such models, and (iii) considering the bigger picture of molecular mechanisms underpinning disease. All modeling studies rely on a set of methods and tools to run, inspect and interpret them. We conclude with a perspective on current trends to improve and

extend the portfolio of tools, with the potential to provide important breakthroughs in the future.

2.1 Learning from Molecular Models

How to build molecular models. In the simplest case, a disease may be directly linked to a specific single-point mutation of a key molecule, the understanding of which may provide important clues for therapies. Hence, building a 3-dimensional all-atom model is a fundamental step on the way to better treatment. When the crystal or NMR structure of the key molecule is known, model building follows a standard procedure. Typical approaches and setups are described in [2, 3], highlighting specific issues that may arise with membrane proteins. In a typical setup, it is required to choose among potential alternative conformations, correct for mutations that may have been required to achieve crystallization, and possibly predict the protonation states of ionizable amino acids including His, Asp, Glu, Arg and Lys residues. A relation to diseases may be established by analyzing the 3D positions of mutations and their molecular

environment. This is the case for the low density lipoprotein receptor [4], contributing to cholesterol cleansing in the blood. We analyzed four point mutation sites involved in familiar hypercholesterolemia, the main risk factor in atherosclerosis, and understood their molecular origin through visual inspection revealing an influence of nearby calcium ions, disulfide bridges, electrostatic and steric effects as illustrated in Fig. 2.

The effects of the four point mutations we studied were interpreted as follows. **C113R** is involved in a stabilizing disulfide bridge (Fig. 2a) which will be lost upon mutation. The positively charged Arg-mutant will furthermore repel the nearby calcium ion. The **G266C** residue shown in Fig. 2b sits between two close and several more distant disulfide bridges. The cysteine mutant might lead to the formation of alternative disulfide bridges. Its negative charge might lead to a change in coordination of the nearby calcium. **P664L** is in contact with a beta-sheet and part of a loop (Fig. 2c). The Leu mutant is bulkier and no kink is induced. **C690S** is involved in a disulfide bridge (Fig. 2d) which seems essential to maintain the local geometry.

Modeling without a crystal structure. The most common case is that the precise structure of the molecule of interest is unknown. In the absence of any structurally exploitable data (e.g. indirect experimental measurements), homology modeling is a common choice. We employed such an approach to model a full-length Fzo1 mitofusin, involved in membrane fusion, a fundamental mechanism which remains unclear [5]. Mutations in the related human mitofusin MFN2 cause Charcot–Marie–Tooth disease type 2a [6], which is characterized by degeneration of long peripheral nerves. Furthermore, mitofusins can be linked to the etiology of Parkinson disease [7]. The predicted architecture of our

model improves upon the current domain annotation, with a precise description of the helical spans linked by flexible hinges, and provided indications for several interesting mutations that were carried out and tested experimentally.

A slightly different situation is observed when experimental data is available to guide the modeling process. For example, the molecular knowledge of dystrophin, a protein mutated in myopathy patients, remains limited, yet it is amenable to Small-angle X-ray Scattering (SAXS) investigations. We designed an original interactive docking method to model full-length dystrophin based on its fragments, integrating qualitative experimental data restraints [8]. This model allowed us to show that the central dystrophin domain is a tortuous and complex filament, profoundly disorganized by the most severe Becker muscular dystrophy deletions. The structural description gained through our model represents a first necessary step to improve the design of microdystrophin constructs in the goal of a successful gene therapy for the severe Duchenne muscular dystrophy [9].

2.2 Adding Dynamics and Linking to Function

So far, we mostly considered static three-dimensional models, yet, dynamics is a key factor in biological systems and processes. Typical simulation setups are described in the literature [3, 10]. An interesting and straightforward application example are pharmacological chaperones (PC) used for the treatment of Fabry disease [11, 12]. Fabry disease is a rare pathology caused by mutations of lysosomal alpha-galactosidase. About 40% of all the disease missense mutations occur at flexible sites of the protein [13], destabilizing it and leading to clearance by the quality control system of the cell. An oral PC therapy uses

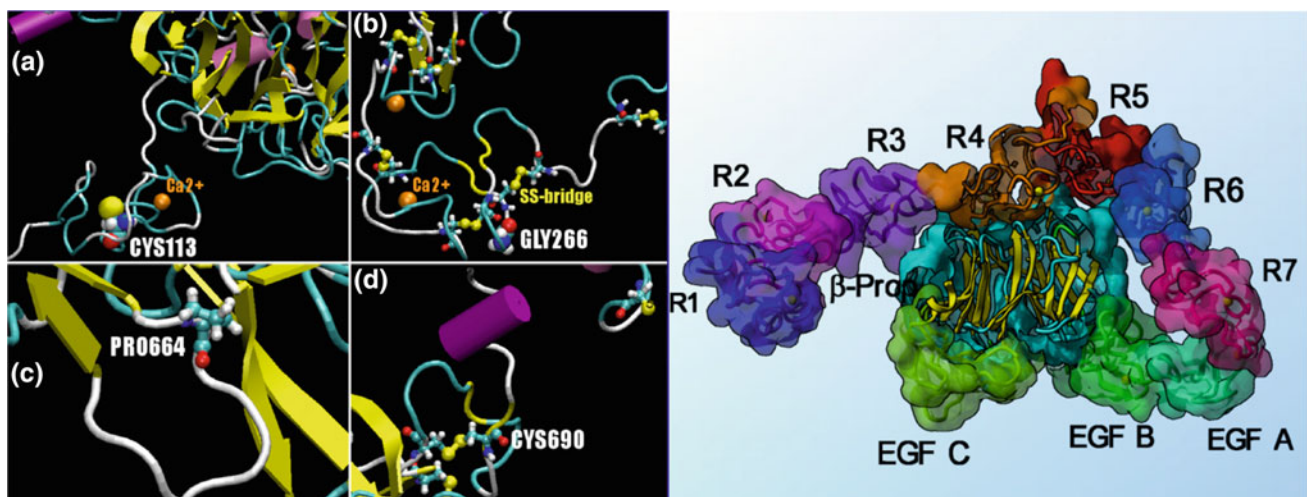


Fig. 2 Closeup of the low density lipoprotein receptor (LDLR) mutation sites and nearby points of interest are shown on the left panel and labelled a to d. The right panel shows the extracellular domain of LDLR at pH5 where these mutations are located

1-deoxygalactonojirimycin that reversibly binds to the active site of the enzyme and stabilizes it. We demonstrated the effectiveness of molecular dynamics (MD) simulations to correlate the genotype to the severity of the disease. More generally, destabilizing mutations are widely encountered in other proteins, hence MD may be useful for diagnostic purposes in other human diseases.

2.3 Moving Towards Mechanisms

Previous examples focused on simple relationships between molecular models, static or dynamic, and disease conditions. For many diseases the situation is more intricate, requiring to understand entire complex molecular mechanisms leading to disease. The modeling task may involve multi-step molecular processes with several actors in complex environments such as the membrane. General anesthesia (GA) is such an example. Although GA is not a disease, a better understanding of its mechanism is of medical relevance as it would enable us to design better compounds and more efficient palliative treatments. The mechanism of action remains a matter of controversy. One proposed mode of action involves binding of anesthetic molecules to ligand gated ion channels, modulating their function. We explored this mode at the molecular level by studying the membrane-inserted pentameric ligand-gated ion channel GLIC for which many anesthetic binding sites were characterized. By performing MD simulations to gain key insights on binding location and affinity, in particular microsecond-long flooding simulations, combined with free energy calculations, we characterized access to binding sites and quantified binding affinities. This study revealed a complex network of interconnected binding sites, possibly all contributing in concert to the anesthetic effect [14].

Another fundamental mechanism of medical importance is aggregation, leading to proteinopathies and neurodegenerative disorders. Modeling approaches have been widely used to study Alzheimer's, as reviewed in [15, 16]. In particular multi-scale and multi-physics simulations may be required to address the sampling and time-scale challenges imposed by the underlying processes [17], with some involved molecules being possibly intrinsically disordered.

2.4 Towards New and Improved Tools

All studies described in this article require adequate modeling tools. Continuous improvement of algorithms, hardware and technology lead to new approaches to be explored. Key trends and upcoming new tools in computational biology may involve for instance interactive model building and simulation as a very promising approach, in particular when

the methods are rendered robust enough such that non-specialists can use them. In the current era of integrative modeling, much is yet to come in terms of combining experimental data with modeling approaches. Another development is next-level computational power, increasingly exploited through GPU computing, and soon to be boosted by exa-scale high performance computing. These developments lead to a much increased amount of data to interpret, and hence advanced analysis tools are the next big challenge. Interactive approaches such as visual analytics help the rationalization process, deep learning approaches may uncover complex relationships in the data. Closely related are advanced visualization techniques, in particular immersive ones such as virtual reality and augmented reality. They allow us to scrutinize complex three-dimensional datasets in a natural and intuitive way.

3 Conclusion

Computational modeling approaches bear great promise for understanding disease conditions and to design improved and novel therapies. A few examples on how to establish a link between the atomistic modeling scale and the medical implications were discussed. Two strategies for treatments can be envisaged. In the symptomatic approach, a better understanding of the function and pharmacology of macromolecular key players is targeted. For curative approaches, a deeper understanding of disease-inducing molecular processes is required such that e.g. molecular inhibitors for critical steps can be designed. With the current developments in terms of computational power, intuitive, immersive and interactive analysis and manipulation methods, much progress is yet to be expected in the near future.

Acknowledgements This work was supported by the Fondation pour la Recherche Médicale, grant number FRM DBI20141231801, the Air Liquide, Servier and UCB Biopharma companies, and the "Initiative d'Excellence" program from the French State (Grants "DYNAMO", ANR-11-LABX-0011-01 and ANR-11-EQPX-0008).

Conflict of Interest The author declares that he has no conflict of interest.

References

1. Sinha, D.K., Neveu, P., Gagey, N., Aujard, I., Benbrahim-Bouzidi, C., Le Saux, T., Rampon, C., Gauron, C., Goetz, B., Dubruille, S., Baaden, M., Volovitch, M., Bensimon, D., Vrız, S., Jullien, L.: Photocontrol of protein activity in cultured cells and zebrafish with one- and two-photon illumination. *ChemBioChem* **11**(5), 653–663 (2010). <https://doi.org/10.1002/cbic.201000008>
2. Hénin, J., Baaden, M., Taly, A.: Foundations of biomolecular simulations: a critical introduction to homology modeling,

- molecular dynamics simulations, and free energy calculations of membrane proteins. In: *Membrane Proteins Production for Structural Analysis*. Springer, New York (2014)
- Murail, S.: Simulation of ligand binding to membrane proteins. In: *Membrane Protein Structure and Function Characterization. Methods in Molecular Biology*, vol. 1635, pp. 359–381. Humana Press, New York (2017)
 - El Messal, M., Ait Chihab, K., Chater, R., Vallve, J.C., Bennis, F., Hafidi, A., Ribalta, J., Varret, M., Loutfi, M., Rabes, J.P., Kettani, A., Boileau, C., Masana, L., Adlouni, A.: Familial hypercholesterolemia in Morocco: first report of mutations in the LDL receptor gene. *J. Hum. Genet.* **48**(4), 199–203 (2003). <https://doi.org/10.1007/s10038-003-0010-x>
 - De Vecchis, D., Cavellini, L., Baaden, M., Henin, J., Cohen, M.M., Taly, A.: A membrane-inserted structural model of the yeast mitofusin Fzo1. *Sci. Rep.* **7**(1), 10217 (2017). <https://doi.org/10.1038/s41598-017-10687-2>
 - Zuchner, S., Mersiyanova, I.V., Muglia, M., Bissar-Tadmouri, N., Rochelle, J., Dadali, E.L., Zappia, M., Nelis, E., Patitucci, A., Senderek, J., Parman, Y., Evgrafov, O., Jonghe, P.D., Takahashi, Y., Tsuji, S., Pericak-Vance, M.A., Quattrone, A., Battaloglu, E., Polyakov, A.V., Timmerman, V., Schroder, J.M., Vance, J.M.: Mutations in the mitochondrial GTPase mitofusin 2 cause Charcot-Marie-Tooth neuropathy type 2A. *Nat. Genet.* **36**(5), 449–451 (2004). <https://doi.org/10.1038/ng1341>
 - Chen, Y., Dorn 2nd, G.W.: PINK1-phosphorylated mitofusin 2 is a Parkin receptor for culling damaged mitochondria. *Science* **340** (6131), 471–475 (2013). <https://doi.org/10.1126/science.1231031>
 - Molza, A.E., Ferey, N., Czjzek, M., Le Rumeur, E., Hubert, J.F., Tek, A., Laurent, B., Baaden, M., Delalande, O.: Innovative interactive flexible docking method for multi-scale reconstruction elucidates dystrophin molecular assembly. *Faraday Discuss.* **169**, 45–62 (2014). <https://doi.org/10.1039/c3fd00134b>
 - Delalande, O., Molza, A.E., Dos Santos-Morais, R., Cheron, A., Pollet, E., Raguene-Nicol, C., Tascon, C., Giudice, E., Guilbaud, M., Nicolas, A., Bondon, A., Leturcq, F., Ferey, N., Baaden, M., Perez, J., Roblin, P., Pietri-Rouxel, F., Hubert, J.F., Czjzek, M., Le Rumeur, E.: Dystrophin's central domain forms a complex filament that becomes disorganized by in-frame deletions. *J. Biol. Chem.* (2018). <https://doi.org/10.1074/jbc.m117.809798>
 - Laurent, B., Murail, S., Da Silva, F., Corringer, P.-J., Baaden, M.: Modeling complex biological systems: from solution chemistry to membranes and channels. *Pure Appl. Chem.* **85**(1) (2013)
 - Germain, D.P., Hughes, D.A., Nicholls, K., Bichet, D.G., Giugliani, R., Wilcox, W.R., Feliciani, C., Shankar, S.P., Ezgu, F., Amartino, H., Bratkovic, D., Feldt-Rasmussen, U., Nedd, K., Sharaf El Din, U., Lourenco, C.M., Banikazemi, M., Charrow, J., Dasouki, M., Finegold, D., Giraldo, P., Goker-Alpan, O., Longo, N., Scott, C.R., Torra, R., Tuffaha, A., Jovanovic, A., Waldek, S., Packman, S., Ludington, E., Viereck, C., Kirk, J., Yu, J., Benjamin, E.R., Johnson, F., Lockhart, D.J., Skuban, N., Castelli, J., Barth, J., Barlow, C., Schiffmann, R.: Treatment of Fabry's disease with the pharmacologic chaperone Migalastat. *N. Engl. J. Med.* **375**(6), 545–555 (2016). <https://doi.org/10.1056/nejmoa1510198>
 - Hughes, D.A., Nicholls, K., Shankar, S.P., Sunder-Plassmann, G., Koeller, D., Nedd, K., Vockley, G., Hamazaki, T., Lachmann, R., Ohashi, T., Olivotto, I., Sakai, N., Deegan, P., Dimmock, D., Eyskens, F., Germain, D.P., Goker-Alpan, O., Hachulla, E., Jovanovic, A., Lourenco, C.M., Narita, I., Thomas, M., Wilcox, W.R., Bichet, D.G., Schiffmann, R., Ludington, E., Viereck, C., Kirk, J., Yu, J., Johnson, F., Boudes, P., Benjamin, E.R., Lockhart, D.J., Barlow, C., Skuban, N., Castelli, J.P., Barth, J., Feldt-Rasmussen, U.: Oral pharmacological chaperone migalastat compared with enzyme replacement therapy in Fabry disease: 18-month results from the randomised phase III ATTRACT study. *J. Med. Genet.* **54**(4), 288–296 (2017). <https://doi.org/10.1136/jmedgenet-2016-104178>
 - Cubellis, M.V., Baaden, M., Andreotti, G.: Taming molecular flexibility to tackle rare diseases. *Biochimie* **113**, 54–58 (2015). <https://doi.org/10.1016/j.biochi.2015.03.018>
 - Laurent, B., Murail, S., Shahsavari, A., Sauguet, L., Delarue, M., Baaden, M.: Sites of anesthetic inhibitory action on a cationic ligand-gated ion channel. *Structure* **24**(4), 595–605 (2016). <https://doi.org/10.1016/j.str.2016.02.014>
 - Nguyen, P., Derreumaux, P.: Understanding amyloid fibril nucleation and abeta oligomer/drug interactions from computer simulations. *Acc. Chem. Res.* **47**(2), 603–611 (2014). <https://doi.org/10.1021/ar4002075>
 - Nasica-Labouze, J., Nguyen, P.H., Sterpone, F., Berthoumieu, O., Buchete, N.V., Cote, S., De Simone, A., Doig, A.J., Faller, P., Garcia, A., Laio, A., Li, M.S., Melchionna, S., Mousseau, N., Mu, Y., Paravastu, A., Pasquali, S., Rosenman, D.J., Strodel, B., Tarus, B., Viles, J.H., Zhang, T., Wang, C., Derreumaux, P.: Amyloid beta protein and Alzheimer's disease: when computer simulations complement experimental studies. *Chem. Rev.* **115**(9), 3518–3563 (2015). <https://doi.org/10.1021/cr500638n>
 - Sterpone, F., Doutreligne, S., Tran, T.T., Melchionna, S., Baaden, M., Nguyen, P.H., Derreumaux, P.: Multi-scale simulations of biological systems using the OPEP coarse-grained model. *Biochem. Biophys. Res. Commun.* **498**(2), 296–304 (2018). <https://doi.org/10.1016/j.bbrc.2017.08.165>

Part VII

Regenerative Medicine and Tissue Engineering

Optimization of High Resolution Melting (HRM) Method for Genotyping and Estimating Frequency of SNP rs4284505 in the Vietnamese Breast Cancer

Hoang Mai Le Nguyen, Thi Nga Nguyen, Dien Thanh Giang Nguyen, Thi Ngoc Thanh Nguyen, and Thi Hue Nguyen

Abstract

Breast cancer is one of the most common and dangerous disease among women throughout the world whose incidence continues to increase rapidly, particularly in several Asian countries. Among well-known causative breast cancer genes like: BRCA1/2, PTEN, p53..., microRNAs (miRNAs), recently, have been proven to play a critical role in breast cancer development and can serve as a new potential biomarker for breast cancer detection. SNP rs4284505 located on miRNA 17–92 cluster host gene exhibits the strong association with breast cancer in Caucasian Australian. In this study, SNP rs4284505 is investigated to determine whether it can relate to breast cancer in Vietnamese patients. High Resolution Melting (HRM) method has been optimized to screen selected SNP, aiming at predicting the correlation of the chosen SNP and breast cancer in Vietnam. 100 breast cancer samples were examined. The optimal HRM protocol was constructed with high sensitivity (95%), specificity and stability. The polymorphism of SNP rs4284505 does occur in Vietnamese population with the MAF (G) = 44.27%. The G allele seems likely to have the protective effect to breast cancer [OR (95% CI) = 0.80 (0.54–1.18)]. Nevertheless, this SNP is predicted not to be associated with breast cancer risk (p -value >0.05) due to small size and the computed control. Because of high polymorphism in patients, a further research should be conducted in a larger scale and in a suitable control group to validate the relationship between SNP rs4284505 and breast cancer in Vietnam.

Keywords

Breast cancer • SNP rs4284505 • High resolution melting (HRM)

1 Introduction

Breast Cancer (BC) has been becoming the common disease and ranked the most popular leading cause of cancer death in women throughout the world [1]. According to GLOBOCAN 2012 in Vietnam, breast cancer became the first leading cause of cancer death which accounted up to 20.3% in the total of 54,476 cases at all ages. Hence, there is an urgent need in developing a low cost, high sensitivity, specificity, and simplicity method which is suitable for Vietnam.

To develop breast cancer prognosis methods, we need to understand deeply two main causes affecting them including the extrinsic factors mostly from unhealthy life style, and intrinsic factors which are: menopause state, family history, or genetic disorders [2]. A research conducted in 2006 reported that germ-line mutations in well-identified breast cancer susceptibility genes cause 5–10% of all breast cancers [3]. Therefore, these genes can be served as the potential biomarkers for early prognosis.

In recent studies, microRNAs (miRNAs) have been proved to play a critical role and can become new potential biomarkers for breast cancer detection. Many Genome-Wide Association Studies have found numerous Single Nucleotide Polymorphisms (SNPs) which are located on miRNA and correlate with various human cancers with the function as tumor suppressors or oncogenes [4]. Among them, SNP rs4284505 was confirmed to have strong association with breast cancer in individuals of Caucasian Australians [5]. This SNP's position is in the upstream region of miRNA 17–92 cluster regulating the expression of important genes which related to breast cancer development such as: Cyclin D1 (CCND1) [6], Estrogen Receptor α (ESR1) [7],

H. M. L. Nguyen (✉) · D. T. G. Nguyen
School of Biotechnology, International University, Vietnam
National University HCMC, Ho Chi Minh City, Vietnam
e-mail: maile.nguyenhoang.0803@gmail.com

T. N. Nguyen · T. N. T. Nguyen · T. H. Nguyen
Faculty of Biology-Biotechnology, University of Science,
Vietnam National University, Ho Chi Minh City, Vietnam
e-mail: nthue@hcmus.edu.vn

Amplified In Breast Cancer 1 (AIB1) [8] proteins. Therefore, SNP rs4284505 is selected as a promising candidate for investigation of the association with the risk of breast cancer in Vietnamese.

HRM is a sensitive technique for detection of single base change between otherwise identical nucleotide sequences based on difference in melting characteristic of variants [9]. Due to the benefits of time saving, low cost, and highly sensitive, this method becomes increasingly popular and innovative one. Hence, this study was conducted to optimize the HRM condition which is suitable for genotyping the selected SNP and to predict the association between SNP rs4284505 and breast cancer status in Vietnamese.

2 Material and Method

2.1 Subjects

100 whole blood samples were collected from breast cancer patients (40–67 years old) who were confirmed to have tumors in their breast at Oncology Hospital, Binh Thanh District, Ho Chi Minh City. DNA from blood samples was extracted by Salting-out method followed protocol of Hue et al. [10].

2.2 Development HRM Method

In Silico Design The sequence of SNP rs4284505 was identified using Gene Bank database. Primers for HRM Analysis was designed by Primer3plus, NCBI Blast, UCSC In silico PCR, Oligo Analyzer, and Umelt Hets.

HRM Optimization The annealing temperature (T_a) optimization was performed in range 59–69 °C by thermal cycle PCR Eppendorf instrument and HotStarTaq DNA polymerase, Qiagen. Components for 10 μ L PCR reaction included: 1X PCR buffer, 0.2 μ M dNTP, 0.2 μ M per each primer (forward and reverse), 0.05 units HotStarTaq, 20 ng DNA and H₂O.

The three control samples were identified based on the displayed different melting curve patterns thanks to SYBR family dye and confirmed by sequencing (ABI3130).

Further optimization by adjusting the [MgCl₂] was conducted at 1.5, 2.0, and 2.5 mM MgCl₂ to achieve the best discrimination between three identified controls.

HRM Method Validation The evaluation is examined through three parameters: sensitivity, specificity, and stability.

2.3 Genotyping and Association Prediction

The optimal condition for HRM was applied to genotype 100 cases. The results were analyzed using LightCycler[®] 96 SW 1.1 software.

Then, three main genetic and an allelic model were used to determine the association between SNP rs4284505 and breast cancer in Vietnamese population. These tests were analyzed by R software version 3.4.2.

3 Result

3.1 Development of HRM Method

A primer set has been selected (Table 1) which is suitable for amplifying the amplicon containing the selected SNP and also gave three distinguished melting curves for three genotypes of rs4284505 (Fig. 1).

HRM Optimization

After running conventional PCR to figure out the best T_a , the result was analyzed by gel electrophoresis. From Fig. 2, 67 °C can be served as the optimal temperature for annealing because this band is the brightest and sharpest.

Since T_a was determined, seven random samples were chosen to run HRM assay, under the condition of 3.0 mM MgCl₂ and T_a = 67 °C. Three controls were identified and confirmed by sequencing (Fig. 3).

After identifying, these controls were used as template for adjusting the [MgCl₂] to obtain the best HRM optimization. With the [Mg²⁺] = 1.5 mM, the ΔT_m between two homozygous equaled 0.11 °C and three standard curves group together (Fig. 4a1). For the [Mg²⁺] = 2.0 and 2.5 mM, three different genotypes were grouped into three

Table 1 Primer sets for HRM

Primer	Sequence (5' → 3')	T _m
HRM-F	TCCTGCCCGGTCTCTGTTCCCT	65.4
HRM-R	GCAACGACGAGCCTGCCTTTT	64.7

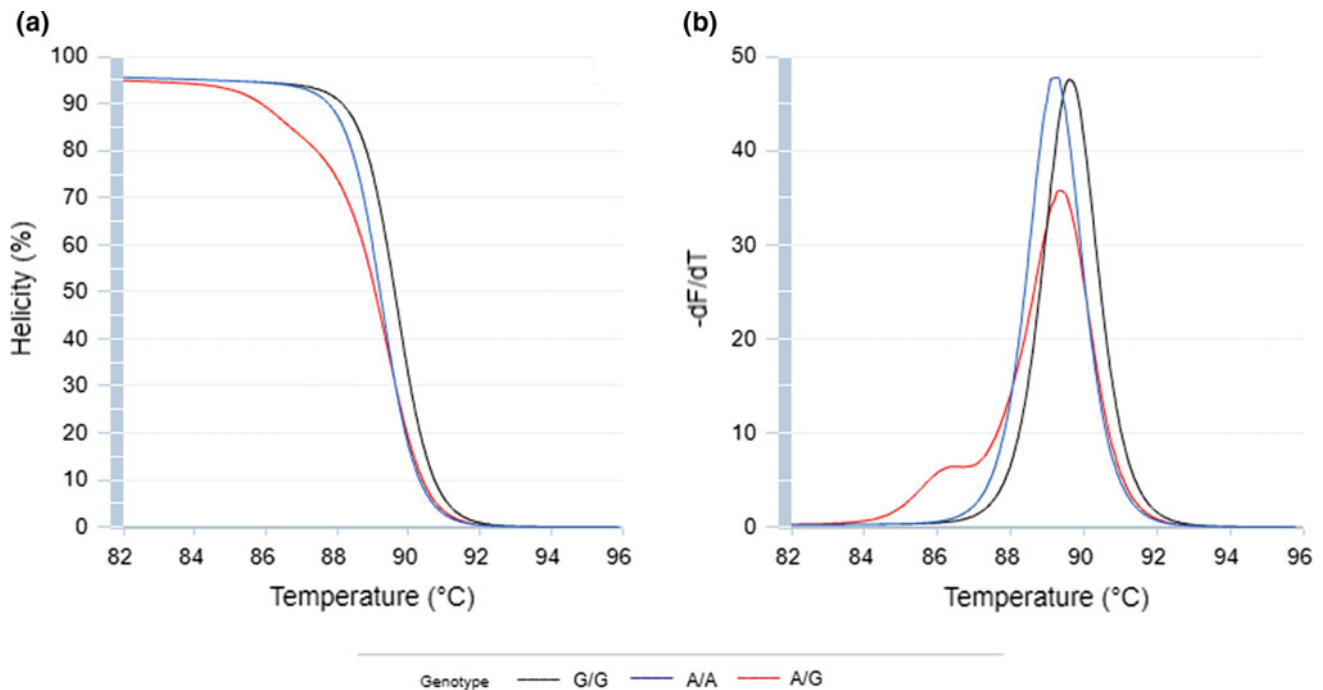


Fig. 1 The predicted melting curves (a) and melting peaks (b) of rs4284505 on Umelt Hets at $[Mg^{2+}] = 3.0$ mM

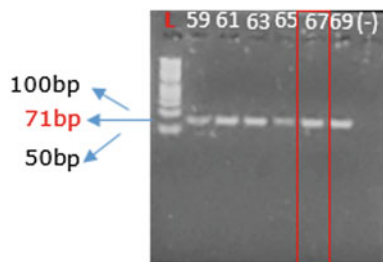


Fig. 2 Annealing temperature for HRM primer set

distinct curves (Fig. 4b2; b3) and ΔT_m was >0.4 °C which was acceptable. Hence, $[Mg^{2+}] = 2.0$ and 2.5 mM were run for clearer observation in the bigger scale.

Of $[Mg^{2+}] = 2.0$ mM, all samples were clustered clearly into three groups (Fig. 5a1). From Fig. 5b1, the blue curve was sharper and smoother compared to that at 2.5 mM Mg^{2+} (Fig. 5b2). About $[Mg^{2+}] = 2.5$ mM, all samples were not well clustered in Fig. 5a2. There seemed to be a small peak appeared in both blue and red curve when T_m was in range of 82 – 84 °C (Fig. 5b2). Thus, $[MgCl_2] = 2.0$ mM was selected as the optimal condition in this HRM performance.

Validation of HRM Method

Sensitivity: 5/100 samples did not show the amplification. Hence, the method's sensitivity was 95%.

Specificity: The T_m of the three genotypes expressed a significant difference (p -value <0.001) in either control samples (Table 2) or tested samples (Table 3).

Stability

Each genotype can be distinct from others via T_m , which were seen in the positive control (Table 4) and the tested samples (Table 5), except the heterozygote in tested samples. However, the heterozygote, with two-peaks unique pattern compared to the other two homozygotes, is easily identified without mistake.

A. Genotyping and Association prediction

100 samples of Breast Cancer patients were genotyping by the optimal HRM assay above. The typical result based on three types of curves was illustrated in Fig. 6.

Table 6 presented the frequencies of each genotype as well as each allele. The HWE was adequate for genotyping results. The frequencies of the three genotypes of SNP rs4284505: AA, AG, and GG were 32.29, 46.88 and 20.83% in 100 cases and 24.75, 50.50, and 24.75% in controls (1000 Genome), respectively.

The association analysis in neither allelic nor genotypic model did not show the significant difference in the frequencies of alleles or genotypes between cases and controls

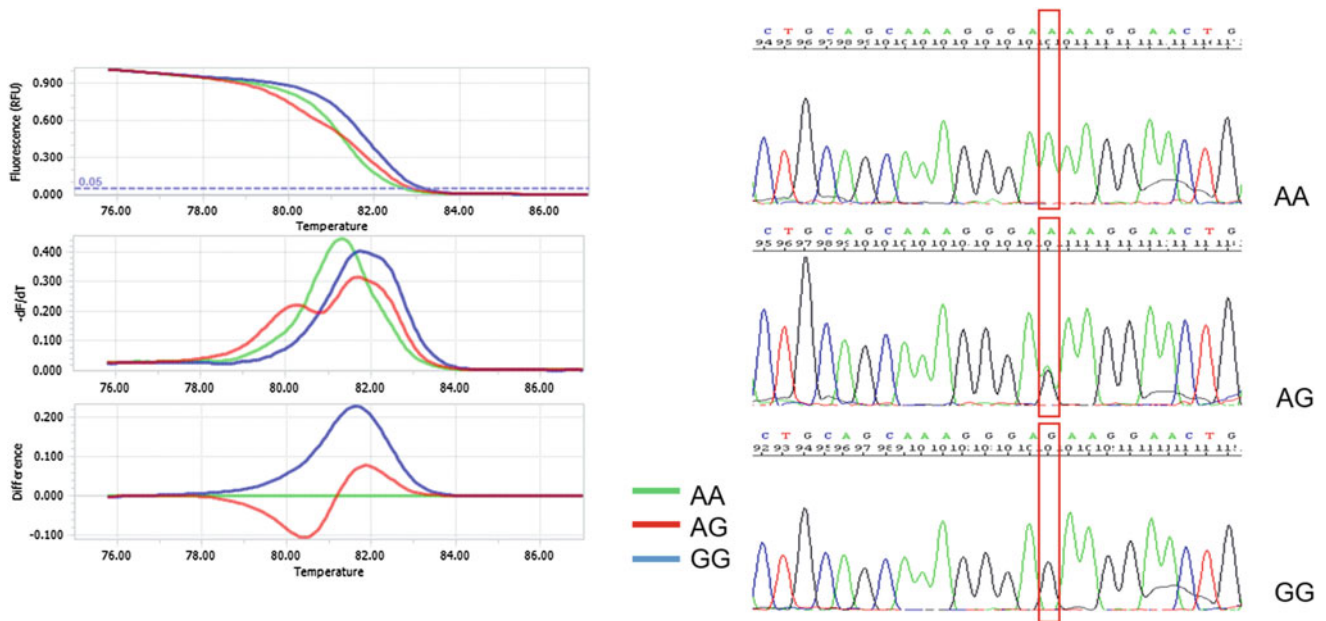


Fig. 3 Identifying control samples by sequencing

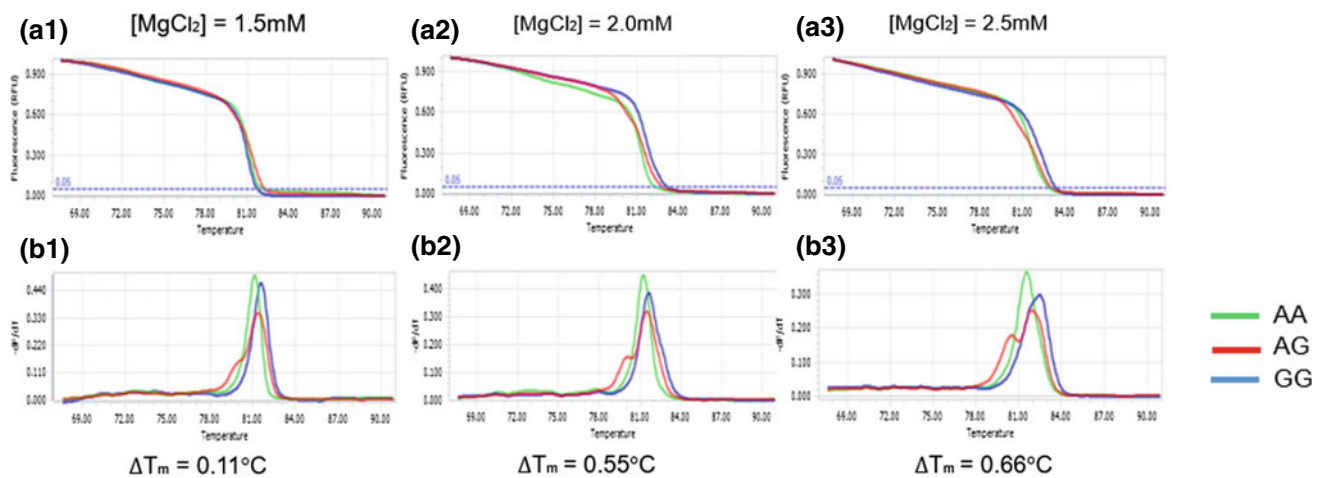


Fig. 4 The three tested $MgCl_2$ concentration. Note a1, a2, and a3: Normalized melting curve; b1, b2, and b3: Normalized melting peak

(p -value >0.05) (Table 7). However, the G allele may show as a protective function (OR [95%CI] = 0.8 [0.54–1.18]).

4 Discussion

With the successful in developing HRM method, SNP rs4284505 has been screened in the Vietnamese breast cancer patients with the Minor Allele Frequency (MAF) G is 44.27%. This frequency was also high in Kinh healthy control 50% (compute from 1000 Genome). This indicated the highly polymorphism of the SNP rs4284505 in Vietnamese population. Comparing to Caucasian Australian [5],

the MAF (A) in Genomic Research Center Breast Cancer (GRC-BC), and Griffith University-Cancer Councils Queensland Breast Cancer Biobank (GU-CCQ BB) patients equals 38.3, and 35.9%, respectively while this frequency is 46.9, and 41.2% in GRC-BC, and GU-CCQ BB control (Table 8).

The association prediction conducted in this study did not reveal the SNP rs4284505 is a good candidate for association. However, due to the computed data and the small sample size that make the result of analysis is not strongly reliable. With OR (95% CI) = 0.80 (0.54–1.18), p -value = 0.2596, this result pointed out that the existence of G allele might reduce the breast cancer risk up to 0.80 times compared to A

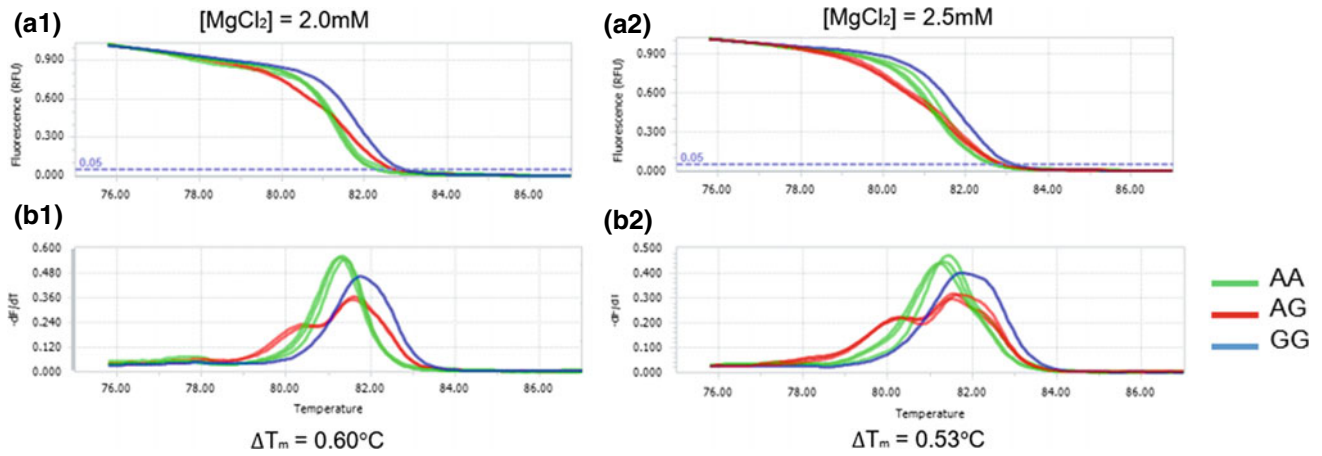


Fig. 5 Eight testing samples for [Mg²⁺] = 2.0, and 2.5 mM. *Note* a1, a2: Normalized melting curve; b1, b2: Normalized melting peak

Table 2 The melting temperature specificity in positive controls

Genotype	Positive controls		<i>p</i> -value (ANOVA test)
	No. test	$\bar{T}_m \pm SD$ (°C)	
AA	6	81.09 ± 0.10	<0.001
AG	6	81.11 ± 0.16	
GG	6	81.60 ± 0.11	

Table 3 The specificity of melting temperature in tested samples

Genotype	Tested samples		<i>p</i> -value (ANOVA test)
	No. test	$\bar{T}_m \pm SD$ (°C)	
AA	30	81.14 ± 0.15	<0.001
AG	43	81.26 ± 0.18	
GG	19	81.56 ± 0.12	

Table 4 The stability of positive controls

Genotype	Positive controls		<i>p</i> -value (t test)
	No. test	$\bar{T}_m \pm SD$ (°C)	
AA	6	81.09 ± 0.10	1.00
AG	6	81.11 ± 0.16	1.00
GG	6	81.60 ± 0.11	1.00

Table 5 The stability of tested samples

Genotype	Tested samples		<i>p</i> -value (t test)
	No. test	$\bar{T}_m \pm SD$ (°C)	
AA	30	81.14 ± 0.15	0.09
AG	43	81.26 ± 0.18	2.44 × 10 ⁻⁶
GG	19	81.56 ± 0.12	0.16

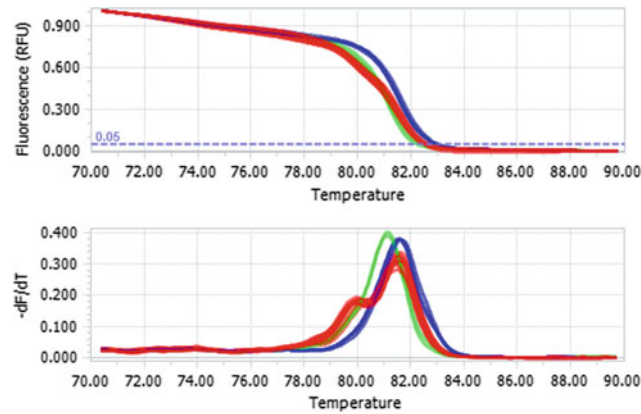


Fig. 6 The melting curves and melting peaks analysis of rs4284505 by HRM showed 3 different genotypes. The green, blue and red curve presented AA, GG and AG genotype, respectively

Table 6 Genotyping of rs4284505 in Vietnamese population

Sample	Genotype			Allele		<i>p</i> -value (HWE)
	AA	AG	GG	A	G	
Case	31	44	20	107	85	0.68
	32.29%	46.88%	20.83%	55.73%	44.27%	
Control (1000 Genome)	25	51	25	101	101	1.00
	24.75%	50.50%	24.75%	50%	50%	

Table 7 Allelic and genotypic association analysis

Analysis model		OR	95% CI	<i>p</i> -value
Allele	G versus A	0.80	0.54–1.18	0.2596
Addictive	GG versus AA	0.65	0.29–1.42	0.4845
	AG versus AA	0.71	0.37–1.38	
Dominance	[GG+AG] versus AA	0.69	0.37–1.29	0.2407
Recessive	GG versus [AG+AA]	0.80	0.41–1.56	0.5121

Table 8 Frequency of rs4284505 in Australian population [5]

Population		Allele		<i>p</i> -value
		A (%)	G (%)	
GRC-BC population	Control	46.9	53.1	0.01
	Cases	38.3	61.7	
GU-CCQ BB population	Control	41.2	58.8	0.03
	Cases	35.9	61.4	

allele. However, all genetic models exhibited the high *p*-value (>0.05) indicated no significant differences between distinct genotypes or alleles on incident rate in Vietnamese patients. According to Chacon-Cortes et al. [5], SNP rs4284505 was proved to have a strong association to breast cancer at the allelic level in two Caucasian-Australian study

cohorts (GRC-BC *p* = 0.01 and GC-CCQ BB *p* = 0.03) and the presence of A allele seems to have the protective effect on susceptibility to breast cancer. There is a conflict in the function of the G allele in Vietnamese and Australian.

Main reasons for difference between Australian Caucasian and Vietnamese might be come from the sample size

of the research and the gene pool. In Australian, they studied in total of 431 individuals (in GRC-BC) and 679 samples (in GU-CCQ BC) while there were only 100 breast cancer patients that had been collected and identified in this study. Another factor that impact to the contrast can be explained by the distinct in genetic variants. Two countries are separated by the huge geographic distance so that, there is no close-relationship among these populations and SNP may be evolved in different way under the natural selection. Therefore, sample size and genetic information can be considered as the most important parameters to evaluate the association of SNP with breast cancer in case/control studies in specific population. Thus, based on high polymorphism, SNP rs4284505 is needed to be continued study in a bigger sample size and suitable control group to confirm the type of association between its alleles and the breast cancer risk.

5 Conclusion and Suggestions

This study has been success in developing the HRM method for genotyping SNP rs4284505. This is the first study investigating SNP rs4284505 in Vietnamese breast cancer patients. Nevertheless, due to the high polymorphism with MAF (G) = 44.27% in case population, our finding requires further validation in suitable control group, larger scales or different ethnicities to obtain the clearer association between SNP and breast cancer.

Acknowledgements We are appreciated all physicians and staffs of Oncology Hospital of Ho Chi Minh City, Vietnam for providing blood samples. This research is funded by NAFOSTED under grant code 106-YS.01-2013.09.

Conflict of Interest Statement We declare that there is no conflict of interest in this study.

References

1. Maxmen, A.: The hard facts. *Nature* **485**(7400), S50 (2012)
2. McCormack, V.A., Boffetta, P.: Today's lifestyles, tomorrow's cancers: trends in lifestyle risk factors for cancer in low- and middle-income countries. *Ann. Oncol.* **22**, 2349–2357 (2011)
3. Oldenburg, R.e.a.: Genetic susceptibility for breast cancer: how many more genes to be found? *Crit. Rev. Oncol./Hematol.* **63**(2), 125–149 (2007)
4. Esquela-Kerscher, A., Slack, F.J.: Oncomirs—microRNAs with a role in cancer. *Nat. Rev. Cancer* **6**(4), 259 (2006)
5. Chacon-Cortes, D., et al.: Association of microRNA 17–92 cluster host gene (MIR17HG) polymorphisms with breast cancer. *Tumor Biol.* **36**(7), 5369–5376 (2015)
6. Yu, Z., Wang, C., Wang, M., Li, Z., Casimiro, M.C., Liu, M., Wu, K., Whittle, J., Ju, X., Hyslop, T., McCue, P., Pestell, R.G.: A cyclin D1/microRNA 17/20 regulatory feedback loop in control of breast cancer cell proliferation. *Cell Biol.* **182**, 509–517 (2008)
7. Leivonen, S.-K., Makela, R., Ostling, P., Kohonen, P., Haapa-Paananen, S., Kleivi, K., Enerly, E., Aakula, A., Hellstrom, K., Sahlberg, N., Kristensen, V.N., Borresen-Dale, A.-L., Saviranta, P., Perala, M., Kallioniemi, O.: Protein lysate microarray analysis to identify microRNAs regulating estrogen receptor signaling in breast cancer cell lines. *Oncogene* **28**, 3926–3936 (2009)
8. Hossain, A., Kuo, M.T., Saunders, G.F.: Mir-17-5p regulates breast cancer cell proliferation by inhibiting translation of AIB1 mRNA. *Mol. Cell. Biol.* **26**(21), 8191–8201 (2006)
9. Reed, G.H., Kent, J.O., Wittwer, C.T.: High-resolution DNA melting analysis for simple and efficient molecular diagnostics. *Pharmacogenomics* **8**, 597–609 (2007)
10. Hue, N.T., et al.: Extraction of human genomic DNA from dried blood spots and hair roots. *Int. J. Biosci. Biochem. Bioinform.* **2** (1), 21 (2012)

Dental Implant or Dental Transplant: A Two Case Report

L. Truong, N. Doan, P. Reher, and Q. T. Duong

Abstract

Aim This report intends to illustrate the different outcomes between a dental implant and transplant. **Materials and methods** Our literature review showed 812 papers related to the use of concentrated growth factors (CGF) in implantology, but none of them report on the study of the application of CGF on dental implant and transplant. Therefore, this paper will be a two-case report instead of systematic review. The first case is the application of CGF on dental implant therapy on a thirty-year-old male. Case two is the application of CGF on a tooth transplant in a fifteen-year-old male patient. **Results and discussion** Case one—CGF has facilitated the osseointegration process effectively with no complications. Case two—Healing was uneventful, however, there was some evidence of root resorption. **Conclusion** CGF application in dental implant treatment appears to be more predictable compared to its application in transplants within the limits of this two-case report.

Keywords

Dental implant • Dental transplant • CGF

1 Introduction

Some studies show that the addition of growth factors in wound tissue effectively accelerate the growth of wound healing consequently increasing the success rate of bone grafting and implant therapy [1]. The process of bone healing is affected by several factors such as the size and type of defect as well as the ability to obtain primary stability [2]. Primary stability at implant placement is critical for successful osseointegration. To overcome vertical deficiencies and insufficient bone volume; autografts, allografts, xenografts, alloplastic grafts, or combinations of different graft materials have been used to accommodate dental implants. To date, there are limited studies indicating implant survival rate on bone formation using concentrated growth factors (CGF) alone [3]. Thus, clinicians can use a CGF barrier membrane to speed up soft tissue healing on top of mixing it with bone graft [3]. The barrier membrane is necessary to prevent ingrowths of soft tissue. Pain, inflammation and bleeding are reduced when CGF is applied to grafted areas [3].

Another technique used to replace missing teeth is with tooth transplants. Autogenous tooth transplantation (auto-transplants) allow primary wound healing, preservation of bone contours as well as faster repair or damaged tissue regeneration. It is the surgical movement of a vital or endodontically treated tooth from a donor site to another area in the mouth. Autotransplants are a viable option for tooth replacement for carefully selected patients, donor tooth and the recipient site. Ideally, candidates should be in good health and demonstrate adequate oral hygiene as well as follow post-operative directions properly. The recipient site preferably should have enough bone support with attached keratinized tissue. Most importantly, the patient's donor tooth needs to be extracted as atraumatic as possible with optimal results obtained when roots are one half to two thirds developed. Minimal time between transfer from donor to recipient site and no injury to the periodontal ligament assists in the success rate [4].

L. Truong (✉) · N. Doan · P. Reher
School of Dentistry and Oral Health, Griffith University,
Gold Coast, Australia
e-mail: lauratruong1996@gmail.com.au

N. Doan
e-mail: nvtdoan123@gmail.com

N. Doan · Q. T. Duong
The University of Queensland, Brisbane, Australia

N. Doan
Queensland University of Technology, Brisbane, Australia

There has been a recent spotlight placed on tissue engineering involving the use of stem cell therapy to repair or replace injured tissue [5]. In addition, there is no evidence to suggest biological concerns with the use of CGF as they are recruited and used from the blood of the same individual [1].

Regenerative processes can be affected by dead space formation, coagulum contraction, serum extrusion or microbial infections [2]. Nowadays, CGF is being explored for the prospect of its application in tissue regeneration [6]. CGF is a fibrin matrix rich in growth factors, which prevents the displacement of the bone graft particles during healing. CGF is the condensation from blood, therefore, it contains most of the growth factors available such as vascular endothelial growth factor (VEGF), platelet derived growth factor (PDGF), transforming growth factor (TGF), insulin like growth factor 1 (IGF 1) and epidermal growth factor (EGF) as well as stem cell progenitors such as CD34+ and CD45 [7]. The platelet gel helps accelerate the migration of fibroblasts and revascularization [8, 9]. They play a role in cell migration, cell proliferation and angiogenesis in tissue regeneration phase [10]. These factors that regulate complex processes during wound healing are primarily found in blood plasma and platelets.

Kim et al. [1] found that many parameters are involved in the use of growth factors to obtain the desired result in bone regeneration such as the concentrations of growth factors and the individual's state of health at the recipient site. They concluded that it accelerates bone regeneration thus reducing the time before the placement of implants [3]. In addition, Sohn, Moon [3] advised that when combined with guided bone regeneration (GBR) and guided tissue regeneration (GTR), CGF was more effective in bone formation. Hence, the objective of this paper is to document two clinical cases on a transplant and implant case as well as draw some conclusions/recommendations.

2 Materials and Methods

Griffith University has provided human ethics approval (Ref No: 2018/213). All patients were informed about the treatment, oral and written consent was obtained.

In this two-case report, the two patients were selected for from records of a private dental clinic. Patient details that were taken into consideration included medical history, demographic details and environmental factors. Case one—thirty-year-old male who underwent dental implant therapy with CGF. Case two—fifteen-year-old male who underwent tooth transplant with CGF.

CGF corpuscles were harvested as per procedure of [7]. Preparation of the CGF was performed within 30–60 min with the use of standard equipment. Using the patient's forearm, 40 mL of venous blood was obtained and divided

into 4 Vacutainer® (2 red and 2 white) 10 mL glasscoated test tubes. The red tube is internally coated with serum activator while the white tube has no adaptive coating. Hence, the red tube is used for making fibrin membrane and the white tube is used for making sticky bone. The tubes were then centrifuged with a CGF centrifuge (MEDIFU-GETM, Silfradentsrl, S. Sofia, Italy). It was programmed with the following speeds: 2700 rpm 2 min, 2400 rpm 4 min, 2700 rpm 4 min, and 3000 rpm 3 min. The blood sample is then represented by four layers, however, it was the buffy coat (second layer) consisting of large and dense polymerized fibrin block and the growth factor layer (third layer) including white cells and stem cells that made up the CGF. Isolated CGF was harvested through these layers after pouring off the top serum layer (Platelet Poor Plasma or PPP). The uppermost layer was represented by serum (blood plasma without fibrinogen and coagulation factors) and the lowest red layer was platelet-rich coagulation. Care was taken to continually agitate the samples as platelets would begin to settle to the bottom.

Following manufacturer protocols, the CGF was used to make sticky bone and fibrin membrane. Condensing the coagulum from the red tube constitute the fibrin membrane while the extract from the white tube is used for fabricating sticky bone. Sticky bone is a mixture of Geistlich Bio-Oss® (bovine demineralized freeze-dried bone) and Osteon (hydroxyapatite and calcium triphosphate, MIS 4Bone®).

Surgery was performed under local anesthesia using 4% Articaine with 1:100,000 epinephrine with a maxillary infiltration/block. Antibiotic prophylaxis is taken one day before the procedure: Augmentin Duo 500/125, Metronidazole 200 mg and Dexamethasone 20 mg (3 days). Standardized intraoral radiographs were taken (60 kV, 7 mA, and 0.25 s) of the grafted regions using Super-Bite™ Kerr X-ray holders. ASA laser was used to maximize the wound healing process using the setting recommended by the manufacturer for these surgical protocols. Hence, MLS® (Multiwave Locked System) impulse was used to radiate the sites for three minutes.

3 Results

3.1 Case One

The thirty-year old male was initially referred to an oral surgeon by a general practitioner for treatment of the upper left first premolar (tooth 24). The 24 suffered from trauma as a result from an assault in a mental institution. On examination, intraoral periapical radiograph and cone beam CT revealed the tooth had a vertical crack consequently leading to a poor prognosis. Due to the injury, the 24 warranted an extraction. It was noted that the adjacent tooth (25) was

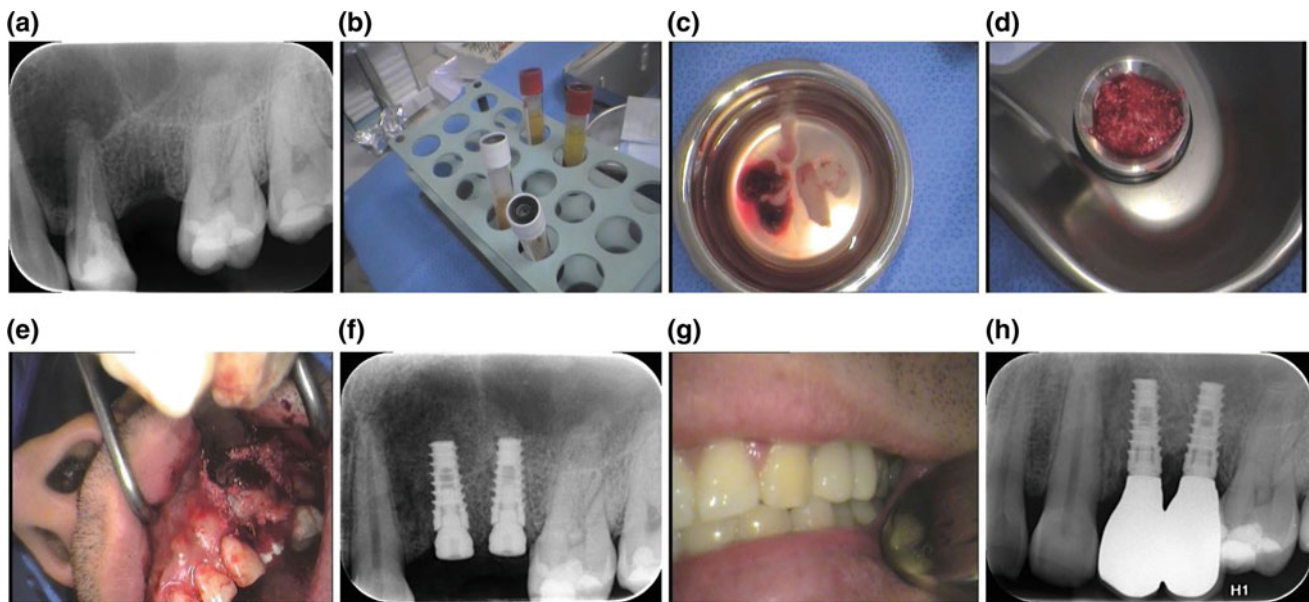


Fig. 1 CASE ONE **a** Pre-operative radiograph before extraction of the 24 with vertical root fracture. **b** CGF in the Vacutainer[®] glasscoated test tubes. **c** CGF fibrin membrane. **d** Sticky bone was formed by mixing CGF with bone graft material using Geistlich Bio-Oss[®] (bovine demineralized freeze-dried bone) and Osteon (hydroxyapatite and calcium triphosphate, MIS 4Bone[®]). **e** Placement of CGF sticky bone

and membrane after the placement of two implant fixtures. **f** Intraoral periapical radiograph of the two implant fixtures with healing abutments. **g** Clinical photo after final restoration with two-unit PFZ bridge. **h** Intraoral periapical radiograph of the two implant fixtures final restoration with two-unit PFM bridge

extracted more than two years ago. Bone resorption was detected in horizontal and vertical dimensions for both the 24 and 25. In addition, the root of the 24 extruded into the left maxillary sinus. As such, both teeth also had a minor soft tissue defect. The 24 was subsequently extracted and left to heal for ten weeks.

Thereafter, two screw type titanium implant fixtures were placed in the 24 and 25 regions in conjunction with GBR, GTR and CGF. Initial site stability of implants was achieved by a 1-step down undersized osteotomy and the placement of a self-tapering surface modified titanium alloy implant (Blue Sky Bio bone level internal hexagon) similar to that of Straumann SLA (sandblasted large grit and acid etched) implant. This technique was chosen due to the autologous nature of the procedure as described in the method. Throughout the procedure there was no evidence wound dehiscence or complications thus the result was very satisfactory. This was left in place for six months before the two implants were exposed for second stage surgery. This involved placing healing abutments. The wound was left for one month intended for soft tissue maturation prior to implant crown impression. After three weeks, two abutments in conjunction with a two-unit porcelain fused to Zirconia (PFZ) bridge was inserted in the implant fixtures.

The implant has been stable for a period of 6 months loading. CGF as an adjunct to bone grafting and simultaneous implantation is efficient and efficacious. Post

prostheses insertion X-rays showed successful new bone formation. During the period of post-implantation observation, there was no wound infection, or loss of any implant. The patient was very happy with the final outcome in terms of function, aesthetics and ease of cleaning (Fig. 1).

3.2 Case Two

The fifteen-year-old male patient had previous history of surgical removal of all upper right molars (teeth 16, 17 and 18) due to fibrosis. As a result of the surgery there was severe bone and soft tissue defects. Because of the patient age and financial reasons, implants were not a feasible treatment option at this stage. Due to the advancement of CGF technology, there was a glimpse of hope that tooth transplantation was possible at the 16 location using an extracted 28.

The 28 was extracted with minimal invasion using a surgical technique with a mucoperiosteal flap. To ensure there was no damage to the entire crown and pulp, the 16 transplant sites was prepared by means of trephination. The 28 was then implanted into the prepared site and covered with CGF sticky bone and fibrin membrane to complete the GTR and GBR technique. Post-operative instructions are to avoid mastication on the transplanted tooth and maintain a soft food diet.

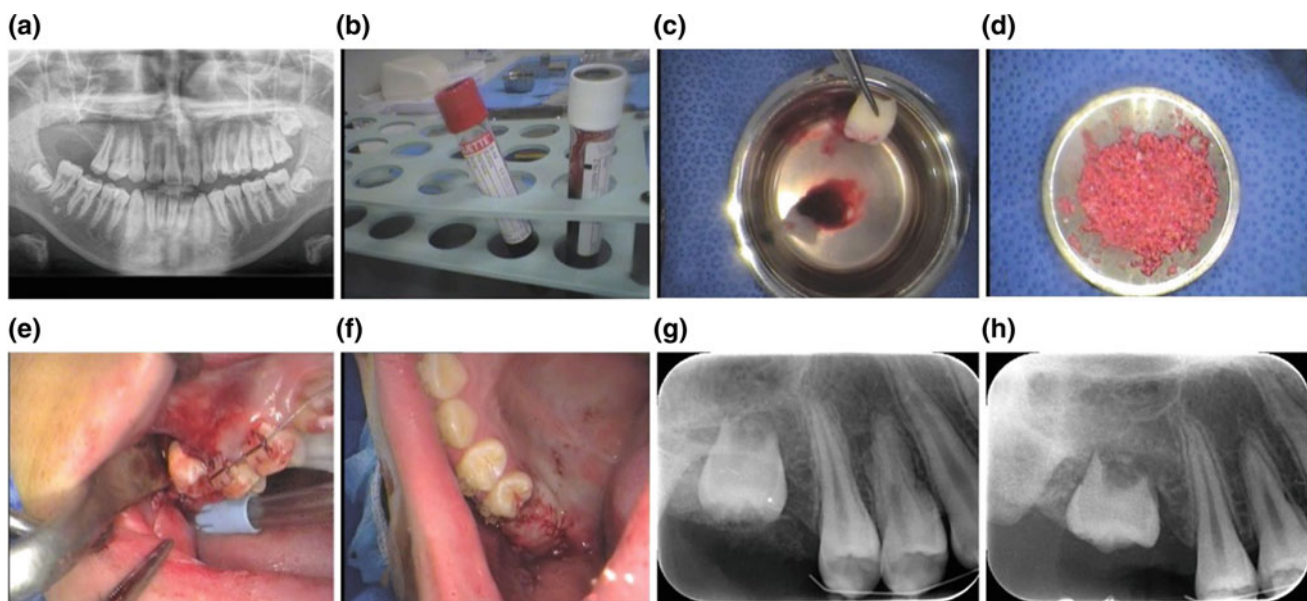


Fig. 2 CASE TWO **a** Pre-operative panoramic illustrating the recipient and donor site. **b** CGF in the Vacutainer[®] glasscoated test tubes. **c** CGF blood clot. **d** CGF was mixed with sticky bone and membrane using Geistlich Bio-Oss[®] (bovine demineralized freeze-dried bone) and Osteon (hydroxyapatite and calcium triphosphate, MIS 4Bone[®]). **e** Placement of the atraumatically extracted 28 in the position of the

16. **f** Suturing of the socket after placement of the CGF sticky bone and membrane. **g** Intraoral periapical radiograph of the auto transplanted tooth immediately after the procedure. **h** Intraoral periapical radiograph of the auto transplanted tooth three months after the procedure

The transplant therapy was uneventful. Patient experienced minimal pain and swelling. Clinically, there was no evidence of wound dehiscence or infection. The endogenous graft is entirely autologous as it is produced from the patient's own blood. However, root resorption was evident, which was expected as it is the most common cause of failure in autotransplantation (Fig. 2).

4 Discussion

There are advantages and disadvantages to each surgical procedure. The auto-transplantation was a much more time-consuming procedure (approximately 3 h) as two minor surgical procedures had to be performed. The use of implants using was less time consuming (2 h) and provided good predictability regarding function and aesthetics. In term of cost in both procedures, implants were more expensive than auto transplant. However, the outcome of the auto transplant was unpredictable, nevertheless, this does not mean that the procedure should be disregarded. Overall, implants are an efficient, predictable, and a well-established technique, which offers good functional and aesthetic outcome compared to autotransplants.

This study agrees with literature [1, 3, 6] that the use of GCF with GBR and GTR is an effective method to reduce

healing time and increase bone regeneration. Layers of growth factors that make up the fibrin-rich CGF clot await stimulation and differentiation into specialized cell types. Furthermore, CGF contains cytokines that promote cell proliferation, growth, maturation, and matrix production [5]. In these two cases, the CGF acted as a tissue sealant, scaffold and a drug delivery system. The ability to obtain autologous CGF quickly makes it easy and inexpensive. As it is the patient's own blood, there is little to no risk of transmissible and allergic diseases.

5 Conclusion

Despite limited literature on the use of autotransplantation compared to implants, this report shed some light on the applications/benefits of each technique. The implants used in case one did not result in adverse effects. However, the auto transplanted tooth in case two displayed signs of root resorption. Within the limits of this two-case study, it showed that implants are an efficient and cost-effective method to replace missing teeth as opposed to auto transplantation.

Conflict of Interest The authors declare that they have no conflict of interest.

References

1. Kim, T.-H., et al.: Comparison of platelet-rich plasma (PRP), platelet-rich fibrin (PRF), and concentrated growth factor (CGF) in rabbit-skull defect healing. *Arch. Oral Biol.* **59**(5), 550–558 (2014)
2. Mirkovic, S., Djurdjevic-Mirkovic, T., Pugkar, T.: Application of concentrated growth factors in reconstruction of bone defects after removal of large jaw cysts—the two cases report. *Vojnosanit. Pregl.* **72**(4), 368–371 (2015)
3. Sohn, D., et al.: The use of concentrated growth factors (CGF) for sinus augmentation. *J. Oral Implant* **38**(1), 25–38 (2009)
4. Clokie, C.M., Yau, D.M., Chano, L.: Autogenous tooth transplantation: an alternative to dental implant placement? *J.-Can. Dent. Assoc.* **67**(2), 92–96 (2001)
5. Honda, H., et al.: Bone tissue engineering with bone marrow-derived stromal cells integrated with concentrated growth factor in *Rattus norvegicus* calvaria defect model. *J. Artif. Organs* **16**(3), 305–315 (2013)
6. Rodella, L.F., et al.: Growth factors, CD34 positive cells, and fibrin network analysis in concentrated growth factors fraction. *Microsc. Res. Tech.* **74**(8), 772–777 (2011)
7. Doan, N., et al.: Application of concentrated growth factors (CGF) and Mphi laser to treat defects in the oral and maxillofacial region. A two—case report. *Int. J. Oral Maxillofac. Surg.* **46**, 203–204
8. Thorn, J.J., et al.: Autologous fibrin glue with growth factors in reconstructive maxillofacial surgery. *Int. J. Oral Maxillofac. Surg.* **33**(1), 95–100 (2004)
9. Tayapongsak, P., et al.: Autologous fibrin adhesive in mandibular reconstruction with particulate cancellous bone and marrow. *J. Oral Maxillofac. Surg.* **52**(2), 161–165 (1994)
10. Clark, R.A.: Fibrin and wound healing. *Ann. N. Y. Acad. Sci.* **936**, 355–367 (2001)

Fabrication of N,O Carboxymethyl Chitosan (NOCC)—Aldehyde Hyaluronic Acid (AHA)—Biphasic Calcium Phosphate (BCP)—Poly (Vinyl Phosphonic Acid) (PVPA) Hydrogel for Bone Regeneration

Le Nguyen My An, Nguyen Thanh Truc, Vo Ngoc My Tuyen, Vo Van Toi, and Thi-Hiep Nguyen

Abstract

N,O carboxymethyl chitosan—aldehyde hyaluronic acid (NOCC-AHA) hydrogel has been proved for successfully cutaneous wound healing due to its porosity, water uptake and biocompatibility. Modification of poly (vinyl phosphonic acid) (PVPA) and biphasic calcium phosphate (BCP) nanoparticles into NOCC-AHA matrix is expected to fabricate a hydrogel for bone regeneration. BCP is main factor of osteogenesis, which shows excellent osteoconductivity, osteoinductivity, biodegradability. Besides, PVPA containing P-C groups in structure support bonding between bone and hydrogel matrix, and increase of bone formation by eliminating osteoclast apoptosis. This research investigates an optimal NOCC: AHA ratio loaded PVPA and BCP in order to optimize the formulation of injectable bone hydrogel. The optimal NOCC-AHA-PVPA-BCP was biocompatible, and showed the porosity, pore size were favorable for bone regeneration, which was confirmed through scanning electron microscope. However, degradation rate of this hydrogel needs improving in further research.

Keywords

Hydrogel • Bone • N,O carboxymethyl chitosan • Aldehyde hyaluronic acid • Poly (vinyl phosphonic acid) • Biphasic calcium phosphate

1 Introduction

Bone is a highly-vascularized component of the skeletal system and is considered as a living tissue with the regenerative ability. Bone can regenerate the injury from 6 to 10 months depending on its extent, individual physical and age. Cast immobilization, bone transplantation and stem cell therapy are the most common treatments for bone defects [1]. However, patients usually either feel uncomfortable when wearing a plaster or fiberglass cast for a long time or having inflammation, swelling after a transplantation surgery. To overcome these obstacles, novel biomaterials for bone fracture regeneration are continually developed, which aims at favoring optimal bone integration in the scaffold, up to complete bone regeneration [2]. This new bone should ideally replace the bone graft through repeated remodeling cycles, enabling repair of the defect site to maintain an optimal balance between form and function [3]. Hydrogels are among the most promising biomaterials in regenerative medicine applications: they are very flexible materials that allow a number of different properties to be targeted for different applications, through appropriate chemical modifications [4].

Hydrogel formulated by N,O—Carboxymethyl Chitosan (NOCC)—Aldehyde Hyaluronic Acid (AHA) has been known for cutaneous wound healing capacity [5] and having the same structure of hard bone matrix [6], which makes a biodegradable environment to load some potential biomaterial enhancing bone regeneration. However, almost hydrogel systems, including NOCC-AHA, lack the capacity to mineralize preventing the application in bone substitutes.

Le Nguyen My An, Nguyen Thanh Truc, Vo Ngoc My Tuyen—contributed equally.

L. N. M. An (✉) · N. T. Truc · V. N. M. Tuyen · V. Van Toi · T.-H. Nguyen
 Department of Biomedical Engineering, International University, Vietnam National University- Ho Chi Minh City (VNU-HCMC), Ho Chi Minh City, 700000, Vietnam
 e-mail: myanlenguyen@gmail.com

T.-H. Nguyen
 e-mail: nthiep@hcmiu.edu.vn

The concept of combining a hydrogel with inorganic phase is inspired by the composite nature of bone itself [7]. There are many advantages of adding an inorganic phase such as providing nucleation for apatite layer formation, providing cell adhesion sites for enable integration with surrounding bone tissue [8, 9].

Poly (vinyl phosphonic acid) (PVPA), a phosphonate-containing polymer, is hypothesized to mimic the action of bisphosphonates, a group of drugs used in the treatment of osteoporosis. Due to the P-C groups in structure, it is speculated to imitate the P-C-P backbone found in bisphosphonates which act by eliminating osteoclast apoptosis leading to an increase in bone formation [10]. One of the most important functions of PVPA is that they can assist in the bone-bonding between the restorative material and the native bone tissue [11] due to its similarity to the phosphate groups of the natural bone hydroxyapatite [12].

Biphasic calcium phosphate (BCP) composed of Hydroxyapatite (HAp: $\text{Ca}_{10}(\text{PO}_4)_6(\text{OH})_2$) and beta Tricalcium phosphate (β -TCP: $\text{Ca}_3(\text{PO}_4)_2$), synthetic materials for bone replacement and novel biomaterials with similar properties to native bone. Its composition and structure are similar to mineral phase of bone and be processed to have osteoconductive properties, allow osteogenesis to occur and form tight bonds with host tissues [13]. BCP showed excellent osteoinductivity, osteoconductivity, bioactivity, and biodegradability among potential calcium phosphate substances. It offers the capable of supporting bone cells adhesion and evenly distribute over injured area.

Hence, the aim of the research is optimization of NOCC-AHA-PVPA-BCP hydrogel.

The ratio between NOCC and AHA was varied and loaded constant PVPA and BCP. Porosity and pore size of samples acquired were compared and confirmed through scanning electron microscope. Additionally, degradation rate and cell viability were also determined in order to conclude an optimal hydrogel formulation for bone regeneration. This hydrogel is expected to stimulate bone forming and mineralization thanks to the support of the AHA-NOCC network, calcium and phosphate ions from BCP and PVPA.

2 Materials and Methods

2.1 Fabrication NOCC-AHA-PVPA-BCP Hydrogel

Synthesis of AHA 0.8 g of Hyaluronic acid sodium salt (HA, Sigma-Aldrich) was added with 80 mL of distilled water and 4 mL of 4.25% NaIO₄ and stirred within 2 h, 60 °C. After that, 0.4 mL of ethylene-glycol was added in the solution and continued to stir in 1 h, 60 °C. The final solution dialysed in 3 days.

Synthesis of NOCC 2 g of chitosan (CS, Sigma-Aldrich) was added with 20 mL of Isopropanol and 20 mL of 50% NaOH (w/v) and stirred in 2 h, 60 °C. Then, 20 mL of cinnamylidene acetic acid (CAA) was added by drops into the mixture within 20 min and stirred in 2 h, 60 °C. The residue was washed with 80% ethanol three times and finally added with 66.67 mL distilled water and stirred until it dissolved completely, and the final solution was dialysed in three days.

Fabrication of NOCC-AHA-PVPA-BCP hydrogels 5 mg Biphasic calcium phosphate (BCP) is mixed with 3 μ l of Poly (vinyl phosphonic acid) 30% (PVPA, War-rinton, PA, USA) 30%. Then, NOCC and AHA are added into an envedop, respectively. Three NOCC: AHA ratios which are 7:3, 6:4, and 5:5 were selected to investigate the effect of PVPA and BCP on the formation of this system since the homogeneous AHA/NOCC hydrogel was form at 7NOCC and 3AHA [5].

2.2 Characterization of NOCC-AHA-PVPA-BCP Hydrogel

Scanning electron microscope (SEM) observation The hydrogel samples were freeze-dried, Au-coated for 1 min and observed under Scanning Electron Microscope (SEM, JEOL, 12 keV), at magnification of 100x and 5000x.

Degradation behavior. The samples were incubated in a 1 mL of 1X PBS solution (pH = 7.4) at 37 °C. After regular time intervals (one-day), surface water was removed from the samples and the samples were weighed (W_i). Fresh PBS was then added to the samples. The weight ratio of hydrogels (W_t/W_i) was calculated as a function of incubation time.

Fourier Transform Infrared Spectroscopy (FTIR) Three samples of hydrogel: AHA-NOCC, AHA-NOCC-BCP, and AHA-NOCC-BCP-PVPA were prepared. The hydrogel samples after freeze-drying were sent to Institute of Life Material Science, HCMC for FTIR measurement. Data from FTIR was analysed by Sigmaplot software (ver.13).

Cytotoxicity The samples were sterilized under UV light for 20 min. The hydrogel extract was collected by placing the hydrogel in DMEM medium at a concentration of 0.1 mg/mL and incubated at 37 °C for 24 h. After incubation, the hydrogel extract was collected and diluted in order to have 50 and 100% extract solution. The DMEM medium was used as a control. L-929 fibroblast cells were seeded in 96-well culture plates, at a density of 10^4 cells/well. The plate was incubated for 24 h at 37 °C. After incubation, the

media was discarded and replaced with 100 μL of hydrogel extracts. The 96-well culture plate was then placed in the incubator for 24 h. At the end of the culture time, the hydrogel extracts were discarded from the 96-well plated and the plate was added with 100 μL of DMEM media and 10 μL of 1X MTT solution. After a brief incubation time of 4 h, the absorbance of the solution was measured at 600 nm using Multiplate Reader (Varioskan). Samples were tested in quadruplicate.

3 Results and Discussion

3.1 Morphology Observation

Gel formation of NOCC-AHA-PVPA-BCP with variation of NOCC: AHA ratio was depicted in Fig. 1. The hydrogel formulation was investigated according three NOCC: AHA ratios (7:3; 5:5; 6:4). However, the sample (5:5) did not form gelation in case of loading PVPA and BCP. Therefore, the optimal NOCC-AHA-PVPA-BCP hydrogel was investigated following two ratios (7:3 and 6:4).

Under SEM observation (Fig. 2), these scaffolds created interconnected pore structure at low magnifications (100x) with the presence of BCP observed at higher magnifications (5000x). However, NOCC: AHA (7:3) had higher porosity and larger pore size (>100 μm) compared with NOCC: AHA (6:4). Moreover, the sparsely distribution of BCP particles on NOCC: AHA (7:3) hydrogel membrane suggested that it should increase the loading of BCP on the hydrogel system. Meanwhile, the aggregation of BCP on NOCC: AHA (6:4) depicted the partial reaction and non-homogeneity in the hydrogel system.

3.2 Degradation Behavior

The AHA-NOCC-PVPA loading BCP hydrogels with two different ratios of AHA and NOCC (4:6 and 3:7) degraded substantially at third day (37 and 61% respectively). Both

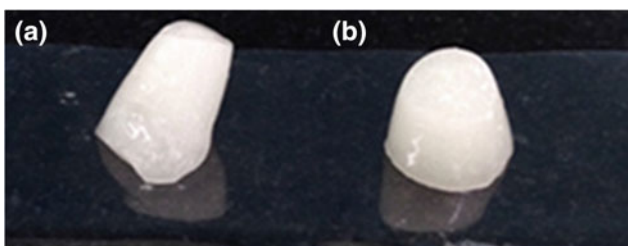


Fig. 1 Gelation of AHA-NOCC-PVPA-BCP hydrogel with NOCC: AHA ratio **a** 6:4, **b** 7:3

these two hydrogels system completely degraded after one week. This degradation rate cannot fully support for the whole process of bone regeneration (Fig. 3).

3.3 Fourier Transform Infrared Spectroscopy (FTIR)

Figure 4 shows the spectra of obtained hydrogel (NOCC-AHA, NOCC-AHA-BCP, and NOCC-AHA-PVPA-BCP). FTIR spectroscopy indicates the all of the three hydrogels investigated had very strong absorption band in 1000–1627 cm^{-1} region (due to Schiff base reaction between aldehyde and amine group of AHA and NOCC). There is no sharp difference peak obtained in NOCC-AHA-BCP when comparing with NOCC-AHA hydrogel, only a slight absorption at band of 480 and 719 cm^{-1} is observed. These band express the phosphonate group PO_4^{3-} of BCP. The presence of new peaks in NOCC-AHA-PVPA-BCP at 571 and 604 cm^{-1} may be due to PO_4^{3-} in PVPA, and the formation of covalent bond $\text{P}=\text{O}$ between PVPA and aldehyde group in AHA as being mentioned in previous study.

3.4 Cytotoxicity

The effect of 100 and 50% hydrogel extracts on L-929 fibroblast cell are shown in Fig. 5. In these experiments, the remaining cell viability was over 75% for both 50% and 100 vol% hydrogel extracts after incubation, indicating that the hydrogel extracts were not cytotoxic. Specifically, the AHA-NOCC-PVPA-BCP hydrogel (7:3) had cell viability which was approximately 5% higher than the hydrogel (6:4), corresponding 50 vol% hydrogel extracts. However, regarding 100 vol% hydrogel extract, the former accounted for lower cell viability at nearly 88% comparing with the later at around 92%. Therefore, it can be concluded that the AHA-NOCC-PVPA-BCP fabricated did affect the cell proliferation due to decrease in cell viability in different volume extracts.

4 Conclusion

Two different ratios of NOCC: AHA in NOCC-AHA-PVPA-BCP hydrogel namely 6:4 and 7:3 were investigated, respectively, the later has larger inter-connected pore structure and more porous than the former, and all the formulations showed biocompatibility. In conclusion, this hydrogel is favorable for bone regeneration. However, limitation of this study is to control the biodegradation rate of hydrogel

Fig. 2 SEM morphology of NOCC-AHA-PVPA-BCP hydrogel with variation of NOCC: AHA ratio (7:3, and 6:4), at 100x and 5000x

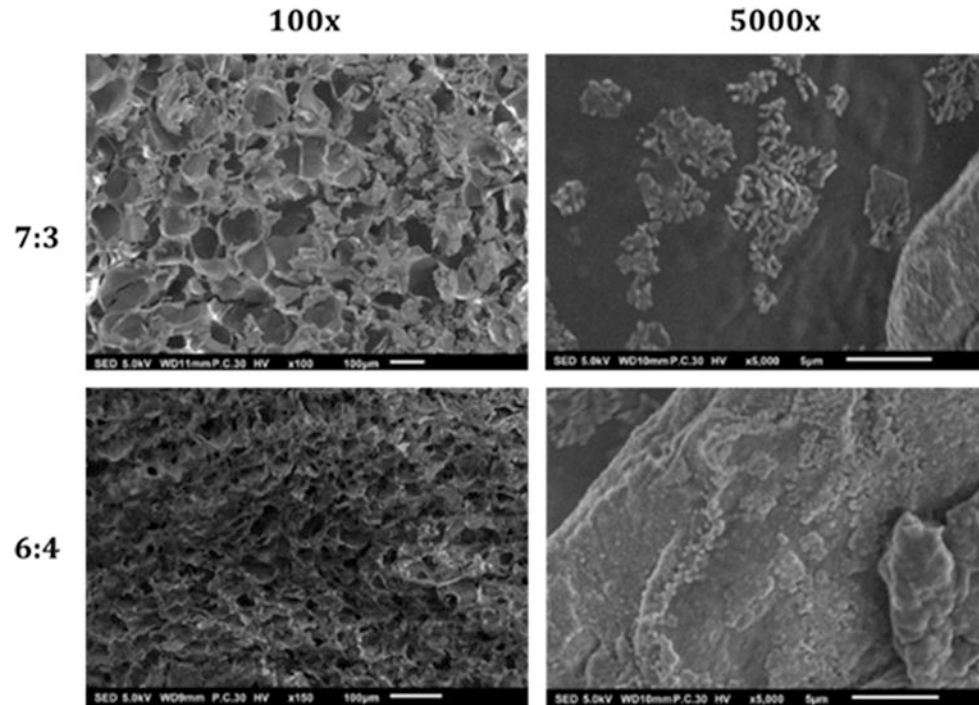


Fig. 3 Degradation rate of NOCC-AHA-PVPA-BCP hydrogel with variation of NOCC: AHA ratio 7:3 (blue), and 6:4 (orange)

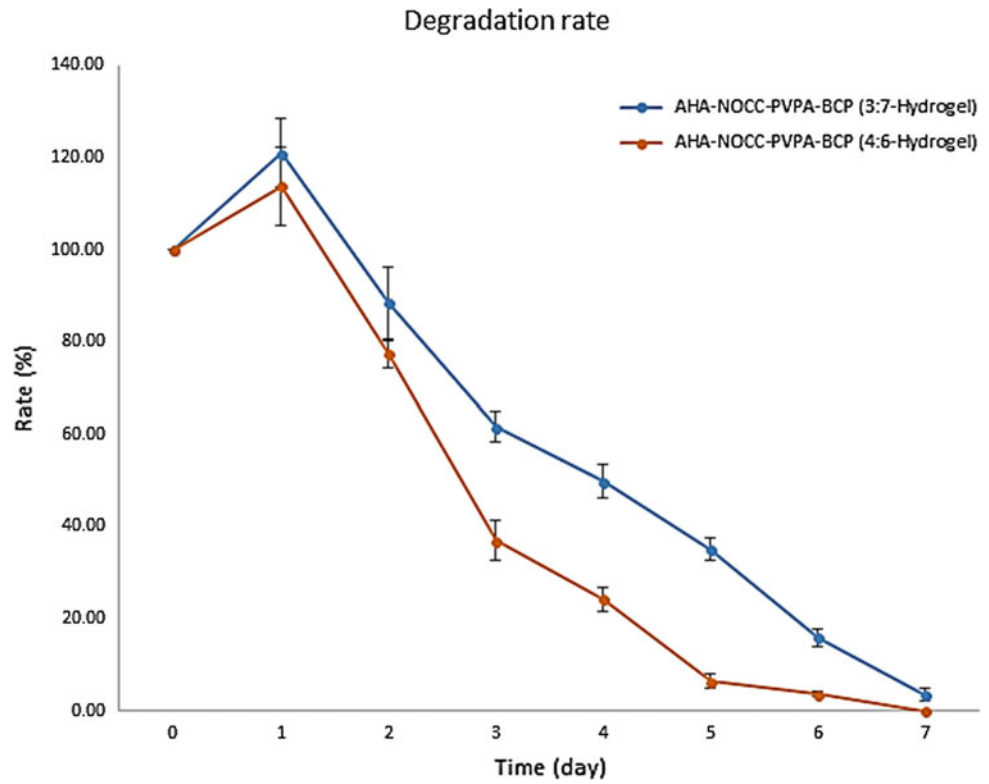


Fig. 4 Fourier Transform Infrared Spectra of NOCC-AHA (red), NOCC-AHA-BCP (green) and NOCC-AHA-PVPA-BCP (black)

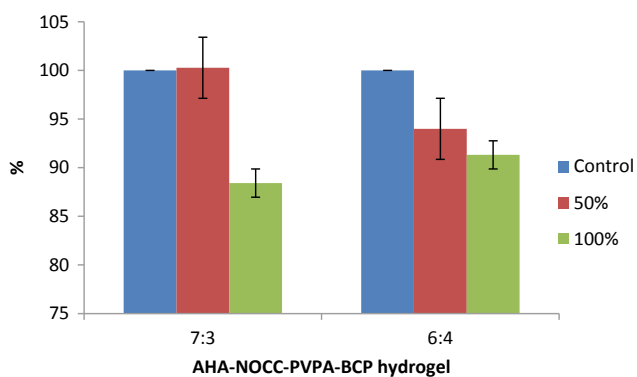
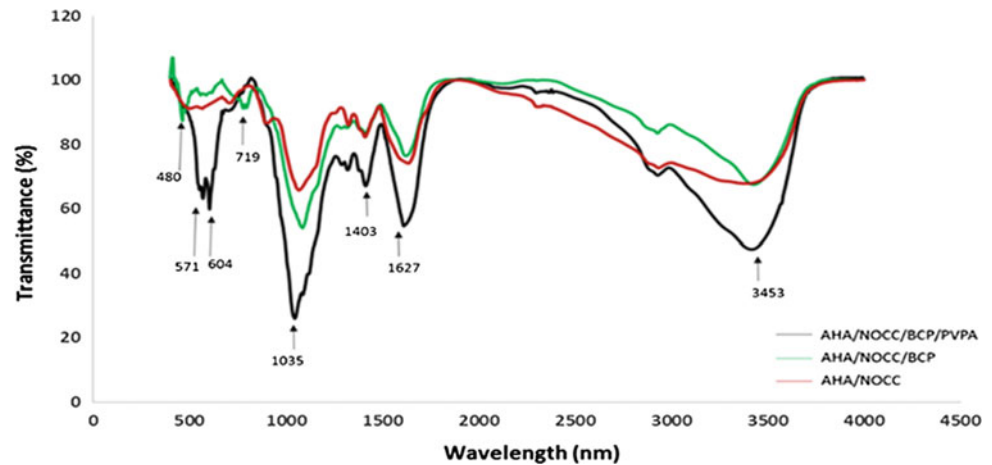


Fig. 5 Cell viability of AHA-NOCC-PVPA-BCP hydrogel with variation of NOCC: AHA ratio (7:3 and 6:4)

for bone regeneration within several months while current optimal NOCC-AHA-PVPA-BCP hydrogel is degraded totally after one week.

Acknowledgements This research is funded by International University—VNUHCM under grant number T2017-03-BME. **Conflict of Interest** The authors declare that they have no conflict of interest.

References

- Sadiasa, A., Nguyen, T.-H., Lee, B.-T.: In vitro and in vivo evaluation of porous PCL-PLLA 3D polymer scaffolds fabricated via salt leaching method for bone tissue engineering applications. *J. Bio. Mat. Sci. Polym. E* **25**(2), 150–167 (2014)
- Thi-Hiep, N., et al.: A novel fibrous scaffold composed of electrospun porous poly(ϵ -caprolactone) fibers for bone tissue engineering. *J. Biomater. Appl.* **28**(4), 514–528 (2012)
- Jang, D.W., Nguyen, T.-H., Sarkar, S.K., Lee, B.-T.: Microwave sintering and in vitro study of defect-free stable porous multilayered HAP–ZrO₂ artificial bone scaffold. *Sci. Technol. Adv. Mater.* **13** (2012)
- Nguyen, T., Ventura, R., Min, Y., Lee, B.: Genipin cross-linked polyvinyl alcohol-gelatin hydrogel for bone regeneration. *J. Biomed. Sci. Eng.* **9**, 419–429 (2016)
- Nguyen, N.T.-P., et al.: Synthesis of cross-linking chitosan-hyaluronic acid based hydrogels for tissue engineering applications, 671–675 (2018)
- Thi-Hiep, N., Van Hoa, D., Van Toi, V.: Injectable in situ crosslinkable hyaluronan-poly (vinyl phosphonic acid) hydrogels for bone engineering. *J. Biomed. Sci. Eng.*, **6** (2013)
- Gkioni, K., et al.: Mineralization of hydrogels for bone regeneration **16**, 577–585 (2010)
- Hoffman, A.S.: Hydrogels for biomedical applications. *Adv. Drug Deliv. Rev.* **54**(1), 3–12 (2002)
- Huaping, T., Marra, K.: Injectable, biodegradable hydrogels for tissue engineering applications, **3** (2010)
- Russell, R., Rogers, M.: Bisphosphonates: from the laboratory to the clinic and back again, **25**, 97–106 (1999)
- Franco, R.A., et al.: On stabilization of PVPA/PVA electrospun nanofiber membrane and its effect on material properties and biocompatibility. *J. Nanomater.* **2012**, 9 (2012)
- Macarie, L., Iliu, G.: Poly(vinylphosphonic acid) and its derivatives. *Prog. Polym. Sci.* **35**(8), 1078–1092 (2010)
- Ebrahimi, M., Botelho, M.: Biphasic calcium phosphates (BCP) of hydroxyapatite (HA) and tricalcium phosphate (TCP) as bone substitutes: importance of physicochemical characterizations in biomaterials studies. *Data Brief* **10**, 93–97 (2017)

Overcoming Single Dental Implant Failure Using Two Small Implant Support for One Crown: Five Year Retrospective Study

N. Doan, L. Truong, J. Doan, and P. Reher

Abstract

Introduction Overcoming a dental implant failure/osseointegration is still a dilemma for implantologists. Using two implants to support for one crown is a novel approach to resolve this issue. *Aim* The aim of this study is to carry out a five-year retrospective study on how to overcome shortfalls in single implant failures by using two small implants to support one crown. *Materials and methods* An audit of a group of 23 patients who had issues with single implant failures underwent two implant fixture placements for future restoration of a single crown. The patient demographic variables collected were medical history, systemic and genetic conditions (Type 1 & 2 Diabetes Miletus), and social habits (smoking and alcohol). Digital x-rays, implant survival assessment, and clinical evaluation were used to analyze the data. *Results and discussion* There was a 100% implant survival rate over five years. Patients reported to be very happy and satisfied with the outcome. *Conclusion* With respect to this retrospective paper, the study found that the use of two implants to support one crown is a favorable and advantageous method to overcome a single implant failure.

Keywords

Dental implant failures • Osseointegration • Osseointegration • Survival rate
Satisfaction • Audit

N. Doan · L. Truong (✉) · P. Reher
School of Dentistry and Oral Health, Griffith University,
Gold Coast, Australia
e-mail: lauratruong1996@gmail.com

N. Doan
e-mail: nvtdoan123@gmail.com

N. Doan · J. Doan
The University of Queensland, Brisbane, Australia

N. Doan
Queensland University of Technology, Brisbane, Australia

1 Introduction

Due to an increase in the popularity of implant placement, dental clinicians also must deal with more failure and complication rates despite previously reported success rates [1, 2]. Literature reports high success rates for dental implants; however, there are still insufficient reports regarding functions of implants for more than 5 years [1]. In a systemic review conducted by [3], they found that >98% of implants will successfully osseointegrate, 95% have a 5-year survival rate, and 89% have a 10-year survival rate. However, figures decline with success rate even when bioactive surfaces are used [4]. This means that implant failures do occur in a minority of patients, consequently leading to more treatment required or further costs [1, 5]. The survival/success rates of implant replacements are generally lower compared to the initially placed implants [1, 2].

Numerous studies reported in the literature document lists of factors associated with implant failure that include but are not limited to: patient-related factors, implant-related characteristics and dental clinician [6]. Patient-related factors are poor bone quantity and quality, systemic diseases, smoking, unresolved infection or parafunctional habits [7, 8]. In addition, implant characteristics like osseointegration, the number or position of the implant, inappropriate loading and/or ill-suited prosthesis design may contribute to failure [1, 9]. From a clinical view, several different etiologies, for instance, bacterial infection, occlusal load and technical errors like micromovement during insertion, trauma should be considered [5, 10].

From time to time, failed implants present with symptoms, such as continuous pain and mobility [1, 6]. Implant failures can present differently in clinical and radiographic presentation including pain, bleeding, swelling, suppuration, and radiographic signs of bone loss [10]. Nevertheless, marginal alveolar bone loss is usually asymptomatic but may compromise the implant in the long term. If undetected, it might make replacing the failed implant difficult or

compromise the outcome [1]. Therapeutic methods should be attempted in cases without definite failure; however, to prevent further bone loss, failed implant needs to be removed [6].

There is still a lack of literature for evidence-based data concerning the replacement of a failed implant [6]. The ultimate challenge is to achieve osseointegration in a non-pristine bone site of the previously failed implant [11]. At this site, latent inflammation or scar tissue from the previous surgical intervention may remain [12]. The replacement implant will always be subjected to all the factors that led to the initial failure. Survival rates of re-implantation typically do not compare to first time single implants placed [1, 11].

There have only been limited studies reporting on the success of replacing implants at the same site [2, 6, 8, 10, 13]. Immediate replacement of implants directly into the previously failed site has not been widely reported. Nevertheless, it is possible with the use of larger diameter screws [10, 14]. Glavas and Moses [2], Alsaadi et al. [12] found that even if a remaining bone lesion tends to compromise the osseointegration, improved surface implants (rather than machine milled surfaces) would have high predictability and better prognosis when an implant is to be replaced. However, it is traditional to re-enter the site after primary closure with a flap after 9–12 months. This is because sufficient socket bone needs to be maintained and preserved for endosseous regeneration to allow placement of new implants in the future [5].

A way of diminishing the potential overload and screw loosening is to use wide implants [15]. Wide-diameter implants are not always a treatment option and hence, the use of two implants to support a single-molar replacement is another method to reduce the stress on implant and bone [16]. This increases surface area for osseointegration and more accurately represent the crown to root ratio of molars [15, 17, 18]. It can reduce mesio-distal bending and increase support capacity buccolingually [15, 17, 18]. The ability to reduce rotation forces adds to the biomechanical advantage to minimize problems such as screw loosening [17, 19]. However, a downside is that enough interdental space (12 mm) is needed; otherwise, it could lead cleaning difficulties for the patient [20].

Most implant failures occur in the posterior maxilla and/or in type 4 bone [7, 21]. Thus, towards the posterior region, sufficient space is present to place implants directly next to the failed implant site rather than in the previously compromised bone through two-implant supported crowns.

2 Materials and Methods

2.1 Inclusion and Exclusion Criteria

All subjects gave their informed consents (Griffith University Ref no: 2018/224) to carry out the treatment according to the described protocol. Patient selection was based on demographic variables: medical history, systemic and genetic conditions (Type 1 & 2 Diabetes Miletus), and social habits (smoking and alcohol). The surgical implant procedures were explained and chosen because of the patient characteristics and the anatomic peculiarities of the insertion places.

All implant failures occurred after restorative procedures. Conditions that resulted in implant failure included implant mobility, pain, infection, fracture, intolerable paresthesia, anesthesia or dysesthesia, and greater than 50% radiographic bone loss. The failed implants were made of surface modified titanium alloy Ti–6Al–4V. The 3.75–4.1 mm-diameter tissue level type internal octagons implants (Mistral Implant, MIS Schlomi, Israel) while the 4.1- and 3.75 mm-diameter screw-type internal hexagons implants (Internal hexagon Implant, Blue Sky Bio, Grayslake, IL USA) in varying lengths.

2.2 Surgical and Prosthetic Procedures

The superior aspect of the implant was exposed through vertical releasing incisions to raise a mucoperiosteal surgical flap extending over the mucogingival junction. The failed implants were unthreaded and removed with sterile forceps or manual implant driver tip. The remaining site is to be examined for soft tissue lining and any granulation tissue. Meticulous removal (manual curettage) of these tissues to minimize trauma and time should be allowed for alveolar walls to regenerate in the socket before reimplantation. A mucoperiosteal flap is then mobilized and the site is tightly closed. There were three rare cases, one person had peri-implantitis, hence the implant was removed then GTR was done. Another case after 3 months after removal of failed implant, the replacement implant was placed then GTR was done. Lastly, all GTR required a minimum of 6–9 months wait.

After 3 months, the replacement implants were most likely to be a 3.75-mm-diameter surface modified implant, Ti–6Al–4V tissue level type implants (Mistral Implant, MIS) with internal octagons. The 4.1- and 3.75 mm-diameter

implants were the most commonly used in this study. No fracture occurred with any implant wider than 3.75 mm during the study period. Antibiotic prophylaxis is taken one day before the surgery: Augmentin Duo 500/125, Metronidazole 200 mg and Dexamethasone 20 mg (3 days). For penicillin allergic patients, alternative antibiotics such as Clindamycin would be used instead.

An internally irrigated spade drill, stepped-down 2.0- to 3.7-mm-diameter spade drill was used to increase the diameter of the receptor site. Before installation, implants were carefully embedded in liquid concentrated growth factor (CGF) with the aim of bioactivating the implant surface and promoting the osseointegration. The replacement implant was then placed into the freshly prepared socket according to the manufacturer's instructions, preferably using flapless technique, as it is minimally invasive with good implant survival rate [21]. In certain cases, guided tissue regeneration techniques were employed utilizing barrier membranes with or without additional bone fill augmentation material. Care was taken to ensure that the implant was firmly stabilized within the receptor site. If a flap was raised then it was sutured, and primary closure was attempted whenever possible, sutures were removed 1 week later. The patients were told to avoid chewing and tooth-brushing the area for the first 2 weeks post-operatively. The medication that was prescribed to all patients consisted of antibiotics, anti-inflammatories, and 0.12% chlorhexidine mouthwash. Removable prostheses were worn for the first 3 weeks for esthetic reasons only.

2.3 Maintenance Procedures

All patients were recalled for follow-up through a regular implant maintenance program at the 6- and 12-month recall appointments and annually thereafter. However, all patients were encouraged to contact the clinic whenever they had problems. Generally, all recipients' sites took up to one year to heal. The parameters recorded at visits were clinical evaluations of implant stability, function, signs of inflammation, and radiographic assessment of marginal bone loss using standardized intraoral radiographs compared with baseline immediately after prosthesis placement. Even though the same standard posterior periapical X-ray holders were used (Super-Bite™ Kerr), error still exists. Any instance that involved implant complications were also recorded and in certain situations, sulcular debridement was performed if deemed necessary.

2.4 Criteria for Success and Failure

The implant is deemed to be successful if it does not have any surgical or prosthetic issues. Surgical complications include infection, wound dehiscence, osseointegration. While a prosthetic complication consists of screw loosening, crown fracture, crown detachment and aesthetics dissatisfaction. Survival is defined as the presence of the implant and associated prosthesis at the end of the observed period. Hence, data was recorded regarding the success and survival rates of these implants.

3 Results

Osseointegration is deemed after percussion with a metal instrument that produces a sharp, solid sound, and no movement/rotation was caused in all directions. After restoration, all subjects were followed up for a minimum of 5 years. During this period, all implants have successfully maintained osseointegration. Radiographs showed crestal bone exhibited less than 0.5 mm of bone loss in the first year. There has been successful soft tissue attachment, without sign of inflammation in all cases. Patients report uneventful outcomes and high satisfaction.

The average age in this study was 62.72 ± 9.926 with 11 females (47.8%) and 12 males (52.2%). More than half the implants were placed in the lower posterior region, suggesting that this area has higher failure rates. Due to the small sample size, inferential statistics cannot be calculated and deemed statistically significant (Fig. 1; Tables 1 and 2).

4 Discussion

The purpose of this study was to evaluate the clinical effectiveness of two implants being placed after the removal of a pre-existing fixture that failed in 23 patients. All the implants included in the study were clinically stable, asymptomatic, and did not show any bone defects. None of the implants were observed to have failed or been affected by peri-implantitis at the 12-month follow-up. This surgical approach offers some clinical advantages when faced with failed implants; however, it is technique sensitive and many factors should be taken into consideration.

It is important to examine the patient's general health status, smoking habits, quantity and quality of bone, oral hygiene maintenance, etc. Implant characteristics to watch

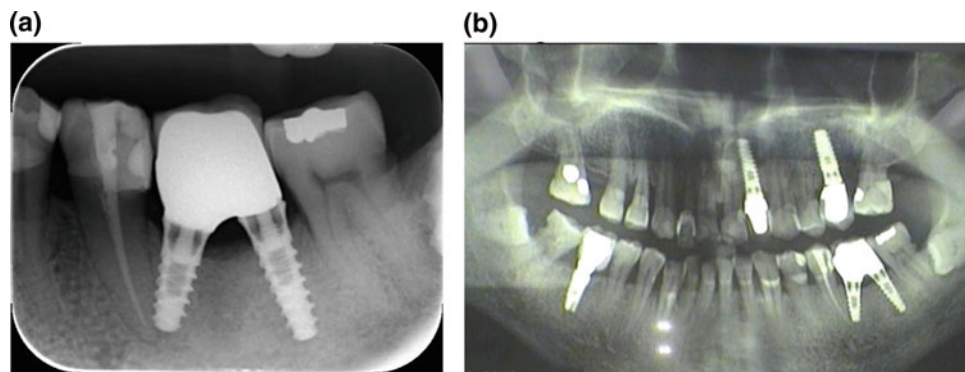


Fig. 1 **a** Intraoral periapical radiograph of the final restoration supported by the two narrow implants. **b** Panoramic radiograph of the final restoration supported by the two narrow implants. Panoramic

were examined to determine whether the two implants were splinted to any adjacent structures and to note opposing and neighboring dentitions

Table 1 Characteristics of participants

Patient characteristics	n (%)
<i>Sexton of implant</i>	
Upper anterior	4 (17.4)
Upper posterior	6 (26.1)
Lower anterior	1 (4.3)
Lower posterior	12 (52.5)
<i>Diabetes</i>	
No	21 (91.3)
Yes	2 (8.7)
<i>Bruxer</i>	
No	4 (17.4)
Yes	19 (82.6)
<i>Smoking</i>	
Non-smoker	18 (78.3)
Past smoker	3 (13.0)
Current smoker	2 (8.7)
<i>Bone type</i>	
2	2 (8.7)
3	15 (65.2)
4	6 (26.1)
<i>Periodontal status</i>	
No	18 (78.3)
Mild	2 (8.7)
Mod	3 (13.0)

out for are dimensions, coating, loading, location, and clinician skills [1]. Patients should be given a detailed explanation of all alternative treatment options according to the relevant parameters and informed about personalized treatment plans [1]. Replacement of a failed implant presents a challenge to achieve osseointegration in a healed bone site and is likely to result in a lower survival rate [11]. In this

Table 2 Outcome of implant characteristics

Implant characteristics	n (%)
<i>Radiographic bone loss</i>	
Normal (0.5 mm/year)	23 (100.0)
<i>Implant stability</i>	
Yes	23 (100.0)
<i>Pain</i>	
No	23 (100.0)
<i>Swelling</i>	
No	23 (100.0)
<i>Bleeding</i>	
No	22 (95.7)
Mild	1 (4.3)
<i>Screw loosening</i>	
No	23 (100.0)
<i>Function</i>	
Yes	23 (100.0)

study, the two replaced implants are placed more laterally to the adjacent teeth to maximize bone quantity available and enable it to be in a fresh site. This can be explained as the alveolar socket may undergo continuous remodeling after removal of the failed implant.

Although there is limited long-term data, it has been suggested that failed implants can be replaced with a wider diameter; however, the replacement implant may fail again [17]. Two-implant-supported crown should then be considered a suitable alternative for failed implants if spatial constraints do not exist [20]. The use of two narrow implants has been successfully demonstrated to be a functional and more biomechanically sound method of molar replacement [16].

This approach allows the implants to achieve proper fixation even if the position is not conventional, especially

for molars that are more susceptible to occlusal forces. Nevertheless, the present analysis of the fate of failed implants remains uncertain. Furthermore, all the implants were placed and restored by the same operator, thus providing statistical evidence of high implant survival [21].

Further clinical studies with a larger cohort over a longer follow-up period are warranted to obtain establish data on long-term benefits and feasibility of this therapy.

5 Conclusion

The results of this study suggest that placement of two small implants at directly adjacent sites to the failed implant showed very favorable outcomes. All patients reported uneventful healing with no specific symptoms. The clinical parameters identified in the success of this procedure included primary implant stability and an extreme level of precision and techniques during implant removal and reimplantation to maintain the integrity of endosseous socks of the failed implant. Further clinical studies, with more extensive cases and an extended follow-up period are necessary to provide additional findings and validate the success of this treatment protocol. Within limitations of this study, the techniques and benefits of using two-implant-supported crowns can be transferred to the site of a failed implant. This is a viable and versatile approach that is conservative to the adjacent bone.

Conflict of Interest The authors declare that they have no conflict of interest.

References

- Levin, L.: Dealing with dental implant failures. *J. Appl. Oral Sci.* **16**(3), 171–175 (2008)
- Glavas, P., Moses, M.S.: Stage I indexing to replace a failed implant in an edentulous arch: a clinical report. *J. Prosthet. Dent.* **89**(6), 533–535 (2003)
- Sailer, I., et al.: A systematic review of the survival and complication rates of all-ceramic and metal-ceramic reconstructions after an observation period of at least 3 years. Part II: fixed dental prostheses. *Clin. Oral Implants Res.* **18**(Suppl 3), 86–96 (2007)
- Buser, D., et al.: 10-year survival and success rates of 511 titanium implants with a sandblasted and acid-etched surface: a retrospective study in 303 partially edentulous patients. *Clin. Implant Dent Relat. Res.* **14**(6), 839–851 (2012)
- Anitua, E., Orive, G.: A new approach for atraumatic implant explantation and immediate implant installation. *Oral Surg. Oral Med. Oral Pathol. Oral Radiol.* **113**(3), e19–e25 (2012)
- Kim, Y.-K., et al.: Prognosis of the implants replaced after removal of failed dental implants. *Oral Surg. Oral Med. Oral Pathol. Oral Radiol. Endodontol.* **110**(3), 281–286 (2010)
- Moy, P.K., et al.: Dental implant failure rates and associated risk factors. *Int. J. Oral Maxillofac. Implants* **20**(4), 569–577 (2005)
- Muroff, F.I.: Removal and replacement of a fractured dental implant: case report. *Implant Dent.* **12**(3), 206–210 (2003)
- Porter, J.A., von Fraunhofer, J.A.: Success or failure of dental implants? A literature review with treatment considerations. *Gen. Dent.* **53**(6), 423–432; quiz 433, 446 (2005)
- Evian, C.I., Cutler, S.A.: Direct replacement of failed CP titanium implants with larger-diameter, HA-coated Ti–6Al–4V implants: report of five cases. *Int. J. Oral Maxillofac. Implants* **10**(6) (1995)
- Grossmann, Y., Levin, L.: Success and survival of single dental implants placed in sites of previously failed implants. *J. Periodontol.* **78**(9), 1670–1674 (2007)
- Alsaadi, G., Quirynen, M., van Steenberghe, D.: The importance of implant surface characteristics in the replacement of failed implants. *Int. J. Oral Maxillofac. Implants* **21**(2), 270–274 (2006)
- Watanabe, F., et al.: Retrieval and replacement of a malpositioned dental implant: a clinical report. *J. Prosthet. Dent.* **88**(3), 255–258 (2002)
- Covani, U., et al.: Clinical outcome of implants placed immediately after implant removal. *J. Periodontol.* **77**(4), 722–727 (2006)
- Balshi, T.J., et al.: A comparative study of one implant versus two replacing a single molar. *Int. J. Oral Maxillofac. Implants*, **11**(3) (1996)
- Shah, Z., Shah, A., Raiyani, P.: Two narrow implants replacing a mandibular right first molar: a case study. *J. Dent. Implants* **6**(2), 75–78 (2016)
- Wolfinger, G.J., et al.: A retrospective analysis of 125 single molar crowns supported by two implants: long-term follow-up from 3 to 12 years. *Int. J. Oral Maxillofac. Implants* **26**(1), 148–153 (2011)
- Penmetsa, R., Venkatesh Murthy, K.R.: Replacement of a molar with two narrow-diameter dental implants. *J. Indian Soc. Periodontol.* **20**(6), 651–654 (2016)
- Jackson, B.J.: Small diameter implants: Specific indications and considerations for the posterior mandible: a case report. *J. Oral Implantol.* **37**(sp1), 156–164 (2011)
- Balshi, T.J., Wolfinger, G.J.: Two-implant-supported single molar replacement: interdental space requirements and comparison to alternative options. *Int. J. Periodontics Restorative Dent.* **17**(5), 427–435 (1997)
- Doan, N.V., et al.: Flapless dental implant surgery: a retrospective study of 1,241 consecutive implants. *Int. J. Oral Maxillofac. Implants* **29**(3), 650–658 (2014)

A Three Year Retrospective Study on the Use of Concentrated Growth Factor (CGF) on Dental Patients Who Undergo Oral Regenerative Treatment

J. Doan, L. Truong, P. Reher, and N. Doan

Abstract

Aim The purpose of this study is to carry out a three-year retrospective study on the use of autologous Concentrated Growth Factor (CGF) on dental patients undergoing oral regenerative treatment. **Materials and methods** Data was gathered from 46 patients who received oral regenerative therapy using CGF within the last three years in a private dental clinic. CGF mixture of demineralized freeze-dried bone (DFDB sticky bone) and fibrin membrane was obtained from the patient's centrifuged blood. Patient medical history, demographic details, social habits, vital signs, oral hygiene status, digital radiographs, clinical observation and photos, survival rate as well as numeric pain intensity scale and visual analogue satisfaction scale were used to evaluate the clinical outcomes. **Results and discussion** All patients had uneventful outcomes in terms of wound healing complications and satisfaction. No patients reported of failure. Though factors like smoking, poor oral hygiene status, periodontitis, and medical conditions such as diabetes have been recognized in the literature, they had no statistical significance in this study. However, gender and age showed statistical significance with the following variables: more males with SDB than females; more older patients (>50 years old) with SDB and high blood than those under 50. **Conclusion** Using the limited patient data available in the last three years in this study, it was found that CGF is a novel approach for

regeneration of defective oral tissues, especially in males and older patients with SDB and high blood pressure. Furthermore, CGF renders good outcomes in terms of uneventful wound healing, biocompatibility, minimal pain, and high satisfaction rate.

Keywords

Oral regeneration • Concentrated growth factor (CGF) • Patient outcomes

1 Introduction

In order to achieve adequate regeneration of tissue structures such as bones, many environmental factors play a critical role [1]. Literature has shown that one approach to increase the quality and quantity of bone healing is through the use of growth factors. Growth factors are bioactive substances, including steroids, proteins or hormones, which contribute to the regulation of wound healing [2]. They play a role in angiogenesis, hemostasis, osteogenesis, and bone growth as they are responsible for cell migration and proliferation [3]. Growth factors can be found in blood and concentrates of platelet-rich-plasma (PRP), platelet-rich fibrin (PRF), and concentrated growth factor (CGF), and all three have been used for tissue regeneration [4, 5].

Studies [2, 4, 6–8] suggest that growth factors have major effects on all stages of bone regeneration. Various studies [4, 6] demonstrated PRP, PRF, and CGF had significantly increased bone formation and may be useful to increase the success rate of bone grafting [4]. CGFs are simple as they do not require additional synthetics or biomaterials, such as bovine thrombin and calcium chloride, which therefore reduces the likelihood of cross-contamination [9]. Despite the similar components, CGF has a higher thickness and tensile strength to better prevent proteolysis of the growth factors [4]. Recently, growth factor-containing CGF preparations with or without bone graft substitutes or transplants

J. Doan (✉) · N. Doan
The University of Queensland, Brisbane, Australia
e-mail: doan.joshua@gmail.com

N. Doan
e-mail: nvtdoan123@gmail.com

L. Truong · P. Reher · N. Doan
Griffith University Schools of Dentistry and Oral Health,
Gold Coast, Australia

N. Doan
Queensland University of Technology, Brisbane, Australia

have been used with the intention of shortening the time after bone graft placement [4]. Bone regeneration requires an osteoconductive scaffold and growth factors for osteoinduction [1]. This is made possible through soft and hard tissue applications of CGF.

Platelet aggregation fibrin-rich gel can be produced from the venous blood by single centrifugation and unlike other growth factors such as PRF, CGF uses different speeds (2400–2700 rpm) to separate cells [1]. Due to this, the CGF clots are more abundant in growth factors and are larger and denser, resulting in a greater regenerative capacity [2]. The agglutination of fibrinogen, factor XIII, and thrombin and the fact that clotting is initiated through thrombin activating factor XIIIa provides protection from plasmin degradation. This cascade allows CGF to have high cohesion, tensile strength, and stability [3]. Aside from the osteoinductive growth factors derived from platelets, there is an osteoconductive fibrin matrix [4]. Furthermore, [5] demonstrated CGF contained TGF- β 1 and VEGF.

Removal of cysts or other pathologies provides an opportunity for microbiological infections. Therefore, primary healing and preservation of blood clots through methods such as CGF is important [6]. Studies [1, 6] have in the past solely used CGF fibrin-rich blocks to aid in wound healing. However, the addition of CGF with bone substitutes may have its advantages, especially in cases with larger defects.

2 Materials and Method

2.1 Experimental Design

Griffith University has provided human ethics approval (Ref No: 2018/182) and all patients gave informed consent.

In this study, 46 patients were selected from the records of a private dental practice. The main inclusion criteria were that the patients have undergone oral regenerative procedures in the last three years. Patient details that were taken into consideration included medical history, demographic

details, social habit (smoking), vital signs (blood pressure), and oral hygiene status. Exclusion criteria were patients with compromised medical conditions or ASA (American Society of Anesthetists) scores of III and above.

2.2 CGF Collection and Placement

The process of CGF collection starts from the venipuncture of the patient's blood. Four sterilized 10 mL Vacutainer[®] tubes, two red and two white, were fully filled with the collected blood. The white tubes are used for making sticky bone and the red tubes are for making fibrin membrane. Each tube was promptly centrifuged using Medifuge MF 200 (Silfradent, Italy) following the manufacturer's instructions. Afterwards, sedimentation of the tubes was allowed for 20 min, resulting in the following layers seen in Table 1.

The top PPP layer from a red tube was then either tipped off or saved for other cosmetic injection techniques such as dermal fillers, allowing the CGF mixture to be methodically obtained. The next step for making CGF membrane was to obtain the CGF clot using tweezers and with scissors, it was separated from the lower red layers. This was then put into saline bath, and then the final shape was determined by the individual application. For example, if it was used for implant GBR/GTR, it was most likely to be converted into a membrane-type configuration. On the other hand, if socket preservation was required, then the CGF was molded into the shape of the defect.

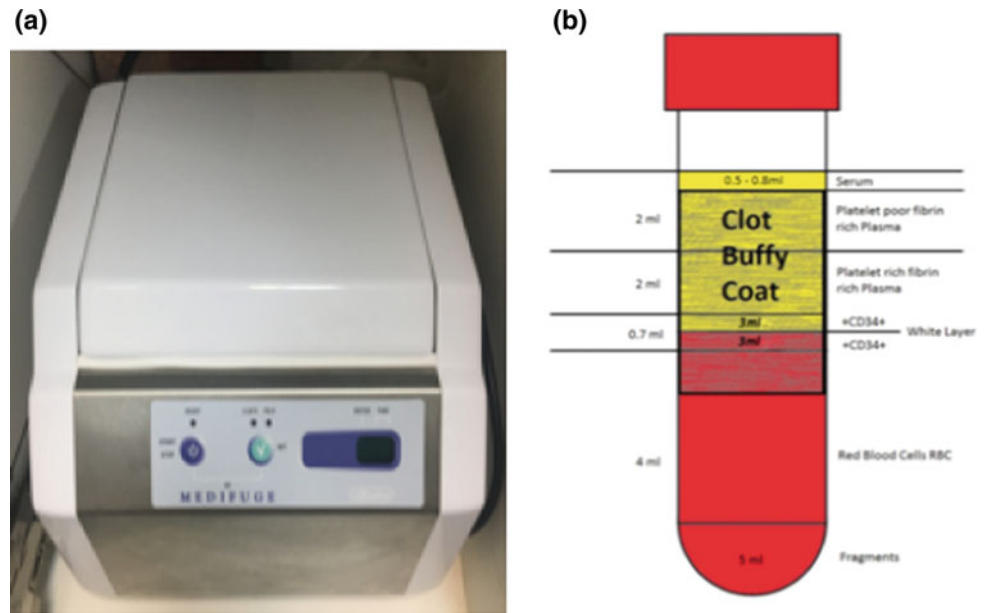
For the white tube, to make sticky bone, the 0.7 mL stem cells/white layer at the interface between the red and creamy phase was mixed with bone filler. Following protocols of the manufacturer, this was made using Geistlich Bio-Oss[®] (bovine demineralized freeze-dried bone, Geistlich Biomaterials), and Osteon (hydroxyapatite and calcium triphosphate, Genoss[®]) was used rather than calcium triphosphate (Fig. 1).

Patients presented to the dental clinic complaining of pain or swelling with no significant medical history. Clinical

Table 1 Layers of centrifuged blood

Serum layers	Amount
PPP—platelets poor plasma	2 mL
PRP—platelets rich plasma	2 mL
Stem cells/white layer	0.7 mL
Fibrin-rich mass with CGF clot	Central
Red blood cells	4 mL
Sedimentary blood fragments	1 mL

Fig. 1 Apparatus used in CGF procedure. **a** Medifuge MF200 (Silfradent, Italy). **b** CGF, which is characterized by four phases: (1) a superior phase, PPP; (2) an interim phase, PRP; (3) a liquid phase or Stem cells/white layer; and (4) the lower red portion is a viscous, dense, platelet-rich coagulation [12]



assessment would indicate a variety of lesions including, but not limited to, periapical periodontitis, infections, or periapical/radicular cysts. The treatments to remove the pathology include surgical periapical drainage, periapical curettage, apicectomy, retrograde filling, decompression, and marsupialization. The patients were prescribed a combination of clindamycin or Augmentin and metronidazole and instructed about appropriate hygienic-dietary regimen.

Clinical outcomes were evaluated using digital radiographs, clinical observation and photos, and survival rate. The patients were monitored for pain, swelling, and trismus using the numeric pain intensity scale [NPIS (0–10)]. To measure the degree of satisfaction, visual analogue satisfaction scale [VASS (1–5)] was used (Fig. 2).

3 Results

All patients had uneventful outcomes in terms of wound healing complications and satisfaction. No patients reported of failure. Though factors like smoking, poor oral hygiene status, periodontitis, and medical conditions like diabetes have been recognized in the literature, they had no statistical significance in this study. However, gender and ages showed statistical significance ($p < 0.05$) with the following variables: more males with SDB than females; more older patients (>50 years old) with SDB and high blood than those under 50. All (46 patients) reported being satisfied with CGF treatment (VASS 4 and 5), with this result shown to be associated with NPIS ($p < 0.001$) (Tables 2 and 3).

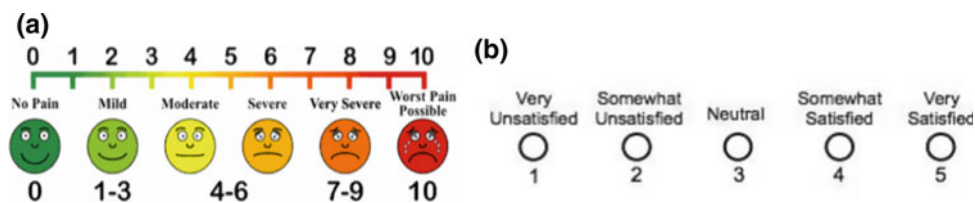


Fig. 2 Visual analogue scales used in the study. **a** Numeric pain intensity scale (NPIS: 0–10 with 0 = no pain and 10 = worst pain) [13]. **b** Visual analogue satisfaction scale (VASS: 1–5 with 1 = very unsatisfied and 5 = very satisfied) [14]

Table 2 Results of 46 patients treated with concentrated growth factors (CGF), visual analogue satisfaction scale (VASS) and numeric pain intensity scale (NPIS) and associated statistical significance where $*p < 0.05$

	Mean ± SD	(Min, Max)	Chi-square	P-value
NPIS	2.20 ± 0.885	1–4	20.649	.000
VASS	4.50 ± 0.506	4–5		

NPIS: verbal rating scale (0–10); VASS: visual analogue scale score (1–5)

Table 3 Descriptive analysis of CGF treatment outcomes stratified by gender and age

	Total	Female	Male	Gender χ^2	Young	Old	Age χ^2
<i>Sexton</i>							
Upper anterior	17 (37.0)	10 (58.8)	7 (41.2)	6.17	2 (11.8)	15 (88.2)	1.87
Upper posterior	13 (28.3)	10 (76.9)	3 (23.1)		3 (23.1)	10 (76.9)	
Lower anterior	3 (6.5)	0 (0.0)	3 (100.0)		1 (33.3)	2 (66.7)	
Lower posterior	13 (28.3)	7 (53.8)	6 (46.2)		4 (30.8)	9 (69.2)	
<i>Procedure</i>							
Apicectomy	2 (4.3)	1 (50.0)	1 (50.0)	.08	1 (50.0)	1 (50.0)	2.95
Bridge	20 (43.5)	12 (60.0)	8 (40.0)		6 (30.0)	14 (70.0)	
Single implant	24 (52.2)	14 (58.3)	10 (41.7)		3 (12.5)	21 (87.5)	
<i>Medical history</i>							
Diabetes	3 (6.5)	1 (33.3)	2 (66.7)	.85	0 (0.0)	3 (100.0)	.89
<i>Periodontal status</i>							
Mild	22 (47.8)	14 (63.6)	8 (34.4)	1.28	7 (31.8)	15 (68.2)	2.96
Moderate	20 (43.5)	10 (50.0)	10 (50.0)		3 (15.0)	17 (85.0)	
Severe	4 (8.7)	3 (75.0)	1 (25.0)		0 (0.0)	4 (100.0)	
<i>Smoking</i>							
Non-smoker	42 (91.3)	26 (61.9)	16 (38.1)	3.08	10 (23.8)	32 (76.2)	1.22
Past smoker	2 (4.3)	0 (0.0)	2 (100.0)		0 (0.0)	2 (100.0)	
Current smoker	2 (4.3)	1 (50.0)	1 (50.0)		0 (0.0)	2 (100.0)	
<i>Vital signs</i>							
Yes	33 (71.7)	17 (51.5)	16 (48.5)	2.48	2 (6.1)	31 (93.9)	16.87*
<i>Oral hygiene status</i>							
Adequate	30 (65.2)	20 (66.7)	10 (33.3)	2.26	9 (30.0)	21 (70.0)	3.46
Inadequate	16 (34.8)	7 (43.8)	9 (56.3)		1 (6.3)	15 (93.8)	
<i>Digital radiographs</i>							
No	46 (100.0)	27 (58.7)	19 (41.3)	–	10 (21.7)	36 (78.3)	–
<i>SBD signs</i>							
Yes	36 (78.3)	17 (47.2)	19 (52.8)	8.99*	5 (13.9)	31 (86.1)	6.00*
<i>Complications</i>							
No	46 (100.0)	17 (47.2)	19 (52.8)	–	10 (21.7)	36 (78.3)	–
<i>NPIS</i>							
1	11 (23.9)	5 (45.5)	6 (54.5)	2.96	1 (9.1)	10 (90.9)	2.64
2	18 (39.1)	11 (61.1)	7 (38.9)		5 (27.8)	13 (72.2)	
3	14 (30.4)	8 (57.1)	6 (42.9)		4 (28.6)	10 (71.4)	
4	3 (6.5)	3 (100.0)	0 (0.0)		0 (0.0)	3 (100.0)	
<i>VAS</i>							
4	23 (50.0)	15 (65.2)	8 (34.8)	.81	6 (26.1)	17 (73.9)	.51
5	23 (50.0)	12 (52.2)	11 (47.8)		4 (17.4)	19 (82.6)	

**p*-value < 0.05

4 Discussion

Conventional stem cell research is usually high in cost and can come with many risks. On the other hand, CGF has a low affordable cost with no need for good manufacturing practice. Due to its autologous nature, it is easy to obtain and hence efficacious for the patients with a reduced chance of rejection. This study has demonstrated the above notions as all patients had uneventful outcomes in terms of wound healing complications and satisfaction. Furthermore, no patients reported of failure, reinforcing the efficacy of CGF in this study. Thus, CGF procedure is safe and simple with no evidence of side effects.

Factors like smoking, poor oral hygiene status, periodontitis, and medical conditions like diabetes have been recognized in the literature as contributing factors in periodontal disease and tooth loss [10]. These patients tend to require more regenerative procedures using CGF. However, no such statistical findings were found in this study. Once again, this might be due to the small sample size of the study. Therefore, future studies should have a larger sample size. The medical literature has well-documented the strong association between gender and age with SDB and high blood pressure [11]. Fortunately, this research study illustrated this statistically significant ($p < 0.005$) association. If a patient was to be a male who presents with SDB, high blood pressure, and a need for implant treatment, the results of this study indicate that CGF seems to be the regenerative procedure of choice. This is due to its high success rate, minimal pain and complication, and high level of treatment satisfaction.

5 Conclusion

Using the limited patient data available in the last three years in this study, it was found that CGF is a novel approach for regeneration of defective oral tissues, especially in males and older patients with SDB and high blood pressure. Furthermore, CGF renders good outcomes in terms of uneventful wound healing, biocompatibility, minimal pain, and high satisfaction rate.

Conflict of Interest The authors declare that they have no conflict of interest.

References

1. Honda, H., et al.: Bone tissue engineering with bone marrow-derived stromal cells integrated with concentrated growth factor in Rattus norvegicus calvaria defect model. *J. Artif. Organs* **16**(3), 305–315 (2013)
2. Rodella, L.F., et al.: Growth factors, CD34 positive cells, and fibrin network analysis in concentrated growth factors fraction. *Microsc. Res. Tech.* **74**(8), 772–777 (2011)
3. Clark, R.A.: Fibrin and wound healing. *Ann. N. Y. Acad. Sci.* **936**, 355–367 (2001)
4. Kim, T.-H., et al.: Comparison of platelet-rich plasma (PRP), platelet-rich fibrin (PRF), and concentrated growth factor (CGF) in rabbit-skull defect healing. *Arch. Oral Biol.* **59**(5), 550–558 (2014)
5. He, L., et al.: A comparative study of platelet-rich fibrin (PRF) and platelet-rich plasma (PRP) on the effect of proliferation and differentiation of rat osteoblasts in vitro. *Oral Surg. Oral Med. Oral Pathol. Oral Radiol. Endod.* **108**(5), 707–713 (2009)
6. Thorn, J.J., et al.: Autologous fibrin glue with growth factors in reconstructive maxillofacial surgery. *Int. J. Oral Maxillofac. Surg.* **33**(1), 95–100 (2004)
7. Doan, N., et al.: Application of concentrated growth factors (CGF) and Mphi laser to treat defects in the oral and maxillofacial region. A two—case report. *Int. J. Oral Maxillofac. Surg.* **46**, 203–204
8. Tayapongsak, P., et al.: Autologous fibrin adhesive in mandibular reconstruction with particulate cancellous bone and marrow. *J. Oral Maxillofac. Surg.* **52**(2), 161–165 (1994)
9. Sohn, D., et al.: The use of concentrated growth factors (CGF) for sinus augmentation. *J. Oral Implant* **38**(1), 25–38 (2009)
10. Nazir, M.A.: Prevalence of periodontal disease, its association with systemic diseases and prevention. *Int. J. Health Sci.* **11**(2), 72–80 (2017)
11. Knutson, K.L., et al.: Association between sleep and blood pressure in mid life: the CARDIA sleep study. *Arch. Intern. Med.* **169**(11), 1055–1061 (2009)
12. Concentrated Growth Factors. Concentrated growth factors and CD34+ (2018) (cited 2018 5 May 2018). Available from: <https://cgf.global/pl/produkty/concentrated-growth-factors-2/>
13. Ahuja, D.: Utilising functional pain scales in physiotherapy clinical practice (2018) (cited 2018 5 May 2018). Available from: <http://www.physioguru.com/physiotherapy-blog/clinical-physiotherapy-blog/54-utilising-functional-pain-scales-in-clinical-practice>
14. Research, M.: 5 essential customer satisfaction survey questions (2017) (cited 2018 5 May 2018). Available from: <http://www.mymarketresearchmethods.com/customer-satisfaction-survey-questions/>

Composite Nano-fiber Mats Consisting of Biphasic Calcium Phosphate Loaded Polyvinyl Alcohol—Gelatin for Bone Tissue Engineering

Linh Thuy Ba Nguyen, Thi-Hiep Nguyen, Chan-Khon Huynh, Byong-Taek Lee, and Hua Ye

Abstract

Electrospun blends of biphasic calcium phosphate (BCP) loaded polyvinyl alcohol (PVA)-gelatin (GE) were created with the aim of fabricating biodegradable scaffolds for bone tissue engineering. The process parameters including the electrical field and tip-to-collector distance (TCD) were investigated. The morphology of these hybrid scaffolds were characterized by scanning electron microscope (SEM). X-ray diffraction (XRD) was used to determine the crystallinity of the membrane. Adhesion of osteoblastic cells (MG-63) onto the BCP loaded PVA/GE composite nano-fiber mat was performed to assess potential of the product as a bone scaffold. This result suggests that the BCP loaded PVA/GE composite nano-fiber mat has a high potential for use in the field of bone regeneration and tissue engineering.

Keywords

Electrospinning • Nano-fiber • Biphasic calcium phosphate nanoparticles • Bone tissue engineering

1 Introduction

Several requirements are necessary in the design of tissue engineering scaffolds, including a high porosity, large surface area, adequate pore size, and uniformly distributed interconnected porous structures throughout the matrix [1]. Biodegradable polymeric fiber structures can provide a large surface area, and a relatively high porosity, which can be optimized for specific applications. Due to the structural similarity between electro-spun polymeric mats and the collagen fiber arrangement in the natural extracellular matrix component of bone, the electrospinning process has drawn a great deal of attention in scaffold processing for tissue engineering [2]. Within the last few years, this technique has proven to be especially suitable for biomedical applications, including tissue engineering of scaffolds, wound dressings, drug delivery, and in other fields such as medical implants [3–6].

Biodegradable polymers have been proposed as a possible alternative to other tissue engineering materials and have garnered a large amount of attention. These polymers can be easily processed into 3-D porous structures with the proper degradation behavior and mechanical strength [7]. Among the biodegradable and biocompatible polymers, polyvinyl alcohol (PVA), gelatin (GE) and their blends have extensive applications as surgical sutures, implant materials, drug carriers, and scaffolds for tissue engineering [3, 8]. PVA is a non-hazardous material and does not cause any injuries to the skin upon contact. Due to their excellent biocompatibility and biodegradability, gelatin fibers are widely used in a variety of biomedical applications, including wound or burn dressings, surgical treatments, and tissue engineering of bone, skin, and cartilage [3, 4, 8]. PVA/GE nano-fibrous membranes with different compositions could have different clinical applications, especially the controlled release of drugs and bone tissue engineering [9, 10].

The most common strategy employed to engineer bone is to use a scaffold combined with osteoblast cells, or cells that

L. T. B. Nguyen (✉) · H. Ye
Department of Engineering Science, Institute of Biomedical Engineering, University of Oxford, Oxford, OX3 7DQ, UK
e-mail: linh.nguyen@eng.ox.ac.uk

T.-H. Nguyen · C.-K. Huynh
Tissue Engineering and Regenerative Medicine Laboratory,
Department of Biomedical Engineering, International University,
Vietnam National University-Ho Chi Minh City (VNU-HCM), Ho
Chi Minh City, 700000, Vietnam

B.-T. Lee
Department of Regenerative Medicine, College of Medicine,
Soonchunhyang University, Cheonan, 330-090, Republic of
Korea

can mature/differentiate into osteoblasts and regulatory factors that promote cell attachment, differentiation, and mineralized bone formation [11]. However, the requirements for designing and production of an ideal scaffold for bone regeneration are very complex and not yet fully understood. It is generally agreed that the scaffold must be a biocompatible, porous (more than 90% and pore sizes between 100 and 350 μm), interconnected and permeable in order to permit the ingress of cells and nutrients [12]. Clearly, structures designed with biodegradable fibers can meet all these criteria and may serve as a scaffold for the engineering of bone. Many different fiber-based polymeric matrices have been tested with different cell types to create a bone construct. Recently, biphasic calcium phosphate (BCP) ceramic, which consists of hydroxyapatite (HAp) and β -tri calcium phosphate (TCP), has received attention for applications as bone substitutes and scaffold materials. In addition, BCP ceramics exhibit various mechanical properties and biological responses depending on their compositional ratio of HAp and β -TCP. BCP showed good resorption, osteoconductivity, biodegradable bone, and replacement material.

The fabrication of a composite material from PVA/GE nano-fibers for using in tissue engineering or in guided tissue regeneration, particularly for bone regeneration, has already been reported earlier [8, 13]. In this study, nano-structured scaffolds of BCP nano-particles loaded in PVA/GE nano-fibers were fabricated via electrospinning for bone regeneration.

2 Materials and Methods

Poly (vinyl alcohol) (PVA, 99+% hydrolyzed, Sigma) was obtained from Aldrich Chemical Co (USA). Gelatin Type A (Approx. 300 Bloom, Sigma, St. Louis, MO) from porcine skin was obtained in powder form. The MG-63 cell line was obtained from Korean Cell Bank. Dulbecco's Modified Eagle's Medium (DMEM, HyClone, Logan, UT), fetal bovine serum (FBS, Grand Island, NY), penicillin-streptomycin (antibiotics) and trypsin-EDTA were purchased from GIBCO (Carlsbad, CA, USA). BCP nano-powder was synthesized by microwave hydrothermal method using $\text{Ca}(\text{OH})_2$ (99.995%, Aldrich Chemical) and H_3PO_4 (85–87%, Dongwoo Fine Chemicals, Korea) as precursors.

For electrospinning (eS-robot, Electrospinning/Spray system), the solutions were placed into a 10 ml syringe fitted to a needle with a tip (diameter of 25 gauges, inner diameter 0.25 mm), a syringe pump (lure-lock type, Korea) for controlling feed rates, and a grounded cylindrical stainless steel mandrel was used to collect the mat. The morphology of

the electro-spun fibers was examined by scanning electron microscopy (SEM, JSM-7401F). The crystal structures of the BCP-PVA/GE composite membranes were subjected by X-ray diffraction (XRD) (Rigaku, D/MAX-2500 V).

MG-63 cells were maintained and suspended in a humidified incubator at 37 °C and a 5% CO_2 atmosphere (incubator, ASTEC, Japan) in DMEM supplemented with 10% FBS and 1% penicillin–streptomycin. MG-63 cells were seeded on the PVA/GE and BCP-PVA/GE scaffolds at a density of 10^4 cells/ cm^2 . The attachment behaviors of MG-63 were observed after 1 h of incubation.

3 Results and Discussion

The electrospinning conditions were optimized to produce a uniform PVA/GE and BCP-PVA/GE nano-fiber. The optimized parameters were determined by examining the effect of different electrospinning parameters, including applied voltage and tip to collection distance (TCD) on fiber diameter. The amount of GE added to the PVA solution was up to 80 v/v% as previous report [13] and the amount of BCP loaded PVA/GE as 20, 40 and 50 wt/v% [5]. In this study, the concentration of BCP loaded in PVA/GE was increased up to 60 wt/v%. Figure 1 showed SEM images of the PVA/GE, BCP nanoparticles and BCP-PVA/GE prepared by electrospinning. The applied voltage and TCD were fixed at 22 kV and 10 cm, respectively. As shown in Fig. 1, nano-scale PVA/GE and BCP-PVA/GE blends were obtained with diameters ranging from 300 to 500 nm.

The diameter of 60% BCP-PVA/GE fibers was found to be larger than PVA/GE fibers. The appearance of Ca, P spectrum in EDS profile confirmed that the BCP nanoparticles were presence in the PVA/GE fibers. BCP nano-particles were well distributed in the PVA-GE nano-fibrous matrix and appeared on the surface of PVA/GE fibers. Due to the nano-size of the BCP-PVA/GE scaffolds, the electrospun fibers had a high, specific surface area, which is beneficial for tissue engineering applications.

XRD profile of BCP-PVA/GE membrane was performed to examine the crystalline structure of the composite as shown in Fig. 2. PVA/GE fibers showed a crystalline property with the peak around 20 2θ . The strong peaks of HAp at 26, 31, 32, 40, 47, 49, 53, and few peaks of TCP at 27, 28, 33, 48 and 52 are clearly observed in Fig. 2. The results confirmed that BCP nanoparticles were loaded into PVA/GE nano-fibers and retained their crystalline structure during electrospinning.

Pore of various diameters were formed within the nano-fiber structures and the interconnected porous structure

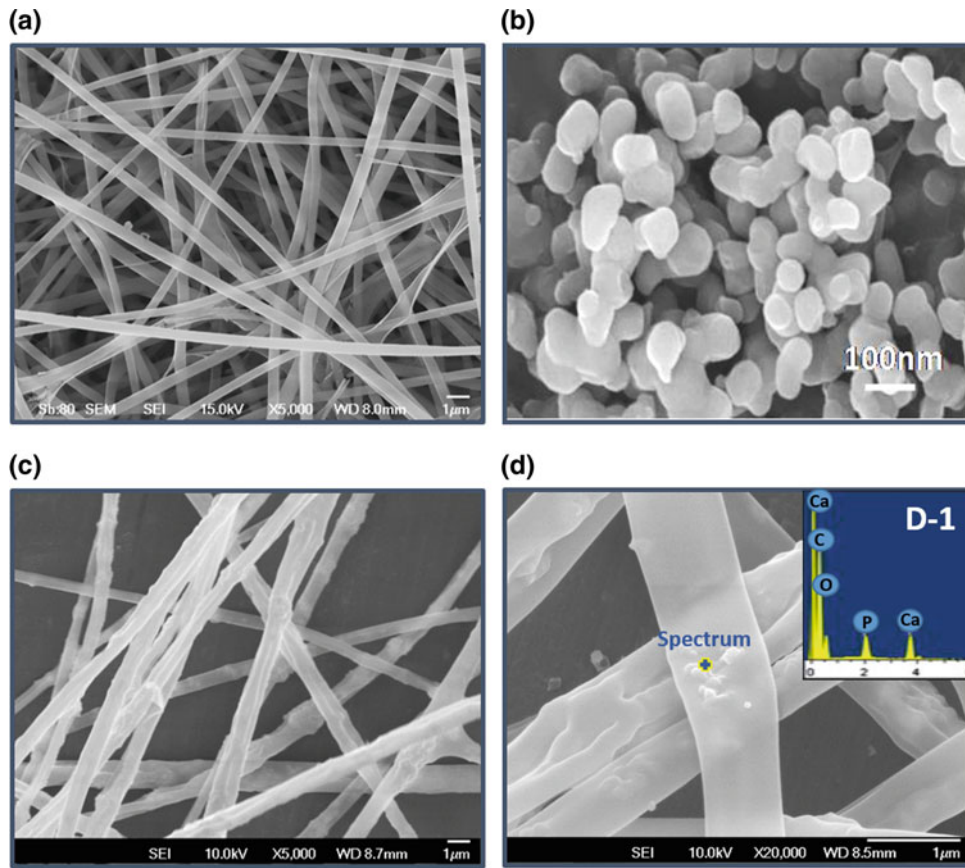


Fig. 1 The morphology of nano-fiber PVA/GE (a), BCP nano-particles (b), BCP loaded PVA/GE in low magnification (c) and high magnification (d) and EDS spectrum (D-1)

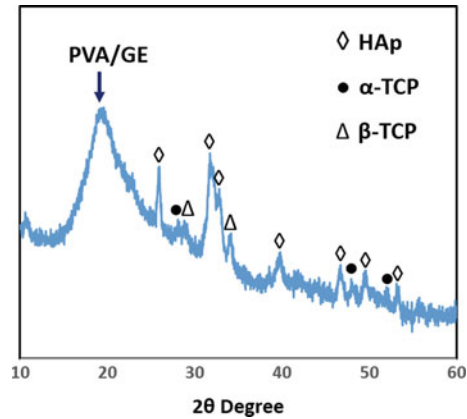
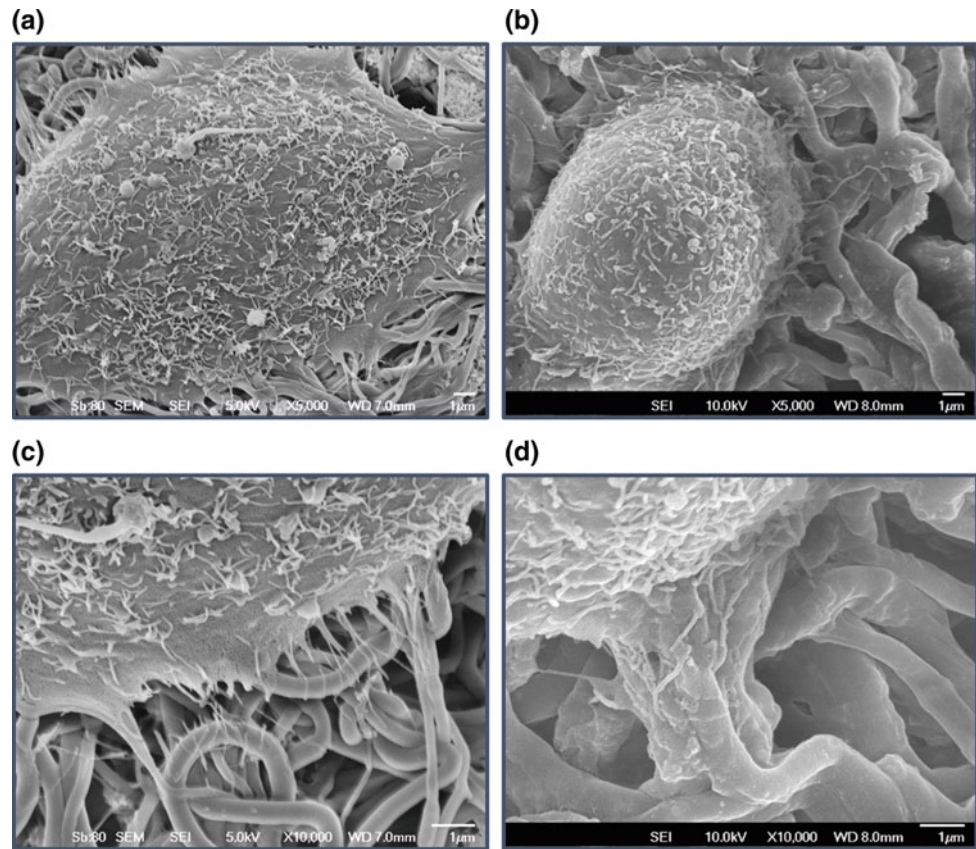


Fig. 2 XRD profile of 60% BCP nanoparticles loaded PVA/GE fibers

Fig. 3 The morphology of MG-63 on PVA/GE scaffolds (a and c) and on BCP-PVA/GE scaffolds (b and d) after 1 h of seeding



provided a large surface area for cell residence and proliferation, and effectively simplified the exchange of nutrients between the scaffold environments. Figure 3 showed that the osteoblast cells were attached on both PVA/GE and BCP-PVA/GE after 1 h of incubation. The surface topography of nano-fibers plays an important role in cell behavior, including cell adhesion [14]. It is known that human cells can attach and organize themselves well around fibers with diameters smaller than those of the cells [15]. This might explain the behavior of the MG-cells on the combined scaffolds, which had a nano-scale structure.

4 Conclusions

PVA/GE and BCP-PVA/GE fibers were produced using the electrospinning technique. Fibers could also be formed into 3D structures, which have the potential for use as bone tissue engineering scaffolds. BCP nano-particles were well distributed in the PVA-GE nano-fibrous matrix for improving similarity to bone component. We also found that the mesh structures of the scaffold were suitable for cell adhesion containing BCP nano-particles. This was confirmed by the results of the *in vitro* cell culture studies. In addition, osteoblasts that grew over the scaffold surfaces exhibited the

appropriate morphology and displayed good attachment, suggesting that the developed scaffolds might be used for bone tissue engineering applications.

Conflicts of Interest Statement The author(s) declared no potential conflicts of interest with respect to the research, authorship, and/or publication of this article.

References

1. Patrick, C.W., Mikos, A.G., McIntire, L.V.: *Frontiers in Tissue Engineering*. Elsevier (1998)
2. Greiner, A., Wendorff, J.H.: *Angew. Chem. Int. Ed.* **46**(30), 5670–5703 (2007)
3. Zhang, Y., Ouyang, H., Lim, C.T., Ramakrishna, S., Huang, Z.M.: *J. Biomed. Mater. Res. Part B: Appl. Biomater.* **72**(1), 156–165 (2005)
4. Rujitanaroj, P.-O., Pimpha, N., Supaphol, P.: *Polymer* **49**(21), 4723–4732 (2008)
5. Linh, B., Thuy, N., Lee, K.H., Lee, B.T.: *J. Biomed. Mater. Res. Part A* **101**(8), 2412–2423 (2013)
6. Zhang, H., Xia, J., Pang, X., Zhao, M., Wang, B., Yang, L., Wan, H., Wu, J., Fu, S.: *Mater. Sci. Eng. C* **73**, 537–543 (2017)
7. Lutolf, M., Hubbell, J.: *Nat. Biotechnol.* **23**(1), 47 (2005)
8. Linh, N.T.B., Lee, B.-T.: *J. Biomater. Appl.* **27**(3), 255–266 (2012)
9. Yang, D., Li, Y., Nie, J.: *Carbohydr. Polym.* **69**(3), 538–543 (2007)

10. Jayaraman, P., Gandhimathi, C., Venugopal, J.R., Becker, D.L., Ramakrishna, S., Srinivasan, D.K.: *Adv. Drug Deliv. Rev.* **94**, 77–95 (2015)
11. Tateishi, T., Chen, G., Ushida, T.: *J. Artif. Organs* **5**(2), 77–83 (2002)
12. Liu, X., Ma, P.X.: *Ann. Biomed. Eng.* **32**(3), 477–486 (2004)
13. Linh, N.T.B., Min, Y.K., Song, H.Y., Lee, B.T.: *J. Biomed. Mater. Res. Part B: Appl. Biomater.* **95**(1), 184–191 (2010)
14. Teixeira, A.I., Nealey, P.F., Murphy, C.J.: *J. Biomed. Mater. Res. Part A* **71**(3), 369–376 (2004)
15. Laurencin, C.T., Ambrosio, A., Borden, M., Cooper Jr., J.: *Annu. Rev. Biomed. Eng.* **1**(1), 19–46 (1999)

Effect of Polyvinyl Alcohol Concentration on Properties of Polyvinyl Alcohol-Chitosan Hydrogel Loading Silver Nanoparticles

Ngoc Thi-thanh Nguyen, Nam Minh-phuong Tran[✉],
and Thi-Hiep Nguyen[✉]

Abstract

Moisturizing ability makes hydrogel wound dressing the optimal treatment for dry wound, but this feature also creates a convenient environment for proliferation of microorganisms. The loading of silver nanoparticles (AgNPs), which exhibit wide-spectrum antimicrobial activity, into the wound dressing helps counter this problem. However, a hydrogel matrix with suitable properties is required to maintain the size and activity of AgNPs as well as control their release kinetic. Here this research formulated hydrogel composites from polyvinyl alcohol (PVA) and chitosan (Cs) loading with AgNPs and initially examined their qualities. Microwave irradiation was used to synthesize AgNPs by reducing silver nitrate and crosslink PVA with Cs. Based on its sensitive crosslinking behavior, the concentration of PVA was varied in the composition to investigate its effect on the characteristics of the hydrogels. Fourier transform infrared (FT-IR) spectroscopy and thermogravimetric analysis (TGA) were performed to observe the interaction between the components of the hydrogels and the change in thermal property of the hydrogels caused by this variation.

Keywords

Polyvinyl alcohol • Silver nanoparticles • Chitosan • Hydrogel • Wound dressing

Ngoc Thi-thanh Nguyen and Nam Minh-phuong Tran—contributed equally.

N. T. Nguyen (✉) · N. M. Tran · T.-H. Nguyen
Department of Biomedical Engineering, International University,
Vietnam National University- Ho Chi Minh City (VNU-HCMC),
700000 Ho Chi Minh City, Vietnam
e-mail: thanhngocvn1989@gmail.com

T.-H. Nguyen
e-mail: nthiep@hcmiu.edu.vn

1 Introduction

Wound dressings play a key role in wound healing process due to their ability to preserve moisture at the wound site and protect the wound against pathogens [1]. Thus, hydrogel, typically a network of three-dimensional cross-linked polymers which retains large amount of water, is recommended for dry or minimally exudative wounds [2]. However, a moist environment is also favorable for bacterial invasion and proliferation so hydrogel dressing is preferred to have decent and prolonged antibacterial activity [3].

In avoidance of antibiotic usage, silver nanoparticles (AgNPs) are proposed as a suitable agent to be loaded into hydrogel dressing to offer antibacterial and anti-inflammatory activity. Their antibacterial efficacy is sufficient even with low concentration due to their high surface area to volume ratio [4]. Moreover, the effective duration of AgNPs is extended since they can release silver ions, which maintain the antibacterial efficacy of the agent with similar but not fully-understood mechanisms. AgNPs have also been reported to have a wide antimicrobial effect on virus, fungi and antibiotic-resistance bacteria [5]. Among various physical or chemical methods used to synthesize AgNPs, the microwave irradiation synthetic method applied on silver nitrate solution were known to be safe, do not required toxic chemical and highly effective. However, the nanoparticles synthesized by this procedure are unable to maintain their shape and size in solution due to rapid oxidation and aggregation tendency, which can mitigate their antibacterial activity [6]. Therefore, the encapsulation by a carrying matrix is required to maintain the size and activity of AgNPs as well as control the release kinetic of silver ions.

Between a variety of polymers suitable for biomedical application, chitosan (Cs) and polyvinyl alcohol (PVA) are promising hydrogel-forming and capping agents. Their combination allows the fabrication of composite hydrogels with antimicrobial activity, biocompatibility and biodegradability provided by Cs [7], as well as the

mechanical strength and thermal stability of synthetic PVA [8]. The characteristics of this mixture can be further improved using microwave irradiation, which can crosslink PVA and Cs without any chemical agent [9]. However, PVA exhibits thermal-sensitive, radiation-sensitive crosslinking behavior which can destabilize its properties and its interaction with Cs.

Thus, the variation of PVA concentration can produce significant changes in the thermal properties and chemical interaction of PVA-Cs mixture together with its silver-stabilizing ability. This work investigated the effect of such variation on PVA loading AgNPs (PA) hydrogel and PVA-Cs loading AgNPs (PCA) hydrogel which were fabricated using microwave irradiation. The hydrogels were examined by Fourier transform infrared (FT-IR) spectroscopy and thermogravimetric analysis (TGA) to observe the interaction between their components and the change in thermal property of the hydrogels.

2 Materials and Methods

2.1 Materials

Polyvinyl alcohol (hydrolysis degree of 99.0–99.8%) and chitosan (from shrimp shells, $\geq 75\%$ deacetylated) were purchased from Sigma Aldrich, USA. Acetic acid and silver nitrate were purchased from Xilong Chemical Co., Ltd (China). Deionized water (DI) was used as the solvent in all experiments.

2.2 Methods

Synthesis of PA hydrogels and PCA hydrogels. Chitosan solution (2% w/v) was prepared by dissolving and continuously stirring Cs in diluted acetic acid solution (2% v/v) for 24 h at room temperature. PVA solutions (6, 8 and 10% w/v) were prepared by dissolving PVA in deionized water at 90 °C for 4 h. Silver nitrate was dissolved in deionized water in dark room to create silver nitrate solution (1% w/v). Each of PVA solutions were blended and stirred for 30 min with silver nitrate solution (1% w/v) to create solution with silver concentration of 120 ppm. Then, each of the solutions was poured into a separate beaker and irradiated in microwave (Whirlpool, China) at 800 W for 90 s to create PA solutions. Immediately after the treatment, Cs solution was blended with PA solutions with the v/v ratio of 1:1 to create PCA hydrogels with silver concentrations of 60 ppm. All sample compositions were showed in Table 1.

Fourier transform infrared (FTIR) spectroscopy. FT-IR spectra of hydrogels were examined using a FT-IR

spectrometer (Tensor 27, Bruker, USA) with wave number from 500–4000 cm^{-1} .

Thermogravimetric analysis. TGA profile of the hydrogels was acquired by TA Instrument—Series Q500. The analyses were performed on specimens of 7–10 mg at 10 °C/min from 30 to 900 °C, in a nitrogen flow rate of 60 ml/min.

3 Results and Discussion

3.1 FT-IR Analyses

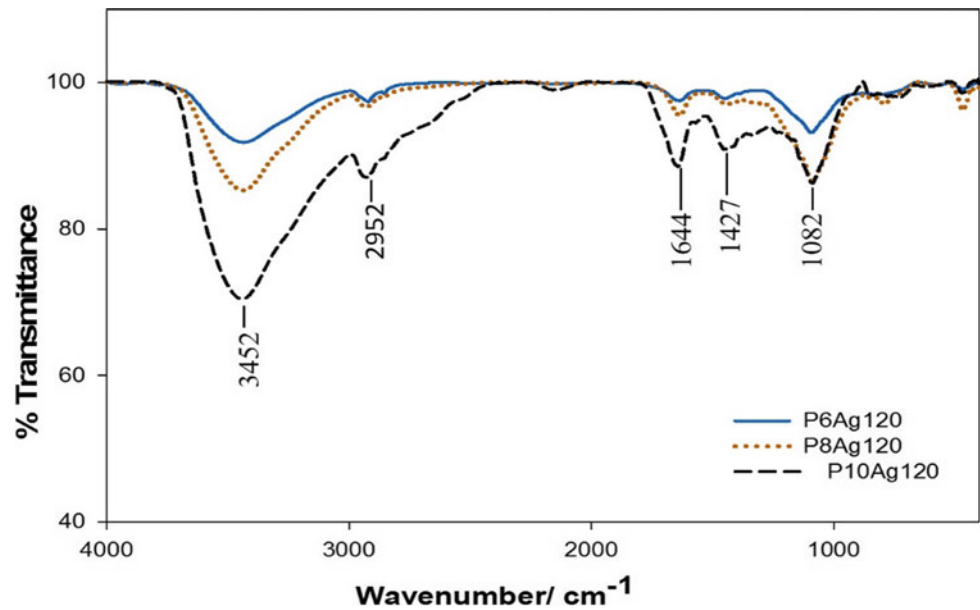
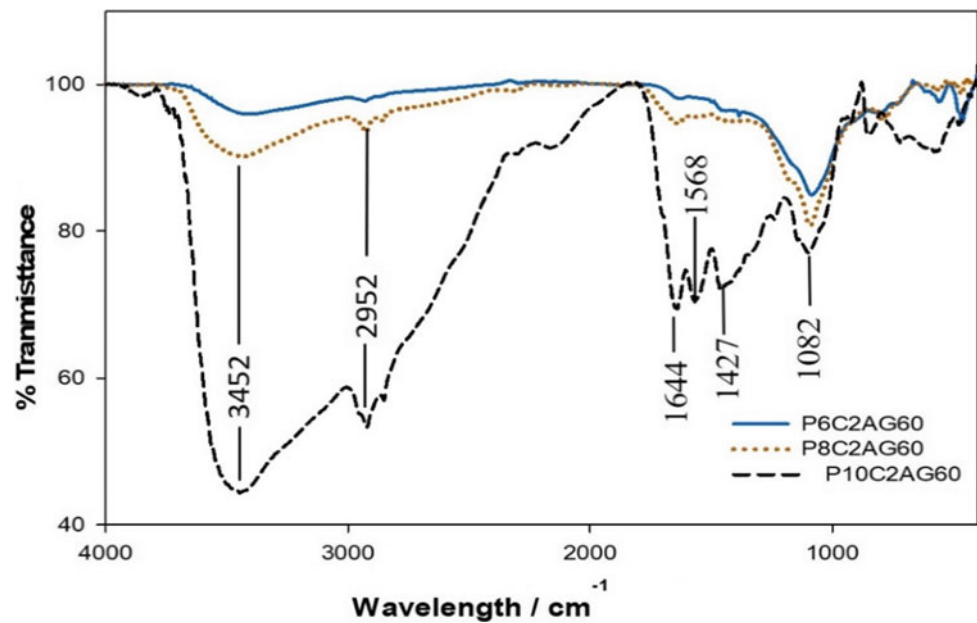
FTIR spectra of the PA and PCA hydrogels were obtained to examine their chemical functional groups and the interaction between PVA and Cs after microwave treatment. Figure 1 illustrates the FTIR spectra of three PA hydrogel samples: P6AG120, P8AG120 and P10AG120. Similar absorption bands at 3452, 2952, 1427 and 1082 cm^{-1} , which are assigned respectively to O–H stretching, C–H stretching, C–H bending and C–O stretching, were observed in all spectra [10, 11]. Moreover, a peak was observed at 1644 cm^{-1} which can be attributed to both $-\text{CH}_2-$ bending and C=O stretching [11]. The existence of these usual peaks suggests that there is no evidence of PVA degradation due to microwave irradiation, but the oxidation changing hydroxyl groups into aldehyde groups may have occurred. In addition, the absorption of P10AG120 was notably more intense than which of P6AG120 and P8AG120. We attribute this change to the increase of crosslink density of the polymer induced by the increase of PVA concentration.

In Fig. 2, the absorption bands in the spectra of PCA hydrogels indicated the occurred changes when PA hydrogel was blended with Cs. Beside absorption bands similar to FT-IR spectra of PA samples, all the PCA hydrogels exhibited new peaks around 896 and 1160 cm^{-1} expressing polysaccharide structure of Cs. Furthermore, the broadening of the region around 3444 cm^{-1} can be attributed to the presence of hydrogen bonds between hydroxyl groups of PVA and amine groups of Cs causing O–H/N–H stretching [12]. In the spectra of P10C2AG60, an additional peak was identified at 1568 cm^{-1} . This peak was unobservable in the profile of the other two samples and it is strongly associated with amide II group [13]. Thus, the appearance of this peak may suggest the interaction between amine group of Cs and the newly formed aldehyde group of PVA to form covalent bonds through Schiff base linkage. The notation that this peak was only detected in the latter sample may also indicate that the PVA concentration of 10% is critical to initiate this reaction.

Expectedly, the absorption of P10C2AG60 was significantly higher than which of P6C2AG60 and P8C2AG60.

Table 1 The compositions of the fabricated hydrogel samples

Sample	Polyvinyl alcohol (%w/v)	Chitosan (%w/v)	AgNO ₃ (ppm)
P6AG120	6	0	120
P8AG120	8	0	120
P10AG120	10	0	120
P6C2AG60	6	2	60
P8C2AG60	8	2	60
P10C2AG60	10	2	60

Fig. 1 FTIR spectra of P6AG120, P8AG120 and P10AG120**Fig. 2** FTIR spectra of P6C2AG60, P8C2AG60 and P10C2AG60

trait is preferable in wound dressing application or not, further investigations on biocompatibility and bioactivity of the hydrogels are necessary.

4 Conclusion

In this study, the effect of PVA concentration on chemical composition and thermal stability of PA and PCA hydrogels was investigated to determine the suitable matrix for AgNPs loading and stabilization. The results of FT-IR suggest the formation of hydrogen bonds and covalent bonds between PVA and Cs, which induced an elevated crosslink density along with the increase in PVA concentration. A sharp rise of these intermolecular interactions in PCA hydrogel with 10% PVA w/v was observed. Thus, TGA analyses indicate that P10C2AG60 provided the highest thermal stability, which can be favorable in immobilization of AgNPs. Nevertheless, further tests need to be conducted to examine the effect of these changes on the biological performance of this type of hydrogel system, specifically in wound dressing application.

Acknowledgements This research is funded by Vietnam National University HoChiMinh City (VNU-HCM) under grant number C2018-28-02.

Conflict of Interest The authors declare that they have no conflict of interest.

References

- Perry, A.G., Potter, P.A., Ostendorf, W.: *Clinical Nursing Skills and Techniques8: Clinical Nursing Skills and Techniques*. Elsevier Health Sciences (2013)
- Kopeček, J.: Hydrogel biomaterials: a smart future? *Biomaterials* **28**(34), 5185–5192 (2007)
- Trudgian, J.: Investigating the use of aquaform hydrogel in wound management. *Br. J. Nurs.* **9**(14), 943–948 (2000)
- Iravani, S., Korbekandi, H., Mirmohammadi, S.V., Zolfaghari, B.: Synthesis of silver nanoparticles: chemical, physical and biological methods. *Res. Pharm. Sci.* **9**(6), 385 (2014)
- Lara, H.H., Garza-Treviño, E.N., Ixtapan-Turrent, L., Singh, D.K.: Silver nanoparticles are broad-spectrum bactericidal and virucidal compounds. *J. nanobiotechnol.* **9**(1), 30 (2011)
- Hiep, N.T., Khon, H.C., Niem, V.V.T., Toi, V.V., Ngoc Quyen, T., Hai, N.D., Ngoc Tuan Anh, M.: Microwave-assisted synthesis of chitosan/polyvinyl alcohol silver nanoparticles gel for wound dressing applications. *Int. J. Polym. Sci.* **2016** (2016)
- Jayakumar, R., Prabakaran, M., Kumar, P.S., Nair, S., Tamura, H.: Biomaterials based on chitin and chitosan in wound dressing applications. *Biotechnol. Adv.* **29**(3), 322–337 (2011)
- Abraham, A., Soloman, P., Rejini, V.: Preparation of chitosan-polyvinyl alcohol blends and studies on thermal and mechanical properties. *Procedia Technol.* **24**, 741–748 (2016)
- Hennink, W.E., van Nostrum, C.F.: Novel crosslinking methods to design hydrogels. *Adv. Drug Deliv. Rev.* **64**, 223–236 (2012)
- Xiao, C., Yang, M.: Controlled preparation of physical cross-linked starch-g-PVA hydrogel. *Carbohydr. Polym.* **64**(1), 37–40 (2006)
- Lambert, J.B.: *Organic Structural Spectroscopy*. Pearson College Division (1998)
- Al Sagheer, F., Al-Sughayer, M., Muslim, S., Elsabee, M.Z.: Extraction and characterization of chitin and chitosan from marine sources in Arabian Gulf. *Carbohydr. Polym.* **77**(2), 410–419 (2009)
- Li, L., Wang, N., Jin, X., Deng, R., Nie, S., Sun, L., Wu, Q., Wei, Y., Gong, C.: Biodegradable and injectable in situ cross-linking chitosan-hyaluronic acid based hydrogels for postoperative adhesion prevention. *Biomaterials* **35**(12), 3903–3917 (2014)
- Hezma, A., Elashmawi, I., Rajeh, A., Kamal, M.: ISSN 0975-413X CODEN (USA): PCHHAX
- Bonilla, J., Fortunati, E., Atarés, L., Chiralt, A., Kenny, J.: Physical, structural and antimicrobial properties of poly vinyl alcohol–chitosan biodegradable films. *Food Hydrocoll.* **35**, 463–470 (2014)
- Casey, L.S., Wilson, L.D.: Investigation of chitosan-PVA composite films and their adsorption properties. *J. Geosci. Environ. Prot.* **3**(02), 78 (2015)

Fabrication Drug Loaded Polycaprolactone Microparticles by Electrospraying Method

Viet Linh Nguyen-Vu and Dai Phu Huynh

Abstract

The drugs such as Insulin and Paclitaxel were encapsulated in Polycaprolactone (PCL) by electrospraying method. Some fabricated factors which influenced the morphology of PCL microparticles were investigated. Electrospraying is an effective and approachable method to produce considerable solid drug-loaded microparticles for drug delivery system. Using the Scanning electron microscopy to observe the morphology and size of particles and Thermal Analysis evaluated the compatibility of drug and polymer matrix. The toxicity of products was determined by checking the existence of solvent inside the electrosprayed particles. The results showed that the drug-loaded microspheres were fabricated at 15–20% drug (w/w), 4.5% PCL in Dichloromethane. Besides, the hydrophobic drug (Paclitaxel) had a good compatibility with PCL matrix, therefore, the surface of particles was smoother. In case of Insulin, it and PCL created a suspension and consequently generated the undesirable morphology with holes and wrinkled surfaces. The drug-loaded microparticles didn't contain toxic solvent so that it can be applied in pharmacy.

Keywords

Electrospraying • Drug-loaded particles • Polycaprolactone • Insulin • Paclitaxel

1 Introduction

Electrospraying is an efficient method to fabricate solid drug-loaded microparticles in drug carrier system over the conventional treatment due to some advantages such as macromolecules high penetration, high loading capacity, simple process, and ability for encapsulating both hydrophobic and hydrophilic drug [1–3]. Besides some drug delivery systems such as liposome, micro-emulsion, solvent evaporation, hydrogel, spray drying, layer by layer, etc..., the electrospraying technique fabricated solid micro(nano)-particles has been studying to lengthen the release time of drug or protein; increase safety and the patient compliances [4, 5]. Depend on the desirable degradation of the drug carrier and the release of drug from the polymer matrix, the sort of polymer would be chosen. Thank more ester groups on polymer backbone than PCL, Poly(lactic-co-glycolic)acid (PLGA) and Polylactic acid (PLA) are suitable for short-term drug release while PCL microparticles are suitable for long-term release system [1, 2, 6]. In previous studies, PLGA and PLA encapsulated some hydrophilic drugs (Salbutamol sulfate, Bovine serum albumin, oestradiol, etc...) and hydrophobic drugs (Beclomethasone dipropionate, Paclitaxel, Celecoxib) [7–10]. In case of PCL, a hydrophobic polymer, it combined with Paclitaxel (PTX) to form the PTX-loaded PCL microparticles for the brain tumor treatment [9, 10]. Besides PTX, some kind of drug was encapsulated with PCL such as β - Oestradiol, Bovine serum albumin (BSA) [11, 12]. In this research, the insulin-loaded PCL microparticles were fabricated and compared with PTX-loaded PCL particles about the morphology, compatibility of polymer and drug.

V. L. Nguyen-Vu (✉)

Faculty of Materials Technology, Ho Chi Minh City University of Technology, VNU-HCM, Ly Thuong Kiet Street, District 10, Ho Chi Minh City, Vietnam
e-mail: nguyenvvietlinh@hcmut.edu.vn

D. P. Huynh

National Key Laboratory of Polymer and Composite Materials, Ho Chi Minh City University of Technology, VNU-HCM, Ly Thuong Kiet Street, District 10, Ho Chi Minh City, Vietnam

2 Materials and Methodology

2.1 Materials

Polycaprolactone (PCL) (average $M_n = 80$ kDa) and Paclitaxel (PTX) were purchased from Sigma-Aldrich, Singapore. Insulin, Human Recombinant was obtained from SAFC Biosciences, US. Dichloromethane (DCM) was used as an organic solvent and supplied by Fisher Scientific, Vietnam, 99.5% purified.

2.2 Fabrication Drug-Loaded Polycaprolactone by Electrospaying

The polymer solution was prepared by dissolving PCL in DCM at room temperature for 1.5 h. Then, the drug (insulin or PTX) was added to PCL solution and stirred for 1 h. Next, they were filled in a 10 ml glass syringe with a flat stainless steel needle on top (Gauge 20G). Next, this syringe was placed in a Micropump Top-5300 (Japan) with adjustable flow rate. Finally, the solid drug-loaded PCL particles were collected in aluminum foil thanks to the solvent evaporation and Coulomb fission when the electrospaying happened [13].

2.3 Methods

Scanning Electron Microscopy (SEM), Hitachi S4800-Japan, was used to determine the morphology of drug-loaded microparticles. The accelerating voltage of SEM was set at 5 kV during scanning. The DCM solvent in the drug-loaded particles was detected by Gas Chromatography—Mass Spectrometry (GC-MS), GC 7890A/5975C MS detector (Agilent Technology, US) and equipped with a

non-polar column DB-5 (Agilent Technology, US). The detector was operated in electron impact ionization mode (electron energy 70 eV). The injection port was operated in split mode 1:10, Helium (99.99% purity) was used as a carrier gas, 280 °C. The column temperature was kept at 50 °C for 3 min, increasing at 10 °C/min to 150 °C.

The Differential scanning calorimetry (DSC) spectrum (NETZSCH DSC 204F1 Phoenix—Germany) evaluated the interaction of drug and PCL. The temperature was increased gradually from 30 to 250 °C, with step 5 °C/min, in the Nitrogen environment.

3 Results and Discussion

3.1 Effect of PCL Concentration and Flow Rate on the Morphology of the PTX-Loaded and Insulin-Loaded PCL Particles

Polymer concentration and flow rate are main factors influence the morphology of the PCL particles. The high number of chain entanglements can be created by high polymer concentration or low flow rate due to increasing the density of polymer chains in the electrospay droplets [1, 13].

With high chain entanglements in solution, the heterogeneous morphology of PTX-loaded PCL particles such as tapered particles, beaded fibers and spheres were generated (Fig. 1a). Whereas, lower PCL concentration (4.2%) and higher flow rate (1.3 mL/h) created homogeneous spheres (Fig. 1b, c) although their size was different.

In case the insulin-loaded particles, lower PCL concentration (4.5%) created the hollow and corrugated particles (Fig. 2a, b) while 4.75% PCL generated microspheres (Fig. 2c). Moreover, the microparticles were deformed and sticky on the collector due to the presence of the solvent in the particles at a high flow rate (Figs. 1c and 2b, c).

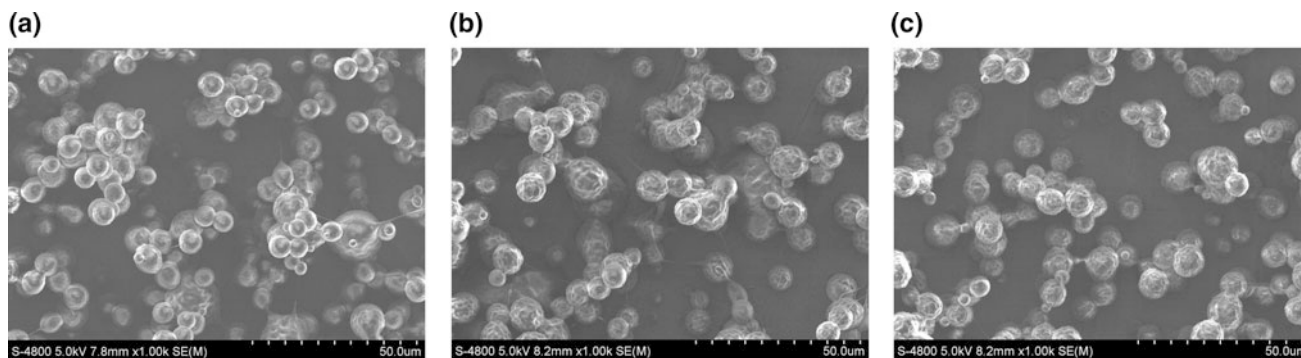


Fig. 1 SEM images of 15% PTX-loaded PCL particles; **a** 4.5% PCL, 1.2 mL/h; **b** 4.2% PCL, 1.2 mL/h; **c** 4.2% PCL, 1.3 mL/h (voltage 18 kV, collecting distance 21 cm)

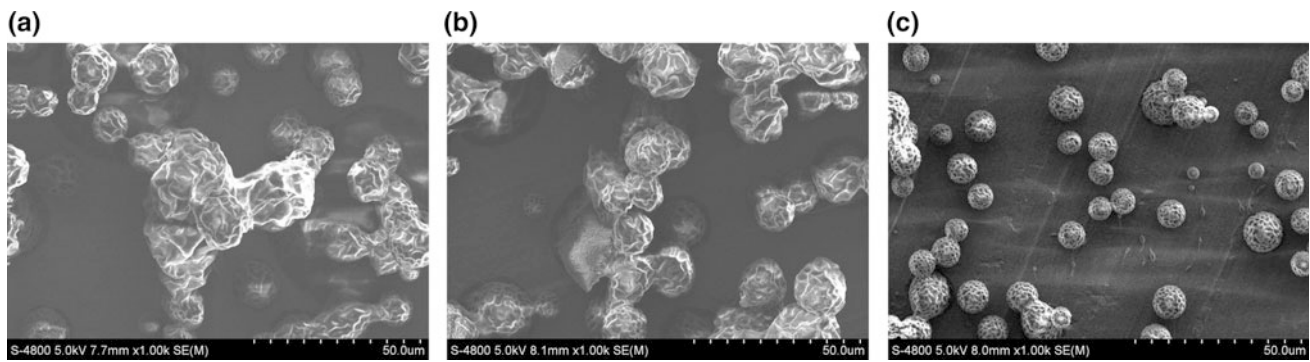


Fig. 2 SEM images of 20% insulin-loaded particles: **a** 4.5% PCL, 1 mL/h; **b** 4.5% PCL, 1.2 mL/h; **c** 4.75% PCL, 1.2 mL/h (voltage 18 kV, collecting distance 21 cm)

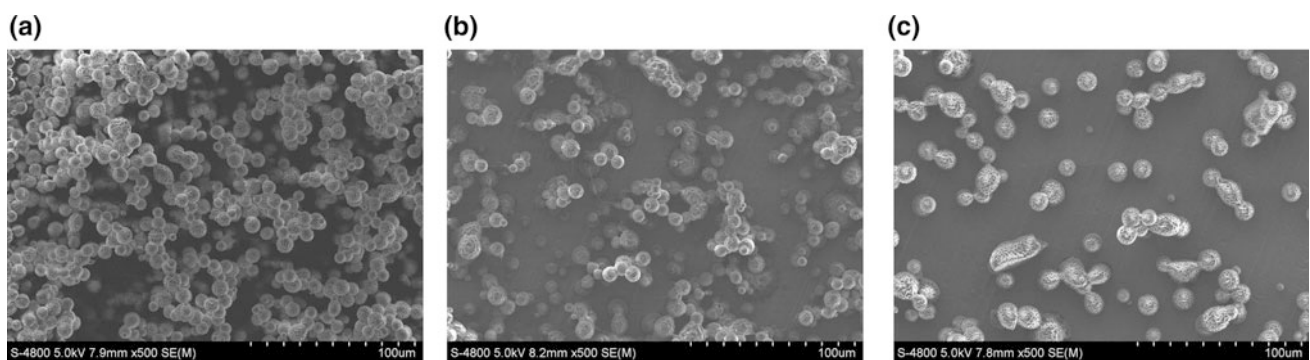


Fig. 3 SEM micrograph of drug-loaded PCL microparticles; 4.5% PCL in DCM, applied voltage 18 kV, gauge 20G, collecting distance 21 cm, flow rate 1.2 ml/h with **a** no drug, **b** 15% PTX in PCL particles and **c** 15% insulin in PCL particles (w/w)

3.2 Fabrication Drug-Loaded PCL Particles by Electrospaying

The results indicated that the nature of drug impact on the distribution of drug inside the polymer matrix and the particles' morphology. The hydrophobic drug (PTX) was compatible effectively with PCL, the hydrophobic polymer, therefore small molecule of PTX could fill the hollow and pore inside the microparticles [9]. The PTX-loaded particles were dense microspheres with smoother surfaces (Fig. 3b). In case of a hydrophilic drug, insulin was suspended in PCL solution due to insolubility and incompatibility with polymer. Therefore, the sedimentation and the migration of drug on and near the surface particles were formed during spraying. Figure 3c showed that the morphology of the

insulin-loaded particles was irregularly corrugated and aggregated.

3.3 Evaluate the Properties of Electrospayed Drug-Loaded PCL Microparticles

According to the results of GC-MS, the DCM solvent cannot be detected in the drug-loaded PCL microparticles due to the completed solvent evaporation (Fig. 4). Therefore, the drug-loaded particles are non-toxic and safe in drug delivery system application.

The DSC Thermogram showed that the melting transition peak of Paclitaxel (180–250 °C) [9] was indistinct, as a result of the PTX is well dispersed and compatible in the

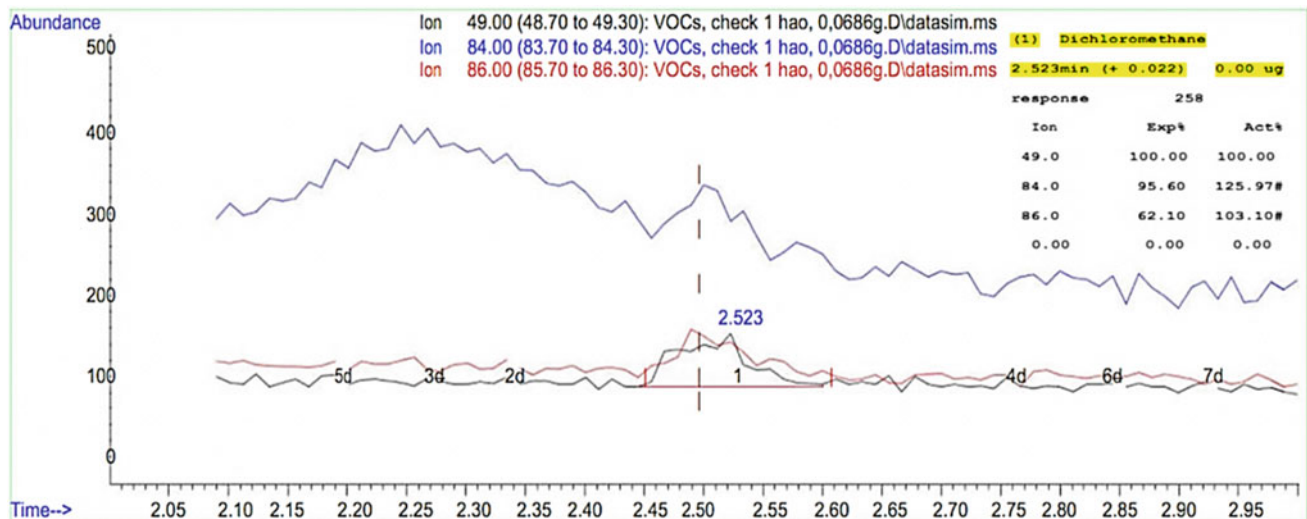


Fig. 4 The GC-MS spectrum of detecting DCM in PCL particles

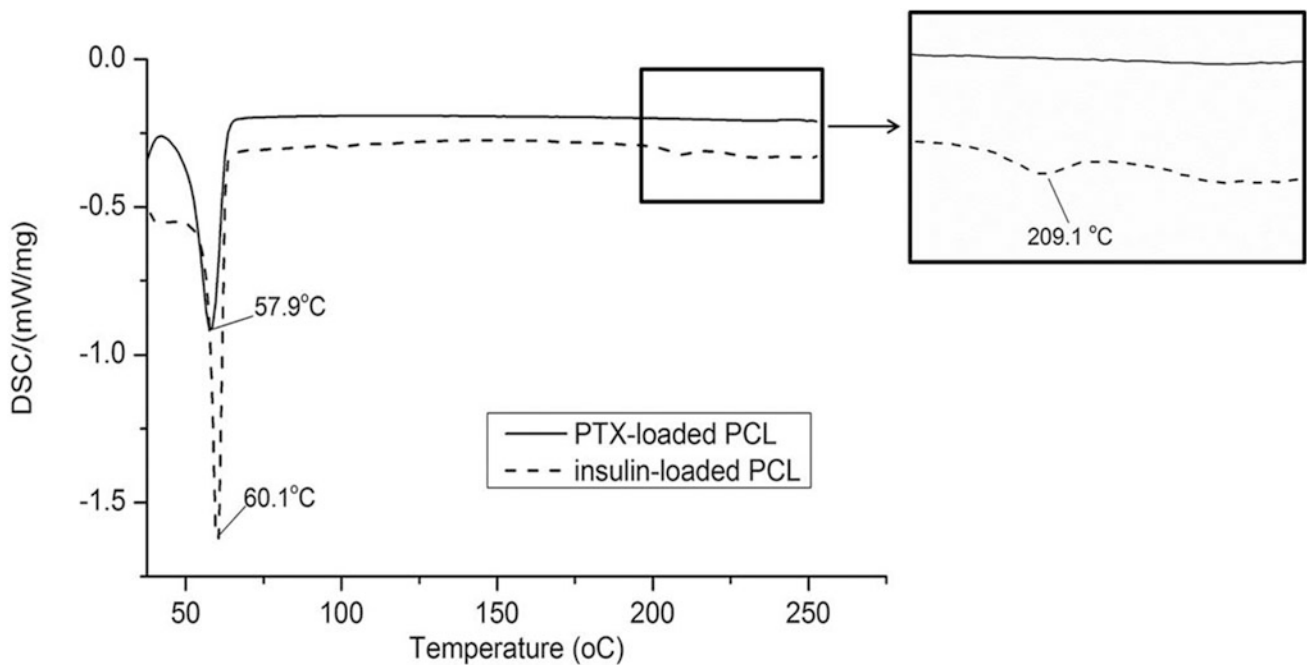


Fig. 5 DSC thermogram of electrosprayed drug-loaded PCL particles (drug: insulin and PTX)

PCL matrix. While insulin wasn't integrated with Polymer, therefore, the melting transition peak of Insulin (200–220 °C) was detected (Fig. 5).

4 Conclusion

The homogeneous drug-loaded microspheres can be generated by tailoring the electrosprayed parameters such as PCL concentration and flow rate. Besides, PCL can combine both

hydrophobic drug (PTX) and hydrophilic drug (insulin) and create the drug-loaded particles. PTX is more compatible with PCL matrix than insulin thank to the similar hydrophobic property. They don't contain the toxic solvent (DCM) after drying so that they can be applied to drug carrier system.

Acknowledgements This research is funded by Ho Chi Minh City University of Technology, VNU-HCM, under grant number BK-SDH-2019-1585030.

Conflict of Interest Statement The authors declare that they have no conflict of interest.

References

1. Bock, N., Dargaville, T.R., Woodruff, M.A.: Electrospraying of polymers with therapeutic molecules: state of the art. *Prog. Polym. Sci.* **37**(11), 1510–1551 (2012)
2. Xie, J., Jiang, J., Davoodi, P., Srinivasan, M.P., Wang, C.-H.: Electrohydrodynamic atomization: a two-decade effort to produce and process micro-/nanoparticulate materials. *Chem. Eng. Sci.* **125**, 32–57 (2015)
3. Nguyen, D.N., Clasen, C., Van den Mooter, G.: Pharmaceutical applications of electrospraying. *J. Pharm. Sci.* **105**(9), 2601–2620 (2016)
4. Chakraborty, S., Liao, I.-C., Adler, A., Leong, K.W.: Electrohydrodynamics: a facile technique to fabricate drug delivery systems. *Adv. Drug Deliv. Rev.* **61**(12), 1043–1054 (2009)
5. Bruschi, M.L.: *Classification of Therapeutic Systems for Drug Delivery: ‘Strategies to Modify the Drug Release from Pharmaceutical Systems’*, pp. 29–36. Woodhead Publishing (2015)
6. Woodruff, M.A., Hutmacher, D.W.: The return of a forgotten polymer Polycaprolactone in the 21st century. *Prog. Polym. Sci.* **35**(10), 1217–1256 (2010)
7. Valo, H., Peltonen, L., Hirvonen, J., et al.: Electrospray encapsulation of hydrophilic and hydrophobic drugs in poly(l-lactic acid) nanoparticles. *Small* **5**(15), 1791–1798 (2009)
8. Bohr, A., Kristensen, J., Stride, E., Dyas, M., Edirisinghe, M.: Preparation of microspheres containing low solubility drug compound by electrohydrodynamic spraying. *Int. J. Pharm.* **412**(1), 59–67 (2011)
9. Ding, L., Lee, T., Wang, C.H.: Fabrication of monodispersed Taxol-loaded particles using electrohydrodynamic atomization. *J. Control Release* **102**(2), 395–413 (2005)
10. Xie, J., Marijnissen, J.C., Wang, C.H.: Microparticles developed by electrohydrodynamic atomization for the local delivery of anticancer drug to treat C6 glioma in vitro. *Biomaterials* **27**(17), 3321–3332 (2006)
11. Enayati, M., Ahmad, Z., Stride, E., Edirisinghe, M.: Size mapping of electric field-assisted production of polycaprolactone particles. *J. R. Soc. Interface* **7**, S393–S402 (2010)
12. Xu, Y., Hanna, M.A.: Electrosprayed bovine serum albumin-loaded tripolyphosphate cross-linked chitosan capsules: synthesis and characterization. *J. Microencapsul.* **24**(2), 143–151 (2007)
13. Nguyen-Vu, V.L., Tran, N.H., Huynh, D.P.: Taylor cone-jet mode in the fabrication of electrsprayed microspheres. *Vietnam J. Sci. Technol.* **55**(1B), 216–222 (2017)

Observation of Fibroblast Cell Attachment and Proliferation on Different Titanium Surface Textures: Morphology and In Vitro Study

Minh Thuy Vo, Thanh Truc Nguyen, Hieu Minh Ho, Loan Khanh Ly, Vo Van Toi, Le Minh Huynh, and Thi-Hiep Nguyen

Abstract

For dental implant, Titanium abutments were statically reported failure of long-term implantation related to soft tissue defects, unpredictable esthetic outcome and bacterial leakage by positioning failure. Recently, a dominant influence of the surface modification for the soft tissue integration at the Titanium implant tissue interface has found in a lot of experimental studies. The purpose of present study is evaluation of fibroblast cell behaviors on different modified Titanium surface including Titanium (Ti) alloys, Titanium dioxide (TiO₂) and Ti modified with Collagen type I (TiCol-1) at various time intervals of cell culturing. Titanium plates were treated with NaOH and Collagen type I (Col-1) deposition in 2 different patterns. Polished and sand-blasted titanium plates were used as control group. Specimen surface properties were determined using scanning electron microscopy (SEM). Fibroblast cell behavior on modified surfaces was analyzed by SEM images for cell adhesion, viability, proliferation. The results suggested that modified Ti surfaces had significant affect the viability of fibroblast cells and improved adhesion was measured in Col-1 modification groups after 1 h and 1 day. Proliferation study showed that the density of

fibroblast cells after 3 days cultured on TiCol-1 was higher and comparable with that of other groups. As for cell membrane adhesion, cells grew after 5 days on Collagen modified surfaces also had higher expression as compared with titanium treated by NaOH. In conclusion, TiCol-1 surface seems to favor fibroblast adhesion.

Keywords

Titanium • Adhesion • Proliferation • Collagen type I

1 Introduction

Considerable effort in dental implants is currently being devoted to the design, synthesis and fabrication of biomaterials in order to obtain a long-term secure anchoring and provide retention for a fixed or removable prosthesis. Meanwhile, previous studies have mainly focused on enhancing the osseointegration of biomaterials implant, the dental implant failure come from the loss of soft tissue support in abutment. The soft tissue defects often happen with the volume loss of soft tissue or connective tissue detachment around the implant abutment leads to dislocation and imbalance of dental implant. The soft tissue around the implant, peri-implant mucosa, is similar in many ways to the Gingiva found around the tooth. The peri-implant tissue has important clinical implications that not only contribute to the anchorage of the tooth in the jaw, but also defend against foreign invaders at the interface between the teeth and the soft tissues and stabilize the tooth position. Thus, the need for establishment of a dense connective tissue around the implant abutment and supports the latter in the task of mucosa attachment is therefore becoming an increasing concern.

Titanium and its alloys have been widely discussed as a popularly metallic materials used for implantation thanks to its biocompatibility and excellent resistance. Ti is a proven material with attractive mechanical properties to replace

Vo Minh Thuy, Nguyen Thanh Truc, Ho Hieu Minh and Ly Loan Khanh—Contribution of Authors is similar.

M. T. Vo (✉) · T. T. Nguyen · H. M. Ho · L. K. Ly · V. Van Toi · T.-H. Nguyen

Department of Biomedical Engineering, International University, Vietnam National University-Ho Chi Minh City (VNUHCM), Ho Chi Minh City, 700000, Vietnam
e-mail: vmtbach153@gmail.com

T.-H. Nguyen
e-mail: nthiep@hcmiu.edu.vn

L. M. Huynh
Board of Management of Saigon High Tech Park of Ho Chi Minh City, Vietnam Department of Science, Technology Management and International Collaboration Lot T2-3, D1 Road, Saigon Hi-Tech Park, 9 Dist., Ho Chi Minh city, Vietnam

missing teeth and to repair fractured bone and joints. Even though Ti's bio-inert property is a positive factor to prevent the rejection of implant from the body immunogenesis, it simultaneously hinders a weak cell-implant interaction between the gingival fibroblast, lack of connective tissue support resulting in formation of a gap between abutments, hence, it is required to remove such implants [1–3].

Up to now, considerable effort to modify Ti surface with various types of biomaterials using different methods to restrict its bio-inert property [4], enhance the soft tissue integration and avoid its failure in implantation as mentioned above. In fact, Type I Collagen is the dominating type found in dense gingival fiber apparatus not only attaches the gingiva to the root cementum and the alveolar bone but also provides the rigidity and resistance of the gingiva [5]. Collagen type I is also a promising candidate for surface immobilization, regulating various aspects of cell behaviors, such as controlling cell migration and attachment by interacting integrin located on cell membrane [6]. The supposition is that the addition of Col-1 to a dental implant surface may similarly enhance its barrier capability and reduce the failure rate.

Besides the method using ECD method to obtain strong Collagen coating adhesion (under support of the bottom Ca-P layer) to Ti was reported the effective bone-implant interface [7]. Col-1 also functions as a component of gingival fibroblast's extracellular matrix [8, 9] while ECD is an optimal choice for Col-1 modification on Ti (without the existence of Calcium and phosphate ions) in respect to the fibroblast adhesion and soft tissue attachment. At previous study, Ti surface was successfully optimized using Col-1 by electrochemical deposition method [10]. TiCol-1 surface was proven for higher expression of fibroblast adhesion and proliferation compared with uncoated-Ti. The present studies have been concentrated giving facts from surface materials science and from biocompatibility testing to improve the cell behavior on modified materials with either a bio-inert coating (TiO₂) or a bio-interactive coating (Col-1). SEM images obtained from different Ti surfaces-cell culture was used to observe cell attachment and proliferation within 1 h, 1 day, 3 days and 5 days. The knowledge of these initial cell activities is important for studying and improving the biocompatibility of biomaterials.

2 Materials and Methods

2.1 Preparation of Titanium Samples Modified Different Surfaces

Polished and sand-blasted Titanium plates: Ti alloy 6AL-4V foil (BAOJI Energy Titanium CO., China) was cut in similar strips before being cleaned ultrasonically in ethanol 70° and distilled water by Elma Ultrasonic Cleaning machine.

Titanium dioxide: Ti plates were then soaked in 4 M NaOH solution for 2 h at 90 °C to produce sodium titanate hydrogel layer [11, 12].

Titanium modified Collagen type I: Bovine Type I Collagen Ligament purchased from Sigma Aldrich was dissolved in 5 M acetic acid (Xilong Chemical Co., Ltd.) to achieve Col-1 solutions 0.5 mg/ml, pH 5.5. Ti plate and Platinum (Pt) net acted as Cathode (–) and Anode (+) respectively. These two electrodes were placed opposite each other; at a distance of 15 mm; and in Col-1 solution. Time for ECD was set at 20 min, the coated Ti plates were then rinsed with distilled water and dried at room temperature [10].

2.2 Characterization of the Coating Ti/Col-1

All samples were analyzed by using a scanning electron microscope (SEM, JEOL JSM-IT100) at 5 and 16 kV to observe the changed morphology on Ti surfaces investigated. The chosen magnification was 5000×.

2.3 In Vitro Studies of Fibroblast Cell

Cell maintenance: Cell culture studies were carried out using the mouse fibroblast L929 cell line, which was obtained from ATCC. The cells were maintained in culture flask containing DMEM media. Cells were dissociated using trypsin-EDTA (GIBCO), were then centrifuged and resuspended in medium. The culture medium was changed every two days. After sterilization, 2 samples of each group (Ti, TiO₂, TiCol-1) were placed in 24-well plate and seeded with L929 fibroblast cells with 5×10^4 cells per well and incubated at 37 °C.

Sterilization: the samples including Ti, TiO₂, and TiCol-1 were sterilized by UV for 20 min and then in 70° ethanol for 20 min, finally rinsed with PBS.

SEM observation: the samples after distinct incubation time (1 h, 1 day, 3 days and 5 days) were washed with PBS, then fixed in 4% glutaraldehyde within 20 min; and rinsed thoroughly with PBS before being dehydrated with ethanol at room temperature. Once being dried, the samples were observed under SEM at 5 and 16 kV, with magnifications of 1000× and 8000×.

3 Results and Discussion

3.1 Morphology Observation

To further examine the surface of the processed samples, SEM images of the Ti plates were captured at high magnification. Figure 1a showed the native Ti alloy 6AL-4V foil

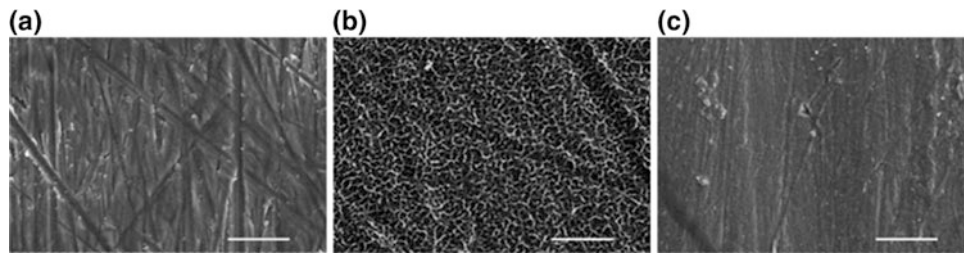


Fig. 1 SEM images of Ti surface: **a** Ti, **b** TiO₂ and **c** TiCol-1 by ECD (E = 2.0 V; t = 20 min; d = 1.5 cm; pH = 5.5) at 5000× (scale bar 5 μm)

plates were polished and sand-blasted at 5000×, respectively. Figure 1b showed Ti surface after being soaked in 4 M NaOH solution for 2 h at 90 °C. A uniform TiO₂ layer with a nanoporous scale was successfully created by heat treatments. This nanoporous, hydrophilic TiO₂ surface was seem to be very thin and resulting to changes of surface properties such as energy conversion efficiency and adhesion resistance. In addition, rough porous surface of TiO₂ layer can support the adhesion and stable adsorption of Collagen molecule [13]. This is a reason why we treated Ti plates with NaOH before electrochemically depositing Col-1. After coating Col-1 by EDC method, it can be seen that Ti plate was massively covered with uniform membrane of Collagen in Fig. 1c. The disappearance of nanopores created sodium titanate hydrogel layer became evidence for successfully modifying collagen on Ti surface.

3.2 Cell Attachment and Proliferation

The SEM images of Titanium demonstrated cell adhesion of untreated Ti, TiO₂ and TiCol-1 substrates after reseeding with L929 fibroblast in 1 h, 1 day, 3 days and 5 days. The morphologies of cell were different among three samples reflecting the compatibility of the substrate's surfaces to the cell.

The Ti sample was found to have the largest number of cell lying on surface after 1 h, but still kept spherical morphologies. Ti surface was started showing the appearance of filopodia from the fibroblast formed focal adhesions with the substrate and linked to it to the cell surface. After 1 day, filopodia-mediated cell spreading lead to dendritic cell shapes in the absence of typical lamellipodia-like membrane protrusions. Spreading rate of Ti sample increased and began to process of cell migration after passing 3 days. Following to 5 days, the number of fibroblasts significantly increased to form a plasma membrane attach on Ti disc.

Simultaneously, it can be observed that the TiO₂ layer seems to be not a promising substrates for cell attachment and proliferation. There are very few numbers of filopodia attach spherical cells in the first hour of substrate contact. After 1 day, fibroblast made effort to spread and began to

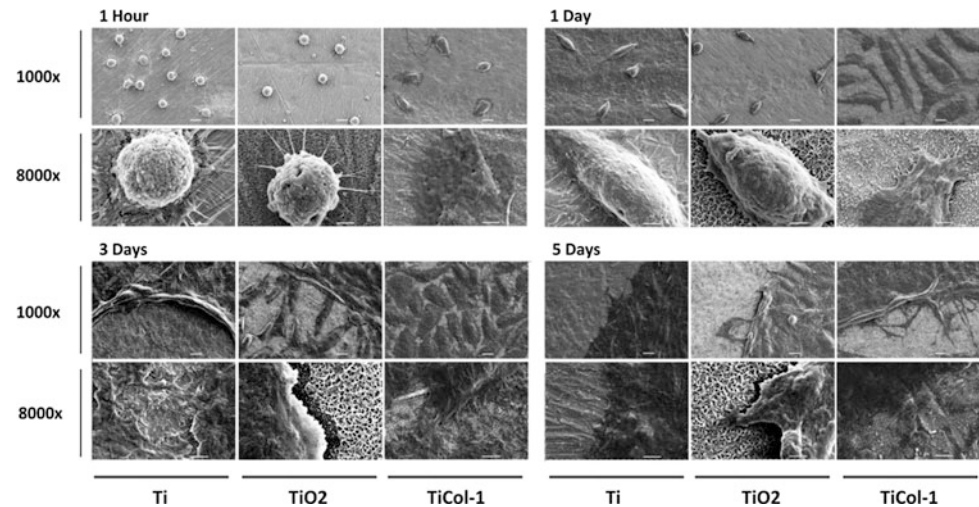
change their morphology, however neither filopodia nor lamellipodia were identified from cell morphology, this suggested lower capacity of TiO₂ in biological functions than TiCol-1 and Ti. As seeding cell took place for 3 days, the original associations between the fibroblast and the underlying TiO₂ layer were lost although cell continued to spreading and interact with each other. Due to the relatively poor cell-material interaction of TiO₂, Lamellipodia on cell-substrate interaction, ribbon-like flat cellular protrusions that are formed at the periphery of a moving or spreading cell, appeared interruption.

Fibroblasts were seeded on the collagen matrix modified on Ti surface have been considered the most important parameters for altering cell activity. Adhesion to Col-1 is accompanied by pronounced cell spreading and cell adhesion in the first hour. The actin-rich lamellipodium replaced the initial surface adherent filopodia contacts where a full circumferential lamellipodium had occurred after the first step of cell–biomaterial interactions. The efficacy of this early phase significantly influenced the subsequent ability to adhesion and proliferation of fibroblast. Lamellipodial extension gave the assembly more stable and resistance to bend than single filaments of filopodia, and therefore drove fibroblast migration and supported a long extension of the plasma membrane [14, 15]. Within the first day, most fibroblasts completely spread and attached closely on Col-1 membrane. The proliferation and migration rates were observed to increase dramatically after 3 days and 5 days of culture with a starting similar number of seeded cells. A uniform plasma membrane under supporting Col-1 was formed to massively cover Ti disc. It demonstrated that Col-1 providing the first important step for long-term survival and development of cell and tissue (Fig. 2).

4 Conclusion

The study initially evaluated fibroblast cell behaviors among Ti surface properties. While Titanium alloys surface allowed for fibroblast cell adhesion and proliferation, TiO₂ layer were seem to inappropriate substrate for fibroblast attachment. The attendance of Col-1 on Ti plates provided the first

Fig. 2 SEM micrographs of L929 Fibroblast cell reseeded on Ti, TiO₂ and TiCol-1 after various time intervals of cell culturing (1 h, 1 day, 3 days and 5 days) at magnification of 1000× (scale bar 10 μm) and 8000× (scale bar 2 μm)



support of cell–biomaterial interactions and promoted the speed of cell spreading and attachment on substrate. Simultaneously, the efficacy of this early phase set a milestone for the subsequent ability to proliferation and migration, as well as the formation of plasma membrane onto biomaterial interface. The knowledge of these initial cell activities is important for further study to improve the biocompatibility of biomaterials.

Acknowledgements This research is funded by International University, Vietnam National University Ho Chi Minh City under grant number: 02-BME-2016/HĐSV-QLKH.

Conflict of Interest Statement The authors declare that they have no conflict of interest.

References

1. Pye, A.D., et al.: A review of dental implants and infection. *J. Hosp. Infect.* **72**(2), 104–110 (2009)
2. Gómez-Florit, M., Ramis, J.M., Xing, R., Taxt-Lamolle, S., Haugen, H.J., Lyngstadaas, S.P., Monjo, M.: Differential response of human gingival fibroblasts to titanium-and titanium-zirconium-modified surfaces. *J. Periodont. Res.* **49**, 425–436 (2014)
3. Kasemo, B.: Biocompatibility of titanium implants: surface science aspects. *J. Prosthet. Dent.* **49**(6), 832–837 (1983), June
4. Liu, X., Chu, P.K., Ding, C.: Surface modification of titanium, titanium alloys, and related materials for biomedical applications. *Mater. Sci. Eng.: R Rep.* **47**, 49–121 (2004)
5. Welander, M.: Soft tissue integration to dental implants (2008)
6. Mizuno, M., Fujisawa, R., Kuboki, Y.: Type I collagen-induced osteoblastic differentiation of bone-marrow cells mediated by collagen- $\alpha 2\beta 1$ integrin interaction. *J. Cell. Physiol.* **184**(2), 207–213 (2000)
7. Ling, T., et al.: Mineralized collagen coatings formed by electrochemical deposition. *J. Mater. Sci. Mater. Med.* **24**(12), 2709–2718 (2013)
8. Ao, H., et al.: Improved hMSC functions on titanium coatings by type I collagen immobilization. *J. Biomed. Mater. Res. A* **102**(1), 204–214 (2014)
9. Kato, E., Sakurai, K., Yamada, M.: Periodontal-like gingival connective tissue attachment on titanium surface with nano-ordered spikes and pores created by alkali-heat treatment. *Dent. Mater.* **31**(5), e116–e130 (2015)
10. Truc, N.T., et al.: Modification of type I collagen on TiO₂ surface using electrochemical deposition. *Surf. Coat. Technol.* **344**, 664–672 (2018)
11. Chang, Q., et al.: Toughening mechanisms in iron-containing hydroxyapatite/titanium composites. *Biomaterials* **31**(7), 1493–1501 (2010)
12. Kokubo, T., Matsushita, T., Takadama, H.: Titania-based bioactive materials. *J. Eur. Ceram. Soc.* **27**(2–3), 1553–1558 (2007)
13. Friedrichs, W., et al.: Adsorption of collagen nanofibrils on rough TiO₂: a molecular dynamics study. *Adv. Eng. Mater.* **13**(10), B334–B342 (2011)
14. Rikitake, Y., Takai, Y.: Directional cell migration: regulation by small G proteins, nectin-like molecule-5, and afadin (Chap. 3). In: Jeon, K.W. (ed.) *International Review of Cell and Molecular Biology*, pp. 97–143. Academic Press, New York (2011)
15. Thomas Parsons, J., et al.: Integrin signaling: cell migration, proliferation, and survival A2—Bradshaw, Ralph A (Chap. 66). In: Dennis, E.A. (ed.) *Handbook of Cell Signaling*, 2nd edn, pp. 491–499. Academic Press, San Diego (2010)

Comparison of Nail Polish Meth(Acrylates) (MA) Gel Photoresist and Vinyl Adhesive Paper for Low-Cost Microfluidics Fabrication

Ha Thach, Hoang-Tuan Nguyen, Uyen Tong, Tuan Hoang, Tuan-Anh Vuong, Cecile M. Perrault, and Khon Huynh

Abstract

There are variety methods and materials for fabrication of the master mold for microfluidic system. In this report, two simple low-cost methods for fabrication of master molds for microfluidic chips are described and compared in quality of molds, thickness and resolution of micro-channels, design complexity, error tolerance and executive time. The first approach can create a master mold just in 5 min by using cutting plotter to cut the design out from vinyl adhesive paper based on the previous design; after that, the assembly attached into the petri dish to fabricate the complete mold. The second one is using nail polish meth(acrylates) (MA) gel as photoresist material to alter expensive SU-8 photoresist in soft photolithography technique and LED-UV light. These processes are simple, short time prototyping, inexpensive materials and no requirement for sophisticated equipment. Both methods can achieve the channels with the depth up to 80 μm . However, the channels of UV gel method are less affected by changes in temperature which enables more complex design as narrow as 200 μm in width compared to 500 μm of craft cutter method. The comparison of two proposed methods shows that UV gel satisfies the important demand for microfluidic master mold fabrication: low cost, possibility of more complex pattern in short time (15 min).

Keywords

Microfluidics • Low-cost fabrication • Vinyl paper • Meth(acrylates)

1 Introduction

Microfluidics field has been making a considerable impact on advanced applications (cell biology, chemical analysis) and healthcare applications (typically point-of-care diagnostic devices) [1]. Currently, there are distinctly various methods and techniques to fabricate microfluidic systems by utilizing different materials [2–9]. The state-of-the-art approach of manufacturing microfluidic systems is photolithography technology [10]. It works based on a projection-printing system in which the image of a photo-mask is reduced and projected onto a thin film of photoresist that is spin-coated on a wafer through a high numerical aperture lens system [11]. However, photolithography has some limitations including excessive cost, necessity in high standard clean room and full of modern facilities for procedure, additionally tolerating little variations in the materials that can be used. Moreover, it is difficult to find an alternative method being better than photolithography. Therefore, researchers address soft-lithography whose main features are printing and replica molding using of elastomeric materials (mechanically soft like PDMS) to create complex pattern for fabrication of microfluidic systems [12]. Nevertheless, the fabrication of the molds for soft-lithography usually requires not only an advanced cleanroom but also expensive materials such as SU-8. For those reasons, many efforts have been made to develop low-cost alternatives for the fabrication of microstructures, avoiding the use of cleanroom facilities. The current requirement is to develop a low-cost method of fabricating microfluidics systems with flexible materials replacing for SU-8 and short-time prototyping process while still meet the requirement of high quality and avoiding the use of cleanroom facilities. This article provides two alternative materials for molding are vinyl adhesive paper [13] and meth(acrylates) (MA) gel photoresist (UV nail polish gel). Both methods aim to create different molds of the microfluidics

H. Thach (✉) · H.-T. Nguyen · U. Tong · T. Hoang · T.-A. Vuong · K. Huynh
International University, Ho Chi Minh City, Vietnam
e-mail: hatuny97@gmail.com

C. M. Perrault
The University of Sheffield, Sheffield, UK

systems for various using purposes, in different sizes with high accuracy.

With vinyl adhesive paper (two-layer decal paper), the master mold is directly created after using cutting plotter machine. On the other hand, nail polish MA gel photoresist method has the same principle of photolithography technique. In this paper, two simple low-cost methods for fabrication of master molds for microfluidic systems were described clearly and compared visually in quality of molds, thickness and resolution of micro-channels, design complexity. Moreover, error tolerance and executive time were examined to verify which one is suitable for low-cost fabrication microstructures.

2 Materials and Methods

Vinyl decal paper also known as a wall sticker, normally used on advertisement. In this report, Firstmark Chemicals 184 Sun Yellow 1235C vinyl decal is used. It basically consists of two layers: decal layer (or vinyl decal) and backing paper. The top layer is decal layer that will be usable mask for the experiment and the bottom layer is to protect the adhesive side of the decal.

Cutting plotter named Mimaki CG- 60SRIII is used to generate master molds.

MA gel is a kind of UV-gel using in nail polish field, it is very popular in market (costs about 1\$ for 15 ml). MA gel hereby is a special material that lab-on-a-chip laboratory used to replace SU-8 polymer with many advantages for replica molding, such as fast process, simple way but effective procedure, flexibility for any complex designed without increasing of the cost.

Apparently, MA gel, which is hardened under exposing of UV light, can do the trick. Gel nails are formulated with several combinations of oligomers. Oligomers is a polymer formed when a few number of monomers are linked together by covalent bonds. Photo-initiators are compound of oligomers and monomers that can absorb and transform physical energy of light into chemical energy (one well-known photo-initiator is 2,2-dimethoxy-1,2-diphenylethan-1-one). When a UV gel photoresist contained photo-initiator components is put under a UV lamp, it absorbs UV light and becomes a hard, insoluble crosslinked polymer network. Thanks to the similar property as photoresist, in laboratory, we apply gel nail in photography to fabricate the microfluidic channel. With this method, the minimum size of micro-channels we could obtain is down to 200 μm .

Lithographic machine or UV-light source is specially designed for the microfabrication of micro devices. It emits light in the correct spectrum to activate the photo-initiator in MA gel. In this article, UV- light source with wavelength of 365 nm is used. Photoresist is exposed under the UV-light

source in a short period time depending on the thickness of photoresist and distance from sample to source.

2.1 Molding Using Cutting Plotter with Decal Paper

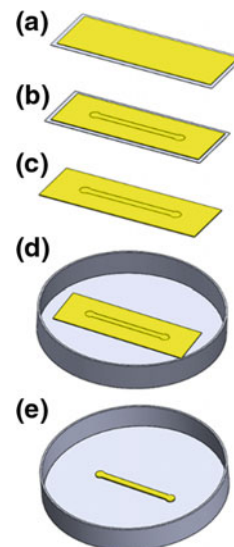
2D drawing being generated in any design software on the computer are loaded onto the cutting plotter to cut the pattern creating the foil on a one-side of the vinyl decal paper (Fig. 1a, b). Next, peel and paste the adhesive top layer of the foil on to the clean petri dish (Fig. 1c, d). The master mold is generated after totally peeling off the remaining needless part (Fig. 1e).

2.2 Molding Using MA Gel

2D drawing of the chip is formed by using common design software on the computer (AutoCAD, Solidworks). After that, chip design drawings are printed into the transparent film by a dedicated laser printer with high resolution to form a photomask.

The process of molding using MA gel get start in an essential step is preparation materials. Glass slide washed by using respectively acetone, alcohol and distilled water to ensure clean and dry on the surface (Fig. 2a). Next, the glass surface is applied by MA gel photoresist with a certain thickness (normally 80 μm in thickness). Place the baser on four edges of the glass to control the thickness of the gel layer (Fig. 2b). After the MA gel photoresist is covered by a photomask, then metal rod is used carefully laminate the combination. Scroll the rod along the longer edge, repeat in different dimensions to guarantee the gel spread evenly onto

Fig. 1 Fabrication process diagram of molding using cutting plotter with decal paper



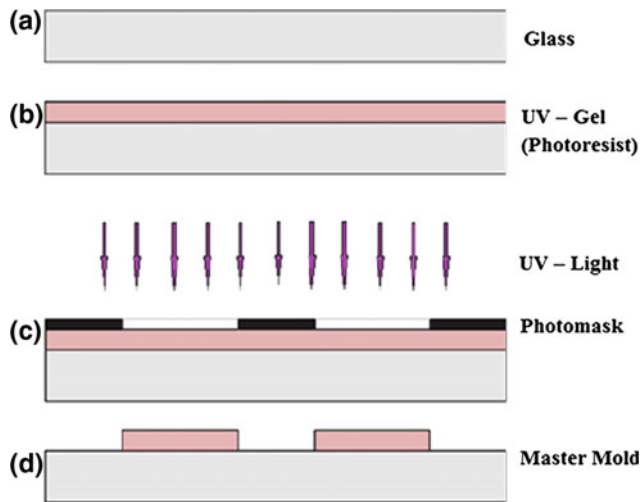


Fig. 2 Fabrication process diagram of molding using MA gel

the glass surface. This apparatus is directly exposed under UV-light (wavelength: 365 nm) for a certain duration. The exposure time depends on UV source wavelength and distance from the apparatus placing to UV source (Fig. 2c). Peel the photomask off the glass, the unexposed area of photoresist is dissolved in a solution mixed from acetone and alcohol (1:4) (Fig. 2d).

3 Results

As a demonstration, a series of templates with various patterns are designed and fabricated following two methods. The important parameters indicating the resolution and quality of soft-lithography are surface of the master mold and width of channel.

3.1 Molding Using Cutting Plotter with Decal Paper

The design having simple patterns (straight and zigzag channels) and increasing gradually width channel is to detect minimum width channel value achieved. Such geometries were studied due to their common use in almost microfluidics systems. The demonstration shows that straight line pattern can be generated at width of 200 μm . In zigzag pattern, it was found that it is very difficult to achieve a smooth and clean cut at width below 500 μm ; therefore, very hard to peel the remaining needless part off. Figure 4 shows the cutting quality of sophisticated microfluidics template with relative channel width about 300 μm . Overall

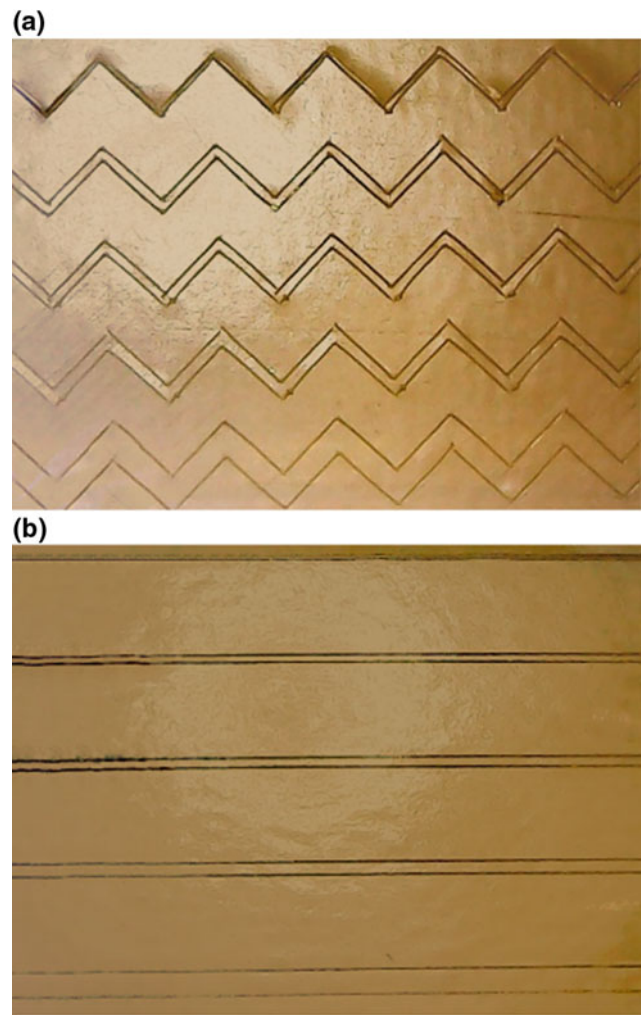


Fig. 3 Vinyl decal template with simple pattern. **a** zigzag pattern; **b** straight line pattern. Figure 5 shows the cutting quality of sophisticated microfluidics template with minimum channel width about 500 μm . Surface of master mold is not clean and smooth; wall channel is not completely straight channel. Overall, the master molds have large error

template is severely damaged because channels are not continuous and overlap (Fig. 3).

3.2 Molding Using UV Gel

The quality of master mold from MA gel is showed in Fig. 6. Some patterns in Fig. 6b, e, f are similar to the design in Fig. 4 but the quality of MA gel master mold is much better. Figure 7 demonstrate some photomask whose sophisticated pattern design can be generated at 200 μm minimum channel width by using MA gel.

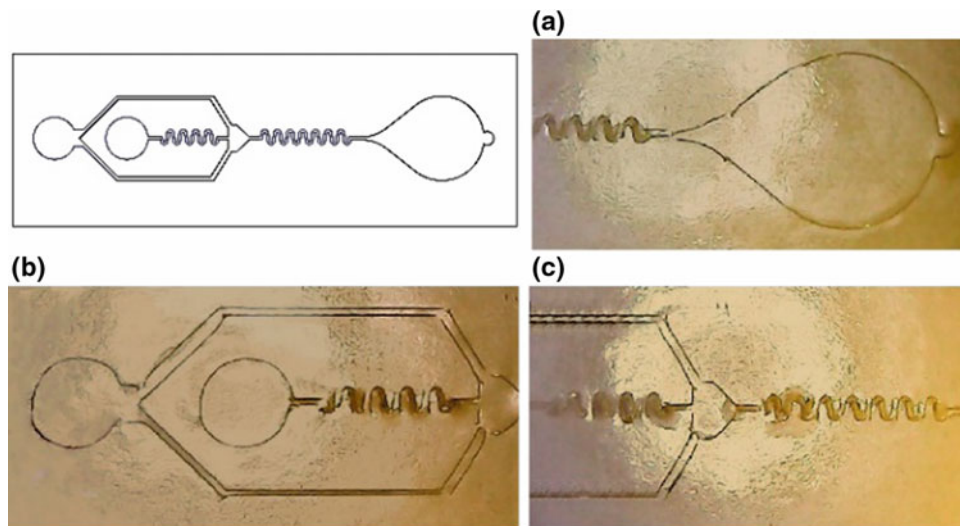


Fig. 4 The cutting quality of complex microfluidics system under microscope (40× magnification) (relative channel width about 300 μm)

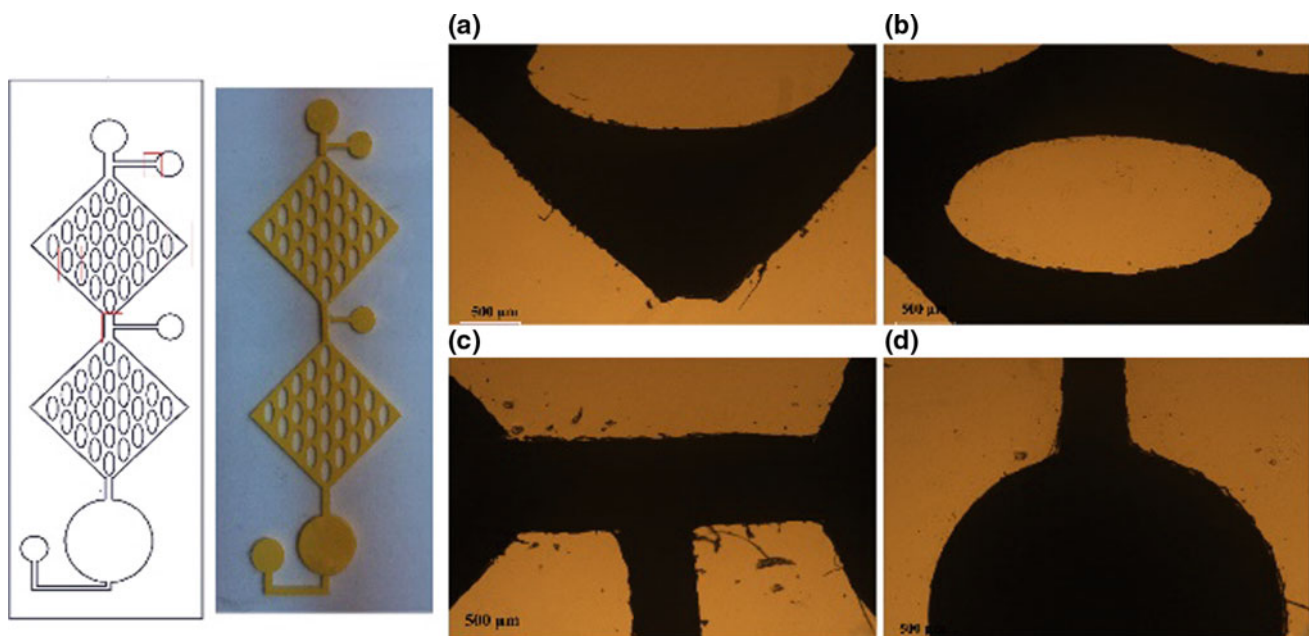


Fig. 5 The cutting quality of sophisticated microfluidics system under microscope (40× magnification). (Minimum channel width is about 500 μm)

Boxplot in Table 1 demonstrates visually error tolerance of channel width of two methods. The difference means and standard errors of method using vinyl decal paper is larger than method using MA gel. (Shown in detailed in Fig. 8.) Using paired samples test is to evaluate the error tolerance of each methods. For method of using vinyl decal paper and cutting plotter, the difference between measured channel width and real value in design is significant statistically ($p < 0.05$). On the other hand, when using UV gel for master molds, the difference between measured channel width and real value in design is not significant statistically ($p > 0.05$).

4 Discussion

4.1 The Method of Molding Using Cutting Plotter with Decal Paper

The cutting quality of the model relies on the sharpness of the knife, the thickness of cutting media, the cutting plotter setting and the complexity of the pattern. The material used to fabricate the pattern of the chip in this research is one-sided vinyl decal paper. This type of decal is almost

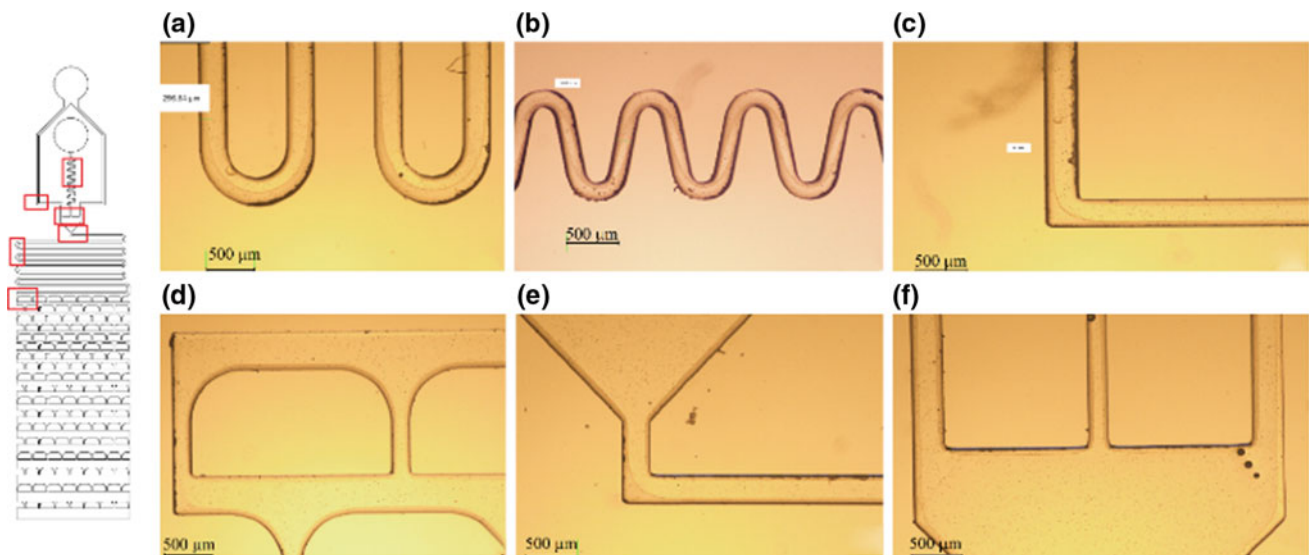
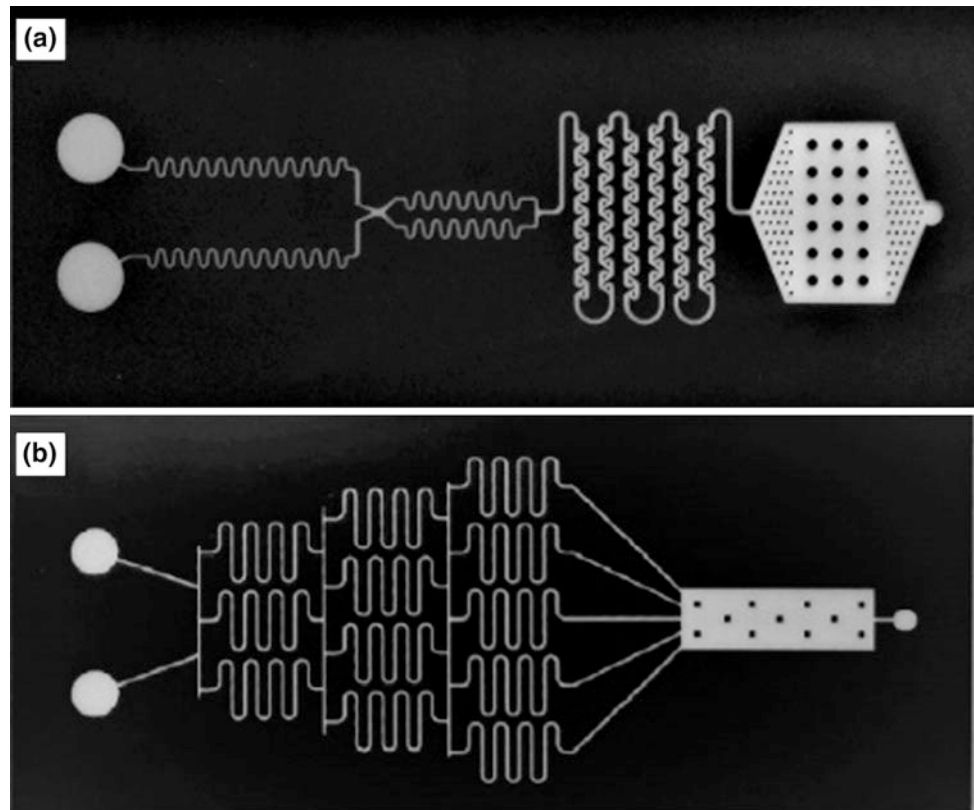


Fig. 6 Surface of UV-gel master mold under microscope (40× magnification)

Fig. 7 Photograph of photomask
a micromixer; **b** gradient generator



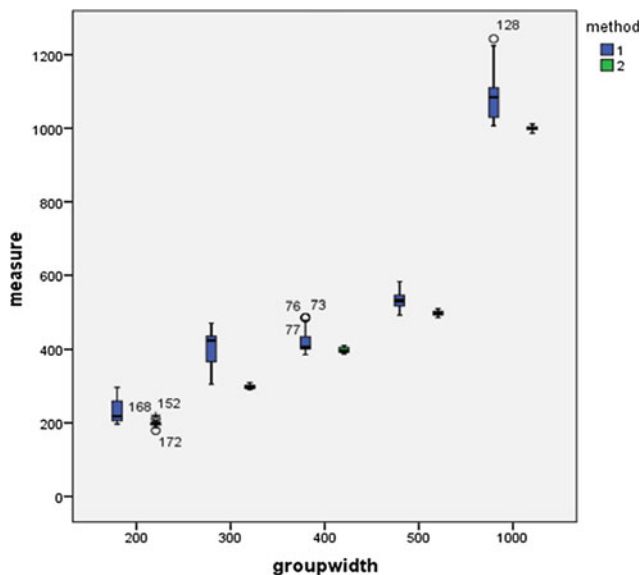
thinner than the others due to the lack of protective materials on the surface; therefore, it can be easily broken by the knife. In order to achieve the best cutting quality, the setting of the cutter, especially speed, need to be adjusted correctly. Moreover, and even more importantly, though, because cutting media is breakable during cutting, for simple patterns, including line, zigzag the minimum width that can be

reached is 200 μm , while this value should be 500 μm for sophisticated models such as micromixer. In addition, the thickness of decal only varies from 80 to 100 μm ; therefore, it is required to stacked over each other in an attempt to increase the entire volume of the microfluidic system.

The total duration for an entire process of making master mold is around 15 min including cutting the designed

Table 1 Statistic of channel width of both methods

Channel width		200	300	400	500	1000
Vinyl decal	N	34	20	32	40	25
	Mean	231.66	403.35	423.52	535.83	1095.29
	Std. deviation	34.37	55.32	32.66	25.48	71.48
UV gel	N	25	20	29	25	20
	Mean	197.96	298.54	397.61	497.78	999.9
	Std. deviation	7.47	4.6	6.44	6.43	6.13

**Fig. 8** Boxplot of channel width (unit: micrometer) on average in each method. Method 1: using vinyl decal paper; method 2: using MA gel

pattern and several other steps to accomplish a complete mold before moving to the next process which is casting the PDMS. It takes approximately 5 min in order to cut the design pattern and this step is performed by Mimaki CG-60SRIII cutting plotter. The mold is required to be cleaned the surface after being peeled and applied into petri dish. It is noticed that the vinyl-paper pattern should be carefully stick to the petri dish because any negligent action can be damaged during degassing in vacuum desiccator which affect the mold fabrication process. These steps take about 10 min for simple pattern and could be longer for sophisticated patterns.

4.2 The Method of Molding Using MA Gel

The quality of master molds depends on photomask, UV-light source wavelength, distance from UV-light source to the combination, exposure duration and handling of laboratory technician. The quality of photomask based on the resolution of laser printer is the most important factor to

fabricate a good master mold which is the darker the ink is, the higher resolution is. In this report, the wavelength 365 nm LED UV-light source is used. Conventionally, the distance from LED-UV source is 3 cm and the time exposure is 25 s, which are the standard conditions for the exposure 80 μm photoresist (depth of channel). The distance from UV-light source increases resulting the time exposure also increases, holding the depth of channel is constant. Similarly, the time exposure is directly proportional to the depth of channel while holding constant for the distance from UV-light source. Compare to the previous method, this one allows to design the complex design but still meet the high resolution. The minimum channel width is able to achieve was 200 μm . In this range of channel width, it requires the careful preferment and the sample was not exposed in long time under washing solution. From 200 μm up, microfluidics system can be generated varying different size, shape and geometry with high precision at both the small curves and angles in the pattern. Surface of UV gel master mold is better than vinyl decal paper master mold because UV gel material is quite stable with the change in temperature. The depth of channel depends on the thickness of spacers, that is vinyl decal paper spacer or plastic spacer in this report with range from 80 to 1000 μm . Duration for fabrication of each master mold is from 15 to 20 min. Moreover, this method can be and applied to develop multilayers design microfluidic system.

5 Conclusion

In summary, two low-cost soft-lithography techniques for fabrication master mold using two different material was described. Both methods are simple, out-of-cleanroom, using inexpensive materials and no requirement for sophisticated devices. The use of vinyl decal paper allows to create master molds in short period time but having various difficulties. The use of UV-gel nail polish can achieve complex designs and vertical side walls as well as allow control the height of channels by selecting the thickness of spacer. The special developments include 200 μm in minimum width channel and smooth channel. Overall, the comparison of two

methods indicates that UV gel satisfies the important demand for microfluidic master mold fabrication: low cost, possibility of more complex pattern in short time (15 min).

Acknowledgements This research is funded by International University – VNUHCM under grant number T2017-02-BME.

Conflict of Interest The authors declare that they have no conflict of interest.

References

1. Whitesides, G.M.: The origins and the future of microfluidics. *Nature* **442**(7101), 368 (2006)
2. Khademhosseini, A., Langer, R.: Microengineered hydrogels for tissue engineering. *Biomaterials* **28**(34), 5087–5092 (2007)
3. Ren, K., Zhou, J., Wu, H.: Materials for microfluidic chip fabrication. *Acc. Chem. Res.* **46**(11), 2396–2406 (2013)
4. Martinez, A.W., Phillips, S.T., Butte, M.J., Whitesides, G.M.: Patterned paper as a platform for inexpensive, low-volume, portable bioassays. *Angew. Chem. Int. Ed.* **46**(8), 1318–1320 (2007)
5. Sollier, E., Murray, C., Maoddi, P., Di Carlo, D.: Rapid prototyping polymers for microfluidic devices and high pressure injections. *Lab Chip* **11**(22), 3752–3765 (2011)
6. Lin, C.H., Lee, G.B., Lin, Y.H., Chang, G.L.: A fast prototyping process for fabrication of microfluidic systems on soda-lime glass. *J. Micromech. Microeng.* **11**(6), 726 (2001)
7. Nge, P.N., Rogers, C.I., Woolley, A.T.: Advances in microfluidic materials, functions, integration, and applications. *Chem. Rev.* **113**(4), 2550–2583 (2013)
8. McDonald, J.C., Whitesides, G.M.: Poly (dimethylsiloxane) as a material for fabricating microfluidic devices. *Acc. Chem. Res.* **35**(7), 491–499 (2002)
9. Nguyen, N.T., Wereley, S.T.: *Fundamentals and Applications of Microfluidics*. Artech House (2002)
10. Rothschild, M.: Projection optical lithography. *Mater. Today* **8**(2), 18–24 (2005)
11. Whitesides, G.M., Ostuni, E., Takayama, S., Jiang, X., Ingber, D. E.: Soft lithography in biology and biochemistry. *Annu. Rev. Biomed. Eng.* **3**(1), 335–373 (2001)
12. Xia, Y., Whitesides, G.M.: Soft lithography. *Annu. Rev. Mater. Sci.* **28**(1), 153–184 (1998)
13. Yuen, P.K., Goral, V.N.: Low-cost rapid prototyping of flexible microfluidic devices using a desktop digital craft cutter. *Lab Chip* **10**(3), 384–387 (2010)

Part VIII

Lab-on-a-chip and Point of Care Technologies

Improvements in DNA Extraction and Loop-Mediated Isothermal Amplification (LAMP) Assist Application of LAMP on Malaria Point-of-Care Diagnostic Devices

Han Ly, Thanh-Xuan Le, Hoang-Tuan Nguyen, Vo Van Toi, Thanh-Dong Le, Thuy-Vy Pham-Nguyen, Cécile M. Perrault, and Khon Huynh

Abstract

Early detection right at epidemic areas can prevent infectious diseases from propagation. Currently, the most common nucleic acid test—polymerase chain reaction (PCR) is time-consuming, complex, expensive and thermocycler required, thus limiting its utility in poor laboratory conditions or even non-laboratory condition of epidemic areas. Loop-mediated isothermal amplification (LAMP) is quick, cheap, sensitive and isothermal assay could be combined with a simple DNA extraction method to integrate into Lab-on-a-chip (LOC) device. Here, we attempted to improve LAMP method for malaria diagnosis on portable microfluidics chip platform by optimizing DNA extraction using boil and spin method and altering Tris-containing amplification buffer for ascertaining changing in pH of reaction solution. Basically, blood sample was mixed with extraction buffer containing Sodium Dodecyl Sulfate (SDS) concentration and treated under high temperature condition. Four concentrations of SDS (0, 0.4, 0.8 and 1%) were tested along with different temperature (65 and 95 °C) to adapt into LOC platform and avoid denaturation of LAMP reagent. All samples treated at 65 °C showed the presence of DNA after extraction. Furthermore, DNA amplification buffer was minimized Tris concentration to facilitate result read-out step. The releasing of hydrogen ion from amplification reaction causes increasing in pH which could be recognized by color of pH indicator paper or dye, for example,

phenolphthalein. Throughout a series of experiments, LAMP is demonstrated that it can also occur in low-Tris buffer with pH indicator dye, efficiently. The positive sample will have a change from pink to transparent in solution color, otherwise, the negative sample will maintain pink. These improvements allowed us to adapt LAMP technique into Point-of-care (POC) devices in which the whole process run under isothermal condition (65 °C) and non-instrument required visual detection. The LAMP microfluidics chip will be potential tool for early detection infectious diseases and several other diseases in non-laboratory condition.

Keywords

LAMP • DNA extraction • Colorimetric detection • Malaria • Microfluidics chip

1 Introduction

In 2016, 91 countries reported a total of 216 million cases of malaria, an increase of 5 million cases over the previous year [1]. The global malaria deaths reached 445,000 deaths [1]. Although malaria case incidence has fallen globally since 2010, the rate of decline and mortality has stalled and even reversed in some regions since 2014 [1]. The most heavily affected countries are least developed countries and developing one, those countries oftenly have poor medical systems. Therefore, to have impressive reductions in cases and deaths, those countries must be our primary focus. The most effective way to reduce malaria is preventing it from transmission by early diagnosis right at epidemic areas [1]. However, due to the poor medical systems of epidemic areas, they need a rapid, simple-use point-of-care device.

At present, microscopy of blood smears is still considered as the gold standard for diagnosing malaria infections. However, microscopic diagnosis is unable to detect low-density infections and required skilled expertise [2–4].

H. Ly (✉) · T.-X. Le · H.-T. Nguyen · V. Van Toi · K. Huynh
Department of Biomedical Engineering, International University
—Vietnam National University Ho Chi Minh City, Ho Chi Minh
City, Vietnam
e-mail: lybaohanmb@gmail.com

T.-D. Le · T.-V. Pham-Nguyen
Institute of Malariology—Parasitology—Entomology in Ho Chi
Minh City, Ho Chi Minh City, Vietnam

C. M. Perrault
Department of Mechanical Engineering, University of Sheffield,
Sheffield, UK

Therefore, rapid diagnostic tests (RDTs) are now widely used, especially when fast and easy diagnosis is needed [5]. The momentous disadvantage of RDTs is that they are rather expensive and inaccurate in some cases, similar to microscopy, RDTs are incapable to detect low-density infections [6, 7]. Currently, PCR is a unique method that can achieve highest detection rates and specificity. PCR uses expensive thermocycler and reagents as well as molecular laboratories and well-trained technician. Moreover, it consumes quite long time, thus, it is not appropriate when rapid, simple diagnoses are mandatory. LAMP may offer the best of both aspects for malaria diagnosis, with sensitivity of PCR and speed of RDTs.

LAMP is a simple method to amplify DNA with high sensitivity, specificity, speed and tolerance to inhibitors under isothermal conditions [8, 9]. LAMP uses a DNA polymerase with strand displacement activity, usually from *Bacillus stearothermophilus*, eliminating the need for a thermocycler. Besides, Bst polymerase which is less sensitive to inhibitors compared to PCR, allows the use of simple and rapid DNA extraction methods such as “boil and spin” [10, 11]. LAMP assay has high specificity because amplification only occurs when six separate regions of target DNA are recognized. Specifically, amplification requires two inner and two outer primers, two additional loop primers for acceleration. This working mechanism enhances the sensitivity of the reaction and speeds up the amplification time to less than an hour. With those characteristics, LAMP is appropriate assay for applying on POC devices.

When a DNA polymerase incorporates a deoxynucleoside triphosphate into the nascent DNA, a pyrophosphate moiety and a hydrogen ion are released as the by-products. There are a number of studies that demonstrated the ability of a DNA polymerase to perform efficient synthesis in weakly buffered or non-buffered solutions [12–15]. The release of hydrogen ion can cause a significant change from initial alkaline pH to final acidic pH in low-Tris buffer. Such a significant change in pH offers the possibility of detecting DNA amplification through the use pH indicator dyes.

The combination of three rapid and simple steps (boil and spin DNA extraction, LAMP and pH change observation) can be applicable on POC devices, especially microfluidic chips which can run DNA amplification at single temperature, presence of inhibitors, and results can be read through colorimetric pH detection easily by naked eye (Fig. 1).

2 Materials and Methods

2.1 Materials

DNA template. *Plasmodium falciparum* 18S rRNA gene (gen bank M19173.1).

DNA extraction. Sodium Dodecyl Sulfate (SDS) was purchased from Bio-Rad, Singapore. Sodium Chloride, Sodium hydroxide were purchased from Merck Millipore, Germany. Tris-HCl was from Sigma Aldrich, USA.

LAMP. MgSO₄, Bst polymerase 3.0 were purchased from New England BioLabs. dNTPs 10 mM mix, primers F3, B3, FIP, BIP, Loop F, Loop B (Table 1) were produced by PHUSABiochem, Vietnam.

Colorimetric pH detection. Phenolphthalein was purchased from Sigma Aldrich, USA.

2.2 Methods

Boil and spin extraction. Extraction buffer was prepared comprising: 400 mM NaCl, 40 mM Tris-HCl pH 6.5 and various SDS concentration 0, 0.4, 0.8, 1%. Then, 60 µL of EB was mixed with 60 µL of infected blood and heated at two temperature 65 and 95 °C for 3 min. Extracted DNA was stored at 4 °C and used as DNA template for PCR and LAMP.

LAMP

Normal-Tris buffer. A Normal-Tris mastermix 2X was prepared comprising 40 mM Tris-HCl, 20 mM (NH₄)₂SO₄, 300 mM KCl, 4 mM MgSO₄, 0.2% Tween 20, pH 8.8 at 25 °C, 12 mM MgSO₄, 2.8 mM dNTPs mix, 0.64 U/µL. The primer 10X mixture was prepared with 1.6 µM of FIP and BIP, 0.8 µM of Loop F and Loop B, 0.2 µM of F3 and B3 primers. All reactions were carried out in total volume of 25 µL using 12.5 µL standard mastermix 2X, 2.5 µL of primer 10X mixture, 1 µL of DNA template which extracted under condition of 0%SDS, 65 °C. All tubes were heated at 65 °C for 45 min in a water bath. Result was analysed using agarose gel electrophoresis.

Low-Tris buffer. A Low-Tris mastermix 2X was prepared comprising 20 mM (NH₄)₂SO₄, 100 mM KCl, 16 mM MgSO₄, 2.8 mM dNTPs mix, 0.2% Tween 20. All



Fig. 1 Block diagram of the whole procedure

Table 1 List of primers and sequence for *Plasmodium falciparum* 18S rRNA gene

Primer name	Sequence (5'–3')
F3	TGTAATTGGAATGATAGGAATTTA
B3	GAAAACCTTATTTTGAACAAAGC
FIP (F1c-F2)	AGCTGGAATTACCGCGGCTGGGTTTCCTAGAGAAACAATTGG
BIP (B1-B2c)	TGTTGCAGTAAAAACGTTTCGTAGCCCAAACCAGTTTAAATGAAAC
Loop F	GCACCAGACTTGCCCT
Loop B	TTGAATATTAAGAA

components were mixed in water, and 1 M NaOH was used to adjust the pH to 8.4–9.0, as measure by pH paper. The primer 10X mixture was similar to that for Normal-Tris. Reagent taken volume and other amplification conditions are the same to Normal-Tris.

Colorimetric pH detection. 1 µL Phenolphthalein 0.5% was added to the amplified reaction mixture and visually inspected to check final pH of positive and negative samples. Color change was observed by naked eye and recorded using a camera.

3 Results

3.1 Boil and Spin DNA Extraction

From Table 2, generally, DNA concentration showed higher value when increasing SDS concentration. Among 4 samples treated at 95 °C, 1%SDS extracted sample had highest concentration (188.1 ng/µl). However, with 65 °C condition, the most concentrated DNA was 0.8%SDS sample. This also the highest concentration within 8 extracted samples. Additionally, it can be seen that 65 °C demonstrated better results in DNA extraction than 95 °C when using the same extraction buffer. For instance, 0%SDS extraction buffer gave only 77.2 ng/µl when heated at 95 °C while it accounted for 183.9 ng/µl with 65 °C condition. Moreover, A₂₆₀/A₂₈₀ ratios of all samples were below 1.8 that indicated the low purity of products derived from Boil and Spin

Table 2 The concentration of extracted DNA at different conditions

Sample	Concentration (ng/µl)	A ₂₆₀ /A ₂₈₀
0%SDS, 65 °C	183.9 ± 4.3	0.67
0.4%SDS, 65 °C	204.6 ± 8.9	0.82
0.8%SDS, 65 °C	235.3 ± 5.5	0.86
1%SDS, 65 °C	198.8 ± 2	0.83
0%SDS, 95 °C	77.2 ± 10.8	1.14
0.4%SDS, 95 °C	145.6 ± 9.2	0.90
0.8%SDS, 95 °C	156.8 ± 1.9	0.92
1%SDS, 95 °C	188.1 ± 4.3	0.88

method. All extracted samples were tested by PCR reaction and demonstrated the presence of genome of *Plasmodium falciparum*. As a result, 0%SDS extraction buffer, heat at 65 °C can provided sufficient concentration for LAMP.

3.2 Loop-Mediated Isothermal Amplification (LAMP)

LAMP can occur under Low-Tris condition though gel results shown that it has shorter amplified fragments with less number of copies compared to Normal-Tris buffer. On the other hand, Low-Tris buffer allowed the change in pH which can be easily observed with phenolphthalein color. In Low-Tris buffer, negative sample had clear pink color while positive sample was colorless. Normal-Tris buffer shown the same color of both positive and negative samples whereas Low-Tris buffer shown significant change in color. Initially, pH of buffers were measured by using pH paper, thus pH might not be precise at the same value for both of buffers and it led to the small difference in color of negative sample in Fig. 2c and negative sample in Fig. 2d.

4 Discussion

In regions where malaria is epidemic, parasites spreads very quickly, so a test for diagnosis malaria at early stage is extremely crucial. PCR is the most common used test. Nevertheless, in epidemic areas, they usually have no

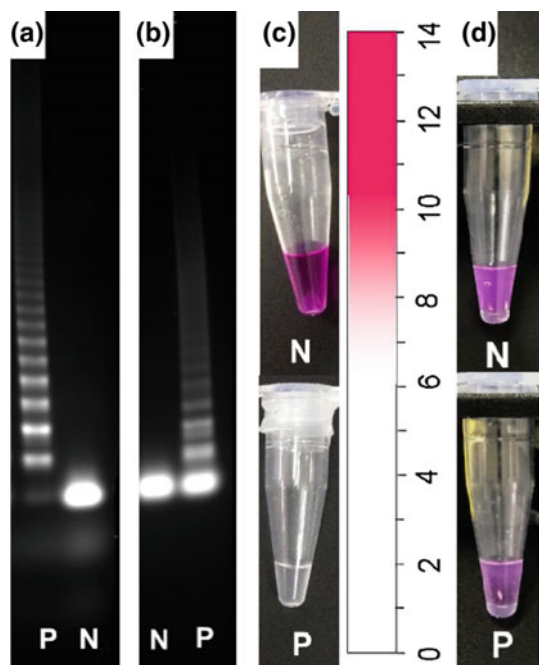


Fig. 2 a and b are agarose gel electrophoresis result of LAMP with Normal-Tris and Low-Tris buffer, respectively. c and d are results of colorimetric pH detection by Phenolphthalein in Low-Tris and Normal-Tris buffer, respectively. P: positive sample, N: negative sample (without DNA template)

thermocycler. Correspondingly, LAMP completely fits those requirements: quick, simple, high sensitivity, specificity.

Moreover, unlike PCR, LAMP has high tolerance to inhibitors. Therefore, DNA extracted by Boil and Spin method can be apply directly to LAMP without purification. Although Boil and Spin extraction method is performed at 95 °C as usual [16, 17], it not suitable for applying on microfluidic system together with LAMP reaction, since Bst polymerase efficient temperature range is 57–72 °C [18]. Providentially, Boil and Spin method can provide sufficient efficiency at 65 °C. This improvement helps facilitating microfluidics platform fabrication and also protect LAMP reagents from being inactivated by high temperature.

In other hands, Bst polymerase can work efficiently during amplification process under Low-Tris condition. Furthermore, Low-Tris buffer allows the pH to change, which cause by the release of proton only if the amplification occurred while Normal-Tris buffer maintains pH of reaction mixture during LAMP reaction. Then, users can easily recognize the change in color of reaction mixture by observing the color of Phenolphthalein chamber on microfluidic chip when reaction mixture passes through.

Acknowledgements This research is funded by International University, VNU-HCM under grant number T2017-02-BME.

Conflict of Interest The authors declare that they have no conflict of interest.

References

1. World malaria report 2017. Geneva: World Health Organization (2017)
2. Chinkhumba, J., et al.: Comparative field performance and adherence to test results of four malaria rapid diagnostic tests among febrile patients more than five years of age in Blantyre, Malawi. *Malar. J.* **9**(1), 209 (2010)
3. Endeshaw, T., et al.: Performance of local light microscopy and the ParaScreen Pan/Pf rapid diagnostic test to detect malaria in health centers in Northwest Ethiopia. *PLoS one* **7**(4), e33014 (2012)
4. Mekonnen, S.K., et al.: Return of chloroquine-sensitive *Plasmodium falciparum* parasites and emergence of chloroquine-resistant *Plasmodium vivax* in Ethiopia. *Malar. J.* **13**(1), 244 (2014)
5. Chou, M., et al.: Performance of “VIKIA Malaria Ag Pf/Pan” (IMACCESS[®]), a new malaria rapid diagnostic test for detection of symptomatic malaria infections. *Malar. J.* **11**(1), 295 (2012)
6. Aydin-Schmidt, B., et al.: Loop mediated isothermal amplification (LAMP) accurately detects malaria DNA from filter paper blood samples of low density parasitaemias. *PLoS one* **9**(8), e103905 (2014)
7. Cunningham, J., Gatton, M.L., Kolaxinski, K.: Malaria rapid diagnostic test performance: results of WHO product testing of malaria RDTs: Round 7 (2015–2016) (2017)
8. Notomi, T., et al.: Loop-mediated isothermal amplification of DNA. *Nucl. Acids Res.* **28**(12), e63–e63 (2000)
9. Han, E.-T., et al.: Detection of four Plasmodium species by genus- and species-specific loop-mediated isothermal amplification for clinical diagnosis. *J. Clin. Microbiol.* **45**(8), 2521–2528 (2007)
10. Mori, Y., Kanda, H., Notomi, T.: Loop-mediated isothermal amplification (LAMP): recent progress in research and development. *J. Infect. Chemother.* **19**(3), 404–411 (2013)
11. Poon, L.L.M., et al.: Sensitive and inexpensive molecular test for falciparum malaria: detecting *Plasmodium falciparum* DNA directly from heat-treated blood by loop-mediated isothermal amplification. *Clin. Chem.* **52**(2), 303–306 (2006)
12. Pourmand, N., et al.: Direct electrical detection of DNA synthesis. *Proc. Natl. Acad. Sci.* **103**(17), 6466–6470 (2006)
13. Purushothaman, S., Toumazou, C., Ou, C.-P.: Protons and single nucleotide polymorphism detection: a simple use for the ion sensitive field effect transistor. *Sens. Actuators B: Chem.* **114**(2), 964–968 (2006)
14. Rothberg, J.M., et al.: An integrated semiconductor device enabling non-optical genome sequencing. *Nature* **475**(7356), 348 (2011)
15. Toumazou, C., et al.: Simultaneous DNA amplification and detection using a pH-sensing semiconductor system. *Nat. Methods* **10**(7), 641 (2013)
16. Hopkins, H., et al.: Highly sensitive detection of malaria parasitemia in a malaria-endemic setting: performance of a new loop-mediated isothermal amplification kit in a remote clinic in Uganda. *J. Infect. Dis.* **208**(4), 645–652 (2013)
17. Cook, J., et al.: Loop-mediated isothermal amplification (LAMP) for point-of-care detection of asymptomatic low-density malaria parasite carriers in Zanzibar. *Malar. J.* **14**(1), 43 (2015)
18. Tanner, N.: Improve reagents for isothermal DNA amplification. Feature article. New England Biolabs Inc. Available online: http://www.neb-online.de/isothermal_amp.pdf (2015)

Recent Developments in Continuous Monitoring Diagnostics with Microneedle Arrays

Anthony E. G. Cass[✉], Danny O'Hare[✉], and Sanjiv Sharma[✉]

Abstract

Compared with therapeutics, diagnostic devices account for a relatively small proportion of healthcare expenditure (less than 10%) and yet timely diagnosis as well as continuous monitoring of molecular markers can have a major impact on disease outcomes. In particular point of care (or near patient) tests can empower individuals to become active participants in the management of their conditions, giving them and their medical support greater insight into both their conditions and their response to treatment. In an extension of the point of care paradigm, continuous monitors of biomarkers and/or therapeutics allow high frequency data to be gathered and patterns of variation to be analyzed in ways that are not possible with infrequent and sporadic testing. The advent of novel materials, fabrication methods and data analysis have opened the way to new devices, assay formats and molecular targets. In this paper we will discuss some aspects of our work in this area with a particular focus on microneedles for continuous, minimally invasive sensing and the use of nucleic acid aptamers in both electrochemical and lateral flow assays.

Keywords

Microneedles • Electrochemical • Aptamers

1 Microneedle Sensor Arrays

Continuous measurement of physiological parameters such as blood pressure, heart rate, electrophysiological patterns (electrocardiograms, electroencephalograms), and respiration

rate are very familiar procedures whether in hospital or, increasingly at home. However, as a general observation this approach has not been applied to the measurement of molecular parameters (biomarker and drugs). The only significant exception is in continuous glucose monitoring (CGM) in Type 1 diabetes and even here only a small proportion of individuals with Type 1 diabetes regularly use CGM devices. There are several well documented reasons for this including cost, discomfort, inconvenience and concerns over reliability. Typically, such CGM is performed with a subcutaneously implanted needle modified to generate a glucose dependent current when an electrical potential is applied. Over the past several years we have taken a different approach to the design and fabrication of continuous sensing devices that we believe overcome many of the limitation of current implanted sensors and allow a straightforward extension to continuous monitoring of many other molecular species. These microneedle sensor arrays are fabricated by low cost, scalable and flexible methods, reside in the dermal interstitial compartment, less than 1 mm below the surface of the skin, whose fluid (interstitial fluid or ISF) is very close in composition to serum. This compartment sits above the capillary bed and nerve endings and so the microneedles cause neither pain nor bleeding upon insertion. The microneedles are shown in Fig. 1 and are typically configured as four separate arrays, each array comprising 16 electrically contiguous solid microneedles. This format offers a large sensing area whilst resulting in no adverse tissue response (inflammation or irritation) or collagen capsule formation.

The base structures are made in polycarbonate by injection moulding and then metallized with gold, silver or platinum. Finally, they are functionalized with the relevant sensing chemistries. A complete set of protocols are described in our recent *Methods in Enzymology* chapter [1] and here the use of the devices in continuous amperometric and potentiometric sensing will be described. Both these sensing modalities are well established and have been used with a range of molecular recognition chemistries, in the case of amperometric sensors through oxidation or reduction

A. E. G. Cass (✉) · D. O'Hare
Imperial College London, London, UK
e-mail: t.cass@imperial.ac.uk

S. Sharma
Swansea University, Swansea, UK

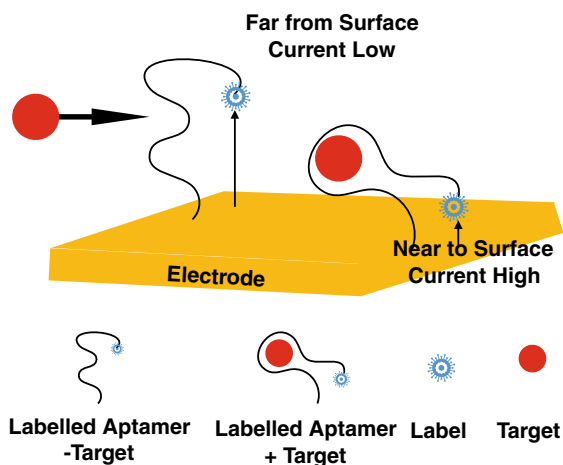
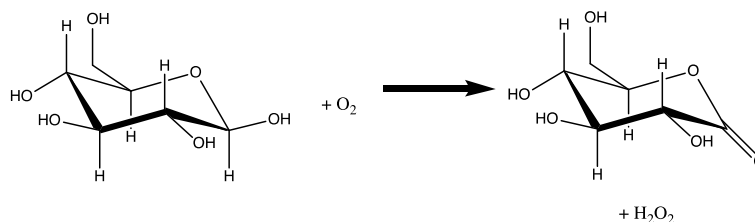


Fig. 1 Electrochemical transduction of structure switching in an aptamer. MB is the redox group methylene blue and k_{CT} is the charge transfer rate constant

generating an electrical current and in the case of potentiometric sensors through reactions generating an electrical potential via a local ion flux (most commonly of protons).

1.1 Amperometric Sensing

Many different substrate oxidizing enzymes are known, but one of the earliest and still a widely used example is glucose oxidase from *Aspergillus niger* which catalyses the following reaction:



The reaction is characteristic of the class of enzymes that utilize oxygen as the electron acceptor and reduce it to hydrogen peroxide. This product is then reoxidised at a positive potential producing a glucose dependent current. The high turnover number, robustness, low cost and

specificity for glucose, when linked to the importance of glucose measurements in the management of diabetes has made it the major application for microneedle sensors of many different designs [2]. In our current design the enzyme is entrapped in a polyphenol coating which provides sufficient mechanical robustness to survive skin insertion. We have recently published data from 24-h monitoring of 5 study participants with Type 1 diabetes [3]. In this case the calibration of the sensor was based on a single point at the start of the monitoring period with no further recalibration. Although glucose has been the most intensively studied metabolite in ISF with microneedles, others are both tractable and relevant. Perhaps the example of lactate is a good one. Like glucose there is an accessible lactate oxidase and continuous monitoring of lactate has applications in both sports performance and in the management of sepsis.

1.2 Potentiometric Sensing

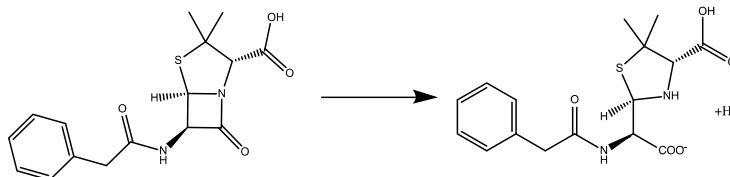
Classically, potentiometric sensors are based on establishing a potential difference across an ion selective membrane due to differences in concentration between the two compartments separated by the membrane. More recent developments have replaced the two-compartment/membrane configuration by solid-state ion sensing electrodes (ISE's) that offer greater robustness and more straightforward fabrication procedures. Miller and colleagues have demonstrated the combination of a solid-state potassium ISE with

hollow microneedles to produce a transdermal potassium sensor [4].

Enzyme linked ISE's have typically linked hydrolytic enzymes to pH sensors and we have recently demonstrated microneedle sensing of penicillin with an iridium oxide

(IrOx) pH sensor coated with a hydrogel layer containing entrapped β -lactamase [5].

the redox group and the electrode surface and so changes the current flowing [10].



This device could have particular utility in enabling dynamic dosing of antibiotics based upon continuous monitoring and a feedback loop [6].

Conflict of Interest The authors declare that they have no conflict of interest.

2 Beyond Enzyme Sensing-Aptamers

2.1 Affinity Sensing

Enzymes exhibit the dual properties of molecular recognition and catalysis, transforming the target analyte and in the process generating a detectable product (hydrogen peroxide and protons in the above examples). Affinity reagents simply bind with the requisite specificity and affinity to the target analyte and that process then needs to be coupled to signal generation. There are many possible affinity reagents and signal generation schemes, in respect of compatibility with microneedle sensors we have chosen redox labelled nucleic acid aptamers as the basis for sensing target molecules that are not amenable to enzymatic sensing. This group comprises protein biomarkers and drug molecules amongst others and offers the opportunity to move the single measurement, point of care paradigm to continuous monitoring.

If the application of microneedle sensor arrays is to be of use here, then the target analytes should be present in the dermal ISF and studies over the past few years have shown that this is indeed the case for both proteins [7] and therapeutic drugs [8].

Nucleic acid aptamers are short single stranded DNA or RNA sequences selected to bind target molecules with good affinity and specificity. The selection typically uses the SELEX (Systematic Evolution of Ligands by Exponential Enrichment) to identify binding sequences in a large (10^{14}) pool of random sequences [9]. Once known the DNA sequence can be synthesized and modified, for example with a redox active group, such that analyte binding brings about a structure switch (Fig. 1). This alters the distance between

References

1. Cass, A.E.G., Sharma, S.: Microneedle enzyme sensor arrays for continuous in vivo monitoring. *Meth. Enzymol.* **589**, 413–427 (2017)
2. El-Laboudi, A., Oliver, N.S., Cass, A., Johnston, D.: Use of microneedle array devices for continuous glucose monitoring: a review. *Diabetes Technol. Ther.* **15**(1), 101–115 (2013)
3. Sharma, S., El-Laboudi, A., Reddy, M., Jugnee, N., Sivasubramaniyam, S., El Sharkawy, M., Georgiou, P., Johnston, D., Oliver, N., Cass, A.E.G.: A pilot study in humans of microneedle sensor arrays for continuous glucose monitoring. *Anal. Methods* **10**(18), 2088–2095 (2018)
4. Miller, P.R., Xiao, X., Brener, I., Burckel, D.B., Narayan, R., Polsky, R.: Microneedle-based transdermal sensor for on-chip potentiometric determination of K(+). *Adv. Healthc. Mater.* **3**(6), 876–881 (2014)
5. Rawson, T.M., Sharma, S., Georgiou, P., Holmes, A., Cass, A., O'Hare, D.: Towards a minimally invasive device for beta-lactam monitoring in humans. *Electrochem. Commun.* **82**, 1–5 (2017)
6. Rawson, T.M., O'Hare, D., Herrero, P., Sharma, S., Moore, L.S.P., de Barra, E., Roberts, J.A., Gordon, A.C., Hope, W., Georgiou, P., Cass, A.E.G., Holmes, A.H.: Delivering precision antimicrobial therapy through closed-loop control systems. *J. Antimicrob. Chemother.*, pp. 1–9 (2017)
7. Tran, B.Q., Miller, P.R., Taylor, R.M., Boyd, G., Mach, P.M., Rosenzweig, C.N., Baca, J.T., Polsky, R., Glaros, T.: Proteomic characterization of dermal interstitial fluid extracted using a novel microneedle-assisted technique. *J. Proteome Res.* **17**(1), 479–485 (2017)
8. Kiang, T.K.L., Ranamukhaarachchi, S.A., Ensom, M.H.H.: Revolutionizing therapeutic drug monitoring with the use of interstitial fluid and microneedles technology. *Pharmaceutics* **9**(4) (2017)
9. Famulok, M., Mayer, G.: Aptamers and SELEX in chemistry & biology. *Chem. Biol.* **21**(9), 1055–1058 (2014)
10. Arroyo-Currás, N., Dauphin-Ducharme, P., Ortega, G., Ploense, K. L., Kippin, T.E., Plaxco, K.W.: Subsecond-resolved molecular measurements in the living body using chronoamperometrically interrogated aptamer-based sensors. *ACS Sens.* **3**(2), 360–366 (2018)

Towards the Digital Hospital: From Implant Design to In-Clinic Bio Fabrication

J. Munguia, Zhichao Ma, and Y. Ugurluoglu

Abstract

The application of biocad, digital manufacturing and virtual visualization techniques for healthcare purposes is on a steady growth, with different medical units such as anesthetics, genetic medicine, dentistry and medical physics gradually adopting them on a normal basis. Whilst University-Hospitals have the advantage of having support from mechanical, bioengineering and design departments, some common questions arising from other independent healthcare systems wanting to apply digital technologies are: who can perform the design? What software is available and what is need it to operate it? How can manufacturing be adopted at point of care? This work describes the experience of different units across the Newcastle Hospitals NHS Foundation Trust on how digital design and manufacturing technologies are permeating the conventional Healthcare structure, including an insight into how the in-clinic fabrication possibilities afforded by digital technologies can change the medical devices supply chain for a variety of purposes including: medical devices development, design of teaching aids, advanced visualization and bio fabrication.

Keywords

Digital hospital • 3D printing • NHS

1 Introduction

1.1 The Digital Hospital

The word “Digital” has been indistinctly to a number of concepts ranging from “Digital health”, “Digital healthcare”, “Digital Medicine” or “Digital diagnostics”. Most sources

J. Munguia (✉) · Z. Ma · Y. Ugurluoglu
School of Engineering, Newcastle University, Newcastle upon Tyne, NE17RU, UK
e-mail: Javier.munguia@ncl.ac.uk

discussing the feasibility of future “Digital hospitals” do it in the context of Information and Communication Technologies (ICT), Artificial Intelligence (AI) for diagnostics, patient data systems automation and big data mining [1]. In fact, the UK National Health Care Service (NHS) has designed a 2020 vision prioritizing: patient data management, data standardization and cybersecurity [2] which has resulted in a number of ICT initiatives across the NHS trust including patient records digitalization and encryption [3]. This communication addresses a different side of the “Digital Hospital” which also acknowledges the importance of patient and health data, but goes beyond to explore the increasing digitalization occurring across different medical fields in public and private healthcare, as well as the new enabling design and manufacturing technologies which will tend to replace or “digitize” conventional provision services.

1.2 The Trend Towards Digitalization

The proposed concept of a digital hospital is that in which not only all sources of patient data are digitized and inter-linked, but also includes the ‘digital literacy’ of clinical staff in the handling of medical imaging software, proficiency in biocad/bio design, as well as in-house expertise in the use of digitalization equipment of various forms and the generation of in-clinic medical devices, medical aids and potentially the means to produce these (Table 1).

2 A Map of Medical Digitalization

2.1 Newcastle University and NHS Trust

There is evidence of different medical applications of digital design and manufacturing technologies (aka 3D Printing) since the late 1990s [4, 5] however it wasn’t until the past decade where the use of such technologies became widespread across different health systems. Recent reviews

Table 1 Some medical fields and common digitalization taking over conventional practice

Biomechanics	<ul style="list-style-type: none"> • Digital scan data of upper and lower limbs replacing plaster casts and foam impressions • Inertial and image based gait analysis replacing markers • Standardized anatomic implants replaced by Custom CAD-based design of anatomic implants
Prosthetics/orthotics	<ul style="list-style-type: none"> • 3D scanning of foot/ankle-foot orthotics, splints, bracing • Plantar Pressure mapping for computational analysis • Digitizing of remaining limb for prosthetic socket design
Medical imaging	<ul style="list-style-type: none"> • Image segmentation/reconstruction from CT, MRI, US • BioCAD (Computer Aided Design based on biomedical data) • Preparation of 3D digital files for digital manufacturing
Dentistry	<ul style="list-style-type: none"> • Intraoral and external dentures 3D image acquisition • Replacement of silicone mold impressions via dental scanning • Replacement of plaster casts with 3d dental CAD • Crown, bridge and dentures design via BioCAD

Table 2 Different medical units adopting digitalization approaches in the Newcastle area ('UNEW' denotes Newcastle University units)

Medical device development	Surgical aids and bio printing	Teaching and training aids
Freeman Hospital, Lung Function Unit/UNEW CPAP masks provision	Dental Hospital, (UNEW) Mandibular 3D models	RVI Anesthetics unit Ultrasound 3D training kit
RVI, Medical Physics 3D Printing of home-use devices	Mechanical Engineering (UNEW) Custom hip/joint implants	Institute of Neuroscience (UNEW) 3D Scanning sensorial models
PCK Medical Group 3D Scoliosis Bracing	Mechanical Eng. (UNEW) Cell printing/osteocondral plugs	Inst. Genetic Medicine Embryonic Digital Database

describe the use of Digital Manufacturing to produce bones, ears, exoskeletons, windpipes, jaws, prosthetics, cell cultures, stem cells, blood vessels, vascular networks, tissues, and organs, as well drug delivery devices [5–7]. We have mapped a number of key actors from the Newcastle university/healthcare ecosystem, which is representative recent “digitalization” initiatives in the UK (Table 2), splitting the activity into: (1) medical device development, (2) Surgical aids and bioprinting and (3) Teaching and training aids. The next section describes a number of selected case studies.

3 Towards the Digital Hospital: Projects Across the Newcastle (UK) Ecosystem

3.1 On-Site Medical Device Design and Development

Home-use devices: Uroflowmeter. A number of Hospitals across the NHS trust operate internal units which have the capacity to provide specialists services such as gait analysis, clinical measurement (urodynamic, spinal cord monitoring, etc.) and mechanical engineering for the manufacture of specialist parts and instruments not commercially available [8]. A feasibility study with the Regional Medical Physics

Department (Royal Victoria Infirmary, Newcastle) explored the potential of in-clinic digital manufacturing of a uroflowmeter which had been previously developed by the RVI team (Fig. 1). The six month project [9] took the team through 3 new product iterations concluding that in-house digital manufacturing could modify the existing supply chain for this device which is currently manufactured in Asia, assembled in continental Europe and calibrated in the UK.

CPAP masks provision. A project involving Obstructive Sleep Apnea (OSA) patient observation at Freeman Hospital (Newcastle Trust. Lung Function Department) is exploring the design and optimization of custom CPAP masks via 3D scanning and digital manufacturing. Currently over 50% of patients quit OSA treatment after 4 weeks and only 4% comply with full use of overnight sleep masks [10]. A digital measurement and prescription method is expected to optimize the prescription and design of respiratory interfaces leading to an increase in compliance, improving acceptance and optimizing the treatment (Fig. 2).

Custom Foot orthoses. The first attempts to produce customized foot orthoses via Digital Manufacturing started by an EU funded initiative in 2010 [11] which aimed at establishing a novel supply chain for the provision of custom

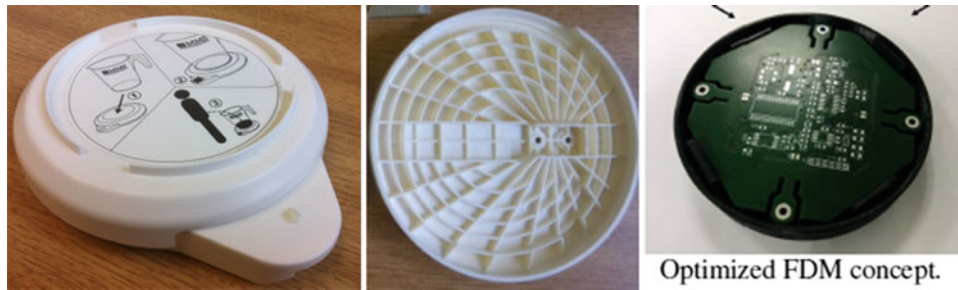


Fig. 1 RVI Medical Physics Department. Design and 3D printing of home-use medical devices (Dr. Michael Drinnan). Injection molded device (left) and 3D printed equivalent (right)

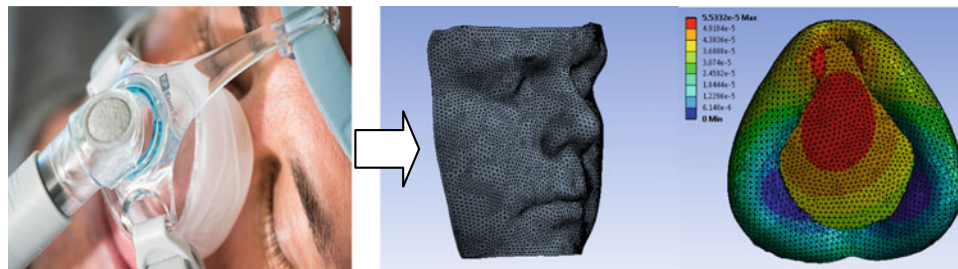


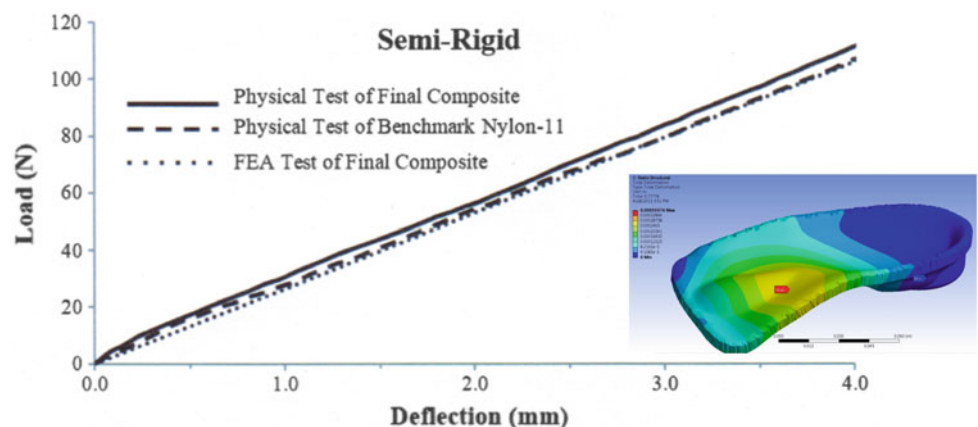
Fig. 2 Development of a novel prescription method for OSA masks based on Digital facial scanning, measurement and computational pressure analysis of CPAP mask interfaces

orthotic devices to the NHS. In Newcastle, this initiative was commercially exploited by the local startup PODFO Ltd who partnered with Newcastle University for the long-term mechanical stability and materials behavior of a number of 3D printed materials including Nylon12, Nylon11 and a range of Polyurethane flexible formulations. The results conformed the basis for an internal system for integrity/product validation (Fig. 3) which is currently followed by the company to supply custom devices through the UK and Europe.

3.2 Medical 3D Imaging and Surgical Aids

Embryonic Digital Database. The Institute of genetic Medicine (Institute of Child Health) has developed a Biology Resource (HDBR; www.hdbr.org) consisting on a human fetal tissue bank comprising: (i) High-quality materials from embryonic and early fetal stages, tissues for cell culture (ii) An In-House Gene Expression Service that undertakes studies for registered researchers; (iii) A web-based database (HuDSeN) for dissemination of human

Fig. 3 Load versus deflection analysis of several conventional, 3D printing materials and virtual simulation of a typical foot orthotic design



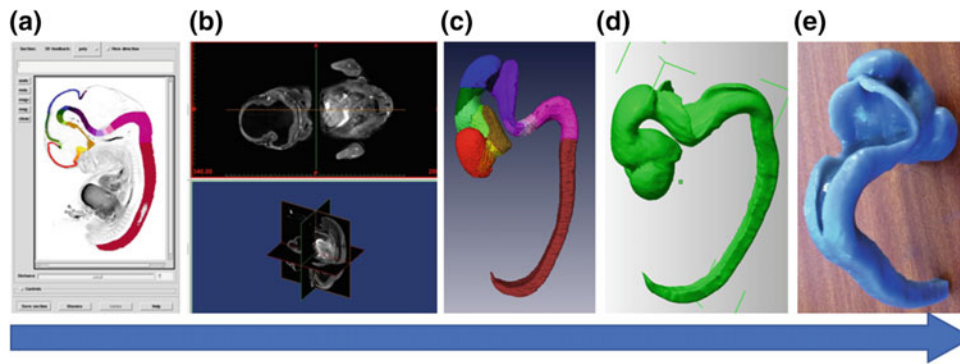


Fig. 4 Embryonic model conversion: From **a** organ ‘Coloring’ to **b** MRI, **c** BioCAD, **d** Slicing, **e** 3D Printing. Institute of Genetic Medicine (Dr. Susan Lindsay)

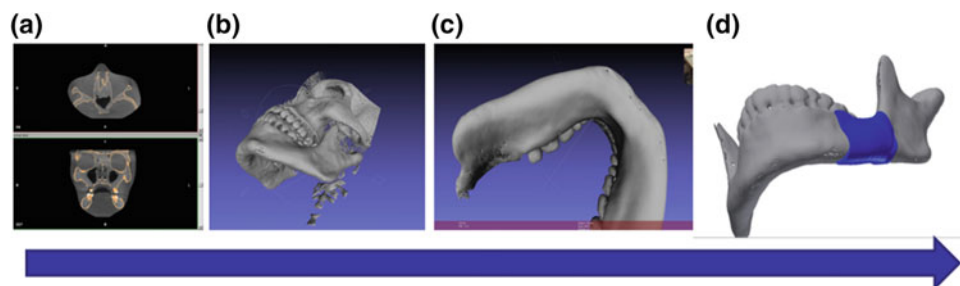


Fig. 5 Conversion of CT patient data (**a**) into a high quality mandibular model (**b–c**) for surgical simulation. Newcastle Dental Hospital, (Dr. Mat German), Newcastle University (J. Munguia)

gene expression data spatially mapped to 3D models. Some of these models have been digitalized and converted to real models (Fig. 4) so that students can benefit from a close interaction with models that otherwise could only be visualized as 2D medical datasets.

Anatomic mandibular plaques from CT scan data. Digital maxillofacial and neuroanatomical models can be particularly helpful to dental and neurosurgeons by providing a representations of complicated structures in the human body [12]. The Dental Hospital at Newcastle University has explored the conversion of CT datasets for the feasibility evaluation of custom mandibular implants via BioCAD and 3D printing (Fig. 5). Early datasets were originally converted using Open source software such as Invesalius and 3DSlicer, however there is an increasing amount of surgical teams within the hospital adopting commercial BioCAD alternatives due to the automatic segmentation and model smoothing options embedded within the software (Materialise MIMICS, Simpleware).

4 Conclusions

Digital imaging, visualization, diagnosing and manufacturing technologies are increasingly permeating across different medical disciplines. In the UK it is now commonplace to find internal units with complete design, manufacturing and testing capabilities and that includes an increasing amount of BioCAD software and Digital manufacturing.

One of the main challenges remains the training and recruitment of professionals that have the technical background and expertise required on digital technologies on the medical field. Only until 2017 Swansea Morriston Hospital (Wales) created a new biomedical 3D technician position, which is believed to be the first such designation in the UK National Health Service (NHS). This trend is expected to expand and permeate other trusts and clinical units across the country.

Conflicts of Interest The authors certify that they have NO affiliations with or involvement in any organization or entity with any financial interest, or non-financial interest in the subject matter or materials discussed in this manuscript.

References

1. Oxford University Hospitals (OUH): Building the Digital Hospital (2018). (<https://www.ouh.nhs.uk/about/building-the-digital-hospital.aspx>). Accessed May 2018
2. Sheffield Teaching Hospitals: Information and Technology Strategy 2020. NHS Foundation trust (2017)
3. Wachter, R.: Making IT Work: Harnessing the power of health information technology to improve care in England (2016)
4. Chua, et al.: Rapid Prototyping: Principles and Applications (2nd ed) (2003)
5. Schubert, et al.: Innovations in 3D printing: a 3D overview from optics to organs. *Br. J. Ophthalmol.* **98**(2), 159–161 (2014)
6. Klein, et al.: 3D printing and neurosurgery—ready for prime time? *World Neurosurg.* **80**(3–4), 233–235 (2013)
7. Banks, J.: Adding value in additive manufacturing: researchers in the United Kingdom and Europe look to 3D printing for customization. *IEEE Pulse* **4**(6), 22–26 (2013)
8. NHS Foundation Trust: Newcastle Upon Tyne Hospitals services (2018). (<http://www.newcastle-hospitals.org.uk/services/index.aspx>) Accessed May 2018
9. RiHN: Redistributed manufacturing for home-use medical devices (2016). (<http://rihn.org.uk/feasibility-studies/redistributed-manufacturing-for-home-use-medical-devices>). Accessed April 2018
10. Munguia & Ma: Design considerations to prevent pressure ulcers: optimising the respiratory mask interface. In: TVC-Tissue Viability Conference, Newcastle, UK, March 2018 (2018)
11. Munguia, J., et al.: A-Footprint: Ankle and Foot Orthotic Personalization via Rapid Manufacturing. 5th VRAP Leiria, CRC Press, Portugal (2012)
12. Ventola, C.L.: Medical applications for 3D printing: current and projected uses. *Pharm. Ther.* **39**(10), 704–711 (2014)

Integration of Microfluidic Sensors for Interactive Remote Wireless Data Transmission

Enobong E. Bassey and Philip Sallis

Abstract

Recently, applications of nanotechnology in trace analyses of substances have increased very significantly. With improvements in properties of nanomaterials, such as larger surface area and surface effect, and quantum size and quantum tunnel effects, nanomaterials have been integrated to improve the sensing capabilities of microfluidic chemical sensors. This has resulted in an increase in the range of applications of microfluidics in nanotechnology and biotechnology. With the increasing miniaturization into lab-on-a-chip, chemical sensors are widely employed in various applications for the direct correlation of physical signal with incidences of chemical phenomena in health and environment. These have resulted in faster processing of samples of analytes for biotechnology and clinical diagnosis. Current applications could be extended to analyze ultra-trace analytes, and easily incorporate the information into a wireless network for real-time analyses. Therefore, this paper will explore technologies for coupling nanomaterials and microfluidic chemical sensors for interactive data transmission to a remote central server, along with analyses, retrieval and visualization over the wireless sensor network.

Keywords

Nanomaterials • Microfluidics • Chemical sensors • Interactive data transmission • Remote wireless system • Metal oxide

E. E. Bassey (✉)
School of Energy, Construction and Environment, Coventry University, Coventry, UK
e-mail: enobong.bassey@coventry.ac.uk

E. E. Bassey · P. Sallis
School of Engineering, Computer and Mathematical Sciences, Auckland University of Technology, Auckland, New Zealand

1 Introduction

Nanomaterials and nanotechnology have attracted extensively applications in energy, sensor devices, medical/health, environment and safety, nanoelectronics and machinery. Interests are mostly focused on multidisciplinary analyses of the transport phenomena and behaviors of nanomaterials for the development of nanodevices and new nanomaterials in many areas. Methodologies include innovations in design, fabrication, synthesis, processing and analyses at nanoscale. Recently, interest and applications have expanded very significantly into the combination of nanomaterials into microfluidic system. But the challenge remains real-time analyses and applications, especially at remote locations.

This paper presents the vital properties of nanomaterials as they apply in analyses of ultra-trace analytes. We will explore technologies for coupling nanomaterials and microfluidic chemical sensors for central interactive data transmission at remote locations, along with analyses and retrieval over the wireless sensor network.

2 Nanomaterials and Nanotechnologies

Nanomaterials can be classified based on different dimensions and shapes. These include nanoparticles, nanocomposites and nanostructures. The best nanomaterials are from metal oxides, such as tin oxide and zinc oxides [1].

Using nanotechnologies, there has been significant research in the physical, chemical and electro-mechanical properties of nanomaterials, resulting in improvement in their applications. With good surface area and surface effects, increase in surface atoms and reduction in particle sizes, nanomaterials are characterized by specific surface behavior, larger functional group density, and selective adsorption capacity. The quantum size and tunneling effects in nanomaterials are caused by the confinement of electrons within particles of dimensions smaller than the bulk

counterpart [2, 3], and the flow of electrical current between two conductors separated by a sufficiently thin insulator [4], respectively.

Improvements in the understanding of these properties (i.e., larger surface area and surface effect, quantum size and quantum tunnel effects) by nanomaterials have promoted more reactive surfaces for transportation of microfluidics and increased the capabilities and applications in a wide number of areas. In a blend of methods and techniques, nanotechnology and microelectronics have governed the development of a new generation of high-density, smart and innovative multi-analyte sensing devices from nanomaterials to meet the rising demand for highly sensitive and highly selective smart sensor systems capable of simultaneously detecting multiple species and transmission/interpretation of signals in real-time for effective decision making.

3 Microfluidics and Flow Patterns

Microfluidics involves the systematic manipulation of fluids through micro-cellular channels in submillimeter scale. This technology has offered new capabilities for the control of molecular fluids and concentrations in spatiotemporal flow condition. Whitesides [5] discussed the fundamentals of microfluidics and the vital possibilities of the technology. Applications abound in the biology, physics and chemistry of microscale fluid transport phenomena, where microfluidics platforms are used for dosing, mixing and separation. Usually, the major components of the microfluidic system consist of a network of microchannels, fluid/sample delivery ports and mixer, microanalyzer, micro-synthesizers, and electrodes, mounted on a three-dimensional structure (Fig. 1).

The flow mechanisms through the microfluidic network could be continuous flow, discrete (droplet or digital) systems. A continuous flow is controlled in the microchannel by applying a continuous hydrostatic pressure between the channel ends [7]. However, continuous flows in interconnected channels could limit the scalability of the number of independent fluid in operations [8].

The discrete flow (digital) systems could be reclassified as a droplet-based microfluidic. Usually, the droplets are transported by modifying the wetting property of the substrate by application of electric potential or optical control. As observed in electrowetting process (Fig. 2), when a suitable voltage is applied on the platform, the droplet moves towards a more wetting regions, e.g., towards the electrode Point B.

This results in the reduction in the contact angle of liquid droplet on a surface due to application of electrical potential [9]. By embedding microelectrodes beneath the dielectric

layer, the local wettability can be modulated using the electrowetting process [7].

Generally, droplet-based microfluidic systems based on multiphase flows can be categorized as discrete microfluidics since there is no independent control of individual droplets [8]. The process involves manipulation of droplets in multiphase flow systems in microchannels. This is different from digital microfluidics, where droplets are manipulated on open, planar surfaces under programmable software control providing real-time control of individual droplets. But, the limitation is the lack of active control of individual droplets during the multiphase flows. Nevertheless, the technology associated with discrete-flow microfluidics can still be applied in discrete microreactors, for rapid mixing and dead volumes reduction [8].

4 Microfluidic Sensing Platforms

The manipulation of sensors and their transport behaviors have resulted in the development of various microfluidic platforms for detection and analyses. These platforms have presented fast detection for comprehensive analytical results, reducing the cost of the analyses and processes, and improving easy implementation of the technology. Various processes have been developed for microfluidics using physical and chemical sensing platforms.

Physical sensing platforms form the fundamental building blocks of a multitude of advanced applications that detect and monitor the surroundings and communicate with the acquired physical data [10]. Some of the physical data include pressure, shear, strain, torsion, temperature, and humidity. The platforms operate based on relative variations in their electrical parameters to detect and quantify the desired physical data, such as pressure and temperature. There are many sensors and actuators operating by the modification of these electrical properties, such as piezoelectricity, triboelectricity, capacitance, or resistance variations.

Chemical sensing platforms, acting as microreactors, present substrates for analysis of conductive fluids using the microfluidic sensor technology. These have been applied in the characterization of chemical and biological assays by employing only a small volume of working fluid to detect an external load. Quantification of the fluid concentration is based on the variations in the electrical parameters (i.e., capacitance or resistance) of the sensing device. These microfluidics-enabled devices provide an ideal platform for the exploration and development of functional liquid-state devices [10]. Applications include biotechnology, biological, chemical and medical analysis methods, such as micro total analysis systems [11].

Fig. 1 Microfluidic system
(Adapted from Boyd-Moss et al. [6])

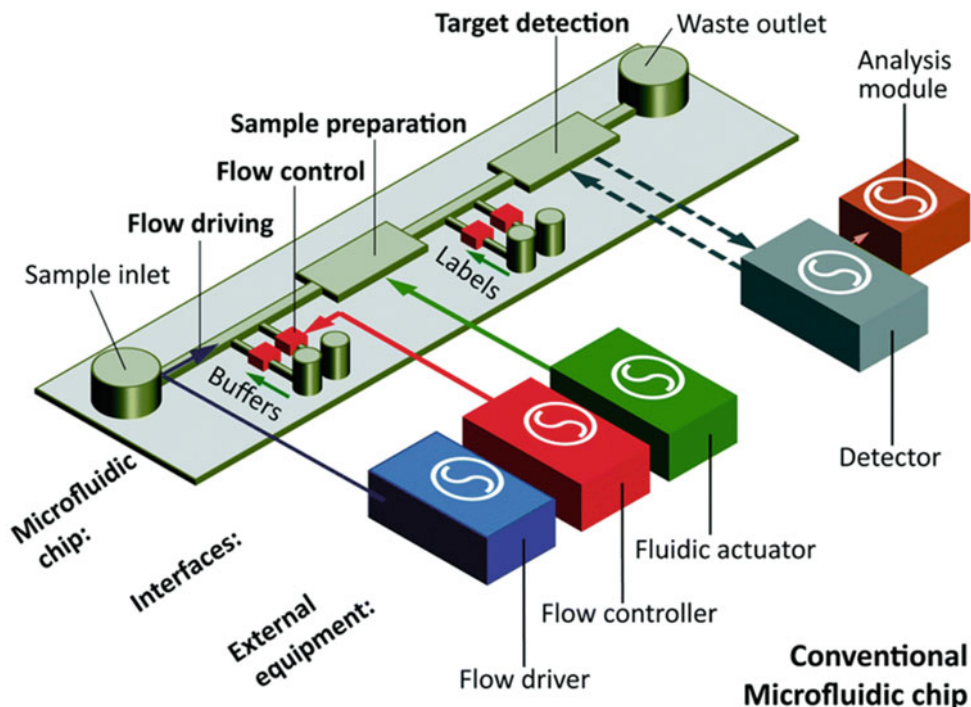
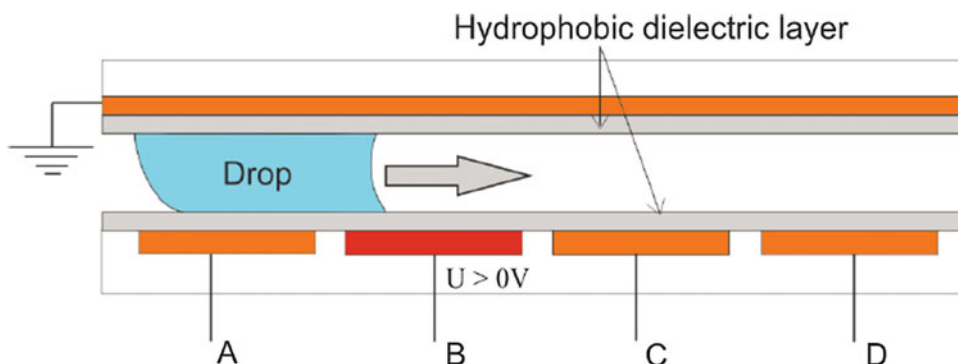


Fig. 2 Droplets can be transported using electrowetting [7]



However, there are some platforms that could be characterize as hybrid platforms. For example, Coelho et al. [12] described a digital microfluidic in which each droplet acts as a single reactor, by allowing for extensive multiparallelization of biological and chemical reactions at a much smaller scale. Kim et al. [13] described an integrated and automated digital microfluidic system for preparing DNA libraries for personal sequencers (Fig. 3). Advantages of this portable and fully automated microfluidic system include volume reduction, shorter reaction time, increased process sensitivity and decrease in sample cross-contamination [12, 13].

Therefore, the basic sensing procedure in microfluidics involve the large-scale integration of various microfluidic

components, such as micropumps, microvalves, microfluidic mixers, microchannels, and other electrodes to control and maintain fluids at the microscale. Detection procedures in microfluidics can be undertaken by mass spectrometry, electrochemical detection, and optical methods.

The combination of nanomaterials and microfluidics through nanotechnology have presented a platform for real-time nanoparticle delivery, reaction monitoring and microcellular processing of analytes microscale. Mostafalu et al. [14] developed a suite of physical and chemical sensors integrated with microfluidic networks to monitor physiochemical tissue properties, all made from thread, for direct integration with tissues toward the realization of a thread-based diagnostic device platform (Fig. 4).

Fig. 3 Schematic representation of the DMF platform proposed, evidencing the location of all the reagents required for DNA sequencing (Adapted from Kim et al. [13])

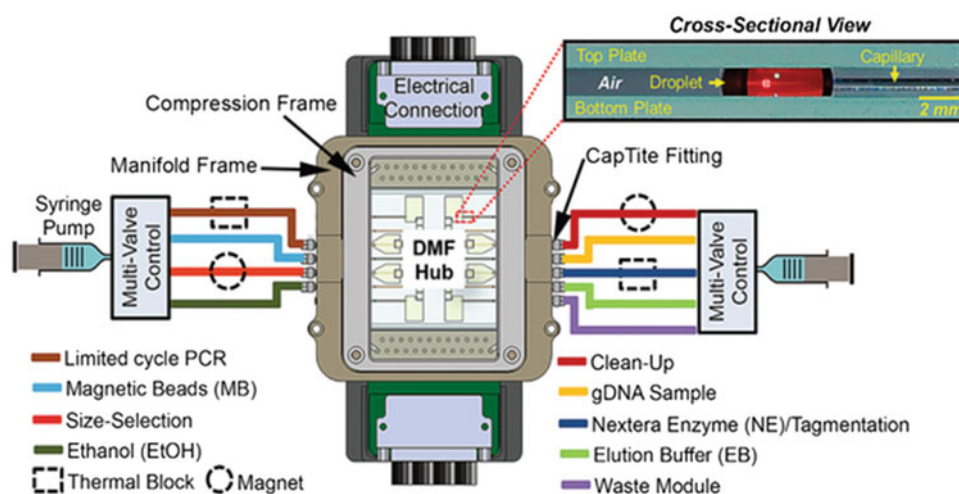
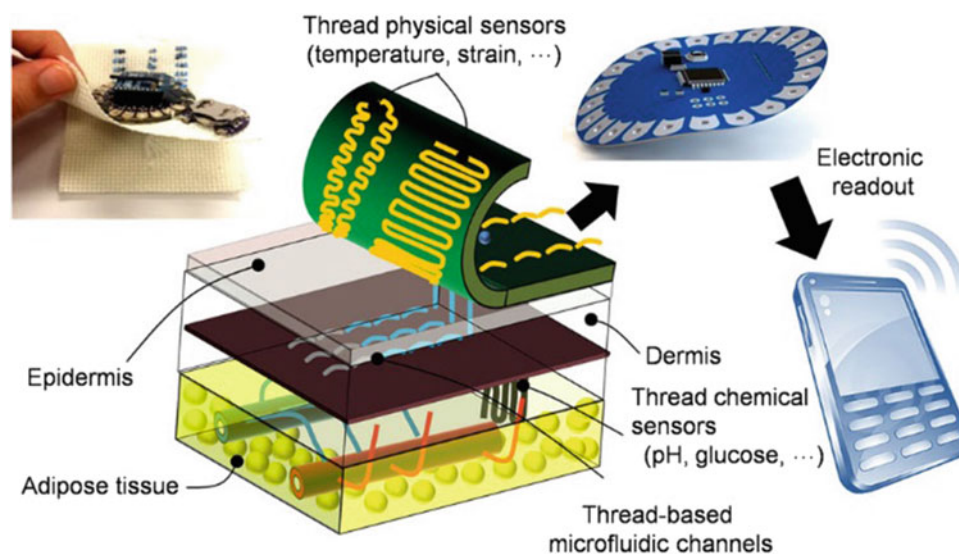


Fig. 4 A toolkit of thread-based chemical and physical sensors, microfluidic channels, and interconnects for the realization of a thread-based diagnostic device Mostafalu et al. [14]



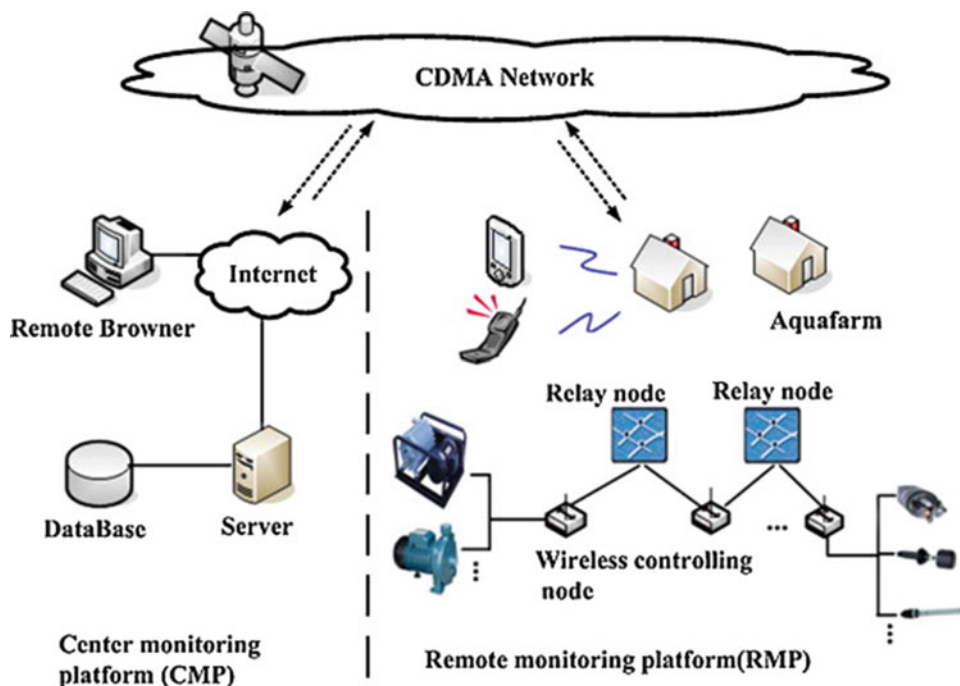
5 Integration of Remote Wireless Microfluidic Sensors

Despite substantial research and innovations in microfluidics and chemical sensor technologies, real-time practical applications with interactive data analyses have remained a major challenge, especially in remote locations. Practical in situ environmental sensing systems must be fully autonomous, operate for extended periods of time, sample at periods when “events” occur, reflect needs in terms of spatial and/or selective measurements, successfully communicate the sensor data remotely, and present the data to relevant users in an easy to use and understandable manner [15, 16]. Therefore, integration of the multi-functional operations of chemical sensors and microfluidics into autonomous wireless sensor networks for real time applications using multi-disciplinary team would be vital for this to be successful.

The basic architecture of the remote wireless system (Fig. 5) is composed of the remote monitoring platform (RMP) and the central monitoring platform (CMP) for data acquisition and data analysis, respectively [17]. The wireless telecommunication system establishes and maintains communication between the remote monitoring platform and the central monitoring platform. The remote monitoring platform involves analyte detection, data acquisition, data transformation and transmission, and quality control components. Non-electrical signals of the analytes from various sensors are obtained by the data-acquisition component. The components of data transformation and transmission are signal conditioning circuits, data-acquisition board, core-processing chip and code-division multiple access (CDMA) module.

Physicochemical parameters of the analytes are converted to electrical signals by the sensors and the signal conditioning circuits. Through the A/D conversion, the signal is

Fig. 5 Structural diagram of our proposed remote wireless network [17]



transmitted to the web-based monitoring chip, and further converted into the digital signal. The on-site data-acquisition nodes compose a wireless local area network (LAN), and the CDMA module enables the RMP to receive the data and transmit them to a PC for further analysis [17].

The function of the central monitoring platform includes acting as a receptor, storage and pre- and post-processor of data/signal from RMP [17, 18]. It analyzes the data and predicts the trend of the parameters according to previous and current interactive information. Real-time signals are relayed via web-based servers at scheduled intervals. If the signals are above preset trace or toxicity level, early warning signals are relayed to the stakeholders for immediate action.

6 Conclusion

This paper will explore technologies for coupling nanomaterials and microfluidic chemical sensors for interactive data transmission to a remote central server, along with analyses, retrieval and visualization over the wireless sensor network. A typical multi-functional system would consist of the chemical sensors, microfluidic network, electrodes, detectors, pumps, valves, etc., designed and integrated by a team of chemists, chemical/mechanical/electrical/electronic/telecommunication engineers and technologists, computer scientists, visualization experts, and web designers. In order to develop this system effectively, every component of the system must be integrated into the remote architecture for

real-time end-to-end sensing, microfluidic analyses, transmission and decision making.

Conflict of Interest The authors declare that they have no conflict of interest.

References

1. Bassey, E.E., Sallis, P., Prasad, K.: Analysis of methanol sensitivity on SnO₂-ZnO nanocomposite. In: Ikhmayies, S.J., Li, B., Carpenter, J.S., Hwang, J.-Y., Monteiro, S.N., Li, J., Firrao, D., Zhang, M., Peng, Z., Escobedo-Diaz, J.P., Bai, C. (eds.) *Characterization of Minerals, Metals, and Materials 2016*, pp. 287–291. Wiley, Hoboken, NJ (2016)
2. Daniel, M.-C., Astruc, D.: Gold nanoparticles: assembly, supramolecular chemistry, quantum-size-related properties, and applications toward biology, catalysis, and nanotechnology. *Chem. Rev.* **104**(1), 293–346 (2004)
3. Mittal, A.K., Banerjee, U.C.: Current status and future prospects of nanobiomaterials in drug delivery A2—Grumezescu, Alexandru Mihai (Chap. 5). In: *Nanobiomaterials in Drug Delivery*, pp. 147–170. William Andrew Publishing (2016)
4. Zhang, P.: Scaling for quantum tunneling current in nano- and subnano-scale plasmonic junctions. *Sci. Rep.* **5**, 9826 (2015). <https://doi.org/10.1038/srep09826>
5. Whitesides, G.M.: The origins and the future of microfluidics. *Nature* **442**, 368 (2006)
6. Boyd-Moss, M., Baratchi, S., Di Venere, M., Khoshmanesh, K.: Self-contained microfluidic systems: a review. *Lab Chip* **16**(17), 3177–3192 (2016)
7. Mampallil, D., George, S.D.: Microfluidics—a lab in your palm. *Resonance* **17**(7), 682–690 (2012)

8. Sista, R., Hua, Z., Thwar, P., Sudarsan, A., Srinivasan, V., Eckhardt, A., Pollack, M., Pamula, V.: Development of a digital microfluidic platform for point of care testing. *Lab Chip* **8**(12), 2091–2104 (2008)
9. Cooney, C.G., Chen, C.-Y., Emerling, M.R., Nadim, A., Sterling, J.D.: Electrowetting droplet microfluidics on a single planar surface. *Microfluid. Nanofluid.* **2**(5), 435–446 (2006)
10. Kenry, Y., Yeo, J.C., Lim, C.T.: Emerging flexible and wearable physical sensing platforms for healthcare and biomedical applications. *Microsyst. Nanoeng.* **2**, 16043 (2016)
11. Imai, S.: Rolling performance of liquid marbles enhanced by optimizing particles as digital microfluidics actuators. *Sens. Actuators, A* **274**, 73–84 (2018)
12. Coelho, B., Veigas, B., Fortunato, E., Martins, R., Águas, H., Igreja, R., Baptista, P.V.: Digital microfluidics for nucleic acid amplification. *Sensors (Basel, Switzerland)* **17**(7), 1495 (2017)
13. Kim, H., Jebraill, M.J., Sinha, A., Bent, Z.W., Solberg, O.D., Williams, K.P., Langevin, S.A., Renzi, R.F., Van De Vreugde, J. L., Meagher, R.J., Schoeniger, J.S., Lane, T.W., Branda, S.S., Bartsch, M.S., Patel, K.D.: A microfluidic DNA library preparation platform for next-generation sequencing. *PLoS ONE* **8**(7), e68988 (2013)
14. Mostafalu, P., Akbari, M., Alberti, K.A., Xu, Q., Khademhosseini, A., Sonkusale, S.R.: A toolkit of thread-based microfluidics, sensors, and electronics for 3D tissue embedding for medical diagnostics. *Microsyst. Nanoeng.* **2**, 16039 (2016)
15. Diamond, D., Collins, F., Cleary, J., Zuliani, C., Fay, C.: Distributed environmental monitoring. In: Filippini, D. (ed.) *Autonomous sensor networks: collective sensing strategies for analytical purposes*, pp. 321–363. Springer, Berlin (2013)
16. Glasgow, H.B., Burkholder, J.M., Reed, R.E., Lewitus, A.J., Kleinman, J.E.: Real-time remote monitoring of water quality: a review of current applications, and advancements in sensor, telemetry, and computing technologies. *J. Exp. Mar. Biol. Ecol.* **300**(1), 409–448 (2004)
17. Zhu, X., Li, D., He, D., Wang, J., Ma, D., Li, F.: A remote wireless system for water quality online monitoring in intensive fish culture. *Comput. Electron. Agric.* **71**, S3–S9 (2010)
18. Capella, J.V., Campelo, J.C., Bonastre, A., Ors, R.: A reference model for monitoring IoT WSN-based applications. *Sensors (Basel, Switzerland)* **16**(11), 1816 (2016)

An Electrochemical DNA Sensor Based on Conducting Polymer Electrode

Trieu Van Vu Quan, Tran Quang Thinh, Le Binh Dươg, Tran Hong Thuy, Chu Thi Xuan, and Mai Anh Tuan

Abstract

In this paper, a DNA aptamer was detected by electrochemical DNA sensors. To enhance the sensitivity and selectivity, the working electrode surface of the electrochemical sensor was modified by a synthesis of poly-pyrrole nanowires. Characterization of poly-pyrrole nanowire was verified by SEM images. The evaluation of DNA sensors was implemented using EC301 Potentiostat from SRS. The sensor can detect the DNA concentration as low as 10^{-12} mol/l. A series of measurement were conducted, which showed the relationship between DNA concentrations and peak current.

Keywords

Electrochemical DNA sensors • Potentiostat • Conducting polymer

1 Introduction

DNA diagnostics have significant applications in many fields as agriculture, medicine, molecular biology and forensics [1–3]. Since the first widely adopted method for DNA sequencing of Maxam-Gilbert in 1977 [4], much effort has been made to improve the performance of the test [5–8]. DNA assay based on hybridization [9], where bio-recognition event occurs due to the affinity between

complementary single-stranded DNA, has been utilized since the early 90s. Today, the method, combined with the advancement of micro-technology, lead to a development of DNA sensors, Lab-on-a-chip (LOC) or Point-of-care-test (POCT). Many approaches have been proposed to improve a detection of hybridization event with high sensitivity and selectivity, including acoustic, optical and electrochemical techniques [10]. One challenge to the DNA sensor lies in the immobilization process, where the DNA must be effectively linked to the solid support for secure signal transduction. Some conventional immobilization techniques could be listed, such as retention in a polymeric matrix, covalent attachment on a functionalized support and polypyrrolization [11].

Conducting polymers play the role of active substrate that has unique electronic, chemical and biochemical properties and was utilized widely in numerous applications, including energy storage, electro-catalysis and chemical sensors [11]. They contain π -backbone which is responsible for unusual electronic properties such as electrical conductivity, low ionization potential and high electronic affinity [12]. The characteristics could be explained through the formation of non-linear defects in polymer structure, which are polarons, bipolarons and solitons [12, 13]. A number of conducting polymer materials have been used extensively in many applications, such as drug delivery, environmental and clinical monitoring, super capacitors, batteries and biosensors, etc. In biosensors, the conducting polymer formed suitable matrices of biomolecules, which enhance speed, sensitivity and versatility of the biosensors [14]. On top of that, polypyrrole was used extensively in DNA biosensors due to its good bio-compatibility and polymerization ability at neutral pH.

This paper shows the procedure used for synthesis of polypyrrole nanowire and immobilization process. The immobilized sensors were then used to detect label-free DNA through the voltammetric technique.

T. Van Vu Quan (✉) · T. Q. Thinh · L. B. Dươg · M. A. Tuan
National Center for Technological Progress, Hanoi, Vietnam
e-mail: quan.trieu@mph.vn

M. A. Tuan
e-mail: tuan.maianh@mph.vn; tuan.maianh@gmail.com

T. H. Thuy · C. T. Xuan
Hanoi University of Science and Technology, Hanoi, Vietnam

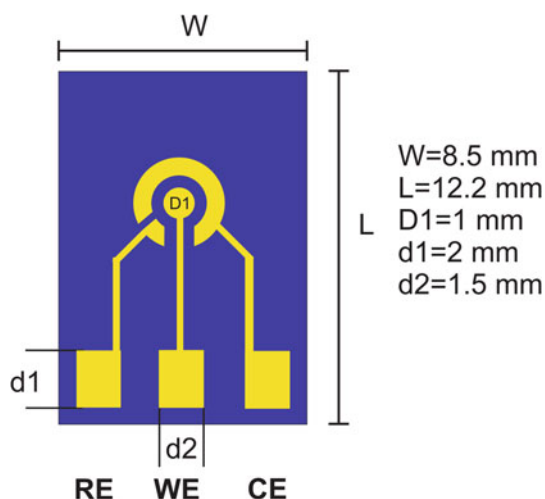


Fig. 1 Triple electrode configuration

2 Experimental

2.1 Triple Electrode Configuration

Triple-electrode configuration is the most common structure for design and development of electrochemical sensor. The structure comprises three distinct electrodes, namely Working electrode (WE), Reference electrode (RE) and Counter electrode/Auxiliary electrode (CE).

A pre-defined voltage was applied between Working and Reference electrode while the current was measured between Working and Counter electrode. The Working electrode is where the reaction occurs in the analysis, and they are often made of noble or inert materials, such as gold, platinum or glassy carbon to not participate in the electron transfer process. In this work, gold has been chosen for electrode material due to its stability, wide range potential and linking ability with biological substances [15]. Three electrodes, including WE, RE and CE, are all integrated on one sensor of which the dimension is $8.5 \times 12.2 \text{ mm}^2$ and WE's area is 3.14 mm^2 . All electrodes were deposited on SiO_2/Si substrate by cathode sputtering technique. The electrodes were designed and fabricated at ITIMS, HUST. The sensors' structure is shown in Fig. 1.

2.2 Immobilization Process

Electrochemical synthesis of Poly-pyrrole nanowire

Pyrrole was purchased from Merck & Co., Inc (Germany). Monomer Pyrrole solution was prepared by mixing phosphate buffer solution (pH 7.4), Gelatin Solution 0.08% weight, LiClO_4 and Monomer Pyrrole 1M in order.

Table 1 Aptamer sequence

Probe sequence	Thiol-C ₆ -5'- AGACCTCCAGTCTCCATGGTACGTC-3'
Target sequence	5'-GACGTACCATGGAGACTGGAGGTCT-3'

Poly-pyrrole nanowire (PPy-NWs) was grown on working electrode by electrochemical polymerization with chronoamperometry technique. The electrode was immersed in pyrrole solution, a fixed voltage, 0.75 V compared to Ag/AgCl reference electrode, will be applied to working electrode to start the deposition process in a period of 200 s.

DNA Probe immobilization

Both DNA Probe and DNA Target are chemicals from Integrated DNA Technologies (IDT) as shown in Table 1.

For immobilization process, DNA probe was taken out of the fridge, at 4 °C, to be defrosted, then it was dropped onto surface-modified working electrode. The electrodes would be stored in a dry place at room temperature (28 °C) for one day. After that, they were taken out and rinsed off to clean the unlinked components. The characterization would be demonstrated by Cyclic Voltammetry (CV) technique.

DNA hybridization

The DNA target was prepared and diluted to be 10^{-6} , 10^{-7} , 10^{-8} , 10^{-9} , 10^{-10} , 10^{-11} and 10^{-12} mol/l in, 7.4 pH, PBS solution. For DNA probe immobilized sensors, 10 μL sample of each concentration was dropped onto the WE surface. The interaction between complementary target and probe would occur in 5 min at 28 °C, then the unlinked molecules will be removed by rinsing with DI water. The polymerization, immobilization and hybridization processes were shown in Fig. 2.

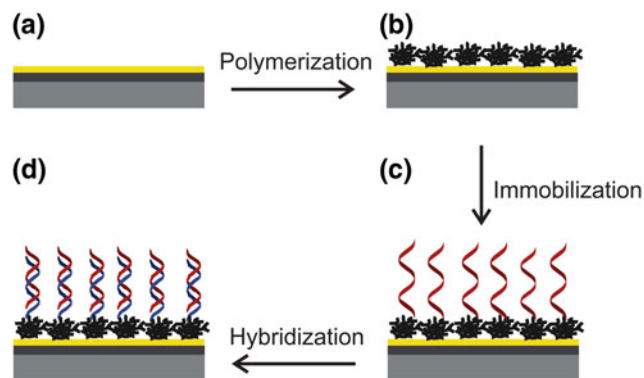


Fig. 2 Polymerization, DNA immobilization and hybridization on the sensor's working electrode

Measurement

The sensors were immersed in electrolyte composing of 0.1M KCl and 0.03M $\text{Fe}(\text{CN})_6^{3-/4-}$ (1:1) as a redox couple. A CV scan by EC301 Potentiostat was performed and the change in current amplitude as well as the voltage where current peak appears were observed and recorded. Voltage was applied from -0.3 to 0.6 V then reversed versus reference electrode at the scan rate of 50 mV/s and temperature at 28 °C.

3 Results and Discussion

3.1 Immobilization Characterization

In PPy-NWs synthesis by electrochemical method, gelatin was used as soft mold [16]. As can be seen in Fig. 3, nanowires were uniformly distributed on the surface of the electrode. The size of PPy-NWs ranges from 60 to 105 nm.

The multi-cycle voltammogram of the sensors is shown in Fig. 4. The highest peak corresponds to the CV scan of bare electrode (line a), the next one belongs to the sensor when PPy was synthesized onto the bare electrode (line b). The lowest peak shows the result of the sensor when the DNA probe had been immobilized (line c). The decreasing trend of current when growing Polypyrrole to the electrode's surface and then the DNA probe was immobilized could be explained for two reasons. First, the impedance of PPy is

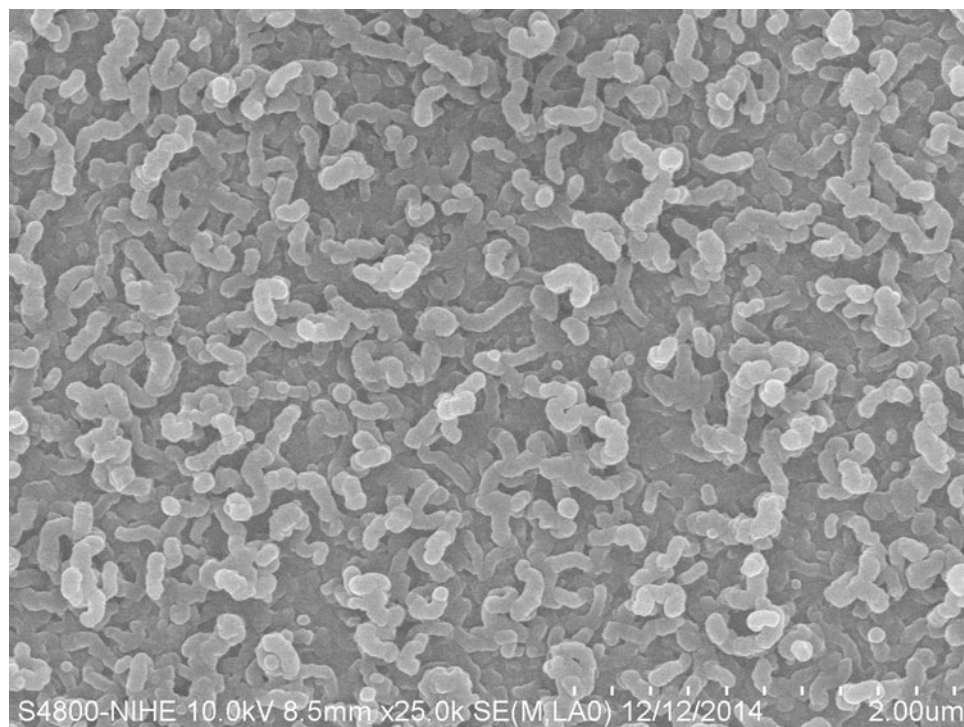
higher than that of Au, which partly inhibits the charge transfer process between electrolyte and the Working electrode surface. Second, the inhibition was also caused by the presence of negatively charged ions (ClO_4^- , HPO_4^{2-} , etc.) on PPy structure that was doped during the electrochemical polymerization. When DNA probe was immobilized onto the surface of polymers, the binding occurs via the reaction between a phosphate group at 3' terminal of DNA and a N-H group of PPy [16]. The presence of phosphate group onto PPy impedes the transfer process of $\text{Fe}(\text{CN})_6^{3-/4-}$ ions with the electrode surface, which further enhances the charge transfer resistance and decreases the current peak response.

3.2 Label-Free DNA Detection

Figure 5 shows the CV response of a sensor before and after hybridization. A decrease in peak current and positive voltage shift in oxidation potential of the polymer film were observed. The reason of potential shift lies in the formation of bulky double-stranded DNA during hybridization, thus increasing the energy required for polymer oxidation. The double layer model suggests that when adding a layer of chemical component onto the electrode surface, a charge barrier will be created. Also, the electron transfer resistance through double stranded DNA is higher than that of single stranded DNA, which caused the decrease in current peak.

The decrease of the peak current after DNA target detection indicates the concentration of the DNA target. For

Fig. 3 SEM Image of working electrode with PPy-NWs



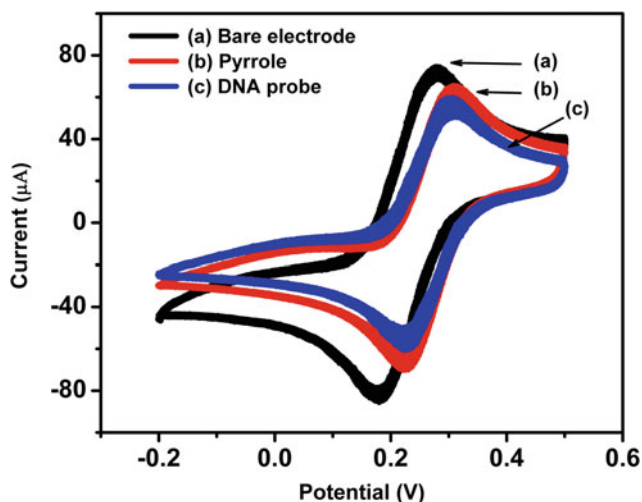


Fig. 4 Voltammogram after each steps: **a** bare electrode, **b** electrode pyrrolization and **c** DNA probe immobilization

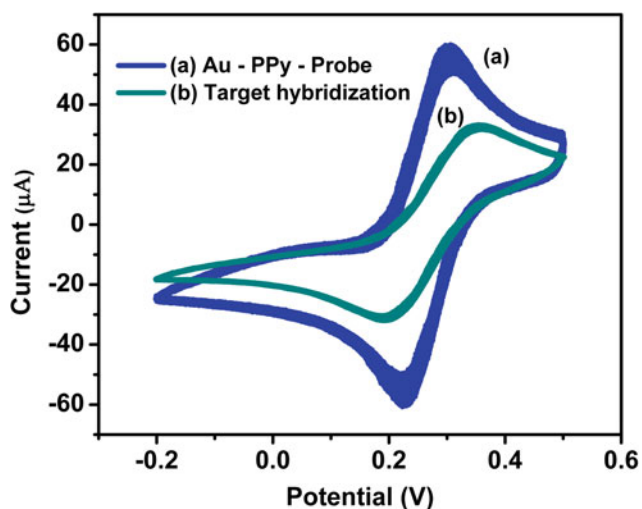


Fig. 5 CV Voltammogram after each step at Target $C = 10^{-6}$ mol/l by EC301

this application, the value ΔI_p as calculated in Eq. (1) will be employed to view on the change after each steps.

$$\Delta I_p = (I_{pa\ Probe} - I_{pc\ Probe}) - (I_{pa\ Target} - I_{pc\ Target}) \quad (1)$$

As the concentration decreases from 10^{-6} to 10^{-12} mol/l, the number of bindings between DNA probe and DNA target also decreases. Naturally, this affects the amplitude of current reduction. The less DNA bindings, the less inhibition they caused to the charge transfer process, thus the difference between the probe peak current and target peak current

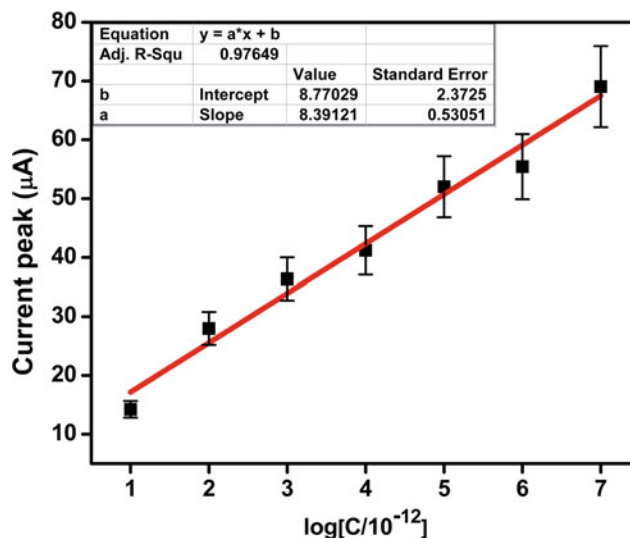


Fig. 6 Relation between ΔI_p and the concentrations of DNA target

decreased. Figure 6 shows that there is a linear relation between ΔI_p and the concentrations of the DNA target. The lowest detectable concentration is 10^{-12} mol/l.

4 Conclusion

This work presented the mechanism and implementation of a label-free electrochemical DNA sensor. The experimental results show that the sensors were successful in detection of DNA aptamers at different concentrations. The sensor also shows high sensitivity as its lowest detectable concentration is 10^{-12} mol/l.

Acknowledgements This research is supported by The World Academy of Science (TWAS) under Grant no. 16-169 RG/PHYS/AS_I-FR3240293345.

Conflict of Interest Statement The authors declare that there is no conflict of interest.

References

- Dewey, F., Pan, S., Wheeler, M., Quake, S., Ashley, E.: DNA sequencing: clinical applications of new DNA sequencing technologies. *Circulation* **125**, 931–944 (2012)
- Liu, G.E.: Recent applications of DNA sequencing technologies in food, nutrition and agriculture. *Recent. Pat. Food Nutr. Agric.* **3**, 187–195 (2011)

3. Weber-Lehmann, J., Schilling, E., Gradl, G., Richter, D., Wiehler, J., Rolf, B.: Finding the needle in the haystack: differentiating “identical” twins in paternity testing and forensics by ultra-deep next generation sequencing. *Forensic Sci. Int.: Genet.* **9**, 42–46 (2014)
4. Maxam, A., Gilbert, W.: A new method for sequencing DNA. *Proc. Natl. Acad. Sci.* **74**, 560–564 (1977)
5. Reinartz, J.: Massively parallel signature sequencing (MPSS) as a tool for in-depth quantitative gene expression profiling in all organisms. *Brief. Funct. Genomics Proteomics* **1**, 95–104 (2002)
6. Edwards, J., Ruparel, H., Ju, J.: Mass-spectrometry DNA sequencing. *Mutat. Res./Fundam. Mol. Mech. Mutagen.* **573**, 3–12 (2005)
7. Zwolak, M., Di Ventra, M.: DNA sequencing via electron tunneling. In: 2012 IEEE International Symposium on Circuits and Systems (2012)
8. Drmanac, R., et al.: Sequencing by hybridization (SBH): advantages, achievements, and opportunities. In: Hoheisel, J., et al. (eds.) *Chip Technology. Advances in Biochemical Engineering/Biotechnology*, vol. 77. Springer, Berlin (2002)
9. Drummond, T., Hill, M., Barton, J.: Electrochemical DNA sensors. *Nat. Biotechnol.* **21**, 1192–1199 (2003)
10. Homs, M.: DNA sensors. *Anal. Lett.* **35**, 1875–1894 (2002)
11. Peng, H., Zhang, L., Soeller, C., Trivas-Sejdic, J.: Conducting polymers for electrochemical DNA sensing. *Biomaterials* **30**, 2132–2148 (2009)
12. Bredas, J., Street, G.: Polarons, bipolarons, and solitons in conducting polymers. *Acc. Chem. Res.* **18**, 309–315 (1985)
13. Malhotra B, Chaubey A, Singh S.: Prospects of conducting polymers in biosensors. *Anal. Chim. Acta.* **578**, 59–74 (2006)
14. Ronconi, L., Marzano, C., Zanello, P., Corsini, M., Miolo, G., Maccà, C., Trevisan, A., Fregona, D.: Gold(III) dithiocarbamate derivatives for the treatment of cancer: solution chemistry, DNA binding, and hemolytic properties. *J. Med. Chem.* **49**, 1648–1657 (2006)
15. Nhan B, Tuan M.: Electrochemical synthesis of polypyrrole for biosensor application. *Int. J. Nanotechnol.* **10**, 154 (2013)
16. Tran, T., Chu, T., Do, P., Pham, D., Trieu, V., Huynh, D., Mai, A.: In-channel-grown polypyrrole nanowire for the detection of DNA hybridization in an electrochemical micro-fluidic biosensor. *J. Nanomater.* **2015**, 1–7 (2015)

Part IX

**Technological Development in Microfluidics, and
Point-of-Care**

Microfluidic Droplets and Their Applications: Diagnosis, Drug Screening and the Discovery of Therapeutic Enzymes

Liisa D. van Vliet  and Florian Hollfelder 

Abstract

Microfluidic droplets are a unique tool for performing biological and chemical experiments. The compartmentalization of single entities, such as plasmids or cells, into microdroplets separated by an immiscible carrier fluid allows for (i) experimentation in the nL- and pL-range which reduces reagent consumption (ii) the generation of highly monodisperse droplets resulting in homogeneous reaction conditions and (iii) microdroplets can be generated with frequencies up to 10 kHz allowing high-throughput screens of up to 100 million reaction conditions per day. If ultrahigh throughput is not necessary, devices interfacing with multiple handling and optical analysis systems provide additional capabilities with more control over the content of each droplet. Microfluidic droplets are used for a variety of biochemical and biomedical assays. They can be used to encapsulate single cells in 3D hydrogel matrices to monitor the effect of specific soluble factors or drugs on differentiation, or follow clonal spheroid formation and drug response. And finally, microfluidic devices enable the high-throughput screening of millions of metagenomic genes to discover new enzymes for improved catalytic efficiency or new therapeutic activities.

Keywords

Microdroplets • Microfluidics • Drug screening • Therapeutic enzymes

1 Microfluidic Droplets

1.1 Introduction

Microfluidics, the control and study of fluids in the micrometer scale, has become an increasingly popular tool for the biomedical researcher, based on its promise to reduce costs by minimizing reagent usage and waste, its potential for high-throughput screening, for point-of-care testing and for mimicking organ behavior and blood flow in microscale body-on-a-chip devices. Further miniaturization can be achieved by segmenting the microfluidic flow into pL to nL water-in-oil droplets. Micron scale droplets were initially used for biological assays as poly-disperse emulsions, where each droplet linked a genotype with its phenotype by encapsulating single DNA plasmids into individual droplets for in vitro transcription and translation (IVTT)—or protein expression—and analysis [1–4]. Microfluidic droplets or microdroplets [5, 6] are now routinely used for a variety of assays as mono-disperse water-in-oil droplets that can be generated at rates in the hundreds of kHz range and provide uniform assay conditions across up to 10^8 to 10^9 droplets per day [7–12].

1.2 High-Throughput Generation of Droplets from a Single Sample

Droplet generation.

The most popular method for producing microfluidic droplet is to use flow-focusing, T-junction or co-flow devices [5, 6, 13, 14], whereby an aqueous stream is split into monodisperse droplets by an immiscible oil flow (see Fig. 1). Depending on the size of the flow focusing junction (e.g. 30 μm in Fig. 1b) and the flow rates of the oil and aqueous phases, highly monodisperse droplets can be generated at frequencies of up to several kHz, allowing for the generation and screening of around 10^8 droplets per day.

L. D. van Vliet (✉) · F. Hollfelder
Department of Biochemistry, University of Cambridge, 80 Tennis
Court Road, Cambridge, CB2 1GA, UK
e-mail: ldv20@cam.ac.uk

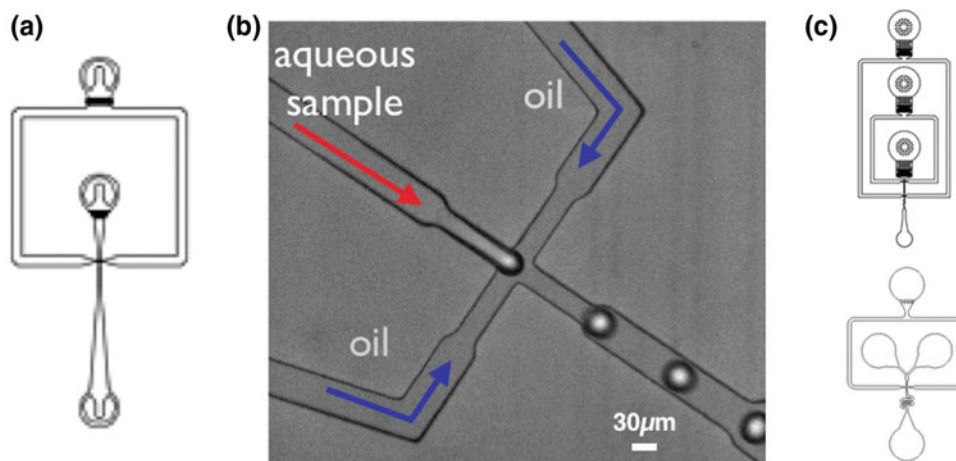


Fig. 1 Flow focusing device. **a, b** This example of a flow focusing device design has a first inlet for the oil and a second inlet for the aqueous samples. The height of the channels and width of the

flow-focusing junction vary from a few to a few hundred μm . **c** Designs can include filters, multiple inlets and various geometries to allow for mixing of reagents immediately prior to droplet formation

The droplets are stabilized in their monodisperse format by adding surfactants to the carrier oil phase. A variety of oil and surfactant combinations have been used [15, 16]. However the consensus is to use fluorinated oils and surfactants that are compatible with biological assays by allowing oxygen diffusion and stabilizing proteins within the aqueous droplets [17–21]. The majority of the surfactants currently used are based on a protocol for making the most successful and bio-compatible surfactant to date, the so-called EA surfactant first described by Holtze et al. [22]. Block co-polymer surfactants are synthesized by coupling perfluorinated polyether (PFPE) and polyethyleneglycol (PEG); they are typically made ‘in-house’ but are commercially available (originally by Raindance and now by Ran Technologies).

Designs for biological assays.

Droplets have been used to perform a variety of biological assays (PCR, cell-based assays, immunoassays, transcriptomics) and various tools or device designs (as in Fig. 1a, c) have been established to replace the conventional liquid handling steps for adding, mixing, diluting and analyzing reagents: devices for droplet generation, droplet storage, droplet merging and pico-injection, droplet immobilization or droplet sorting have been developed [9, 23–26].

The most powerful advantages of the microdroplet technology are (i) its ability to encapsulate single “genotype” entities, such as single fragments of DNA [4, 27–29] or single cells from bacteria [30] to yeast cells [22] and mammalian cells [31–33] (Fig. 2a, b) and (ii) its confinement of the “phenotype” of the enzymatic reactions, substrates and products within these single compartments (Fig. 2c, d).

The distribution of these entities across single droplets follows the ‘Poisson Distribution’, where k is the number of

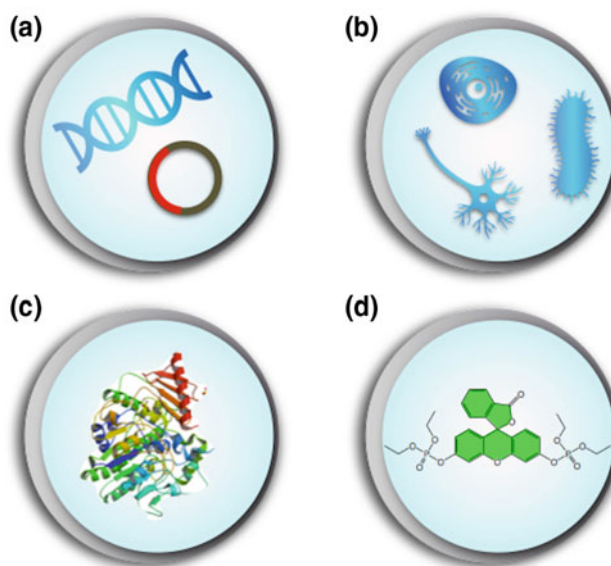


Fig. 2 Biology in droplets. Water-in-oil droplets are stabilized by surfactants. **a** Single fragments of DNA as linear transcription template, plasmids or fosmids can be individually encapsulated for protein expression by IVTT or amplification **b** a variety of cells types have been encapsulated as gene expression hosts, but also for single cell studies, for drug screening or detection of rare cells from clinical samples and **c** enzymes can be directly encapsulated with **d** a variety of chromo- and fluorogenic substrates to analyze their activity

entities (e.g. cells) per droplet and λ is the mean number of entities per droplet volume.

$$P(k; \lambda) = \lambda^k e^{-\lambda} / k! \quad (1)$$

In addition to manipulating and studying these droplets in their water-in-oil emulsion format, they can be re-emulsified via a hydrophilic flow-focusing device to generate water/oil/water compartments or double emulsions [28, 34–36].

1.3 Lower Throughput, Precise Control Over the Droplet Content and Handling

While droplets generated by microfluidic flow-focusing devices offer the ability of high-throughput screening, the main limitation is that all droplets are generated from a single sample (e.g. library of plasmids, or cell solution). We have recently developed several tools to allow precise control over the content of each droplet, with the trade-off of lower throughput (up to several Hz).

Droplets-on-demand platforms generate specific sequences of droplets to create high-precision dilution gradients for drug screening [37–39] (commercialized as the MitoDroplex[®]), to miniaturise immuno-assays [40, 41] or digital PCR reactions (such as the ddPCR[™] system commercialized by QuantaLife, and now Bio-Rad) [15, 27, 42]. A few of these platforms provide the desperately needed interface between droplet generation and the multi-well plate format [43–45].

2 Microdroplets for Diagnosis, Drug Screening and the Discovery of Therapeutic Enzymes

2.1 Diagnostics

The power of microdroplets to encapsulate single cells has been highlighted by the recent breakthroughs in single-cell transcriptomics, namely the inDrop [46] or Drop-Seq [47] methods. This will undoubtedly lead to a better understanding of the cellular processes and diagnostic biomarkers involved in a range of diseases from cancer to diabetes and neurodegenerative disorders [48, 49].

The current gold standard of immuno-assays (ELISA) is limited to detections in the picomolar (10^{-12}) range; by fragmenting the samples into thousands of pL droplets, microfluidic immuno-assays have been shown to detect cancer biomarkers and circulating tumour cells (CTCs) in the fM range (10^{-15}) [50–52] and have been shown to detect the Alzheimer's disease biomarker amyloid-beta [41].

In a future of eHealth and telemedicine, droplets will be used not only for diagnosis, but also for continuous health monitoring and detection of a variety of molecular markers [53, 54]. In short, microfluidic droplets offer the unique capability of detecting rare cells and low concentration of biomarkers while using minimal amounts of sample, and in so doing they promise point-of-care methods for earlier diagnosis.

2.2 Cells in Gels

The ability to study single cells provides insight into the cellular subtypes in heterogenic populations and an

understanding of the mechanisms of cellular behavior. Cells have been encapsulated into culture media droplets for high-throughput drug screening or diagnostics [31, 32] but in order to study cells in their more natural state, these droplets can be turned into 3D hydrogel matrices (Fig. 3). The mechanism of droplet generation is identical, but the aqueous droplets are turned into a gel format by replacing the media with liquid forms or precursors of hydrogels. Agarose and alginate are the most commonly used hydrogels for cell encapsulation, but a variety of hydrogels have been used for microdroplet generation [55–62] (see Fig. 3a). This enables the monitoring of the effect of specific soluble factors or drugs on differentiation, following clonal spheroid formation [63] (Fig. 3c) and drug response on tumors [64, 65], but also encapsulating cells for therapeutic treatment [66].

In addition to encapsulating mammalian cells, hydrogel beads have also been used to form gel shell beads (GSBs) that can retain proteins and small molecules by forming a layer-by-layer polymeric shell around agarose beads during the de-emulsification step (Fig. 3b, d) [67, 68].

2.3 Drug and Enzyme Discovery

As described above, microdroplet assays have been developed for assessing drug toxicity on single cells and tumor models, but they are also used for high-throughput drug discovery. Indeed microdroplet systems for generating combinatorial, dilution gradients or multiplexed drug collections have been used to characterize drug efficacy and enzyme kinetics [44, 68–71].

The key advantages of using microdroplets—high-throughput and encapsulation of single entities—have been successfully used to screen for antibodies and enzymes with new or improved activity. The general scheme of high-throughput screening for enzymes by directed evolution or metagenomic screening (Fig. 4) has now been well established [9, 35, 72].

High-affinity antibody have been screened for by two-hybrid systems [73], phage or snap display [3, 9, 74, 75], and bead surface display (BeSD) [76, 77].

In the search for improved enzymes or completely new ones, libraries of DNA (so far linear templates, plasmids, DNA in *E. coli* hosts, in the future possibly also fosmids) are encapsulated and expressed in microdroplets for functional screening [10]. These libraries can be generated by controlled or random mutations for directed evolution or they can come from metagenomic sources (Fig. 5a). Plasmid DNA can be expressed in droplets via IVTT (in vitro transcription and translation) kits [74–77] or by using an expression host (Fig. 5b). To select for the active genotype, microfluidic droplets can be sorted for fluorogenic [23, 78] or chromogenic [24] reactions at typical rates of up to a few

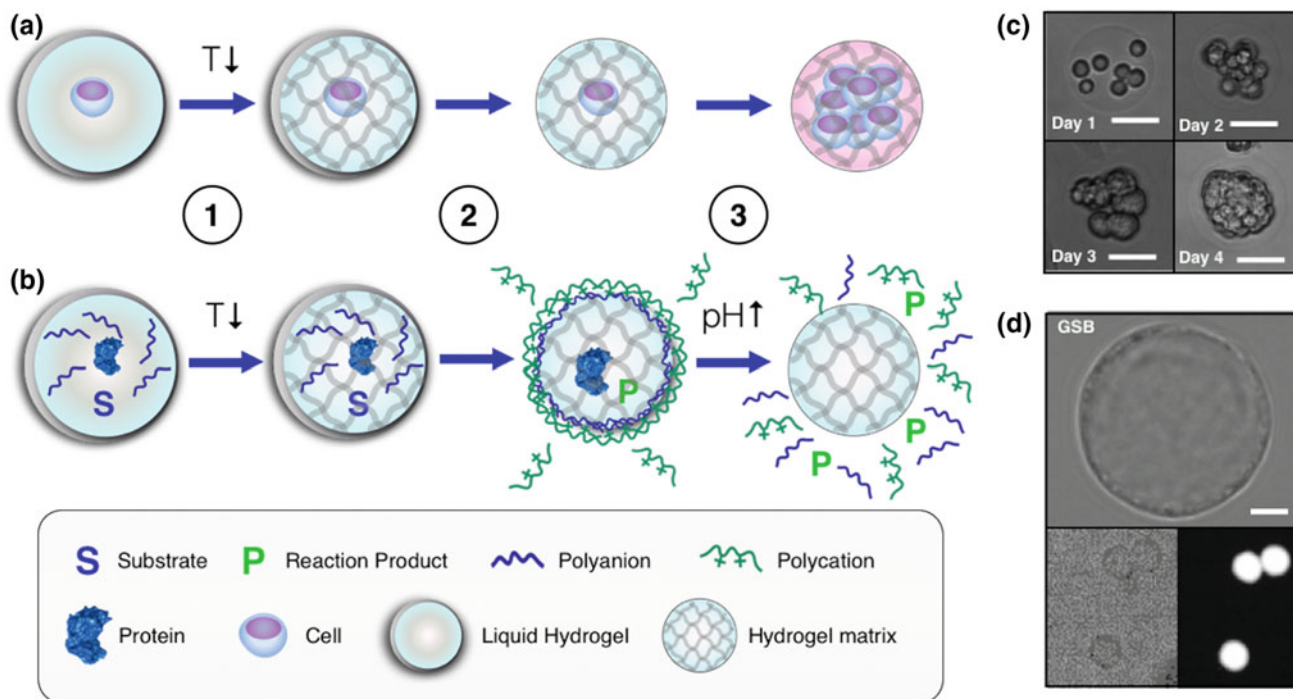
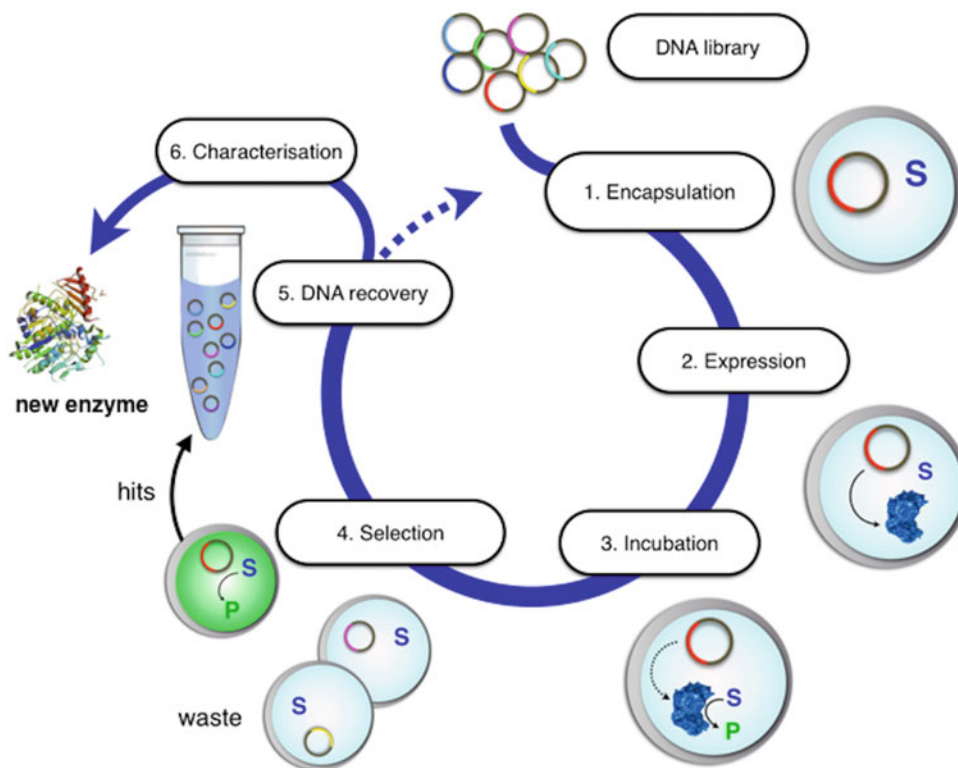


Fig. 3 Hydrogel droplets for (a) cell encapsulation or (b) the formation of gel-shell beads (GSBs). **a** Cells are encapsulated into liquid agarose, which is cooled (1) to form mono disperse hydrogels, which are demulsified (2) and can be perfused by media to allow for cell growth and monitoring (3). **b** To generate GSBs, enzymes and substrate are encapsulated into liquid agarose and alginate (a polyanion), these liquid droplets are cooled to allow for gellification (1) these hydrogel

beads are de-emulsified into a polycation solution which forms a shell layer at the surface of the polyanionic bead that retains the reaction product inside the bead (2). By raising the pH (3), the anion-cation interaction is lost and the hydrogel contents leak out of the bead. **c** Encapsulated HeLa cells form spheroids after 4 days of incubation, scale bars = 200 μm . **d** A GSB in PBS, and bright field and fluorescence images that show retention of fluorescein within the 50 μm GSB, scale bar = 10 μm

Fig. 4 Workflow for enzyme discovery by directed evolution or metagenomic screening.

Single nucleic acids from a DNA library are encapsulated into droplets with a chromo- or fluorogenic substrate (1), which, if it encodes for an enzyme, is expressed (2). After incubation (3) the droplets containing active enzymes are sorted (4) and the “active” DNA is recovered (5) for further characterization (6) or a new round of mutations and selection



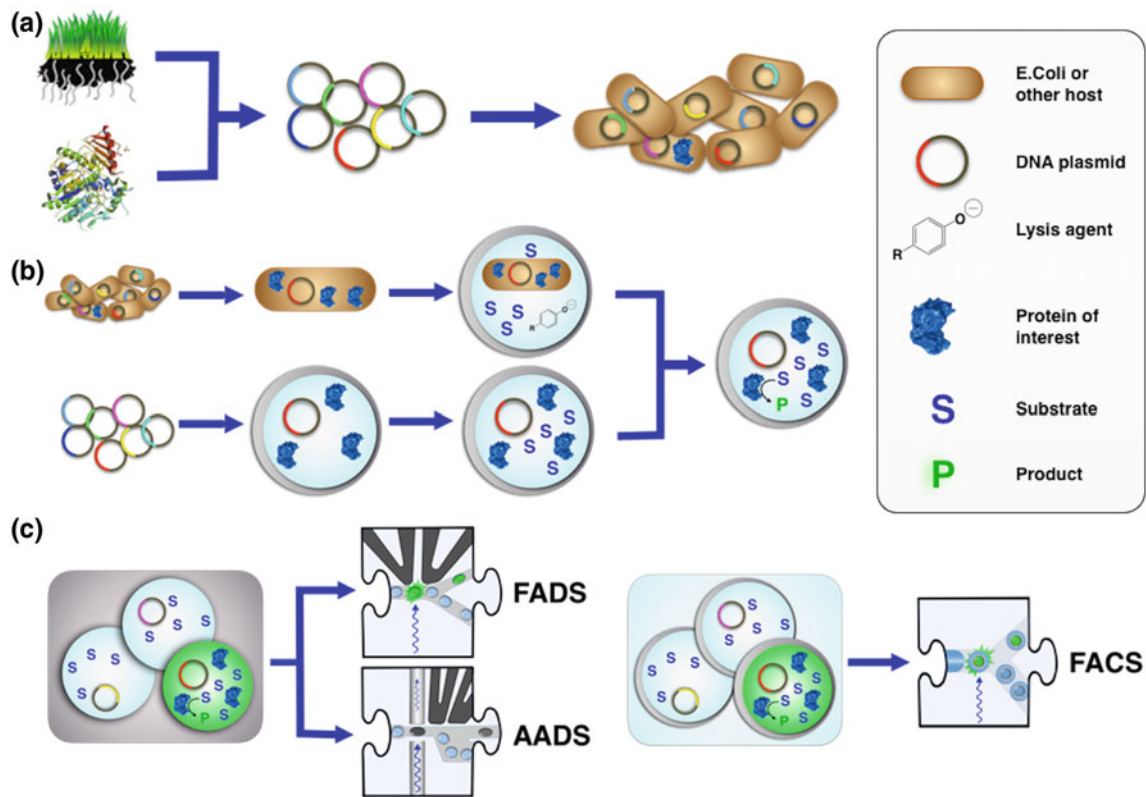


Fig. 5 High-throughput functional screening in droplets. **a** First, a DNA library is generated from metagenomic DNA or enzyme mutants that are cloned into a host (most commonly *E. Coli*). **b** The host is used to express the enzyme and are encapsulated with substrate, but plasmid DNA can also be used to directly express proteins by encapsulation with and IVTT mix. The droplets containing active genes will turnover the

fluoro- or chromogenic substrate. **c** These droplets with active clones (green droplet) can be sorted in their oil emulsion using either a fluorescence (FADS) or an absorbance (AADS) activated droplet sorter. Alternatively, the water-in-oil droplets can be re-injected into a hydrophilic flow-focusing device to generate water/oil/water double emulsions that can be sorted by Fluorescence Activated Cell Sorting (FACS)

kHz, but they can also be re-encapsulated to form cell-like double-emulsions and be sorted using commercial FACS instruments [34].

3 Conclusion

Microfluidic droplets can be made using a variety of microfluidic devices or droplet-on-demand platforms. The promise of great savings in costs and reagents through the miniaturization of screening is starting to be realized and droplet formats emerge as solution for many biomedical applications from diagnosis to drug screening.

Cells-in-gels provide useful research tools for understanding cellular processes and for discovering transcription factors involved in diseases, and they may be a useful tool to monitor drug efficacy directly from patient cells, helping pave the way towards personalized medicine. However, due to the infrastructure required for making droplets, these will not be immediately used for diagnosis, safe for the detection of rare cells within a sample, and will need further

development to provide highly specific and sensitive point-of-care tests.

The main contribution of microdroplets to the biomedical field will be their unparalleled ability to find new therapeutic enzymes. By harnessing their ability for ultrahigh-throughput (up to 10^8 conditions screened per day) and for retaining the genotype-phenotype linkage, it is possible to find rare hits within billions of conditions.

Conflict of Interest The authors declare that they have no conflict of interest.

References

1. Tawfik, D.S., Griffiths, A.D.: Man-made cell-like compartments for molecular evolution. *Nat. Biotechnol.* **16**, 652–656 (1998). <https://doi.org/10.1038/nbt0798-652>
2. Devenish, S.R.A., Kaltenbach, M., Fischlechner, M., Hollfelder, F.: Droplets as Reaction Compartments for Protein Nanotechnology in Protein Nanotechnology: Protocols, Instrumentation and Applications. Humana Press, New York (2012)

3. Kaltenbach, M., Hollfelder, F.: SNAP display. In: *In Vitro Protein Evolution in Microdroplets*, pp. 101–111. https://doi.org/10.1007/978-1-61779-379-0_7
4. Miller, O.J., Bernath, K., Agresti, J.J., Amitai, G., Kelly, B.T., Mastrobattista, E., Taly, V., Magdassi, S., Tawfik, D.S., Griffiths, A.D.: Directed evolution by in vitro compartmentalization. *Nat. Methods* **3**, 561–570 (2006). <https://doi.org/10.1038/NMETH897>
5. Song, H., Tice, J.D., Ismagilov, R.F.: A microfluidic system for controlling reaction networks in time. *Angew. Chem. Int. Ed. Engl.* **42**, 768–772 (2003). <https://doi.org/10.1002/anie.200390203>
6. Anna, S.L., Bontoux, N., Stone, H.A.: Formation of dispersions using “flow focusing” in microchannels. *Appl. Phys. Lett.* **82**, 364–366 (2003). <https://doi.org/10.1063/1.1537519>
7. Huebner, A., Sharma, S., Srisa-Art, M., Hollfelder, F., Edel, J.B., Demello, A.J.: Microdroplets: A sea of applications? *Lab Chip* **8**, 1244–1254 (2008). <https://doi.org/10.1039/b806405a>
8. Schaerli, Y., Hollfelder, F.: The potential of microfluidic water-in-oil droplets in experimental biology. *Mol. BioSyst.* **5**, 1392–1404 (2009). <https://doi.org/10.1039/b907578j>
9. van Vliet, L.D., Colin, P.-Y., Hollfelder, F.: Bioinspired genotype–phenotype linkages: mimicking cellular compartmentalization for the engineering of functional proteins. *Interface Focus* **5**, 20150035 (2015). <https://doi.org/10.1098/rsfs.2015.0035>
10. Mair, P., Gielen, F., Hollfelder, F.: Exploring sequence space in search of functional enzymes using microfluidic droplets. *Curr. Opin. Chem. Biol.* **37**, 137–144 (2017). <https://doi.org/10.1016/j.cbpa.2017.02.018>
11. Kintsies, B., van Vliet, L.D., Devenish, S.R.A., Hollfelder, F.: Microfluidic droplets: new integrated workflows for biological experiments. *Curr. Opin. Chem. Biol.* **14**, 548–555 (2010). <https://doi.org/10.1016/j.cbpa.2010.08.013>
12. Guo, M.T., Rotem, A., Heyman, J.A., Weitz, D.A.: Droplet microfluidics for high-throughput biological assays. *Lab Chip* **12**, 2146 (2012). <https://doi.org/10.1039/c2lc21147e>
13. Garstecki, P., Stone, H.A., Whitesides, G.M.: Mechanism for flow-rate controlled breakup in confined geometries: a route to monodisperse emulsions. *Phys. Rev. Lett.* **94**, 4 (2005). <https://doi.org/10.1021/ma0343986>
14. Umbanhowar, P.B., Prasad, V., Weitz, D.A.: Monodisperse emulsion generation via drop break off in a coflowing stream. *Anal. Chem.* **16**, 347–351 (2000). <https://doi.org/10.1021/la990101e>
15. Theberge, A.B., Courtois, F., Schaerli, Y., Fischlechner, M., Abell, C., Hollfelder, F., Huck, W.T.S.: Microdroplets in microfluidics: an evolving platform for discoveries in chemistry and biology. *Angew. Chem.-Int. Edit.* **49**, 5846–5868 (2010). <https://doi.org/10.1002/anie.200906653>
16. Huebner, A.M., Abell, C., Huck, W.T.S., Baroud, C.N., Hollfelder, F.: Monitoring a reaction at submillisecond resolution in picoliter volumes. *Anal. Chem.* **83**, 1462–1468 (2011). <https://doi.org/10.1021/ac103234a>
17. Baret, J.-C.: Surfactants in droplet-based microfluidics. *Lab Chip* **12**, 422–433 (2012). <https://doi.org/10.1103/physrevlett.101.164502>
18. Wagner, O., Thiele, J., Weinhart, M., Mazutis, L., Weitz, D.A., Huck, W.T.S., Haag, R.: Biocompatible fluorinated polyglycerols for droplet microfluidics as an alternative to PEG-based copolymer surfactants. *Lab Chip* **16**, 65–69 (2016). <https://doi.org/10.1039/c3lc51427g>
19. Chiu, Y.-L., Chan, H.F., Phua, K.K.L., Zhang, Y., Juul, S., Knudsen, B.R., Ho, Y.-P., Leong, K.W.: Synthesis of fluorosurfactants for emulsion-based biological applications. *ACS Nano* **8**, 3913–3920 (2014). <https://doi.org/10.1021/nn500810n>
20. Etienne, G., Kessler, M., Amstad, E.: Influence of fluorinated surfactant composition on the stability of emulsion drops. *Macromol. Chem. Phys.* **218**, 1600365 (2016). <https://doi.org/10.1021/ma971016l>
21. Roach, L.S., Song, H., Ismagilov, R.F.: Controlling nonspecific protein adsorption in a plug-based microfluidic system by controlling interfacial chemistry using fluorinated-phase surfactants. *Anal. Chem.* **77**, 785–796 (2005). <https://doi.org/10.1021/ac049061w>
22. Holtze, C., Rowat, A.C., Agresti, J.J., Hutchison, J.B., Angilè, F.E., Schmitz, C.H.J., Köster, S., Duan, H., Humphry, K.J., Scanga, R.A., Johnson, J.S., Pisignano, D., Weitz, D.A.: Biocompatible surfactants for water-in-fluorocarbon emulsions. *Lab Chip* **8**, 1632–1639 (2008). <https://doi.org/10.1039/b806706f>
23. Baret, J.C., Miller, O.J., Taly, V., Ryckelynck, M., El-Harrak, A., Frenz, L., Rick, C., Samuels, M.L., Hutchison, J.B., Agresti, J.J., Link, D.R., Weitz, D.A., Griffiths, A.D.: Fluorescence-activated droplet sorting (FADS): efficient microfluidic cell sorting based on enzymatic activity. *Lab Chip* **9**, 1850–1858 (2009). <https://doi.org/10.1039/b902504a>
24. Gielen, F., Hours, R., Emond, S., Fischlechner, M., Schell, U., Hollfelder, F.: Ultrahigh-throughput–directed enzyme evolution by absorbance-activated droplet sorting (AADS). *Proc. Natl. Acad. Sci. U.S.A.* 201606927 (2016). <https://doi.org/10.1073/pnas.1606927113>
25. Fidalgo, L.M., Whyte, G., Bratton, D., Kaminski, C.F., Abell, C., Huck, W.T.S.: From microdroplets to microfluidics: selective emulsion separation in microfluidic devices. *Angew. Chem.-Int. Edit.* **47**, 2042–2045 (2008). <https://doi.org/10.1002/anie.200704903>
26. Abate, A.R., Hung, T., Mary, P., Agresti, J.J., Weitz, D.A.: High-throughput injection with microfluidics using picoinjectors. *Proc. Natl. Acad. Sci. U.S.A.* **107**, 19163–19166 (2010). <https://doi.org/10.1073/pnas.1006888107>
27. Schaerli, Y., Wootton, R.C., Robinson, T., Stein, V., Dunsby, C., Neil, M.A.A., French, P.M.W., Demello, A.J., Abell, C., Hollfelder, F.: Continuous-flow polymerase chain reaction of single-copy DNA in microfluidic microdroplets. *Anal. Chem.* **81**, 302–306 (2009). <https://doi.org/10.1021/ac802038c>
28. Bernath, K., Hai, M., Mastrobattista, E., Griffiths, A.D., Magdassi, S., Tawfik, D.S.: In vitro compartmentalization by double emulsions: sorting and gene enrichment by fluorescence activated cell sorting. *Int. J. Gastron. Food Sci.* **325**, 151–157 (2004). <https://doi.org/10.1016/j.ab.2003.10.005>
29. Courtois, F., Olguin, L.F., Whyte, G., Bratton, D., Huck, W.T.S., Abell, C., Hollfelder, F.: An integrated device for monitoring time-dependent in vitro expression from single genes in picoliter droplets. *ChemBioChem* **9**, 439–446 (2008). <https://doi.org/10.1002/cbic.200700536>
30. Huebner, A., Olguin, L.F., Bratton, D., Whyte, G., Huck, W.T.S., de Mello, A.J., Edel, J.B., Abell, C., Hollfelder, F.: Development of quantitative cell-based enzyme assays in microdroplets. *Anal. Chem.* **80**, 3890–3896 (2008). <https://doi.org/10.1021/ac800338z>
31. Hufnagel, H., Huebner, A., Gülch, C., Güse, K., Abell, C., Hollfelder, F.: An integrated cell culture lab on a chip: modular microdevices for cultivation of mammalian cells and delivery into microfluidic microdroplets. *Lab Chip* **9**, 1576–1582 (2009). <https://doi.org/10.1039/b821695a>
32. Clausell-Tormos, J., Lieber, D., Baret, J.-C., El Harrak, A., Miller, O.J., Frenz, L., Blouwolf, J., Humphry, K.J., Köster, S., Duan, H., Holtze, C., Weitz, D.A., Griffiths, A.D., Merten, C.A.: Droplet-based microfluidic platforms for the encapsulation and screening of mammalian cells and multicellular organisms. *Chem. Biol.* **15**, 427–437 (2008). <https://doi.org/10.1016/j.chembiol.2008.04.004>
33. Köster, S., Angilè, F.E., Duan, H., Agresti, J.J., Wintner, A., Schmitz, C., Rowat, A.C., Merten, C.A., Pisignano, D., Griffiths,

- A.D., Weitz, D.A.: Drop-based microfluidic devices for encapsulation of single cells. *Lab Chip* **8**, 1110 (2008). <https://doi.org/10.1039/b802941e>
34. Zinchenko, A., Devenish, S.R.A., Kintses, B., Colin, P.-Y., Fischlechner, M., Hollfelder, F.: One in a million: flow cytometric sorting of single cell-lysate assays in monodisperse picolitre double emulsion droplets for directed evolution. *Anal. Chem.* **86**, 2526–2533 (2014). <https://doi.org/10.1021/ac403585p>
35. Colin, P.-Y., Zinchenko, A., Hollfelder, F.: Enzyme engineering in biomimetic compartments. *Curr. Opin. Struct. Biol.* **33**, 42–51 (2015). <https://doi.org/10.1016/j.sbi.2015.06.001>
36. Utada, A.S., Lorenceau, E., Link, D.R., Kaplan, P.D., Stone, H.A., Weitz, D.A.: Monodisperse double emulsions generated from a microcapillary device. *Science* **308**, 537–541 (2005). <https://doi.org/10.1126/science.1109164>
37. Niu, X.Z., Gielen, F., Edel, J.B., deMello, A.J.: A microdroplet dilutor for high-throughput screening. *Nat. Chem.* **3**, 437–442 (2011). <https://doi.org/10.1038/nchem.1046>
38. Gielen, F., Van Vliet, L., Koprowski, B.T., Devenish, S.R.A., Fischlechner, M., Edel, J.B., Niu, X., Demello, A.J., Hollfelder, F.: A fully unsupervised compartment-on-demand platform for precise nanoliter assays of time-dependent steady-state enzyme kinetics and inhibition. *Anal. Chem.* **85**, 4761–4769 (2013). <https://doi.org/10.1021/ac400480z>
39. Clausell-Tormos, J., Griffiths, A.D., Merten, C.A.: An automated two-phase microfluidic system for kinetic analyses and the screening of compound libraries. *Lab Chip* **10**, 1302 (2010). <https://doi.org/10.1039/b921754a>
40. Ali-Cherif, A., Begolo, S., Descroix, S., Viovy, J.-L., Malaquin, L.: Programmable magnetic tweezers and droplet microfluidic device for high-throughput nanoliter multi-step assays. *Angew. Chem.-Int. Edit.* **51**, 10765–10769 (2012). <https://doi.org/10.1002/anie.201203862>
41. Mai, T.D., Ferraro, D., Aboud, N., Renault, R., Serra, M., Tran, N. T., Viovy, J.-L., Smadja, C., Descroix, S., Taverna, M.: Single-step immunoassays and microfluidic droplet operation: Towards a versatile approach for detection of amyloid-beta peptide-based biomarkers of Alzheimer's disease. *Sens. Actuators B: Chem.* **255**, 2126–2135 (2018). <https://doi.org/10.1016/j.snb.2017.09.003>
42. Chabert, M., Dorfman, K.D., de Cremoux, P., Roeraade, J., Viovy, J.-L.: Automated microdroplet platform for sample manipulation and polymerase chain reaction. *Anal. Chem.* **78**, 7722–7728 (2006). <https://doi.org/10.1021/ac061205e>
43. Du, W.-B., Sun, M., Gu, S.-Q., Zhu, Y., Fang, Q.: Automated microfluidic screening assay platform based on DropLab. *Anal. Chem.* **82**, 9941–9947 (2010). <https://doi.org/10.1021/ac1020479>
44. Gielen, F., Buryska, T., Vliet, L.V., Butz, M., Damborsky, J., Prokop, Z., Hollfelder, F.: Interfacing microwells with nanoliter compartments: a sampler generating high-resolution concentration gradients for quantitative biochemical analyses in droplets. *Anal. Chem.* **87**, 624–632 (2015). <https://doi.org/10.1021/ac503336g>
45. Sun, S., Kennedy, R.T.: Droplet electrospray ionization mass spectrometry for high throughput screening for enzyme inhibitors. *Anal. Chem.* **86**, 9309–9314 (2014). <https://doi.org/10.1021/ac502542z>
46. Klein, A.M., Mazutis, L., Akartuna, I., Tallapragada, N., Veres, A., Li, V., Peshkin, L., Weitz, D.A., Kirschner, M.W.: Droplet barcoding for single-cell transcriptomics applied to embryonic stem cells. *Cell* **161**, 1187–1201 (2015). <https://doi.org/10.1016/j.cell.2015.04.044>
47. Macosko, E.Z., Basu, A., Satija, R., Nemesh, J., Shekhar, K., Goldman, M., Tirosh, I., Bialas, A.R., Kamitaki, N., Martersteck, E.M., Trombetta, J.J., Weitz, D.A., Sanes, J.R., Shalek, A.K., Regev, A., McCarroll, S.A.: Highly parallel genome-wide expression profiling of individual cells using nanoliter droplets. *Cell* **161**, 1202–1214 (2015). <https://doi.org/10.1016/j.cell.2015.05.002>
48. Wang, D., Bodovitz, S.: Single cell analysis: the new frontier in “omics”. *Trends Biotechnol.* **28**, 281–290 (2010). <https://doi.org/10.1016/j.tibtech.2010.03.002>
49. Casamassimi, A., Federico, A., Rienzo, M., Esposito, S., Ciccodicola, A.: Transcriptome profiling in human diseases: new advances and perspectives. *Int. J. Mol. Sci.* (2017). <https://doi.org/10.3390/ijms18081652>
50. Shim, J.-U., Ranasinghe, R.T., Smith, C.A., Ibrahim, S.M., Hollfelder, F., Huck, W.T.S., Klenerman, D., Abell, C.: Ultrarapid generation of femtoliter microfluidic droplets for single-molecule-counting immunoassays. *ACS Nano* **7**, 5955–5964 (2013). <https://doi.org/10.1021/nn401661d>
51. Del Ben, F., Turetta, M., Celetti, G., Piruska, A., Bulfoni, M., Cesselli, D., Huck, W.T.S., Scoles, G.: A method for detecting circulating tumor cells based on the measurement of single-cell metabolism in droplet-based microfluidics. *Angew. Chem.-Int. Edit.* **55**, 8581–8584 (2016). <https://doi.org/10.1002/ange.200704903>
52. Chiu, T.-K., Lei, K.-F., Hsieh, C.-H., Hsiao, H.-B., Wang, H.-M., Wu, M.-H.: Development of a microfluidic-based optical sensing device for label-free detection of circulating tumor cells (CTCs) through their lactic acid metabolism. *Sensors* **15**, 6789–6806 (2015). <https://doi.org/10.1016/j.jbiosc.2011.03.019>
53. Chou, W.-L., Lee, P.-Y., Yang, C.-L., Huang, W.-Y., Lin, Y.-S.: Recent advances in applications of droplet microfluidics. *Micromachines* **6**, 1249–1271 (2015). <https://doi.org/10.1016/j.jfoodeng.2013.06.046>
54. Yesiloz, G., Boybay, M.S., Ren, C.L.: Label-free high-throughput detection and content sensing of individual droplets in microfluidic systems. *Lab Chip* **15**, 4008–4019 (2015). <https://doi.org/10.1039/c5lc00314h>
55. Zhang, H., Tumarkin, E., Sullan, R.M.A., Walker, G.C., Kumacheva, E.: exploring microfluidic routes to microgels of biological polymers. *Macromol. Rapid Commun.* **28**, 527–538 (2007). <https://doi.org/10.1002/marc.200600776>
56. Tan, W.H., Takeuchi, S.: Monodisperse alginate hydrogel microbeads for cell encapsulation. *Adv Mater* **19**, 2696–2701 (2007). <https://doi.org/10.1002/adma.200700433>
57. Nicodemus, G.D., Bryant, S.J.: Cell encapsulation in biodegradable hydrogels for tissue engineering applications. *Tissue Eng. Part B: Rev.* **14**, 149–165 (2008). <https://doi.org/10.1089/ten.teb.2007.0332>
58. Tumarkin, E., Tzadu, L., Csaszar, E., Seo, M., Zhang, H., Lee, A., Peerani, R., Purpura, K., Zandstra, P.W., Kumacheva, E.: High-throughput combinatorial cell co-culture using microfluidics. *Integr. Biol.* **3**, 653–662 (2011). <https://doi.org/10.1039/c1ib00002k>
59. Velasco, D., Tumarkin, E., Kumacheva, E.: Microfluidic encapsulation of cells in polymer microgels. *Small* **8**, 1633–1642 (2012). <https://doi.org/10.1002/sml.201102464>
60. Utech, S., Prodanovic, R., Mao, A.S., Ostafe, R., Mooney, D.J., Weitz, D.A.: Microfluidic generation of monodisperse, structurally homogeneous alginate microgels for cell encapsulation and 3D cell culture. *Adv. Healthcare Mater.* **4**, 1628–1633 (2015). <https://doi.org/10.1002/adhm.201500021>
61. Wan, J.: Microfluidic-based synthesis of hydrogel particles for cell microencapsulation and cell-based drug delivery. *Polymers* **4**, 1084–1108 (2012). <https://doi.org/10.3390/polym4021084>
62. Allazetta, S., Negro, A., Lutolf, M.P.: Microfluidic programming of compositional hydrogel landscapes. *Macromol. Rapid Commun.* (2017). <https://doi.org/10.1002/marc.201700255>

63. Kleine-Brüggeney, H., van Vliet, L.D., Mulas, C., Gielen, F., Agle, C.C., Silva, J.C.R., Smith, A., Chalut, K., Hollfelder, F.: Long-term perfusion culture of monoclonal embryonic stem cells in 3D hydrogel beads for continuous optical analysis of differentiation. *Small* **15**, 1804576 (2019). <https://doi.org/10.1002/sml.201804576>
64. Dolega, M.E., Abeille, F., Picollet-D'ahan, N., Gidrol, X.: Controlled 3D culture in Matrigel microbeads to analyze clonal acinar development. *Biomaterials* **52**, 347–357 (2015). <https://doi.org/10.1016/j.biomaterials.2015.02.042>
65. Yu, L., Chen, M.C.W., Cheung, K.C.: Droplet-based microfluidic system for multicellular tumor spheroid formation and anticancer drug testing. *Lab Chip* **10**, 2424 (2010). <https://doi.org/10.1039/c004590j>
66. Orive, G., Hernández, R.M., Gascón, A.R., Calafiore, R., Chang, T.M.S., Vos, P.D., Hortelano, G., Hunkeler, D., Lacik, I., Shapiro, A.M.J., Pedraz, J.L.: Cell encapsulation: promise and progress. *Nat. Rev. Drug Discov.* **9**, 104–107 (2003). <https://doi.org/10.1038/nm0103-104>
67. Fischlechner, M., Schaerli, Y., Mohamed, M.F., Patil, S., Abell, C., Hollfelder, F.: Evolution of enzyme catalysts caged in biomimetic gel-shell beads. *Nat. Chem.* **6**, 791–796 (2014). <https://doi.org/10.1038/nchem.1996>
68. Zhu, Z., Yang, C.J.: hydrogel droplet microfluidics for high-throughput single molecule/cell analysis. *Acc. Chem. Res.* **50**, 22–31 (2017). <https://doi.org/10.1021/acs.accounts.6b00370>
69. Brouzes, E., Medkova, M., Savenelli, N., Marran, D., Twardowski, M., Hutchison, J.B., Rothberg, J.M., Link, D.R., Perrimon, N., Samuels, M.L.: Droplet microfluidic technology for single-cell high-throughput screening. *Proc. Natl. Acad. Sci. U.S.A.* **106**, 14195–14200 (2009). <https://doi.org/10.1073/pnas.0903542106>
70. Chen, D.L., Ismagilov, R.F.: Microfluidic cartridges preloaded with nanoliter plugs of reagents: an alternative to 96-well plates for screening. *Curr. Opin. Chem. Biol.* **10**, 226–231 (2006). <https://doi.org/10.1016/j.cbpa.2006.04.004>
71. Miller, O.J., El-Harrak, A., Mangeat, T., Baret, J.C., Frenz, L., El Debs, B., Mayot, E., Samuels, M.L., Rooney, E.K., Dieu, P., Galvan, M., Link, D.R., Griffiths, A.D.: High-resolution dose-response screening using droplet-based microfluidics. *Proc. Natl. Acad. Sci. U.S.A.* **109**, 378–383 (2012). <https://doi.org/10.1073/pnas.1113324109>
72. Gielen, F., Colin, P.-Y., Mair, P., Hollfelder, F.: Ultrahigh-throughput screening of single-cell lysates for directed evolution and functional metagenomics, pp. 297–309. https://doi.org/10.1007/978-1-4939-7366-8_18
73. Cui, N., Zhang, H., Schneider, N., Tao, Y., Asahara, H., Sun, Z., Cai, Y., Koehler, S.A., de Greef, T.F.A., Abbaspourrad, A., Weitz, D.A., Chong, S.: A mix-and-read drop-based in vitro two-hybrid method for screening high-affinity peptide binders. *Sci. Rep.* **6**, 292 (2016). https://doi.org/10.1007/978-1-4939-1053-3_7
74. Kaltenbach, M., Stein, V., Hollfelder, F.: SNAP dendrimers: multivalent protein display on dendrimer-like DNA for directed evolution. *Chembiochem* **12**, 2208–2216 (2011). <https://doi.org/10.1002/cbic.201100240>
75. Houlihan, G., Gatti-Lafranconi, P., Kaltenbach, M., Lowe, D., Hollfelder, F.: An experimental framework for improved selection of binding proteins using SNAP display. *J. Immunol. Methods* **405**, 47–56 (2014). <https://doi.org/10.1016/j.jim.2014.01.006>
76. Diamante, L., Gatti-Lafranconi, P., Schaerli, Y., Hollfelder, F.: In vitro affinity screening of protein and peptide binders by megavalent bead surface display. *Protein Eng. Des. Sel.* **26**, 713–724 (2013). <https://doi.org/10.1093/protein/gzt039>
77. Mankowska, S.A., Gatti-Lafranconi, Pietro, Chodorge, M., Sridharan, S., Minter, R.R., Hollfelder, F.: A shorter route to antibody binders via quantitative in vitro bead-display screening and consensus analysis. *Sci. Rep.* **6**, 36391 (2016). <https://doi.org/10.1038/srep36391>
78. Colin, P.-Y., Kintsjes, B., Gielen, F., Miton, C.M., Fischer, G., Mohamed, M.F., Hyvönen, M., Morgavi, D.P., Janssen, D.B., Hollfelder, F.: Ultrahigh-throughput discovery of promiscuous enzymes by picodroplet functional metagenomics. *Nat. Commun.* **6**, 10008 (2015). <https://doi.org/10.1038/ncomms10008>

A Microfluidic Device for Nucleic Acid-Based Analysis of *Helicobacter pylori* and Antibiotic Susceptibility Testing

Leah Greenhalgh, Mamun Rashid , Patricia E. Linton , and Kirsty J. Shaw 

Abstract

Rapid diagnosis of bacterial infections enables earlier implementation of appropriate and effective treatment regimens, therefore improving patient outcomes. We have previously demonstrated a microfluidic device for nucleic acid-based analysis of *Helicobacter pylori*, which can cause peptic ulcers and increase the risk of stomach cancer. One of the major challenges to overcome has been the use of challenging real-world samples, e.g. stool, and urine allowing use at the point-of-care. Here we present results for bacterial identification as well as initial studies on the use of screen-printed electrodes (SPE) for miniaturised electrochemical detection for determining antibiotic susceptibility of pathogenic *Escherichia coli*. Resazurin was used as an indicator of bacterial viability, with reduction of resazurin demonstrating continued cell growth. Differential pulse voltammetry was used to measure potential reduction and showed measurement at -0.58 V or -0.38 V to be the most discriminatory. A fixed voltage of -0.58 V was then used to monitor current changes as a function of increasing gentamycin (antibiotic) concentration, with the results showing a significant reduction in current with increasing amounts of gentamycin (ANOVA, $p < 0.001$), within 90 min. The ability to integrate diagnosis with antibiotic susceptibility testing would allow administration of timely and specific treatment to patients with serious infections in low-resource settings.

Keywords

Microfluidics • Bacterial infection • Antibiotic susceptibility

1 Introduction

Bacterial infections affect hundreds of thousands of people annually worldwide. Rapid diagnosis of bacterial infections enables earlier implementation of appropriate and effective treatment regimens, therefore improving patient outcomes. Patient samples are preferentially collected using non-invasive methods, i.e. urine or stool samples, for both ease of collection and improved patient compliance. However, both sample types present challenges for analysis in terms of low target analyte concentrations and heterogeneity. Bacterial strain identification is important as different strains can have varying pathogenicity, for example, the phenotype of *Helicobacter pylori* (*H. pylori*) that expresses cytotoxin-associated protein (CagA) causes a higher degree of acute inflammation and is three times more likely to lead to gastric carcinogenesis than *H. pylori* strains which do not express CagA [1]. We have previously demonstrated a microfluidic device for nucleic acid-based analysis of *H. pylori*, from clinical stool samples, which identified the bacterial infection and whether or not it expressed the pathogenic CagA [2].

The growing emergence of antibiotic resistance is a global concern and has been identified as a high priority for the World Health Organisation [3]. Therefore the ability to not only identify the type of infection but also which antibiotics can be prescribed to successfully treat the infection (i.e. antibiotic susceptibility) is crucial to improve clinical outcomes. The use of microfluidics to integrate these steps together offers the potential to create cost-effective diagnostics for point-of-care applications.

Resazurin has been commonly used as a redox indicator to measure the metabolic rate of bacteria, which can be indicative of antibiotic resistance/susceptibility. In aqueous buffer solution, resazurin (blue) undergoes an irreversible two-electron reduction to resorufin (pink) due to the elimination of oxygen from the dye molecule. An additional two electron reversible reduction process to convert resorufin to

L. Greenhalgh · M. Rashid · P. E. Linton · K. J. Shaw (✉)
Manchester Metropolitan University, Manchester, M1 5GD, UK
e-mail: k.shaw@mmu.ac.uk

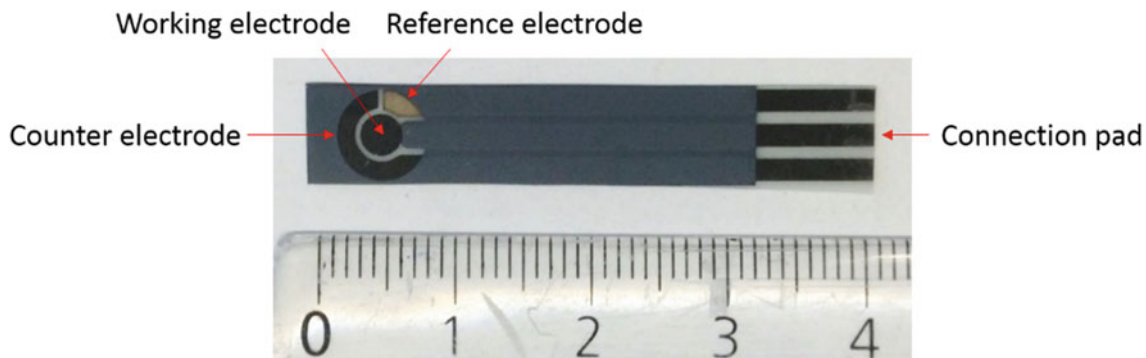


Fig. 3 Screen-printed electrode

selected on the basis that they had previously been tested for *H. pylori* during routine clinical testing.

3 Results and Discussion

Chemical lysis of bacterial cells was achieved on-chip using guanidine hydrochloride powder stored in the sample chamber, and reconstituted upon sample addition. Lysis efficiencies of 80.2 and 69.3%, respectively, for *E. coli* (Gram negative) and *S. aureus* (Gram positive) were demonstrated. DNA extraction efficiencies, using *E. coli* as a model organism, were shown to be greater (~75%) when smaller amounts of DNA were present, which is ideal for dealing with low levels of infection in clinical specimens. The use of multiple wash chambers (Fig. 2, chambers B–D) was shown to be necessary when analysing stool samples to provide DNA of sufficient purity for amplification of target markers: Ure C (for identification of *H. pylori*) and CagA (indicator of severe pathogenic phenotype) [2].

As resazurin and resorufin have different electrochemical signals in aqueous buffer solution, by using differential pulse voltammetry it is possible to identify the oxidation/reduction states of resazurin and thus specify whether the target bacteria is susceptible or not [5]. Figure 4, shows the differential pulse voltammogram recorded during the reduction of resazurin in the three electrode configuration. It is observed that the two electron reduction of resazurin to resorufin occurs at -0.38 V (Peak I). An additional two electron reversible reduction process is observed at -0.58 V (Peak II) that corresponds to formation of dihydroresorufin in the same aqueous medium.

A fixed voltage of -0.58 V was then used to monitor current changes as a function of increasing gentamycin concentration (10, 20, 30, 40 and 50 mg/mL), with the results showing a significant reduction in current with increasing amounts of gentamycin (ANOVA, $p < 0.001$), within 90 min (Fig. 5). In Fig. 5, it was observed that, both

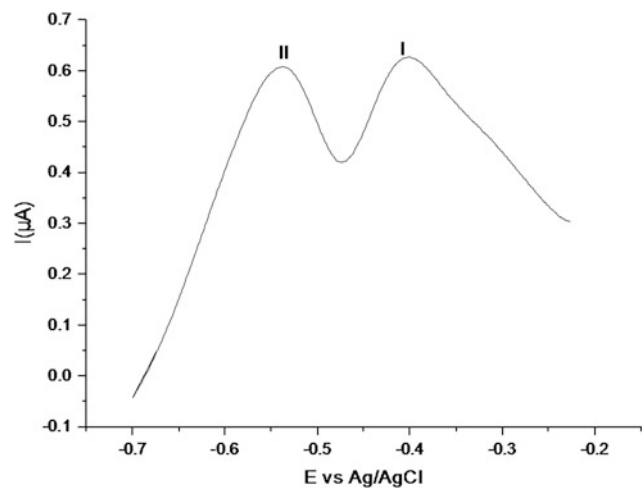


Fig. 4 Representative differential pulse voltammogram recorded during the reduction of buffered resazurin solution (1 mM)

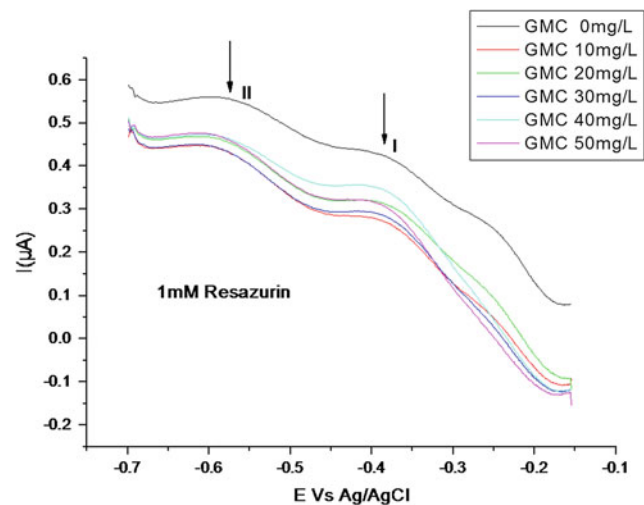


Fig. 5 Representative differential pulse voltammograms obtained from cultured *E. coli* for 80 min with resazurin and gentamycin (GMC)

peaks I and II decreased systematically as metabolism was affected by the antibiotic, indicating antibiotic susceptibility.

4 Conclusions

The ability to integrate diagnosis with rapid antibiotic susceptibility testing would allow administration of timely and specific treatment to patients with serious infections in low-resource settings. The work presented here shows how PDMS microfluidic devices can be used for identification of bacterial infections (including phenotypic indications) using genetic testing and also monitoring of the metabolic state of the bacteria using SPEs within 90 min.

Conflict of Interest The authors declare no conflict of interest.

References

1. Parsonnet, J., Friedman, G.D., Orentreich, N., Vogelman, H.: Risk of gastric cancer in people with CagA positive or CagA negative *H. pylori* infection. *Gut* **40**, 297–301 (1997)
2. Mosley, O., Melling, L.M., Tarn, M.D., Kemp, C., Esfahani, M.M.N., Pamme, N., Shaw, K.J.: Sample introduction interface for on-chip nucleic acid-based analysis of *Helicobacter pylori* from stool samples. *Lab Chip* **16**(11), 2108 (2016)
3. World Health Organisation, <http://www.who.int/en/news-room/fact-sheets/detail/antibiotic-resistance>. Accessed 10th May 2018
4. Khazalpour, S., Nematollahi, D.: Electrochemical study of Alamar Blue (resazurin) in aqueous solutions and room-temperature ionic liquid 1-butyl-3-methylimidazolium tetrafluoroborate at a glassy carbon electrode. *RSC Adv.* **4**, 8431–8438 (2014)
5. Besant, J.D., Sargent, E.H., Kelley, S.O.: Rapid electrochemical phenotypic profiling of antibiotic-resistant bacteria. *Lab Chip* **15**, 2799–2807 (2015)

Part X
Biophotonics

Coherent Hemodynamics Spectroscopy for Dynamic Measurements of Absolute Cerebral Blood Flow

Thao Pham, Kristen Tgavalekos, Angelo Sassaroli, and Sergio Fantini

Abstract

Coherent Hemodynamics Spectroscopy (CHS) is a novel technique for quantitative assessment of cerebral hemodynamics based on dynamic near infrared spectroscopy (NIRS) measurements. Here, we present a new approach for dynamic measurements of absolute cerebral blood flow (CBF) with NIRS and CHS in one healthy subject during transient changes of mean arterial pressure (MAP) in normal breathing and in hyperventilation conditions. Hyperventilation is known to reduce blood flow and enhance cerebral autoregulation. During hyperventilation, with respect to normal breathing at baseline, we found a lower absolute CBF (hyperventilation: 32 ± 3 ml/100 g/min; normal breathing: 35 ± 3 ml/100 g/min) and a faster CBF recovery to baseline (time of half recovery: 6 s for hyperventilation; 11 s for normal breathing). These results demonstrate the application of NIRS and CHS for quantitative, noninvasive, dynamic measurements of cerebral perfusion and cerebral autoregulation in the local cerebral microcirculation.

Keywords

Near-infrared spectroscopy • Coherent hemodynamics spectroscopy • Cerebral blood flow • Cerebral autoregulation

1 Introduction

Cerebral blood flow (CBF) is a measure of the rate of blood supply to brain tissue. Measurements of CBF are critically important to monitor brain perfusion and assess tissue via-

bility. In fact, adequate blood flow to the brain tissue is necessary to ensure sufficient oxygen supply for oxidative metabolism occurring in brain tissue. Keeping a relatively constant CBF is vital to prevent brain damage associated with hypoperfusion or hyperperfusion [1]. Cerebral autoregulation is one of the homeostatic mechanisms in the brain to keep CBF constant despite changes of mean arterial blood pressure (MAP) [2].

Current techniques for continuous monitoring of CBF include transcranial Doppler ultrasound (TCD) and diffuse correlation spectroscopy (DCS). While TCD is only sensitive to the cerebral macrovasculature, DCS can only measure local relative CBF changes but not absolute CBF. In this article, we describe a novel optical technique, coherent hemodynamics spectroscopy (CHS), for continuous monitoring of absolute CBF in the microvasculature [3–5]. This technique translates cerebral concentrations of oxyhemoglobin (O) and deoxyhemoglobin (D) measured noninvasively with near-infrared spectroscopy (NIRS) into the dynamics of cerebral blood volume (CBV), cerebral blood flow (CBF) and cerebral metabolic rate of oxygen ($CMRO_2$). We use the thigh-cuff method of Aaslid et al. [6] to induce transient changes in MAP and we measure the associated cerebral hemodynamic response with NIRS. By fitting the measured transient changes in $O(t)$ and $D(t)$ with the CHS model, we can obtain quantifiable parameters and a time trace of absolute CBF under the assumption of constant $CMRO_2$. Cerebral autoregulation could be assessed by either the recovery of CBF to baseline following the cuff release or by the fitted parameter of autoregulation cutoff frequency [6, 7]. In this study, partial pressure of carbon dioxide (pCO_2) was modulated when the subject performed normal breathing and hyperventilation to induce predictable changes in CBF and cerebral autoregulation [6, 8]. Hyperventilation causes hypocapnia-induced vasoconstriction, which will reduce CBF and enhance cerebral autoregulation. We show that CBF measured with NIRS and CHS is sensitive to different levels of perfusion and autoregulation in the cerebral microvasculature.

T. Pham (✉) · K. Tgavalekos · A. Sassaroli · S. Fantini
Department of Biomedical Engineering, Tufts University, 4 Colby St., Medford, MA 02155, USA
e-mail: Thao.Pham@tufts.edu

2 Methods

2.1 Experimental Setup

Data measured from a 33 year old female healthy subject are presented. The subject provided written informed consent approved by the Tufts University Institutional Review Board. NIRS measurements on the human brain were performed using a frequency-domain tissue spectrometer (Imagent, ISS, Inc., Champaign, IL), which utilizes laser diodes emitting at 690 and 830 nm. Prior to the experiment, absolute baseline concentrations of oxy-, deoxy-, and total-hemoglobin (O_0 , D_0 , and T_0) were obtained from measurement collected using an optical probe with eight source-detector distances in the range 0.5–4.0 cm [9]. Then, a probe with a single source-detector distance at 3.5 cm was used to measure optical intensity changes during the experiment, which were translated into changes in the concentrations of oxy-, deoxy-, and total-hemoglobin [$\Delta O(t)$, $\Delta D(t)$ and $\Delta T(t)$] by applying the modified Beer-Lambert law [10]. In either case, the probe was placed on the right side of the subject's forehead. Two pneumatic cuffs were wrapped around both subject's thighs and connected to an automated cuff inflation system (E-20 Rapid Cuff Inflation System, D.E. Hokanson, Inc., Bellevue, WA). Mean arterial pressure (MAP) was recorded with a finger plethysmography system (NIBP100D, BIOPAC Systems, Inc., Goleta, CA). Respiration effort was monitored with a strain gauge

minute, guided by a metronome. The subject continued hyperventilating for 30 s following the second cuff release.

2.2 Data Analysis

The superposition of relative changes to the absolute baseline values provides temporal traces of absolute concentrations of oxy-, deoxy-, and total-hemoglobin [$O(t)$, $D(t)$ and $T(t)$], in units of microMolar, μM . The dynamic responses of $O(t)$ and $D(t)$ within 7 s following the thigh cuff release were fitted with time-domain CHS [3, 4] to give the following parameters: the capillary blood transit time $t^{(c)}$, the venous blood transit time $t^{(v)}$, the autoregulation cutoff frequency f_c^{AR} , the inverse of the modified Grubb's exponent k , and the capillary blood volume ratio $\mathcal{F}^{(c)}\text{CBV}_0^{(c)}/\text{CBV}_0$ (where $\mathcal{F}^{(c)}$ is the Fåhræus factor). The fitting procedure was performed using the least-square method, with lower and upper bounds of parameters chosen on the basis of physiological ranges [4]. Errors on the parameters were estimated by running bootstrapping 20 times based on the data errors compared to the fit residues [11]. For the second cuff release, we fixed $\text{CBV}_0^{(c)}$ and k to the values obtained from the first step response while fitting for the remaining parameters.

By assuming a constant CMRO_2 , dynamic changes in CBF with respect to baseline ($\text{cbf}(t)$) was computed as the inverse Fourier transform of the following equation [4, 5]:

$$\widetilde{\text{cbf}}(\omega) = \frac{\frac{\widetilde{\Delta O(\omega) - \Delta D(\omega)}}{T_0} - (2S^{(a)} - 1) \frac{\text{CBV}_0^{(a)}}{\text{CBV}_0} \widetilde{\text{cbv}}^{(a)}(\omega) - (2S^{(v)} - 1) \frac{\text{CBV}_0^{(v)}}{\text{CBV}_0} \widetilde{\text{cbv}}^{(v)}(\omega)}{2 \left[\frac{\langle S^{(c)} \rangle}{S^{(v)}} (\langle S^{(c)} \rangle - S^{(v)}) \frac{\mathcal{F}^{(c)}\text{CBV}_0^{(c)}}{\text{CBV}_0} \mathcal{H}_{\text{RC-LP}}^{(c)}(\omega) + (S^{(a)} - S^{(v)}) \frac{\text{CBV}_0^{(v)}}{\text{CBV}_0} \mathcal{H}_{\text{G-LP}}^{(v)}(\omega) \right]} \quad (1)$$

(Sleepmate Piezo Effort Sensor, Ambu, Inc., Colombia, MD). All optical and auxiliary signals from the finger plethysmograph and respiratory strain gauge were acquired synchronously at a sampling rate of 9.9 Hz.

The experiment consisted of two thigh cuff occlusion protocols, separated by at least 2 min of baseline. Each cuff occlusion protocol included two minutes of cuff inflation to a pressure of 200 mmHg and then a rapid release of the cuff pressure to induce a transient decrease in systemic MAP, which resulted in changes in the cerebral NIRS signals. The first cuff protocol was performed while the subject was breathing normally. The second cuff protocol was performed while subject was hyperventilating at a rate of 20 breaths per

where the tilde symbol indicates Fourier transformation (ω is the Fourier conjugate of t), S is the oxygen saturation of hemoglobin with superscripts (a) , (c) , and (v) for the arterial, capillary and venous compartments, and $\langle S^{(c)} \rangle$ denotes the spatial average saturation over the capillary bed. $S^{(a)}$ is set to 0.98, while $S^{(v)}$ and $\langle S^{(c)} \rangle$ are computed from the transit times $t^{(c)}$, $t^{(v)}$ and from the rate constant of oxygen diffusion α , which is set to 0.8 s^{-1} . The two low-pass filters $\mathcal{H}_{\text{RC-LP}}^{(c)}(\omega)$ and $\mathcal{H}_{\text{G-LP}}^{(v)}(\omega)$ are the transfer functions associated with the blood transit time in the capillary bed and in the venous compartment, respectively. We also set the quantity $\text{CBV}_0^{(a)}/\text{CBV}_0$ to 0.3 [12].

The baseline cerebral blood flow, CBF_0 (in units of ml/100 g/min) can be obtained using the following equation:

$$CBF_0 = \frac{1}{\rho_T} \frac{\mathcal{F}^{(c)} CBV_0^{(c)}}{t^{(c)}} = \frac{1}{\rho_T} \frac{T_0}{ctHb} \frac{\mathcal{F}^{(c)} CBV_0^{(c)}}{t^{(c)}} \quad (2)$$

where the hemoglobin concentration in blood $ctHb$ is set to 2.3 mM, the mass density of brain tissue ρ_T is taken to be 1.04 g/ml. From Eqs. (1) and (2), the absolute time trace of cerebral blood flow can be written as $CBF(t) = CBF_0(1 + cbf(t))$.

3 Results

Rapid thigh cuff release resulted in a drop in mean arterial pressure (MAP), which induced a transient decrease in cerebral oxy-hemoglobin ($\Delta O(t)$) and increase in deoxy-hemoglobin concentration ($\Delta D(t)$) within 7 s following the cuff release. By fitting this segment of NIRS signals with the hemodynamic model, we retrieved the parameters reported in Table 1. The baseline total-hemoglobin concentration (T_0) was $45.7 \pm 0.1 \mu\text{M}$ at the cuff release during normal breathing and $45.9 \pm 0.1 \mu\text{M}$ during hyperventilation. The inverse of the modified Grubb's exponent $k = 3.6 \pm 0.2$ and the capillary baseline

cerebral blood volume $CBV_0^{(c)} = 0.0091 \pm 0.0001 \text{ ml}_{\text{blood}}/\text{ml}_{\text{tissue}}$, were obtained from the fit of the first step response, and then fixed at these values in the fit of the second step response to obtain the parameters $t^{(c)}$, $t^{(v)}$ and $f_c^{(AR)}$.

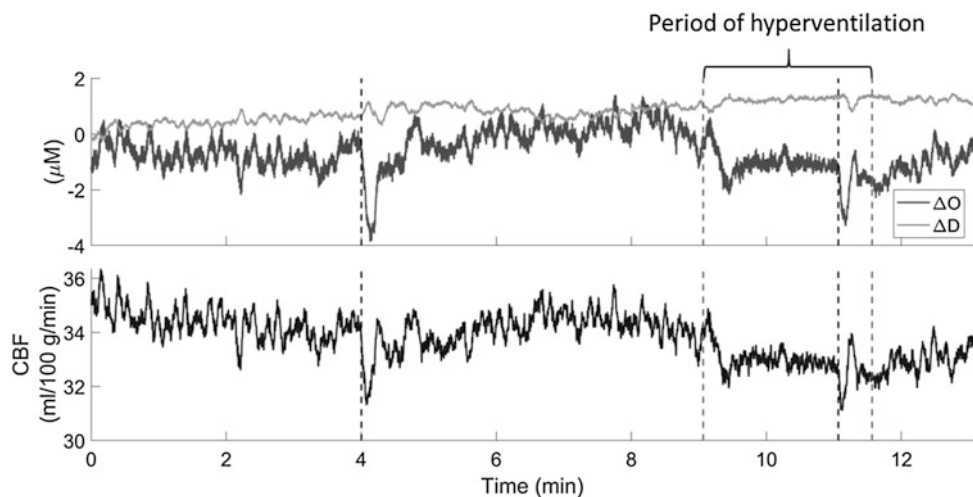
The absolute baseline cerebral blood flow (CBF_0) and the time trace $CBF(t)$ were obtained from the measured NIRS signals and the fitted parameters. The time traces of $\Delta O(t)$, $\Delta D(t)$, and temporal dynamics of $CBF(t)$ in the overall experiment are shown in Fig. 1. CBF dropped during hyperventilation (which started at $t = 9$ min), with a decrease in CBF_0 from 35 to 32 ml/100 g/min and an associated increase in $t^{(c)}$ from 1.2 to 1.3 s.

Due to the systemic decrease in MAP induced by the rapid release of the thigh cuffs, CBF itself features a transient decrease. This transient decrease in CBF with respect to baseline during normal breathing and hyperventilation are reported in Fig. 2. The measured CBF dropped by 6% from its baseline value at the thigh cuff release during normal breathing and by 3% during hyperventilation. The CBF trace during hyperventilation featured a faster recovery to baseline in comparison to normal breathing, with the time of half recovery (i.e., the time at which the CBF trace reaches 50% of the baseline-to-minimum range) approximately at 11 s for normal breathing and 6 s for hyperventilation. This result indicates an increase in cerebral autoregulation during hyperventilation, as expected [6].

Table 1 Parameters obtained from the model fit (mean \pm standard deviation)

	$t^{(c)}$ (s)	$t^{(v)}$ (s)	$f_c^{(AR)}$ (Hz)	CBF_0 (ml/100 g/min)
Normal breathing	1.18 ± 0.02	4.6 ± 0.2	0.04 ± 0.01	35 ± 3
Hyperventilation	1.30 ± 0.01	5.6 ± 0.1	0.07 ± 0.01	32 ± 3

Fig. 1 Measurement time series throughout the protocol. Black vertical dashed lines indicate the thigh cuff releases. Hyperventilation occurred between the gray vertical dashed lines



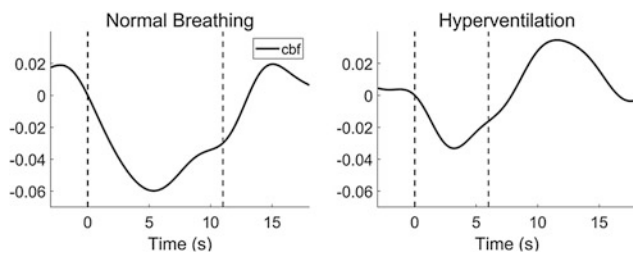


Fig. 2 Time traces of CBF following the thigh cuff releases during normal breathing (left) and hyperventilation (right). The thigh cuff release is at time $t = 0$ s (black vertical dashed line). The time of half recovery for each trace is indicated by the gray vertical dashed line

4 Discussion

We presented a method that uses standalone NIRS in conjunction with a hemodynamic model (CHS) to measure temporal dynamics of absolute cerebral blood flow ($CBF(t)$). Representative measurements from one healthy subject during transient MAP changes in normal breathing and hyperventilation conditions demonstrate that our method is sensitive to changes in CBF and cerebral autoregulation due to perturbations in partial pressure of carbon dioxide (pCO_2). This proposed NIRS-CHS technique can enhance research and clinical applications of real-time monitoring of cerebral perfusion and autoregulation in humans.

We found a value of absolute CBF (CBF_0) in the prefrontal cortex of 32–35 ml/100 g/min, which is lower than the reported range of typical cerebral blood flow of 55–60 ml/100 g/min [13]. This could be due to confounding effects from the extracerebral tissues to NIRS measurements [14], or to systematic errors in our parameter estimation with CHS. We are currently working on methods for depth-resolved CHS to discriminate contributions from extracerebral and intracerebral tissues hemodynamics. We are also working on refining the CHS model, protocols, and fitting methods to improve the robustness of parameter recovery.

The magnitude of the CBF decrease measured with our technique during the MAP transient drop (6% at baseline, 3% during hyperventilation) is lower than the one reported with transcranial Doppler ultrasound (TCD) (11–14%) [15]. This discrepancy result from the fact that NIRS-CHS provides an indirect measurement of microvascular cerebral blood flow based on blood oxygen diffusion in the capillaries. Instead, blood flow from TCD is estimated from the more direct measurement of red blood cells velocity in the macrovasculature (e.g., the middle cerebral artery). Future work would focus on further validation of the NIRS-CHS technique in concurrent measurements with TCD and diffuse correlation spectroscopy (DCS).

Acknowledgements This research is supported by the National Institutes of Health (Grants R01-NS095334 and R21-EB020347).

Conflicts of Interest The authors declare no conflicts of interest.

References

1. Tzeng, Y.C., Ainslie, P.N.: Blood pressure regulation IX: cerebral autoregulation under blood pressure challenges. *Eur. J. Appl. Physiol.* **114**(3), 545–559 (2014)
2. Panerai, R.B.: Assessment of cerebral pressure autoregulation in humans—a review of measurement methods. *Physiol. Meas.* **19**, 305–338 (1998)
3. Fantini, S.: Dynamic model for the tissue concentration and oxygen saturation of hemoglobin in relation to blood volume, flow velocity, and oxygen consumption: implications for functional neuroimaging and coherent hemodynamics spectroscopy (CHS). *NeuroImage* **85**, 202–221 (2014)
4. Kainerstorfer, J.M., Sassaroli, A., Hallacoglu, B., Pierro, M.L., Fantini, S.: Practical steps for applying a new dynamic model to near-infrared spectroscopy measurements of cerebrovascular oscillations and transient changes. Implications for cerebrovascular and functional brain studies. *Acad. Radiol.* **21**(2), 185–196 (2014)
5. Fantini, S., Sassaroli, A., Kainerstorfer, J.M., Tgavalekos, K.T., Zang, X.: Non-invasive assessment of cerebral microcirculation with diffuse optics and coherent hemodynamics spectroscopy. *Proc. SPIE. USA* **9690B**, 1–9 (2016)
6. Aaslid, R., Lindegaard, K.F., Sorteberg, W., Nornes, H.: Cerebral autoregulation dynamics in humans. *Stroke* **20**(1), 45–52 (1989)
7. Kainerstorfer, J.M., Sassaroli, A., Tgavalekos, K.T., Fantini, S.: Cerebral autoregulation in the microvasculature measured with near-infrared spectroscopy. *J. Cereb. Blood Flow Metab.* **35**(6), 959–966 (2015)
8. Carrera, E., Lee, L.K., Giannopoulos, S., Marshall, R.S.: Cerebrovascular reactivity and cerebral autoregulation in normal subjects. *J. Neurol. Sci.* **285**(1–2), 191–194 (2009)
9. Fantini, S., Franceschini, A., Fishkin, J., Barbieri, B., Gratton, E.: Quantitative determination of the absorption spectra of chromophores in strongly scattering media: a light emitting diode technique. *Appl. Opt.* **33**(22), 5204–5213 (1994)
10. Sassaroli, A., Fantini, S.: Comment on the modified Beer-Lambert law for scattering media. *Phys. Med. Biol.* **49**(14), N255–N257 (2004)
11. Efron, B., LePage, R.: Introduction to Bootstrap. Exploring the Limits of Bootstrap (1st ed). Springer Science+Business Media (1992)
12. Ito, H., Kanno, I., Iida, H., Hatazawa, J., Shimosegawa, E., Tamura, H., Okudera, T.: Arterial fraction of cerebral blood volume in humans measured by positron emission tomography. *Ann. Nucl. Med.* **15**(2), 111–116 (2001)
13. Henriksen, O.M., Larsson, H.B.W., Hansen, A.E., Grüner, J.M., Law, I., Rostrup, E.: Estimation of intersubject variability of cerebral blood flow measurements using MRI and positron emission tomography. *J. Magn. Reson. Imaging* **35**(6), 1290–1299 (2012)
14. Hallacoglu, B., Sassaroli, A., Fantini, S.: Optical characterization of two-layered turbid media for non-invasive, absolute oximetry in cerebral and extracerebral tissue. *PLoS ONE* **8**(5), e64095 (2013)
15. Panerai, R.B., Saeed, N.P., Robinson, T.G.: Cerebrovascular effects of the thigh cuff maneuver. *Am. J. Physiol. Heart Circ. Physiol.* **308**(7), H688–H696 (2015)

Investigation of Cerebral Hemodynamic Changes in Mild Cognitive Impairment Due to Alzheimer's Disease During a Verbal Fluency Task

Minhee Kim, Thien Nguyen, Jeonghwan Gwak, Jang Jae Lee, Kyu Yeong Choi, Kun Ho Lee, and Jae Gwan Kim

Abstract

In this study, we used functional near-infrared spectroscopy to measure the brain hemodynamic responses during a verbal fluency task in both healthy controls (HC) and mild cognitive impairment patients (MCI). We found a greater amplitude of oxy-hemoglobin and deoxy-hemoglobin changes, and a significantly higher value of maximum slope calculated from oxy-hemoglobin change in MCI compared to HC during the task. Our experimental results suggest the potential of using the cerebral hemodynamic responses, especially the maximum slope of oxy-hemoglobin change, as a biomarker for MCI.

Keywords

Functional near-infrared spectroscopy • Alzheimer's disease • Semantic verbal fluency task • Phonemic verbal fluency task

1 Introduction

Mild cognitive impairment (MCI) is a progressive stage of dementia, which reduces the cognitive and memory functions more than the normal aging but not serious enough to disturb the patient's daily life [1]. Because there is a high risk for MCI to develop into Alzheimer's disease (AD), it is important to diagnose MCI in the early stage. Several imaging techniques have been used to develop a diagnostic method for MCI such as fMRI, PET, and EEG [2–4]. PET/fMRI provide whole brain images with high spatial resolution but PET uses radioactive agents, fMRI restricts people with metal-implanted devices, and both PET/fMRI systems are extremely expensive. EEG has a high temporal resolution, but its signal is not localized. In addition, the above-mentioned techniques are highly sensitive to movement noises. As a result, diagnosing MCI with these techniques is still challenging.

Hence, we suggest using functional near-infrared spectroscopy (fNIRS) to investigate MCI. fNIRS is a noninvasive optical technique to measure brain hemodynamic changes. It is a low-cost system that can be applied harmlessly on everyone. Additionally, it is relatively stable with motion-induced artifacts. Currently, fNIRS has been used for researches to diagnose MCI using dual-task [5], working memory task [6], and verbal fluency task (VFT) [7–9]. In this study, we measure fNIRS signals during a VFT. We hypothesize that the compensatory mechanism may alter the cerebral hemodynamic responses in MCI during the task. We also compare our results with the other fNIRS studies using VFT. Because fNIRS can measure the brain

Minhee Kim and Thien Nguyen—These authors contributed equally to this work.

M. Kim · T. Nguyen (✉) · J. G. Kim
Department of Biomedical Science and Engineering, Gwangju
Institute of Science and Technology, Gwangju, 61005, Republic
of Korea
e-mail: thien@gist.ac.kr

J. G. Kim
School of Electrical Engineering and Computer Science, Gwangju
Institute of Science and Technology, Gwangju, 61005, Republic
of Korea
e-mail: jaekim@gist.ac.kr

J. Gwak
Biomedical Research Institute, Seoul National University
Hospital, Seoul, 03080, Republic of Korea

Department of Radiology, Seoul National University Hospital,
Seoul, 03080, Republic of Korea

J. J. Lee · K. Y. Choi · K. H. Lee
Department of Biomedical Science, Chosun University, Gwangju,
61452, Republic of Korea

K. H. Lee
National Research Center for Dementia, Chosun University,
Gwangju, 61452, Republic of Korea

hemoglobin oxygenation without any restrictions, we believe that it will play an important role in diagnosing MCI.

2 Method

2.1 Participant

A total of 69 right-handed elderly subjects living in Gwangju and adjacent cities (Republic of Korea) participated in this study. Based on the AD diagnosis criteria at Chonnam National University Hospital (Gwangju, Republic of Korea), subjects were divided into two groups: a healthy control (HC) group and a MCI group. The HC group has subjects without any psychiatric disorders (39 subjects, 18 males, ages: 72.2 ± 5.6 years). The MCI group includes subjects who were diagnosed as MCI due to AD (30 subjects, 21 males, ages: 76.0 ± 3.5 years). Before the experiment, all subjects signed an agreement to participate in the experiment after a technician explained the experimental procedure. This study was approved by Institutional Review Board at GIST.

2.2 fNIRS Device

A lab-built four channels fNIRS device was designed to measure signals from the subject's forehead. Channel 1 and 2 were located at the right forehead and channel 3 and 4 were at the subject's left forehead. Our fNIRS device has been tested and applied in several previous studies [10, 11]. The device in this study consists of 2 LEDs (OE-MV7385-P, OptoENG), which emit light at 730 nm and 850 nm and 3 photodiodes (OPT101, Texas Instruments). The separation between a LED and a photodiode was 3 cm (Fig. 1). The device sampling rate was 8 Hz and intensity of the LED light was 5 mW. The LED and photodiodes were attached to the subject's forehead using a medical double layer tape. The ambient light was shielded using a black-colored hairband covering the entire forehead.

2.3 Experimental Protocol

Verbal fluency task (VFT) comprised of two different tasks, phonemic and semantic and 30 s of rest period between

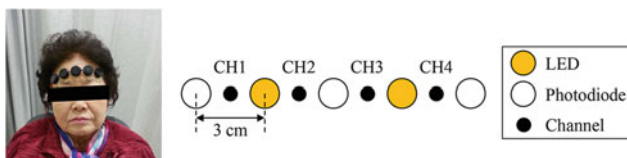


Fig. 1 A lab-built 4 channels fNIRS system

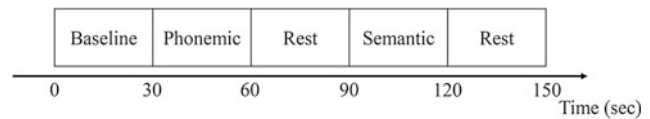


Fig. 2 The paradigm of a verbal fluency task

them. In a phonemic task (30 s), the subjects were asked to speak words beginning with a certain letter (e.g. letter “P” with pig, power, paper, etc.), and in a semantic task (30 s), the subjects had to tell words belonging to a certain category (e.g. “animal” category with dog, cat, lion, etc.). Including the baseline period, total experimental time was less than 3 min (Fig. 2). During the experiment, subjects were asked not to move their body to prevent motion artifact.

2.4 Processing Method

Firstly, relative concentration changes of oxy-hemoglobin ($[\Delta\text{OHb}]$) and deoxy-hemoglobin ($[\Delta\text{RHb}]$) were calculated from the light intensity using modified Beer-Lambert's law [12]. Unit of $[\Delta\text{OHb}]$ and $[\Delta\text{RHb}]$ is $\mu\text{M}/\text{DPF}$ where DPF is the differential path length factor. Secondly, $[\Delta\text{OHb}]$ and $[\Delta\text{RHb}]$ were band-pass filtered with 2nd order Butterworth at 0.01–0.1 Hz. Thirdly, the maximum increase of $[\Delta\text{OHb}]$ and the minimum decrease of $[\Delta\text{RHb}]$ within a 35-second window (30 s during the task and 5 s after the task) were computed. Both $[\Delta\text{OHb}]$ and $[\Delta\text{RHb}]$ were corrected to 0 $\mu\text{M}/\text{DPF}$ when the task started and there was no other normalization process. After that, the highest positive slope was calculated from the 1st derivative of $[\Delta\text{OHb}]$. Finally, an unpaired two-sample t-test was applied to the computed features to check the significance of the difference between two groups.

3 Result

3.1 Behavioral Results

In the phonemic task, the HC group produced 6.6 ± 2.8 words, and the MCI group produced 5.5 ± 3.1 words. The HC and MCI groups in the semantic task generated 9.6 ± 3.1 and 8.8 ± 3.2 words, respectively. In both tasks, HC group spoke more words compared to MCI group, but not statistically significant ($p > 0.1$).

3.2 fNIRS Results

Figure 3 plot the averaged time traces of $[\Delta\text{OHb}]$ and $[\Delta\text{RHb}]$ from channel 1 in 50 s (10 s before and after the task). During the task, $[\Delta\text{OHb}]$ increased in both groups, but

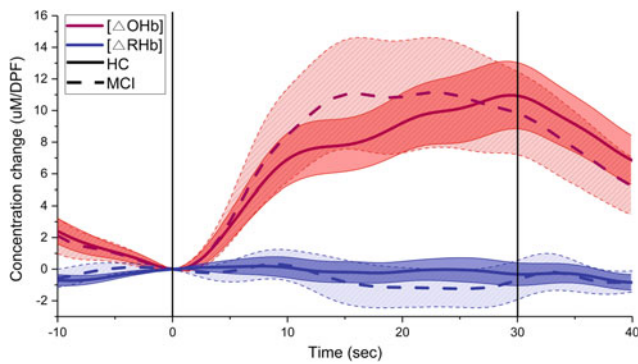


Fig. 3 The averaged $[\Delta\text{OHb}]$ and $[\Delta\text{RHb}]$ during a VFT in HC and MCI groups from channel 1. The shades represent standard error

$[\Delta\text{OHb}]$ of MCI reached its maximum earlier than the one in HC. In contrast, $[\Delta\text{RHb}]$ was constant in HC, while it decreased in MCI.

The maximum increase in $[\Delta\text{OHb}]$ in MCI group was higher than HC group for all the channels from both tasks, but there was no significance due to large variation within a group (Fig. 4a). In agreement with the increase in $[\Delta\text{OHb}]$, the maximum decrease in $[\Delta\text{RHb}]$ of MCI group was greater than the one in the HC group. A significant difference was found during a phonemic task in channels 1 and 4 ($p < 0.05$), while there was no significant difference during a semantic task (Fig. 4b). The maximum slope of $[\Delta\text{OHb}]$ was significantly higher in the MCI group than HC group during

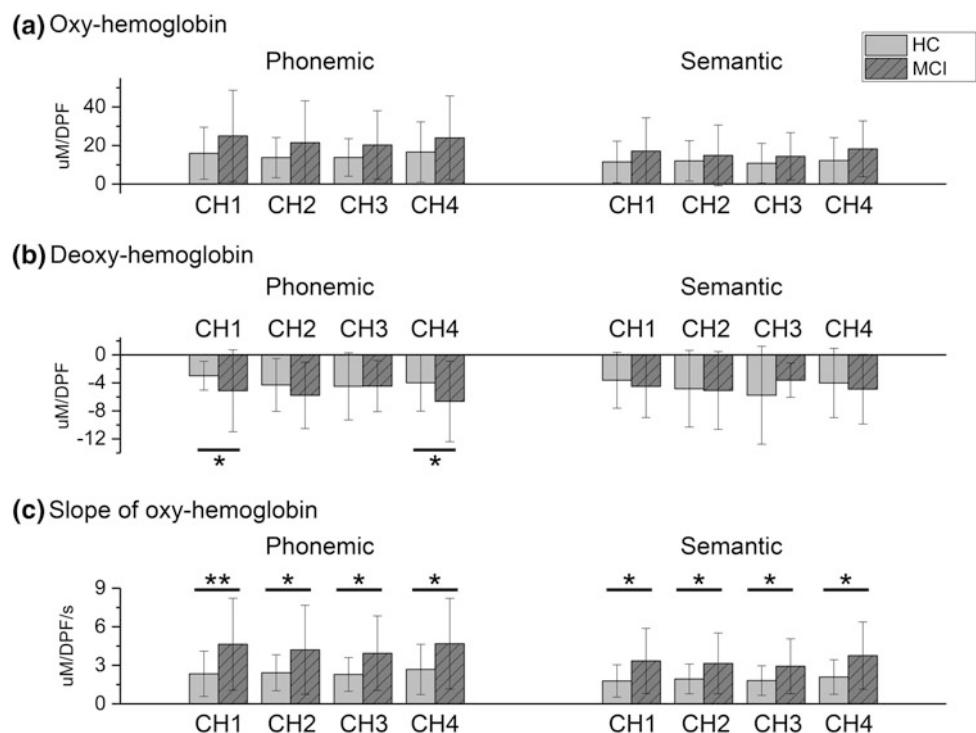
the phonemic tasks ($p < 0.05$), and especially, channel 1 showed $p < 0.001$ (Fig. 4c).

4 Discussion

The cerebral hemodynamic responses were monitored during a process of generating words, mainly related to the memory function. Most previous studies showed an increased $[\Delta\text{OHb}]$ and a decreased $[\Delta\text{RHb}]$ during a VFT [7–9]. In agreement with former studies, our study showed a similar trend in both groups but with a higher amplitude of $[\Delta\text{OHb}]$ and $[\Delta\text{RHb}]$ in MCI patients. This result can be explained by the compensation theory [13]. The compensation theory is a hypothesis to explain a natural aging process in elderly. When dealing with the same amount of workload, the elders' brain recruits more energy than the youngsters' one. The former study revealed that MCI also followed this theory showing a higher level of activation [8]. Hence, even with age-matched, MCI group required more energy than HC group to perform the VFT.

Since oxy-hemoglobin is a major factor to represent regional cerebral blood flow (rCBF) [14], the slope of $[\Delta\text{OHb}]$ represents how fast the oxygen is carried to the brain through the blood. The higher the slope is, the more blood supply to the brain is. Therefore, we focused on analyzing the slope of $[\Delta\text{OHb}]$ rather than the one of $[\Delta\text{RHb}]$. In addition, depending on the study purpose, the

Fig. 4 Experimental result. **a** The maximum increase of $[\Delta\text{OHb}]$, **b** The maximum decrease of $[\Delta\text{RHb}]$, and **c** The maximum $[\Delta\text{OHb}]$ slope. Error bars represent standard deviation



selection of window size for processing the data affects the result of the group analysis. The slope change when the subjects start to generate words has been studied and showed a significantly lower value in AD compared to HC and MCI [8]. In this study, we extracted the maximum slope from 35 s window to observe brain activity during the whole task and this parameter was able to provide a significantly higher value in MCI compared to HC. Furthermore, we noticed that MCI subjects tended to speak words without any restriction at the beginning of the task, but they felt difficulties from the middle of the task. It may be an evidence that the greater neural activity was recruited when workload became larger during VFT. These results imply that MCI patients tried to come up with matching words during verbal fluency tasks, which is shown by an increased $[\Delta\text{OHb}]$ slope but failed to speak as many words as HC group.

In summary, we performed VFT study to assess altered hemodynamic responses in MCI. Compared to previous studies, our study has two new aspects. Firstly, instead of focusing on one type of VFT, we assessed the prefrontal hemodynamic changes using both alphabet and category VFT. In general, both tasks successfully tested the cognitive function by observation of the prefrontal activation. However, because the mechanism to generate the words from the phonemic and semantic conditions is different, it is valuable to compare the performance and hemodynamic response between two groups in each condition. In fact, the minimum amplitude of $[\Delta\text{RHb}]$ was found to be significant between two groups in phonemic (channel 1 and 4) but not semantic. Secondly, rather than computing $[\Delta\text{OHb}]$ slope during first several seconds of the task, we calculated the maximum $[\Delta\text{OHb}]$ slope during the whole task (35 s). By doing so, we were able to reveal the significant difference between MCI and HC groups in term of $[\Delta\text{OHb}]$ slope. From our experimental results, we suggest using the slope of $[\Delta\text{OHb}]$ during a VFT as a biomarker to characterize MCI.

5 Conclusion

We investigated the cerebral hemodynamic responses in normal healthy controls and mild cognitive impairment patients. We found a higher increase in the oxy-hemoglobin concentration, a larger decrease in the deoxy-hemoglobin concentration, and a significantly greater slope of oxy-hemoglobin change in MCI during a verbal fluency task. These results suggest that the maximum slope of oxy-hemoglobin change during a verbal fluency task may be a promising biomarker to diagnose MCI due to the AD when

further studies are conducted to compare MCI from AD and MCI from other causes.

Conflict of Interest The authors declare that they have no conflict of interest.

References

1. Albert, M.S., et al.: The diagnosis of mild cognitive impairment due to Alzheimer's disease: recommendations from the National Institute on Aging-Alzheimer's Association workgroups on diagnostic guidelines for Alzheimer's disease. *Alzheimers Dement. J. Alzheimers Assoc.* **7**(3), 270–279 (2011)
2. Petrella, J.R., Prince, S.E., Wang, L., Hellegers, C., Doraiswamy, P.M.: Prognostic value of posteromedial cortex deactivation in mild cognitive impairment. *PLOS ONE* **2**(10), e1104 (2007)
3. Jelic, V., Kowalski, J.: Evidence-based evaluation of diagnostic accuracy of resting EEG in dementia and mild cognitive impairment. *Clin. EEG Neurosci.* **40**(2), 129–142 (2009)
4. Marcus, C., Mena, E., Subramaniam, R.M.: Brain PET in the diagnosis of Alzheimer's disease. *Clin. Nucl. Med.* **39**(10), e413–e426 (2014)
5. Doi, T., et al.: Brain activation during dual-task walking and executive function among older adults with mild cognitive impairment: a fNIRS study. *Aging Clin. Exp. Res.* **25**(5), 539–544 (2013)
6. Niu, H.-J., Li, X., Chen, Y.-J., Ma, C., Zhang, J.-Y., Zhang, Z.-J.: Reduced frontal activation during a working memory task in mild cognitive impairment: a non-invasive near-infrared spectroscopy study. *CNS Neurosci. Ther.* **19**(2), 125–131 (2013)
7. Arai, H., et al.: A quantitative near-infrared spectroscopy study: a decrease in cerebral hemoglobin oxygenation in Alzheimer's disease and mild cognitive impairment. *Brain Cogn.* **61**(2), 189–194 (2006)
8. Yap, K.H., et al.: Visualizing hyperactivation in neurodegeneration based on prefrontal oxygenation: a comparative study of mild Alzheimer's disease, mild cognitive impairment, and healthy controls. *Front. Aging Neurosci.* **9**, 287 (2017)
9. Yeung, M.K., et al.: Altered frontal lateralization underlies the category fluency deficits in older adults with mild cognitive impairment: a near-infrared spectroscopy study. *Front. Aging Neurosci.* **8**, 59 (2016)
10. Ahn, S., Nguyen, T., Jang, H., Kim, J.G., Jun, S.C.: Exploring neuro-physiological correlates of drivers' mental fatigue caused by sleep deprivation using simultaneous EEG, ECG, and fNIRS data. *Front. Hum. Neurosci.* **10**, 219 (2016)
11. Nguyen, T., Ahn, S., Jang, H., Jun, S.C., Kim, J.G.: Utilization of a combined EEG/NIRS system to predict driver drowsiness. *Sci. Rep.* **7**, 43933 (2017)
12. Phillips, Z., Kim, E., Kim, J.G.: Preliminary study of gender-based brain lateralization using multi-channel near-infrared spectroscopy. *J. Opt. Soc. Korea* **19**(3), 284–296 (2015)
13. Reuter-Lorenz, P.A., Cappell, K.A.: Neurocognitive aging and the compensation hypothesis. *Curr. Dir. Psychol. Sci.* **17**(3), 177–182 (2008)
14. Hoshi, Y., Kobayashi, N., Tamura, M.: Interpretation of near-infrared spectroscopy signals: a study with a newly developed perfused rat brain model. *J. Appl. Physiol.* **90**(5), 1657–1662 (2001)

Designing and Building the Vein Finder System Utilizing Near-Infrared Technique

Long Thanh Tran and Hien Thi-Thu Pham

Abstract

The process of venipuncture is a necessity for obtaining intravenous access for intravenous therapy or blood sampling of venous blood. Therefore, a vein finder system is an effective solution not only to make venipuncture safe and accurate but also to reduce anxiety and stress of patients and to improve donation comfort and efficiency. Vein visualization technology utilizes noninvasive infrared technology in capturing the real-time venous image on the patient's skin and making it observable. In the procedure executed by this system, the sample's skin is exposed to the near-infrared (NIR) light transmitted from an 850 nm 12 W 6-LED array. Following this, Raspberry Pi 3 Model B, connected with NoIR Camera Board, is utilized as an image acquisition equipment to capture the NIR illuminated skin area. Next, the raw data will be transferred to the computer to perform the filtering and processing technique before being displayed on the monitor. The system is examined on 24 volunteers with various age and gender groups. The output venous image is also imported to a pico-projector (Texas Instrument Inc.) for the attempt of back-projection onto the patient's hand. In overall, the experimental results are capable of distinguishing the differences in the contrast and brightness between the veins and the surrounding tissues on the wrists of the samples. It is anticipated that, with further investigation and experiments, a verification method for accurate and real-time projection of the enhanced imaged onto the human skin can be developed.

Keywords

Venipuncture • Near-infrared • Camera board • Filtering and processing • Back-projection

1 Introduction

Recently, Near-Infrared (750–1400 nm) Imaging (NIR) has significantly attracted the attention of many medical scientists and practitioners as a non-invasive method of acquiring images of veins near the surface of skin efficiently. It has been scientifically proven to be useful assistance in phlebotomy procedure performed on patients and a remarkable tool in medical diagnostic [1]. Hence, this device aids more support in the vein tracking process of the phlebotomists because venipuncture is an essential part of clinical testing, donation, or medical research.

The principle of this project is the method of vein imaging, which relies on the variation of light absorption parameters between venous blood and surrounding tissue to capture the image of the venous system non-invasively. Together with some digital image enhancement techniques, a system is designed with a NIR light source (850 nm), a Raspberry Pi 3 Model B micro-controller, a NoIR camera board, DLPDL2010EVM projector, and a laptop (or computer) with MATLAB installed as an image processor.

The experimental results exhibit an acceptable venous image of some chosen samples. The image projection is also initially possible using the adjustments in the projector's software and the method of reference points. This vein finder system is believed to have a lot of future potentials to be developed in many orientations such as venous disease diagnosis, more accurate image re-projection, or vein finder smartphone application.

L. T. Tran · H. T.-T. Pham (✉)
Biomedical Engineering Department, International University—
Vietnam National University HCMC, Ho Chi Minh, Vietnam
e-mail: ptthien@hcmiu.edu.vn

2 Principle of Near-Infrared Imaging in Vein Illuminator

The unique characteristic of NIR radiation is it can penetrate into biological tissue up to a depth of about 3 mm, in which the veins are located. Arteries are more deeply seated than veins and NIR cannot penetrate further beyond 3 mm. Moreover, in contrast with arterial blood which is mostly occupied by oxygenated hemoglobin (HbO_2), the reduced, or deoxygenated, hemoglobin (Hb) in the venous blood absorbs more of the radiation in this spectrum than the surrounding tissue. This concept is illustrated in Fig. 1 [2], which describes the absorption spectra of Hb and HbO_2 and water, main component of the neighbor tissues such as fat, and muscle.

According to the figure, only Hb and HbO_2 are the primary absorbers of NIR light (600–1300 nm). In this region, venous blood still maintains a higher absorption capability when the absorption coefficients of both oxygenated and deoxygenated blood dramatically fall with the wavelength beyond 600 nm. Also, there exists a peak at approximately 760 nm for HbO_2 , and the absorption difference between both kinds of hemoglobin is most prominent within the 700–900 nm range. Therefore, it is significant that the wavelength of the NIR light source is chosen to be between 700 and 900 nm or around 760 nm, ideally.

3 Methodology

3.1 System Design

The system is built up by some essential components such as a 12 W NIR 6-LED array (850 nm), an image capturing device (NoIR camera), a camera controller (Raspberry Pi 3 Model 3), a computer with MATLAB installed, and a DLPDLCR2010EVM projector.

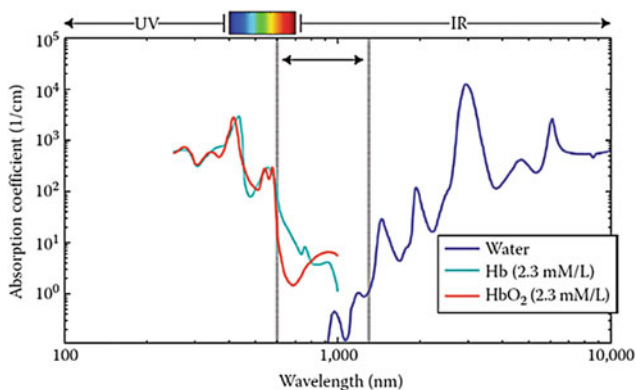


Fig. 1 The absorption spectra of water, Hb, and HbO_2

As can be seen from Fig. 2, at the first stage, the NIR light source will be operated to emit NIR light to the skin surface of the skin. Because of the absorption of Hb, the image of the venous system can be captured by a NoIR Camera Board connected to Raspberry Pi. From the controller, the image is transferred to the computer to perform the image enhancement and noise filtering process on MATLAB. Finally, the resulting image is either display on the screen or re-projected on the skin by the projector.

3.2 Software Implementation

Figure 3 illustrate the programming procedure of the system. Two most crucial image processing technique will be discussed thoroughly: median filtering and adaptive histogram equalization.

3.3 Median Filtering

Median filtering is a nonlinear method used to remove noise from images without eliminating the edges and lines. Specifically, the median filter works by replacing each pixel of the image with the median of all pixels in a neighborhood ω .

$$y[m, n] = \text{median}\{x[i, j], (i, j) \in \omega\} \quad (1)$$

where ω represents a neighborhood defined by the user whose center is around location $[m, n]$ in the image. In this approach, 2D median filter, in which the median of all pixel value inside the window is applied as the replacement for the pixel at the center is performed on the snapshot image [3].

3.4 Adaptive Histogram Equalization

This technique is only executable as long as the image is converted to grayscale. The histogram is the plot of the number of pixels for each intensity value. In this method, the image is divided into distinct sections whose histograms are computed separately. After that, the tonal values of the image are redistributed according to their probability distribution function. Consequently, the visual contrast is considerably enhanced along with the sharpness. In our implementation, adaptive histogram equalization is performed twice to increase the effectiveness of the method [4].

3.5 Back-Projection Methodology

It can be analyzed that the real-time image of the veins as a consequence of the MATLAB program only occupies a

Fig. 2 The system components

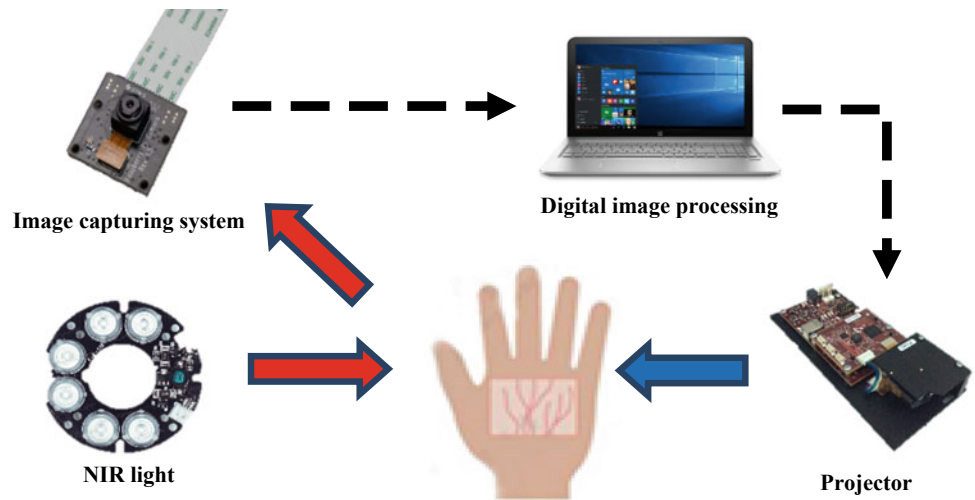
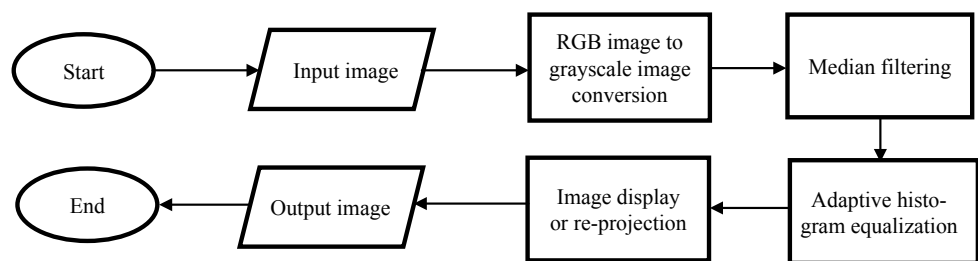


Fig. 3 Flowchart of the system



central part of the computer screen. This means that the output of the projection through the HDMI port will be extremely distracted as the whole screen is projected on the skin. Therefore, it is required that the input need to be cropped to only the part of the venous image.

As can be seen from Fig. 4, the cropping transaction is accomplished by controlling the 24-bit parallel I²C interface of the DLPDLR2010EVM with a unique programming language that is not compatible with other prevalent and standardized ones such as C++, Python, MATLAB. First of all, from the resolution of the input HDMI display, the coordinate (X, Y) of the pixel where the crop will be started is determined. Following that, the number of lines and pixels per line are called to indicates the width and height of the cropped image. At the last stage, the cropped pixels can be scaled to an arbitrary resolution as long as it is rational with the input venous image before being projected [5].

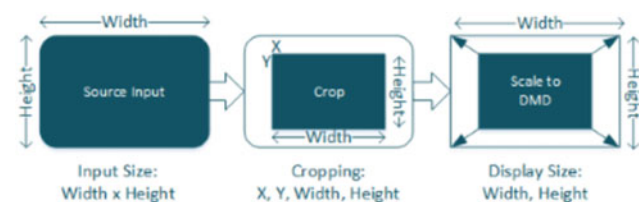


Fig. 4 Steps of image cropping procedure

4 Results

4.1 Hardware Design and On-Screen Results of Volunteers

Figure 5 describes the design of the image capturing system including a camera board attached at the center of a 6-LED array ring, all of which are connected to the ports of Raspberry Pi 3 Model B. The computer controls this system via the Ethernet port on Raspberry Pi.

In the next part of the research, 24 volunteers (14 females, 10 males) with various age groups and BMI indexes representing the amount of fat under the skin are invited to examine the operation of the design. There are 5 children and teenagers (8–14 years old), 11 adults (18–34 years old) in the volunteer’s group, whereas, the remaining people are in middle ages (44–64 years old). Their left or right wrist is NIR illuminated and captured by the system, the resulting images are displayed on the screen of the computer, as shown in Fig. 6.

4.2 Back-Projection of the Results onto the Skin

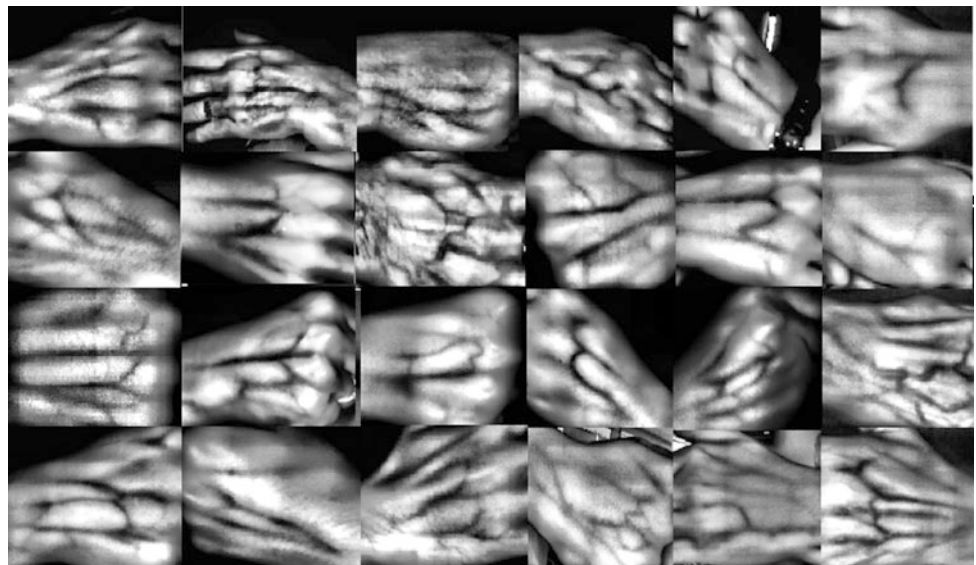
The research is currently investigated on the projection of the venous image onto the volunteers’ wrists. Two subjects



Fig. 5 Hardware design of the image capturing system

are undergoing the experiments of this process. Subject 1 is a 21-year-old man, while the other is a 55-year-old woman, whose right hands are the location for image capturing and re-projecting. Their hands are stabilized on the table in both cases.

Fig. 6 Resulting venous images of the wrists of 24 volunteers



However, to assure that the venous image accurately illuminates the subject's hand at the right position, a calibration method is proposed, in which the subject's wrist is marked with three white dots by a special ink that prevents transmittance of NIR light. Therefore, the on-screen enhanced image also contains these dots. After that, these images are projected back onto the skin in a way such that the reference points must be accurately fixed with their original ones, indicating the accurate projection [4]. The procedure is illustrated in Fig. 7.

5 Discussion and Implementations

5.1 Evaluation of the Results

According to Fig. 6, after the contrast enhancement process, in almost every subject, the veins are more easily located as their color is significantly darkened and conversely, the other tissues appear with a higher brightness. Furthermore, there is a development in the re-projection of the image onto human's skin although the procedure only pauses at the experiments. Indeed, the application of the DLP LightCrafter Display 2010 EVM in a new approach of the project is considerable because the problems of operating a new projector module that uses I2C interface to control is overcome and the quality of the output is comparable to the commercialized products regarding resolution.

Nevertheless, it can be easily observed that the current design has a bunch of raw connection wires to link the components together such USB, HDMI, power supply cable... which makes the product look extraordinarily anesthetic and not portable. In case of tiny and deep veins such as those from the children and teenagers group, the

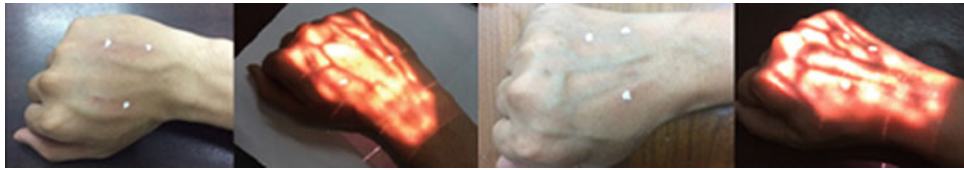


Fig. 7 Original hands and venous image re-projection on the hands of subject 1 (two leftmost images) and subject 2 (two rightmost images)

image is blurred or may not be obtained. In addition, the task of image projection has no guarantee that the venous image is illuminating the right anatomical parts because the method using reference points are temporary and it contains many errors regarding distance and angle.

5.2 Implementations

The next progression, the research can develop the software and graphical user inter-face to obtain more emphasizing venous images and a friendlier program for every-one other than the engineers to operate the system. Moreover, innovative system will be designed with proper components arrangement for both the NIR camera and the projector for the real-time operation. Therefore, a method in which a camera and projector are placed in different axes is proposed. On account of the modification of the axes, the visual conflict between the input of the camera and the output of the projector is completely eliminated. In the proposed method, the software program requires an additional technique called homography transformation to correct the angle variances between the camera and projector [6, 7].

6 Conclusion

To sum up, this analyzing vein image system will provide the safest way for venipuncture shortly due to non-invasive characteristic of NIR technology. The hardware components are the state-of-the-art modules that are popularly available on the market. In addition, the image processing algorithm is an innovative version of other researches. By looking at the vein-illuminating images displayed on the screen, the

phlebotomists would deal with no trouble in searching for the accurate vessels for blood drawing or venipuncture as the venous image appears clearly and sharply among the surrounding tissues. In the future, the achievement of a real-time projectable vein finder device, together with an aesthetically satisfying design will even emphasize the beneficial effects of this research in Vietnam's medical system.

Acknowledgements This research is funded by International University—VNUHCM under grant number T2017-01- BME.

Conflict of Interest The authors declare that they have no conflict of interest.

References

1. Marathe, M., et al.: A novel wireless vein finder. In: International Conference on Circuits, Communication, Control and Computing (2014)
2. Vo-Dinh, T.: Biomedical Photonics Handbook: Fundamentals, Devices, and Techniques. CRC Press Inc, Boca Raton, FL (2014)
3. Median Filter, fourier.eng.hmc.edu/e161/lectures/smooth_sharpen/node2.html
4. Sureshkumar, V., Elizabeth Kurien, S., Sunny, S., James, S., Lakshmy, S.: Electronic vein finder. *Int. J. Adv. Res. Comput. Commun. Eng.* **4**(10) (Oct, 2015)
5. DLPC3430, DLPC3435, DLPC3433, and DLPC 3438 Software Programmer's Guide. DLPDLCR2010EVM DLP LightCrafter™ Display 2010 Evaluation Module | TI.Com
6. Dai, X., et al.: A fast vein display device based on the camera-projector system. In: 2013 IEEE International Conference on Imaging Systems and Techniques (IST), pp. 146–149 (2013)
7. Sukthankar, R., Stockton, R.G., Mullin, M.D.: Smarter presentations: exploiting homography in camera-projector systems. In: Eighth IEEE International Conference on Computer Vision, 2001. ICCV 2001. Proceedings, vol. 1. IEEE, New York (2001)

Characterization of Non-melanoma Skin Cancer Utilizing the Optical Polarizing System

Dan Linh Le, Trinh Ngoc Huynh, and Thi-Thu-Hien Pham

Abstract

Defining the true of skin pathologies non-invasively is still an unsolved problem for the dermatology community. In this study, a new noninvasive method to visualize skin pathologies using polarized light imaging is discussed. This technology will assist doctors as well as dermatologists in making a quick assessment of skin pathologies. Researching on the propagation of polarized light in randomly scattering media have been investigated as a new and a huge potential methodology for disease early detection. Accordingly, a fundamental understanding of how polarized light propagates through tissue is essential for the development clinically useful optical diagnostic systems because of its practical application, especially in non-invasive diagnosis. The purpose of this research concentrated on the interaction of polarized light and biological tissues utilizing Mueller matrix and Stokes parameter description for extracting nine optical parameters such as linear birefringence (LB), linear dichroism (LD), circular birefringence (CB), circular dichroism (CD), linear depolarization (L-Dep), and circular depolarization (C-Dep) properties. The samples of the healthy skin and the non-melanoma skin cancer extracted from mouse were analyzed and compared their effective optical characterization. The experimental results illustrated that the LB and LD of the disease samples tend to be larger than the standard samples, creating an innovating solid foundation for the diagnosis of skin cancer in the future.

Keywords

Polarized light • Mueller matrix • Stokes polarimeter • Tissue characterization

1 Introduction

Recently, optical measurement methods are becoming more widely used because of its advantages. Most components in the measurement system are available, so it is easy to assemble and use. One position of optical measurement methods is that noninvasive. A non-contact optical measuring device, the probe does not touch the object being measured, and the device is not based on demolition measurement techniques. These techniques were applied in many applications, especially for samples that wish to remain intact throughout the measurement. Therefore, utilizing the Mueller matrix decomposition method to extract the effective linear birefringence (LB), linear dichroism (LD), circular birefringence (CB), circular dichroism (CD), linear depolarization (L-Dep), and circular depolarization (C-Dep) properties of the anisotropic material. Estimation of the linear birefringence of tissue might create a useful provision for noninvasive diagnostic of different obsessive diseases and a helpful insight into the characteristics of the photo-elasticity of human tissue [1–3]. Circular birefringence (CB) measurements of human blood, however, provide a reliable indication of diabetes [4]. Circular dichroism (CD) analysis offer a reliable means of classifying different proteins [5, 6], while linear dichroism (LD) measurements of human tissue can facilitate tumor diagnosis [7]. Additionally, valuable experience of the characteristics of tumor surface measurements can be gained through analyzing linear depolarization parameters [8].

Furthermore, of the long and high history from polarimetry as a thorough tool for characterizing unique materials, polarized light and biological tissue interaction show the basis for quantitative descriptions which are

D. L. Le · T.-T.-H. Pham (✉)

Department of Biomedical Engineering, International University
—Vietnam National University HCMC, Ho Chi Minh, Vietnam
e-mail: pthien@hcmiu.edu.vn

T. N. Huynh

Department of Pharmacognosy, University of Medicine and
Pharmacy of Ho Chi Minh City, Ho Chi Minh, Vietnam

essential for biomedical diagnostics. Wood et al. suggested a Monte Carlo model for polarized light propagation in birefringent, optically active, multiply scattering media for accurately representing the propagation of polarized light in biological tissue [9]. Wood et al. suggested a Monte Carlo model for polarized light propagation in birefringent, optically active, multiply scattering media for accurately representing the propagation of polarized light in biological tissue [10]. Mueller matrix decomposition is used for extraction of individual polarization parameters from complex turbid media exhibiting multiple scattering, optical activity, and linear birefringence [9, 10]. Pham and Lo [11, 12] proposed a decoupled analytical technique for extracting six effective, i.e. linear birefringence (LB), linear dichroism (LD), circular birefringence (CB), and circular dichroism (CD) parameters of anisotropic optical materials. Due to providing independent parameters, the advantages of decoupling the extraction process and avoiding multiple solutions problem in the previous method are an exceptional effort of presented technique. However, the ability to extract linear depolarization (L-Dep) and circular depolarization (C-Dep) properties of turbid sample incompletely promote in the method. In the present study, all effective LB, LD, CD, CB, L-Dep, C-Dep parameters were extracted in a decoupled manner of turbid media by an advanced proposed analytical method. Base on the achievement in [11–13], the validity of technique is established by obtaining the effective properties of the various optical samples.

2 Methodology

2.1 Technique

We applied the analytical technique of Pham and Lo [11, 12], termed Mueller matrix decomposition and Stokes vector polarimetry. In this method, the values of the Stokes output parameters for the six input light (S_{0° , S_{45° , S_{90° , S_{135° , S_{RH} , and S_{LHC}) are based on the input values of the samples and the Stokes input vectors. The Stokes output values are then taken respectively for the calculation of all elements of the Mueller matrix. As a consequence, nine effective parameters α , β , γ , θ_d , D , R , e_1 , e_2 , e_3 and Δ should be extracted.

2.2 Experiment Setup

The polarized light system included a Helium-Neon laser (wavelength of 632 nm, power < 5mW), a quarter-wave plate, polarizers, and a Stokes polarimeter to characterize the LB, LD, CB, CD, L-Dep and C-Dep properties of turbid media. In performing the experiments, the input light was provided by a frequency-stable He-Ne laser (JDSU—Model 1125P) with a

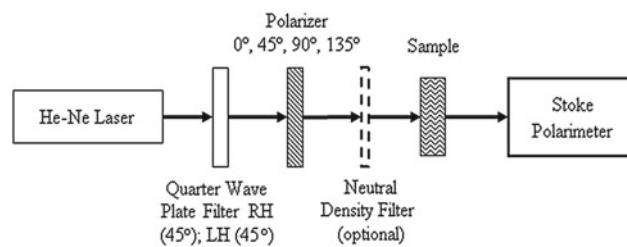


Fig. 1 Schematic illustration of a model of measurement

central wavelength of 632.8 nm. Also, a polarizer (GTH5M, Thorlabs Co.) and a quarter-wave plate (QWP0-63304-4-R10, CVI Co.) were used to produce four linear polarization lights (0° , 45° , 90° and 135°) and two circular polarization lights (right-handed and left-handed). Finally, a neutral density filter (NDC-100-2, ONSET Co.) was used to ensure that each of the input polarization lights had the equal intensities. The output Stokes parameters were computed from the intensity measurements obtained using a commercial Stokes polarimeter (PAX5710, Thorlabs Co.) at a sampling rate of 33.33 samples per second. A minimum of 1024 data points were obtained for each sample. Of these data points, 100 points were chosen and used to calculate the mean value of each effective parameter. Figure 1 shows the installation of the system. The samples were placed between the polarizer and detector by being fixed to a side stand.

3 Sample Preparation

3.1 Experimental Animals

White male rats, 6–8 weeks old, completely healthy, no malformations, no abnormal expression were stabilized one week before the experiment. One day before the test, the rats were shaved on their back with 2×2 cm in area and 1.5 cm in the tail. They were then randomly assigned to different batches. Each mouse was housed separately in $12 \times 12 \times 15$ cm; one cage six boxes.

3.2 Combination Model with DMBA and Croton Oil

Mice were induced by applying DMBA (7,12-dimethyl benz[a]anthracen)- one of the potential carcinogenic compounds that damage the genetic and carcinogenic genes and croton oil- a potent tumor enhancer in mice to the shaved scalp. The skin cancer then formed in squamous cells that make up the middle and the outer layer of the skin. The trial period is 20 weeks. DMBA is mixed in acetone to create a solution of 0.2%. The croton oil is diluted in acetone to give

a solution of 2%. These solutions are mixed right before starting to apply on mice. On the first day of testing, mice were sprayed with 50 μl of a 0.2% DMBA solution (0.1 mg DMBA respectively) as a single-onset agent. Two weeks after DMBA application, mice continued to apply 50 μL of 2% croton oil solution (1 μL croton oil) twice daily for 20 weeks.

Application: DMBA or croton oil was applied on mouse skin with 20–200 μL micropipettes. Gradually remove the shaved scalp, keep the micropipette upright and small from the center of the solution and move the micropipette around to ensure that the substance is evenly applied over the area of the skin.

3.3 Sample Extraction

2 non-melanoma mouse skin cancer samples and 2 normal mouse skin samples were extracted after 20 weeks and soaked in formalin to preserve the samples in a 10% formalin solution. To perform test procedure, the paraffin molded tissues were applied to make the sample holders. Molded paraffin wrapped into the sample, make easy to cut the tissues into thin slices to study the structure and proceed the experiment with He–Ne laser 633 nm wavelength.

Figure 2 shows the paraffin block of non-melanoma mouse skin cancer and healthy mouse skin.

Each sample was extracted into 3 slices with the conducted thickness of 5 μm due to the ability of intensity of the light. Those sliced samples were assumed that they come from equivalent healthy mouse as the weight and the non-melanoma mouse skin cancers are at the same stage. Subsequently, their similarity of optical parameters were comparable in their own characteristics for further investigation.

3.4 Hematoxylin and Eosin Staining

The process promoted simultaneously with the optical sample measuring. Extracted wounded skin was taken to the Tu Du Hospital for H&E staining process. The result is the signature verification for the presence of the interaction between biological tissue a polarized light. Histological results (hematoxylin and Eosin staining) for all these images showed the skin surface and collagen fibers in the dermis layer under a microscope. Figure 3 shows the result of H&E staining give the strength of the validation of the product research.

Fig. 2 Non-melanoma mouse skin cancer (a) and healthy mouse skin (b)

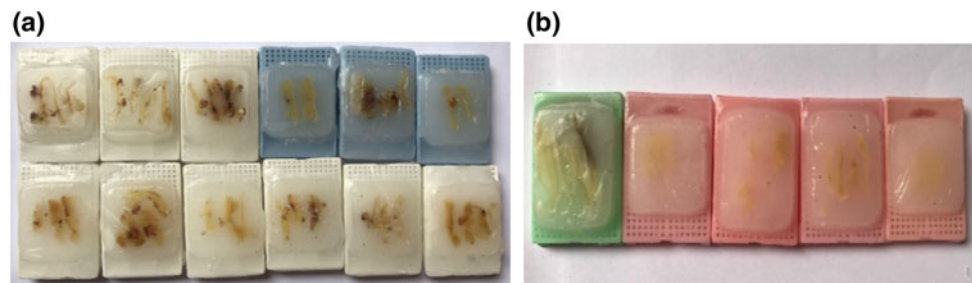


Fig. 3 H&E staining image

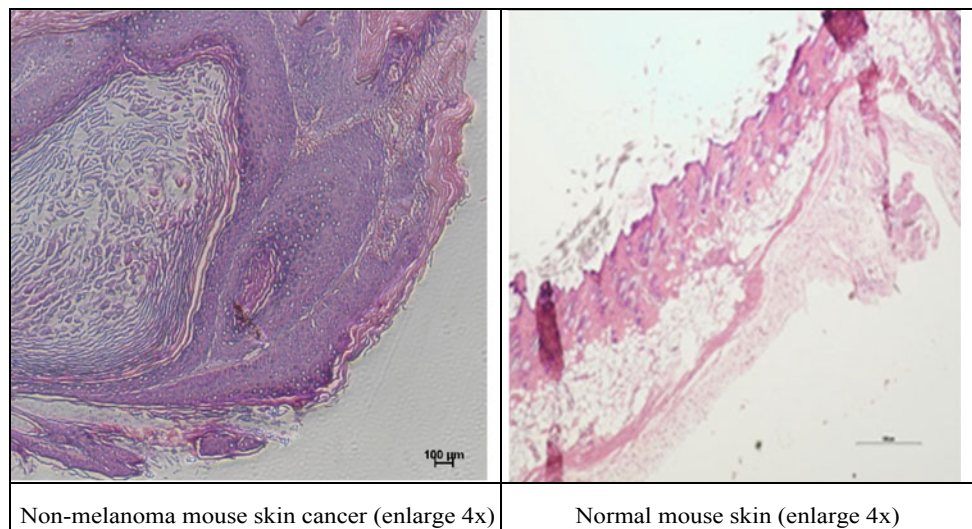


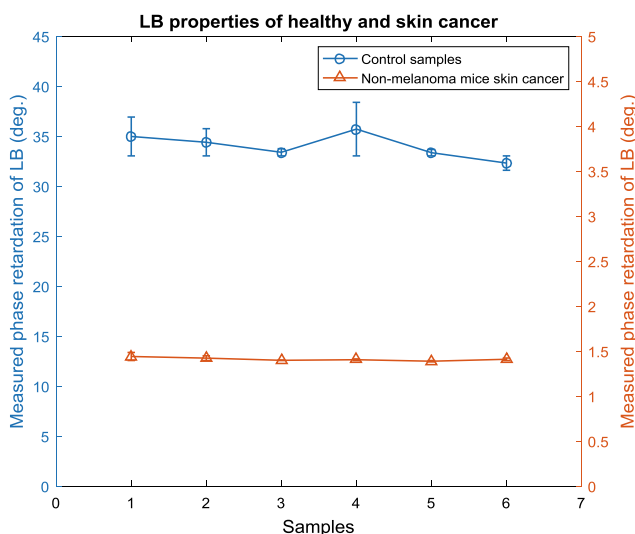
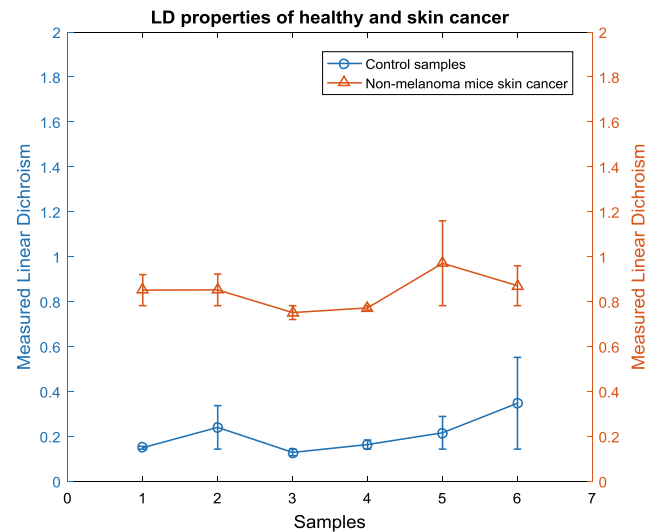
Table 1 Comparison between effective parameters of non-melanoma skin cancer with controlling mouse

		α	β	γ	θd	D	R	e1	e2	e3	Δ
Control	Mean	160.53	34.03	90.59	0.62	2.13	0.35	0.21	0.41	0.56	0.85
	Standard deviation	1.36	1.24	2.21	0.035	0.27	0.04	0.03	0.04	0.06	0.03
Non melanoma mouse skin cancer	Mean	99.45	1.41	156.96	0.10	1.31	0.03	0.78	0.87	0.51	0.17
	Standard deviation	1.47	0.02	2.24	0.01	0.18	0.02	0.04	0.01	0.05	0.03

4 Experimental Result and Discussion

The experimental results illustrate the relationship between polarized light with characteristics of non-melanoma mouse skin tissue samples and normal mouse skin by extracting the characteristics of these anisotropy materials by promoting the proposed analytical method, however, depending on distinct characteristics of biological materials have only meaningful properties need to be analyzed. Table 1 illustrates the comparative result of effective parameters after measuring 2 samples of non-melanoma mouse skin cancer and 2 sample of healthy skin. It can be seen that the linear birefringence and linear dichroism property showed the statistical significance.

As shown in Fig. 4, the distinct differences between the samples of non-melanoma mouse skin cancer and controlling mouse skin of the linear birefringence property are observed with the large disparity, varying about 32–35°. The cancer disease tissue has a marked reduction compared to healthy skin tissue. Specifically, for further investigation on

**Fig. 4** Comparison between non-melanoma skin cancer with controlling mouse, in which linear fitting results of linear birefringence**Fig. 5** Comparison between non-melanoma skin cancer with controlling mouse, in which linear fitting results of linear dichroism

cancer, tissue becomes cancerous can affect the optical properties of the tissue because of the alteration of the number of morphology and physiology. When cancerous tissue uncontrollable growth, the ordered collagen fibers break down causing the change of linear birefringence.

Characteristics of linear dichroism from non-melanoma mouse skin cancer and healthy mouse skin as the control samples are investigated and validated by the current polarization system and proposed a method. Figure 5 showed that the LD between healthy and diseased tissue has a difference of approximately 0.5. Meanwhile Fig. 6 illustrated significantly the difference of measured CB values between healthy and cancer mice skin. Finally, Fig. 7 presented the comparison between the depolarization index of non-melanoma skin cancer and healthy skin of mice.

5 Conclusion

The research has illustrated obviously the interaction between polarized light with biological anisotropy using the decoupled analytical technique that based on Stokes

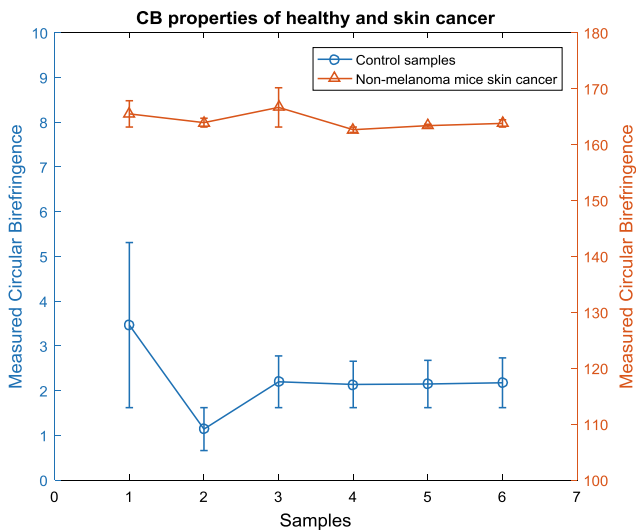


Fig. 6 Comparison between non-melanoma skin cancer with controlling mouse, in which linear fitting results of circular birefringence

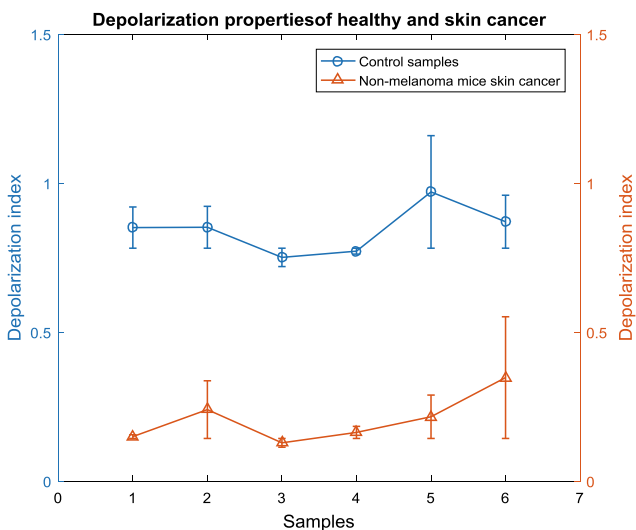


Fig. 7 Comparison between non-melanoma skin cancer with controlling mouse, in which linear fitting results of depolarization

polarimetry and Mueller matrix decomposition method. This technique has shown its potential application to the study. Thanks to the powerful technique, effective optical parameters consisting of linear birefringence (LB), linear dichroism (LD), circular birefringence (CB), circular dichroism (CD), linear depolarization (L-Dep) and circular depolarization (C-Dep) were extracted for characterizing optical

properties of the samples. The experimental result showed a good comparison non-melanoma cancerous skin cancer and healthy skin. It also claims that linear dichroism appears in biological material relating to carcinoma while comparing to a standard sample. All obtained results came out as the expectation that based on a consistent experiment was done on previous literature which confirms the reliability of the method. However, the method remains some limitations coming from sample preparation, sensitivity and irrelevant optical alignment for clinical study and their solution have been mentioned in the discussion above.

Acknowledgements The authors gratefully acknowledge the financial support provided to this study by Vietnam National Foundation for Science and Technology Development (NAFOSTED) under grant number 103.03-2016.86

Conflict of Interest The authors declare that they have no conflict of interest.

References

- de Boer, J.F., Milner, T.E., van Gemert, M.J., Nelson, J.S.: Two-dimensional birefringence imaging in biological tissue by polarization-sensitive optical coherence tomography. *Opt. Lett.* **22** (12), 934–936 (1997)
- Maitland, D.J., Walsh, J.T.: Quantitative measurements of linear birefringence during heating of native collagen. *Lasers Surg. Med.* **20**(3), 310–318 (1997)
- Wu, P.J., Walsh, J.T.: Stokes polarimetry imaging of rat tail tissue in a turbid medium: degree of linear polarization image maps using incident linearly polarized light. *J. Biomed. Opt.* **11**(1), 14031 (2006)
- Sun, P., Ma, Y., Liu, W., Yang, Q., Jia, Q.: Mueller matrix decomposition for determination of optical rotation of glucose molecules in turbid media. *J. Biomed. Opt.* **19**(4), 46015 (2014)
- Kelly, S.M., Jess, T.J., Price, N.C.: How to study proteins by circular dichroism. *Biochim. Biophys. Acta Proteins Proteomics* **1751**(2), 119–139 (2005)
- Swords, N.A., Wallace, B.A.: Circular-dichroism analyses of membrane proteins: examination of environmental effects on bacteriorhodopsin spectra. *Biochem. J.* **289**(Pt 1), 215–219 (1993)
- Angelskaya, A., Gruia, I., Yermolenko, S., Ivashko, P., Gruia, M.: Manifestations of linear dichroism changes in cancer biotissues. *Rom. Reports Phys.* **65**(3), 1052–1062 (2013)
- Wang, W., Lim, L.G., Srivastava, S., Yan, J.S.B., Shabbir, A., Liu, Q.: Roles of linear and circular polarization properties and effect of wavelength choice on differentiation between ex vivo normal and cancerous gastric samples. *J. Biomed. Opt.* **19**(4), 46020 (2014)
- Wood, M.F.G., Guo, X., Vitkin, I.A.: Polarized light propagation in multiply scattering media exhibiting both linear birefringence and optical activity: Monte Carlo model and experimental methodology. *J. Biomed. Opt.* **12**(1), 14029 (2007)
- Ghosh, N., Wood, M.F.G., Vitkin, I.A.: Mueller matrix decomposition for extraction of individual polarization parameters from

- complex turbid media exhibiting multiple scattering, optical activity, and linear birefringence. *J. Biomed. Opt.* **13**(4), 44036 (2008)
11. Pham, T.-T.-H., Lo, Y.-L.: Extraction of effective parameters of anisotropic optical materials using decoupled analytical method. *J. Biomed. Opt.* **17**(2), 25006-1-25006-17 (2012)
 12. Pham, T.-T.-H., Lo, Y.-L.: Extraction of effective parameters of turbid media utilizing the Mueller matrix approach: study of glucose sensing. *J. Biomed. Opt.* **17**(9), 0970021–09700215 (2012)
 13. Pham, H.-T.-T., Nguyen, A.L.-T., Vo, T.-V., Huynh, K.-C., Phan, Q.-H.: Optical parameters of human blood plasma, collagen, and calfskin based on the Stokes-Mueller technique. *Appl. Opt.* **57**(16), 4353–4359 (2018)

Investigating on the Effective Wound Healing Therapy Utilizing Laser Optical System

Xuan-Hieu Le, Ngọc-Bao-Tran Nguyen, Minh-Vy Huynh, Thi-Phuong-Trinh Vo, and Thi-Thu-Hien Pham

Abstract

Recent advances in wound healing treatment and management using Low-level Laser Therapy (LLLT) has been emphasized in many types of research for wound healing stimulation. Many studies have indicated the effects of this method; and thus, there is a concern that which wavelength and dosages would take more benefits, in term of wound closure and collagen synthesis. This research is conducted to re-emphasize and improve the efficiency of this therapy in chronic wounds and standard rat model to study and analyze the best conditions and protocol for these kinds of wound healing treatment. By utilizing red laser beams from an optical system to treat excisions on mice's dorsal regions, we aim to determine the irradiation parameters (i.e., wavelength, light intensity, time irradiation) that provide the optimal conditions to promote the healing process. Two round excision wounds are created on the back of each mouse: one for a control group and one for treated group. The treated group wound were irradiated with the red (635 nm wavelength), following these intensities: 2; 3; 5 J/cm². After every one week, the wound skins were taken and stained for results comparison. The experimental results showed that the wound closures were significantly different between treated and control group. At day 5th, 10th the follow-up tests indicated that the laser group had smaller wound areas compared to control group (non-diabetes and untreated). The improvement of impairment (>20%) and the faster time to wound closure indicated that this phototherapy could be used to heal chronic wounds in diabetic subjects. The healing progress analysis shows that the positive result and promising application of this therapy in future aid of wound control and healing.

Keywords

Wound healing • Diabetes • Chronic wounds • Healing process • LLLT

1 Introduction

There are many methods used in treating the wound. For example, electrical stimulation, electromagnetic stimulation, ultrasound, and ultraviolet light have been used extensively in wound healing [1]. Among these methods—there is a therapy receiving much attention, and expected to be long-standing and promising research in the application of healing and wound healing as light therapy—Low-Level Light Therapy (LLLT).

Laser means “amplification of light by stimulating emission,” was invented in 1960 [1]. Since their inception in 1960, lasers have been used for many applications in different fields. In 1980, Endre Master discovered that there is a positive effect on the wound of the rats by using 694 nm wavelength [2]. Also more and more research has been done on the development and application of lasers in the medical field, especially wound healing. These studies have more or less demonstrated the positive effect of lasers on wound healing [3, 4]. There are two types of light commonly used in this field, including blue light and red light. Blue light has been shown to have antibacterial effects, and red light has been considered capable of shortening wound healing and cell proliferation [5, 6].

In fact, blue light and red light have been introduced to the direct treatment of acne inflammatory disease in humans and have resulted in significant results, which demonstrate that the effect of blue light and red light is effective and reliable [7]. However, the exact biological mechanisms of low-intensity light in tissues are still not explained.

The application of light, especially laser, in wound healing and stimulation has been proposed and discussed long time ago. The first report on this field is the work of

X.-H. Le · N.-B.-T. Nguyen · M.-V. Huynh
T.-P.-T. Vo · T.-T.-H. Pham (✉)
Biomedical Engineering Department, International University—
VNU HCMC, Ho Chi Minh City, Vietnam
e-mail: ptthien@hcmiu.edu.vn

Andrew Mester, a professor at Semmelweis University [1]. In 1968, by utilizing defocused ruby laser on the shaved dorsum of rats. Andrew Mester accidentally found out that during the experiment, the laser can stimulate the growth of rat hair. This discovery is one of the first and basic reports on the effect of the laser in bio stimulation. Later, inspired by the work of Mester, many types of research have been conducted in the same direction. Despite many reports, the biomechanical mechanism of LLT is not fully understood yet. However, among the influence factor, dosage dependent effect of LLLT can be expressed by a curve, called Arndt-Schulz curve.

According to Arndt-Schultz Law, a dose too small cannot promote any biological effect while a dose too large can inhibit cellular activities. Thus, choosing dosage within the acceptable range of Arndt-Schultz curve is significantly necessary. For the choice of dosage in previous researches, based on figures of a literature review of 68 studies from 1992 to 2012 published in 2014 by Maria Emilia de Abreu Chaves [8], it can be seen that dosage range varies from 0.1 to 10 J/cm², with the predominance of 5 J/cm². This dosage is also seen with the most biological effects.

There are three primary therapeutic parameters of LLLT, i.e. wavelength, intensity, and irradiance. This study was designed to find the optimal parameters to maximize the wound healing rate by utilizing and combining the use of both red and blue light in *in vivo* on mouse skin.

2 Methodology

2.1 Animal Preparation

A group of twelve male mice obtained in the Institute Pasteur in Ho Chi Minh City, Vietnam was applied for the investigation. Their ages ranged from 20 to 30 weeks with the body weight of 10–15 g. Animals were feed and hold in a plastic cage. They were maintained in a constant condition of temperature (23 °C) and provided laboratory food. The mice were all physically alike.

2.2 Anesthetic Procedure

Initially, the dorsal surface hair of all mice was trimmed with an electrical clipper. The trimmed area was then hair-removed by a hair removal cream (Cleo) and entirely cleaned by alcohol. The anesthetic procedure was performed including two steps. Firstly, a single injection of a pre-anesthesia drug (Atropine Sulfate, 10 mg/kg) with the dose of 0.2 ml was applied at one side of the groin. Then, 0.2 ml anesthetic drug (Zoletil, 12 mg/kg) was injected on the other side of the groin to anesthetize the mouse completely.

2.3 Wound Infliction

In each mouse, two full-thickness round wounds (8-mm diameter) were created on the dorsal surface using a punch biopsy and a scalpel. One wound was considered as control group and the other wound was considered as treated group. Until the end of the surgical procedure, both groups were physically treated with the same way.

2.4 Laser Irradiation

Six hours after the wound conffiction, treated group was exposed to a red (635 nm) laser light system (Thorlabs Inc, US) while the control group was totally shielded to avoid the effect of the laser beam. Output power was measured by a photometer. The duration time was determined according to the wound area and output power to produce an intensity of 2, 3 or 5 J/cm². Twelve mice were equally divided into three small groups, each of which received one dose. The laser beam was aligned directly perpendicular to the wound in 1 mm distance, project the entire wound area. Laser treatment was performed day by day and repeated until wholly healed to stimulate the wound healing process. The diameter of the wound is recorded at day 5 and day 10 after surgery, and every 7 days, each group was photographed to evaluate the wound's size. A full-thickness wound skin of each group was then captured. To collect the sample from wound-healing skin, cryotome (Shandon Cryotome Thermo Scientific), in which the cold condition is the critical factor for making very thin sections of tissue after they have been removed from body and frozen, was used. Each specimen was extracted with a thickness of 10 µm. Samples were stained with Hematoxylin-e Eosin and observed in a light microscope for evaluation.

3 Results

For each time of measurement (at day 5 and day 10 after surgery), the wound diameter is recorded to compare the difference between groups. The rate of wound healing can be expressed as a graph of Wound diameter versus Treatment days. Also, the wounded area is sectioned utilizing freezing microtome technique for histological analysis after 7 days of therapy.

Table 1 shows that 5 J/cm² dosage treatment reduces the wound size the most efficiently when compared to other laser dosages.

The result and figure indicates that, the diameter of the wounds decrease after 5 days of treatment for all cases and even get smaller after 10 days of exposure to red laser beam.

Table 1 Wound diameter recorded initially and on the 5th and 10th day

Wound diameter in cm	2 J/cm ²	3 J/cm ²	5 J/cm ²
Initially	0.8	0.8	0.8
Day 5	0.74 ± 0.006	0.75 ± 0.006	0.71 ± 0.006
Day 10	0.42 ± 0.026	0.39 ± 0.015	0.38 ± 6.8 × 10 ⁻¹⁷

5 J/cm² dosage seems to give the best result among others (Fig. 1).

The relationship between the wound diameter and healing time of each dosage can be expressed as quadratic equation models in which correlation coefficient can be calculated utilizing Eq. (1):

$$r = \sqrt{1 - \frac{\sum(d_i - (A + Bt + Ct^2))^2}{\sum(d_i - \bar{d})^2}} \tag{1}$$

Equation (2) demonstrates the best fit-curve model for 2 J/cm²:

$$Y = -0.0053 * x^2 + 0.0153 * x + 0.8 \tag{2}$$

Similarly, Eq. (3) is obtained to illustrate the best fit curve for 3 J/cm² as shown.

$$Y = -0.0064 * x^2 + 0.0233 * x + 0.8 \tag{3}$$

For 5 J/cm², the curve is indicated by Eq. (4):

$$Y = -0.0047 * x^2 + 0.0047 * x + 0.8 \tag{4}$$

All of these models have high correlation coefficient which is $r \approx 1$, calculated utilizing Eq. (1).

After 7 days of LLLT, the entire wounded area is sectioned using freezing microtome technique. The sample is then fixed with formaldehyde and embedded in paraffin for

histological evaluation with hematoxylin and eosin (H&E) staining.

Figure 2 showed the damage of the dermis with necrotic cells sighted, very low level of granulation and matrix formation characterized by minimal amount of collagen fiber deposition, absence of hair follicles and sebaceous gland, scarce vascularity.

Figure 3 indicated that necrotic cell remnants are less dense compared to that of the untreated control group. A thin layer of epidermis is reforming. The dermis showed signs of ongoing healing process with sightings of granulation tissue formation, fibroblast infiltrates and a moderate number of capillaries.

As shown in Fig. 4, epidermis development is noticeable. Wound healing is predominantly demonstrated with the onset of granulation tissue formation, numerous capillary sightings, reformation of hair follicles and adipose tissues, together with a large number of fibroblasts (Fig. 5).

Signs of advanced wound healing and ongoing remodeling process are displayed with the proliferation of epithelial and matrix components, thickening of the epidermis, completion of angiogenesis and granulation characterized by the abundance of granulation tissues and vascular content, prominent regeneration of skin appendages such as hair follicles and sebaceous gland.

These histological findings suggest that LLLT does accelerate wound healing rate and when we increase the laser dosage from 2 to 5 J/cm², the healing process is promoted accordingly. Beneficial effects are the most profound in treatment with 5 J/cm² laser dosage. This is in agreement with the results obtained from wound diameter measurement in the previous part of the study.

The results obtained from both histological assessment and wound diameter measurement lead us to the conclusion that treatment with 5 J/cm² laser dosage has the most prominent positive effects on wound healing dynamics. In several experiments in the literature, evidence has been provided that laser irradiation at 5 J/cm² promotes wound healing [8]. In contrast to our findings, 5 J/cm² lies within the range of energy dosages inducing cell retardation on the Arndt-Schultz curve. This may be confusing at first, however, a three-dimensional extension model of this curve can solve this conflict [9]. The three-dimensional graph suggests that a seemingly adverse dosage can also have “sweet spots” that promote maximal bio-stimulation and deliver no

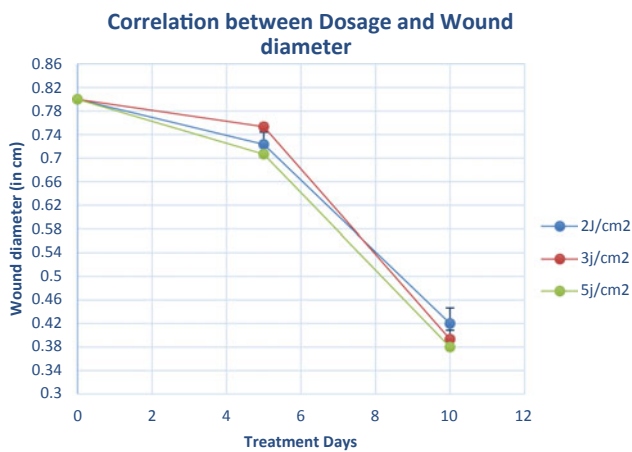


Fig. 1 The graph showing the correlation between wound diameter and treatment day

Fig. 2 Control sample—
magnification: **a** 10× and **b** 20×

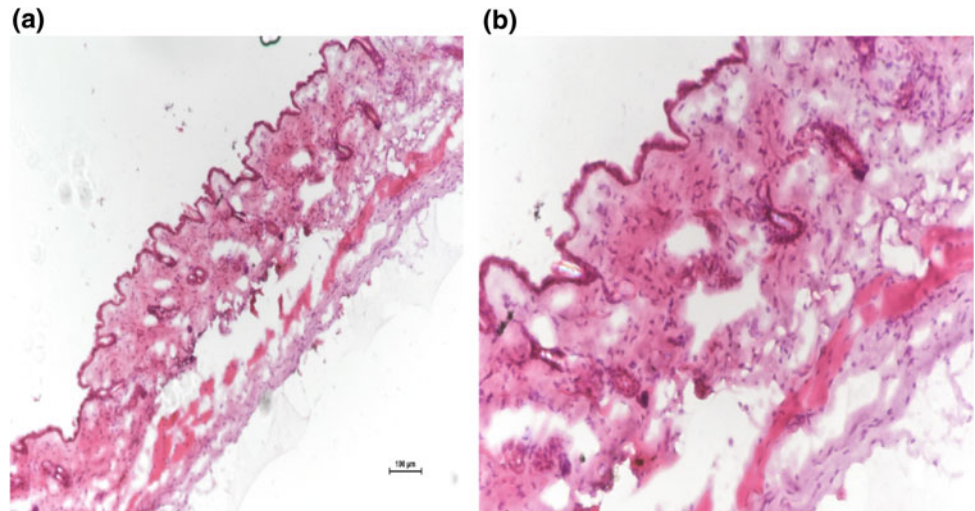


Fig. 3 Treatment with 2 J/cm²
laser dosage—magnification:
a 10× and **b** 20×

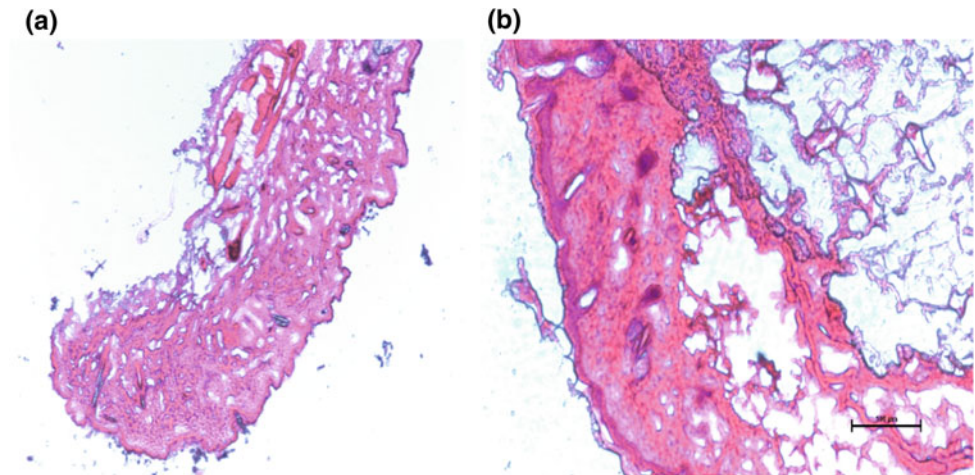
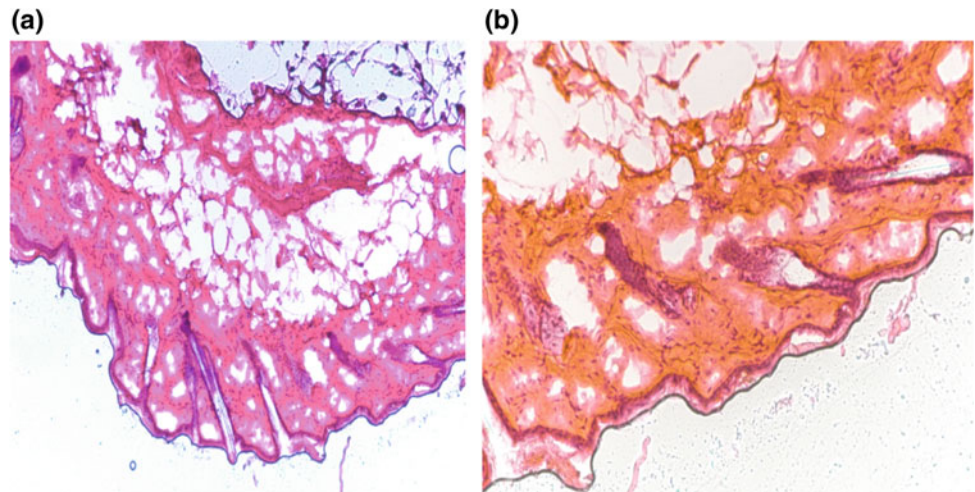


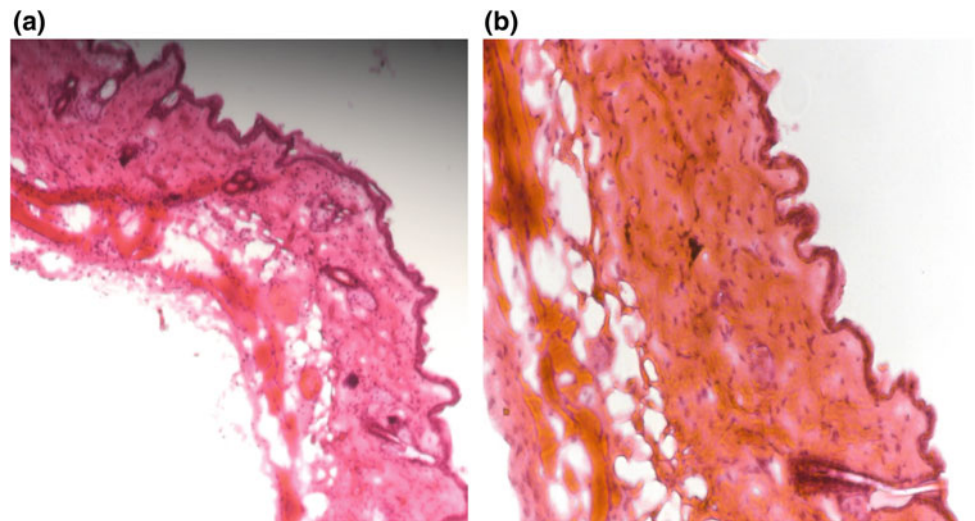
Fig. 4 Treatment with 3 J/cm²
laser dosage—magnification:
a 10× and **b** 20×



bio-inhibition when the appropriate balance between power density and irradiation time is achieved. Furthermore, whilst the Arndt-Schultz curve can provide a general view of

theoretical LLLT dose response, in real-life research context many factors have to be taken into account such as wavelength, pulse width, beam area while exploring the

Fig. 5 Treatment with 5 J/cm² laser dosage—magnification: **a** 10× and **b** 20×



relationship between energy dosage and its effect on wound healing. Those factors all contribute to the inconsistency between theory and real-life experiment.

4 Conclusion and Discussion

The proposed study applied an optical system with red laser beams to characterize the efficiency of the wound healing treatment in chronic wounds and standard rat model. The results showed that the phototherapy could be used to heal chronic wounds with the improvement of impairment and the faster time to wound closure. In the future, we hope to overcome the existing limitations with a new model that can utilize different parameters (wavelength, power density, treatment duration, and frequency) as well as a larger sample ($N > 100$). In the next phase of our research, diabetic mice instead of normal healthy mice will be used since diabetes mellitus is a significant international health concern. The goal is to examine whether the use of LLLT is effective in healing diabetes in comparison with the standard of care and to provide an evidence-based recommendation for the treatment of diabetes using LLLT. Last but not least, we are seeking to incorporate tissue engineering and regenerative medicine into our study by combining LLLT treatment with the use of the wound-healing gel to see whether the healing progress can be further accelerated.

Acknowledgements This research is funded by International University—VNUHCM under grant number T2017-01- BME.

Conflict of Interest The authors declare that they have no conflict of interest.

References

1. Parker, S.: Introduction, history of lasers and laser light production. *Br. Dent. J.* **202**(1), 21–31 (2007)
2. Purohit, G., Pandey, H., Sharma, R.: Effect of cross focusing of two laser beams on the growth of laser ripple in plasma. *Laser Part. Beams* **21**(04), 567 (2003)
3. Kana, J.S.: Effect of low—power density laser radiation on healing of open skin wounds in rats. *Arch. Surg.* **116**(3), 293 (1981)
4. Dawood, M.S., Salman, S.D.: Low level diode laser accelerates wound healing. *Lasers Med. Sci.* **28**(3), 941–945 (2012)
5. Ganz, R.: Helicobacter pylori in patients is killed by visible light. *Am. J. Gastroenterol.* **98**(9), S47 (2003)
6. Fekrazad, R., Mirmoezzi, A., Kalhori, K.A., Arany, P.: The effect of red, green and blue lasers on healing of oral wounds in diabetic rats. *J. Photochem. Photobiol. B* **148**, 242–245 (2015)
7. Lee, S.Y., You, C.E., Park, M.Y.: Blue and red light combination LED phototherapy for acne vulgaris in patients with skin phototype IV. *Lasers Surg. Med.* **39**(2), 180–188 (2007)
8. de Chaves, M.E.A., de Araújo, A.R., Piancastelli, A.C.C., Pinotti, M.: Effects of low-power light therapy on wound healing: LASER LED. *Anais Brasileiros de Dermatologia* **89**(4), 616–623 (2014)
9. Huang, Y.-Y., Sharma, S.K., Carroll, J., Hamblin, M.R.: Biphasic dose response in low level light therapy—an update. *Dose-Response* **9**(4), 602–618 (2011)



Non-invasive Glucose Monitoring System Utilizing Near-Infrared Technology

Duc Trinh-Minh Dinh, Viet Anh Truong, An Nhu-Phu Tran, Hieu Xuan Le, and Hien Thi-Thu Pham

Abstract

Regular monitoring of glucose concentration is essential and urgency, especially diabetics. However, those methods which involve finger puncturing are invasive, expensive as well as painful. Also, there are risks of infectious diseases using these techniques due to the contact of the needle on human skin. This paper proposed a non-invasive glucose monitoring system utilizing the near-infrared (NIR) light to measure the glucose concentration in the human blood. The designed system uses a 980 nm-wavelength NIR LED transmitting through D-glucose phantom samples, a photo-sensor for analyzing the transmitting optical parameters, a filter & an amplifier circuit, and a Nano Arduino microcontroller. For calculating the values of glucose concentration, the R programming with the methodology of the artificial neural network (ANN) was applied. This type of methodology is considered as one of the most useful technique in the world of data analysis and because it is adaptive, learns from the provided information and optimizes for better prediction outcomes. The ANN is used to predict the correlation equation between collected voltage and glucose concentration. The obtained glucose level is demonstrated directly on the system's screen or further sent to the user's mobile phone. The result obtained shows a correlation between the transmittance and the concentration of D-glucose solution. The correlation parameter of the technique is $R^2 = 0.9957$. Despite having the acceptable results, there are still some improvements that could be carried out for more accurate measurement (angle of the LED, a procedure of filtering and amplifying, usage of an optical instrument...). For further investigation and development, it is predicted that

the result can be more accurate, precise and sensitivity as much as possible.

Keywords

Near-infrared • Non-invasive • Blood glucose • Diabetes

1 Introduction

Diabetes is a pathological metabolic condition that occurs when the amount of glucose (sugar) in the blood is too high, which affects other organs if not diagnosed and left untreated. Nowadays, it has become a significant health problem globally. Nowadays, the number of people getting diabetes is rising, and the need for the blood glucose monitoring is the obvious outcome. Checking the blood pressure regularly not only let people know what state they are in but also help them to have suitable prevent diabetes [1–5].

With the available devices, the users can check their blood glucose quickly and regularly. The most popular device is the invasive type. The user has to make a finger prick by using a test strip, and the device uses their blood to calculate the glucose amount. Although giving precise results but this method has some disadvantages: not suitable for people who afraid of needles, waste of money and time to buy the test trip, painful and discomfort. Moreover, using the invasive method could increase the risk of infection. Hence, finding another method is the concern at the moment.

Indeed, there is a sharp rise of the non-invasive method for checking the blood glucose level. The majority of these methods is the application of the LED and the properties of light for measurement. These devices can deliver painless and comfortable progress for the users. Although this type of method is new, it shows the potential of making a device which is more user-friendly, painless and could give reliable results.

D. T.-M. Dinh · V. A. Truong · A. N.-P. Tran ·
H. X. Le · H. T.-T. Pham (✉)
Biomedical Engineering Department, International
University- Vietnam National University HCMC,
Ho Chi Minh City, 70000, Vietnam
e-mail: pthien@hcmiu.edu.vn

The non-invasive method works base on the light properties. For each substance, there is always a specific wavelength at which the absorbance of that substance is that strongest. Each substance has its wavelength. Using this property, the system consists of two main components which are the LED and the photo-sensor. The LED emit the light through the skin area where it is put, and the photo-sensor is placed on the opposite side. By choosing the appropriate wavelength which absorbed mostly by blood glucose, the amount of light that reaches the photo-sensor is calculated and analyzed.

Choosing the appropriate wavelength for the system is the most important key. To achieve the good result, the wavelength must be the one that has the most interaction with blood glucose and also not be affected too much by the other substances. There have been many options for the wavelength that is proposed by the previous research since glucose has light absorption peaks at wavelengths of 940, 1150, 1450, 1536 nm [1–5]. The wavelength of 940 nm is chosen the most in research since, at this wavelength, the attenuation of optical signals by other constituents like platelets, red blood cells or water is at a minimum.

2 Methodology

The proposed system consists of an adapter and a voltage converter for converting 220–24 and 24–5 V for the power supply. A NIR light source and an optical sensor are the main parts of the system. When the light reaches the optical sensor, the signals go through amplifying and filter circuits, and an Arduino is used to convert the data from analog to digital signals. After the processing, the value of blood glucose level is shown on the computer. Figure 1 validates the operation of the system.

2.1 Emitting System

The NIR LED used in the system is TSAL 6100 with the wavelength of 940 nm. This LED has an emitting angle and the power that suitable for the system, and that leads to the

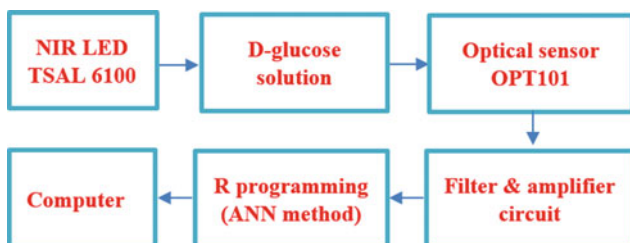


Fig. 1 The block diagram of the system

decrease of scattering light. A constant current circuit is designed for emission of NIR to minimize the fluctuation in the current through the NIR LED. For this circuit, the BC557 PNP transistor is used along with LM358. LM358 op-amp plays the role as a current stabilizer to adjust the suitable current goes into the LED. The output of LM358 is given to the base of the transistor for controlling the average power transmitted by the NIR LED. Figure 2 demonstrates the emitter circuit diagram.

2.2 Receiving System

The OPT101 is used as the optical sensor. The reason for using this sensor is because the sensitivity is high enough thus it would not be affected too much by another light source from the environment or scattering light. LM358 is also used in the designed circuit. Therefore, the signal collected from the optical sensor is then amplified and filtered. Figure 3 shows the receiver circuit diagram.

2.3 Black Box System

A black box system is built to keep the sample and the sensor from getting noise. There is a slit put in front of the LED, and the size of the slit would fit the emitting angle so the intensity transferred from the LED to sample is the most. The purpose is to focus the light into a line and lead it directly to the sample, and it could reduce the noise since most of the

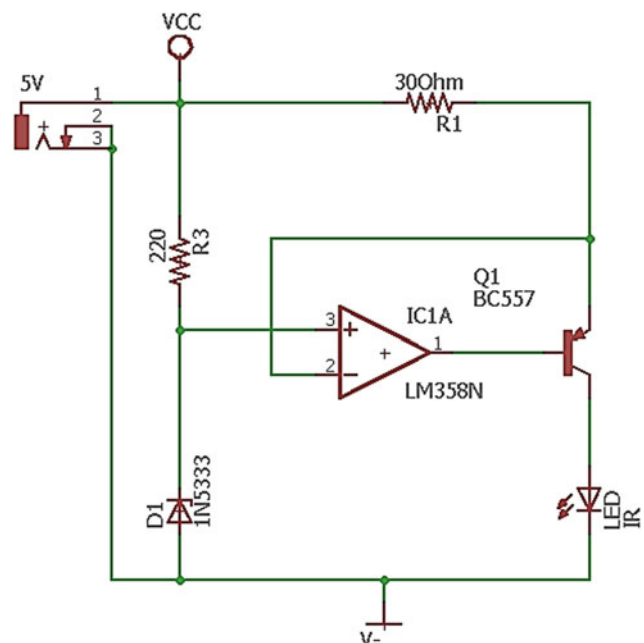
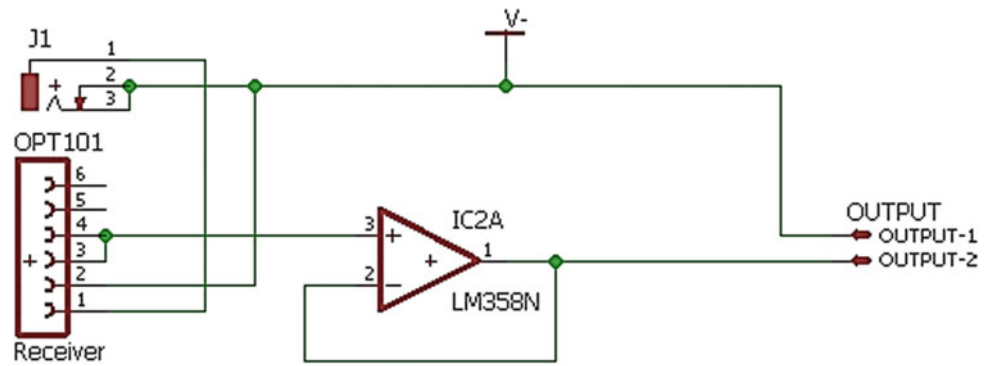


Fig. 2 Emitter circuit

Fig. 3 Receiver circuit



sensitivity contact with the sample. All the light leaving the sample goes into the optical sensor put behind the sample. The box is painted black to absorb the scattering light goes out from the sample. There is an area in the box for putting the circuits. Figure 4 shows the illustration of black box system.

2.4 Analyzing System

The method for processing the data getting from the LED is by using machine learning. ANN method is chosen for processing and analyzes the data since it is more appropriate with the complex data [6]. Figures 5 and 6 show the component of ANN were used in this study.

The network consists of one input layer, one output layer, and several hidden layers. Each input node maps to all hidden nodes, and each hidden node maps to all nodes of the next hidden layers till it reaches the output

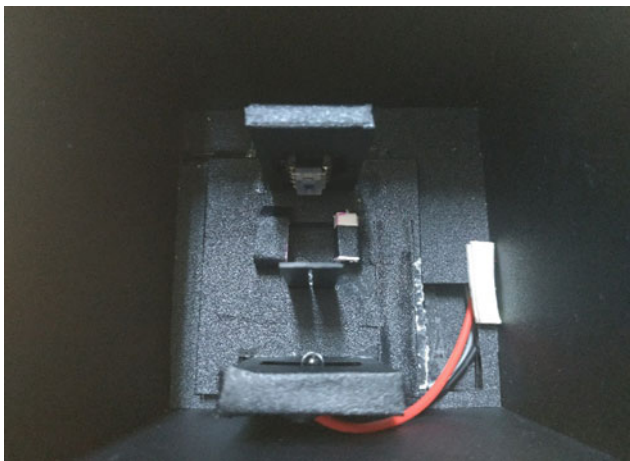


Fig. 4 Black box system

Since one node in hidden layers may connect with several others nodes, the value of that node can be calculated with the formula:

$$Y = f(w_1.X_1 + w_2.X_2 + \dots + W_n.X_n) \quad (1)$$

where Y is the output of that node and X1, X2, ..., Xn are the input nodes; W1, W2, ..., Wn is the weights corresponding to each node respectively.

The final node- output node is utilized to compare the accuracy of the model to the training data. The weights is updated continuously until we obtain the minimum in “Error estimation” between actual output and model output [6, 7].

$$J(w) = \frac{1}{2} \sum_i (target^{(i)} - output^{(i)})^2 \quad (2)$$

where J(w) is the error/loss, target⁽ⁱ⁾ is the actual output and output⁽ⁱ⁾ is the network output.

Following, Fig. 7 shows the flowchart of the ANN network for better illustration

There were D-glucose samples prepared with a variant of concentrations. Every time a sample with known concentration is measured, the output voltage is recorded. After multiple measurements and records for each concentration, a set of data with corresponding output voltages is created for ANN. This set of data is used to train the ANN, and from the trained data, appropriate function and algorithm is generated to calculate the connection between D-glucose concentration and the output voltage. The sample for the training data must be assured with unification (in the way of making the sample: the weight of 12 sample for each concentration must be identical and also the amount of water) to reduce the error between each measurement and increase the accuracy for the predicted result.

Fig. 5 ANN diagram

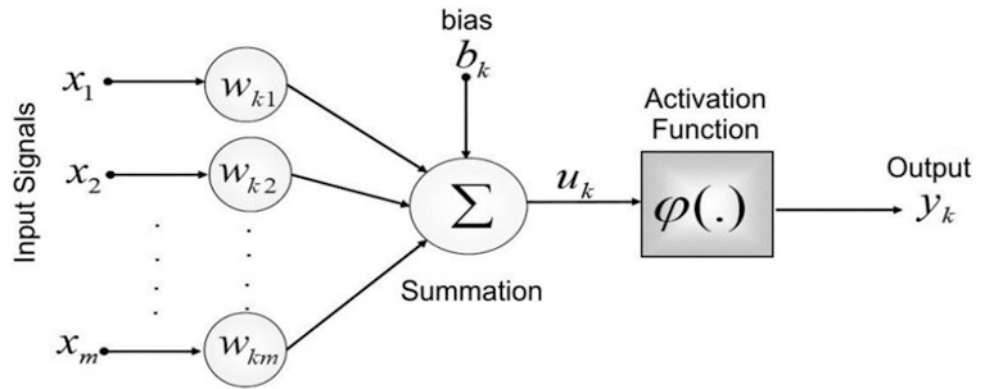


Fig. 6 The layers of ANN

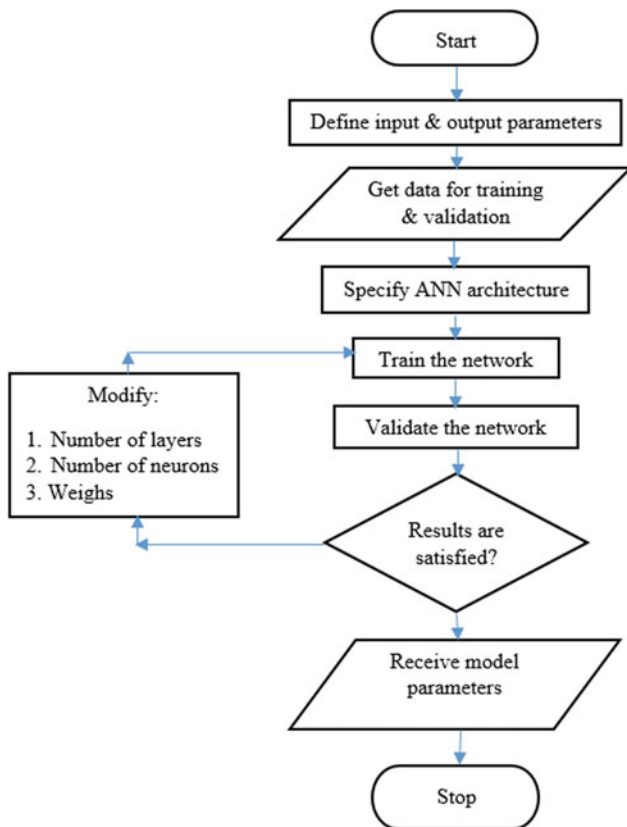
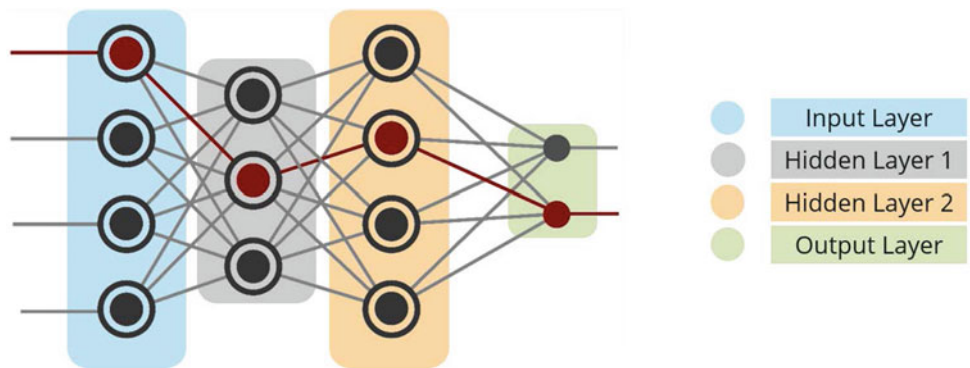


Fig. 7 Flowchart of ANN network

3 Results and Discussion

The results were taken from twelve samples of five different concentrations (500, 1000, 1500, 1800 and 2000 ppm). The mean of each sample were chosen to make the correlation line between the concentration and the output voltage. Table 1 and Fig. 8 show the collected data (with standard deviation) and the correlation.

As data at two concentrations 1500 and 1800 ppm shows no linearity, the 1500 ppm concentration is removed in order to increase the accuracy of the system (by comparing the R^2 of the model while removing 1500 and 1800 ppm respectively). Figure 9 shows the fit line and trend line of the data after removing 1500 ppm concentration point.

The results illustrate the linear correlation of the output voltage and glucose concentration chosen from the data table. It reveals that the more concentration of the sample, the more output voltage measured. The trend line has the $R^2 = 0.9957$ comparing with another reliable source is the UV-VIS 730 machine with $R^2 = 0.9999$.

The results approve that wavelength and the method of processing chosen for the research are appropriate and have the potential to develop further. As the few number of samples, the use of ANN cannot be optimized and the produced result is not enough sensitivity. Some improvements

Table 1 The collected data table

Samples (ppm)	1	2	3	4	5	6	7	8	9	10	11	12
500	3.936	3.937	3.945	3.945	3.924	3.924	3.915	3.915	3.922	3.921	3.922	3.93
1000	3.955	3.942	3.945	3.958	3.941	3.942	3.94	3.932	3.933	3.939	3.948	3.945
1500	3.971	3.979	3.969	3.979	3.979	3.97	3.963	3.974	3.98	3.976	3.98	3.977
1800	3.976	3.972	3.979	3.978	3.979	3.974	3.975	3.971	3.98	3.972	3.973	3.972
2000	3.985	3.987	3.985	3.984	3.982	3.987	3.983	3.978	3.981	3.987	3.988	3.983

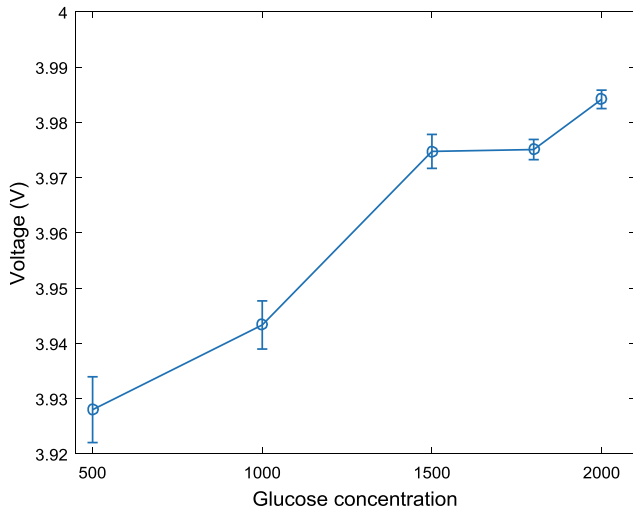


Fig. 8 Correlation between the output voltage and concentration

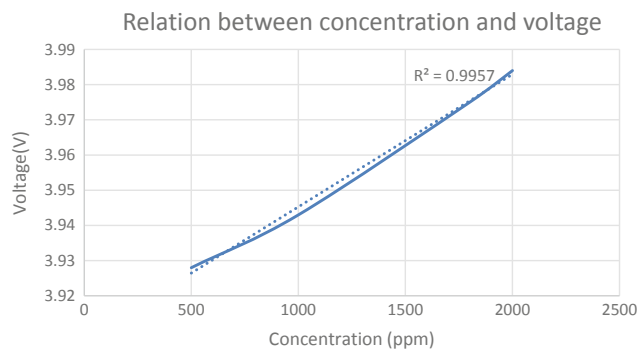


Fig. 9 Model after removing 1500 ppm data

should be carried out for more accurate and reliable results in future: the emitting angle of the LED, the amplifying and filtering circuit, the structure of the black box, increasing the size of the data set for the better fit with ANN in predicting the fit line, usage of another optical instrument.

4 Conclusion

The work in this study provides the way for measuring the glucose concentration non-invasively. For further development, the system is expected to be able to work with more complicated solutions such as a microsphere, animal blood as well as other liquid composition in the human body.

Acknowledgements This research is funded by International University, VNU-HCM under grant number SV2017-BME-07.

Conflict of Interest The authors declare that they have no conflict of interest.

References

1. Bobade C.D., Mahadev, S.P.: Non-invasive monitoring of glucose level in blood using near-infrared spectroscopy
2. Narkhede, P., Dhalwar, S., Karthikeyan, B.: NIR based non-invasive blood glucose measurement. *Indian J. Sci. Technol.* **9**(41) (2016)
3. Yadav, J., et al.: Near-infrared LED based non-invasive blood glucose sensor. In: 2014 International Conference on Signal Processing and Integrated Networks (SPIN). IEEE, New York (2014)
4. Lawand, K., Parihar, M., Patil, S.N.: Design and development of infrared LED based noninvasive blood glucometer. In: 2015 Annual IEEE India Conference (INDICON). IEEE, New York (2015)
5. Malin, S.F., et al.: Noninvasive prediction of glucose by near-infrared 1651–1658
6. Guo, D., et al.: Noninvasive blood glucose measurement based on NIR spectrums and double ANN analysis. *J. Biosci. Med.* **3**(06), 42 (2015)
7. Coster, S., et al.: Monitoring blood glucose control in diabetes mellitus: a systematic review. *Health Technol. Assess.* (Winchester, England), **4**(12), i–iv, 1–93 (1999)

Characterization of Liver Cancer Tissues Utilizing the Optical Polarized System

Thao-Vi Nguyen, Chi-Bao Bui, and Thi-Thu-Hien Pham

Abstract

According to GLOBOCAN, in 2012, liver cancer with 782,000 cases was diagnosed, and 746,000 patients died from this disease in the world. The rate of liver cancer was ranked 5th in the types of cancer in men and ranked 9th in women, but the death rate accounted for 2nd in both sexes. In Vietnam, the liver cancer rate was ranked 2nd in men and ranked 3rd in women on morbidity, while the highest death rate occurred in both sexes. Meanwhile, the prognosis for liver cancer is quite sad, which depends on many factors. Currently, there are many methods to monitor the treatment of liver cancer depends on the stage of the disease, in which the noninvasive process is considered a new study on cancer diagnosis without pain or injury to patients, and one of them is the use of optical measurement systems. Study on the interaction between bio-samples and polarized light received significant attention because of its potential for developing non-invasive detection methods. In this work, an analytical technique based on Stokes polarimetry and the Mueller matrix decomposition method was applied to extract the effective linear birefringence (LB), linear dichroism (LD), circular birefringence (CB), circular dichroism (CD), linear depolarization (L-Dep), and circular depolarization (C-Dep) properties. The experimental results showed that the LB properties of normal and liver cancer tissues have a great difference, with 15° – 20° and 150° – 160° in that order. In addition, CB properties and depolarization properties of two kinds of samples are also described in a significant disparity. Thus,

it has promising potential for detecting liver cancer by an optical polarized light system.

Keywords

Liver cancer • Polarization state • Stokes polarimeter • Mueller matrix • Liver tissue

1 Introduction

Recently, optical diagnostic techniques from turbid media such as biological tissues, human or animal muscle are essential experimental tools employed in facilitating the development of advanced inspection and/or diagnostic applications. Based on polarimetric measurements of effective parameters, a number of these techniques are able to determine the optical properties of turbid media. Examples of applications are numerous: linear birefringence (LB) measurements provide a useful insight into the characteristics of LCD compensator films or the photo-elasticity of human tissue, while circular birefringence (CB) measurements of human blood give a reliable indication of diabetes [1–4]. Similarly, linear dichroism (LD) measurements of human tissue can facilitate tumor diagnosis, while circular dichroism (CD) measurements are an effective means of characterizing and classifying protein structures [5–7]. Moreover, linear depolarization (L-Dep) and circular depolarization (C-Dep) measurements provide valuable experience of the characteristics of tumors or surface measurements [8]. In a recent study, Pham and Lo [9–12] proposed a decoupled analytical technique for extracting the six effective Linear Birefringence (LB), Linear Dichroism (LD), Circular Birefringence (CB) and Circular Dichroism (CD) parameters of anisotropic optical materials. By decoupling the extraction process, the “multiple solutions” problem inherent in previous models [9–12] was avoided. However, the method was unable to extract the Linear Depolarization (L-Dep) and Circular Depolarization (C-Dep)

T.-V. Nguyen · T.-T.-H. Pham (✉)

Biomedical Engineering Department, International University-Vietnam National University HCMC, Ho Chi Minh, 70000, Vietnam
e-mail: ptthien@hcmiu.edu.vn

C.-B. Bui

Ho Chi Minh City Medicine and Pharmacy University, HCM City, Ho Chi Minh, 70000, Vietnam

properties of turbid samples. Accordingly, an enhanced analytical model is proposed by Lo et al. [10] for extracting all the effective LB, CB, LD, CD, L-Dep and C-Dep parameters of a turbid medium in a decoupled manner. The validity of the proposed method is demonstrated by extracting the parameters of various optical samples. In contrast to existing analytical models, the proposed model extracts the effective optical parameters in a decoupled manner and considers not only the circular dichroism properties of the sample but also the depolarization properties. The results show that the proposed method enables all of the effective optical parameters to be measured over the full range.

2 Methodology

2.1 Theory

This section introduces the analytical model proposed in the proposed study for determining the effective LB, LD, CB, CD, L-Dep and C-Dep properties of a turbid medium. In summary, for a turbid media with hybrid properties, a total of nine effective optical parameters need to be extracted, namely the principal axis angle (α), the retardance (β), optical rotation angle (γ), the dichroism axis angle (θ_d), the dichroism (D), the circular dichroism (R), the degrees of linear depolarization (e_1 and e_2), and the degree of circular depolarization (e_3). Table 1 summarizes the notations, ranges, and definitions of the nine effective parameters and the depolarization index, respectively.

The output Stokes vector can be calculated as

$$S_c = \begin{bmatrix} S_0 \\ S_1 \\ S_2 \\ S_3 \end{bmatrix}_c = [M_\Delta][M_{lb}][M_{cb}][M_{ld}][M_{cd}]\hat{S}_c = \begin{pmatrix} m_{11} & m_{12} & m_{13} & m_{14} \\ m_{21} & m_{22} & m_{23} & m_{24} \\ m_{31} & m_{32} & m_{33} & m_{34} \\ m_{41} & m_{42} & m_{43} & m_{44} \end{pmatrix} \begin{pmatrix} \hat{S}_0 \\ \hat{S}_1 \\ \hat{S}_2 \\ \hat{S}_3 \end{pmatrix}_c \quad (1)$$

where $[M_\Delta]$, $[M_{lb}]$, $[M_{cb}]$, $[M_{ld}]$, and $[M_{cd}]$ are the effective Mueller matrices describing the depolarization, LB, CB, LD and CD properties of the turbid sample, respectively, and \hat{S}_c is the input Stokes vector. In the methodology proposed in this study, the sample is illuminated by six input polarization lights, namely four linear polarization lights (S_{0° , S_{45° , S_{90° , and S_{135°) and two circular polarization lights (S_{RHC} and S_{LHC}).

The corresponding output Stokes vectors can be obtained from Eq. (1) as follows:

$$S_{0^\circ} = [m_{11} + m_{12}, \quad m_{21} + m_{22}, \quad m_{31} + m_{32}, \quad m_{41} + m_{42}]^T \quad (2)$$

$$S_{45^\circ} = [m_{11} + m_{13}, \quad m_{21} + m_{23}, \quad m_{31} + m_{33}, \quad m_{41} + m_{43}]^T \quad (3)$$

$$S_{90^\circ} = [m_{11} - m_{12}, \quad m_{21} - m_{22}, \quad m_{31} - m_{32}, \quad m_{41} - m_{42}]^T \quad (4)$$

Table 1 Symbols, ranges, and definitions of effective parameters of turbid media with hybrid properties [10]

Name	Symbol	Range	Definition (*n)
Orientation angle of LB	α	0° – 180°	
Linear birefringence of LB	β	0° – 360°	$2\pi(n_s - n_f)l/\lambda_0$
Optical rotation of CB	γ	0° – 180°	$2\pi(n_- - n_+)l/\lambda_0$
Orientation angle of LD	θ_d	0° – 180°	
Linear dichroism of LD	D	0–1	$2\pi(\mu_s - \mu_f)l/\lambda_0$
Circular dichroism of CD	R	–1 to 1	$2\pi(\mu_- - \mu_+)l/\lambda_0$
Linear depolarization	e_1 and e_2	–1 to 1	
Circular depolarization	e_3	–1 to 1	
Depolarization index	Δ	0–1	

(*) n is refractive index, μ is absorption coefficient, l is path length through medium (thickness of material), and λ_0 is vacuum wavelength. Furthermore, subscripts f and s represent the fast and slow linearly polarized waves, respectively, when neglecting the circular effects. Finally, + and – represent the right and left circular polarized waves, respectively, when neglecting the linear effects

$$S_{135^\circ} = [m_{11} - m_{13}, \quad m_{21} - m_{23}, \quad m_{31} - m_{33}, \quad m_{41} - m_{43}]^T \tag{5}$$

$$S_{RHC} = [m_{11} + m_{14}, \quad m_{21} + m_{24}, \quad m_{31} + m_{34}, \quad m_{41} + m_{44}]^T \tag{6}$$

$$S_{LHC} = [m_{11} - m_{14}, \quad m_{21} - m_{24}, \quad m_{31} - m_{34}, \quad m_{41} - m_{44}]^T \tag{7}$$

Equations from (2) to (7) are sufficient to calculate all of the elements of the Mueller matrix product given in Eq. (1).

Note that full details of the experimental procedure used to extract the various parameters are available in Refs. [10, 11]. In summary, the LB orientation angle (α), phase retardance (β), optical rotation angle (γ), LD orientation angle (θ_d), linear dichroism (D), circular dichroism (R), linear depolarization (e_1, e_2), and circular depolarization (e_3) can be extracted using Stokes—Mueller technique from Refs. [9–12]. Notably, this methodology does not require the alignment of the principal birefringence axes and diattenuation axes. Although only four different input polarization lights, namely three linear polarization lights (i.e. \hat{S}_{0° , \hat{S}_{45° , \hat{S}_{90° , and \hat{S}_{135°) and two circular polarization lights (i.e. right-handed \hat{S}_{RHC} and left-handed \hat{S}_{LHC}) are enough for obtaining all elements of Mueller matrix.

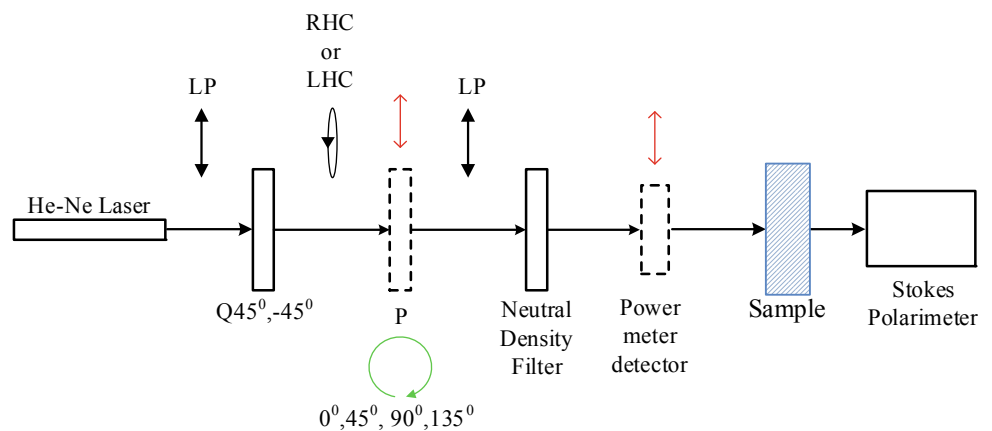
Moreover, the ability of the analytical model for extracting all the optical parameters of interest over the measurement ranges was verified using an analytical simulation and error analysis technique. Thus, the analytical model yielded accurate results even when the output Stokes parameters had errors in the range of ± 0.005 , or the samples

had the minimum measurement of birefringence or dichroism [10, 11].

2.2 Experimental Setup

Figure 1 presents a schematic illustration of the experimental setup used in the present study to characterize the LB, LD, CB, CD, L-Dep and C-Dep properties of turbid media. In performing the experiments, the input light was provided by a frequency-stable He–Ne laser (JDSU—Model 1125P) with a central wavelength of 632.8 nm. Also, a polarizer (GTH5M, Thorlabs Co.) and a quarter-wave plate (QWP0-633-04-4-R10, CVI Co.) were used to produce four linear polarization lights ($0^\circ, 45^\circ, 90^\circ$ and 135°) and two circular polarization lights (right-handed and left-handed). Finally, a neutral density filter (NDC-100-2, ONSET Co.) was used to ensure that each of the input polarization lights had equal intensities. (Note that for samples with no linear dichroism, the output Stokes parameters can be normalized. Thus, there is no need to calibrate the intensity of the input light. However, for samples with dichroism, the output Stokes parameters cannot be normalized in this way, and thus the neutral density filter and power meter detector are required). The output Stokes parameters were computed from the intensity measurements obtained using a commercial Stokes polarimeter (PAX5710, Thorlabs Co.) at a sampling rate of 33.33 samples per second. A minimum of 1024 data points was obtained for each sample. Of these data points, 100 points were chosen and used to calculate the mean value of each effective parameter. It is noted that the experimental data were chosen from the average result of four to five multiple measurements.

Fig. 1 Schematic illustration of the model of measurement



2.3 Preparation Procedure

The calibration procedure was to adjust the polarization states of input lights and the incident angle of light. To ensure the light to pass through the optical element normally, the system was inserted a pinhole in front of the optical element. The light reflected by the optical element was then adjusted to pass through the pinhole. Following the same procedure, the sample placed into the system can typically be adjusted to the input light, and then the incident angle of input light can be controlled by a stage controller. Subsequently, the polarization state of input light can be adjusted by a stage controller through checking Poincare sphere in a polarimeter.

The effective optical parameters of the biologic turbid medium were studied using frozen human liver cancer tissues obtained from University Medical Center (HCMC, Vietnam) approved protocol with patient consent prior to the procedure. It was stored at $-80\text{ }^{\circ}\text{C}$ immediately after production in a freezer. The samples thawed at $37\text{ }^{\circ}\text{C}$ and were used within 24 h post-mortem to ensure the best data collection.

2.4 Hematoxylin and Eosin Staining

The process was simultaneously conducted with the optical measurement at the laboratory after the tissues were cut by a cryostat and put on distinct glass slices. Histopathological

images with H&E stain showed clearly the differences between cancer and normal (healthy) tissues under a microscope. Figure 2 shows the results of H&E staining give the strength of the validation of the product research.

3 Result and Discussion

This section presents the value of effective parameters in optical measurement of two distinct samples of liver cancer tissues and two samples of healthy tissues. Table 2 illustrates the comparative result of these parameters. Apparently, it can be seen that the linear, circular birefringence properties and depolarization index showed the considerable differences.

As seen from Fig. 3, the differences between the samples of liver cancer tissues and normal liver tissues of the linear birefringence properties are observed with a significant disparity, varying from around 150° to 160° . The cancer tissues have a slight increase compared to healthy tissues. To be more specific, for further investigation on cancer, tissues becoming cancerous can affect the optical properties because of the change of the number of morphology and physiology. When cancerous tissues uncontrollable growth, the ordered tissues layers break down and cause the change of linear birefringence.

Figure 4 indicated that the circular birefringence between healthy and diseased tissues has a disproportion of

Fig. 2 H&E staining image

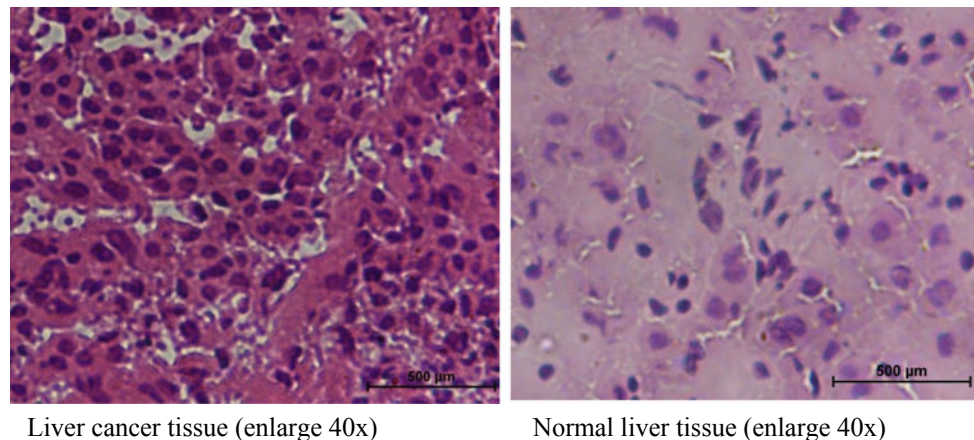


Table 2 Comparison between effective parameters of liver cancer tissues and healthy (normal) liver tissues

		α	β	γ	θ_d	R	D	Δ	e1	e2	e3
Liver cancer tissues	Mean standard deviation	157.44	5.27	79.51	96.82	0.01	0.15	0.029	0.58	0.72	0.35
		5.28	0.11	0.07	5.39	0.005	0.05	0.023	0.08	0.09	0.06
Normal liver tissues	Mean standard deviation	15.07	0.53	179.58	59.34	0.008	0.08	0.68	0.82	0.78	0.28
		1.45	0.06	0.13	4.89	0.005	0.02	0.078	0.09	0.04	0.06

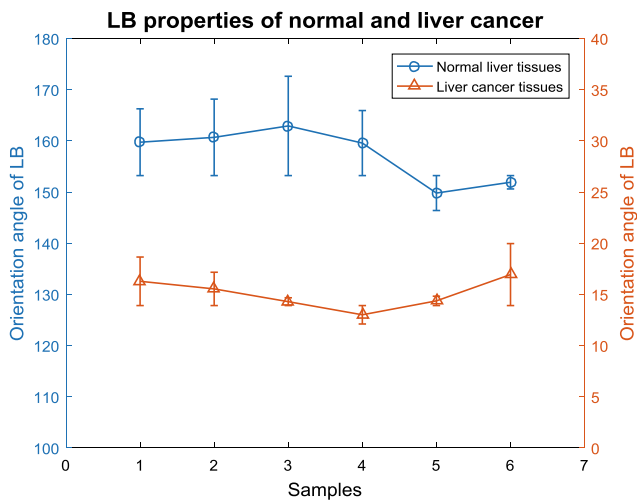


Fig. 3 Comparison between liver cancer tissues and normal liver tissues, in which linear fitting results of linear birefringence

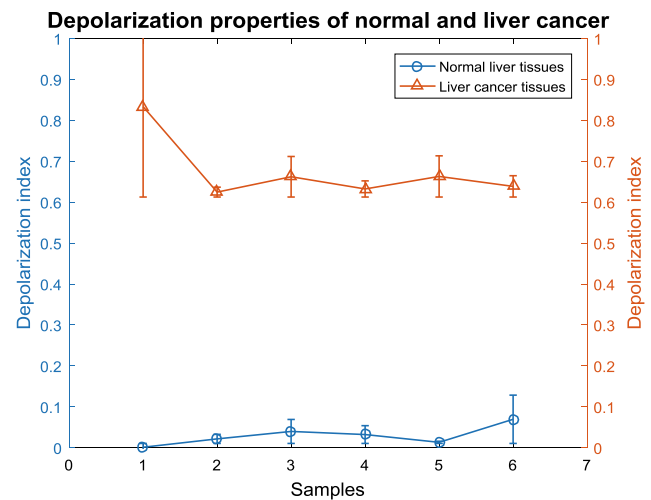


Fig. 5 Comparison between liver cancer tissues and normal liver tissues, in which linear fitting results of depolarization index

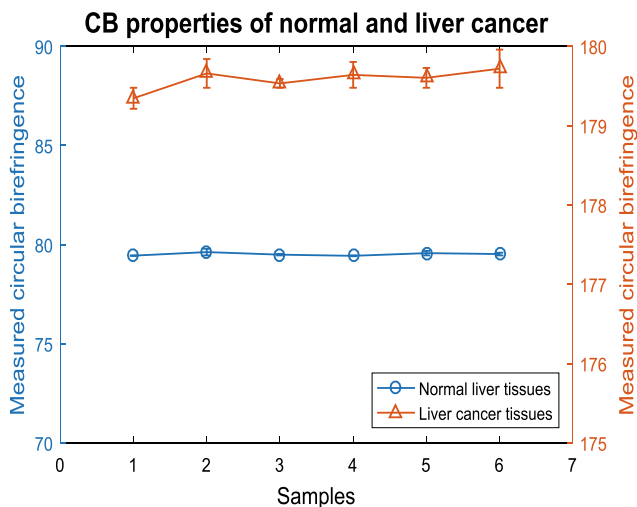


Fig. 4 Comparison between liver cancer tissues and normal liver tissues, in which linear fitting results of circular birefringence

approximately 100°. The cancer tissues have a gradual rise compared to healthy tissues. Meanwhile Fig. 5 illustrated substantially the comparison of depolarization index values between healthy and cancer liver tissues.

4 Conclusion

The research has indicated the interaction between polarized light with biological anisotropy using the decoupled analytical technique that based on Stokes polarimetry and Mueller matrix decomposition method. This technique has shown its potential application to the study. Thanks to the

powerful technique, effective optical parameters consisting of linear birefringence (LB), linear dichroism (LD), circular birefringence (CB), circular dichroism (CD), linear depolarization (L-Dep) and circular depolarization (C-Dep) were extracted for characterizing optical properties of the samples. The experimental result showed a good comparison between liver cancer tissues and healthy tissues. It also claims that depolarization index appears in biological material relating to carcinoma while comparing to a standard sample. All obtained results came out as the expectation that based on a consistent experiment was done on previous literature which confirms the reliability of the method. However, the method remains some limitations coming from sample preparation, sensitivity and irrelevant optical alignment for clinical study and their solution have been mentioned in the discussion above.

Several difficulties arise from samples preparation for study. First, tissues could not adhere to quartz-slide. Hence, a new protocol was built for tissue culture in slides. Second, the limitation of laser power was low, so signally is unstable. Therefore, we needed to perform the test many times than the collected data. Since the range of linear dichroism (LD) and error bar especially in the liver cancer tissue of sample 2 was considerable variation, the culture protocol needs to be improved in the future.

Acknowledgements The authors gratefully acknowledge the financial support provided to this study by Vietnam National Foundation for Science and Technology Development (NAFOSTED) under grant number 103.03-2016.86.

Conflict of Interest The authors declare that they have no conflict of interest.

References

1. Huang, X.R., Bagga, H., Greenfield, D.S., Knighton, R.W.: Variation of peripapillary retinal nerve fiber layer birefringence in normal human subjects. *Invest. Ophthalmol. Vis. Sci.* **45**, 3073–3080 (2004)
2. Wood, M.F., Ghosh, N., Wallenburg, M.A., Li, S.H., Weisel, R. D.: Polarization birefringence measurements for characterizing the myocardium, including healthy, infarcted, and stem-cell-regenerated tissues. *J. Biomed. Opt.* **15**, 047009 (2010)
3. Cameron, B.D., Li, Y., Nezhuvinal, A.: Determination of optical scattering properties in turbid media using Mueller matrix imaging. *J. Biomed. Opt.* **11**, 054031 (2006)
4. Huang, X.R., Knighton, R.W.: Diattenuation and polarization preservation of retinal nerve fiber layer reflectance. *Appl. Opt.* **42**, 5737–5743 (2003)
5. Berova, N., Nakanishi, K., Woody, R.W.: *Circular dichroism: principles and applications* (2000)
6. Swords, N.A., Wallace, B.A.: Circular-dichroism analyses of membrane proteins: examination of environmental effects on bacteriorhodopsin spectra. *J. Biochem.* **289**, 215–219 (1993)
7. Zsila, F., Molnár, P., Deli, J., Lockwood, S.F.: Circular dichroism and absorption spectroscopic data reveal binding of the natural cis-carotenoid bixin to human [alpha]1-acid glycoprotein. *Bioorg. Chem.* **33**, 298–309 (2005)
8. Ghosh, N., Wood, M.F., Vitkin, I.A.: Mueller matrix decomposition for extraction of individual polarization parameters from complex turbid media exhibiting multiple scattering, optical activity, and linear birefringence. *J. Biomed. Opt.* **13**, 044036 (2008)
9. Pham, T.-T.-H., Lo, Y.-L.: Decoupling six effective parameters of anisotropic optical material using Stokes polarimetry. *Opt. Meas. Model. Metrol.* **5**, 365–370 (2011)
10. Pham, T.-T.-H., Lo, Y.-L.: Extraction of effective parameters of anisotropic optical materials using decoupled analytical method. *J. Biomed. Opt.* **17**(2), 25006-1–25006-17 (2012)
11. Pham, T.-T.-H., Lo, Y.-L.: Extraction of effective parameters of turbid media utilizing the Mueller matrix approach: study of glucose sensing. *J. Biomed. Opt.* **17**(9), 0970021–09700215 (2012)
12. Pham, T.-T.-H., Nguyen, A.L.-T., Vo, T.-V., Huynh, K.-C., Phan, Q.-H.: Optical parameters of human blood plasma, collagen, and calfskin based on the Stokes-Mueller technique. *Appl. Opt.* **57**(16), 4353–4359 (2018)

Using UVB 311 nm Narrow-Band Medical Lamp for the Treatment of Psoriasis

Si-Nguyen Mai, Gia-Phu Pham, Vo Van Toi, Khon Huynh, and Thi-Thu-Hien Pham

Abstract

Ultraviolet B (UVB) light is effective in eliminating symptoms of psoriasis and the overall dosage of the narrow-band radiation can be closely controlled, which makes UVB lamps suitable for home therapy. Utilizing phototherapy, this study proposes a psoriasis treatment method which applies 311 nm narrow-band UVB (NB-UVB) to improve efficacy and reduce long-term toxicity comparing to other recent treatments. One device was designed and built—from a Philips UVB Narrow-band medical lamp and a controlling digital circuit comprising of an 89S52 microcontroller, a LCD screen, and a DS1307 real-time clock—to illuminate the psoriasis lesions in a controllable exposing time. An *in vitro* study was established on mouse skin fibroblasts to investigate the effect of NB-UVB on cell proliferation and morphology. The efficacy and safety of the lamp were also examined on two patients of psoriasis. The obtained results showed no significant abnormal change in morphology and growth of the irradiated fibroblasts. Furthermore, in patients undergoing the therapy, improvement was observed after 6 weeks of treatment. The psoriasis scales were fewer and the skin was softer and less flushed. The skin lesions also did not itch and spread out. The mechanism of action of the proposed treatment, however, remains not fully understood and would be further studied by investigating the effect of NB-UVB on key cell types involved in the pathogenesis of the disease including the keratinocytes and the T lymphocytes. The system will also be upgraded with various components, such as UV light sensor, for safe uses.

Keywords

Psoriasis • UVB • Fibroblast • 311 nm wavelength

1 Introduction

Psoriasis is a common disease influencing 5% of Europe's population, 2% of the population in Asia and Africa, and the vast majority of whom experience first indications at <40 years old [1]. In Vietnam, as indicated by the Department of Dermatology of Hanoi Medical University, psoriasis affects roughly 1.5% of the country population. The disease is chronic with recurring symptoms causing unpleasant, exhausted or even painful feelings, which could greatly affect patient's daily activities as well as mental wellness.

Normally, skin cells grow gradually and flake off about every 4 weeks. New skin cells grow to replace the outer layers of the skin as they shed. In psoriasis, however, new skin cells move rapidly to the surface of the skin in days rather than weeks (3–5 days) [2]. They build up and form thick patches called plaques. The patches range in size from small to large. They most often appear on the knees, elbows, scalp, hands, feet, or lower back. The five main types of psoriasis are plaque, guttate, inverse, pustular, and erythrodermic [2]. Psoriasis can be mild, moderate or severe based on coverage percentage of body. Mild psoriasis covers less than 3% of the body. Moderate psoriasis covers between 3 and 10% of the body. If psoriasis covers more than 10% of your body, it is severe [3]. It is widely accepted that the immune system and genetics play major roles in the development of the disease [4]. Most of the identified genes relate to the immune system, particularly the major histocompatibility complex (MHC) and T cells.

Besides topical treatments, doctors usually also prescribe phototherapy or systemic medications, including biologic drugs, to their patients. In natural sunlight, ultraviolet B (UVB) is an effective treatment for psoriasis. UVB penetrates the skin and slows the growth of affected skin cells [5].

S.-N. Mai · G.-P. Pham · V. Van Toi · K. Huynh
T.-T.-H. Pham (✉)

Department of Biomedical Engineering, International University,
Vietnam National Universities of Ho Chi Minh City
(VNU-HCMC), Quarter 6, Linh Trung Ward, Thu Duc District,
Ho Chi Minh City, 70000, Vietnam
e-mail: ptthien@hcmiu.edu.vn

During UVB treatment, the symptoms may worsen temporarily before showing improvement. The skin may redden and itch from exposure to the UVB light [6]. To avoid further irritation, the amount of UVB administered may need to be reduced. Wavelengths of 305–315 nm are most effective and specialized lamps have been developed for this application [7]. Increasing rate of cancer from treatment applying wavelengths in this range was also indicated to be small [8]. However, like many other kinds of medical lamp utilizing the UV light, in order to avoid any skin damage, the exposure time in these devices needs to be controllable for users, since the effective and safe amount of UV exposure highly varies among people.

In this study, we proposed a medical system with narrow-band UVB (NB-UVB) lamp whose operation can be closely controlled as an efficient, safe, and economical solution for psoriasis patients. An *in vitro* study was established on mouse skin fibroblasts to initially investigate the effect of NB-UVB on cell proliferation and morphology. The efficacy and safety of the medical system were also characterized on 2 patients of psoriasis in a pilot study where the two patients strictly followed the treatment protocol utilizing our system for 6 weeks.

2 Materials and Method

2.1 Materials

PHILIPS UVB311 nm Narrow-band medical lamp was purchased from Philips (PL-S 9 W/01/2Plamp). L929 murine fibroblast cells were obtained from American Type Culture Collection (ATCC, Rockville, USA). Cell culture

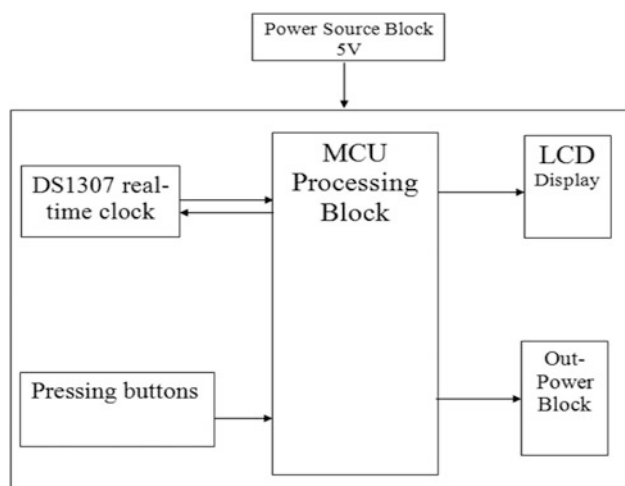


Fig. 1 Block diagram of the medical lamp system

media Dulbecco's Modified Eagle's Medium (DMEM, CAT No. D6429), Ham's Nutrient Mixture F12 (CAT No. 516512C), Gentamicin (G1272) were purchased from Sigma-Aldrich. All other materials and chemicals were from major suppliers.

System diagram of medical lamp

Resource blocks create 5 V DC for the circuit. MCU processing block process and perform the requirements of temperature measurement and reading time, while DS1307 real-time block counts time and transits time parameters on the MCU, then converts data to display on the LCD. The keystroke sets time parameters match with real-time for IC measurement DS1307 (Fig. 1).

Fibroblast cell culture

Fibroblast cells were cultured in Dulbecco's modified Eagle Medium Ham's 12 (DMEM/F12) supplemented with 10% fetal bovine serum (FBS) and 1% gentamicin at 37 °C in atmosphere of 5% CO₂ and 98% relative humidity. Cells were grown to 80% confluency prior to the experiments.

2.2 Exposure of Cultured Fibroblast Cells to UVB 311 nm Narrow Band Irradiation

L929 murine fibroblast cells were placed into wells of 24-well cell culture plate at a density of 104 cells/well in DMEM/F12 media containing 10% FBS and 1% Gentamicin. Fibroblast cells were exposed to NB-UVB light for 1, 2, 3 and 4 min. Control experiments were performed with unexposed cells. In order to ensure all samples have received correct doses as expected, whenever a group of wells were exposing to the UV light, wells in other experimental groups were being covered by a UV-resistant glass. Following NB-UVB irradiation, cells were cultured in a humid incubator (37 °C, 5% CO₂, 98% humidity) and examined under light microscope at 24-h intervals for 4 days. Data was collected from four repeated experiments.

2.3 UVB 311 nm Narrow Band Irradiation for Psoriasis Treatment—Initial Pilot Study

Subjects

We obtained IRB approval from to study the effect of UVB 311 nm narrow-band medical lamp treatment in two psoriasis patients. The first patient was a 22-year-old male who had pustular psoriasis on his scalp for over 10 years.

Second patient was a 53-year-old female who had had erythrodermic psoriasis on her right leg also for over 10 years. After proper diagnosis and consultation, two patients have agreed to participate in the study.

UVB treatment protocol

The protocol was applied for both patients. Personal safety protection was taken by following manufacturer's instruction. Patients' psoriatic skins were exposed to periodic illumination three times per week. Starting dose for NB-UVB therapy was 2 min irradiation with the distance from lamp bulb to psoriatic skin was 10–15 cm. After 8 h of irradiation, patient's skin was checked for any change in color. Irradiation time was increased 1–2 min if there was no change in skin color until 20 min. The time increment was stopped if skin turned pink.

3 Results and Discussion

3.1 Medical Lamp System

Figures 2 and 3 represent the prototype of our medical lamp device for psoriasis treatment. The system included a microcontroller system, a transformer changing 220–60 V and a Philips UVB Narrow-band PL-S 9W/01/2Plamp. The front side of the system comprised a display LCD and four keystrokes corresponding to start, pause, up and move. On the back side, there was an on/off button and a power port for microcontroller. Irradiation time was controllable. Distance between bulb and skin also could be controlled by adjusting the angle (30° to 120°) of the base and of the lamp.



Fig. 2 UVB 311 nm narrow-band medical lamp system

3.2 In Vitro Study

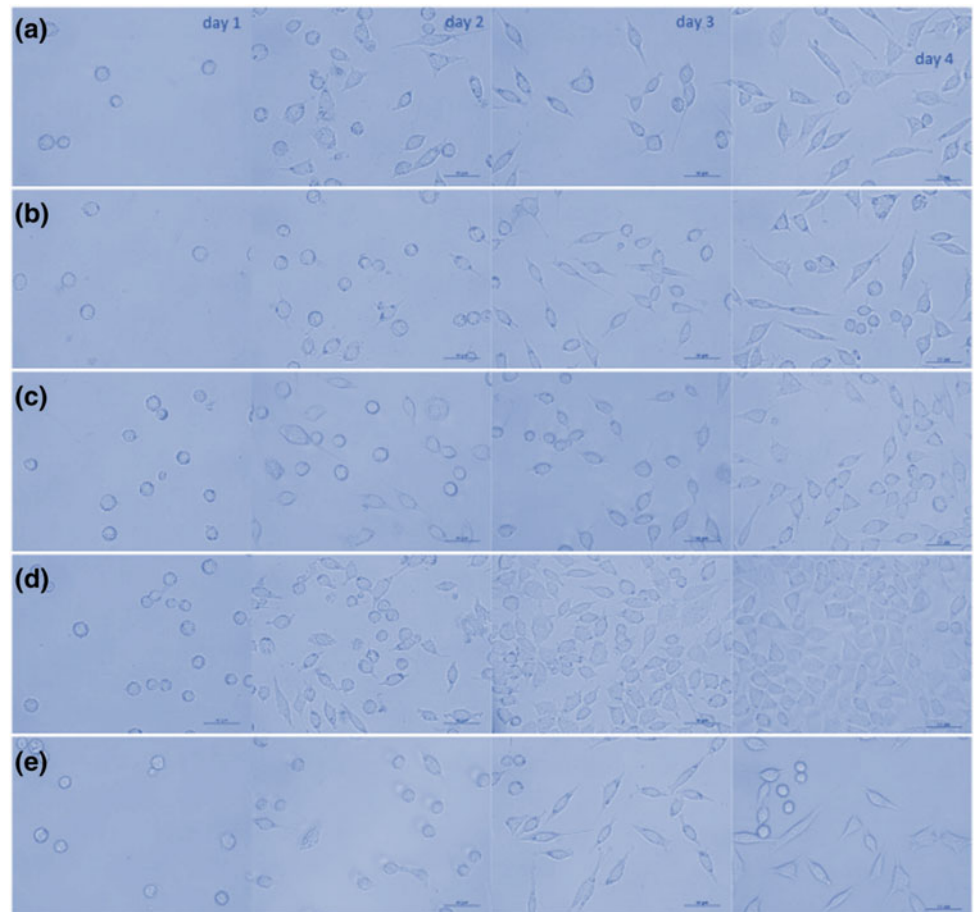
To optimize the therapy, it is important to understand the biological effects of NB-UVB on skin cells. As has been shown in a case-control study, the level of cell-cycle suppressor protein p-53 was lower and the level of cell-cycle promoter protein cyclin D1 was higher in skin biopsies of psoriatic lesions. These levels were normalized after exposure of NB-UVB. Nonetheless, it is also known that UV light has various harmful effects on human skin cells, by modulating many signaling pathways or directly damaging the DNA [9, 10]. There were numerous studies about UV-induced genetic changes and UV-induced skin carcinogenesis. It was shown that UVB exposure can lead to skin inflammation, cancer development and progression through the modulations of gene expression or signal transduction response of skin cells [9, 11]. Therefore, before applying the phototherapy using UVB light, it is essential to initially evaluate at which doses the side effect is reduced.

In our study, we established in vitro experiments examining the proliferation and morphology of fibroblast cells under the NB-UVB light in different amounts of time. The results for the effect of this light on fibroblast were illustrated as light microscopic images of the cells after irradiation 1, 2, and 3 days (Fig. 4). As has been shown, there was a slight increase in proliferation of cells being exposed to NB-UVB for 4 min, as compared to other groups, but the overall growth rates of irradiated cells were not significantly different from that of the non-irradiated cells. In terms of morphology, there was also no difference either between irradiated cells of different doses or between irradiated cells and the control.

Besides the NB-UVB, there is also another subtype of UVB, which is the broad-band UVB (BB-UVB). The NB-UVB is similar to the BB-UVB in many ways, and the major difference between them is that NB-UVB light bulbs release a smaller range of ultraviolet light [12]. From a research which evaluated the cytotoxic doses of narrow-band and broad-band UVB in different types of human skin cells, it was indicated that minimal cytotoxic doses of NB-UVB are exceed than those of BB-UVB, and for NB-UVB, the minimal cytotoxic doses in keratinocytes, melanocytes, and fibroblasts are 100, 100, and 400 mJ/cm², respectively [11]. In our study, no significant abnormal change was observed in the proliferation and morphology of the fibroblasts after 1, 2, 3 and 4 min of NB-UVB exposure.

3.3 Initial Pilot Study

First patient is a 22-year-old male patient who has had pustular psoriasis for over 10 years. The main symptom is

Fig. 3 Front and back panel**Fig. 4** 1 min (a), 2 min (b), 3 min (c), 4 min (d) and control (e)

that psoriasis lesion appears on the scalp, and particularly in cold weather, the number of psoriasis usually increases rapidly (Fig. 5).

Figures 6 and 7 show the improvements observed in symptoms of the first patient after respectively 2 and 6 weeks of treatment. The number of psoriasis lesions were reduced and became no longer itchy. In the course of treatment, the patient's scalp also showed no irritation or redness (Fig. 7).

The second patient is a 53-year-old female patient who has had erythrodermic psoriasis for also over 10 years. The

main symptom is that a psoriasis lesion is on the right leg which often starts itching from around 19–20 pm or at midnight and causes unpleasant feelings for the patient (Fig. 8).

After the treatment following our protocol, the patient was still not out of irritation, however, her psoriatic lesion became no longer flushed and it also did not spread out (Fig. 9).

It is known that NB-UVB, with an emission peak at 311 nm, is particularly effective in the treatment of psoriasis. From our pilot study treating on 2 psoriasis patients,

Fig. 5 Pustular psoriasis on scalp of patient 1



Fig. 6 After 2-week treatment (patient 1)



Fig. 7 After 1.5-month treatment (patient 1)



improvements were observed after 6 weeks following the treatment protocol using NB-UVB light. Overall, the psoriasis scales were fewer and the skin was softer and less flushed. The skin lesions also did not itch and spread out. Although for one patient (patient 2), the irritation was not

eliminated but it remains unknown whether prolonging the treatment course could give better result.

Comparing to other wavelengths, few studies have shown that NB-UVB clears psoriasis lesions speedier and creates longer reductions than BB-UVB. It also likewise



Fig. 8 Erythrodermic psoriasis on right leg of patient 2



Fig. 9 After 1-month treatment (patient 2)

might be powerful with less medication every week than the BB-UVB [13]. Moreover, the NB-UVB also has been demonstrated to be as effective as PUVA but with less side effects [13].

4 Conclusion

Using UVB 311 nm narrow-band wavelength for the treatment of psoriasis has been discovered and used widely in the world, however in Vietnam, this method is emergent and not common. Hence, we aimed to develop a medical system utilizing NB-UVB that is efficient, safe and economical for Vietnamese psoriasis patients. Experimenting with the prototype of such a system, it was demonstrated that NB-UVB, when exposed to fibroblast cells for 1–4 min, did not promote significant abnormal change to the cells, as well as clinically improved the symptoms in psoriasis patients after 6 weeks of treatment. These preliminary results are good stepping stones to further research and development on the proposed medical device.

Finally, as the mechanism of action of the proposed treatment remains not fully understood, the future work

would comprise of investigating the effect of NB-UVB on key cell types involved in the pathogenesis of psoriasis, including the keratinocytes and the T lymphocytes. The hardware system will also be upgraded with various components, such as UV light sensor, for safe uses.

Acknowledgements This research is funded by International University—VNUHCM under grant number T2017-01-BME.

Conflicts of Interest Statement The authors declare that they have no conflict of interest.

References

1. Christophers, E.: Psoriasis—epidemiology and clinical spectrum. *Clin. Exp. Dermatol.* **26**, 314–320 (2002). <https://doi.org/10.1046/j.1365-2230.2001.00832.x>
2. Farber, E.M., Nall, L.: The natural history of Psoriasis in 5,600 patients. *Dermatology* **148**, 1–18 (1974). <https://doi.org/10.1159/000251595>
3. Krueger, G., Koo, J., Lebwohl, M., Menter, A., Stern, R.S., Rolstad, T.: The impact of Psoriasis on quality of life: results of a 1998 National Psoriasis Foundation patient-membership survey. *Arch. Dermatol.* **137**, 280–284 (2001). doi:10-1001/pubs. ArchDermatol.-ISSN-0003-987x-137-3-dst0024

4. Lowes, M.A., Kikuchi, T., Fuentes-Duculan, J., Cardinale, I., Zaba, L.C., Haider, A.S., Bowman, E.P., Krueger, J.G.: Psoriasis vulgaris lesions contain discrete populations of Th1 and Th17 T Cells. *J. Invest. Dermatol.* **128**, 1207–1211 (2008). <https://doi.org/10.1038/sj.jid.5701213>
5. Weelden, H.V., Faille, H.B.D.L., Young, E., Leun, J.C.V.D.: A new development in UVB phototherapy of psoriasis. *Br. J. Dermatol.* **119**, 11–19 (1988). <https://doi.org/10.1111/j.1365-2133.1988.tb07096.x>
6. Behrens, S., Grundmann-Kollmann, M., Schiener, R., Peter, R.-U., Kerscher, M.: Combination phototherapy of psoriasis with narrow-band UVB irradiation and topical tazarotene gel. *J. Am. Acad. Dermatol.* **42**, 493–495 (2000). [https://doi.org/10.1016/S0190-9622\(00\)90225-1](https://doi.org/10.1016/S0190-9622(00)90225-1)
7. Storbeck, K., Hölzle, E., Schürer, N., Lehmann, P., Plewig, G.: Narrow-band UVB (311 nm) versus conventional broad-band UVB with and without dithranol in phototherapy for psoriasis. *J. Am. Acad. Dermatol.* **28**, 227–231 (1993). [https://doi.org/10.1016/0190-9622\(93\)70032-O](https://doi.org/10.1016/0190-9622(93)70032-O)
8. Green, C., Ferguson, J., Lakshminpathi, T., Johnson, B.E.: 311 nm UVB phototherapy—an effective treatment for psoriasis. *Br. J. Dermatol.* **119**, 691–696 (2006). <https://doi.org/10.1111/j.1365-2133.1988.tb03489.x>
9. Soriani, M., Hejmadi, V., Tyrrell, R.M.: Modulation of c-jun and c-fos transcription by UVB and UVA radiations in human dermal fibroblasts and KB cells. *Photochem. Photobiol.* **71**, 551–558 (2007). [https://doi.org/10.1562/0031-8655\(2000\)0710551mocjac2.0.co2](https://doi.org/10.1562/0031-8655(2000)0710551mocjac2.0.co2)
10. de Gruijl, F.R.: Photocarcinogenesis: UVA vs UVB. In: *Methods in Enzymology*. pp. 359–366. Academic Press, Cambridge (2000)
11. Tyrrell, R.M.: Activation of mammalian gene expression by the UV component of sunlight—from models to reality. *BioEssays* **18**, 139–148 (2005). <https://doi.org/10.1002/bies.950180210>
12. Lowes, M.A., Bowcock, A.M., Krueger, J.G.: Pathogenesis and therapy of psoriasis. *Nature* **445**, 866–873 (2007). <https://doi.org/10.1038/nature05663>
13. Van, H.W., de la Faille Baart, H., Young, E., van der Leun, J.C.: Comparison of narrow-band UV-B phototherapy and PUVA photochemotherapy in the treatment of psoriasis. *Acta Derm. Venereol.* **70**, 212–215 (1990)

Pyramid Hologram in Projecting Medical Images

Minh H. N. Than, Minh M. N. Pham, and Hien Thi-Thu Pham

Abstract

To read 2D slices from medical scanners on a flat screen and analyze them into full 3D structure in one's own mind requires long-time training and experiences. Therefore, aside from doctors and experts, it is very difficult for patients to follow their own state of illness only by mere explanation from their physicians and a series of 2D slices displayed on flat screens. Up until now, pyramid holograms have only been used for advertising and entertainment, but not in medical field since it was not able to interact. Hence, the research of our team is to enhance this system with the interactive ability. The first step for this is to compute a hologram from multi-layer images captured by CT or MRI scanners in the form of DICOM via pyramid hologram, with the use of MATLAB programming language and a lot of its available functions for image processing. The whole procedure of the team research contains six main steps. The first four steps include: reconstructing 3D images from a folder of CT or MRI multi-layer images, capturing four orthogonal projections of the 3D image, arranging these four side views into one appropriate png image, saving the final image. Step five is to reduce a layer from the original folder of CT or MRI multi-layer images and repeating the first four steps until running out of layers inside the folder, gradually. All the saved images for each layer reduction will be computed into a video which can show the outside through the inside of the images from CT or MRI scanner via a pyramid hologram. Users can pause the video at any time to show the structure of the images they desire. This paper traces the design concept but can only confirm the first four steps for coding function of creating a hologram image from the original medical devices by a prototype demonstration. Future work for this research will include

full six steps and designing for a hardware system that can be combined with the pyramid hologram for interaction between users and the model.

Keywords

Pyramid hologram • MATLAB • 3D volume CT

1 Introduction

Holography is a technique that was invented in the 1940s by Hungarian scientist Dr. Dennis Gabor and has become a very useful tool in many areas, such as in commerce, scientific research, business, education, entertainment, art, industry, medicine, healthcare and so forth. In the medical field nowadays, many medical systems generate complex data using advanced imaging technology, such as Magnetic Resonance Imaging (MRI), Computed Tomography (CT) scans, Emission Tomography (PET) or ultrasound scans. Normally, the electronic information from these types of technology is used to display flat images on a computer screen, which are understandable by many doctors and experts, but may be difficult for patients and students to follow. Although in this paper, the hologram created is still in the stage of virtual image, it could be developed into a real and interactive image in near future. The coding in this paper for the pyramid hologram is only the first step for applying the real-interactive 3D holographic images in teaching and training students and patients for reading data from medical scanner devices through a non-expensive and easy technique.

The holographic design our team is working with is focus on the pyramid hologram. This is a simple device that is made by cutting a transparent acrylic sheet into the special shape of a hollow pyramid so that all four panes of this pyramid will make a suitable angle with the horizontal surface [1]. The more view sides from different angles of the 3D structures are shown, the more panes or faces of the

M. H. N. Than · M. M. N. Pham · H. T.-T. Pham (✉)
Biomedical Engineering Department, International
University-Vietnam National University, HCM City,
70000, Vietnam
e-mail: ptthien@hcmiu.edu.vn

pyramid hologram system are needed to be computed, which will lead to more complicated calculation, coding, and wasting time. On the other hand, four-main-angle hologram is simpler, but still give enough information of the outward structure of the 3D image. The technique is not only simple and easy for all to compute, but also has the ability to change sizes depending on users' demand. Pyramid hologram was made based on the Pepper's ghost illusion, named after John Henry Pepper who implemented a working version of the device in 1862, creating illusion for observer by the principle of reflection [2]. Since the pyramid hologram generator is extremely easy to create, anyone can make one for themselves with any size of the pyramid they desire.

The objective of our team in this paper is to design a system that can stimulate or aid in capturing 3D holographic images from these medical scanners, display them on screen with the major help of MATLAB programming language for image processing. The final product is in form of a software that people can use to turn images from medical scanners directly into holograms shown on screens with the dimensions that can satisfy any demand of any pyramid size. We hope that this product should be not only users-friendly and cost-effective, but also a great and convenient tool for visualizing patient data while training patients and students in Vietnam.

2 Methods and Materials

2.1 Requirements

Programming languages and software use

Digital Imaging and Communication in Medicine (DICOM) has become one of the most popular standards in medicine. In the beginning, DICOM was used for the exchange and management of images and image-related information between different systems. Actual developments of the standardization enable increasingly more DICOM-based services for the integration of modalities and information systems (e.g., RIS, PACS) [3].

MATLAB is a high-level programming language and interactive environment for data analysis and mathematical computing functions. It provides a variety of interactive tools including threshold, correlation, Fourier analysis, filtering, basic statistics, curve fitting, matrix analysis, 2D and 3D plotting functions. These tools allow users to perform noise reduction and image enhancement, image transformation, colormap manipulation, color-space conversions,

region-of-interest processing, and geometric operation [4]. Furthermore, the open sources for exchanging files of MATLAB language users are enormous also beneficial.

Pyramid projecting hologram system

The result of the hologram image or video displays were to be projected by a pyramid hologram device. The system is a simple device that was made by cutting a transparent acrylic sheet into the distinctive shape of a hollow pyramid so that all four faces of this pyramid will make a suitable angle with the horizontal surface. Many parameters could be applied for pyramid holograms, but by some simple calculation, the pyramid hologram specifications chosen for this project were shown in Table 1.

2.2 Process

There were five main steps in the flow chart (Fig. 1) shows how images taken from CT/MRI scanners were processed and displayed by the MATLAB programming language. However, only four first steps were able to be conducted, and the process is shown below.

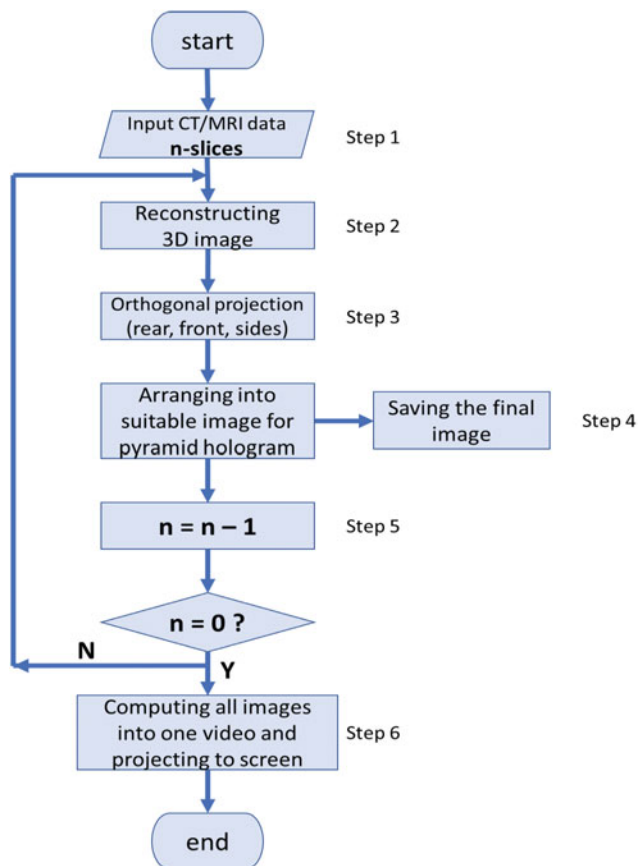
A total of 142 CT slices of a brain (patient Doe Pierre [54879843]—1 January 2006) with the post-concussive syndrome (PCCS) were taken from Patient Contributed Image Repository (PCIR) website in the form of DICOM files (*.dcm). These files were stored in the same folder so that they could be called out via graphical user-interface (GUI) of MATLAB programming language. Usually, after a scan from CT/MRI, these DICOM files are automatically organized in an appropriate sequence for easy detection. Hence no manual naming was required for arranging these files.

There were many available filtering and enhancement tools in MATLAB, but based on a research of Thanh and Hai [5], the Otsu method (Otsuthresh) were especially applied for all CT slices before reconverting them into a full 3D image and extracted out onto the GUI figuring of MATLAB (Fig. 2). The color for the axes framing of the figure was made black so that it could reduce the background light when projected out by the pyramid hologram.

With the glass box approach, the algorithm designed an object camera and adjusted its position at six views of the 3D figure (top, bottom, front, rear, left and right views), represent the six orthogonal projections. When running the code on MATLAB, the camera automatically took an image from each position and saved all six of which as Portable Network Graphic (*.png) files (Fig. 3). However, based on the

Table 1 The pyramid hologram specifications

Material	Thin transparent acrylic sheet
Length	Upper side 6 [cm] Bottom side 1 [cm]
Height	3.5 [cm]
Angle	45°

**Fig. 1** Six main steps for creating hologram video projected via pyramid

principle of pyramid hologram, only 4 out of 6 views, which were the front, the rear, and two side views were required (Fig. 4). As introduced above, more angles of the 3D image can be taken for projecting on a system that has more than just 4 sides. However, there was only one object camera in MATLAB, hence, to take more views from more angle of the 3D image, there will be more coding for changing the camera position and hence, very time consuming. On the other hand, four main angles still give enough information for the outward structure of the 3D image, so more angle views are not necessary.

Similar to a work done on OpenGL screen by using glViewport by Salih et al. [6], a square-shaped frame on a

flat 2D image was created and separated by a grid into 9 equal invisible segments. All the saved png images of the set of four projections of the 3D image were mirrored and scaled at the same ratio so that each of them would be able to fit in one small square. Figure 5 illustrated the arrangement and the final image that was saved as a png to be displayed on wide range of devices and projected out by the appropriate pyramid projector.

3 Results and Discussions

The image was displayed on an LCD screen of Samsung A5 with the screen size of 13.22 cm (5.2), resolution 1920×1080 (FHD) and 16M color depth. The resulting hologram image was shown in Fig. 6 through the pyramid hologram prototype. Even though ambient light can be bright, to create a better environment for the quality of the hologram projected via the pyramid hologram system, the ambient light was turned off. Although the pyramid hologram was a quite simple system to make within a short amount of time, the level of transparency of this system can affect the sharpness and quality of the hologram. The higher the transparency, the clearer the hologram image will be observed.

The result of our team is so far completed through step 4 (Fig. 1) and projected the outward hologram image of the 3D multi-layer CT images via a pyramid hologram prototype, but step 5 has yet to be able to run and test. This is due to each layer of DICOM multi-layer images from medical scanners is huge (about 150 KB), hence, the procedure just from step 1 to step 4 takes up too long processing time (about 7 min). Furthermore, instead of the whole 3D image, only a set of four projections of it is needed, but the method we used to capture these projections required a camera object, hence, we have to show the 3D volume image out in a GUI of MATLAB to be able to use this function, which is also very time consuming. Aside from that, in step 5, after reducing a CT layer, the first four steps will be repeated until running out of layers inside the folder, gradually. Since we used 142 CT layers, this all means that continuing to run step 5 will lead to about 16 h processing time. More code work and solution should be done to modify the processing time of the first four steps before going to the next step.

4 Conclusion and Future Work

The goal of this study is to create a final product in the form of software that people can use to turn images from medical scanners into a hologram easily via holographic pyramid

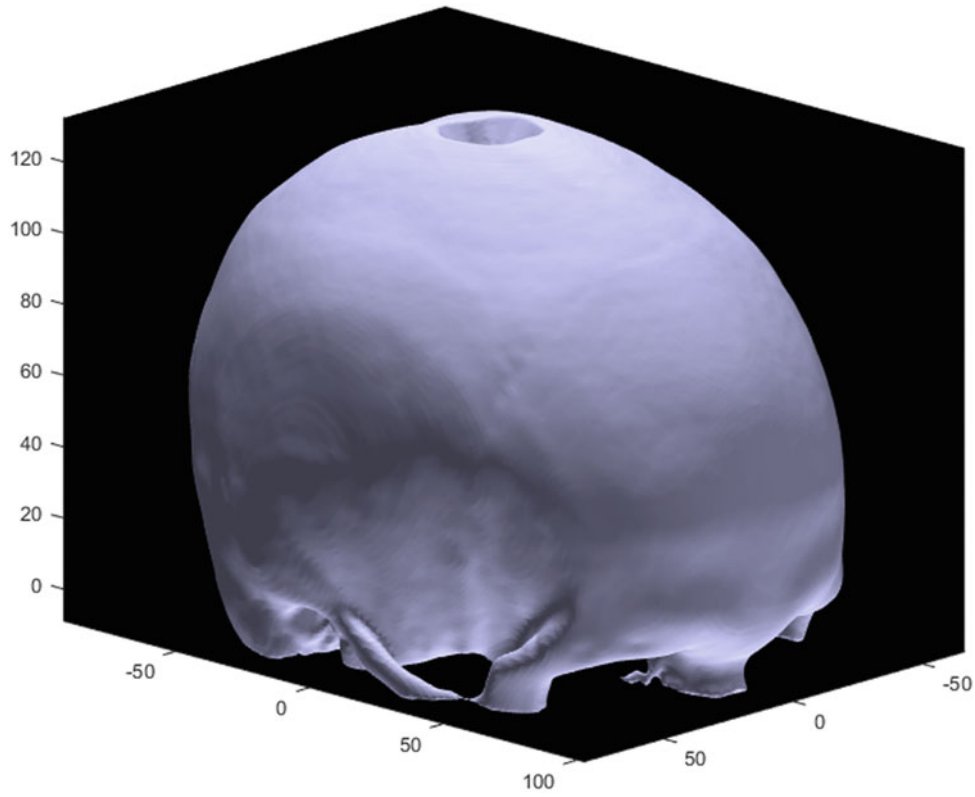


Fig. 2 3D volume of the brain

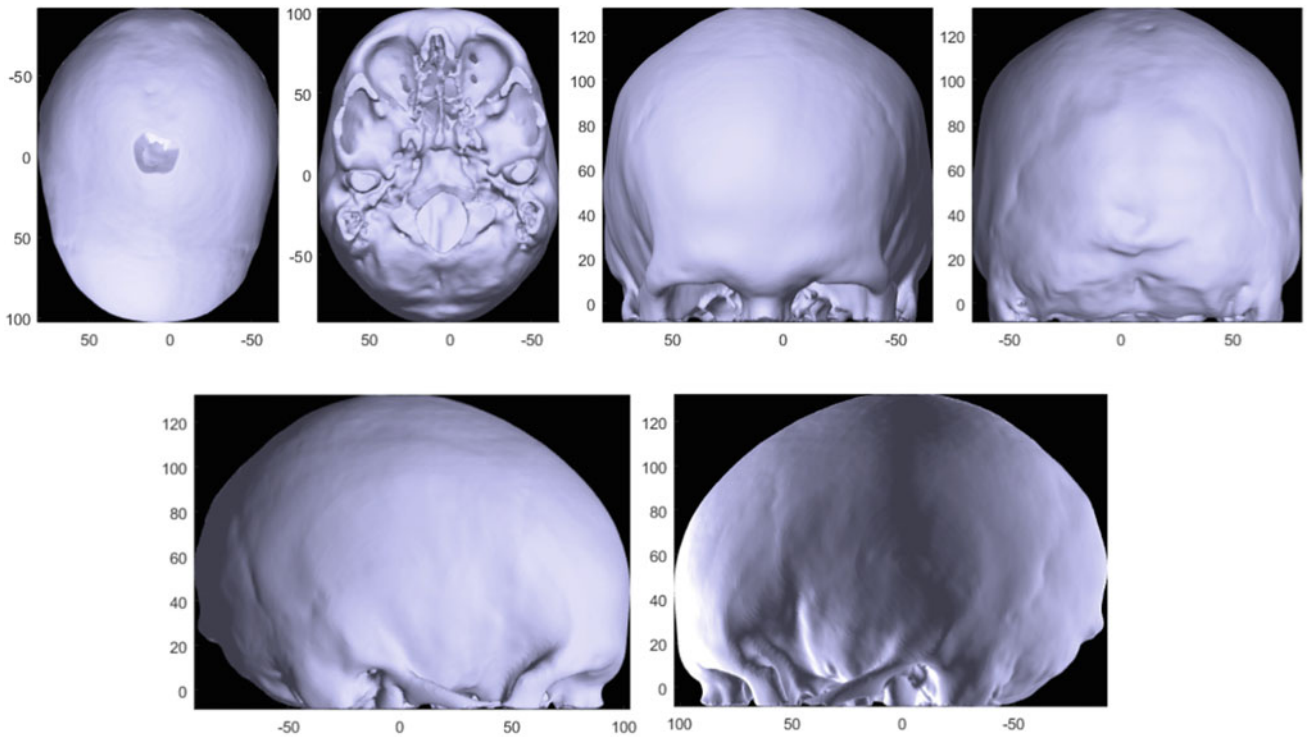


Fig. 3 Using MATLAB object camera to take a picture of the constructed 3D image; from left to right, top to bottom are the view of top, bottom, front, rear, right, and left

Fig. 4 From left to right, top to bottom are the front, left, rear and right viewed projections of the 3D volume

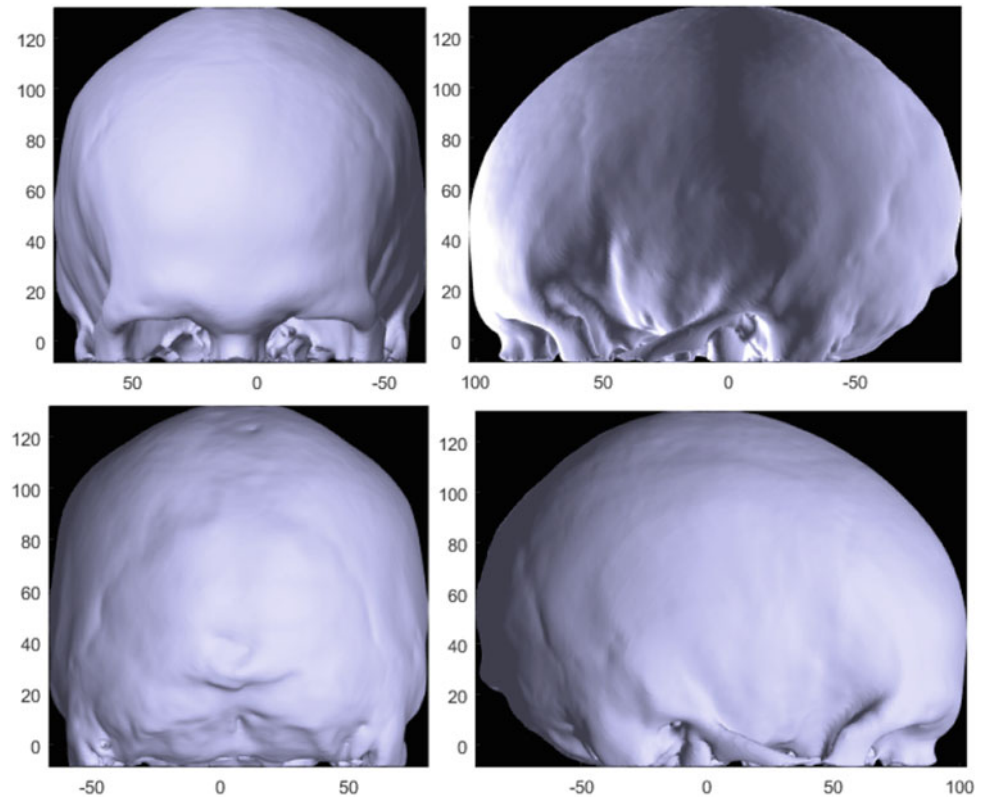
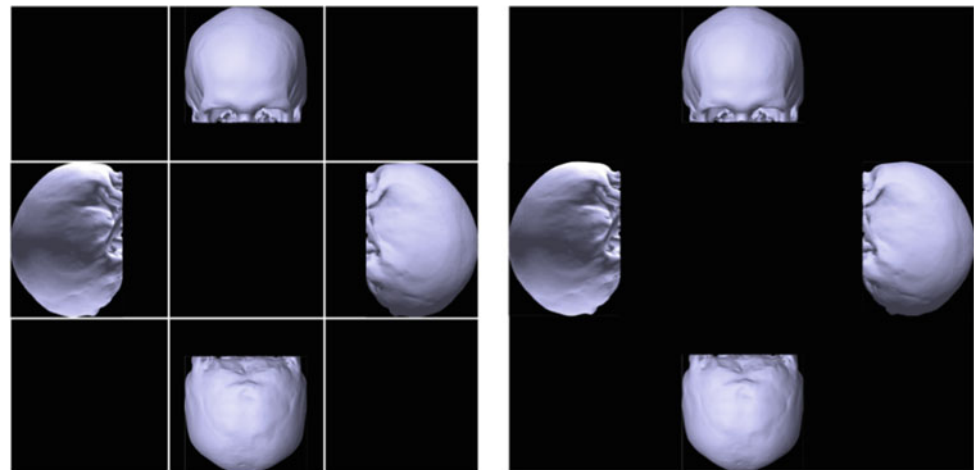


Fig. 5 Arrangement of four-sided projections of the 3D image with nine segment method (left) and the final image (right)



system. Although the hologram was successfully built, displayed and projected via the pyramid hologram system, there are a lot of future works that still need to be done. All steps of the coding procedure (Fig. 1) should be enhanced for faster processing to be able to continue with the next step to create a real-time hologram video that could show people the complete structure inside the objects. Furthermore, although the hologram computed by this technique may not be interactive, Jiono Mahfud and Takafumi Matsumaru have presented an interactive aerial projection of 3D hologram objects by using the pyramid hologram and parabolic

concave mirror system (Fig. 7). Further studies on this technique can help create a device that not only displays the 3D images but also help users to interact with it. This is a very new method that can create real and interactive images from the simple pyramid holographic projector—cheap and simply made system—and hence, very suitable for individual studies of students, and training material for patients with low income.

Acknowledgements This research is funded by International University, VNU-HCM under grant number SV2016-BME-01. This

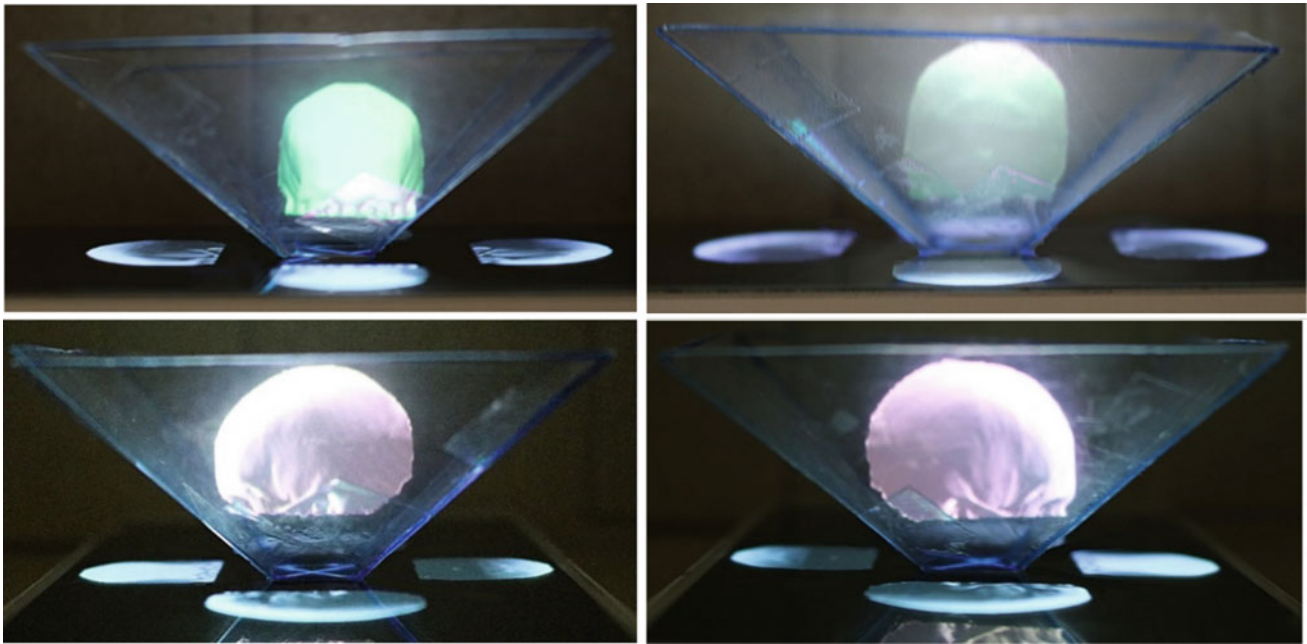
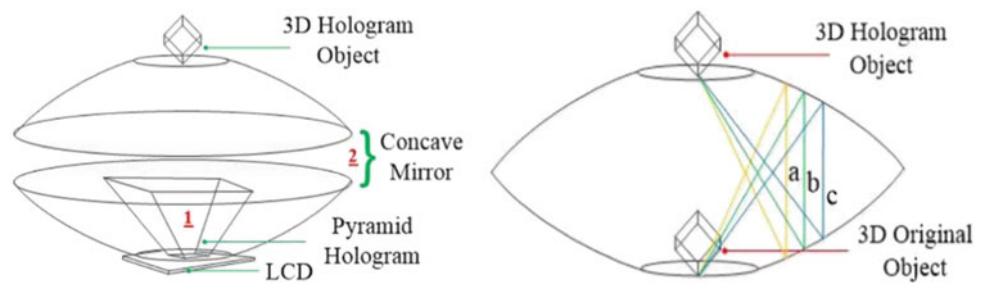


Fig. 6 Image displaying the pyramid hologram prototype via an LCD screen

Fig. 7 The structure and working principle of the parabolic concave mirror system [1]



research received a significant help from Hung T. Lam for advising cleaner coding, MATLAB open source for useful information of MATLAB programming language, and the Patient Contributed Image Repository (PCIR) website for providing DICOM files source. We would like to express our sincere gratitude.

Conflict of Interest The authors declare that they have no conflict of interest.

References

1. Mahfud, J., Matsumaru, T.: Interactive aerial projection of 3D hologram object. In: 2016 IEEE International Conference on Robotics and Biomimetics, ROBIO 2016, pp. 1930–1935 (2016)
2. Thange, R., Sugdare, P., Kaudare, V., Jain, V.: Interact. Holograms Pepper Ghost Pyramid **4**(1), 1221–1224 (2016)
3. Mildenerger, P., Eichelberg, M., Martin, E.: Introduction to the DICOM standard. *Eur. Radiol.* **12**(4), 920–927 (2002)
4. Mcandrew, A.: An introduction to digital image processing with MATLAB notes for SCM2511 image processing 1. *Image Rochester NY* **1**(1), 1–13 (2005)
5. Thanh, C.Q.T., Hai, N.T.: Trilinear Interpolation Algorithm Reconstr. *3D MRI Brain Image* **7**(1), 1–11 (2017)
6. Salih, S.Q.M., Sulaiman, P.S., Ramlan, M., Rahmat, R.W.O.K.: 3D holographic rendering for medical images using manipulates lighting in a 3D pyramid display. *J. Adv. Sci. Eng. Res.* **7**, 14–26 (2017)

Building an Automatic Control System for Measuring the Stokes Parameters

Minh Lai-Nhat Phan, Minh Nhat Nguyen, and Hien Thi-Thu Pham

Abstract

Many researches have shown the potential of polarized light in inspection and diagnostic. Such as the ability to determine sugar concentration in the cornea which could be developed to non-invasive polarimetric glucose detector for diabetic's detection; or diagnose vascular disease and brain function by detecting the concentration of the deoxygenated hemoglobin in vein. Additionally, the Polarization properties of scattered light from turbid media such as biological tissues and certain plastics have also received considerable attention. From the scattered light of a sample, fundamental optical properties of the sample could be revealed. From this information, some diseases could be detected, including diabetes, cancer. In this research, an automatic Stokes parameters measurement system is introduced to determine the fundamental optical properties i.e., the effective linear birefringence (LB), linear dichroism (LD), circular birefringence (CB), circular dichroism (CD), linear depolarization (LDep), and circular depolarization (CDep) of a biological sample. By measuring Stokes parameters of 6 kinds of polarized lights (right-hand circular, left-hand circular, 0° , 45° , 90° , 135° of linear polarized lights) which are projected through the biological sample. The results showed that the system can automate measure Stokes parameters of a biological sample with the accuracy $\pm 5\%$ to compare with the commercial device, Stokes polarimeter. From this raw system, the developing of the system is improved for diagnosing cancer.

Keywords

Polarized light • Linear birefringence • Linear dichroism • Circular birefringence • Circular dichroism • Stokes parameters

M. L.-N. Phan · M. N. Nguyen · H. T.-T. Pham (✉)
Biophotonics Laboratory, Biomedical Engineering Department,
International University—VNU HCM, Ho Chi Minh City,
Vietnam
e-mail: ptthien@hcmiu.edu.vn

1 Introduction

Since being found, polarized light has shown its endless potential in photography, display technology, chemistry, biology, microscopy, astronomy and especially medical [1–6]. It already has many applications in therapy, beauty industry and shown many potentials in diagnostics and medical imaging [4–6]. In this research, an automatic Stokes measurement system was built with the desire to develop a medical device that could detect tumor or cancer in early stage. Based on the analytical method of Pham and Lo [7, 8], the system was designed and built for measuring the Stokes polarization parameters to determine the fundamental optical properties of biological samples for distinguishing the differences between the healthy and abnormal tissues/cells. The designed system sequentially generates six polarized light (i.e., left-hand circular (LHC), right-hand circular (RHC), linear polarized lights in 0° , 45° , 90° and 135°) to illuminate through a biological sample. After that, the system measures the analog signal and calculate the Stokes parameters of these output lights.

2 Methodology and Structure

2.1 Methodology

Based on the analytical method of Pham and Lo [7, 8], we propose an automatic control system for measuring the Stokes parameters of anisotropic optical materials or biomedical samples. The automatic control system can determine the fundamental optical properties of samples; then it could help to distinguish healthy and abnormal tissue from that early detect some disease especially tumor or cancer. The measured optical parameters are linear birefringence (LB), circular birefringence (CB), linear dichroism (LD), circular dichroism (CD), linear depolarization (LDep),

and circular depolarization (CDep). Thus, the automatic control system of Stokes measurement is built as following shown in Fig. 1.

As shown in Fig. 1, the laser source (633 nm wavelength) firstly went to a fixed linearly horizontal polarizer (GTH5 M, Thorlabs Co.) to make the polarization state at 0° for normalization and calibration the light source. Then, the light source with a rotating quarter-wave plate (QWP0-633-04-4-R10, CVI Co.) and a rotating polarizer (GTH5 M, Thorlabs Co.) generated sequentially six polarized light, i.e., two circular polarized lights (LH and RH) and four linear polarized light at 0° , 45° , 90° , 135° . After that, these input lights went through the sample and touched to the Stoke Analyzation block which includes a rotating quarter-wave plate (QWP0-633-04-4-R10, CVI Co.), a fixed vertical polarizer (GTH5 M, Thorlabs Co.) and a photodiode (BNC mount#53-373 silicon detector, Edmund Co.). Based on the Stoke quarter-wave plate measurement method [9] with $N = 50$, the system controlled the rotating quarter wave plate (AR-Q2) rotates from 0° to 180° interval and the detector taken 50 points data sample from the interval. Then, the system received 50 points measurement data with the steps equal to 3.6° ($\theta_{n+1} - \theta_n = 180/50 = 3.6^\circ$), that mean each of every angle at $\theta_1 = 0.0^\circ$, $\theta_2 = 3.6^\circ$, $\theta_3 = 7.2^\circ \dots \theta_{49} = 172.8^\circ$, $\theta_{50} = 176.4^\circ$; the system read the analog signal for every angles. Then, the analog signal was calculated and converted to digital signals. The Stoke parameters was calculated by the following equations [9].

$$A = \frac{2}{N} \sum_{n=1}^N I_n \quad | \quad B = \frac{4}{N} \sum_{n=1}^N I_n \sin 2\theta_n \quad (1a)$$

$$C = \frac{4}{N} \sum_{n=1}^N I_n \cos 4\theta_n \quad | \quad D = \frac{4}{N} \sum_{n=1}^N I_n \sin 2\theta_n \quad (1b)$$

$$S_0 = A - C, \quad S_1 = 2C, \quad S_2 = 2D, \quad S_3 = B \quad (1c)$$

Additionally, the Degree of Polarization (DOP), Azimuth and Ellipticity of each data point were calculated by the following equations.

$$DOP = \frac{\sqrt{S_1^2 + S_2^2 + S_3^2}}{S_0} \quad (2a)$$

$$Azimuth = 90^\circ - \frac{\tan^{-1}\left(\frac{S_1}{S_2}\right)}{2} \quad (2b)$$

$$Ellipticity = \frac{\tan^{-1}\left(\frac{S_3}{\sqrt{S_1^2 + S_2^2}}\right)}{2} \quad (2c)$$

Finally, the output results of the system (i.e., Stoke parameters, DOP, Azimuth and Ellipticity of a biological sample) was displayed as values and graphical results in the User Interface designed by MatLab.

2.2 Hardware Design

For the hardware of the system is designed into 2 main parts. The first part is light former including a laser source, fixed polarizer, one rotating quarter wave plate, one rotating polarizer for creating six input polarized light. The second part is Stokes analyzer including rotating quarter wave plate, fixed polarizer and one photodetector for receiving the analog signal of the detector and calculating the intensity corresponding to different input lights.

The laser beam is created by a He-Ne laser source (JDSU —Model 1125P) with wavelength at 633 nm. For controlling the rotating quarter wave plates and polarizers, three stepper motors were utilized with a resolution of 1.8° per step which is controlled by Arduino Uno integrated with CNC module. All transmission gears, auto-rotation block of quarter-wave plate, and polarizers were designed by Solidwork 2016 and printed by using a 3D printer.

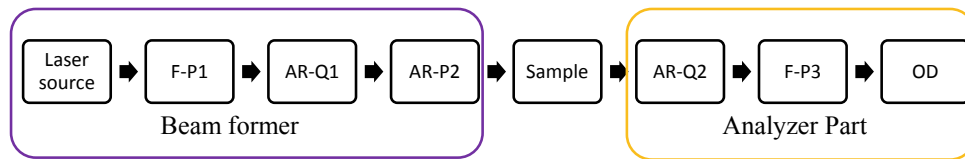


Fig. 1 The automatic optical system for measuring the Stokes parameters

3 Results and Discussion

3.1 Designed Hardware

Rotating quarter-wave plate blocks (AR-Q1 and AR-Q2) were designed to put the lens in the quarter-wave plate holder and controlled by a stepper motor. The quarter-wave plate holder is designed to plug the lens M-MT-RS metric polarizer rotation mount from Newport Co. (Fig. 2).

Auto-rotation polarizer block (AR-P2) was designed to assemble the stepper motor to control the angle of the polarizer lens. The holder of lens polarizer rotation mount was built to compatible with the lens RM25A polarizer (Newport Co.) (Fig. 3).

Fixed polarizer blocks (F-P1 and F-P3) were designed to assemble and fix the lens RM25A polarizer rotation mount from Newport Co. (Fig. 4).

The cage of the whole system also was designed to assemble all blocks of the automatic controlling system (Fig. 5).

3.2 Analyzed Results

A rotating motorized stage (SGSP-60YAW-0B, SIGMA KOKI Co.) was used to rotate a polarizer 36 steps to create 36 angles from 0° to 180° each step being 5°. Then, both the

designed system and commercial Stokes polarimeter (PAX5710, Thorlabs Co.) were applied to measure the polarization state of a polarizer and a quarter wave plate with 36 different angles from 0° to 180°; and D-glucose solution polystyrene microsphere (diameter = 5 μm) containing D-glucose with the different concentration. Each samples were tested from two to three times repeatability. The output Stokes vectors of the Stokes polarimeter were compared to the output Stokes vectors of the designed system. Then the % error was calculated by the Eq. (3).

$$\%error = \left| \frac{\text{The system values} - \text{Stoke polarimeter values}}{\text{Stoke polarimeter values}} \right| \times 100\% \quad (3)$$

Figure 6 showed the comparing results for measuring polarizer of the commercial Stoke polarimeter and the designed system.

Continuously, the system also applied to experiment the D-glucose solution. The samples are the solution of polystyrene microsphere beads (diameter = 5 μm) containing D-glucose with the different concentration in 0.2, 0.4 and 0.6 M.

Figures 6 and 7 showed that the designed system operates with the % error <5% to compare with a commercial Stokes polarimeter. Although the accuracy is acceptable, the system could be improved the quality also the sensitivity of the system by increasing the quality of stepper motor, especially

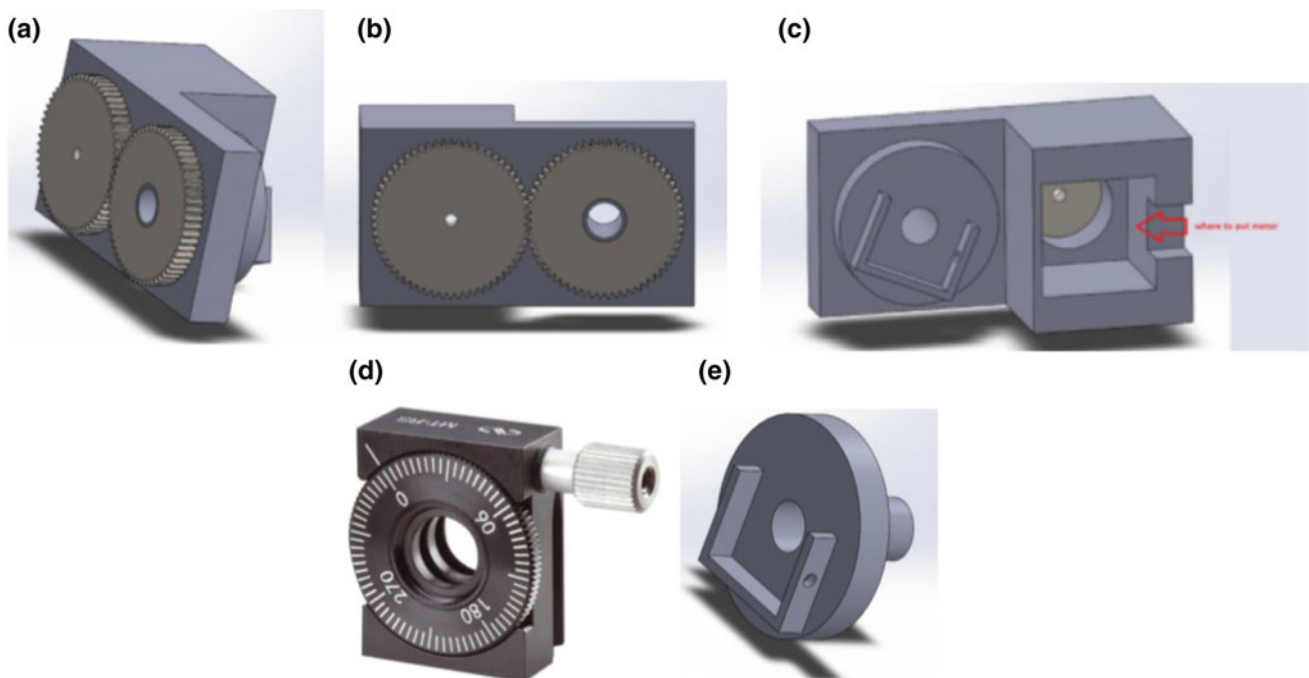


Fig. 2 a–c Rotating quarter-wave plate block with different angle view, d lens M-MT-RS metric polarizer rotation mount, e lens M-MT-RS metric polarizer rotation mount holder

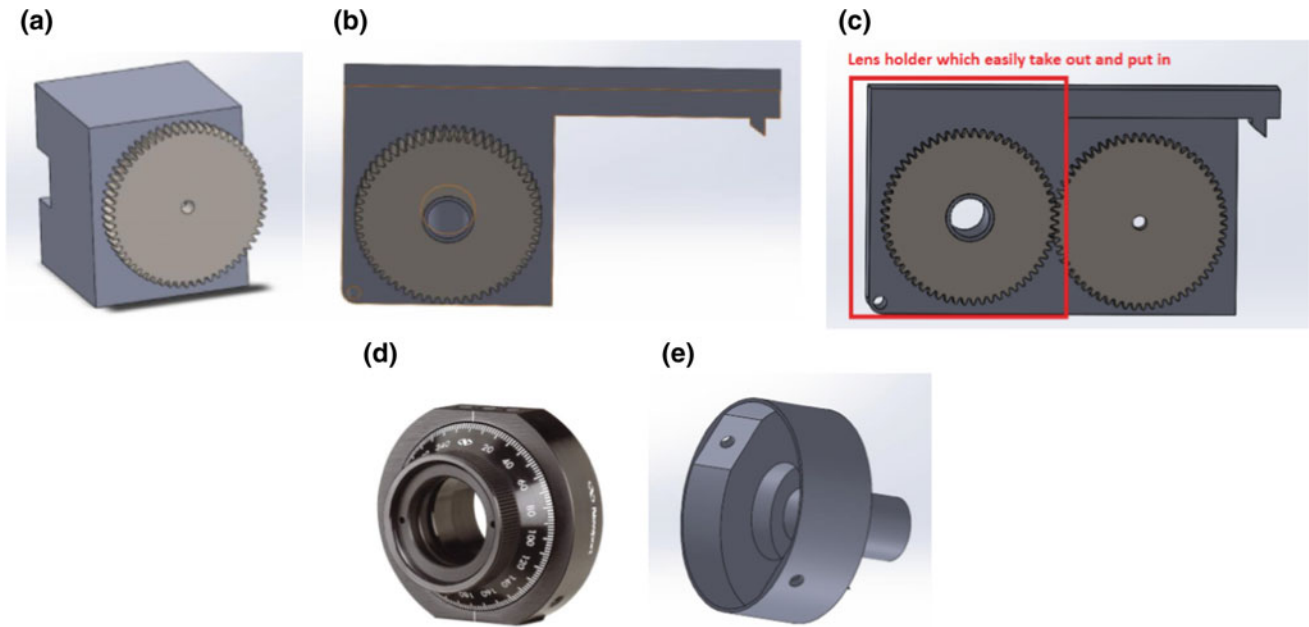


Fig. 3 a Step motor jointing gear, b rotating hooker, c rotating polarizer block, d lens RM25A polarizer, e rotating polarizer holder

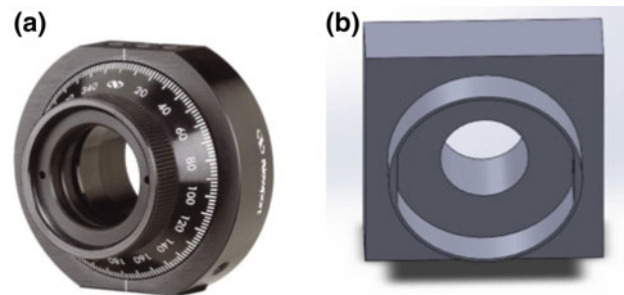


Fig. 4 a RM25A polarizer rotation mount, b fixed polarizer holder

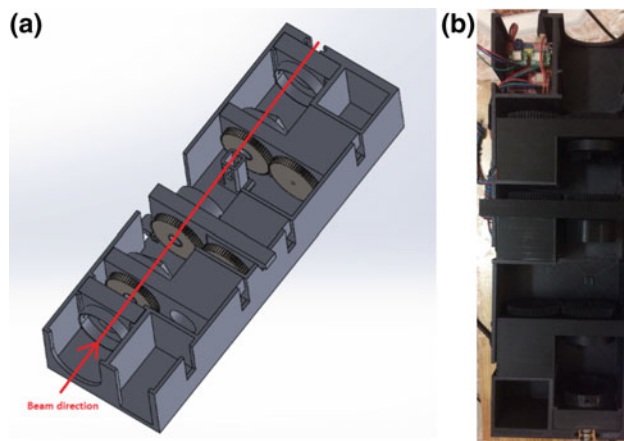
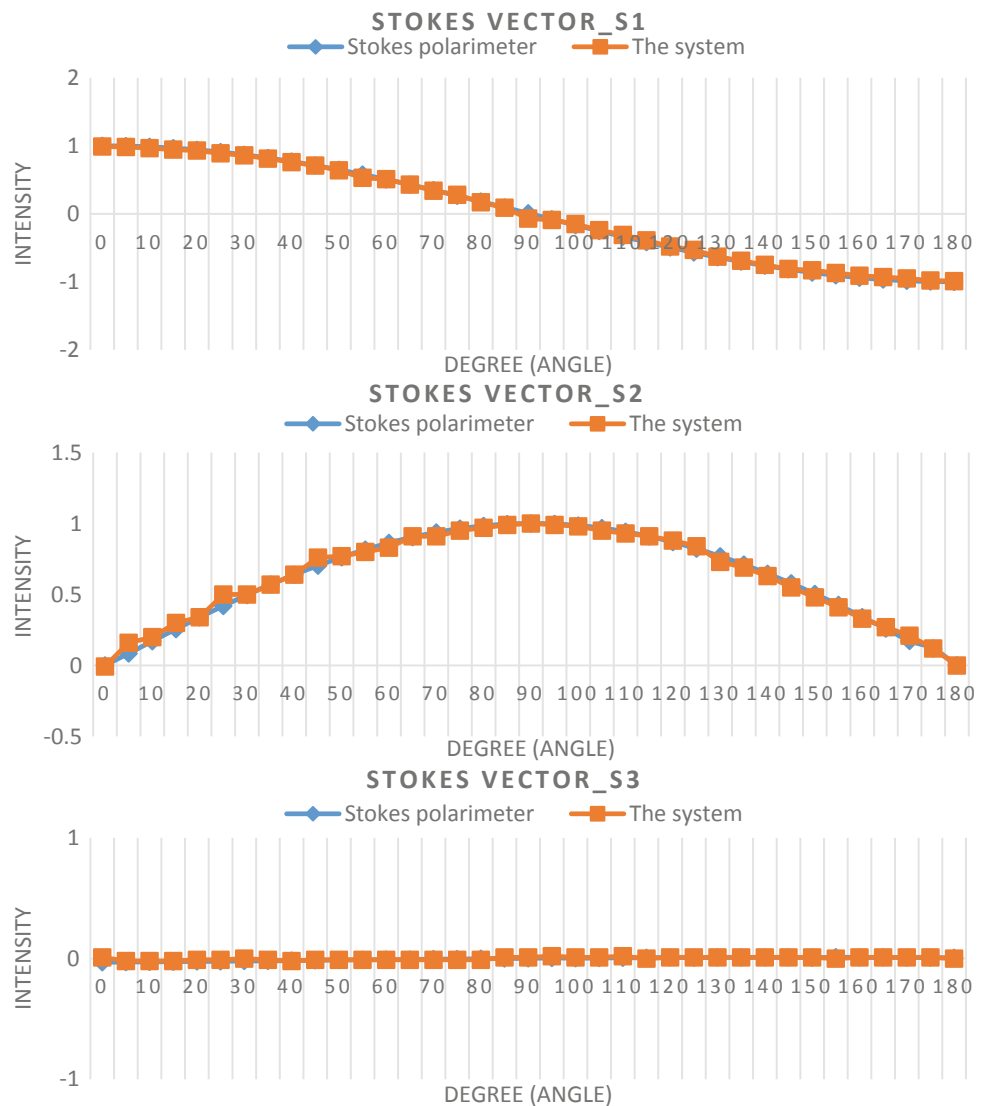


Fig. 5 The cage of the designed system. a Assembled system on solidwork, b final result after assembling all 3D printed part of system

Fig. 6 The comparison measurement results of a polarizer between the Stokes polarimeter and the designed system



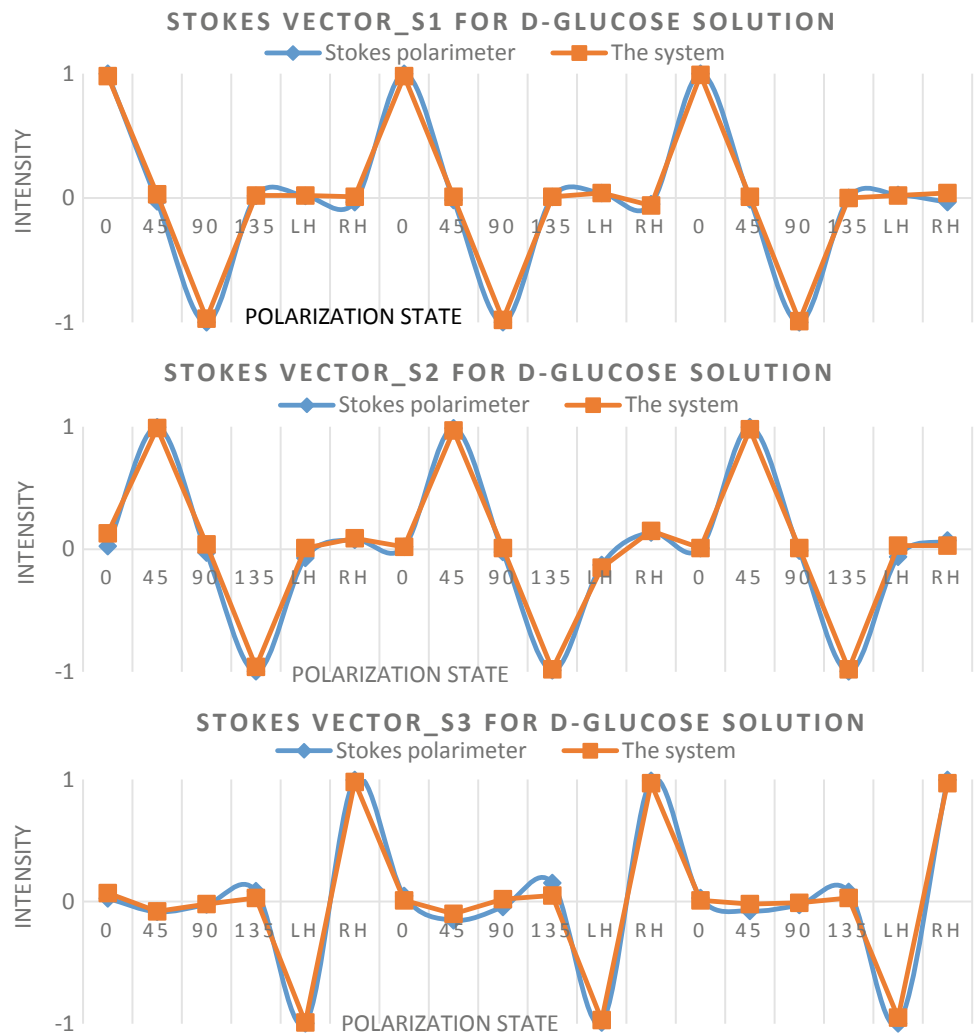
their gear system; and the number of sample N in each Stokes measurement. One advantage of the designed system is that we can change the laser source by UV, Blue or IR for other experimental purposes.

4 Conclusion

In conclusion, the system can automate to measure the Stokes parameter of a biological sample, and the results showed that the accuracy $<5\%$. The designed system can

help to minimize the experiment time. Moreover, the system can apply to different laser sources such as UV, Blue, IR for other experimental purposes. However, the system is not enough fully-automatic system; the user has to follow the manual to ensure the measurement accuracy. In the future, the quality of the system will be improved by (1) avoiding the motors noises; (2) developing the system into a fully automatic system; and (3) increasing the accuracy of the detector and the sampling numbers. We expect that the system is a feasibility method in diabetic diagnosis and monitoring or detecting cancer.

Fig. 7 The comparison measurement results of D-glucose solution between the stokes polarimeter and the system



Acknowledgements This research is funded by International University, VNU-HCM under grant number SV2016-BME-02.

Conflict of Interest The authors declare that they have no conflict of interest.

References

1. Wu, P.J., Walsh, J.T.: Stokes polarimetry imaging of rat tail tissue in a turbid medium: degree of linear polarization image maps using incident linearly polarized light. *J. Biomed. Opt.* **11**(1), 14031 (2006)
2. Sun, P., Ma, Y., Liu, W., Yang, Q., Jia, Q.: Mueller matrix decomposition for determination of optical rotation of glucose molecules in turbid media. *J. Biomed. Opt.* **19**(4), 46015 (2014)
3. Wood, M.F., Ghosh, N., Wallenburg, M.A., Li, S.H., Weisel, R.D.: Polarization birefringence measurements for characterizing the myocardium, including healthy, infarcted, and stem-cell-regenerated tissues. *J. Biomed. Opt.* **15**, 047009 (2010)
4. Bargo, P.R., Prah, S.A., Goodell, T.T., Slevin, R.A., Koval, G., Blair, G., Jacques, S.L.: In vivo determination of optical properties of normal and tumor tissue with white light reflectance and an empirical light transport model during endoscopy. *J. Biomed. Opt.* **10**, 034018-1-03401815 (2005)
5. Moffitt, T., Chen, Y.C., Prah, S.A.: Preparation and characterization of polyurethane optical phantoms. *J. Biomed. Opt.* **11**, 041103-1 - 041103-10 (2006)
6. Pickering, J.W., Prah, S.A., van Wieringen, N., Beek, J.F., Sterenberg, H.J.C.M., van Gemert, M.J.C.: Double-integrating-sphere system for measuring the optical properties of tissue. *Appl. Opt.* **32**, 399–410 (1993)
7. Pham, T.T.H., Lo, Y.L.: Extraction of effective parameters of anisotropic optical materials using decoupled analytical method. *J. Biomed. Opt.* **17**(2), 25006-1-25006-17 (2012)
8. Pham, Thi-Thu-Hien, Lo, Yu-Lung: Extraction of effective parameters of turbid media utilizing the Mueller matrix approach: study of glucose sensing. *J. Biomed. Opt.* **17**(9), 0970021–09700215 (2012)
9. Schaefer, B., Collett, E., Smyth, R., Barrett, D., Fraher, B.: Measuring the stokes polarization parameters. *Am. J. Phys.* **75**(2) (2007)

Part XI
Healthcare Informatics

An Efficient Solution to Secure Embedded Information in DICOM Images for Telemedicine

Tuan T. Nguyen, Luan M. Tran, Ngoc C. Nguyen, and Thuong T. Le

Abstract

Digital Imaging and Communications in Medicine (DICOM) is an international data standard used worldwide to store and transmit various medical images. In addition to the image pixel data, DICOM files also consist of private information and other important information for diagnosis. However, they are easily modified, and alterations are not detectable with current DICOM file format. Consequently, the security of this kind of data over the Internet arises more challenges. This paper presents an efficient solution to secure embedded information in DICOM images by exploiting different techniques of data encoding, encryption and watermarking. Firstly, the proposed method encodes personal information, encrypts it and then embeds it into the DICOM images by two secret keys to increase the security. After that, personal information is removed from the DICOM images. As a result, medical images are still handled in both normal mode and secure mode without leakage of personal information. Finally, the experimental results on different medical images demonstrate the imperceptibility, capacity and efficiency of the proposed design to discuss its use in telemedicine.

Keywords

Embedded information • Encryption • Watermarking • DICOM • Telemedicine

1 Introduction

The terminology “telemedicine” was defined as the delivery of healthcare services from a distance using information and communication technologies. These technologies have

facilitated the exchange of digital data and images between patients and medical staff through remote connection devices [1]. Meanwhile, DICOM, which stands for Digital Imaging and Communications in Medicine, is a set of industrial standards progressing in the demand of connecting, storing, exchanging and printing medical images. Various modalities such as CT (Computed Tomography), MR (Magnetic Resonance), US (Ultra Sound), DX (Digital Radiography), and so on are accompanied by a table that meets the DICOM standards to clarify the service classes that these devices support. DICOM has gradually gained widespread acceptance in hospitals and clinics. Nowadays, the management of this standard system belongs to DICOM Standards Committee consisting of many large companies operating in manufacturing medical devices and health organizations in North America, Japan and Europe. DICOM is also ISO 12052:2006 standard.

A DICOM file is not only a type of image data but also contains information relating to patients and modalities that create the images. It has a.dcm extension and consists of a number of information attributes with different data types and one special attribute containing image pixel data up to 65,536 (16 bits) grayscales for excellent image quality [2].

The rapid progress of digital imaging technique and Internet brings convenience to remote medical treatment, diagnosis and academic exchange, and effectively solves the problem of uneven distribution of medical resources. However, the individualized medical information sharing over public networks may violate the privacy of the patient. In order to improve information security, many different kinds of solutions have been developed so far, but mostly for non-DICOM images. Hence, the paper focuses on information security in DICOM medical images. It means that the embedded image is still compatible with the DICOM standard. The rest of this paper is organized as follows. Literature review in various technologies used to maintain medical image security, such as encryption and watermarking is included in Sect. 2. In Sect. 3, the new solution to secure embedded information in DICOM images is introduced and

T. T. Nguyen (✉) · L. M. Tran · N. C. Nguyen · T. T. Le
Ho Chi Minh City University of Technology (VNU-HCM),
268 Ly Thuong Kiet, Dist. 10, Ho Chi Minh City, Vietnam
e-mail: nttuan@hcmut.edu.vn

analyzed. Experimental results are implemented on various medical images to evaluate the imperceptibility, capacity and efficiency of the proposed method. Section 4 summarizes and concludes the paper.

2 Literature Review

Patient information such as name, age, sex, date of birth, identification information, and so on is formatted in some DICOM common tags, specifically in group “0010”. Data may or may not be displayed on the screen, but anyone can also extract this kind of private information from those tags when accessing to the DICOM file. A simple and easy method to secure patient information is to convert and export the DICOM file into common image formats such as PNG (Portable Network Graphics), TIFF (Tagged Image File Format) or JPEG (Joint Photographic Experts Group). However, all additional information excluding image data from original DICOM file will be lost. Moreover, the quality of resulting image may be degraded significantly due to the limitation of bit depth or the lossy compression of these image formats. Another solution is removing or replacing all

patient information with “anonymization”. It obtains the same quality of the resulting image due to keeping the DICOM format. However, private information is still not reconstructed from the resulting image so that it is only suitable for training purposes [3].

Therefore, some authors exploited the cryptography to obtain security with DICOM file such as Advanced Encryption Standard (AES). AES has a fixed block size, which has three levels of 128, 192 or 256 bits. It works on data managed in the form of matrices in the order of 4×4 byte principal column, called state. This technique is based on the combination of both substitutions and permutations as shown in Fig. 1, which has a great advantage in implementing both software and hardware [4].

However, applying encryption for whole DICOM file is not efficient because its size is extremely large. By contrast, encryption solution for only personal information in DICOM file may have latent errors because encrypted data can overlap with the control characters such as Patient Name (PN) tag and most DICOM patient information tags only support text characters as shown in Table 1. Moreover, encrypted data is completely not protected after decryption and easy to be realized, thus it may be hacked or simply removed by attackers.

Fig. 1 AES encryption and decryption algorithm

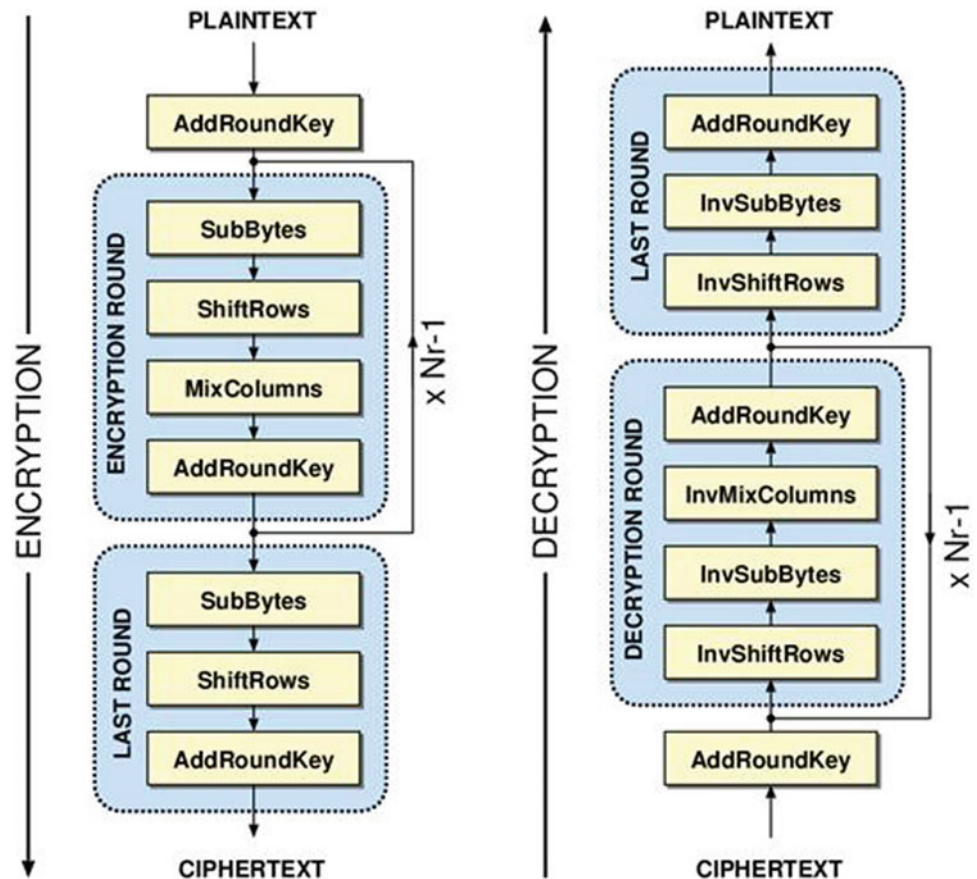


Table 1 Several patient information attributes

Tag	Name	VR	Character repertoire	Value
(0010, 0010)	Patient Name	PN	Excluding Control Characters LF, FF, and CR	64 chars maximum
(0010, 0020)	Patient ID	LO	Excluding Control Characters Except for ESC	64 chars maximum
(0010, 0030)	Patient's Birth Date	DA	YYYYMMDD: "0"–"9"	8 bytes fixed
(0010, 0032)	Patient's Birth Time	TM	HHMMSS.FFFFFFF: Uppercase characters, "0"–"9", the SPACE character, and underscore "_"	16 bytes maximum
(0010, 0040)	Patient's Sex	CS	Uppercase characters, "0"–"9", the SPACE character, and underscore "_"	16 bytes maximum

To solve this problem, watermarking has recently been applied in the field of medicine for hiding information in medical image to increase usability. The advantage of watermarking technology is that it supports enhanced security, which cryptography simply cannot meet the need for secure medical data. By using digital watermarking with invisibility characteristics, the patient information as the watermark is hidden in medical images in order to ensure the transmission security on the Internet, and thus plays a role in protecting patient privacy [5–7].

Usually, medical image watermarking is to use traditional watermarking techniques to embed patient information in spatial domain [8] or transform domain [9]. Due to their simplicity and high capacity, Least Significant Bit (LSB) algorithms are the most studied in watermarking [10]. However, these methods are not secure, because no encryption technique is used for embedding information in images. In order to improve the security, some solutions exploit a private key from a pseudo random number generator to determine the pixels used for embedding [11]. Unfortunately, most proposed methods are applied for non-DICOM images. To overcome the above issues, our research on design of a new solution to secure embedded information in DICOM images for telemedicine applications by exploiting different techniques of data encoding, encryption and watermarking. Especially, the resulting image is fully compatible with DICOM standard.

3 Proposed Method

The main steps of the proposed method for embedding personal information are presented as below:

Step 1 Binary encoding personal information based DICOM data structure as shown in Table 2. It is implicit encoding where each data element consists of a tag that identifies the attribute, includes Group Number (2 bytes) and Element Number (2 bytes)

Table 2 Implicit VR encoding

Group number	Element number	Value length	Value
2-byte	2-byte	4-byte L	L bytes

and a Value Representation (VR) that describes the data type and format of the attribute value [2].

Step 2 AES encryption of binary data from step 1 with a secret key as shown in Fig. 1.

Step 3 Insertion of encrypted data into original image through LSB planes by another key. The LSB bits of each pixel in original image are replaced by bitstream of encrypted data. In this way, the embedded image is obtained as shown in Table 3. Finally, personal information is removed completely from DICOM tags.

Correspondingly, the extraction process is also implemented in three main steps:

Step 1 Extraction of encrypted data from embedded image through LSB planes by the same embedded key.

Step 2 AES decryption of binary data from step 1 with the same secret key in encryption as shown in Fig. 1.

Step 3 Decoding personal information based DICOM data structure as shown in Table 2.

As a result, with our method, in the normal mode, any physician can also view medical images with full support of DICOM standard without leakage of personal information, even if one key is known, while in the secure mode, personal information can only be extracted and decrypted to the user having the rights to access patient's complete data.

To measure the amount of visual quality degradation between original image x and embedded image s , this paper uses the mean squared error (MSE) and the peak signal-to-noise ratio (PSNR), as shown in Eqs. (1) and (2), where b is bit depth of original image with $M \times N$ size.

Table 3 LSB watermarking algorithm

Original image (pixels)				Bitstream of data					Embedded image (pixels)			
				1	1	0	0	...				
			LSB	←	←	←	←	←				LSB
...	1	0	1	←	←	←	←	←	...	1	0	1
...	0	0	0	←	←	←	←	←	...	0	0	1
...	1	1	1	←	←	←	←	←	...	1	1	0
...	0	1	0	←	←	←	←	←	...	0	1	0
...	←	←	←	←	←

These measures are popular because they are simple to implement and it is relatively suitable to design systems.

$$MSE = \|s - x\| = \frac{1}{M.N} \sum_{i=1}^M \sum_{j=1}^N (s_{ij} - x_{ij})^2 \quad (1)$$

$$PSNR = 10 \log_{10} \frac{(2^b - 1)^2}{MSE} \quad (2)$$

It is clear that a good watermarking technique should have high *PSNR* value and low *MSE* value. It can be derived that *MSE* metric only depends on the number of embedded LSB planes, while *PSNR* also depends on bit depth of

original image. It means that with the same *MSE*, the larger bit depth of image is, the better the quality of image obtains. Figure 2 shows the embedded images with different number of LSB planes corresponding with original CT image. Due to the effect of Human Visual System, the quality degradation of the embedded image is not perceptible in the case of using three LSB planes, somehow perceptible with four LSB planes and noticeable significantly for five LSB planes. Similarly, the 3-LSBs embedded images corresponding with original images of US, DX and MR are shown in Figs. 3, 4 and 5. From these results, it can be derived that the *PSNR* should be more than around 37 dB in order to obtain the imperceptible embedded image.

Fig. 2 Original CT image and embedded images with different number of LSB planes

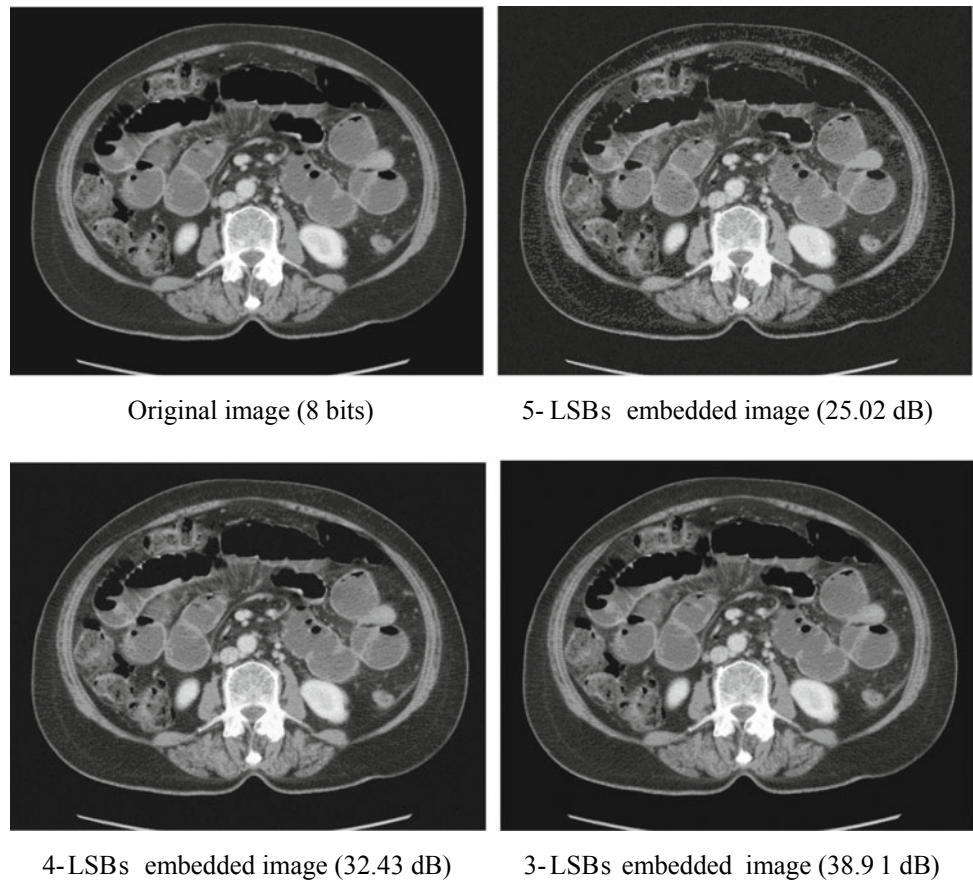
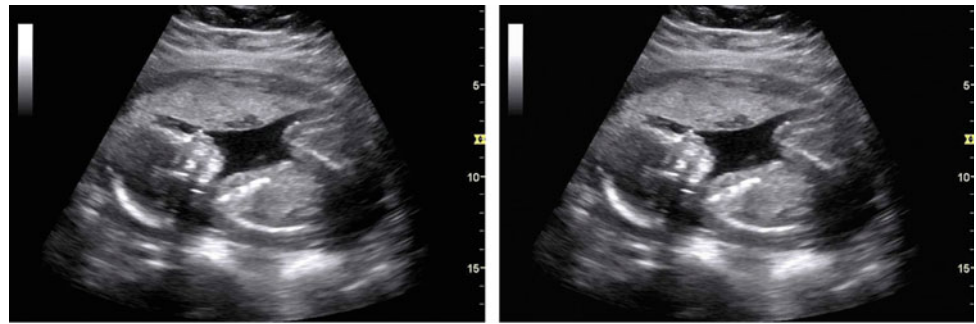


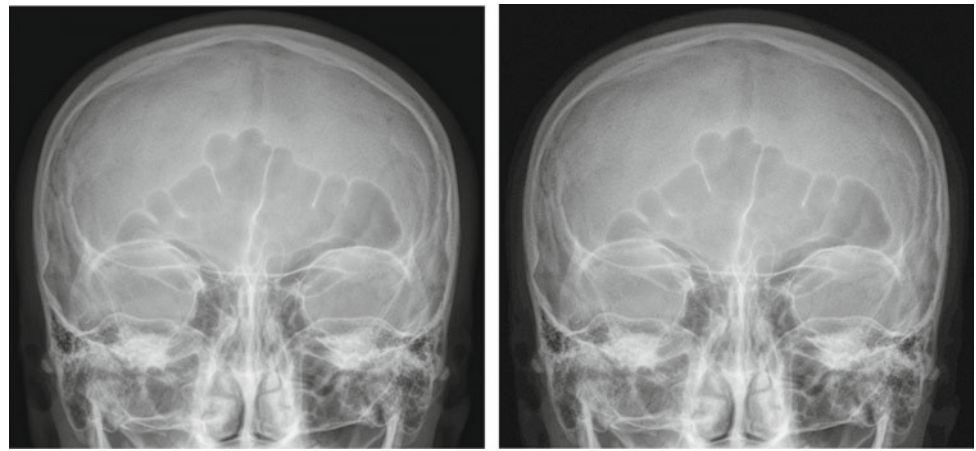
Fig. 3 Original US image and 3-LSBs embedded image



Original image (8 bits)

3-LSBs embedded image (36.89 dB)

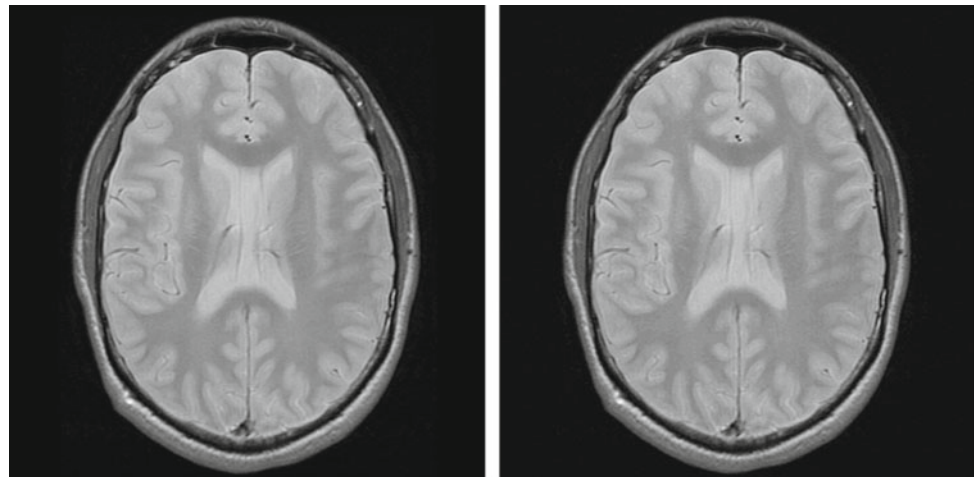
Fig. 4 Original DX image and 3-LSBs embedded image



Original image (8 bits)

3-LSBs embedded image (38.02 dB)

Fig. 5 Original MR image and 3-LSBs embedded image



Original image (8 bits)

3-LSBs embedded image (37.40 dB)

Table 4 shows theoretical values of *PSNR* versus bit depth of original image and the number of embedded LSB planes. From this table, the maximum number of LSB planes for embedding can be derived corresponding to different bit

depth images in order to obtain imperceptible degradation. Moreover, with high capacity up to 1 bit per pixel (bpp) for each embedded LSB plane, our solution allows to secure a large amount of private information; in particular, we can

Table 4 Theoretical values of PSNR (dB)

Bit depth	Number of embedded LSB planes										
	1	2	3	4	5	6	7	8	9	10	11
8	51.1	44.2	37.9								
10	63.2	56.2	50.0	43.9	37.7						
12	75.3	68.3	62.0	56.0	49.9	43.9	37.9				
16	99.3	92.4	86.1	80.1	74.0	68.0	62.0	56.0	49.9	43.9	37.9

embedded 98,304 bytes of private information into the grayscale image with the size of 512×512 in the case of using three embedded LSB planes. When comparing between our solution for DICOM images and the algorithm in [10] for nature images, we obtain the same results of them about the quality of embedded image and the capacity of embedded information. However, the security of their method is extremely weak due to using only inverse bit. Unlike them, our solution is supplemented the security property for embedded information by cryptography technique and fully compatible with DICOM standard, adapting to the requirements for the practice of telemedicine.

4 Conclusions

Even though there are some disadvantages, DICOM is one of the most ambitious international standards for medical imaging archiving and exchanging and has proved to be a very helpful standard in telemedicine. However, when the patients' medical images are transmitted through the network, interception and tampering of medical information become easier so that there is a risk of leakage of patient information. Hence, in this paper, we proposed an efficient solution to secure embedded private information in DICOM images to adapt to telemedicine. By the combination of encoding, encryption and watermarking, our method allows two-level security (one key for encryption and one key for watermarking), and lossless retrieval of the embedded information without the original image. As a result, in the normal mode, any physician can also view medical images with full support of DICOM standard while in the secure mode, personal information can only be extracted and decrypted to the user with complete access to the patient's data. In addition, the proposed solution not only improves information security but also obtains the high capacity and

good imperceptibility with various DICOM images. The simulation results agree with the theoretical derivation.

Acknowledgements This research is funded by Ho Chi Minh City's Department of Science and Technology (HCMC-DOST) under grant number 82/2017/HD-SKHCN. **Conflict of Interest** The authors declare that they have no conflict of interest.

References

1. Ekeland, G., Bowes, A., Flottorp, S.: Effectiveness of telemedicine: a systematic review of reviews. *Int. J. Med. Inform.* **79**(11), 736–771 (2010)
2. Oleg, S. Pinykh: *Digital Imaging and Communications in Medicine (DICOM): A Practical Introduction and Survival Guide*, 2nd edn. Springer, Heidelberg (2012)
3. Gackowski, et al.: Development, implementation and multicenter clinical validation of the TeleDICOM–advanced, interactive teleconsultation system. *J. Digit. Imaging* **24**(3), 541–551 (2011)
4. Canavan, J.E.: *The Fundamentals of Network Security*. Artech House (2001)
5. Panchal, U.H., Srivastava, R.: A comprehensive survey on digital image watermarking techniques. In: *Fifth IEEE International Conference on Communication Systems and Network Technologies*, pp. 591–595 (2015)
6. Mousavi, S.M., Naghsh, A., Abu-Bakar, S.A.R.: Watermarking techniques used in medical images: a survey. *J. Digit. Imaging* **27**(6), 714–729 (2014)
7. Priya, S., Santhi, B., Swaminathan, P.: Study on medical image watermarking techniques. *J. Appl. Sci.* **14**(14), 1638–1642 (2014)
8. Acharya, R., Anand, D., Bhat, S., Niranjana, U.C.: Compact storage of medical images with patient information. *IEEE Trans. Inf. Technol. Biomed.* **5**(4), 320–323 (2001)
9. Singh, A.K., Kumar, B., Dave, M., Mohan, A.: Multiple watermarking on medical images using selective DWT coefficients. *J. Med. Imag. Health Inform.* **5**(3), 607–614 (2015)
10. Bamatraf, A., Ibrahim, R., Salleh, M.: A new digital watermarking algorithm using combination of least significant bit and inverse bit. *J. Comput.* **3**(4), 1–8 (2011)
11. Hajjaji, M.A., Mtibaa, A., Bourennane, E.L.: A watermarking of medical image: method based LSB. *J. Emer. Trends Comput. Inf. Sci.* **2**(12), 656–663 (2011)

A Wireless Hemodialysis Blood Oozing Detection and Alarm System

Jia-Huang Zeng and Yuh-Show Tsai

Abstract

During the hemodialysis treatment, two needles, for drawing to dialyzer and for returning filtered blood to the body, respectively, will be inserted into an AV shunt. Occasionally, the blood leaking is occurred on the interface of needle and artificial fistula. This incident not only increased the risk of infection, it also caused many conflicts between patients and nurses. This paper presents a wireless alarm system that can detect the blood leaking and send the alarm signal to nurse station. The system is consisting of two optical blood detectors, an adjustable threshold comparator, a Wi-Fi embedded MCU, and an user-friendly management APP. The system continuously send green light on the gauze. When certain amount of blood pass though the gauze, the decreasing of reflection light would activate alarm event. A MS-Windows APP is installed on the nurse station. It monitors the front-end sensing devices and, upon receiving alarm signal, it pop-up a warning dialog to remind medical staffs to take care of the event. The primary test shows the system can effectively provide early blood leaking detection and reduce the rate of aforementioned problems.

Keywords

Wireless alarm system • Hemodialysis • Blood oozing

1 Introduction

Due to renal failure or end-stage renal disease, there are 85 thousands patients who are suffered from regularly hemodialysis treatment in Taiwan. On hemodialysis preparation stage, patients will need to have a procedure to create a vascular access. The access create a way for blood to be removed from the body, and circulate through dialysis machine, where the body's waste products are filtered, and then return to the body. A synthetic bridge graft is a quite common type of vascular access. A surgeon can use a flexible, rubber-like tube to create a path between an artery and vein, so called AV-shunt. The graft sits under the skin, so that the needles used for hemodialysis are placed into the graft material rather than the patient's own vein [1, 2].

During the hemodialysis process, due to the unintentional arm movement, the blood bleeding often occurs at the interface between needles and graft. This incident not only increased the risk of infection [3, 4], it also causes many conflicts between patients and nurses. It is desired to have an automatic blood leaking detection and alarm system so that the medical staff's workload can be reduced and the incident can be prevented at early stage. The followings describe requirements, architecture, implementation, and results of the system.

2 System Requirement and Architecturer Introduction

By reviewing the commercial available blood leaking detection products [5, 6], we found that most devices are designed for patient aware-fashion, which is not suitable for centralized monitoring applications. After survey from medical staffs, a list of system requirements are:

1. The device shall be able to monitor both arterial and vein needle-fistula interfaces.

J.-H. Zeng · Y.-S. Tsai (✉)
Institute of Biomedical Engineering, Chung Yuan Christian University, Taoyuan, Taiwan
e-mail: yuhshow@gmail.com

Y.-S. Tsai
Biomedical Instrument Development and Accreditation Service Center, Chung Yuan Christian University, Taoyuan, Taiwan

2. The device shall have clear indicators to show which end is blood oozing.
3. The device shall provide switchable warning sound.
4. The device shall transmit the sensing status wirelessly to nurse station.

Based on the requirements, a blood leaking detection device was proposed as Fig. 1. Two photo Transceivers with Trans-Impedance Amplifier (TIA) are placed on arterial and vein sides for blood detection. The sensed signal with polling by an analog switch controlled by MCU. A voltage follower is placed between the switch and ADC to perform impedance match. A low-power MCU with built-in Wi-Fi communication is the heart of the device.

3 Material and System Implementation

Sensor: The compact surface mount type photo sensor, which is built in two green LED and a high sensitive photo diode, NJL5310R [7], is selected for the blood detection (Fig. 2). This part is generally used for pulse rate detection. As seen on Fig. 2, the peak wavelength of NJL5310R is 525 nm, which makes it perfect for blood sensing.

TIA: Each photo sensor will generate current, based on incident light intensity. The current will convert to voltage by a high gain, high noise immunity Trans-Impedance Amplifier.

MCU: ESP8266EX, a Wi-Fi built-in Microcontroller is chosen as the main process unit, due to its compact size and low power consumption. The ESP8266 [8] is operated at 40 MHz. It offers full TCP/IP stack. Its single-channel, 10-bit resolution Analog-to-Digital Converter is suitable for photo sensing signal acquisition. The 32 KB flash memory is accommodated for most Internet of Things applications.

Analog switch: The proposed device has two photo sensing analog signals and one battery voltage-monitoring signal, whereas there is only one ADC channel. Therefore, a CD4066 quad bilateral switch is utilized to multiplex the analog signals. The MCU polling the signals by on-off of the switches sequentially.

Alarm indicators: Two LEDs are installed to illustrate whether the arterial side (RED led), or Vein side (BLUE) blood-leaking event occurred. An accompanied buzzer with on-off switch is used to provide audio alarm.

Firmware flow: To prevent the background signal from photo sensor causes false alarm, the MCU will initially get the each sensor signal at the startup stage. Once the

Fig. 1 The block diagram of hemodialysis blood leaking detection device

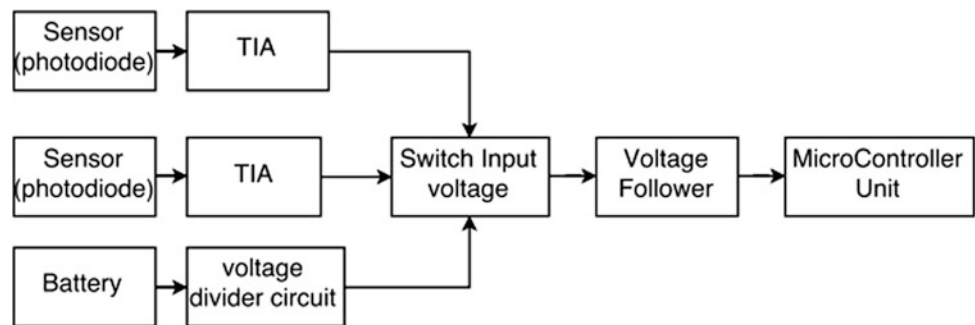
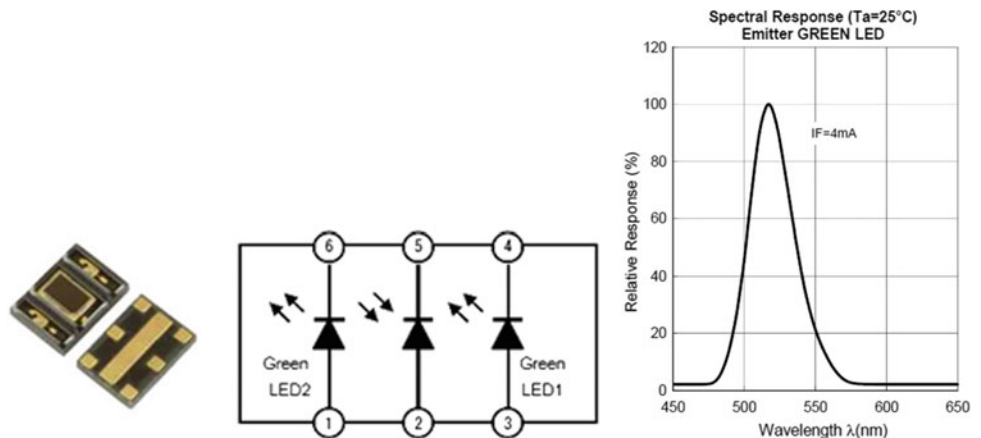


Fig. 2 The NJL5310R, its block diagram and spectral response



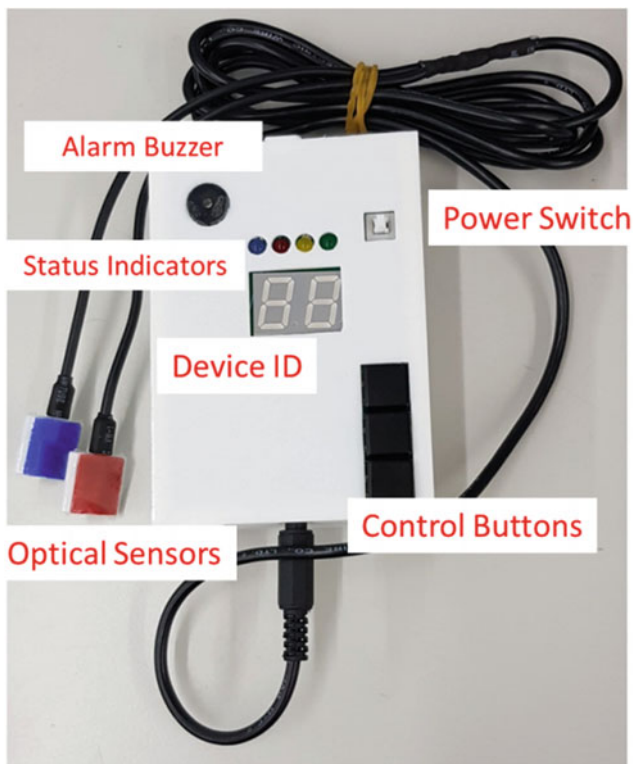


Fig. 3 The prototype system with optical sensors, status indicators, device ID display, alarm buzzer, control buttons and power switch

difference between the incoming signal and the background over a threshold, MCU will trigger alarm LED and buzzer. The threshold can be manually adjusted, by medical staffs based on their clinical experience, to either increase or decrease the sensitivity of the alarm. The detection flow executed every 5 s.

APP on nurse station: A Windows APP is developed and installed on a nurse station computer for distant monitoring each blood leaking device status. The APP is programmed with Visual Studio 2017. It scans each device status through

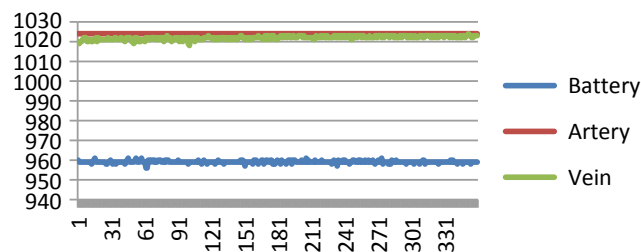


Fig. 5 Signal acquired from the static stability test

Wi-Fi Chanel and paring patient ID by checking the MAC address. From the monitor display, medical staffs can easily check activity of each device and, if blood leaking event occurs, locate which bed needs to be take care of. The MS SQL database is applied to store the status every 5 s. These record will be furtherly integrated to hospital hemodialysis information system.

4 Experimental Results

All the components and power module are integrated and packed as a prototype device (Fig. 3). A series of experiments have been conducted to evaluate the system stability, sensitivity, and function verification (Fig. 4). Red pigment with different intensities are used to emulate human blood. The first trial is to test the sensing stability on both stationary table and moving arm.

Figure 5 shows when the sensors are placed on a stationary table, the signals are very stable. However, when placed the sensors on an arm, the fluctuation is quite evident (Fig. 6). Based on the finding, a moving-average low pass filter is applied to smooth the signal for reducing the false alarm.

Sensitivity test is performed by applying different intensity of red color cards. The results shown on Fig. 7 reveal



Fig. 4 The stability test: blood emulation kit, static test, and dynamic test

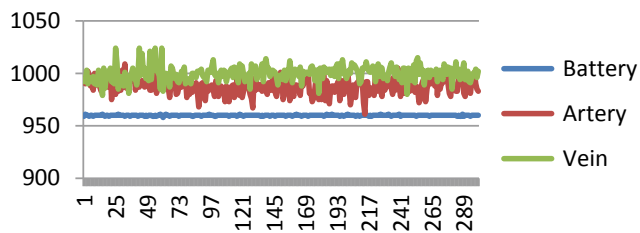


Fig. 6 Signal acquired from the dynamic stability test

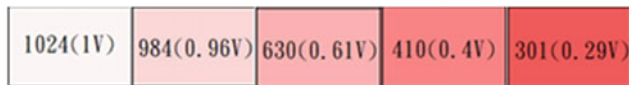


Fig. 7 Sensitivity test results with different intensity of red color. The numbers on each block represent ADC reading and voltage value

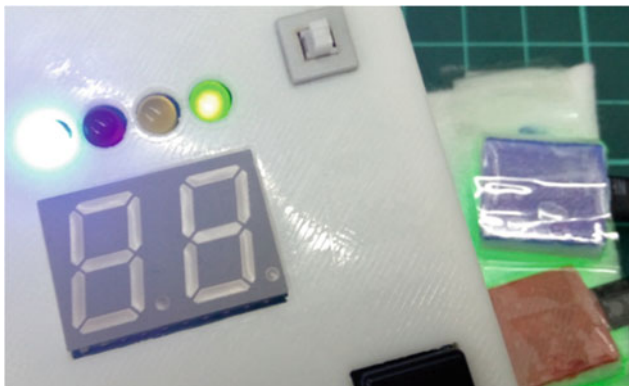


Fig. 8 The blue LED lights up when venous site blood leaking is detected

that the darker of red signal, the lower the signal strength. These results help to justify the optimum threshold. To maintain the flexibility, a manually threshold adjustable mechanism, by applying these color cards on clinical sites is also implemented on the experimental system.

The function tests are exhibited on both device side and nurse station computer side. By slowly dripping the blood emulates on cotton gauge, once the blood leaking emulation reaches predefined threshold, the LEDs and busser start issue alarm signals (Fig. 8). In the meantime, the App on the nurse station computer will display the warning immediately (Fig. 9).

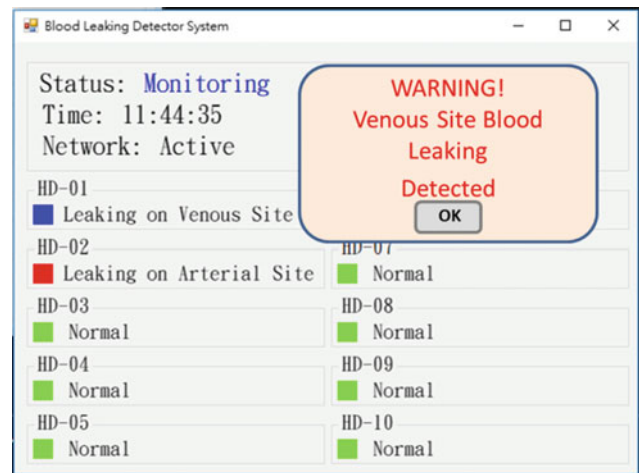


Fig. 9 The APP on nurse station displays each device status. The green square indicates the device is in normal condition. The blue square (venous site) and red square (arterial site) are flashing upon blood-leaking detected. Upon receiving alarm signal, it pop-up a warning dialog

5 Conclusions

The preliminary performance test shows very promising results. However, further robustness test and determination of optimum probe placement are still undergo. An IRB application has been filed. It is expected to process clinical trial in coming summer.

Compliance with Ethical Standards The authors declare no conflict of interest.

References

1. Kidney Disease, <https://www.niddk.nih.gov/health-information/kidney-diseaseSmith>
2. Hemodialysis, <https://www.niddk.nih.gov/health-information/kidney-disease/kidney-failure/hemodialysis>
3. Sandroni, S.: Venous needle dislodgement during hemodialysis: an unresolved risk of catastrophic hemorrhage. *Hemodialysis Int.* **9**, 102 (2005)
4. Lindley, E.J.: "Venous needle dislodgement during hemodialysis", summary of the EDTNA. *ERCA J. Club Discuss. EDTNA/ERCA J.* **31**(4), 220–227 (2005)
5. HEModialert™—Home <http://www.hemodialert.com/>
6. Redsense, <http://www.redsensemedical.com/>
7. NJL5310R datasheet, New Japan Radio Co., Ltd
8. ESP8266 Wikipedia, <https://en.wikipedia.org/wiki/ESP8266>

Part XII

Biomedical Signal and Image Processing

Detecting and Counting Eyes Blinking Using Haar Cascade—A Handy Way to Diagnose Dry Eyes Disease

Nguyen D. Nguyen, Nguyen D. Quang, Dang T. Tin, and Anh Dinh

Abstract

This paper presents the design of the program, called Eye Blinking Detection Program, to define eye state as well as eye blinking by using Haar Cascades. Based on the result of the opened-eye detection process, eye state is determined and the eye blinking can be counted. All the results are displayed on a friendly user interface. By checking eyes state, the program determines if the object is asleep or awake and activate the alert. In addition, the program also has dry-eyes disease diagnostic feature and an eye health-training program. This program is very useful for drivers by helping them stay awake or apply to patients who has eye-related disease.

Keywords

Face detection • Eyes detection • Haar cascade • Eyes blink detection • Warning avoid sleeping • Dry eyes diagnose system

1 Introduction

According to 2017s statistics, the number of handheld devices is increasing rapidly. That mean the time we spend on electronics devices is longer every year too. That is the main reason cause many of eye diseases, for example Dry eyes diseases because people look at the screen continuously for many hours and make eyes tired. On working time, people need a convenient way to avoid accident from lack of sleep and get healthy eyes too. Eyes blink detection come as a handy way to solve these problems.

N. D. Nguyen · N. D. Quang · D. T. Tin (✉)
Faculty of Electrical and Electronics Engineering, Ho Chi Minh City University of Technology, Ho Chi Minh City, Vietnam
e-mail: dttin@hcmut.edu.vn

A. Dinh
Department of Electrical and Computer Engineering, University of Saskatchewan, Saskatoon, Canada

Object Detection using Haar feature-based cascade classifiers [1] is the core method of detecting eyes. We use Haar-Cascade classifiers to detect face and eyes from face. Then, we research other papers and find the relationship between the number of blinks and Dry Eyes disease. We count the number of blinks and the time during blinking eyes. Using these parameters, compared to the parameters of healthy eyes, then we can tell that person got problems with eyes or not. After that, we develop an application to diagnose Dry Eyes, warn avoid sleeping and do eyes exercise automatically.

This paper comprises six sections including this introduction. Section 2 presents some methods to detect and track the eyes. Section 3 shows the methodology and algorithms. Section 4 shows the results from our applications in real life. Section 5 describes the addition of some features to the application. Finally, Sect. 6 concludes the work.

2 Related Works

The idea of having an application that counts the number of blinks is not new. Looking back on the published researches about face and eyes detection, we've seen many effective and precise algorithms such as works done by [1–3]. Most of them are well done with many constraints. An advance face detection [4] is having Graphic Processing Unit (GPU) support, Central Processing Unit (CPU) to speed-up the detection process. They got success speed up 3.3 times for 640×480 . Among related works in this field of application, Ito [5] has applied circular Hough transform and histogram of gradient to detect the apple of the eye. This algorithm is rather complex and seems impossible to apply to blinking detection because it depends on eye color and the environment conditions. But it's good for tracking eyes movement.

We rely on this research [8], and take sample parameters to check if the eyes are dry or not

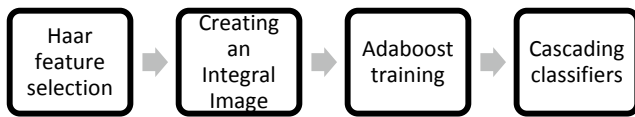


Fig. 1 Object detection using Haar-like feature based

3 Methodology

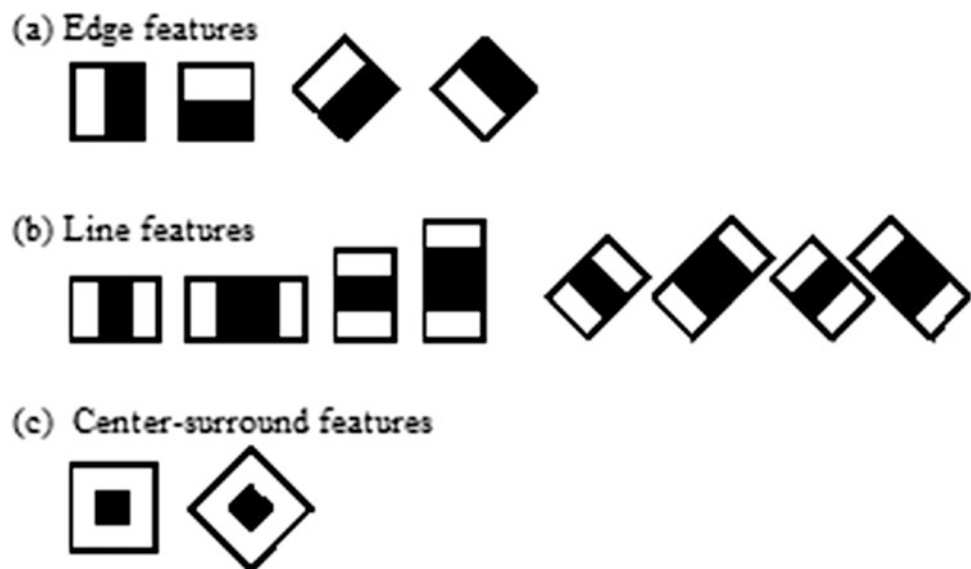
3.1 Object Detection Using Haar-like Feature-Based Cascade Classifier

Figure 1 shows the four stages of object detection step using Viola Jones object detection framework: Haar feature selection, creating an integral image, Adaboost training, and cascading classifiers.

In the Haar feature selection, a simple rectangular Haar-like feature can be defined as the difference of the sum of pixels of areas inside the rectangle, which can be at any position and scale within the original image.

This modified feature set is called 2-rectangle feature. Viola and Jones also defined 3-rectangle features and 4-rectangle features. Haar-like features are rectangles demonstrate the most significant common properties of all pixels in that area. For example, a few properties common to human faces: the nose bridge region is brighter than the eyes, the eye region is darker than the upper-cheeks, etc. Each feature results in a single value which is calculated by subtracting the sum of pixels under white rectangle from the sum of pixels under black rectangle. The resultant classifier includes multiple simpler classifiers of 3 types: (a) edge features, (b) line features, and (c) center-surround features as shown in Fig. 2.

Fig. 2 Types of rectangular features



The algorithm applies all of these simple classifiers to the region of interest. These simple rectangular features include upright features and tilted features are respectively calculated by using integral image and rotated integral image also known as Summed Area Table (SAT) and Rotated Summed Area Table (RSAT). These equations below show how to determine the integral image $AI[x', y']$ and the rotated integral image $AR[x', y']$ from an original image $A[x, y]$.

$$AI[x, y] = \sum_{x' \leq x, y' \leq y} A(x', y') \quad (1)$$

$$AR[x', y'] = \sum_{x' \leq x, x' \leq x - |y - y'|} A(x', y') \quad (2)$$

After calculating the Summed Area Table, we can get the sum of rectangular pixel area by using value of four pixels at the corner as shown in Fig. 3. *Adaptive Boosting*, is a machine learning meta-algorithm formulated by Freund and Schapire [5]. Adaboost helps in finding only the best features among all these Haar-features which match on the original image. After these features are found, a weighted combination of all these features is used in evaluating and deciding any given window has a face or not. Each of the selected features are considered good to be included if they can at least perform better than random guessing (detecting more than half the cases).

3.2 Detect Face and Eye Blinking with OpenCV Cascade Classifier

The face detection is based on [6]. Image pre-processing is required in order to make detection effortless. These steps are (a) down sampling and (b) contrast enhancement. The

Fig. 3 **a** Upright summed area table and **b** rotated summed area table; calculation scheme of the pixel sum of SAT (c) and RSAT (d)

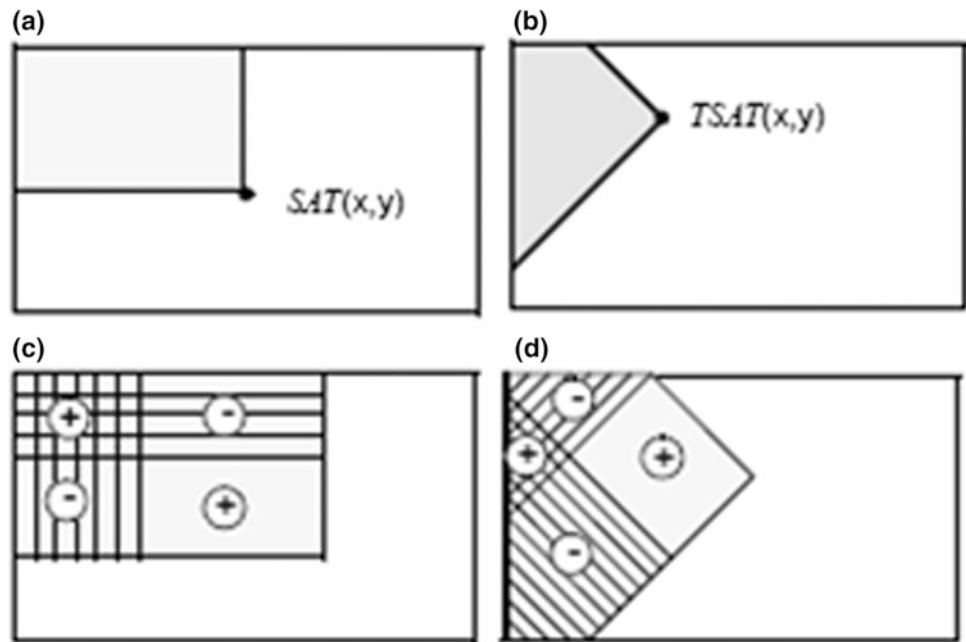


Fig. 4 Shrinking the image then calculate the face rect on the original size image

algorithm will scan the whole image to fit Haar features. If the image is too large, it would take more time to finish; the image is down sampled as illustrated in Fig. 4.

For face and eye detect we will have 2 variables: face_scale and eye_scale. They are ratio between detect size and original size of the image. We recorded the minimum eye_scale that detect both eye smoothly with different video resolution at 15 and 20 cm. Original and detect columns are sizes of eye region before and after shrinking. Original eye region is calculated from face Rect (face region get from face detection process) by determining relatively eye position on face. From the table, we can see that eye can be easily detected if detect region is about 165×55 pixels. We designed an automatic mode that define best eye scale according to detected face Rect. Then, we equalize the histogram to differ the bright and dark areas [7]. Besides equalizing histogram for entire image, we process a separate equalizing by splitting the image into

left and right halves of the face as shown in Fig. 5. This process will remove unbalance lighting on each side of the face. The process of detecting eyes is demonstrated as shown in Fig. 6. By using the specific trained data to detect eye, program only detects opened eye. Therefore, after a face is detected, if there is no eye detected, the eye state will be close, otherwise, if eyes are detected, the eye state will be open.

4 Result and Discussion

4.1 Specifications

In Table 1, we show specifications of our application in real-time mode, and Table 2 presents the parameter FPS in different brightness environments, along with the interfacing of our tool in Fig. 7.

Fig. 5 Separate histogram equalizing

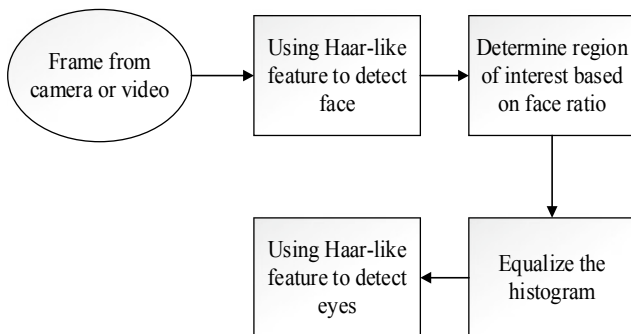
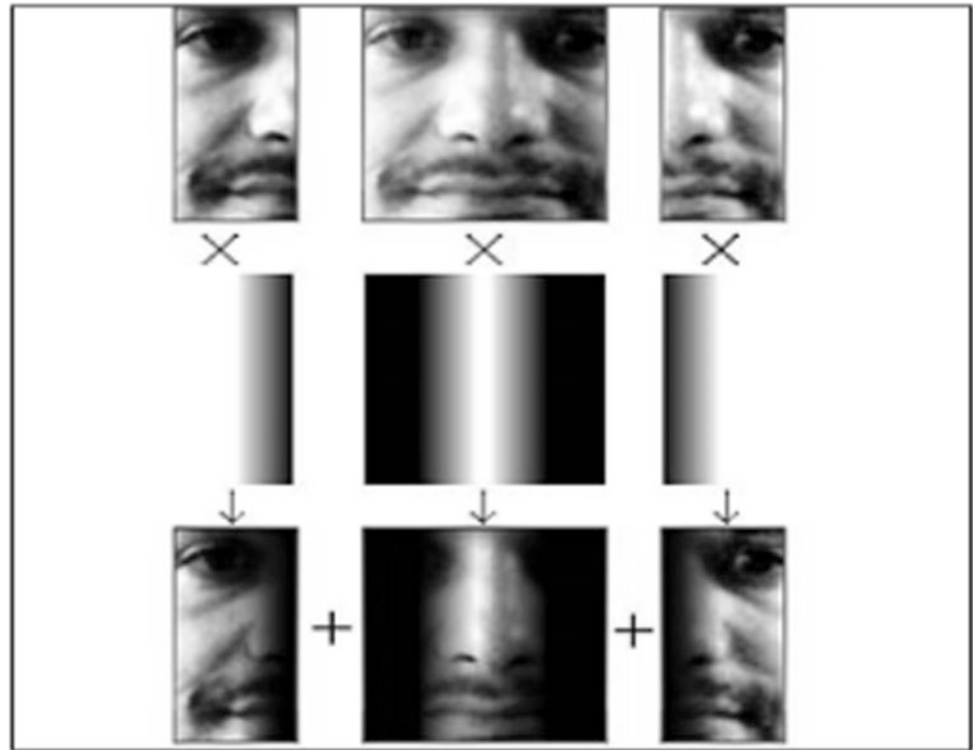


Fig. 6 Algorithm flowchart

Table 1 Application's specifications in real-time mode

Parameters	Value
Distance operation range (face is only detected within this range)	15–55 cm
Optimal operating distance (for highest accuracy)	35 cm
Frame size	640 × 480
Frame per second average	20
Frame per second maximum	22
Frame per second minimum	18
Brightness operation range	30–400 lx
Optimal operating brightness	200 lx
Video source	From camera

Table 2 FPS in different brightness environments

Room brightness	Max FPS	Average FPS
Full-light room (200 lx)	20	19
Half-light room (100 lx)	18	17
Room without light (40 lx)	15	14

4.2 Experiments

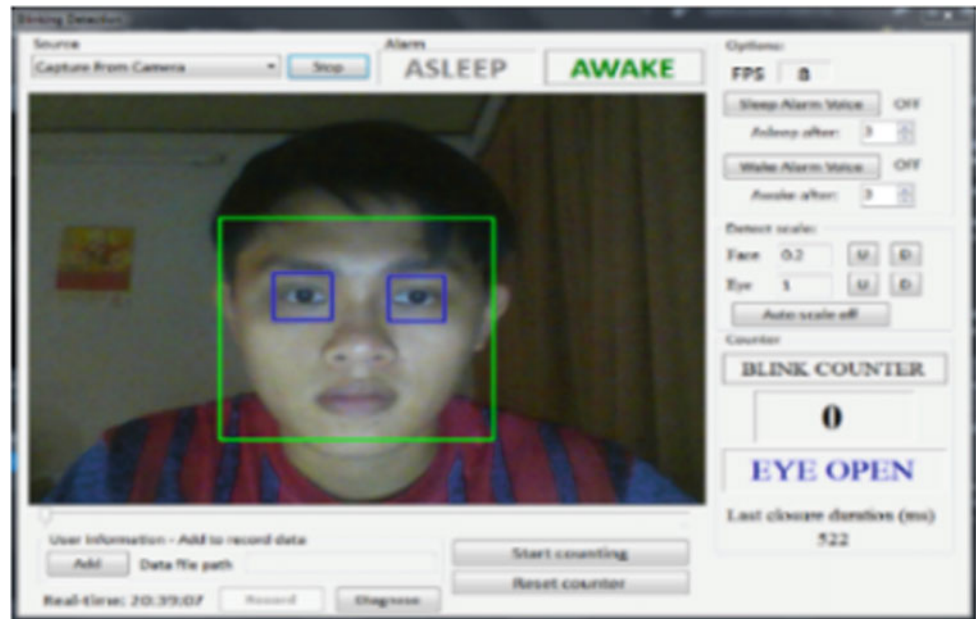
We check the correctness of this application on three different objects by manually counting the number of blinks. For 480p videos, FPS is at 25 and would be 11 with Full-HD (1080p) videos. Full-HD make FPS decrease but the detection is more accurate. In Table 2, the FPS is the result in different brightness environments. In Table 3, we calculated the error percentage per case. The average error percentage of this app is around 9%.

5 Additional Features

5.1 Support Features

As mentioned, the program supports source video from a real-time camera or video by selecting on the application. The external interface supports real-time observation. The interface is shown in Fig. 7.

Fig. 7 Detecting eyes in real-time on our app



5.2 Diagnosis of Eye Condition

We choose the mean of lid-contact rate and the mean duration of lid closure/blink as parameters. Based on above table [8], we realize that these parameters differ noticeably between normal eyes and dry eyes. For each parameter, we classify closure into 3 different groups depending on the duration of eyes closure. Specifically, we have 3 groups as follows: all full lid closure (>0 s in duration)—type I, extended lid closures (>0.1 s in duration)—type II—and

super-extended lid closures (>0.5 s in duration)—type III. In total, we have six parameters to measure, corresponding to six conditions within the value of confidence interval that need to be verified. Then we split them up into 3 cases that the eye can encounter. That is “Non Dry Eyes”—when only meet below 2 conditions, “Dry Eyes Potential”—when meet from 2 to 4 conditions, and the rest is Dry Eyes. Table 5 are the results of eyes examination and result of this test is: Dry Eyes Potential (Table 4).

Table 3 The accuracy when measuring blinking

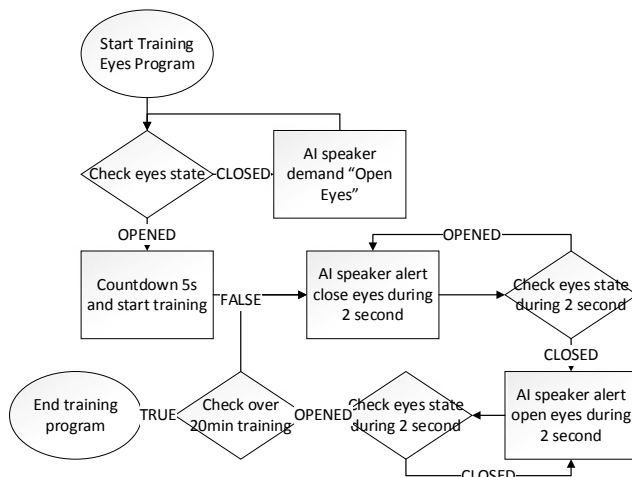
Category	Brightness (lux)	Blink measured	Blink actuality	Error percentage
Object 001	~40	18	20	10
Object 002	~40	20	20	0
Object 003	~100	24	20	20
Object 004	~100	20	20	0
Object 005	~200	20	23	15

Table 4 Sample of normal eyes [7]

Category	Type of blink	95% Confidence interval
The contact rate	All full lid closure	2.47–16.46
	Extended lid closure	3.35–47.26
	Super-extended lid closure	17.73–113.16
Mean duration of lid closure/blink (s)	All full lid closure	2.46–20.33
	Extended lid closure	1.65–11.07
	Super-extended lid closure	3.28–6.15

Table 5 Result of our measured information on 3 different objects

Category	Patients		
Name	Object 001	Object 002	Object 003
Age	21	17	21
Gender	Male	Male	Male
Examine time	25/06/2017 7:39:36	06/07/2017 20:22:16	06/07/2017 15:16:12
Duration of the test	110	113	120
Number of closure type I	42	53	21
Number of closure type II	19	12	12
Number of closure type III	4	0	1
Contact rate closure type I	6.70228	3.54713	2.431
Contact rate closure type II	5.54223	1.38272	1.82283
Contact rate closure type III	2.18019	0	0.5721
Mean duration of type II	0.321105	0.13075	0.181083
Mean duration of type III	0.6	0	0.682

**Fig. 8** Algorithm flowchart for eyes training programs

5.3 Healthy Eyes Training Programs

Based on [9], the training program includes the following steps: the user close both eyes for 2 s normally. and then open the eyes for 2 s. Moreover, people should do this exercise 20 times daily to get healthy eyes (Fig. 8).

Moreover, users should do this exercise 20 times daily to get healthy eyes.

6 Conclusion

In this paper we had introduced a real-time eyes blink detection system, consist of many techniques like Haar-like Feature, image preprocessing, etc. Thanks to that, this system allows us detect blinking eyes precisely. Furthermore,

we had boosted the number of Frame Per Second to enable working in real-time environment like video surveillance system. First of all, we apply a smaller region of interest (ROI) by using Haar-like Feature for face detection, then we equalize the histogram of ROI to enhance detect ability and apply Haar-like Feature for eye detection lastly. From then, by checking eye detected or not, we can easily verify that eyes are opened or closed.

Specially, only with a cheap camera or low resolution video, we had come up with a system that automatically counts number of times a patience blinks in a medical examination. We create a patient management tool that enable doctor to track status or number of times blink of each patience. Then, we proposed a parameter list that help doctors diagnose dry eyes diseased based on related parameters like the contact rate and the mean of duration per type of blink. Besides, we also offer a warning system to check if a patient is asleep or awake. Thanks to this feature, doctor can easily track the activities or warning patients automatically to avoid many eyes diseased.

Conflict of Interest The authors declare that they have no conflict of interest.

References

1. Viola, P., Jones, M.: Rapid object detection using a boosted cascade of simple features. In: Proceedings of the 2001 IEEE Computer Society Conference on Computer Vision and Pattern Recognition. CVPR 2001, vol. 1, pp. I-511–I-518 (2001)
2. Morris, T., Blenkhorn, P.: Blink detection for real-time eye tracking. *J. Netw. Comput. Appl.* **25**, 129–143 (2002)
3. Martinez-Zarzuela, M., D'iaz-Pernas, F.J., Ant'ón-Rodr'iguez, M.: AdaBoost face detection on the GPU using haar-like features. In:

- IWINAC'11 Proceedings of the 4th International Conference on Interplay Between Natural and Artificial Computation: New Challenges on Bioinspired Applications, vol. Part II, pp. 333–342 (2011)
4. Ito, Y., Ohya, W., Wakabayashi, T., Kimura, F.: Detection of eyes by circular hough transform and histogram of gradient. In: 21st International Conference on Pattern Recognition, ICPR, Japan. pp. 1795–1798 (2012)
 5. Freund, Y., Schapire, R.E.: A short introduction to boosting. *J. Jpn. Soc. Artif. Intell.* (1999)
 6. Fernandez, J., Wilson, P.I.: Facial feature detection using Haar classifiers. *J. Comput. Sci. Coll., JCSC* **21**(4), 127–133 (2006)
 7. Baggio, D.L., Emami, S., Escrivá, D.M., Ievgen, K., Mahmood, N., Saragih, J., Shilkrot, R., et al.: *Mastering OpenCV with Practical Computer Vision Projects*, 1st edn. Packt Publishing, Birmingham, UK (2012)
 8. Ousler 3rd, G.W., Abelson, M.B., Johnston, P.R., et al.: Blink patterns and lid-contact times in dry-eye and normal subjects. *Clin. Ophthalmol.*, **8**, 869–874 (2014)
 9. Dry eye sufferers try blinking exercises app, <http://www.skyvisioncenters.com/blog/dry-eye-sufferers-try-blinking-exercises-app/>. Last accessed 15 Apr 2018

Edge Detection in Low-Quality Medical Images Based on Augmented Lagrangian Method and B-Spline

Vo Thi Hong Tuyet, Nguyen Thanh Binh, and Nguyen Chi Thanh

Abstract

Medical images are very important for the treatment process of specialists because of containing a lot of important information in patient's body. The edge detection is a prepared process for object boundaries. Therefore, the edge detection in medical images is very important and necessary with low-quality medical images. Other previous methods must sacrifice time to have the accurate results. In this paper, we proposed a new method to detect edges in low-quality medical images which have impurities by using augmented Lagrangian method and B-spline. Our method improves the ability for smoothing and detecting faster.

Keywords

Edge detection • Augmented lagrangian method • B-spline • Low-quality medical images

1 Introduction

We cannot deny the usefulness of medical images in this life. So, their quality is very noticeable for using. Because the diagnosis or the treatment process also depends on the

quality and strong objects, the medical images which have clear objects will give much useful information about boundary, size or the limit between objects in images. In computer vision, the edge detection is a preparatory step for contour detection or segmentation. A medical image contains one or more objects. They have noised or blurred pixels or both, and they are called as weak objects, low-quality medical images. So, in low-quality medical images, it is a great obstacle for image processing. However, when the edge detection or segmentation has no good results, the limit between boundaries of objects is not clear. This is a difficult problem for specialists. The limit can refer as fracture, enlargement or tumor.

In the past, there are many algorithms which are proposed for edge detection [1]. But the usefulness of B-spline in [2–4] shows that this is an appropriate method. After that, the transform, such as wavelet transform [5] is continued for process. Although transform gives good results to remove noise, blur pixels, and improves the quality of images [6, 7]. But the previous methods are limited with weak objects in medical images. Curvelet transform could overcome this disadvantage and keep much information of medical images for specialists, but the time processing was very long. In recent years, the snake is proposed for active contour which has edge detection step in [8] or the combination with curvelet in [9]. And Cuckoo search [10, 11] is also to give many notes. With the comeback of B-spline surfaces [12] is a wind revived to detect sharp edges. We repeat about the slow time in processing. Although it can be accepted in medicine as long as the result is good. However, the time can be smaller, the life can be longer. With this problem, augmented Lagrangian method [13] is a good resolution.

In this paper, we propose a new method to detect the edges in low-quality medical images. The proposed method included two periods. Firstly, we use Augmented Lagrangian method (ALM) to remove noise and detect edges in low-quality medical images. Secondly, the ALM coefficients and B-spline curve are also calculated in there. And finally is the comparison between distances to choose the showing

V. T. H. Tuyet (✉) · N. C. Thanh
Faculty of Information Technology, Ho Chi Minh City Open
University, Ho Chi Minh City, Vietnam
e-mail: tuyet.vth@ou.edu.vn

N. C. Thanh
e-mail: thanhngch1982@gmail.com

N. T. Binh
Faculty of Computer Science and Engineering, Ho Chi Minh City
University of Technology, VNU-HCM, Ho Chi Minh City,
Vietnam
e-mail: ntbinh@hcmut.edu.vn

edges. The contributions of this paper are: to introduce the problems that exist; to present the basic concept about edge detection, ALM and B-spline; to propose a new method for edge detection in low quality medical images. The rest of this paper is as follows: the basic concepts are presented in Sect. 2. The proposed method is described clearly in Sect. 3. Our experiments and results are accentuated in Sect. 4, and conclusions is presented in final section.

2 Basic Knowledge

2.1 Edge Detection

The boundary of two different regions in an image is called edges. The difference is between the colors or gray, with medical images is usually gray. The purpose of edge detection is to keep the important features of the combination pixels together, such as: lines, corners, curves, etc. The combination of pixels to strong or weak also presents acreage of objects. Edge detection includes four steps [14], as follows:

Firstly, the smoothing. This is to remove noise from the input images but it must keep the features of edges. In this step, it bases on the types of noisy or blur or both. The truth is the suitability between pixels and filters or threshold.

Secondly, the enhancement. We use the filters to improve the quality of edges. By the values of the calculating, the input images are improved.

Thirdly, the detection. The thresholding is the basis of the detection. And *finally* is localization. This step bases on the location of each edge.

Edge detection bases on estimating the gradient: strength the combination, gradient direction by -90° . The gradient is the two-dimensional (2D) equivalent of the first derivate and is defined as the vector:

$$G[f(x, y)] = \begin{bmatrix} G_x \\ G_y \end{bmatrix} = \begin{bmatrix} \frac{\partial f}{\partial x} \\ \frac{\partial f}{\partial y} \end{bmatrix} \quad (1)$$

where, vector $G[f(x, y)]$ points in the direction of the maximum rate of increase of the function $f(x, y)$. And the direction of the gradient is defined as:

$$\alpha(x, y) = \tan^{-1} \left(\frac{G_y}{G_x} \right) \quad (2)$$

where α is measured with respect to the x axis. In this process, the smoothing and detection base on the threshold. So, the threshold is very important for this.

2.2 Augmented Lagrangian Method

Augmented Lagrangian method (ALM) depends on the idea to minimize a total variation optimization problem for spatial temporal data [13]. It is used to solve the constrained problem in image or video processing but, the main problem which [13] solves to be denoising and deblurring in video.

A vector denoting the unknown (potentially sharp) image which has size $M \times N$ is called f ($f \in R^{MN \times 1}$). f is an ingredient of equation to find the observed image g , $g \in R^{MN \times 1}$. It is a linear shift invariant imaging system to calculate as:

$$g = Hf + \eta \quad (3)$$

where, f is a vector denoting the unknown (potentially sharp) image of size $M \times N$, g is a vector denoting the observed image, $\eta \in R^{MN \times 1}$ is a vector denoting the noise/blur, and the matrix $H \in R^{MN \times MN}$ is a linear transformation representing convolution operation.

Two problems were mentioned to define as:

$$\text{minimize}_f \frac{\mu}{2} \|Hf - g\|^2 + \|f\|_{TV} \quad (4)$$

and

$$\text{minimize}_f \mu \|Hf - g\|_1 + \|f\|_{TV} \quad (5)$$

where, μ is the regularization parameter.

The authors were to find a saddle point of $L(f, u, y)$. Then, they used the alternating direction method (ADM) to solve f -subproblem, u -subproblem and r -subproblem. This algorithm can be summarized as follows in Fig. 1.

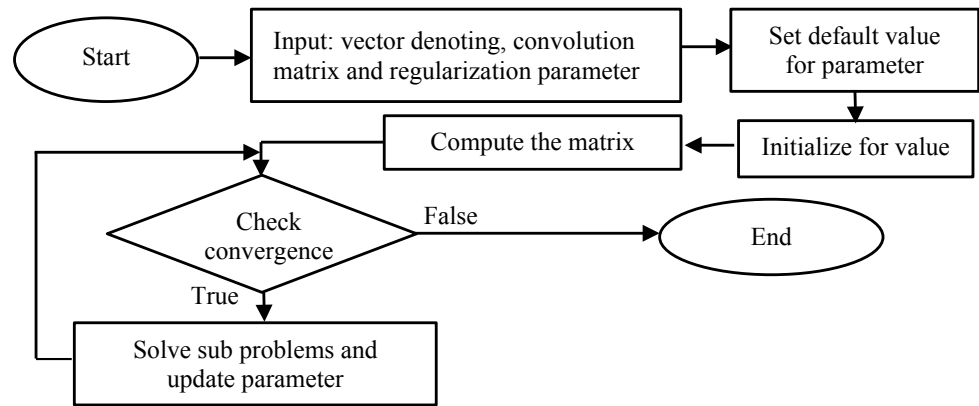
2.3 B-Spline and Curves

Similar to Bézier curve, a parametric curve, the B-spline curve [2] gives more information and very fit for medical images. B-spline, basis spline, can be used for curve-fitting and numerical differentiation of data. From the set of $(n + 1)$ control points, knot vector of $(m + 1)$ knots and a degree p . But must satisfy: $m = n + p + 1$. The B-spline curve of degree p ($N_i, u(u)$) defined by these control points and knot vector U is:

$$C(u) = \sum_{i=0}^n N_{i,p}(u)P_i \quad (6)$$

where, $(n + 1)$ control points P_0, P_1, \dots, P_n and a knot vector $U = \{u_0, u_1, \dots, u_m\}$.

$N_i, u(u)$ looks like $B_n, i(u)$. The basis function of Bézier bases on the number of control points and B-spline with the

Fig. 1 The augmented lagrangian method

smoothing function $\beta_{2^{-1}}^{n+1}$ and $\beta_{2^{-1}}^{n+2}$ uses 2^{-1} level. In these function, n is the order of wavelet transform. We can see B-spline to create the smooth curves. It calls knots or breakpoints in images, but must be in non-descending of locations. The calling process is the range between the first and last of these knots and may be zero elsewhere. The knots have the same distance from predecessor. Then, the surfaces of degree can be defined as the condition statement. And this statement shows or not to base many in u values, similar to the presentation of threshold or filter in image processing.

3 Edge Detection in Low-Quality Medical Images

Many algorithms had proposed to detect edges in medical images. In [2–4], the B-spline curve is used for detection. And, [5, 7] are the using transform—spatial domain—for this process. The reason of using transform because of the positive results of them in denoising [6] is useful for smoothing step. In recent, the B-spline surface appears in [12] to detect sharp edges. We notice that: any methods based on transform are to use much time to detect edges. Although the time can be sacrificed in medical treatment, the speed is necessary.

In the proposed method, ALM is used for the smoothing step and based on this value to enhance the quality of medical images. After that, we use B-spline curve for the combination between edges and show the edge detection of output images. The proposed method is presented clearly in Fig. 2.

In the smoothing and enhancing step, ALM has many input values: vector denoting the observed image, convolution matrix, regularization parameter and the isotropic total variation. The default value is set for parameter. And the step continues with the computation the matrices of the first-order forward finite difference operators along the horizontal, vertical and temporal directions. Then, it is the check coverage and update parameter as Fig. 1. In here, the problem to be solved is the:

$$\text{minimize}_{f,r,u} \mu \|r\|_1 + \|u\|_1 \quad (7)$$

to solve the problem of (7), we perform sequentially as:

- (i) We call g is vector denoting the observed image, H is the convolution matrix, μ is the regularization parameter the isotropic total variation $\beta_x, \beta_y, \beta_t$, go to (ii) step.
- (ii) Set parameter with value default for $\rho_r = 2, \rho_0 = 100$ (ρ_r is a regularization parameter) and $\alpha_0 = 0.7$, next to (iii) step.
- (iii) Initialize $f_0 = g, u_0 = Df_0, y_0 = 0, r_0 = Hf_0 - g, z_0 = 0$. (where, y is the Lagrange multiplier), go to (iv).
- (iv) Compute the matrices of the first-order forward finite difference operators along the horizontal, vertical and temporal directions. And begin the loop statements:

While (not coverage) do:

+ Solve the f-subproblem is:

$$\text{minimize}_f = \frac{\rho_0}{2} \|r - Hf + g\|^2 + \frac{\rho_r}{2} \|u - Df\|^2 + z^T Hf + y^T D \quad (8)$$

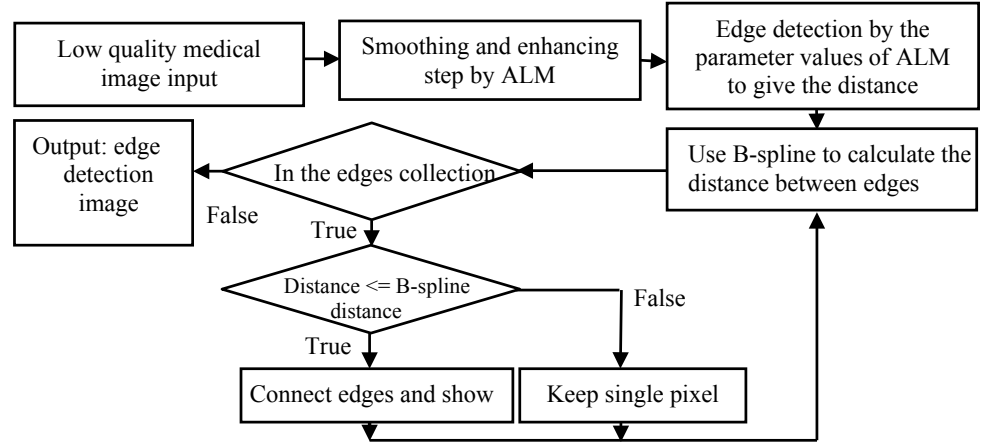
where, $D = [D_x^T \ D_y^T \ D_t^T]^T$, D_x, D_y, D_t are the first—order forward finite-difference operators along the horizontal, vertical, and temporal directions.

f-subproblem is improved by equation:

$$f = \mathcal{F}^{-1} \left[\frac{\mathcal{F}[\rho_0 H^T g + H^T (\rho_0 r - z) + D^T (\rho_r u - y)]}{\rho_0 |\mathcal{F}[H]|^2 + \rho_r (|\mathcal{F}[D_x]|^2 + |\mathcal{F}[D_y]|^2 + |\mathcal{F}[D_t]|^2)} \right] \quad (9)$$

where, \mathcal{F} denotes the three-dimensional Fourier Transform operator.

+ Solve the u-subproblem is:

Fig. 2 The proposed method

$$u_{k+1} = \arg \min_u \|u\|_1 - y_k^T(u - Df_{k+1}) + \frac{\rho_r}{2} \|u - Df_{k+1}\|^2 \quad (10)$$

by Eq. (11):

$$u_x = \max \left\{ |v_x| - \frac{1}{\rho_r}, 0 \right\} * \text{sign}(v_x) \quad (11)$$

+ Solve the r-subproblem:

$$\text{minimize}_r \mu \|r\|_1 - z^T r + \frac{\rho_0}{2} \|r - Hf + g\|^2 \quad (12)$$

by equation:

$$r = \max \left\{ \left| Hf - g + \frac{1}{\rho_0} z \right| - \frac{\mu}{\rho_0}, 0 \right\} * \text{sign} \left(Hf - g + \frac{1}{\rho_0} z \right) \quad (13)$$

+ Update the Lagrange multiplier y and z:

$$y_{k+1} = y_k - \rho_r (u_{k+1} - Df_{k+1}) \quad (14)$$

and

$$z_{k+1} = z_k - \rho_0 (r_{k+1} - Hf_{k+1} + g) \quad (15)$$

+ Update:

$$\rho_r = \begin{cases} \gamma \rho_r, & \text{if } \|u_{k+1} - Df_{k+1}\|_2 \geq \alpha \|u_k - Df_k\|_2 \\ \rho_r, & \text{otherwise} \end{cases} \quad (16)$$

+ Check convergence: if $\|f_{k+1} - f_k\|_2 / \|f_k\|_2 \leq \text{tol}$ then break

End while.

$$\psi^n(x) = \frac{d}{dx} \beta_{2^{-1}}^{n+1}(x) = 4(\beta^{n+1})^{(1)}(2x) \quad (17)$$

$$\psi^n(x) = \frac{d^2}{dx^2} \beta_{2^{-1}}^{n+2}(x) = 8(\beta^{n+2})^{(2)}(2x) \quad (18)$$

where, n is the order of wavelet transform. The distance measure is the Euclidean equation (E), edge strengths, as:

$$E = \left(\sum_{i=1}^n |x_i - y_i|^2 \right)^{1/2} \quad (19)$$

where, x and y are the coordinates of image pixels.

The B-Spline curves and surfaces of degree is defined as Eq. (20) for degree zero and other degree (p) as Eq. (21):

$$N_{i,0}(u) = \begin{cases} 0, & \text{if } u_i \leq u \leq u_{i+1} \\ 1, & \text{otherwise} \end{cases} \quad (20)$$

$$N_{i,p} = \frac{u - u_i}{u_{i+p} - u_i} N_{i,p-1}(u) + \frac{u_{i+p+1} - u}{u_{i+p+1} - u_{i+1}} N_{i+1,p-1}(u) \quad (21)$$

Based on the values of B-spline distance, we apply this for the showing results. From the edge collection which collects from ALM to compare with E distance (19). If true for the condition as in Fig. 2, the proposed method uses Eqs. (20) and (21) to show edges. If false, our idea will only keep pixel values and show. And finally, the results of algorithm are the low-quality medical images which are detected edges.

4 Experiments and Results

After the smoothing and enhancing step, the distance values is calculated by B-spline. Equation (17) is the equation of B-spline curve with 4-scales and Eq. (18) with 8-scales:

Based on the method which is presented in previous section clearly, our experiments are developed in Matlab 2013b and carried out on computer of Intel core i5, 2.4 GHz CPU and 08 GB DDR memory. Our dataset is the medical images

collected in many hospitals. There are more than 600 medical images and in many sizes: 256×256 , 512×512 . We test many medical images from this dataset. Our dataset has many types of quality of medical images also is difference. Some images have strong objects, but others are weak objects because of many reasons. But the quality of them is very difficult for edge detection.

As mentioned in Sect. 3, we improve the smoothing step quality by ALM. After that, we detect the strong points and connect the strong point together based on the coefficients of ALM to enhance the quality of low-quality medical images. We implement the proposed method and compare its results to wavelet transform method [5] (WT), Cuckoo method [11] and the bicubic B-splines surfaces method [12]. The results of our proposed method are to detect many edges more than other methods. Specially, the time processing of our method is the shortest. In Fig. 3, we report the results from some images. In these figures, we observe that the proposed method performs well.

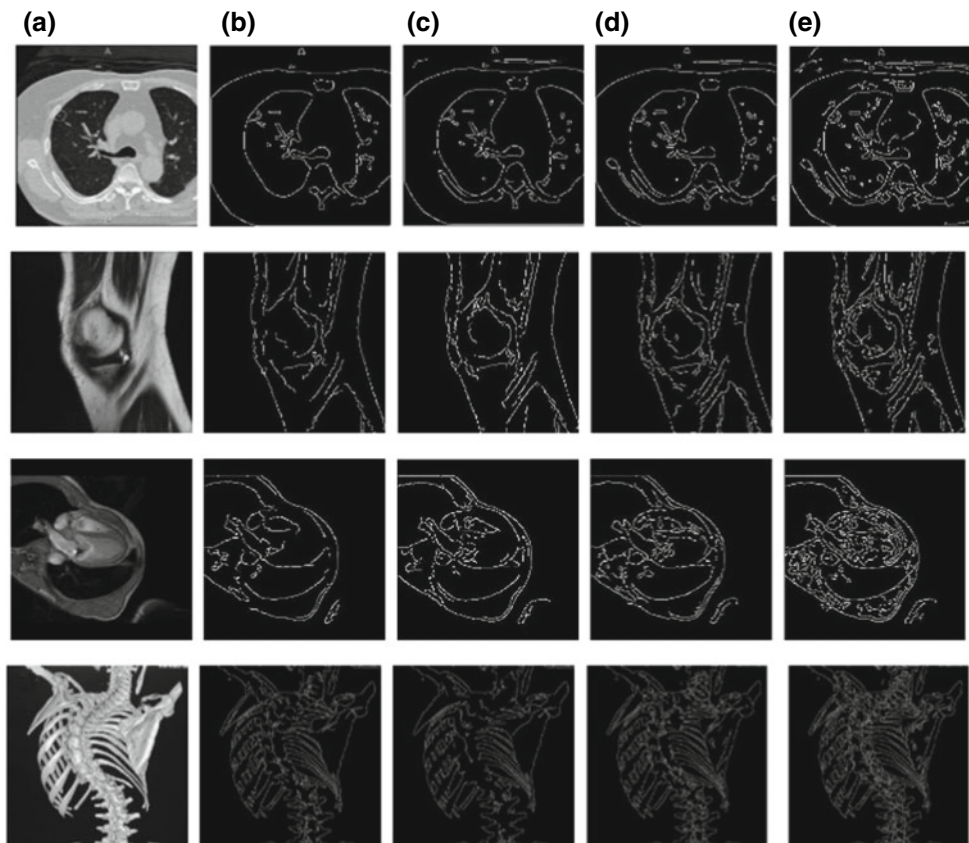
Figure 3a is the original medical images. The edge-detection result of wavelet transform method [5] is to

present in Fig. 3b. The result of Cuckoo method [11] is to present in Fig. 3c. The result of the bicubic B-splines surfaces method [12] is to present in Fig. 3d and of the proposed method is to present in Fig. 3e.

In Fig. 3e, the number of edges detection is better than the result in Fig. 3b, c, d. And the average time processing of Fig. 3e is the shortest between all methods.

We can see the quality of medical images in dataset is not good. This is low-quality medical images and they have weak objects. However, the proposed method has detected many strong edges and faster than the other methods, such as: wavelet transform method, Cuckoo method and the bicubic B-splines surfaces method. With medical images, the number of edges is useful for the next process such as: contour detection or segmentation. The edges are detected to be the important pixels. They are connected by the curves or transform. With natural images, the weak objects can found and not useful. However, medical images must keep many edges because any the change may be a sign of disease. The reason of the results of the proposed method which are better and faster than the other methods can explain as follows:

Fig. 3 The results of edge detection by the proposed method and the other methods in low quality medical images. **a** The original medical images. **b** Edge detection by WT [5] with the average time processing ~ 1.752 s and ~ 2342 edges. **c** Edge detection by Cuckoo method [11] with the average time processing ~ 1.611 s and ~ 2910 edges. **d** Edge detection by the bicubic B-splines surfaces method [12] with the average time processing ~ 1.32 s and ~ 3562 edges. **e** Edge detection by the proposed method with the average time processing ~ 0.937 s and ~ 4582 edges



Firstly, ALM is used in first, smoothing and enhancing step, to be necessary. The quality of low-quality medical images has improved and made from weak into strong objects.

Secondly, we calculate distance between edges two times by ALM coefficients and E distance (in B-spline curve). We compare them and choose less distance. Because the medical images differ from other type of images, medical images have much information and easy to lost this. We choose less distance to keep the close together. This is a method to keep the precious information of input images.

Finally, on the other hand, the proposed method does not use transform or threshold or filter to combine together. The images do not fit with many coefficients. And also do not use the time for the decomposition and reconstruction.

5 Conclusions

In medical images, the adaptation of threshold and filter is a big problem. Because of their complex, any image processing is to lose much important information and to use much time for processing. The proposed method used ALM and B-spline for edge detection. With medical images, ALM can denoise faster and better with low-quality images. Then, B-spline gives better results for connecting edges together. The results of the proposed method are compared with other methods such as: Cuckoo Search method [11], wavelet transform method [5] and the bicubic B-splines surfaces method [12]. The comparison of the results shows that the proposed method detects more edges than other methods. Specially, the time processing of proposed method is the shortest.

Acknowledgements This research is funded by Vietnam National University Ho Chi Minh City (VNU-HCM) under grant number C2017-20-20.

Conflict of Interest The authors declare that they have no conflict of interest.

References

1. Zhai, L., Dong, S., Ma, H.: Recent methods and applications on image edge detection. In: International Workshop on Geoscience and Remote Sensing, pp. 332–335 (2008)
2. Wang, Y., Cai, Y.: Multiscale B-spline wavelet for edge detection. *Sci. China (Series A)* **38**(4), 499–512 (1995)
3. Bhatt, A.D., Warkhedkar, R.V.: Reverse engineering of human body: a B-Spline based heterogeneous modeling approach. *Comput. Aided Des. Appl.* **5**, 194–208 (2008)
4. Bhatt, A.D., Warkhedkar, R.V.: Material-solid modeling of human body: a heterogeneous B-Spline based approach. *Comput. Aided Des.* **41**, 586–597 (2009)
5. Zhang, L., Bao, P.: Edge detection by scale multiplication in wavelet domain. *Pattern Recogn. Lett.* **23**, 1771–1784 (2002)
6. Binh, N.T., Tuyet, V.T.H.: The combination of adaptive filters to improve the quality of medical images in new wavelet domain (Chap. 3). In: Classification and Clustering in Biomedical Signal Processing, pp 46–76. IGI Global Publication (2016)
7. Moslemi, A., Movafeghi, A., Moradi, S.: CT medical images denoising based on new wavelet thresholding compared with curvelet and contourlet. *Int. J. Comput. Electr. Autom. Control Inf. Eng.* **9**(10), 2174–2179 (2015)
8. Saadatmand-Tarzjan, M., Ghassemian, H.: Self-affine snake for medical image segmentation. *Pattern Recogn. Lett.* **59**, 1–10 (2015)
9. Shan, H., Ma, J.: Curvelet-based geodesic snakes for image segmentation with multiple objects. *J. Pattern Recog. Lett.* **31**, 355–360 (2010)
10. Srishti. Technique based on Cuckoo's search algorithm for exudates detection in diabetic retinopathy. *Int. J. Ophthalmol. Res.* **2**(1), 43–54 (2014)
11. Gonzalez, C.I., Castro, J.R., Melin, P., Castillo, O.: Cuckoo search algorithm for the optimization of type-2 fuzzy image edge detection systems. In: IEEE Congress on Evolutionary Computation, pp. 449–455 (2015)
12. Liew, K.J., Ramli, A., Hamid, N.N.A., Majid, A.A.: Sharp edge preservation using bicubic B-spline surfaces. *ScienceAsia* **43S**, 20–26 (2017)
13. Chan, S.H., Khoshabeh, R., Gibson, K.B., Gill, P.E., Nguyen, T. Q.: An augmented lagrangian method for total variation video restoration. *IEEE Trans. Image Process* **20**(11), 3097–3111 (2011)
14. Morse, B.Y.: Edge detection. Brigham Young University (2000). <http://homepages.inf.ed.ac.uk>. Last accessed 13 Apr 2018

Analysis of the Brain's Response to Visual Stimulation in Reality and Imaginary

Tran Thanh Huy, Le Quoc Khai, and Huynh Quang Linh

Abstract

The brain always responds to any stimulations. Analyzing the correlation between imaginary and reality of stimulus signals set up a standard of the process in collecting targeted response signal. The major of this study is focused on the portable electroencephalography (EEG) device in acquisition signals. The methodology estimates the relation by using correlation coefficient and eigenvector. The results show that the correlation of signals in stimulus and imaginary is high (above 70%) and the power of imaginary signals is higher than the power of signals in stimulus.

Keywords

Imaginary • Reality • Visual stimulation • Correlation coefficient

1 Introduction

The human brain is the central organ of the human nervous system. It controls lots of the activities of the human body, processing, integrating, coordinating the information and making decisions as to send signals to the rest of the body for activities. Visual stimulation, the use of positive stimulation images such as waterfalls, sunsets, and animals are commonly used in mental and cognitive therapy. In visual function, photoreceptors in the retina receive the light, transduce the sensory stimulus of light into an electrical waves signal. Vision from the left side passes through tracts on the opposite side of the brain.

In general, despite the way of stimulation by the objects in the surrounding environments, the brain always reacts to the stimulus and creates electrical waves as a response. Particularly, the brain responds to the lights reflected by objects (such as a red car, green leaf, ...), the sound of things [1] (including the human voice, bell sounds, bird songs ...), physical and chemical stimulus [2] to generate the reality signals. The brain still reacts to the signals from organs inside (such as heart-attack, headache, stomachache ...) and mental thinking which is like imaginary as how things are reminded of. In addition, those studies were just about the stimulations and the analysis of response signals and their objectives, however, are to find false signals and new kinds of stimulation. Besides, they still have some problems in noise analysis [3] and more superior ways of controlling memories foundation [4].

In this study, the brain's response is analyzed to visual stimulation in both cases. Firstly, visual stimulus signals are recorded. This electrical wave signals may have the same form as the one created in daily, especially, the beta waves dominating the waking state of consciousness and the alpha waves being the dominant during the quiet thought. Secondly, the brain reacts to the imaginary picture, the signals are saved. Correlation analysis helps to determine the value of relationship between two variables, in this case, the visual stimulation in reality and imaginary visual stimulus. This case is to analyze both visual stimulus and imaginary response signals. The purpose is to evaluate the correlation between visual stimulus and imaginary signals.

The visual stimulates signal has the same form of the imaginary signal although the components of the spectrum are totally different. The correlation between them is at a high rate (above 0.7). If this result is right, I will find a way to stimulate the subjects' brain and to make them see the objects that I want. This may make a new effective step in Brain Computer Interface (BCI) [5] and many utilizations in controlling machines in real time by thinking.

T. T. Huy (✉) · L. Q. Khai · H. Q. Linh
Biomedical Engineering Department, Faculty of Applied Science,
Ho Chi Minh City University of Technology, Vietnam National
University, Ho Chi Minh City, Vietnam
e-mail: 1411513@hcmut.edu.vn

2 Experiments

2.1 Data Acquisition and Procedure

The data is taken from Nicolet One V32 by Natus—CareFusion—USA, which has 32 channels and is designed for contextualized research. Due to 10–20 EEG Systems [6], A1 and A2 are selected as reference electrodes; the occipital electrodes O1, O2 receive the main data of experiment and the parietal electrode Pz can help to detect changes and to support the major leading through.

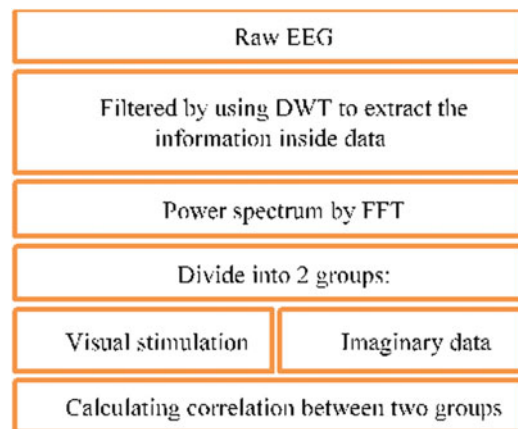
The aim of the experiment is to detect the symptoms of alpha and beta waveforms in visual and imaginary stimulus samples. The experiment is conducted in the brain electroencephalography laboratory. The subject is a 20-year-old-boy and he has no mental disease. Subjects are under relaxation as well as the way they do not concentrate on things around them in daily life. The recorded data gets through two main processing including pre-processing and correlation comparison by using Matlab.

In the first stage, the subject sits in front of the screen, his hands are free. The subject relaxes with no thinking in 4 min. In this 4-min period, he must open his eyes in one minute and close them in next one minute then repeats. It is a necessary step to remove the subjective noise, besides, it let the subject's eyes relax and adjust to the specific colors as the object should be watched later.

After the first 4-min period, the image is shown in blinking in an interval of 100 ms and faster after times. In this stage, the subject must not blink their eyes. Then the subject can relax in one minute and repeat until completing five cycles. The expectation is to stimulate the subject so that they must see the object as the way they see things in daily life, not glance at them. The black screen is shown between 2 stimulations in an interval of over 100 ms so as not to involve in the persistence of vision.

The subject must image what they see in the final stage. When he images things successfully, opens his eyes and blinks two or three times to determine the frames of the signal. They image the picture as many times as they can, at least three times in a period.

2.2 Data Analysis



The pre-processing proceeds two functions, Wavelet to cut the modified bandwidth of frequency from 8 to 30 Hz. This range is the fundamental frequency band and represents the most basic characteristics of the states. Because of awakening statements of the subject, the frequency bandwidth should be focused on is from 8 to 30 Hz. The result is the distributed according to the cut-off frequency [7, 8].

The Fast Fourier Transform (FFT) can provide the information about the signal frequency quickly and accurately [9]. The Discrete Wavelet Transform helps to filter the noise and to extract the data in the time-domain [10].

Applying the FFT on modified data to check the bandwidth of the signals and form of signals' volume. This process is required to recheck the filtered noise removed, to distinguish the noise and to identify the beta waves in the data, especially the beta 1 and beta 2 from 13 to 20 Hz.

The power spectrum of alpha (7–14 Hz) and beta (15–20 Hz) wave is used to determine the signal in phases. The data consists of 5 visual stimulus samples and 1 imaginary sample for a subject. Also, there are 22 image signals in a visual stimulation period and 3 in an imaginary period. Therefore, a data contains about 110 visual stimulation and 3 imaginary samples. The data is divided into 2 groups called a 'visual stimulation' and 'imaginary', as a result of time marked, it is easy to be seen and calculated.

The main purpose of this step is to calculate the correlation coefficient (CC). The range of value of the CC is from -1.0 to 1.0 . A correlation value of -1.0 indicates a perfect negative, while a value of 1.0 means a perfect of positive [11]. As a result of evaluating CC value, the similarities between stimulation signals are appraised more precisely.

3 Discussion

The recorded data is grouped into 2 groups, 'visual stimulus signal' and 'imaginary stimulus signal'. Then, they are filtered to be in the bandwidth of alpha and beta waves. After that, FFT applies to the data to transform the signals into the frequency domain. As a result, elements of alpha and beta waves can be identified precisely.

In Fig. 1, the two graphs show the signal form in time-domain. Stimulation signal can be found instantly because of markers. The second graph shows the information of alpha (from 7 to 14 Hz) and beta (from 14 to 30 Hz) at the same time. The red line shows the shape of the alpha wave and the beta wave is plotted with green dot and these are the spectrums of them in the frequency domain.

In Fig. 2, both alpha and beta waves are shown in the frequency spectrum of visual stimulus and imaginary data. In visual stimulation period, the alpha spectrum has a higher percentage of the value than the beta. Besides, the alpha spectrum, from 7 to 14 Hz, is absolutely stronger than the spectrum of low-beta, between 15 and 19 Hz. Thus, it is

identified that the subjects are totally relaxed when they are in visual stimulation period. They do not have to concentrate on what is shown on the screen. Also, this statement is like the way people reacts as they look at things in the environment in their daily life.

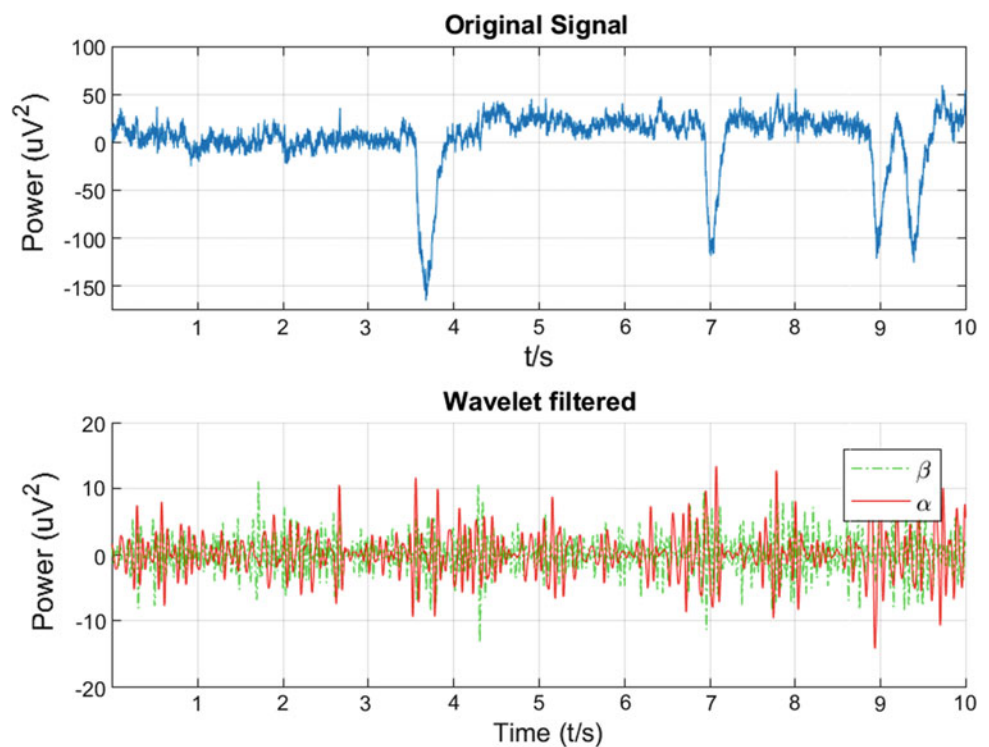
However, in the frequency spectrum of the imaginary group, both alpha and beta waves have a high amplitude. Especially, the extremely high spectrum is around 16 Hz, within the low-beta range. This can be seen as an effect of imaginary practices. While imaging the object, the subjects have to close their eyes and image it as much as they can. Besides that, the subjects have to close their eyes, this may make alpha waves increased its amplitude in the frequency spectrum. Also, the subjects try to image the picture, this causes the high amplitude of beta waves (Fig. 3).

As a result of the graphs, the alpha wave always shows the higher percent in the visual stimulus period while the beta gets the lower percentage. Particularly, in this period, the objects are in an awakening statement, they just look at the picture without thinking. The element of alpha has a stronger signal than beta in this state. In contrast, in the period of imaginary, the low-beta has the higher percentage of the spectrum. The element of the beta wave is usually stronger when subjects think about something, particularly, they think about the object.

In Fig. 4, most of the samples have the latency time while the others do not have it.

The visual stimulus signals are shown as blue and the imaginary signals are red lines. In Fig. 4, both graphs show the

Fig. 1 The original data is recorded by Nicolet V32 Amp and filtered by using DWT



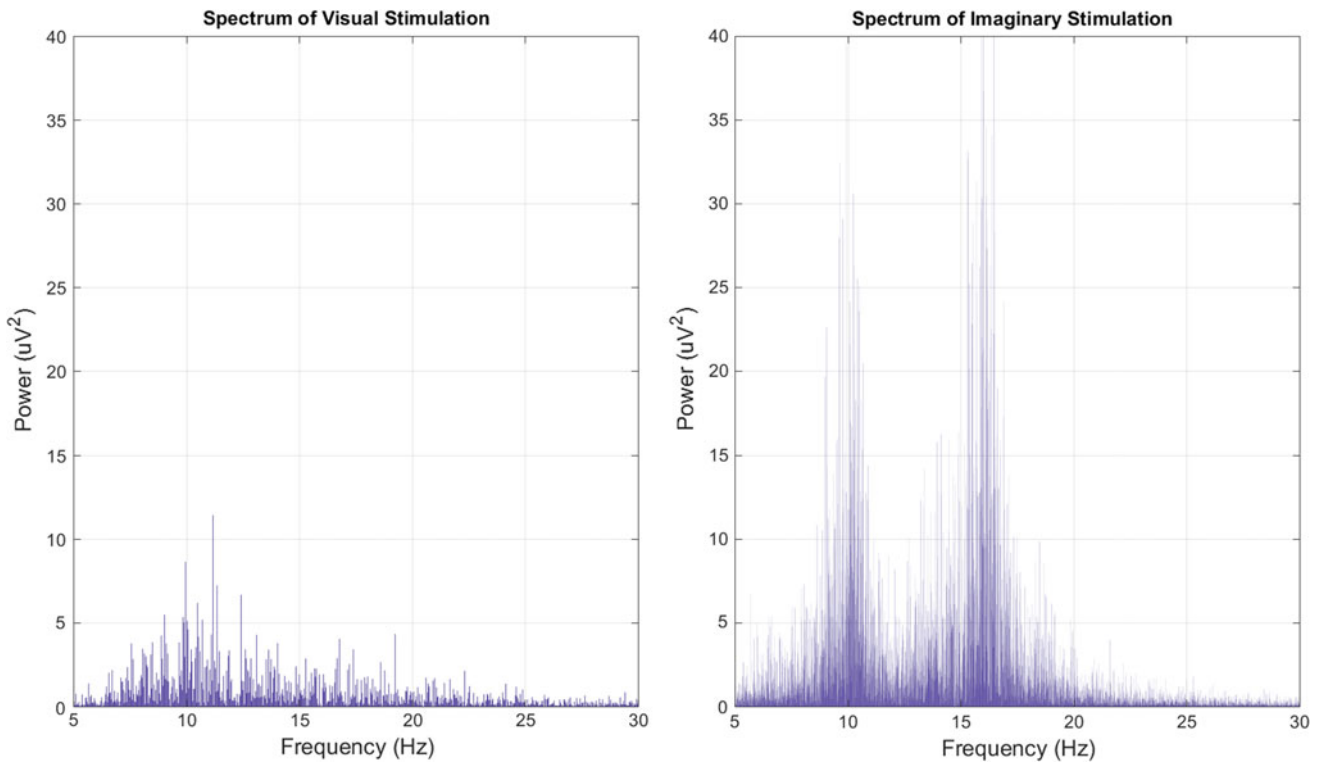


Fig. 2 The graphs demonstrate the power spectrum of signals of visual stimulus (on the left side) and imaginary (on the right side). Both signals are filtered by the same bandwidth of DWT, from 7 to 30 Hz

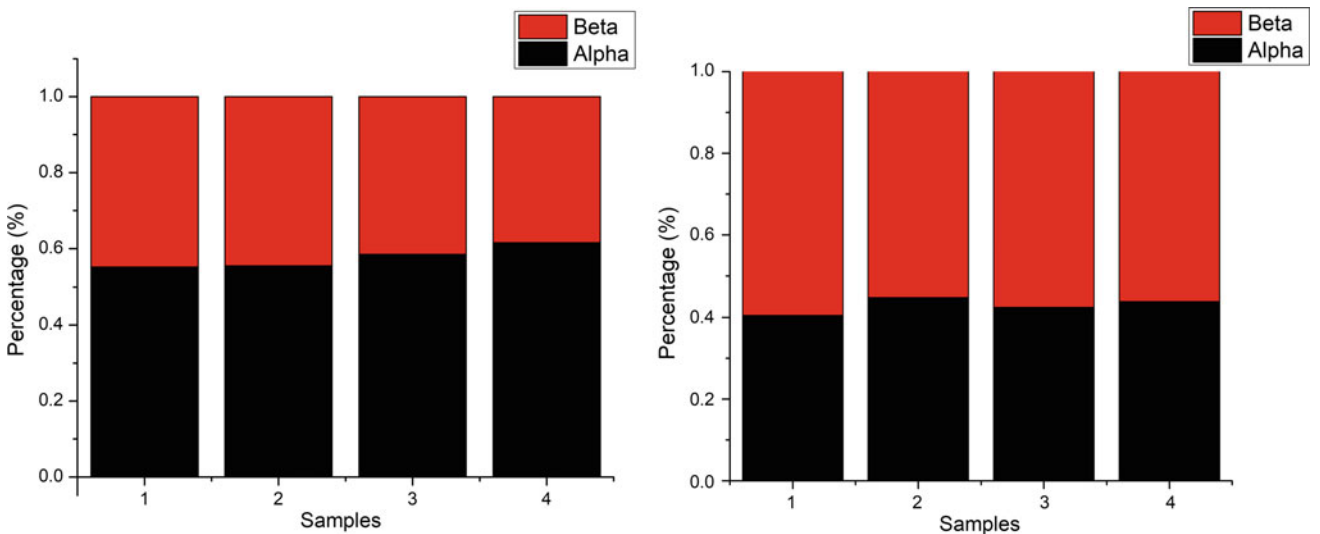


Fig. 3 The graphs illustrate the spectrum percentage of alpha and beta waves in samples. On the left side, it shows the information in visual stimulation data while it is the imaginary information on the right side

stimulation signals and they have the same shape. On the first graph, the signals of visual stimulation and imaginary are slightly different in shape and amplitude. Particularly, the visual stimulation peak happens earlier than that of imaginary. This may be the cause of hard imagination, the subjects need time to image the object sharply. As a result, the first pair's

correlation value (on the left) is approximate 0.55. Meanwhile, on the second graph, the time and shape of the pair are quite similar. The difference is only the amplitude, the amplitude of imaginary is weaker than the one of visual stimulation, this may be caused by the familiar to the action. As a result, the CC of the sample in the right graph is around 0.95 (Fig. 5).

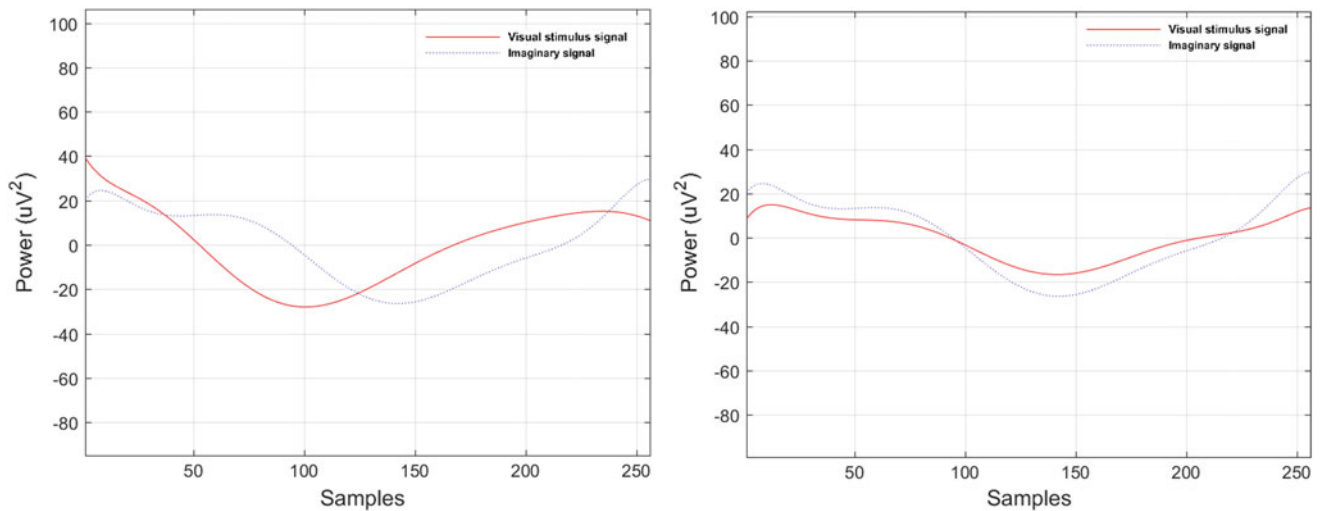


Fig. 4 The graphs demonstrate troughs covering the stimulus signals, between a visual stimulus signals and two imaginary signals

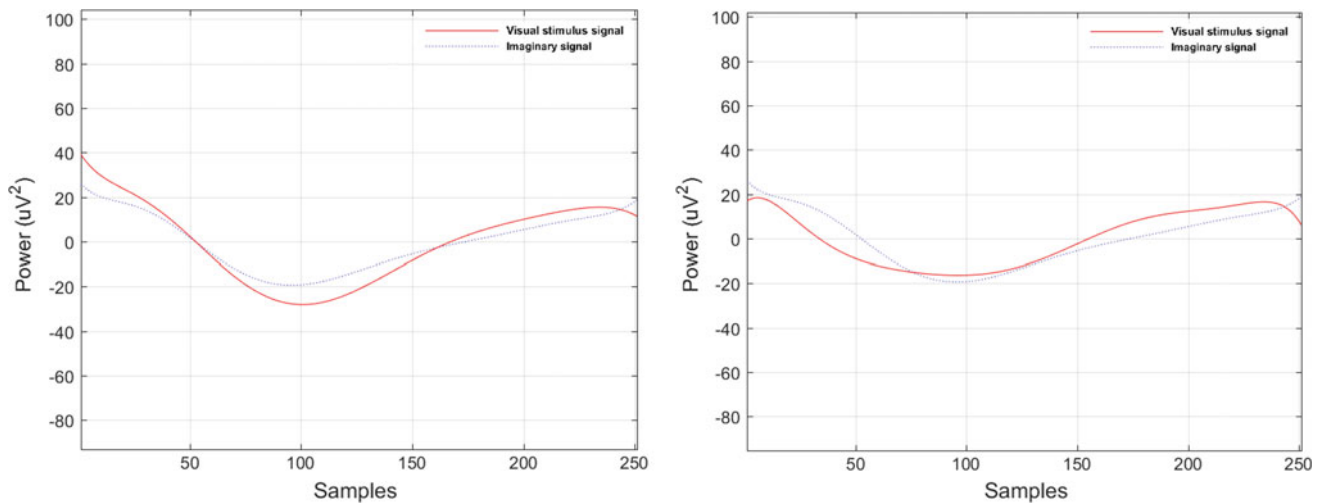


Fig. 5 The shape comparison between a visual stimulus signal and two imaginary signals. The visual stimulus signals are shown as blue and the imaginary signals are red lines

In addition, many peaks covering the signals have the similarities and differences. Some peaks have high correlation values while the others are in weak correlation. The differences are usually led by the latency time between the samples. However, the shapes of samples are related.

4 Conclusion

In the visual stimulation period, the subjects stay awaken and look at the screen without thinking. The alpha wave shows the higher percentage while the beta waves demonstrate the lower percentage on the whole spectrum. However,

in the period of imaginary, the subjects must close their eyes and image the object. The beta waves show the stronger element and the amplitude of the imaginary signals is stronger. In addition, the correlation values of the pairs are mostly middling to higher percent. Some pairs have the latency times and amplitude differences, this causes the less correlation between them. Although the correlation coefficient value is just over the middling rate, the visual stimulation and imaginary signals are similar.

Acknowledgements This research is funded by the University of Technology, VNU-HCM under grant number SVCQ_2017_KHUD_99.

Conflict of Interest The authors declare that they have no conflict of interest.

References

1. Gao, S., Wang, Y., Gao, X., Hong, B.: Visual and auditory brain-computer interfaces. *IEEE Trans. Biomed. Eng.* **61**, 1436–1447 (2014)
2. Zao, J.K., Jung, T.P., Chang, H.M.: Augmenting VR/AR applications with EEG/EOG monitoring and oculo-vestibular recoupling, pp. 121–131 (2016)
3. Hou, J., Morgan, K., Tucker, D.M., Konyn, A., Poulsen, C.: An improved artifacts removal method for high dimensional EEG. *J. Neurosci. Methods* **268**, 31–42 (2016)
4. Li, P., Baker, T.E.: Oscillatory profiles of positive, negative and neutral feedback stimuli during adaptive decision making. *Int. J. Psychophysiol.* **107**, 37–43 (2016)
5. Martišius, I., Damaševičius, R.: A prototype SSVEP based real time BCI gaming system (2016)
6. Klem, G., Luders, H.O., Jasper, H.H., Elger, C.: The ten-twenty electrode system of the international federation. *The international federation of clinical neurophysiology. In: Electroencephalography and Clinical Neurophysiology*, 52, pp. 3–6 (1999)
7. Rangaswamy, M., Porjesz, B., Chorlian, D.B., Wang, K.: Beta power in the EEG of alcoholics. *Biol. Psychol.* **52**, 831–842 (2002)
8. Gerrard, P., Malcolm, R.: Mechanisms of modafinil: a review of current research. *Neuropsychiatr. Dis. Treat.* **3**, 349 (2007)
9. Nussbaumer, H.J.: *Fast Fourier Transform and convolution algorithms*. Springer, New York (2012)
10. Kshirsagar, P.: *Diagnosis of Autism with EEG Analysis Using Discrete Wavelet Transform*. Lamar University, Beaumont (2017)
11. Darrel, P.F., Coats, A.J.S., Derek, G.G.: How high can a correlation coefficient be? Effects of limited reproducibility of common cardiological measures. *Int. J. Cardiol.* **69**(2), 185–189 (1999)

Real Time 3D Pose Estimation of Both Human Hands via RGB-Depth Camera and Deep Convolutional Neural Networks

Geon Gi, Tae Yeon Kim, Hye Min Park, Jeong Min Park,
Dong-Luong Dinh, Soo Yeol Lee, and Tae-Seong Kim

Abstract

3D human hand pose estimation (HPE) is an essential methodology for smart human computer interfaces. Especially, 3D hand pose estimation without attached or hand-held sensors provides a more natural and convenient way. In this work, we present a HPE system with a single RGB-Depth camera and deep learning methodologies which recognizes 3D hand poses of both hands in real-time. Our HPE system consists of four steps: hands detection and segmentation, right and left hand classification using a Convolutional Neural Network (CNN) classifier, hand pose estimation using a deep CNN regressor, and 3D hand pose reconstruction. First, both hands are detected and segmented from each RGB and depth images using skin detection and depth cutting algorithms. Second, a CNN classifier is used to distinguish right and left hands. Our CNN classifier consists of three convolutional layers and two fully connected layers, and uses the segmented depth images as input. Third, a trained

deep CNN regressor estimates the key sixteen joints of hands in 3D from the segmented left and right depth hands separately. The regressor is hierarchically composed of multiple convolutional layers, pooling layers and dense fully connected layers to estimate the hand joints from the segmented hand depth images. Finally, 3D hand pose of each hand gets reconstructed from the estimated hand joints. The results show that our CNN classifier distinguishes the right and left hands with an accuracy of 96.9%. The 3D human hand poses are estimated with an average distance error of 8.48 mm. The presented HPE system can be used in various application fields including medical VR, AR, and MR applications. Our presented HPE system should allow natural hand gesture interfaces to interact with various medical contents.

Keywords

Convolutional neural network • 3-D hand pose recognition • Both hands • RGB-depth • Deep learning

G. Gi · T. Y. Kim · H. M. Park · J. M. Park

S. Y. Lee · T.-S. Kim (✉)

Department of Biomedical Engineering, College of Electronics and Information, Kyung Hee University, Yongin, Republic of Korea

e-mail: tskim@khu.ac.kr

G. Gi

e-mail: geon@khu.ac.kr

T. Y. Kim

e-mail: ky@khu.ac.kr

H. M. Park

e-mail: hmp9669@khu.ac.kr

J. M. Park

e-mail: jmpark@khu.ac.kr

S. Y. Lee

e-mail: sylee01@khu.ac.kr

D.-L. Dinh

Department of Information Technology, Nha Trang University, Nha Trang, Vietnam

e-mail: luongdd@nut.edu.vn

1 Introduction

Recently, a demand is growing in 3D human hand pose recognition (HPE) due to the expanding fields of virtual reality (VR), augmented reality (AR), and mixed reality (MR) for various biomedical applications. Conventionally, HPE has been achieved using hand-held sensors or controllers. However, this methodology only recognizes hand gestures or motions, no hand poses in 3D. Recently, due to the commercialization of structured-light and time-of-flight depth cameras such as Microsoft Kinect and Intel Real-sense camera, active research works are underway to develop 3D hand pose estimation methodologies from color and depth images of human hands. In addition, recent emergence of deep learning techniques enhances the development of HPE.

Among various deep learning methodologies, convolutional neural network (CNN) is one of well-known architectures for its good performance in the problems of hand pose estimation. Previous CNN-based methods used a single depth image as an input to their system and predicted heat maps of each joint of hand [1, 2] or regressed 3D joint positions directly [3, 4]. Recently, 3D CNN, residual, and region ensemble networks have been applied to improve performance of HPE [5, 6]. So far, most HPE systems focus on 3D pose estimation of a single hand. In this work, we propose a 3D pose estimation system of both hands in real-time. In our system, first, skin detection algorithm finds both hands from a color image. Second, based on the detected hands, the corresponding hands are cropped from the depth image via a depth cutting algorithm. Then, a CNN classifier distinguishes the left or right hand. Finally, a CNN regressor estimates 3D joints of both hands and their poses are reconstructed in 3D. Our presented system can be used in various applications providing natural hand interfaces in the fields of medical AR, VR, and MR applications.

2 Methods

As shown in Fig. 1, our system consists of four stages: hand detection and segmentation, right or left hand classification, 3D hand joints estimation, and finally 3D hand pose reconstruction with the estimated 3D hand joints.

2.1 Hand Detection and Segmentation

We use a skin detection algorithm [7] to recognize the color of hand skin. It was applied to a HSV image converted from a RGB image. We set the HSV value from the minimum of (0, 20, 48) to the maximum of (200, 255, 255) for skin detection. After detecting the blobs of hands with a threshold in the HSV image, the Region of Interests (ROIs) are

obtained with a margin of 20 pixels to the blobs of hands. On the synchronized depth map from the corresponding RGB image, the depth hand is detected in the corresponding ROI. In each corresponding hand ROI, we set a distance threshold to remove the depth background and crop the depth hand which are used as input for hand classification and pose estimation later. The cropped hand images are resized to 128×128 , and normalized to $[-1, 1]$.

2.2 Right and Left Hands Classification

To distinguish the right and left hand, we have designed a CNN classifier using the ICVL hand pose dataset [8] which contains 180K frames for training and 1.5K for testing. Since 160K frames are provided as augmented frames from the original 22K data, we trained our classifier with the original 22K data for each hand. The hand depth images of 128×128 are used to create the depth dataset of the right and left hands for training. Our CNN classifier consists of three convolutional layers, three pooling layers and two fully connected layers as shown in Fig. 2. Every output after every layer goes through the ReLU function except the pooling layers and final fully connected layer. The final fully connected layer takes each hand depth image and decides whether it is the right or left hand.

2.3 3D Hand Pose Estimation

To reconstruct hand poses from the hand depth images after classification, a CNN regressor is designed as shown in Fig. 3 and implemented to estimate the hand joints in 3D. We constructed a CNN regressor with a total of twelve convolutional layers, four pooling layers, and three fully connected layers. From the hand-depth image, twelve convolutional layers increase feature maps from 16 and finally 128 feature maps are extracted through multiple

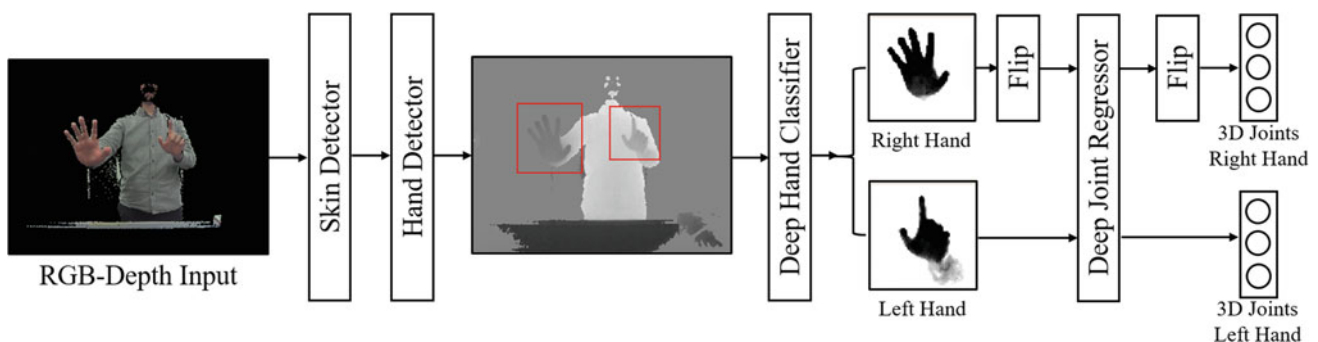


Fig. 1 Overview of our proposed 3D hand pose estimation system. The system takes color and depth images as input. The hands are extracted by the skin and hand detectors. The deep hand classifier

recognizes each extracted depth hand either as the right or left hand. Finally, the deep joint regressor predicts 3D hand joints from each depth hand

Fig. 2 Structure of our CNN classifier. The classifier consists of three convolutional layers, three pooling layers and two fully connected layers. It classifies the input depth image of hand as the right or left hand

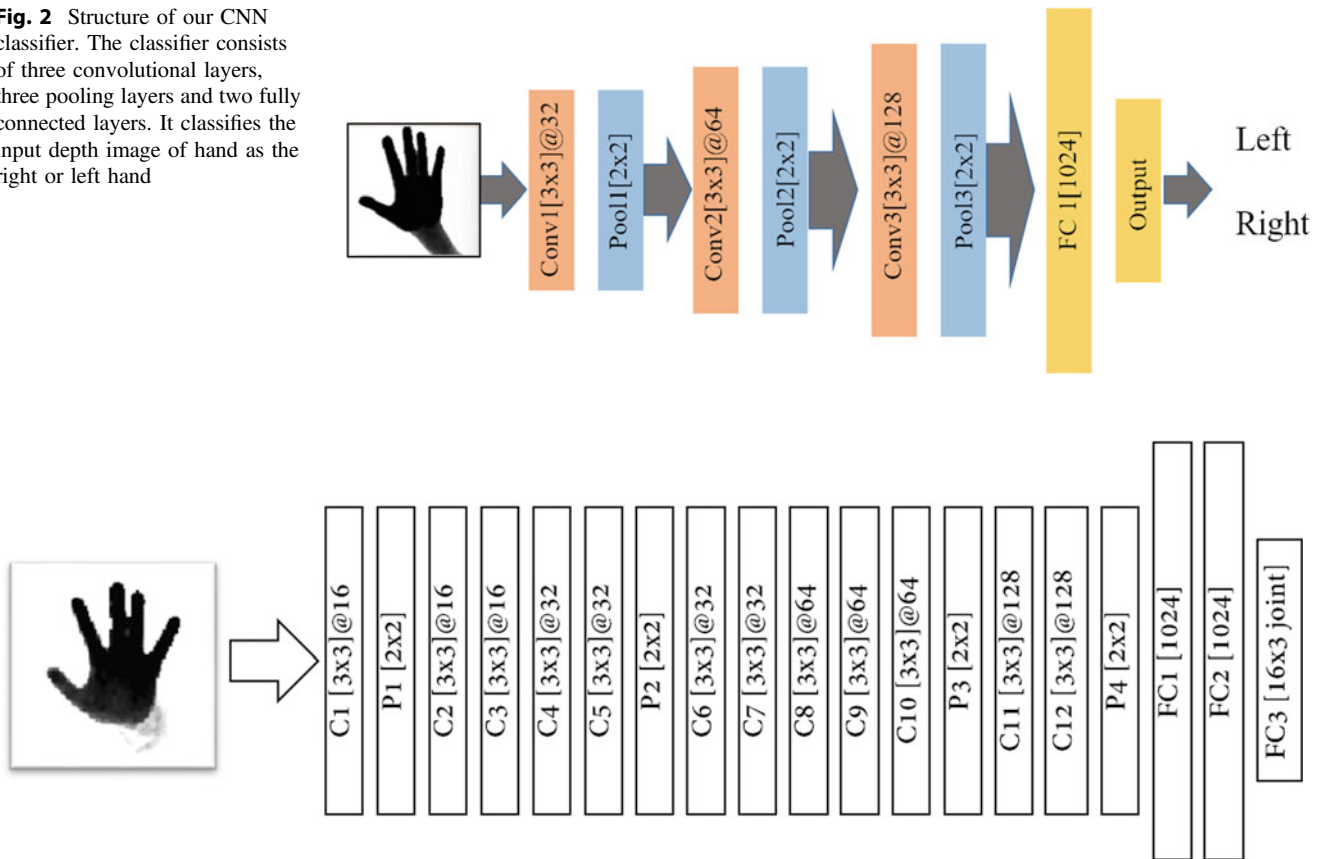


Fig. 3 Structure of CNN regressor. The regressor takes a depth map as an input. It is hierarchically composed of twelve convolutional layers and four pooling layers. Through the three fully connected layers, the regressor estimates hand joints of 16×3 in 3D

convolutional layers using a kernel of 3×3 with one stride and zero-padding to keep the size. Four pooling layers using a kernel of 2×2 with two strides are located between the convolutional layers to reduce the size of feature maps extracted from the convolutional layer, and the computational complexity. The hierarchically structured regressor extracts the appropriate features from the input and predicts the final sixteen hand joint positions in 3D (i.e., 16×3). The regressor is trained with only the left hand training dataset. For the right hand, its depth hand image is flipped as input to the regressor. After the regression, the estimated hand joints are flipped back.

2.4 Implementation Details

We implemented our CNN models using TensorFlow [9] on a PC with i7-6850K CPU, 16 GB RAM and NVIDIA Geforce GTX 1080ti GPU. After passing through the final fully connected layer, Adam optimizer minimized the mean squared error with a learning rate of 0.0001 to find the

minimum error of the regressor, which is back propagated across the whole layers during 100 epochs.

3 Result and Discussion

3.1 Hand Classification

Table 1 shows the performance of our CNN classifier. The classifier is able to classify the right and left hand with the average accuracy of 96.94%. The left-hand image is classified with an accuracy of 97.29%, whereas the right-hand image classified with an accuracy of 96.58%.

3.2 3D Hand Pose Estimation

We evaluate the performance of hand pose estimation in two different metrics. We compared our method against the hand pose estimators of Tang et al. [8] and Zhou et al. [2]. The first evaluation metric is the average Euclidean distance between

Table 1 Confusion matrix of the CNN classifier with the ICVL hand dataset

Classification rates (%)		Predicted value	
		Right	Left
Actual value	Right	96.58	2.71
	Left	3.42	97.29

Table 2 Comparison of the proposed HPE with other works on the ICVL dataset [8]

Model	Mean error (mm)
Tange et al. [8] (LRF)	12.57
Zhou et al. [2] (DeepModel)	11.56
Our proposed	8.48

Mean error indicates the average 3D distance error

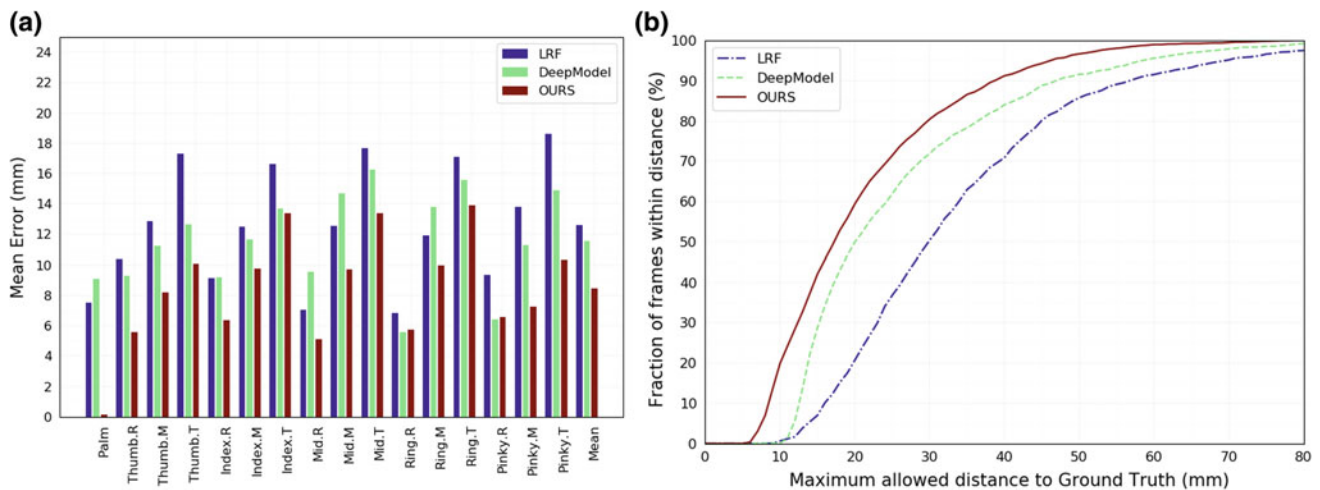


Fig. 4 **a** Comparison with other methods on the ICVL dataset showing the average error distance per key hand joints across all test set. **b** Comparison of our HPE against other estimators on the ICVL

dataset. The fraction of frames within the maximum distance from the ground truth is shown

the ground-truth and predicted hand joint positions in 3D. The mean error of our estimator is 8.48 mm as shown in Table 2 and compared to others. Figure 4a shows the mean error for each joint. The second metric is the percentage of frames which reflect all errors of joints below a threshold [3]. Figure 4b shows the threshold of error versus the percentage of testing examples for our and other estimators.

3.3 3D Hand Pose Reconstruction

Figure 5 shows some exemplary 3D hand poses reconstructed from real-time sequences of depth hands captured

with a Creative Senz3D (RGB-D) camera. The first and third rows show the cropped depth hands. The second and fourth rows show the corresponding 3D hand poses reconstructed with the estimated 3D hand joints. The first and third columns show the left hands whereas the second and fourth columns show the right hands.

4 Conclusion

We present a deep CNN based hand pose estimation system with a RGB-D camera in 3D. Our HPE system estimates 3D poses of both hands in real-time (25 fps). As the presented

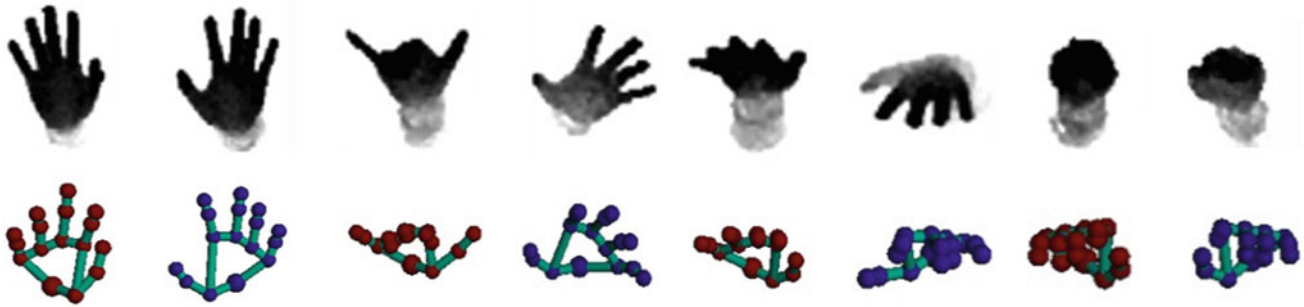


Fig. 5 Reconstructed 3D hand poses in 3D: (first rows) depth hands; (second rows) reconstructed 3D hand poses; (odd columns) right hand; (even columns) left hand

HPE system works in real-time, we believe that the system can be used in various application fields including medical VR, AR, and MR applications.

Acknowledgements This work was supported by International Collaborative Research and Development Programme (funded by the Ministry of Trade, Industry and Energy (MOTIE, Korea) (N0002252).

Conflict of Interest The authors declare that they have no conflict of interest.

References

1. Ge, L., Liang, H., Yuan, J., et al.: Robust 3D hand pose estimation in single depth images: from single-view CNN to multi-view CNNs. In: Proceedings of the IEEE Conference on Computer Vision and Pattern Recognition, pp. 3593–3601 (2016)
2. Zhou, X., Wan, Q., Zhang, W., et al.: Model-based deep hand pose estimation. In: Proceedings of the Twenty-Fifth International Joint Conference on Artificial Intelligence, pp. 2421–2427. AAAI Press (2016)
3. Oberweger, M., Wohlhart, P., Lepetit, V.: Hands deep in deep learning for hand pose estimation. In: Proceedings of Computer Vision Winter Workshop, pp. 21–30 (2015)
4. Sun, X., Wei, Y., Liang, S., et al.: Cascaded hand pose regression. In: Proceedings of the IEEE Conference on Computer Vision and Pattern Recognition, pp. 824–832 (2015)
5. Ge, L., Liang, H., Yuan, J., et al. (2017). 3D convolutional neural networks for efficient and robust hand pose estimation from single depth images. In: Proceedings of the IEEE Conference on Computer Vision and Pattern Recognition, vol. 1, p. 5
6. Guo, H., Wang, G., Chen, X., et al.: Region ensemble network: improving convolutional network for hand pose estimation. In International Conference on Image Processing, pp. 4512–4516 (2017)
7. Shaik, K.B., et al.: Comparative study of skin color detection and segmentation in HSV and YCbCr color space. *Procedia Comput. Sci.* **57**, 41–48 (2015)
8. Tang, D., Jin Chang, H., Tejani, A., Kim, T.K.: Latent regression forest: structured estimation of 3D articulated hand posture. In: Proceedings of the IEEE Conference on Computer Vision and Pattern Recognition, pp. 3786–3793 (2014)
9. Abadi, M., Agarwal, A., Barham, P., et al.: Tensorflow: large-scale machine learning on heterogeneous distributed systems. arXiv preprint, [arXiv:1603.04467](https://arxiv.org/abs/1603.04467) (2016)

Automatic Facial Expression Recognition System Using Convolutional Neural Networks

Hung Ngoc Do, Kien Trang, Bao Quoc Vuong, Van-Su Tran, Linh Mai, Minh-Thanh Vo, and Mai Hoang Nguyen

Abstract

Facial expression recognition (FER) has attracted the interest of many scholars because it plays an important role in human-computer interaction, image analysis, and artificial intelligent. The main purpose of FER is to classify a given facial image into one of the seven basic emotions: angry, disgust, fear, happy, sad, surprise, and neutral. In recent years, convolutional neural networks (CNN) have been studied and applied in the fields of image processing and computer vision with great success. One of the main properties of CNN is the training stage that needs a large-scale data set for having a good performance. In this paper, we present a FER system using CNN in which the training and testing images are extracted from the AffectNet facial expression database. Compared to the traditional facial expression databases, AffectNet provides over one million images which are annotated by manual and automatic methods. The performance of the proposed model is analyzed via evaluations of the correct recognition rates, in comparison with the published ones, with the use of the same database.

Keywords

Facial expression • Image analysis • Convolutional neural networks • Computer vision

1 Introduction

Facial expression recognition has been an interesting research topic due to its applications in many areas such as human-computer interaction, entertainment, e-learning,

H. N. Do (✉) · K. Trang · B. Q. Vuong · V.-S. Tran
L. Mai · M.-T. Vo · M. H. Nguyen
School of Electrical Engineering, Vietnam National University,
Ho Chi Minh City, Vietnam
e-mail: dnhung@hcmu.edu.vn

robotics, etc. In recent years, many FER methods have been introduced to classify a facial image into one of seven emotions defined by the American psychologist Ekman and Friesen in 1971 [1]. Although many of them show good results in testing with well-known databases, they have a limitation in applying in reality because of the small number of images and the insufficient background conditions in these databases. For example, NMI [2], JAFFE [3], and Cohn-Kanade [4] databases contain from hundreds to several thousands of images.

Deep learning networks such as convolutional neural networks (CNN) or deep belief network (DBN) have been applied in many fields of computer vision with great success in the past few years. One of the key factors affects to the performance of this framework is the size of dataset for training. AffectNet is considered as one of a good database for this method with over one million images with a large amount of subject variations in the wild conditions [5]. In this paper, we propose a CNN architecture for FER and test that system by using AffectNet. In particular, the scale-invariant feature transform (SIFT) feature of the points in facial landmark will be extracted for training or classifying our networks. The large amount of features can be trained in an effective way with the advantage of a graphical processing unit (GPU). The trained network will be saved for classifying purpose. The rest of this paper is organized as follows. Section 2 describes our methodology in details. Some information about the database and the performance of our system are shown in Sect. 3. Finally, Sect. 4 concludes our paper and gives some recommendations.

2 System Description

Figure 1 shows the processing chart of our facial expression recognition system which contains five main stages. The images for training and testing are taken from AffectNet database. We use the same process for feature extraction in training and classifying works. The Viola-Jones method [6]

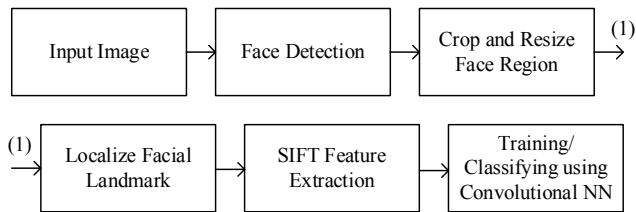


Fig. 1 System model

is applied to detect face in the input image. Then facial landmark contains important points in the face will be extracted and moved to SIFT descriptor to extract the facial expression features for training or recognizing.

2.1 Facial Landmark Localization

Before taking feature extraction stage, a facial landmark will be detected to point out the exactly position of important parts on a face (eyes, eyebrows, nose, mouth, face line). In analyzing emotion on a face region, it is not very useful to collect all the feature data because there are just some main parts have strong contribution to decide the state of an emotion. Besides, an enormous data of features also leads to lower computational process and ravel in the classification stage. Extracting facial landmark location will be treated as the initial step in pre-processing stage. In this paper, the method in [7] is used to cover this task which is based on the elastic deformations model with a simpler tree-structured mesh. Furthermore, the mixture of trees model is also applied to deal with multi-pose of face in the wild. Every facial landmark and global mixtures are modeled and used to capture topological changes due to viewpoint. The result of this stage is 68 facial landmark points are marked as in Fig. 2a.

2.2 Scale-Invariant Feature Transform Feature Extraction

Scale-invariant feature transform (SIFT) is a local feature extraction method which is used popularly in the computer vision field. It is proposed by D. G. Lowe in [8] and applied in object recognition with high performance. SIFT also is known as a descriptor which is robust to the change of illumination, rotation and scaling. Each descriptor is extracted from the sub-region will have magnitude and orientation of gradient which can be defined in Eqs. (1) and (2)

$$\eta(x, y) = \sqrt{(L(x+1, y) - L(x-1, y))^2 + (L(x, y+1) - L(x, y-1))^2} \quad (1)$$

$$\sigma(x, y) = \tan^{-1} \left(\frac{L(x, y+1) - L(x, y-1)}{L(x+1, y) - L(x-1, y)} \right) \quad (2)$$

where $\eta(x, y)$ is gradient magnitude and $\sigma(x, y)$ is the orientation which are calculated by the difference of pixels for each image sample.

In this paper, the SIFT features will be extracted based on the 68 facial landmark points which are treated as central points for SIFT description. This gives that each key point will have an associated SIFT feature descriptor which is corresponding to a 128 dimensional vector. Besides, normalization stage will be done in order to reduce the changes in illumination. Figure 2b shows the visualization of SIFT features based on the facial landmark points.

2.3 Convolutional Neural Network Architecture

The convolutional neural network is known as advanced version of multilayer neural network [9]. CNN is a deep neural network which is commonly used for image classification. This brings in a significant breakthrough in image processing and computer vision which can improve the efficiency and accuracy. There are some basic layers in CNN such as Convolutional, Max Pooling, Rectified Linear Units, Fully Connected and Softmax layer. In this paper, we proposed a structure of CNN to deal with facial expression recognition based on SIFT feature. Figure 3 shows the architecture of the proposed convolutional neural network for facial expression with SIFT feature.

3 Results

3.1 AffectNet Facial Expression Database

The AffectNet consists of over 1,000,000 facial expression images which are collected from the Internet based on related keywords. This can give a huge number of human expression in wild which could challenge some traditional algorithms for facial expression recognition. There are 8 emotion categories and nearly 450,000 images are annotated manually by the expert labelers. Besides, the authors of AffectNet also provide a model deep neural networks to classify emotions in their database.

3.2 Experiments

A confusion matrix of the proposed model SIFT-CNN is shown in Table 1. The average recognition rate is 72%. It is clearly that two expressions of happy and surprise have the

Fig. 2 **a** Facial landmark localization, **b** the visualization of SIFT features based on facial landmark points

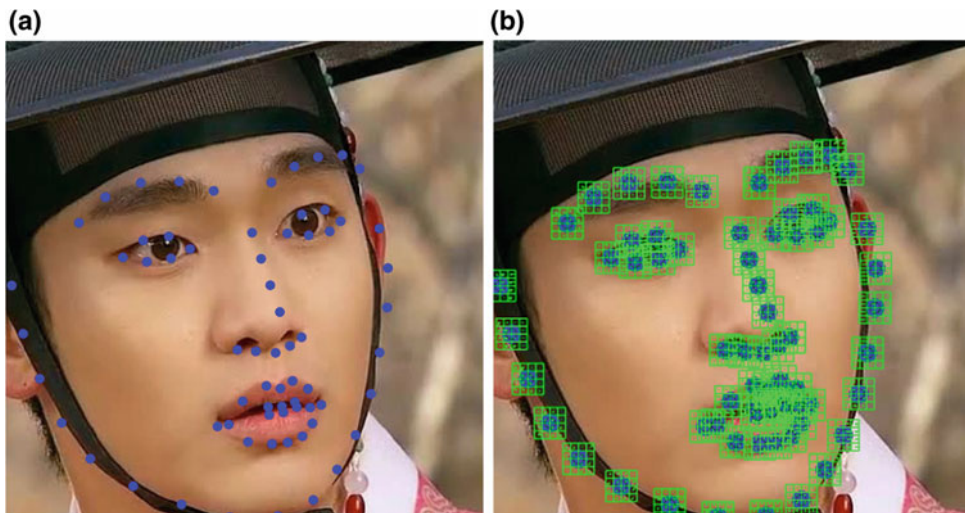


Fig. 3 Convolutional neural network

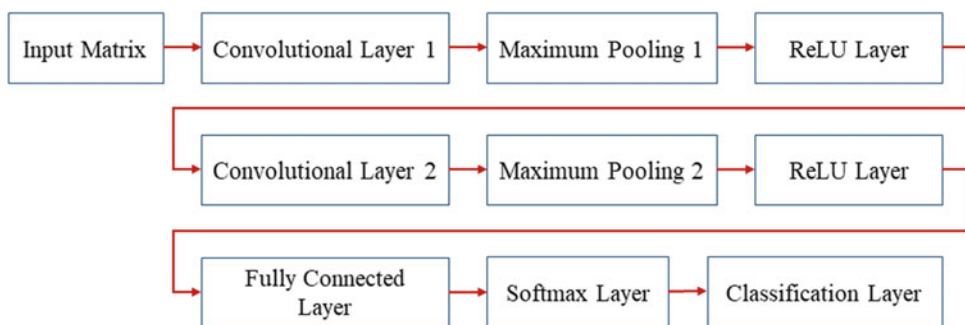


Table 1 Confusion matrix of proposed model

%	Angry	Neutral	Disgust	Fear	Happy	Sad	Surprise
Angry	70.3	2.35	8.5	4.95	3.25	7.1	3.55
Neutral	4.3	74.95	2.3	7.45	6.9	2.85	1.25
Disgust	6.45	6.35	68.35	6.85	4.4	5.8	1.8
Fear	7.5	6.8	4.5	69.25	2.75	6.65	2.55
Happy	4.2	3.35	2.35	3.15	76.6	4.55	5.8
Sad	7.45	5.35	5.5	6.2	3.65	69.5	2.35
Surprise	3.5	3.95	5.8	2.6	5.35	3.45	75.35

highest recognition rate which are 76.6 and 75.35%, respectively. Besides, the fear and disgust expression are much difficult to recognize which the accuracy are 69.25 and 68.35%, respectively. Table 2 shows the confusion matrix of method which is proposed by the authors in [5]. In the original paper, the authors consider 8 type of expression, however, we ignore the contempt expression for having the same size of confusion matrices. We can see that an improvement of accuracy in the combination of SIFT-CNN to the results in [5].

4 Conclusion

In this paper, a CNN structure is proposed to deal with the FER problem by using SIFT features and large-scale dataset. The use of a huge number of images and the diversity in the background, head pose, occlusion, and illumination conditions in AffcetNet can help the trained CNN to work well with a similar database which was well tested and documented. Although the recognition rates are rather high when

Table 2 Confusion matrix of model in [5]

%	Angry	Neutral	Disgust	Fear	Happy	Sad	Surprise
Angry	65.8	6.2	11.1	5.8	1.2	5.0	3.2
Neutral	10.4	53.3	2.5	1.7	2.8	9.8	8.7
Disgust	10.6	2.0	68.6	6.2	2.2	5.8	3.3
Fear	4.3	1.5	4.2	70.4	1.5	4.6	13.5
Happy	1.0	4.5	1.7	0.6	72.8	1.1	6.0
Sad	9.2	13.0	4.4	5.8	1.3	61.7	3.6
Surprise	2.8	3.4	1.7	18.9	1.2	1.7	69.9

considering the complexity of the dataset, in order to have a better result, the further studies will focus on combinations of additional features, with new training algorithms or new network models.

Conflict of Interest The authors declare that they have no conflict of interest.

References

- Ekman, P., Friesen, W.V.: Constant across cultures in the face and emotion. *J. Pers. Soc. Psychol.* **17**(2), 124 (1971)
- Pantic, M., Valstar, M., Rademaker, R., Maat, L.: Web based database for facial expression analysis. In: *IEEE International Conference on Multimedia and Expo (ICME)*, pp. 1–5 (2005)
- Kamachi, M., Lyons, M., Gyoba, J.: *The Japanese Female Facial Expression (JAFFE) Database* (1998)
- Kanade, T., Cohn, J.F., Tian, Y.: Comprehensive database for facial expression analysis. In: *Fourth IEEE International Conference on Automatic Face and Gesture Recognition*, pp. 46–53 (2000)
- Mollahosseini, A., Hasani, B., Mahoor, M.H.: AffectNet: a database for facial expression, valence, and arousal computing in the wild. In: *The IEEE Transactions on Affective Computing* (2017)
- Viola, P., Jones, M.J.: Robust real-time face detection. *Int. J. Comput. Vis.* **57**(2), 137–154 (2004)
- Zhu, X., Ramanan, D.: Face detection, pose estimation, and landmark localization in the wild. In: *Computer Vision and Pattern Recognition (CVPR) Providence, Rhode Island* (2012)
- Lowe, D.G.: Distinctive image features from scale-invariant keypoints. *Int. J. Comput. Vis.* **60**(2), 91–110 (2004)
- Li Deng, D.Y.: Deep learning: methods and applications. *Found. Trends Sig. Process.* **7**(3), 197 (2014)

Design of Classifier for Electrocardiography Classification

Duong Van Binh, Nguyen Thanh Nghia, Nguyen Thanh Hai,
and Nguyen Manh Hung

Abstract

The Electrocardiography classifier is an essential tool for helping doctors in diagnosing early heart problems. This paper proposes with an electrocardiography classifier for analyzing accuracy in case of non-long-tail effect. Data are obtained from MIT-BIH arrhythmia database. Therefore, a discrete wavelet transform decomposition algorithm is employed for feature extraction and a principal component analysis is used for dimension reduction of data. In addition, the heart beat can be classified using a neural network method. In order to evaluate the classifier accuracy, the confusion matrix and Receiver Operating Characteristic curve are applied.

Keywords

Principal component analysis • Discrete wavelet transform decomposition • Neural networks • Confusion matrix and receiver operating characteristic curve

1 Introduction

In recent years, dead people due to heart disease have fast increased. Early diagnosis of arrhythmia is very necessary for doctors. Electrocardiography (ECG) shows the electrical activity of heart changes over time through displaying on a screen or paper pages for presenting ECG data. Therefore,

D. Van Binh (✉) · N. T. Nghia · N. T. Hai · N. M. Hung
FEEE, HCMC University of Technology and Education, Ho Chi Minh City, Vietnam
e-mail: 11141013@student.hcmute.edu.vn

N. T. Nghia
e-mail: nghiant@hcmute.edu.vn

N. T. Hai
e-mail: nthai@hcmute.edu.vn

N. M. Hung
e-mail: hungnm@hcmute.edu.vn

doctor can show clinical diagnosis of heart disease based on the ECG graphical presentation with waveform characteristics P, Q-R-S, T [1]. In this waveform, some of characteristics such as PR interval, PR segment, QRS complex interval, ST segment, ST interval, QT interval, and RR interval contains features of ECG data that doctor can use for diagnosis.

The noisy component in ECG data needs to be considered. In particular, noisy source in ECG data is from all of leads and the variety of frequency bands of the system. Thus ECG data need to be removed the noisy component by using filters. Some algorithms for removing ECG noise is often used such as baseline wander, low pass and high pass filters, wavelet filter, and discrete wavelet transform [2, 3].

ECG data after removing the noisy component is converted into one beat, in which each heart beat is considered as one feature. Because dimensions of feature are large, some techniques are applied to reduce the feature dimensions. In particular, the techniques applied for dimensional reduction often are Principal Component Analysis (PCA), Independent Component Analysis (ICA) and Linear Discriminant Analysis (LDA) [4, 5]. The new ECG data with the low dimension will allows the action of classifier faster.

To determine the heart beat type, a classifier is applied for recognition. The classifier for recognition of ECG data can be one of the following kinds such as Support Vector Machine (SVM), Neural Networks (NNs), fuzzy logic, Hidden Markov Model (HMM) [6, 7]. The ECG feature after dimensional reduction will be employed for training the classifier. In particular, a part of ECG feature will be used for testing in the classifier. Moreover, some algorithms are utilized for testing the classifier such as confusion matrix, accuracy index, and Receiver Operating Characteristic (ROC).



Fig. 1 The block diagram of the propose method

is the error between the desired response and the actual response.

In order to classify ECG data, steps are shown as in Fig. 1. In particular, in the first stage, ECG data is split into heartbeats, the second stage is that ECG data feature extraction is executed using the DWTD algorithm, the next stage means that the ECG data dimensions is reduced using the PCA algorithm, and at the final stage, the neural network is employed to classify ECG heartbeats.

3 Result and Discussion

Features of ECG data are extracted using the DWTD with Mayer wavelet function, in which Approximate coefficients and detail coefficients at fourth level is obtained. The original ECG heartbeat, approximate coefficient (a_4) and detail coefficient (d_4) are described in Fig. 2.

The ECG features of a_4 and d_4 consist of 214 samples corresponding to 214 dimensions of ECG data. To reduce the ECG data dimensions, the PCA algorithm was applied in this research. Figure 3 shows the sum of the cumulative distributions of information with Approximate coefficient a_4 . In particular, the principal information in six first features of a_4 is about 96.5% compared to the whole information. After reducing its dimensions, coefficients of a_4 and d_4 are twelve dimensions which are considered as the ECG features in the classifier. Therefore, the neural network with twelve input

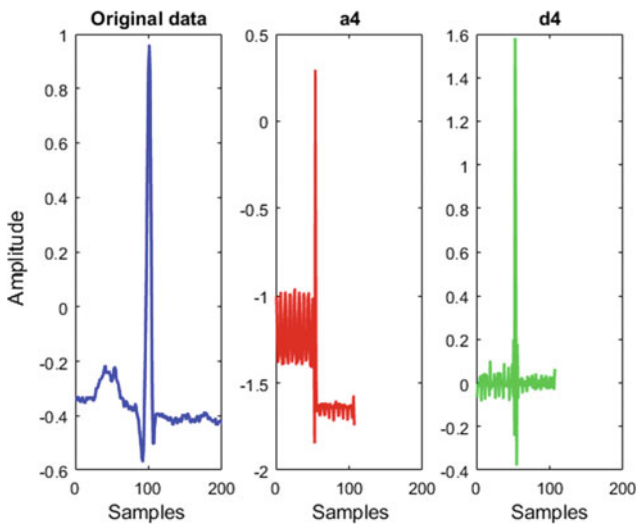


Fig. 2 Original data, approximate (a_4) and detail (d_4)

neurons is applied for calculating the accuracy (ACC) of classifier as follows:

$$ACC = \frac{TP + TN}{TP + FP + TN + FN} \quad (5)$$

in which parameters are defined as the True Positive (TP), True Negative (TN), False Positive (FP), False Negative (FN).

The ECG heartbeats are classified for evaluating the performant of classifier and a confusion matrix is described as in Table 2.

In this paper, the training and testing data are designed as in Tables 3 and 4 for evaluation of the accuracy. In particular, In Table 3, the ECG data in large class (situation-1) is extracted randomly to equal another class. Because of the number of heartbeats in each class is small, the accuracy of classifier is low. While the ECG data in small class

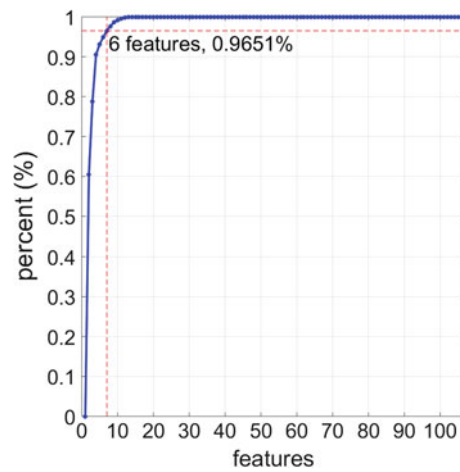


Fig. 3 Sum of the cumulative distributions of the relative weights

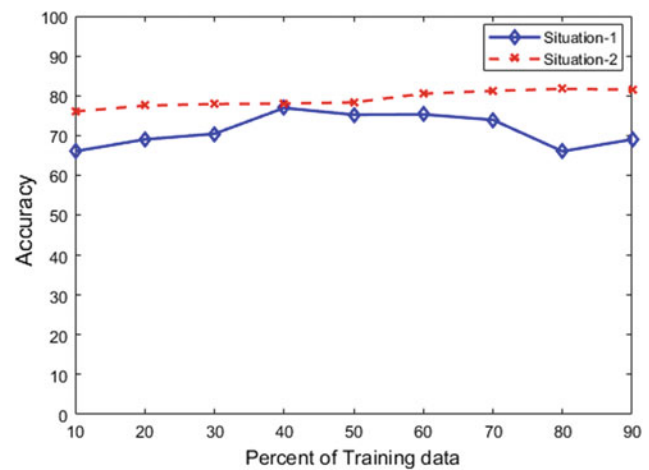


Fig. 4 The accuracy of the classifier

Table 2 Structure of the confusion matrix

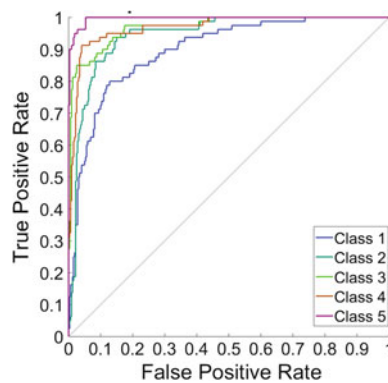
		True condition	
		Positives	Negatives
Predicted	Positives	True positives (<i>TP</i>)	False positives (<i>FP</i>)
	Negatives	False negatives (<i>FN</i>)	True negatives (<i>TN</i>)

Table 3 The accuracy of classifier in case of ECG data with large class is extracted randomly

Training (%)	10	20	30	40	50	60	70	80	90
Testing (%)	90	80	70	60	50	40	30	20	10
ACC (%)	66.0	69.0	70.4	76.9	75.2	75.3	73.9	66.0	69.0

Table 4 The accuracy of classifier in case of ECG data with small class was duplicated

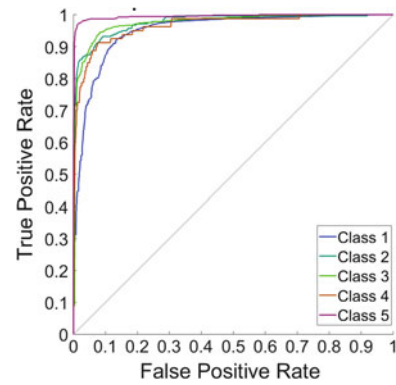
Training (%)	10	20	30	40	50	60	70	80	90
Testing (%)	90	80	70	60	50	40	30	20	10
ACC (%)	80.7	82.8	83.1	82.7	84.2	83.9	84.1	85.1	84.5

**Fig. 5** ROC curve of classifier in situation-1

(situation-2) is duplicated for equal to large class, so the accuracy of this classifier is higher as described in Table 4. In addition, both cases above are recognized as the long-tail effect which is cancelled.

From Table 3, the accuracy of two classifiers are described in Fig. 4, the blue line with the accuracy in case of ECG data is extracted randomly in each class and the red line with the accuracy of ECG data is duplicated. As a result of the classifier, the accuracy of the ECG classifier of situation-2 is higher than that of situation-1.

In addition, the ROC curves of classifiers shown in Figs. 5 and 6 of Situation-1 and Situation-2 are to present the true positive rates and compare them together for evaluation. While authors of research in [5] just shows the high accuracy of classifier, but the number of heartbeat in each

**Fig. 6** ROC curve of classifier in situation-2

class is not mentioned. The original data in Table 1 shows that the number of normal heartbeats (in class 1) is 83.5% of the total heartbeat. Therefore, the long-tail effect still exists on the classifier. In this paper, ECG data on each class is equal, so the distribution of ECG data on each class is similar to the classifiers as shown in Figs. 5 and 6.

4 Conclusions

The DWT algorithm was applied for feature extraction of ECG data from MIT-BIH database in this study. Therefore, the PCA algorithm was applied to reduce the number of dimensions of feature vectors for accurate evaluation. The ECG heartbeats were classified using the neural network. The experimental results showed the better performance of the classifiers of two situations and the distribution of ECG data between classes. In addition, the accuracy of the classifiers with the non-long-tail effect by duplicating ECG data is a little lower long-tail effect, but the distribution of ECG data between classes is better.

Acknowledgements The authors would like to acknowledge the support of Ministry of Education and Training, Vietnam with Grand No. B2017.SP.K.03 and HCMC University of Technology and Education, Vietnam.

Conflicts of Interest The authors declare that they have no conflict of interest.

References

- Gajendra, E., Kumar, M.J.: A novel approach of ECG classification for diagnosis of heart diseases: review. *Int. J. Adv. Res. Comput. Eng. Technol.* **4**(11), 4096 (2015)
- Hesar, H.D., Mohebbi, M.: ECG denoising using marginalized particle extended Kalman filter with an automatic particle weighting strategy. *IEEE J. Biomed. Health Inform.* **21**(3), 635–644 (2017)

3. Vidya, M.J., Sadasiv, S.: A comparative study on removal of noise in ECG signal using different filters. *Int. J. Innovative Res. Develop.* **2**(4), 915–927 (2013)
4. Bakir, C.: Classification of ECG signals with the dimension reduction methods. *J. Math. Stat. Sci.* **2007**(12), 353–363 (2017)
5. Martis, R.J., Acharya, U.R., Min, L.C.: ECG beat classification using PCA, LDA, ICA and discrete wavelet transform. *Biomed. Sig. Process. Control* **8**(5), 437–448 (2013)
6. Behadada, O., Chikh, M.: An interpretable classifier for detection of cardiac arrhythmias by using the fuzzy decision tree. *Artif. Intell. Res.* **2**(3), 45–58 (2013)
7. Liu, S.-H., Cheng, D.-C., Lin, C.-M.: Arrhythmia identification with two-lead electrocardiograms using artificial neural networks and support vector machines for a portable ECG monitor system. *Sensors (Basel, Switzerland)* **13**(1), 813–828 (2013)
8. Physionet: MIT-BIH Arrhythmia database. <http://physionet.org/physiobank/database/mitdb/>. (10 Nov 2014)
9. Thai, N.H., Nghia, N.T., Binh, D.V., Hai, N.T., Hung, N.M.: Long-tail effect on ECG classification. In: *Proceedings of the International Conference on System Science and Engineering 2017 (ICSSE 2017)*, pp. 34–38 (2017)

DWT Algorithm for Iris Recognition

Vien Phuc Nguyen, Hai Thanh Nguyen, and Dat Duc Ngo

Abstract

This paper proposes with a Discrete Wavelet Transform (DWT) method to extract features for iris recognition. In particular, Daugman's Integro—differential operator is applied to extract iris image from human eye image and the iris image is analyzed to extract features using the DWT for iris recognition of one person. From the iris features, a threshold method is proposed to estimate similarity between irises of people for recognition of one corresponding person. Results show that contribution of this research illustrates the effectiveness of the human recognition method.

Keywords

Iris recognition • Discrete wavelet transform • Biometrics • Daugman's integro—differential operator

1 Introduction

In recent years, man systems for human identification based on signals or images have been developed with increased reliability. In particular, different ways of identification of voices, faces, obstacles, eyes and others people have attracted researchers [1, 2]. Identification of iris part in human eye image for recognition of one corresponding person is one interesting issue.

Biometrics are the reliable and secure instrument for access control systems and physical assets provided by individual characteristics or based on physiological or behavioral characteristics [3, 4]. Related to human

recognition of characteristics, particularly the physiological characteristics are iris, fingerprint, face and hand geometry or behavioural characteristics consist of voice, signature, gait and keystroke dynamics [5, 6]. Moreover, methods can be applied for biometric recognition based on properties and they cannot be forgotten or stolen like traditional authentication such as passwords or PIN's [7, 8].

To successfully perform iris recognition, iris segmentation in eye image is a very important [9]. Two methods, which are often used for iris segmentation, are Wildes method and Daugman's one. In particular, Wildes proposed the iris segmentation with two steps: firstly, eye image is converted into binary image base on gradient of intensities of the pixels in an iris image; the secondly, the iris inner and outer borders are detected using Hough transform [10]. Daugman's algorithm is an integro differential operator that allows to search over an eye image for the circular pupil and borders of the iris image [11]. Therefore, the circular edge is detected for determining parameters of circular border.

The performance of an iris recognition system is affected by iris features. In recent decade, 2D Gabor filters developed by Daugman have been applied for filtering noises of images. Therefore, Wavelet transform algorithm are employed for feature extraction [12]. It means that this is one of the methods is applied for improvement of the human iris recognition system. Some other research results showed that the method of identifying human iris is highly accurate compared to that of biometric fingerprint identification. In particular, the structure of the human iris has 240 distinct characteristics compared to only 20 to 40 fingerprint recognition features [13]. It means that using the structure of the iris for recognition is more accurate than that of the fingerprint.

In this paper, the threshold method is proposed to estimate iris recognition of people based on eye images. In addition, this research shows statistics of many iris images of different people and between two eyes of one human for estimating the effectiveness of the proposed method. This paper is organized as follows: Sect. 2 describes the materials

V. P. Nguyen (✉) · H. T. Nguyen
Faculty of Electrical-Electronics Engineering, HCMC University
of Technology and Education, Ho Chi Minh City, Vietnam
e-mail: nguyenphucvien@gmail.com

D. D. Ngo
HCMC Navy Technical College, Ho Chi Minh City, Vietnam

and methods related to the DWT and DIDO, in Sect. 3, results and discussion of iris recognition are obtained, Sect. 4 provides the overall conclusion.

2 Materials and Methods

The collection of eye image with iris for identification is one of the major challenges due to requiring its high-quality image and they are not obscured by human eyelashes. In addition, in this research, the eye image database with iris is obtained from the website of the organization of Biometrics Ideal Test (CASIA-Iris-Interval) and there are 249 persons with one left eye or one right eye only. Which each eye image with an iris has the resolution of 320×280 pixels. From these eye images, an iris image of each eye image needs to extract for recognition, then the methods of normalization and feature extraction for estimating and decision are employed as shown in Fig. 1.

2.1 Extraction of Iris Image

The algorithm of Daugman's Integro-Differential Operator (DIDO) [5] is applied to find an iris image in an eye image as described.

$$\max_{(r, x_0, y_0)} \left| G_\sigma(r) * \frac{\partial}{\partial r} \oint_{r, x_0, y_0} \frac{I(x, y)}{2\pi r} ds \right| \quad (1)$$

where $I(x, y)$ is the intensity of the pixel at coordinate (x, y) in the iris image, r denotes the radius of the various circular region with the center coordinate at (x_0, y_0) , σ is the standard deviation of the Gaussian distribution, $G_\sigma(r)$ denotes the Gaussian filter of the scale sigma (σ), (x_0, y_0) is the assumed centre at the iris coordinate and s is the contour of the circle determined by the parameters of (r, x_0, y_0) .

In Daugman's Operator, a Gaussian filter is employed to make smooth image and to reduce noise of eye image. In

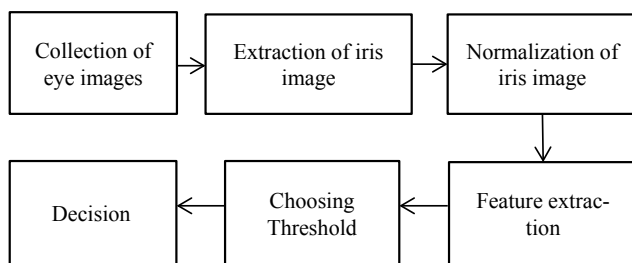


Fig. 1 Block diagram of iris recognition

order to find an iris image in an eye image, one needs to set up parameters as described in Table 1. From these parameters, circles of pupil and iris are drawn as shown in Fig. 2. Therefore, in order to calculate the iris, the iris image needs to be normalized by using the model as shown in Fig. 3.

2.2 Normalization of Iris Image

After determining the iris area in the eye image, all iris images need to be resized for comparison. The spatial conflict between eye images is mainly due to dilated iris from different lighting levels. In particular, the main causes of inconsistencies include the projecting distance, the rotations of the camera and the eye in the eye socket. Thus, the normalization of iris image is necessary and the normalization process will produce the same irregularly shaped iris areas. With this iris normalization, two images with the same iris under different conditions will have the same structure at the same locations.

The homogenous rubber sheet model was devised by Daugman [14, 15], in which each point within the iris region corresponding to a pair of polar coordinates is (r, θ) , where r is on the interval $[0, 1]$ and θ is the angle of $[0, 2\pi]$. This model allows to convert an iris image into a homogenous rubber sheet image as described in Fig. 3. From this model, the rubber sheet used for remapping of the iris image can be represented as follow.

$$I(x(r, \theta), y(r, \theta)) \rightarrow I(r, \theta) \quad (2)$$

where

$$x(r, \theta) = (1 - r)x_p(\theta) + rx_l(\theta) \quad (3)$$

$$y(r, \theta) = (1 - r)y_p(\theta) + ry_l(\theta) \quad (4)$$

From Operator (2), an iris image is calculated and normalized to be a rubber sheet image as shown in Fig. 4. Therefore, all iris images after normalization are calculate to extract features for iris recognition.

2.3 Discrete Wavelet Transform Algorithm for Feature Extraction

The Discrete Wavelet Transform (DWT) algorithm is applied to analyze features in iris regions into components appearing at different resolutions [16]. The DWT allows to collect coefficients for extracting features of iris images. Therefore, the coefficient output of the DWT is encoded to provide a compact and distinctive representation of the iris model and its equations are described as follows.

Table 1 Description of parameters of finding the iris image

	X coordinate	Y coordinate	Radius
Pupil	142	159	34
Iris	152	152	109

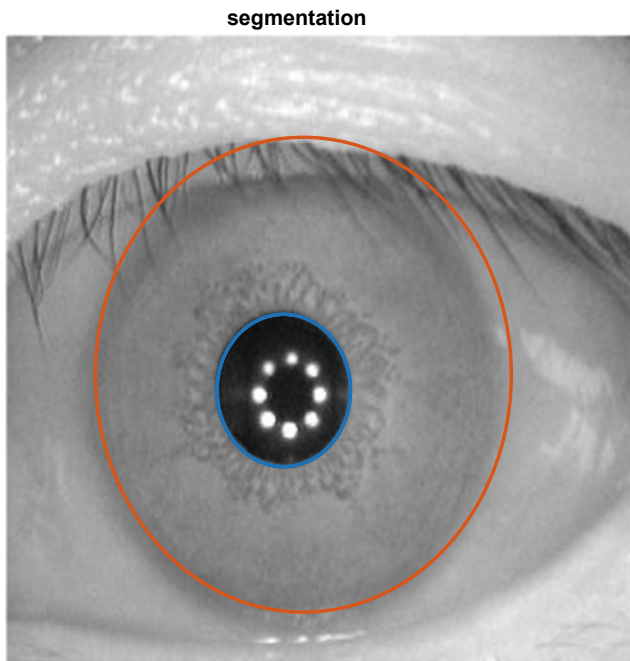


Fig. 2 Representation of finding an iris image in an eye image

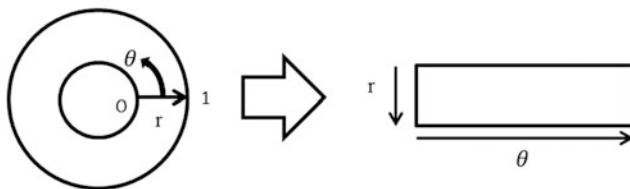


Fig. 3 Daugman's rubber sheet model

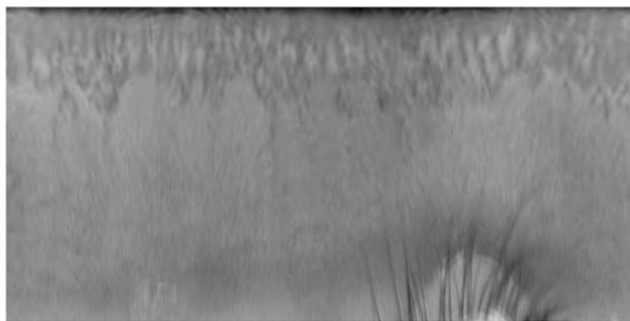


Fig. 4 Normalization of the iris image

$$W_{\phi}(j_0, m, n) = \frac{1}{\sqrt{MN}} \sum_{x=1}^{M-1} \sum_{y=1}^{N-1} I(x, y) \phi_{j,m,n}(x, y) \quad (5)$$

$$W_{\psi}^i = \frac{1}{\sqrt{MN}} \sum_{x=1}^{M-1} \sum_{y=1}^{N-1} I(x, y) \phi_{j,m,n}^i(x, y), i = H, V, D \quad (6)$$

where $I(x, y)$ is the normalization iris image with $M \times N$ pixels, $M = N = 2^J$, $j = 0, 1, 2, \dots, J - 1$; $m, n = 0, 1, 2, \dots, 2^j - 1$. j_0 denotes the random starting scale and is commonly chosen to be $j_0 = 0$.

Figure 5 shows the result of the iris image using the DWT with Harr function, in which the approximate image contains features. After extracting features, the iris image needs to be encoded in binary. Thus, the DWT algorithm was employed at level-2 to produce three coefficient components H, V, D which can be utilized for binary coding by using the following equation.

$$\begin{cases} C(i) = 0, & C(i) < 0 \\ C(i) = 1, & C(i) \geq 0 \end{cases} \quad (7)$$

where C represents the iris feature space after the DWT, $C = \{LH3, HL3, HH3\}$ after the DWT with level 3, and $C(i)$ is the element of C .

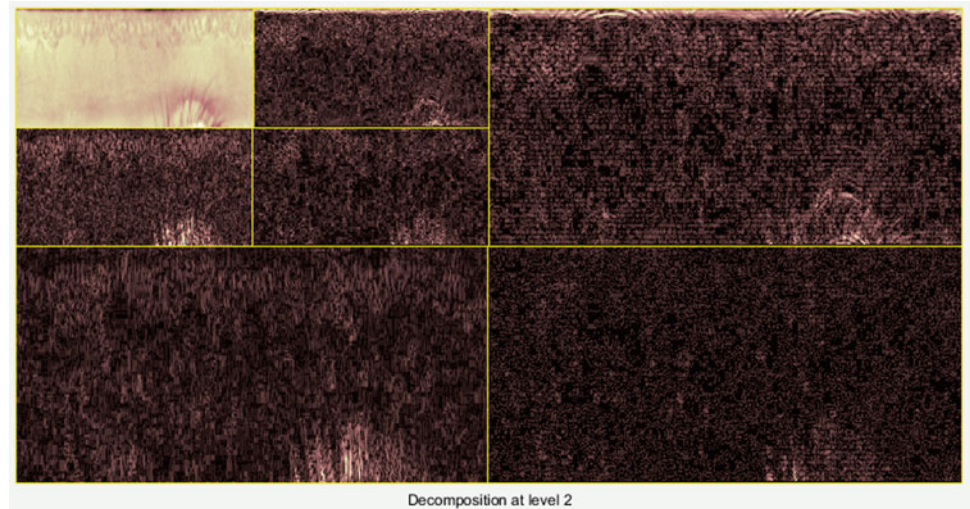
2.4 Threshold Algorithm for Iris Identification

From features of the iris image, the Hamming Distance (HD) indicates the number of bits that are the same between two bit patterns. Using the HD of the two bit patterns, one decision can be made whether two samples of different irises or from they are the same iris. It means that when one compares between samples A and B , the $HD(A, B)$ is defined as the sum of the bits not to be the same per the total number of bits of a sample and its equation is described as follows.

$$HD(A, B) = \frac{1}{N} \sum_{j=1}^n A_j \oplus B_j \quad (8)$$

in which N is the size of an iris feature code, A and B are denoted as different iris feature codes, A_j and B_j are corresponding bits of the iris feature codes.

Fig. 5 An iris image is analysed using the discrete wavelet transform



For evaluating the similarity of two iris samples, the Similarity Degree (SD) method is applied and its equation is defined as follows.

$$SD(A, B) = 1 - HD(A, B) \quad (9)$$

In general, the SD and HD are the same, but the SD is the same direction to the similarity of the two irises. Finally, the threshold T is employed for estimating, particularly if $SD(A, B) \geq T$, then A and B comes from an iris and else that is not.

3 Results and Discussion

In this research, each iris of one person is encoded to be S1011L08, in which S1011 is assigned a person; letters of L or R are assigned to be the left iris or right iris; 08, 09 or 02 is the number of the sample. Therefore, the algorithm was applied to calculate values of SD on the iris images and one is based on it to estimate and make decision. The results in Table 2 show that the SD value of iris from two eyes is

Table 2 The results of matching iris images of the left eye images between different samples



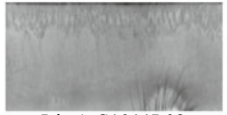

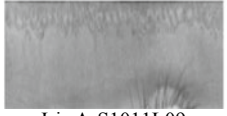
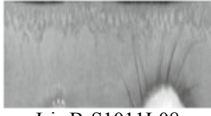
Images		Matching Results
 Iris A-S1011L02	 Iris B-S1011L09	SD=0.628
 Iris A-S1011L02	 Iris B-S1011L08	SD=0.6308
 Iris A-S1011L09	 Iris B-S1011L08	SD=0.6276

Table 3 The results of matching iris images with different people


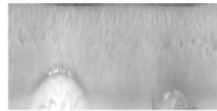
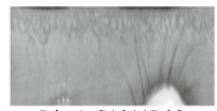
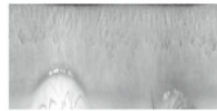



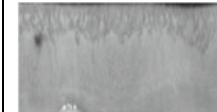
Image		Matching Result
 Iris A- S1011L02	 Iris B- S1019L01	SD=0.6176
 Iris A-S1011L08	 Iris B-S1019L01	SD=0.6215
 Iris A-S1011L02	 Iris B-S1016L02	SD=0.6201

Table 4 The results of matching with left iris with right iris of a person

Image		Matching Result
 Iris A- S1011L02	 Iris B- S1011R02	SD=0.6184

always less than 0.625, so the threshold $T = 0.625$ can be installed to identify matching. In particular, the SD values, which are smaller than T , mean that two iris images are estimated not to be the same and inversely it is the same. Therefore, to be able to select an optimal T threshold, the database with different iris samples is large.

In case of two irises of different people as shown in Table 2, in which the SD values are considered differently for recognition. In similarity, Table 3. shows matching an iris image compared with that of other iris images corresponding to the different SD values.

In Table 4, two iris images show the difference in structure of the left and right iris images of one person corresponding to one SD value.

From the above results, with $SD = 0.6184 < T$, it shows that there is the difference in the structure of the iris images between the left and the right iris images. Therefore, one can be based on this difference to identify one typical person with higher accuracy.

In this paper, the proposed method of iris recognition showed that using the iris structure for human recognition is useful and needs to develop in the future. In this research, the feature extraction for recognition was worked out using the DWT based on the DIDO model and its simulation results showed the effectiveness.

4 Conclusions

In this research, an iris recognition system was applied to analyze the iris features of human for recognizing a typical person. In particular, the DIDO model was used to extract iris image from eye image for feature extraction and the DWT algorithm was employed to determine the iris features for identification. The threshold method was utilized to exactly determine the iris feature for finding the corresponding person. Simulation results are that one T threshold suitably chosen allows to determine difference between two

right and left irises of one person, as well as between two irises of two persons. These results mean that the proposed method is the effectiveness and the basic step for development of iris identification with more optimal methods.

Acknowledgements The authors would like to thank Faculty of Electrical-Electronics, HCMC University of Technology and Education and the organization of Biometrics Ideal Test (CASIA-Iris). Moreover, we would like to thank students and colleagues for this research.

Conflicts of Interest The authors declare that they have no conflict of interest.

References

1. Choraś, M.: Perspective methods of biometric human identification. In: The SPA Conference, pp. 195–200 (2008)
2. Cruz, R.G., et al.: Iris recognition using Daugman algorithm on Raspberry Pi. In: The IEEE Conference (TENCON), pp. 2126–2129 (2016)
3. Pradhan, M.: Next generation secure computing: biometric in secure e-transaction. *Int. J. Adv. Res. Comput. Sci. Manag. Stud.* **3** (4), 473–489 (2015)
4. Choras, M.: Emerging methods of biometrics human identification. In: The Second International Conference on Innovative Computing, Information and Control (ICICIC), p. 365 (2007)
5. Zhou, X., Bhanu, B.: Integrating face and gait for human recognition. In: The Conference on Computer Vision and Pattern Recognition Workshop (CVPRW'06), p. 55 (2006)
6. Mil'shtein, S., Pillai, A., Shendye, A., Liessner, C., Baier, M.: Fingerprint recognition algorithms for partial and full fingerprints. In: The IEEE Conference on Technologies for Homeland Security, Waltham, MA, pp. 449–452 (2008)
7. Patil, S., Gudasalamani, S., Iyer, N.C.: A survey on iris recognition system. In: The International Conference on Electrical, Electronics, and Optimization Techniques (ICEEOT), pp. 2207–2210 (2016)
8. Bajwa, G., Dantu, R., Aldridge, R.: Pass-pic: a mobile user authentication. In: The IEEE International Conference on Intelligence and Security Informatics (ISI), Baltimore, MD, p. 195 (2015)
9. Proenca, H.: Iris recognition: on the segmentation of degraded images acquired in the visible wavelength. *IEEE Trans. Pattern Anal. Mach. Intell.* **32**, 1502–1516 (2010)
10. Wildes, R.P.: Iris recognition: an emerging biometric technology. *Proc. IEEE* **85**(9), 1348–1363 (1997)
11. Daugman, J.: How iris recognition works. *IEEE Trans. Circ. Syst. Video Technol.* **14**(1), 21–30 (2004)
12. Tajbakhsh, N., Misaghian, K., Bandari, N.M.: A region-based iris feature extraction method based on 2D-wavelet transform. In: The European Workshop on Biometric ID Management and Multimodal Communication, pp. 301–307 (2009)
13. Adler, F.H.: *Physiology of the Eye*, p. 143. Mosby, Maryland Heights (1953)
14. Sanderson, S., Erbetta, J.: Authentication for secure environments based on iris scanning technology. In: The IEE Colloquium on Visual Biometrics, pp. 1–12 (2000)
15. Thomas, T., George, A., Devi, K.P.I.: Effective iris recognition system. *Procedia Technol.* **25**, 464–472 (2016)
16. Yao, Z.W., Jun, Z., Yu, F.W., Ming, J.W.: Iris feature extraction based on Haar wavelet transform. *Int. J. Secur. Appl.* **8**(4), 265–272 (2014)

Development of a Fingerprint Singularity Detection Method Based on Moment Invariants for Biometrics and Medical Applications

L. V. Dang, S. S. Makhanov, L. C. Hieu, M. S. Packianather, H. L. Minh, and L. H. Quoc

Abstract

The biometric technologies have long been used for identification and authentication purposes; and fingerprint is one of the most widely used biometric technologies. In medicine and healthcare applications, biometric systems are used to identify patients and retrieve crucial medical records. In this paper, we propose a fingerprint singularity detection algorithm based on a very well-known pattern recognition technique. The successfully developed algorithm was tested for different fingerprint image resolutions, noise levels, and it was directly compared to the traditional technique, Poincare index which is the scalar values representing the geometrical behavior of basic patterns. The test of the proposed algorithm shows the outperformed results in both the high noise and low resolution images. Especially, the descriptors can be extracted directly from the suspect original and sample fingerprint images. The proposed method is therefore robust and can be adopted to any special descriptors rather than the pure core and delta points. With the recent advancement in data science, the successfully developed algorithm is potential for development of innovative biometric and medical applications, especially for telehealth and e-health systems.

Keywords

Biometrics • Poincare index • Singularity detection • Medical records • Patient identification

1 Introduction

Patient's privacy and data are the first and foremost important issues in today's healthcare, and security of Electronic Health Records (EHRs) which are the most vulnerable and tempting targets to cyber-attacks. To access confidential EHRs, the security systems for human authentication are normally used, including iris, DNA, voice recognition, fingerprint, retina and finger vein [1, 2], in which the fingerprint is one of the most widely used and well researched [3]. The use of fingerprint authentication to safeguard privacy and grant access to EHRs has been successfully developed and applied in healthcare [1, 4]. Generally, the applications of biometrics such as fingerprint in healthcare include: (1) to fight against health care fraud and abuse; (2) to manage and protect confidential EHRs; (3) to identify patients, especially for cases in which unconscious individual could be identified, and for speeding up patient intake and improving record accuracy, as well as preventing the duplication of medical records and potential medical record errors; (4) to safely operate medical facilities and equipment; and (5) to have a continuous and secure access to EHRs, especially in the cloud-based telehealth and telemedicine. There is an emerging need to enhance the security, effective managements and use of patient data and medical records, especially in telehealth, management of confidential medical records, and e-health systems.

This study aims to investigate the use of fingerprints for biometrics and medical applications, in which the fingerprint singularity detection method is used to correctly locate the singular points (core and delta points) of a fingerprint image for the fingerprint recognitions, based on the *moment*

L. V. Dang (✉) · S. S. Makhanov
Sirindhorn IIT, Thammasat University, Bangkok, Pathum Thani,
Thailand
e-mail: haidang3a2009@gmail.com

L. C. Hieu
Faculty of Engineering and Science, University of Greenwich,
Kent, UK

M. S. Packianather
School of Engineering, Cardiff University, Cardiff, UK

H. L. Minh · L. H. Quoc
Department of S&T Management, Saigon Hi-Tech Park, Ho Chi
Minh, Vietnam

invariant which is an excellent technique for pattern recognition and classification.

In fingerprint singularity detection, the global structure of the fingerprint image is required and usually represented as a direction field or orientation field (OF) [5]. The pattern around a singularity has its unique structure and can be prescribed as flow template [6]. These special structures are used to allocate type of singularity and its location [7]. There is a huge number of well-documented methods used to identify singularities of fingerprint images [8], especially the Poincare index method [7]. Major methods work well for high quality images; however, when the images include high level of noises or irregular structures, spurious points are obtained [9]. Several methods such as phase portrait analysis [10] or Poincare index are suffered from fixed size of searching window; consequently, the singularities near boundary image are unable to detect [11]. Moment invariants [12] are properties of connected regions in binary images that are invariant to translation, rotation and scale. The use of moment invariants to determine the singularity of a fingerprint image has not been well investigated and applied, especially for development of algorithms to detect the singularity of fingerprint images.

The rest of the paper is organized as follows. Section 2 presents the procedure to extract the orientation field (OF) of fingerprint images. The moment invariant formulation for the resulted OF is presented in Sect. 3. The proposed fingerprint singularity detection algorithm is presented in Sect. 4. Finally, Sect. 5 presents the test results, conclusions and brief discussions.

2 Estimation of the Orientation Fields

The flow patterns established by the ridge and valley of fingerprint images are represented by bi-direction vector fields (VFs) or orientation fields (OFs). Usually, the ridge orientation ranges from 0 to π . Conveniently, the range of orientation is defined in $(-\pi/2, \pi/2)$. A number of methods have been proposed to extract the OF from the fingerprint images [5]. A robust and efficient method to noise images proposed in [13] is used to extract the OFs of fingerprint images in this study. For a given normalized image $I(x, y)$, five steps (S1 to S5) to evaluate the orientation at pixel (x, y) are presented as follows: (S1) A block size $W \times W$ is centered at (x, y) ; (S2) For each pixel in the block, compute the gradient $\partial_x I(x, y)$ and $\partial_y I(x, y)$; (S3) The local orientation $\theta(x, y)$ then can be estimated using the equations: $\theta(x, y) = \frac{1}{2} \tan^{-1} \frac{V_y(x, y)}{V_x(x, y)}$

where $V_x(x, y) = \sum_{u=x-\frac{W}{2}}^{x+\frac{W}{2}} \sum_{v=y-\frac{W}{2}}^{y+\frac{W}{2}} 2\partial_x I(u, v)\partial_y I(u, v)$ and $V_y(x, y) = \sum_{u=x-\frac{W}{2}}^{x+\frac{W}{2}} \sum_{v=y-\frac{W}{2}}^{y+\frac{W}{2}} \partial_x^2 I(u, v)\partial_y^2 I(u, v)$;

(S4) Smooth the OF in a local neighborhood using the Gaussian filter to correct the corrupted orientation which is resulted from noises; and (S5) Finally, the orientation at the pixel (x, y) now can be re-assigned as: $\theta(x, y) = \frac{1}{2} \tan^{-1} \frac{U_x(x, y)}{U_y(x, y)}$, where $U_x(x, y)$ and $U_y(x, y)$ are the components of the continuous vector field with the Gaussian filter. Examples of fingerprint orientation extractions and estimations are presented in Fig. 1.

3 Formulation of the Moment Invariant

Let us represent the orientation of the ridge at the location (x, y) by a unit vector (v_x, v_y) and express it in form of a complex number $V = v_x + iv_y$ defined in the reference coordinate system. The ‘‘argument’’ of the complex number is defined by $\theta(x, y) = \begin{cases} \tan^{-1}(v_y/v_x), & \text{if } v_x \neq 0, \\ -\pi/2, & \text{otherwise.} \end{cases}$. Clearly, $\theta(x, y) = \theta(-x, -y)$ and $\theta(-x, y) = \theta(x, -y)$. Therefore, $f(x, y) = e^{i2\theta(x, y)}$ is ‘‘flip invariant’’, integrable, and can represent the OF (Note that the orientation have been double to resolve the integration problem of the single phase). A complex moment c_{pq} is defined by [12]: $c_{pq} = \int_{-\infty}^{\infty} \int_{-\infty}^{\infty} (x + iy)^p (x - iy)^q f(x, y) dx dy$. We replace the integral $\int_{-\infty}^{\infty} \int_{-\infty}^{\infty}$ by an integral over a sampling circle with the radius R_s . In the polar coordinates $c_{pq} = \int_0^{R_s} \int_0^{2\pi} r^{p+q+1} e^{i(p-q)\varphi} f(r, \varphi) dr d\varphi$. Substituting $f(r, \varphi) = e^{i2\theta(r, \varphi)}$ yields $c_{pq} = \int_0^{R_s} \int_0^{2\pi} r^{p+q+1} e^{i(p\varphi - q\varphi + \theta(r, \varphi))} dr d\varphi$. Note that $0 \leq \varphi \leq 2\pi$, whereas $-\frac{\pi}{2} \leq \theta < \frac{\pi}{2}$. If $f(r, \varphi) = e^{i2\theta(r, \varphi)}$ is rotated by an angle α , $f_{new}(r, \varphi) = e^{i(2\theta(r, \varphi) - \alpha)}$, then $c_{pq, new} = e^{i(p-q+1)\alpha} c_{pq}$. Therefore, any moment constructed as $\prod_{j=1}^n c_{p_j, q_j}$ with $\sum_{j=1}^n (p_j - q_j + 1) = 0$ is rotationally invariant. A change of variables $\hat{x} = x - \bar{x}$, $\hat{y} = y - \bar{y}$ and normalizing c_{pq} implies the translation and scale invariance as follows: $c_{pq} = \frac{1}{v^{\gamma}} \int_0^{\infty} \int_0^{\infty} (\hat{x} + i\hat{y})^p (\hat{x} - i\hat{y})^q f(\hat{x}, \hat{y}) d\hat{x} d\hat{y}$, where $\gamma = \frac{p+q+2}{2}$, $v = \int_{-\infty}^{+\infty} \int_{-\infty}^{+\infty} \chi(\hat{x}, \hat{y}) d\hat{x} d\hat{y}$,

$$\chi(x, y) = \begin{cases} 1, & \text{if } (x, y) \in W \\ 0, & \text{otherwise,} \end{cases}$$

$$\bar{x} = \frac{\int_{-\infty}^{+\infty} \int_{-\infty}^{+\infty} x\chi(x, y) dx dy}{\int_{-\infty}^{+\infty} \int_{-\infty}^{+\infty} \chi(x, y) dx dy},$$

$$\bar{y} = \frac{\int_{-\infty}^{+\infty} \int_{-\infty}^{+\infty} y\chi(x, y) dx dy}{\int_{-\infty}^{+\infty} \int_{-\infty}^{+\infty} \chi(x, y) dx dy}.$$

Finally, Flusser [12] derives a set of independent moments of the order $p + q \leq 2$ as follows: $\mu_2 = \{c_{01}, c_{00}c_{02}, c_{11}c_{02}, c_{10}c_{02}^2, c_{20}c_{02}^3\}$. The moments are considered as a feature vector in a multi-dimensional space. In order to identify the



Fig. 1 Fingerprint orientation field extraction

patterns a straightforward test is applied to compare a vector μ_2 with a template vector $\mu_{2,\text{pattern}}$ and an identification threshold ζ is introduced [14, 15].

4 Algorithm for Detection of Singularity of Fingerprint Images

The proposed algorithm is presented as follows.

1. **Generation of a singularity template.** From a set of fingerprint images with well defined singularities, a sample of patterns centered at the singularity pixels with different radiuses is selected for each type of singularity. Moment invariant vectors are evaluated, averaged, and stored as template vector $\mu_{2,\text{pattern}}$.
2. **Calculation of the pyramid moment invariant.** For an input fingerprint image of size $M \times N$. Define a moving square window centered at (x, y) with the radius k . For each position (x, y) , a sequence of moments $B_{x,y}^k$ is evaluated. The increasing radius of the window $k = k_{\min}, \dots, k_{\max}$ creates a pyramid structure [16].
3. **Calculation of the similarity pyramid.** For each type of singularity, a same structure of pyramid moment is constructed by replacing the value in each cell by the Euclidean distance between the vector in the cell and the template vector.
4. **Detection of singularities.** The pyramid moment is expressed in a matrix form and sorted in descending order of similarity (higher similarity means lower the distance, thus closer matching pattern). An ε_1 — threshold cut-off level is performed. A new set of ε_1 — similarity with different window sizes is obtained. Now, the obtained set is sorted by descending the order of a window radius. The similarity value corresponding to the smallest window size will again be used as the minimum

similarity threshold, ε_2 . Remove any rows that have a similarity smaller than ε_2 . The process is repeated until the singularities are found.

5 Results, Discussions and Conclusions

The proposed fingerprint singularity detection algorithm was successfully developed and it was then verified by using two common sources of data bases FVC2002/DB1 and FVC2002/DB2 [17]. The data DB1 is used for the singularity template extraction. The searching window radius is selected from 10 to 50 with the increment size 10. The proposed algorithm and the Poincare index method were then tested using both databases. The experiment results are shown in Table 1. Note that the size of the OFs can be defined for appropriate image resolutions and to reduce the computational cost.

Figure 2 presents the core and delta detection examples. The obtained results show that the moment invariant algorithm in this study outperforms the Poincare index and it is able to detect the singularity that is very closed to the image boundary (Fig. 2b).

In conclusion, the fingerprint singularity detection algorithm was successfully developed and tested for different fingerprint image resolutions and noise levels. The proposed

Table 1 Experiment results: a singularity detection rate

	DB1		DB2	
	Core	Delta	Core	Delta
Actual value	80	34	79	60
Poincare index [7]	80	27	73	47
Moment invariant	80	33	76	55
PI—detection rate (%)	100	79.4	92.4	78.3
MI—detection rate (%)	100	97.0	96.2	91.6

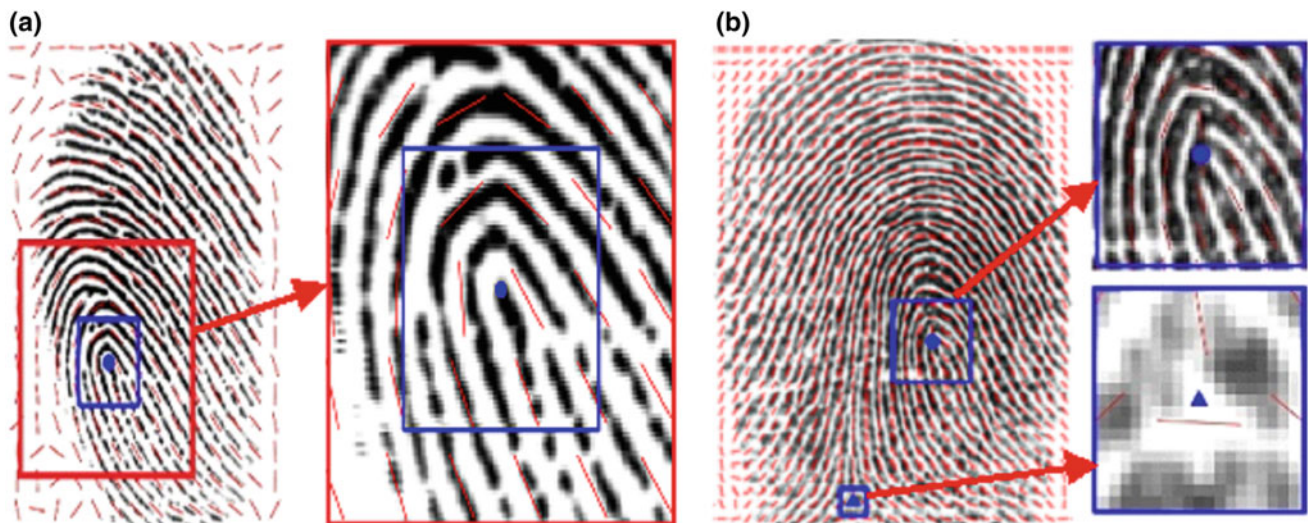


Fig. 2 a Core and delta detection. b Detection of a singularity closed to the image boundary

algorithm is robust and can be adopted to any special descriptors rather than the pure core and delta, with potentials for biometrics and medical applications. The outcome of a study is directly used for further development of a complete fingerprint authentication system to safeguard privacy and grant access to EHRs, aimed to enhance the security as well as effective managements and use of patient data and medical records in telehealth, management of confidential medical records, and e-health systems.

Acknowledgements This research is sponsored by the Center of Excellency in Biomedical Engineering, Thammasat University of Thailand, British Council and Newton Fund.

Disclosure Statement The authors declare that they have no conflict of interest.

References

- Chen, Y.-C., Chen, L.-K., Tsai, M.-D., Chiu, H.-C., Chiu, J.-S., Chong, C.-F.: Fingerprint verification on medical image reporting system. *Comput. Methods Programs Biomed.* **89**(3), 282–288 (2008)
- Sadhya, D., Singh, S.K.: Privacy risks ensuing from cross-matching among databases: a case study for soft biometrics. *Inform. Process Lett.* **128**, 38–45 (2017)
- Yang, W., Wang, S., Hu, J., Zheng, G., Valli, C.: A fingerprint and finger-vein based cancelable multi-biometric system. *Pattern Recogn.* **78**, 242–251 (2018)
- Weerasinghe, D., Rahulamathavan, Y., Rajarajan, M.: Secure trust delegation for sharing patient medical records in a mobile environment. *Health Policy Technol.* **2**, 36–44 (2013)
- Gupta, P., Gupta, P.: An accurate fingerprint orientation modeling algorithm. *Appl. Math. Model.* **40**, 7182–7194 (2016)
- Dass, S.C., Jain, A.K.: Markov models for directional field and singularity extraction in fingerprint images. *IEEE Trans. Image Process.* **13**(10), 1358–1367 (2004)
- Kawagoe, M., Tojo, A.: Fingerprint pattern classification. *Pattern Recogn.* **17**(3), 295–303 (1984)
- Iwasokun, G.B., Akinyokun, O.C.: Fingerprint singular point detection based on modified Poincare index method. *Int. J. Sig. Process. Image Process. Pattern Recog.* **7**(5), 259–272 (2014)
- Zacharias, G.C., Lal, P.S.: Singularity detection in fingerprint image using orientation consistency. In: 2013 International Multi-Conference on Automation, Computing, Communication, Control and Compressed Sensing (iMac4s), pp. 150–154 (2013)
- Ram, S., Bischof, H., Birchbauer, J.: Detection fingerprint singularity using linear phase portraits. In: *Handbook of Remote Biometrics. Advances in Pattern Recognition*, Springer, London, pp. 349–362 (2009)
- Li, J., Yau, W.-Y., Wang, H.: Combining singular points and orientation image information for fingerprint classification. *Pattern Recogn.* **41**, 353–366 (2008)
- Flusser, J., Suk, T., Zitová, B.: *Moments and Moment Invariants in Pattern Recognition*. Wiley, Chichester (2009)
- Thai, R.: *Fingerprint image enhancement and minutiae extraction*. The University of Western Australia, Perth (2003)
- Flusser, J., Suk, T.: Affine moment invariants: a new tool for character recognition. *Pattern Recogn. Lett.* **15**, 433–436 (1994)
- Hu, M.-K.: Visual pattern recognition by moment invariants. *IRE Trans. Inf. Theory* **8**, 179–187 (1962)
- Schlemmer, M., Heringer, M., Morr, F., Hotz, I., Bertram, M.H., Garth, C., Kollmann, W., Hamann, B., Hagen, H.: Moment invariants for the analysis of 2D flowfields. *IEEE Trans. Vis. Comput. Graph.* **13**, 1743–1750 (2007)
- Maio, D., Maltoni, D., Cappelli, R., Wayman, J. L., Jain A. K.: FVC2002: fingerprint verification competition. In: *Proceedings of the International Conference on Pattern Recognition (ICPR)*, pp. 744–747 (2002)

Pancreas Segmentation in Medical Images Based on Gaussian Mixture Model in Bandelet Domain

Nguyen Huu The, Vo Thi Hong Tuyet, Nguyen Mong Hien, and Nguyen Thanh Binh

Abstract

The pancreas is one of important organs in human body. The pancreas segmentation from medical images is a difficult task. Because adjacent organs have the similar intensity values. In this paper, we proposed a new method for pancreas segmentation in bandelet domain. Our method includes two stages. Firstly, applying the Gaussian mixture model for foreground and background is estimated using marked pixels by the user in bandelet domain. Finally, that is pancreas segmentation in medical images in the first stage by objcut. Our dataset is pancreas images that have been collected in many hospitals. We undervested the proposed method by calculating the Jaccard index values. The results of the proposed method are better than the other recent methods.

Keywords

Pancreas segmentation • Gaussian mixture model • Bandelet

1 Introduction

Located deep in the abdomen, the pancreas is a long, flat organ where enzymes and hormones are produced that support digestion. These enzymes are secreted into the small intestine, where they help break down protein and fat after they have left the stomach. Therefore, pancreas segmentation is hard work and challenge. In recent years, many methods have been built to pancreas segmentation [1]. Shimizu [2, 3] proposed an automatic pancreas segmentation method from contrast-enhanced multiphase computed tomography (CT). Marius [4] uses liver and spleen as starting points for detection of splenic. Shimizu [3] proposed pancreas segmentation using atlas-guided segmentation and level-sets. However, each method has strengths and weaknesses. In this paper, we propose a new method for pancreas segmentation in bandelet domain. Our method includes two stages. Firstly, applying the Gaussian mixture model for foreground and background is estimated using marked pixels by the user in bandelet domain. Finally, pancreas segmentation in medical images in the first stage by objcut. Our dataset is pancreas images, which have been collected in many hospitals. We underveste the proposed method by calculating the Jaccard index values. We use the Jaccard index (J.I) measure to calculate an extracted region and a true one. To evaluate the results, we compare the results of the proposed method and the results of Shimizu method [2] and Marius method [4]. The results of the proposed method are higher than the other recent methods. The rest of the paper is organized as follows: in Sect. 2, we describe bandelet transform and details of the proposed method. The experiment results and conclusion are presented in Sects. 3 and 4.

N. H. The (✉)

Faculty of Engineering Technology, Mekong University,
Vinh Long, Vietnam
e-mail: nguyenhuuthe@mku.edu.vn

V. T. H. Tuyet

Faculty of Information Technology, Ho Chi Minh City Open
University, Ho Chi Minh City, Vietnam
e-mail: tuyet.vth@ou.edu.vn

N. M. Hien

Tra Vinh University, Tra Vinh, Vietnam
e-mail: hientvu@tvu.edu.vn

N. M. Hien · N. T. Binh

Faculty of Computer Science and Engineering,
Ho Chi Minh City University of Technology,
VNU-HCM, Ho Chi Minh City, Vietnam
e-mail: ntbinh@hcmut.edu.vn

2 Pancreas Segmentation in Medical Images in Bandelet Domain

2.1 Bandelet Transform

Bandelets are adapted to a multi-scale geometry defined over the coefficients of a wavelet basis. The bandelets [5, 6] have optimal approximation results for geometrically regular functions. The bandelets are defined as smooth functions on smoothly bounded domains [5]. As bandelet construction utilizes wavelets, many of the results follow. Similar approaches to take account of geometric structure were taken for contourlets and curvelets. The bandelet decomposition is computed with geometric orthogonal transform. It has basis functions elongated along the singularity.

A dyadic segmentation of wavelet coefficients and choice of a polynomial flow inside each square define a bandelet $B(T)$. This bandelet depends on the geometry of the local flows. The bandelet is an orthogonal, multiscale transform [5, 7]. The bandelet decomposition is applied on orthogonal wavelet coefficients. It is computed with a geometric orthogonal transform. We consider a wavelet transform at a fixed scale 2^j . The wavelet coefficients $\langle f, \psi_{jn} \rangle$ are samples of an underlying regularized function [8].

$$\langle f, \psi_{jn} \rangle = f * \psi_j(2^j n) \text{ where } \psi_j(x) = \frac{1}{2^j} \psi(-2^{-j} x) \quad (1)$$

The coefficients $\psi_v[n]$ are the coordinates of the bandelet function $b_v \in L^2([0,1]^2)$ in the wavelet basis. A bandelet function [7] is defined by,

$$b_v(x) = \sum_n \psi_v[n] \psi_{jn}(x) \quad (2)$$

It is a combination of wavelets and its support along a band as Fig. 1 [7]. Bandelets are as regular as the underlying wavelets. The support of bandelets overlaps in the same way that the support of wavelets overlaps [7]. This is particularly

important for reconstructing image approximations with no artifacts. Figure 1 presents a combination of wavelets along a band and its support is thus also along a band.

From an orthogonal wavelet basis with an orthogonal transformation, they are obtained from bandelets. Apply this transformation to each scale 2^j , an orthogonal basis of $L^2([0,1]^2)$ is defined as [7]:

$$B(T) = \stackrel{\text{def}}{=} \bigcup_{j \leq 0} \{b_v | \psi_v \in B(T_j)\}, \quad \text{where } T = \stackrel{\text{def}}{=} \bigcup_{j \leq 0} T_j \quad (3)$$

2.2 Pancreas Segmentation in Bandelet Domain

In this section, we propose a method to segment pancreas from medical images based on Gaussian mixture model (GMM) in bandelet domain. The proposed method includes two stages. Firstly, applying the GMM for foreground and background is estimated using marked pixels by the user in bandelet domain. Finally, that is pancreas segmentation in medical images in the first stage by objcut. The proposed method can be summarized as follows in Fig. 2.

From Fig. 2, the procedure for pancreas segmentation in medical images based on Gaussian mixture model in bandelet domain is as follows:

- (i) The medical image input is the CT image, which contains pancreas.
- (ii) Region information by GMM in bandelet domain. We got foreground and background, which are estimated from GMM method in bandelet domain. The image is a matrix. Each element in these matrixes is a pixel. The value of the pixel is intensity of these pixel. Let X is random value of the pixel. For probability model, support to have mixture of Gaussian distribution as [9]:

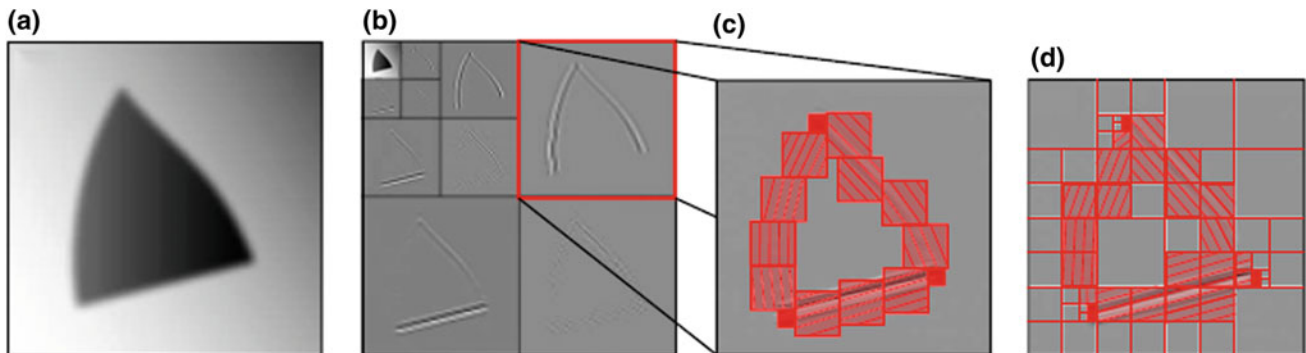


Fig. 1 a A geometrically regular image. b Wavelet coefficients. c A non-dyadic segmentation into squares together with bands over each square crossing the singularities. d A dyadic subdivision of the coefficients together with a dyadic subdivision into bands. Source [7]

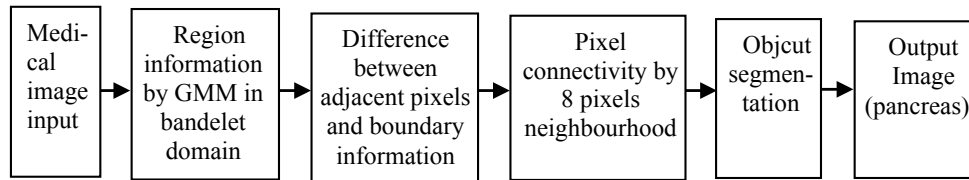


Fig. 2 The process flow of the proposed method

$$f(x) = \sum_{i=1}^k p_i N(x|\mu_i, \sigma_i^2) \quad (4)$$

where, k is the number of region and $p_i > 0$ are weights and $\sum_{i=1}^k p_i = 1$. For a given image I , the lattice data are the values of pixel and GMM is pixels base model. Pixel-based background modeling update all pixel information every region. We find difference between adjacent pixels and boundary information. After that, we use 8-pixels neighborhoods to connect the adjacent pixels together.

- (iii) Objcut to segment the pancreas from medical images. The objcut algorithm [10] was apply to segment pancreas with the input image I , a nonarticulated object category and the initial estimate of pose using edges and texture.

3 Experiments and Results

Experiments are developed in Matlab 2013a and carried out on computer of Intel core i7, 3.2 GHz CPU, 16 GB DDR3 memory. Our dataset is the medical images collected in many hospitals. There are 110 medical images with the sizes: 256×256 and 512×512 in dataset. We test the proposed method, Shimizu method [2] and Marius method [4] by these above dataset.

To evaluate the results, we computed the Jaccard index ($J.I$) between an extracted region and a true one [11], which were manually defined by a medical expert.

$$JI(A, B) = \frac{|A \cap B|}{|A \cup B|} \times 100 \quad (5)$$

where, A is extracted region, B is true region. If A and B are both empty, we define $J.I(A, B) = 100$. The index ranges from 0 to 100%, with higher values representing better performance [12].

We test on 110 medical images in the above dataset. In here, we only present two cases as Figs. 3 and 4. In addition, the value of $J.I$ is every case, which is calculated.

Figure 3 shows results for the original images and the result of the proposed method with others. Figure 3a is the original medical image. The result of Shimizu method [2] for pancreas segmentation is Fig. 3b. The result of Marius method [4] for pancreas segmentation is Fig. 3c and of the proposed method is Fig. 3d. In Fig. 3d, the $J.I$ value is higher than the result in Fig. 3b, c. Therefore, the result of the proposed method is better than the result of Shimizu method [2] and Marius method [4].

Figure 4 also shows results of the original images and the result of the proposed method with others. Figure 4a is the original medical image. The results of Shimizu method [2], Marius method [4] and the proposed method for pancreas segmentation are Fig. 4b, c, d. In Fig. 4d, the $J.I$ value is higher than the result in Fig. 4b, c. We see that, the result of the proposed method is also better than the result of Shimizu method [2] and Marius method [4].

As the above presented, our dataset has 110 pancreas images. The average $J.I$ value of all pancreas images is presented in Table 1.

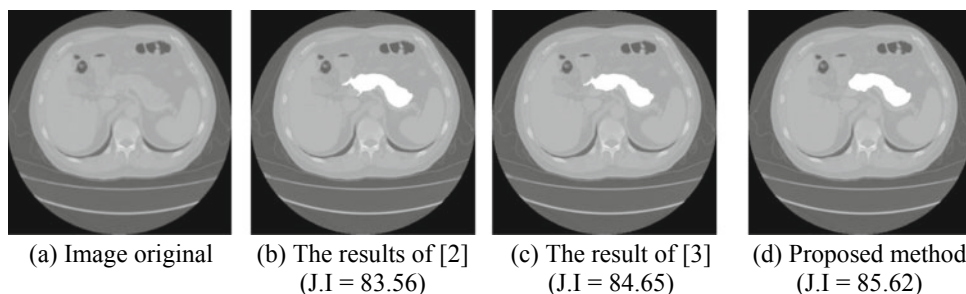


Fig. 3 The results of pancreas segmentation by proposed methods and the other method. **a** The original medical image. **b** Pancreas segmentation by Shimizu method [2]. **c** Pancreas segmentation by Marius method [4]. **d** Pancreas segmentation by the proposed method

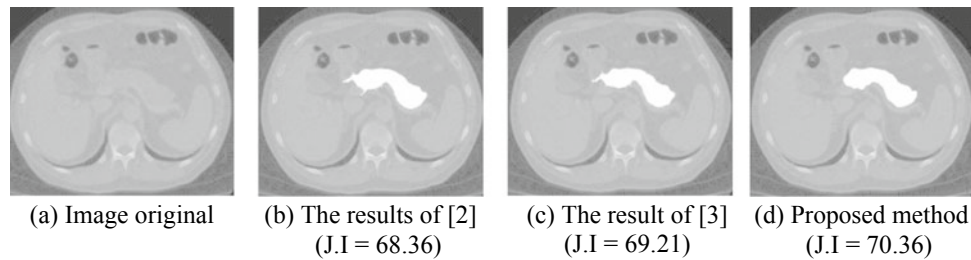


Fig. 4 The results of pancreas segmentation by proposed methods and the other method. **a** The original medical image. **b** Pancreas segmentation by Shimizu method [2]. **c** Pancreas segmentation by Marius method [4]. **d** Pancreas segmentation by the proposed method

Table 1 The average J.I value of three methods

Total of pancreas images	The average J.I value of Shimizu method [2]	The average J.I value of Marius method [4]	The average J.I value of the proposed method
110	75.342	76.268	77.274

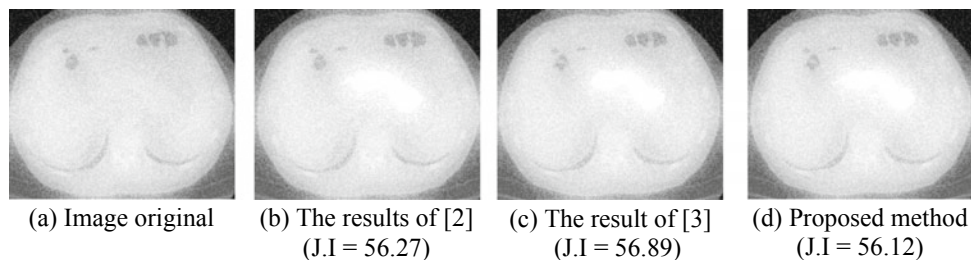


Fig. 5 The results of pancreas segmentation by proposed methods and the other method in case of blur images. **a** The original medical image. **b** Pancreas segmentation by Shimizu method [2]. **c** Pancreas

segmentation by Marius method [4]. **d** Pancreas segmentation by the proposed method

From Table 1, we see that: the result of the proposed method is better than the other methods. The reason of the results of the proposed method, which are better than those of the other methods because the bandelets have optimal approximation results for geometrically regular functions (smooth functions on smoothly bounded domains). Therefore, the result of the region information by GMM in bandelet domain step is very clear and smooth. Moreover, the object segmentation step helps group regions in the image.

Figure 5 also shows results for the original images and the result of the proposed method with others. From Fig. 5, the result of the proposed method is not better than the result of Shimizu method [2] and Marius method [4] in cases of blur images.

As mentioned in Sect. 2, we got foreground and background, which are estimated from GMM method in bandelet domain. If the medical images are very blur. The proposed method is difficult to get foreground and background. Therefore, the proposed method is effective.

4 Conclusions

Most people are only interested in the stomach, small intestine and colon but usually pay little attention to the pancreas. However, the pancreas is an important part of the digestive tract, which helps control blood sugar. The pancreas segmentation in medical image is a difficult task. In this paper, we proposed a new method for pancreas segmentation based on Gaussian mixture model in bandelet domain. Bandelets are adapted to a multi-scale geometry defined over the coefficients of a wavelet basis. It is combined with GMM to create region information. If the medical image is of high quality then the proposed method can be applied. The results of the proposed method are better than the other recent methods by calculating the Jaccard index values. In case the quality of medical images is low quality, the task of the pancreas segmentation is a challenge.

Conflict of Interest The authors declare that they have no conflict of interest.

References

1. Shimizu, A., Nawano, S., Shinozaki, K., Tateno, Y.: Medical image processing competition in Japan, WC 2009. In: IFMBE Proceedings 25/IV, pp. 1814–1817 (2009)
2. Shimizu, A., Kimoto, T., Kobatake, H., et al.: Automated pancreas segmentation from three-dimensional contrast-enhanced computed tomography. *Int. J. Comput. Assist. Radiol. Surg.* **5**(1), 85–98 (2010)
3. Shimizu, A., Ohno, R., Ikegami, T., Kobatake, H., Nawano, S., Smutek, D.: Segmentation of multiple organs in non-contrast 3D abdominal images. *Int. J. Comput. Assist. Radiol. Surg.* **2**, 135–142 (2007)
4. Erdt, M., Kirschner, M., Drechsler, K., Wesarg, S., Hammon, M., Cavallaro, A.: Automatic pancreas segmentation in contrast enhanced CT data using learned spatial anatomy and texture descriptors. In: 2011 IEEE International Symposium on Biomedical Imaging: From Nano to Macro, pp. 2076–2082 (2011)
5. Le Pennec, E., Mallat, S.: Sparse geometric image representations with bandelets. *IEEE Trans. Image Process.* **14**(4), 423–438 (2005)
6. Le Pennec, E., Mallat, S.: Bandelet image approximation and compression. *SIAM J. Multiscale Simul.* **4**(3), 992–1039 (2005)
7. Mallat, S., Peyré, G.: Orthogonal bandelet bases for geometric images approximation. *Commun. Pure Apply Math.* LXI **61**(9), 1173–1212 (2008)
8. Binh, N.T., Tuyet, V.T.H., Vinh, P.C.: Ultrasound images denoising based context awareness in bandelet domain. In: Proceedings of the 2nd International Conference on Context-Aware Systems and Applications, vol. 128, pp. 115–124 (2013)
9. Permuter, H., Francos, J., Jermyn, I.: A study of Gaussian mixture models of color and texture features for image classification and segmentation. *Pattern Recogn.* **39**, 695–706 (2006)
10. Kumar, M.P., Torr, P.H.S., Zisserman, A.: In: OBJ CUT, IEEE Computer Society Conference on Computer Vision and Pattern Recognition, pp. 1–8 (2005)
11. Real, R., Vargas, J.M.: The probabilistic basis of Jaccard's index of similarity. *Syst. Biol.* **45**(3), 380–385 (1996)
12. Tam, T.D., Binh, N.T.: Efficient pancreas segmentation in computed tomography based region growing. In: Proceedings of the International Conference on Nature of Computation and Communication, pp 332–340 (2014)

Elevator Motion States Recognition Using Barometer Support Indoor Positioning System

Duong Van Nguyen, Thanh Van Pham, An Van Tran, Khai NguyenTuan, Hang Duong ThiThuy, Hop Hoang The, and Tan Tran Duc

Abstract

Indoor positioning is widespread applications in health monitoring, navigation and other indoor position services. There are a variety of researches focusing on solving indoor position problems, but most of them are using the accelerometer to solve horizontal positions. Nevertheless, there are a lot of buildings and houses where people are using the elevator to move among the floors. Hence, it is difficult to estimate the positions vertically when the users use the elevator in motion. This paper aims to integrate a barometer in indoor positioning system (IPS) for elevator motion recognition and proposes a new feature name “pressure standard deviation” from barometer recording data to distinguish among elevator up, elevator down, still, stairs up, stairs down to track the position of user in vertical axis. Our experimental results achieve 100% accuracy in distinguishing the state of elevator up, elevator down, still, stairs up, stairs down and estimate exactly and real-time in vertical axis.

Keywords

Indoor positioning system • Barometer • Elevator • Vertical position • Pressure standard deviation

1 Introduction

Activity recognition is important for widespread applications like IPS, patient tracking, health monitoring. Recently, most of the researches have focused on using acceleration data for activities classification. Nevertheless, the limitations of acceleration data are difficult to estimate the activities in vertical. Using built-in smartphone sensor like accelerometer, barometer, Global Positioning System (GPS), Wi-Fi, Bluetooth,... is more and more popular because these sensors are integrated in a smartphone. The GPS is unreliable for IPS because it is unstable in indoor environments. Using Wi-Fi and Bluetooth requires pre-installed system to emit and transfer the signal among the insides and between the inside and the outside. Hence, it is not applicable for indoor positioning applications like firefighting and rescue because the pre-installed system may be destroyed by flame and heat from burning fire.

In Refs. [1, 6, 7], the authors proposed to use the accelerometer for state classification. The accelerometer is only suitable to estimate the states of walking, running and still state horizontally. The accelerometer reading in the vertical is not very different among in-elevator up, in-elevator down and still states. Furthermore, using accelerometer in stairs up, stairs down and walking classification achieves low accuracy because the accelerometer reading values are not very different in these states.

The publication [8, 9] used barometer in vertical estimation, the authors proposed to integrate this sensor for measuring the pressure without eliminating abnormal parts in barometer reading. Hence, the reading values of the barometer will be affected by environment like weather, temperature and humidity and noise in sensor or the sudden change of air pressure.

Based on the above limitations, this paper proposes to integrate barometer in our IPS and to add new feature “pressure standard deviation” to eliminate abnormal part in barometer reading.

D. Van Nguyen · T. Van Pham (✉) · K. NguyenTuan · H. Duong ThiThuy · H. Hoang The · T. Tran Duc
VNU Hanoi University of Engineering and Technology,
Hanoi, Vietnam
e-mail: phamvanthanh1209@gmail.com

T. Van Pham · A. Van Tran
The University of Fire Fighting and Prevention (UFFP),
Hanoi, Vietnam

2 System Design

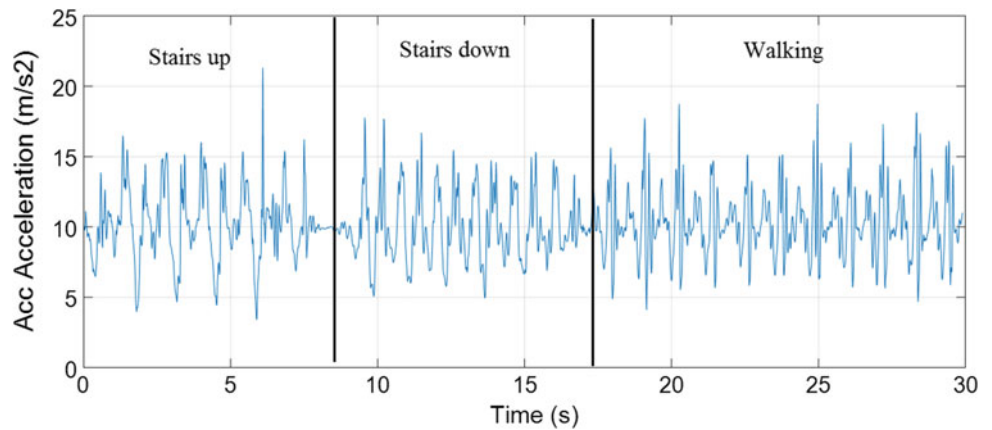
2.1 The 3-DOF Accelerometer

The 3-DOF accelerometer is used to acquire the acceleration in three axis A_x , A_y and A_z . This kind of sensor is also popular in outdoor positioning system [9–14]. Nevertheless, the accelerometer is only applicable to distinguish among activities like running, walking and still states by using the magnitude of acceleration as:

$$A_n = \sqrt{A_x^2 + A_y^2 + A_z^2}, \quad (1)$$

The acceleration data is difficult to recognize amongst still states, in-elevator up, in-elevator down and walking stairs up, walking stairs down and walking on the floor. It can be seen that, the Fig. 1 shows the acceleration (m/s^2) of walking stairs up, walking stairs down and walking on the floor (see Fig. 1). Also, it is difficult to distinguish among these states when using only the accelerometer for states classification.

Fig. 1 Acceleration magnitude of walking stairs up, walking stairs down and walking on the floor



2.2 Barometer BMP180 and Map Information

(a) *Barometer BMP180*

BMP180 is a sensor used to measure pressure and temperature. The temperature parameter supports to calculate the pressure of the environment because the pressure depends directly on the temperature, weather and humidity of the environment. Based on current measured pressure p and the pressure at sea level $p_0 = 1013.25$ hPa to calculate the altitude by using the international barometric formula [5]:

$$altitude = 44,330 * \left(1 - \left(\frac{p}{p_0} \right)^{\frac{1}{5.255}} \right), \quad (2)$$

Based on the *altitude* value and map information (see Figs. 2b and 3) we can estimate the vertical position of the user. Nevertheless, the barometer reading has always existed an abnormal signal (see Fig. 2a), it leads to the wrong position estimation (see Fig. 2) when we integrate barometer

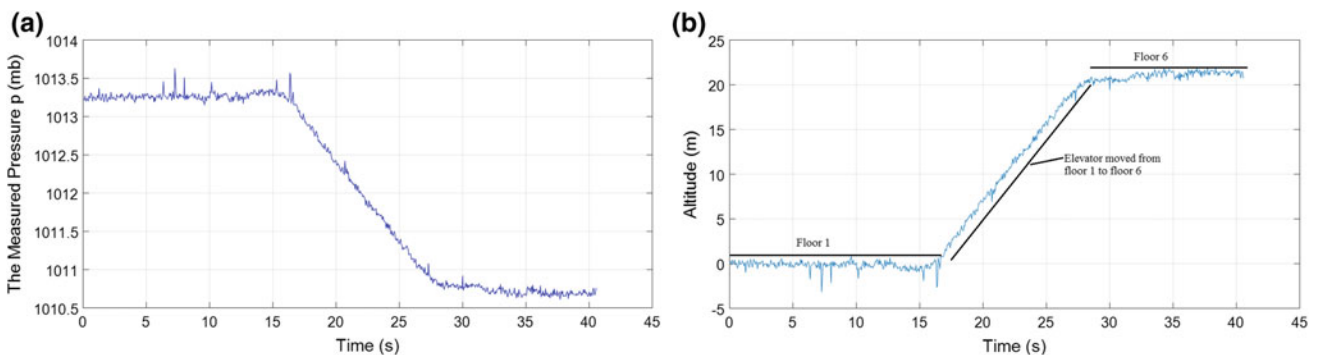


Fig. 2 a The raw measured pressure p (mb) and b the altitude based on the raw measured pressure

into an IPS without eliminating abnormal parts in the signal. The raw measured pressure data may cause the wrong prediction vertical position as the Fig. 2:

(b) Map Information

All buildings need designing before constructing, and there are all parameters like the height of the building, the height of each floor, stairs and elevators positions...etc. that are also clarified (see Fig. 3). These are useful information to support for finding the position of users inside of the building.

2.3 The Proposed Method

(a) System Design

The proposed IPS integrates of a micro controller unit (MCU) STM32F103C8T6, a low-cost 9-DOF IMU MPU-9250 (9-axis Motion Processing Unit), a wireless data transmitter/receiver, a barometer BMP180 and other supporting sensors for data fusion.

Figure 4 is the flowchart of our proposed method. Firstly, BMP180 sensor will record pressure data. In order to find out exactly the pressure data, the sensor is integrated temperature sensor. Based on recorded data, we have proposed new feature “pressure standard deviation” to solve abnormal parts in recorded data. Then, basing on the changing of pressure to estimate in-elevator states and floor level.

(b) The Pressure Standard Deviation

To detect the level of the floor, we uses the height which is calculated from the processed pressure data by the formula (2). The data in each window are a group of 4 barometer samples ($baro(i)$, $baro(i + 1)$, $baro(i + 2)$, $baro(i + 3)$). The pressure standard deviation algorithm is used for calibration data as Fig. 5.

To eliminate abnormal signal recorded from a barometer, we proposes that: if $abs(baro(i) - D) \leq Th1$ then $baro(i) = baro(i)$ else $baro(i) = baro(i - 1)$. Then the altitude can be derived from the measured pressure as in (1). We can distinguish being still from being in a vertical motion state by calculating the difference of data after 2 s. If the

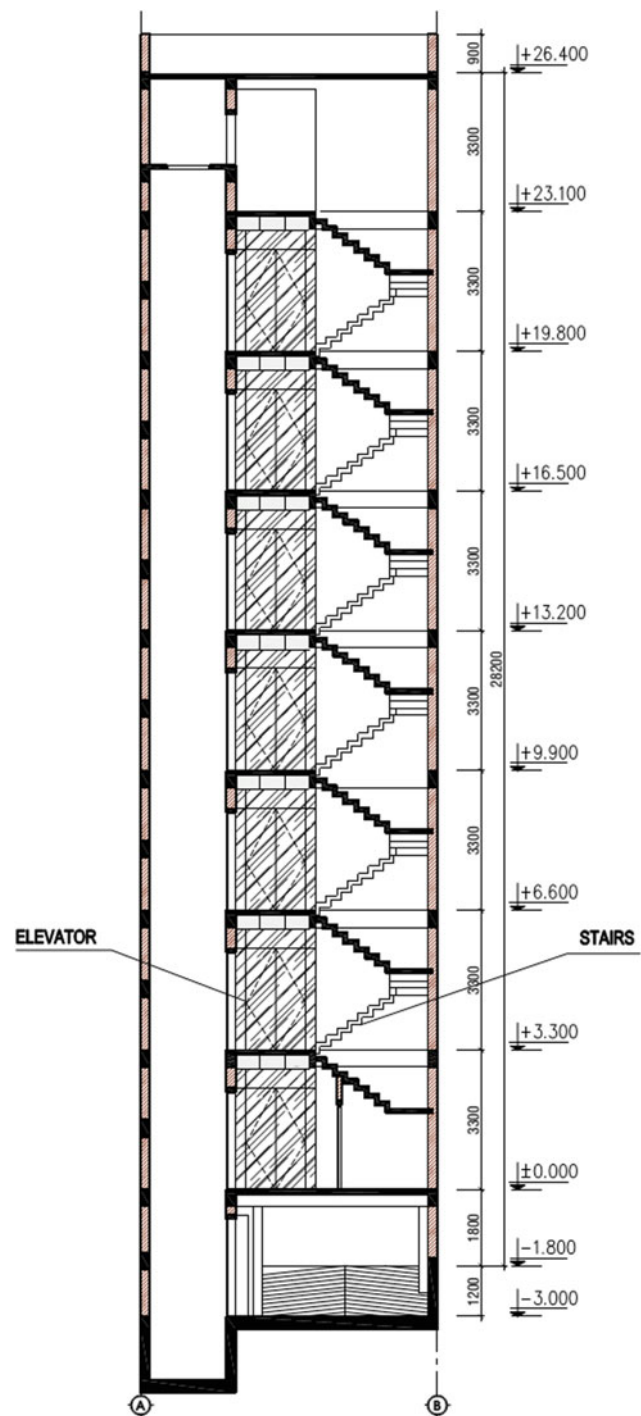


Fig. 3 The map information of a building (the building height, floor height, elevators and stairs positions)

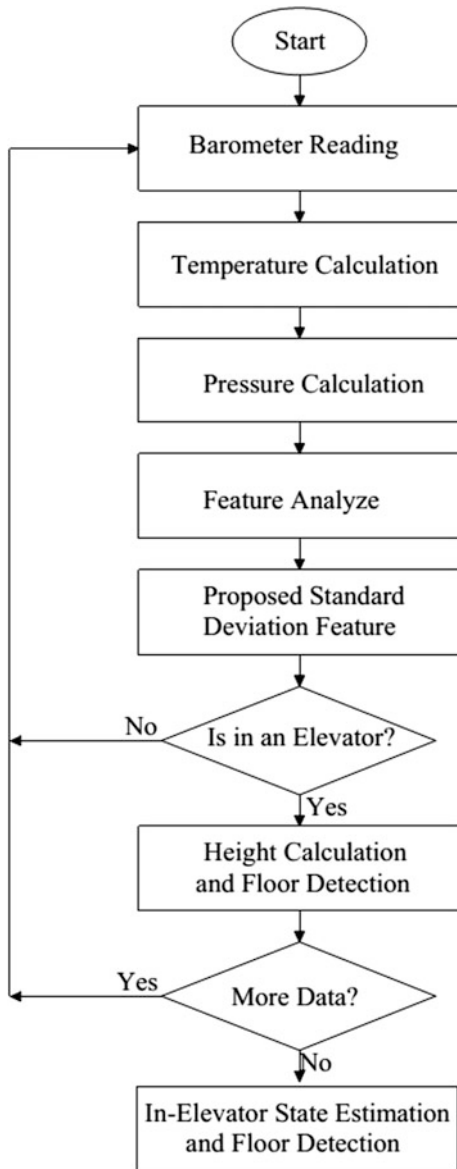


Fig. 4 The flowchart of our proposed method

difference is larger than the threshold, it can be considered that the user is moving vertically. With the given building schematics, we are able to estimate the instant altitude of the user and which floor the user is currently in.

3 Results and Discussions

For the experiment testing, we carried out a test on 6 firefighters selected from The University of Fire Fighting and Prevention (UFPF) age range of 18–22, height: 1.65–1.78 m,

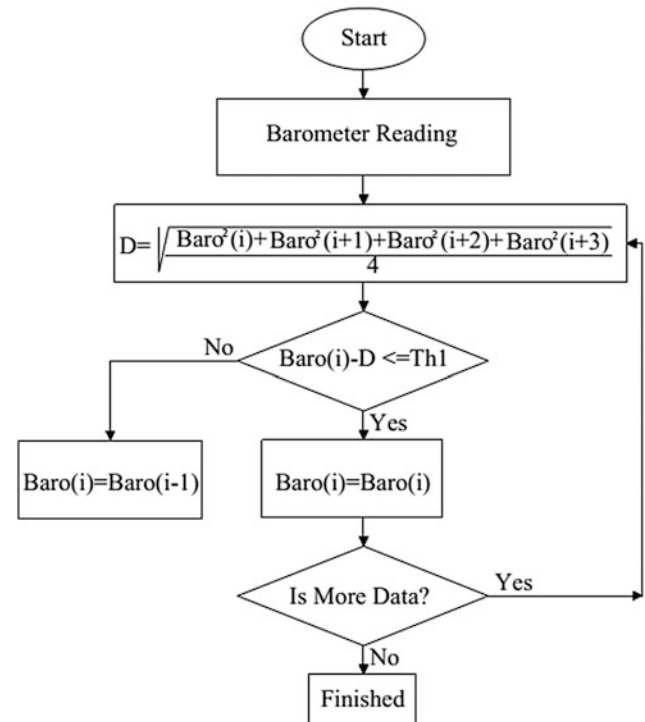


Fig. 5 The flow chart of our proposed “pressure standard deviation” feature

weight: 65–79 kg. The volunteers recorded two types of data: walking—elevator up—walking—elevator down—walking and stairs up—stairs down. For each type of data, the volunteer would record 3 times.

Figures 6 and 7 illustrates the altitude and position of firefighters in vertical position

In Fig. 6a, the volunteer carries our device and walks on floor 1, then uses the elevator to move to floor 6 and walks on it. The achievement results in Fig. 6 illustrates clearly of the states of walking—in-elevator up—walking from floor 1 to floor 6; (a) the measured pressure (mb) (b) the altitude (m).

The result in Fig. 7a is also very clear about the changing pressure and altitude among the floors. The proposed pressure standard deviation features will eliminate all abnormal parts in the signal (see Figs. 6 and 7).

4 Conclusion

In this paper, we proposed to use barometer integrated into an IPS and a new feature “pressure standard deviation” for states classification. The achievement results are significant improvements in states classification and floors estimation. In future work, we will combine recording data from IMU,

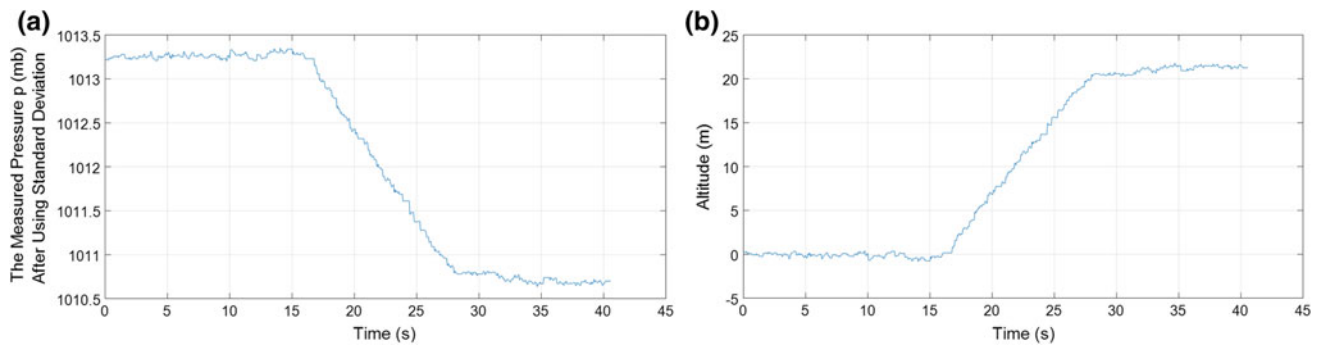


Fig. 6 a The measured pressure (*mb*) and b The altitude (*m*) after using the “pressure standard deviation” feature in elevator up

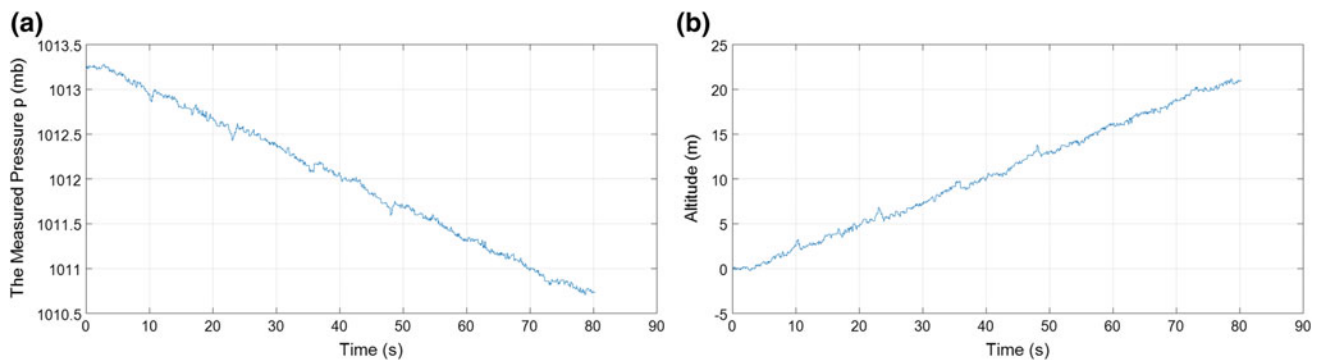


Fig. 7 The altitude and vertical position of volunteer after using the “pressure standard deviation” feature in walking stairs up

Barometer and other supporting sensors for data fusion and build map information to enhance the performance of our proposed IPS.

Conflict of Interest The authors declare that they have no conflict of interest.

References

- Gu, F., Kealy, A., Khoshelhamand, K., Shang, J.: User-independent motion state recognition using smartphone sensors. *Sensors* (2015)
- Rantakokko, J., Rydell, J., Strömbäck, P., Händel, P., Callmer, J., Törnqvist, D., Gustafsson, F., Jobs, M., Grudén, M.: Accurate and reliable soldier and first responder indoor positioning: multisensor systems and cooperative localization. *IEEE Wirel. Commun.* **18** (2), 10–18 (2011)
- Kales, S.N., Soteriades, E.S., Christoudias, S.G., Christiani, D.C.: Firefighters and on-duty deaths from coronary heart disease: a case control study. *Environ. Health: A Glob. Access Sci. Source* (2003)
- Figo, D., Diniz, P.C., Ferreira, D.R., Cardoso, J.M.P.: Preprocessing techniques for context recognition from accelerometer data. *Pers. Ubiquit. Comput.* **14**, 645–662 (2010)
- BMP180 Data sheet, downloaded at <https://cdn-shop.adafruit.com/datasheets/BST-BMP180-DS000-09.pdf>. Accessed 22 Mar 2018
- Van Thanh, P., Thi, A.D.N., Quynh, T.T.T., Phuong, D.C.T., Mau, V.H., Tran, D.T.: A novel step counter supporting for indoor positioning based on inertial measurement unit. In: The 7th International Conference on Integrated Circuits, Design, and Verification (ICDV 2017), Hanoi, Vietnam, Oct 5–6, 2017
- Pham, V.T., Nguyen, T.-A., Nghia T. D., Nguyen D., Tran D.-T.: Development of a real time supported program for motorbike drivers using smartphone built-in sensors. *Int. J. Eng. Technol. (IJET)*, Apr–May 2017
- Chen, Z., Zou, H., Jiang, H., Zhu, Q., Soh, Y.C., Xie, L.: Fusion of WiFi, smartphone sensors and landmarks using the Kalman filter for indoor localization. *Sensors* **15**, 715–732 (2015)
- Shang, J., Gu, F., Hu, X., Kealy, A.: APFiLoc: An infrastructure-free indoor localization method fusing smartphone inertial sensors, landmarks and map information. *Sensors* **15**, 27251–27272 (2015)
- Tran, D.T., Luu, M.H., Nguyen, T.L., Nguyen, D.D., Nguyen, P. T.: Land-vehicle MEMS INS/GPS positioning during GPS signal blockage periods. *J. Sci.* **23**(4), 243–251 (2007). (Vietnam National University, Hanoi)
- Tran, D.T., Luu, M.H., Nguyen, T.L., Nguyen, P.T., Huynh, H.T.: Performance improvement of MEMS-based sensor applying in inertial navigation systems. *Posts Telematics Inform. Technol. J.* **2**, 19–24 (2007)

12. Tan, T.D., Ha, L.M., Long, N.T., Tue, H.H., Thuy, N.P.: Novel MEMS INS/GPS integration scheme using parallel Kalman filters. In: IEEE/SICE International Symposium on System Integration, pp. 72–76 (2008)
13. Tan, T.D., Ha, L.M., Long, N.T., Tue, H.H., Thuy, N.P.: Feedforward structure of Kalman filters for low cost navigation. In International Symposium on Electrical-Electronics Engineering (ISEE2007), pp. 1–6 (2007)
14. Duc-Tan, T., Fortier, P., Huynh, H.T.: Design, simulation, and performance analysis of an INS/GPS system using parallel Kalman filters structure. REV J. Electron. Commun., **1**(2) (2011)

Predictive Modelling for Cardiovascular Disease Mortality in Intensive Care Units

Anh Thi Ngoc Vo, Trung Quoc Le, Trieu Nguyen Hai Le,
and Vo Van Toi

Abstract

The study develops a prognostic model for the mortality prediction of patients with cardiovascular diseases in Intensive Care Units (ICUs). Using clinical data, physiological measurements and vital signs during the first 48-hour after their admissions, the model specified the patients' death correlations therefrom identified high-risk patients and their survival probability. Cox Proportional Hazards model is used to classify the patients as dead or survival with the accuracy measured by Score 1—the minimum of sensitivity and positive predictivity-of 0.45, which is 1.5 times better than that of the baseline ICU scoring system. Meanwhile, Lasso (least absolute shrinkage and selection operator) removes redundant variables and Regression analysis estimates the patients' death time. The model excels in clinical prediction in terms of good classification, hybrid usage of data analysis, machine learning and signal processing for more insightful extraction of clinical features. Furthermore, the fast response time and heterogeneous multivariate diagnosis in multidimensional dataspace, including temporal changes of time-variant physiological measurements proposed a effective solution for real-time ICU monitoring system. Ultimately, this work serves as a predictive indicator of patient status, helping physicians and clinicians get insight into each individual for the most optimal treatment and resources allocation.

Keywords

Mortality prediction • Regression • Cox proportional hazards model

1 Introduction

The advancements in sensing technology and healthcare informatics have been widely adopted in healthcare area. Especially, patients admitted to Intensive Care Units (ICUs) with cardiovascular diseases, who commonly require life-sustaining treatment, have provided research community with a rich data source [1]. Their mortality, which is predictive by a cumulative deterioration of clinical abnormalities, could be utilized for better care prioritization and resource allocation [2]. Moreover, recently automated healthcare systems have significantly increased the amount of medical information collected. However, the large storage of test results and extensive monitoring over long periods of time has challenged care providers to utilize them quickly and effectively, leading to uneven resource distribution, shortage of ICU beds, higher mortality rate and premature discharge [3, 4]. These concerns call for new prognostic models, which can interpret that huge pool of information, predict patients' survival outcome and assist care providers in patient care. Various scoring metrics, computational calibration and mortality models are available, yet simplistic in the influence of diverse predictive variables, and often fails to precisely investigate the representation from complex data sources [5]. Hence, the accuracy of conventional models needs to be decisively better. Rather than statistical summary, more powerful forecasting models with intelligent monitoring are in demand.

This study proposes a predictive model to forecast the survival probability of ICU patients with cardiovascular disease, using their clinical measurements during the first 2 days throughout ICU stay. One of the most popular and strictly studied method for mortality prediction is survival analysis, which refers to the analysis of time-to-event data and the prediction of the event occurrence for an individual, such as biological death, mechanical or physiological failure, hospital discharge or admission [6, 7]. Three popular approaches for survival analysis are Kaplan-Meier method—

A. T. N. Vo (✉) · T. Q. Le · T. N. H. Le · V. Van Toi
Department of Biomedical Engineering, International University,
Vietnam National University, Ho Chi Minh City, Vietnam
e-mail: atv55@msstate.edu

a non-parametric statistic measuring the fraction of patients living and estimating survival curves, Accelerated Failure Time (AFT) model—a parametric model describing the direct covariate effects on survival time with prior distribution, and Cox Proportional Hazards model—a semiparametric model that estimates effect parameters with no particular survival distribution and unspecified hazard function, indicating the variables associated with hazard rate and identify the effects of covariates on the hazard occurrence of the event [8, 9]. In this study, Cox Proportional Hazards (CPH) model is used for survival binary classification (die or survive) of the patients. Not only dealing with static and fix-length data such as age, gender, race, weight, height, etc. which is assumed to have constant effect on the survival overtime, Cox model also investigates time-varying factors such as laboratory test results, clinical measurements, etc., and studies the dependence of the survival time on those covariate predictors [10, 11].

Besides classification, time to death of the patients is estimated based on the set of their clinical features, using least square regression, which tries to minimize the sum of the squares of the residuals between predicted and observed values [12]. Furthermore, prior to the classification or estimation process to derive the output prediction, various techniques are used prepare and justify the input, which include acquiring and preprocessing data, selecting and extracting predictors or clinical features of the patients [13, 14]. Lasso (least absolute shrinkage and selection operator) helps to remove redundant features by shrinking their regression coefficients to zero, thus preventing multicollinearity which happens when independent variables are too highly correlated with each other (one predictor can be linearly inferred from the others with a substantial degree of accuracy, adding no relevant information or contribution to the accuracy of the predictive model) [15, 16]. In general, beyond statistical analysis, utilizing signal processing techniques (frequency transform and phase synchronization), data mining and machine learning (regression model), this

model is constructed to identify high-risk patients and forecast mortality rate from their state. It would be able to analyze and interpret the large amounts of data, which considerably empowers clinicians to prioritize resources, target healthcare budget and limit hospital cost. Above all, by estimating the survival based on patient-specific characteristics, healthcare provider can get insight into each individual and identify high-risk patients, as well as apply proper therapeutics and optimal treatment to potentially reduce their mortality risk [17, 18].

2 Methodology

2.1 Data Acquisition and Preprocessing

The data were extracted from MIMIC II Database into Matlab files. 4000 subjects were selected due to 4 main ICU types: (1) Coronary care, (2) Cardiac Surgery Recover, (3) Medical ICU, (4) Surgical ICU. Then 1451 patients with ICU type 1 and type 2 are targeted, since the study focuses on cardiovascular diseases. Up to 42 features, or predictors, or variables were recorded during the first 48 h (2880 min) after their admission (Table 1).

The dataset used in this study contains much more missing data than collected data (approximately 80% of the dataset are missing values), since different patients have different time point of collecting data ranging from minutes to hours, but measurement value in each minute needs to be filled for each patient because the Cox model requires equally divided data points across all patients. For this reason, piecewise interpolation is used to fill missing data between time points to get value in each minute for each patient. For n data points, there are $(n - 1)$ intervals and thus $4(n - 1)$ unknowns to solve for all the coefficients in the i th function of a third-order interpolation. The third order exhibits the desired smoothness and minimizes round-off error caused by higher orders.

Table 1 Recorded features

Demographic	Vital signs	Pathological readings
Record ID	Heart rate (HR)	Blood urine nitrogen (BUN)
Age	Invasive and non-invasive of systolic and diastolic arterial blood pressure (SysABP, NISysABP, DiasABP, NIDiasABP)	Urine, hematocrit (HCT)
Gender	Temperature (Temp)	White blood cell count (WBC) Glucose, K, Na, Mg
Height	Respiration rate (RespRate)	Serum bicarbonate (HCO_3)
ICU Type	Mechanical ventilation respiration (MechVent)	Glasgow coma score (GCS) Creatinine, albumin
Weight	Invasive and non-invasive mean arterial blood pressure (NIMAP, MAP)	Alkaline phosphatase (ALP) Alkaline transaminase (ALT) Cholesterol, lactate, pH
		Fractional inspired O_2 (FiO_2)
		Partial pressure of arterial O_2 and CO_2 (PaO_2 , PaCO_2)
		Platelets, O_2 saturation (SaO_2)

$$s_i(x) = a_i + b_i(x - x_i) + c_i(x - x_i)^2 + d_i(x - x_i)^3 \quad (1)$$

2.2 Feature Selection and Extraction

Since not all features are available for all patients, 24 common features are defined, together with a subset of 717 patients having those common features. A regression analysis named Lasso (Least absolute shrinkage and selection operator) is applied, modelling the regressive correlation of each feature X to the death time T by coefficients β . Lasso removes redundant features by shrinking their coefficients to zero by a penalty λ , preventing multicollinearity (too highly correlated variables that can be linearly inferred from each other, adding no contribution to the model accuracy).

$$\min_{\beta_0-\beta} \left(\frac{1}{2N} \sum_{i=1}^N (y_i - \beta_0 - x_i^T \beta)^2 + \sum_{j=1}^p |\beta_j| \right) \quad (2)$$

where N is number of observations; y_i is response at observation i; x_i is data (p values at observation i); λ is a nonnegative regularization parameter; β_0 and β are scalar. As λ increases, nonzero components of β decreases. Features selected by Lasso are then double checked for multicollinearity using Variance Inflation Factor (VIF), indicating the degree that the variances in the regression estimates increased due to multicollinearity. Any features with $VIF > 2$ is removed.

Another approach is applied to obtain model input, going deeper into fewer but more meaningful features. Using statistical distribution (Mean, Median, Variance, Skewness, Kurtosis), variability magnitude (Standard deviation, RMS of the intervals), signal processing (frequency domain transformation, power of VLF, LF, HF and LF/HF), chaos and information theory (detrended fluctuation analysis, entropy), 16 more features are extracted [19]. Then for each feature pair, their phase synchronization is analyzed by calculating phase locking values. The study also comes up with another selection method using graph theory [20]. A graph is constructed using features selected by Lasso. Each node is a feature, and the weight between each feature pair is their phase locking value. The larger the phase locking, the stronger interaction between the two features. Because strongly related features give redundant information, they need to be removed. If the weight between 2 nodes is greater than a set threshold, the link between them is disconnected. The remaining (not strongly correlated) features are selected (Fig. 1).

Additionally, time slicing window is used to exploit the temporal changes and time-variant information of clinical time-series data. Each time series is divided into multiple windows (window length = 60 min = 1 h) and features are

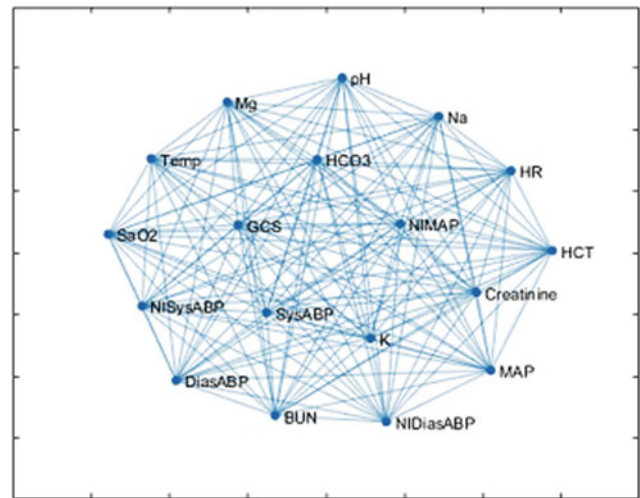


Fig. 1 The graph constructed using features selected by Lasso

extracted for each window, decreasing a patient time frame from 2880 rows in minutes into 48 rows in hours, and the total run time from 10 h to 5 min, saving a huge computational cost and being much more reasonable in ICU (Fig. 2).

2.3 Model Construction, Validation and Evaluation

The data of those features for 717 patients is merged into a matrix X (each column is each feature, each row is data in each hour). Matrix X is then split into 2 parts: the top 80% (513 patients) is training data for building model, the rest 20% (144 patients) is for testing. Another similar matrix T containing time-to-death corresponding to each row of data is also split with the same ratio. T has 1 column and the same number of rows as X). These two matrixes X and T are the input into the model, which consists of two parts: classification of patients as die or survive, and the estimation of patients' death time.

Cox Proportional Hazard model is used for classification. It analyzes time-to-event data and predict the occurrence of the event by quantifying the relation between the features X and the hazard rate at a particular time through hazard function [11, 21]. In this study, the event of interest is the mortality of ICU patients, and time-to-event data are their clinical measurements until death time. *coxphfit* function in Matlab is used to derive the set of coefficients β from the input of the independent variables X (features) and dependent variables T (time to death of the patients), then the proportional hazard rate $h(t)$ is calculated. Threshold c is set so that patients with hazard rate greater than c belong to one class (1-‘death’) and the rest belong to another class (0-‘survival’).

Fig. 2 Time slicing window

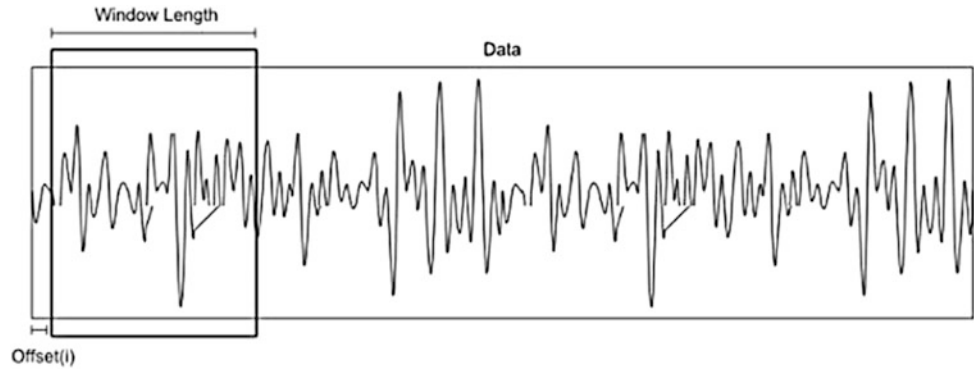


Table 2 Predicted classification compared with real observation

Hazard rate ($c = 0.5$)	Patient 1	Patient 2				Patient n
	0.43	0.53	0.39	0.63	...	0.71
Predicted (0 = <i>survived</i> , 1 = <i>death</i>)	0	1	0	1	...	1
Recorded (0 = <i>survived</i> , 1 = <i>death</i>)	0	0	0	1	...	1

$$h(t|X) = \underbrace{h_0(t)}_{\text{baseline hazard function}} \times \underbrace{\exp(\beta_1 x_1) \times \dots \times \exp(\beta_m x_m)}_{\text{proportional hazards}} \quad (3)$$

The prediction is compared with the real observation and model accuracy is evaluated. True positive (TP), false positive (FP), true negative (TN) and false negative (FN), then Score 1—the smaller between sensitivity and positive predictive values—is calculated to evaluate model performance and reliability (Table 2; Fig. 3).

Besides classification, time to death T of the patients who dies in hospital is estimated using least square estimation, which tries to minimize the sum of the squares of the residuals between predicted and observed values [12]. Assumptions on linearity, normality, multicollinearity and homoscedasticity are tested to see whether the relationship between independent variables X and dependent variable T is linear. However, since the data is not always error-free, those assumptions are sometimes relaxed and nonlinearity is considered as noisy linearity [22]. Also, 124 patients that die in hospital is targeted for estimation because their death is exactly recorded and not affected by other uncontrollable external factors as that of patients dying out of hospital. Multiple Linear Regression is used to calculate T from X , generalizing the relationship of T and X in multivariate dimension, and preventing overfitting by higher orders. Finally, root-mean-square error between the predicted and observed T is obtained.

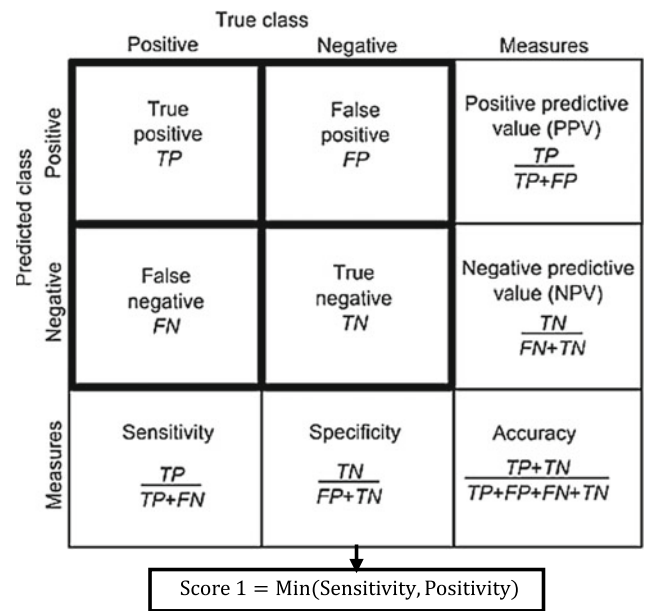


Fig. 3 Model performance evaluation

$$T_{\text{predicted}} = \beta_0 + \beta_1 X_1 + \beta_2 X_2 + \beta_3 X_3 + \dots + \beta_m X_m \quad (4)$$

$$RMSE = \sqrt{\frac{\sum_{i=1}^n (T_{\text{predicted}(i)} - T_{\text{observed}(i)})^2}{n}} \text{ (days)} \quad (5)$$

3 Result and Discussion

3.1 Data Preprocessing, Feature Selection and Extraction

After filling all missing values, each patient will have data at every minute saved in Matlab cells, with the first column is the name of a feature, the second column contains raw data, and the third column contains interpolated data. Each cell of the second and third column is a 2D matrix—1D is time and 1D is corresponding value at that time. Next, in the selection step, overall Lasso selects a subset X of 18 out of 24 features with their corresponding 18 regression coefficients β . Those 18 features are then checked for multicollinearity, reduced to 10 using VIF and to 8 selected features using graph theory. In Fig. 4, the highlighted rows on the left side indicates the VIF values of the 10 selected features. Meanwhile, on the right side, in the graph constructed from 18 features selected by Lasso, the pair of features with by phase locking greater than 0.65 is removed, resulting in the selected group of 8 features linked together.

Then for each pair of features, 16 further features are extracted as discussed above (Mean, Median, Variance, Skewness, Kurtosis, Standard Deviation (SD), Root Mean

Square of Standard Deviation (RMSSD), power of Very Low Frequency (VLF), Low Frequency (LF), High Frequency (HF) and ratio of LF/HF, Detrended Fluctuation Analysis (DFA), Approximate Entropy, Sample Entropy, Permutation Entropy, and Phase Synchronization), with their corresponding coefficients β in Cox model. Feature selection and extraction methods help to enhance the performance of the predictors, provide more effective variables, simplify the complexity, improve the accuracy and interpretability of the model, and provide a better understanding of the underlying process generating the data.

3.2 Model Implementation

Among different methods, the pair of Blood Urea Nitrogen (BUN)—Heart Rate (HR) and their extracted features yield the largest Score 1 in both training and testing set, which are roughly 0.47 and 0.45 respectively—1.5 times better than that of the baseline ICU scoring system of 0.3. The result is shown in Table 3.

In fact, BUN and HR have been proven to have a strong link to cardiovascular disease in many scientific works [20–24]. Furthermore, time to death of ICU patients is

Feature name	Lasso coefficients	VIF
BUN	-42.603	1.896
Creatinine	16.919	1.912
HCT	-28.666	1.291
Platelets	0.274	1.330
GCS	91.702	1.498
HR	-6.023	1.584
Temp	40.850	1.350
WBC	0.492	1.249
HCO3	33.798	3.733
Na	33.755	1.257
Urine	0.770	1.201
Mg	360.290	1.410
K	186.996	1.558
Glucose	0.102	1.125
MAP	-6.043	2.693
DiasABP	3.033	3.308
SysABP	1.480	2.785
pH	-53.213	3.116
PaO2	-0.148	1.334
PaCO2	-0.808	3.421
NISysABP	1.160	19.095
NIDiasABP	2.006	389.872
NIMAP	-1.850	490.160
SaO2	-14.498	1.397

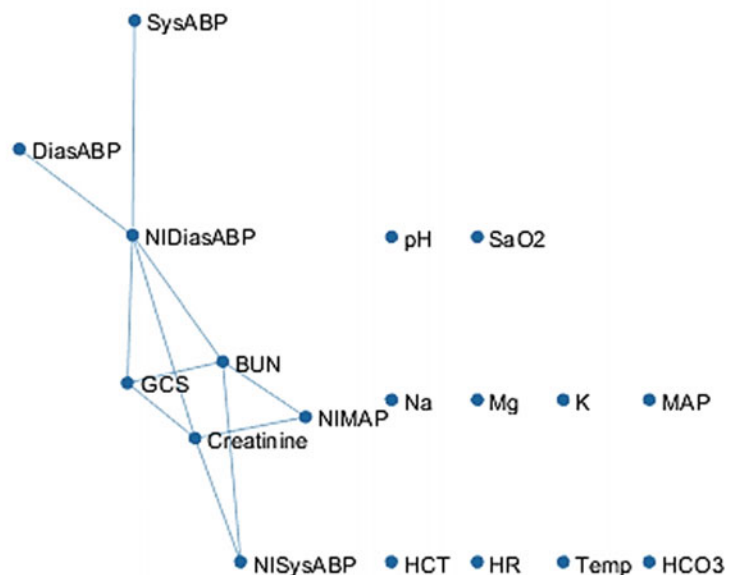


Fig. 4 Features selected by Lasso, VIF and graph theory

Table 3 Different algorithms and the associated classification score 1

	Dataset	TP	FP	TN	FN	SEN	SPEC	POS	Score 1
18 features—Lasso	Train	41.0	112.0	103.0	317.0	28.5	73.9	26.8	26.8
	Test	19.0	22.0	29.0	74.0	39.6	77.1	46.3	39.6
10 features—Lasso + VIF	Train	44.0	121.0	100.0	308.0	30.6	71.8	26.7	26.7
	Test	19.0	23.0	29.0	73.0	39.6	76.0	45.2	39.6
8 features—Lasso + graph	Train	54.0	148.0	90.0	281.0	37.5	65.5	26.7	26.7
	Test	22.0	32.0	26.0	64.0	45.8	66.7	40.7	40.7
Feature pair HR—BUN	Train	72.0	77.0	82.0	342.0	46.8	81.6	48.3	46.8
	Test	17.0	21.0	15.0	91.0	53.1	81.3	44.7	44.7

estimated, using selected features and their β -coefficients as input to the multi linear regression: $T_{\text{predicted}} = \beta_0 + \beta_1 X_1 + \beta_2 X_2 + \dots + \beta_m X_m$ (X_i is the value of the i th feature and β_i is the corresponding coefficient). $T_{\text{predicted}}$ is compared with T_{observed} , then finally RMSE is calculated, giving a brief overview of model performance. Higher regression orders were also applied; however, the higher the order is, the more unstable the model becomes, and the larger the RMSE is,

$$RMSE = \sqrt{\frac{\sum_{i=1}^n (T_{\text{predicted}(i)} - T_{\text{observed}(i)})^2}{n}} = 19(\text{days}) \quad (6)$$

There are several reasons that may contribute to this high RMSE, mainly because the original data has lots of errors (missing data, negative values, limited features recorded, the focus on cardiovascular diseases omitting many patients from the dataset, etc.). Hence, a larger dataset with better collecting method may significantly enhance the model performance.

4 Conclusion

The study has developed and validated a prognostic model using ICU measurements of patients with cardiovascular disease to forecast their mortality, specifically by quantifying the stochastic correlation between those data and patients' death. An alert will be triggered when preset criteria are met, and death time estimation would help physicians in identifying high risk patients, as well as in planning the most optimal therapy for each individual patient. So far the pair of BUN and HR is the best feature for survival analysis of patients with cardiovascular concern. Although there are rooms for improvement, the potential use in the future for

this predictive model can be interdisciplinary. Combining statistic, machine learning, data mining, and signal processing gives more insightful mortality investigation, dealing with heterogeneous multivariate analysis in multidimensional dataspace. Also, to the best of my knowledge, binary classification is conventional, but time to death regressive estimation is a novel approach proposed in this study. The research claims no conflict of interest, and the developed model not only saves cost and time, but also provides a feasible tool for better treatment, healthcare prioritization and resource distribution.

Conflict of Interest The authors declare that they have no conflict of interest.

References

1. Johnson, A.E., et al.: Patient specific predictions in the intensive care unit using a Bayesian ensemble. In: Computing in Cardiology (CinC), IEEE (2012)
2. Ha, D.T., et al.: Development and validation of a prognostic model for predicting 30-day mortality risk in medical patients in emergency department (ED). *Sci. Rep.* **7** (2017)
3. Hug, C.W.: Predicting the Risk and Trajectory of Intensive Care Patients Using Survival Models. Massachusetts Institute of Technology, Massachusetts (2006)
4. Goldhill, D.R., Sumner, A.: Outcome of intensive care patients in a group of British intensive care units. *Crit. Care Med.* **26**(8), 1337–1345 (1998)
5. Rocker, G., et al.: Clinician predictions of intensive care unit mortality. *Crit. Care Med.* **32**(5), 1149–1154 (2004)
6. Hosmer, D.W., Lemeshow, S., May, S.: Applied Survival Analysis. Wiley, Hoboken (2011)
7. Miller Jr., R.G.: Survival Analysis, vol. 66. Wiley, Hoboken (2011)
8. Hu, Y.: Survival Analysis of Cardiovascular Diseases (2013)
9. Kaplan, E.L., Meier, P.: Nonparametric estimation from incomplete observations. *J. Am. Stat. Assoc.* **53**(282), 457–481 (1958)
10. George, B., Seals, S., Aban, I.: Survival analysis and regression models. *J. Nucl. Cardiol.* **21**(4), 686–694 (2014)

11. Cai, J., Zeng, D.: Cox Proportional Hazard Model. Wiley Encyclopedia of Clinical Trials (2008)
12. Sun, H., Wu, Q.: Least square regression with indefinite kernels and coefficient regularization. *Appl. Comput. Harmonic Anal.* **30**(1), 96–109 (2011)
13. Le, T.Q., Bukkapatnam, S.T.: Nonlinear dynamics forecasting of obstructive sleep apnea onsets. *PloS One* **11**(11), e0164406 (2016)
14. Le, T.Q., et al.: Wireless wearable multisensory suite and real-time prediction of obstructive sleep apnea episodes. *IEEE J. Trans. Eng. Health Med.* **1**, 2700109 (2013)
15. Ohlemüller, R., et al.: The coincidence of climatic and species rarity: high risk to small-range species from climate change. *Biol. Lett.* **4**(5), 568–572 (2008)
16. Tibshirani, R.: Regression shrinkage and selection via the Lasso. *J. Royal Stat. Soc. Series B (Methodol.)* **58**, 267–288 (1996)
17. Panahiazar, M., Taslimitehrani, V., Pereira, N., Pathak, J.: Using EHRs and machine learning for heart failure survival analysis. *Stud. Health Technol. Inform.* **216**, 40 (2015)
18. Knaus, W.A., et al.: APACHE II: a severity of disease classification system. *Crit. Care Med.* **13**(10), 818–829 (1985)
19. Wang, Y., et al.: Mortality prediction in ICUs using a novel time-slicing cox regression method. In: AMIA Annual Symposium Proceedings, American Medical Informatics Association (2015)
20. Le, T.Q., et al.: Topology and random-walk network representation of cardiac dynamics for localization of myocardial infarction. *IEEE Trans. Biomed. Eng.* 2325–2331 (2013)
21. Kalbfleisch, J.D., Prentice, R.L.: *The Statistical Analysis of Failure Time Data*, vol. 360. Wiley, Hoboken (2011)
22. Weisberg, S.: *Applied Linear Regression*, vol. 528. Wiley, Hoboken (2005)
23. Ostfeld, R., et al.: The association of blood urea nitrogen levels and coronary artery disease. *Einstein J. Biol. Med.* **25**(1), 3–7 (2016)
24. Perret-Guillaume, C., Joly, L., Benetos, A.: Heart rate as a risk factor for cardiovascular disease. *Prog. Cardiovasc. Dis.* **52**(1), 6–10 (2009)

The Characteristics of the Event-Related Potentials with Visual Stimulus

Nguyen Thi Minh Huong, Nguyen Trong Nguyen,
and Huynh Quang Linh

Abstract

With a huge development of neuroscience, the abilities for remote control of devices without manual direct interaction by brain wave have become a convinced reality. In this paper, five volunteers carrying Emotiv EPOC headsets were performed Brain-computer interface (BCI) experiments due to visual stimulus. The Electroencephalogram (EEG) signals were collected and analyzed in real time to extract features. P300 signals with largest amplitude occurs remarkably at the occipital and frontal channels. There were two methods to be used to classify P300 BCI for comparisons. The Artificial Neural Network (ANN) combined EEGLAB for offline analyzing and the Linear Linear Discriminate Analysis (LDA) of OpenVibe were employed for online detection. The accuracy percentage of ANN is 80% and test results of online detection is above of 85%. These good results promised real assistance application for disabled.

Keywords

EEG • ERP • ANN • OpenVibe • EEGLAB

1 Introduction

Brain Computer Interface (BCI) is technology that enables the use of the brain's neural activity to communicate with others or to control machines, artificial limbs, or robots without direct physical movements. BCI based on electroencephalogram (EEG) can be applied to disabled individuals. Present-day BCIs determine the intent of the user from different electrophysiological signals: for instance, the

N. T. M. Huong (✉) · N. T. Nguyen · H. Q. Linh
Ho Chi Minh University of Technology, Ho Chi Minh City,
Vietnam
e-mail: nguyentmhuong@hcmut.edu.vn

N. T. Nguyen
e-mail: trongnguyen1408@gmail.com

user may control the modulation of some brain waves (e.g., mu or beta rhythms) or the BCI may exploit natural automatic responses of the brain to external stimuli (e.g., event-related potentials [1]). The P300 (P3) wave is an event related potential (ERP) component elicited in the process of decision making. It is considered to be an endogenous potential, as its occurrence links not to the physical attributes of a stimulus, but to a person's reaction to it. The algorithm proposed by Farwell and Donchin [2] provides an example of a simple BCI that relies on the unconscious decision-making processes of the P300 to drive a computer. A 6×6 grid of characters is presented to the subject, and various columns or rows are highlighted. When a column or row contains the character a subject desires to communicate, the P300 response is elicited (since this character is "special" it is the target stimulus described in the typical oddball paradigm). The combination of the row and column which evoked the response locates the desired character. A number of such trials must be averaged to clear noise from the EEG. The speed of the highlighting determines the number of characters processed per minute. Results from studies using this setup show that normal subjects could achieve a 95% success rate at 3.4–4.3 chars/min. Such success rates are not limited to non-disabled users; a study conducted in 2000 revealed that 4 paralyzed participants (one with complete paraplegia, three with incomplete paraplegia) performed as successfully as 10 normal participants.

In order to find an optimum ERPs feature extraction from EEG data for controlling a mouse pointer, Shirnogasa and Higa [4] designed a visual stimulus flicker program, measured an able-bodied subject's EEG using it as an oddball paradigm, processed, and classified the EEG data to control a mouse pointer. The ERP components of P300 and N100 were extracted from the ERPs using an artificial neural network (ANN). The experimental results showed 95% of rates of the correctly classified directions for trigger signals of upward, downward, leftward and rightward movements of a mouse device.

With the aims of designing a real-time EEG-based communication aid using brain-computer interface (BCI) technologies, Alkhater [3] used the Emotive headset to detect P300 waves used as the control signals for the P300 BCI. The users' performance with the verbal and graphical versions of the speller is similar to the performance obtained when using the typical alphanumeric speller, although with higher spelling speed. Accordingly, the use of these new versions is highly recommended. The obtained accuracies are comparable to those presented in other studies in which expensive medical EEG recording systems were utilized.

In this paper, we focus on BCI technologies with the real-time EEG signals from Emotiv Epoch. First, we detected ERP waveforms from Emotiv Epoch device with advanced P300 speller paradigm. Then, BCI used ERP signals to communicate with able-volunteers for identified targets in oddball paradigm with different matrixes and also to classify directions in the controlling experiment.

2 Methods

2.1 Experimental Procedure and EEG Data

For EEG data collection, five healthy volunteers accepted to contribute in our BCI's experiments. They are all 22 years old and study biomedical engineering in the Ho Chi Minh University of Technology. The used device is Emotiv Epoch which contains 14 EEG channels and the sampling rate is at 128 Hz. Each volunteer sit on the short stool placed in front of the monitor which presents stimuli. Based on the answers of all volunteer who have different types of eyes condition, it was set nearly 55 cm from the screen to the volunteers'

eyes. This experiment was placed in the Faraday room to reduce the electrical noises. There are two tasks designed for obtaining ERP signals (Fig. 1):

Task 1: Using OpenVibe designer, the P300 speller structure was created based on the odd-ball paradigm. The communication interface is the matrix of letter showing in two forms: 2×2 and 6×6 . In the first stage, the subject was asked to pay his attention to the letter which was colored in blue in the letter matrix. Further more, to increase the accuracy for getting P300, he needs to count the number of times of the selected flashed cell in their mind and during the experiment. The operator has to ensure that the comfortable feeling of the volunteer has to be maintained as much as possible. After he finished 6 marked letters, the two-class training module of Openvibe was applied to classify. Finally, the subject was asked to choose any his favourite word which wasn't marked and performed the online testing to verify if the Openvibe can recognize one-by-one letter or not.

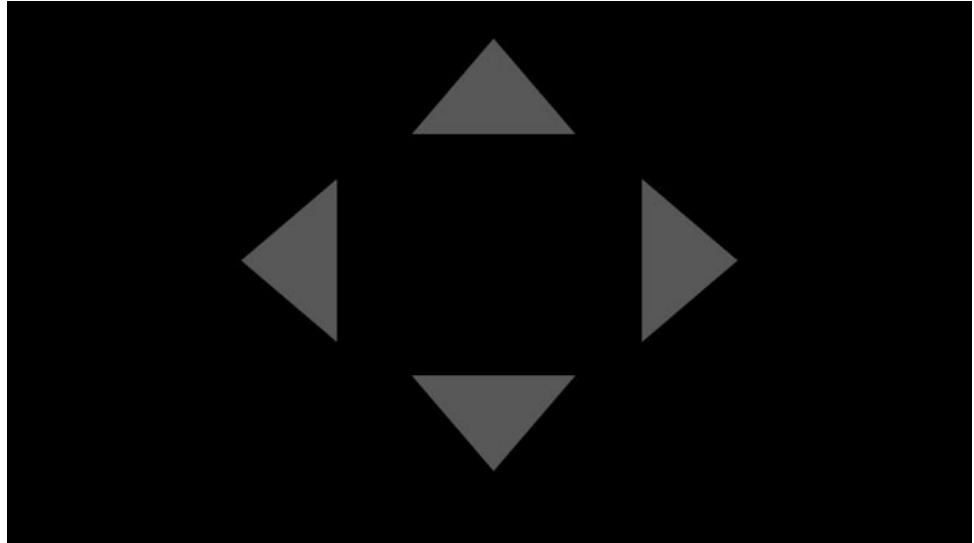
Task 2: The OpenVibe test was used to do the experiments as Fig. 2 [4]. The display shows a picture including four triangles as direction pointers which is presented for leftward, rightward, upward and downward. The target is flashed over time and changed manually until all four directions are tested. The subject was asked to quietly count the number of flashed times from the target. The classifying and online detection stages for four directions of this experiment were performed similarly as those of the task 1.

In two tasks, data were saved in files with format .ov and the event file was derived from Test Bench. They were thus analyzed offline by EEGLAB. A quite clear P300-ERP components appear with the largest amplitude shown at the occipital and frontal channels. To classify the P300 BCI, we

Fig. 1 P300 speller using Emotiv Epoch



Fig. 2 Direction pointer experiment



have tried to create a sample model by using interpolation a sample model becomes a reliable target for the Artificial Neural Network (ANN).

2.2 EEG Signal Processing

The raw EEGs signals contains not only pure P300 evoked potentials but also muscular, 50 Hz of power supply and/or ocular artifacts. First, the EEG data was filter by band-pass filter from 1 to 45 Hz. Besides, the xDAWN algorithm was used to enhance evoked potentials because P300 signals are very small compared with normal EEGs. It estimates a subspace which contains most of the P300 evoked potentials. The classification between target/non-target stimuli is so simplified leading to a faster spelling device. The data consists of two characteristic reactions, one is generated by the flashing targets and one is generated by all stimuli (target and non-target). Finally, Linear Discriminant Analysis (LDA) and Support Vector Machine classifier were applied to classify for online and Artificial Neural Network (ANN) is used for offline analyzing.

2.2.1 xDAWN Algorithm

For many factors, the raw EEG is easy to have plenty types of artifact signal so the signal-to-noise ratio (SNR) is very low and that's a huge barrier for classification. For that reason, Rivet [1] and his colleagues developed xDAWN algorithm which creates the evoked subspace and set the data to follow the structure of that subspace. In this research, the training data set is projected to P300 evoked potential subspace before it come to the classification session.

Suppose the data followed with:

$$X = D_1 A_1 + D_2 A_2 + N \quad (1)$$

where $X \in R^{N_t \times N_s}$ is the collected data, N_t is the number of samples, N_s is the number of channels. $A_1 \in R^{N_t \times N_s}$ are the signals synchronized with the target stimuli and $A_2 \in R^{N_t \times N_s}$ are signal related with the non-target stimulus. $D_1 \in R^{N_t \times N_t}$ and $D_2 \in R^{N_t \times N_t}$ are Toeplitz matrices in which the first column entries are zero with the exception of the one corresponding to the target stimuli time indexes, respectively.

Then, to maximize the signal-to-signal plus noise ratio, the spatial filters is applied:

$$g(U) = \frac{T_r(U^T \hat{\Sigma}_1 U)}{T_r(U^T \hat{\Sigma}_x U)}, \hat{U}_1 = \arg \max g(U) \quad (2)$$

where $T_r(\cdot)$ is the trace operator and $\hat{\Sigma}_1 = \hat{A}_1^T D_1^T D_1 \hat{A}_1$, $\hat{\Sigma}_x = X^T X$. \hat{A}_1 is the least mean square estimated of the not known target evoked reactions A_1 . A_1 , A_2 , D_1 , A_1 and D_2 , A_2 may overlap, \hat{A}_1 is calculated from:

$$\begin{pmatrix} \hat{A}_1 \\ \hat{A}_2 \end{pmatrix} = (D^T D)^{-1} D^T X \quad (3)$$

with $D = [D_1, D_2]$. After computing the QR factorization [5] $X = Q_x R_x$, $D = Q_D R_D$ and replacing \hat{A} by (3) in $\hat{\Sigma}$, criterion (2) can be expressed as,

$$\hat{U} = R_x^{-1} \Psi_s$$

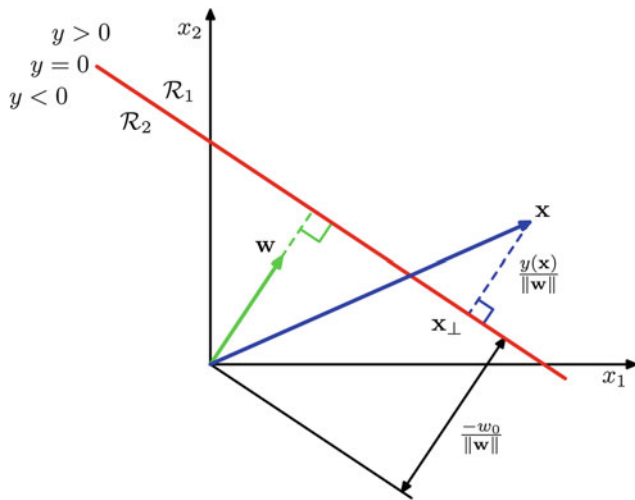


Fig. 3 Visualization of LDA [6]

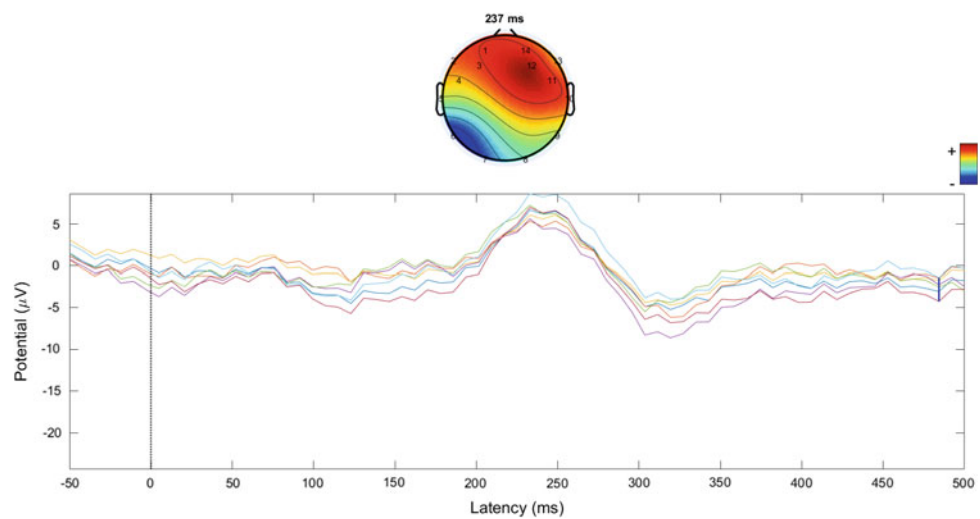
with Ψ_s is the sequence of the signal individual vectors given by the value factors of $Q_D^T Q_X = \Phi \Lambda \Psi^T$ where Λ is a diagonal matrix, Φ and Ψ^T represent the unitary matrices. In this case, the enhanced signals are specified by the following formula in the final stage:

$$\hat{S} = X\hat{U} = DR_D^{-1}\Phi_s\Lambda_s + NR_X^{-1}\Psi_s$$

2.2.2 Linear Discriminant Analysis (LDA)

Linear discriminant analysis (LDA) is a classification method that based on the information in a learning data set, the prediction is performed to separate the predefined classes. This kind of supervised learning is developed by R. A. Fisher in 1936. In our case, the result is expected that our training data is divided into 2 classes: P300 and non-P300 [6].

Fig. 4 P300 images of AF3, F7, F3, T8, FC6, F4, F8, and AF4 of volunteer 1



Linear discriminant function:

$$y(x) = \omega^T x + \omega_0$$

where ω is called a weight vector, x is an input vector and ω_0 is a bias. If $y(x) \geq 0$, the input vector x is assigned to first class and to second class otherwise. To be clear about how it works, the visualization is show at Fig. 3

Basically, LDA helps to reduce the dimension of the data basing on the information from two criteria and maximize the separation of known categories. In the past, many of BCI experiment used it and achieved high classification performance [7, 8].

3 Experimental Results

In terms of the ERP analysis, for each recording by the OpenVibe, the virtual trigger was simultaneously running and marking to the Emotiv Test Bench. Collected event files from Test Bench were transferred to EEGLAB to extract and analyze P300 signals. The significant positive waveforms around 300 ms were shown in Figs. 4, 5, 7 and 8 of two volunteers. A quite clear P300-ERP components with the largest amplitude appear at the occipital and frontal channels. These results are in agreement with published articles such as of Escolano, Antelis and Minguez at Fig. 6 [9]. With the average of 192 trials, the average P300's amplitude reached to 8.6 μ V.

In this section, the accuracy of BCI is presented when BCI communicates with five volunteers in different oddball paradigms. As above mentioned, oddball paradigms in this experimental procedure are 2×2 and 6×6 letter matrices. For the letter matrix 2×2 , the obtained accuracy was 100%. For classifying four directions in task 2, accuracy is

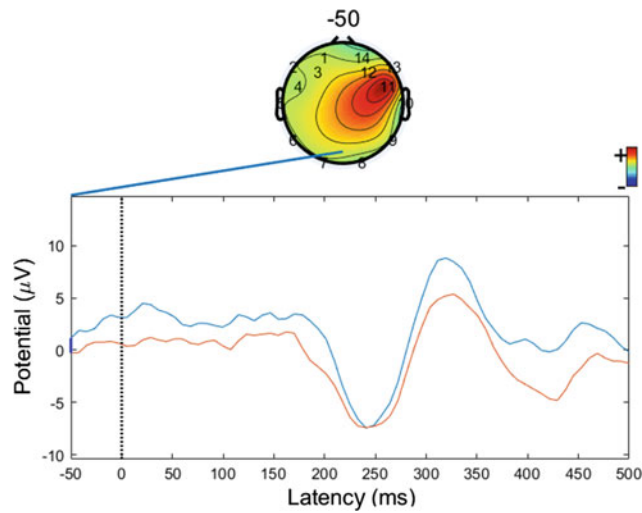


Fig. 5 P300 images of O1 and O2 of volunteer 1

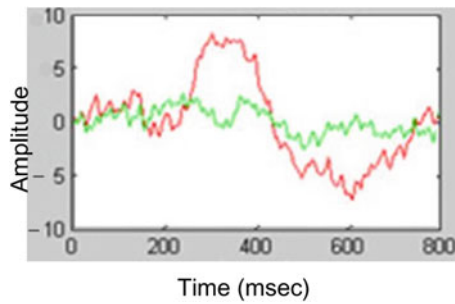
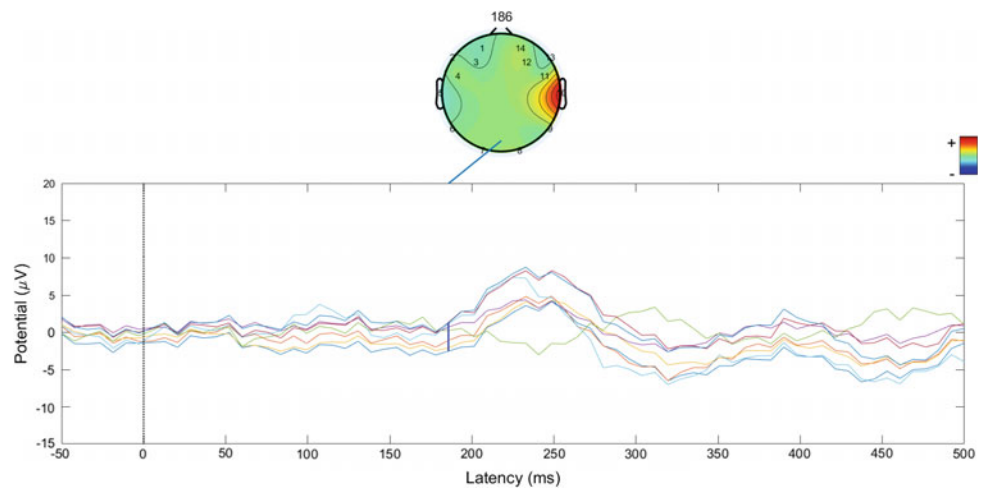


Fig. 6 P300 waveforms generated by a target (in red) and a non-target (in green) [9]

Fig. 7 P300 images of AF3, F7, F3, T8, FC6, F4, F8, and AF4 of volunteer 2



above 85%. For the letter matrix 6×6 , after training section, the classification is performed and its result show on Table 1. The accuracy in two types of accuracy is both above 80% and it was also shown that the Emotiv system may be suitable for P300 acquisition.

For offline analyzing, we have tried to create a P300 sample model by using interpolation based on theory of P300 about latency and amplitude of our experimental data. The Artificial Neural Network (ANN) used this sample as reliable target for classifying offline data. The obtained accuracy is 80%.

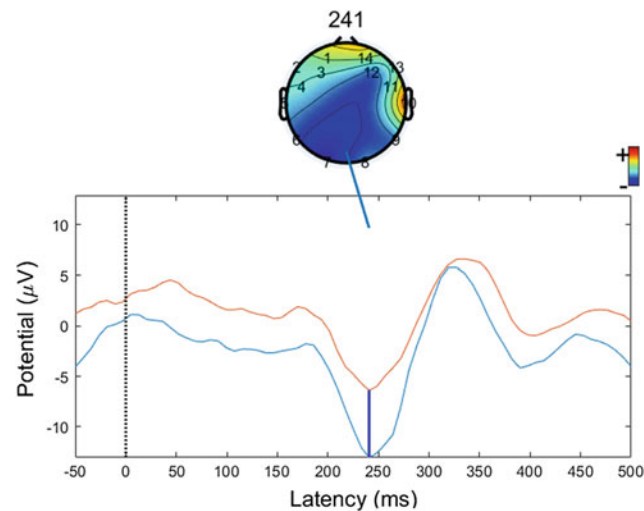


Fig. 8 P300 images of O1 and O2 of volunteer 2

Table 1 Training set accuracy for 6×6 letter matrix oddball paradigm

Subjects	Subject 1	Subject 2	Subject 3	Subject 4	Subject 5
Classification rate (%)					
Cross-validation accuracy	83.31	85.94	88.12	89.27	86.99
Training set accuracy	87.37	88.89	90.54	91.75	89.87

Finally, at the online detection section, the result is remarkable as how well the volunteer can accomplish. In case of using 6×6 matrix, the best result is volunteer who achieved five/six letters. With the 2×2 matrix and the directions experiments, the results are better with four/four of letters and of directions.

4 Conclusions

The purpose of this research is to test and examine the reactions of the neurological system visual stimulation and EEG signal processing in real time. The differential neural activities between the elicited cell and non-elicited cell exists mostly around the frontal region of the head. The differential neural activities demonstrated by P300 signal between the elicited cell and non-elicited cell occur mostly around the frontal region of the head. Mentioned promising P300 signals could be used in BCI applications to assist disabled. Besides, the OpenVibe is helpful for collecting real time EEG signals.

In term of usability, the mobile EEG device as Emotiv headset has many advantages and disadvantages. The user, especially the disabled, can bring and perform flexible BCI application because of the simplicity and mobility of Emotiv

headsets. However, compared to professional medical equipment, they are not reliably stable and the experimenters feel uncomfortably when they use them for a long time.

Conflict of Interest The authors declare that they have no conflict of interest.

References

- Rivet, B., Souloumiac, A., Attina, V., Gibert, G.: xDAWN algorithm to enhance evoked potentials: application to brain-computer interface. *IEEE Trans. Biomed. Eng.* **56**(8), 2035–2043 (2009)
- Donchin, E., Spencer, K., Wijesinghe, R.: The mental prosthesis: assessing the speed of a P300-based brain-computer interface. *IEEE Trans. Rehabil. Eng.* **8**(2), 174–179 (2000)
- Alkhatir, R.M.: Real-time detection of P300 brain events: brain-computer interfaces for EEG-based communication aids. MS thesis, Auckland University of Technology (2012)
- Shirnogasa, T., Higa, H.: Toward a control of a mouse pointer: EEG analysis for feature extraction. In: 14th International Conference on Intelligent Systems Design and Applications, IEEE, Japan, pp. 151–155 (2014)
- Golub, G.H., Loan, C.F.V.: *Matrix Computation*, 3rd edn. The Johns Hopkins Univ. Press, Baltimore, MD (1996)
- Bishop, C.M.: *Linear models for classification*. In: *Pattern Recognition and Machine Learning*. Springer Science + Business Media, LLC, pp. 181, 182 (2006)

7. Bostanov, V.: Feature extraction from event-related brain potentials with the continuous wavelet transform and the t-value scalogram. *IEEE Trans. Biomed. Eng.* **51**, 1057–1061 (2004)
8. Scherer, R., Muller, G.R., Neuper, C., Graimann, B., Pfurtscheller, G.: An asynchronously controlled EEG-based virtual keyboard: improvement of the spelling rate. *IEEE Trans. Biomed. Eng.* 51(6), 979–984 (2004)
9. Escolano, C., Antelis, J., Minguez, J.: Human brain-tekeioerated robot between remote places. In: *IEEE International Conference on Robotics and Automation*, Kobe, Japan, pp. 4430–4437 (2009)

Application of Portable EEG Device in Detection and Classification Drowsiness by Support Vector Machine

Thi Tram Anh Pham, Thi Diem Hang Nguyen, Quoc Khai Le, and Quang Linh Huynh

Abstract

Sleeplessness and driver's drowsiness is one of the reasons leading to accidents. Many studies as well as applied products have been recently developed and integrated into car. However, almost research concentrated on eyes-movement and pupillary stretch. Especially, mobile Electroencephalography (EEG) measurement device becomes new trend thanks to its convenience and affordable price. This research focused on using portable EEG device—EPOC Emotiv for detecting sleep-onset by analyzing power spectrum after filtering frequency band of brain waves. The processed features become the input of Support Vector Machine (SVM) classification and the prerequisite for real-time drowsiness detection. The changes of vigilance state classified by SVM in analysis show the result with over 70% data samples, reliably used in driving safety system in the future.

Keywords

Drowsiness • Portable EEG device • Support vector machine

1 Introduction

Sleep is a naturally recurring state of mind and body, characterized by altered consciousness, relatively inhibited sensory activity, inhibition of nearly all voluntary muscles, and

reduced interactions with surroundings [1]. So impairing performance and ultimately leading to the inability to resist falling asleep at the wheel cause the accident on the road [2]. Some features such as eyes blinking and head nodding have developed to detect drowsiness [3]. Though, drivers still feel sleepy while trying to hold the eyes open, or regularly wearing glasses. So the primary reason of sleep focused on this study is from inside the brain—Electroencephalography (EEG) signals.

EEG is an electrophysiological monitoring method to record electrical activity of the brain. The electrical patterns observed are called brain waves. Brain waves change according to behavior and feeling. Investigate alteration in brain waves make distinctions states possible to detect and go to further applications [4, 5].

Many recent studies analyze EEG signals acquired by Emotiv EPOC. Main research areas based on Brain-Computer Interface (BCI), which apply in reality for visual [6] and wheelchair control [7]. Because of the inconvenience in using traditional multiple-electrode device and good performance of Emotiv EPOC in many studies before, Emotiv EPOC is chosen in this study to collect data for analyze EEG signals.

Differences discrimination methods have been used recently and Support Vector Machine (SVM) has become an increasingly popular tool for Machine Learning. In real life, SVM have been successfully used in three main areas: text categorization, image recognition, and bioinformatics [8, 9]. An automatic detection of drowsiness EEG is possible by SVM with the classification accuracy reached 99.3% [10].

This study applies SVM to create an automatic separation between alert and drowsy states based on EEG signals required from a low-cost portable device with expected accuracy over 70%. To achieve this, particular signal frequency parameters in EEG signals that correlate with two labels: awake and sleepy will be identified and used as the input for pattern recognition.

T. T. A. Pham (✉) · T. D. H. Nguyen · Q. K. Le · Q. L. Huynh
Biomedical Engineering Department, Faculty of Applied Science,
Ho Chi Minh City University of Technology, Vietnam National
University, Ho Chi Minh City, Vietnam
e-mail: phamthitramanht2@gmail.com

T. D. H. Nguyen
e-mail: ntdhang96@gmail.com

2 Methods

2.1 Materials

Subjects from 18 to 40 years old with no alcohol, caffeinated drinks and drowsiness-causing medications are provided an EEG headset. All experiments are in the same light condition. Task performances are playing racing game (Asphalt8—time limited solo racing option) and taking own self-assessment about status after every three-minute round. Some questions in survey make sure that subjects can favorably participate in the experiment. Noise of electrical power sources are minimized by using battery mode on device. Behavior in preprocessing is monitoring to confirm the preciseness of the value input. Sequence of experiment is shown in Table 1.

2.2 Devices

Emotiv EPOC contains 14 electrodes (AF3, F7, F3, FC5, T7, P7, O1, O2, P8, T8, FC6, F4, F8, and AF4) and two reference sensor (CMS as P3 and DRL as P4). Sampling rate is 128 sample per second, meet requirement signals which have frequency under 64 Hz. The necessary EEG wave is ranged from 0.5 to 35 Hz, so Emotiv is passably accepted according to the Nyquist frequency. The electrodes located in relation based on the standard design of the 10–20 system receive signals, connect with processor by Bluetooth and battery life is up to about 12 h [11].

2.3 Data Analysis

Fast Fourier Transform (FFT) is a popular method to determine energy spectrum of signals. It is used to transform time domain into frequency field. However, density of the specific frequency after FFT is an important argument. However, that is also a trouble to recognize the time when the events start or suddenly change.

The Wavelet Transform acts as a useful tool for filtering and separating raw EEG signals into primary frequency bandwidth. While Fourier Transform is constituted by sinusoid, Wavelet Transform uses some Wavelet families as the mother-waves describe the data by scaling the signals. This method analyses original data into constituent wavelet of the different scale and position. Discrete Wavelet Transform (DWT) is also called multi-levels unattached process [12]. In this research, the seventh Debauchies's wavelet family is chosen for evaluation and reconstruction of signals. The wavelet filter is an effective way to reduce artifact noise. It can extract data in the necessary frequency (Theta: 0.5–4 Hz, Alpha: 4–13 Hz, Beta: 13–35 Hz). Hence, combining DWT and FFT is an ultimate process to both show the power spectrum and specific the expected frequency bandwidth.

After preprocessing with necessary frequency, features of drowsiness can be dissociated. There is a gradual increase of theta activity and a concurrent decrease of alpha activity [13]. According to AASM, Sleep-Onset begins with the fragmentation of the alpha wave and the emergence of theta waves, or the occurrence of slow waves (2–7 Hz). The alpha waves will decrease less than 50% epoch and the low frequency waves will dominate over 50% epoch. Changes of the EEG signal usually occur from a few seconds to a few minutes. This alteration happens after the beginning of slow eye movement (SEM) and transition state that lasts minimum 3 s and maximum 15 s, usually within 10 s [14, 15]. Thus, the decline of alpha activity and the growth of theta rhythm are the sign of drowsiness. Be based on those characteristics, the Ratio of Power Spectrum (RPS) is a reasonable indicator, identified by formula:

$$RPS_X = \frac{P_X}{\sum P}, \quad (1)$$

X are theta, alpha and beta.

Pair of RPS_{theta} , RPS_{alpha} with each label matching with alert/drowsy state, becomes the input of SVM. The goal in this research is to build an optimal separating hyper-plane with the largest margin in training data and correctly classify

Table 1 Task performance

Time	Task
Before	Training how to play game + Tutorial: getting started + Try getting on with game
Stage 1	Relax (two minutes)
Stage 2	Play game (3 min/round * 15 rounds)
Stage 3	After 1 round: Check status + Sleepy (eyestrain/yawn/lack of mental agility) + Tired but still control the car + Alert (awake) Note the scores and go back to the game again immediately
After	Survey

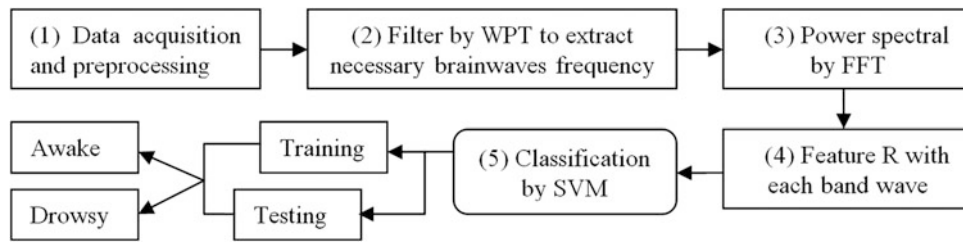


Fig. 1 System processing flowchart

new one called testing data. Training data contains target values and two correlative features. SVM predicts the target in testing data with the attributes provided. The alert state refers to relaxed wakefulness in EEG with dominant beta activity and the drowsy state is shown with decreasing occipital alpha rhythm in the amplitude and/or frequency [10]. In order to make the training data more reliable, RPS_{β} , RPS_{α} and RPS_{θ} are used for confirming with self-assessment and all unsatisfactory data will be ignored. Figure 1 shows the diagram of the proposed system.

This range is unfamiliar with EEG signal. Thus, Wavelet Transform is used to eliminate the offset and also filters EEG bandwidth in the second one. Therefore, the range of pre-processing signal fluctuates from -100 to $100 \mu V$. The last graph indicates the power spectrum of filtered data by FFT, it present the dominant of frequency bands in EEG signal. All graphs about segment of EEG signal are shown on Fig. 2.

3 Results and Discussion

3.1 Pre-processing Data

The first graph shows the baseline offset which makes the amplitudes of original data in the first graph over $4000 \mu V$.

3.2 Statistic of RPS

Table 2 presents a pair of RPS from a subject. The proposed features were based on the power spectrum of each 10-s EEG epoch. The figure presents a drowsiness appearing in epoch from 90 to 100. It is matched with the record of subject (shown on Fig. 3). In this graph, the blue line is created by using polyfit function with RPS_{α} and the red

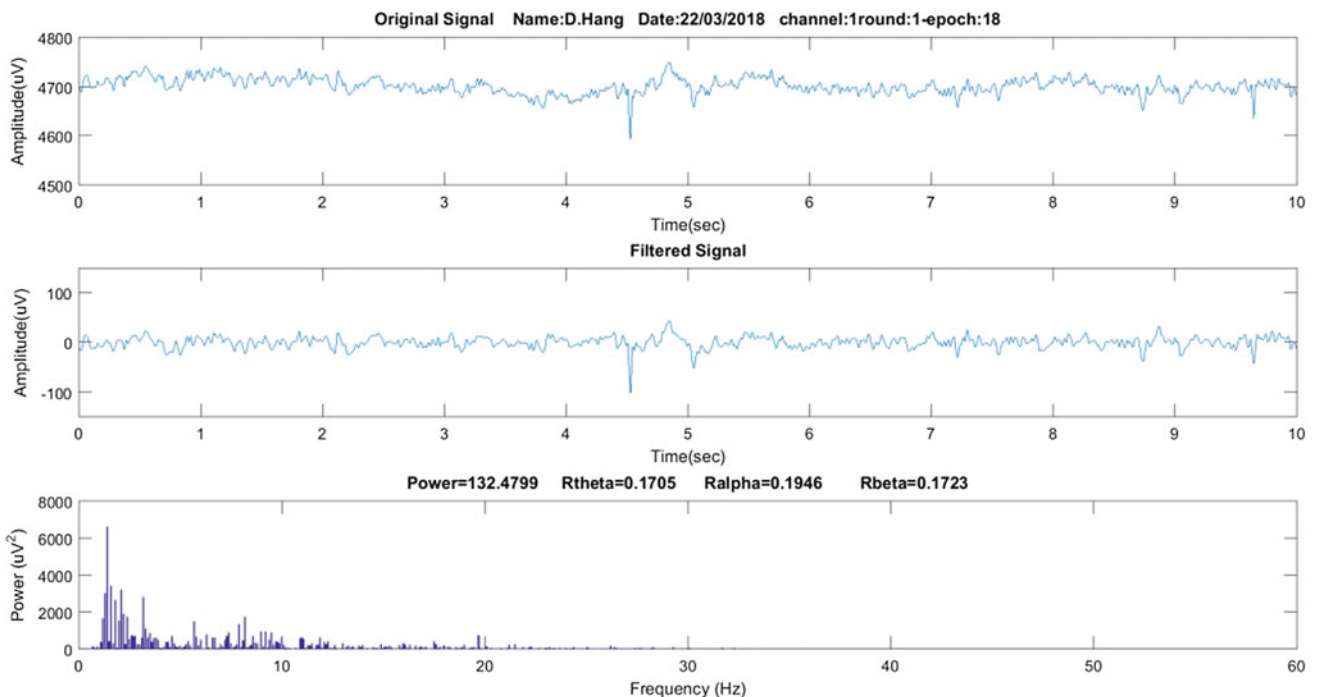


Fig. 2 The raw EEG and the data filter with Wavelet

Table 2 Quote RPS of Subject 1—Channel O1

Epoch	RPS _{theta}	RPS _{alpha}
1	0.33542	0.26895
2	0.43158	0.2636
3	0.33833	0.34766
...
94	0.29359	0.31224
95	0.36744	0.31857
96	0.40461	0.29367
...
269	0.32716	0.21224

line is the same way for RPD_{theta}. When RPD_{theta} is rising and RPD_{alpha} is decreasing, it warns a drowsiness signal will appear soon. Drowsiness appearing marked by green circle in Fig. 3 indicates that subject feel tired and hard to control working. So we can choose the suitable time to alarm drivers from dangerous situation before that state appears.

3.3 SVM Classification

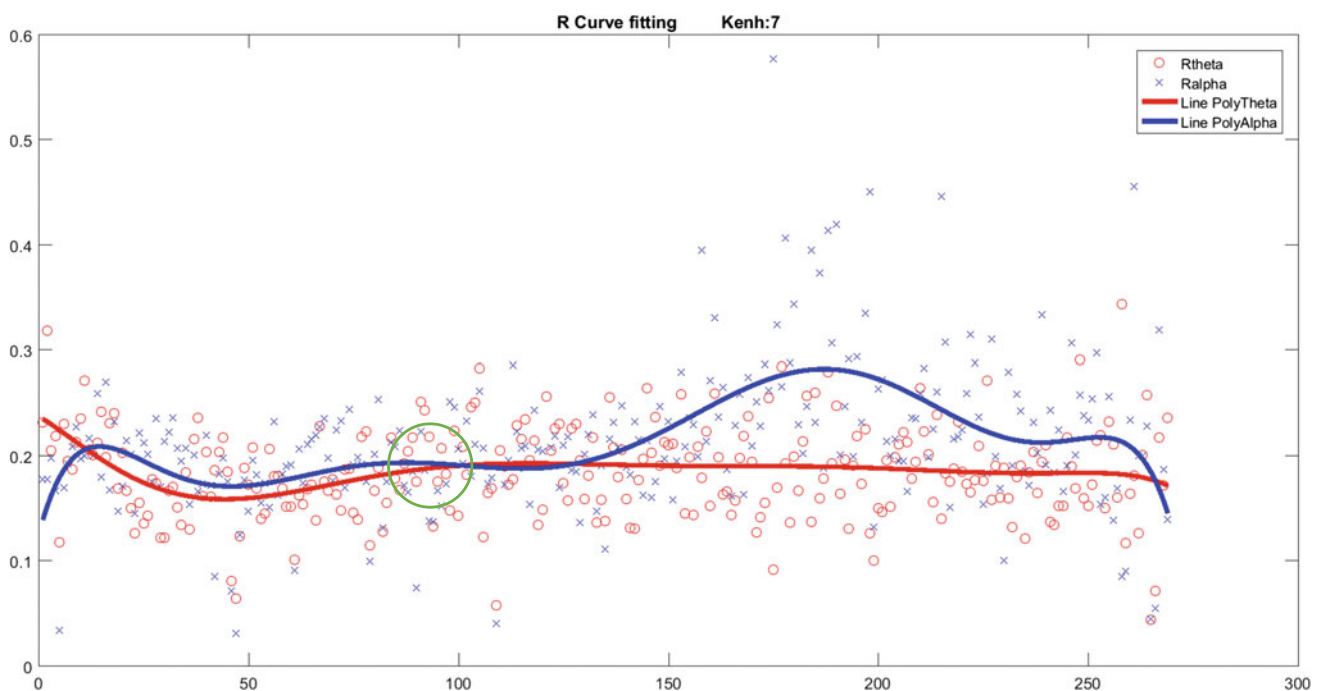
In this part, Fig. 4 presents the training data are drawn by dots, the testing data are drawn by circles. Hyper-plane separate two areas of drowsy and alert, which colored by red

and blue. The support vectors are shown as black circles. This figure shows the projection view of the hyper-plane in two dimensions (RPS_{theta} and RPS_{alpha}) in the transformed space. Classification accuracy achieved over 80%, so it proves that SVM can predict the tendency of drowsiness based on attributes provided in real-time with the low sampling rate EEG device. This means that the trained SVM could match the standards of manual classification and showed encouraging results for the automatic detection of driving drowsiness.

One of the strength of this study is less time consumption for classification into two states. Besides, the portable device brings advantage with the convenience in acquiring data and doing long-time experiments. Although expected results for SVM classification was performed, a large number of challenges need to be consider. The quality of signal makes accuracy lower than the similar methods. Comparing with other approaches, this study needs improving to get higher precision and reliability.

4 Conclusion

This research aims to design an optimal model for detecting vigilance state and warning drivers. Alpha and Theta power spectrum ratio are chosen as the feature extraction in this study. Polyfit function is a method applied to present

**Fig. 3** Statistic of RPS during the experiments and the curve fitting on O1 channel

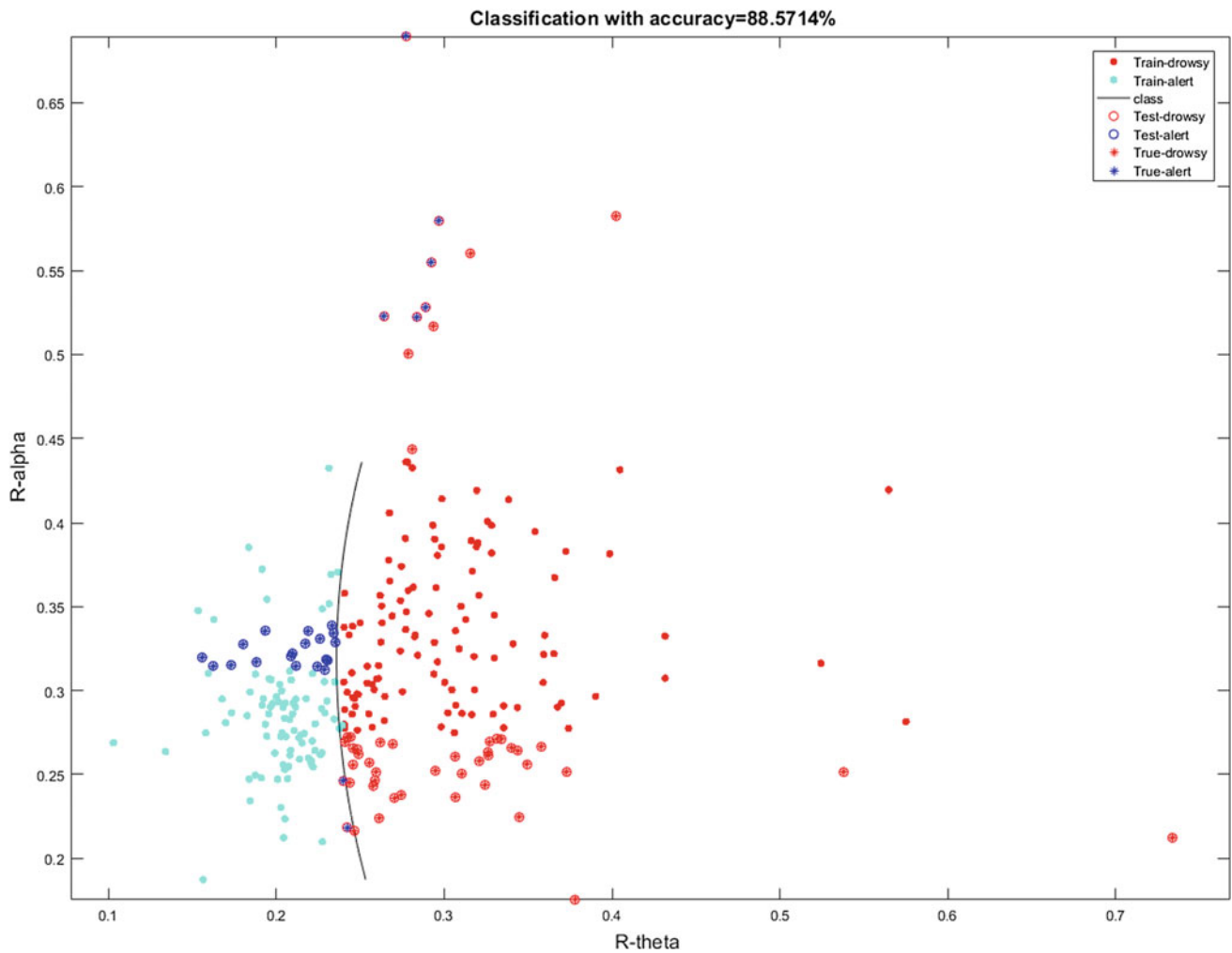


Fig. 4 SVM classify two separated data: drowsy and alert

tendency of them and the curve fitting on O1 channel is better than the others. Even for the number of training data and the features is low, SVM commonly can still give result over 80% in predicting testing data. By increasing training data dimension to achieve high confidence, SVM can be able to predict the same switching point as identified and then select the rational time to alarm in further study. When EEG sections are unable to be correctly classified, it is necessary to develop algorithms in the SVM classification and adjusting parameters in algorithms for accurate prediction of unseen samples are proposed methods for solving problems existed.

Conflict of Interest About the paper, the authors declare that they have no conflict of interest.

References

1. NIH: <https://www.ninds.nih.gov/Disorders/Patient-Caregiver-Education/Understanding-Sleep>. Last modified 22 May 2017, Last accessed 4 Apr 2018
2. NCSDR/NHTSA Expert Panel on Driver Fatigue and Sleepiness: Drowsy Driving and Automobile Crashes: Report and Recommendations. National Highway Traffic Safety Administration, US (1998)

3. Qiong, W., Jingyu, Y., Mingwu, R., Yujie, Z.: Driver fatigue detection: a survey. In: Proceedings of the 6th World Congress on Intelligent Control and Automation, IEEE, China, pp. 8587–8591 (2006)
4. Zhang, W., Cheng, B., Lin, Y.: Driver drowsiness recognition based on computer vision. *Tsinghua Sci. Technol.* **17**, 354–362 (2012)
5. Šušmáková, K.: Human sleep and sleep EEG. *Measur. Sci. Rev.* **4** (2), 59–74 (2004)
6. Yue L., Jiang, X., Teng, C., Feng, W., Mak, P.U., Mak, P.I., Vai, M.I.: Implementation of SSVEP based BCI with Emotiv EPOC. In: 2012 IEEE International Conference on Virtual Environments Human-Computer Interfaces and Measurement Systems (VECIMS), IEEE, China, pp. 34–37 (2012)
7. Ramirez, E.J.R., Huosheng, H., McDonald M.K.: Head movements based control of an intelligent wheelchair in an indoor environment. In: 2012 IEEE International Conference on Robotics and Biomimetic (ROBIO), IEEE, China, pp. 1464–1469 (2013)
8. Cristianini, N., Shawe, T.J.: An Introduction to Support Vector Machines, 1st edn. Cambridge University Press, New York, USA (2000)
9. Kowalczyk, A.: Support Vector Machines Succinctly, 1st edn. Syncfusion, USA (2017)
10. Yeo, M.V.M., Xiaoping, L., Kaiquan, S., Wilder-Smith, E.P.V.: Can SVM be used for automatic EEG. *Saf. Sci.* **47**, 115–124 (2008)
11. Emotiv Company Limited: User Manual Emotiv Software Development Kit (2012)
12. Paul, S.A.: The Illustrated Wavelet Transform Handbook: Introductory Theory and Applications in Science, Engineering, Medicine and Finance, 2nd edn. CRC Press, Scotland (2017)
13. Lin, C.T.: Assessment of driver's driving performance and alertness using EEG-based fuzzy neural networks. In: International Symposium on Circuits and Systems, IEEE, Japan, pp. 152–155 (2008)
14. Malaekah, E.: Automatic sleep-wake detection using electrooculogram signals. In: 2014 IEEE Conference on Biomedical Engineering and Sciences, IEEE, Malaysia, pp. 724–728 (2014)
15. Iber, C.: AASM Manual for the Scoring of Sleep and Associated Event: Rules, Terminology and Technical Specification, 1st edn. American Academy of Sleep Medicine, Westchester (2007)

Effect of Trehalose on Preservation of Mouse Freeze-Dried Spermatozoa at Room Temperature

Daiyu Ito, Sayaka Wakayama, Yuko Kamada, Masatoshi Ooga, and Teruhiko Wakayama

Abstract

Freeze-drying has been frequently used to preserve food at room temperature for extended periods of time; however, its application to mammalian spermatozoa is difficult because it is impossible to preserve spermatozoa at room temperature for long periods. It is known that trehalose is one of the best cryoprotectant agents, but not yet clear whether trehalose is effective for the protection of freeze-dried spermatozoa. In this study, we examined DNA damage of mouse freeze-dried spermatozoa preserved for one week at room temperature with or without trehalose. When freeze-dried spermatozoa were preserved for one week, the DNA damage of spermatozoa and in vitro developmental potential after fertilization had no difference between any concentrations of trehalose. However, when those embryos were transferred into recipient females, the highest birth rate was obtained from embryos fertilized with trehalose treated spermatozoa. These results suggest that the trehalose can protect freeze-dried spermatozoa and increased the quality of embryo for full term development.

Keywords

Freeze dry • Spermatozoa • Trehalose • Room temperature • Preservation • ICSI

1 Introduction

Preservation of spermatozoa in liquid nitrogen (LN₂) plays an important role in the treatment of infertility, domestic production of animals, preservation of genetically-modified mouse strains, and protection of endangered or extinct species [1]. However, the use of LN₂ for freezing spermatozoa may not be ideal for many reasons, for example, LN₂ must be handled very carefully because of its extremely low temperature or the use of LN₂ adds to the cost of spermatozoa preservation, which is incumbent on the couples seeking infertility treatment [2]. By contrast, freeze-drying is a reliable and commonly used technique in many countries. Previously, we demonstrated for the first time that spermatozoa can be freeze-dried (FD) and stored for three months at 4 °C or for one month at room temperature (RT) without losing their reproductive potential [3]. The preservation of FD spermatozoa at RT enables cost-effective transportation of spermatozoa [3, 4]. This preservation method does not require any electric power or other expensive inputs because the use of a desk drawer is sufficient. Benefiting from this advantage, we recently sent FD spermatozoa to the International Space Station to examine the effect of space radiation on the integrity of sperm DNA [5]. Despite its advantages the method of freeze-drying spermatozoa has not yet been utilized because of its poor reliability for long-term preservation at RT.

To improve the reliability of freeze-dried spermatozoa, here we investigated the effect of trehalose and tried to determine the appropriate concentration of that for the protection of DNA damage of freeze-dried spermatozoa for one week preservation at RT.

2 Materials and Methods

2.1 Animals

ICR male and female mice (8–10 weeks of age) were obtained at from SLC Inc. (Hamamatsu, Japan). The

D. Ito · Y. Kamada · M. Ooga · T. Wakayama (✉)
Faculty of Life and Environmental Sciences, University of Yamanashi, Yamanashi, 400-8510, Japan
e-mail: twakayama@yamanashi.ac.jp

S. Wakayama · T. Wakayama
Advanced Biotechnology Centre, University of Yamanashi, Yamanashi, 400-8510, Japan

surrogate pseudopregnant ICR females, used as recipients of embryos, were mated with vasectomized ICR males, whose sterility had been previously demonstrated. On the day of the experiments or after finishing all experiments, mice were euthanized by CO₂ inhalation or cervical dislocation and used for experiments. All animal experiments followed the Guide for the Care and Use of Laboratory Animals and were approved by the Institutional Committee of Laboratory Animal Experimentation of the University of Yamanashi.

2.2 Media

HEPES–CZB medium and CZB were used for oocyte/embryo manipulation in air and incubation in 5% CO₂ at 37 °C. HTF medium was used for the capacitation of spermatozoa. Tris-EGTA medium with trehalose was used for the freeze drying of spermatozoa. The final concentration of trehalose were 0.1, 0.5, 2.0 M, respectively.

2.3 Preparation and Preservation at RT of FD Spermatozoa

Both epididymides were collected from the male mice and ducts were cut with a pair of sharp scissors. After the capacitation, the concentration of spermatozoa was measured. Then, 50- μ l aliquots of the spermatozoa suspension of Tris-EGTA with or without trehalose were dispensed into glass ampoules. The ampoules were flash-frozen in LN₂ and then FD using the FDU-2200 freeze dryer (EYELA, Tokyo, Japan). The cork of the freeze dryer was opened for at least 5 h until all samples were completely dry. After drying, ampoules were sealed by melting the ampoule necks using a gas burner under vacuum. All ampoules were placed in small plastic bags and then in paper boxes and stored in a desk drawer at RT (15–25 °C) until further use. No additional protective measures were taken for the preservation of the spermatozoa.

3 Results

3.1 Effect of Trehalose on One Week Preserved FD Spermatozoa for Embryo Development in vitro and in vivo

As shown in Figs. 1, 2 and 3, when one week preserved FD sperm were used, we could obtain a lot of blastocysts in vitro and healthy offspring after embryo transfer. However, those

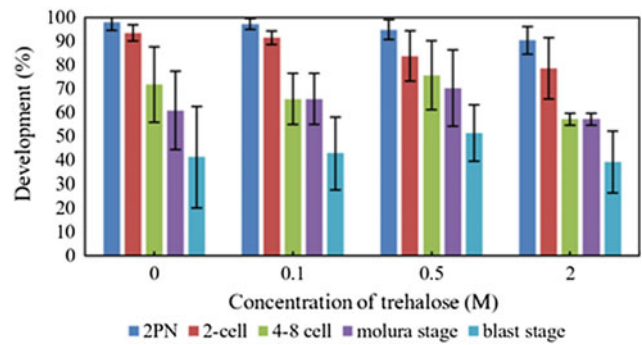


Fig. 1 Developmental rates of mouse oocyte injected with FD sperm preserved with or without trehalose for 1 week at RT. Developmental rates were calculated as means for each stage of embryos at 24, 48, 72 and 96 h after injection. The blastocyst rates were evaluated using chi-squared tests. Statistical significance of the differences between variables was determined at $P < 0.05$

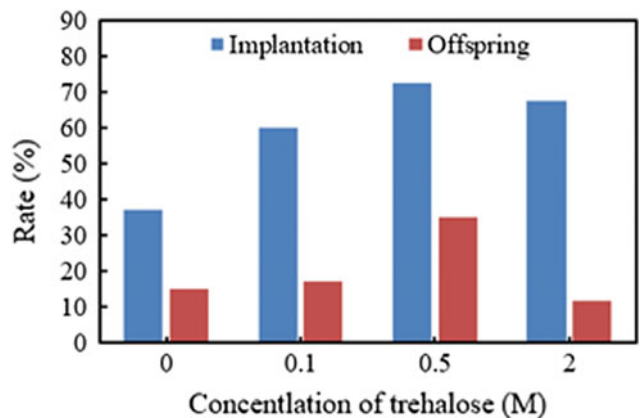


Fig. 2 Implantation and offspring rates of embryos derived from FD sperm preserved with or without trehalose for 1 week at RT. Embryos at two-cell stage were transferred to a day 0.5 pseudopregnant mouse that had been mated with a vasectomized male the night before transfer. Six to ten embryos were transferred into each oviduct

rate did not increased with increased the concentration of trehalose.

3.2 Examination of the DNA Integrity of FD Spermatozoa Preserved for One Week with or Without Trehalose by the Comet Assay

The DNA integrity of FD spermatozoa with or without trehalose was examined using the comet assay. When one week preserved FD spermatozoa were examined, the DNA damage did not differ between with or without trehalose.

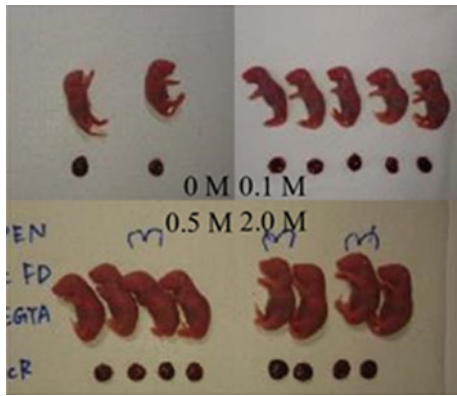


Fig. 3 Live offspring derived from FD spermatozoa stored with or without trehalose at RT for 1 week. At day 18.5 of gestation, the offspring were delivered by caesarean section

4 Discussion

In this study, the highest success rate of blastocyst in vitro and full term were obtained when trehalose were used for preservation of FD spermatozoa at RT for more than one month. Interestingly, the protection effect of trehalose was not observed when embryos were cultured in vitro for up to blastocyst stage. When trehalose was used, the preservation

period at RT and full-term developmental rate will be increased comparing to without trehalose.

Acknowledgements This work was supported by JSPS KAKENHI Grant (Numbers 17K15394 to MO, and 16H02593 to TW), and Asada Science Foundation.

References

1. Benson, J.D., Woods, E.J., Walters, E.M., Critser, J.K.: The cryobiology of spermatozoa. *Theriogenology* **78**, 1682–1699 (2012)
2. Gil, L., Olaciregui, M., Luno, V., Malo, C., Gonzalez, N., Martinez, F.: Current status of freeze-drying technology to preserve domestic animals sperm. *Reprod. Domest. Anim.* **49**(Suppl 4), 72–81 (2014)
3. Wakayama, T., Yanagimachi, R.: Development of normal mice from oocytes injected with freeze-dried spermatozoa. *Nat. Biotechnol.* **16**, 639–641 (1998)
4. Kaneko, T.: Simple sperm preservation by freeze-drying for conserving animal strains. *Methods Mol. Biol.* **1239**, 317–329 (2015)
5. Wakayama, S., Kamada, Y., Yamanaka, K., Kohda, T., Suzuki, H., Shimazu, T., Tada, M.N., Osada, I., Nagamatsu, A., Kamimura, S., Nagatomo, H., Mizutani, E., et al.: Healthy offspring from freeze-dried mouse spermatozoa held on the International Space Station for 9 months. *Proc. Natl. Acad. Sci. USA* **114**, 5988–5993 (2017)

Breast Cancer Histopathological Image Classification Utilizing Convolutional Neural Network

Tuan Dinh Truong and Hien Thi-Thu Pham

Abstract

Breast cancer is a significant health concern prevailing in both developing and advanced countries where early and precise diagnosis of the disease receives significant attention from the scientific community. In this work, we proposed a deep learning approach using Convolutional Neural Network (CNN) to address the problem of classifying breast cancer using the public histopathological image dataset BreakHis. We propose a CNN model that takes input as preprocessed and augmented images from the available dataset and finally evaluate the classification performance of the model based on accuracy. The result shows that data preprocessing and augmentation significantly improve the performance of the model and help avoid overfitting due to class imbalance from the raw image set. The performance of our model also indicates the high capability of CNN in learning the representation that substantially improves the overall classifying accuracy of cancerous breast tissue.

Keywords

Computer-aided diagnosis • Deep learning • Image processing • Breast cancer

1 Introduction

Besides common screening examination using various imaging techniques to detect breast cancer, the analysis of breast tissue under microscopy serves as a crucial step in definitive diagnosis that includes evaluation of the spread as well as determining the type of the disease. Even though image analysis on the histopathological image is a gold standard for detection of breast cancer compared to other

imaging modalities, the manual performing of this task still faces many challenges, one of which is the extensive use of time as well as experienced and skilled pathologists [1]. Therefore, the need for automated analysis of the histopathological image is undoubtedly one of the most promising topics in CAD.

Conventional image classification in CAD involves engineering tasks in feature extraction where information about the tumor (i.e., size or color) or the background is extracted as the representative for the model to classify. Some of the obstacles faced by this method are that we do not know if these features are strong enough to represent the characteristics of the image and how many features are enough for classifying, which as a result leads to extensive engineering work for feature extraction and selection. A technique like Principle Component Analysis (PCA) for feature selection is commonly utilized such as in the work of Zhang et al. [2], who performs PCA on handcrafted features to classify benign and malignant tumors and achieve an accuracy of 92%. Some of the other techniques in engineering feature extraction include scale-invariant feature transform (SIFT), gray-level co-occurrence matrix (GLCM), a histogram of oriented gradient (HOG).

Even though many computer-aided diagnosis (CAD) techniques have been developed to assist pathologists in performing analysis, it is only until recently that Deep Learning has proved to have considerable potential in achieving high diagnostic accuracy compared to previous CAD systems. One of the most potential and powerful techniques is Convolutional Neural Network (CNN), which has been profoundly utilized in many image classification models. The advantage of CNN is its capability to automatically extract features without prior knowledge about the content of the image. The recent implementation of CNN in breast cancer classification includes Spanhol et al. [3], whose works utilizing CNN for patch-based image classification of the benign and malignant tumor and Hou et al. [4] who also introduces a patch-based model for multiclass classification of breast cancer. As the implementation of CNN requires a

T. D. Truong · H. T.-T. Pham (✉)
Biomedical Engineering Department, International University—
Vietnam National University, Ho Chi Minh City, Vietnam
e-mail: ptthien@hcmiu.edu.vn

Table 1 Distribution of BreakHis database

Magnifying factor	Benign	Malignant	Total
40X	652	1370	1995
100X	644	1437	2081
200X	623	1390	2013
400X	588	1232	1820
Total	2480	5429	7909

significantly large number of training examples, the employment of data augmentation in which the image is transformed in various ways such as flipping, translation, rotation or noise addition can help create more examples for small image sets. The implementation of data augmentation has been utilized extensively during the training as in [5–7].

While CNN is mighty in feature extraction, preprocessing tasks before feeding into the model is still essential to improve the quality of features generated. In our experiment, the whole model is implemented on Keras API with Tensorflow backend and is trained with the supported Nvidia Geforce GTX 1080 Ti.

2 Experiment

2.1 Data Background

BreakHis (Breast Cancer Histopathological Database) [8] is a publicly available database consisting of 9109 RGB microscopic images of breast cancer tumors collected from 82 patients using four different magnifying factors (40X, 100X, 200X, 400X). The dataset is divided into 2480 benign and 5429 malignant samples in an image size of 460 by 700. The distribution of samples is shown in Table 1 (Fig. 1).

2.2 Preprocessing

Preprocessing the dataset includes image augmentation and normalization. As can be seen from Table 1, the training phase can be overfitted because of the lack of quantity and diversity of the training examples. More images are thus generated from the original ones by flipping horizontally and

vertically, blurring and adding more noise. The image augmentation is employed in the training set whereas validation and test set contains only original data. In doing so, the size of the training set is increased about five times of the original ones. In the next step, all samples are resized into $(64 \times 64 \times 3)$ and normalized.

2.3 Training and Classification

The architecture for CNN used in this experiment is a simple one consisting of 3 convolutional blocks and two fully-connected layers at the end as shown Table 2. The computation of convolution is described by the formula as shown in Eq. (1).

$$(f \otimes h)(m, n) = \sum_i \sum_j h(i, j) f(m - i, n - j) \quad (1)$$

In other words, the convolutional layer is formed by sliding a kernel h across the width and height of the input image volume f and computing at each position the dot product between the elements in the kernel and those in the input volume, which results in an activation map showing the response of that filter.

The classification part in this architecture utilizes Fully-connected Neural Network with two layers of 1024 neurons and the last layer of 2 neurons corresponding two classes: benign and malignant (labeled as respectively 0 and 1). The loss is calculated as in the Softmax classifier, which is defined as:

$$L_i = -\log \left(\frac{e^{f_{y_i}}}{\sum_j e^{f_{y_j}}} \right) \quad (2)$$

The Softmax classifier gives probabilities of each class, and the loss function tries to maximize the probability of the class belonging to a particular label. In case of binary classification, a loss function is a generalized form of binary cross-entropy loss, which is commonly used with the sigmoid function.

At the beginning of the training process, all the filters are initialized by Xavier initialization [9] which draws the weights from a Gaussian distribution. Xavier initialization

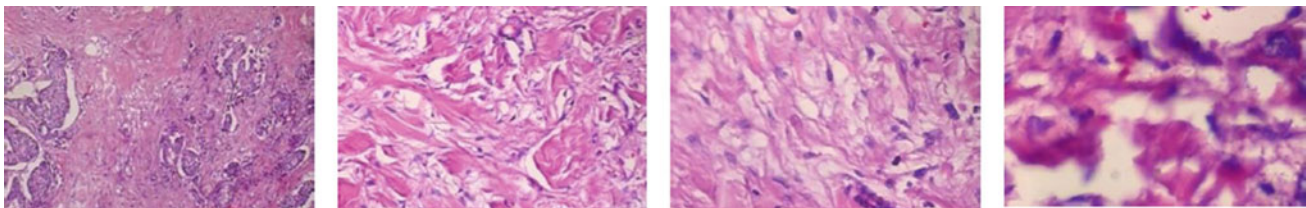


Fig. 1 A malignant tumor in 4 magnifying factors (40X, 100X, 200X, 400X) from left to right

Table 2 CNN architecture

Layer	Filter size, Filter	Stride
Conv + ReLU	3×3 , 64	1
Max Pooling	2×2	2
Conv + ReLU	3×3 , 96	1
Max Pooling	2×2	2
Conv + ReLU	3×3 , 128	1
Max Pooling	2×2	2
FC + ReLU	1024	–
FC + ReLU	1024	–
FC	2	–
Softmax	–	–

helps the loss function to converge faster. All the weights after each iteration are updated based on Adam (Adaptive Moment Estimation) [10] algorithm:

$$\theta_{t+1} := \theta_t - \frac{\alpha}{\sqrt{\hat{v}_t + \epsilon}} \hat{m}_t \quad (3)$$

In Eq. (3), α is the learning rate and \hat{m}_t and \hat{v}_t are respectively bias-corrected first moment (the mean) and second moment (the uncentered variance) estimate of the gradients. The bias-corrected first and second moment estimate are computed as:

$$\hat{m}_t := \frac{m_t}{1 - \beta_1^t} \quad (4)$$

$$\hat{v}_t := \frac{v_t}{1 - \beta_2^t} \quad (5)$$

In Eqs. (4) and (5), β_1 and β_2 are exponential decay rates for moment estimate. In this experiment, the default values of these decay rates are taken as $\beta_1 = 0.9$ and $\beta_2 = 0.999$ [10]. The term ϵ has the value of 10^{-8} and is taken to prevent division by 0. As can be seen from Eqs. (3), (4) and (5), Adam takes into account the first and second moment of the gradients and is thus effective in the convergence of the calculated loss. The learning rate for the whole training process is set as 10^{-5} moreover, batch size is 32 in a total of 50 epochs.

Initial training shows massive sign of overfitting, so regularization techniques as dropout and L2 kernel regularization are used to avoid too early overfitting. After successfully being trained, the test set is used to evaluate the model with accuracy as assessment metric.

3 Results

3.1 Training and Validation Accuracy

Figures 2, 3, 4 and 5 show the training and validation accuracy of 4 different magnifying factors. These figures are obtained from Tensorboard, a visualization tool from Tensorflow. As Tensorboard does not provide any means for high resolution downloading of graphs, the above figures are of the best resolution we can achieve. The training and validation accuracy are respectively evaluated on the training and validation set. While the model uses the training set to learn the parameters, the validation set is only exposed to the model for evaluation at the end of every epoch. Accordingly, the validation accuracy is a reliable estimation of learning progress and can be used to assess how well the

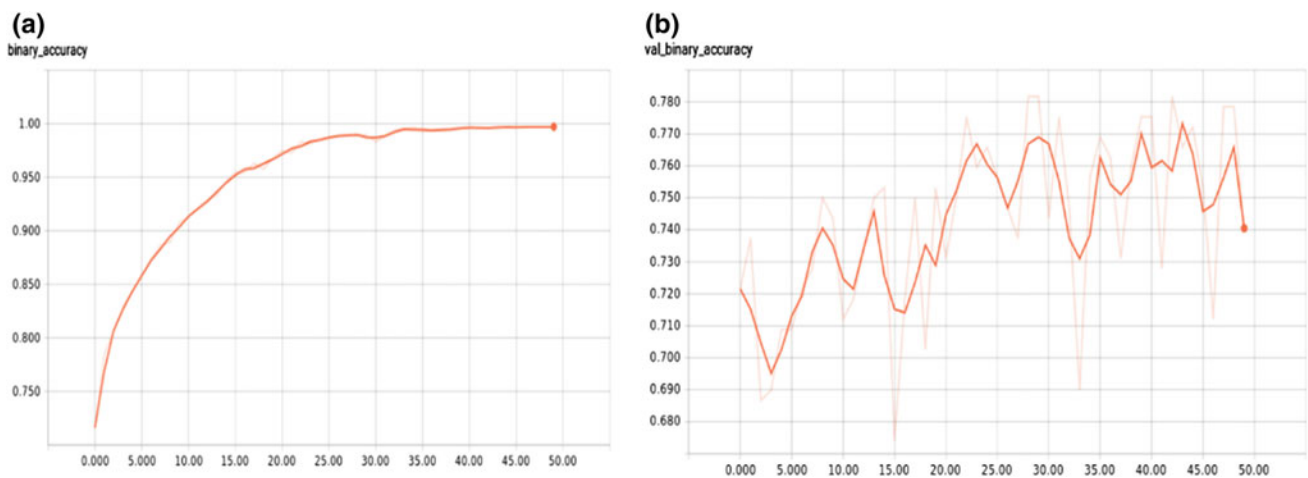


Fig. 2 The training accuracy (a) and validation accuracy (b) in 40X

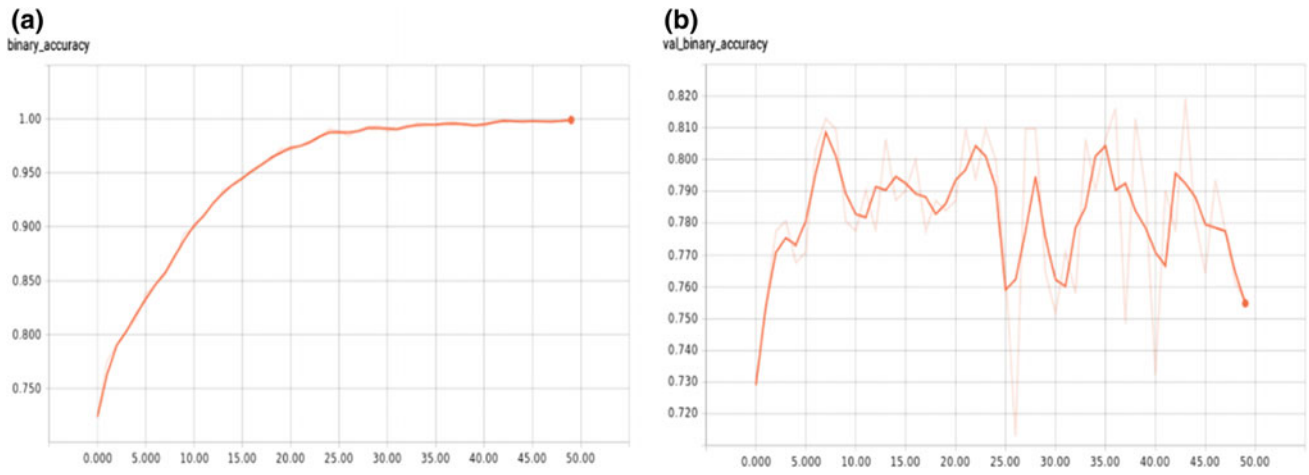


Fig. 3 The training accuracy (a) and validation accuracy (b) in 100X

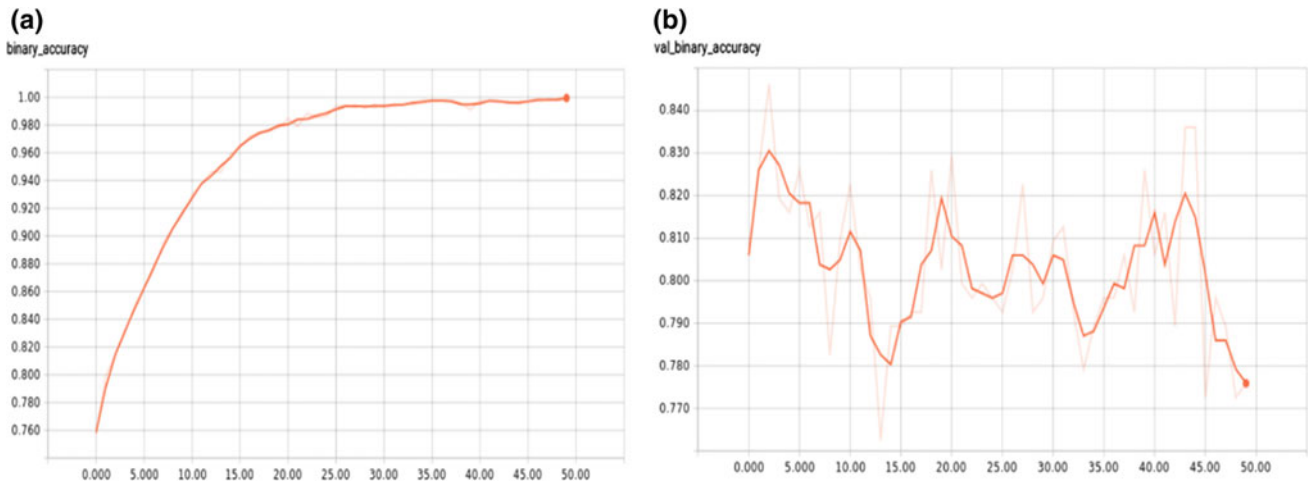


Fig. 4 The training accuracy (a) and validation accuracy (b) in 200X

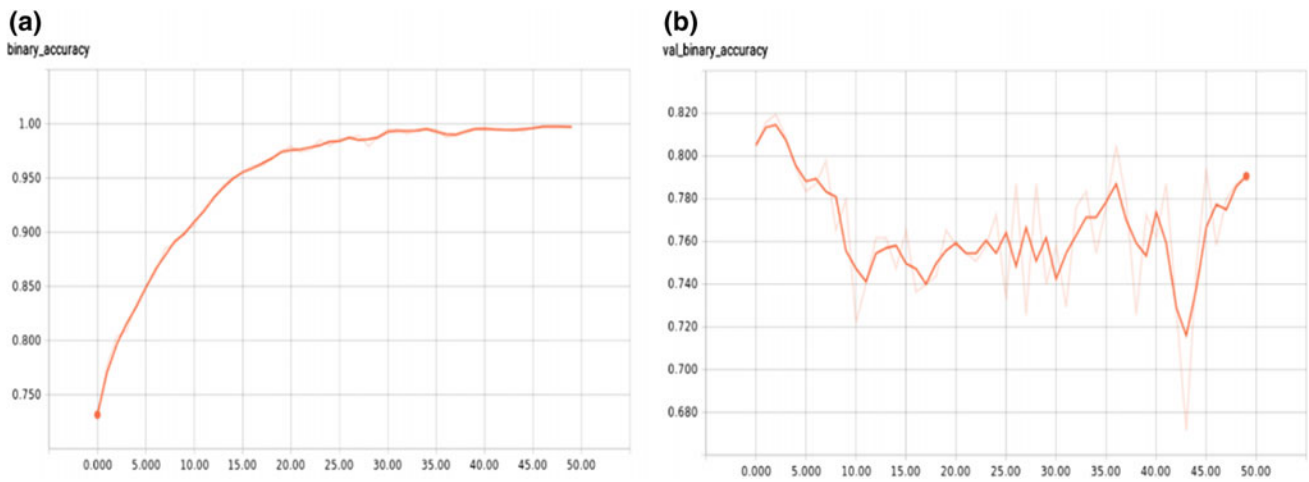
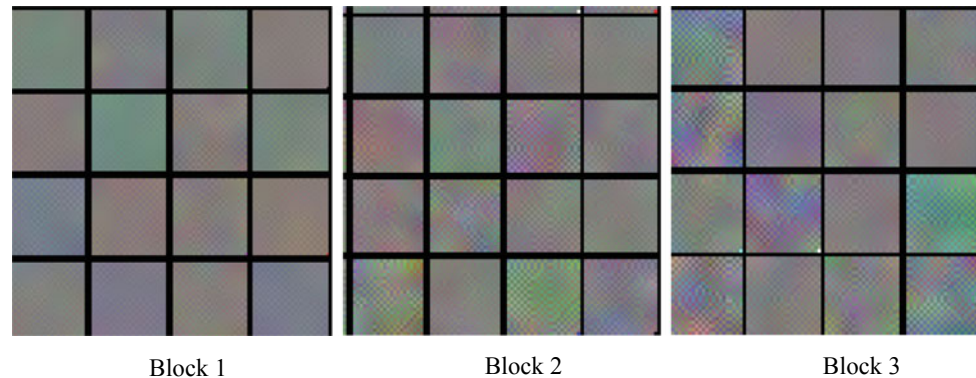


Fig. 5 The training accuracy (a) and validation accuracy (b) in 400X

Table 3 Test accuracy in 4 magnifying factors

Magnifying factor	40X	100X	200X	400X
Accuracy	73.41	76.77	83.22	75.81

Fig. 6 Visualization of some filters in each convolutional block using Keras-Vis [11]

model responds to new data apart from the training set. From Figs. 2, 3, 4 and 5, there is a clear difference between the graphs of training and validation accuracy. Whereas the training accuracy approaches to 1 after 50 epochs, which is a clear sign that the model successfully fits the training set, there is a fluctuation around 0.7–0.8 in the validation accuracy across 50 epochs. The instability of validation accuracy indicates the difficulty of the model in responding to new data.

3.2 Test Accuracy

See Table 3.

4 Discussion

The model fits the training set perfectly after ten epochs whereas there is fluctuation within the validation set, a sign of overfitting. The fact that the size of the training set is about 6000 samples included the generated ones is still insufficient for Neural Network classification. Moreover, from the visualization of some filters in each convolutional block, it can be seen that model can learn some basic shape of the tumor in training set, but it is still not enough to distinguish between benign and malignant tumors. A possible solution, in this case, can be increasing the size of the training set and simultaneously the depth of the model. It is possible to achieve a larger size of training set by using the patch-based approach as many recent works such as [3, 4] have investigated so far (Fig. 6).

5 Conclusions

The experiment with initial result shows that the model has achieved a moderate accuracy score but is insufficient to generate a significant result in cancer detection. The future approach to this problem includes a solution to prevent overfitting as well as new methods to better the image quality to improve the learning of CNN model.

Conflict of Interest The authors declare that they have no conflict of interest.

References

1. Veta, M., Pluim, J.P.W., van Diest, P.J., Viergever, M.A.: Breast cancer histopathology image analysis—a review. *IEEE Trans. Biomed. Eng.* **61**(5), 1400–1411 (2014)
2. Zhang, Y., Zhang, B., Coenen, F., Xiao, J., Lu, W.: One-class kernel subspace ensemble for medical image classification. *EURASIP J. Adv. Signal Process.* **2014**(1), 1–13 (2014)
3. Spanhol, F.A., Oliveira, L.S., Petitjean, C., Heutte, L.: Breast cancer histopathological image classification using convolutional neural network. In: *International Joint Conference on Neural Networks* (2016)
4. Hou, L., Samaras, D., Kurc, T.M., Gao, Y., Davis, J.E., Saltz, J.H.: Patch-based Convolutional Neural Network for Whole Slide Tissue Image Classification (2015)
5. Korbar, B., Olofson, A.M., Mirafior, A.P., Nicka, C.M.: Deep learning for classification of colorectal polyps on whole-slide images. *J. Pathol. Inform.* **8**, 30 (2017)
6. Motlagh, N.H., Jannesary, M., Aboulkheyr, H.R., Khosravi, P., Elemento, O., Totonchi, M., Hajirasouliha, I.: *Breast Cancer Histopathological Image Classification: A Deep Learning Approach* (2018)

7. Rakhlin, A., Shvets, A., Iglovikov, V., Kalinin, A.A.: Deep Convolutional Neural Networks for Breast Cancer Histology Image Analysis. (2018)
8. Breast Cancer Histopathological Database (BreakHis) [Online]: Available: <https://web.inf.ufpr.br/vri/databases/breast-cancer-histopathological-database-breakhis/>
9. Glorot, X., Bengio, Y.: Understanding the difficulty of training deep feedforward neural networks. In: Proceedings of the Thirteenth International Conference on Artificial Intelligence and Statistics (2010)
10. Diederik, J.B., Kingma, P.: Adam: a method for stochastic optimization. In: The 3rd International Conference for Learning Representations, San Diego (2015)
11. Keras Visualization Toolkit [Online]. Available: <https://github.com/raghakot/keras-vis>

Electrooculography Feature Extraction Techniques for Classification of Eye Movements

Toan Le, Ngu Bui, and Trung Le

Abstract

Understanding of eye movement is crucial for viewers' behavior recognition. The movement of eyeballs in space can be described by a nonlinear differential equation that should be processed with a special identification approach due to its nonlinearities. Electrooculography (EOG) is a technique for measuring the cornea—retinal standing potential that exists between the front and the back of the human eye. The EOG signal can be processed separately through the horizontal and vertical channel from the surface muscle around the eye. In this paper, we propose a method to describe the characteristic of EOG signals that can be used to detect eye movements. The method consists of two (2) main parts: recurrence quantification analysis to estimate the behavior of EOG signal and state space analysis to identify different types of eye movement. The assessment of the data suggests the potential parameters in characterizing EOG signal. The preliminary results indicate that state space analysis is promising in classifying different types of eye movement for activity recognition.

Keywords

Electrooculography • Feature extraction • State space

1 Introduction

The development of researching about human activities have been observed in different fields, especially computer-science applications, which rely on neuroscience and

biobehavioral theories. Human activity recognition is the most important research direction in this field, which can recognize activities from a series of observations on the actions of subjects and the environmental conditions. The vision-based HAR research is the basis of many applications which are investigated to collect the stabilizing the eyes with regard to the outside world and aiming the eyes toward moving or stationary targets. In order to understand these motions, eye movements tracking and processing are considered.

Electrooculography (EOG), is a common method for analyzing eye movement which is measured by two pairs of skin electrodes placed at the periorbital positions of the eye, plus an additional reference electrode on the forehead [1]. By this way, the vertical movement and the horizontal movement of the eye are identified in two different signal components. Thus, the characterizing EOG signal for deterministic dynamics demonstrates the classification of types of eye movement by chaos theory application (Fig. 1).

2 Background

2.1 Electrooculography

The electro-oculography (EOG) is a technique to measure the electrical signal of the eye which varies depending on the eye's position. Essentially, the eye is the origin of a standing electrical potential field which is considered as a dipole, where the negative pole represented by the retina (posterior part of the eye) is oriented towards the positive pole, represented by the cornea (anterior part of the eye) [2]. By recording changes the rotation of the dipole, the eye movement can be tracked and its characteristics: amplitude, duration, and speed, can be obtained [3]. Typically, EOG shows signal amplitudes ranging from 5 to 20 $\mu\text{V}/\text{degree}$ and a frequency range between 0 and 30 Hz [4].

T. Le (✉) · N. Bui · T. Le
Department of Biomedical Engineering, International University
—VNU HCM, Ho Chi Minh City, Vietnam
e-mail: lthtoan.pctcr11@gmail.com

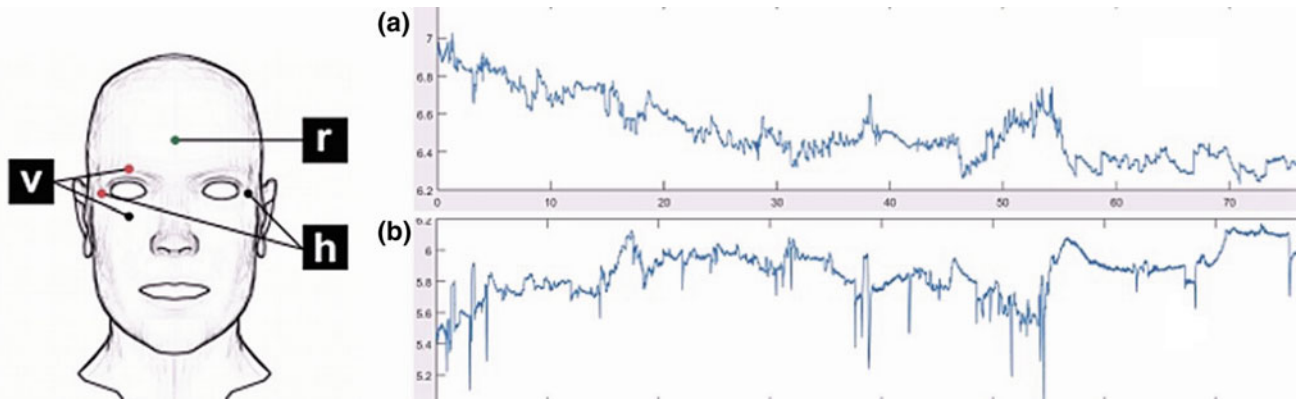


Fig. 1 Electrode placement for measuring EOG signal; The raw EOG signal **a** Horizontal EOG signal, **b** Vertical EOG signal

However, EOG signal is unstable because of the strongly affected by different sources of noise. For example, the activity of muscles tends to become a considerable number of artifacts in the EOG (eyelid closure, movement of the opposite eye, muscle action potential spike at the onset of a saccade) [5, 6]. Furthermore, the noise generated by the contact resistance between skin and electrodes and the unstable attachment of the electrodes to the skin represents an interruption and impairment of the signal. In addition, a particular interference called baseline drift that deforms the raw EOG signal. Essentially, it affects to the signal of the eye movements, except for the saccades, as their duration is so short that the drift cannot be distinguished. Thus, the removing noise and baseline drift contamination is necessary to enhance the quality of EOG signal (Fig. 2).

2.2 Eye Movements Types

To understanding the characteristic of eye movements from EOG signal collected, there are three basic eye movement types which are fluently detected by using this signal: saccades, fixations, and blinks.

A saccade is a rapid movement of both eyes between two or more phases of fixation in the same direction. The saccade duration depends on the angular distance the eyes travel during this movement: the so-called saccade amplitude. In general, the characteristics of saccadic eye movements are 20° for the amplitude, and 10–100 ms for the duration [7].

Fixations are states when eyes essentially stop scanning the scene. Normally, fixations are defined as the time intervals of apparent ocular immobility between two

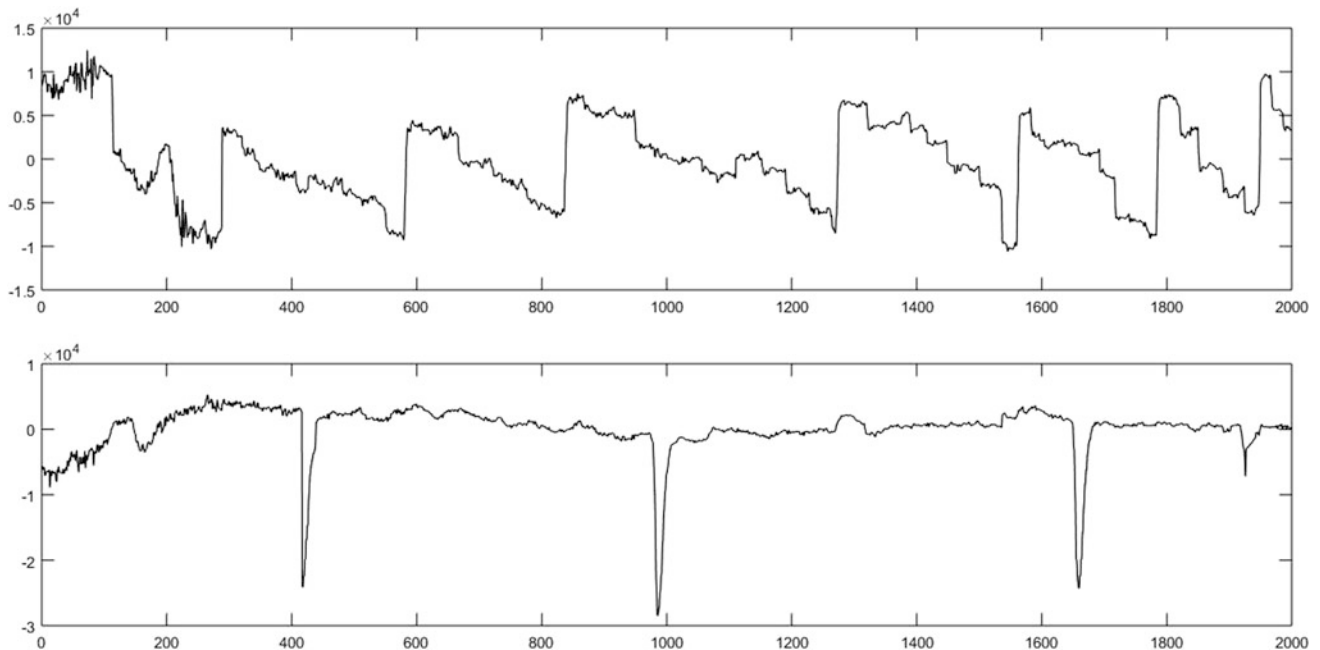


Fig. 2 The EOG signal after remove baseline drift and noise

saccades. The average duration of fixation is between 100 and 200 ms [8].

Blinks are defined as regular opening and closing of the eyelids to spread the tear across the corneal surface. There are three types: spontaneous blinking, reflex blinking, voluntary blinking [9]. The average blink rate varies between 12 and 19 blinks per minute while at rest [10] and duration is between 100 and 400 ms [11].

3 Methodology

3.1 Recurrence Quantification Analysis

Recurrence analysis is a technique to investigate the time evolution of data series which was developed to characterize the behavior of time series [12].

EOG signals are denoted as time series in this study, which has the time sequence of the form $\{x_0; x_1; x_2; \dots x_i; \dots x_n\}$, where x_i denotes the signal at time i .

To characterize this signal a set of five recurrence variables which are investigated to defined that functioned as complexity measures based on diagonal line structuring in Recurrence Plots and recurrence quantification analysis (RQA).

$\%REC(RR)$ is the percentage of recurrence or global recurrence measure, defined as:

$$\%REC = 100 \times \frac{NREC}{NP} \quad (1)$$

where $NP = \frac{n(n-1)}{2}$ is the size of recurrent point.

$\%DET$ is the percentage of determinism, defined as:

$$\%DET = 100 \times \frac{NPD}{NREC} \quad (2)$$

where NPD is the number of points on lines parallel to the main diagonal, considering that a line is formed with a minimum of at least two adjacent points.

ENT is shannon entropy or a measure of the average information contained in the line-segment distribution, defined as:

$$ENT = - \sum_{k=1}^{n-1} p_k \log_2(p_k) \quad (3)$$

where p_k is the proportion of diagonal lines of length k over the total diagonal lines.

3.2 State Space Reconstruction

The reconstruction of state space can be obtained by using the concept of delayed time series a certain number of times. The number of the displaced time series with a time delay t is called the embedding dimension m [13]. To estimate time delay t and the embedding dimension m various approaches have been proposed. The most common techniques used to calculate the time delay are the first zero of the autocorrelation function or the first minimum of the mutual information function [14]. In this study, we choose the mutual information to estimate time delay t .

Fundamental to the notion of information among measurements of mutual information between two measurements a_i and b_j drawn from sets A and B of possible measurements. This theorem asserts the formula:

$$MI(T) = \sum_{s(n), s(n+T)} P(s(n), s(n+T)) \log_2 \left[\frac{P(s(n), s(n+T))}{P(s(n))P(s(n+T))} \right] \quad (4)$$

When T becomes large, the chaotic behavior of the signal makes the measurements $s(n)$ and $s(n+T)$ become independent in a practical sense, and $MI(T)$ tends to zero [15]. The first minimum of $MI(T)$ is a prescription, this means that for values of T near this minimum the coordinate system produced by time delay vectors is essentially as good as that for the T which is the actual first minimum of $MI(T)$ [16].

To estimate the embedding dimension m , the False Nearest Neighbour algorithm is used which is based on the increasing the dimension until the percentage of neighbors of the points in the reconstructed space stops to decrease [17, 18].

4 Results

Figure 4 shows the typical RPs for EOv, EOGh, and fixations segments. The delay and embedding dimension used for generating the RPs are 10 and 6 respectively. These figures indicate the dynamic behavior of the signal. Detection of types of eye movements by using CWT-coefficients (continuous wavelet transform) graph show that in EOGh corresponds with the structure follow on RPs plot: fixation and saccades points were highly concentrated on diagonal line while the blink points which are detected by the pair of neighbor symmetric-peak by CWT which presents a white region in RPs [e.g. (405 : n)]. Therefore, these plots are unique for fixations-saccades and blink class, and hence, can

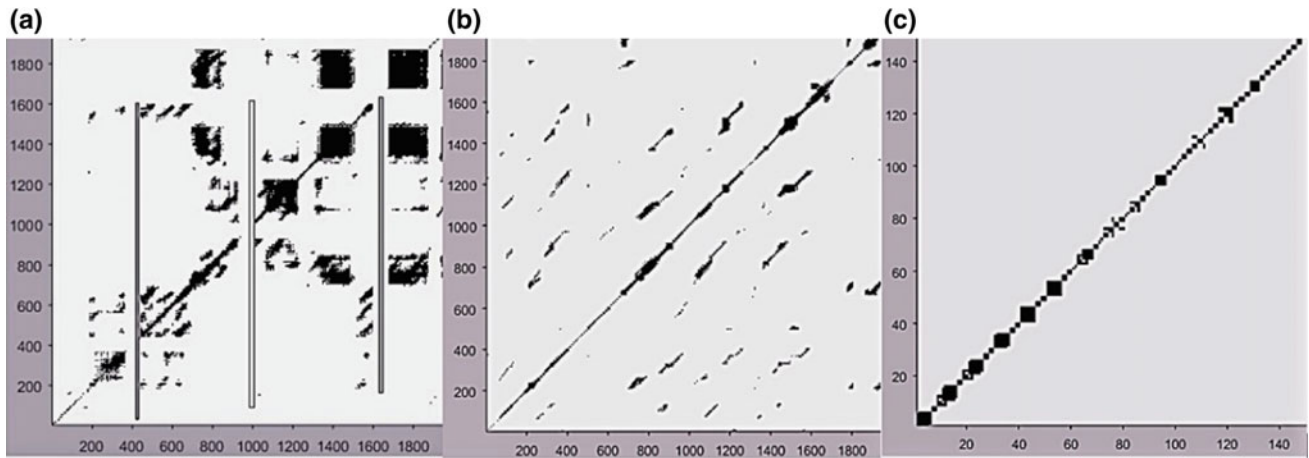


Fig. 3 Recurrence plots (RP) of EOG signals: **a** RP of EOGv indicate blinks, **b** RP of EOGh, **c** indicate only fixations

Table 1 Results of RQA features for EOGh and EOGv

Subject	EOGh			EOGv		
	%RR	%DET	ENT	%RR	%DET	ENT
S1	0.0254	0.9675	2.2325	0.0948	0.9726	2.6634
S2	0.0166	0.9599	2.5501	0.0263	0.9446	2.2467
S3	0.0345	0.9403	2.4423	0.1587	0.9803	2.9481
S4	0.0228	0.9356	2.5586	0.0980	0.9942	3.9387

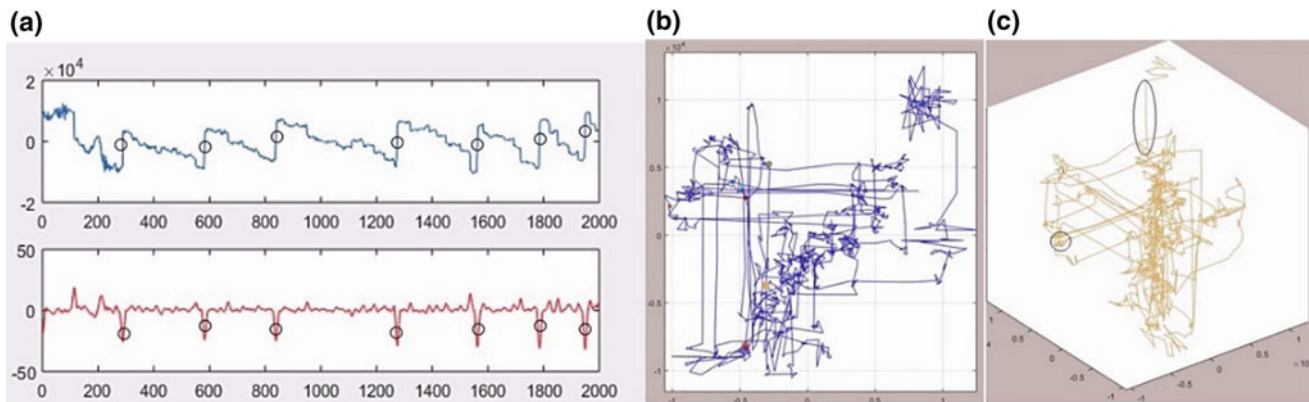


Fig. 4 $N = 2000$ samples are reconstruction by using state space: **a** EOGh signal and CWT coefficients to detect saccades-fixation (peak > 20); **b** State space reconstruction in 2D, State space reconstruction in 3D (c)

be used to identify the unknown class easily even for shorter series of data (Fig. 3).

Table 1 shows the range of RQA features for a dataset includes 4 subjects while working with laptop. The results from Table 1 confirm the information which are described in RPs, RQA shows the characteristic of EOG signal which can be predicted (mean of %DET > 0.9 , %RR < 0.1 , ENT > 2 and the p -value < 0.01).

The behavior of saccades in which signal is the interrupted between two fixations, the state-space shows this behavior in the movement of dots in space. By estimate the immediate switch point (Fig. 4c), the saccades event can be collected. In addition, Fig. 5 shows the structure of blink in EOGv, the number of structures equal to the number of blinks. The confidence level of this method is concluded with the accuracy above 80% for whole subjects (80,000 samples).

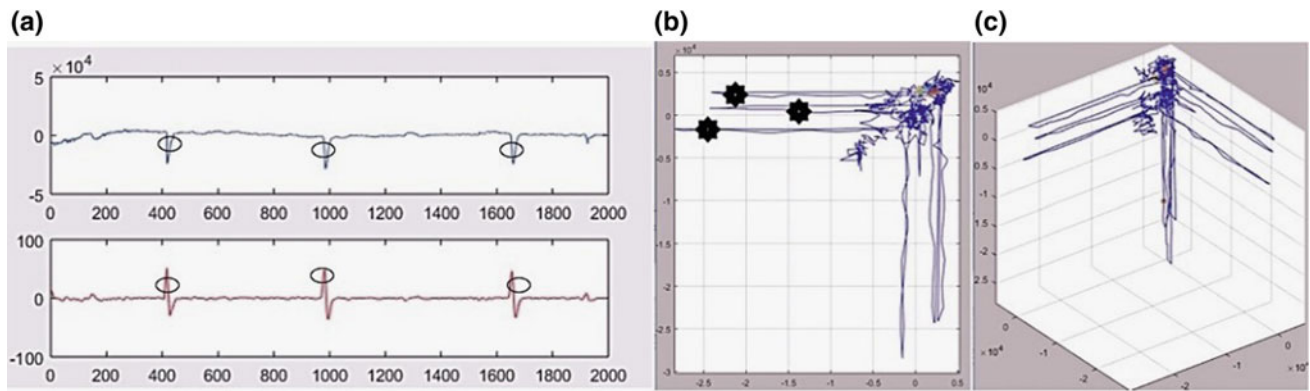


Fig. 5 $N = 2000$ samples are reconstruction by using state space: **a** EOGv signal and CWT coefficients to detect blinks; **b** State space reconstruction in 2D, **c** State space reconstruction in 3D

5 Discussion

RQA parameters and state space provide new efficient methods to detect the types of eye movements from EOG signal. Beside RQA and RPs also describe the periodic of EOG signal which can be predicted in future work such as prediction of eye-movement from EOG which opened discussions about how to observe activity and changing recognition of human.

Conflict of Interest The authors declare that there are no conflict of interests.

References

- Chenamma, H.R., Yuan, X.: A survey on eye-gaze tracking techniques. arXiv preprint [arXiv:1312.6410](https://arxiv.org/abs/1312.6410) (2013)
- Cafasso, A., Karlsson, S.: Automatic detection of saccadic eye movements using EOG for analysing effects of cognitive distraction during driving
- Duchowski, A.T.: Eye tracking methodology. *Theor. Pract.* **328**, 614 (2007)
- Bulling, A., et al.: Eye movement analysis for activity recognition using electrooculography. *IEEE Trans. Pattern Anal. Mach. Intell.* **33**(4), 741–753 (2011)
- Duchowski, A.: *Taxonomy and Models of Eye Movements*, pp. 41–48. Springer London, London (2007)
- Leigh, R.J., Zee, D.S.: *The Neurology of Eye Movements*, 5th edn. Oxford University Press, Oxford (2015)
- Duchowski, A.T.: *Eye Tracking Methodology: Theory and Practice*. Springer-Verlag, New York Inc (2007)
- Manor, B.R., Gordon, E.: Defining the Temporal Threshold for Ocular Fixation in Free-Viewing Visuocognitive Tasks. *J. Neurosci. Methods* **128**(1/2), 85–93 (2003)
- Karson, C.N., Berman, K.F., Donnelly, E.F., Mendelson, W.B., Kleinman, J.E., Wyatt, R.J.: Speaking, thinking, and blinking. *Psychiatry Res.* **5**(3), 243–246 (1981)
- Schleicher, R., Galley, N., Briest, S., Galley, L.: Blinks and saccades as indicators of fatigue in sleepiness warnings: looking tired? *Ergonomics* **51**(7), 982–1010 (2008)
- Schiffman, H.R.: *Sensation and Perception: An Integrated Approach*, 5th edn. Wiley & Sons, New York (2001)
- Vaidyanathan, P., et al.: Recurrence quantification analysis reveals eye-movement behavior differences between experts and novices. In: *Proceedings of the Symposium on Eye Tracking Research and Applications*. ACM (2014)
- Marwan, N., et al.: Recurrence plots for the analysis of complex systems. *Phys. Rep.* **438**(5–6), 237–329 (2007)
- Webber Jr., C.L., Zbilut, J.P.: Recurrence quantification analysis of nonlinear dynamical systems. *Tutorials in Contemporary Nonlinear Methods for the Behavioral Sciences*, pp. 26–94 (2005)
- Abarbanel, H.: *Analysis of Observed Chaotic Data*. Springer Science & Business Media, Berlin (2012)
- Hendi, S.F., et al.: Characterizing EOG signal from the Chaotic Point of View. In: *3rd Kuala Lumpur International Conference on Biomedical Engineering 2006*. Springer, Berlin, Heidelberg (2007)
- Kennel, M.B., Brown, R., Abarbanel, H.D.I.: Determining embedding dimension for phase-space reconstruction using a geometrical construction. *Phys. Rev. A* **45**(6), 3403 (1992)
- Rhodes, Carl, Morari, Manfred: The false nearest neighbors algorithm: An overview. *Comput. Chem. Eng.* **21**, S1149–S1154 (1997)

Feature Extraction Techniques for Automatic Detection of Some Specific Cardiovascular Diseases Using ECG: A Review and Evaluation Study

Trieu Hai-Nguyen Le, Triet Minh Le, Trung Q. Le, and Vo Van Toi

Abstract

Cardiovascular diseases (CVDs) are the leading cause of death globally. For an effective treatment of CVDs, automatic CVDs detection based on Electrocardiograph (ECG) monitoring is highly desirable. One major challenge in ECG classification is feature learning. This paper reviews developed techniques for feature extraction and compared their performances in Atrial Fibrillation (AF), Myocardial Infarction (MI) and Pericarditis detection. Feature extraction methods in the literature reviews can be divided into mainly four categories: linear feature, nonlinear feature, wavelet transform, deep learning. Three studies were implemented using database from PhysioNet to evaluate the effectiveness of different feature extraction techniques. The AF detection algorithm use morphology features, statistic features, spectral feature, and wavelet entropy, presented a sensitivity of 96%, specificity of 93% and accuracy of 94.1%. In the case of Pericarditis and MI classification, information theory-based features including subband energy, permutation entropy, and approximate entropy are the most noteworthy features. The study of detecting MI using machine learning based model of Convolutional Neural Network showed a sensitivity of 92.04% which yield the most promising results.

Keywords

Cardiovascular diseases detection • Feature extraction techniques • ECG • Linear feature • Nonlinear feature • Wavelet transform • Deep learning

T. H.-N. Le · T. M. Le · V. Van Toi
Department of Biomedical Engineering, International University
—Vietnam National University, Ho Chi Minh City, Vietnam

T. Q. Le (✉)
North Dakota State University, Fargo, ND, USA
e-mail: trung.q.le@ndsu.edu

1 Introduction

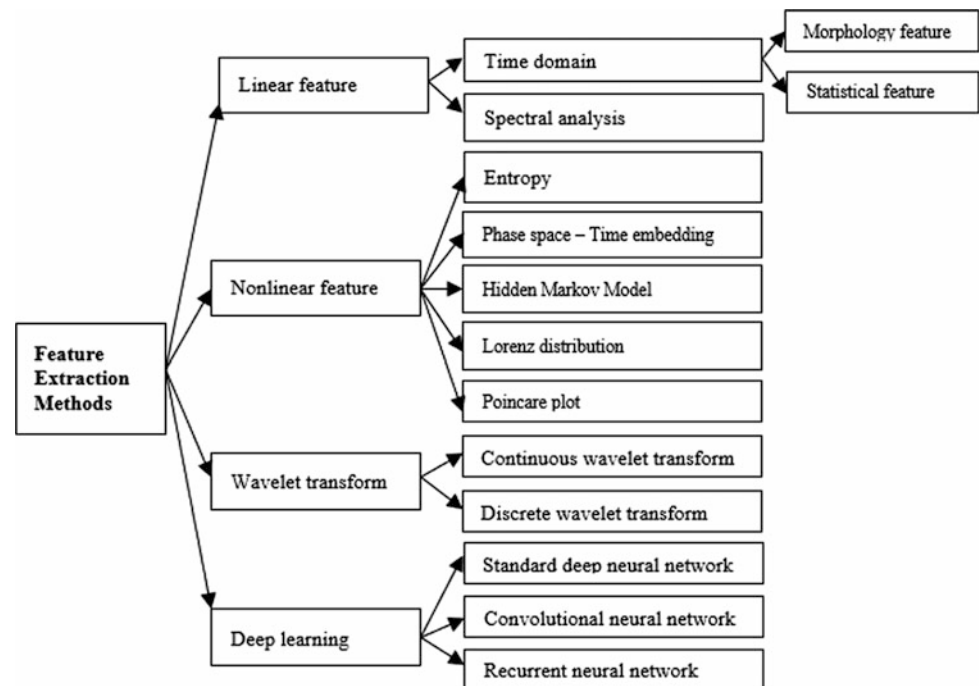
Cardiovascular diseases (CVDs) are the principal cause of death globally. The analysis of the ECG has been extensively used for diagnosing many cardiac disorders. ECG is a realistic record of the magnitude and direction of the electrical activity generated by depolarization and repolarization of the atria and ventricles. One cardiac cycle in ECG signal typically comprises the P wave, QRS complex and T wave. In order to accurately characterize ECG signals, time series feature extraction is especially important to locate the characteristic of cardiac abnormalities. The improvement of precise and rapid methods for automatic ECG feature extraction is extremely necessary, particularly for the examination of long recordings. In this work, the advantages and limitations of different methods of feature extraction are studied.

2 Literature Review

In this study, we investigate four main techniques of feature extraction, including Linear feature, Nonlinear feature, Wavelet transform and Deep Learning. Figure 1 is the summary of the methodologies which we are going to review thoroughly to reveal these characteristics and applications.

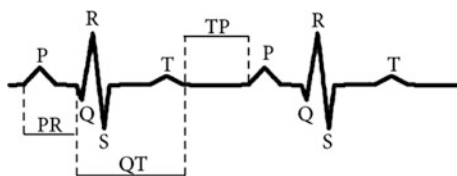
2.1 Linear Feature

ECG feature extraction system provides significant features for classification. Most of the previously proposed method based on linear feature method. It includes time domain and frequency domain features.

Fig. 1 Methodologies summary

Time domain feature

Time-domain is the analysis of mathematical functions, multidisciplinary signals, and data, respect to time. ECG components such as P-wave, QRS complex, ST-segment, and RR intervals are analyzed to extract fundamental features of CVDs, including amplitude, duration and the number of waves, etc. They were considered in disease related to atrial fibrillation (AF), premature atrial contraction [1–4]. PR segment deviation analysis is an effective tool in differential diagnosis of myopericarditis and ST-Elevation MI for patients presenting with ST elevation as well as arrhythmia detection [1, 5]. In addition, duration of QRS complex, QT interval and TP down-sloping segment (Spodick's sign) in ECG signal with ST-segment elevation can be used to detect acute pericarditis [6, 7]. T wave amplitude and ST deviation are significant features of myocardial infarction [8–11]. Q, R, and S amplitudes and the Q and S duration in V2–V4 were used for diagnosing anterior infarct [12]. RR intervals or heart rate variability

**Fig. 2** Morphology feature of ECG

(HRV) is the salient feature in arrhythmia detection, especially AF and MI diagnosis [13, 14].

Other RR interval statistical features as mean, max, and standard deviation are proved giving expected performance [1, 15, 16]. Yaghouby et al. combined statistical and geometrical features from a histogram of RR intervals of HRV data as well as improved forward floating selection analysis to increase performance of AF detection [17]. In [18], the coefficients of variation of the RR and Δ RR intervals computed from the standard density histograms are used to detect AF.

Frequency domain feature

Another approach of feature extraction is a spectral-domain perspective, the transformation of ECG signal from time domain to frequency domain. After spectrum frequency is found by applying fast Fourier transform, a set of following spectral features should be used for CVDs classification: main frequency peak, spectral component with maximal power content, spectral content below the main peak, spectral concentration in the band of the peak, first-order moment, normalized first order spectral moment, second order moment, main peak amplitude to first harmonic amplitude ratio. These above features have shown their effectiveness in arrhythmia detection [18–21]. In [22], the number of harmonics (peaks) in this certain spectrum was counted to differentiate between atrial fibrillation and atrial flutter. (Fig. 2).

2.2 Nonlinear Feature

The linear feature is unable to take into account the nonlinear dynamics of the ECG signal. On the other hand, the nonlinear features try to encompass and quantify the complexity of ECG signal or heart rate variability (HRV).

Entropy, defined as a measure of the amount of information within a random process, has been playing a key role in biomedical and image analysis during the last few years. Indeed, entropy-based parameters have recently provided a significant ability to reveal useful information from diseases. Shannon entropy (ShEn) provides a quantitative measure of uncertainty for a random variable which is lower in normal sinus rhythm than AF [23, 24]. Approximate entropy quantified the amount of regularity of data while permutation entropy estimates the signal complexity.

Phase space—Time embedding is the method reconstructing the R-R intervals and investigating the structure of the reconstructed attractor to diagnose cardiac arrhythmias [25, 26].

Hidden Markov Model is a statistical model for predicting the state of a state machine based on observations. The RR sequence was modeled as a three-state Markov Process, the probabilistic distribution and transition between states for both normal rhythms and AF episodes are studied [3, 16, 27].

Lorenz distribution is used for AF and tachycardia detection [28]. The Lorenz plot is a scatter plot of RR(i + 1) versus RR(i), encodes the uncorrelated nature of RR intervals in the direction of change of three consecutive RR intervals.

Poincare plot is applied to exploit the number of clusters, mean stepping increment of inter-beat intervals, and dispersion of the points around a diagonal line in the plot [29] to classify non-AF and AF episodes.

2.3 Wavelet Transform

Most of the time, the desired ECG signals are either corrupted or embedded in noises; therefore proper classification is not always easy. Wavelet theory holds the property of multi-resolution analysis to give both time and frequency domain information of a signal. When analyzing signal of a non-stationary nature, it is often beneficial to be able to acquire both the time and frequency domains of a signal.

Continuous Wavelet Transform (CWT)

CWT equation is given by:

$$C(a, b) = \frac{1}{\sqrt{|a|}} \int_{-\infty}^{\infty} x(t) * \Phi\left(\frac{t-b}{a}\right)$$

where Φ is mother wavelet, a is scale parameter, and b is translation parameter. In [30], the use of wavelet coherence (WTC) differentiates the normal and AF ECG signal. They calculated the WTC of two ECG signals (normal template and analyzed signal) of 10 s duration using the ‘db4’ mother wavelet for integer scales from 1 to 100.

Discrete Wavelet Transform (DWT)

DWT of a signal is calculated by passing it through a series of filters (Fig. 3). Filters of different cutoff frequencies are to analyze the signal at different scales. In the wavelet domain, entropy at various decomposition levels of WT of ECG signal could be indicative of signal properties. The energy and entropy at each level have shown their effectiveness in myocardial infarction and arrhythmias analysis [31, 32]. Sarma et al. proposed an ECG arrhythmia classification scheme based on the wavelet subband energy features [33]. After approximate and detailed coefficients are obtained, subband energy (SE) is calculated. SE is given by $\sum_{n=1}^N |C_n|^2$ where C means coefficients, n represents sub-band, and N is the total number of coefficients in the sub-band. In [34], two features are extracted for each coefficient: peak-to-average power ratio and log-energy entropy.

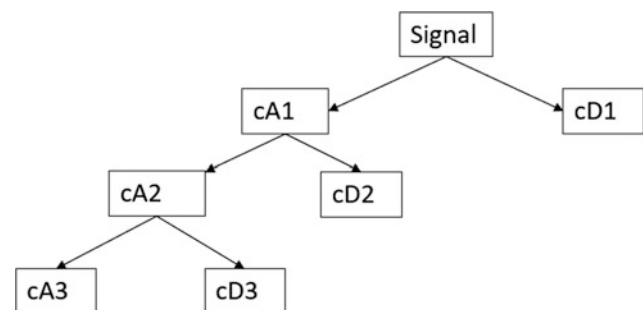


Fig. 3 DWT 3 level

2.4 Deep Learning

Nowadays, deep learning has acquired significant interest in multidimensional signal processing due to their robust capabilities and functionalities for different applications, such as object detection and classification in computer vision, natural language processing, and time-series data analysis [35]. Deep learning's sophisticated technology and self-learning capabilities result in higher accuracy and faster processing. Deep neural networks do not require manual feature engineering; rather, they learn on their own by processing and learning the high-level and nonlinear features from raw data. There are three common types of deep learning in ECG analysis: standard deep neural network, convolutional neural network, recurrent neural network.

Standard Deep Neural Network

A deep neural network is an artificial neural network with multiple hidden layers between the input and output layers. Jun et al. extracted six features from raw data and used them as input of premature ventricular contraction (PVC) beat classification phase. They built a deep neural network with six nodes of input layer, multiple hidden layers, and two nodes of output layer. This model classifies normal and PVC beats with the high performance of 99.41 and 96.08% for accuracy, and sensitivity, respectively [36].

Convolutional Neural Network (CNN)

Adoption of CNN as a feature learning mechanism, it is shown to be capable of generating robust features without requiring the domain knowledge and a feature selection algorithm, as opposed to conventional feature extraction schemes. CNNs are deep artificial neural networks that are used primarily to classify images and object recognition. They consist of three main layers: convolutional layer, max-pooling layer, and fully-connected layer. The short-term Fourier transform (STFT) and stationary wavelet transform (SWT) were used to analyze ECG segments to

obtain two-dimensional (2-D) matrix input suitable for deep CNNs [37]. Tan et al. propose the implementation of long short-term memory network with CNN to automatically diagnose Coronary Artery Diseases ECG signals accurately [38]. Limam et al. implemented atrial fibrillation detection using convolutional recurrent neural network (CRNN) [39].

3 Case Studies

3.1 Automatic Atrial Fibrillation Detection Using Linear Features

Atrial Fibrillation (AF) is the most common disease of arrhythmia, and its abnormally irregular heart rate indication allows us to detect at an early stage. Table 1 shows nine features that are used for analyzing RR series variability and atrial activity in this work. First-hour ECG of six patients with sampling frequency 250 Hz from MIT-BIH Atrial Fibrillation Database obtained from PhysioNet, were used [40]. There are 1200 30-second windows (observations) for training and testing with 752 normal and 521 AF episodes. Through R-R variability, AF can be detected by comparing with Normal Sinus Rhythm. However, to improve the diagnostic accuracy, it is necessary to separate the electrical activity of the atria and then analyzing both characteristics with 30 s sliding window. First, raw data is denoised by 4-order Butterworth highpass filter with cutoff frequency of 0.5 Hz. Then discrete wavelet transform was used to extract cD2 so that signal only contains QRS complex (high-frequency component). R peak location was found by applying the adaptive threshold ($0.3 \times \text{maximum of R peak's amplitude}$). After that, four features which measure RR series variability is extracted for training classification model: mean, minimum, maximum of RR intervals and wavelet entropy. In addition, a QRST cancellation method is used to extract atrial activity (AA). The R-peak location is calculated by Pan-Tompkin algorithm and a time window where the atrial activity can be localized is defined (from $R + 0.75 \times RR$ to $R + 0.95 \times RR$ with R is R peaks location)

Table 1 Extracted features for AF detection

RR variability	Atrial activity
Wavelet entropy	Spectral analysis
Mean RR	Standard deviation
Min RR	P-peak deviation
Max RR	Area

[41]. Then area, peak value, standard deviation and spectral analysis of AA are calculated as features for detection. Finally, Support Vector Machines with Gaussian kernel function is used as a classifier. The result shows the effective of extracted feature to detect AF episodes with the specificity and sensitivity are 96, 93% respectively.

3.2 Differentiate Myocardial Infarction and Pericarditis Using Nonlinear Features

The most confusing element in the diagnosis of acute pericarditis is ECG misinterpretation, especially as acute myocardial infarction. Abnormal MI only occur in few leads, while pericarditis makes ST elevation in all leads. 142 ECG data are collected from PhysioNet—PTB Diagnostic ECG Database [40]. After beat segmentation, 5000 normal beats, 8000 MI beats and 330 pericarditis beats per lead are used for training classifier. First, baseline-wandering and high-frequency noise were removed by using wavelet transform 11 levels. Then, R-peaks are detected by Pan-Tompkin algorithm [41]. In beat segmentation step, 250 samples to the left and 400 samples to the right of R peak was considered one beat due to sampling frequency is 1000. Discrete wavelet transform four levels with db6 mother wavelet is applied for each beat to obtain totally eight subband coefficients. The following features are extracted: Approximate entropy (ApEn), Shannon Entropy (ShEn), Wavelet entropy (WaEn), Signal energy (SiEn), Fuzzy entropy (FuEn), Permutation entropy (PeEn) for each DWT coefficient. Finally, 48 features are used for feature selection step to validate their significance. There are eight class's features (normal, 6 types of MI and pericarditis), ANOVA test is used in this work. The one-way analysis of variance (ANOVA) is used to determine whether there are any statistically significant differences between the means of eight independent (unrelated) groups. F is large when the difference in means is large comparing to the variability of the data.

From the results in Table 2, features which are extracted from low-frequency subband, are seemly higher rank due to the information of heart electrical activity it contains. In

addition, subband energy, permutation entropy, and approximate entropy are the most significant features. There are differences in energy distribution and complexities between normal, MI and pericarditis ECG signal.

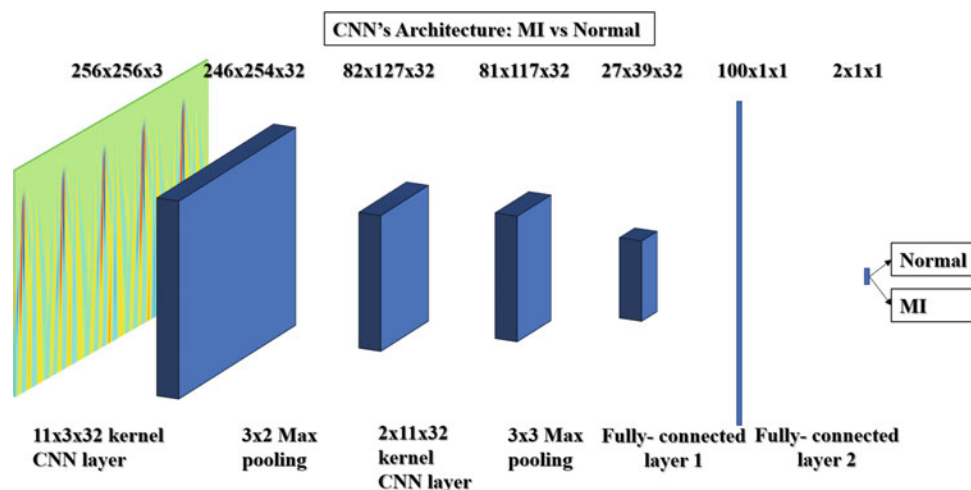
3.3 Detecting Myocardial Infarction by Continuous Wavelet Transform and Convolutional Neural Networks

The existing MI detection algorithms analyze ST deviation, T peak. However, if relevant peaks are missed or detected by mistake, their performance may significantly decrease. Using hand-crafted and fixed features may not represent the key features of the signal. In this study, convolutional neural network (CNN) is used to detect myocardial infarction without the detection of ST deviation or T peak and the extraction of handcrafted manual features. The ECG lead V6 of 147 subjects (48 normal and 99 MI) of PTB Diagnostic ECG database were collected from PhysioNet [40]. Forty normal and eighty-eight MI cases are used for training and the rest of subjects are used for validation. The raw ECG signal is divided every five seconds and normalized to the normal distribution. The data segment is passed to continuous wavelet transform with bior1.5 mother wavelet and scale from 1 to 256. The transformation enables an ECG signal (1-D) to be applied to CNN which process two-dimensional (2-D) data. Then 2-D matrix data is mapped to RGB images with size of 256×256 as input of CNN. Figure 4 shows the architecture of CNN which consists of two convolutional layers, two max-pooling layers, two ReLU layers, two fully-connected layers, and a softmax layer. The learning rate is set to 0.0001, batch size of each iteration is 32 observations and network is built by training 10 epochs. Adam optimizer—a method for stochastic optimization—is used to update weights of kernel filter. The sensitivity and specificity of the proposed method are 92.04 and 82.85% respectively. The results show that learning of convolutional layer is a promising extraction technique. In the future, hyperparameters will be tuned to improve the performance of the algorithm.

Table 2 Extracted features' significance ranking

	SiEn(A4)	SiEn(A1)	SiEn(A2)	SiEn(A3)	PeEn(A3)	ApEn(D4)	ApEn(D3)
F-value	928.6740	928.5141	928.5136	928.5092	809.4399	722.3456	661.8763

Fig. 4 CNN's architecture: MI detection



4 Comparison Between Methodologies

The following table is the detailed comparison between methodologies to show the advantages and weaknesses of each method which would give the readers more information to choose their methods they should apply.

		Advantages	Disadvantages
Linear feature	Time-domain	<ul style="list-style-type: none"> • Quite simple and evolvable • Real-time ECG monitoring due to low computational complexity 	<ul style="list-style-type: none"> • Performance depends on peaks detection, significantly decrease when noise is present • Not specific and generalized
	Frequency-domain	<ul style="list-style-type: none"> • Capable of analyzing atrial activity source 	<ul style="list-style-type: none"> • Need to combine with other features to improve accuracy • Performance is affected by noise • Frequency band of ventricle activity overlaps atrial activity
Nonlinear feature		<ul style="list-style-type: none"> • More suitable and stable for ECG analysis due to its nonstationary characteristic • Capture nonlinear behavior of ECG signal 	<ul style="list-style-type: none"> • High computation • Need of feature selection
Wavelet	Continuous (CWT)	<ul style="list-style-type: none"> • Capture both time and frequency information • Effectiveness in noise condition 	<ul style="list-style-type: none"> • Loss of information when transformation
	Discrete (DWT)		
Deep learning		<ul style="list-style-type: none"> • Machine-crafted features • No need of predefined formula to calculate features and choose appropriate features • More generalized than conventional features 	<ul style="list-style-type: none"> • Require large of training data • High computational training

5 Conclusion

Feature extraction extensively affects classification performance. Therefore, we need to find appropriate features for different CVDs detection. In this paper, we have reviewed the recent feature extraction techniques in ECG. Time domain, frequency domain, wavelet domain of signal is analyzed to exploit key features for classification. Deep learning can extract features without predefined formula (machine-crafted features). The evaluated performance of different features in cardiovascular diseases detection is provided. Linear features are fast and straightforward computation; however, missing information in the presence of noise. Nonlinear features are promising features due to nonlinear and nonstationary characteristics of ECG signal. Deep learning is the most modernized technique for feature extraction. It does not require manual feature engineering as it could learn on their own by processing and learning the high-level and nonlinear features from raw data. However, it requires a much larger amount of data for training compared to conventional methods.

Conflict of Interest The authors declare that they have no conflict of interest.

References

1. Gutiérrez-Gnechchi, J.A., et al.: DSP-based arrhythmia classification using wavelet transform and probabilistic neural network. *Biomed. Signal Process. Control* **32**, 44–56 (2017)
2. Pourbabaee, B., Lucas, C.: Automatic detection and prediction of paroxysmal atrial fibrillation based on analyzing ecg signal feature classification methods. In: 2008 Cairo International Biomedical Engineering Conference, CIBEC 2008. IEEE (2008)

3. Couceiro, R., et al.: Detection of atrial fibrillation using model-based ECG analysis. In: 2008 19th International Conference on Pattern Recognition, ICPR 2008. IEEE, 2008
4. Clavier, L., et al.: Automatic P-wave analysis of patients prone to atrial fibrillation. *Med. Biol. Eng. Comput.* **40**(1), 63–71 (2002)
5. Porela, P., et al.: PR depression is useful in the differential diagnosis of myopericarditis and ST elevation myocardial infarction. *Ann. Noninvasive Electrocardiol.* **17**(2), 141–145 (2012)
6. Rossello, X., et al.: New electrocardiographic criteria to differentiate acute pericarditis and myocardial infarction. *Am. J. Med.* **127**(3), 233–239 (2014)
7. Makaryus, J.N., Makaryus, A.N., Boal, B.: Spodick's sign. *Am. J. Med.* **121**(8), 693–694 (2008)
8. Arif, M., Malagore, I.A., Afsar, F.A.: Detection and localization of myocardial infarction using k-nearest neighbor classifier. *J. Med. Syst.* **36**(1), 279–289 (2012)
9. Lu, H., K. Ong, Chia, P.: An automated ECG classification system based on a neuro-fuzzy system. In: *Computers in Cardiology 2000*. IEEE (2000)
10. Devika, M., et al.: Myocardial infarction detection using hybrid BSS method. In: *International Conference on Communication Systems and Networks (ComNet)*. IEEE (2016)
11. Sun, L., et al.: ECG analysis using multiple instance learning for myocardial infarction detection. *IEEE Trans. Biomed. Eng.* **59**(12), 3348–3356 (2012)
12. Reddy, M., et al.: Neural network versus electrocardiographer and conventional computer criteria in diagnosing anterior infarct from the ECG. In: *Proceedings of Computers in Cardiology*. IEEE (1992)
13. Ghodrati, A., Murray, B., Marinello, S.: RR interval analysis for detection of atrial fibrillation in ECG monitors. In: 2008 30th Annual International Conference of the IEEE Engineering in Medicine and Biology Society, EMBS 2008. IEEE (2008)
14. Le, T.Q., et al.: Topology and random-walk network representation of cardiac dynamics for localization of myocardial infarction. *IEEE Trans. Biomed. Eng.* **2325–2331** (2013)
15. Logan, B., Healey, J.: Robust detection of atrial fibrillation for a long term telemonitoring system. In: *Computers in Cardiology*. IEEE (2005)
16. Young, B., Brodnick, D., Spaulding, R.: A comparative study of a hidden Markov model detector for atrial fibrillation. In: *Proceedings of the 1999 IEEE Signal Processing Society Workshop Neural Networks for Signal Processing IX*. IEEE (1999)
17. Yaghouby, F., et al.: Robust genetic programming-based detection of atrial fibrillation using RR intervals. *Expert Syst.* **29**(2), 183–199 (2012)
18. Tateno, K., Glass, L.: Automatic detection of atrial fibrillation using the coefficient of variation and density histograms of RR and Δ RR intervals. *Med. Biol. Eng. Comput.* **39**(6), 664–671 (2001)
19. Millet-Roig, J., et al.: Surface-ECG atrial activity extraction via blind source separation: spectral validation. In: *Computers in Cardiology*. IEEE (2002)
20. Nolle, F., et al.: Evaluation of a frequency-domain algorithm to detect ventricular fibrillation in the surface electrocardiogram. In: *Proceedings Computers in Cardiology*. IEEE (1988)
21. Rieta, J., et al.: Atrial fibrillation, atrial flutter and normal sinus rhythm discrimination by means of blind source separation and spectral parameters extraction. In *Computers in Cardiology*. IEEE (2002)
22. Mrochek, A.G., et al.: Identification and spectrum analysis of the atrial electrical activity for differential diagnostics of the atrial fibrillation. *Int. J. Biomed.* (2011)
23. Zhou, X., et al.: Automatic online detection of atrial fibrillation based on symbolic dynamics and Shannon entropy. *Biomed. Eng. Online* **13**(1), 18 (2014)
24. Dash, S., et al.: Automatic real time detection of atrial fibrillation. *Ann. Biomed. Eng.* **37**(9), 1701–1709 (2009)
25. Hong-wei, L., et al.: A probability density function method for detecting atrial fibrillation using R-R intervals. *Med. Eng. Phys.* **31**(1), 116–123 (2009)
26. Lahiri, T., et al.: Analysis of ECG signal by chaos principle to help automatic diagnosis of myocardial infarction (2009)
27. Artis, S.G., Mark, R., Moody, G.: Detection of atrial fibrillation using artificial neural networks. In: *Proceedings Computers in Cardiology*. IEEE (1991)
28. Sarkar, S., et al.: A detector for a chronic implantable atrial tachyarrhythmia monitor. *IEEE Trans. Biomed. Eng.* **55**(3), 1219–1224 (2008)
29. Park, J., Lee, S., Jeon, M.: Atrial fibrillation detection by heart rate variability in Poincare plot. *Biomed. Eng. Online* **8**(1), 38 (2009)
30. Padmavathi, K., Ramakrishna, K.S.: Detection of atrial fibrillation using continuous wavelet transform and wavelet coherence. *Int. J. Syst. Control Commun.* **6**(4), 292–304 (2015)
31. Kalra, M., et al.: Continuous wavelet transform for the analysis of arrhythmia. *Int. J. Latest Res. Sci. Tech.* **4**(3), 80–84 (2015)
32. Jayachandran, E.: Analysis of myocardial infarction using discrete wavelet transform. *J. Med. Syst.* **34**(6), 985–992 (2010)
33. Sarma, P., Nirmala, S., Sarma, K.K.: ECG classification using wavelet subband energy based features. In: 2014 International Conference on Signal Processing and Integrated Networks (SPIN). IEEE (2014)
34. Asgari, S., et al.: Automatic detection of atrial fibrillation using stationary wavelet transform and support vector machine. In: *Computers in Biology and Medicine*, vol. 60, pp. 132–142 (2015)
35. LeCun, Y., Bengio, Y., Hinton, G.: Deep learning. *Nature* **521**(7553), 436 (2015)
36. Jun, T.J., et al.: Premature ventricular contraction beat detection with deep neural networks. In: 2016 15th IEEE International Conference on Machine Learning and Applications (ICMLA). IEEE (2016)
37. Xia, Y., et al.: Detecting atrial fibrillation by deep convolutional neural networks. *Comput. Biol. Med.* **93**, 84–92 (2018)
38. Tan, J.H., et al.: Application of stacked convolutional and long short-term memory network for accurate identification of CAD ECG signals. In: *Computers in Biology and Medicine* (2018)
39. Limam, M., Precioso, F.: Atrial fibrillation detection and ECG classification based on convolutional recurrent neural network. *Computing* **44**, 1 (2017)
40. Goldberger, A.L., et al.: Physiobank, physiotoolkit, and physionet. *Circulation* **101**(23), e215–e220 (2000)
41. Pan, J., Tompkins, W.J.: A real-time QRS detection algorithm. *IEEE Trans. Biomed. Eng.* **3**, 230–236 (1985)

Feature Extraction and Electrophysiological Modeling in Personalized Deep Brain Structure Using Electroencephalography Signal

Linh Luu, Phong Pham, and Trung Q. Le

Abstract

The knowledge attained from deep brain structure allows for the establishment of novel computational-based methods for yielding insights into pathophysiology and electrophysiology of neurological and degenerative brain disorders for aiding medical treatment and diagnosis, namely Epilepsy, Parkinson's disease, and Alzheimer's disease. To support those purposes, Electroencephalography is a readily accessible, noninvasive and relatively inexpensive monitoring method to serve diagnostic purposes, analytical tools for brain investigation, and inherently features an excellent temporal resolution for recording behaviors of brain's spontaneous electrical activities over a period of time which follow a non-stationary dynamic process. In fact, the representation of the system also differs across individuals due to the identification of person-specific parameters. This paper proposes a scheme that extracts features characterizing the personalized spatial-temporal structure contained in EEG associated with Parkinson's disease and Epilepsy, then build an electrophysiological model using only EEG signal for the individual to enhance accuracy for detection of these diseases. The primary result of classifying some non-linear features (Approximate entropy, Sample entropy, Fractal Dimension, and Hurst exponent) between normal and epilepsy segments showed high performance in classifiers (Decision tree: $80.5 \pm 1.24\%$, K-nearest neighbor: $81.6 \pm 1.52\%$, Support vector machine: $82.6 \pm 0.34\%$).

Keywords

EEG • Non-linear features • Electrophysiological model • Deep brain activity

1 Introduction

Electroencephalography (EEG) is a non-invasive technique that records the electrical field produced by the neural electrical activity in the brain. EEG has good temporal resolution and high test-retest which help recognizing some fundamental hallmark of cortical functions and might provide some important biomarkers for brain disorders such as Epilepsy, Alzheimer's disease, major depressive disorder and so on [1, 2].

This study focus on two common neurological disorders proceeding from deep brain structure, namely Parkinson's Disease (PD) and Epilepsy. PD is a long term disorder of the central nervous system that mainly affects the motor system. In normal human, the neurons from the Substantia Nirga in the basal nuclei of basal ganglia in midbrain will produce dopamine (a neurotransmitter) to corpus striatum (the region in brain controls muscle movement). In PD's patient, that neurons are reduced, lead to the missing of dopamine. Consequences are performance of many symptoms (Tremors, Muscle rigidity, Brandykinesia, Postural instability...), and their severity will increase ascending in 5 stages. To diagnosis PD, doctors usually rely on a physical examination, symptoms and the patient's family history with the help of some methods that are blood test, imaging test (EEG, CT or MRI), PET. Main treatment options are pharmacology (Levodopa, Anticholinergic...), surgery (implanted Deep Brain Stimulation) [3]. In PD, EEG was researched to use in diagnosing and optimizing effectiveness and minimizing complications of PD treatment (surgery). However, EEG

Linh Luu and Phong Pham—Contributed equally to this work.

L. Luu (✉) · P. Pham · T. Q. Le
Biomedical Engineering Department, International University—
Vietnam National University, Ho Chi Minh City, Vietnam
e-mail: luuhoanglinh.0603@gmail.com

contains no objective diagnostic markers and just provides some hallmarks associated with dopamine loss such as rhythm, changes in firing rates, burst activity, neuronal oscillation, and synchrony which may present early signs of cortical dysfunction [4].

In term of Epilepsy, a chronic disorder, the hallmark of which is recurrent, unprovoked seizure. Many people with epilepsy have more than one type of seizure and may have other symptoms of neurological problems as well. Those decrease patient's quality of life, limit their activity from joining traffic or doing recreation. The causes that make Epilepsy are unidentifiable, but there are some factors such as genetic influence and brain conditions (stroke, tumor...) which could change some neurons become "burster cells" then cause epileptic seizure. Unlike PD, EEG is the most common test in diagnosing Epilepsy, but it is not the most useful test in confirming a diagnosis of Epilepsy because an abnormal EEG result do not always associate with an Epilepsy. Doctor often combines EEG with video records to have important clues for determine either Epilepsy or not and what type of Epilepsy is. In addition, although EEG remains critical in seizure localization, it is often inconclusive [5].

The main purpose of our study is to investigate a method to enhance the efficiency of EEG signal processing not only in detecting PD and Epilepsy (what it is), but also localize the source having abnormal activity in brain (where it comes from). To achieve this goal, we apply some nonlinear feature extraction method such as Approximate entropy, Sample entropy, Fractal Dimension, and Hurst exponent to quantify nonlinear information, and using them to train machine learning models. Furthermore, the electrophysiological model is also a method is considered to extend dynamic property in EEG, and it is expected to provide a detailed picture about brain structure in both spatial and temporal resolution.

2 Background

Machine learning is a powerful tool using statistical technique to give computer systems the ability to learn with data, without being explicitly programed. Machine learning task was applied to solve the classification problem in this study that is supervised learning. From training set which consists of example pairs (data-label), it can infer a function generalizing the training data to predict outcome of new input [6]. There are many machine learning algorithms applied to the problem such as Support Vector Machine, Decision Tree, K-Nearest Neighbor.

3 Method

3.1 Prepared Data

The EEG dataset used in this work was available at the University of Bonn [7] which contain three categories: normal segments, interictal segments, and ictal segments. For each categories, 100 segments were taken. Each EEG segments were recorded using 128-channel amplifier system, digitized with a sampling rate of 173.61 Hz and 12-bit A/D resolution, and filtered using a 0.53–40 Hz (12 dB/octave) band pass filter. Figure 1 illustrates three types of segments. We select 5 s of each segment for feature extraction and classification.

3.2 Feature Extraction

Entropy

Approximate entropy (ApEn)

ApEn describes the predictability of a time series data [8]. In other words, these entropy features represent the possibility of the next values in time series would be in a specific range. In term of calculation, consider a time series $u(1), u(2), \dots, u(N)$ with N is length of time series, an integer m is the length of sequences to be compared, and a positive real number r is the tolerance for accepting matches. A sequence of vectors $\mathbf{x}_m(i)$ with $1 \leq i \leq N - m + 1$ are formed where $\mathbf{x}_m(i) = \{u(i), u(i+1), \dots, u(i+m-1)\}$. The distance between two vectors $d[\mathbf{x}_m(i), \mathbf{x}_m(j)]$ with $1 \leq j \leq N - m + 1$ is the maximum difference between their corresponding scalar components. Let A_i is the number such that $d[\mathbf{x}_m(i), \mathbf{x}_m(j)] \leq r$ and B_i is the number such that $d[\mathbf{x}_{m+1}(i), \mathbf{x}_{m+1}(j)] \leq r$ (vector $\mathbf{x}_{m+1}(i)$ is created similarly with $\mathbf{x}_m(i)$ by replacing m with $m+1$), the probability of any vector $\mathbf{x}_m(j)$ is within r of $\mathbf{x}_m(i)$ and the probability of any vector $\mathbf{x}_{m+1}(j)$ is within r of $\mathbf{x}_{m+1}(i)$ are given by

$$C_i^m(r) = \frac{A_i}{N - m + 1} \quad (1)$$

$$C_i^{m+1}(r) = \frac{B_i}{N - m} \quad (2)$$

ApEn is given by

$$\text{ApEn} = \frac{1}{N - m + 1} \sum_{i=1}^{N-m+1} \log C_i^m(r) - \frac{1}{N - m} \sum_{i=1}^{N-m} \log C_i^{m+1}(r) \quad (3)$$

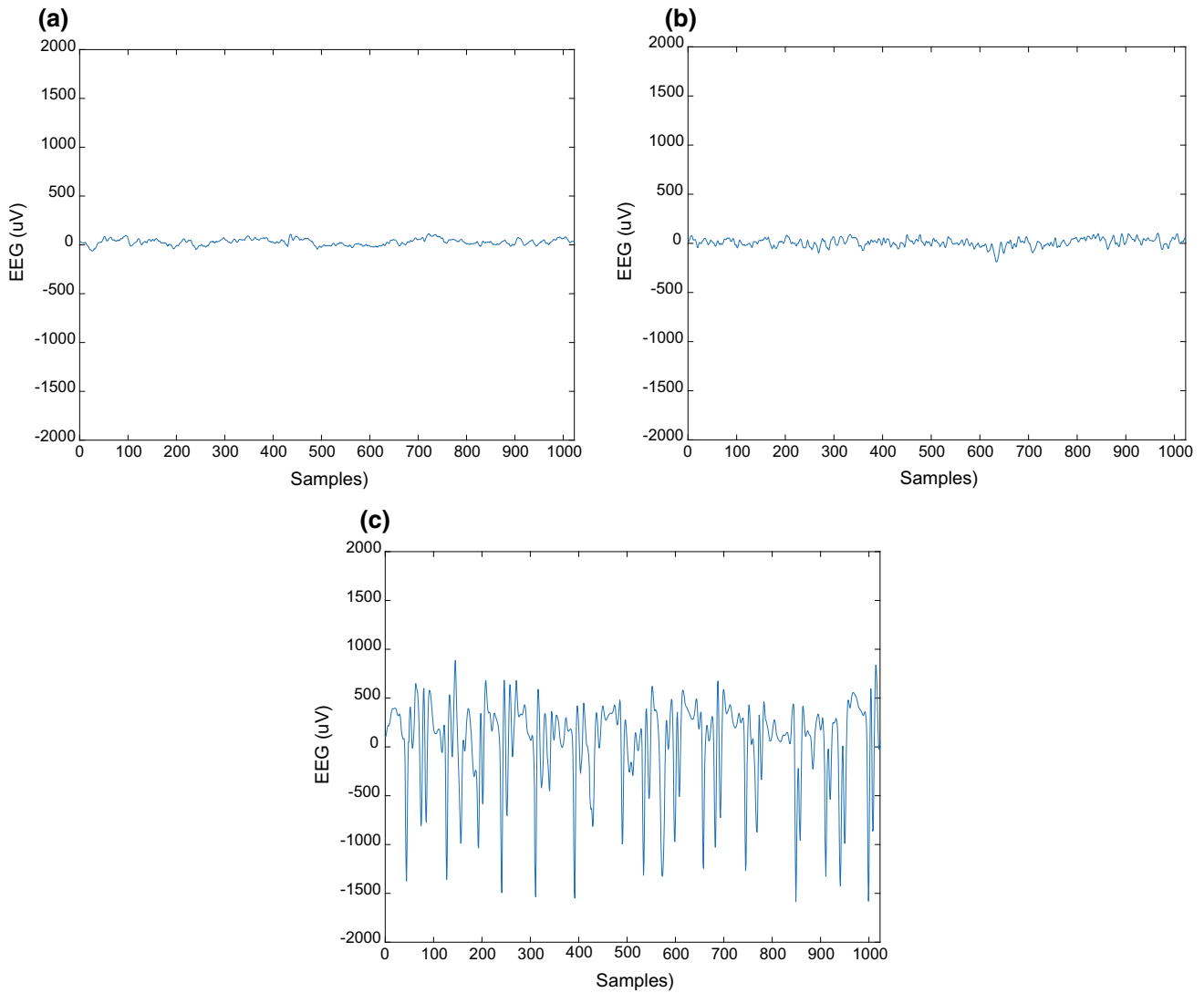


Fig. 1 EEG signal **a** normal, **b** interictal, and **c** ictal

Sample Entropy (SampEn)

SampEn reduces the bias by not considering self-matches in calculation of ApEn [8]. Given a time series $u(1), u(2), \dots, u(N)$, form two sequence of vector $\mathbf{x}_m(i)' = [u(i), u(i + 1), \dots, u(i + m - 1)]$ and $\mathbf{x}_{m+1}(i)' = [u(i), u(i + 1), \dots, u(i + m)]$ with $1 \leq i \leq N - m$. Let A'_i is the number such that $d[\mathbf{x}_m(i)', \mathbf{x}_m(j)'] \leq r$ and B'_i is the number such that $d[\mathbf{x}_{m+1}(i)', \mathbf{x}_{m+1}(j)'] \leq r$, the probability of any vector $\mathbf{x}_m(j)$ is within r of $\mathbf{x}_m(i)$ and the probability of any vector $\mathbf{x}_{m+1}(j)$ is within r of $\mathbf{x}_{m+1}(i)$ are given by

$$C_i^m(r)' = \frac{A'_i}{N - m + 1} \tag{4}$$

$$C_i^{m+1}(r)' = \frac{B'_i}{N - m + 1} \tag{5}$$

SampEn is given by

$$\text{SampEn} = \ln \frac{\sum_{i=1}^{N-m} C_i^m(r)'}{\sum_{i=1}^{N-m} C_i^{m+1}(r)'} \tag{6}$$

Higuchi Fractal Dimension (FD)

FD is a powerful tool for transient detection and it can be used to measure the dimensional complexity of biological signals [7]. In term of calculation, given a time series

$u(1), u(2), \dots, u(N)$, decompose original time series into each k , an integer, time series given by

$$u(k, m) = \left\{ u(m), u(m+k), u(m+2k), \dots, u\left(m + \text{int}\left(\frac{N-m}{k}\right)k\right) \right\} \quad (7)$$

where $m = 1, 2, \dots, k$ and $\text{int}()$ is an integer function. The length of each time series is computed by

$$L(m, k) = k^{-1} \left(\sum_{i=1}^{\frac{N-m}{k}} |u(m+ik) - u(m+(i-1)k)| \right) \frac{N-1}{\left(\frac{N-m}{k}\right)_k} \quad (8)$$

and the average length for each $L(k)$ is $L(k) = \frac{\sum_{m=1}^k L(m, k)}{k}$. FD is given by

$$\text{FD} = \log(L(k)) / \log\left(\frac{1}{k}\right) \quad (9)$$

Hurst Exponent (H)

Hurst exponent is a measure of the degree of long-range dependence in a time-series. The high value indicate smooth trend while the low value show the roughness [7]. The value of Hurst exponent vary between 0 and 1. The formula is

$$H = \frac{\log\left(\frac{R}{S}\right)}{\log(N)} \quad (10)$$

where R is difference between maximum and minimum deviation from the mean of the time series, S is standard deviation and N is length of that time series.

3.3 Electroencephalography Model

Despite nonlinear features and phase space can capture some dynamic properties of brain system through EEG, we want to have further steps in investigating brain structure due to limitation in low spatial resolution of EEG [9]. Recently, Electroencephalography model emerged as state-of-the-art methods help improving brain-structure analysis. We expect to create a model based on EEG that can characterize some personal information of brain and infer behaviors of current sources—source localization. This problem is also called EEG inverse problem including two parts: one estimating a gain matrix which contains information about geometry and

conductivities of compartments in brain, location and orientation of dipoles; one estimating current voltage of sources/dipoles. The problem can be described by following mathematical formulation [10].

$$Y = AX + e \quad (11)$$

where Y is EEG measurement, X is EEG sources, A is lead field/gain matrix and e is noise.

In Eq. (11), there just has one given information that is EEG measurement Y , while remaining variables need to be estimated from EEG. This is an ill-posed problem because there are many solutions (A and X) can correspond with EEG measurement. In term of noise, we have two ways to treat it that are considering noise as a distribution controlled by parameters and estimating them, or modeling noise but increasing the complexity of problem.

Our approach is applying novel techniques of data-driven forward inference and deep learning to solve conductivity and source estimation problem respectively [11].

Data-driven forward model

The accuracy of solution for source localization is highly sensitive to how we correct the geometry and the conductivity of brain, because the dissimilarities among individuals can lead to errors in the EEG inverse problem [12]. The data-driven forward inference is applied to estimate an optimal person-specific model based on EEG without structural scans or conductivity measurement. The method include two parts: generating forward models from training data containing structural scans of the corpus subjects, and minimizing the free energy of new test subject to infer best suited forward model for the EEG provided. The assumption of this method is that the source distribution of interest is sparse.

Free energy of MarkoVG

The Variation Garrote (VG) introduces new binary variables $S \in \{0, 1\}^{N \times T}$ that indicate the spatio-temporal activation states (inactive or active) to forward model in Eq. (11).

$$Y_{kt} = \sum_{n=1}^N A_{kn} S_{nt} X_{nt} + E_{kt} \quad (12)$$

where N presents for number of sources, K for number of electrodes and T is time samples. The solution is found by computing the expectation of binary variable S and remaining variables.

Marko prior is applied for controlling degree of temporal smoothness and spatial sparsity of S_{nt} . For dipole location n

the transition probabilities of S_{nt} thus depend on the activation state at previous time $t - 1$.

$$\Gamma_{ji} = P(S_{nt} = j | S_{n,t-1} = i), \text{ where } i, j = 0, 1.$$

$$\Gamma = \begin{bmatrix} \Gamma_{00} & \Gamma_{01} \\ \Gamma_{10} & \Gamma_{11} \end{bmatrix} = \begin{bmatrix} 1 - \Gamma_{10} & \Gamma_{01} \\ \Gamma_{10} & 1 - \Gamma_{01} \end{bmatrix} \quad (13)$$

Instead of optimizing the posterior $p(S, X, \beta | D, \Gamma)$, we

4 Classification and Results

We calculate ApEn, SampEn, Higuchi Fractal Dimension (FD), and Hurst Exponent (H). ANOVA test is used to determine the significant features. Table 1 show the range and p-value of four features for three EEG classes. We see that p-values are very low, which mean all features are significant.

$$\begin{aligned} F_t(M, X, \beta, Z, \lambda) = & -\frac{Kt}{2} \log \frac{\beta}{2\pi} + \frac{\beta}{2} \sum_k (Y_k - Z_k)^2 + \frac{K\beta}{2} \sum_n M_n (1 - M_n) X_n^2 \chi_{nn} \\ & - \sum_n \left[M_n \log \frac{\Gamma_{10}}{\Gamma_{00}} + M_{n,t-1} \log \frac{\Gamma_{01}}{\Gamma_{00}} + (M_n * M_{n,t-1}) \log \frac{\Gamma_{00}\Gamma_{11}}{\Gamma_{01}\Gamma_{10}} \right] \\ & + Nt \log \frac{1}{\Gamma_{00}} + \sum_n [M_n \log(M_n) + (1 - M_n) \log(1 - M_n)] \\ & + \sum_k \lambda_k \left(Z_k - \sum_n A_{kn} M_n X_n \right) \end{aligned} \quad (14)$$

can minimize the free energy with Markovian prior which describes an upper bound on the negative log-likelihood to find optimal solution. where M is variational mean which describes the probability of source n being active at time t , β is controlling parameter of noise variance, $Z_k = \sum_n A_{kn} M_n X_n$ and λ are Lagrange multipliers. With X , these parameters are updated by Gradient descent, and estimated by minimizing free energy function. Before minimizing the function, two parameters $\gamma_1 = \log \frac{\Gamma_{10}\Gamma_{01}}{\Gamma_{00}^2}$ and $\gamma_2 = \log \frac{\Gamma_{00}\Gamma_{11}}{\Gamma_{01}\Gamma_{10}}$ indicate level of sparsity and smoothness respectively should be find using four fold cross-validation.

Minimizing free energy also is minimizing the difference between real signal Y and simulated signal Z . In addition, the free energy function prefers a dynamic system which has high probability to transit into another state of dipoles; to a stationary system.

We use three machine learning algorithms, which are Decision Tree (DT), K-Nearest Neighbor (KNN), and Support Vector Machine (SVM), to classifier three classes based on four significant features mentioned above. Table 2 shows the results of the sensitivity (Sn), specificity (Sp), accuracy (Acc), and Positive Predict Value (PPV) recorded by three classifiers using all four features.

The result of electroencephalography model is working for ongoing conversation.

5 Discussion

SVM give the highest value in classification with 82% for accuracy and about 81% for sensitivity, specificity, and PPV. However, the results in classification are lower than our

Table 1 Range (mean \pm standard deviation) of features for normal, interictal, and ictal EEG classes

Features	Normal	Interictal	Ictal	p-value
ApEn	1.327 \pm 0.178	0.761 \pm 0.237	0.969 \pm 0.197	<0.001
SampEn	1.223 \pm 0.114	0.670 \pm 0.231	0.732 \pm 0.196	<0.001
FD	1.197 \pm 0.051	1.272 \pm 0.045	1.087 \pm 0.031	<0.001
H	0.766 \pm 0.072	0.770 \pm 0.078	0.529 \pm 0.121	<0.001

Table 2 The Sensitivity, specificity, accuracy and positive predict value presented by the three classifiers using four six features for training and testing (mean \pm standard deviation)

Classifiers	Acc (%)	PPV (%)	Sn (%)	Sp (%)
DT	80.5 \pm 1.24	80.7 \pm 4.88	80.5 \pm 3.12	80.5 \pm 1.83
KNN	81.6 \pm 1.52	81.8 \pm 5.92	81.0 \pm 5.92	81.0 \pm 3.00
SVM	82.6 \pm 0.34	81.7 \pm 3.26	81.8 \pm 4.33	81.8 \pm 2.61

expectation (need to greater than 90%). We would like to enhance the results by applying Electroencephalography model. We suppose to use the EEG sources in the model for the implementation instead of EEG. We expect the result better than the current results.

6 Conclusion

PD and epilepsy are two subjects researched to investigate the dynamic properties of deep brain structure. However, we will work for epilepsy's data first to complete the scheme of method for analyzing the attribute and dynamic of deep brain activity, because epilepsy was proved as a dynamic disease of neuronal networks. Machine learning and non-linear futures are significant tools to recognize the patterns of EEG in epilepsy, and their results will be used to combine with the analysis of electrophysiological model.

Conflict of Interest This work doesn't have any conflict of interest.

References

- Han, C.X., et al.: Investigation of EEG abnormalities in the early stage of Parkinson's disease. *Cogn. Neurodyn.* **7**(4), 351–359 (2013)
- Al-Qazzaz, N.K., et al.: Role of EEG as biomarker in the early detection and classification of dementia. *Sci. World J.* **2014**, 906038 (2014)
- Colcher, A., Simuni, T.: Clinical manifestations of Parkinson's disease. *Med. Clin. North Am.* **83**(2), 327–347 (1999)
- Ellens, D.J., Leventhal, D.K.: Review: electrophysiology of basal ganglia and cortex in models of Parkinson disease. *J. Parkinsons Dis.* **3**(3), 241–254 (2013)
- Smith, S.J.: EEG in the diagnosis, classification, and management of patients with epilepsy. *J. Neurol. Neurosurg. Psychiatry* **76** (Suppl 2), ii2–ii7 (2005)
- Bishop, C.M.: *Pattern Recognition and Machine Learning*. Springer, New York (2006)
- Acharya, U.R., et al.: Application of non-linear and wavelet based features for the automated identification of epileptic EEG signals. *Int. J. Neural Syst.* **22**(2), 1250002 (2012)
- Richman, J.S., Moorman, J.R.: Physiological time-series analysis using approximate entropy and sample entropy. *Am. J. Physiol. Heart Circ. Physiol.* **278**(6), H2039–H2049 (2000)
- Burle, B., et al.: Spatial and temporal resolutions of EEG: Is it really black and white? A scalp current density view. *Int. J. Psychophysiol.* **97**(3), 210–220 (2015)
- Grech, R., et al.: Review on solving the inverse problem in EEG source analysis. *J. Neuroeng Rehabil* **5**, 25 (2008)
- Hansen, S.T., Hauberg, S., Hansen, L.K.: Data-driven forward model inference for EEG brain imaging. *Neuroimage* **139**, 249–258 (2016)
- Awada, K.A., et al.: Effect of conductivity uncertainties and modeling errors on EEG source localization using a 2-D model. *IEEE Trans. Biomed. Eng.* **45**(9), 1135–1145 (1998)

Part XIII
Public Health

Model of Information Technology in Management of Medical Equipment

Men Nguyen Thi, Hang Dang Thuy, Minh Nguyen Hong, and Do Tran Quang

Abstract

In the Hospital of Vietnam, Medical equipment is being managed quite simple without using information technology. So, the health care is increasingly developed, the management, investment as well as effective using are more difficult. For that reason, this paper proposes a model of information technology application in management of medical equipment. The model was built after survey and evaluation of some hospitals in the North of Vietnam. Later, it will be tested in the E-Hospital in Hanoi.

Keywords

Information technology • Management of medical equipment

1 Introduction

The management of investment and construction equipment is one of the important tasks of the medical branch. Medical equipment includes specific types of machinery and equipment. Medical equipment includes special devices. However, as with other types of machinery, the process of using and operating medical equipment will gradually appear technical problems, weaknesses. Therefore, the management of medical equipment also needs to pay special attention to maintenance management. This is an important basis to adjust and repair in time when equipment is damaged.

M. N. Thi (✉) · H. D. Thuy · M. N. Hong
Department of Control Technique, Le Quy Don Technical
University, Ha Noi, Viet Nam
e-mail: mennguyen.hy95@gmail.com

D. T. Quang
Department of Medical Equipment and Materials, E-Hospital, Ha
Noi, Viet Nam

2 Methods

In developing countries, the application of software maintenance management equipment has become quite familiar, in Vietnam maintenance work is only in the manual management. At present, most of the hospital maintenance management in the form of paper or Excel file, MS word.... In particular, the management of data on paper also causes the risk of missing, damage to the regular maintenance of equipment. Therefore, to ensure the comprehensive management of maintenance activities, to repair quickly and accurately, applying information technology to management is an effective solution, thoroughly solve the inadequacies of equipment management.

To support the equipment in the hospital need an effective intelligent maintenance management system, to ensure effective monitoring and management of maintenance activities, quickly update information of device status.

The construction of models helps to save time, work efficiency in maintenance issues. The device information is gathered quickly and accurately, helps to shorten maintenance time of equipment. In addition, the equipment in the hospital will be controlled optimally, more easily. Users can control the expiry date of the equipment.

Management of medical equipment should pay attention to maintenance of equipment, guarantee optimizing the performance of purchased equipment.

In fact, in some hospitals the maintenance process is done through the following steps [1].

Step one: Make maintenance schedule.

Step two: Announce the schedule to relevant departments.

Step three: Do the maintenance schedule.

The maintenance schedule is based on the following principles:

- Follow recommendation of manufacturers.
- Time to use the equipment.
- According to the actual situation of equipment.
- According to the request of the department using the equipment.
- Regular maintenance schedule is usually made at the beginning of the year.

When regular maintenance schedule has been approved by the manager, medical equipment department shall send it to departments using equipment to do maintenance together.

Before do maintenance, technical staffs of the medical equipment department have to survey, test run to determine the current working status of the equipment [1].

Depending on the quantity, the complexity of the device and warranty period, the leader of the medical equipment department will suggest equipment will be maintained by the service provider and equipment will be maintained by the medical equipment department. Hire other units or do it by technical staffs of the medical equipment department is specified while make maintenance schedule [1].

With equipment required labor safety, service providers must establish the process of detailed maintenance for each part of the equipment. During the maintenance, service providers must make daily maintenance logs that are confirmed by the user of the equipment [1].

Model of medical equipment maintenance plan and model listing medical equipment are built based on the actual process.

Prior to performing maintenance, technical staff of medical equipment and supplies department will carry out the survey and check the condition of equipment and make a list of broken equipment, replacement materials for each device.

List of broken devices, with full information device such as device name, department, serial number or year of use, will be brought to the repair department to fix them immediately. List of replacement materials includes all equipment information, help the equipment department know what equipment is available in the store or equipment that need to buy outside. This is to reduce maintenance time as well as budget for maintenance (Fig. 1).

The list of medical equipment is being used in the hospital is stored in the database of equipment management software. After checking the equipment information such as device name, department, serial number, country of manufacture, year of use, equipment code,... are saved on software system, technicians will have a list of equipment that need to maintain in the hospital and its warranty period to select the maintenance is done by the equipment supplier or

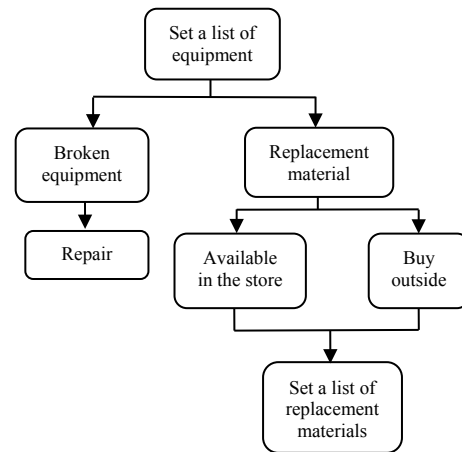


Fig. 1 Model listing medical equipment

the technical staff of the material department. From that, maintenance cycle of equipment often are made by month, quarter, or year or made by device type. Then set the projected time for each device of each department. Finally, the maintenance plan for the equipment is built.

The purpose of planning is to perform regular and full work and to guide the steps of maintenance of medical equipment. In addition planning indicates future direction, avoid waste, excess resources and promote effective maintenance, achieving the goal. Therefore, the planning step is quite important in the management and maintenance of medical equipment (Fig. 2).

3 Results

The management software for medical equipment maintenance is built based on the model and process management that is showed before.

The database of “maintenance management” software is stored in the SQL Server software. With SQL Server software, the database is stored on a server, connected to an internal network or the Internet. It allows users to use the software on any computer that has LAN network, access to the database and use these databases. The database structure consists of data tables:

- Table_KeHoachBaoDuong: Stores maintenance plans of medical equipment (Fig. 3).
- Table_DonVi: Stores names of departments in hospital (Fig. 4).
- Table_BaoCaoBaoDuong: Stores reports about results of equipment maintenance (Fig. 5).
- Table_DS_TTBAYT: Stores information of medical equipment in hospital (Fig. 6).

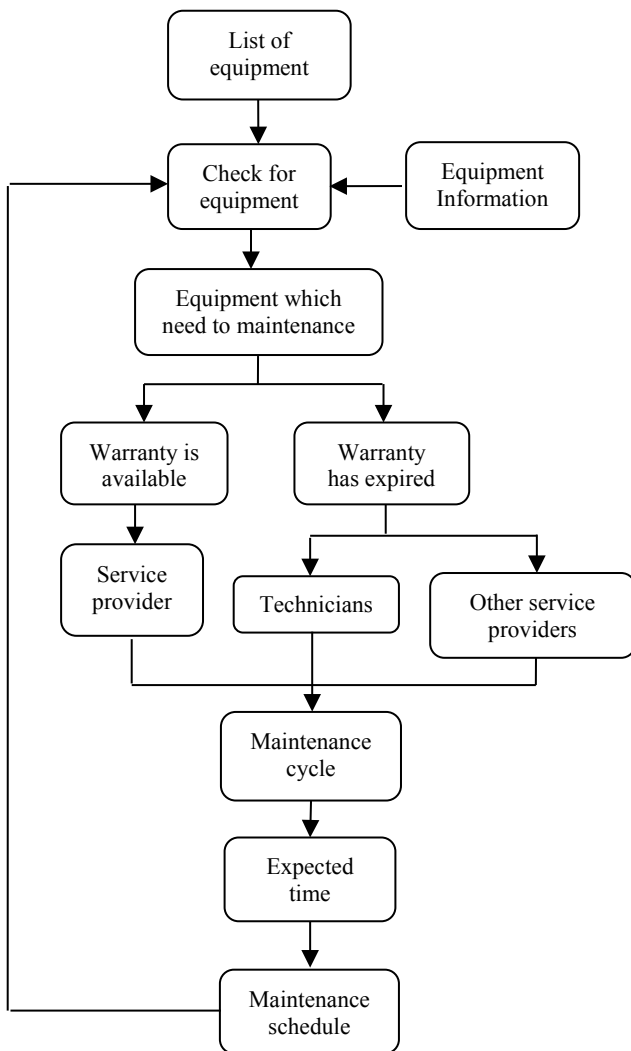


Fig. 2 Model of medical equipment maintenance plan

The main functions of the software:

- Display the maintenance plan of medical equipment that is established in this year.
- Display the maintenance plan of medical equipment that is established in this month.
- Look up information about the equipment, allow edit information.
- Establish the maintenance plan of medical equipment each year or each department, and Print out the plan for approval.
- Establish report after maintain medical equipment, save to database and print out the plan for approval.
- Look up the maintenance history of each of equipment to assess the frequency, extent of damage, replacement materials by each of equipment. Since, offer specific solutions to make the operation of the equipment easier and to improve equipment life, durability of use...

Column Name	Data Type	Allow Nulls
TenKeHoach	nvarchar(MAX)	<input type="checkbox"/>
ThoiGianLap	date	<input checked="" type="checkbox"/>
TenThietBi	nvarchar(MAX)	<input checked="" type="checkbox"/>
MaDinhDanh	nvarchar(50)	<input checked="" type="checkbox"/>
SerialNumber	nvarchar(50)	<input checked="" type="checkbox"/>
Model	nvarchar(MAX)	<input checked="" type="checkbox"/>
DonViSuDung	nvarchar(MAX)	<input checked="" type="checkbox"/>
ChuKyBaoDuong	nvarchar(50)	<input checked="" type="checkbox"/>
CachThucHien	nvarchar(50)	<input checked="" type="checkbox"/>
DonViThucHien	nvarchar(MAX)	<input checked="" type="checkbox"/>
NamThucHien	int	<input type="checkbox"/>
Thang1	bit	<input checked="" type="checkbox"/>
Thang2	bit	<input checked="" type="checkbox"/>
Thang3	bit	<input checked="" type="checkbox"/>
Thang4	bit	<input checked="" type="checkbox"/>
Thang5	bit	<input checked="" type="checkbox"/>
Thang6	bit	<input checked="" type="checkbox"/>
Thang7	bit	<input checked="" type="checkbox"/>
Thang8	bit	<input checked="" type="checkbox"/>
Thang9	bit	<input checked="" type="checkbox"/>
Thang10	bit	<input checked="" type="checkbox"/>
Thang11	bit	<input checked="" type="checkbox"/>
Thang12	bit	<input checked="" type="checkbox"/>

Fig. 3 Data structure of the table “Table_KeHoachBaoDuong”

Column Name	Data Type	Allow Nulls
ID	int	<input type="checkbox"/>
TenDonVi	nvarchar(MAX)	<input type="checkbox"/>

Fig. 4 Data structure of the table “Table_DonVi”

Column Name	Data Type	Allow Nulls
TenThietBi	nvarchar(MAX)	<input type="checkbox"/>
MaDinhDanh	nvarchar(MAX)	<input checked="" type="checkbox"/>
SerialNumber	nvarchar(50)	<input checked="" type="checkbox"/>
Model	nvarchar(MAX)	<input checked="" type="checkbox"/>
DonViSuDung	nvarchar(50)	<input checked="" type="checkbox"/>
VatTuThayThe	nvarchar(MAX)	<input checked="" type="checkbox"/>
TinhTrang	nvarchar(MAX)	<input checked="" type="checkbox"/>
NgayBaoDuong	date	<input type="checkbox"/>
Nam	int	<input type="checkbox"/>
Thang	int	<input type="checkbox"/>
Ngay	int	<input type="checkbox"/>
ID	int	<input type="checkbox"/>

Fig. 5 Data structure of the table “Table_BaoCaoBaoDuong”

Column Name	Data Type	Allow Nulls
TenThietBi	nvarchar(MAX)	<input checked="" type="checkbox"/>
MaDinhDanh	nvarchar(MAX)	<input checked="" type="checkbox"/>
SerialNumber	nvarchar(MAX)	<input checked="" type="checkbox"/>
HangSanXuat	nvarchar(MAX)	<input checked="" type="checkbox"/>
NamSuDung	date	<input checked="" type="checkbox"/>
Model	nvarchar(MAX)	<input checked="" type="checkbox"/>
ThoiHanBaoHanh	date	<input checked="" type="checkbox"/>
NhaCungCap_ConBaoH...	nvarchar(MAX)	<input checked="" type="checkbox"/>
NhaCungCap_HetBaoHa...	nvarchar(MAX)	<input checked="" type="checkbox"/>
DonViSuDung	nvarchar(MAX)	<input checked="" type="checkbox"/>
ChuKyBaoDuong	nvarchar(MAX)	<input checked="" type="checkbox"/>
TinhTrang	nvarchar(MAX)	<input checked="" type="checkbox"/>
GhiChu	nvarchar(MAX)	<input checked="" type="checkbox"/>
Lan_BaoDuong_GanNhat	date	<input checked="" type="checkbox"/>
ID	int	<input type="checkbox"/>

Fig. 6 Data structure of the table “Table_DS_TTYT”

- Make a list of replacement materials of each of equipment for the maintenance.
- Edit information about departments which use medical equipment when departments are renamed or hospital has a new department (Fig. 7).

Main interface displays the maintenance plan of medical equipment which is established in this year. It allows the

technical staff can manage all medical equipment, maintenance time, and departments where maintain equipment. Besides that, main interface also displays the maintenance plan of medical equipment which is establish in this month to help the technical staffs don't forget maintenance time. It helps the manager to organize work and working time in a scientific way, to be able to carry out full equipment maintenance, do not miss (Fig. 8).

The medical equipment available in the hospital will be listed and saved to the database on the server, with all necessary information for searching or establishing the maintenance plan on each of equipment. With management software, users can easily edit information or add new medical equipment [2] (Fig. 9).

With a large number of medical equipment operating in the hospital, finding information or looking for particular medical equipment often takes a long time to check on paper books (Fig. 10).

With the search feature of the software, finding information or searching for equipment become quick and easy. Search options are built very useful include search by equipment name, equipment identifier, serial number, model, or department which use equipment. You can search by multiple options at the same time to shorten the search range.

At the moment, maintenance planning usually takes a lot of work because Managers must check the identity of each of equipment, take maintenance cycle information, maintenance times to evaluate and plan maintenance (Fig. 11).



Fig. 7 Main interface of the software

Fig. 8 The list of medical equipment interface

DANH SÁCH TRANG THIẾT BỊ Y TẾ TRONG BỆNH VIỆN					
		Danh sách	Thêm thiết bị	Xóa thiết bị	Sửa
Tên thiết bị	Mã định danh	Serial Number			
Máy thận nhân tạo	MTNT1	22572			
Máy thận nhân tạo	MTNT2	22573			
Máy thận nhân tạo	MTNT3	25612			
Máy thận nhân tạo	MTNT4	22576			
Máy thận nhân tạo	MTNT5	25598			
Máy thận nhân tạo	MTNT6	5369			
Máy thận nhân tạo	MTNT7	CM5369			

Fig. 9 Medical equipment information interface

THÔNG TIN THIẾT BỊ Y TẾ

Tên thiết bị: Máy thận nhân tạo

Mã định danh: MTNT1

Serial Number: 22572

Hãng sản xuất: B.BRAUN

Năm sử dụng: 01/01/2014 01/01/2014

Model thiết bị: 710501C

Thời hạn bảo hành: 01/01/2016 01/01/2016

Nhà cung cấp 1: Nhà cung cấp thiết bị (còn bảo hành)

Nhà cung cấp 2: Công ty thiết bị y tế (hết bảo hành)

Đơn vị sử dụng: Khoa thận nhân tạo Khoa thận nhân tạo

Chu kỳ bảo dưỡng: 3 3

Tình trạng: Bình thường

Ghi chú:

Lần bảo dưỡng gần nhất: 07/04/2017 07/04/2017

Fig. 10 Interface for searching medical equipment

Tim thiết bị y tế

Lựa chọn cách thức:

Tên thiết bị: Máy thận nhân tạo Mã định danh:

Đơn vị sử dụng: Khoa thận nhân tạo Serial Number:

Model thiết bị:

Danh sách thiết bị tìm kiếm

Tên thiết bị	Mã định danh	Serial Number	Model thiết bị	Đơn vị sử dụng
Máy thận nhân tạo	MTNT1	22572	710501C	Khoa thận nhân tạo
Máy thận nhân tạo	MTNT2	22573	710501C	Khoa thận nhân tạo
Máy thận nhân tạo	MTNT3	25612	710501C	Khoa thận nhân tạo
Máy thận nhân tạo	MTNT4	22576	710501C	Khoa thận nhân tạo

Tên thiết bị	Mã định danh	Thời gian thực hiện											
		1	2	3	4	5	6	7	8	9	10	11	12
Máy thận nhân tạo	MTNT1	<input checked="" type="checkbox"/>	<input type="checkbox"/>	<input type="checkbox"/>	<input checked="" type="checkbox"/>	<input type="checkbox"/>	<input type="checkbox"/>	<input checked="" type="checkbox"/>	<input type="checkbox"/>	<input type="checkbox"/>	<input checked="" type="checkbox"/>	<input type="checkbox"/>	<input type="checkbox"/>
Máy thận nhân tạo	MTNT2	<input type="checkbox"/>	<input type="checkbox"/>	<input checked="" type="checkbox"/>	<input type="checkbox"/>	<input type="checkbox"/>	<input checked="" type="checkbox"/>	<input type="checkbox"/>	<input type="checkbox"/>	<input checked="" type="checkbox"/>	<input type="checkbox"/>	<input type="checkbox"/>	<input checked="" type="checkbox"/>
Máy thận nhân tạo	MTNT3	<input checked="" type="checkbox"/>	<input type="checkbox"/>	<input checked="" type="checkbox"/>	<input type="checkbox"/>	<input type="checkbox"/>	<input checked="" type="checkbox"/>	<input type="checkbox"/>	<input type="checkbox"/>	<input checked="" type="checkbox"/>	<input type="checkbox"/>	<input checked="" type="checkbox"/>	<input type="checkbox"/>
Máy thận nhân tạo	MTNT4	<input checked="" type="checkbox"/>	<input type="checkbox"/>	<input type="checkbox"/>	<input checked="" type="checkbox"/>	<input type="checkbox"/>	<input type="checkbox"/>	<input checked="" type="checkbox"/>	<input type="checkbox"/>	<input type="checkbox"/>	<input checked="" type="checkbox"/>	<input type="checkbox"/>	<input type="checkbox"/>

Fig. 11 Interface for establishing the maintenance plan

Tên thiết bị	Mã định danh	Serial Number	Model thiết bị	Đơn vị sử dụng
Máy điện tim 6 cân	MDT6C	13551	ECG-9020	Khoa nhi
Máy thận nhân tạo	MTNT1	22572	710501C	Khoa thận nhân tạo

Fig. 12 Interface for reporting maintenance results

Lịch sử bảo dưỡng trang thiết bị

Lựa chọn

Tra cứu theo thiết bị

Tra cứu theo năm: 2018

Tra cứu theo tháng: 1

Tra cứu theo ngày: 1

In lịch sử bảo dưỡng

Ngày in báo cáo: 11/04/2018

Tra cứu lịch sử bảo dưỡng

Fig. 13 Interface equipment maintenance history

Tên thiết bị	Mã định danh	Đơn vị sử dụng	Vật tư thay thế
Máy điện tim	MDT2	Khoa Thận	điện cực
Máy thận nhân tạo	MTNT1	Khoa thận nhân tạo	bầu lọc, dây truyền

Fig. 14 Interface list of replacement materials

To simplify this process, reduce work, save time, this software is built features that automatically establish maintenance plan for all equipment or for each department which use medical equipment. Equipment required for maintenance will be automatically entered into the maintenance plan, based on the maintenance information of each device is stored in the database. Manager can also edit, add, delete in the plan table and save the plan into database (Fig. 12).

After maintaining the device, technical staff can use this feature to report maintenance results and save them into

database. This is a great advantage if manager want to check the maintenance history of each of equipment. He can have the necessary assessment of the operation of the equipment to determine the next maintenance plan. It help the device can work most effectively (Fig. 13).

History maintenance searching feature is built very useful include search by equipment name, equipment identifier, serial number, model, department which use equipment or maintenance time (Fig. 14).

List of replacement materials is established with full equipment information, help the equipment department know what equipment is available in the store or equipment that need to buy outside. In addition feature finding information about replacement materials of equipment allows the user to quickly find the replacement materials to be prepared before each of maintenance. It helps to reduce maintenance time as well as budget for maintenance [3, 4].

4 Conclusions

This paper presents a model of management process for medical equipment. The model was built in software on a database of nearly 800 medical devices at hospital E. Software has brought positive effects in maintenance management such as limiting delay time or missing in the maintenance process, helps to shorten maintenance time, saves energy in the planning maintenance of medical equipment. It helps managers and technicians can have the

necessary assessments about the operation of the equipment to make it as efficient as possible. Software is developed at the level of testing and assessing stability of it to apply in reality.

Acknowledgements The authors would like to thank Department of Medical equipment in E-Hospital.

Conflict of Interest The authors declare that they have no conflict of interest.

References

1. Management process of medical equipment in Bach Mai- Hospital
2. List of medical equipment in E-Hospital
3. Trần Nguyễn Phong, Giáo trình SQL, nhà xuất bản đại học khoa học Huế (2004)
4. Hoàng Hữu Việt, Lập trình C# cho ứng dụng cơ sở dữ liệu, nhà xuất bản đại học Vinh (2015)

Establishing a Healthcare Research Network in Vietnam: A Platform for Collaborative Quality Improvement

Anh The Bui, Dung Dao Trung, Ky Le Minh, Trung Nguyen, Hung Le Dinh, Lien Tran, Nga Nguyen, Priya Vohra, Keven Seung Yong Ji, Eunice Lee, James Campbell, and Walter T. Lee

Abstract

There is both a demand and need for delivering patient centered care in health systems. This is especially challenging in developing countries in which resources are limited, population health burdens are extensive, and coordination between facilities is fractured. The development of a low cost, centralized, real time data collection platform would be a powerful tool in understanding patient centered healthcare needs and issues. We report a pilot project that seeks to establish such a healthcare research network in Vietnam. This pilot used a web-based database collection tool called REDCap (Research Electronic Data Capture). We programmed a validated general health quality of life questionnaire in both English and Vietnamese that was used to collect patient responses. A total of four hospitals located in Hanoi, Vietnam participated in the pilot project of patients presenting with otolaryngology-head and neck complaints and concerns between January 23 and January 26, 2018. We report

outpatient responses and their associated quality of life in ten specific domains. This pilot demonstrates the successful international collaboration among academic, non-profit, clinical entities in establishing this low-cost research network. This will be a platform that could easily be expanded to include other healthcare facilities in conducting quality improvement and research projects. We envision this approach as an important tool in improving health care quality in developing countries throughout the world.

Keywords

Practice based research • Network • Quality of life • Otolaryngology • Quality improvement

A. T. Bui · K. Le Minh
Department of Otolaryngology—Head and Neck Surgery,
National ENT Hospital, Hanoi, Vietnam

D. D. Trung
Vietnam-Cuba Friendship Hospital, Hanoi, Vietnam

T. Nguyen
Hanoi Medical University Hospital, Hanoi, Vietnam

H. Le Dinh
E Hospital, Hanoi, Vietnam

L. Tran · N. Nguyen
Resource Exchange International (REI)—Vietnam, Colorado
Springs, USA

P. Vohra · E. Lee · J. Campbell · W. T. Lee (✉)
Duke University School of Medicine, Durham, USA
e-mail: walter.lee@duke.edu

K. S. Y. Ji · W. T. Lee
Department of Surgery, Duke University Medical Center,
Durham, USA

1 Introduction

In developing countries such as Vietnam, healthcare can be a major challenge due to high patient needs, limited resources for clinical and research activities, and fractured healthcare networks among facilities. Delivery of healthcare can vary among individual practices as well as institutions. Policies, protocols and practices have been developed to improve the overall quality of healthcare and better standardize the quality of care regardless of facility or institution [1]. These steps often do not incorporate an important perspective—that of the patient.

Assessing and incorporating patient reported outcomes (PRO) have been recognized as an important part of improving healthcare [2]. PRO are data collected about a certain outcome based on the patient's own experience. Thus, PRO involves valuable information on measurements based on actual patient experience. Healthcare quality is improved when patient quality of life experiences (i.e. eating, communication) are improved [3, 4].

Practice based research networks (PBRN) have been established as a means to collect and perform research in a

way that seeks to understand related practices as a whole [5]. Indeed, in the US as of October 2016, there were 178 PBRNs registered that involved all 50 states and over 25 countries [6]. PBRN have been used to assess important practice trends within a system. For example, the CHEER (Creating Health Excellence and Education through Research) network is an otolaryngology based network of 30 practices with half being academic and the other half being private practice [7]. CHEER has demonstrated how quality improvement and research projects that can inform how different individual sites compare to each other [8]. This facilitates opportunities for improving patient care and standardizing best practices.

Having such a PBRN in developing countries would be an important tool in understanding current practices and identifying areas in which healthcare delivery could be improved. Therefore, we sought to establish a pilot practice based research network based in otolaryngology practices in Hanoi, Vietnam. Our pilot included a web-based quality of life (QOL) tool centered on global health in both physician and emotional domains (PROMISE Global Health v.1.2). Our goals were (1) to establish feasibility of collecting PRO from patients at different hospitals and (2) to report on the global health of patients having ear, nose/sinuses and/or throat problems at otolaryngology head and neck clinics.

2 Materials and Methods

This work was considered quality improvement (QI) due to its focus on studying care delivery processes and thus did not require IRB approval. Data collection was done in a manner that did not collect any personal health information and was completely anonymous. Furthermore, we sought to improve care delivery to patients by using available validated tools to assess physical and emotional health at presentation at the otolaryngology clinic.

We collaborated with Research Exchange International (REI) Vietnam, an established non-governmental non-profit organization based in Colorado Springs, CO USA. REI has been working within the healthcare sector for over 20 years and has been instrumental in improving otolaryngology related healthcare throughout the country. REI provided logistical and administrative support throughout the QI project.

An initial cohort of four hospital based otolaryngology practices were chosen for this pilot study. These were chosen based on existing relationships with REI, as well as representative of different types of hospitals in Hanoi. These hospitals were National ENT Hospital (quaternary national referral center), E Hospital (general and national level facility), Vietnam-Cuba Friendship Hospital (city level facility), and Hanoi Medical University Hospital (academic training facility).

An informational session was held with key stakeholders and partners prior to implementation. The goals of the project were shared and workflow pathways were created to capture data during patient intake. Administrative approvals were obtained from all locations for this pilot study.

The Global Health QOL tool v.1.2 was chosen as the pilot tool. This tool is a 10 question tool that is not disease specific. It also has been translated into several languages and is available on line through the PROMIS (Patient-Reported Outcomes Measurement Information System) Health Measures website (<http://www.healthmeasures.net/explore-measurement-systems/promis>). This Global Health tool was translated into Vietnamese by a native speaker and was independently reviewed by another two native Vietnamese speakers. Data was scored according to instructions and cumulative raw sum scores for emotional and physical health were calculated. These raw sum scores are then converted to a T-score. T-Score distributions are standardized in that 50 represents the average (mean) for the US general population. One standard deviation from the mean is 10 points. Higher scores are considered better. Incomplete surveys were censored from analysis because incomplete surveys are invalid. Furthermore, the survey tool has only been validated for adults and therefore respondents <18 years of age were excluded.

The REDCap database was used to collect the data from the PROMIS Global Health survey v1.2. REDCap is a web-based, secure, HIPAA-compliant, system for building and managing web-based research projects such as surveys and databases [9]. The survey was coded electronically and available to be used on Kindle tablets. Paper copies were also available for use.

3 Results

The pilot project was implemented over four days from January 23–26, 2018. A total of 762 surveys were collected from outpatients having self reported ear, nose/sinuses, and/or throat problems (206, 167, 389 respectively). The number of surveys that were collected from each site varied. The National ENT Hospital collected a total of 354 surveys. Vietnam-Cuba Friendship Hospital collected 229 surveys. Hanoi Medical University collected 88 surveys, and E Hospital collected 91 surveys. There was an approximate 99% completion rate of surveys (750 of 762 surveys complete). Most data was collected on paper and then transcribed into the REDCap database using the Kindle tablets.

A total of 66 surveys were excluded, 54 surveys were <18 years and 12 were incomplete. This resulted in 696 adult patients who had ear, nose/sinuses, and/or throat issues available for analysis.

Survey data was reviewed and scored per instructions. The mean Physical Health T-scores for ears, nose & sinus,

Fig. 1 Physical Health T-Scores (50 is equivalent to the average for the US population.) A change in 10 represents one standard deviation

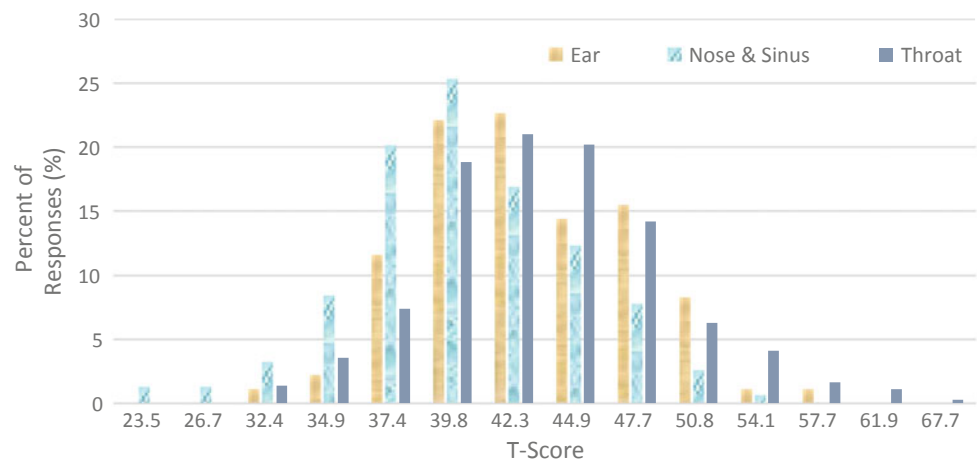
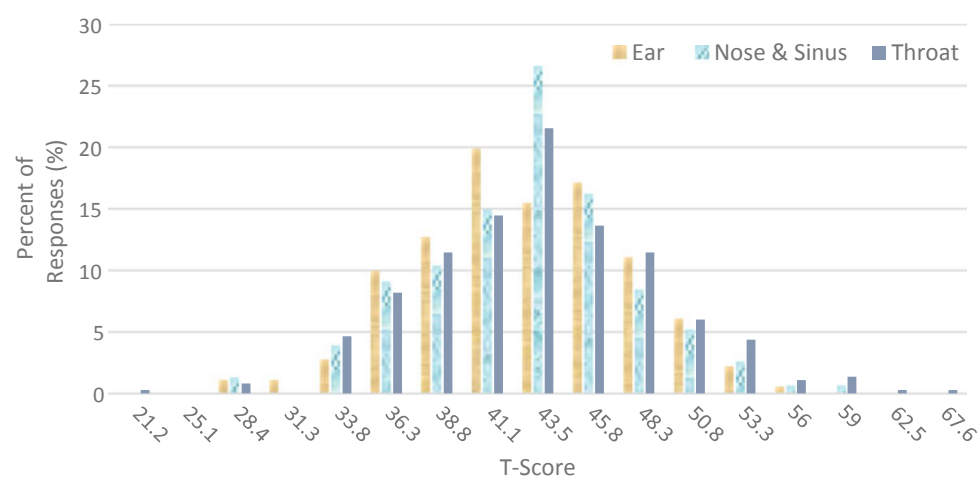


Fig. 2 Mental Health T-Scores (50 is equivalent to the average for the US population.) A change in 10 represents one standard deviation



and throat were 42.3, 39.8, and 42.3 respectively. The mean Mental Health T-score for ears, nose & sinus, and throat were 43.5, 43.5, and 43.5 respectively. The physical health and mental health T-scores for patients presenting with ears, nose/sinuses, and throat concerns are represented in Figs. 1 and 2 respectively.

4 Discussion

We report on the first otolaryngology based PBRN in Vietnam. We describe the approach to setting up the PBRN and describe results in an initial pilot to collect anonymous QOL data. This data was collected in REDCap, allowing for monitoring, data auditing, and also initial analysis. This web based data is accessible to all participating sites. Our data show the QOL effects from ear, nose & sinuses, and/or throat complaints in both the physical and mental health domains. Although the data demonstrate a normal

distribution of responses, there appears to be more of a negative impact on physical health from those with nose & sinuses complaints and concerns.

We demonstrate that healthcare teams can implement this approach into current practice routines as well as collect patient reported outcome. Data from this validated survey and other validated surveys could facilitate interventions to improve healthcare delivery. For example, healthcare teams may be able to screen and identify patients whose scores are outside of one deviation from the mean. This relatively simple survey would enable healthcare teams to better address mental and physical needs of the patient and their families. Follow-up using these same tools would provide longitudinal assessment of treatment effectiveness of these needs.

The outpatient clinics at these study sites, like others in developing countries, have significant daily clinical demands. Some otolaryngology clinics in Hanoi see over 100 patients per day. This heavy clinical demand may be an

advantage in QI projects such as this one. It makes the ability to capture large number of subjects possible over a few days. Such large volumes open an opportunity for rapid project enrollment and meeting recruitment target. QI or research projects will need to work with clinical staff and faculty to minimize the impact of such data collection projections on clinical workflow.

Further steps include expanding the network to other hospitals not only in and around Hanoi, but also throughout the country. Data could also be collected from the general public to compare with the average from the US. Specific data analysis as defined by the area of concern is ongoing to identify interventions than may address some of the needs as reported by patients. Future studies would potentially incorporate electronic input by the patient with immediate scoring to be available to the treating clinician at the point of care.

5 Conclusions

This pilot work demonstrates the feasibility of establishing a PBRN in Vietnam. It also demonstrates the advantages of using a web-based data collection system such as REDCap to collect data from multiple sources. Finally, through using validates survey tools, areas of improvement can be identified from PRO that can be in the clinical care of patients. Key partnerships among different collaborators is vital for establishing a PBRN. This approach may be an important step in developing research and improving healthcare delivery in other countries.

Acknowledgements We would like to thank Erika Juhlin for her assistance in coding the REDCap survey as well as programming the electronic tablets. We thank the nursing staff at the hospitals for data collections. We would also like to acknowledge the Duke—NUS collaboration grant that provided support travel (WTL).

Conflict of Interest The authors declare that they have no conflict of interest.

References

1. Kagan, J., et al.: Assessing clinical research capacity in Vietnam: a framework for strengthening capability for clinical trials in developing countries. *Public Health Rep.* **131**(3), 396–403 (2016)
2. Carroll, T.L., et al.: Evidence-based medicine in otolaryngology, part 6: patient-reported outcomes in clinical practice. *Otolaryngol. Head Neck Surg.* **158**(1), 8–15 (2018)
3. Liu, J.B., et al.: Patient-reported outcomes in surgery: listening to patients improves quality of care. *Bull. Am. Coll. Surg.* **102**(3), 19–23 (2017)
4. Church, J.: Quality of life and patient-reported outcomes. *Br. J. Surg.* **105**(3), 157–158 (2018)
5. Baldwin, L.M., et al.: Developing a practice-based research network by integrating quality improvement: challenges and ingredients for success. *Clin. Transl. Sci.* **5**(4), 351–355 (2012)
6. Agency for Health Care, R.a.Q.A. Available from: <https://pbm.ahrq.gov/>
7. Bellmunt, A.M., et al.: Does an otolaryngology-specific database have added value? a comparative feasibility analysis. *Otolaryngol. Head Neck Surg.* **155**(1), 56–64 (2016)
8. Lee, W.T., et al.: Tonsillectomy bleed rates across the CHEER practice research network: pursuing guideline adherence and quality improvement. *Otolaryngol. Head Neck Surg.* **155**(1), 28–32 (2016)
9. Harris, P.A., et al.: Research electronic data capture (REDCap)—a metadata-driven methodology and workflow process for providing translational research informatics support. *J. Biomed. Inform.* **42**(2), 377–381 (2009)

Value Signposts in MedTech Development: An Experience from the Field

K. T. Nguyen, P. P. Lee, P. G. Yock, N. C. Tan, H. K. Tan, and W. T. Lee

Abstract

Medical technology (MedTech) is traditionally seen as enabling the delivery of health in a better, innovative fashion. For example, the Da Vinci robot enables robotic surgeries, and Ardian enables surgical treatment of refractory hypertension. More recently, there has been a profound shift in emphasis on technologies that can provide cost-saving values to the payers. To this end, value signposts are fundamental in identifying and addressing clinical needs on a global scale. These value signposts include the potential to keep patients out of the hospital, change location of care to less expensive venues, and diagnose a condition earlier to reduce complications and/or slow disease progression. These presentations will review the key value signposts for translating health science technology and apply them to two case studies. *Case 1*: Even with readily available Emergency Medical Service and well equipped tertiary medical centres dotted across Singapore, the rate of patients with ischemic stroke receiving thrombolysis is low at 6.3%. Patients missing the window for thrombolysis have worse clinical outcome and require expensive rehabilitation. Our Singapore Stanford Biodesign team developed an app to identify the three most common symptoms of stroke and automatically activate medical response. *Case 2*: Our team of physicians from Singapore and the United States identified a scarcity of nasoendoscope in Vietnam. Only 45% of central and regional hospitals have nasoendoscopes whereas no

community or district hospitals have such capacity. The team developed an affordable, LED-based, cord-free, AAA-battery-powered nasoendoscope system with data acquisition and transmission circuitry. This device can potentially add significant value to the delivery of ENT care in Vietnam and beyond. The objective is to demonstrate how innovations with strong focus on reducing the costs to healthcare systems have global appeal.

Keywords

MedTech • Stroke • Health app • HealthTech
telemedicine • Head and neck cancer •
Nasoendoscope • Endoscopy

1 Introduction

MedTech is seen broadly as any healthcare product used to treat a wide range of medical conditions to save lives, and to alleviate symptoms and sufferings. From the contact lens used in the home to the sophisticated Da Vinci machines in modern operating theatres, MedTech devices shared the common thread of benefiting health and improving quality of life. Entrepreneurs entering the MedTech space, the authors included, are often drawn to the appeal and seduction of inventing a next generation catheter, a better robotic surgical system, or an avant-garde device that makes existing technologies obsolete, enable new procedures and disrupt how care is being delivered. Intuitive Surgical (Netherlands) pioneered the field of robotic surgery. Ardian (USA) enabled minimally invasive renal denervation for the treatment of hypertension. BrainSpec (USA) is an example of a medical device that enable needleless brain biopsy that seeks to enable accurate, efficient, and non-invasive diagnosis of brain disorders. Cam Med (USA) is a medical device startup that aims to replace existing drug-delivery devices that are often bulky and complex with a flexible, bandage-like patch pump. These devices are examples of

K. T. Nguyen (✉) · N. C. Tan · H. K. Tan
Singapore Health Services, Singapore, 229899, Singapore
e-mail: thienkhanh.nguyen@mohh.com.sg;
drkhanhnguyen@gmail.com

P. P. Lee
Institute of Materials Research and Engineering, Singapore,
138634, Singapore

P. G. Yock
Stanford University, Palo Alto, 94305, USA

W. T. Lee
Duke University Medical Center, Durham, NC 27710, USA

Table 1 Practice-based signposts that may reduce healthcare spending [1]

Potential to keep patients out of the hospital
Potential to shorten length of stay
Potential to change the location of care to less expensive venues
Potential to reduce the procedure time or resource use
Potential to shift a service to a lower-cost provider
Potential to reduce the number of staffs required to carry out a procedure
Potential to diagnose a condition earlier to reduce complications and/or prevent/slow diseases progression

MedTech companies that are extremely innovative and continue to push the overall boundaries of MedTech.

However, innovation is not always about pushing the boundaries on what we can do. Arguably, it is becoming progressively essential for MedTech entrepreneurs to deliver technologies that can provide cost-saving values to the healthcare systems while maintaining equivalent or better outcomes. Understanding some of these value signposts can help guide the entrepreneur toward delivering MedTech innovations with global appeal. Table 1 summarises some of the potentials to reduce healthcare spending. The case studies that follow draw from the authors' own experience using these signposts to identify and attempt to address compelling clinical needs in Singapore and in Vietnam, two countries with starkly different healthcare environments, structures, regulations, and challenges.

2 Case Studies

2.1 Case I: My Stroke Alert Technology: MyStAT

Stroke is one of the leading causes of mortality and the leading cause of adult disability in the world. In the United States of America alone, stroke consumes approximately \$65 billion in direct and indirect healthcare costs [2]. At the individual level, the toll of stroke is infinite with most elderly patients preferred death over a disabling stroke [3]. Most strokes are ischemic, for which exist established treatments such as intravenous recombinant tissue plasminogen activator (tPA) and endovascular thrombectomy. Both treatments have been shown to improve functional outcomes, but must be initiated within 4.5 and 6 h respectively [4].

Thus, in the treatment of stroke, emergency medical help is crucial for improved outcomes. Singapore, with state-of-the-art hospitals sprawling across the city state and a well-trained and well-staffed emergency medical service (EMS), is well-positioned to provide timely and efficient stroke management to its population. Ambulance statistics in Singapore reports a response time and delivery time of 11 and 20 min respectively [5]. The door-to-drug time could be

as soon as 60 min [6]. Unfortunately, the percentage of a patients receiving thrombolysis treatment in Singapore is a paltry 6.3% [7]. The reality is that there is no chain of survival without detection of symptoms.

Most stroke patients in Singapore miss out on the treatment window because they fail to recognize stroke signs and symptoms. In 2007, only 9% of patients presented to the hospital emergency department (ED) within 2 h of symptoms onset and the median time to hospital arrival was 16 h and 5 min [8]; in 2009, only 6% of patients presented within 2 h and the median time to hospital arrival was 20 h and 45 min [9]. In fact, poor patient awareness of symptoms and delay in seeking medical care have long been reported to affect tPA rates in other countries as well [10, 11]. Currently, the most widely adopted method to combat this problem is through national campaigns to increase public awareness. The acronym FAST has been used to represent the 3 major signs and symptoms of stroke—namely, Face for any signs of facial droop, Arms for any signs of arm weakness, Speech for any slurring of speech and Time, a reminder to alert EMS. However, just having knowledge of symptoms may not help. In the DASH II study, the authors found no association between knowledge of stroke symptoms and the increased use of EMS for stroke [12]. Thus, the deficiency in the detection of the signs and symptoms at the onset of stroke creates a gap in the delivery of care that is currently unresolved.

Our team at the Singapore-Stanford Biodesign program adopted the design thinking and innovation methods taken from the Stanford Biodesign program to address this need. One part of our solutions is the first interactive mobile app of its kind, the MyStAT App. The app utilizes the sensors in the phone to help the user self-monitor for the same 3 major signs of stroke as mentioned above—F, A, S. Our app uses a simple, easy-to-understand user interface design to help users monitor for changes in facial features, arm weakness and slurred speech. We designed an intuitive process where users are instructed to lift the phone, take an image with the front-facing camera and read out a simple line of text. Our proprietary algorithm will then analyze these inputs for any anomalies. If the user displays any significant variation from their baseline, the app will offer the user a quick-call option

for EMS or a caregiver. By providing a fast, intuitive and intelligent way to assist these at-risk patients, we aim to decrease time to treatment, increase tPA rates and thus, improve the chance of stroke victims receiving time-sensitive acute care. The team has secured funding to complete the development of the technology and is aiming to work with nursing homes, senior activity centers and hospitals to optimize the app. We are also currently in discussions with key insurance providers in Singapore to adopt various forms of the technology and secure a wide distribution among the local population.

2.2 Case II: ENSiTe

Head and neck cancers (HNC) are the 6th most common cancers worldwide, with an incidence of 550,000 patients a year and a mortality rate of 356,000 patients a year [13]. In addition to the high mortality rate, HNC is extremely morbid and survivors experienced decreased quality of life [14]. HNC can significantly impair a person appearance as well as basic life functions such as breathing, eating, and speaking [15–17]. The mortality and morbidity of HNC are even more severe in Third World countries. Firstly, the highest prevalence of the disease is found in Asia and Southeast Asia countries with resource poor healthcare infrastructures, including Vietnam [18]. Not only the population in these areas have genetic predisposition to develop cancer of the nasopharynx but lifestyle factors such as alcohol, tobacco, and betel nut usage and environmental factors such as heavy metal pollution are also commonplace in these regions. Secondly, due to the lack of access to care, HNC are often diagnosed late, resulting in significantly higher cancer morbidity and mortality [19]. Thirdly, with almost no existing allied health services such as speech therapists, physiotherapists, or psychologists, patients who survive the treatments are often disabled by resection and left with poor quality of life.

The flexible nasopharyngoscope (FNS) is an invaluable tool in the standard-of-care assessment of the upper aerodigestive tract in developed countries. The flexible scope is inserted through the nasal cavity into the back of the throat, enabling a full assessment of all the head and neck areas that are at risk for cancer. In developing countries like Vietnam, the gold standard for upper aerodigestive examinations is the rigid scope. The rigid scope has significant drawbacks compared to the flexible one as it is more uncomfortable for the patients and offered limited view of the larynx, nasopharynx, and nasal cavity. However, rigid scopes are more affordable than flexible. Base on focus group discussion and pilot site visits with Vietnamese physicians in 2014, due to lack of skills and fundings, only 45% of national level hospitals located in major cities are equipped with FNS. This

represents a significant gap in the ability to properly diagnose HNC and during follow up to assess for treatment response or for recurrences.

Our team of physicians and engineers from Duke University (USA) and Singapore designed a low-cost and portable FNS using complementary metal-oxide semiconductor (CMOS) camera and LED technology. The device includes a CMOS camera with built in LED lights at the tip of the endoscopic shaft. The handle carries a tungsten wires-pulley mechanism that enables bidirectional control of the endoscopic tip, the CMOS camera processor, a connector to an LED screen, and a power source. In our earliest iteration, the power provided by 4 AAA-batteries powered both the LED-CMOS camera complex and the LED light. With these early prototypes, the team carried out an early pilot study in Vietnam in 17 patients. The initial responses were positive. Most physicians were able to handle the prototypes well and completed all the exams. The LED brightness was sufficient and the image captured by the CMOS camera is clear and focus (Fig. 1). The physicians also find the prototypes no more difficult to handle than the rigid. Patients also find our device less painful than the rigid, as evidenced by a much lower pain score with our device than the rigid.

In our most up-to-date iteration, the LED screen is replaced by a smart device and the power is drawn directly from the smartphone or tablet. The app on this device allows recording and secure sharing of images, enabling the procedurist to be instantaneously connected to an ecosystem of global users for second opinions and/or referrals. Encouraged by fundings from angel investors in Vietnam and



Fig. 1 ENSiTe was used to assess a tracheostomy site of a patient who recently underwent a total laryngectomy. The trachea rings and the carina can be clearly seen on the LED screen of ENSiTe

supported by local physicians, the team goal is to make ENsiTe available for targeted screening of HNC in three major cities in Vietnam: Hanoi, Ho Chi Minh City, and Danang by the first quarter of 2019.

3 Discussions

The above case studies demonstrate that medical technologies that can reduce healthcare spending have universal appeal, whether it is in a top 3 GDP per capita country like Singapore or an emergent country like Vietnam. ENsiTe was developed to be used in underserved populations in emerging markets. However, due to its focus on being low-cost and being able to be used in less expensive venues by primary care physicians, ENsiTe carries a strong value proposition to be used in developed countries for screening. If ENsiTe screens and detects a laryngeal tumor when it is stage I, it can be treated definitively with primary radiotherapy at €1773 compared to a stage III tumor that requires elaborate laryngectomy at €22,298 [20]. A medical device with a potential of reducing healthcare spending has a strong and enduring appeal globally.

Perhaps, at this time, an important distinction between healthcare cost and healthcare spending needs to be established. Healthcare cost refers to the cost of delivering a healthcare service. Healthcare spending refers to the total money spent for a particular group of patients over a period of time. A patient suffering from ischemic stroke who does not receive tPA requires higher healthcare spending than a patient who received tPA due to longer hospital stay, complications, longer rehabilitation, and nursing home. Another study designed to look at the overall, societal economic benefit of increasing utilization of TPA shows a net savings of as much as US\$7.4 millions for every 2% increase in tPA-treated patients and as high as US\$73.9 millions for an increase of 20% in proportion of ischemic stroke patients that receive tPA [21]. Similarly, a patient who is diagnosed with early nasopharyngeal carcinoma can be treated with local resection and thus, requires less healthcare spending than an advanced cancer that requires invasive and complex nasopharyngectomy, lengthy hospitalization, and sophisticated rehabilitation. The distinction between cost and spending is important because new procedures or treatments will usually incur new healthcare costs. What is critical is that, as illustrated in our case studies, the new devices may not necessarily incur additional spending and therefore, provide good value for money. New procedures that incur significant spending will face a significant barrier to entry in an increasingly cost-conscious healthcare culture.

An inescapable fact about new medical technology is that patient outcome is not the only driver for technology diffusion. Certainly, veracity of clinical data can facilitate

diffusion among clinicians. However, economic considerations such as the insurer's willingness to pay or the payer's funding policies may hasten or slow down diffusion of technology. To this end, innovators should strongly consider obtaining economic data endpoints while designing clinical trials for their technologies. Being able to offer convincing economic evidence will build a robust value proposition to payers and thus enhance the diffusion and adoption of new technologies. The plethora of high quality publications on the economic advantages of receiving tPA vs not receiving tPA enable the authors to gather support from insurance providers and to obtain further funding to continue MyStAT's development. The HNC space is a younger and less studied fields than stroke, particularly in the area of cost effectiveness and cost analysis. However, we will be collecting prospective economic data in our future studies as part of our comprehensive strategy to advocate for the routine screening of HNC in high risk populations.

4 Conclusions

Increasingly, payers and governments will stop spending indiscriminately for health care products and services. MedTech entrepreneurs and innovators will benefit from being cognizant about value, healthcare cost and healthcare spending to develop effective and long-lasting solutions with global impact.

Conflict of Interest The authors declare that they have no conflict of interest.

References

1. Yock, P., Zenios, S., Makower, J., et al.: *Biodesign*, 2nd edn. Cambridge University Press, UK (2015)
2. Solomon, N.A., Glick, H.A., Russo, C.J., Lee, J., Schulman, K.A.: Patient preferences for stroke outcomes. *Stroke* **25**(9), 1721–1725 (1994)
3. Troke, S.T.S., Roup, S.T.G.: Tissue plasminogen activator for acute ischemic stroke. *N. Engl. J. Med.* **231**(16), 1240–1241 (1999)
4. Fonarow, G.C., Smith, E.E., Reeves, M.J., Grau-sepulveda, M.V., Hernandez, A.F., Peterson, E.D., Schwamm, L.H.: Time to treatment with intravenous tissue plasminogen activator and outcome from acute ischemic stroke. *JAMA* **309**(23), 2480–2488 (2013)
5. Saver, J.L., Goyal, M., van der Lugt, A., Menon, B.K., Majoie, C. B.L.M., Dippel, D.W.: Time to treatment with endovascular thrombectomy and outcomes from ischemic stroke: a meta-analysis. *JAMA* **316**(12), 1279 (2016)
6. Lin, C.B., Peterson, E.D., Smith, E.E., Saver, J.L., Liang, L., Xian, Y., Olson, D.M., Shah, B.R., Hernandez, A.F., Schwamm, L.H., Fonarow, G.C.: Emergency medical service hospital prenotification is associated with improved evaluation and treatment of acute ischemic stroke. *Circ. Cardiovasc. Qual. Outcomes* **5**(4), 514–522 (2012)

7. National Registry of Diseases Office Singapore: Stroke Registry Report 2014 (2014)
8. De Silva, D.A., Ong, S.H., Elumbra, D., Wong, M.C., Chen, C.L., Chang, H.M.: Timing of hospital presentation after acute cerebral infarction and patients' acceptance of intravenous thrombolysis. *Ann. Acad. Med. Singapore* **36**(4), 244–246 (2007)
9. De Silva, D.A., Yassin, N., Toh, A.J., Lim, D.J., Wong, W.X., Woon, F.P., Chang, H.M.: Timing of arrival to a tertiary hospital after acute ischaemic stroke—A follow-up survey 5 years later. *Ann. Acad. Med. Singapore* **39**(7), 513–515 (2010)
10. Kothari, R., Sauerbeck, L., Jauch, E., Broderick, J., Brott, T., Khoury, J., Liu, T.: Patients' awareness of stroke signs, symptoms, and risk factors. *Stroke* **28**(10), 1871–1875 (1997)
11. Mandelzweig, L., Goldbourt, U., Boyko, V., Tanne, D.: Perceptual, social, and behavioural factors associated with delays in seeking medical care in patients with symptoms of acute stroke. *Stroke* **37**(5), 1248–1253 (2006)
12. Schroeder, E.B., Rosamond, W.D., Morris, D.L., Evenson, K.R., Hinn, A.R.: Determinants of use of emergency medical services in a population with stroke symptoms: the second delay in accessing stroke healthcare (DASH II) study. *Stroke* **31**(11), 2591–2596 (2000)
13. Jemal, A., Bray, F., Center, M.M., Ferlay, J., Ward, E., Forman, D.: Global cancer statistics. *CA Cancer J. Clin.* **61**(2), 69–90 (2011)
14. Alicikus, Z.A., Akman, F., Ataman, O.U., Dag, N., Orcin, E., Bakis, B., Kinay, M.: Importance of patient, tumor and treatment related factors on quality of life in head and neck cancer patients after definitive treatment. *Eur. Arch. Otorhinolaryngol.* **266**(9), 1461–1468 (2009)
15. Abendstein, H., Nordgren, M., Boysen, M., Jannert, M., Silander, E., Ahlner-Elmqvist, M., Hammerlid, E., Bjordal, K.: Quality of life and head and neck cancer: a 5 year prospective study. *Laryngoscope* **115**(12), 2183–2192 (2005)
16. Osthus, A.A., Aarstad, A.K., Olofsson, J., Aarstad, H.J.: Health-related quality of life scores in long-term head and neck cancer survivors predict subsequent survival: a prospective cohort study. *Clin. Otolaryngol.* **36**(4), 361–368 (2011)
17. Hanna, E.Y., Mendoza, T.R., Rosenthal, D.I., Gunn, G.B., Sehra, P., Yucel, E., Cleeland, C.S.: The symptom burden of treatment-naïve patients with head and neck cancer. *Cancer* **121**(5), 766–773 (2015)
18. Sankaranarayanan, R., Masuyer, E., Swaminathan, R., Ferlay, J., Whelan, S.: Head and neck cancer: a global perspective on epidemiology and prognosis. *Anticancer Res.* **18**(6B), 4779–4786 (1998)
19. Psoter, W.J., Aguilar, M.L., Levy, A., Baek, L.S., Morse, D.E.: A preliminary study on the relationships between global health/quality of life and specific head and neck cancer quality of life domains in Puerto Rico. *J. Prosthodont.* **21**(6), 460–471 (2012)
20. Erika, W., Griebisch, I., Lungershausen, J., Foster, T., Pashos, C. L.: The economic burden of head and neck cancer: a systematic literature review. *Pharmacoeconomics.* **32**(9), 865–882 (2014)
21. Demaerschalk, B.M., Yip, T.R.: Economic benefit of increasing utilization of intravenous tissue plasminogen activator for acute ischemic stroke in the United States. *Stroke* **36**(11), 2500–2503 (2005)
22. Emergency medical services statistics: Singapore Civil Defence Force Statistics (2014). Retrieved from <http://scdf.gov.sg>

Design of a Medical Expert System for Consulting Tuberculosis Diagnosis in Vietnam Rural Areas

Thi Ngoc Mai Nguyen, Quang Chung Tran, Tien Dat Duong, and Ngoc Anh Mai

Abstract

Tuberculosis is a serious infectious disease. Vietnam is one of the 20 countries with the highest TB incidence, and the mortality rate due to tuberculosis each year in Vietnam is nearly double than that due to traffic accidents. To assist physicians in Vietnam rural areas dealing with tuberculosis and reducing pressure on central hospitals, a medical expert system has been developed based on fuzzy logic rules to give advice for diagnosis and treatment of tuberculosis.

Keywords

Medical expert system • Tuberculosis • Diagnosis

1 Introduction

According to [1], Tuberculosis (TB) is an infectious disease caused by bacteria (*Mycobacterium tuberculosis*). TB can be seen at any parts of a human's body, of these, pulmonary tuberculosis (PTB) poses the most popular type and is the main source of TB transmission. Africa and Asia are two places having the majority number of TB incidence rates every year.

When *Mycobacterium tuberculosis* bacteria enter the lungs, they are usually walled off into harmless capsules (granulomas) in the lung, causing infection but not disease. These capsules may later wake up weeks, months or decades later causing active TB disease [2].

Under the report of WHO in 2016 [3], Vietnam is one of the 20 high TB burden countries and also experiences the highest rate of multidrug-resistant cases. Every year, it is estimated that there are 17,000 deaths relating to TB, nearly twice as much as the mortality rate caused by traffic accidents. However, central hospitals in the cities, where facilitate with advanced technologies to diagnose and cure the disease, seem to be overloaded due to the large number of patients. For this reason, it is necessary to have a solution of remoting coordination in order to reduce the burden of overloading patients for the central hospitals.

In the past decades, medical expert system (MES) has been strongly investigated into diagnosis of diseases in many hospitals. MESs are usually used for diagnosing a specific disease, teaching to medical students, advising to patients. However, this is not popular in Vietnam due to spending too much time and money on physicians and bioengineers.

There have been a lot of successful MESs for medical diagnosis in the world such as MYCIN [4], HERMES [5], PUFF [6]. Basically, they are a computer program that represents and reasons with knowledge of some specialist subjects with a view to solving problems or giving advice. With the tremendous growth of applying artificial intelligence in medical field, the automated and fast response programs allow reducing high risks of human errors process. Generally, MES is a computer program utilizing expert's knowledge to give advice about specific disease.

In some MESs, the fuzzy rules are used in inference engine because this kind of rules can deal with specificity, sensitivity, positive and negative predictive values for diagnosing. The fuzzy logic rules offer better results in cases of dealing with uncertainties and inexactness because they permit to align with human's thinking in evaluating and processing disease data.

In this research, an expert system, named QCTuber, for consulting diagnosis of Tuberculosis is programmed in Matlab software and uses fuzzy rules for its inferences. This expert system gets data from a patient to serve rule-based reasoning to address a consultancy for the clinical decision

T. N. M. Nguyen · Q. C. Tran (✉) · T. D. Duong
Biomedical Engineering Department, Le Quy Don Technical University, Hanoi, Vietnam
e-mail: chungbme@gmail.com

N. A. Mai
Advanced Technology Center, Le Quy Don Technical University, Hanoi, Vietnam
e-mail: maingocanh.atc@mta.edu.vn

of pulmonary tuberculosis and to assist physicians in rural areas dealing with the significant development of tuberculosis, multidrug-resistant and reducing pressure on central hospitals.

The structure of the paper is organized as follows: The design of search tree for the fuzzy-based MES is introduced in the second section; the setup of the fuzzy inference system is presented in the third section; after that, the user interfaces are described.

2 Design of Fuzzy-Based MES

The principle diagram of the fuzzy-based MES for diagnosis is shown in Fig. 1 with four modules: Fuzzifier, Rules, Inference Engine, and Defuzzifier.

The input data of the system are the symptoms and test results of a tuberculosis patient. These symptoms and test results are then fuzzified into fuzzy sets by the module Fuzzifier and provide them for the module Inference Engine, where the input data are compared to the given rules (in module Rules) represented from the physician expert knowledge to produce the fuzzy result set. After the fuzzy inference, the fuzzy results are defuzzified to crisp results by the module Defuzzifier. Based on the crisp results, the system produces an output decision for consulting PTB diagnosis.

The physician expert knowledge of tuberculosis diagnosis is stored in the module Rules and is represented by a search tree in Fig. 2. This is a search tree for diagnosis of pulmonary tuberculosis (PTB) consisting of two main branches: Clinical diagnosis and Definitive diagnosis.

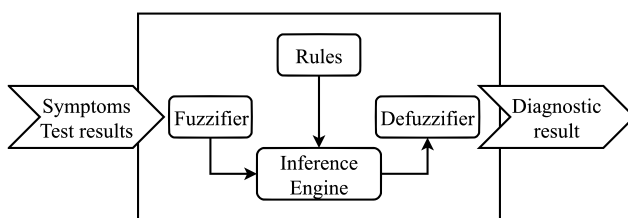


Fig. 1 Principle diagram of the fuzzy-based MES for PTB diagnosis

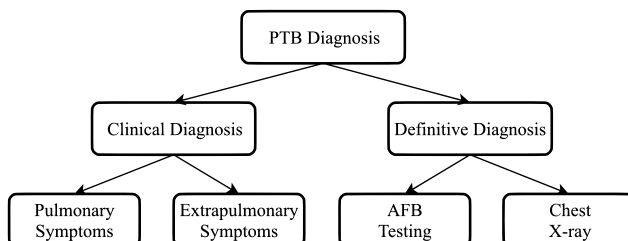


Fig. 2 The search tree for PTB diagnosis

In the nodes of the search tree, the rules for diagnosis are added. In fact, the rules taken from the knowledge of the physician experts are normally vague and rather complicated for the computer to understand. Therefore, it is necessary to make the complicated rules simpler and turn the vague rules into fuzzy logic ones.

The fuzzy logic rules in the module Rules are formulated by the basic form:

$$\text{IF } A_i \text{ THEN } X_i \quad (1)$$

From the basic form, several variant forms can be created as follows:

$$\text{IF } A_i \text{ AND } B_i \text{ THEN } X_i \quad (2)$$

$$\text{IF } A_i \text{ OR } B_i \text{ THEN } X_i \quad (3)$$

where

- A_i and B_i are crisp values defined under physician expert's knowledge of PTB;
- X_i is a crisp value represented for a singular conclusion of the expert.

During developing a fuzzy-based MES, we may cope with many complex and vague rules such as:

$$\text{IF } A_i \text{ AND } B_i \text{ THEN } X_i \text{ OR } Y_i \quad (4)$$

For example, the rule “IF *extreme-cough* AND *high-fever* THEN *acute-pneumonia* OR *severe-tuberculosis*” is rather complicated for programming. Fortunately, by using the formula (2) and (3), we can simplify (4) as follows:

$$\left\{ \begin{array}{l} \text{IF } A_i \text{ AND } B_i \text{ THEN } X_i \\ \text{IF } A_i \text{ AND } B_i \text{ THEN } Y_i \end{array} \right. \quad (5)$$

Let us see again the given example, the rule “IF *extreme-cough* AND *high-fever* THEN *acute-pneumonia* OR *severe-tuberculosis*” now becomes less complicated with two new rules: (i) “IF *extreme-cough* AND *high-fever* THEN *acute-pneumonia*”; (ii) “IF *extreme-cough* AND *high-fever* THEN *severe-tuberculosis*.”

It can be recognized that from a complex rule, we can simplify to many simpler ones. This allows the fuzzy-based MES easier to setup fuzzy logic rules and allows the computer program to operate more effectively. For this reason, the method of simplifying complicated rule to simple rules is adopted as the basic principle of developing diagnosis rules for the fuzzy-based MES.

Now we analyze again the search tree in Fig. 2, the clinical diagnosis is executed based on the tuberculosis symptoms concerning sputum, urine, or cerebrospinal fluid. These symptoms can be divided into two kinds of

pulmonary and extrapulmonary symptoms. Pulmonary symptoms usually concern lung symptoms and cough symptoms. The lung symptoms and cough symptoms are used as A_i and B_i to create fuzzy rules similar to the formula (5). On the other hand, extrapulmonary symptoms usually related to larynx, pleura, brain, bones, and joints [7] are utilized as A_i and B_i to create fuzzy rules. The clinical symptoms are pre-screened by a physician in a rural hospital.

The definitive diagnosis is completed in a laboratory of bacteriologic examination involving Acid-Fast Bacilli (AFB) tests and chest X-ray. Technically, definitive diagnosis is performed in higher-level hospitals such as district or provincial hospitals.

According to [8], to make the diagnosis easier for the patient during the daytime, two sputum samples should be tested instead of three sputum samples. The AFB tests use 2 patient's sputum samples to find out the presence of tuberculosis bacteria. Clinical diagnosis indicates whether the patient's symptoms that they present are related to tuberculosis, so clinical diagnosis should be made prior to the definitive diagnosis.

Normally, AFB tests concern in five periods: AFB specimen collection, processing, and review; AFB smear classification and results; Direct detection of tuberculosis in AFB specimen; AFB specimen culturing and identification; Drug-susceptibility testing [9].

The module of Inference Engine executes an inference algorithm as the illustration in Fig. 3. First of all, the MES accomplishes a fuzzy inference based on the inputs as a result of AFB test. If the result of AFB test is positive (1 out of 2 sputum samples is positive), the result of fuzzy inference is a fuzzy value in a range of 0–1. The fuzzy logic rules in the module Inference Engine have the similar forms as (1), (2), and (3). The only difference is that the value of A_i and B_i are fuzzy instead of crisp.

For example, if the results of AFB test are 2 values at the boundary of negative and positive values. They must be fuzzified into 2 fuzzy values a and b , with both a and b in the interval $[0, 1]$. These fuzzy values represent the membership levels of a with A_i and b with B_i . Assuming that two fuzzy rules i and j concern in the input values a and b , as follows:

$$\begin{cases} \text{IF } a_i = \text{positive} \text{ OR } b_i = \text{positive} \text{ THEN } x_i = \text{positivePTB}(k_i) \\ \text{IF } a_j = \text{negative} \text{ AND } b_j = \text{negative} \text{ THEN } x_j = \text{chestXray}(k_j) \end{cases} \quad (6)$$

where k_i and k_j are certain factors of possibility.

In the case of multiple output like (6), a fuzzy inference must be carried out as the following:

$$X = \frac{k_i x_i + k_j x_j}{k_i + k_j} \quad (7)$$

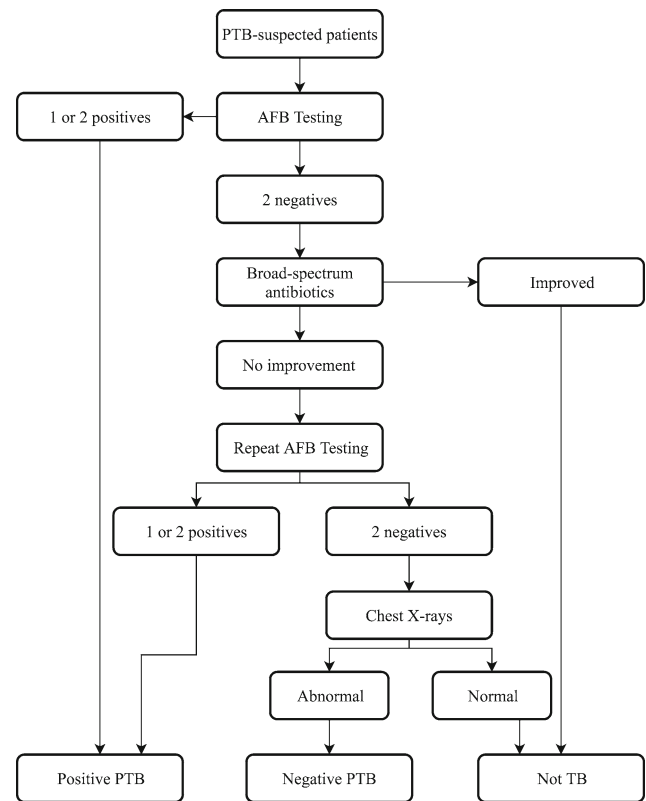


Fig. 3 Fuzzy inference algorithm of PTB diagnosis

where X is a fuzzy conclusion that harmonizes the output values of the possible rules concerning the patient.

Equation (7) represents the principle of fuzzy inference in the MES. The output of the Eq. (7) is a fuzzy value. Hence, it is defuzzified at the module Defuzzifier.

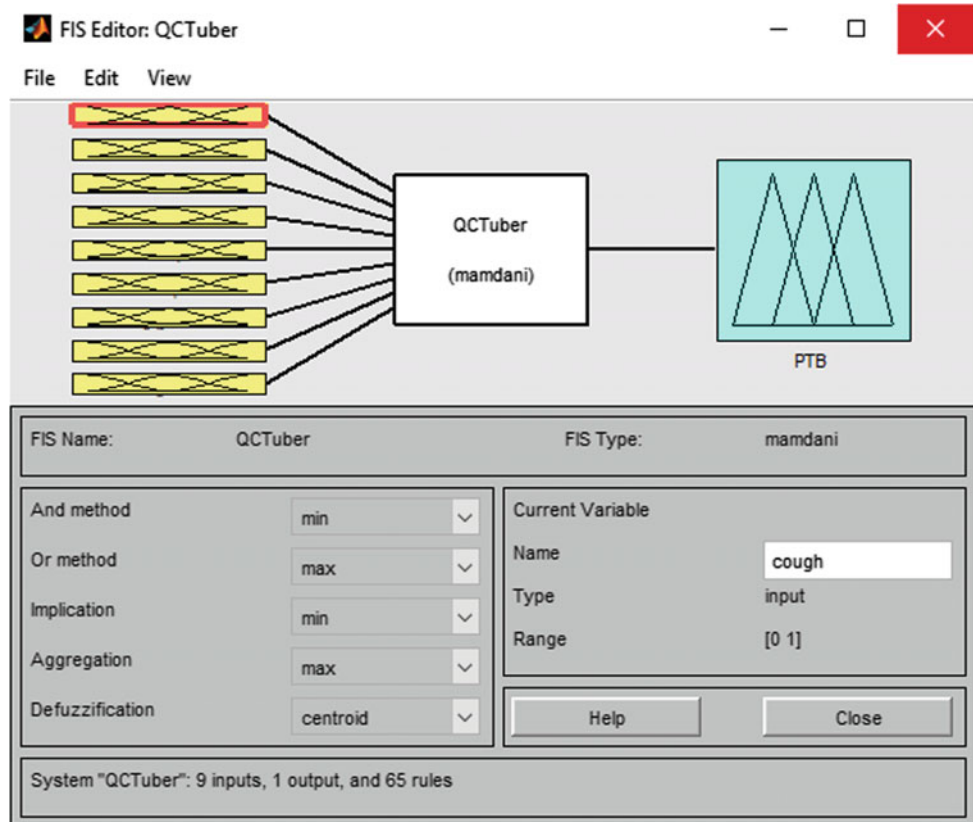
The broad-spectrum antibiotics treatment (not anti-TB drugs) is only effective against respiratory bacteria that does not work with PTB bacteria. Therefore, if symptoms are improved, the patient is not infected with PTB. In contrast, the AFB test should be repeated. It is noticeable that there are two times of performing AFB tests, which are similar to each other but not the same.

Once the second AFB test result is positive, the patient is diagnosed with having positive PTB, and chest X-ray scan is carried out when the result is negative. The injury in the patient's pulmonary shows that the patient has smear-negative PTB. Otherwise, if there is no injury found in the X-ray image, the patient is not infected with PTB.

3 Setup Fuzzy Inference System

Based on the expert's knowledge of tuberculosis, the fuzzy inference system called QCTuber is settled with 9 inputs and 1 output as demonstrated in Fig. 4. The inputs include 8

Fig. 4 The fuzzy inference system for PTB diagnosis



common clinical symptoms of PTB and 1 outcome of chest X-ray scan described in [9]. The clinical symptoms are lingering cough, coughing up blood, mild fever in the afternoon, unexplained weight loss, chest pain, loss of appetite, fatigue, night sweats. The output of the fuzzy inference system is the suggestion for the patient concerning PTB diagnosis.

We denote:

$S = \{S_1, S_2, \dots, S_9\}$: set of symptoms.

μ (degree value) is a number in the interval $[0, 1]$. The value μ is divided into μ_S and μ_D as follows:

- $\mu_S = 1$ means the symptom definitely present in patient;
- $\mu_S = 0$ indicates that the symptom definitely absents in patient;
- $0 < \mu_S < 1$ is equivalent to the possibility of appearance of symptom. μ_r is a number in the interval $[0, 1]$;
- $\mu_D = 1$ means patients definitely have PTB;
- $\mu_D = 0$ indicates patients do not have PTB;
- $0 < \mu_D < 1$ is equivalent to the possibility of PTB infection.

The membership value of μ is illustrated in Fig. 5.

The inference machine structure of the QCTuber is based on the standard structure of MESs such as the TUBERDIAG

Inputs/Output	Levels	Geometric shape	Interval
cough	less	trapmf	[0 0 0.2 0.3]
	moderate	trapmf	[0.55 0.65 1 1]
	extreme	trapmf	[0.2 0.35 0.6 0.65]
hemoptysis (coughing up blood)	no	zmf	[0.4 0.6]
	yes	smf	[0.4 0.6]
fever	no	zmf	[0.4 0.6]
	yes	smf	[0.4 0.6]
weight_loss	no	zmf	[0.4 0.6]
	yes	smf	[0.4 0.6]
chest_pain	no	zmf	[0.4 0.6]
	yes	smf	[0.4 0.6]
lost_of_appetite	no	zmf	[0.4 0.6]
	yes	smf	[0.4 0.6]
fatigue	no	zmf	[0.4 0.6]
	yes	smf	[0.4 0.6]
night_sweats	no	zmf	[0.4 0.6]
	yes	smf	[0.4 0.6]
cxr (chest x -ray)	no	trapmf	[0 0 0.05 0.1]
	low	trapmf	[0.05 0.1 0.25 0.3]
	high	trapmf	[0.2 0.3 0.65 0.75]
PTB (output)	severe	trapmf	[0.65 0.7 1 1]
	no	zmf	[0.4 0.6]
	yes	smf	[0.4 0.6]

Fig. 5 The membership values μ for PTB diagnosis

expert system [10] for TB diagnosis and LDDS expert system [11] for detecting the lung diseases.

The knowledge base of QCTuber comprises 65 fuzzy rules with the basic form as follows:

$$\text{IF } \langle S_1, S_2, \dots, S_9 \rangle \text{ THEN level of PTB} = \mu_{D_i}, (k_i) \quad (8)$$

After all the rules are implemented, system will aggregate the outputs of the rules by the maximizing method. Then, defuzzification is the last step of inference process. The defuzzification used in QCTuber is the centroid method. The mathematical expression for fuzzy inference is similar to (7):

$$\mu_D = \frac{\sum_{i=1}^n \mu_{D_i} \cdot k_i}{\sum_{i=1}^n k_i} \quad (9)$$

where n is a number of invoked fuzzy rules concerning the situation of the patient.

The inference engine of QCTuber performs diagnosis in 3 steps:

Step 1: Clinical diagnosis: Evaluate patient's symptoms to find out chances they have level of PTB (μ_D). If μ_D is greater than certain number ε (the number ε is determined based on the experience of the physician, where $\varepsilon = 0.3$), then go to step 2. If not, go straight to step 3.

Step 2: Definitive diagnosis: The system requires 2 sputum samples to look for bacteria, the AFB test and the result of chest X-ray image. QCTuber utilizes those inputs in combination with symptoms in step 1 to recalculate μ_D .

Step 3: Conclusion: Using results from step 1 and step 2 in the combination of Eq. (9) to give out the final result concerning the possibility of PTB.

4 Design of User Interface

The whole program of the MES is written in Matlab, one of the most popular programming software for biomedical engineers. The MES, namely QCTuber, has 4 layers of user interface: Beginning layer; Clinical diagnosis layer; Definitive diagnosis layer and Diagnostic Consult layer.

The beginning interface is displayed in Fig. 6. The interface gives instructive information about diagnostic steps

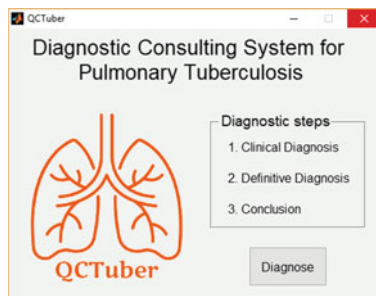


Fig. 6 User interface for first instruction

including Clinical diagnosis, Definitive diagnosis, and Conclusion.

The next layer is the first clinical diagnosis. This window pops up when users click on the Diagnosis button in the beginning interface. Eight typical symptoms of PTB that have been mentioned above will be listed in this interface.

After pressing the Next button in Fig. 7 (right), the system will evaluate the possibility that the patient has PTB μ_D based on user's answers. If μ_D is not greater than ε then QCTuber will show the Diagnostic result interface like in Fig. 9 on the left. In contrast, the definitive diagnosis is recommended.

The left side of Fig. 8 displays the user interface of definitive diagnosis on AFB test results. If μ_D is greater than ε , this interface will show up. The right side of Fig. 8 is the definitive diagnosis of any injury in patient's lung based on chest X-ray image.

There are 2 kinds of information on the left side of Fig. 9. The written information in the above white box tells user that he/she is not infected with PTB. The below pie chart implies the percentage of PTB infection (red color) and not PTB infection (green color). Similarly, the diagnostic consultancy on the right side of Fig. 9 tells the user that the patient is diagnosed with PTB and the percentage of its possibility.

As a result of the study, the designed program is not meant to use for the doctors at the district or provincial hospitals because they can directly give the diagnosis as the experts. However, this program is really useful in rural hospitals where competent physicians are both lack in quality and quantity. The outputs of the program are used as suggestions for giving followed-up treatment regimen whether they will be treating at home, inpatient or transferring to the provincial hospitals. The significance of the suggestions is to reduce the over-crowded problems in the provincial hospitals.

5 Conclusion

The paper presents the design of medical expert system QCTuber for consulting diagnosis of Tuberculosis. QCTuber is written in Matlab and uses fuzzy logic tools for designing the fuzzy inference system.

The program is designed with the simple and intuitive user interface to help physicians in Vietnam rural areas be more confident throughout medical practices.

In the next period, QCTuber needs enriching the knowledge base, increasing the number of fuzzy rules, and improving the user interface. After that, several experiments will be performed under the patient data of the rural hospitals

Fig. 7 User interface for first clinical diagnosis and for final clinical diagnosis

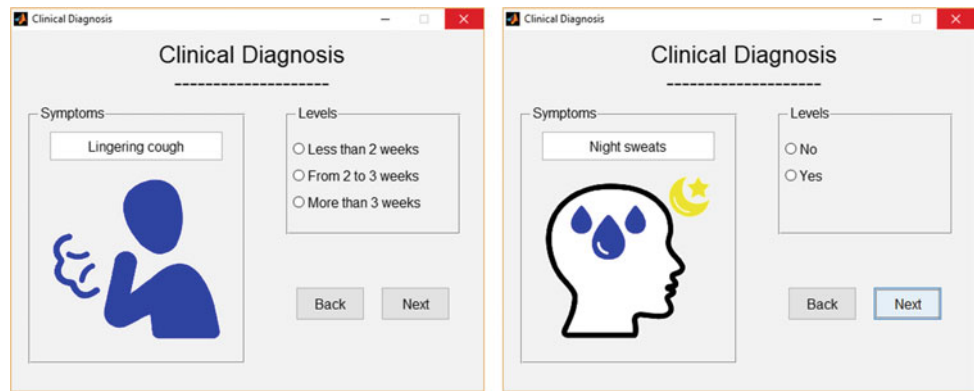


Fig. 8 User interface of definitive diagnosis for AFB test and Chest X-ray results

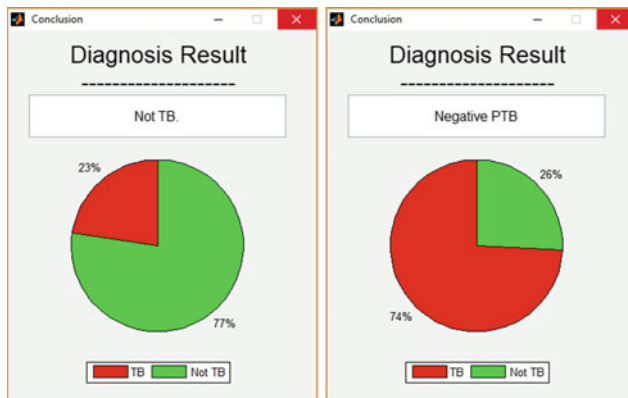
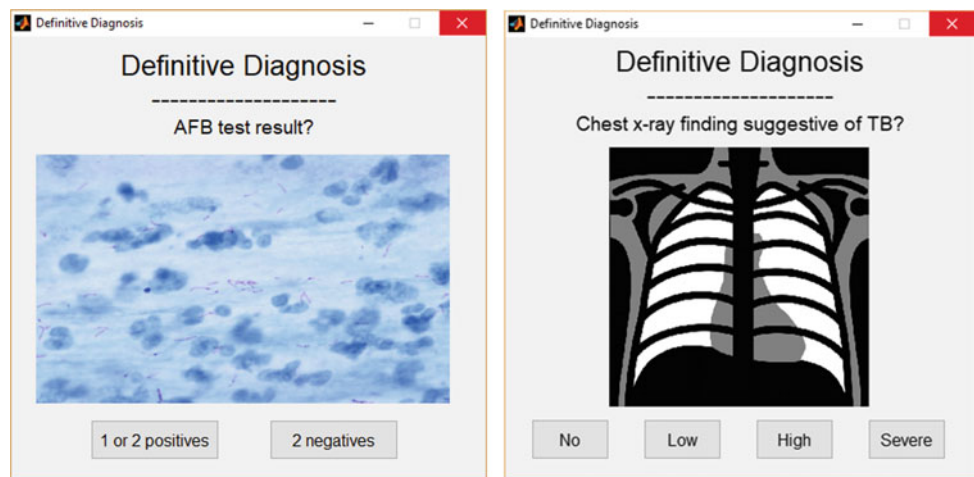


Fig. 9 User interface for consulting

Acknowledgements The biomedical engineers express the highly appreciation to the Department of Biomedical Engineering of Le Quy Don Technical University for their supports.

Conflict of Interest The authors declare that they have no conflict of interest.

References

1. WHO: Global Tuberculosis Report 2017. WHO, Geneva (2017)
2. ATS: We help the world breathe. *Am. J. Respir. Crit. Care Med.* **195**, 7–8 (2017)
3. WHO: Global Tuberculosis Report 2016. WHO, Geneva (2016)
4. Meena, A.K., Kumar, S.: Study and analysis of MYCIN expert system. *Int. J. Eng. Comput. Sci.* **4**(10), 14861–14865 (2015), ISSN 2319-7242

5. Bonfa, I., Sarti, F., Maioli, C., Monte, P.D.: HERMES: an expert system for the prognosis of hepatic diseases. In: Technical Report UBLCS-93-19 (1993)
6. Aikins, J.S., Kunz, J.C., Shortliffc, E.H., Fallat, R.J.: PUFF: an expert system for interpretation of pulmonary function data. In: Technical report No. STAN-CS-82-931, Stanford University (1982)
7. CDC: Core Curriculum on Tuberculosis: What the clinician should know. National Center for HIV/AIDS, Viral Hepatitis, STD, and TB Prevention, Chap. 2, p. 30 (2013)
8. Vietnam Ministry of Health: Guidance of diagnosis, treatment, and prevention of Tuberculosis. In document 4263/QD-BYT, 13.10.2015, p. 1, Sect. 2.2
9. CDC: Core Curriculum on Tuberculosis: What the clinician should know. National Center for HIV/AIDS, Viral Hepatitis, STD, and TB Prevention, Chap. 4, p. 79–83 (2013)
10. Phuong, N.H., Hung, D.H., Co, N.V., Duong, B.D., Thinh, P.T., Hoa, N.P., Linh, N.N.: TUBERDIAG: an expert system for pulmonary tuberculosis diagnosis. *Int. J. Uncertainty Fuzziness Knowl. Based Syst.* **7**(4), 371–381 (1999)
11. Phuong, N.H., Nghi, L.H., Cho, H., Kwak, Y.S.: LDDS—a fuzzy rule based lung diseases diagnostic system combining positive and negative knowledge

Oral Impacts on Daily Performances of Children 12 and 15-Year-Old in Can Tho City

H. G. Do, K. N. Truong, D. H. Pham, L. T. Quynh Ngo, H. T. Tran, and N. Doan

Abstract

The oral discomforts are still popular and impact on daily activities, reduce quality of life of the patients. *Aim* The objectives of this study were to determine the prevalence, intensity, and extent of the impacts, caused by oral problems on 12- and 15-year-old children in Can Tho city. *Materials and methods* 407 children at 12 and 402 children at 15 from 10 out of 62 secondary schools in 9 urban and suburban districts in Can Tho city were selected into the study by probability proportional to size sample selection method. Vietnamese child version of the Oral Impact of Daily Performances (Child-OIDP) was employed to evaluate oral impacts on 8 daily activities. *Results and discussion* The prevalence of oral impacts was 87% of children at 12 and 78.6% of those at 15. The most frequently impacted among daily performances was eating (64.6% 12-year-old pupils, 53% those at 15), then next was cleaning mouth, emotion, and smiling. Among children with impacts, 36.4 and 15.2% children (at 12 and 15 respectively) reported impacts on more than five daily activities and with severe to very severe intensity

relatively high (16.7 and 11% sequentially). *Conclusion* Oral impacts on daily performances were very common, rather wide but not severe among children at 12 and 15 years old in Can Tho province. Affects on the former were more than on latter, in urban districts were higher than suburban ones significantly. The common reasons were tooth decay, toothache, oral ulcer, swollen gums and sensitive tooth.

Keywords

Child-OIDP • Oral impact • Daily activities

1 Introduction

Report of the World Health Organization in 2008 [1] on global oral health, periodontal disease and tooth decay were still two common oral diseases, affecting human health, psychological, physiological and social activities, daily life and reducing quality of life of the patient.

The methods of treatment as well as researches of oral health in traditional way usually concentrated on studying and solving the problems of diseases, mainly focusing on having or not having the diseases, reporting health status according to clinical indicators and ignoring subjective perception of patients about health and illness as well as their impact on patients' daily lives. Therefore, the concept of "Oral Health-Related Quality of Life" was born, fully met the definition of health and oral health of the World Health Organization. Along with the launch of this, the socio-dental health indicators appeared and were more and more widely used to assess the impacts of oral health problems on quality of life.

However, generally in Vietnam and particularly in Can Tho city, there were very few studies about oral health, using socio-dental indicators. Therefore, this study was undertaken to assess the impact of oral health problems on daily activities of 12 and 15-year-old children in Can Tho.

H. G. Do · K. N. Truong · D. H. Pham
Faculty of Odonto-Stomatology, Can Tho University of Medicine and Pharmacy, Can Tho, Vietnam

L. T. Q. Ngo
Faculty of Odonto-Stomatology, Ho Chi Minh University of Medicine and Pharmacy, Ho Chi Minh City, Vietnam

H. T. Tran
Can Tho Medical College, Can Tho, Vietnam

N. Doan (✉)
Griffith University School of Dentistry and Oral Health,
Gold Coast, Australia
e-mail: nvtdoan123@gmail.com; nvtdoan23@gmail.com

N. Doan
The University of Queensland & Queensland University of Technology, Brisbane, Australia

2 Materials and Methods

The research targeted all children at 12 and 15 years old in the Can Tho city in 2011 as the children are in pre and early teen and are prone to oral health diseases due to poor habit. No previous similar study has been done in Can Tho province before. Furthermore, the principal research is a staff of Can Tho University and Pharmacy. Therefore, it is feasible to conduct the study at the chosen location. Sample population was 6th and 9th class pupils of the 2010–2011 school year in secondary schools. Using sample size calculation with type 1 error probability of a maximum of 5% and sampling method of cluster sampling of Probability Proportional to Size, 400 of 6th and 400 of 9th grade pupils were selected from 10 schools (6 schools in urban and 4 ones in rural area) among 62 junior high schools in 9 districts of Can Tho city. There were 3 interviewers who were qualified and trained dentists for this survey at the above-mentioned schools. These interviewers collected all the identified information. The University of Medicine and Pharmacy Ethics Committee approved this study as well as local authority. Consent from participants also was obtained.

The Vietnamese version of the questionnaire Child Oral Impacts on Daily Performance (Child-OIDP) [8] was used. This Vietnamese version was previously validated and used in two previous studies in Ho Chi Minh City. First, children were delivered questionnaire, listing dental discomforts and under the guidance and interpretation of the investigators, they marked a cross on those that they had encountered in the past three months. Secondly, they were interviewed to assess whether these oral problems had impacted on their daily activities, including: (1) eating food, (2) speaking clearly, (3) cleaning mouth, (4) relaxing including sleeping and resting, (5) laughing (smiles, big laughs without embarrassment), (6) spiritual comfort, (7) learning and doing homework, (8) contacting to people. If the answer is “yes” in any activities, interviewers would ask about the frequency, the severity and the reasons for that daily activity impact. The frequencies were evaluated with a scale between 1 and 3. If impaction was on regular basis, scale was classified: (1) 1 or 2 times/month; (2) 3 or more than 3 times/month or 1 or 2 times/week; (3) 3 or more than 3 times/week. If impaction was infrequently or less than 1 times/month, scale was based on the total number of affected days during the last 3 months: (1) 1 to 7 days; (2) 8 to 15 days; (3) over 15 days. The severity was scored from 1 to 3: (1) effected slightly (slightly difficult to perform activities); (2) average impacted (difficult to implement activities); (3) severely impacted (unable to perform activities). Thirdly, from the questionnaire about the dental discomforts that children completed crossing at first step, interviewers asked which of them were the causes of impactions. If at the second stage,

children answered “no”, score of 0 would be filled for both the frequency and severity of the impact on daily activities.

For data analysis, the Child-OIDP score of each affected daily activity was calculated by multiplying the frequency scale with severity scale (the lowest score was 0 and the highest one was 9). The total OIDP score of eight daily activities were the total Child-OIDP score of eight activities (ranging from 0 to 72) divided by 72 and then multiplied by 100 to render percentage score, valuing from 0 to 100%. The prevalence of oral impact on daily activities was measured by the proportion of children having at least one daily activity with Child-OIDP scores greater than 0. The intensity of impact on each activity was categorized into five levels based on its child-OIDP score: (1) very slight (1 score); (2) slight (2 score); (3) moderate (3 to 4 score); (4) severe (5 to 6 score), and (5) very severe (7 to 9 score). The extent of influences is the number of daily activities impacted (lowest was 0 and the largest was 8).

When comparing the impacts of oral problems on daily activities between 12 and 15 years-old children, between urban and rural areas, Chi-squared test and Fisher’s test were used to compare the percentages, Mann-Whitney test was used to compare means.

3 Results

The sample had a total of 809 children, including 407 children of 12 years old and 402 children of 15 years old [Table 1 and 2]. No differences on the distribution ratio of male and female in each age group as well as between urban and rural areas.

3.1 Effects of Oral Discomforts on Children Activities

In 12-year-old sample, the percentage of children, affected by oral issues on daily activities was 87%, Child-OIDP mean score was 9.16 ± 9.28 , and average number of impacted daily activities was 3.7 ± 1.9 . All were higher than that of 15-year-old children (78.6%; $5.63 \pm 7.07\%$; 2.8 ± 1.62 respectively) (Tables 1 and 2).

The most affected activity in both ages was eating, whereas the least one was speaking. In the impacted group, 83.3% of children at 12 and 88.9% those at 15 suffered from very slight to moderate level, while those with severe to very severe level were 16.7 and 11% sequentially. Laughing, eating, cleaning mouth of children at 12 years old were impacted severely to very severely, while in 15-year-old ones, they were speaking, relaxing and contacting to people.

Comparison between urban and rural areas had statistically significant difference in all activities in both

Table 1 The proportion of affected children, Child-OIDP scores and levels of impacts of dental issues on 12 year-old children’s daily activities

Activities	n	%	Child-OIDP mean score	Impact level (%)				
				Very slight	Slight	Moderate	Severe	Very severe
Eating	263	64.6	1.31	56.7	17.9	17.9	6.1	1.5
Speaking	45	11.1	0.20	60	22.2	11.1	6.7	0
Cleaning	213	52.3	1.10	54.5	18.8	19.2	4.2	3.3
Relaxing	87	21.4	0.44	50.6	21.8	21.8	4.6	1.1
Spirits	206	50.6	1.01	54.9	21.8	17.5	3.9	1.9
Laughing	202	49.6	1.19	42.1	23.3	22.3	9.9	2.5
Learning	107	26.3	0.47	57.9	24.3	13.1	4.7	0
Contacting	185	45.5	0.88	54.6	21.1	19.5	2.7	2.2
Whole	354	87	9.16	33.3	20.3	29.7	11.6	5.1

Table 2 The proportion of affected children, Child-OIDP scores and levels of impacts of dental issues on 15-year-old children’s daily activities

Activities	n	%	Child-OIDP MEAN score	Impact level (%)				
				Very slight	Slight	Moderate	Severe	Very severe
Eating	213	53	0.90	65.3	18.3	11.7	3.8	0.9
Speaking	14	3.5	0.07	64.3	7.1	14.3	14.3	0
Cleaning	161	40	0.64	68.3	12.4	17.4	1.9	0
Relaxing	48	11.9	0.27	56.2	14.6	16.7	10.4	2.1
Spirits	158	39.3	0.75	60.1	17.7	15.8	4.4	1.9
Laughing	123	30.6	0.61	57.7	14.6	21.1	4.1	2.4
Learning	57	14.2	0.28	50.9	26.3	15.8	5.3	1.8
Contacting	112	27.9	0.53	65.2	11.6	16.1	4.5	2.7
Whole	316	78.6	5.63	48.4	19	21.5	8.2	2.8

percentages and means of child-OIDP score (except for cleaning mouth in both ages and for eating and speaking in 15-year-olds) but only cleaning mouth of children at 15 ages had significant difference in impact level. 12-year-old urban children had more affected daily activities than rural ones significantly (3.28 ± 1.79 vs. 4.24 ± 1.92), but it was contrast in the age of 15 (2.48 ± 1.46 vs. 3.27 ± 1.72).

3.2 Reasons of Daily Activity Impact

94.1% children at 12 and 92.5% that of 15 had encountered at least one dental discomfort in the last 3 months. Among them, 93.2% of former and 84.7% of latter had impact on daily activities with an average of 3.41 ± 2.08 and 2.37 ± 1.8 activities.

Five major dental discomforts blamed for impacting on children’s daily lives were shown in Figs. 1 and 2.

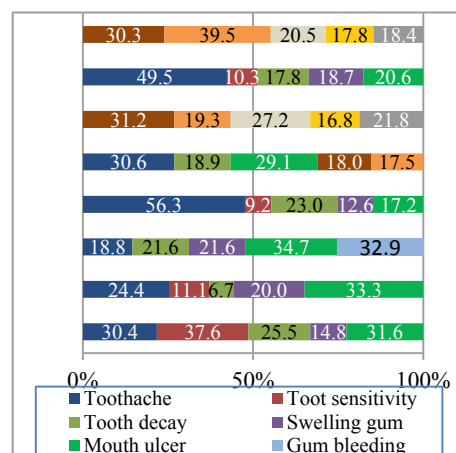


Fig. 1 The most common causes of 12 year-old children affecting their daily activities

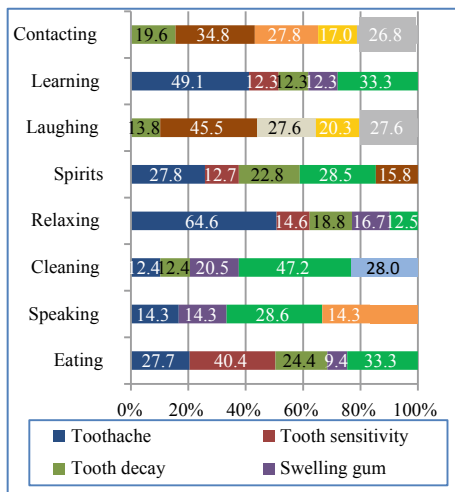


Fig. 2 The most common causes of 15 year-old children affecting their daily activities

Toothache, tooth decay and mouth ulcer were the most common dental problems in children at 12 age, affecting 6 out of 8 daily activities; swollen gum was the second, impacting 5 activities; tooth sensitivity was the third popular, causing 4 activities' difficulty. In children at age of 15, dental decay was still the most popular reason, accounting for 7 activities; toothache and ulcers in the mouth became second cause with 6 activities affected; swelling of the gums fell to third position with 5 activities; tooth sensitivity and tooth colored were ranked third place with 3 activities.

4 Discussion

The impact of oral health on daily activities of children in Can Tho city was very common, 87% of 12-year-old and 78.6% of 15-year-old children when interviewed said at least one daily activity was affected in the past three months, the most affected one was eating (64.6% of children at age 12 and 53% of age 15). This result was consistent with studies, in Ho Chi Minh City [2] the percentage of pupils at grade 5 in an elementary schools impacted by dental problems was 80.6%, in Peru [3] was 82%, in South Africa [4] was 88%, New Zealand [5] and France [6] was 73%, in Thailand [7] was 85.2%. This indicated that the impact of oral health on quality of life were common in children of this age and influence on eating always accounted for the highest percentage of all the activities.

Extent of oral health impact was quite wide. On average, each child at 12 years old when affected would have difficulty in the implementation of 3.7 ± 1.9 activities higher than that of 15-year-old children (2.8 ± 1.62). The percentage of children at age 12 affected more than 5 daily activities was 36.4% also higher than that of age 15 (15.2%).

This result was higher than study in Peru [3], 2.7 ± 1.5 activities in average and only 12.3% of children were affected more than 5 activities.

The effect of oral health on quality of life of Can Tho children was not severe. 83.3% children at 12 and 88.9% ones at 15 were affected at level from very slight, slight to moderate. Activities with highest proportion of severe to very severe impacted level among 12 year olds was laughing (12.4%), eating (7.6%), mouth cleaning (7.5%), speaking (6.7%); while 15 year olds had speaking (14.3%), relaxing (12.5%), contacting (7.2%), learning (7%). This result was consistent with study in Thailand [7] that the impact of oral health on quality of life of the child was not serious; eating food, laughing and mouth cleaning was three activities that had highest proportion of severely to very severely impacted level in children at 12 and 15 years old.

94.1% of children age 12 and 92.5% of age 15 had at least 1 among 18 dental discomforts in the past 3 months. Each child at age of 12 encountered 4.22 ± 2.8 dental problems, maximum value was 14; this value was higher than that of 15-year-old child, which was 3.33 ± 2.26 , maximum was 13. The most frequent discomforts in children at 12 years old were calculus (45.5%), dental caries (42.5%), tooth sensitivity (40%), ulcers in the mouth (36.6%), bad tooth color (33.4%). The order in age-15 children were different, tooth decay (41.3%), calculus (39.1%), tooth sensitivity (38.6%), bad teeth color (37.1%), ulcers in the mouth (32.8%).

Among children at age 12 and 15 having dental discomforts, 93.2% and 84.7% respectively felt that at least one daily activity was affected. One 12 year-old child was impacted 3.41 ± 2.08 daily activities, much higher than in child of age 15, 2.37 ± 1.8 . Common dental problems that 12 year-old children met and usually affected on their lives were toothache (91.4%), swelling gums (84.4%), mouth ulcers (80.5%), tooth sensitivity (69.3%), bad breath (68.8%) and dental caries (66.5%). 15-year-old children had dental pain (82%), ulcers (74.2%), swelling gums (67.6%), tooth sensitivity (62.6%), bad breath (60%).

In brief, tooth decay, gum disease and mouth ulcers are the common dental problems that children age 12 and 15 encountered in the past three months and affected most on children's daily activities. This result was consistent with studies in Thailand [7] showed that ulcers in the mouth was at the second position after tooth decay in both the proportion of encounter and impact score. Although the influence of mouth ulcers on the children's daily activities was pretty much but due to one characteristic of the ulcers which was often in a short time, they was not adequately noticed in the program of oral health care as well as rarely discovered in studies using clinical indicators. Therefore, to achieve the goal of health as definition of health and dental health by the World Health Organization, in addition to the problems of tooth decay and periodontal

disease, we need to pay more attention on the issue of mouth ulcers in both comprehensive treatment and prevention for individuals. Mouth ulcers were the unexpected major finding in this study. Hence, it is recommended for future study to carry out clinical assessment to validate the survey findings especially the extent of mouth ulcers in students.

5 Conclusion

The oral impact on daily activities of 12 and 15 year-old children in the Can Tho city was quite common, occurred in all three types of activities: physical, mental and social, was rather broad in extent, influencing many activities but was not severe. The impact was higher on children at age 12 than ones at age 15, higher in rural areas than in urban areas. The main dental problems that were blamed for impacting on the daily activities of children living in Can Tho city were tooth decay, toothache, mouth ulcers, swollen gums and tooth sensitivity.

Conflict of Interest The authors declare that they have no conflict of interest.

References

1. Petersen, P., et al.: Global oral health of older people-call for public health action. *Community Dent. Health* **27**(4), 257–267 (2010)
2. Khanh, N.T.N.: Oral impact on daily performances of pupils at grade 5 of 2 elementary school in district 5, Hochiminh city. Graduation essay of doctor of odonto-stomatology, university of medicine and pharmacy at Hochiminh city (2005)
3. Bernabé, E.: Intensity and extent of oral impacts on daily performances by type of selfperceivedoral problems. *Eur. J. Oral Sci.* **115**, 111–116 (2007)
4. Naidoo, S., Chikte, U.M., Sheiham, A.: Prevalence and impact of dental pain in 8–10-year-olds in the western Cape. *S Afr. Dent. J.* **56**, 521–523 (2001)
5. Chen, M.S., Hunter, P.: Oral health and quality of life in New Zealand: a social perspective. *Soc. Sci. Med.* **43**, 1213–1222 (1996)
6. Tubert-Geannin, S., Pegon-Machat, E., Griemeau-Richard, C., Lecuyer, M., Tsakos, G.: Validation of a French version of the Child-OIDP index. *Eur. J. Oral Sci.* **113**, 355–362 (2005)
7. Krisdapong, S.: Oral health-related quality of life of 12- and 15-year-old Thai children: findings from a national survey. *Community Dent. Oral Epidemiol.* **37**, 509–517 (2009)
8. Gherunpong, S.: Developing and evaluating an oral health-related quality of life index for children, the CHILD-OIDP. *Community Dent. Health* **21**(2), 161–169 (2004)

An Evaluation on Initial Deficiency of Left Ventricular Systolic Function in Patients with Systemic Hypertension by Speckle Tracking Echocardiography

D. T. Nguyen, V. A. Nguyen, L. D. Do, and N. Doan

Abstract

Background Speckle tracking echocardiography 2D (STE 2D), a new technology, allows rapid and accurate analysis of regional and global left ventricular systolic function. **Aim** The aim of this study was to assess subclinical left ventricular systolic dysfunction in the patients with systemic hypertension with preserved ejection fraction by using STE 2D. **Methods** 2D echocardiography images of left ventricular were acquired in six sections-apical 4-chamber, 2-chamber, 3-chamber, parasternal short axis at the basal, mid, and apical levels in 194 subjects (151 hypertensive patients and 43 healthy controls). The images were analysed by QLAB software version 9.0. Long, circumferential and radial strain were quantified in 18-segments. **Result** Peak systolic long strain, circumferential strain, radial strain and longitudinal-circumferential systolic index were markedly decreased in patients with systemic hypertension comparing with control group ($-11.57 \pm 2.37\%$ vs. $-16.52 \pm 1.19\%$; $-13.52 \pm 4.97\%$ vs. $-17.92 \pm 2.39\%$; $10.24 \pm 3.4\%$ vs. $12.33 \pm 1.94\%$; $-12.55 \pm 2.83\%$ vs. $-17.22 \pm 1.44\%$, $p < 0.001$). Besides, the average of systolic blood pressure in normal longitudinal-circumferential systolic index group is lower than abnormal that group (127.93 ± 9.02 mmHg vs. 139.92 ± 12.51 mmHg, $p < 0.001$) and the average of systolic blood pressure in normal systolic index group is lower than abnormal that group (128.57 ± 8.1 mmHg vs.

141.96 ± 12.39 mmHg, $p < 0.001$). **Conclusion** although left ventricular ejection fraction is normal by conventional echocardiography, there is an early decline in systolic function by STE method and mean systolic blood pressure in the groups with normal systolic strain parameters are lower than that with abnormal strain parameters.

Keywords

Left ventricular systolic deficiency • Hypertension • Speckle tracking echocardiography

1 Introduction

The incidence of systemic hypertension in Vietnam is increasing rapidly. In 1960, the prevalence of systemic hypertension was about 1%, in 1992 was 11.7% and after 10 years the frequency up to 16.9%. Most recently (2008) the frequency of systemic hypertension in Vietnam was 25.1% [1]. Systemic hypertension causes many complications in many organs; cardiovascular complications are one of the early complications of hypertension. Although there are many facilities for diagnosis and treatment, the frequency of cardiovascular mortality remains high. Therefore, early detection of cardiac complications can improve the frequency of heart failure and reduce cardiovascular mortality. Echocardiography is a common method of assessing cardiac function, especially systolic function. Left ventricular ejection fraction is a commonly used parameter in assessment of systolic function. However, the old technique of measurement of this parameter is based on the change in volume so it is affected by loading conditions [2]. Recent studies show that speckle-tracking echocardiography may detect early subclinical systolic dysfunction despite normal ejection fraction [3, 4] this novel technique can assist identify initial

D. T. Nguyen
Can Tho University of Medicine and Pharmacy, Can Tho, Vietnam

V. A. Nguyen
Hue University of Medicine and Pharmacy, Hue, Vietnam

L. D. Do · N. Doan (✉)
Ha Noi Medical University, Ha Noi, Vietnam
e-mail: nvtdoan123@gmail.com; nvtdoan23@gmail.com

N. Doan
Griffith University, The University of Queensland & Queensland University of Technology, Brisbane, Australia

cardiac problems owing to hypertension. Therefore, this study carries out “An Evaluation On Initial Deficiency Of Left Ventricular Systolic Function In Patients With Systemic Hypertension By Speckle Tracing Echocardiography”.

2 Materials and Method

2.1 Population

The cross-sectional description study consisted of 194 subjects: 151 hypertensive patients with normal left ventricular ejection fraction and 43 healthy patients from Bach Mai Hospital in Hanoi and National Institute. All subjects were asked for history, clinical examination, taking blood pressure, blood glucose test, lipid test, electrocardiogram and echocardiography. Hypertension: according to the standards of the Vietnam Heart Association in 2015 and according to the European Society of Hypertension/European Cardiovascular Association in 2013 [5].

- Control group: healthy people are those with no cardiovascular disease, no diabetes, no hypertension, and normal systolic ultrasonographic indexes in accordance with the American Heart Association standard.
- Exclusion criteria: non-sinus rhythm, extra ventricular tachycardia, coronary artery disease, cardiac movement abnormalities, mitral stenosis or aortic stenosis, congenital heart disease, cardiomyopathy, pericarditis and cardiomyopathy, poor visual quality (loss > 3 segments of cardiac muscle).

2.2 Conventional Echocardiography

Cardiac ultrasonography was performed in all subjects using the Philips iE33 ultrasound, probe scanner S4-2. Measurement of left ventricular ejection fraction was done by M-mode and Simpson method. Calculate relative wall thickness and left ventricular mass index.

2.3 Application of Speckle Tracking Echocardiography

Using offline QLAB software version 9.0. The parameters are strains of 17 cardiac muscle regions at 3 consecutive cardiac cycles. Analysis of longitudinal deformations conducts on parasternal long axis, 2-chamber and 4 chambers in the apex. Analysis of circumferential and radial deformation conducted on short axis sections at the bottom, middle and apex level of the heart [6].

2.4 Statistics

Means \pm standard deviation was used to denote for continuous variables. The difference between the hypertensive and control groups was determined by independent t-test (by standard deviation). Statistical significance was established at $p < 0.05$. The outcomes were investigated using SPSS 18.0.

3 Results

3.1 General Characteristics of the Sample

See Tables 1, 2, Figs. 1, 2, 3 and 4.

4 Discussion

4.1 General Characteristics of the Sample

There was no difference in age, sex, BMI, BSA, ejection fraction, left ventricular diastolic diameter between the hypertensive group and the control group.

4.2 Evaluating Systolic Function Along the Longitudinal, Circumferential and Horizontal Axis

In Figs. 1 and 2, longitudinal, circumferential and radial strains were reduced in hypertensive patients compared to controls. This finding is consistent with the results of several studies, such as those of Kosmala [7] and Imbalazano [4]. GLS and GRS decline in hypertensive patients. According to Altiok E and et al., the cause of this changes is due to increase in chronic pressure to the heart wall which promotes collagen synthesis in sub-endothelium layer. Along with this biochemical change, cardiac fibrosis is one of the contributing factors to myocardial dysfunction in hypertensive patients [2]. Therefore, the longitudinal strain declines.

Sengupta [8] studied on 59 hypertensive patients. It found that in hypertensive patients without left ventricular hypertrophy, GLS of the endothelium and peripheral layer were reduced, GCS decreased only in the peripheral layer.

In young patients, Galderisi also found that GLS declined very early phase of complication [9] and even in the pre-hypertension [10] with speckle tracking echocardiography. Kosmala [7] also reported that GLS was an early indicator of preclinical left ventricular dysfunction.

Mizuguchi Y's study in Asian subjects, longitudinal, circumferential and radial strain were reduced in hypertensive patients with left ventricular hypertrophy [11].

Table 1 General characteristics of the sample

Characteristics	Control (n = 43) (\bar{X} + SD)	Hypertension (n = 151) (\bar{X} + SD)	p
Age	58.33 ± 8.21	60.91 ± 8.13	0.068
Sex (male) %	39.7	37.7	0.831
BMI	22.13 ± 2.27	22.83 ± 2.23	0.71
BSA (m ²)	1.58 ± 0.144	1.58 ± 0.141	0.96
Systolic BP (mmHg)	114.19 ± 10.63	137.62 ± 12.8	<0.001
Diastolic BP (mmHg)	68.02 ± 9.01	81.52 ± 8.54	<0.001
LVMI (g/m ²)	72.44 ± 14.92	87.43 ± 23.68	<0.001
EF- Mode (%)	69.53 ± 5.54	70.65 ± 6.18	0.29
EF-Simpson (%)	65.79 ± 5.71	65.28 ± 6.33	0.65
LVIDd (cm)	4.58 ± 0.38	4.5 ± 0.45	0.3
RWT	0.35 ± 0.05	0.42 ± 0.21	0.02

Remarks There was no difference in age, sex, BMI, BSA, ejection fraction, left ventricular diastolic diameter between the hypertensive group and the control group

Table 2 Systolic blood pressure levels by longitudinal-circumferential index and systolic index

Systolic BP (mmHg)	Longitudinal-circumferential		p
	Normal	Reduction	
	127.93 ± 9.02	139.92 ± 12.51	<0.001 (95%CI 7.94 ± 16.04)
Systolic BP (mmHg)	Systolic index		p
	Normal	Reduction	
	128.57 ± 8.1	141.96 ± 12.39	<0.001 (95%CI 10.05 ± 16.73)

Remarks Mean systolic BP in the group with lower longitudinal-circumferential index and systolic index is higher than that with normal index

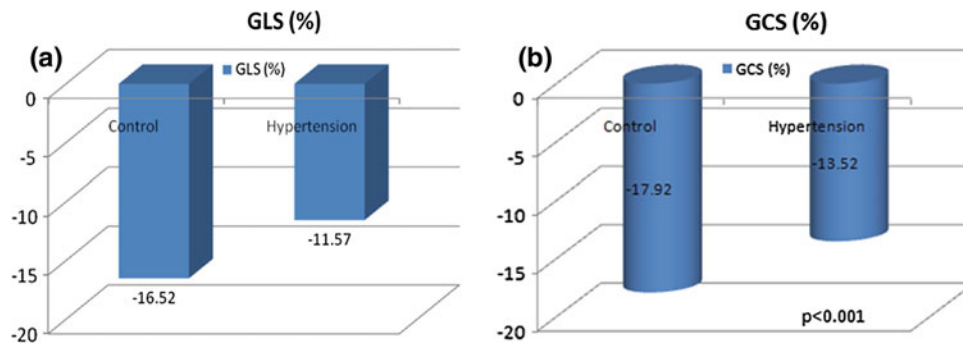


Fig. 1 Illustration of longitudinal strain and circumferential strain: **a** Longitudinal strain in the hypertensive group was lower than that of the control group with $p < 0.001$. **b** Circumferential strain was lower in the hypertensive group than in the control group with $p < 0.001$

4.3 Evaluation of Left Ventricular Systolic Function in Multiple Directions

Kouzu and et al. reported that total systolic function was the result of myocardial contractility in many directions, such as longitudinal, circumferential and radial axis [7]. Therefore, the evaluation of systolic function by conventional method was only a partial evaluation of systolic function.

Daniel and et al. found that longitudinal-circumferential index and systolic index are more sensitive than longitudinal systolic strain and left ventricular ejection fraction. On the other hand, longitudinal-circumferential index and systolic index correlated negatively with NYHA [12]. Our study of perimeter and systolic indexes decreased in hypertensive patients and decreased the most in hypertensive patients with normal ejection fraction.

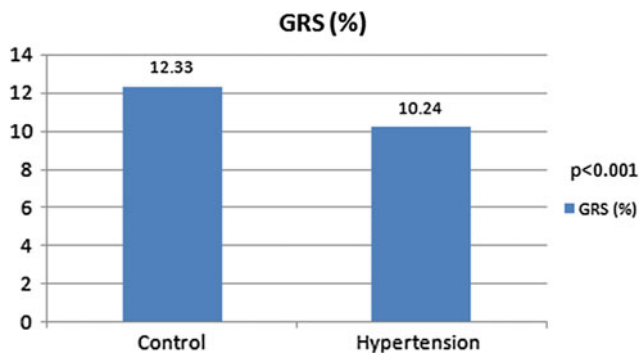


Fig. 2 Radial strain: Mean radial strain was lower in the hypertensive group than in the control group with $p < 0.001$

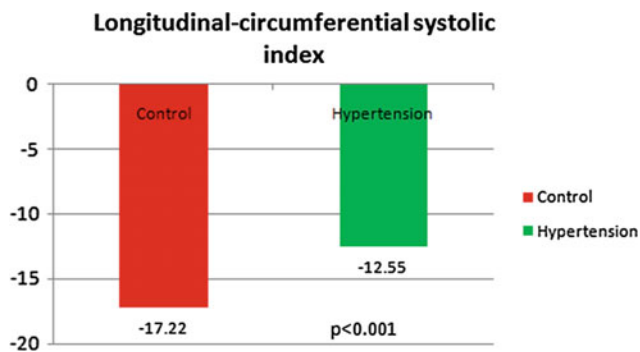


Fig. 3 Comparison of longitudinal-circumferential indexes in hypertensive patients and control groups: The longitudinal-circumferential index in patients with hypertension was lower than controls

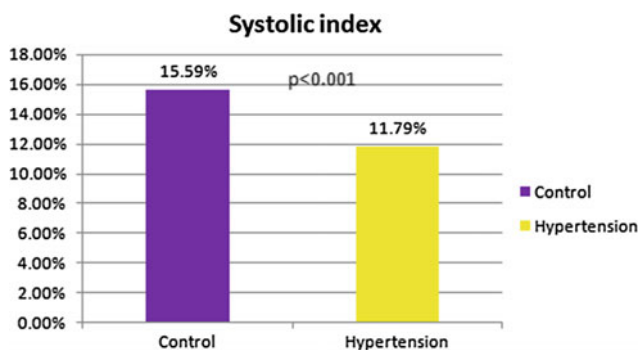


Fig. 4 Systolic index in hypertensive patients and control groups: Systolic index in hypertensive patients is lower than control group

4.4 Systolic Blood Pressure Level by Longitudinal-Circumferential Index and Systolic Index

In Table 2, we found that mean systolic blood pressure in the group with normal longitudinal-circumferential index and systolic index was <130 mmHg.

In fact, many authors also reported that in patients with hypertension, the rate of cardiovascular events increased with blood pressure [13]. According to SPRINT study, the mean systolic blood pressure was 121.4 mmHg in the intensive treatment group and 136.2 mmHg in the standard-treatment group. The intervention was stopped early after a median follow-up of 3.26 years owing to a significantly lower rate of the primary composite outcome in the intensive-treatment group than in the standard-treatment group [14].

In addition, the American Heart Association, American Heart Association and other American associations agree that the level of systolic blood pressure for reducing cardiovascular risk is $<130/80$ mmHg [15].

This paper indicated that Speckle tracking echocardiography could detect early sub-clinical left ventricular systolic dysfunction in hypertensive group that could not be detected by conventional method, which is ventricular ejection fraction, by echocardiography. Nevertheless, no longitudinal report was carried out to ratify whether clinical left ventricular systolic dysfunction truly established in this group. It implies that we still don't know the sensitivity and specificity of the existing technique. Thus, further longitudinal studies are required. Recently, Three-dimensional (3D) speckle-tracking echocardiography (3DSTE) [16] 3DSTE has the prospective to overwhelm various inherent restraints of two-dimensional STE (2DSTE) in the evaluation of complicated LV myocardial mechanism, proposing extra distortion parameters (such as area strain) and a wide-ranging quantitation of LV geometry and work from a single 3D acquirement.

5 Conclusion

This study illustrated left ventricular systolic strain, such as longitudinal, circumferential and radial strain; longitudinal-circumferential index, systolic index diminished in hypertensive sufferers with typical left ventricular ejection fraction in contrast to control group. At the same time, the mean systolic blood pressure in the group with normal longitudinal-circumferential index, systolic index was lower than 130 mmHg. Additional clinical assessment, novel technique, and vigorous substantiation with this method are required so as to enhance its clinical practice and to recognize its benefits in contrast with the traditional approaches. Therefore, future longitudinal studies are required.

Conflict of Interest The authors declare that they have no conflict of interest.

References

1. Son, P.T., Quang, N.N., Viet, N.L., Khai, P.G., Wall, S., et al.: Prevalence, awareness, treatment and control of hypertension in Vietnam -results from a national survey. *J. Human Hypertens.* 1–13 (2011)
2. Carluccio, E., Biagioli, P., Alunni, G., Murrone, A., et al.: Advantages of deformation indices over systolic velocities in assessment of longitudinal systolic function in patients with heart failure and normal ejection fraction. *Eur. J. Heart Fail.* **13**, 292–302 (2011)
3. Altiok, E., Neizel, M., Tiemann, S., Krass, V., et al.: Quantitative analysis of endocardial and epicardial left ventricular myocardial deformation-comparison of strain-encoded cardiac magnetic resonance imaging with two-dimensional speckle-tracking echocardiography. *J. Am. Soc. Echocardiogr.* **25**, 1179–1188 (2012)
4. Imbalzano, E., Zito, C., Carej, S., et al.: Left ventricular function in hypertension: new insight by speckle tracking echocardiography. *Echocardiography* **28**, 649–657 (2011)
5. Viet Nam Heart association: Guideline on diagnosis and treatment of systemic hypertension (2015)
6. Phan, T.T., Shivu, G.N., Abozguia, K., Gnanadevan, M., et al.: Left ventricular torsion and strain patterns in heart failure with normal ejection fraction are similar to age-related changes. *Eur. J. Echocardiogr.* **10**, 793–800 (2009)
7. Kosmala, W., Plaksej, R., Strotmann, J.M., et al.: Progression of left ventricular function abnormalities in hypertension patients with heart failure: an ultrasonic two dimensional speckle tracking study. *J. Am. Soc. Echocardiogr.* **21**, 1309–1317 (2008)
8. Sengupta, S.P., Caracciolo, G., Thompson, C.: Early impairment of left ventricular function in patients with systemic hypertension: new insights with 2- dimensional speckle tracking echocardiography. *Indian Heart J.* **65**, 48–52 (2013)
9. Galderisi, M., Lomoriello, V.S., Santoro, A., et al.: Differences of myocardial systolic deformation and correlates of diastolic function in competitive rowers and young hypertensives: a speckle-tracking echocardiography study. *J. Am. Soc. Echocardiogr.* **23**, 1190–1198 (2010)
10. Di Bello, V., Talini, E., Dell’Omo, G., et al.: Early left ventricular mechanics abnormalities in prehypertension: a two- dimensional strain echocardiography study. *Am. J. Hypertens.* **23**, 405–412 (2010)
11. Mizuguchi, Y., Oishi, Y., Miyoshi, H., et al.: Possible mechanism of left ventricular torsion evaluated with hypertension. *Eur. J. Echocardiogr.* **11**, 690–697 (2010)
12. Morris, D.A., Boldt, L.-H., Eichstadt, H., et al.: Myocardial systolic and Diastolic performance derived by 2-Dimensional speckle tracking echocardiography in heart failure with normal left ventricular ejection fraction clinical perspective. *Circ. Heart Fail.* **5**, 610–620 (2012)
13. Kuroda, K., Kato, T.S., Amano, A.: Hypertensive cardiomyopathy: a clinical approach and literature review. *World J. Hypertens.* **5**(2), 41–52 (2015)
14. Wright, J.T., Williamson, J.D., Whelton, P.K., et al.: A randomized trial of intensive versus standard blood-pressure control, <https://doi.org/10.1056/nejmoa1511939> (2015)
15. Whelton, P.K., Carey, R.M., Carey, R.M.: ACC/AHA/AAPA/ABC/ACPM/APHa, Guideline for the prevention, detection, evaluation, and management of high blood pressure in adults. <https://doi.org/10.1016/j.jacc.2017.11.006> (2017)
16. Mararu, D., et al.: Three-dimensional speckle-tracking echocardiography: benefits and limitations of integrating myocardial mechanics with three-dimensional imaging. *Cardiovasc. Diagn. Ther.* **8**(1), 101–117 (2018)



Biological Alterations of Lung Carcinoma

T. Q. Huynh, D. N. Tran, T. P. Chau, M. T. Nguyen, and N. Doan

Abstract

Tumorigenesis of the lung cancer is a multistep transformation involving genetic and epigenetic alterations. *Aims* To evaluate the general genetic pathways, their involvement, determining how they relate to the biological behavior of lung cancer, and their utility as diagnostic and therapeutic targets. *Materials and method* Online literature search through Google scholars, Pubmed, and hard copies, using keywords “biological alterations and lung carcinoma” yielded 9,380,000 publications. The 16 selected papers were used as a basis to formulate this report, and to evaluate the general pathways and involved genes, determining how they relate to the biological behaviour of lung cancer and their utility as diagnostic and therapeutic targets. *Results and discussion* Growth signals and lung cancer: In tumours cell, the activated oncogenes encode the molecules relating to the signalling growth factors either by direct initiation of the cell growths as an imitation of other growth factors or neutralization of the growth factor inhibitor. *Conclusion* Significant advances in molecular biologic research during recent decades have resulted in a substantial insight into critical signalling pathways and mediators contributing to lung cancer pathogenesis.

Keywords

Biological • Alterations • Lung carcinoma

1 Introduction

The carcinogenesis of lung cancer is the multistep progress of transformation from normal epithelial cells of bronchi to cancer cells. Decades of research have contributed to our understanding of these processes, through which resulting DNA damage transforms normal lung epithelial cells into the lung cancer cells. The conclusion of these alterations leads to lung cancers, displaying every marks of lung malignancy, comprising self-sufficiency of growing signs, unresponsive to grow-inhibitory signs, avoidance of predetermined cell decease, unlimited proliferation ability, nonstop angiogenesis and tissue penetration and metastasis.

Clinically, lung cancer is a heterogeneous disease, biologically, histologically and molecularly. The molecular mutations lead to the deregulation of the critical genetic pathways, relating to cellular proliferation, differentiation, program cell death, invasion, migration and other progress harboring the malignant particularities [1]. Hanahan and Weinberg [2] suggested classification according to hallmarks of cancer: Unrestrained cell production; elusion of scheduled cell mortality; deficit of reliance on growing stimulatory indications; uninhibited replicative ability; unrestricted Angiogenesis; envasion and metastasis. This review presented the progress of each hallmark as expressed by clinical and genetic properties of carcinogenesis.

2 Materials and Method

An online literature search through Google scholars, PubMed, and hard copies, using keywords “biological alterations and lung carcinoma” yielded 9,380,000 publications. The 16 selected papers were used as a basis to

T. Q. Huynh · D. N. Tran · M. T. Nguyen
Can Tho Oncology Hospital, Can Tho, Vietnam

T. P. Chau
Department of General and Thoracic and Oncologic Surgery
of Cho Ray Hospital, Ho Chi Minh City, Vietnam

N. Doan (✉)
Griffith University Schools of Dentistry and Oral Health,
Gold Coast, Australia
e-mail: nvtdoan123@gmail.com; nvtdoan23@gmail.com

N. Doan
The University of Queensland & Queensland University
of Technology, Brisbane, Australia

formulate this report, and to evaluate the general pathways and involved genes, determining how they relate to the biological behavior of lung cancer and their utility as diagnostic and therapeutic targets.

3 Results and Discussion

3.1 Growth Signals and Lung Cancer

In tumors cell, the activated oncogenes encode the molecules relating to the signaling growth factors either by direct initiation of the cell growths as an imitation of other growth factors or neutralization of the growth factor inhibitor [3]. The tumor cell, losing the dependency on stimulatory growth signals from surrounding environment, have the ability of independent growth [4]. This phenotype of auto growth, by the influence of intracellular changes as molecular alterations and gene mutations, express the “self-supporting of growth factors,” then produce the necessary growth factors and receptors from “self-stimulatory autocrine signaling loop” leading to the uncontrolled proliferation [5].

In non-small cell lung cancer (NSCLC), these phenomena include the mutation of up regulating of some EPHB4 receptor tyrosine kinase (RTK), specifically epidermal growth factor receptor [EGFR (Erb1)] and other members of ErbB RTK family.

In SCLC, the overexpression of Insulin-like growth factor-1 (IGF-1) and its receptor, as well as its neuro-stimulating growth factors often observed.

3.1.1 Over-Expression of Epidermal Growth Factor and Signaling in NSCLC

Overexpression of EGFR was observed in 50–90% of NSCLC and especially in SCC, but rare in SCLC. Entire EGFRs comprise an extracellular ligand-binding area, a trans membrane area, and a cytoplasmic protein tyrosine kinase field. Binding of the ligand epidermal growth factor leads to receptor homo or heterodimerization with another member of EGFR family and activation of TK domain through the phosphorylation of thymidine kinase (TK) residues [6].

Signal transduction stimulated by EGFR occurs through PI3 K/AKT/mTOR →→ Inhibits the regulator of the cell cycle (glycogen synthase kinase—GSK-3 and pro-apoptotic protein BAD. RAS/RAF/MAPK →→ cell proliferation, and JAK/STAT/PLC- γ signaling pathways →→ affecting the cell motility, migration, and invasion of the cancer cell.

EGFR involves the regulation of numerous oncogenic functions such as proliferation, survival, differentiation, neoangiogenesis, invasion, and metastasis. Also, it relates to

the constitutive TK activation and oncogenic transformation of pulmonary epithelial cell in vitro.

EGFR activates other pathways leading to effects anti-apoptotic, invasion, metastasis and proliferation, cross-act among pathways. A mutant EGFR—called IIIv EGFR found in different malignancies, about 16% in NSCLC. The EGFRvIII analysis assay is capable of detecting the EGFRvIII mutation. The mutant receptor is incapable of binding any known ligand. The pro-tumorigenic effects of EGFRvIII seem to rely directly on its ability to signal. EGFRvIII activates several downstream pathways; EGFRvIII is the most common mutation in glioblastoma multiforme (GBM), occurring in 25–64% of these tumors. It is also found in 20–36% of breast cancers and about 33% of head and neck squamous cell carcinoma (HNSCC) patients. Some trials report that this kind of mutant EGFR was present in about 5% of NSCLC, compared with wild-type EGFR, EGFRvIII appears to be relatively resistant to treatment with conventional anti-EGFR agents [7].

In NSCLC, EGFR mutations occur in the first four exons of the intracellular tyrosine kinase domain: most commonly exon 19 in-frame deletions (# 45%), of which there are over 20 variants, the universal being delE746-A750. The next most familiar EGFR are missense mutations, particularly L858R (# 40%) in exon 21. Another insertion mutation of EGFR in exon 20 (5–10%) of which there are many variants often resistant to EGFR-TKIs [8].

Secondary mutations in EGFR develop or clonally selected in patients that develop resistance to EGFR-TKIs. The most typical being the T790M activating point mutation in exon 20 which substitutes a bulkier methionine for threonine that interferes with binding of reversible TKIs. T790M found in about 50% of tumors from patients who develop acquired TKI resistance [9].

Another member of ErbB family is Her2/neu is overexpressed about 30% in NSCLC. Until now, there is not yet an adequately identified ligand for Her2 but can form heterodimers with other ligand-bound members of the receptor family. Oncogenic driver mutations identified in non-small cell lung cancer (NSCLC) have triggered the development of drugs capable of interfering in intracellular signaling pathways involved in tumorigenesis. Tyrosine kinase inhibitors, such as erlotinib or gefitinib, have demonstrated promising results in patients with advanced NSCLC that harbor EGFR mutations. Human epidermal growth factor 2 (HER2) mutations in NSCLC, described exclusively in adenocarcinoma histology, are present in approximately 4% of this subset of lung cancer patients, suggesting that thousands of patients per year may benefit from targeted therapy. Therefore, it can conclude that systematic genotypic testing in this subgroup of NSCLC patients should include detection of HER2 mutations.

3.1.2 Overexpression of Other Growth Factor Receptor and Ligand

The expression level of mitogen IGF-1 is elevated in the majority of SCLC, resulting in the formation of a “self-stimulatory autocrine signaling loop” involving IGF-1 receptor, which is commonly co-expressed in this malignancy. IGF signaling proceeds through binding of IGF ligands to cell surface RTK. The biologic activity of signaling system modulated by binding of IGF protein, which present in extracellular fluid, and serum to the IGF ligands. As for EGFR, activated IGF-1R signaling is complex but primarily occurs through the Ras/Raf/EEK and Pi3 K/AKT pathways. A correlation between significantly elevated IGF-1 serum level and lung cancer risk has been reported [10].

RTK c-kit and its ligand SCF (stem cell factor) is another receptor/ligand system, upregulated in more than 80% of SCLC tumors. A study of c-kit expression in SCLC patients identified c-kit as a marker for increased survival.

c-MET is another RTK often overexpressed in SCLC. Signaling through this receptor system has been reported to be associated with tumor growth and metastasis. In contrast to the c-Kit SCF system, the c-MET ligand hepatocyte growth factor (HGF) is rarely co-expressed with the receptor in SCLC.

3.1.3 Activating Ras Mutations

As mentioned, mutation of the intracellular membrane-associated signaling mediator Ras with a high overrepresentation of mutations in the Kras gene detected in up to 30% of NSCLC, but rarely in SCLC. Ras protein becomes activated by the binding of guanine triphosphate (GTP), allowing for transmission of growth stimulatory signals to the cell nucleus.

Downregulation of Ras signaling occurs by hydrolysis of GTP to GDP, mediated by GTPase activating protein (GAP).

In NSCLC and other malignancies, activating point mutations in the K-ras gene result in resistance to GAP activities, thereby trapping the Ras protein in a constitutively active state, capable of continuous growth promoting signaling [11].

3.1.4 Overexpression of Neuropeptides

Highly elevated expression of different neuropeptides is a hallmark of SCLC, and many of these markers have also detected in some (mainly poorly differentiated) NSCLC tumors. Neuropeptides exert their effect via binding to seven transmembrane G-protein coupled receptors, resulting in activation of various downstream signaling pathways including PLC. Gastrin-releasing peptide (GRP) signaling via the GRP-receptor has become one of the most intensively studied neuropeptide signaling pathways in SCLC. Other neuropeptides highly expressed in lung cancer include

bradykinin, neuron-specific enolase, and l-Dopa decarboxylase.

In recent years, the expression of neuroendocrine transcription factor Achaete-scute homolog-1 (ASH-1) in SCLC has gained increased attention. ASH-1 usually is expressed in neuronal progenitor cell during early fetal development of various tissues including the central nervous system and the lung. The expression is virtually absent in normal adult organism but reactivated and highly expressed in SCLC and In other lung tumors with a neuroendocrine phenotype.

3.1.5 Amplification of Myc Gene

Myc is a member of a proto-oncogene family comprising N-myc, c-myc, and L-myc, commonly amplified in NSCLC and SCLC, resulting in overexpression of transcription factor Myc. Although the contribution of myc-amplification to the pathogenesis of lung cancer remains to be elucidated; a recent study has pointed out to a role of myc to promote cell cycle progression. Also, myc in combining with loss of TSG such as Rb has been shown to significantly contribute to decreased cell cycle arrest and deregulate tumor growth.

3.1.6 Anaplastic Lymphoma Kinase (ALK)

Rearrangement of RTK ALK is most common in the fusion of the intracellular kinase domain with the amino-terminal end of Echinoderm Microtubule-associated protein-Like 4 (EML4) occur in a subset of lung cancers. The rearrangement result from a short inversion in chromosome 2p whereby in the best-known variant, intron 13 of EML4 is fused to intron 19 of ALK. Numerous variants of EML4-ALK fusions have identified due to different lengths of EML4, the commonest being exons 1–13 of EML4 joining to exon 20–29 of ALK. More recently, various partner gene has identified in a small subset of ALK rearrangements including KIF5B (kinase family member 5b), TFG (TRK-fuse gene) and KLC-1 (kinesin light chain1). Activation of ALK is linked to cell proliferation and inhibition of apoptosis mediated through RAS/RAF/MAPK1, PI3K/AKT, and JAK3-STAT3 signaling pathways.

ALK rearrangement has identified in approximately 4% of unselected NSCLC. ALK inhibition with TKI Crizotinib produce a profound response, drug resistance develops with evidence of secondary ALK point mutations.

3.1.7 ROS1 Proto-Oncogene

Ros1 is a proto-oncogene located on chromosome 6q22, which encodes a transmembrane RTK that has high homology with ALK in its protein kinase domain. ROS1 activation leads to signaling through the PI3K/AKT/mTOR, STAT3 and RAS/MAPK/ERK pathways [4]. ROS1 rearrangements appear to be more common in patients who are younger, never smoker or of Asian Ethnicity similar to ALK

rearrangement. Furthermore, there is *in vitro* and early clinical evidence that lung cancers with ROS1 rearrangement are sensitive to kinase inhibitors including inhibitor Crizotinib.

3.1.8 RET

RET is located on chromosome 10q11.2 and encodes a receptor tyrosine kinase in neural crest development. Alteration of the crest has long been known to play a role in papillary and medullary thyroid carcinoma. But it was not until recently that activation of RET through chromosomal rearrangement has identified in a small proportion of lung cancer. Similar to ALK and ROS1, rearrangements of RET also appear to be associated with ADC from never smoker [4, 5].

3.1.9 Experimental Therapeutic Targeting of Growth Factors and Oncogenes

Some different growth factors and oncogenes of importance for lung cancer biology have presented. A research area of the significant locus in recent years has been the therapeutic targeting of EGFR in NSCLC.

There are two global strategies: one is to prevent binding of the ligand through blocking the ligand-binding site (belonging to this group Cetuximab is a humanized mAb anti EGFR). The other is to directly inhibit receptor signaling by blocking activities of cytoplasmic tyrosine kinase domain (the two most clinical advanced are erlotinib and gefitinib).

Recently, some others newer agents: Afatinib (GilotrifR—Chemocare); Crizotinib (XalkoriR—Pfizer) for uses of EML4-ALK, ROS1, RET; Ceritinib (ZykadiaR—Novartis) used for NSCLC patient who has developed resistance to crizotinib.

3.2 Aberrant Anti-growth Signaling

In contrast to an oncogene, TSG act to prevent and control cell growth, often via tight control of cell cycle progression. Full inhibition of tumor suppressors activity often requires inactivation of both alleles of a TSG in the cancer cell. This dual inactivation is frequently accomplished by a two-step process, involving a chromosomal translocation or deletion resulting from loss of heterozygosity (LOH), followed by inactivating point mutation of the remaining allele. In lung cancer cells, LOH of distinct chromosomal regions frequently detected, and many of these regions harbor genes encoding central tumor suppressor, known or speculated to be involved in cancer pathogenesis.

3.2.1 TP53 Gene Mutations

The TP53 gene located within a region of chromosome 17 (17p13), which is mutated or altered in the majority of lung cancer with a specific high prevalence in SCLC or SCC.

The type of TP53 alterations observed in lung cancer range from gross chromosomal changes such as LOH, homozygous deletion, and DNA rearrangements, to local point mutations, all of which contribute to TP53 malfunction or inactivation.

The cellular enzyme MDM2 play an important role in the downregulation of p53. It serves as a p53 binding partner, which facilitate the attachment of ubiquitin tags to p53, thereby targeting it for degradation. MDM2-p53 interaction generates an oscillating feedback loop of p53 and MDM2 degradation and synthesis within the cell.

Active p53 regulates transcription of some genes involved in cell cycle control, resulting in cell cycle arrest, allowing for repair of damaged DNA by the cellular repair machinery. Activation of p53 also induces apoptosis via activation of some apoptotic mediator (including BAX) and inhibits blood vessel formation by activation of genes encoding antiangiogenic factors. P53 mutations suggest a poorer prognostic in NSCLC and SCLC as well.

3.2.2 Mutated RB and P16INK4A

A central tumor is suppressing signaling cascade, frequently altered in human lung cancer, is the p16INK4A/CDK-cycling/Rb pathway. The retinoblastoma (Rb) tumor suppressor gene at 13q14 encodes a transcription factor involved in the regulation of G1 to S phase transition in the cell cycle. The tumor-suppressing activity of Rb depends on its level of phosphorylation. In its hypo-phosphorylated state, Rb binds to and inhibit the activity of different binding partners, including members of the E2F family of transcription factors. Upon phosphorylation of Rb, E2F is released and activated, resulting in transcription of the gene responsible for G1 to S phase cell cycle progression. The formation of these complexes inhibited by p16INK4A which thereby serves as a tumor suppressor upstream of Rb by indirect inhibiting its phosphorylation and thereby promoting Rb association with its binding partner.

3.2.3 Aberrant TGF- β Signaling

The transforming growth factor β (TGF- β) receptor system is also commonly altered in lung cancer. The effects of signaling by TGF- β mostly associated with inhibited cellular proliferation in many cell types. TGF- β signaling related to some cell functions, the best described of which relate to inhibition of the cell cycle. Growth inhibitory effects of TGF- β signaling have associated with inhibition of expression and assembly of some of cyclin/CDK components responsible for Rb activation.

3.2.4 Loss of Chromosome 3p and Related Genes

Probably the most frequent chromosomal abnormality in lung cancer is a loss of regions within chromosome 3p. LOH at chromosome 3p has been reported in 70–100% of all

NSCLC and more than 90% of SCLC. Some genes within this region have suggested as putative tumor suppressors.

The loss of the fragile histidine triad (FHIT) gene located at position 3p14, 2 is frequent in lung cancer. Expression of FHIT protein in NSCLC cell line and mouse xenograft models have been showed to suppress tumor growth and induce apoptosis. And recently FHIT has been found to stabilize p53 presumably by interaction with MDM2 [10, 12].

RASSF1A is a different candidate tumor suppressor gene residing at chromosome 3p (position 3p21). This gene inactivated in virtually all SCLC and more than 60% NSCLC. RASSF1A has been found to reduce motility of NSCLC cell and increase cell adhesion, suggesting a role for RASSF1A in cell migration and metastasis.

Several other genes reside at the frequently deleted regions of chromosome 3p but much remains to be learned about the role of these genes in tumor suppression.

3.2.5 Experimental Treatment: The Reintroduction of Tumor Suppressors

Since the loss of activity of specific tumor suppressor pathways is a distinctive characteristic of human lung cancer, the reinstatement of tumor suppressor activity is an attractive strategy for the therapeutic intervention. For this purpose, replacement therapy by delivery of lost tumor suppressor genes to cancer has become increasingly attractive. Most reports of tumor suppressor replacement gene therapy involve reintroduction of TP53 in NSCLC, where some clinical trials have published. However, the limiting factor of gene therapy today remains poor delivery of the therapeutic gene to the cancer cells. The clinical study performed to date have all used modified viruses for gene delivery, but a significant drawback of using viruses for gene delivery is the induction of immune responses against the virus in the patients. Results in the production of antibodies, which target the virus for degradation and limit the efficiency of repeated treatment. Novel non-viral delivery vehicles developed. Which may in the future provide a potent alternative to viral gene therapy [11, 13].

3.3 Apoptosis in Lung Cancer

Apoptosis is a morphologically and biochemically distinct form of cell death that occurs under various physiologic and pathologic conditions triggered by extrinsic and intrinsic cellular and molecular damage. It characterized by the activation of a specific event of molecular processes followed by specific morphologic changes such as shrinkage of the cell, condensation of chromatin, and disintegration of the cell into small fragments [6, 16].

Apoptosis activated by a family of intracellular cysteine proteases called caspases. They are synthesized as zymogens and activated by proteolytic cleavage. They divided into two distinct classes, initiator caspase, which include caspase P8, P9 and P10; and effector caspase, which provides for P3, P6, and P7. There are two separate pathways of caspase activation: one starts with binding of an extracellular ligand to its cell surface receptor. The ligands are TNF, FasL, and Trail, and their respective receptors are TNFR1, FAS, and DR4 and DR5. The other caspase activation pathway starts with the release of cytochrome C from the intermembrane space of mitochondria. Two proapoptotic family members, BAX and BAK, appear to facilitate cytochrome C release by participating in the formation of a pore that releases mitochondrial intermembrane space protein. Once discharge, cytochrome C fixes to apoptotic protease activating factor 1 (APAF-1) fastening to procaspase 9 establishing a multi-protein compound, named an apoptosome. Inhibitor of apoptosis protein (IAP) binds and inhibits apoptosome related caspases. The most widely studied IAP is survivin, which elevated in the majority of NSCLC and it has shown that absence of its expression might associate with improved prognosis. Activators and inhibitors are influenced by several other proteins including p53, Rb, PTEN, Raf-ERK, PI3K-PKB and Hsp70 [5].

Another member of apoptosis in lung cancer: programmed cell death 1 (PD-1) is also CD279, a cell surface receptor encoded by PDCD-1 gene, member of the superfamily of immunity. It expressed on the surface of T and preB cell, NSCLC and SCC cells. PD-1 binds to two ligands: PD-L1 and PD-L2, member of family B7-homolog and encoded by CD 247. PD-1 and its ligand regulate downstream immune system [12].

3.3.1 Targeting Apoptotic Pathway

Treatment with TNF has undertaken. However, due to pronounced general toxicities, its potential as a therapeutic drug is limited; Recently, Trail agonist have approved for clinical trials, but no data are presently available [7].

Small molecule inhibitor of Bcl-2 have been developed and are at the moment being tested in preclinical trial and phase I test.; antisense constructs against survivin have been produced and test in phase I clinical trial. In addition, adenovirus-based gene therapy is under development.

Inhibition of PD-1 leads to promote an immune system for the treatment of non-squamous NSCLC. Nivolumab (Opdivo—BMS; FDA approved 12/2014; Pembrolizumab (Keytruda—MERCK) target PD-1; FDA approved 9/2014 for NSCLC and HCC; other agents PALIVIZUMAB—BMS; MPDL—Roche also target PD-1, on the study of phase III [14].

3.4 Angiogenesis

Good vascularity is vital for cell task and existence in each matter as oxygen and nutrients delivered by the vessels. The growth of new blood vessel, called the process of angiogenesis, is a typical physiologic process-taking place under angiogenesis, which under these conditions, is transitory and carefully regulated. Similarly, tumors must develop angiogenic ability to progress. This ability appears by activating the angiogenetic switch. Once cancer has activated its angiogenic switch, it becomes able to grow. Many different pro and anti-angiogenic factor have identified. The angiogenesis instigating signs are demonstrated by vascular endothelial growth factors (VEGF)/vascular permeability factor (VPF) and acidic (FGF1) and basic fibroblast growth factors (FGF2), which completely attach to transmembrane tyrosine kinase receptor presented by endothelial cell. VEGF has been proven to be a important prognosticator of insignificant diagnosis in NSCLC.

3.4.1 Targeting Angiogenic Factors

Inhibition of angiogenesis is through anti-angiogenic and/or vascular targeting agents seem logical, as the new anti-cancer treatment strategy. There has been increasing attention focused on targeting VEGF and VEGFR. The recent clinical trial has shown that the anti-VEGF antibody bevacizumab, combined with standard first-line chemotherapy in NSCLC, provided a statistically and clinically significant survival advantage with tolerable toxicity. Also, more recently tested compounds characterized as an anti-vasculature agent have been shown to be effective against multiple targets Sunitinib, regorafenib, ramucirumab. The efficacy of such compounds currently investigated in a clinical trial for NSCLC.

3.5 Replicative Potential and Telomerase

After some division, the cells are predetermined to enter a crisis, a state characterized by extensive cell death and chromosomal aberrations. This phenomenon has been termed the mitotic clock and is part of the precise regulation of healthy cell growth. In contrast, cancer cells propagated in culture have an unlimited potential for continuous cell division, and said to be immortalized.

The molecular explanation for the mitotic clock resides in the chromosomal structure and mechanism of DNA replication. Upon cell division, the cell initiates DNA replication which proceeds to produce new leading and lagging strands from the DNA double helix. Since DNA replication can only proceed in one direction (3'–5'), only the leading strand of the double helix is continuously synthesized, whereas the new lagging strand assembled by ligation of smaller DNA

fragments. The discontinuous replication of the lagging strand results in a gap at the 5' end of the newly synthesized DNA strand, resulting in loss of chromosomal material during each mitotic cycle. Due to the continuous shortening of telomeric DNA following cell division, lack of telomere maintenance ultimately results in chromosomal degradation and end-to-end chromosome fusion. For the cells to overcome the limitation of telomere shortening, cancer cell activates a program for telomere maintenance, which is usually shut down in fully differentiated normal cells. Most frequently, this accomplished by activation of an enzyme complex known as telomerase, but a subset of cancer cell lacks telomerase activity and immortalized by a process known as alternative lengthening of telomerase (ALT).

3.5.1 Telomere Maintenance in Lung Cancer

The core telomerase enzyme comprises an RNA subunit (hTERC) which provides the template for synthesis of new telomeric DNA facilitated by the catalytic subunit human telomerase reverse transcriptase (hTERT). Some studies have shown that increased telomerase activity and increased level of hTERT mRNA are mainly found in patients with poorly differentiated tumor (such as SCLC) and advanced disease and correlate with poor survival, suggesting telomerase activity as an important prognostic marker for patients with lung cancer.

3.5.2 Experimental Therapeutic Targeting of Telomerase in Lung Cancer

Due to the central role of telomerase in the transformation of lung cancer cell, and the lack of telomere maintenance in normal tissue, blocking the activity of this enzyme appear an intriguing target for therapeutic intervention.

The compound GRN136L is a lipid-modified oligonucleotide, which binds to the hTERC subunit of telomerase with high affinity, thereby inhibiting reverse transcription by blocking access of hTERT to its RNA template. GRN 136L has recently been reported to successfully inhibit telomerase activity, leading to telomere shortening and resulting in decreased growth of adenocarcinoma cell in vitro and effective prevention of tumor metastasis in a xenograft mouse model [11].

3.6 Tissue Invasions and Metastasis

Tumor cell can produce some proteolytic enzyme, which can degrade these protein structures. Including matrix metalloproteinase (MMPs), collagenase, urokinase plasminogen activator (uPA), Plasmin, cathepsin, and others [6, 14]. MMPs are known to play a functional role in the metastatic spread of lung cancer. Different MMPs are active in various steps of the invasive and metastatic process, and a better

understanding of the involvement of MMPs in the invasion and regulation of growth of both primary and metastatic tumors may help to implement these as anti-cancer therapy targets. Cathepsin has demonstrated to have a prognostic value in NSCLC and levels of the receptors for uPA and other components of the plasminogen activation system associated with survival in NSCLC.

3.6.1 Targeting Protease and the Metastatic Process

It expected that inhibition of the metastatic potential of the tumor by interaction with extracellular protein degradation could be an essential target, especially during early tumor development. Drug targeting MMPs have been in a clinical trial but have shown little or no activity in lung cancer. Inhibition of MMPs has primarily focused on targetting MMP-2 and -9. At the moment, new MMP inhibitors such as CP471.358 are being evaluated in Phase I and II studies in some malignancies including lung cancer [13, 15].

4 Conclusion

Significant advances in molecular biologic research during recent decades have resulted in a substantial insight into critical signaling pathways and mediators contributing to lung cancer pathogenesis. The identification of driver mutations in EGFR, ALK, and others heralded a new era of targeted therapy in lung adenocarcinoma, and advanced sequencing technologies are providing more sophisticated insights into the molecular alterations underlying lung cancer. These researchers have also identified a range of potentially targetable genetic modifications for lung cancer, have also encountered a troubling complexity and heterogeneity posing significant challenges for diagnosis as well as targeted therapy for lung cancer, a genuinely multi-mechanistic and heterogeneous malignant disease.

Conflict of Interest The authors declare that they have no conflict of interest.

References

- Weinberg, R.A.: Multi-step Tumorigenesis. The biology of cancer, 2nd edn, pp. 31–70. Garland Science (2014)
- Hanahan, D., Weinberg, R.A.: The hallmarks of cancer. The next generation. *Cell* **144**(5), 646–674 (2011) (Elsevier. Inc)
- Cagle, P., Allen, T., Beasley, M.B., et al.: Molecular pathology of lung cancer. Springer, New York (2012)
- Bergethon, K., Shaw, A.T., Ou, S.H., et al.: ROS1 rearrangements define a unique molecular class of lung cancers. *J. Clin. Oncol.* **30**, 863–870 (2012)
- Thang, H.Q.: Basically molecular in Cancer. *J. Med. HCM city* **19** (5–2015), 1–7 (2015)
- Cooper, W.A., Lam, D.C.L., O’Toole, S.A., Minna, J.D.: Molecular biology of lung cancer. *J. Thorac. Dis.* **5**, 1–22 (2013)
- Thang, H.Q.: Molecular alterations in lung cancer. *J. Med. HCM city* **19**(5–2015), 8–15 (2015)
- Thang, H.Q.: Up dating biology, diagnosis, and treatment of lung cancer. Training documentations of Cantho Cancer Society 2014 (2014)
- Larsen, Jill E., Minna, John D.: Molecular biology of lung cancer: clinical implications. *Clin. Chest Med.* **32**(2011), 703–740 (2011)
- Tan, W.W.: Nonsmall cell lung cancer treatment and management. *Medscape Updated* 17 Aug 2017, pp 01–40 (2017)
- Zappa, C., Mousa, S.A.: Nonsmall cell lung cancer: current treatment and future advances. *Transl. Lung Cancer Res. TLCR* **5** (3), 288–300 (2016)
- Berinstein, N.L.: Biological therapy of cancer. In: *Basic Science of Oncology*, 4th edn, pp. 453–484. McGraw Hill, New York (2005)
- Zarogoudilis, K., Zarogoudilis, P., Darwiche, K., Machairiolis, N., et al.: Treatment of NSCLC. *J. Thorac. Dis.* **5**(4), 389–396 (2013)
- Mackinnon, A.C., Kopatz, J., Sethi, T.: The molecular and cellular biology of lung cancer: Identifying novel therapeutic strategies. *Br. Med. Bull.* **95**, 57–61 (2010)
- Reck, M., Rabe, K.F.: Precision diagnosis and treatment for advanced NSCLC. Review article *New England J. Med.* 31 Aug 2017, pp. 849–861 (2017)
- Shivapurkar, N., Reddy, J., Chaudhary, P.M.: Gazdar AF (2003) Apoptosis and lung cancer: a review. *J. Cell. Biochem.* **88**, 885–898 (2003)

Evaluation of the HBV Genotype, Viral Load and Antivirus Drug Resistance Mutation in Tay Ninh Hospital, Vietnam by Real-Time PCR

Thuan Duc Lao, Hung Chi Lieu, Thuy Thanh Thi Ho, and Thuy Ai Huyen Le

Abstract

HBV infection is a leading cause of chronic hepatitis. The new advances in diagnosis and treatment of hepatitis B have significantly contributed in limiting several complications of hepatitis including the usage of molecular biotechnological method such as real-time PCR, typically, which become a helpful method in diagnosis, monitoring, and treatment of disease. The study aimed at developing a real-time PCR assay in order to quantify viral load in blood, genotype and characteristic antiviral drug (Lamivudine—LAM, Adefovir—ADV) resistance mutation in hepatitis B in patients of Tayninh Hospital, Tayninh province, Vietnam. According to results, in Tay Ninh, we certainly recorded several clinical parameters of HBV infections. The patient's age at HBV infection was 37.5 ± 13.7 . Impact of HBV infection in female was counted for 58.5%, the proportion of persons without consideration they are infected with HBV was up to 55.5%, the main of HBV infection through the spread of blood was 94.5%. The ALT value with normal range, HBeAg negative and without any recommendation for hepatitis treatment were counted for 74.5, 71, 68.5% in turn. In HBsAg positive group, 73.5% HBV DNA positive for predominant genotype B was counted for 78.2%. The group with high viral load with $\geq 20,000$ UI/mL was counted for 27.5%. The proportion of antiviral drug resistance mutation in LAM, both LAM and ADV were counted for 67.3, 43.3% in turn. In the group of LAM resistance, double mutations at 204I,

204 V was 52.6%. In cases of ADV resistance, double mutations at 181 V, 181T was reached to the highest proportion with 48.2%. Antiviral drug resistance mutation frequently occurred in the younger group, associated with the high ratio of HBeAg positive, increasing of ALT and high viral load, whereas there is no difference in genotype effected on clinical and subclinical factors.

Keywords

Antiviral drug resistance • Chronic hepatitis B • Hepatitis B • Genotype • Real-time PCR • Viral load

1 Introduction

According to the report of WHO, currently over two billion people were infected with hepatitis virus B worldwide, the prevalence of acute infection was 6%, of which about 5–10% will turn into chronic infection in adult population and up to 90% in child population. The mortality rate in the cases with acute infection was 1%. Hepatitis B virus infection was leading to the chronic hepatitis, cirrhosis, primary liver cancer that lead to one million deaths per year [11, 15]. In Vietnam, the prevalence of HBV infection was 15–20%. Besides, the ratio of HBV infection in cirrhosis and primary liver cancer patient was 80–92% [16, 18, 21]. In Vietnam, the common HBV genotype were B and C [5, 12, 13]. Recent studies showed that there was a strong relationship between genotype and hepatitis B incubation period, disease process, viral escape from immune system, and drug response [6, 14, 15]. In hepatitis therapy, Lamivudine (LAM), Adefovir (ADV) were the common drug used for treatment due to oral solution and fewer side effects [9]. However, currently use was limited by drug resistance status, which increased during the duration of HBV treatment [10]. In Tayninh province, Vietnam, hepatitis B was the common disease with predicted proportion was 10% of

T. D. Lao (✉) · T. A. H. Le
Ho Chi Minh City Open University, Ho Chi Minh City, Vietnam
e-mail: thuan.ld@ou.edu.vn

T. A. H. Le
e-mail: thuy.lha@ou.edu.vn

H. C. Lieu
Tay Ninh Hospital, Tay Ninh Province, Vietnam

T. T. T. Ho
Viet A Corporation, Binh Duong, Vietnam

HBsAg tests. The implementary of HBV therapy in Tayninh hospital was preliminary, because they lacked of means for diagnosis. Therefore, the current study aimed to evaluate the HBV genotype, viral load and antiviral drug resistance mutation in Tay Ninh Hospital, Vietnam.

2 Materials and Methods

This study was carried out on patient, treated in Tayninh Hospital, Vietnam, whose positive HBsAg which tested by serology test and without any treatment by using antiviral HBV. Blood samples were collected, then, having a ALT and HBeAg test. The sample with the average of ALT level less than 42 UI/ml was used in this study.

2.1 Real-Time PCR Reaction

DNA was collected from patient's serum using *iVA*pDNA Extraction Kit (Code: VA.A92-002D). Real-time PCR reaction was carried out using Real-time PCR kit supported by Viet A Technologies Joint Stock (Vietnam) including Lightpower *iVA* HBV qPCR Plus Kit (to quantify viral load in blood with a detection threshold of 60 IU/ml); LightPower *iVA* HBV LamP rPCR Plus Kit: VA. A02-001G and LightPower *iVA* HBV AdeR rPCR Kit: VA. A02-001I (to examine common types of Lamivudine resistance mutation including L180M, M204I, M20V and Adefovir resistance mutation including A181T, A181V, N236T); LightPower *iVA* HBV genotype rPCR Plus Kit: VA. A02-001E (to identify three common genotypes of HBV in Vietnam including A, B and C).

2.2 Data Statistical Analyzing

SPSS software was used to statistical analyze research data with p value <0.05 which was considered significant. χ^2 test was applied to determine the correlation between variances, if χ^2 test was not appropriate, the method likelihood ratio will be replaced. t test and ANOVA-one way were used to compare variances. The Mann-Whitney and kruskal-Wallis method will be replaced if previous methods were not appropriate.

3 Results and Discussions

3.1 Characteristics of Samples

200 cases of HBsAg positive out of 1928 cases, which had a serological test, were collected from February, 2012 to

October, 2012. It was accounted for 10.4%. 200 cases showed the patient's age with the average age is 37.5 ± 13.7 range from 10 to 83 years old. Moreover, male and female are accounted for 83 cases (41.5%), 117 cases female (58.5%). In general, HBV infection at Tay Ninh is fluctuation in the patient age, it means that the rate of infected in women is higher than in men, more and a half patient without any consideration that they are HBV infected (55.5%). The majority of cases were outpatients, purpose of their tests was in order to check for HBV infected or uninfected, moreover, monitoring the case of HBV infected counted for 61.5%. The number of cases that had normal ALT was 149/200 (74.5%), ALT that was above normal from 1 to 2 fold was 32/200 (16.0%), and ALT that was above 2×42 UI/ml was 19/200 (9.5%). In 200 HBsAg positive cases, only 58 cases of which had HBeAg positive, which accounted for 29%. With the HBV DNA detection threshold, in 200 cases, 52 samples (26.5%) of which were negative and 147 samples (73.5%) were positive, only 55 cases (27.5%) of which had the viral load over 20,000 UI/ml. The viral load was the helpful method to estimate exactly the viral replication and it also was a necessary criterion to determine the method, that will be used for HBV treatment.

In 147 HBV DNA positive cases, the results showed that genotype B, C made up 115 cases (78.2%), 26 cases (17.7%) and both genotype B, C infections were counted for 6 cases (4.1%). The genotype B/C rate was round 4/1. Moreover, in this study, no other genotypes were found out except genotype B and C. The results of this study were no any differences to previous studies including the contribution of HBV genotypes, which were various depended on geography, continents, and countries. The genotype B and C were common in Asian countries, Japan and Pacific region, moreover, the infectious rate of genotype B was higher than genotype C [1–3, 16, 17, 21].

In this study, we used the Real-time PCR kit, which was supported by Viet A company to detect the mutation of HBV. The positions of LAM resistance located regularly on the domain C of HBV reverse transcriptase gene segments, mainly YMDD type (Tyrosine-Methionine-Aspartate-Aspartate), in which Methionine replaced by Valine and Isoleucine (rtM204 V/I). Other mutations associated to LAM resistance were the replacement Leucine by Methionine on B domain (rtL236T, rtA181T/V mutations) [7, 8], and some mutations occurred on 3 rt regions belonged to HBV polymerase [4].

In 147 cases were found out LAM and AVD resistance, 99 cases of which were drug mutation (67.3%) and 48 (32.7%) of which were without any drug mutation. There were 43 cases (43.4%) of LAM resistance, 21 cases (21.2%) of ADV resistance and 35 cases (35.4%) of both LAM and ADV resistance out of 99 cases of drug resistance. The

results of this study showed that double LAM resistance mutation occurred on two positions M204I and M204V, moreover, dual DAV resistance mutation on two positions A181V and A181T with the high proportion, corresponding to 41/78 cases (52.6%) and 27/56 cases (48.2%). 5 mutation L180M cases were detected with M204I/V and only 1 case of L180M mutation was detected; there was no any cases of N236T mutations with ADV resistance out of 147 positive samples. According to a study was performed from August, 2004 to May, 2006 on 122 patients at Medic medical center, Vietnam by Ho et al. [3], authors used sequencing method on OpenGene system with TruGene reagent (Bayer), as the results, 78 cases (63.9%) carried LAM mutation with the following types and ratio of mutations: L180M & M204I (11.5%); L180M & M204V (36.1%); L180M, M204V & V173L (0.8%); L180M, M204V & V207I (0.8%); M204I (12.3%); M204I & V207I (0.8%); M204V (1.6%). To make a comparison with this study, at the time of 2012, it meant that was 8 years later; the percentage of LAM resistance was increased by more than 15%. Compared with mutations which detected on our study, these results were different from us, however, L180M and/or M204I, and/or M204V regularly appeared either alone or combined together, in some case, it combined with other mutations such as V173L or V207I with a very low rate (0.8%). A previous study which was found out by Nguyen et al. [4] showed that Nested PCR-RFLP was used to detect mutation resistance; LAM resistance mutations were detected with the high frequency counted for 74.4%, common types of mutations were M204I (39.2%) and L180M/M204I (14.7%). Nested PCR-RFLP was considered as more advantages in detection—discrimination between wild HBV and HBV mutation. To have a comparison of LAM resistance with our study conducted 4 years later, 2012, the rate of LAM resistance counted for 79.2%, it was equivalent to study of Nguyen's study. However, there were differences in the common types of mutation: single mutation was detected in 26.9%, dual mutations M204I/V were 52.6%.

In spite of consideration on the characteristics: the high frequency of mutations occurred commonly (such as L180M, M204I/V, A181V/T and N236T), addition to these mutations almost occurred with the low frequency mutation; the protocol for detecting mutation based on Real-time PCR technique in this study show that 99 cases carried mutations out of 147 cases. In 48/147 (32.7%) negative cases: patients were probably without any mutations, or the Real-time PCR method did not detect all mutations which may be occurred separately. Therefore, we temporarily concluded that all of these cases did not have any mutations of drug resistance, in future, sequencing method will be applied in detect other mutations in these 48 cases.

3.2 The Effects of Drug Resistance on Other Clinical Factors

The results of this study indicated that there were no any significant differences between resistance mutation and patient's sex ($p = 0.583$) (Data not shown). Moreover, the drug resistance status is colerated to the age of patients ($p = 0.046$) (Table 1).

Table 2 showed that drug resistance mutation combined with high the proportion of HBeAg positive and vice versa. These results also were similar to the study of Tan et al. [20], it meant that there was a difference between two groups of HBeAg positive and negative with YMDD mutation.

ALT concentration of the patients with drug resistance mutation was higher than the patients without mutation ($p = 0.022$, Table 3). Patients with mutation had viral load higher: median of viral load in case of mutation was 79.600 (1.726–18,800,000 IU/ml), in the case without mutations was 235 (60–510 UI/ml). These were significant differences ($p < 0.001$, Table 4). Drug resistance mutation was the changes in viral material that occurred to lose the prohibition of DNA replication of LAM and ADV. It could be deduced that HBV had more convenience on replication, so that, leading to increase the viral load.

In the study of Sinn et al. [19], the results were recorded that viral load in the group of patients with LAM resistance combined with ADV resistance (rtA181V/T and/or rtN236T) was higher. So that viral load due to being used as the important marker for monitoring the hepatitis therapy.

From above data, according to our suggestions, it was very necessary and important to screen resistance mutation including the LAM resistance such as M204I/V, L180M; ADV resistant such as A181V/T, N236T. With the characteristics of LAM, ADV resistance was study on this initial research, if the protocol treatment with NUCs \pm /interferon was applied in Tay Ninh hospital, the

Table 1 The correlation of resistance mutation and age of patients

	Drug resistance mutation		p
	Resistance	Non-resistance	
Age (SD)	36.2 (14.3)	41.0 (13.4)	0.046

Table 2 The relationship between drug resistance mutation and HBeAg

HBeAg (%)	Drug resistance mutation		p
	Resistance	Nonresistance	
Positive	47 (47.5)	5 (10.4)	<0.001
Negative	52 (52.5)	43 (89.6)	

Table 3 The relationship between drug resistance mutation and ALT

	Drug resistance mutation		P
	Resistance	Non-resistance	
ALT (UI/mL)	32 (21–52)	25 (15.75–35.75)	0.022

Table 4 The relationship between drug resistance mutation and viral load

	Drug resistance mutation		P
	Resistance	Non-resistance	
Virus load (IU/mL)	79,600 (1726–18,800,000)	253 (60–510)	<0.001

screening and selection of mutations were very essential. The protocol for detecting the resistance mutation by using Real-time PCR was proved to have more effective in clinical application.

4 Conclusion

The average age of patient was 35.5 ± 13.7 ; HBV infection in female was counted for 58.5%, the proportion of persons without consideration they are infected with HBV was up to 55.5%, the main of HBV infection through the spread of blood was 94.5%. The ALT value with normal range, HBeAg negative and without any recommendation for hepatitis treatment are counted for 74.5, 71, 68.5% in turn. In HBsAg positive group, 73.5% HBV DNA positive for predominant genotype B was counted for 78.2%. Group with high viral load with $\geq 20,000$ UI/mL was counted for 27.5%. The proportion of antiviral drug resistance mutation in LAM, both LAM and ADV were counted for 67.3, 43.3% in turn. In the group of LAM resistance, double mutations at 204I, 204V was 52.6%. In cases of ADV resistance, double mutations at 181 V, 181T was up to the highest proportion with 48.2%. The effects of genotypes on clinical and sub-clinical factors were not significant differences. Resistance mutation regularly occurred in young people with high HBeAg positive, ALT and viral load.

Conflicts of Interest The authors declared that they have no conflict of interests.

References

1. Đông thị Hoài An, Cao Minh Nga. 2003. Kỹ thuật định typ gene siêu vi viêm gan B bằng Multiplex PCR trên bệnh nhân nhiễm siêu vi viêm gan B mạn. *Từ khoa học sinh học phân tử đến cuộc sống và chăm sóc sức khỏe*, pp. 17–25

2. Đỗ Thị Thùy Dương và Lê Huyền Ái Thủy: Ứng dụng kỹ thuật real-time PCR trong xác định kiểu gen của virus gây viêm gan siêu vi B tại Đắk Lắk. *Tạp chí Khoa học – Kỹ thuật*, 1(19)-2011: 118–123 (2010)
3. Hồ Tấn Đạt, Phạm Thị Thu Thủy, Nguyễn Bảo Toàn, Nguyễn Thị Kiều Oanh, Nguyễn Thanh Tòng. Trung Tâm Y Khoa MEDIC, TP. HCM. Ứng dụng kỹ thuật giải trình tự chuỗi để xác định kiểu gen và các đột biến kháng thuốc của siêu vi viêm gan B. Trích từ nguồn: <http://www.drthuthuy.com/reseach/HBVGenotype.html>
4. Nguyễn Chí Vinh. Báo cáo nghiệm thu, đề tài “Xây dựng quy trình phát hiện đột biến kháng Lamivudine rt180 – rt204 và thử nghiệm ứng dụng quy trình trên huyết thanh bệnh nhân”, Sở KHCN, TP. HCM (2008)
5. Thuy, H. T. T., Hung, N. V., Toan, N. B., Thuy, L. H. A.: Phát hiện đột biến rtN236T và rtA181T/V kháng adefovir dipivoxil ở những bệnh nhân nhiễm virus HBV mạn tính bằng real-time PCR. Báo cáo khoa học Hội nghị CNSH toàn quốc, pp. 888–890 (2009)
6. Thuy, H. T. T.: Phát hiện đột biến rtL180 M và rtM204 V/I kháng Lamivudine ở bệnh nhân nhiễm HBV mạn tính bằng kỹ thuật real-time PCR”. Hội nghị khoa học kỹ thuật đại học y dược TP. HCM lần thứ 27 (2010)
7. Angus, P., Vaughan, R., Xiong, S., Yang, H., Delaney, W., Gibbs, C., et al.: Resistance to adefovir dipivoxil therapy associated with the selection of a novel mutation in the HBV polymerase. *Gastroenterology* **125**(2), 292–297 (2003)
8. Bartholomeusz, A., Locarnini, S., Ayres, A., Thompson, G., Sozzi, V., Angus, P., et al.: Molecular modelling of hepatitis B virus polymerase and adefovir resistance identifies three clusters of mutations. *Hepatology* **40**(1), 246A (2004)
9. Hadziyannis, S.J., Tassopoulos, N.C., Heathcote, E.J., Chang, T. T., Kitis, G., Rizzetto, M., et al.: Long-term therapy with adefovir dipivoxil for HBeAg-negative chronic hepatitis B for up to 5 years. *Gastroenterology* **131**(6), 1743–1751 (2006)
10. Jia-Hong, K.: Molecular epidemiology of hepatitis B virus. *Korean J. Intern. Med.* **26**, 255–261 (2011)
11. Liang, T.J.: Hepatitis B: The virus and diseases. *Hepatology* **48** (2009)
12. Linda, D., Michael, J.C., Jonathan, D., Linh, T.N., Thu, H.T.T., Binh, T.N., Jeff, C., Suzie, C., Hien, T.N., William, W.H., Lan, A.N. T.: A multicentre molecular analysis of hepatitis b and blood-borne virus coinfections in VietNam. *PLoS ONE* **7**(6), 1–11 (2012)
13. Long, H.N., Nghiem, B.H., Philip, V., Nghi, B.H., Ruel, T.G., Huy, N.T., et al.: Prevalence of hepatitis B virus genotype B in Vietnamese patients with chronic hepatitis B. *Hepatol. Int.* **3**, 461–467 (2009)
14. Niesters, H.G., Pas, S., de Man, R.A.: Detection of hepatitis B virus genotypes and mutants: current status. *J. Clin. Virol.* **34**(1), S4–S8 (2005)
15. Norder, H., Courouce, A.M., Magnius, L.O.: Complete genome, phylogenetic relatedness and structural proteins of six strains of the hepatitis B virus, four of which represent two new genotypes. *Virology* **198**, 489–503 (1998)
16. Norder, H., Hammas, B., Lee, S.D., Bele, C., Courouce, A.M., Mushawar, I.K., et al.: Genetic relatedness of hepatitis B viral strains of diverse geographical origin and natural variation in the primary structure of the surface gene. *J. Gen. Virol.* **74**, 1341–1348 (1993)
17. Norio, A., Hiromitsu, K.: Influence of hepatitis B virus genotypes on the response to antiviral therapies. *J. Antimicrob. Chemother.* **55**, 139–142 (2005)
18. Okamoto, H., Tsuda, F., Sakagawa, H., Sastrosoewignjo, R.I., Imai, M., Miyakawa, Y.: Typing hepatitis B virus by homology in nucleotide sequence comparison of surface antigen subtypes. *J. Gen. Virol.* **69**, 2575–2583 (1988)

19. Sinn, D.H., Lee, H.I., Gwak, G.Y., Choi, M.S., Koh, K.C., Paik, S. W., Yoo, B.C., Lee, J.H.: Virological response to adefovir monotherapy and the risk of adefovir resistance. *World J. Gastroenterol.* **17**(30), 3526–3530 (2011)
20. Tan, Y.W., Ge, G.H., Zhao, W., Gan, J.H., Zhao, Y., Niu, Z.L., Zhang, D.J., Chen, L., Yu, X.J., Yang, L.J.: YMDD motif mutations in chronic hepatitis B antiviral treatment naïve patients: a multi-center study. *Brazilian J. Infect. Dis.* **16**(3), 250–255 (2012)
21. Tran, H.T., Ushijima, H., Quang, V.X., Phuong, N., Li, T.C., Hayashi, S., Lien, X.T., Sata, T., Abe, K.: Prevalence of hepatitis virus types B through E and genotypic distribution of HBV and HCV in Ho Chi Minh City, Vietnam. *Hepatol. Res.* **26**(4), 275–280 (2003)

A Meta-Analysis of *Apolipoprotein B* Gene Mutation in Hypercholesterolemia Based on Previous Studies

Phuong Kim Truong, Phuong Mai Thi Nguyen, Thuan Duc Lao, and Thuy Ai Huyen Le

Abstract

Apolipoprotein (Apo) B gene consists of 28 introns, 29 exons and encodes the protein component of LDL particles, which plays a central role in human lipoprotein metabolism. Mutations in the *ApoB-100* will drastically alter its functional activity leading to a decrease in its binding to LDLR, resulting in high blood cholesterol levels. However, previous publications related to the mutations of ApoB-100 were not always unification. In current study, therefore, a meta-analysis was performed. A systematic literature analysis was conducted based on previous studies published in Pubmed, Pubmed Central (NCBI), Google by using following keywords: *Apolipoprotein B* gene, hypercholesterolemia, Familial Defective Apolipoprotein B-100 by the end of March, 2018. The prevalence of *ApoB* mutation was calculated and accessed by MedCalc[®]. Additionally, the meta-regression analysis and subgroup analysis were conducted. As the results, the total of 22 cohort studies, that includes 17,303 hypercholesterolemic blood samples, were enrolled into current study. The analysis results indicated that the prevalence of *ApoB* mutation was 31.774% (95%CI = 8.288 – 61.912, $p < 0.0001$). Additionally, R3500Q was identified as the common mutation occurred in *ApoB*. The association between ApoB mutations and hypercholesterolemia was effected by different methods analysis (PCR-sequencing: prevalence = 30.731%; 95% CI = 4.561 – 67.104, $p < 0.001$; Other methods: prevalence = 32.265%; 95% CI = 10.739 – 58.846, $p < 0.0001$, Random model) and ethnic groups (European: prevalence = 35.929%; 95% CI = 6.956 – 72.486, $p < 0.0001$, Random model; Asian: prevalence = 33.806%; 95%CI = 3.681 – 75.061, $p < 0.0001$). In conclusion, the prevalence of mutations of

ApoB-100 is high in hypercholesterolemia. R3500Q mutation is the frequent type of *ApoB-100* mutations. The identification of prevalence of mutations of *ApoB-100* was depended on ethnic group, methods.

Keywords

Apolipoprotein (Apo) B gene • Hypercholesterolemia • R3500Q • Meta-analysis

1 Introduction

Familial hypercholesterolemia (FH; OMIM#143890), which was the first described in 1930s by Carl Müller, is a common dominant disorder of cholesterol metabolism characterized by elevated level of serum cholesterol [5]. Many factors had been proven to affect the manifestation of FH including age, gender, lifestyle, and genetic disorders. According to the molecular mechanisms, the pathogenesis of FH comprise of a variety of genetic alterations in many genes, including *Low Density Lipoprotein Receptor (LDLR)*, *Apolipoprotein B-100 (ApoB-100)*, *Low density lipoprotein receptor adaptor protein (LDLRAP)*, *proprotein convertase subtilisin/kexin type 9 (PCSK9)* [6]. Among them, *ApoB* is localized at 2p24.1 and consists 28 introns, and 29 exons, that codes for the protein component of LDL particles, plays a central role in human lipoprotein metabolism [3, 4, 6]. APOB-100 is the protein component responsible for the cellular recognition and catabolism of LDL via the LDLR pathway, thus, the APOB-100 mediates the binding of LDL to LDLR, leading the clearance of LDL particles [6, 8]. The mutation in *ApoB-100*, will drastically alter its functional activity leading to a decrease in its binding to LDLR, which is proven to be associated with, named as “Familial

P. K. Truong (✉) · P. M. T. Nguyen · T. D. Lao · T. A. H. Le
Faculty of Biotechnology, Ho Chi Minh City Open University,
Ho Chi Minh City, Vietnam
e-mail: phuong.tk@ou.edu.vn

T. A. H. Le
e-mail: thuy.lha@ou.edu.vn

Defective Apolipoprotein B-100" (FDB) [1]. However, many studies relevant to types and frequency of mutation were various. It could be explained that the previous studies were carried on different populations, sample sizes, methods for mutation detection. The significant difference of frequency of *ApoB-100* mutation has been reported in patients with FH. Thus, we performed the meta-analysis to clarify the differences in previous published results regarding to the proportion of *ApoB-100* gene mutation and analyze the factors that affect the frequency of *ApoB-100* mutation, such as ethnicity, methods for detection, clinical characteristics of FDB.

2 Materials and Methods

2.1 Search Strategy, Inclusion and Exclusion Criteria of Literature

The systematic review of relevant literature was conducted by using many keywords for the literature search: Familial hypercholesterolemia, Apolipoprotein B-100, Familial Defective Apolipoprotein B-100 on four electronic databases: PUBMED, Web of Science, Embase database, updated to March, 2018.

The studies were included if they satisfied the following inclusion criteria: (1) The investigation/identification of *ApoB* mutation, which correlated with FDB; (2) The correlation between *ApoB* mutation and clinicopathological features of FDB; (3) cohort design studies of APOB mutation and FDB; (4) the identification method was not excluded. Additionally, only studies written in English were included for current study. Types of case reports, abstracts, review, and letter to editor were eliminated.

2.2 Data Extraction and Statistical Analysis

The following data from each available study were extracted, including the last name of the first author, publication year, country, ethnicity, cohort design study, method for identification of mutation, clinical features of FH. In current study, meta-analysis of data was performed using Medcalc[®]2018. The proportion of APOB mutation was calculated to determine the strength of the association between APOB mutation and FDB. Additionally, the statistical heterogeneity among the studies was tested based on the Cochran's Q and I² tests. The random-effects model was employed when the *p* value was less than 0.1 in the Q-test, indicating the presence of substantial heterogeneity.

3 Results and Discussion

3.1 Identification of Relevant Study and Characteristics of Studies

A total of 158 studies were initially identified by literature search. After selection based on the inclusion and exclusion criteria, finally, 22 studies were included in the meta-analysis. The detail of characteristics was summarized in Table 1.

3.2 Meta-Analysis: The Proportion of APOB Mutation in FDB and Subgroup Analysis

In the meta-analysis, the heterogeneity among included studies was significant for Q test ($p < 0.0001$). Therefore, the random-effect model was employed to access the proportion of *ApoB* mutation. The proportion of APOB mutations were observed in a range of from 1.77% to 100%. Based on the random-effect model, our results revealed that the proportion of *ApoB* mutation was 37.77% (95% = 8.288 – 61.912), which was significantly associated with FH, based on the calculation of 17,303 cases (Fig. 1).

To further assess the potential methods, as well as the distribution of ethnicity, types of mutation, we conducted the subgroup analysis according to the methods used in literatures, types of identified mutation, ethnicity (Table 2). With the respect to the subgroups categorized by the method, the results showed that PCR—sequencing method is the prior method in identification of *APOB-100* mutation compared to other methods, such as AS-PCR, real-time-PCR, melting curve analysis, Multiplex ligation probe amplification (MLPA), polymerase chain reaction-single-strand conformation polymorphism (PCR-SSCP), Denaturing gradient gel electrophoresis (DGGE), restriction fragment length polymorphism (RFLP). Subgroup analysis based on the ethnicity showed that the mutations of *ApoB-100* gene was significantly correlated with the FDB in among Asian, European and Americans populations investigated. Particularly, the highest proportion of *ApoB-100* was observed in European (Proportion = 35.929%; 95%CI = 6.956 – 72.486) and Asian (Proportion = 33.806%; 95%CI = 3.681 – 75.061). It suggested that the Asia and European population, may be more susceptible to *ApoB-100* mutation. However, due to the limitation of the small sample size, the analysis of the American and Australian population subgroup in the current study should be cautiously interpreted. Concerning to types of mutation, the R3500Q mutation, meant that G → A transition at nucleotide 10,708, subsequently the substitution

Table 1 Characteristics of studies included in the meta-analysis of APOB-100 mutation and FH

First author, year	Country	Ethnicity	Method	Total	Even	Types of mutation	Age	TC (mmol/L)	LDL-C (mmol/L)
Gabčová, 2017	Slovakia	European	Realtime PCR	235	14	R3527Q	27.1 ± 4.4	8.2 ± 0.4	6 ± 0.3
Truong, 2017	Viet Nam	Asian	PCR & Sequencing	40	27	R3500Q			
Xiang, 2017	China	Asian	Sequencing	219	11	R3527Q			
Benn, 2016	Denmark	European	Realtime- PCR, MLPA	76	49	R3500Q	20–100		
Du, 2016	China	Asian	PCR & Sequencing	11	1	R3527W	7–48	7.52–20.15	5.47–18.21
Pandey, 2016	United Kingdom	European	PCR, Melting-Curve Genotyping	10	4	R3527Q	1–46	5.5–9.2	4–7.2
Sharify, 2016	Poland	European	PCR & Sequencing	161	13	R3527Q			
Wald, 2016	United Kingdom	European	PCR & Sequencing, MLPA	10,095	10,015	R3527Q	1–2		
Han, 2015	Korean	Asian	PCR & Sequencing	69	46	R3527Q	54 ± 13	8.2 ± 1.24	6 ± 1.06
Maglio, 2014	Sweden	European	NGS	77	4	R3527Q, R3500W			
Bertolini, 2013	Italy	European	Northern blot, RT-PCR	1018	18	R3527Q	2–86		
Chatzistefanidis, 2013	Greece	European	AS-PCR	6	6	R3527Q			
Pecin, 2011	Croatia	European	PCR & Sequencing	8	1	R3527Q	21–60	6.1–10.7	4.4–8.41
Futema, 2012	USA	American	PCR & Sequencing, MLPA	48	3	R3527Q			
Tichý, 2012	Czech Republic	European	PCR & Sequencing, MLPA, PCR & RFLP	2239	265	R3527Q			
Chmara, 2011	Poland	European	PCR & Sequencing, MLPA	378	25	R3527Q	18–95	9 ± 2.5	6.94 ± 2.4
Liyanage, 2008	Australia	Australian	PCR & Sequencing	35	8	R3527Q, R3500W			
Yang, 2007	Taiwan	Asian	PCR & Sequencing	30	3	R3527Q	14–70	8.2 ± 1.8	5.7 ± 1.4
Tosi, 2008	United Kingdom	European	PCR & Sequencing, MLPA	200	14	R3500W			
Soufi, 2004	Germany	European	PCR & Sequencing, DGGE	853	844	R3500Q	42–69	2.46–8.8	1.6–6.2
Real, 2003	Spain	European	Southern blot, PCR-SSCP	213	106	R3500Q			
Bochmann, 2001	Germany	European	PCR & Sequencing, SSCP	31	22	R3500Q	33–71	7.4–16	5.4–13.7
Kalina, 2001	Hungary	European	AS-PCR	21,000	2	R3500Q			
Lombardi, 2000	Netherlands	European	PCR & Sequencing, DGGE	1223	30	R3500Q			
Haddad, 1999	Utah	American	SSCP, Sequencing	47	3	R3500Q			

of Arginine by Glutamine at codon 3500, was announced in all of studies. It could be explained that *ApoB* R3500Q was demonstrated as changing ApoB protein structure, completely broke the link between LDLR receptor with carrier cholesterol (LDLC) and therefore this is the cause of familial defective apolipoprotein (FDB), consequently, accumulate of cholesterol in the blood which lead to cardiovascular

disease risk [2, 7]. In the subgroup of major clinical parameter, the results of the meta-analysis suggested that individuals with *ApoB-100* mutations are associated with the levels of total cholesterol and LDL cholesterol. In the characteristic of total of cholesterol ≥ 5 mmol/L, the significantly proportion of *ApoB-100* mutation was observed (Proportion = 29.563; 95% CI = 10.240 – 53.855).

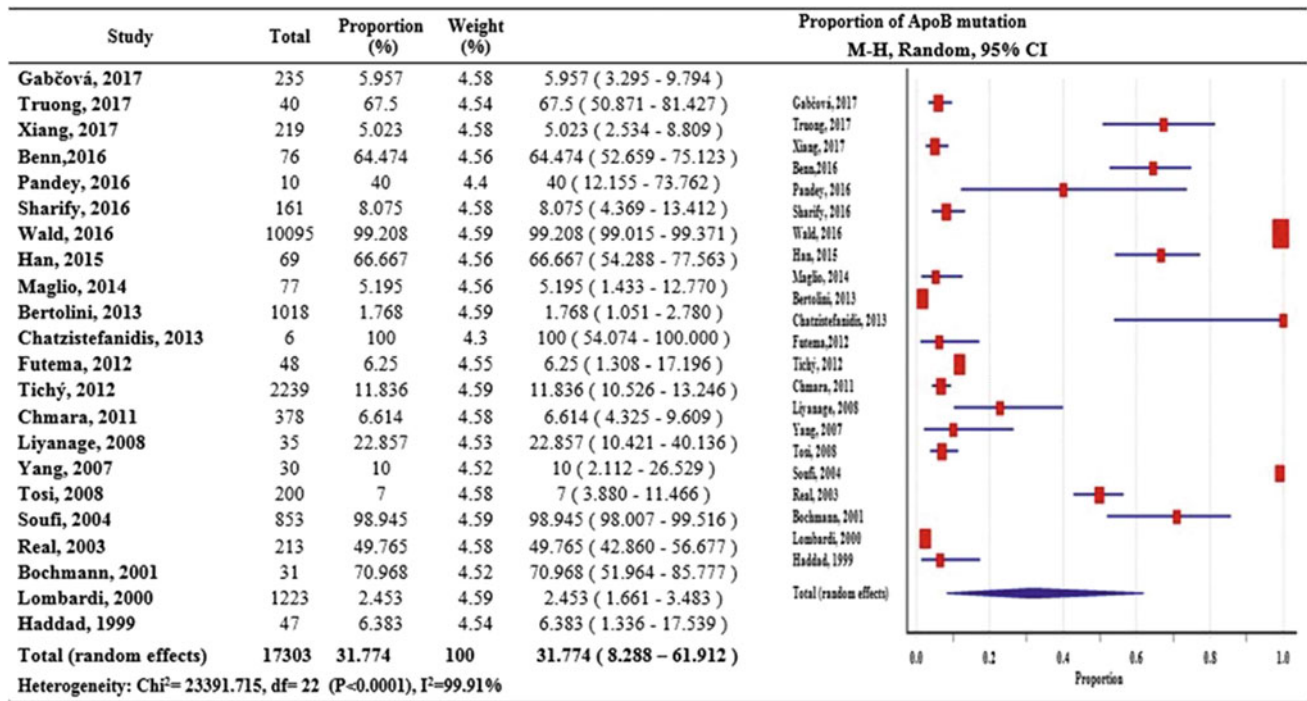


Fig. 1 Forest plots of APOB mutation associated with FH

Table 2 The subgroup analysis of APOB-100 mutation in FH

Test of association			Test of heterogeneity			
	Variables	N	Proportion (95% CI)	Model	Ph	I2 (%)
Total		22	31.774 (8.288–61.912)	R	<0.0001	99.91
Method						
PCR—Sequencing		15	30.731 (4.561–67.104)	R	<0.0001	99.93
Other methods		7	32.265 (10.739–58.846)	R	<0.0001	98.74
Types of mutation						
R3527Q/R3500Q		19	35.650 (9.206–68.177)	R	<0.0001	99.92
R3500W		1	7 (3.880–11.466)	NA	NA	NA
R3527Q/R3500Q & R3500W		2	12.92 (1.168–34.427)	R	0.0085	85.55
Ethnicity						
Asian		4	33.806 (3.681–75.061)	R	<0.0001	98.09
European		15	35.929 (6.956–72.486)	R	<0.0001	99.94
American		2	7.182 (2.923–13.132)	F	0.978	0.00
Australian		1	22.857 (10.421–40.136)	NA	NA	NA
Clinical parameters						
Total of cholesterol (≥ 5 mmol/L)		6	29.563 (10.240–53.855)	R	<0.0001	97.23
LDL Cholesterol (≥ 5 mmol/l or ≥ 190 mg/dl)		5	27.774 (7.896–53.987)	R	<0.0001	97.72
Total of cholesterol & LDL Cholesterol (≥ 5 mmol/l)		5	27.774 (7.896–53.987)	R	<0.0001	97.72

4 Conclusion

The present study found that the prevalence of *ApoB* mutation was 31.774% (95%CI = 8.288 – 61.912, $p < 0.0001$) in FDB. The major method for *ApoB-100* mutation identification was PCR-sequencing (prevalence = 30.731%; 95% CI = 4.561 – 67.104, $p < 0.001$). The criteria for clinical characteristics selection was based on the total of cholesterol (Total of cholesterol ≥ 5 mmol/L). Additionally, R3500Q was the prior type of *ApoB-100* mutations, leading to the FDB, own type of FH. The high proportion of *ApoB-100* was observed in European population (prevalence = 35.929%; 95%CI = 6.956 – 72.486, $p < 0.0001$) and Asian population (prevalence = 33.806%; 95%CI = 3.681 – 75.061, $p < 0.0001$).

Conflicts of Interest The authors declared that they have no competing interests.

References

- Hansen, P.S.: Familial defective apolipoprotein B-100. *Dan. Med. Bull.* **45**(4), 370–382 (1998)
- Hevonoja, T., Pentikäinen, M.O., Hyvönen, M.T., Kovanen, P.T., Ala-Korpela, M.: Structure of low density lipoprotein (LDL) particles: basis for understanding molecular changes in modified LDL. *Biochim. Biophys. Acta* **1488**(3), 189–210 (2000)
- Knott, T.J., Rall Jr., S.C., Innerarity, T.L., Jacobson, S.F., Urdea, M. S., Levy-Wilson, B., et al.: Human apolipoprotein B: Structure of carboxyl-terminal domains, sites of gene expression, and chromosomal localization. *Science* **230**(4721), 37–43 (1985)
- Law, S.W., Lackner, K.J., Hospattankar, A.V., Anchors, J.M., Sakaguchi, A.Y., Naylor, S.L., Brewer Jr., H.B.: Human apolipoprotein B-100: cloning, analysis of liver mRNA, and assignment of the gene to chromosome 2. *Proc. Natl. Acad. Sci. USA* **82**(24), 8340–8344 (1985)
- Najam, O., Ray, K.K.: Familial hypercholesterolemia: a review of the natural history, diagnosis, and management. *Cardiol. Ther.* **4**(1), 25–38 (2015)
- Soutar, A.K., Naoumova, R.P.: Mechanisms of disease: genetic causes of familial hypercholesterolemia. *Nat. Clin. Pract. Cardiovasc. Med.* **4**(4), 214–225 (2007)
- Truong, P.K., Van Bui, C., Lao, T.D., Le, T.H.A.: Detection of defective Apolipoprotein B-100 R3500Q mutation caused familial hypercholesterolemia in Vietnamese patients. In: Vo Van T., Nguyen Le T., Nguyen Duc T. (eds.) 6th International Conference on the Development of Biomedical Engineering in Vietnam (BME6). BME 2017. IFMBE Proceedings, vol 63. Springer, Singapore (2018)
- Twisk, J., Gillian-Daniel, D.L., Tebon, A., Wang, L., Barrett, P.H., Attie, A.D.: The role of the LDL receptor in apolipoprotein B secretion. *J. Clin. Invest.* **105**(4), 521–532 (2000)

Part XIV

**Public Health—Cancer Therapy and
Reconstructive Surgery**



An Overview of Immune Checkpoints and Immunotherapy in Cancer

T. Q. Huynh, D. N. Tran, T. P. Chau, T. M. Huynh, C. H. Trinh, and N. Doan

Abstract

Immune checkpoints are molecules in the immune system that either turn-on a signal (co-stimulatory molecules) or turn-off a signal for maintaining self-tolerance and modulating the duration and amplitude of physiological immune responses. Many cancers protect themselves from the immune system by inhibiting the T cell signal Inhibitory receptors such as anti-cytotoxic T-lymphocyte antigen 4 (CTLA-4) and programmed death 1 (PD-1), expressed on tumor-specific T cells, lead to compromised activation and suppressed effector functions such as proliferation, cytokine secretion, and tumour cell lysis. Modulating these receptors using monoclonal antibodies, an approach termed “immune checkpoint blockade,” has gained momentum as a new approach in cancer immunotherapy. This treatment concept was first introduced in patients with advanced melanoma: In this patient population, the anti-CTLA-4 antibody Ipilimumab was the first drug ever to show improved overall survival in phase III trials. Antibodies directed against PD-1 and its ligand, PD-L1, have shown much promise in the treatment of melanoma, renal cell cancer, non-small cell lung cancer, and other tumours, as evident by encouraging rates and durability of tumour responses. Because of the successes with immune checkpoint inhibitors in cancer immunotherapy, many new agents and strategies,

including combination approaches, are being developed at a fast pace.

Keywords

Immune checkpoint • CTLA4, PD-1 • PD-L1

1 Introduction

Immune checkpoints are regulators of the immune system, play the critical role in the maintenance of the self-tolerance, prevention of autoimmune and protection of tumor tissue from the immune collateral damages [1]. The above immune checkpoints are often appropriated by the tumors, to contain the capacity of the immune system to post an efficient anti-tumor reaction.

To reboot anti-tumor immunity, stalling immune checkpoints is therefore an encouraging tactic [2]. Lately, the antibody-based medications delaying the immune checkpoints CTLA4 and PD-1 appeared as “game changers” in cancer treatment, running to strong clinical reactions even in patients with progressive malignancy. The discovery achievements in melanoma, lung and kidney cancers offered a remedial confirmation for this method for a novel age of cancer management [3] (Table 1).

2 Immune’s Checkpoints Proteins in Immune System

Notwithstanding the achievement of CTLA4 and PD-1 blockers, numerous patients do not react to these managements. Additionally, clinical value is still restricted to a small subset of cancer indications, and only a minority achieves the promise of ongoing survival [5, 6]. It is consequently obvious there is added immune avoidance means facilitated by extra immune checkpoint proteins. In this appraisal, we

T. Q. Huynh · D. N. Tran · T. M. Huynh · C. H. Trinh
Can Tho Oncology Hospital, Can Tho, Vietnam

T. P. Chau
Department of General and Thoracic and Oncologic Surgery
of Cho Ray Hospital, Ho Chi Minh City, Vietnam

N. Doan (✉)
Griffith University Schools of Dentistry and Oral Health,
Gold Coast, Australia
e-mail: nvtdoan123@gmail.com; nvtdoan23@gmail.com

N. Doan
The University of Queensland & Queensland University
of Technology, Brisbane, Australia

Table 1 The clinical progress of agents that focus immune-checkpoint routes

Target	Biological function	Antibody or Ig fusion protein	State of clinical development ^a
CTLA4	Inhibitory receptor	Ipilimumab	FDA approved for melanoma, Phase II and Phase III trials ongoing for multiple cancers
Tremelimumab	Previously tested in a Phase III trial of patients with melanoma; not currently active		
PD1	Inhibitory receptor	MDX-1106 (also known as BMS-936558)	Phase I/II trials in patients with melanoma and renal and lung cancers
MK3475	Phase I trial in multiple cancers		
CT-011 ^b	Phase I trial in multiple cancers		
AMP-224 ^c	Phase I trial in multiple cancers		
PDL1	Ligand for PD1	MDX-1105	Phase I trial in multiple cancers
Multiple mAbs	Phase I trials planned for 2012		
LAG3	Inhibitory receptor	IMP321 ^d	Phase III trial in breast cancer
Multiple mAbs	Preclinical development		
B7-H3	Inhibitory ligand	MGA271	Phase I trial in multiple cancers
B7-H4	Inhibitory ligand	Preclinical development	
TIM3	Inhibitory receptor	Preclinical development	

CTLA4, cytotoxic T-lymphocyte-associated antigen 4; FDA, US Food and Drug Administration; Ig, immunoglobulin; LAG3, lymphocyteactivation gene 3; mAbs, monoclonal antibodies; PD1, programmed cell death protein 1; PDL, PD1 ligand; TIM3, T cell membrane protein 3

^aAs of January 2012. ^bPD1 specificity not validated in any published material. ^cPDL2–Ig fusion protein. ^dLAG3–Ig fusion protein [4]

discuss separately about two utmost reviewed immune checkpoints.

3 Cytotoxic T-Lymphocyte-Related Proteins 4 (CTLA4)

This protein, correspondingly identified as cluster of differentiation 152 (CD152), is a receptor, which works as an immune checkpoint and down synchronizes the immune reactions. CTLA4 is presently conveyed in regulatory T cell once initiation of a occurrence, which is specifically noted in cancers. It behaves as an “off” switch when attached to CD80 or CD86 on the exterior of antigen exhibiting cell (APC). The *ctla4* gene in mice and CTLA4 gene in human encrypt the CTLA4 protein.

3.1 Function

Generally, CTLA4 is a representative of the immunoglobulin superfamily that is conveyed by stimulated T cells and conducts an inhibitory wave to T cell. The stimulation of T cell, across the TCR and CD28, results in increasing manifestation of CTLA-4.

CTLA4 is similar to the T-cell co-stimulatory protein, CD28, and the two molecules join to CD80 (B7-1) and CD86 (B7-2), localizing on the cell exterior of antigen-presenting cells (APC), permitting to contest CD28 from its ligands. CTLA4 diffuses an inhibitory sign to T cells, while CD28 conveys a stimulatory signal. CTLA4 is similarly located in Treg cells and provides to its inhibitory role.

The method by which CTLA-4 works in T cells remnants being described by biochemical proof that implied CTLA-4 employs a phosphatase to the TCR, hence weakening the sign. This work stays unverified in the literature. More contemporary research has implied that CTLA-4 may work in vivo by seizing and eliminating B7-1 and B7-2 from the membranes of antigen-presenting cells, consequently creating these inaccessible for activating of CD28. Furthermore, it has been discovered that dendritic cell (DC)—Treg collaboration produces repossession of Fascin-1, an actin-bundling protein vital for immunological synapse establishment, and twists Fascin-1–dependent actin polarity in antigen exhibiting DCs to the T reg cell connection region [6]. Though it is rescindable on T regulatory cell detachment, this requisitioning of crucial cytoskeletal constituents triggers an exhausted condition of DCs, resulting in lessened T cell preparing. This indicates Treg-mediated immune

clampdown is a many-step development. Also the CTLA-4 CD80/CD86 communication, the fascin related polarity of cytoskeleton concerning DC-Treg immune synapse performs a key function.

CTLA-4 may also function via modulation of cell motility and/or signal through PI3 kinase. Early multi-photon microscopy studies observing T-cell motility in intact lymph nodes appeared to give evidence for the so-called “reverse-stop signaling model”. In this model CTLA-4 reverses the TCR-induced ‘stop signal’ needed for firm contact between T cells and antigen-presenting cells (APCs). The purpose of these reports is to equate CTLA-4 positive cells, which are primarily supervisory cells and are at least partly stimulated, with CTLA-4 negative naïve T cells whilst other clusters, having investigated the influence of antibodies to CTLA-4 *in vivo*, have established slight or no consequence on motility in the framework of anergic T-cells [7].

3.2 Structure

The protein comprises an extracellular V area, a trans-membrane field, and a cytoplasmic tail. Different link variations, encrypting diverse isoforms, have been depicted. The membrane-bound isoform works as a homodimer interlocked by a disulfide bond, whilst the resolvable isoform behaves as a monomer. The intracellular area is analogous to that of CD28, in that it has no inherent catalytic action and includes one YVKM motif able to fix PI3K, PP2A and SHP-2 and one proline-rich motif capable to fix SH3 comprising proteins. The principal function of CTLA-4 in impeding T cell reactions appear to be candidly through SHP-2 and PP2A dephosphorylation of TCR-proximal indicating proteins for example CD3 and LAT. CTLA-4 can additionally influence signing subtly thru opposing with CD28 for CD80/86 attachment [8]. CTLA-4 can similarly attach PI3 K, though the significance and outcomes of this interface are undefined.

3.3 Clinical Significance

The variations of this gene have been linked with various conditions such as insulin-dependent diabetes mellitus, Hashimoto’s thyroiditis, Graves’ disease, celiac disease, thyroid-associated orbitopathy, systemic lupus erythematosus primary biliary cirrhosis and further autoimmune disorders. Polymorphisms of the CTLA-4 gene are coupled with autoimmune syndromes for example autoimmune thyroid disorder and numerous scleroses; nevertheless this

relationship is frequently feeble. In Systemic Lupus Erythematosus (SLE), the link alternative sCTLA-4 found to be abnormally formed and located in the serum of patients with vigorous SLE.

3.4 Germline Haploinsufficiency

Generally, germline haploinsufficiency of CTLA4 results in CTLA4 deficit or CHAI and LATAIE disorder (CTLA4 haploinsufficiency with autoimmune penetration), an uncommon genetic syndrome of the immune structure. Patients with CHAI and LATAIE, present with autoantibody-mediated cytopenias, lymphadenopathy/splenomegaly, hypogammaglobulinemia, organ-specific autoimmunity, and lymphocytic infiltration of nonlymphoid organs. Although features of CHAI and LATAIE are similar, a notable difference is the typically earlier age of onset with LATAIE, where disease onset is often apparent in preschool-age children, whereas CHAI presents in older children or young adults. The autoantibody-mediated cytopenias (i.e., autoimmune hemolytic anemia, autoimmune thrombocytopenia, and neutropenia), lymphadenopathy, and splenomegaly resemble the autoimmune lymphoproliferative syndrome [9].

3.5 Clinical and Laboratory Indications

For any symptomatic patients with CTLA4 mutations categorized by an immune dysregulation condition involving widespread T cell penetration in some organs, involving the gut, lungs, bone marrow, central nervous system, and kidneys [2]. Most patients have diarrhea or enteropathy. Lymphadenopathy and hepatosplenomegaly are likewise as autoimmunity. The tissues disturbed by autoimmunity differ nonetheless involve thrombocytopenia, and thyroiditis, psoriasis, type I diabetes, and arthritis. Furthermore, respiratory contagions are very usual. Notably, the clinical appearances and illness progressions are alterable with certain persons relentlessly affected, while others display minor symptom of complaint. This disorder is defined to have partial penetrance of complaint. Penetrance is thought to be partial when particular persons stop to carry the characteristic and appear fully asymptomatic, though they pass the allele. The penetrance is expected to be approximately 60%.

The clinical signs are initiated by anomalies of the immune arrangement. Majority of patients acquire reduced quantities of at least one immunoglobulin isotype, and have trivial CTLA4 protein manifestation in T regulatory cells, hyperactivation of effector T cells, muted switched memory B cells, and gradual damage of travelling B cells [10].

3.6 Treatment

After a diagnosis is completed, the management is established on an person's clinical circumstance and may involve typical treatment for autoimmunity and immunoglobulin defects. A new report cured a Korean CHAI ailment patient with CTLA4 mimetic, CTLA4-Ig (e.g., abatacept) and was capable to manage immune action and recuperate patient signs [10].

3.7 Agonists to Diminish Immune Action

The moderately greater attraction of CTLA4 has created it an impending treatment for autoimmune disorders. Synthesis proteins of CTLA4 and antibodies (CTLA4-Ig) have been employed in clinical experiments for rheumatoid arthritis. The mixture protein CTLA4-Ig is commercially obtainable as Orencia (abatacept). A succeeding group form of CTLA4-Ig recognized as belatacept lately ratified by the FDA established on encouraging outcomes from the randomized Phase III BENEFIT report. It was accepted for renal transplantation in patients that are exposed to Epstein-Barr virus (EBV) [11].

3.8 Antagonists to Surge Immune Endeavor

Equally, there is growing attention in the conceivable remedial aids of hindering CTLA4 (exploiting antagonistic antibodies alongside CTLA such as ipilimumab (FDA accepted for melanoma in 2011) as a ways of stopping immune system acceptance to tumors and thus offering a hypothetically valuable immunotherapy scheme for patients with malignance [5]. This is the initial permitted immune checkpoint deter treatment. Alternative is tremelimumab, however it is still not ratified [12].

4 Programmed Cell Death Protein 1 (PD-1)

Planned cell death protein 1, similarly recognized as PD-1 and cluster of differentiation 279 (CD279), is a cell exterior receptor participating an vital function in down-regulating the immune structure and stimulates self-tolerance by over-powering T cell inflammatory endeavor.

PD-1 is an immune checkpoint and protects alongside autoimmunity over a twofold mechanism of encouraging apoptosis (programmed cell mortality) in antigen-specific T-cells in lymph nodes whilst concurrently decreasing apoptosis in regulatory T cells (anti-inflammatory, suppressive T cells). PD-1 impedes the immune system, inhibits autoimmune disorders, although it can similarly block the immune system from extermination of tumor cells.

A latest group of medications that impede PD-1, the PD-1 inhibitors, trigger the immune system to assault cancers and are thus employed with variable realization to handle specific sorts of malignancy. The PD-1 protein in humans programmed via the PDCD1 gene. PD-1 is a cell superficial receptor that fits to the immunoglobulin superfamily and is conveyed on T cells and pro-B cells. PD-1 attaches dual ligands, PD-L1 and PD-L2 [2, 3].

4.1 Structure

Predetermined death 1 is considered a type I membrane protein of 268 amino acids. PD-1 is a affiliate of the expanded CD28/CTLA-4 family of T cell regulators. The protein's configuration embraces an extracellular IgV field pursued by a transmembrane area and an intracellular end. The intracellular end includes double phosphorylation locations situated in an immunoreceptor tyrosine-based inhibitory motif and an immunoreceptor tyrosine-based control motif, which indicates that PD-1 depressingly regulates T-cell receptor TCR signals. This is coherent with fastening of SHP-1 and SHP-2 phosphatases to the cytoplasmic end of PD-1 on ligand attachment. Additionally, PD-1 ligation up-regulates E3-ubiquitin ligases CBL-b and c-CBL that trigger T cell receptor down-modulation. PD-1 is conveyed on the exterior of stimulated T cells, B cells, and macrophages, proposing that contrasted to CTLA-4, PD-1 extra mostly negatively controls immune reactions [12].

4.2 Ligand

PD-1 has dual ligands, PD-L1 and PD-L2, which are partners of the B7 family. Normally, PD-L1 protein is upregulated on macrophages and dendritic cells (DC) in reply to LPS and GM-CSF therapy, and on T cells and B cells on TCR and B cell receptor marking, while in quiescent rats, PD-L1 mRNA can be identified in the heart, lung, thymus, spleen, and kidney. PD-L1 is conveyed on nearly entirely murine cancer cell lines, involving PA1 myeloma, P815 mastocytoma, and B16 melanoma on therapy with IFN- γ . The PD-L2 manifestation is further constrained and is communicated chiefly by DCs and a limited cancer cell lines [6, 13].

4.3 Function

Numerous literatures indicate that PD-1 and its ligands adversely control immune reactions. PD-1 knockout mice have been revealed to grow lupus-like glomerulonephritis and enlarged cardiomyopathy on the C57BL/6 and BALB/c

settings, correspondingly. In vitro, management of anti-CD3 encouraged T cells with PD-L1-Ig leads to reduced T cell fabrication and IFN- γ production. IFN- γ is an important pro-inflammatory cytokine that encourages T cell inflammatory commotion. Downgraded T cell production was likewise associated with reduced IL-2 production. Mutually these facts imply that PD-1 deleteriously controls T cell reactions.

Trials employing PD-L1 transfected DCs and PD-1 conveying transgenic (Tg) CD4+ and CD8+ T cells indicate that CD8+ T cells are further vulnerable to inhibition by PD-L1, though this could be reliant on the potency of TCR signaling. Coherent with a function in adversely controlling CD8+ T cell reactions, exploiting an LCMV viral vector standard of chronic disease, Rafi Ahmed's group revealed that the PD-1-PD-L1 collaboration deters stimulation, growth, and attainment of effector roles of virus-specific CD8+ T cells, which can be overturned by impeding the PD-1-PD-L1 communication [2, 14].

Since CTLA-4 undesirably controls anti-tumor immune reactions, the diligently associated molecule PD-1 has been freely discovered as a goal for immunotherapy. Manifestation of PD-L1 on tumor cells constrains anti-tumor action within arrangement of PD-1 on effector T cells. Manifestation of PD-L1 on cancers is linked with reduced survival in esophageal, pancreatic and other types of cancers, highlighting this pathway as a target for immunotherapy. Triggering PD-1, conveyed on monocytes and up-regulated upon monocytes initiation, via its ligand PD-L1 stimulates IL-10 manufacture, which reduces CD4 T-cell task [15].

In mice, manifestation of this gene is produced in the thymus when anti-CD3 antibodies are introduced, and great amounts of thymocytes experience apoptosis. Mice lacking for this gene raised on a BALB/c setting acquired enlarged cardiomyopathy and perished from congestive heart failure. These reports indicate that this gene outcome may also be essential in T cell role and add to the inhibition of autoimmune disorders.

Overexpression of PD1 on CD8+ T cells is only sign of T-cell fatigue (e.g., in prolonged infection or malignancy).

4.4 Clinical Significance

Cancer

PD-L1, the ligand for PD1, is highly expressed in several cancers and hence the role of PD1 in cancer immune evasion is well established. Monoclonal antibodies targeting PD-1 that boost the immune system are being developed for the treatment of cancer. Numerous tumor cells express PD-L1, an immunosuppressive PD-1 ligand; inhibition of the interaction between PD-1 and PD-L1 can enhance T-cell

responses in vitro and mediate preclinical antitumor activity. This is known as immune checkpoint blockade.

Assortment therapy employ dual anti-PD1 and anti-CTLA4 therapeutics have seemed as significant cancer managements in the arena of checkpoint inhibition.

A mixture of PD1 and CTLA4 antibodies has been revealed to be additional efficient than any antibody only in the management of various malignancies. The outcomes of the double antibodies do not emerge to be superfluous. Anti-CTLA4 therapy results in a superior antigen-specific T cell-dependent immune response whilst anti-PD-1 seems to resurrect CD8+ T cells capability to destroy tumor cells.

In clinical experiments, mixture remedy has been revealed to be successful in lessening cancer magnitude in patients that are insensitive to solo co-inhibitory barricade, notwithstanding growing quantities of noxiousness owing to anti-CTLA4 management [8]. A mixture of PD1 and CTLA4 produced up to a ten-times greater amount of CD8+ T cells that are dynamically penetrating the cancer mass. The writers postulated that the greater concentrations of CD8+ T cell insinuation were owing to anti-CTLA-4 subdued the transformation of CD4 T cells to T regulator cells and supplementary decreased T regulatory destruction with anti-PD-1. This amalgamation encouraged a further strong inflammatory reaction to the cancer that condensed the extent of tumor. Recently, the FDA has accepted a mixture treatment with dual anti-CTLA4 (Ipilimumab) and anti-PD1 (Nivolumab) in October 2015.

The molecular influences and receptors are crucial creation a cancer responsive to anti-PD1 therapy stay undetermined. The PDL1 manifestation on the exterior of tumor cells shows a major function. PDL1 positive cancers were twofold as probable to react to mixture therapy. Nonetheless, patients with PDL1 negative growths additionally have restricted reaction to anti-PD1, signifying that PDL1 manifestation is not an utter factor of the efficiency of treatment [8].

The greater mutational problem in the cancer is associated with a superior influence of the anti-PD-1 usage. In clinical experiments, patients who gained from anti-PD1 management had malignancies, for example melanoma, bladder cancer, and gastric cancer, that had a usual greater than normal number of mutations than the patients who do did not counter to the treatment. Yet, the relationship amid advanced cancer problem and the clinical efficiency of PD-1 immune blockade is remained unclear.

Anti-PD-1 therapeutics

Certain malignancy immunotherapy vehicles that focus the PD-1 receptor have been established.

An example of such anti-PD-1 antibody medicine, Nivolumab, (Opdivo—Bristol Myers Squibb), made far-reaching or fractional reactions in non-small-cell lung cancer,

melanoma, and renal-cell cancer, in a clinical trial with a overall of 296 patients 38 Colon and pancreatic cancer did produce a reaction. Nivolumab (Opdivo, Bristol-Myers Squibb) ratified in Japan in July 2014 and by the US FDA in December 2014 to cure metastatic melanoma [16].

A typical agent such as Pembrolizumab (Keytruda, MK-3475, Merck) aims at PD-1 receptors accepted by the FDA, in Sept 2014 to use for metastatic melanoma. Pembrolizumab has been made available to radical melanoma patients in the UK via UK Early Access to Medicines Scheme (EAMS) in March 2015. It has been employed in clinical studies in the US for patients with lung cancer, lymphoma, and mesothelioma. It has had reasonable achievement, with a few reported complications. It is up to the producer of the medication to ask to the FDA for endorsement for application in these illnesses. On October 2, 2015, FDA approved Pembrolizumab for radical (metastatic) non-small cell lung cancer (NSCLC) patients who are exhausted with othertherapies [17].

Further drugs in early-phase of development directing PD-1 receptors (checkpoint inhibitors) are Pidilizumab (CT-011, Cure Tech) and BMS-936559 (Bristol Myers Squibb). Both Atezolizumab (MPDL3280A, Roche) and Avelumab (Merck KGaA, Darmstadt, Germany & Pfizer) aim the analogous PD-L1 receptor.

4.5 Animal Illness

HIV Medications aiming PD-1 in amalgamation with further negative immune checkpoint receptors, for example (TIGIT), may supplement immune reactions and/or accelerate HIV abolition. T lymphocytes display higher manifestation of PD-1 in situation of long-lasting HIV infection. Increased occurrence of the PD-1 receptors relates to collapse of the HIV specific CD8+ cytotoxic and CD4+ helper T cell residents that are fundamental in fighting the virus. Immune barricade of PD-1 led to the renewal of T cell inflammatory phenotype indispensable to battle the development of the illness.

Alzheimer's disease Impeding of PD-1 tips to a decrease in cerebral amyloid- β plaques and develops intellectual functioning in mice. Immune block of PD-1 induced an IFN- γ dependent immune reaction that enlisted monocyte-derived macrophages to the brain that were then proficient of clearance the amyloid- β plaques from the mass. Continual admin with

anti-PD-1 were discovered to be essential to uphold the remedial outcomes of the therapy. Amyloid plaques are immunosuppressive, and this discovery has been independently established by inspecting the properties of the fibrils in neuroinflammatory disorders. PD-1 offsets the results of the fibrils by encouraging immune activity and activating an immune route that permits for brain restoration.

4.6 Future Consideration

The clinical realizations have unlocked a renewed range of remedial: FDA approval of anti-CTLA4, rapidly pursued by anti-PD-1 therapy [18]. A recently discovered understanding of prospective antitumor endeavor in cancer patients have helped to clarify the role of ICs in immune reactions in different levels. The investigation of ICS yields two challenges: Is the classification of possible biomarkers that can control which IC foremost pathway in specific cancer therapy a difficult decision? Is it conceivable that particular oncogenic pathway such as PI3k-AKT or STAT3 may provoke and can be employed as a replacement biomarker? The clinical development of combined therapy: vaccine associated with anti-ICs? The above-mentioned questions allow the following conclusions to be reached: Clinical effects of CTLA4 and PD-1/PD-L1 inhibitors indicate that B7-H1/PD-1 passageway is a significant objective for the successful antitumor immune reaction. Encouragement and toxicity synopsis of PD-1/B7-H1 inhibitors confirms that they are very useful for the treatment of advanced cancers.

The conceivable perpetuation of response of PD-1 and CTLA4 pathways lasting up to ten years, leading to the conduct of extensive international clinical trials on the their effect on solid tumors. This open up future research opportunities in blockades of ICS associated with new vaccines, angiogenesis, MAPK inhibiting targeted therapy.

5 Conclusions

Immune checkpoint blockade has gained momentum as a new approach in cancer immunotherapy. Due to its successes, many new agents and strategies, including combination approaches, are being developed at a fast pace.

Conflict of Interest The authors declare that they have no conflict of interest.

References

1. Thang, H.Q.: Basic molecular biology of cancers. *J. Med. HCM city Vietnam* **19**(5–2015), 1–7 (2015)
2. Abbas, A.K., Lichtman, A.H., Pillai, S.: Lymphocyte development and Antigen receptor gen rearrangement. In: *Cellular and Molecular Immunology*, 9th edn, pp. 179–208. Elsevier (2018)
3. Hanahan, D.: Weinberg RA. The hallmarks of a cancer cell **144**, 646–674 (2011)
4. Marin-Acevedo, J.A., et al.: Next generation of immune checkpoint therapy in cancer: new developments and challenges. *J. Hematol. Oncol.* **11**, 39 (2018)
5. Harrington, L., Bristow, R.G., Hill, R.P., Tannock, I.F: Introduction to cancer biology. In: *The Basic Science of Oncology*, pp. 1–4 (2005)
6. Franklin, M., Kratzke, R.: Molecular biology for the oncologist: the essentials 2013. http://clinicaloption.com/Practice/Oncology/General_Oncology
7. Bristow, R.G., Harrington, L.: Genomic stability and DNA repair. In: *The Basic Science of Oncology*, pp. 77–100 (2005)
8. Baroja, M.L., Vijayakrishnan, L., Bettelli, E., Darlington, P.J., Chau, T.A., Ling, V., Collins, M., Carreno, B.M., Madrenas, J., Kuchroo, V.K.: Inhibition of CTLA-4 function by the regulatory subunit of serine/threonine phosphatase 2A. *J. Immunol.* **168**(10), 5070–5078 (2002). <https://doi.org/10.4049/jimmunol.168.10.5070>. PMID11994459
9. Weinberg, R.A.: Multi-step tumorigenesis. In: *The Biology of Cancer*, pp. 439–510 (2014)
10. Enderling, H., Hyatky, L., Hahnfeldt, P.: Immunoediting: evidence of the multifaceted role of the immune system in self-metastatic tumor growth. *Theor. Biol. Med. Model.* **9**, 31 (2012)
11. Cahill, D.P., Lengauer, C.: Tumor genome instability. In: *The Genetic Basis of Human Cancer*, pp. 129–130 (2002)
12. Abbas, A.K., Lichtman, A.H., Pillai, S.: Cell and tissue of the immune system. In: *Cellular and Molecular Immunology*, 9th edn, pp. 13–38. Elsevier, Amsterdam (2018)
13. Thang, H.Q.: Biological alterations in lung cancer. *J. Med. HCM city Vietnam* **19**(5–2015), 8–15 (2015)
14. Abbas, A.K., Lichtman, A.H., Pillai, S.: Antigen presentation to T lymphocytes and the function of major histocompatibility complex molecules. In: *Cellular and Molecular Immunology*, 9th edn, pp. 117–144, Elsevier (2018)
15. Abbas, A.K., Lichtman, A.H., Pillai, S.: Property and overview of immune responses. In: *Cellular and Molecular Immunology*, 9th edn, pp. 01–12. Elsevier (2018)
16. Alexander, W.: The checkpoint immunotherapy revolution what started as a trickle has become a flood, despite some daunting adverse effects; new drugs, indications, and combinations continue to emerge. *Pharm. Ther.* **41**(3), 185–191 (2016)
17. Dang, O.T., et al.: Pembrolizumab for the treatment of PD-L1 positive advanced or metastatic non-small cell lung cancer. *Expert Rev. Anticancer Ther.* **16**(1), 13–20 (2016)
18. Chae, Y.K., et al.: Current landscape and future of dual anti-CTLA4 and PD-1/PD-L1 blockade immunotherapy in cancer; lessons learned from clinical trials with melanoma and non-small cell lung cancer (NSCLC). *J. Immunother. Cancer* **6**, 39 (2018)

A Molecular Alteration Situations of KRAS, NRAS, BRAF, PIK3C and PTEN Loss in Colorectal Adenocarcinoma at Can Tho Oncology Hospital

T. Q. Huynh, P. H. Nguyen, D. N. Tran, M. T. T. Nguyen, T. P. Chau, T. M. Huynh, and N. Doan

Abstract

Aim To determine the characteristics of KRAS, NRAS, BRAF, PIK3CA gene mutation and loss of PTEN expression in colorectal adenocarcinoma in Can Tho Oncology Hospital. **Materials and methods** A cross-sectional study included 50 cases of colorectal adenocarcinoma were diagnosed and treated at Can Tho Oncology Hospital. KRAS, NRAS, BRAF, PIK3CA mutations identified by Sanger DNA sequencing as well as evaluating the loss of PTEN protein expressed by MHC. **Results and discussion** Among the 50 colorectal cancer patients, we detected 17 (34%) mutations in the KRAS, NRAS (0%), BRAF 1(2%) and PIK3CA 3(6%), all of which were point mutations. Mutation frequencies at codon 12 and codon 13 were 26%. Only one patient harboured a point mutation at codon 10. The KRAS mutation frequency was significantly higher in the rectum than in the colon (26% versus 8%, $p = 0.022$). Other clinic-pathological features, such as gender, histological type, and grade, TNM stage, showed no positive relationship with KRAS gene mutations. The PIK3CA mutation frequency was significantly higher in the <50 years patients or female than in the group ≥ 50 years (6% versus 0%) with $p = 0.042$; $p = 0.036$ respectively.

The incidence of PTEN loss was 14%. Loss of PTEN expression, relative to regional lymph nodes metastatic and distant metastasis was statistically significant. **Conclusion** The KRAS mutation rates of colorectal adenocarcinoma patients in Can Tho Oncology Hospital were 34%. KRAS mutation associated with tumor location. PIK3CA mutation associated with age and gender. In 50 cases, none of NRAS mutations detected. K601E BRAF mutation is also one of several situations that cause over-activation of the BRAF protein. The rate of PTEN loss was 14% and about regional and distant metastasis.

Keywords

KRAS NRAS BRAF PIK3CA mutation • PTEN loss • Colorectal adenocarcinoma

1 Introduction

Colorectal adenocarcinoma is one of the most common malignancies in the world [1], as well as in Vietnam. Recently, the incidence and mortality of colorectal adenocarcinoma have been increasing [2]. Epithelial growth factor receptor (EGFR) plays an important role in the proliferation and differentiation of normal cells. The Ras/Raf/MAP/MEK/ERK signaling pathway leads to cell proliferation, metastasis, evasion of apoptosis, and neovascular proliferation [3]. Cetuximab and panitumumab, the monoclonal antibodies that block EGFR activity, have been approved by the FDA for use in metastatic colorectal cancer treatment. KRAS, NRAS, BRAF, PIK3CA mutations and loss of PTEN expression have implicated in the prognosis and select patients of EGFR Mab indication.

Recently, some studies on KRAS mutations in colorectal adenocarcinoma revealed a mutation rate of 35–40%. In Vietnam, Ta Thanh Van detected 4/10 samples with KRAS mutation. The Ho Huu Tho found ten cases of gastric cancer

T. Q. Huynh · P. H. Nguyen · M. T. T. Nguyen
Can Tho Oncology Hospital, Can Tho, Vietnam

T. P. Chau
Department of General and Thoracic and Oncologic Surgery
of Cho Ray Hospital, Ho Chi Minh City, Vietnam

T. M. Huynh · N. Doan (✉)
Griffith University Schools of Dentistry and Oral Health,
Gold Coast, Australia
e-mail: nvtdoan123@gmail.com

T. M. Huynh · N. Doan
The University of Queensland & Queensland University
of Technology, Brisbane, Australia

D. N. Tran
Can Tho Medical and Pharmacy University's Hospital,
Can Tho, Vietnam

4 of them found to be KRAS mutation. Hoang Anh Vu studied 173 cases, discovered 62 instances of KRAS mutations (35.8%). Nevertheless, very few studies have performed on the BRAF, NRAS, PIK3CA gene mutation or loss of PTEN expression in colorectal adenocarcinoma. This study aimed to identify some mutant characteristics of KRAS, NRAS, BRAF, PIK3CA genes and loss of PTEN expression in colorectal adenocarcinoma at Can Tho Oncology Hospital.

2 Materials and Method

This study was a cross sectional study on 50 cases of colorectal adenocarcinoma at Can Tho Oncology Hospital, Can Tho City, Vietnam. The study gathered recorded clinical information about age, gender, tumor location, and metastatic status. The specimens fixed with neutral buffered formalin 10%, HE stained. Histopathological classification and grading were according to W.H.O. 2010.

Cell harvesting from paraffin-embedded tissue: The tumor area was marked on the HE slides and reconnected to the untreated specimens, and then we shaved the corresponding tumor on the untreated tumor tissue slide.

Genomic DNA extraction with the Promega kit. BRAF, PIK3CA were amplified by PCR, KRAS, NRAS amplified by COL-D-PCR.

Thermal cycles are performed on the GeneAmp® PCR system 9700 (Applied Biosystems, USA). The PCR product detected by electrophoresis and then purified by QIAquick Gel Extraction Kit (Qiagen, USA). The purified PCR product was given a cycle sequencing with Applied Biosystems BigDye Terminator Version 3.1 in both forward and reverse directions for each exon. DNA sequence read by ABI 3130 Genetic Analyzer (Applied Biosystems, USA).

The results were analyzed by Seq Scape software, compared with the KRAS, NRAS, BRAF, PIK3CA reference

sequences on NCBI for the diagnosis of mutations in the genes. Diagnostic procedures for genetic mutations performed at the Center for Molecular Biology, University of Medicine and Pharmacy at Ho Chi Minh City.

Data were processed by SPSS 16.0 software. The relationship between the genetic mutation, loss of PTEN expression with patho-clinical characteristics was verified by the Fisher exact tests, taking $p = 0.05$ to determine the statistical significance of these tests.

3 Results

3.1 Features of KRAS Gene Mutation

In 50 cases (Table 1), we found 17 cases with mutations (34%), all of which were point mutations. Mutations occurred at codon 12 with 13 cases accounting for 26%, followed by codon 13 with three situations accounting for 6%, 1 case with mutations in codon 10 (2%). Among KRAS mutations, there was one mutation in both codons 12 and 13, and one case harbored two forms of a point mutation in the same codon (codon 12).

3.2 The Relationship Between KRAS Mutation and Patho-Clinical Characteristics

Table 2 summarizes the relationship between KRAS gene mutations and some of the patho-clinical features of colorectal cancer, including age, sex, tumor site, histological types, histological grade and TNM staging.

The correlation between KRAS mutation and patho-clinical characteristics such as age, sex, histopathology, histology, the TNM stage were not statistically significant. KRAS mutations were more frequent in the rectum (13/27 cases, 48%) than in the colon (4/23 cases, 17%).

Table 1 Features of *K.RAS* gene mutation (n = 50)

Type of mutation	Amino acid	Number	(%)	
Codon 10	GGA → GAA	Glycine → glutamic acid	01	5.9%
Codon 12	GGT → GAT	Glycine → Aspartic acid	04	23.5%
	GGT → AGT	Glycine → Serine	03	17.7%
	GGT → GTT	Glycine → Valine	04	23.5%
	GGT → GAT	Glycine → Aspartic acid	01	5.9%
	GGT → GTT	Glycine → Glycine		
Codon 13	GGC → GAC	Glycine → Aspartic acid	02	11.8%
	GGC → AGC	Glycine → Serine	01	5.9%
Codon 12 and 13	GGT → AGT	Glycine → Serine	01	5.9%
	GGC → GAC	Glycine → Aspartic acid		

Table 2 Some pathological and clinical characteristics of studied group (n = 50)

Age	Youngest: 23yo; Oldest: 84yo Mean age: 55.5 ± 2.09yo
Sex	Males 58%; females: 42%
TNM staging	T: T ₁ : 03 cases (6%); T ₂ : 06 cases (12%); T ₃ : 24 cases (48%) and T ₄ : 17 case (34%) N: N ₀ : 30 cases (60%); N ₁ : 10 cases (20%); N ₂ : 01 case (02%) M: M ₀ : 43 cases (86%); M ₁ : 07 cases (14%) Stage: I: 09 cases (18%); II: 19 cases (38%); III: 16 cases (32%) and IV: 06 cases (12%)
CEA Plasma concentration	Minimum: 0.2 ng/ml; Maximum: 86.46 ng/ml; Average value: 13.53 ± 1.65; Proportion of increased CEA: 28 cases (56%)
Tumor site	Colon: 23 cases (46%) and Rectal: 27 cases (54%)
Tumor size	Minimal: 3 cm; Maximum: 20 cm; Average size: 6.86 ± 3.57 cm
Type of pathology	Non mucinous adenocarcinoma: 41 cases (82%) Mucinous adenocarcinoma: 09 cases (18%)
Histology grades	Grade I: 19 cases (38%); Grade 2: 18 cases (36%); Grade 3: 13 cases (26%)

3.3 NRAS Gene Mutation

Investigation of NRAS mutations on both exon 2 and three but we have not recorded any mutations.

3.4 BRAF Gene Mutation

Through a BRAF mutation study of 50 cases, the study recorded one case of BRAF mutation in codon 601 (K601E) in a 51-years old male with colon cancer who recurred after 48 months surgery and chemotherapy.

In a study 50 cases of PIK3CA gene mutations in exon 9 and exon 20 showed three situations of mutation PIK3CA (2 instances in exon 20 (4%) and 1 case in exon 9 (2%).

The relation between PIK3CA mutation and age and sex was statistically significant but not with tumor location, type of histopathology, histopathological grade, and pTNM stage.

4 Discussion

4.1 The KRAS Gene Mutation

In this study, we identified 17/48 (34%) cases were having KRAS mutations, which occur quite frequently in colorectal cancer about 35–45% [4, 5]. Hoang Anh Vu, in Ho Chi Minh City, Vietnam, reported the results of KRAS gene mutation in 62/173 cases of colorectal cancer, in proportion to 35.8%. The rate of KRAS mutation in this study was also consistent with the incidence of KRAS gene mutations in colorectal cancer.

Several studies had examined the association between KRAS mutations and some patho-clinical parameters, but the results still are controversial. A correlation existed

between KRAS mutation and sex with a higher rate of mutation in females than males [6]; Elkof (2103) [7] illustrated the relationship between the higher rate of KRAS mutation and the location of the right colon in the delayed stages. Watanabe (2013) [5] showed a correlation between a higher KRAS gene mutation in female patients, with the increase of age, and colon positions more elevated than in left colon and rectum. Of 50 cases in this study recorded a common KRAS mutation in the rectum compared with the colon. Probably because the sample is rather small, and the power of the study was not sufficient to detect other relationships. However, Phipps [8] studied 1989 cases of colorectal cancer and did not find any association between age, sex, tumor location, type of histology, histology, stage of disease with KRAS mutation.

There have been many studies showing that patients with KRAS mutations do not respond to cetuximab or panitumumab, so KRAS mutations are essential predictors of non-response to anti-EGFR drugs [6]. Therefore, all patients with rectal cancer with KRAS mutations in codons 12 or 13 did not receive any treatment for EGFR. De Roock (2010) [9] examined 579 patients with chemo-rectal cancer who treated with cetuximab. and found that patients with KRAS G13D mutation (n = 22) had a lifetime of survival (7.6 months versus 5.7 months, p = 0.005) and the duration of disease did not progress (4 months versus 1.9 months, p = 0.004) longer than patients with other KRAS mutations

4.2 NRAS Mutation

Previous studies have shown that the NRAS mutation rate ranges from 3 to 7%. The NRAS mutation is also a predictor of feeble response to cetuximab or panitumumab in

metastatic colorectal carcinoma [10], Our study has not recorded any mutation case, probably by too small sample number.

4.3 BRAF Gene Mutation

According to COSMIC, the rate of BRAF mutation in colorectal cancer is about 10.7% [11]. This study recorded a BRAF mutation rate of 2%, which was quite consistent with many previous studies [12, 13]. BRAF mutations are mostly mutations in codons 600, V600E (over 95%) [11]. Our study found that a mutation in codon 601 (K601E) was also a mutation that increased BRAF protein activity [14]. Also, Fariña-Sarasqueta [15] identified BRAF mutations as an independent predictor of survival, with a high risk of dying from cancer.

4.4 PIK3CA Mutation

This study found that mutation rates were only 6% lower than previous studies, such as Zhu K. (9.5%), Baldus (21%) [16]. Studies have not shown a significant difference in the PIK3CA mutation rate by gender. Some studies have shown that in the female the frequencies of mutations are significantly higher in the male. But there was no difference in the PIK3CA mutation rate by sex [6, 7].

4.5 Expression of PTEN Protein

This study documented 7/50 (14%) cases of loss PTEN expression in the cytoplasm of invasive tumor cells. Eklof's study [7] reported a 12.5% reduction in PTEN protein expression compared with the Naguib study (30%) and Loupakis (42%). At present, there are not yet facilities in Vietnam, to perform immunohistochemical staining and to evaluate PTEN protein expression for colorectal cancer. On the other hand, there is no uniformed international standard for staining and evaluation of immunohistochemical results of PTEN protein expression in colorectal carcinoma. We recognize that this is a matter that needs to be united and agreed in the future.

5 Conclusion

From 50 cases of colon cancer, this study recorded 34% of KRAS mutation in patients with colorectal carcinoma in Can Tho Oncology Hospital. The mutations were in codons 12 and 13 include G12D, G12V, G12S, G13D, G13S, with the

highest G12D and G12V mutation rates, and a rare mutation in codon 10, G10E. KRAS gene mutations were more common in the rectum than the colon. No report on any of NRAS gene mutations in 50 patients. Only one case of BRAF mutation discovered. The PIK3CA mutation rate was 6%. The PIK3CA mutation rate in female patients aged <50 years was statistical significantly higher in male patients age \geq 50 years. The incidence of PTEN loss was 14% and associated with regional and metastatic distant metastases.

Conflict of Interest The authors declare that they have no conflict of interest.

References

1. American Joint Committee on Cancer: AJCC cancer staging atlas, 7th Edition, pp. 143–164. Springer (2010)
2. Amado, R.G., Wolf, M., Peeters, M., et al.: Wild-type KRAS is required for panitumumab efficacy in patients with metastatic colorectal cancer. *J. Clin. Oncol.* **26**, 1626–1634 (2008)
3. Fang, J.Y., Richardson, B.C.: The MAPK signaling pathways and colorectal cancer. *Lancet Oncol.* **6**, 322–327 (2005)
4. Douillard, J.Y., Siena, S., Cassidy, J., et al.: Randomized, phase III trial of panitumumab with infusional fluorouracil, leucovorin, and oxaliplatin (FOLFOX4) versus FOLFOX4 alone as first-line treatment in patients with previously untreated metastatic colorectal cancer: the PRIME study. *J. Clin. Oncol.* **28**, 4697–4705 (2010)
5. Watanabe, T., Yoshino, T., Uetake, H., et al.: KRAS mutational status in Japanese patients with colorectal cancer: results from a nationwide, multicenter, cross-sectional study. *Jpn. J. Clin. Oncol.* **43**(7), 706–712 (2013)
6. Bando, H., Yoshino, T., Yuki, S., Shinozaki, E., et al.: Clinical outcome of Japanese metastatic colorectal cancer patients harboring the KRAS p. G13D mutation treated with cetuximab + irinotecan. *Jpn. J. Clin. Oncol.* **42**(12), 1146–1151 (2012)
7. Eklof, V., Wikberg, M.L., Edin, S., et al.: The prognostic role of KRAS, BRAF, PIK3CA and PTEN in colorectal cancer. *Br. J. Cancer* **108**, 2153–2163 (2013)
8. Phipps, A.I., et al.: KRAS-mutation status in relation to colorectal cancer survival: the joint impact of correlated tumour markers. *Br. J. Cancer* **108**(8), 1757–1764 (2013)
9. De Roock, W., Jonker, D.J., et al.: Association of RAS p.G13D mutation with outcome in patients with chemotherapy-refractory metastatic colorectal cancer treated with cetuximab. *JAMA* **304** (16), 1812–1820 (2010)
10. De Roock, W., Claes, B., Bernasconi, D., et al.: Effects of KRAS BRAF NRAS and PIK3CA mutations on the efficacy of cetuximab plus chemotherapy in chemotherapy-refractory metastatic colorectal cancer: a retrospective consortium analysis. *Lancet Oncol.* **11**, 753–762 (2010)
11. COSMIC (Catalogue of Somatic Mutations in Cancer) Database, S. Institute, Wellcome Trust Genome Campus, Hinxton, Cambridge. <http://www.sanger.ac.uk/genetics/CGP/cosmic/>
12. Chaiyapan, W., et al.: Somatic mutations of K-Ras and BRAF in Thai colorectal cancer and their prognostic value. *Asian Pac. J. Cancer Prev.* **14**(1), 329–332 (2013)
13. Di Nicolantonio, F., Martini, M., Molinari, F., et al.: Wild-type BRAF is required for response to panitumumab or cetuximab in metastatic colorectal cancer. *J. Clin. Oncol.* **26**, 5705–5712 (2008)

14. Bokemeyer, C., Kohne, C., Rougier, P., et al.: Cetuximab with chemotherapy (CT) as first-line treatment for metastatic colorectal cancer (mCRC): analysis of the CRYSTAL and OPUS studies according to KRAS and BRAF mutation status. *J. Clin. Oncol.* **28** (Suppl.) (2010)
15. Fariña-Sarasqueta, A., van Lijnschoten, G., Moerland, E., Creemers, G.J., Lemmens, V.E., Rutten, H.J., van den Brule, A.J.:
The BRAF V600E mutation is an independent prognostic factor for survival in stage II and stage III colon cancer patients. *Ann. Oncol.* **21**(12), 2396–2402 (2010)
16. Baldus, S.E., Schaefer, K.L., Engers, R., Hartleb, D., Stoecklein, N.H., et al.: Prevalence and heterogeneity of KRAS, BRAF, and PIK3CA mutations in primary colorectal adenocarcinomas and their corresponding metastases. *Clin. Cancer Res.* **16**(3), 790–799 (2010)

Primarily Surgical Treatment of Cervical Cancers Diagnosed in Stages IA–IIA at Can Tho Oncology Hospital: An Overview of 9 Years' Experience 2000–2008

T. Q. Huynh and N. Doan

Abstract

Aims This study aims to evaluate the diagnosis, treatment, and outcomes of early stages cervical cancers. **Materials and methods:** a Randomized descriptive survey of 146 cases/786 cervical cancer patients hospitalized, classified into early stages (IA–IIA) and primarily treated in surgery at Can Tho Oncology Hospital from 06/2000 to 6/2008. **Result** Predominant age of patients was from 40 to 59 year old (85%); mean age were 49 yo; the youngest were 23 yo; the oldest was 75 yo. Postmenopausal patients occupied 18.7%. Proportion of early stages/total cervical cancers is 18.5% among which: stage IA: 5.1%; IB: 8.8% and IIA: 5.5%. The first diagnostic clinical manifestation: intermenstrual bleeding: 73%, postcoital bleeding: 9.5% combined with other favorizing factors: age of first coitus, number of sexual partners, number of children, lifestyle (socioeconomy status, cigarette smoking). Cytology or/and histopathology diagnosis and staging based on Pap-smear with cytological exam: HSIL: 13.3%, Microinvasive: 40%, Invasive: 46.7%; Colposcopy: inflammation: 14.3%, budding: 63.5%, ulcerative: 9.5%. And biopsy of the cervix: epitheliocarcinoma: 85.7%, adenocarcinoma: 14.3%; Post-operative pelvic nodal metastasis: 18.4%; unsafety of cutting field: 3.5%. Essential surgical treatment is Wertheim-Meigs' Operation in conjunction with adjuvant therapy, chemotherapy, Radiotherapy. DFS of 3 years: 77.9%, of 5 years: 62.3%; OS of 3 years: 81.5%, of 5 years: 74.2%. **Conclusion** This study illustrated a low proportion of early-stage cervical cancers in Can Tho, in comparing

with others authors. In the highly populated area of Mekong Delta region, cervical cancer screening programme was vital. The primary surgical treatment was the essential management for the early stages, as early diagnosis implies sooner radically treatment with a high proportion of DFS and OS of 3 or/and five years.

Keywords

Surgical treatment • Cervical cancers • Stages IA–IIA

1 Introduction

Actually, the incidence of cervical cancer tend to be diminished in the developed countries, this kind of gynecological malignant were always ranged as one of the heading cancer and cancerous mortality in the developing countries. There still are a great number of patients were diagnosed in the advanced stages for which the result of treatment still is very modest [1–4].

In Vietnam, according to the results of population-based cancer registration, the incidence of cervical cancer of period 2003–2004 at HCM city were ranked second among most 10 heading kinds of cancer [1] with the prevalence of 16.5/100000. In Hanoi, the cervical cancer was ranged as the 4th with ARS 9/100000 [6].

Can Tho, the fluvial area of Mekong delta, had the ASR 21.5/100000. By the socio-economic situation were still modest, the means of treatment for the malignant diseases were still deficient, the choice of a therapeutic procedure adequate to each of disease stage, for the best response of treatment, were still not easy [7].

The treatment of cervical cancer in initial stages, in practice, still not unanimous among the authors [8–15]: some prefer to do the surgical intervention in advance, following with adjuvant therapy with either radiation or chemoradiation; Others do the initial radiotherapy, in order to downstage, before the surgical procedure.

T. Q. Huynh
Can Tho Oncology Hospital, Can Tho, Vietnam

N. Doan (✉)
Griffith University Schools of Dentistry and Oral Health,
Gold Coast, Australia
e-mail: nvtdoan123@gmail.com; nvtdoan23@gmail.com

N. Doan
The University of Queensland & Queensland University
of Technology, Brisbane, Australia

From that reality, we study the results of treatment for the cervical cancer of early stages at Can Tho Oncology hospital in order to:

- Participate to the evaluation of the cervical cancer state of early stages at an area of Mekong delta region
- To evaluate the role and results of surgical treatment in order to illustrate the necessity of screening and early detection of this common kind of females malignant disease for an area without a network of cancer control and prevention.

2 Materials and Method

Retrospective study describing 146/786 cases of cervical cancers ranged in early stages (IA–IIA) according to the criteria of FIGO [11]. Patients were treated by initially surgical procedure at Can Tho Oncology Hospital from June 2000 to June 2008.

The data of antecedent, clinical, socioeconomic situation, life style of the patients suggest a diagnosis. Paraclinical result of Pap smear, colposcopy, and cervix biopsy help the confirmative diagnosis and staging.

The patients were surgically treated with total hysterectomy associated with superior third of the vagina and bilaterally internal iliac ganglia dissection. Histo-pathological examination of the lesion helps to evaluate the grade of invasion as well as the ganglion metastasis of lesion suggesting an appropriate method of adjuvant treatment; either a radiotherapy, chemoradiotherapy or surveillance.

Results of treatment will be observed randomly: complications, post-operative surveillance, recurrence and metastasis in comparing among different authors.

3 Results

From 6/2000 to 6/2008, 146 cervical cancer patients were diagnosed, staged as IA–IIA and being surgical treated, on a totality of 786 cervical cancer patients examined at outpatient department of Cantho Oncology Hospital (17.1%), distributed as following (Tables 1, 2, 3, 4, 5, 6, 7; Figs. 1, 2, 3 and 4).

3.1 Surgical Intervention

All 146 patients were surgically treated. For patients of stage IA, the basically techniques were Radical Hysterectomy,

Table 1 Distribution per year (n = 146)

Time	Number of patients	Percentage (%)
2000	06	4.1
2001	11	7.5
2002	13	8.9
2003	23	15.7
2004	21	14.4
2005	19	13
2006	27	18.5
2007	18	12.3
2008	08	5.4

comprising total hysterectomy associated with superior third vaginal excision. For the stages IB to IIA, we do further Pelvic lymph nodes dissection (Pelvic lymphadenectomy).

3.2 Results of Treatment

Tumor size: smallest 1 cm, biggest sometime ≥ 5 cm. We had 23 cases of indetermining size due to huge polyposis or lesion invaded into the interior hole of the cervix, very difficult to accurately confirm the dimension of lesion (Tables 8, 9, 10 and 11, 12, 13, 14 and 15).

4 Discussion

4.1 Proportion of Early Cervical Cancers

Cervical cancer diagnosed and ranged as early stages (IA–IIA), was evaluated by clinical examination associated with cytohistological exams. During 9 years 146 cases of early stages detected on the total 786 cases of cervical cancer in general (18.5%). We also ranged all cases pre-IB (even stage O and sin 3) into the IA group (Table 16).

4.2 Other Epidemiological Factors

Age

According to the occidental authors [8–15], cervical cancer were often seen within the limit of age from 48 to 55, the mean age were 53. The statistics of HCM cancer center [3] reported the most common age of 40–69; the mean age were 52.6; Rarely <30 and the age of >60 occupied about 25%.

Table 2 Number of children

Number of children	0	Few (1–2)	Middle (3–5)	Numerous (>5)
Number of patient	10	27	49	60
Percent (%)	6.9	18.5	33.5	41.1

Table 3 Smoking status

Smoking status	No	Light smoker	Medium smoker	Hard smoker
Number of patients	142	4	0	0
Percent (%)	97.2	2.8	0	0

Table 4 First suggesting clinical sign

First clinical sign	Number of patient	Percent (%)
Abnormally vaginal hemorrhage	107	73
Bleeding post-coitus	14	9.5
Hypermenorrhea	7	4.8
Other signs	7	4.8
Diagnosed by Health examination	11	7.9

Table 5 Cyto-histological diagnosis: colposcopy

Colposcopy	Inflammation	Budding	Ulcerative	Infiltrate	Polypous	Mixte
Number	21	93	14	11	5	2
Percent (%)	14.3	63.5	9.5	7.9	3.2	1.3

Table 6 Cyto-histological diagnosis: cytological sign

Cytoexamination	HSIL	Microinvasion	Invasion
Number of patient	12	35	40
Percent (%)	13.3	40	46.7

Table 7 Cyto-histological diagnosis: Pathological examination

Result of anapath	Squamous cell carcinoma	Adenocarcinoma	Other type
Number of patient	110	22	14
Percent (%)	75.3	15.1	9.6

Our statistics reports the most common age of 40–49, mean age were 49. This result differs from the one of Le Phuc Thinh ($p = 0.004$) and the occidental authors ($p=0.002$).

Economical and cultural situations

Economically, >50% of poor patients, only 44% of patients had the mild life level and very few (2%) in comfort. Culturally, more than 60% were in low cultural level or ignorant. By these reasons, the incorrect awareness about diseases as well as the health care rarely being interested, the great number of patients were diagnosed in advanced

periods and that justified the reasons why the proportion of cervical cancers diagnosed in early stages still was very low, the results of treatment was very limited and mortality was not ameliorated as well.

Family status and number of children

Different from the situation in the developed countries, the proportion of cervical cancer were higher in women having many sexual partners, our registration as well as of many other authors of the whole country manifest a higher proportion of cervical cancer in women having

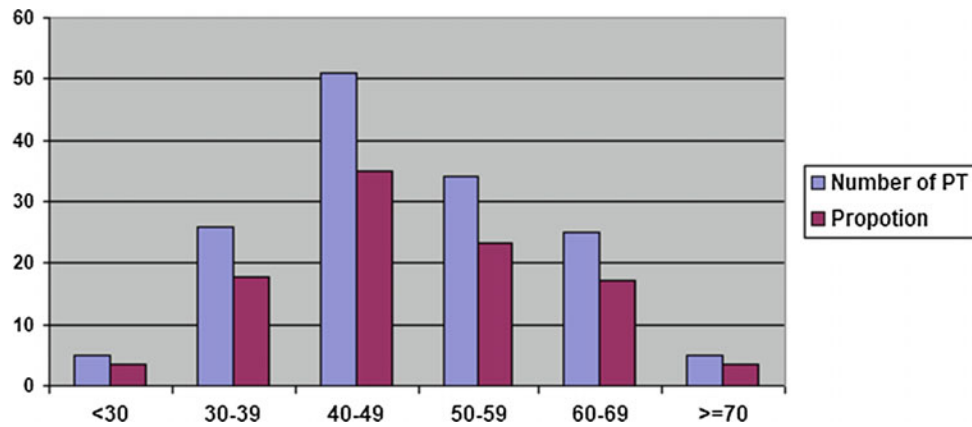


Fig. 1 Age distribution chart with mean age of 49, youngest was 23 and oldest was 75

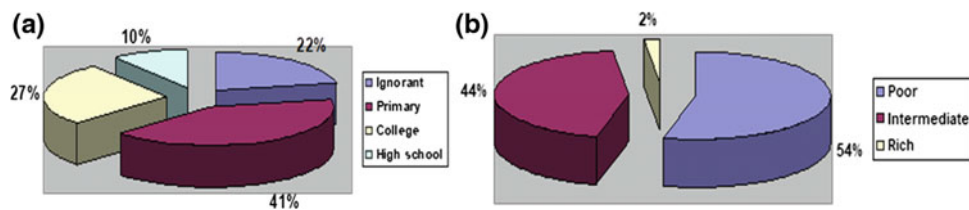


Fig. 2 Pie chart of socioeconomic situations for a Economy and b Culture

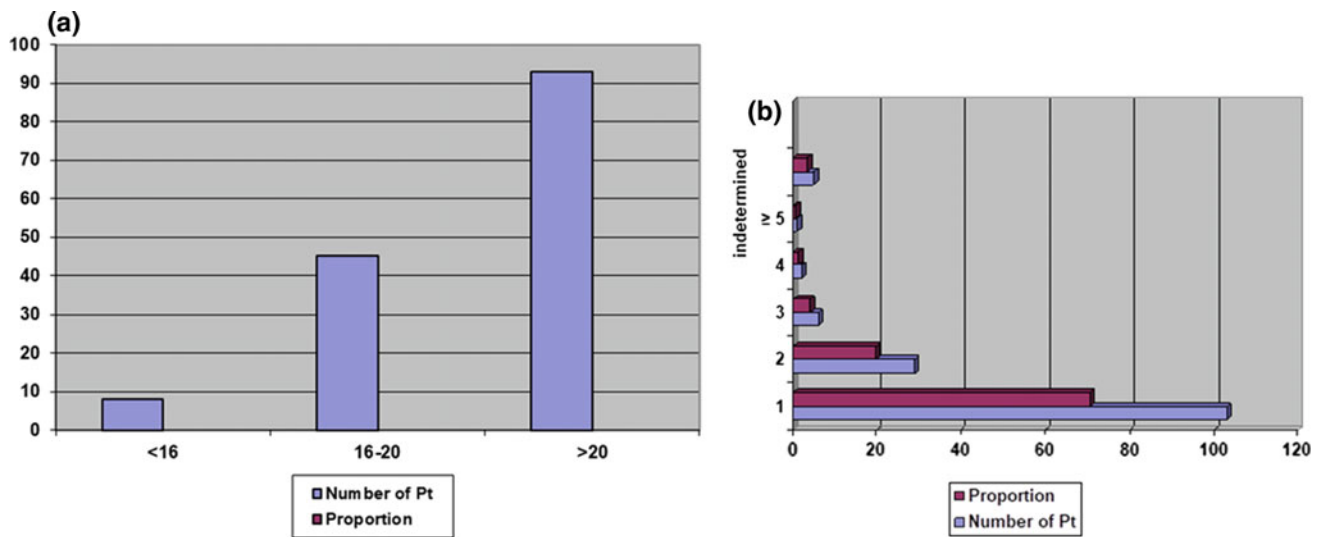


Fig. 3 Charts of familial status for a First coitus age and b Number of sexual partner

a lot of children. Our statistics showed 41% of patients have more than 5 children, and particularly 5 patients have >10 children. So, the factor of “numerous children” was suitable to the relation between “numerous children” and the proportion of cervical cancer, according to many other authors.

Relation between tobacco and cervical cancer

Many documentations worldwide mentioned to the relation between tobacco and cervical cancer. But we didn’t find this factor out in our statistics. In practice, we registered only 4/146 light smoker female patients.

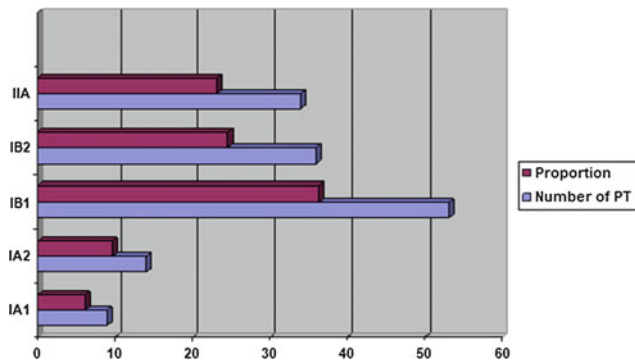


Fig. 4 STAGING: According to FIGO before operation

4.3 About the Clinical Manifestations and the Diagnosis

Similar to the observations of other authors and in the medical literature, we reported 73% cases with abnormal vaginal bleeding and 9.5% with post coitus hemorrhage which were the first abnormality motivating the patients coming to see the doctor. Some other signs as hypermenorrhea (4.8%) were also remarkable.

These was the signs of initially clinical suggests. By gynecological examination, the patients underwent the colposcopy, pap-test and biopsy leading to the positive diagnosis.

Table 8 Tumor size

Tumor size	0–1 cm	1–2 cm	2–3 cm	3–4 cm	4–5 cm	>5 cm
Patient number	4	7	12	38	33	29
Proportion						

Pelvic lymph nodes: 123 cases of pelvic lymphadenectomies, among which, 28 cases had positive metastatic nodes (22.7%). These patents will be transfer to undergo an adjuvant radiotherapy or chemo-radiation

Table 9 Metastatic according to stages

Metastatic lymph nodes	Stage IA	Stage IB1	Stage IB2	Stage IIA
Number of patients	0	3	12	13
Percent (%)	0	4.4	17.9	19.4

Table 10 Metastatic lymph nodes according to tumor size

Tumor size	0–1 cm	1–2 cm	2–3 cm	3–4 cm	4–5 cm	>5 cm
Number of patient	0	1	4	6	10	7
Percent (%)	0	1.5	5.9	8.9	14.9	10.5

Table 11 Recurrence and metastasis: 79 patients are controlled and surveilled (n = 79)

Post treated time	1 year	2 years	3 years	4 years	≥ 5 years
Number of patients	14	15	22	16	12
Percent (%)	17.7	19	27.8	20.2	15.2

The shortest time (from the stop of treatment until revealing of recurrence and/or metastases) 10 months, 14 patients; longest time ≥ 60 month, 13 cases. We have 23 patients of recurrence and/or metastasis

Table 12 The time to recurrence/metastasis after surgical treatment

Times	First year	2nd year	3rd year	4th year	≥ 5th year
Pts. number	3	2	5	8	5
Percent (%)	13	8.7	21.7	34.7	21.7

Table 13 Recurrence/metastasis into pelvic lymph nodes: 21/23 cases of metastasis underwent the pelvic lymph noded dissection with 17/21 of positive anapath results

Recurrence/metastasis/lymph nodes	Pelvic lymph node (-)	Pelvic lymph node (+)	Tổng số
Number of patients	4	17	21
Percent (%)	17.3	74	91.3

Table 14 Recurrence/metastasis according to tumor sizes

Tumor size	0–1 cm	1–2 cm	2–3 cm	3–4 cm	4–5 cm	≥ 5 cm
Number of patients	1	1	4	7	6	4
Percent (%)	4.3	4.3	17.3	30.4	26	17.3

Table 15 Recurrence/metastasis according to the result of Anapath

Anapath	Adenocarcinoma	Squamous Cell carcinoma	Others	Total
Number of patients	13	6	4	23
Percent (%)	56.5	26.1	17.4	100

Table 16 comparison the cancer proportion among other authors

Authors	IA (%)	IB (%)	IIA (%)	Total (%)	p
Thinh et al. [3] (HCM cancer center)	0.15	21.8	23.6	45.4	<0.05
Khuong et al. [6] (K Hospital Ha Noi)	–	18.7	32.1	50.8	<0.05
Thang et al. [16] (Can Tho General Hospital)	2.9	11.3	4.3	18.5	

According to the general evaluation, our proportion of early cervical cancer was 18.5%, this is significantly lower in comparing with the statistics of other authors: Thing [3] (1980–1990) 45.4%; Khuong [6] (1992–1998) 50.8*

Specially, we had 12 cases by the health examination, revealing through a pap-test sin 3, coloscopies end biopsies the intraepithelial carcinoma.

The diagnosis through the health examinations were specially significant in illustrating the interests of the screening and early detection of cervical cancer in community, increasing the proportion of early stage disease, much more patients will be radical treated, signifying an efficacy participation for solving the cancer burden.

4.4 Anatomopathology

Many statistics worldwide of cervical cancer had reported that the great number of cervical cancer was squamous cell carcinoma [16]. Our statistic was also appropriately similar.

Authors	S,C. Carcinoma (%)	Adenocarcinoma (%)
Wolman as in Novak [17]	90	10
Thinh (HCM Cancer Center) [3]	83	10
Binh Dân Hospital [3]	93	7
Cần Thơ Oncology Hospital [18]	75.7	15.1

4.5 Treatment of Early Stages Cervical Cancer

This is a problem being at once dialectic and dedicate, for the therapeutic indications were not yet unanimous among

many authors. According to conditions, situation of materials and equipment, the capacity and even the concepts.

With the cervical cancers before stage IA, the unification of radically or even conservatory surgical indication were no dispute. According to the medial literature, node invasion is rarely and less than 1%.

With stages IB & IIA, the choice of method of treatment depends on different author.

According to Wolman [17], the surgical methods of treatment were preferentially chosen for young patient, fewer risk surgical factor and small lesion. Radiation and/or chemoradiation were chosen for aged patients with higher risk of surgery and extended lesions.

According to Patricia et al. [12] the therapeutic procedure of cervical cancer of early diagnosis as following:

- Epithelial lesions: superficial ablative techniques.
- Microinvasion <3 mm: Conservative surgical treatment (conisation, extracapsular hysterectomy)
- Early invasion (IA2, IB1, IIA): Radical hysterectomy or single radiotherapy.

At HCM city cancer center [3], the stages of cervical cancers were treated as schema:

- Internal radiation
- Surgery
- Completing post-operative radiation (If N+ or surgery were not yet sufficient).

At Can Tho, as the particularity about materials and equipment, there is not yet radiation machine, we treat only

surgically the cervical cancer diseases “in early stages”. By this reason, the choice of patients ranged within the “radically operable group”:

For the \leq IA group: we apply the radical hysterectomy without lymph nodes dissection. For the rest, we opened with bilateral pelvic lymphadenectomy. In the case in suspect, we transfer the patient to an adjuvant radiation or chemoradiation therapy.

4.6 Results and Post Treated Surveillance

During the surgically therapeutic process, we didn't have any case of severe complications: some light infection of the incision and well controlled. Most patients had an almost normal post-operative proceeding. The average post-operative time were 8 days.

There were 123 cases of lymphadenectomy, 84.2%, among which 28 cases were metastatic (22.7%). We had to send the patient to undergo radiation or chemoradiation adjuvant therapy

Nowadays, we manage 79 patients, 54.1%, among which 13 patents had been surveilled more than 5 years after the treatment, most of them were diagnosed at stages of IA and IB. However, about half number of patient were not surveilled through the long time. That couldn't be reexamined or stopped themselves to be surveilled. So that we cannot evaluate accurately the true results of treatment periodically.

According to the medical literature [7], survival proportion of cervical cancer stage I were 72%, stage II 62%, stage III 34% and only 8% for stage IV. Within the country, we didn't find out any documentation talking about 5 years survival for each stage of cervical cancer. The statistics also showed the progressive decrease of reexamined patient number post-treated. There could be several patients of recurrence but impossible to come reexamine, died after and were not reckoned or they also could survive on illness without reexamination. By these reasons, it's so difficult to do a comparison of results of treatment among the therapeutic center within the country.

5 Conclusions

The proportion of early cervical cancer, 14.5%, were significantly lower than the acknowledgments of other institutions within the whole country, participate to reflect the situation of this malignant disease in the region, most populated, of Mekong Delta area. Surgical treatment of cervical cancer in initial stages (IA–IIA) had initially brought many encouraging results participating to solve the burden of

cancer in general and cervical cancer in properly, even in the areas where the means of multidisciplinary treatment were still inadequately. For cervical cancer patients diagnosed in initial stages, with localized lesions, the surgical treatment signified a radical management. This participated to reduce significantly the mortality of this kind of cancer.

The most important problem was how to do for elevating the number of patients diagnosed in initial stages. The screening and early detection of cervical cancers, leading to treat the cancer at an early moment, also signified a radical treatment, were an emergent problem in an area that the prevalence of disease is so high, while the means of diagnostic as well as treatment were still inadequate and lack of a performing cancer control and prevention network.

Conflict of Interest The authors declare that they have no conflict of interest.

References

1. Hung, N.C., et al.: Current aspects of cancer epidemiology at HCM City and some southern provinces in Vietnam. Special issue of Medical Science Magazine of HCM Oncology Hospital, HCM City 65–73 (1995)
2. Hung, N.C.: Cervix uteri cancer. Clinical Oncology, Tome II HCM city University of Medicine and Pharmacy, pp. 135–167 (1982)
3. Thinh, L.P., et al.: (2001) Evaluation of cervical cancer treatment status at HCM City Oncology center from 1990–1996. In: Report in summary record of second scientific conference of Oncology at Cần Thơ, pp. 78–91
4. Truc, N.Q.: Result of treatment of cervical cancer, staged IA-IIA HCM City cancer center. Special issue of medical science magazine of HCM oncology hospital, HCM City, pp. 151–160 (1995)
5. Van Đang, N.: The summation of cervical cancer treatment during 5 years 1990–1994 at Hung Vuong hospital. Special issue of medical science magazine of HCM city oncology hospital, HCM city Vietnam, pp. 34–41 (1995)
6. Loan, Đ.T.P., Duy, K.V.: Cervical cancer patients characteristics at Hanoi city area from 1992–1998. J. Pract. Med. Published by MOH of aaaaavietnam N: 431. National cancer Conference of control and prevention of cancer Oct 2002, pp. 279–282 (2002)
7. UICC: Cervix Uteri Cancer. In: Handbook of clinical oncology (Vietnamese translation), HCM.city's edn, pp. 527–540 (1995)
8. Maingon, P., Barillot, I.: Cancer du col utérin. Thérapeutique du cancer. Spinger Paris, pp. 723–740 (2001)
9. Cappelaere, P., Chauvergne, J., Armand, J.P.: Cancer du col utérin. Manuel pratique de chimiothérapie anticancéreuse, Spinger-Verlag France, pp. 296–300 (1992)
10. Moore, D.H.: The role of Radical Hysterectomy and Neoadjuvant Chemotherapy in carcinoma of the cervix. Curr. Oncol. Rep. 4(2), 145–151 (2002)
11. Benedet, J.L., Bender, H., Jenes III, H., Ngan, H.Y.S., Pecorelli, S.: FIGO Staging classification and clinical practice guidelines in the management of gynecologic cancers. Int. J. Gynecol. Obstet. 70(2), 209–262 (2000)

12. Eifel, P.J., Berek, J.S., Thigpen, J.T.: Cancer of the cervix. In: *Cancer Principle & Practice of Oncology*, pp. 1433–1456. Lippincott—Raven (1997)
13. Blake, P.: Carcinoma of the Cervix. *Treatment of Cancer*, pp. 696–719. Chapman & Hall medical (1995)
14. Look, K.Y.: Carcinoma of the Cervix, pp. 158–161. *Saunders. Current therapy in cancer* (1999)
15. Thigpen, J.T.: Carcinoma of the cervix. In: Perry, M.C. (ed.) *The Chemotherapy Source Book*, pp. 1046–1051. Williams & Wilkins (1992)
16. Paavonen, J.: Human papillomavirus infection and the development of cervical cancer and related genital neoplasias. *Int. J. Infect. Dis.* **11**(2), S3–S9 (2007)
17. Wolman, I.: *Berek and Novak’s Gynecology*, 15th edn. Lippincott Williams and Wilkins (2012)
18. Huynh, T.Q., et al.: *Cervical Cancer. Can Tho General Hospital Data* (2018)

Lymph Node Dissection by Laparoscopic Surgery in Patients Underwent Right Colon Cancer Treatment

T. Q. Huynh, H. L. Ho, K. V. Vo, L. T. Huynh, T. P. Chau, and N. Doan

Abstract

Aim To evaluate the feasibility, safety, and properties of dissected lymph nodes from the specimen of laparoscopic right hemicolectomy for colon carcinoma. **Materials and method** To perform a cross-sectional study of 80 right colon carcinoma patients who underwent laparoscopic right hemicolectomy at K Hospital of Hanoi Medical University and Can Tho Oncology Hospital from June 2012 to June 2016. **Results and discussion** There were 36 male and 44 female patients. Age ranges from 20-87-year-old, the average age was 54.8 ± 1.7 . 15 patients had a history of previous operations. The mean size of tumors was 4.9 ± 0.2 cm (1.5–6 cm). A total of 992 lymph nodes were harvested, the mean number of nodes dissection for each patient was $12.4 \text{ mm} \pm 2.8$ (6–43 mm). The number of nodes dissection whose size from 0.5 to 1 cm were 589 (59.4%). Majority of lymph node's location was closed to the tumor edge and along arteries: ileocolic, right and middle colic arteries (80.1%). Metastatic rate of lymph nodes was moderate (40%). **Conclusion** Within the limit of this study, lymphadenectomy in Laparoscopic surgery for right colon carcinoma was the feasible and safe procedure. It conforms to the oncological principles. Characteristic properties of dissected lymph nodes from the specimen revealed mean of nodes dissection for each patient were 12.4 mm; a majority of node's locations were closed to the tumor edge and along the ileocolic, right colic and middle colic arteries. Metastatic rate of lymph nodes was moderate (40%).

Keywords

Laparoscopy • Colon cancer • Lymphadenectomy

1 Introduction

The presence of lymph node metastases in colorectal cancer is well recognized as one of the most important prognostic factors for long-term outcome [1–3]. Local recurrence and survivals after colon cancer have been reported by standardized surgery with complete mesocolic excision and central vascular ligation [4]. The era of laparoscopic surgery for colon cancer was initiated since 1991 [5]. Moreover, the question regarding to oncology still be posed as: whether the endoscopic surgery ensures the perfect node dissection in comparing with the classically standard operation [6]. The endoscopic surgery had been admitted, worldwide, since a multi-centric randomized, large quantity of patients, clinical trial reporting about the safety as well the interests on regard of oncology [7–9]. Then, the clinical trial COST had concluded the acceptance of endoscopic surgery as one surgical therapeutic modality of choice [9].

Additionally, the AJCC and UICC, and National Cancer Institute consensus panel have all recommended the evaluation of, at least, 12 dissected nodes to ensure an adequate sampling [8]. The college of American pathologist has, for many years, recommended a pathologic examination of at least 12 nodes to accurately predict node negativity. The number of dissected nodes should be at least of 12 to become sufficient to stage the metastatic nodes (N staging) [10, 11]. An accurate node staging of colon cancer post-operative will help us to choose appropriate adjuvant chemotherapy and is an important prognostic factor [12]. From such the reasons and benefits of laparoscopic lymph node dissection, we carry out this study to evaluate the feasibilities, results and clinical applications of node dissection through laparoscopic surgery for adenocarcinoma of the right colon.

T. Q. Huynh · H. L. Ho · K. V. Vo · L. T. Huynh
Can Tho Oncology Hospital, Can Tho, Vietnam

T. P. Chau
Department of General and Thoracic and Oncologic Surgery,
Cho Ray Hospital, Ho Chi Minh City, Vietnam

N. Doan (✉)
The University of Queensland; Griffith University, Queensland
University of Technology, Brisbane, Australia
e-mail: nvtdoan123@gmail.com; ; nvtdoan23@gmail.com

2 Materials and Methods

Patients of right colon adenocarcinoma were selected and treated by endoscopic surgery at central K hospital (Hanoi) and Can Tho oncology hospital (Can Tho). A descriptive cross-sectional study with the duration of study from 2012–2016.

2.1 Targets of Study

- Patient characteristics: age, sex, weigh, height, BMI, location and size of tumors, surgical antecedents
- Results of nodes dissection: quantity, size, locations of dissected node groups, and the metastatic node status according to each section, size and to TNM.

The data of study were processed by statistical algorithm with the software data analysis SPSS 20 and TATA 8. The *p* value <0.05 was considered as statistically significant.

3 Results

The study comprises 36 male and 44 female patients whose mean age was 54.8 ± 1.7 (20–87). The BMI had the mean value of 21 ± 0.3 (14.6–30.8). The mean size of tumor was 4.5 ± 0.2 (1.5–6). 15 patients had the old scar of incision (18.6%).

3.1 Results of Nodes Dissection

The results and characteristics of dissected lymph nodes are clarified in Table 1 according to sites and locations; different halting places of lymph node and metastatic status

depending on N staging as following: N 0 48 cases (69%), N1 24 cases (30%) and N2 008 cases (10%)

The manifested values were mean value \pm standard errors (approximation) or case number (%)

4 Discussion

The nodes dissection in colon cancer was one surgical criterion, an important prognostic factor [2]. There are many factors influencing the number of dissected nodes during the operation of colon cancer: endoscopic or opened surgery, experiences, the technics of nodes dissection, the principles of cancer surgery of the surgeons, the cooperation between the surgeons and pathologists to examine all the dissected nodes [6, 8 and 13]. In our study, 80 patients of colon adenocarcinomas underwent endoscopic surgery, the totality of dissected nodes were 992 nodes among which the most common locations of the nodes were D1, 378 nodes (38.1%) and D2, 417 nodes (42%). D3 had only 197 nodes (19.9%). The most important in prognosticating the cancerological results of treatment in long term were the number of dissected nodes [6]. Goldstein NS and colleagues (1996) and Tekkis PP (2006) recommended the regional nodes should be dissected systematically [11, 12] and the minimum number should be 6–17 nodes and, for pathological exploration, should be at least 12 nodes in order to have a clinical classification appropriate [14, 15]. By this, the indication of adjuvant chemo.

The size of nodes was also a predictive factor for the nodal metastasis of colorectal cancers. therapy will be decided [16]. Analyzing on 80 patients, the size of nodes of 0.5–1 cm were the most commonly seen and found out in 589 nodes (59.4%); 357 cases with nodes ≤ 0.5 cm (36%) and only 46 (4.6%) nodes with the diameter of >1 cm. Braat, in the meta-analysis of 30 studies about the sizes of nodes had

Table 1 Patients characteristics

Characteristics	Results
Ages	54.8 ± 1.7 (20–87)
Sexes	
Males	38 (45)
Females	44 (55)
Weight	52 ± 0.9 (36–76)
Height	157.2 ± 0.7 (143–169)
BMI (kg/m^2)	21 ± 0.3 (14.6–30.8)
Locations of tumor	
Caecum	10 (12.5)
Ascending colon	41 (51.2)
Right angle colon	29 (36.3)
Tumor sizes	4.9 ± 0.2 (1.5–6)
Abdominal surgery antecedents	15 (18.8)

reported: Nodes larger than 1 cm of diameter had a proportional metastasis higher than 90–100%, whereas ≤ 0.5 cm had this proportion of 66–77% [6]. Our study reported a lower metastatic proportion according to nodes sizes: for node group size larger than 1 cm: 38/46 (82.6%); group of 0.5–1 cm: 278/589 (47.2%) and group of <0.5 cm: 81/357 (22.7%). The generally nodal metastasis of the whole patient group was 40%. Nodal metastasis was the independently prognostic factor for the survivals and recurrence after the surgical therapeutic. Moreover, about the nodal metastasis, sometimes the cancer cells, instead of developing by a halting order from “near to far”, skip a passage to a further destination. This is called “skip metastasis. Of our study, we didn’t see any case of skip metastasis. 06 cases of nodal metastasis along the superior mesenteric artery had also the nodal metastatic at other stages of metastasis: beside the tumor and intermediate node groups. N Staging according to TNM we had N1 of 30% (1–3 nodes), N2 of 10% (≥ 4 nodes).

5 Conclusions

Node dissection through laparoscopic surgery for the treatment of colorectal cancers is an operation of high feasibility, but it needs to respect the oncologic principles with the average number of dissected nodes was 12 of which, the most common location was beside the tumor and along the ileocolic, right colic and middle colic arteries (80.1%) with the common size of nodes was 0.5–1 cm (59.4%). The metastatic nodal proportion was 40%.

Conflict of Interest The authors declare that they have no conflict of interest.

References

- McDonald, J.R., Renehan, A.G., O’Dwyer, S.T., Haboubi, N.Y.: Lymph node harvest in colon and rectal cancer: Current consideration. *WJGS* 2012 Jan 27, **4**(1), 9–19 (2012)
- National Comprehensive Cancer Network (NCCN). NCCN practice guidelines in oncology—V.2. 2009. Rectal cancer [Internet]. Washington: NCCN; c2012 [cited 2012 Feb 6]. Available from: <http://www.cchina.net/UserFiles/2009-4/20/20094200133667.pdf>
- Priolli, D.G., et al.: Metastatic lymph node ratio as an independent prognostic variable in colorectal cancer: study of 113 patients. *Tech. Coloproctol.* **13**, 113–121 (2009)
- Uematsu, D., Akiyama, G., Sugihara, T., Magishi, A., Yamaguchi, T., Sano, T.: Laparoscopic radical lymph node dissection for advanced colon cancer close to the hepatic flexure. *Asian J. Endosc. Surg., Issue TQC*, **10**(1), 22–27 (2017)
- Edge, S.B., et al.: Colorectal cancer. In: *AJCC Cancer Staging Handbook*, 7th edn, pp. 173–174 (2010)
- COLOR Study Group: COLOR: a randomized clinical trial comparing laparoscopic and open resection for colon cancer. *Dig. Surg.* **17**, 617–622 (2000)
- Fleshman, J., Sargent, D.J., Green, E., Anvari, M., Stryker, S.J., Beart Jr., R.W., et al.: Laparoscopic colectomy for cancer is not inferior to open surgery based on 5-year data from the COST Study Group trial. *Ann. Surg.* **246**, 655–662 (2007)
- Jayne, D.G., Guillou, P.J., Thorpe, H., Quirke, P., Copeland, J., Smith, A.M., et al.: Randomized trial of laparoscopic-assisted resection of colorectal carcinoma: 3-year results of the UK MRC CLASICC Trial Group. *J. Clin. Oncol.* **25**, 3061–3068 (2007)
- Jayne, D.G., Thorpe, H.C., Copeland, J., Quirke, P., Brown, J.M., Guillou, P.J.: Five-year follow-up of the Medical Research Council CLASICC trial of laparoscopically assisted versus open surgery for colorectal cancer. *Br. J. Surg.* **97**, 1638–1645 (2010)
- Braat, A.E., et al.: Lymphatic staging in colorectal cancer: pathologic, molecular, and sentinel node technique. *Dis. Colon Rectum* **48**, 371–383 (2005)
- Tekkis, P.P., Smith, J.J., Heriot, A.G., Darzi, A.W., Thompson, M. R. Stamatakis, J.D., et al.: A national study on lymph node retrieval in resectional surgery for colorectal cancer. *Dis. Colon Rectum* **49**, 1673–1683 (2006)
- Goldstein, N.S., Sanford, W., Coffey, M., Layfield, L.J.: Lymph node recovery from colorectal resection specimens removed for adenocarcinoma. Trends over time and a recommendation for a minimum number of lymph nodes to be recovered. *Am. J. Clin. Pathol.* **106**, 209–216 (1996)
- Kuhry, E., Schwenk, W., Gaupset, R.: Long—Term Results of Laparoscopic Colorectal Cancer Resection. *The Cochrane collaboration Published by Wiley & Sons*, pp. 1–63 (2008)
- Milsom, W., Bohm, B., Nakajima, K.: *Laparoscopic Colorectal Surgery*. Springer, 2nd edn, pp. 188–202 (2006)
- Lourenco, T., Murray, A., Grant, A., et al.: Laparoscopic surgery for colorectal cancer: safe and effective? A systematic review. *Surg. Endosc.* **22**, 1146–1160 (2008)
- Guillou, P.J., Quirke, P., Thorpe, H.C., et al.: Short—term endpoints of conventional versus laparoscopic—assisted surgery in patients with colorectal cancer (MRC CLASICC Trial): multicenter randomized controlled trial. *The Lancet* **365**, 1718–1726 (2005)

Part XV

**Advanced Technologies in Sleep Diagnosis and
Sleep Medicine**

Study of the Obstructive Sleep Apnea in the Patients with Cardiovascular Risk

Hoang Anh Tien and Nguyen Huu Duc

Abstract

Background Obstructive Sleep Apnea syndrome (OSA) is the syndrome of stopping the breath when sleeping. It is estimated that more than one quarter of the population is at risk for OSA, with increased prevalence noted in populations with hypertension, coronary artery disease, stroke, and atrial fibrillation. In Viet Nam, there are still a few studies of OSA. **Objective** To evaluate the prevalence of cardiovascular risk in OSA patients. Also, the correlation between AHI and BMI, SBP, DBP, blood glucose, Cholesterol, Triglyceride, LDL-C, HDL-C. **Methods** Clinical data of 30 OSA patients admitted to hospital were analyzed and compared to 30 healthy persons, without cardiovascular risk. We evaluated the incidence of cardiovascular risk in the OSA patients. We also find the correlations between AHI and age, BMI, systolic blood pressure, diastolic blood pressure, fasting glucose, Cholesterol, Triglyceride, LDL-C, HDL-C. **Results** 1. The prevalence of cardiovascular risk in the OSA patients: hyperlipidemia was 27.59%, hypertension was 18.97%, obesity was 20.69%, smoking was 13.79%, sedentary lifestyle was 8.62%, diabetes mellitus was 10.34%. 2. AHI correlated with SBS ($r = 0.37, p < 0.05$), Cholesterol ($r = 0.32, p < 0.05$) and BMI ($r = 0.41, p < 0.05$). **Conclusions** Basing on the correlation, cardiovascular risk should be concerned in OSA.

Keywords

Obstructive sleep apnea syndrome • Cardiovascular risk

1 Background

Obstructive sleep apnea (OSA) is a disorder characterized by repetitive collapse and reopening of the upper airway during sleep. The collapse of the airway impairs ventilation and can result in intermittent hypoxemia and hypercapnia. During airway collapse, the resistance to air flow results in increased respiratory effort and intrathoracic pressure swings. Eventually, the increased work of breathing results in disruption of sleep (arousal) and activation of upper-airway muscles that causes reopening of the airway. The repetitive acute physiologic stress of OSA noted above can result in symptoms (sleepiness, awakenings) and/or cardiovascular disease via intermediary mechanisms [1].

OSA has been studied in the last 30 years and the prevalence is becoming more prevalent. OSA is a common disorder with major neurocognitive and cardiovascular sequelae. It is estimated that more than one quarter of the population is at risk for OSA, with increased prevalence noted in populations with hypertension, coronary artery disease, stroke, and atrial fibrillation. A number of epidemiologic and mechanistic studies have recently generated interest in the role of OSA in the pathophysiology of cardiovascular disease, a link that continues to require extensive investigation [2].

In the world, there have been many studies about of OSA but in Vietnam, have not been properly considered compared to the dangers that the syndrome brings. Based on this situation, we conducted the study: “Study of the obstructive sleep apnea in the patients with cardiovascular risk” that aims to two objectives:

1. Evaluate the frequency of cardiovascular risk factors in patients with obstructive sleep apnea syndrome.
2. Find the correlation between AHI (Apnea–Hypopnea Index) with BMI (Body Mass Index), DBP (Diastolic Blood Pressure), SBP (Systolic Blood Pressure), Blood Glucose, Cholesterol, Triglyceride, LDL-C, and HDL-C.

H. A. Tien (✉)
Hue University of Medicine and Pharmacy, Hue, Vietnam
e-mail: bsanhtien@gmail.com

N. H. Duc
Quang Tri Hospital, Quang Tri, Vietnam
e-mail: nguyenhuuduc1986@gmail.com

2 Methods and Study Population

2.1 Study Population

The disease group of 30 patients with obstructive sleep apnea syndrome, with cardiovascular risk factors, admitted to Hue University Hospital. The control group included 30 healthy patients with no cardiovascular risk factors of the same age.

2.2 Methods

Case control study

Agitation of Sleep-Related Sleep Disorders

- The number of apneas 5–15 times/h: light.
- The number of apneas 15–30 times/h: moderate.
- The number of apneas 5–15 times/h: severe [3].

Diagnostic Criteria for Adult Obstructive Sleep Apnea (OSA) Diagnosed with all three criteria A, B, C and have respiratory muscle [3]:

- A. At least one of the following applies:
1. The patient complains of unintentional sleep episodes during wakefulness, daytime sleepiness, unrefreshing sleep, fatigue, or insomnia.
 2. The patient wakes holding his/her breath, gasping, or choking.
 3. The bed partner reports loud snoring or breathing interruptions during the patient's sleep.
- B. Polysomnographic recording shows the following:
1. Five or more score able respiratory events occur per hour. These events can include any combination of obstructive apneas, hypopneas, or respiratory-associated arousals.
 2. There is evidence of respiratory effort during all or a portion of each respiratory event.

- C. This disorder is not better explained by another sleep, medical, or psychiatric disorder, substance abuse, or medication.
- D. Associated features:
Snoring, Obesity, Systemic hypertension, Pulmonary hypertension, Congestive heart failure, Sleep fragmentation, Recurrent awakening from sleep, Sleep-related cardiac dysrhythmias, Nocturnal angina, Gastroesophageal reflux, Impaired quality of life, Impaired concentration, Diabetes, Metabolic syndrome

Epworth Sleepiness Scale How likely are you to doze off or fall asleep in the following situations, use the following scale to choose the most appropriate number for each situation:

0 = would never doze, 1 = slight chance of dozing, 2 = moderate chance of dozing, 3 = high chance of dozing (Table 1).

A score of ≥ 10 indicates significant daytime sleepiness.

3 Results

3.1 Characteristics of Research Subjects

There is significant difference between controls group and disease group in BMI ($p < 0.05$), Heart rate ($p < 0.05$), Diastolic BP ($p < 0.05$), Systolic BP ($p < 0.05$) (Table 2).

3.2 Characteristics of Research Subjects in Polysomnographic Recording

There is significant difference between controls group and disease in Epworth Sleepiness Scale, ($p < 0.01$) AHI ($p < 0.001$), SpO₂ (%) ($p < 0.001$) (Table 3).

Table 1 Epworth Sleepiness Scale [4]

Situation	Chance of dozing (0–3)
Sitting and reading	
Watching TV	
Sitting, inactive in a public place (e.g. a theatre or a meeting)	
Lying down to rest in the afternoon when circumstances permit	
Sitting and talking to someone	
Sitting quietly after a lunch without alcohol	
In a car, while stopped for a few minutes in the traffic	

Table 2 Characteristics of research subjects

Characteristics		Controls group (n = 30)	Disease group (n = 30)	p
Age		46.67 ± 12.48	49.26 ± 11.32	>0.05
Sex	Male	9 (56.25%)	19 (63.33%)	>0.05
	Female	7 (43.75%)	11 (36.67%)	>0.05
BMI (kg/m ²)		19.87 ± 2.99	23.03 ± 4.53	<0.05
Heart rate (bpm)		80.17 ± 8.18	87.16 ± 11.12	<0.05
Systolic BP (mmHg)		130.53 ± 26.14	149.03 ± 28.98	<0.05
Diastolic BP (mmHg)		71.58 ± 15.62	81.67 ± 9.83	<0.05
Glucose (mmol/l)		6.43 ± 1.78	7.20 ± 1.34	>0.05
Cholesterol (mmol/l)		4.93 ± 0.90	5.28 ± 0.83	>0.05
EF (%)		63.46 ± 11.93	58.11 ± 13.45	>0.05
FS (%)		37.92 ± 8.27	33.54 ± 9.66	>0.05

3.3 Distribution of OSA According to AHI

See Table 4.

3.4 Distribution of Pathology and Risk Factors of OSA

Hyperlipidemia accounts accounted for the highest rate with 27.59%. The lowest risk factor is was static lifestyle with 8.62% (Table 5).

3.5 Correlation Between AHI and Cardiovascular Risk Factors

There was a statistically significant positive correlation between AHI and SBP, cholesterol and BMI (Table 6).

4 Discussion

There have been numerous studies showing that OSA is independently associated with hypertension [5] insulin resistance, glucose tolerance [6] hyperlipidemia [7]. The AHI

Table 3 Characteristics of research subjects in polysomnographic recording

	Controls group (n = 30)	Disease group (n = 30)	p
Epworth sleepiness scale	3.45 ± 1.38	8.34 ± 3.37	<0.01
AHI	3.87 ± 0.63	27.66 ± 11.51	<0.001
AHI—supine	4.26 ± 0.43	34.67 ± 12.43	<0.001
AHI—non-supine	3.64 ± 0.57	25.90 ± 11.48	<0.001
SpO ₂ (%)	97.67 ± 0.82	95.05 ± 1.39	<0.001
Snoring index	0.61 ± 0.23	11.32 ± 2.96	<0.001
Blood oxygen saturation reduction index	0.78 ± 0.19	22.17 ± 5.73	<0.001

Table 4 Distribution of OSA according to AHI

AHI	5–14	15–29	≥ 30
BMI	20.27 ± 4.38	21.59 ± 4.49	22.03 ± 6.52
SpO ₂ (%)	95.67 ± 2.52	95.57 ± 0.79	94.44 ± 1.24
Heart rate (bpm)	89.11 ± 9.08	81.86 ± 14.09	93.67 ± 3.06
SBP (mmHg)	124.29 ± 20.82	126.67 ± 26.37	156.67 ± 24.49
DBP (mmHg)	81.67 ± 9.83	78.89 ± 15.37	87.65 ± 11.75
Glucose (mmol/l)	5.32 ± 0.99	6.05 ± 1.74	7.33 ± 2.19
Triglycerid (mmol/l)	1.77 ± 0.43	2.00 ± 0.57	2.31 ± 1.27
Cholesterol (mmol/l)	5.53 ± 0.41	5.50 ± 1.18	5.02 ± 0.56
HDL-Cholesterol (mmol/l)	1.35 ± 0.62	1.06 ± 0.29	1.17 ± 0.17
LDL-Cholesterol (mmol/l)	2.82 ± 0.64	2.80 ± 0.60	2.95 ± 1.10

Table 5 Distribution of risk factors of the sample

Risk factors	(n)	(%)
Hyperlipidemia	16	27.59
Hypertension	11	18.97
Obesity	12	20.69
Smoking history	8	13.79
Static lifestyle	5	8.62
Diabetes mellitus	6	10.34
<i>p</i>	<0.001	

Table 6 Correlation between AHI and cardiovascular risk factors

Correlation	AHI	
	<i>r</i>	<i>p</i>
SBP (mmHg)	0.37	<0.05
Cholesterol (mmol/l)	0.32	<0.05
BMI (kg/m ²)	0.41	<0.05

(Apnea–Hypopnea Index) is the most important parameter in assessing the severity of OSA [1]. In our study, AHI correlated with SBP ($r = 0.37$ $p < 0.05$) and Cholesterol ($r = 0.32$, $p < 0.05$). Steven R. Coughlin et al. concluded that OSA was independently associated with an increase in cardiovascular risk factors and metabolic syndrome. This explains the increased risk and sudden cardiac death in patients with Obstructive Sleep Apnea syndrome [8].

Many studies have shown that OSA, even in middle-aged men, is closely related to the incidence cardiovascular mortality [5, 9].

According to Gami AS et al., OSA increases increased the risk of sudden cardiac death during sleep [10]. According to Yaggi HK et al., OSA is was associated with increased risk of stroke and death from any cause, and increased independence from other causes, including hypertension [11]. According to Baguet [12], there is was a strong correlation between OSA and cardiovascular events, and the treatment of OSA with continuous positive pressure ventilation (CPAP) can could improve cardiovascular risk, specially for hypertension.

Diagnosis and treatment of OSA should be considered in conjunction with the treatment of risk factors such as hypertension, diabetes and obesity. Sleep disturbances associated with OSA should be evaluated in terms of respiratory, cardiovascular, neurological, endocrine, and physical health. This is seen as an intensive diagnostic and treatment strategy for OSA.

5 Conclusions

1. The prevalence of cardiovascular risk factors in obese patients with Obstructive Sleep Apnea syndrome: hyperlipidemia 27.59%, hypertension 18.97%, obesity 20.69% smoking 13.79%, static lifestyle at 8.62%, diabetes mellitus 10.34%
2. There was a significant positive correlation between AHI and SBP $r = 0.37$, $p < 0.05$; Blood cholesterol with $r = 0.32$, $p < 0.05$; BMI $r = 0.41$, $p < 0.05$.

Conflict of Interest I declare that I have no conflict of interest.

References

1. Kapur, V.K.: Obstructive sleep apnea: diagnosis, epidemiology, and economics. *Respir. Care* **55**(9), 1155–1164 (2010)
2. Kohli, P., Balachandran, J.S., Malhotra, A.: Obstructive sleep apnea and the risk for cardiovascular disease. *Curr. Atheroscler. Rep.* **13**(2), 138–146 (2011). <https://doi.org/10.1007/s11883-011-0161-8>
3. Berry, R.B.: Obstructive sleep apnea syndromes: definitions, epidemiology, diagnosis, and variants. In: *Fundamentals of Sleep Medicine*. Elsevier (2012)
4. Johns, M.W.: A new method for measuring daytime sleepiness: the Epworth Sleepiness Scale. *Sleep* **14**, 540–545 (1991)
5. Peppard, P.E., Young, T., Palta, M., Skatrud, J.: Prospective study of the association between sleep-disordered breathing and hypertension. *N. Engl. J. Med.* **19**(342):1378–1384 (2000). <https://doi.org/10.1056/NEJM200005113421901>
6. Ip, M.S., Lam, B.I.N.G., Ng, M.M., Lam, W.K., Tsang, K.W., Lam, K.S.: Obstructive sleep apnoea is independently associated with insulin resistance. *Am. J. Respir. Crit. Care Med.* **165**, 670–676 (2002). <https://doi.org/10.1164/ajrccm.165.5.2103001>
7. Mirrahimov, A.E., Alaa, M.A.: Pathobiology of obstructive sleep apnea-related dyslipidemia: focus on the liver. *ISRN cardiol.* (2013). <https://doi.org/10.1155/2013/687069>
8. Mawdsley, L., Coughlin, S.R., Mugarza, J.A.: Obstructive sleep apnoea is independently associated with an increased prevalence of metabolic syndrome. *Eur. Hear. J.* **25**, 735–741 (2004). <https://doi.org/10.1016/j.ehj.2004.02.021>
9. Whitney, C.W., Shahar, E., Redline, S. et al.: Sleep-disordered breathing and cardiovascular disease: cross-sectional results of the Sleep Heart Health Study. *Am. J. Respir. Crit. Care Med.* **163**, 19–25 (2001). <https://doi.org/10.1164/ajrccm.163.1.2001008>
10. Gami A.S., Howard D.E., Olson E.J., Somers V.K.: Day-night pattern of sudden death in obstructive sleep apnea. *N. Engl. J. Med.* **352**(12), 1206–1214 (2005). <https://doi.org/10.1056/NEJMoa041832>
11. Yaggi, H.K., Concato, J., Kernan, W.N., Lichtman, J.H., Brass, L. M., Mohsenin, V.: Obstructive sleep apnea as a risk factor for stroke and death. *N. Engl. J. Med.* **353**(19), 2034–2041 (2005). <https://doi.org/10.1056/NEJMoa043104>
12. Baguet, J.P., Pépin, J.L., Hammer, L., Lévy, P., Mallion, J.M.: Cardiovascular consequences of obstructive sleep apnea syndrome. *Rev. Med. Interne.* **24**(8), 530–537 (2003). [https://doi.org/10.1016/S0248-8663\(03\)00142-5](https://doi.org/10.1016/S0248-8663(03)00142-5)



Application of Oxygen on Gagging Patients with Sleep Disordered Breathing: Ten Year Retrospective Study

L. Truong, J. Doan, P. Reher, and N. Doan

Abstract

Introduction Application of pure oxygen is an easy method to overcome gagging. **Aim** The objective of this paper is to carry out a ten-year retrospective case series on the application of oxygen on gagging patients diagnosed with sleep disordered breathing (SDB). **Materials and methods** A cohort of 62 private dental patient data was collected for the study over the course of ten years (2007–2017). Patient information used included medical history, vital signs (blood pressure, height, and weight), neck circumference, BMI measurements, lateral cephalometric radiograph, capnograph and a full clinical examination. **Results and discussion** Patients with SDB and gagging issues have associated clinical findings such as scalloped tongue, mandibular and maxillary tori, skeletal class 2 division 1, narrow arch, deep palatal vault and worn-down dentition. Only one patient out of 62 gagging patients did not respond to oxygen therapy. This patient was identified as having SDB with a psychological component. **Conclusion** Oxygen is an excellent method to overcome gagging issues in dental patients with history of SDB.

Keywords

Oxygen • Gag reflex • Sleep disordered breathing • Retrospective study

1 Introduction

In the past, health practitioners have used several methods in an attempt to reduce the likelihood of gagging in patients. The pharyngeal reflex, commonly known as the gag reflex, is a laryngeal spasm in which triggering sensitive areas in the oral cavity causes the contraction of the back of the throat. It is a protective mechanism where the body tries to eliminate an agent or avoid choking [1]. Various causes may be psychogenic or somatogenic in origin with extra and intra oral factors also playing a role [2, 3]. In dentistry, having a hypertensive gag reflex may lead to fear, anxiety or avoidance of treatment [3]. Many dental procedures that may trigger the gag reflex include placement of rubber dam, x-ray films, impression-taking or administration of local anesthesia [2]. This can make treatment very challenging or impossible [3]. Certain areas of the oral cavity can be more sensitive than others; literature [2] suggests trigger regions comprise of the palate, base of the tongue, throat and pharyngeal wall.

This can be particularly true in patients with sleep disordered breathing (SDB) during dental treatment. SDB is defined as the reduction of oxygen or other respiratory irregularities which happen during sleep [4]. It ranges from snoring, upper airway resistance syndrome to obstructive sleep apnoea. The anatomy and neuromuscular functions play a key role in the pathophysiology [5, 6]. Saboisky, Stashuk [7] reported results showing the existence and severity of structural neural remodeling in apneic patients. During treatment, inadequate air may not be obtained through the nose and when the patient lies down in the dental chair, the tongue may be dropped back [8]. It is possible patients may feel they cannot attain supplementary air through their mouth, especially when there is water or other agents/equipment in the oral cavity. Consequently, this leads to higher accumulation of carbon dioxide and thus, maximum end-tidal carbon dioxide levels [9]. The brain then sends alert signals to the body, forcing a powerful gasp or gag. Therefore, the airway is such a vital component for

L. Truong (✉) · P. Reher · N. Doan
School of Dentistry and Oral Health, Griffith University,
Gold Coast, Australia
e-mail: lauratruong1996@gmail.com.au

J. Doan · N. Doan
The University of Queensland, Brisbane, Australia

N. Doan
Queensland University of Technology, Brisbane, Australia
e-mail: nvtdoan123@gmail.com

survival and in this context, the gag reflex is related to the upper airway dimension.

Several pharmacological and psychological approaches such as acupuncture, nitrous oxide, and IV sedation have been used to reduce gagging in dental patients [3, 10]. However, methods such as general anesthesia or acupuncture are considered more invasive and uncomfortable compared to behavior management techniques, oxygen or nitrous sedation.

Chidiac and Chamseddine [10] conducted a study comparing the effectiveness of table salt against nitrous oxide. They found that nitrous oxide had a significant effect on the reduction of time to the gag reflex as opposed to the salt. While a number of researchers [2, 3, 10] support the use of nitrous oxide as an effective technique to prevent the gag reflex, it is also noted that the effect varies depending on the ratio of nitrous oxide to oxygen. Furthermore, De Veaux and Montagnese [3] supports this concept, as his study demonstrated that patients were able to tolerate certain dental treatments better at high ratios of nitrous oxide to oxygen.

However, only licensed practitioners who have undergone appropriate training can legally administer nitrous oxide [11]. Additionally, not every dental surgeon has the right equipment and required training. An alternative to this would be administration of pure oxygen, which is easy, convenient, cheaper, and does not require special training.

One study [12] conducted a similar experiment to test the effects of arterial oxygen saturation on gag reflex in males of similar age. The subjects compressed the lingual root strong enough to induce the gag reflex. Latency, starting from the compression of the tongue to the onset of associated abdominal muscle activity, as well as the duration and activities of these muscles were measured. Their study showed increased latency of gag reflex and decreased integral abdominal muscle activity in those who inhaled 30% oxygen for 3 min. In contrast, subjects who held their breath for 30 s displayed decreased latency of the gag reflex and increased integral abdominal muscle activity [12]. However, the ratio of the number of subjects used for each group was uneven.

Having a system of patients' selection is crucial for any scientific study. In the context of this research, the American Society of Anaesthesiologists (ASA) Score was employed. ASA score is a universal score that measures the physical status of patients prior to surgery. It is also referred to as ASA PS, since it is a quantity of 'physical status'. Thus, ASA I implies a healthy patient, ASA II a patient with mild systemic disease, ASA III a patient with severe systemic disease, and ASA IV a patient with severe systemic disease that is a continuous threat to life.

Table 1 Success rate versus oxygen

Score (VAS)	Success (%)	Gag at the time (%)
0	100	0
1	90	10
2	80	20
3	<70	>30

2 Materials and Methods

All patients selected had a strong gag reflex during dental treatment and gave informed consent (Griffith University Ref no: 2018/169). Inclusion criteria was that all patients had SDB and ASA score of I and II. ASA III and IV were excluded from this study. Gagging is measured when the patient produces laryngeal spasm manifested as coughing when triggering sensitive areas in the oral cavity. Demographic details include gender, medical history (including psychological issues), neck circumference (above average is more than 43 cm for males and more than 40 cm for females), and Body Mass Index (BMI) measurement of 25 or less is considered normal. If the patient was diagnosed by a clinical psychologist or psychiatrist, they will be listed as having a psychological disorder. Full clinical examination and investigations involved intraoral and extraoral examination (forward head posture, lip incompetence), lateral cephalometric radiographs (skeletal pattern and micrognathia), and vital signs such as capnograph, blood pressure, heart rate and arterial oxygen saturation (SpO₂). The vital signs were measured using Biolight M8500 Multi Parameter Patient Monitor, China. A visual analogue scale (VAS) representing success rate is shown in Table 1. Further exclusions are nasal obstruction or contraindications of the use of oxygen, such as complicated medical conditions, that result in ventilation-perfusion imbalance.

They were then administered oxygen using a soft tip nasal cannula for the entire dental procedure ranging from 30 to 120 min. Oxygen flow rate varies from 4–8 L/min depending on patient size (Fig. 1).

3 Results

Summary of the obtained results was found in Table 1. Of the 62 patients (28 males and 34 females), the mean age was found to be 59 years. Their pre-operatively oxygen saturation level (SpO₂) ranges from 94 to 98%. After three minutes, all patients had a SpO₂ improvement by 1.5%. More males with low SpO₂ (<94%) than females existed.

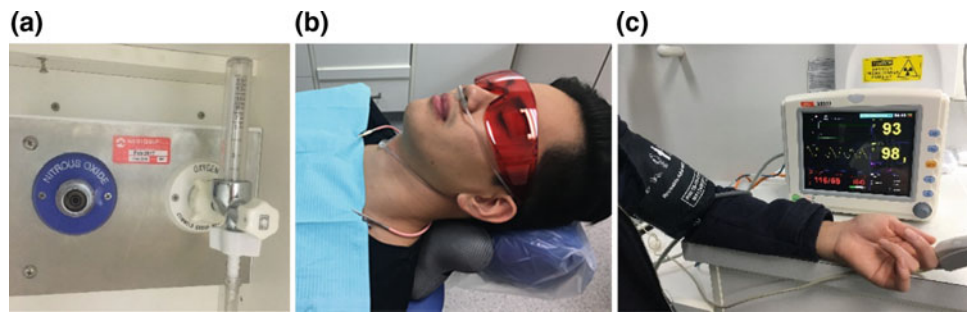


Fig. 1 a Oxygen flow meter b Patient demonstrating the use of the oxygen Softip Nasal Cannula Adult c Vital sign monitor (Biolight M8500 Multi Parameter Patient Monitor)

Statistical analyses were performed using SPSS to evaluate the occurrence of characteristics and the incidence of the gag reflex with statistical significance $P < 0.05$. Despite the above findings, only the V-shape palatal vault was statistically significant in gender. As 61 out of the 62 patients responded to oxygen therapy, this produced a 98.39% success rate with a VAS ≤ 2 . There are significant differences between older patients (≥ 50 years) and younger patients (< 50 years) in the following outcome characteristic findings: psychological issues, forward head posture, lip incompetence and response to oxygen therapy ($P < 0.05$). Despite literature [13] report, there was no association with the other findings (Tables 2 and 3).

4 Discussion

The results indicate that SDB patients benefit from the use of oxygen, especially those with the anatomical, neuromuscular, and pathophysiological conditions that compromise the size of the oral sphincter. The oxygen therapy helps patients with pathophysiological conditions; however, in this study, there was one patient (with psychological issues) who did not respond to oxygen as he did not have a strong oral sphincter. As such, oxygen therapy is less effective in this type of patient. This is an area that should be considered for future research.

Table 2 Characteristic findings of patients

	Total n (%)	Femalen (%)	Male n (%)	Gender χ^2	Young n (%)	Old n (%)	Age χ^2
Heart rate reduction by < 20 BMP	65 (100.0)	37 (56.9)	28 (43.1)	–	11 (16.9)	54 (83.1)	–
Systolic blood pressure > 135 mmHg	49 (75.4)	25 (51.0)	24 (49.0)	2.83	6 (12.2)	43 (87.8)	3.10
BMI > 25	42 (64.6)	21 (50.0)	21 (50.0)	2.32	6 (14.3)	36 (85.7)	0.59
Skeletal II and micrognathia	2 (3.1)	2 (100.0)	0 (0.0)	1.56	1 (50.0)	1 (50.0)	1.61
High capnograph ($> 6\%$)	42 (64.6)	21 (50.0)	21 (50.0)	2.32	6 (14.3)	36 (85.7)	0.59
Psychological issues	1 (1.5)	0 (0.0)	1 (100.0)	1.34	1 (100.0)	0 (0.0)	4.99*
Mallampati score (≥ 2)	42 (64.6)	21 (50.0)	21 (50.0)	2.32	6 (14.3)	36 (85.7)	0.59
Dolichocephalic skeletal pattern	1 (1.5)	1 (100.0)	0 (0.0)	0.77	0 (0.0)	1 (100.0)	0.21
Forward head posture	58 (89.2)	32 (55.2)	26 (44.8)	0.67	8 (13.8)	50 (86.2)	3.75*
Retrognathic mandible	13 (20.0)	9 (69.2)	4 (30.8)	1.00	3 (23.1)	10 (76.9)	0.44
Scalloped tongue	42 (64.6)	21 (50.0)	21 (50.0)	2.32	6 (14.3)	36 (85.7)	0.59
Neck circumference above average	42 (62.6)	22 (51.2)	21 (48.8)	1.72	6 (14.0)	37 (86.0)	0.80
Incompetent lips	7 (10.8)	6 (85.7)	1 (14.3)	2.65	3 (42.9)	4 (57.1)	3.75*
V-shape palatal vault	5 (7.7)	5 (100.0)	0 (0.0)	4.10*	2 (40.0)	3 (60.0)	2.05
Tori	42 (64.6)	21 (50.0)	21 (50.0)	2.32	6 (14.3)	36 (85.7)	0.59
Larger palatal and adenoid tonsils	5 (7.7)	4 (80.0)	1 (20.0)	1.18	2 (40.0)	3 (60.0)	2.05
SpO ₂ increased by 1.5%	65 (100.0)	37 (56.9)	28 (43.1)	–	11 (16.9)	54 (83.1)	–
Responded to O ₂ therapy	64 (98.5)	37 (57.8)	27 (42.2)	1.34	10 (15.60)	54 (84.4)	4.99*

* P value < 0.05

Table 3 Gender versus VAS

VAS	n	Female n (%)	Male n (%)	Gender χ^2	Young n (%)	Old n (%)	Age χ^2
0	47	26 (55.3)	21 (44.7)	5.51	8 (17.0)	39 (83.0)	6.14
1	6	2 (33.3)	4 (66.7)		0 (0.0)	6 (100.0)	
2	11	9 (81.8)	2 (18.2)		2 (18.2)	9 (81.8)	
3	1	0 (0.0)	1 (100.0)		1 (100.)	0 (0.0)	

* *P* value < 0.05

The results show that, on average, patients will have a 1.5% increase in SpO₂ after administration of oxygen. Due to afferent and taste fibers of the nerves in the throat, oxygen can have an effect on gagging by desensitizing these nerves in a similar manner to that of salt as demonstrated by Chidiac and Chamseddine [10]. Ashida and Koga [12] had conducted their experiment for three minutes; however, in this study, there was longer oxygen therapy time, meaning the effect on gagging was more profound.

When there is a sufficient level of oxygen, there is a decrease in heart rate and blood pressure, which is to be expected. Our capnograph demonstrates lower carbon dioxide exhalation levels for those with less oxygen saturation levels. Higher than normal BMI (>25) patients have increased likelihood of greater than average neck circumference and are anticipated to have severe SDB, which is subsequently more advantageous for oxygen therapy. Due to our small sample size and unequal age distribution, these trends were not validated and statistically significant. Of all the analyzed variables, age appears to be the most significant demographic variable that has statistical significance. With increasing age, the optimal physiology is compromised, our results indicated older SDB patients forward head posture, lip incompetence respond well to oxygen therapy. Despite age being statistically associated with psychological issues, there is only one patient in the whole sample thus it is difficult to draw any conclusions from this.

Gagging is associated with any procedure that is more likely to touch the posterior oral tissue and pharyngeal sphincter, which contains the afferent fibers to the three cranial nerves: glossopharyngeal (IX), vagus (X) and hypoglossal (XII) [14]. It is a reflex that is initiated by sensitization of the three cranial nerves that supply the upper airway (CN IX, X, XI). The biological plausibility of oxygen therapy is yet to be explained. However, from similar experiments conducted in dogs, it is suggested that change in saturation of arterial oxygen can affect the stimulation of the sinus nerve composed of afferent fibers of chemoreceptors integrated in the medulla oblongata [12]. From this study, the SpO₂ levels increase with the application of oxygen. This in turn desensitizes the afferent nerve fibers from aortic

baroreceptors. These fibers pass centrally via CN IX and CN X in the nucleus of the tractus solitarius (NTS) in the medulla of the brain [15]. This suggested that when there are higher SpO₂ levels, baroreceptors in the aorta will not send signals to the brain to induce gagging.

People with severe signs of SDB will benefit more than those with less severe SDB. The oxygen flow to the nasal cannula did exert some pressure on the nose, analogous to the principals used in CPAP. Subsequently, more and more oxygen is capable of reaching the lungs and bloodstream. Furthermore, extra oxygen will help to eliminate residual CO₂. In summary, the use of oxygen raises the SpO₂ levels and desensitizes these afferent fibers, thereby reducing the incidence of gag reflex. However, we do not have enough data to substantiate this. Further studies are warranted to accurately measure the pressure of oxygen flow through the nasal cavity.

5 Conclusion

The use of oxygen therapy on SDB patients in this study demonstrated increased levels of oxygen in the blood and a decrease in the gag reflex. Hence, oxygen is an affordable and easy method to overcome gagging problems in dental patients with history of SDB.

Conflict of Interest The authors declare that they have no conflict of interest.

References

1. Yoshida, H., et al.: Management of Exaggerated Gag Reflex Using Intravenous Sedation in Prosthodontic Treatment. *Tohoku J. Exp. Med.* **212**(4), 373–378 (2007)
2. Kaufman, E., et al.: An experimental study of the control of the gag reflex with nitrous oxide. *Anesth. Prog.* **35**(4), 155–157 (1988)
3. De Veaux, C., et al.: The effect of various concentrations of nitrous oxide and oxygen on the hypersensitive gag reflex. *Anesth. Prog.* **63**(4), 181–184 (2016)
4. Alsufyani, N.A., Al-Saleh, M.A.Q., Major, P.W.: CBCT assessment of upper airway changes and treatment outcomes of

- obstructive sleep apnoea: a systematic review. *Sleep & Breathing* **17**(3), 911–923 (2013)
5. Valbuza, J.S., et al.: Oropharyngeal examination as a predictor of obstructive sleep apnea: pilot study of gag reflex and palatal reflex. *Arq. Neuropsiquiatr.* **69**(5), 805–808 (2011)
 6. Hatcher, D.C.: Cone beam computed tomography: craniofacial and airway analysis. *Dent. Clin. North Am.* **56**(2), 343–357 (2012)
 7. Saboisky, J.P., et al.: Neurogenic Changes in the Upper Airway of Patients with Obstructive Sleep Apnea. *Am. J. Respir. Crit. Care Med.* **185**(3), 322–329 (2012)
 8. dos Reis Zinsly, S., et al.: Assessment of pharyngeal airway space using Cone-Beam Computed Tomography. *Dent. Press. J. Orthod.* **15**(5), 150–158 (2010)
 9. Bashaboyina, A.: Investigation of end-tidal carbon dioxide (ETCO₂) and heart rate variations during sleep apnea (2010)
 10. Chidiac, J.J., Chamseddine, L., Bellos, G.: Gagging prevention using nitrous oxide or table salt: a comparative pilot study. *Int. J. Prosthodont* **14**(4), 364–366 (2001)
 11. American Dental Association, Guidelines for use of sedation and anesthesia by dentists (2016)
 12. Ashida, C., Koga, T.: Effects of arterial oxygen saturation on gag reflex in humans. *2, 2005.* **11**, 63–68 (2006)
 13. Heinrich, R.: Sleep apnea for dentists: an overview of signs, symptoms, consequences, and treatment. *Www.needce.com* (Accessed June 2017) (2013)
 14. Monkhouse, S.: *Cranial Nerves: Functional Anatomy.* 2005. Cambridge University Press, Cambridge, United Kingdom
 15. Chappleau, M.W.: Baroreceptor reflexes. In: *Primer on the Autonomic Nervous System*, 3rd edn, pp. 161–165. Elsevier (2012)

Sleep Onset Detection using the Low-Cost Emotiv EPOC Neuroheadset

Le Quoc Khai, Le Nu Ngoc Thuy, Tran Kien, Pham Thi Tram Anh, Nguyen Thi Diem Hang, and Huynh Quang Linh

Abstract

Classification of sleep stages is an important criterion for all sleep studies. Determining the time of transition between stages allows for accurate assessment of sleep quality and development of early alert applications. The major of this study is focused on using the portable electroencephalography (EEG) device for sleep staging. The study used two devices Nicolet One V32 and Emotiv EPOC to analyze the different characteristics of the brain signal in Sleep onset. Analysis results show that the similarity of the two devices reached over 80%, indicating the possibility of using the low-cost device Emotiv EPOC neuroheadset replacing clinical EEG system in sleep studies.

Keywords

Sleep onset • Staging • Portable EEG • Emotiv EPOC

1 Introduction

Electroencephalography (EEG) is a method of recording the biological signals of the brain by electrodes placed on the surface of the scalp. These electrodes are connected together by monopole or bipolar direction. Hans Berger measured EEG activity on humans and laid the foundations for many of current EEG applications. Brain activity is always changing, and it is easy to detect the characteristics of the signal when the state of the subject changes [1]. Although the EEG is designed to measure only the signals obtained from brain activity, EEG also detects signals from other

electrical sources. These signals are generally referred to noise. Noise is divided into physical noise and physiological noise [2]. In the processing EEG signals to detect the features, the important requirement is to eliminate the considerable noise that affects the results.

EEG recording shows the difference in brain waves between wakefulness and sleep. Loomis et al. [3] shows the fragmentation of the alpha wave when sleep onset (SO), followed by the presence of K-complexes, sleep spindles and slow waves. Rechtschaffen and Kales [4] have detected rapid eye movement (REM), which is a separate sleep stage called sleep with rapid eye movement or dreaming state. In 2004, the American Academy of Sleep Medicine (AASM) developed a detailed guideline for sleep assessments, allowing for detecting and monitoring a number of new features such as arousal, respiratory, cardiovascular, and event-related events etc., also known as AASM 2007 [5]. There are three updates in 2012, 2014 and 2017 to amend and supplement sleep assessment standards for infants and children, respiratory, cardiovascular, and use medicine to treat some sleep disorders [6, 7].

In the sleep assessment criteria mentioned above, the transition from waking state to the first state of sleep NREM (Sleep Onset) is very important. Gennaro et al. examined the changes in energy of the EEG signal during sleep and sleep transition by analyzing changes in frequency as well as waves in the EEG [8]. The precise definition of SO is an actual topic of many discussions, because it is difficult to accurately determine the exact time of SO and appropriate methods to determine. The SO determination in this study is based on the analysis of the EEG energy spectrum represented by the energy change of the Alpha and Theta waves. The major device used in the study was the portable EEG device Emotiv EPOC. The clinical EEG device Nicolet One V.32 with 32 channels is used as a reference device to evaluate the reliability of the portable EEG device.

Emotiv EPOC is a multi-channel, wireless device with Bluetooth interface, uses rechargeable battery for continuous use up to 12 h. EPOC uses a set of 14 sensors and 2

L. Q. Khai (✉) · L. N. N. Thuy · T. Kien · P. T. T. Anh · N. T. D. Hang · H. Q. Linh
Biomedical Engineering Department, Faculty of Applied Science,
Ho Chi Minh City University of Technology, Vietnam National
University, Ho Chi Minh City, Vietnam
e-mail: quockhai@hcmut.edu.vn

reference electrodes to record electrical signals from the human brain including thoughts, emotions, and facial expressions in real time [9]. The main advantages of Emotiv EPOC are the low cost, compact, convenient and suitable for studies that do not require high sampling frequency. However, EPOC also has limitations such as the sensors need to be wet with saline solution, the structure of the instrument is not highly customizable so it will not be compatible with different users. However, in general, the Emotiv EPOC device is still a preferred choice for applied research, particularly in the field of EEG monitoring and evaluation of quality of health: ERP, P300 measurements [10, 11], detecting emotion [12].

The main objective of this study was to compare Emotiv EPOC signals and Nicolet One V32 for determining the time of sleep onset. Positive results can ensure Emotiv's reliability in sleep studies, especially for measuring neurological activities related to sleep states in flexible conditions (sleepiness of the driver, sleepwalking etc.)

2 Materials and Methods

As mentioned, the EEG recording samples used for the analysis were obtained from two devices: 06 samples from clinical EEG device Nicolet One V32 (Natus—Care Fussion—USA) and 06 samples from portable EEG device Emotiv EPOC (Emotiv—USA).

As the study focused on determining the timing of transition from waking to the first stage of sleep NREM N1, each measurement was conducted in 80 min. Analytical algorithms include the following steps:

- Preprocessing: Raw data of EEG signals were obtained from O2-A1 channel. The signal quality was checked before transferring to the processing unit. The signal preprocessing included removing noise and correcting baseline drift by Wavelet analysis [13], even removing the noise with 50 Hz of power source.

- Signal analysis: filtered signal was converted from time domain to frequency domain by Fourier transform [14], then was analyzed via the power spectrum of each 10-s epoch. By the average power spectrum analysis of the Theta and Alpha waves for whole domain, the moment of transfer between two waves can be determined as well.

Energy Spectral Density (ESD) or Power Spectral Density (PSD) is a characteristic quantity for evaluating signal quality and filtering noise. The first step in the process is dividing the data into windows with 10-s epoch. Each sample contains nearly 450 epochs. The next step is applying the Fast Fourier Transform for each epoch to determine the features of the EEG signal in the frequency domain and proceed the construction of the transition state recognition algorithm.

By setting the frequency thresholds of the Theta wave (4–7 Hz) and the Alpha wave (8–13 Hz) for the output signal, the energy spectrum of the two waves can be obtained. The power factors for mentioned waveforms were calculated using following formulas:

$$R_Alpha = \frac{P_\alpha}{P_i(i = 0.5 : 30 \text{ Hz})} \quad (1)$$

$$R_Theta = \frac{P_\theta}{P_i(i = 0.5 : 30 \text{ Hz})} \quad (2)$$

Whereas $P_i(i = 0.5 : 30 \text{ Hz})$ is a ratio of energy of each brain waves δ , θ , α , β .

3 Results and Discussions

The signals were filtered in the range from 0.5 to 30 Hz and reduced of the 50 Hz power source noise using Wavelet analysis (Fig. 1).

Analytical data were collected from F3, F4, O1, O2 electrodes to detect the appearance of Alpha and Theta waves in the brain and calculated average power of each

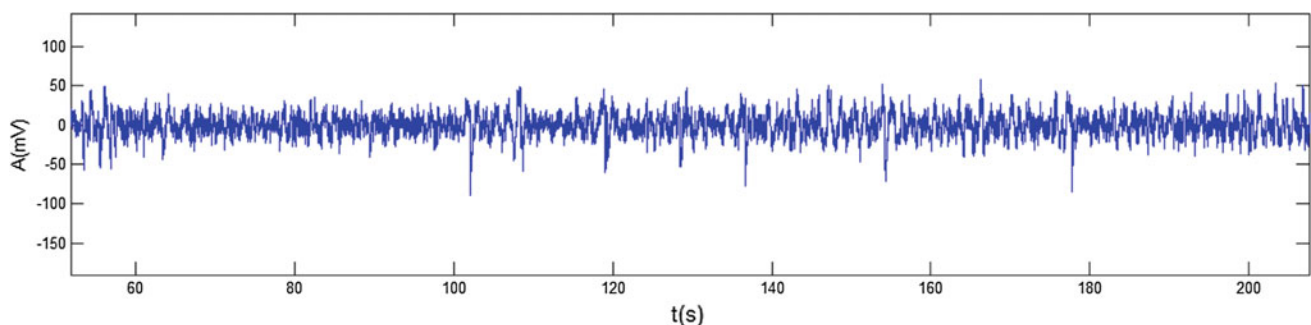


Fig. 1 The filtered EEG signal using wavelet analysis

type of wave. Illustrated values for an epoch are listed in Table 1. Applying formulas (1) and (2) to determine the ratio of energy of each brain waves δ , θ , α , β . The average power factor values R_Alpha and R_Theta were calculated for all epochs of all samples. Using polynomial approximation, the blue and red polynomial curves of all samples measured by Nicolet One V32 and Epoch Emotiv could be obtained as shown in Fig. 2. There exists a phase shift between the power spectrum of Alpha and Theta waves.

The moment of sleep onset could be determine according to following procedure, e.g. in Fig. 2, the Alpha and Theta curves change with moderate fluctuation until to epoch 270, where there is a sudden reduction in the energy spectrum of Alpha wave, meanwhile the energy spectrum of Theta wave increases. These Alpha and Theta curves almost intersect each other at about epoch 290. This time can be considered as the moment of sleep onset (SO). The appropriate time to alarm sleepiness is when the change in wave energy begins, i.e. the location at the epoch 270.

The results determining the time of SO using two different devices are listed in Table 2.

Applying the statistical evaluation to compare the results of two machines, the result could be obtained in Table 3.

The average Emotiv EPOC value differs from the Nicolet One V32 device by less than 20%, i.e. the similarity of Emotiv EPOC and Nicolet One V32 values is greater than 80%.

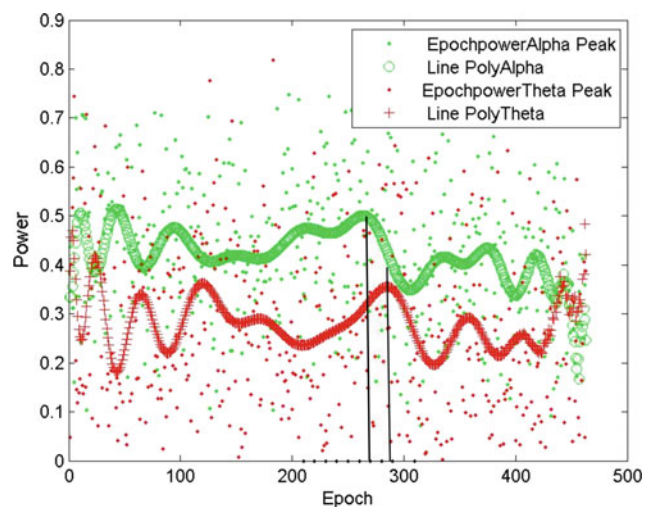


Fig. 2 Characteristics of Alpha and Theta wave energy spectrum

Table 1 The average power of Alpha and Theta of these electrodes F3, F4, O1, O2

	F3	F4	O1	O2
P_Alpha	4,9626	9,5141	10,5581	13,1959
P_Theta	4,0495	3,4841	6,5879	5,7418

Table 2 The comparison of SO timing in Emotiv EPOC and Nicolet One V32

# Sample	Nicolet One V32	Emotiv EPOC
1	265	271
2	262	263
3	255	260
4	239	245
5	260	284
6	275	291

Table 3 The comparison Emotiv EPOC and Nicolet One V32

	Nicolet One V32	Emotiv EPOC
Mean value	259.33	269.33
Standard deviation	11.98	17.77
95% confidence interval (epoch)	259.33 ± 12,57 (epoch)	269.33 ± 13,66 (epoch)
95% confidence interval (min)	43.22 ± 2.1 (min)	44.88 ± 2.28 (min)

4 Conclusion

Analysis results show that the similarity of the two devices reached over 80%, indicating the possibility of using the low-cost device Emotiv EPOC neuroheadset replacing clinical EEG system in sleep studies. Determining the time of SO is a basic factor for assessing sleep quality and a very important parameter for early warning of drowsiness. However, early warning needs to be generally evaluated on larger samples of polysomnography with appropriate additional learning machine algorithms. The results of the analysis show that the present study opens the possibility of using portable EEG devices in sleep studies, especially for measuring polysomnography of flexible conditions related to sleep. Besides, mentioned developed method combined with improved external electrodes could be used for Holter EEG at home, enables remote monitoring for telehomecare services.

Acknowledgements This research is funded by Vietnam National University Ho Chi Minh City (VNU-HCM) under grant number B2016-20-01.

Conflict of interest The authors declare that they have no conflict of interest.

References

1. Dement, W., Kleitman, N.: Cyclic variations in EEG during sleep and their relation to eye movements, body motility, and dreaming. *Electroencephalogr. Clin. Neurophysiol.* **9**(4), 673–690 (1957)

2. Ghandeharion, H., Erfanian, A.: A fully automatic ocular artifact suppression from EEG data using higher order statistics: Improved performance by wavelet analysis. *Med. Eng. Phys.* **32**(7), 720–729 (2010)
3. Loomis, A.L., et al.: Cerebral states during sleep, as studied by human brain potentials. *J. Exp. Psychol.* **21**, 127–144 (1937)
4. Hobson, J.A.: A manual of standardized terminology, techniques and scoring system for sleep stages of human subjects. In: Rechtschaffen, A., Kales A. (eds.) *Electroencephalography and clinical neurophysiology*, **26**(6), 644. (1969)
5. Iber, C., Ancoli-Israel, S., Chesson, A., Quan, S.: *The AASM manual for the scoring of sleep and associated events: rules. Terminology and Technical Specifications*. American Academy of Sleep Medicine, Westchester, IL, USA (2007)
6. Berry, R.B., Brooks, R., Gamaldo, C.E., Harding, S.M., Marcus, C.L., Vaughn, B.V.: *The AASM manual for the scoring of sleep and associated events: rules. Terminology and technical specifications*. American Academy of Sleep Medicine, Darien, Illinois (2012)
7. Berry, R.B., Brooks, R., Gamaldo, C., Harding, S.M., Lloyd, R. M., Quan, S.F., Vaughn, B.V.: *AASM scoring manual updates for 2017 (version 2.4)*. *Journal of clinical sleep medicine*. Official publication of the American Academy of Sleep Medicine, **13**(5), 665 (2017)
8. De Gennaro, L., Ferrara, M., Bertini, M.: The boundary between wakefulness and sleep: quantitative electroencephalographic changes during the sleep onset period. *Neuroscience*, **107**(1), 1–11 (2001)
9. Limited, E.C.: *User Manual Emotiv Software Development Kit* (2012)
10. Badcock, N.A., Mousikou, P., Mahajan, Y., De Lissa, P., Thie, J., McArthur, G.: Validation of the Emotiv EPOC® EEG gaming system for measuring research quality auditory ERPs. **1**, 38 (2013)
11. Duvinage, M., Castermans, T., Petieau, M., Hoellinger, T., Cheron, G., Dutoit, T.: Performance of the Emotiv Epoc headset for P300-based applications. *Biomed. Eng. Online* **12**(1), 56 (2013)
12. Ramirez, R., Vamvakousis, Z.: Detecting emotion from EEG signals using the emotive Epoc device. In: *International Conference on Brain Informatics*, pp. 175–184. Springer, Berlin, Heidelberg (2012)
13. Tumari, S.M., Sudirman, R., Ahmad, A.H.: Selection of a suitable wavelet for cognitive memory using electroencephalograph signal. *Engineering* **5**(05), 15 (2013)
14. Motamedi-Fakhr, S., Moshrefi-Torbati, M., Hill, M., Hill, C.M., White, P.R.: Signal processing techniques applied to human sleep EEG signals—a review. *Biomed. Signal Process. Control.* **10**, 21–33 (2014)

Part XVI
Biotechnology

Interaction Between Fluoro Emulsion and Silane Quaternary Ammonium Salt on Dual Antibacterial and Hydrophobic Fabric of Surgical Gown

Tuan-Anh Nguyen and Vu Thuc Oanh Ta

Abstract

Humans need more protection since environmental pollution becomes more serious problem. In many recent years, the appearance of many infectious diseases has generated the life-threatening and the tremendous challenges have given for medical scientists in diagnosis and treatment methods. Multifunctional protective costumes may be a good solution to protect efficiently human body from such risks. Among initiatives, dual antibacterial and water repellent fabric was able to be a great choice in designing the surgical gown in order to efficiently protect. This work provides usefully interesting information about the synergies among finishing agents on cotton fabric. Accordingly, the experimental results clarified the biocidal and hydrophobic mechanism at the same time under various conditions. In addition, the wearing comforts associated with heat transfer and air exchange between body skin and fabric layers were concerned to increase the product performances.

Keywords

Antimicrobial • Water repellence • Fluoro emulsion • Quaternary ammonium • Comfort

1 Introduction

Multifunctional textiles have been widely developed during recent decades owing to innovative techniques such as nano-technology or plasma technology [1]. These studies not only diversify clothing products more but also please

wearers or consumers. People are living in a bacterial world, in which these tiny creatures are sometime useful and sometime harmful as well [2, 3]. Several reports were clarified that the growth of bioterrorism in a human structure might be successfully controlled through two methods: inhibition (barrier) and extermination (killer). In fact, there were a lot of natural as well as man-made compounds like triclosan, metallic salts, so on, which can apply to commercially produce antibacterial agents for many years. In recent, Messaoud et al., has showed that the antibacterial finishing of cotton-based fabrics might be achieved from quaternary ammonium-based composite particles [4].

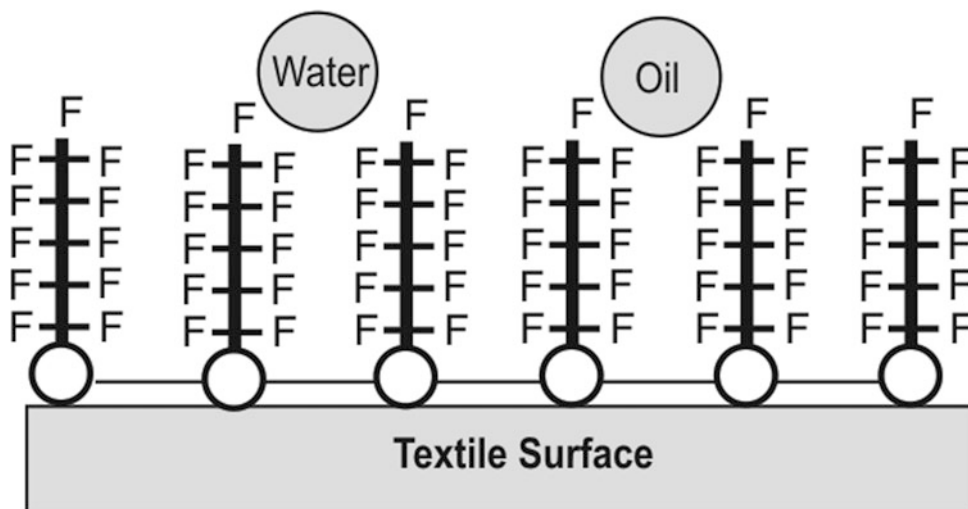
In general, clothing products should have ability of the biocides the dangerous viruses to eliminate the risks of health, especially illness, but they also maintain the convenience for wearers during their daily operations. For instance, a surgeon in hospital is frequently affected by patient's blood and fluid that he must deal with high infection rate, therefore, his gown in operating room needs to not only prevent blood fluid to permeate through cloth layers but also create the most comfort to him [5].

An attaching mechanism of the fluorocarbon agents onto textile surface is illustrated in Fig. 1. Especially, fluorocarbon compound is well known as the best repellent agent, meaning that both water and oil drops are efficiently easy to remove from fabric face (silicone agents or waxes only repel water, not oil) [6–8].

Textile comfort is both physiological and psychological as a human feeling. In this study, the evaluation of thermal comfort was conducted through vapor permeability. Other points such as heat balance, heat loss will be discussed in next investigations.

T.-A. Nguyen (✉) · V. T. O. Ta
Faculty of Garment Technology and Fashion Design,
Ho Chi Minh City University of Technology and Education,
01, Vo van Ngan St, Thu Duc Dist, Ho Chi Minh City, Vietnam
e-mail: nta@hcmute.edu.vn

Fig. 1 The bonding mechanism of fluorocarbon agent with textile fabrics explained to repel both water and oil drops from the textile surface



2 Experiments

The antimicrobial emulsion (AEM-5772/5: 3-trimethylsilylpropyldimethyloctadecyl ammonium chloride) and the water repellent agent (Nuva HPU: fluoro emulsion) on cotton fabric were purchased from Aegis and Clariant, respectively. Because of prevention of dilute solution into water repellent fabric, the antibacterial treatment process should be conducted first. The padding techniques with a stenter were applied for both antibacterial and water repellent processes under some various conditions. Pure cotton fabric were used for all tests due to its wide applications for human health protection. These samples were relaxed in room condition in order to ensure the uniformity of experimental measurements. The experimental results of microbiology, water absorbance, mechanics, comfort and drape were reported according to given standards. The durability of these treatments was determined via the washing cycles and the measurements and results were shown in term of diagram, such as the curve of washing times against agent residue, water resistance, air exchanging ability, so on. The photos were taken to reveal the fabric surface before and after treatments as well. Untreated, antibacterial, water repellent

and dual antibacterial—water repellent cotton fabrics in the experiment named as SO, SA, SW and SAW, respectively.

Chemicals and microorganisms used for this experiments include bromophenol blue (BPB), *Escherichia coli* (*E. Coli*).

3 Results and Discussions

3.1 Biocidal Ability of Silane Quaternary Ammonium Salt on Cotton Fabric Based on Quantitative Decline of Microbes

Antimicrobial activity of treated samples was quantified by counting the growth and reduction of microorganism (*E. coli*) in culture with microbiological measurements. All investigations reported that the amount of microbes on antimicrobial specimens slightly decreased with washing times in an hour of exposure or contact. It is known that the molecular bonds (i.e., the fastness of antimicrobial finish) of substrate (cotton fabric) and antimicrobial agent (ammonium salt) could be seriously affected under washing conditions. In particular, as shown in Table 1, most bacteria were eliminated after 24 contacting hours, meaning that the longer bacteria contacted antimicrobial fabric, the more finished

Table 1 Antibacterial ability of treated samples after 1 and 24 h of contacting with bacteria by microbiological testing method

Sample	Percentage of decreased bacteria	
	After 1 h	After 24 h
S _O	–	–
S _{A0}	55.47	97.91
S _{A5}	62.40	98.73
S _{A10}	74.13	99.17

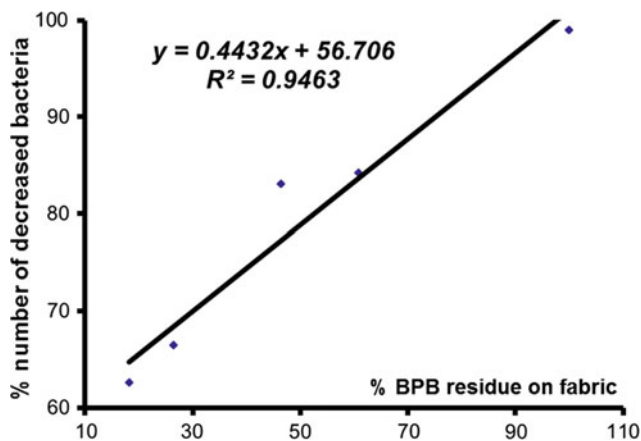


Fig. 2 Linear graph of BPB content against amount of decreased microorganisms on fabric

textile fabric killed bacteria, even lower lost biocidal residue after more washing cycles.

3.2 Determining Antimicrobial Activities by Bromophenol Blue (BPB)

Figure 2 provides an evidence to explain why the content of bromophenol blue (BPB) is linearly proportional to the number of killed bacteria on fabric, corresponding to the residue of silane quaternary ammonium salt. The BPB measurements were quite quick, exact and totally consistent with the microbiological tests. However, such results determined only the content of antimicrobial agent but not biocidal ability of treated fabric because of dependence on contacting time, family of microbes and other additives.

3.3 Investigation of Biocidal Ability on Dual Antimicrobial and Water Repellent Treated Cotton Fabric

The main purpose of this work is to clarify the synergistic interaction among active substances of functional finishes on textile fabric through the efficiency of these treatments. Combining antimicrobial treatment with water repellent treatment is very necessary for some textile products like surgical gown. Due to hydrophobicity of fluorocarbon compound on fabric, the antibacterial treatment should be treated before.

The results of biocidal measurement were indicated in Fig. 3. Interestingly, biocidal ability of dual antimicrobial and hydrophobic material reached the highest value at 10 of washing cycles and decreased rapidly later. In fact, such phenomenon revealed that the productivity of water repellent

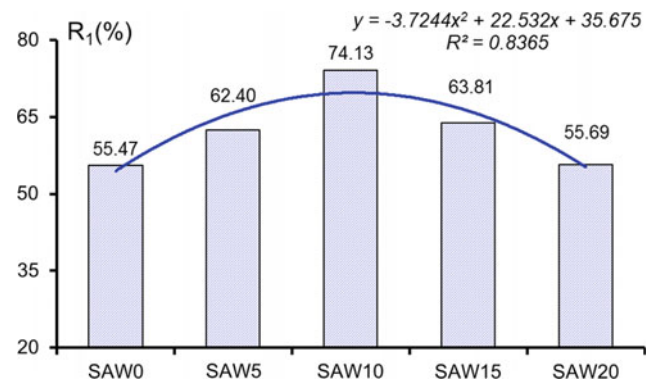


Fig. 3 Biocidal ability of dual antimicrobial and hydrophobic treated fabric for 0, 5, 10, 15 and 20 of washing cycles

finish reduced with washing times but that of antimicrobial finish raised since former one were covered earlier one. When the hydrophobic composition released from material surface, the microbes should be contacted with biocidal substance more, at which the washing cycle was up to 10. On the other hand, the number of microorganisms were killed the most as soon as they were adjacent to antibacterial agent. Nevertheless, at more than 10 times, the efficiency of both treatments declined rapidly because biocides and hydrophobicity were not able to retain enough to either attack or prevent microorganisms.

3.4 Water Repellence of Dual Antimicrobial and Water Repellent Treated Fabric

In case of waterproof finish, water might easily push out of fabric surface, however, the moisture vapor could not transmit through the material. Obviously, the water repellent treatment with fluorocarbon still ensures the ventilation for fabric in which only water in drop form (Fig. 4).

3.5 Drape of Antibacterial and Water Repellent Treated and Untreated Fabrics

The treated agents into fiber structure may basically reduce softness of fabric. Interestingly, the drape of dual functional material is quite higher than untreated or mono-functional samples as shown in Fig. 5. Particularly, the drape of untreated sample was 52.206% while that of antibacterial finish was even 48.485% but that of dual finish was higher previous ones (i.e., 53.630%). It might explain that, after bonding to fabric, these chemicals, thus, might cause the loose yarn system due to the decrease in the coefficient of friction.

Fig. 4 Digital photos of water spraying tests for various types of fabric

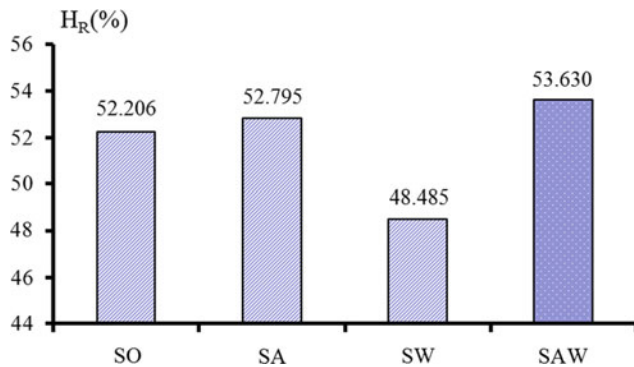
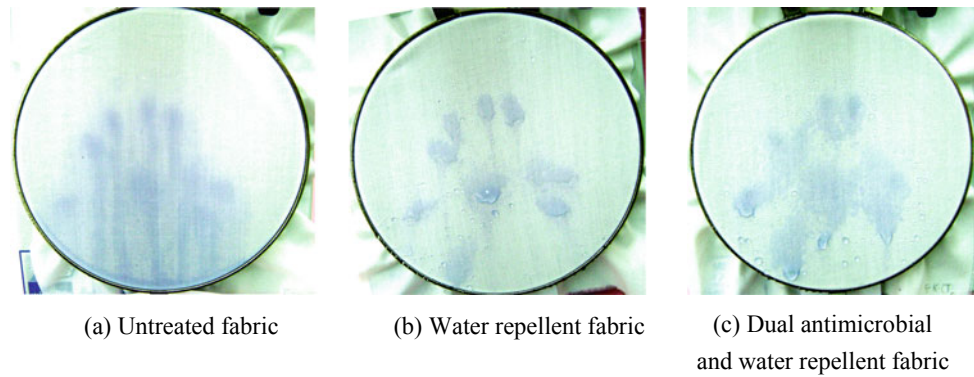


Fig. 5 Drapes of untreated (SO), antimicrobial (SA), water repellent (SW) and dual antimicrobial—water repellent fabric (SAW)

3.6 Change in Air Permeability as Treating Fabric by Antimicrobial and Water Repellent Agents

The obtained results in Table 2 show that vapor exchange of sample S_{AW} after 24 exposure hours occurs more than those

of sample S_A and sample S_W . It can be explained in terms of the agent residue and fastness on treated fabrics.

However, the decrease of vapor permeability on dual functional treated fabric is very little as compared to untreated or mono-functional treated fabrics. On the other hand, this fabric allows air or vapor through its structure close to the untreated material, therefore human body should feel quite comfortable.

4 Conclusions

In this work, an interactive mechanism between antimicrobial and water repellent finishes was investigated through experimental results of microbiological, water absorbent and mechanical tests. Most significantly, synergistic interaction among two various added agents were found that the water repellency might slightly prevent the antimicrobial activity but it still ensured both requirements of finished fabric in hospital gowns. More detailed analysis of studying results will be published in the future work after implementing more investigations.

Table 2 Results of antimicrobial and water repellent treatments based on change in weight after 24 testing hours

Sample	Repeat	W_0 (g)	W_{24} (g)	V_{th}
				(g/dm^2 24 h)
S_O	1	167.27	166.24	1.03
	2	165.57	164.55	1.01
	3	161.64	160.62	1.02
S_A	1	171.42	170.5	0.92
	2	161.2	160.26	0.94
	3	164.23	163.31	0.92
S_W	1	155.53	154.56	0.97
	2	141.59	140.63	0.96
	3	159.87	158.91	0.97
S_{AW}	1	161.57	160.59	0.98
	2	154.73	153.75	0.98
	3	163.97	162.99	0.98

Acknowledgements Authors would like to thank for supporting from Ho Chi Minh City University of Technology and Education. He also thanks to Professor Khanh V. T. H. and his coworkers for their assistance. **Conflict of Interest** The authors declare that they have no conflict of interest.

References

1. AlessioVaresano, et al.: Multifunctional cotton fabrics. *Synth. Met.* **159**(11), 1082–1089 (2009)
2. El-tahlawy, Khaled, F., et al.: The antimicrobial activity of cotton fabrics treated with different crosslinking agents and chitosan. *Carbohydr. Polym.* **60**(4), 421–430 (2005)
3. Windler, L., Height, M., Nowack, B.: Comparative evaluation of antimicrobials for textile applications. *Environ. Int.* **53**:62–73 (2013)
4. Messaoud, M., et al.: Quaternary ammonium-based composite particles for antibacterial finishing of cotton-based textiles. *J. Mater. Sci. Technol.* **30**(1), 19–29 (2014)
5. Thilagavathi, G.: Dual antimicrobial and blood repellent finishes for cotton hospital fabrics. *Indian J. Fiber Text. Res.* **33**:23–29 (2008)
6. Anand, S.C., Kennedy, J.F., Miraftab, M., Rajendran, S. (2010) *Medical and healthcare textiles*, Woodhead Publishing Series in Textiles, ISBN: 978–1-84569-224-7
7. Sayed, U., Dabhi, P.: Waterproof and water repellent textiles and clothing—6: finishing of textiles with fluorocarbons. *The Textile Institute*, pp. 139–252 (2014)
8. Pavlidou, S., Paul, R.: Waterproof and water repellent textiles and clothing—3: soil repellency and stain resistance through hydrophobic and oleophobic treatments. *The Textile Institute*, pp. 73–88 (2018)

Combination of sST2 and BNP in Predicting the Mortality of ST-Elevation Myocardial Infarction

Hoang Anh Tien, Tran Thi Thanh Truc, and Vo Thanh Nhan

Abstract

Serum levels of ST2 are associated with prognosis in non-ischemic heart failure, but the predictive value of ST2 in patients with ST elevation myocardial infarction is unknown. *Methods* The study included 38 STEMI patients at Interventional Cardiology department of Cho Ray hospital. Correlation analysis was used to identify the relationship between the cardiac outcomes within 30 days from the onset of chest pain and sST2 value. *Results* ST2 levels were measured in serum from 38 patients with STEMI. Baseline levels of ST2 were significantly higher in those patients who died (<35 ng/mL vs. >35 ng/mL, $P = 0.01$) or developed new congestive heart failure (<35 ng/mL vs. >35 ng/mL, $P = 0.002$) by 30 days. In an analysis of outcomes at 30 days by ST2 quartiles, both death ($P = 0.01$) and the combined death/heart failure end point ($p = 0.001$) showed a significant graded association with levels of ST2. Furthermore, when sST2 > 35 ng/mL and BNP > 500 pg/mL showed a tightly relationship with cardiac outcomes within 30 days ($P < 0.0001$). *Conclusions* Serum levels of the interleukin-1 receptor family member ST2 predict mortality and heart failure in patients with STEMI. These data suggest that ST2 and BNP are the useful biomarker in short-term prognosis of cardiac events in STEMI.

Keywords

sST2 • BNP • STEMI • Cardiac outcomes

1 Background

B-type natriuretic peptide (BNP) is released from cardiac tissue in response to stress to increase, and measuring its level has recently been shown to assist in diagnosing congestive heart failure (CHF). Therefore, BNP has been proposed as an additional marker for heart damage in the setting of acute coronary syndromes. However, the predictive value of this biomarker in this setting, and especially in the patient with ST-segment elevation myocardial infarction (STEMI) is still unclear.

ST2 is a member of the interleukin-1 receptor family with a soluble form that is markedly upregulated on application of biomechanical strain to cardiac myocytes. ST2 is a biomarker of mechanical stress, and rearrangement of ST2 signals leads to myocardial remodeling. While acute myocardial infarction, Serum levels of soluble ST2 (sST2) are associated is with an increased risk of death or heart failure. In addition, while acute myocardial infarction circulating ST2 levels are elevated in the setting of acute myocardial infarction, but the predictive value of ST2 independent of traditional clinical factors has not been established [4]. Beside, the combination of sST2 and BNP promise the significant predictive value.

2 Methods and Study Population

2.1 Study Population

All patients were diagnosed with acute ST elevation myocardial infarction (by the 3rd European Society of Cardiology (ESC) 2012 definition of myocardial infarction [1]) for the first

H. A. Tien (✉)
Hue University of Medicine and Pharmacy, Hue, Vietnam
e-mail: bsanhtien@gmail.com

T. T. T. Truc · V. T. Nhan
Cho Ray Hospital, Chi Minh City, Vietnam
e-mail: t3truc@gmail.com

time at the Department of Cardiology Intervention, Cho Ray Hospital from April 2015 to July 2015.

All patients with acute myocardial infarction were treated according to guidelines on the management of acute myocardial infarction in patients with ST-segment elevation of European Society of Cardiology (ESC) 2013 [2].

2.2 Methods

Descriptive cross-sectional study with 30-day follow-up.

2.3 Biochemical sST2

All patients were adequately baseline tested and serum levels of sST2 at the time of study. Patients after discharge will be followed-up 30 days for chest pain, heart failure symptoms and response to drug treatment or death in out-patient's clinic or direct telephone contact.

Blood samples are stored in vials containing EDTA (Ethylene Di-Amino-Tetra-Acetic Acid) or heparin, centrifuged for 10 min and plasma separated immediately upon receipt of blood samples. Plasma samples stored at -80°C (hold for 18 months) and wait until the full numbers of patients will be analyzed.

The analysis time is 4 h.

The benchmark was constructed with seven standard concentrations ranging from 3.1 to 200 ng/mL.

The detection limit for the test is 32 pg/mL.

The sST2 cut-off point of was 35 ng/mL according to the Framingham study, which was associated with mortality and progression of heart failure.

2.4 Statistical Analysis

The research data was processed using SPSS statistical software for Windows version 16.0.

Quantitative variables are normally distributed and presented in terms of $\pm\text{SD}$. Qualitative variables are presented as median, minimum, maximum. Qualitative variables are presented in percentage terms. The main statistical tests used are:

- Compare the difference between quantitative variables: If the variables are normalized, then use t-test and take into account differences in variance.
 - If the variables are non-standard, use the Mann-Whitney test or switch to standard distribution and use the t-test.
 - Compare the difference between qualitative variables: Chi square test (Fisher's exact test if needed) to test the difference between the two groups of qualitative variables.
- Relationship assessment with clinical outcome by Wilcoxon test.
- With a 95% confidence interval, the difference was statistically significant when $p < 0.05$.

3 Results

3.1 Characteristics of Research Subjects

There were statistically significant differences in Killip group I and group II ($p < 0.05$) (Tables 1 and 2).

Mean TIMI values increased with age ($p < 0.001$) (Table 3).

Table 1 Killip classification at admission

Killip classification at admission	60–69 year n = 13	70–79 year n = 13	80–89 year n = 12	P-Value
Killip = I	12 (92.3)	11 (84.6)	6 (50.0)	<0.05
Killip \geq II	1 (7.7)	2 (15.4)	6 (50.0)	

Table 2 TIMI risk score for acute myocardial infarction ST elevation

Age (year)	60–69	70–79	80–89	P-Value
n	13	13	12	
TIMI median	6.46 \pm 2.07	7.23 \pm 2.35	10.75 \pm 2.05	<0.001*
TIMI \geq 8 (n, %)	4 (30.8)	6 (46.2)	11 (91.7)	<0.01**

*ANOVA's exact test

**Chi square test

Table 3 Subject's characteristics

Value	60–69 year	70–79 year	80–89 year	<i>p</i>
Male sex, n (%)	11 (84.6)	10 (76.9)	8 (66.7)	0.57
Female sex, n (%)	2 (15.4)	3 (23.1)	4 (33.3)	
Average heart rate	75.23 ± 17.35	76.08 ± 14.04	80.0 ± 17.07	0.74
Systolic BP	131.54 ± 19.19	114.62 ± 19.41	110.83 ± 21.08	<0.05
Diastolic BP	78.46 ± 15.19	68.08 ± 9.03	68.33 ± 10.29	0.06
Mean BMI	22.53 ± 2.49	21.63 ± 2.55	20.15 ± 3.37	0.12
BNP (pg/ml)	109.5 (55.5–163.5)	493.3 (87.0–769.3)	533.0 (190.3–975.2)	<0.05
ECG Anterior MI, n (%)	5 (38.5)	5 (38.5)	7 (58.3)	0.52
ECG Posterior MI, n (%)	8 (61.5)	8 (61.5)	5 (41.7)	
EF > 40%, n (%)	12 (92.3)	11 (84.6)	5 (41.7)	<0.01
EF ≤ 40%, n (%)	1 (7.7)	2 (15.4)	7 (58.3)	

Table 4 Results of coronary angiography and percutaneous coronary intervention (PCI)

Characteristics	n (%)
Coronary Angiography	37 (97.37)
Culprit-Vessel PCI	36 (97.29)
Primary PCI	18 (48.6)
Selective PCI	19 (51.4)
2-vessel disease	23 (62.2)
LM disease	3 (8.1)

There is statistically significant difference ($p < 0.01$) in the EF group >40% versus the EF group ≤ 40% by age group (Table 4).

The rate of coronary angiography was 97.37%.

3.2 The sST2 Concentration in the Study and the Association of sST2 with Clinical and Subclinical Factors

The mean and standard deviation of ST2 were 47.75 ± 3.95 pg/mL (Tables 5 and 6).

There are differences in sST2 subtype ≤ 35 ng/ml and sST2 > 35 ng/ml in hypertension (<0.05) and Killip class II (Table 7).

There are differences in 2 sST2 groups follow age, systolic blood pressure, diastolic blood pressure ($p < 0.05$), TIMI ($p < 0.001$) (Table 8).

There are differences in 2 sST2 groups follow CKMB ($p < 0.05$), BNP ($p < 0.001$), Ejection Fraction—EF ($p < 0.01$) (Table 9).

The mortality after 30 days was 5.26%, the rate of heart failure after 30 days was 26.32% (Table 10).

There is statistically significant difference between Killip I and Killip II in the control group ($p < 0.001$), 1—vessel disease and ≥ 2—vessel disease ($p < 0.05$) (Table 11).

There are statistically significant differences in adverse outcomes for serum creatinine ($p < 0.01$), BNP ($p < 0.001$), EF ($p < 0.001$) (Table 12).

There is statistically significant difference in sST2 < 35 ng/ml and sST2 ≥ 35 ng/ml for mortality ($p < 0.01$), heart failure ($p < 0.001$), mortality or heart failure ($p < 0.001$) (Table 13).

There were statistically significant differences in 3 groups according to sST2 and BNP ($p < 0.001$).

4 Discussion

The mean age of the study participants is higher than studies of Shimpo (mean age 58 ± 1.1) [3] and Sabatine S. (mean age 58.8 ± 9.9) [4]. This difference due to our study only targets on older adults (≥ 60 years), so the average age is higher.

In our study, the proportion of male patients is 76.32% lower than that of the two authors. The proportion of male patients in the study of Shimpo M is 80.11% [3] and that of

Table 5 Statistical values of ST2 concentration in the study

Statistics values	Results (ng/mL)
Mean \pm SD	47.75 \pm 3.95
Interquartile range (IQR)	
25%	20.46
50%	36.05
75%	65.65
Minimum value	10.02
Maximum value	196.98

Table 6 Relationship between sST2 concentration with clinical factors

Characteristics of clinical factors	sST2 \leq 35 ng/ml n = 20	sST2 > 35 ng/ml n = 18	<i>p</i>
Female sex, n	3 (15.0)	6 (33.3)	0.26
Male sex, n	17 (85.0)	12 (66.7)	
Hypertension	12 (60.0)	16 (88.9)	<0.05
Smoking History	10 (50.0)	8 (44.4)	0.73
Hyperlipidemia	17 (85.0)	15 (83.3)	0.88
Diabetes mellitus	5 (25.0)	2 (11.1)	0.41
Obesity	1 (0.05)	4 (22.22)	0.17
Killip class \geq II	1 (0.05)	8 (44.44)	<0.05
Fisher's exact test			

Table 7 Relationship between sST2 concentration with clinical factors

Clinical factors	sST2 \leq 35 ng/mL n = 18	sST2 > 35 ng/mL n = 20	<i>p</i>
Age(year)	70.67 \pm 7.13	74.85 \pm 8.71	<0.05
BMI(kg/m ²)	21.23 \pm 3.54	21.74 \pm 3.39	0.59
Duration of MI (hour)	33.89 \pm 44.41	39.50 \pm 41.25	0.07
Heart rate (bpm)	74.94 \pm 15.75	78.90 \pm 16.20	0.45
Systolic BP (mmHg)	129.17 \pm 16.47	110.25 \pm 21.67	<0.05
Diastolic BP (mmHg)	78.06 \pm 12.26	68.5 \pm 10.89	<0.05
TIMI risk score	6.78 \pm 2.29	9.25 \pm 2.77	<0.001
T student's exact test			

Table 8 Relationship between sST2 concentration and subclinical values

Subclinical values	sST2 \leq 35 ng/mL n = 20	sST2 > 35 ng/mL n = 18	<i>p</i>
Glucose (mg/dL)	118.78 \pm 71.38	152.15 \pm 74.69	0.45
BUN (mg/dL)	13.21 (10.50–16.25)	20.51 (12.50–23.75)	0.07
Creatinin (mg/dL)	1.03 \pm 0.23	1.12 \pm 0.21	0.21
CKMB (U/L)	92.21 \pm 82.24	151.19 \pm 82.69	<0.05
Troponin I > 1 (ng/mL)	17 (94.44)	18 (90)	0.88
BNP (pg/mL)	101.72 (64.62–174.12)	527.95 (152.52–1021.92)	<0.001
Ejection Fraction—EF (%)	51.72 \pm 7.68	41.95 \pm 8.75	<0.01

Table 9 Mortality and heart failure after 30 days

Outcome after 30 days	n	%
Death	2	5.26
Heart failure	10	26.32

Table 10 Relationship between clinical outcomes and other factors

Other factors n (%)	Outcome (death or heart failure)		P-value
	Yes (n = 12)	No (n = 26)	
Male sex	8 (66.7)	21 (80.8)	0.42
Female sex	4 (33.3)	5 (19.2)	
Hypertension	10 (83.3)	18 (69.2)	0.45
Smoking history	4 (33.3)	14 (53.8)	0.30
Diabetes mellitus	9 (75.0)	23 (88.5)	0.35
Hyperlipidemia	1 (8.3)	4 (15.4)	0.55
Obesity	2 (16.7)	5 (19.2)	0.85
Killip class = I	5 (41.7)	25 (96.2)	<0.001
Killip class \geq II	7 (58.3)	1 (3.8)	
Anterior MI	8 (66.7)	9 (34.6)	0.08
Posterior MI	4 (33.3)	17 (65.4)	
1—vessel disease	10 (90.9)	13 (50.0)	<0.05
\geq 2—vessels disease	1 (9.1)	13 (50.0)	

Table 11 Relationship between clinical outcomes and continuous variables

Continuous variables mean \pm SD	Outcome (death or heart failure)		P-value
	Yes (n = 12)	No (n = 26)	
Age (year)	78.92 \pm 6.5	70.08 \pm 7.4	<0.001
Duration of MI (hour)	55.5 \pm 4.8	28.2 \pm 3.5	<0.05
TIMI risk score	9.7 \pm 2.22	6.8 \pm 2.25	<0.001
Heart rate (bpm)	80.92 \pm 15.9	75.23 \pm 15.8	0.31
Systolic BP (mmHg)	107.5 \pm 22.2	124.6 \pm 19.0	<0.02
Diastolic BP (mmHg)	64.17 \pm 9.0	75.19 \pm 12.5	<0.02
BMI (kg/m ²)	20.62 \pm 3.6	21.86 \pm 3.5	0.29
Glucose (mg/dL)	134.5 \pm 6.5	137.2 \pm 7.9	0.92
Creatinin (mg/dL)	1.22 \pm 0.19	1.01 \pm 0.20	<0.01
CKMB (U/L)	137.2 \pm 9.0	116.9 \pm 8.6	0.51
BNP (pg/ml)	898.91 \pm 174.4	160.61 \pm 136.2	<0.001
LV ejection fraction <40%	36.4 \pm 5.3	51.2 \pm 6.3	<0.001

Sabatine S is 79.28% [4]. Our study has higher rates of hypertension, dyslipidemia, diabetes than two studies of two foreign authors. Possible cause is our study participants are elderly patients (\geq 60 years of age) should have a higher rate of cardiovascular risk factors.

The mean sST2 concentration in our study is 47.75 \pm 3.95 ng/mL, with the minimum value being

10.02 ng/ml and the maximum being 196.98 ng/mL. The Framingham study was conducted in 2012 among men and women in the general population, of which 462 men had sST2 concentration limit 11–45 ng/mL, and 674 women had sST2 concentration limit 9–35 ng/mL. In the PRIDE study, the mean value of sST2 concentration in patients with acute decompensated heart failure was 42.7 ng/mL.

Table 12 Relationship between sST2 concentration and cardiovascular adverse events

Cardiovascular adverse events	sST2 < 35 ng/ml (n = 20)	sST2 ≥ 35 ng/ml (n = 18)	<i>p</i>
Death	0 (0)	2 (11.1)	<0.01
Heart failure	2 (10)	8 (44.4)	<0.001
Death or heart failure	2 (10)	10 (55.6)	<0.001

Table 13 Relationship between sST2 concentration and BNP with cardiovascular adverse events

Cardiovascular adverse events	sST2 ≤ 35 ng/ml and BNP < 500 pg/ml	sST2 > 35 ng/ml or BNP ≥ 500 pg/ml	sST2 > 35 ng/ml and BNP ≥ 500 pg/ml	<i>p</i>
No	17 (1)	8 (61.5)	1 (12.5)	<0.001
Yes	0 (0)	5 (38.5)	7 (87.5)	

Two studies of acute ST elevation myocardial infarction showed predictors of events within 30 days based on sST2 levels [5, 6]. Shimpo et al. measured sST2 levels in 810 patients with ST-elevation myocardial infarction, including 362 from TIMI-14 study and 448 from ENTIRE-TIMI 23 study, sST2 > 37 ng/mL predicted heart failure and mortality within 30 days of acute myocardial infarction [3]; Similar to our study, serum sST2 concentrations >35 ng/mL were predictive of mortality and progressive heart failure with $p < 0.001$. In addition, when combining sST2 levels >35 ng/mL with other factors such as hypertension, TIMI score, Killip classification, the prognostic value was higher in patients with ST elevation myocardial infarction.

Study by Bartunek J. et al. in 2008 was found that when combined with BNP or NT-proBNP and sST2 levels, the value of both concentrations increased above the mean increased risk of events (heart failure or death) by 10 times [7], similar to the study of Granger, Dhillon [8, 9]. In our study, 7 patients had serum sST2 > 35 ng/mL and BNP > 500 pg/mL, including 2 deaths and 5 cases of heart failure within 30 days, and difference based on the value of sST2 and BNP for cardiovascular events, statistically significant at $p < 0.0001$.

This study was a first step in investigating the level of sST2 on ST-segment elevation myocardial infarction patients, requiring larger samples size with longer follow-up time to conclude that the value of new biopsy on ST-segment elevation myocardial infarction patients with primary PCI.

5 Conclusion

sST2 ≥ 35 ng/mL associated with heart failure or death with $p < 0.01$.

Cardiovascular events in 3 groups in the order of sST2 > 35 ng/mL and BNP > 500 ng/mL, sST2 > 35 ng/mL or BNP > 500 pg/mL, sST2 < 35 ng/mL and BNP < 500 pg/mL.

6 Recommendations

Clinically, the combination of BNP and sST2 should be used to assess the mortality in the patients with STEMI.

Conflict of Interest I declare that I have no conflict of interest.

References

1. Thygesen, K., Alpert, J.S., Jaffe, A.S.: Third universal definition of myocardial infarction. *Eur. Hear. J.* **33**, 2551–2567 (2012). <https://doi.org/10.1093/eurheartj/ehs184>
2. O’Gara, P.T., Kushner, F.G., Ascheim, D.D.: ACCF/AHA guideline for the management of st-elevation myocardial infarction, a report of the american college of cardiology foundation/american heart association task force on practice guidelines. *Circulation* **127** (2013). <https://doi.org/10.1161/CIR.0b013e3182742cf6>
3. Shimpo, M., Morrow, D.A., Weinberg, E.O., Sabatine, M.S., Murphy, S.A., Antman, E.M., Lee, R.T.: Serum levels of the interleukin-1 receptor family member ST2 predict mortality and clinical outcome in acute myocardial infarction. *Circulation* **109**, 2186–2190 (2004). <https://doi.org/10.1161/01.CIR.0000127958.21003.5A>
4. Sabatine, M.S., Morrow D.A., Higgins L., MacGillivray C., Guo W., Bode C., Rifai N., Cannon C.P., Gerszten R.E., Lee R.T.: Complementary roles for biomarkers of biomechanical strain ST2 and N-terminal prohormone B-type natriuretic peptide in patients with ST-elevation myocardial infarction. *Circulation* **117**, 1936–1944 (2008). <https://doi.org/10.1161/CIRCULATIONAHA.107.728022>
5. Brown, A.M., Wu, A.H.B., Clopton, P., Robey, J.L., Hollander, J. E.: ST2 in emergency department chest pain patients with potential

- acute coronary syndromes. *Ann. Emerg. Med.* **50**, 153–158 (2007). <https://doi.org/10.1016/j.annemergmed.2007.02.015>
6. Weinberg, E.O., Shimpo, M., De Keulenaer, G.W., MacGillivray, C., Tominaga, S., et al.: Expression and regulation of ST2, an interleukin-1 receptor family member, in cardiomyocytes and myocardial infarction. *Circulation* **106**, 2961–2966. (2002)
 7. Bartunek, J., Delrue, L., Van Durme, F., et al.: Nonmyocardial production of ST2 protein in human hypertrophy and failure is related to diastolic load. *J. Am. Coll. Cardiol.* **52**(25), 2166–2174 (2008). <https://doi.org/10.1016/j.jacc.2008.09.027>
 8. Dhillon, O.S., Narayan, H.K., Khan, S.Q., Kelly, D., Quinn, P.A., Squire, I.B., Davies, J.E., Ng, L.L.: Pre-discharge risk stratification in unselected STEMI: is there a role for ST2 or its natural ligand IL-33 when compared with contemporary risk markers. *Int. J. Cardiol.* **167**, 2182–2188 (2013). <https://doi.org/10.1016/j.ijcard.2012.05.073>
 9. Granger, C.B., Goldberg, R.J., Dabbous, O., et al.: Global Registry of acute coronary events investigators. Predictors of hospital mortality in the global registry of acute coronary events. *Arch. Intern. Med.* **163**, 2345–2353 (2003). <https://doi.org/10.1001/archinte.163.19.2345>

Effects of Culture Conditions on the Antimicrobial Activity of *Streptomyces* spp. LTB08

Ngoc Thuy Linh Do, Quynh Ngan Tran, Trong Thuc Nguyen, Ngoc Phuc Chau Do, and Thi Thu Hoai Nguyen

Abstract

The aim of the present study was to find out the optimal culture conditions for *Streptomyces* spp. LTB08 which previously showed strong antimicrobial activity to exert high antimicrobial activity. The effect of each parameter viz., incubation time, pH, sodium chloride concentration, and added carbon on antimicrobial activity was studied by varying single parameter of standard culture condition at a time. The result showed that antimicrobial activity reached the peak after 4 days of culture and remained relatively constant until day 7. Among different tested pHs and salinities, highest antimicrobial activity was obtained at pH 7.0 in comparison to pH 6 and 8 and at the salinity of 0.5% in comparison to 1 and 2%. In contrast, when different carbon sources (glucose, fructose, sucrose, and starch) were supplemented to the culture medium (MHB), there was a marked decrease in the antimicrobial activity of *Streptomyces* spp. LTB08 in comparison to non-supplemented condition which indicated that the production of antimicrobial compounds seemed to be more preferable in restricted media. In summary, 4 days of incubation at pH 7.0; 0.5% NaCl and non-supplemented MHB are optimal conditions to achieve maximum yield of antimicrobial activity of *Streptomyces* in general and of isolate LTB08 in particular.

Keywords

Antimicrobial activity • Culture condition • *Streptomyces*

1 Introduction

Streptomyces is the largest genus of Actinobacteria and belongs to the Streptomycetaceae family [1]. These bacteria are found in a variety of ecological habitats such as soil, fresh water, marine water and plants. The *Streptomyces* is noticeably known as antibiotic producers with approximately 80% of the antibiotics were produced by *Streptomyces* spp. [2, 3]. The growth and production of antimicrobial compounds of *Streptomyces* are often affected by multiple environmental factors particularly temperature and culture medium [4]. Therefore, identifying an optimal culture condition for *Streptomyces* is very important to enhance the growth and production of antimicrobial compounds to serve for isolating, identifying and producing antimicrobial compounds from potential *Streptomyces* isolates. In our previous study, we have obtained a newly isolated *Streptomyces* strain, LTB08 closely related to *Streptomyces griseorubens*, with promising activity against Gram-positive bacteria [5]. However, this isolate LTB08 failed to show its strong antimicrobial activity in when being culture in media such as tryptic soya broth (TSB) and even ISP II broth [5]. Interestingly, when being cultured in Mueller-Hinton broth (MHB), its activity re-appeared and exerted highly [5]. In this study, we aimed to optimize culture conditions including incubation time, pH, salinity and supplemented carbon sources for promoting the antimicrobial activity of this isolate.

2 Materials and Methods

2.1 Bacterial Culture

Streptomyces spp. LTB08 was cultured in Actinomycetes Isolation Agar (AIA, HiMedia, India). Single colony was cultured in Mueller Hinton broth (MHB, Titan Biotech, India) overnight at 25 °C and 120 rpm. 200 µL of overnight

N. T. L. Do · Q. N. Tran (✉) · T. T. Nguyen · N. P. C. Do · T. T. H. Nguyen
School of Biotechnology, International University,
Vietnam National University of Ho Chi Minh City, Quarter 6,
Linh Trung Ward, Thu Duc District, Ho Chi Minh City, Vietnam
e-mail: ntthoai@hcmiu.edu.vn

culture was inoculated into 50 mL MHB and cultured at 25 °C and 120 rpm. Different culture conditions were applied to assess their effect on bacterial growth and antimicrobial activity. At first, *Streptomyces* spp. LTB08 was incubated at different durations 2, 3, 4, 5, 6 and 7 days. Secondly, *Streptomyces* spp. LTB08 was incubated for optimal duration in MHB at different pHs viz. 6.0; 7.0 and 8.0 adjusted using HCl 0.1 N and NaOH 0.1 N. Next, *Streptomyces* spp. LTB08 was incubated for optimal duration in MHB at optimal pH with varying concentrations of NaCl viz. 0.5, 1, 2%. A culture without NaCl added was kept as control. Finally, in the optimized conditions, different carbon sources including Glucose, Fructose, Starch, Sucrose (15 g/L) were added into the culture. A culture with no supplemented carbon source was used as control. After incubation, bacterial cultures were centrifuged to collect supernatant for assessing antimicrobial activity.

2.2 Evaluation of Antimicrobial Activity

Antimicrobial activity was evaluated using agar well diffusion method. Testing bacteria *Staphylococcus aureus* ATCC 29213 (*S. aureus*) and *Pseudomonas aeruginosa* ATCC 9027 (*P. aeruginosa*) were suspended in sterile MHB and adjusted to around 10^6 CFU/mL. 200 µL of testing bacterial suspensions was spread evenly over Mueller Hinton agar plate using sterile cotton swabs. Subsequently, 5-mm wells in agar were made using a sterile tip and 200 µL of cell-free supernatant from *Streptomyces* suspension were added to each well. Plates were then incubated overnight at 30 °C and diameter of inhibition zone surrounding each well was measured in millimeters.

2.3 Statistical Analysis

All experiment was performed in duplicate with two independent replicates for each treatments and controls. The results are presented as mean \pm standard deviation and one-way ANOVA was performed to compare sample means with p value set at 0.05.

3 Results and Discussion

The ability of *Streptomyces* to produce antimicrobial compounds was not consistent. It was remarkably affected by culture conditions. Besides, this inhibition activity was observed with *S. aureus*, Gram-positive bacteria (thus, shown) but not with *P. aeruginosa*, Gram-negative bacteria (thus, not shown).

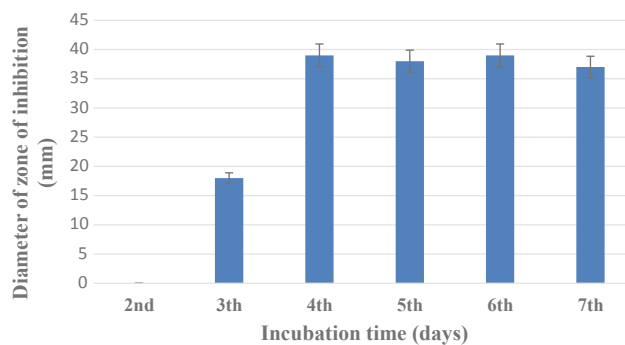


Fig. 1 Effect of incubation time on antimicrobial activity of *Streptomyces*. Testing organisms: *Streptomyces* spp. LTB08 and *S. aureus* ATCC 29213

3.1 Effect of Incubation Time

Data showed that the production of antimicrobial compounds increased with the time of incubation. At second day of culture, no antimicrobial activity was observed. This activity was observed at 3rd day and reached peak at 4th day and kept stable to 6th day (Fig. 1). The data were significantly different among tested values. Our data strongly suggested that incubation time is crucial for the production and collection of bioactive agents and implicated that this duration can be greatly varied among *Streptomyces* species. For example, previous data showed that *Streptomyces* KEH23 produced high antimicrobial metabolites at 96 h of incubation [6] while for *Streptomyces* spp. RUPA-08PR, the maximum production of antimicrobial metabolites was obtained after 10 days of incubation [7].

3.2 Effect of PH

The isolate had different antimicrobial activities against the test bacteria grown on medium with varied pH values (Fig. 2). The antimicrobial activity of isolate LTB08 against *S. aureus* was highest in MHB with pH 7.0, while the lowest activity was exhibited in MHB with pH 6.0. The data were significantly different among tested values. Therefore, pH 7.0 was selected for the followed experiment. Our data was consistent with other previous data showing that pH plays an important role in the production of bioactive compounds by *Actinomycetes* including *Streptomyces*. The optimum pH for the greater growth and metabolite production in *Actinomycetes* is highly varied and usually ranges from 6.0 to 8.0 [8]. For *Streptomyces violates* 22, optimum production of bioactive agents was also observed at pH 7.0 [9]. For *Streptomyces plicatus*, maximum yield of antimicrobial agents was obtained at pH 7.6 [10]. For *Streptomyces* sp. RUPA-08PR, it has been found that optimum production

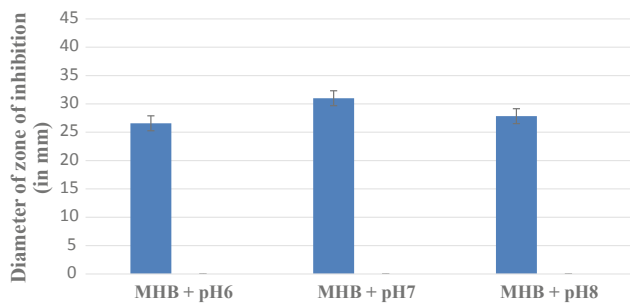


Fig. 2 Effect of pH on antimicrobial activity of *Streptomyces*. Testing organisms: *Streptomyces* spp. LTB08 and *S. aureus* ATCC29213

of bioactive agents at pH 8.0 by [7]. These data suggested that the production of antimicrobial compounds was greatly affected by pH and the optimal value was also varied for each isolate.

3.3 Effect of Sodium Chloride

Effect of NaCl concentration viz., 0.5, 1.0, 2.0% on antimicrobial activities of the strain *Streptomyces* LTB08 was presented in Fig. 3. The highest antimicrobial activity was found in MHB with 0.5% NaCl and the lowest activity was found in MHB with 2.0% NaCl. The data were significantly different among tested values (Fig. 3). Our obtained data was also in agreement with previous ones, which showed that salt is a crucial factor for the production of antibiotics in microorganisms [11, 12] even though its effects vary from one strain to another for example, 1.0% NaCl was optimal for maximum production of antimicrobial metabolites by *Streptomyces* spp. RUPA-08PR [7] while 3.0% NaCl was optimal for *S. sannanensis* strain RJT-1 [12].

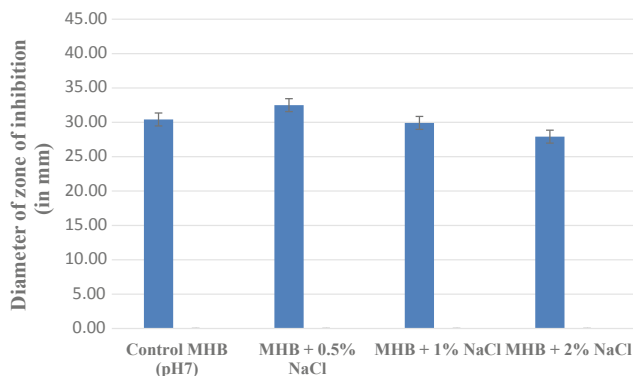


Fig. 3 Effect of NaCl on the antimicrobial activity of *Streptomyces*. Testing organisms: *Streptomyces* spp. LTB08 and *S. aureus* ATCC29213

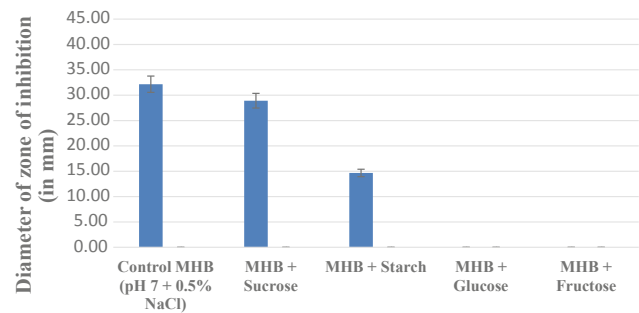


Fig. 4 Effect of supplemented carbon on the antimicrobial activity of *Streptomyces*. Testing organisms: *Streptomyces* spp. LTB08 and *S. aureus* ATCC29213

3.4 Effect of Supplemented Carbon

Antimicrobial activity of *Streptomyces* spp. LTB08 was varied when being grown in MHB supplemented with different carbon sources. The influence of supplemented carbon on the antimicrobial activity of the isolate was shown in Fig. 4. Markedly high inhibitory activity was observed in case of supernatant obtained from culture grown in MHB without supplemented carbon. MHB with added sucrose, starch, fructose and glucose showed much less antimicrobial activity or even no inhibitory activity against *S. aureus*. The data were significantly different among tested conditions. Overall, even though carbon is required for cellular metabolism, it is not necessary to supplement carbons into the culture medium. However, so far previous data on the effect of supplemented carbon are varied. Glucose was found to positively influence the production of antibiotics in *Streptomyces psammoticus* BT-408, *S. sannanensis* strain RJT-1 and *Streptomyces* spp. RUPA-08PR [7, 12–14]. Similarly, *S. plicatus*, *Streptomyces* species and *Streptomyces* sp. MS-266 Dm4 preferred starch as the best carbon source for production of bioactive metabolites [10, 15, 16]. However, starch was found to be poor carbon source for *S. kanamyceticus* M27 [17].

4 Conclusion

Culture media has been known to profoundly influence the antimicrobial activity in *Streptomyces* spp. Since some antimicrobial synthesis pathways could be repressed due to the presence of glucose, inorganic nitrogen sources or inorganic phosphate [18], medium composition should be carefully adjusted for obtaining antimicrobial compounds from *Streptomyces* liquid culture. In this study, we applied MHB which is not only the medium of choice for susceptibility testing [19] but also an optimal one for our LTB08 isolate [5] to study its antimicrobial activity. Our obtained data showed that in MHB, *Streptomyces* spp. LTB08 yielded

high antimicrobial activity at pH 7.0, 0.5% NaCl, 4 days of incubation and without supplemented carbon in culture medium.

Acknowledgements This research is funded by International University—VNUHCM under grant number T2016-02-BT.

Conflict of Interest The authors declare no conflict of interests.

References

- Kämpfer, P.: The family Streptomycetaceae, part I: taxonomy. The prokaryotes, pp. 538–604. Springer, New York (2006)
- Takahashi, Y., Omura, S.: Isolation of new actinomycete strains for the screening of new bioactive compounds. *J. Gen. Appl. Microbiol.* **49**(3), 141–154 (2003)
- Atta, H.M.: An antifungal agent produced by *Streptomyces olivaceiscleroticus*, AZ-SH514. *World Appl. Sci. J* **6**(11), 1495–1505 (2009)
- Rakesh, K.N., Dileep, N., Junaid, S., Prashith, K.T.R.: Optimization of culture conditions for production of antibacterial metabolite by bioactive *Streptomyces* species srdp-tk-07. *An Intern. J. Adv. Pharm. Sci.* **5**, 1809–1816 (2014)
- Bao, L.T., et al.: Investigation of antimicrobial activity of *Streptomyces* isolated from soil in Ho Chi Minh City. B.Sc. Thesis (2017)
- Oskay, M.: Antifungal and antibacterial compounds from *Streptomyces* strains. *Afr. J. Biotechnol.* **8**(13) (2009)
- Ripa, F.A., Nikkon, F., Zaman, S., Khondkar, P.: Optimal conditions for antimicrobial metabolites production from a new *Streptomyces* sp. RUPA-08PR isolated from Bangladeshi soil. *Mycobiology* **37**(3), 211–214 (2009)
- Song, Q., Huang, Y., Yang, H.: Optimization of fermentation conditions for antibiotic production by *Actinomycetes* YJ1 strain against *Sclerotinia sclerotiorum*. *J. Agric. Sci.* **4**(7), 95 (2012)
- Hassan, M.A., El-Naggar, M.Y., Said, W.Y.: Physiological factors affecting the production of an antimicrobial substance by *Streptomyces violatus* in batch cultures. *Egypt. J. Biol.* **3**(1), 1–10 (2001)
- Osman, M.E., Ahmed, F.A.H., El All, W.A.: Antibiotic production from local *Streptomyces* isolates from Egyptian soil at Wady El Natron: isolation, identification and optimization. *Aust. J. Basic. Applied Sci* **5**, 782–792 (2011)
- Pelczar, M.J., Chan, E.C.S., Krieg, N.R.: *Microbiology: Concepts and Applications*, 5th edn. McGraw-Hill, USA (1993)
- Vasavada, S.H., Thumar, J.T., Singh, S.P.: Secretion of a potent antibiotic by salt-tolerant and alkaliphilic actinomycete *Streptomyces sannanensis* strain RJT-1. *Curr. Sci.* 1393–1397 (2006)
- Tadijan, I., Grahovac, J., Dodić, J., Grahovac, M., Maširević, S., Vučurović, D., Dodić, S.: Effect of carbon sources on the production of the biofungicide by *Streptomyces hygrosopicus*. *Acta Univ Sapiientiae Alimentaria* **7**, 54–62 (2014)
- Sujatha, P., Raju, K.B., Ramana, T.: Studies on a new marine *Streptomyces* BT-408 producing polyketide antibiotic SBR-22 effective against methicillin resistant *Staphylococcus aureus*. *Microbiol. Res.* **160**(2), 119–126 (2005)
- Da Silva, I.R., Martins, M.K., Carvalho, C.M., De Azevedo, J.L., de Lima Procópio, R.E.: The effect of varying culture conditions on the production of antibiotics by *Streptomyces* spp. Isolated from the Amazonian Soil. *Ferment. Technol.* **1**(3) (2012)
- Ababutain, I.M., Aziz, Z.K.A., Al-Meshhen, N.A.: Optimization of environmental and nutritional conditions to improve growth and antibiotic productions by *Streptomyces* Sp. isolated from Saudi Arabia Soil. *Int. Res. J. Microbiol.* **4**(8), 179–87 (2013)
- Pandey, A., Shukla, A.N.U.P.A.M., Majumdar, S.K.: Utilization of carbon and nitrogen sources by *Streptomyces kanamyceticus* M27 for the production of an Anti bacterial antibiotic. *Afr. J. Biotechnol.* **4**(9) (2005)
- Hasani, A., Kariminik, A., Issazadeh, K.: *Streptomyces*: characteristics and their antimicrobial activities. *Int. J. Adv. Biol. Biomed. Res.* **2**(1), 63–75 (2014)
- Ericsson, H.M., Sherris, J.C.: Antibiotic sensitivity testing. Report of an international collaborative study. *Acta Pathol. Microbiol. Scand. (Suppl. 217)* (1971)



Optimizing Conditions for *Vibrio Parahaemolyticus* Culture and Preservation

Thi Lan Anh Pham, Quy Khang Le, Trong Thuc Nguyen, Ngoc Phuc Chau Do, and Thi Thu Hoai Nguyen

Abstract

Vibrio parahaemolyticus is a Gram-negative bacterium of research importance nowadays due to its ability to cause diseases in both human and marine organisms. However, the bacterium expresses diminishing potential to grow under in vitro conditions particularly after conventional preservation and serial subculture. In this research, the conditions for *V. parahaemolyticus* culture and preservation were optimized to improve its growth and survival. In brief, *V. parahaemolyticus* XN9 was cultured in different conditions via varying culture medium (TSB, BHI, LB and MB), NaCl concentration (2.5, 3.0 and 3.5%), and pH (7.5, 8.0 and 8.5). The optimal culture condition was then used for optimizing preservation condition with different added glycerol concentrations (20, 30, and 40%). Survival rate was measured after 1, 2 and 3 months using plate counting method. Results showed that, the optimal culture condition for *V. parahaemolyticus* is 2.5% NaCl and pH 8.5 for TSB and BHI medium; 3.0% NaCl and pH 8.0 for LB; 2.5% NaCl and pH 8.0 for MB. For preservation, TSB with 20% glycerol, 2.5% NaCl and pH 8.0 provided best result. In conclusion, media such as TSB, BHI and MB can be applied to culture and preserve *V. parahaemolyticus*. However, to obtain optimal bacterial growth and survival, pH and salt concentration should be of concern for each one.

Keywords

Culture • Preservation • *Vibrio parahaemolyticus*

1 Introduction

Vibrio parahaemolyticus (*V. parahaemolyticus*), a Gram-negative bacterium, belongs to normal flora of multiple marine organisms. This bacterium was found to be major causative agent of Acute Hepatopancreatic Necrosis Disease (AHPND) in shrimps [1]. Although abundant and spreading easily in natural conditions, *V. parahaemolyticus* does not survive well when being preserved and cultured under laboratory condition for long time resulting in some difficulties in carrying out long-term study [2]. In fact, there are multiple media which can be used to culture *Vibrio* species, however, these media have not yet been assessed for optimal growth and survival of *V. parahaemolyticus* [3]. Additionally, being a marine bacterium, *V. parahaemolyticus* requires not only nutrients but also pH and a certain range of salinity for its optimal growth [4]. It has been shown that optimal culture conditions for *V. parahaemolyticus* vary among different strains and the bacterium normally grows well at pH from 7.6 to 8.6 and its optimal growth usually reaches at 1.5–3% NaCl when being cultured between 30 and 37 °C [4–9]. For long-term preservation of *V. parahaemolyticus*, there have yet data suggesting the optimal condition for preserving this bacterium [2]. At current, the most common method for long-term storage of bacteria is using bacterial glycerol stock method. It is no doubt that glycerol concentration influences on the survival of the bacteria during storage particularly in preservation of extremely low temperature (–80 °C) for a long time. In this study, we aimed to investigate the effect of different media including Tryptone Soya broth (TSB), Zobell Marine (MB), Luria Bertani (LB) and Brain Heart Infusion (BHI) on *V. parahaemolyticus* growth. These types of media were used with varying NaCl concentrations and pH to optimize the best condition for culturing and preserving *V. parahaemolyticus*. Different concentrations of glycerol were also applied to find out optimal concentration to preserve this bacterium.

T. L. A. Pham · Q. K. Le (✉) · T. T. Nguyen · N. P. C. Do · T. T. H. Nguyen
School of Biotechnology, International University,
Vietnam National University of Ho Chi Minh City, Quarter 6,
Linh Trung Ward, Thu Duc District, Ho Chi Minh City, Vietnam
e-mail: khanglequy@gmail.com

T. T. H. Nguyen
e-mail: ntthoai@hcmiu.edu.vn

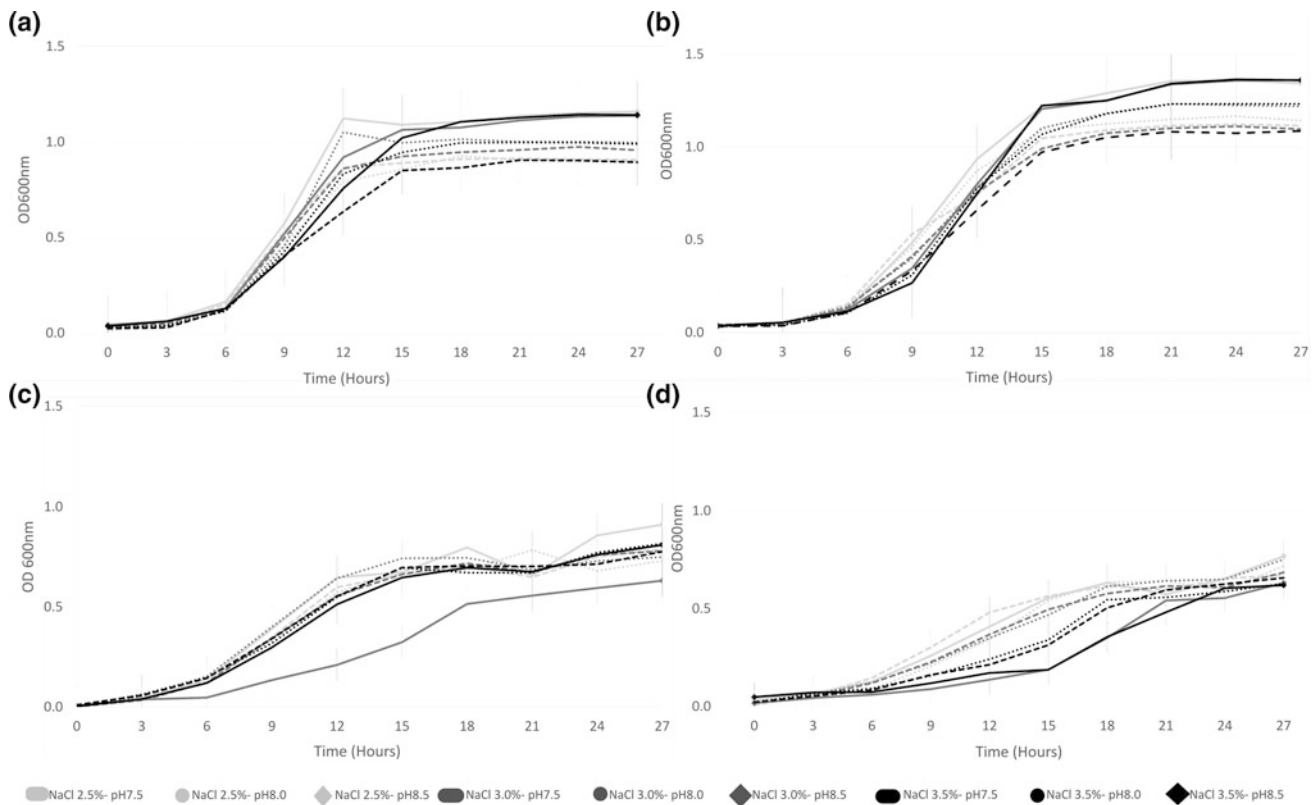


Fig. 1 Growth curve of *V. parahaemolyticus* in TSB (a), BHI (b), LB (c) and MB (d). *V. parahaemolyticus* was cultured at 30 °C and assessed for growth via OD measurement at 600 nm every 3 h for 30 h

parahaemolyticus were 3.0% NaCl and pH range values from 4.7 to 8.0 for TSB [8]; 3.0% NaCl and pH 8.0 for LB [9].

3.2 Effect of Different Preservation Conditions on the Survival of *V. parahaemolyticus*

The effect of glycerol on the survival of *V. parahaemolyticus* is shown in Fig. 2. Obtained results indicated that 20% was the ideal glycerol concentration for glycerol stock of *V. parahaemolyticus* XN9 preservation (Fig. 2). Survival rates of both 20 and 30% group were significantly different with 40% glycerol group. Glycerol with the ability to reduce freezing damage, such as ice crystal formation has long been used as a preserving agent at the range of 20–40% because at lower than 10% the frozen stock is fairly solid at –80 °C, while higher concentrations (over 40%) could result in bacterial death due to bacterial inability to adapt when being thawed. In our study, it again showed its ability to maintain bacterial cells in freezing condition well particularly at the percentage of 20%.

At the same time, the effect of pH, NaCl and media on *V. parahaemolyticus* XN9 survival after preservation were also determined. In order to determine the optimal condition for *V. parahaemolyticus* XN9 storage, all conditions were

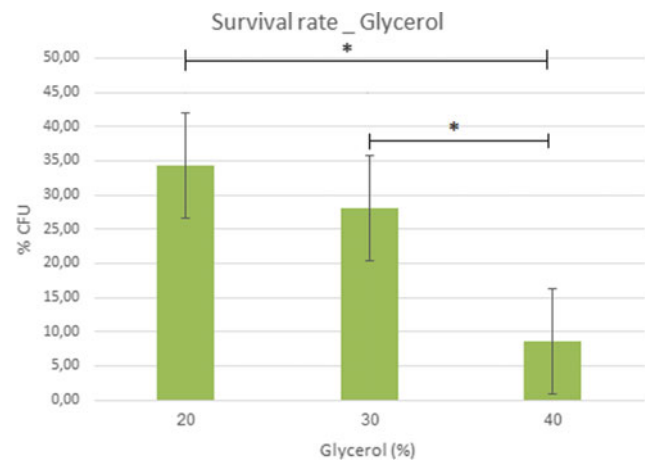


Fig. 2 Survival rate of *V. parahaemolyticus* XN9 after 3-month storage in media containing different glycerol concentrations. Bacteria were cultured in MB, LB, BHI, and TSB then stored at –80 °C in a respective medium of 20, 30 and 40% glycerol. All data were combined in groups of same glycerol concentration; *: Significant difference ($p < 0.05$)

combined for analysis by using 3D Scatter plot software (Plotly, Inc., Canada). Based on survival rate mean and standard deviation, the data showed that for optimal storage condition for TSB medium was 20% glycerol, 2.5% NaCl

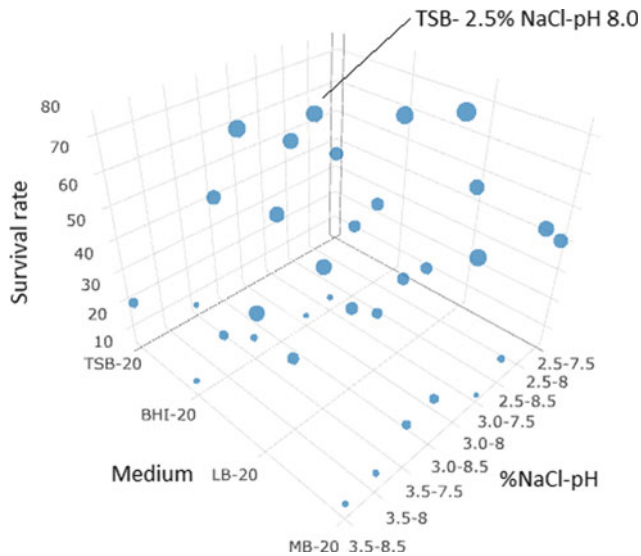


Fig. 3 Survival rates of *V. parahaemolyticus* under different conditions. Dot sizes correspond to mean survival rate in a positive correlation (3D Scatter plot software (Plotly, Inc., Canada))

and pH 8.0 (survival rate is 53.71%) (Fig. 3). This result was fairly different to previous one suggesting that *V. parahaemolyticus* should be maintained at -70°C , 20% glycerol but in nutrient broth with 3.0% NaCl [7].

4 Conclusion

Our study showed that the optimal condition for culturing *Vibrio parahaemolyticus* are 2.5% NaCl and pH 8.5 for TSB and BHI medium; 3.0% NaCl and pH 8.0 for LB; 2.5% NaCl and pH 8.0 for MB, while for preserving, the TSB with 2.5% of NaCl and pH 8.0 provided best result.

Conflict of Interest The authors declare no conflict of interests.

References

1. Loc, T., Linda, N., Rita, M.R., Leone, L.M., Carlos, R.P., Kevin, F., Donald, V.L.: Determination of the infectious nature of the agent of acute hepatopancreatic necrosis syndrome affecting penaeid shrimp. *Dis. Aquat. Organ.* **105**(1), 45–55 (2013)
2. Shen, X., Liu, W., Liu, C.: Effects of cold storage and thermal treatment on growth and survival of pathogenic *Vibrio parahaemolyticus*. In: 2010 International Conference on Bioinformatics and Biomedical Technology, Chengdu, pp. 371–373 (2010)
3. Donovan, T.J., van Netten, P.: Culture media for the isolation and enumeration of pathogenic *Vibrio* species in foods and environmental samples. In: Corry, J.E.L., Curtis, G.D.W., Baird, R.M. (eds.) *Culture media for food microbiology*. Progress in Industrial Microbiology, vol. 34, pp. 203–217 (1995)
4. Whitaker, W.B., Parent, M.A., Naughton L.M., Richards G.P., Blumerman S.L., Boyd E.F.: Modulation of responses of *Vibrio parahaemolyticus* O3:K6 to pH and temperature stresses by growth at different salt concentrations. *Appl. Environ. Microbiol.* **76**, 4720–4729 (2010)
5. Meshack, F.M., Salina, P., Jurgen, S., Tom, R., Anish, C.: The effects of storage temperature on the growth of *Vibrio parahaemolyticus* and organoleptic properties in oysters. *Front. Public Health.* **2**(45), 1–7 (2014)
6. Kalburge, S.S., Whitaker, W.B., Boyd, E.F.: High-salt preadaptation of *Vibrio parahaemolyticus* enhances survival in response to lethal environmental stresses. *J. Food Prot.* **77**(2), 246–253 (2014)
7. Kim, Y.W., Lee, S.H., Hwang, I.G., Yoon, K.S.: Effect of temperature on growth of *Vibrio parahaemolyticus* and *Vibrio vulnificus* in flounder, salmon sashimi and oyster meat. *Int. J. Environ. Res. Public Health.* **9**(12), 4662–4675 (2012)
8. Beuchat, L.R.: Effects of pH, Temperature, and salt concentration on growth and survival of *Vibrio parahaemolyticus*. *Appl. Microbiol.* **25**(5), 844–846 (1973)
9. Lee, J.: Laboratory studies of growth conditions of *Vibrio parahaemolyticus* in pacific oyster (*Crassostrea gigas*) with international considerations to shellfish-associated illnesses in South Korea. Bsc thesis. Oregon State University (2009)

A High M1/M2 Ratio Is Associated with Better Survival in Neuroblastoma

Chi Hoang Linh Pham and Chi-Bao Bui

Abstract

Neuroblastoma is a fatal childhood disease that only 30% are long-term survival for high-risk cases. Tumor-associated macrophages (TAMs) play a crucial role in cancer development. TAMs are classified into classical activated M1 phenotype and alternative activated M2 phenotype under specific stimuli in tumor microenvironment. While M1 macrophages induce pro-inflammation and tumoricidal activity, M2 macrophages promote tumor progression. The poor survival of several cancers (including neuroblastoma) has been assigned to high M2 macrophages presentation. Meanwhile, studies on some cancers reported high M1 infiltration was associated with improved survival. However, the contribution of M1 macrophages has not been well studied in neuroblastoma. In this study, we aimed to elucidate the ratio of M1/M2 macrophages in association with patients' survival expectation. To evaluate activation status of M1 and M2 macrophages, we isolated TAMs from neuroblastoma tumors and quantified their biomarker gene expression using RT-qPCR. A remarkably high infiltration of M1 macrophages in tumor was observed with high event-free survival (EFS) and very low risk. Meanwhile, an M2-populated polarization was the status in poor outcome cases. Collectively, these data suggested that a higher ratio of M1/M2 polarized macrophages resulted in better survival from Very-Low risk (VL) to Intermediate-risk (IR). This study supports promising treatment targeting TAMs polarization for survival improvement in neuroblastoma patients.

Keywords

Neuroblastoma • TAMs • M2/M1 macrophages • Very-Low risk (VL) • Intermediate risk (IR) • Event-free survival (EFS)

1 Introduction

Neuroblastoma is a pediatric cancer of the sympathetic nervous system, which is among fatal diseases, that is responsible for 15% of childhood cancer deaths [1]. The malignant cells usually originated from early nerve cells (called neuroblasts) of the adrenal glands in embryos. Neuroblastoma is classified into High-risk, Intermediate-risk, Low-risk and Very Low-risk group using The International Neuroblastoma Risk Group (INRG) classification system [2] (Fig. 1). The survival rate is over 90% for low-risk neuroblastoma while below 30% patients are long-term survivors [3]. Clinical outcomes remain poor in spite of advances in therapy [4].

Tumor-associated macrophages (TAMs) have significant effects on nearly every stage of cancer development and progression [5]. Not all TAMs under tumor microenvironment maintain their tumoricidal functions, but they may promote tumor invasion, tumor proliferation, angiogenesis and secrete certain immunosuppressive cytokines [6]. TAMs are differentiated into two phenotypes M1 “classically activated” and M2 “alternatively activated” upon distinct stimuli in tumor microenvironment [7]. Th1 cytokines such as interferon- γ (IFN- γ) or lipopolysaccharide (LPS) activate proinflammatory M1 macrophages which promote type I immune response and tumoricidal activities [8]. IL-4 and IL-10 cytokines, on the other hand, stimulate M2 macrophage polarization bias which secretes anti-inflammatory cytokines that induce type II response and tissue repair [9]. While M1 macrophages kill cancer cells, M2 macrophages promote its growth and invasion.

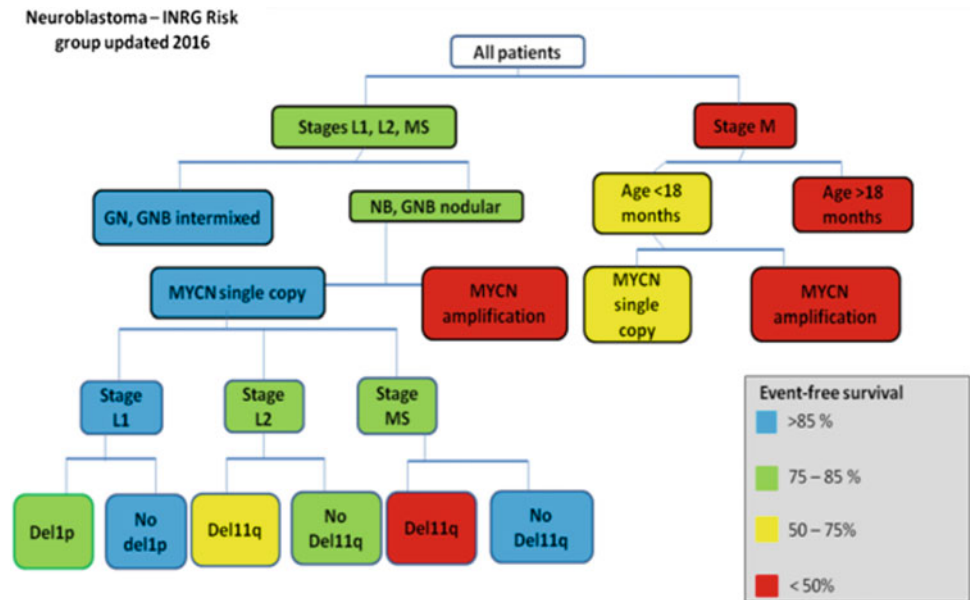
C. H. L. Pham (✉)

School of Biotechnology, International University—Vietnam National University in HCMC, Ho Chi Minh City, Vietnam
e-mail: phamchendi@gmail.com

C.-B. Bui

Center for Molecular Biomedicine, University of Pharmacy and Medicine, HCMC, Ho Chi Minh City, Vietnam
e-mail: bcbao@ump.edu.vn

Fig. 1 The International Neuroblastoma Risk Group classification system. Blue, green, yellow and red indicates Very-Low risk, Low-risk, Intermediate-risk and High-risk, respectively



TAMs, particularly M2-phenotype macrophages, has prognosis potential in neuroblastoma as evidenced by recent research. Hadjidaniel et al. [10] showed that TAMs strongly associated with poor survival in neuroblastoma patients without MYCN amplification by up-regulation of MYC protein through STAT3 pathway. There has been reported on the prognostic significance of only M2 macrophages in combination with cancer-associated fibroblasts in cancer (including neuroblastoma) [11–13]. However, the prognostic importance of TAMs considering the relation of two distinct phenotypes in tumor samples has not been well studied.

In this study, we focused on evaluating the quantitative relation of M1 and M2 macrophages in neuroblastoma tumors and determining its correlation with event-free survival. We aimed to claim the similar activation status of polarized macrophages in neuroblastoma with patients' survival expectation as evidenced in other cancers.

2 Materials and Method

2.1 Materials

Dissociation solution (0.05% Collagenase and 0.01% DNase I solution) was prepared by dissolving 500 µg of Collagenase P from *Clostridium histolyticum* (Roche) and 100 µg of DNase I (Roche) in 1 ml of sterile PBS.

2.2 Method

Sample Collection Surgical resections of primary tumors were collected from NB patients (Children Hospital,

HCMC). The specimens, when received, were taken from the media and stored in -80°C until processed.

There were 6 tumor samples in this study and they were from 2 risk groups: Very Low-risk and Intermediate-risk, equally. The risk was classified based on MYCN amplification and chromosomal aberrations using the INRG (Fig. 1). Data was obtained from the Children Hospital and Center for Molecular Biomedicine, University of Medicine and Pharmacy at HCMC. Informed consent was obtained from all patients for being included in this study.

Tumor dissociation Tumor was mechanically dissociated and 1 ml enzyme solution was added. The mixture was incubated at 38°C for 60 min in the water bath and was gently mixed after each 15 min. The mixture was strained through a 70 µm cell strainer and the solution was collected. Cell suspension was washed 2 times with 10 ml PBS and centrifugation at 400 rcf in 10 min at 4°C . This whole procedure was performed on ice to preserve the cell quality.

Macrophage Isolation Macrophages were isolated by MACS MicroBeads (Miltenyi, Germany). Total cells were suspended in 80 µl MACS buffer and were exposed to 20 µl CD14 antibody for 15 min at 40°C in the dark. The cells were washed with 1 ml MACS buffer by centrifugation for 10 min at 400 g and 40°C . The cell pellet was resuspended in 500 µl MACS buffer. CD14+ cells were positively selected using LS magnetic-bead column (Miltenyi Biotech, Germany) following the manufacturer's instructions.

Flow Cytometric Analysis To confirm the purity of macrophages isolated, flow cytometric analysis was performed. A portion of cells was stained with FITC-labelled

Table 1 Primer pairs for RT-qPCR

Gene	Primer (5'–3')	Amplicon (bp)
<i>GAPDH</i>	For: GTGAAGGTCGGAGTCAACGG Rev: CTCCTGGAAGATGGTGATGGG	228
<i>IL6</i>	For: CCTTCCAAAGATGGCTGAAA Rev: TGGCTTGTTCTCACTACTCTC	149
<i>VSIG4</i>	For: TGGTACAACGTGGCTCAGAC Rev: CTCACGACTTGGTTGCCATC	221

anti-human CD14 mAb and PerCP-labelled anti-human CD45 (Miltenyi Biotech, Germany) following the manufacturer's instructions. Analysis was performed by BD FACSCanto™ II flow cytometer (BD Bioscience) using BD FACSDiva software.

RNA Extraction Total RNA was extracted from macrophages using GeneJET RNA Purification Kit (Thermo Scientific), following the manufacturer's instructions. The quantitative and qualitative analysis were performed by Nanodrop-1000 Spectrophotometer (Thermo Scientific).

RT-qPCR cDNA was synthesized using PrimeScript™ 1st strand cDNA Synthesis Kit (Takara), following the manufacturer's instructions. Realtime PCR was performed using SYBRPremix Ex Taq (Tli RNaseH Plus) (Takara) cDNA derivative from 5 ng total RNA. One reaction (20 µl) contains 10 µl master mix, 1.5 µl of a mixture of 10 µM reverse and forward primers, 7.5 µl nuclease-free water and 1 µl cDNA template. qPCR measurements were performed on Mastercycler ep realplex (Eppendorf North America) with Eppendorf Realplex software. All the reactions were triplicated. The thermal cycle was: 95 °C in 3 min; 40 cycles of 98 °C in 20 s, Ta in 20 s and 72 °C in 50 s; melting-curve analysis followed. The expression was calculated in fold change by $2^{-\Delta\Delta CT}$, normalized to *GAPDH* and relative to the calibrator sample [14]. Primer pairs are as followed (Table 1).

Statistical Analysis Graphs represent means \pm standard deviations (SDs). Shapiro-Wilk and Leneve median test were performed to determine the normality and the equality of variance. All data in this study satisfied the normality and equality assumptions for Student's t-test. Spearman's rank-order test was performed for correlation. Data were analyzed using IBM SPSS Statistics version 23.0 (SPSS Inc., Chicago, Il) and GraphPad Prism 7.0 (GraphPad Software, Inc., San Diego, CA). Significant level is $p < 0.05$.

3 Results

3.1 Macrophages Isolated Was Pure for Further Analysis

To further examine M1/M2 macrophages gene expression, the purity of macrophage isolated from tumors must be evaluated. Cells were stained for CD45 and CD14, specific surface markers for leukocyte and macrophage respectively. In total cells separated by MACS MicroBeads, macrophages are positive for CD45 and CD14 as shown in Fig. 2. The purity of CD14 + macrophages was $86.03 \pm 0.69\%$ and no cell population had purity below the minimum threshold for pure cell fractions ($>85\%$) [15].

3.2 Macrophage Polarization Status Is Precisely Reflected by *IL6* and *VSIG4* MRNA Expression

M1/M2 macrophages population status in a tumor can be reflected by the expression of its marker genes. To study the relative polarization of macrophages, RT-qPCR was carried out to analyze distinctly representative marker genes for each population. *IL6* expression reflects M1 macrophages while *VSIG4* expression is typical for M2 macrophages. Gene expression analysis was performed on 5 ng cDNA and the experiment was triplicated for each sample. Data was calculated for M1/M2 ratio.

M1 marker was statistically significant higher expressed over M2 marker among macrophage populations in VL group, which ratio was 5.875 ± 0.2967 , compared to that of IR group, which ratio is lower than 1 (Fig. 3). There was no great variability among samples in both groups. Spearman's rank-order correlation test was run to determine the relationship between M1/M2 ratio in neuroblastoma tumor and the outcome. There was a strong, positive correlation

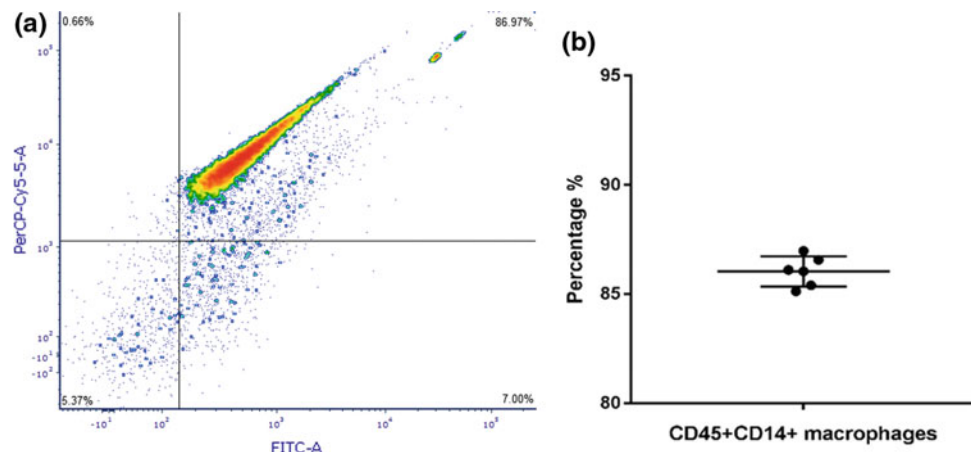


Fig. 2 Flow cytometric analysis. **a** Macrophages are CD45 + CD14 + . The vertical axis shows PerCP-Cy5 fluorescent signal labeled for CD45 and the horizontal axis shows FITC signal labeled for CD14. There are 4

regions gated for positive/negative zones relative to each surface marker. The right upper rectangle is CD45 + CD14 + population. **b** The purity of each sample

between M1/M2 ratio and EFS ($r(4) = 0.878$, $p = 0.021$). A high ratio of M1/M2 polarized macrophages was associated with improved EFS while a low ratio reveals poorer survival rate.

3.3 Macrophage Genes Were Higher Expressed in VL Group Than in IR Group

Interestingly, gene expressions of both M1 and M2 markers were remarkably higher in VL group in comparison to IR group ($p < 0.05$) (Fig. 4).

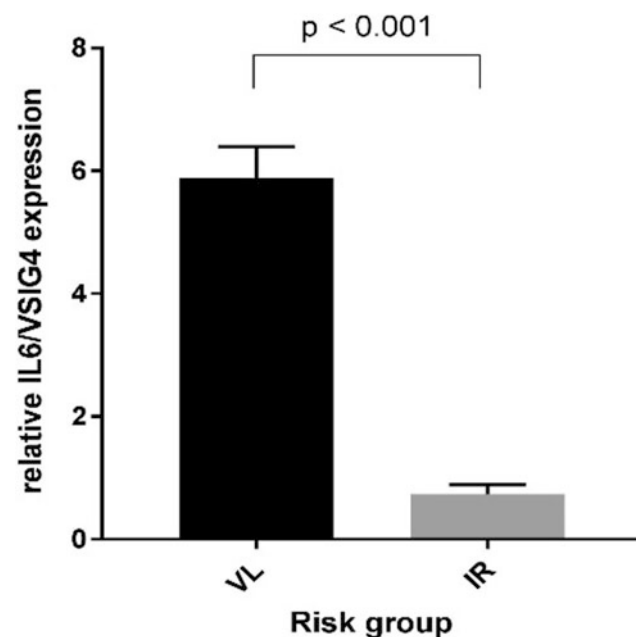


Fig. 3 Relative expression ratio of *IL6/VSIG4*

M1/M2 macrophages expression profiles

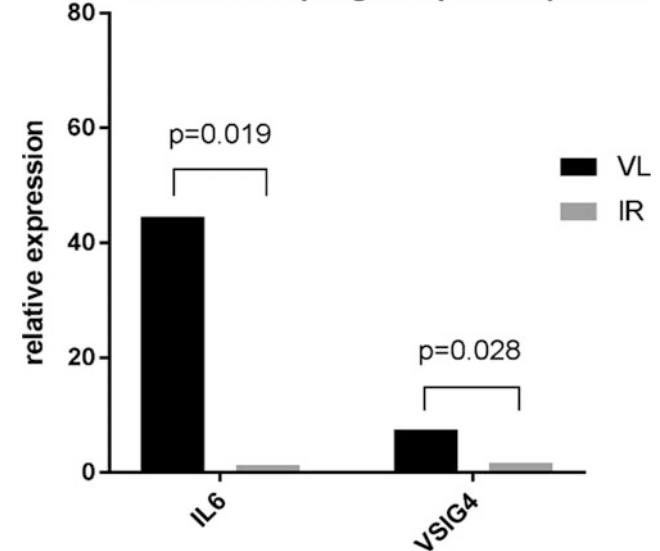


Fig. 4 Relative expression of IL6 and VSIG4 in VL and IR group

4 Discussion

This study enhances the understanding of TAMs activation status and its contribution to the outcome of neuroblastoma patients.

Our observation demonstrated a predominant infiltration of M1-polarized macrophages correlated with a better event-free survival rate. Meanwhile, M2-populated polarization implicated a higher risk and lower event-free survival. Other studies on ovarian cancer, breast cancer and NSCLC also reported the same polarization status of TAMs in association to clinical outcomes [6, 16, 17]. There are several explanations for this phenomenon. First, M1-phenotype

macrophages exhibit tumoricidal activity and recruit several immune cells that target, kill and therefore, suppress the development of tumor [6, 16, 17]. In fact, M1 macrophages were found populated in regressing tumor and necrotic areas of progressing tumor compared to M2-like macrophages [6]. Thereby, an M1-populated polarization might improve the EFS and lower the risk. In contrast, M2-phenotypes, which function in wound repair, misdirectedly promote tumor growth and invasion by secreting several cytokines that induce angiogenesis as well as cell proliferation. Thus, a predominant of M2 macrophages results in poorer outcomes.

In our study, while a higher TAMs density was observed, it exhibited a lower EFS than group of patients who displayed a smaller TAMs population. This is a contrast to some research which reported a decrease in survival in correlation with increased TAMs density [18, 19]. However, these studies had not put the phenotype of TAMs under consideration. Meanwhile, the importance of characterizing macrophage subpopulation in cancer studies was emphasized in many cancerous research findings as different phenotypes drive the outcome adversely [20, 21]. Moreover, as revealed by various research that TAMs in tumor environment are mostly M2 macrophages [22], TAMs density study alone is not sufficient to predict outcomes in cancer. As previously stated by Richards et al. [5] and Zhang et al. [16], our study also indicated that the more predictive factor was the phenotype of TAMs rather than its density in tumors.

Our data supports a cancer therapy targeting a TAMs activation status towards M1-phenotypes for improvements in neuroblastoma. Current treatment of neuroblastoma using retinoic acid was shown to promote Th1-responses [23, 24]. And as M1 macrophages induce Th1 responses, the directed polarization of TAMs to M1-phenotype is promising for treatment of high risk cases. Moreover, the inhibition or suppression of M2 macrophages also auspicious for improvements.

5 Conclusion

In conclusion, the present study demonstrates the strong correlation of M1/M2 polarized macrophage ratio in VL and IR neuroblastoma. The outcome of patients is determined by the polarization status of TAMs. A high M1/M2 ratio is associated with high EFS and lower risk. Therefore, targeting TAMs polarization is promising for neuroblastoma treatment.

Conflicts of Interest Statement The authors certify that they have NO affiliations with or involvement in any organization or entity with any financial interest (such as honoraria; educational grants; participation in speakers' bureaus; membership, employment, consultancies, stock ownership, or other equity interest; and expert testimony or

patent-licensing arrangements), or non-financial interest (such as personal or professional relationships, affiliations, knowledge or beliefs) in the subject matter or materials discussed in this manuscript. Ethical approval has been sought and obtained as necessary and any conflicts of interested stated.

References

- Buckley, P.G., et al.: Chromosomal and miRNA Expression Patterns Reveal Biologically Distinct Subgroups of 11q – Neuroblastoma. *Clin. Cancer Res.* **16**(11), 2971–2978 (2010)
- Cohn, S.L., et al.: The International Neuroblastoma Risk Group (INRG) classification system: an INRG Task Force report. *J. Clin. Oncol.* **27**(2), 289–297 (2009)
- Gowda, M., et al.: Distinct signatures of the immune responses in low risk versus high risk neuroblastoma. *J. Transl. Med.* **9**, 170 (2011)
- Matthay, K.K., et al.: Treatment of high-risk neuroblastoma with intensive chemotherapy, radiotherapy, autologous bone marrow transplantation, and 13-cis-retinoic acid. *Children's Cancer Group. N. Engl. J. Med.* **341**(16), 1165–73 (1999)
- Richards, D.M., Hettinger, J., Feuerer, M.: Monocytes and Macrophages in cancer: development and functions. *Cancer Microenviron* **6**(2), 179–191 (2013)
- Tariq, M., et al.: Macrophage polarization: anti-cancer strategies to target tumor-associated macrophage in breast cancer. *J. Cell. Biochem.* **118**(9), 2484–2501 (2017)
- Taniguchi, K., et al.: Essential role of lysophosphatidylcholine acyltransferase 3 in the induction of macrophage polarization in PMA-Treated U937 Cells. *J. Cell. Biochem.* **116**(12), 2840–2848 (2015)
- Murray, P.J., et al.: Macrophage activation and polarization: nomenclature and experimental guidelines. *Immunity* **41**(1), 14–20 (2014)
- Mantovani, A., et al.: Macrophage polarization: tumor-associated macrophages as a paradigm for polarized M2 mononuclear phagocytes. *Trends Immunol.* **23**(11), 549–555 (2002)
- Hadjidaniel, M.D., et al.: Tumor-associated macrophages promote neuroblastoma via STAT3 phosphorylation and up-regulation of c-MYC. *Oncotarget* **8**(53), 91516–91529 (2017)
- Herrera, M., et al.: Cancer-associated fibroblast and M2 macrophage markers together predict outcome in colorectal cancer patients. *Cancer Sci.* **104**(4), 437–444 (2013)
- Fujii, N., et al.: Cancer-associated fibroblasts and CD163-positive macrophages in oral squamous cell carcinoma: their clinicopathological and prognostic significance. *J. Oral Pathol. Med.* **41**(6), 444–451 (2012)
- Hashimoto, O., et al.: Collaboration of cancer-associated fibroblasts and tumour-associated macrophages for neuroblastoma development. *J. Pathol.* **240**(2), 211–223 (2016)
- Livak, K.J., Schmittgen, T.D.: Analysis of relative gene expression data using real-time quantitative PCR and the 2^{-ΔΔC_T} Method. *Methods* **25**(4), 402–408 (2001)
- Meyer, R.G., et al.: Prophylactic transfer of CD8-depleted donor lymphocytes after T-cell-depleted reduced-intensity transplantation. *Blood* **109**(1), 374–382 (2007)
- Zhang, M., et al.: A high M1/M2 ratio of tumor-associated macrophages is associated with extended survival in ovarian cancer patients. *J. Ovarian Res.* **7**, 19 (2014)
- Jackute, J., et al.: Distribution of M1 and M2 macrophages in tumor islets and stroma in relation to prognosis of non-small cell lung cancer. *BMC Immunol.* **19**(1), 3 (2018)

18. Ryder, M., et al.: Increased density of tumor-associated macrophages is associated with decreased survival in advanced thyroid cancer. *Endocr. Relat. Cancer* **15**(4), 1069–1074 (2008)
19. Subimerb, C., et al.: Tissue invasive macrophage density is correlated with prognosis in cholangiocarcinoma. *Mol. Med. Rep.* **3**(4), 597–605 (2010)
20. de Gaetano, M., et al.: M1- and M2-type macrophage responses are predictive of adverse outcomes in human atherosclerosis. *Front. Immunol.* **7** (2016)
21. Miyasato, Y.: High density of CD204-positive macrophages predicts worse clinical prognosis in patients with breast cancer **108**(8), 1693–700 (2017)
22. Chanmee, T., et al.: Tumor-associated macrophages as major players in the tumor microenvironment. *Cancers (Basel)* **6**(3), 1670–1690 (2014)
23. Cetinkaya, C., et al.: Combined IFN-gamma and retinoic acid treatment targets the N-Myc/Max/Mad1 network resulting in repression of N-Myc target genes in MYCN-amplified neuroblastoma cells. *Mol. Cancer Ther.* **6**(10), 2634–2641 (2007)
24. Austenaa, L.M., Ross, A.C.: Potentiation of interferon-gamma-stimulated nitric oxide production by retinoic acid in RAW 264.7 cells. *J. Leukoc Biol.* **70**(1), 121–9 (2001)

Part XVII
Molecular and Cellular Biology in Medicine

Design and Development of a Novel Anticancer Peptide from Human Gut Microbiome by Using Recombinant Protein Engineering

Thi Kim Cuc Nguyen, Thu Thuy Pham, Thi Bich Mai Huynh, Thanh Hoang Tran, Michael Packianather, Chi Hieu Le, and Van Duy Nguyen

Abstract

Human microbiota is a microbial community that lives on and in the human body. It has received considerable attention and research efforts over the past decade because it exerts a major impact on human health, from metabolism to immunity. In a recent study, we identified novel anticancer Azurin-like peptides from the human gut microbiome using combined molecular biology and bioinformatics based approaches. Herein, we present the cloning, expression and partial purification of one of these peptides as a case study towards the design and development of novel anticancer peptide drugs by the use of recombinant protein engineering. Firstly, the vector pET42a(+) is used for the cloning of a peptide Cnazu8 encoded by *p2seq12* (*cnazu8*) from *Clostridium nexile* DSM 1718 in *E. coli* OmniMAX. Secondly, this vector is further used for expression in *E. coli* BL21 (DE3). Finally, protein purification is performed in a HisPur Ni-NTA column (Thermo). The results show that the plasmid pDT008 allows Cnazu8 to express in fusion with GST-6xHis-TEV in *E. coli*. The optimal conditions for expression of the fusion peptide GST-6xHis-TEV-Cnazu8 (36.7 kDa) include IPTG at 0.05 mM and the temperature at 37 °C. However, most of the expected proteins are expressed in the insoluble forms. Thus, a sonication method for cell disruption is developed to increase the solubility of the desired proteins. The purification results in a relatively low amount of desired fusion proteins. Thus, the purification optimization and

anticancer bioassays of Cnazu8 are required to further consider as a novel anticancer drug candidate.

Keywords

Anticancer peptide • *Clostridium nexile* • Expression • Human gut microbiome • Purification

1 Introduction

Cancer is one of the leading causes of deaths in the world and in Vietnam. The major treatment method is tumor surgical resection followed by radiation and chemotherapy [1]. However, these methods can cause side effects to normal cells and resistant to drugs. Thus, many efforts have been made to develop more effective treatments, including biomedical therapy based on anticancer peptides from bacteria.

Azurin, a bacteriocin produced by the pathogenic bacterium *Pseudomonas aeruginosa*, can reveal selectively cytotoxic and induce apoptosis in cancer cells but cause no apparent effects on normal cells [2]. After overcoming two phase I trials, a functional region of Azurin at amino acids from 50 to 77 (p28) is recommended to use in cancer therapy by several US patents [3] and has been approved as a drug for the treatment of brain tumor glioma by FDA [4]. A recent study indicated that Azurin may be used as an adjuvant to improve the treatment effect to lung cancer [5].

We have recently screened Azurin-like bacteriocins from human gut microbiome with potential anticancer activity [6, 7]. Cnazu8 encoded by the *p2seq12* (*cnazu8*) gene in *Clostridium nexile* DSM 1787 is one of these peptides. In order to design and develop a novel anticancer peptide drug based on Recombinant Protein Engineering, major problems such as the low stability and solubility of recombinant proteins and their unspecific binding during purification must be addressed. In this study, we have overcome these problems to conduct successfully the cloning and expression of the

T. K. C. Nguyen · T. T. Pham · T. B. M. Huynh · T. H. Tran
V. D. Nguyen (✉)
Institute of Biotechnology and Environment, Nha Trang
University, Nha Trang, Vietnam
e-mail: duynv@ntu.edu.vn; V.Nguyen@gre.ac.uk

M. Packianather · V. D. Nguyen
School of Engineering, Cardiff University, Cardiff, UK

C. H. Le · V. D. Nguyen
Faculty of Engineering and Science, University of Greenwich,
Chatham, Kent, UK

cnazu8 gene in *E. coli* and the partial purification of the respective protein.

2 Materials and Methods

2.1 Plasmid, Enzyme, Bacterial Strain, Oligonucleotide and Synthetic Gene

Plasmid pET42a(+) (Novagen) is used for gene cloning and protein expression in *E. coli* (Fig. 1). Enzymes include *Pfu* DNA polymerase (New England Biolabs), *My Taq* DNA polymerase (Bioline), *Bam*HI and *Eco*RI (Fermentas).

E. coli OmniMAX (Invitrogen) for cloning and *E. coli* BL21(DE3) (Novagen) for gene expression were grown aerobically in Luria-Bertani (LB) broth at 37 °C.

A *cnazu8*-carrying synthetic DNA fragment and oligonucleotide primers (Macrogen, Korea) were used in PCR to obtain *cnazu8* gene. Primers include Cnazu8_BamHI_F (GTA CTT CCA GGG ATC CAT GAA TCT GAT ATA CTG TAA ACA CTA CAG AAA G); Cnazu8_EcoRI_R (GGC CTG TAC AGA ATT CTT AAT CAC TAA TTC TGA TTT GAA TTT GG); and pET42a(+)_F_colony (GTT TGG TGG TGG CGA CCA TC).

2.2 The Construction of Expression Plasmid

Cnazu8 gene was obtained by using PCR method based on *cnazu8*-carrying synthetic DNA fragment with specific

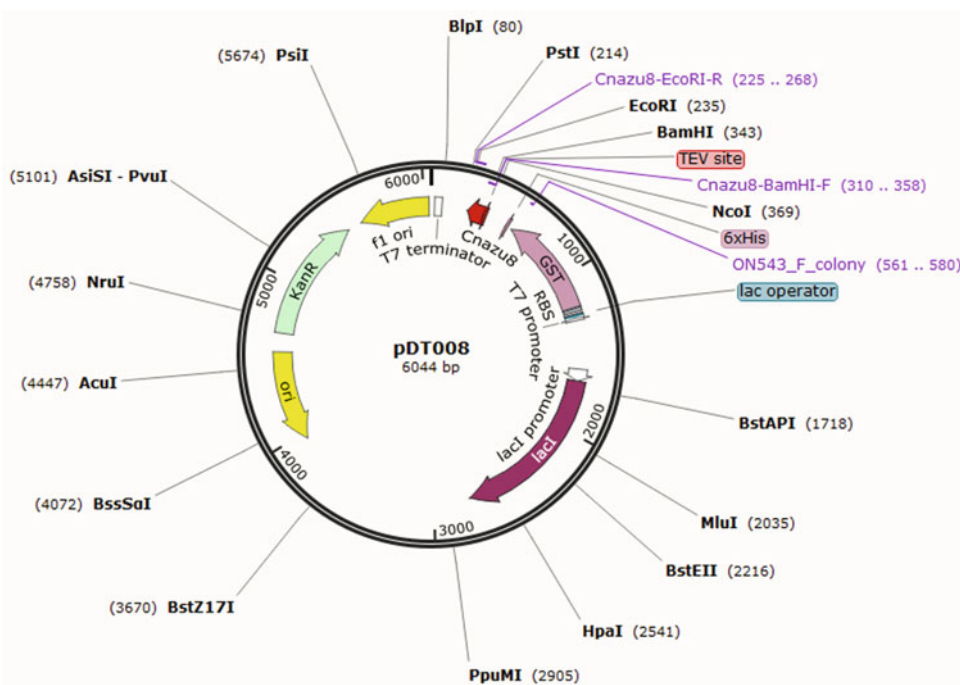
primers Cnazu8_BamHI_F and Cnazu8_EcoRI_R. The purified amplicons and pET42a(+) were then digested with *Eco*RI and *Bam*HI. *Cnazu8* was ligated into pET42a(+) by T4 DNA ligase (Fermentas) to construct a recombinant vector called pDT008 (Fig. 1). The pDT008 was transformed into the competent *E. coli* OmniMAX and *E. coli* BL21 (DE3). Transformants were screened by colony PCR and then recombinant colonies were purified by the GeneJET Plasmid Miniprep Kit (Bioline). The recombinant vectors were confirmed by PCR and DNA sequencing (Macrogen, Korea).

2.3 The Expression of Bacteriocin Cnazu8 in E. Coli

The pDT008-carrying *E. coli* strain BL21(DE3) was selected on LB agar plates with kanamycin (30 µg/ml). The expression was induced by the addition of isopropyl-β-D-thiogalactopyranoside (IPTG) and cultures were grown for 3 h at 37 °C. Two ml of cultures were collected and bacterial cell pellets were harvested by centrifugation at 8000 × g for 30 min at 4 °C, followed by suspended in Tris-Cl buffer (500 mM NaCl, 5% glycerol), pH 8.0 and sonicated on ice. The cell pellet and supernatant were harvested by the same centrifugation. Protein solutions were analyzed by SDS-PAGE and stained with Coomassie Brilliant Blue.

To find the optimal concentration of inducer for expression, the final IPTG concentrations of 0.01, 0.05, 0.1 and

Fig. 1 pDT008 (T7-GST-6xHis-TEV-Cnazu8, Kan)



0.5 mM in cultures were examined at 37 °C in the mid exponential phase for 3 h with shaking at 150 rpm. To find the optimal induction temperature, cultures were incubated at three different temperatures (23, 30 and 37 °C) with the defined optimal inducer concentration at the same condition.

2.4 The Extraction and Purification of Bacteriocin Cnazu8

The extraction of the fusion Cnazu8 was performed by sonication as described above with an exception that a step of freezing the bacterial cell pellet at -40 °C for overnight before sonication was added. The supernatant containing the soluble Cnazu8 was purified by using a HisPur Ni-NTA column (Thermo, USA) according to the manufacturer instructions. Protein fractions were analyzed by SDS-PAGE.

3 Results and Discussions

3.1 The Cloning of Cnazu8 Gene

The *cnazu8* gene (134 bp) was obtained by using PCR and analyzed by agarose gel electrophoresis (*data not shown*). Then it was cloned into the plasmid pET42a(+) for construction of the recombinant plasmid pDT008, which was used to transform into the cloning host *E. coli* OmniMAX and the expression host *E. coli* BL21 (DE3). These purified recombinant plasmids were confirmed by using colony PCR method with the expected sizes of the PCR products (356 bp) (*data not shown*). These results in combination with the DNA sequencing (*data not shown*) confirmed that *cnazu8* was successfully cloned into pET42a(+) in *E. coli* BL21.

3.2 Inducer Concentration Optimization

SDS-PAGE analysis (Fig. 2) showed that the expected fusion Cnazu8 (36.7 kDa) was highly expressed with IPTG induction at the concentrations of 0.5, 0.1 and 0.05 mM but lowly expressed at 0.01 mM IPTG. The expected protein was less expressed in the control sample without IPTG induction. The expected fusion Cnazu8 was not observed in all supernatants (lanes S) but it was observed in the pellets (lanes P). These results have showed that the IPTG concentration of 0.05 mM is enough to induce the recombinant GST-6xHis-TEV-Cnazu8 expression and this protein has a major fraction existing in pellet in an insoluble status. Thus, it is necessary to investigate the optimal temperature in this case after an induction with 0.05 mM IPTG.

3.3 Temperature Optimization

The results revealed that the expression of the recombinant Cnazu8 was the highest at 37 °C under the induced IPTG concentration at 0.05 mM and decreased gradually from 30 to 23 °C with the same IPTG concentration (Fig. 3). However, the fusion Cnazu8 was detected in the component of pellet (lanes P, Fig. 3) under induction at all three temperatures (23, 30 and 37 °C), but not in the components of supernatants (lanes S, Fig. 3). These results indicated that this fusion protein was insoluble, thus, it was very difficult to purify it. Therefore, it is required to improve the solubility of the fusion Cnazu8 by using other purification methods.

E. coli is the most frequently employed host with many available expression systems for producing recombinant proteins. However, its use for the production of recombinant proteins is facing a number of practical problems. For example, the stability and solubility of recombinant proteins produced in *E. coli* can be low due to proteolytic degradation and the formation of inclusion bodies, respectively [8]. The major factors affecting the expression and the solubility of recombinant protein are inducer concentration and induction temperature [9]. Higher temperatures for post-induction (37 °C) often lead to more biomass and more recombinant protein yield [8]. However, reduced or low temperatures can be effective in improving the solubility of some proteins that are difficult to express [10].

In the present study, we found that the best expression of recombinant GST-6xhis-TEV-Cnazu8 occurred at 37 °C with the induction by IPTG at final concentration of 0.05 mM. However, this recombinant Cnazu8 was in insoluble form as inclusion bodies existing in cell pellet. Reducing temperature to 30 and 23 °C for post-induction also did not increase the yield of soluble protein fractions. There are two approaches to overcome these problems that include further expression optimization of soluble recombinant with other factors (culture media, host strains, expression system, etc.) and extraction optimization for improving the solubility of protein [10]. Here we performed a minor modification in extraction method, freezing the cell pellet at -40 °C for overnight before sonication, thus improved significantly the yield of soluble Cnazu8.

3.4 The Extraction and Purification of the Fusion Cnazu8

The soluble fusion Cnazu8 was highly expressed in components of supernatant that were obtained from the sonication with freezing of the cell pellet (lane S3, Fig. 4 left), but very lowly expressed in components of supernatant obtained from the sonication without freezing of the cell pellet (lane

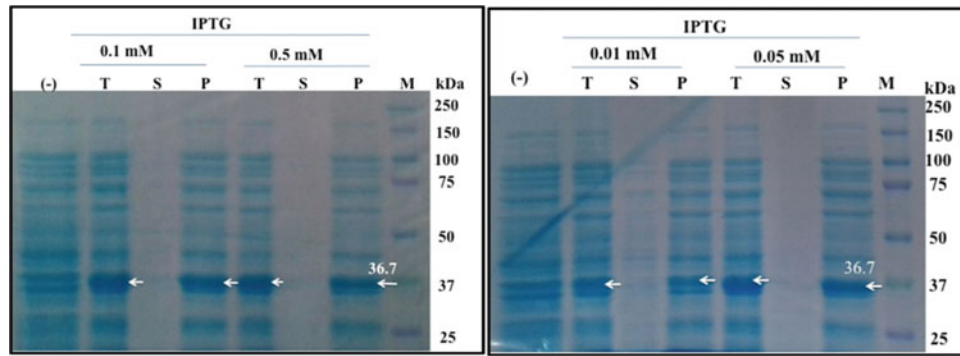


Fig. 2 SDS-PAGE (12%) analysis of Cnazu8 expression in *E. coli* BL21 (DE3) at the different concentrations of IPTG. M: molecular weight marker; T: total protein for 3 h induction at 37 °C; P: pellet

for 3 h induction at 37 °C; S: supernatant for 3 h induction at 37 °C; (-) control (uninduced). The expected protein band is indicated with arrows

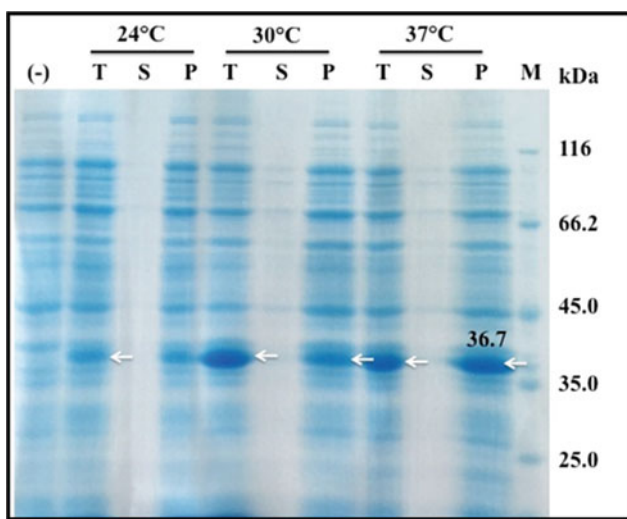


Fig. 3 SDS-PAGE (12%) analysis of the recombinant Cnazu8 expression in *E. coli* BL21 (DE3) at the different temperature conditions. M: molecular weight marker; T: total protein for 3 h induction at 37 °C; P: pellet for 3 h induction at 37 °C; S: supernatant for 3 h induction at 37 °C; (-) control (uninduced)

S2, Fig. 4 left). The results showed that the solubility of the Cnazu8 was improved significantly by the combination of the freezing of the cell pellet with sonication.

The results from Fig. 4(right) indicated that the expected protein band (36.7 kDa) presented in all elution fractions. This suggested that the GST-6xHis-TEV-Cnazu8 bound on column and was eluted from column but the binding of this protein on column was low efficient and non-specific.

According to theory, the fusion GST-6xhis-TEV-Cnazu8 can be purified by specific binding of his-tag with immobilized metal-ion in Ni-NTA column, but our results have indicated that there is at least an unspecific protein in Ni-NTA column. This lead to the low binding efficiency of GST-6xhis-TEV-Cnazu8 with immobilized metal-ion in Ni-NTA column. Several approaches have been used to reduce the unspecific binding of proteins, including the use of higher imidazole concentration in the washing buffer. Moreover, the concentration of imidazole for washing and elution is a powerful tool to increase purity and specificity in the purification process [11]. Therefore, further studies are

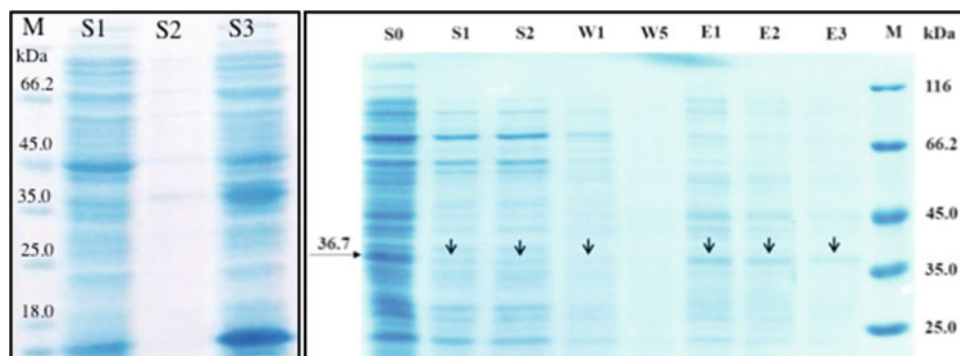


Fig. 4 SDS-PAGE (12%) of soluble fusion protein Cnazu8 in *E. coli* BL21 (DE3) obtained by sonication (left) and purified by HisPur Ni-NTA kit (right). M: molecular weight marker. Left, S1: soluble protein of control (uninduced); S2: soluble protein extract by sonication without storing at -40 °C; S3: soluble protein extract by

sonication stored at -40 °C. Right, S₀: pre-purified sample; S₁₋₂: Samples after column binding (the first time and the second time); W₁₋₅: samples after column washing (the first time and the fifth time); E₁₋₃: samples of eluted fractions (the first time to the third time)

required to define the optimal conditions of purification method and evaluate the anticancer activity of this purified protein.

In conclusions, we report the successful cloning and expression of the recombinant Cnzu8 protein from *Clostridium nextile* DMS in *E. coli*. This recombinant protein is highly expressed with the optimal conditions including 0.05 mM IPTG and the temperature at 37 °C and is extracted by the sonication of biomass stored at -40 °C.

Acknowledgements This work was supported by a grant no.106-YS.04-2014.40 from the Vietnam National Foundation for Science and Technology Development (NAFOSTED).

Conflicts of Interest Statement All authors have no conflicts of interest to declare.

References

1. Chakrabarty, A.M., Bernardes, N., Fialho, A.M.: Bacterial proteins and peptides in cancer therapy: today and tomorrow. *Bioengineered* **5**(4), 234–242 (2014)
2. Taylor, B.N., Mehta, R.R., Yamada, T., Lekmine, F., Christov, K., Chakrabarty, A.M., Green, A., Bratescu, L., Shilkaitis, A., Beattie, C.W., Das Gupta, T.K.: Noncationic peptides obtained from azurin preferentially enter cancer cells. *Cancer Res.* **69**(2), 537–546 (2009)
3. Fialho, A.M., Bernardes, N., Chakrabarty, A.M.: Recent patents on live bacteria and their products as potential anticancer agents. *Recent Pat. Anticancer Drug Discov.* **7**(1), 31–55 (2012)
4. Fialho, A.M., Bernardes, N., Chakrabarty, A.M.: Exploring the anticancer potential of the bacterial protein azurin. *AIMS Microbiol* **2**(3), 292–303 (2016)
5. Bernardes, N., Abreu, S., Carvalho, F.A., Fernandes, F., Santos, N. C., Fialho, A.M.: Modulation of membrane properties of lung cancer cells by azurin enhances the sensitivity to EGFR-targeted therapy and decreased β 1 integrin-mediated adhesion. *Cell Cycle* **15**(11), 1415–1424 (2016)
6. Nguyen, V.D., Nguyen, H.H.C.: Molecular screening of Azurin-like anticancer bacteriocins from human gut microfora using bioinformatics. *Adv. Intell. Syst. Comput.* **358**, 219–229 (2015)
7. Nguyen, C., Nguyen, V.D.: Discovery of azurin-like anticancer bacteriocins from human gut microbiome through homology modeling and molecular docking against the tumor suppressor p53. *Biomed. Res. Int.* **2016**, 8490482 (2016)
8. Choi, J.H., Keum, K.C., Lee, S.Y.: Production of recombinant proteins by high cell density culture of *Escherichia coli*. *Chem. Eng. Sci.* **61**, 876–885 (2006)
9. Vincentelli, R., Cimino, A., Geerlof, A., Kubo, A., Satou, Y., Cambillau, C.: High-throughput protein expression screening and purification in *Escherichia coli*. *Methods* **55**(1), 65–72 (2006)
10. Sheng, J., Yu, H., Li, J., Sheng, G., Zhou, L., Lu, Y.: Cloning and expression of the human augmenter of liver regeneration at low temperature in *Escherichia coli*. *J. Biochem. Biophys. Methods* **70** (3), 465–470 (2007)
11. Arnau, J., Lauritzen, C., Petersen, G.E., Pedersen, J.: Current strategies for the use of affinity tags and tag removal for the purification of recombinant proteins. *Protein Expr. Purif.* **48**(1), 1–13 (2006)

A Label-Free Electrochemical Immunosensor for Detection of Newcastle Disease Virus

Tran Quang Thinh, Trieu Van Vu Quan, Le Binh Dươ̄ng,
Tran Hong Thuy, Chu Thi Xuan, and Mai Anh Tuan

Abstract

In this study, a label-free electrochemical immunosensor system was designed and fabricated with focus on a detection of Newcastle disease virus (NDV). The chicken egg yolk antibodies (IgY) against NDV was used as the biological recognition element to replace IgG antibody, which offers some advantages with respect to animal care, high productivity and special suitability in the source of antibodies. The IgY against NDV was immobilized on sensor surface using the chemical approach. The immunosensor showed high sensitivity with NDV concentration range from 10^6 to 10^2 EID₅₀/mL. This relatively simple fabrication is potential for applications in infection studies.

Keywords

Immunosensor • IgY antibody • Newcastle disease virus (NDV)

1 Introduction

Newcastle disease (ND) has been defined by the World Health Organisation (WHO) as infection of poultry with an avian paramyxovirus (APMV-1 serotype) that belongs to the genus Rubulavirus of the family Paramyxoviridae [1]. Newcastle disease virus (NDV) occurs worldwide and causes severe economic loss to the poultry industry in developing countries, including Vietnam [2]. To date, the conventional qualitative methods such as haemagglutination

inhibition (HI) [3], agar gel precipitation [4] and Latex agglutination tests [5] have been introduced for clinical diagnosis of ND. In addition, enzyme-linked immunosorbent assay (ELISA) [4], polymerase chain reaction (PCR) [7] and immunofluorescence test [8] have also been used for the semi-quantitative analysis. Although these methods effectively determine NDV in infective samples, they require complicated procedures for sample preparations and sophisticated instruments for assays, leading to significant time consuming. Therefore, alternative methods that offer a simple, rapid, cost-effective analytical strategy, and possible on-site and in-field measurements are essential.

Label free electrochemical immunosensor has been developed with rapid analysis, high sensitivity, amenability to miniaturization, and portability purposes [9, 10]. As a type of modern biosensor, it results from a combination of the traditional immunoassay approach with electrochemical analysis in which immunoreactions are coupled to a transducer surface to generate the output electrochemical signal. Antibodies are employed as bio-receptors to capture and detect directly an antigen of interest.

Immunoglobulin Y (IgY) is known as a typical low-molecular-weight antibody of birds, reptiles, amphibian, and lungfish [11]. Antigen-specific IgY antibodies are produced at a large scale by immunization and purification technology from chicken egg yolk. In recent years, development of immunology has allowed the production of highly specific IgY antibodies against a number of antigens [11], such as E. coli bacteria, influenza virus, potato virus, P110 protein (antigen of human stomach cancer), Newcastle disease virus, and so on. In comparison with serum immunoglobulin G antibodies (IgG) extracted from mammalian blood, IgY offers some advantages with respect to animal care, high productivity and special suitability in the source of antibodies.

In this work, chicken egg yolk antibody (IgY) was used as a bioreceptor in electrochemical immunosensor for direct detection of NDV without any labelling step. IgY immobilization on working surface area of gold electrodes (WE) was implemented by combining self-assembly

T. Quang Thinh (✉) · T. Van Vu Quan · L. B. Dươ̄ng
M. Anh Tuan
National Center for Technological Progress, Hanoi, Vietnam
e-mail: thinh.tran@mph.vn

M. Anh Tuan
e-mail: tuan.maianh@mph.vn; ; tuan.maianh@gmail.com

T. H. Thuy · C. T. Xuan · M. Anh Tuan
Hanoi University of Science and Technology, Hanoi, Vietnam

modification of thiol-carboxylic acids (SAM) and the activation based on N-succinimidyl ester (NHS). Furthermore, electrochemical sensors encapsulated with a polydimethylsiloxane (PDMS) microreactor facilitate low-volume immunoassay and help in electrical connection with measuring circuit.

2 Materials and Methods

2.1 Chemicals

Bovine serum albumin (BSA), phosphate buffer solution (PBS, 0.01 M, pH 7.4), $K_4Fe(CN)_6$, $K_3Fe(CN)_6$, KCl, thioglycolic acid (TGA), N,N'-dicyclohexylcarbodiimide (DCC), N-hydroxysuccinimide (NHS), and N,N-dimethylformamide (DMF) were purchased from Sigma-Aldrich. All other reagents were of analytical grade and used without further purification. Chicken egg yolk antibody against NDV (IgY, 60 $\mu\text{g}/\text{mL}$) were obtained from Biotech-Vet Co. (Hanoi, Vietnam). Inactivated NDV (10^6 EID₅₀/mL) was purchased from Hanvet Co. JSc. (Hanoi, Vietnam).

2.2 Measuring Setup

The integrated Au electrodes consisted of a 1 mm in diameter working electrode (WE) and a counter electrode (CE) in an $8.5 \times 12.2 \text{ mm}^2$ chip size. These electrodes were deposited on SiO_2/Si substrate by cathode sputtering technique [12]. The (100 μm in diameter) Ag/AgCl wire, used as a quasi-reference electrode (qRE), was prepared by the ion-exchange reaction of a silver wire with FeCl_3 solution [13]. The micro-reactor with an open chamber (cylindrical shape 5 mm in diameter, 5 mm in depth) on a glass substrate was fabricated by the molding-based PDMS solidification [14]. The three-electrode system were integrated into the PDMS microreactor in which the qRE is immersed in 50 μL

of the electrolyte solution containing 30 mM $\text{Fe(CN)}_6^{3-/4-}$ (1:1) and 100 mM KCl, Fig. 1.

2.3 IgY Antibody Immobilization

To prepare a clean surface before immobilizing IgY antibody, the integrated Au electrodes were pre-treated in acetone, piranha solution ($\text{H}_2\text{O}_2:\text{H}_2\text{SO}_4$, 3:7) and ethanol. The electrodes were then rinsed with deionized water and nitrogen dried. The schematic of antibody immobilization process using SAM/NHS is shown in Fig. 2.

The Au WE was incubated with ethanol solution of 10 mM TGA for 24 h for self-assembly modification (SAM) to occur. The excess TGA molecules on the modified WE was removed by rinsing with ethanol. The SAM-modified Au WE was treated with a DMF solution of 0.2 M DCC and 0.1 M NHS for 1 h at room temperature to convert the terminal carboxylic group to the active NHS ester. After rinsing with deionized water, the WE was incubated with 60 $\mu\text{g}/\text{mL}$ solution (borate buffer, pH = 8.2) of IgY for 12 h at 4 $^\circ\text{C}$. The excess antibodies were then washed off with PBS. BSA solution (1% wt./vol. in PBS) was used to block un-bound sites. Finally, the immunosensor obtained by antibody immobilization was rinsed with PBS, nitrogen dried and stored at 4 $^\circ\text{C}$.

2.4 Newcastle Disease Virus Detection

For an immunoassay, the immunosensor was interfaced into the microreactor as the procedure of measuring setup. 20 μL NDV sample (with various concentrations of the NDV in 0.01 M PBS, pH 7.4) was injected into the chamber. After the system had been incubated for 1 h at 25 $^\circ\text{C}$, it was rinsed three times with PBS buffer. Electrolyte, composing of 0.1 M KCl and 0.03 M $\text{Fe(CN)}_6^{3-/4-}$ (1:1) as a redox couple, was pumped into the microchamber. Cyclic voltammetry (CV) measurements were performed using EC301 Stanford

Fig. 1 a Schematic illustration of the measuring setup and b equivalent circuit of the measuring system

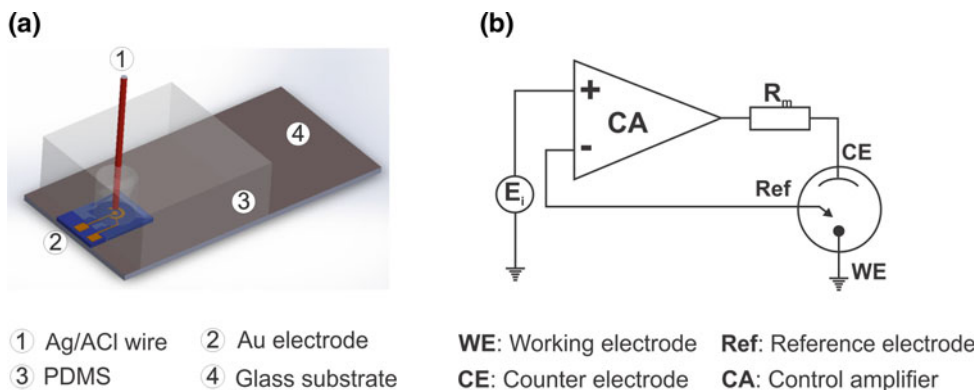
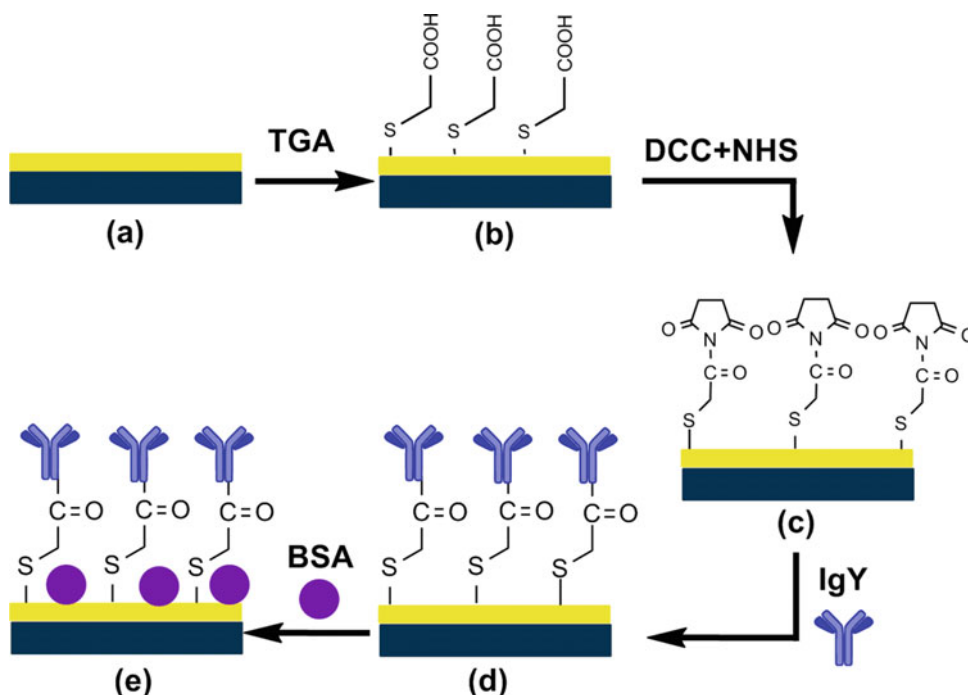


Fig. 2 Steps of antibody immobilization



Research Systems, the potential was cycled from -0.1 to 0.5 V with scan rate 25 mV/s.

3 Result and Discussion

3.1 Electrochemical Sensing System

The three-electrode system in which the fabricated Ag/AgCl electrode used as qRE was electrochemically characterized in $\text{Fe}(\text{CN})_6^{3-/4-}$ solution at 25 mV/s scan rate inside the microchamber. As shown in Fig. 3, two peaks at 0.11 and 0.21 V appear on the cyclic voltammogram, corresponding to the oxidation potential of $\text{Fe}(\text{CN})_6^{4-}$ and reduction potential of $\text{Fe}(\text{CN})_6^{3-}$ versus Ag/AgCl (0.1 M KCl) qRE. The small deviation values of these peaks (E_{pa} and E_{pc}) obtained from CVs of 100 independent measurements, as shown in the insert of Fig. 3, indicate the negligible shift of reversible potentials. The micro chamber not only reduces the analytical volume but also helps keeping the constant potential of Ag/AgCl qRE, and thereby maintaining accuracy of the sensing system.

3.2 Characterization of Immunosensor

Each step of gold WE electrodes modification was examined using CV in the electrolyte including 0.03 M $\text{Fe}(\text{CN})_6^{3-/4-}$ (1:1) as redox marker inside the microchamber. The formation of material layers onto the gold WE electrode leads

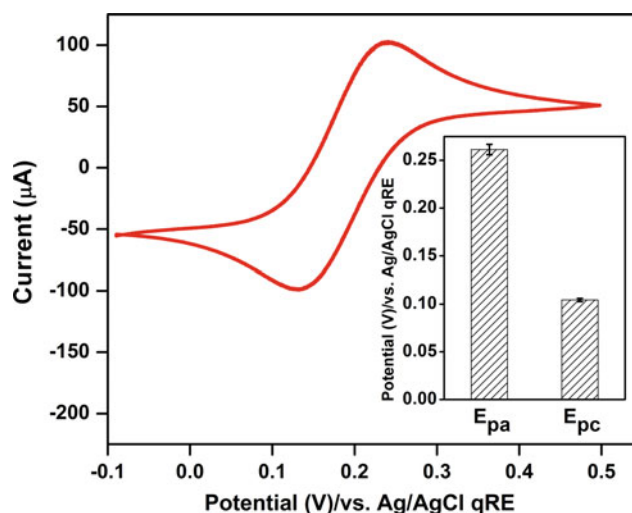


Fig. 3 CV characterization of the electrochemical sensor with bare gold WE measured in the microchamber with Ag/AgCl qRE. Insert shows the repeatability of two potential peaks of CVs obtained from different measurements

to the change of electrode surface processes that recognized in the corresponding CVs as shown in Fig. 4. A reversible CV with the largest peak-to-peak separation (I_p , $I_p = I_{cathodic} - I_{anodic}$) of 202.8 μA was observed (Fig. 4, curve a) at the bare-Au electrode that have no obstacles affecting electron transfer. When a self-assembled modification (SAM) of TGA is formed on the bare-Au electrode (as shown in Fig. 2b), the I_p of the CV response almost disappeared (curve b, Fig. 4). The SAM of TGA built on the electrode

surface through strong gold-thiolate bonds is considered as a highly insulating layer blocking almost all the faradic currents [15]. The reason for this is that the negatively charged terminal carboxyl groups of TGA (formed by the deprotonation in aqueous solution) prevents the transfer of negative $\text{Fe}(\text{CN})_6^{3-/4-}$ redox couple to the electrode surface creating a depleted layer between the sensor surface and solution. As shown in Fig. 2c, when the TGA layer was activated by DCC and NHS, the negatively charged carboxyl groups of TGA were replaced by the neutrally charged NHS-esters that facilitate the transfer of negative $\text{Fe}(\text{CN})_6^{3-/4-}$ at the electrode surface. This is recognized by a significant increase of the I_p (132.3 μA) on the CV (curve c, Fig. 4). The immobilization of IgY antibodies on the sensor's surface in which active NHS-esters are coupled with amine groups of anti-NDV IgY (Fig. 2d) leads to an increase in the charge transfer resistance of $\text{Fe}(\text{CN})_6^{3-/4-}$, thereby reducing the I_p to 124.7 μA . When the immunosensor is treated with BSA, the I_p decreased to 116.7 μA (curve e, Fig. 4), which was attributed to the presence of BSA on the surface of the electrode.

3.3 Newcastle Disease Virus Detection

The proposed immunosensor was employed to directly detect NDV by analysis of peak current shifts in CV responses that were recognized when immunoreaction occurred. As observed in the insert of Fig. 5, the specific IgY-NDV interaction on the surface of the immunosensor causes a considerable decrease of the peak current compared to that of immunosensor without immune bindings. The presence of NDVs inhibits the charge transfer process of Fe

$(\text{CN})_6^{3-/4-}$ on the electrode surface, resulting in a decrease in current response.

The performance of the fabricated immunosensor was evaluated by determining inactivated NDV solution with a range of various concentration from 10^2 to 10^6 EID₅₀/mL. For each NDV concentration, three CV measurements were performed similarly using three immunosensors. The output signal of the immunosensor as $\Delta I_p/I_p$ is calculated by the following equation:

$$\frac{\Delta I_p}{I_p} = \frac{I_{peak}(0) - I_{peak}(i)}{I_{peak}(0)} \quad (1)$$

where $I_{peak}(0)$ is the I_{peak} of the immunosensor treated with 0 EID₅₀/mL NDV (in 0.01 M PBS, pH = 7.4), and $I_{peak}(i)$ is the I_{peak} of the immunosensor obtained after incubating with a certain NDV sample.

As seen from Fig. 5, the $\Delta I_p/I_p$ of the immunosensor decreased when the concentration of NDV was diluted from 10^6 EID₅₀/mL to 10^2 EID₅₀/mL, which reflected the decreased binding of NDV to IgY-immobilized electrode. In this range of concentrations, the immunosensors also showed the linear relationship between $\Delta I_p/I_p$ and $\log[\text{C}_{\text{NDV}}]$ with the regression equation of $\Delta I_p/I_p = 0.0588 \times \log[\text{C}_{\text{NDV}}] + 0.2606$ ($R^2 = 0.991$). According to Michael Swartz [16], the limit of detection (LOD) of a sensor can be determined by the following equation:

$$\text{LOD} = \frac{3.3 \times \sigma}{S} \quad (2)$$

where σ is the standard deviation of the response y-intercept of the regression line and S is the slope of the calibration

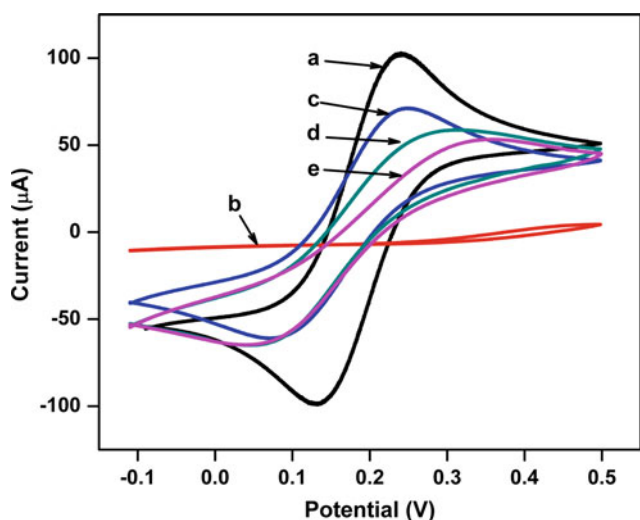


Fig. 4 CVs of the sensor at each a different modification step: **a** bare Au electrode, **b** TGA/Au electrode, **c** NHS/TGA/Au electrode, **d** IgY/NHS/TGA-Au electrode, **e** BSA/IgY/NHS/TGA-Au electrode

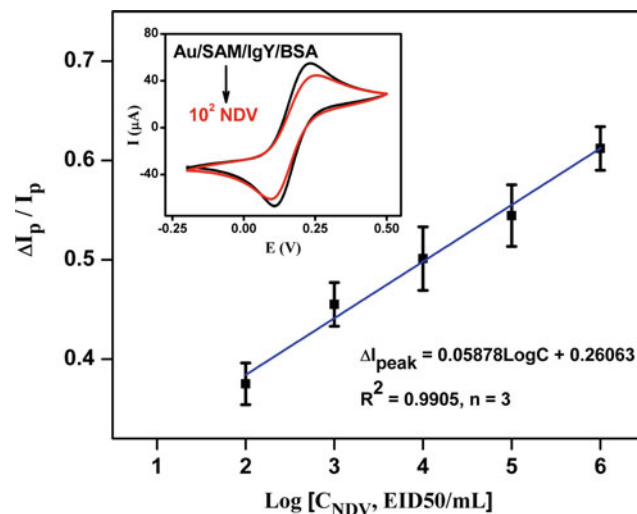


Fig. 5 Calibration curve of the $\Delta I_p/I_p$ versus NDV concentration. Insert shows the change of CV responses when the immunosensor (Au/SAM/IgY/BSA) is employed to directly detect NDV at the concentration of 10^2 EID₅₀/mL (10^2 NDV)

curve. From the data shown in Fig. 5, LOD of the presented immunosensor was 5 EID₅₀/mL. This result shows that the IgY-based immunosensor has a good sensitivity for the NDV detection in comparison with other immunological sensing methods using IgG antibodies and labeling reagents [6, 17].

4 Conclusion

A miniaturized microreactor-integrated electrochemical immunosensor using gold electrodes was prepared for label-free detection of influenza NDV. The anti-NDV IgY antibody as the immune recognition element was immobilized on the electrode surface by the SAM/NHS strategy. The immunosensor exhibited a wide linear range from 10² to 10⁶ EID₅₀/mL with a low detection limit of 5 EID₅₀/mL for NDV. By employing IgY antibodies to replace conventional IgG antibodies on immunoassay, the electrochemical immunosensor may not only reduce analysis costs but also provides an effective solution for rapid detection of infectious diseases in poultry.

Acknowledgements This research is supported by Vietnam Ministry of Education and Training (MOET) under grant number B2015-01-102.

Conflict of Interest Statement The authors declare that there is no conflict of interest.

References

- Alexander, D.J.: Newcastle disease and other avian paramyxoviruses. *Rev. Sci. Tech. Off. Int. Epiz.* **19**(2), 443–462 (2000)
- Choi, K.S., Kye, S.J., Kim, J.Y., To, T.L., Nguyen, D.T., Lee, Y. J., Choi, J.G., Kang, H.M., Kim, K.I., Song, B.M., Lee, H.S.: Molecular epidemiology of Newcastle disease viruses in Vietnam. *Trop. Anim. Health Prod.* **46**(1), 271–277 (2014)
- Chaka, H., Thompson, P., Goutard, F., Grosbois, V.: Evaluation of enzyme-linked immunosorbent assays and a haemagglutination inhibition tests for the detection of antibodies to Newcastle disease virus in village chickens using a Bayesian approach. *Prev. Vet. Medicine.* **119**, 21–30 (2015)
- de Wit, J., Davelaar, F., Braunius, W.: Comparison of the enzyme linked immunosorbent assay, the haemagglutination inhibition test and the agar gel precipitation test for the detection of antibodies against infectious bronchitis and Newcastle disease in commercial broilers. *Avian Pathology.* **21**, 651–658 (1992)
- Thirumurugan, G., Jayakumar, R., Kumanan, K., Venugopalan, T., Nachimuthu, T.: Latex immunoassay for rapid detection of Newcastle disease virus. *Trop. Anim. Health Prod.* **29**(4), 227–230 (1997)
- Gong, L., Gong, C., Zeng, M., Shen, L., Yu, Q.: An amperometric immunosensor for the newcastle disease antibody assay. *Anal. Lett.* **36**, 287–302 (2003)
- Gohm, D., Thür, B., Hofmann, M.: Detection of Newcastle disease virus in organs and faeces of experimentally infected chickens using RT-PCR. *Avian Pathology.* **29**, 143–152 (2000)
- Kothlow, S., Häuslaigner, R., Kaspers, B., Grund, C.: Evaluation of Newcastle disease virus immunoassays for waterfowl using a monoclonal antibody specific for the duck immunoglobulin light chain. *Avian Pathology.* **37**, 323–328 (2008)
- Wang, Y., He, Q., Dong, Y., Chen, H.: In-channel modification of biosensor electrodes integrated on a polycarbonate microfluidic chip for micro flow-injection amperometric determination of glucose. *Sens. Actuators B: Chem.* **145**, 553–560 (2010)
- He, P., Wang, Z., Zhang, L., Yang, W.: Development of a label-free electrochemical immunosensor based on carbon nanotube for rapid determination of clenbuterol. *Food Chem.* **112**, 707–714 (2009)
- Narat, M.: Production of Antibodies in chickens. *Food Technol. Biotechnol.* **41**(3), 259–267 (2003)
- Tran, T., Chu, T., Huynh, D., Pham, D., Luu, T., Mai, A.: Effective immobilization of DNA for development of polypyrrole nanowires based biosensor. *Appl. Surf. Sci.* **314**, 260–265 (2014)
- Shinwari, M., Zhitomirsky, D., Deen, A., Selvaganapathy, R., Deen, M., Landheer, D.: Microfabricated reference electrodes and their biosensing applications. *Sensors* **10**, 1679–1715 (2010)
- Tran, T., Chu, T., Do, P., Pham, D., Trieu, V., Huynh, D., Mai, A.: In-channel-grown polypyrrole nanowire for the detection of DNA hybridization in an electrochemical microfluidic biosensor. *J. Nanomater* **2015**, 1–7 (2015)
- Ding, S., Chang, B., Wu, C., Lai, M., Chang, H.: Impedance spectral studies of self-assembly of alkanethiols with different chain lengths using different immobilization strategies on Au electrodes. *Anal. Chim. Acta* **554**, 43–51 (2005)
- Swartz, M.: Handbook of analytical validation (2012)
- Lee, W., Thompson, H.: Detection of Newcastle disease virus using an evanescent wave immuno-based biosensor. *Can. J. Chem.* **74**, 707–712 (1996)

Part XVIII
Miscellaneous

Determine the Presence of Pathogens on Ticks in the Mekong Delta Region

Le Thanh Dong and Doan Binh Minh

Abstract

Tick-borne diseases are an emerging medical and veterinary problem. Ticks are implicated in the transmission of different pathogens such as viruses, bacteria, protozoa and filarial nematodes. However, up to now researches on these pathogens in Vietnam which has been limited, especially in the Mekong Delta region (Southwestern of Vietnam). We have collected 4763 tick individuals of 7 species, 5 genus, 2 families (*Argas* sp., *Aponomma crassipes*, *Aponomma gervaisi*, *Rhipicephalus (Rhipicephalus) haemaphysaloides*, *Rhipicephalus (Rh.) sanguineus*, *Boophilus microplus*, *Ixodes (Ixodes) granulatus*) at 8 sites in the Mekong delta region on the rainy season and dry season from 2015 to 2016 which determine the presence of pathogens (*Rickettsia* spp. and *Orientia tsutsugamushi*) on ticks. A total of 1457 tick individuals which were subdivided into 299 samples, that determine the presence of *Rickettsia* spp. and *Orientia tsutsugamushi*. Initial results, we have determined the presence of pathogen on ticks.

Keywords

Ticks • *Rickettsia* spp. • *Orientia tsutsugamushi*

1 Introduction

Ticks are ectoparasites infesting many mammals, including humans and their pets. In humans, ticks can cause many serious harms such as paralysis, poisoning, irritation and allergies. Besides they transmit some infectious diseases that are considered to be a major problem in public health [1]. Ticks are recognized as the main vectors and reservoirs of spotted fever group rickettsiae. Tick-borne rickettsioses are

caused by obligate intracellular bacteria belonging to the spotted fever group of the genus *Rickettsia*. These zoonoses are among the oldest known vector-borne diseases, and include Mediterranean spotted fever, which is caused by *Rickettsia conorii* and transmitted by the brown dog tick *Rhipicephalus sanguineus*. Additionally they include most of the emerging tick-borne diseases such as the infection caused by *R. slovaca* which is transmitted by *Dermacentor* spp. [2, 3]. The Mekong delta region is a lowland area of Vietnam which has 13 provinces and cities. This is a typical habitat for mangroves with interminglement of wetlands, lowlands, rural and urban areas. Therefore, the Mekong delta region has typical ecosystem of flora and fauna, including many vertebrates species such as birds, mammals and reptiles. They are the host of ticks.

Our present study aims to capture information on (1) species composition and distribution of ticks in the Mekong delta region (2) and the presence of *Rickettsia* spp. and *Orientia tsutsugamushi* on ticks in this region. Our preliminary data is a basis for the regional monitoring of ticks, in public prevention and control of ticks transmitted diseases.

2 Materials and Methods

From 2015 (the rainy season) to 2016 (the dry season), an investigation was conducted in 8 sites of the Mekong delta region: U Minh Thuong National Park (Kien Giang province); U Minh Ha National Park (Ca Mau province); Tinh Bien district (An Giang province); Thanh Phu district (Ben Tre province); Lung Ngoc Hoang Nature Reserve (Hau Giang province); Lang Sen Wetland Reserve (Long An province); Phu Quoc Island (Kien Giang province), Ninh Kieu District (Can Tho City). This area is located in South West of Vietnam

Ticks were collected from wild animals (rats, bats, squirrels, civets...), Raising animal (dogs, cows, buffalos, goats, rabbits, monkeys...), Wild birds (Junglefowl, greater coucal,...), Raising birds (chickens, ducks, birds...),

L. T. Dong (✉) · D. B. Minh
Institute of Malariaology—Parasitology—Entomology, Ho Chi Minh, Vietnam
e-mail: lethanhdong@gmail.com

Reptiles (python, snake, turtle, geckos...), Garbage and animal nest (chicken nest, plastic sheet, soil, garbage...). Collected ticks were placed into plastic vials containing absolute ethanol and taken to the laboratory, where they were identified based on morphologic criteria following taxonomic keys [4].

For the molecular detection and analysis of *Rickettsia* species, We pooled 1–5 ticks of the same species collected from one animal host for DNA extraction, DNA was extracted by the ISOLATE II Genomic DNA Kit (Bioline, South Korea) according to the manufacturer's instructions. Multiplex PCR reactions were performed with total reaction volume was 50 µl: 25 µl 2x MyTaq HS Mix 2x (Bioline); 2.0 µl Multiplex Primer 25 nmol, to detect *Rickettsia* spp. and *Oriental tsutsugamushi*; 20 µl distilled water; 3 µl of mold DNA. PCR cycle: 94 °C for 5 min, followed by 45 cycles: 94 °C for 30 s, 56 °C for 30 s, and 72 °C for 45 s and ended at 72 °C for 7 min (Applied Biosystem 2720 Thermocycle, America) (Table 1).

PCR products were detected by DNA electrophoresis with 2% agarose in TBE containing ethidium bromide for 30 min at 120 volts and bacteria are identified based on PCR product size on.

3 Results

3.1 Species Composition and Distribution of Ticks in the Mekong Delta Region in 2015–2016

Results of host collecting in the study area

We investigated the host species of ticks on 6 groups of wild animals, raising animals, wild birds, raising birds, reptiles, garbage and animal nests at 8 survey sites in the region in the rainy season and dry season (Table 2).

The two surveys from 2015 (The rainy season)—2016 (the dry season) at 8 sites of Mekong delta region, We collected 2764 tick hosts individuals. Of which, Terrestrial vertebrates were 54 species (25 species of birds, 20 species of mammals,

9 species of reptiles) and 3 groups of Garbage and animal nest (garbage, poultry nets, plastic sheets).

Raising animals had the highest number of individuals (747 individuals of 8 species); wild animals were 648 individuals of 12 species; raising birds were 395 individuals of 8 species; Reptiles were 302 individuals of 9 species. Garbage and animal nest were 407 samples; the lowest was wild birds (266 individuals of 17 species).

Species composition of ticks in the mekong delta region in 2015–2016

There were 4763 tick individuals of 7 species, 5 genus, 2 families were identified (Table 3). In which soft ticks (*Argasidae*) were 1 genus, 1 species: *Argas* sp. (01 individual). Hard ticks (*Ixodidae*) were 4 genus, 6 species, in that *Aponomma* was 2 species: *Aponomma crassipes* (24 individuals), *Aponomma gervaisi* (31 individuals); *Rhipicephalus* has 2 species: *Rhipicephalus (Rhipicephalus) haemaphysaloides* (506 individuals), *Rhipicephalus (Rh.) sanguineus* (2828 individuals); *Boophilus*: *Boophilus microplus* (1372 individuals) and *Ixodes*: *Ixodes (Ixodes) granulatus* (01 individuals)

Distribution of ticks in the Mekong delta region in 2015–2016

Distribution of ticks on the host

Two *Aponomma* species were parasitic on reptile such as *Python molurus*, *P. molurus*, *Varanus bengalensis*, *V. salvator*. *Boophilus microplus* was parasitic on *Bos* sp., *Bubalus bubalis*. *Rhipicephalus (Rh.) Haemaphysaloides* only was parasitic on *Canis familiaris*, *Rhipicephalus (Rh.) sanguineus* was parasitic on *Canis familiaris*, *Bos* sp., *Felis domestica*.

Distribution of ticks at survey sites in Mekong Delta region in 2015–2016 (Fig. 1).

Two tick species parasites on dogs were *Rh. (Rh.) haemaphysaloides* and *Rh. (Rh.) sanguineus* which were distributed in all survey sites; *B. microplus* parasite mainly buffaloes, cows which was distributed in 7 points. *Ap. crassipes* was distributed at 3 sites, *Ap. gervaisi* was distributed in 4 survey sites; *Argas* sp. and *I. (I.) granulatus* were distributed only in one survey site.

Table 1 Primers for groEL gene of Rickettsiaceae

No	Primer	Sequencing primers	Size (bp)	Rickettsiaceae gene segments: groEL
1	SF1	GATAGAAGAAAAGCAATGATG	229	<i>Rickettsia</i> spp.
	SR2	CAGCTATTTGAGATTTAATTTG		
2	TF1	ATATATCACAGTACTTTGCAAC	366	<i>Oriental tsutsugamushi</i>
	TR2	GTTCCCTAACTTAGATGTATCAT		

Table 2 Hosts species of tick at 8 survey sites in the Mekong Delta

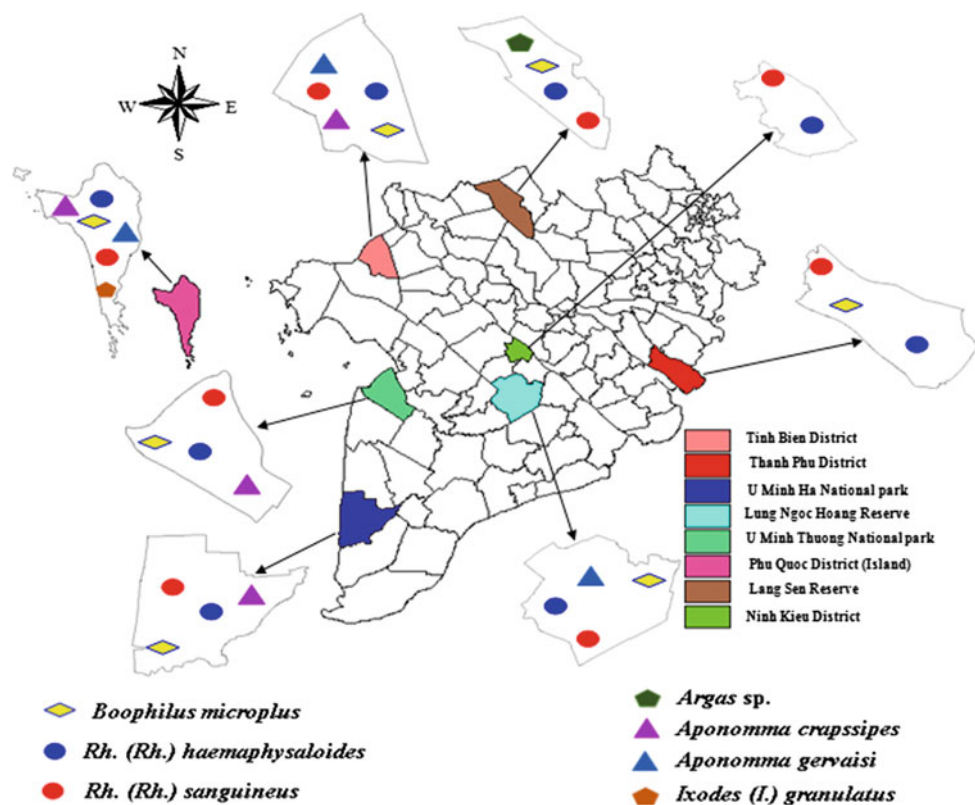
Host groups	8 survey sites in the Mekong Delta region								Total
	LS	LNH	UMH	UMT	PQ	TB	TP	NK	
Wild animals	66	121	84	65	69	71	83	89	648
Raising animals	70	76	113	99	55	130	104	100	747
Reptiles	23	36	48	53	40	33	34	35	302
Wild birds	61	52	55	38	0	22	8	30	266
Raising birds	48	46	48	45	44	60	47	56	394
Garbage and animal nest	46	42	50	41	53	67	51	57	407
Total	314	373	398	341	261	383	327	367	2764

Note LS (Lang Sen Wetland Reserve), LNH (Lung Ngoc Hoang Nature Reserve), UMT (U Minh Thuong National Park), UMH (U Minh Ha National Park), PQ (Phu Quoc Island), TB (Tinh Bien district), TP (Thanh Phu district), NK (Ninh Kieu District)

Table 3 Distribution of ticks on the host in the Mekong delta region

No	Ticks species	The host species
1	<i>Argas</i> sp.	<i>Pipestrellus</i> sp.
2	<i>Ap. crassipes</i>	<i>Python molurus</i> , <i>Varanus bengalensis</i> , <i>Varanus salvator</i>
3	<i>Ap. Gervaisi</i>	<i>P. molurus</i> , <i>V. bengalensis</i>
4	<i>B. microplus</i>	<i>Bos</i> sp., <i>Bubalus bubalis</i>
5	<i>I. (I.) granulatus</i>	<i>Canis familiaris</i>
6	<i>Rh. (Rh.) haemaphysaloides</i>	<i>Canis familiaris</i>
7	<i>Rh. (Rh.) sanguineus</i>	<i>Canis familiaris</i> , <i>Bos</i> sp., <i>Felis domestica</i>

Fig. 1 Distribution diagram of ticks at 8 survey sites (2015–2016)



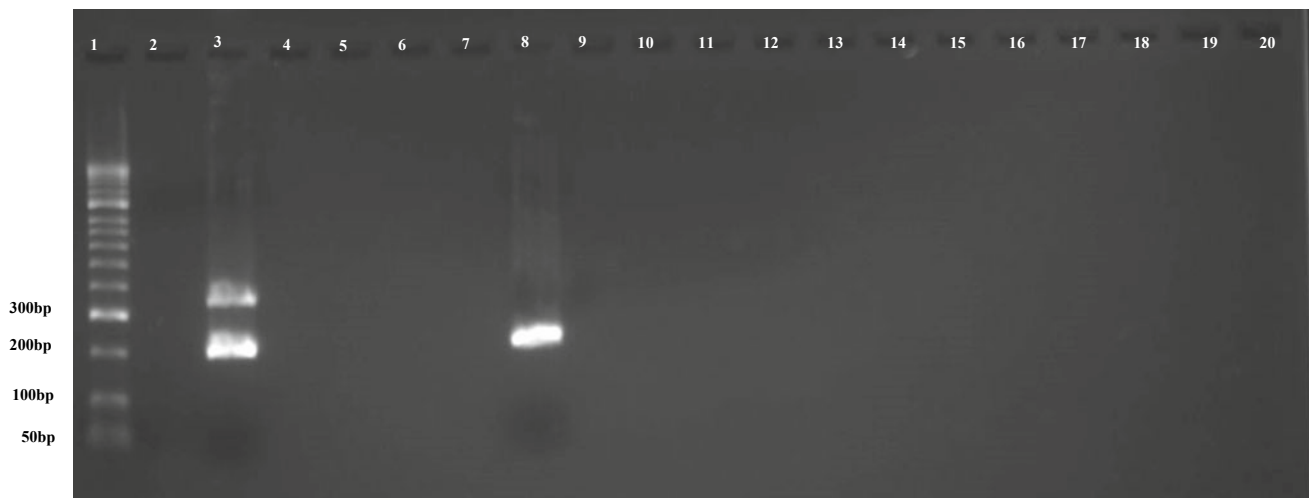


Fig. 2 The results of the PCR detected DNA of *Rickettsia* spp. Note Well 1: DNA bands (50 bp); well 2: negative; well 3: positive of *Rickettsia* spp. (299 bp) and *O. tsutsugamushi* (366 bp); Wells 4–20: tick samples; Well 8: tick sample had positive with DNA of *Rickettsia* spp. (299 bp)

Presence of pathogen on ticks in the Mekong delta region in 2015–2016

Analysis of 299 tick samples (each sample contains 1–5 individuals) to determine the presence of Rickettsiaceae, resulted in the following: ticks collected in the Mekong delta region which had infection rate of *Rickettsia* spp. 1.00%. Of which only 3/153 samples of *Rh. (Rh.) sanguineus* infected *Rickettsia* spp. with infection rate 1.96%. there was no positive sample for *Orientia tsutsugamushi* (Fig. 2).

Three positive tick samples with DNA of *Rickettsia* spp. Which were *Rh. (Rh.) sanguineus*. They were found at three sites: Tinh Bien district, An Giang province in July 2015; Thanh Phu district, Ben Tre province in July 2015 and Lang Sen wetland reserve, Long An province in April 2016.

These 3 positive tick samples which are parasitic in domesticated dogs (*Canis familiaris*).

4 Discussion

The species composition of ticks (Ixodoidea) was discovered in the Mekong delta region of 2 families, 5 genus, 7 species. Tick species composition were collected in 2015–2016 in study region which are higher than tick species composition in other areas such as Quang Binh and Ha Tinh collected 3 ticks species [5]. Quang Nam and Kon Tum collected 4 tick species [6]. Con Dao [7] collected 6 ticks species. Cat Tien National Park [8] collected 4 ticks species [7].

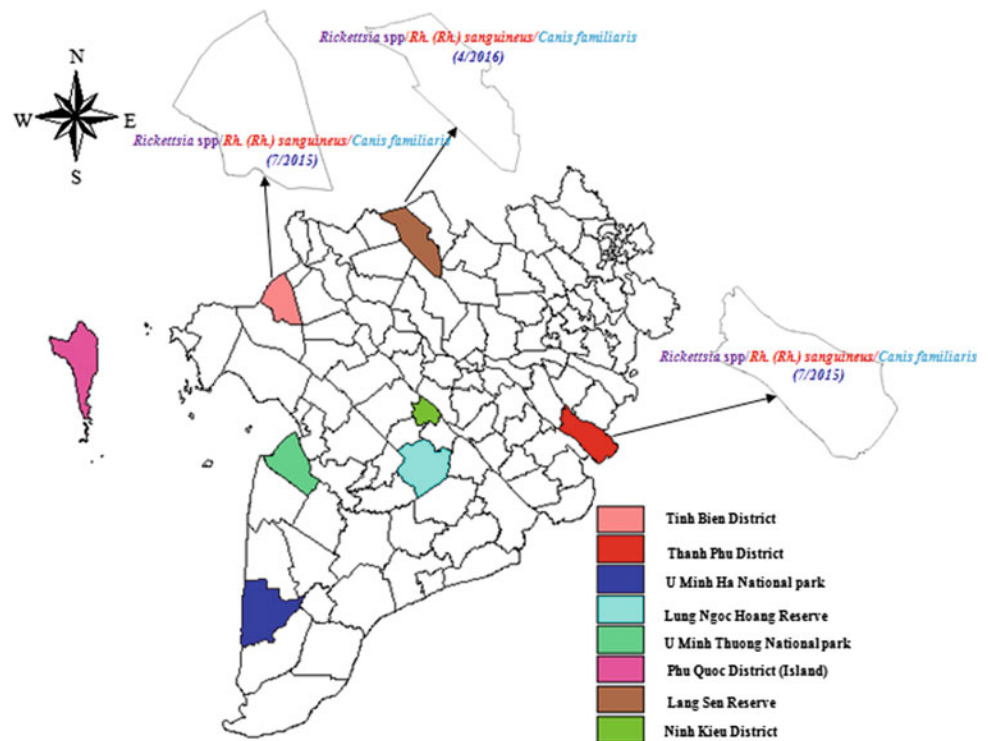
However, ticks species composition in the Mekong delta region which are less than that of the study of [9], First survey of the hard tick (Acari: Ixodidae) fauna of Nakai District, Khammouane Province, Laos, and an updated

checklist of the ticks of Laos. As result, 11 species, 5 genera: *Amblyomma testudinarium*, *Dermacentor auratus*, *D. steini*, *Haemaphysalis colasbelcouri*, *H. hystricis*, *Haemaphysalis* sp. (Similar to *H. aborensis*), *Haemaphysalis* sp. (Similar to *H. darjeeling*), *Haemaphysalis* sp. (Similar to *H. lagrangei*), *Haemaphysalis* spp., *Rhipicephalus haemaphysaloides*, *R. (Boophilus) microplus* were collected; [10], A survey of ticks (Acari: Ixodidae) of companion animals in Australia. A total of 4765 individual of 11 tick species: *Haemaphysalis triglycerides*, *Haemaphysalis bancrofti*, *Haemaphysalis longicornis*, *Ixodes cornuatus*, *Ixodes myrmecobii*, *Ixodes hirsti*, *Ixodes holocyclus*, *Ixodes tasmani*, *Rhipicephalus australis*, *Rhipicephalus sanguineus*, *Bothriocroton* sp.

Distribution of ticks (Ixodoidea) on host: The host of ticks were mainly raising animals, reptiles. Generally in the Mekong delta region, dogs were the main host of *Rh. (Rh.) sanguineus* and *Rh. (Rh.) haemaphysaloides*; Cow were the main host of *B. microplus*. Distribution of ticks (Ixodoidea) at survey sites such as: Phu Quoc island had the highest composition species (6 species), followed by Tinh Bien district (5 species), U Minh Ha national park, U Minh Thuong national park (4 species), Lung Ngoc Hoang nature reserve (4 species), Lang Sen wetland reserve (4 species), Thanh Phu district (3 species) and Ninh Kieu district (2 species).

Compared with previous studies, we recorded additional for Mekong delta region 1 soft ticks species of *Argas* sp. and 3 hard tick species of *Ixodes (I.) granulatus*, *Aponomma crassipes*, *Aponomma gervaisi*. According to [4], the distribution of Ixodoidea in Vietnam such as: there were 6 tick genus appearance in all regions (*Amblyomma*, *Aponomma*, *Boophilus*, *Haemaphysalis*, *Ixodes* and *Rhipicephalus*) with varying amounts. *Dermacentor* genus were not present in delta areas. *Hyalomma* genus were found only in

Fig. 3 Distribution diagrams of *Rickettsia* spp. on ticks in the study region



Central—South and South-West Central. The *Argas* genus were only found in the northern delta but we discovered *Argas* sp. on the bat at Lang Sen—Long An province; For *Ixodes*, there were two species, *Ixodes (I) granulatus* distributed in Quang Ninh, Thai Nguyen, Bac Giang, Gia Lai, Dak Lak, Binh Phuoc, Lam Dong and *Ixodes (Af.) pilosus* in Thai Nguyen [11]. However, species of *Ixodes (I) granulatus* was found in the Phu Quoc Island—Kien Giang province and this tick species parasites on dogs; *Aponomma* had 2 species, *Ap. crassipes* was distributed in Quang Ninh, Cao Bang, Tuyen Quang, Thai Nguyen and *Ap. gervaisi* was distributed in Quang Ninh, Tuyen Quang, Bac Giang, Ha Tinh and parasites on the python, turtles, buffalo, dogs. Species of *Ap. crassipes*, *Ap. gervaisi* were found at the Lung Ngoc Hoang, U Minh Ha and U Minh Thuong, Phu Quoc, Tinh Bien.

A total of 299 tick samples (1457 individuals) were determined *Rickettsia* spp and *O. tsutsugamushi* by PCR. Only three samples were positive for *Rickettsia* spp. and there were no samples which were positive for DNA of *O. tsutsugamushi*. These three tick samples which were *Rhipicephalus sanguineus* species, the remaining tick species were negative. Thus, the ticks samples number were positive with *Rickettsia* spp. per tick samples total which were tested in the South West region (collected from July—October 2015 and March—April 2016) that was 1.00% and the samples of *Rh. sanguineus* were infection of *Rickettsia* spp. for 1.96%. In three ticks samples for DNA of *Rickettsia* spp. positive, a sample was collected at the Tinh Bien in July

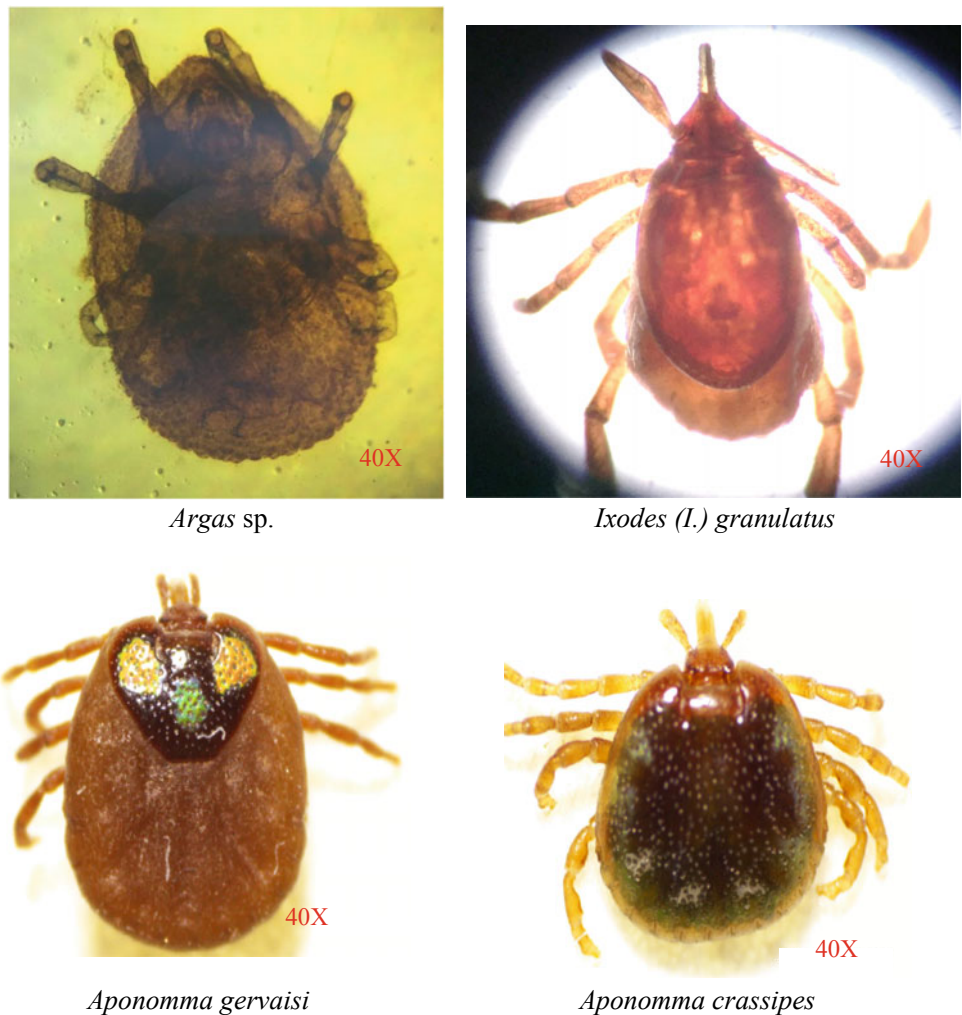
2015, one at Thanh Phu in September 2015 and one at Lang Sen in April 2016. The hosts for the three DNA of *Rickettsia* spp. positive samples which were dogs (Fig. 3). The tick rate of *Rickettsia* spp. infection in this study was much lower than in other studies. Márquez (2008). The rate of *Rhipicephalus sanguineus* ticks in the South West of Spain which were infected rickettsia for 18% [12]. Fatma Khrouf (2013), Detected *Rickettsia* in *Rh. sanguineus* in southeastern of Tunisia for 37.4% [13]. Meng Zhang [13] Determined the presence of *O. tsutsugamushi*, of which 2/13 tick samples was positive for *O. tsutsugamushi* in Shandong Province, China [13].

5 Conclusions

The species composition of ticks (Ixodoidea) in the Mekong delta region in 2015–2016 includes 2 families, 5 genus, 7 species: *Argas* sp., *Aponomma crassipes*, *Aponomma gervaisi*, *Boophylus microplus*, *Ixodes (Ixodes) granulatus*, *Rhipicephalus (Rhipicephalus) haemaphysaloides*, *Rh. (Rh.) sanguineus*. The dominant tick species were *Rh. (Rh.) sanguineus* and *B. microplus*.

Distribution of ticks in Mekong delta region: Ticks were mainly found on dogs and cows. Three ticks species of *B. microplus*, *Rh. (Rh.) sanguineus*, *Rh. (Rh.) haemaphysaloides* were widely distribution (from 6–8 sites), another tick species were narrow distribution (from 1 to 5 survey sites) in this region.

Fig. 4 The first record of ticks species in the Mekong delta region



The sample number of ticks infected *Rickettsia* spp. which was 1.00% (3/299 samples), in which the percentage of *Rh. (Rh.) sanguineus* samples infected *Rickettsia* spp. which was 1.96% (3/153 samples). No ticks samples (0/299 samples) were positive with *Orientia tsutsugamushi* (Fig. 4).

Conflict of Interest Le Thanh Dong and Doan Binh Minh declare that we have no conflict of interest.

References

- Estrada-Peña, A., Jongejan, F.: Ticks feeding on humans: a review of records on human-biting Ixodoidea with special reference to pathogen transmission. *Exp. Appl. Acarol.*, **23**(9), 685–715 (1999)
- Parola, P., Raoult, D.: Ticks and tickborne bacterial diseases in humans: an emerging infectious threat. *Clin. Infect. Dis.* **32**, 897–928 (2001)
- Parola, P., et al.: Update on tick-borne rickettsioses around the world: a geographic approach. *Clin. Microbiol. Rev.* **26**, 657 (2013)
- Cung, P.T., Thu, D.V.: *Acarina. Funa of Vietnam*, Publishing scientific and technical, Hanoi, Episode **11**, 405 (2001)
- Van Chau, N., et al.: Survey on species composition and distribution of some groups of arthropods in 2004 in sites along on Ho Chi Minh Trail in Quang Binh and Ha Tinh Province. *J. Malar. Parasit. Dis. Vietnam* **1**, 54–63 (2005)
- Van Chau, N., et al.: Survey on species and distribution of some groups of arthropods in sites along Ho Chi Minh trail in Quang Nam and Kon Tum Province. *J. Malar. Parasit. Dis. Vietnam* **3**, 73–81 (2004)
- Chinh, V.D., et al.: results of the survey on medical arthropod in CON DAO. *Malaria and Parasitic Diseases in Vietnam*; **4**, 66–74 (2006)
- Ho Dinh Trung.: *Nghiên cứu đa dạng sinh học của các chân đốt y học tại một số khu bảo tồn thiên nhiên và vườn quốc gia đại diện của Việt Nam* (2006)
- Vongphayloth, K., et al.: first survey of the hard tick (Acari: Ixodidae) fauna of Nakai District, Khammouane Province, Laos,

- and an updated checklist of the ticks of Laos. *Syst. Appl. Acarol.* **21** (2): 166–180 (2016)
10. Greay, T.L., et al.: A survey of ticks (Acari: Ixodidae) of companion animals in Australia. *Parasites Vectors* **9**, 207 (2016)
 11. Khrouf, F., et al.: Detection of *Rickettsia* in *Rhipicephalus sanguineus* ticks and *Ctenocephalides felis* fleas from southeastern Tunisia by reverse line blot assay. *J. Clin. Microbiol.* **1**, 268–274 (2013)
 12. Márquez, F.J., et al.: Spotted fever group *Rickettsia* in brown dog ticks *Rhipicephalus sanguineus* in southwestern Spain. *Parasitol. Res.* **103**(1), 119–122 (2008)
 13. Zhang, M., et al.: Molecular epidemiology of *Orientia tsutsugamushi* in chiggers and ticks from domestic rodents in Shandong northern China. *Parasites & Vectors* **6**, 312 (2013). <http://www.parasitesandvectors.com/content/6/1/312>

Integrating Video Recording and Self-reflection to Enhance Communication Skills Training for Dental Students

V. Reher, G. Rehbein, and P. Reher

Abstract

Professional communication skills have a substantial effect on dental patient satisfaction and health outcomes and are one of the core competencies expected of newly graduated dentists in Australia. Acquisition of effective, goal-oriented communication skills has been shown to improve the dentist-patient relationship and requires both practicing skills and reflective thinking. The use of technologies such as video-recording to communicate directly and individually with students can be used to enhance students' engagement and communication skills. This paper aims to present the results of the implementation of the video recording of role-plays and self-reflection in the training of communication skills of first-year dental students at Griffith University, Australia. The year 2015 was used as a control, and in 2016 we introduced video recording, and in 2017 self-reflection. The tools used to measure the impact of these teaching instruments were: (1) student evaluation of courses (SEC) data, and (2) results of the final practical exam grades in the Communication Skills for Oral Health Course. The skills assessed and reflected on include: verbal and non-verbal communication, metacommunication, self-confidence, rapport, active listening, and mindfulness. Recordings and facilitator's feedback can be accessed by each student for their self-reflection on their overall performance, communication skills, patient-centered approach and strategies on how to improve their skills. Results of the SEC data show enhancements in engagement (68–83% +ve answers), assessment (66–78% +ve answers) and feedback (81–89% +ve answers). Results of their average final practical marks increased from 57.82% (control) to 63.34% (with video), and finally 79.64% (with video

and self-reflection). These results strongly suggest that the inclusion of the digital recording of role play interactions and self-reflection increases the quality of communication skills training for dental students by enhancing their dentist-patient relationship skills, engagement, confidence, satisfaction with assessment and the quality of the feedback that can be provided.

Keywords

Communication skills • Self-reflection • Video recording • Dental education • Blended-learning

1 Introduction

The patient interview is the health professional's most important and most frequently used tool in assessing a patient's problem, and poor interviewing technique can lead to loss of important and relevant information [1, 2]. The quality of relationships between patients and health professionals has a significant impact on patient satisfaction, well-being and health outcomes [3, 4]. A key issue in health professional education is developing basic interpersonal skills before actual patient care, and the importance of practice learning has been increasingly recognized to improve health care [5].

In the field of dentistry, knowledge and technical skills are not the only prerequisites for good practice. An ability to communicate effectively with patients—in particular, to use active listening skills, to gather and impart information effectively, to handle patient emotions sensitively, and to demonstrate empathy, rapport, ethical awareness, and professionalism—is critical. When dentists demonstrate effective communication skills, the benefits noted include: increased patient satisfaction, improved patient adherence to dental recommendations, decreased patient anxiety and negative experiences, lower rates of formal complaints and

V. Reher (✉) · G. Rehbein · P. Reher
Griffith University, School of Dentistry and Oral Health, Cnr Olsen Av and Parklands Dr, Southport (Gold Coast), QLD, Australia
e-mail: v.reher@griffith.edu.au

malpractice claims, and increased patient-centered care [6–11].

Due to the critical role of professional communication skills in promoting these relationships, specific educational content for communication skills training has been developed in a growing number of dental schools [12]. Communication Skills teaching is formally recognized in the United Kingdom by the General Dental Council [13], in the United States, by the American Association of Dental Schools [14], and in Australia, by the Australian Dental Council. Efficient communication skills is one of the six competencies expected of the newly graduated dentist to be eligible for professional registration in Australia [15].

However, despite widespread recognition of the importance of communication skills training in the dental curriculum, the reality of what is practiced is somewhat different, and many programs emphasize theoretical aspects of communication rather than provide opportunities for skills-based practice. In several dental schools, the communication skills teaching often take the form of lectures or passive learning, rather than active skills-based practice using simulated or real patients. The assessment of students is conducted by grading participation in class exercises and assessing knowledge via written or oral tests, rather than directly evaluating student's skills performance [16, 17]. This method of education is very similar to rote learning, which makes the students forget most of what they have learned soon after evaluations. Clinical skills in dentistry rely on procedural knowledge, which should be easily transferred to real-world problem-solving situations. This requires both an overall understanding of the situation, which fragmental knowledge does not promote, and a contextual learning experience to store knowledge for a long time [5, 18].

To offer the best teaching experience and prepare dental students for their professional life, a specific course on communication skills for oral health was introduced in 2013 into the curriculum of the School of Dentistry and Oral Health at Griffith University, Queensland, Australia. The course encompasses a comprehensive approach including important principles recommended for effective communication skills teaching. These include the use of a skills-based approach (as opposed to a didactic approach); clinically relevant scenarios; self-assessment by students; video recording methods; trained simulated patients; monitoring of student performance and delivery of feedback, an integrated teaching team and small groups for optimal student learning. By incorporating those elements, it was expected that the program would improve students' interviewing skills, reflective practice and successful life-long learning, all of them cornerstones of patient care [6, 16, 17, 19–21].

The purpose of this article is to describe how the recent implementation of two specific elements of this

comprehensive approach, namely video-recording and self-reflection assessments, have impacted first-years dental science and dental technology students' engagement in the course, their level of satisfaction with the assessments and their communication skills development.

2 Methods

This research was a quasi-experimental control-group. Participants were 312 first year oral health students enrolled across three years in the School of Dentistry and Oral Health at Griffith University located in Queensland, Australia. The number of students enrolled was 110 in 2015, 117 in 2016 and 85 in 2017. Ethical clearance to undertake this study was obtained from the Research Ethics and Integrity Team at Griffith University (GU Ref No: 2018/262). All students received an e-mail informing about the research project and asking their permission for the researchers to use their course marks, student experience of courses (SEC) questionnaire and video recording marks in this study. Students were also advised that all content would be anonymous. Participation was voluntary, and students who didn't want to participate had their marks/evaluation removed from the study.

The same lecturer and instructors delivered this course every year (2015–2017). Also, the content, assessment rubrics, markers, and type and difficulty of scenarios in the role-plays were the same throughout the three years. The year 2015 was used as a control group, then in 2016 we introduced the use of video, and in 2017 the use of video and self-reflection. This allows a comparison of the impacts caused by the introduction of these two teaching instruments.

The tools used to measure the impact of these teaching instruments were: (1) SEC data, and (2) Results of the final practical exam grades in the Communication Skills for Oral Health Course. The SEC questionnaire was used to assess students' engagement and satisfaction with the assessment used. The SEC is a University-wide evaluation tool used to gather feedback from students about their courses, the implementation of which is supported by processes that are effective, efficient, comprehensive, systematic and sustainable. The survey contains eight mandatory fixed items (six quantitative, and two qualitative) measuring student's feedback about their courses. All quantitative items were rated on a 5-point Likert scale (ranging from 1 'strongly disagree'; 2 'disagree'; 3 'neutral'; 4 'agree'; to 5 'strongly agree'). The two open-ended questions related to positive aspects of the course and areas for improvement. The data collection for the SEC is completed between weeks 11–13 each trimester to facilitate the reporting and benchmarking of a course and feedback on teaching data [22].

The second tool used to measure the impact of video and self-reflection techniques was the final practical exam grades

in the Communication Skills for Oral Health Course. This exam uses a rubric based on the literature [23], developed to evaluate dentist-patient communication and patient-centered-approach. The skills assessed included verbal and non-verbal communication, metacommunication, self-confidence, assertiveness, rapport, active listening, and mindfulness. Each item was scored on the following 4-point scale: absent or unacceptable (0), minimal (1), developing (2) and competent (3). The rubric was validated by academics of the dental school and has also been validated in previous studies [24, 25]. To maintain consistency, all assessments were evaluated by a calibrated teaching team, and moderation processes were in place before and after each assessment.

3 Results

Of the 312 oral health students who participated in the communication skills course during the years of 2015, 2016 and 2017, 181 (58%) completed the SEC survey. The number of students enrolled was 110 in 2015, 117 in 2016 and 85 in 2017, with response rates at 62.7, 55.6, and 55.3% respectively. All data collected by the survey was statistically examined centrally by the University, using non-parametric and parametric forms of analyses, and reported back to the course coordinator.

The SEC results between 2015 and 2017 can be seen in Fig. 1. There was a significant enhancement in students' engagement with the course, their satisfaction with the assessments in place and with the feedback received. Comparing the three years, the percentage of students giving the course a rating of 4 or 5 on the Likert scale ranged from 68.1 to 83% positive answers in engagement, 66.7–78.7% positive answers in assessment satisfaction and 81.2–89.4% positive answers regarding the feedback received (Fig. 1).

The results of the comparison between the final practical exam marks in 2015 (control), 2016 (introduction of video) and 2017 (introduction of video and self-reflection) are shown in Fig. 2. The comparison showed an improvement in their communication skills averaged final marks from 57.82% in 2015 to 63.34% in 2016 and reached 79.64% in 2017.

4 Results

The results of this study reinforce previous reports that video-based self-reflection can improve clinical skills performance, promote self-awareness and self-efficacy, and improve the future professional development of students [26]. Self-evaluation using video enhances knowledge retention, promotes critical thinking, and motivates students to become more engaged in their learning. It also allows them to identify their problems and promotes a clearer understanding of the topics to be learned. It indicates a change of attitude in affective dimensions of learning, in that emotions have an important connection to memory and help to store information and trigger its recall [5]. Furthermore, it has been described as a valuable tool for healthcare professionals as they reflect on interpersonal skills [26–28]. The literature also indicates that video is often used in the field of psychology as an effective means of giving feedback and support to students who are learning the subtler aspects of therapeutic communication [29–31]. The results of this study confirm that these instruments are a teaching method that shows a high level of student satisfaction. This was also noted by Epstein et al. (2003), who investigated student satisfaction with video projects on a medical-surgical nursing course. The students reported that using video was a 'fantastic' and 'dramatic' experience and that video-based

Fig. 1 Comparison of SEC results before and after the introduction of video recording and self-reflection

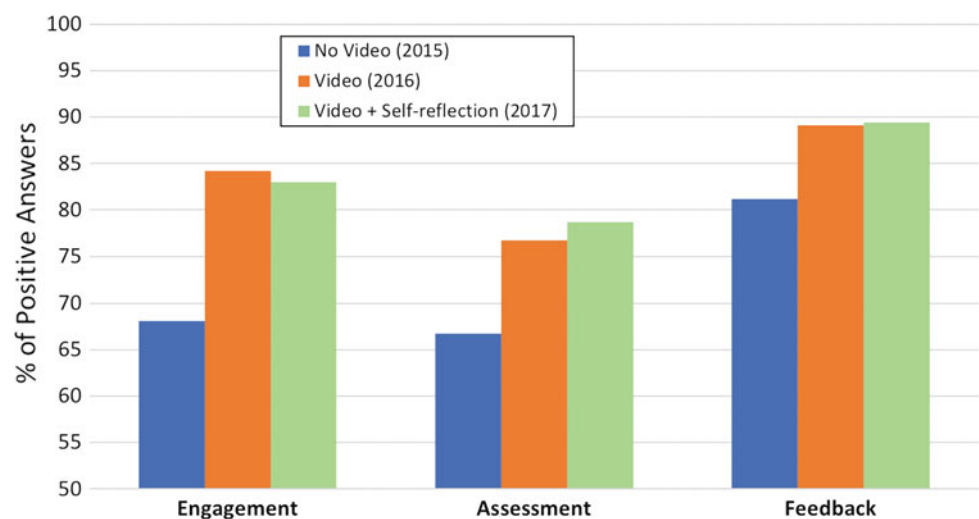
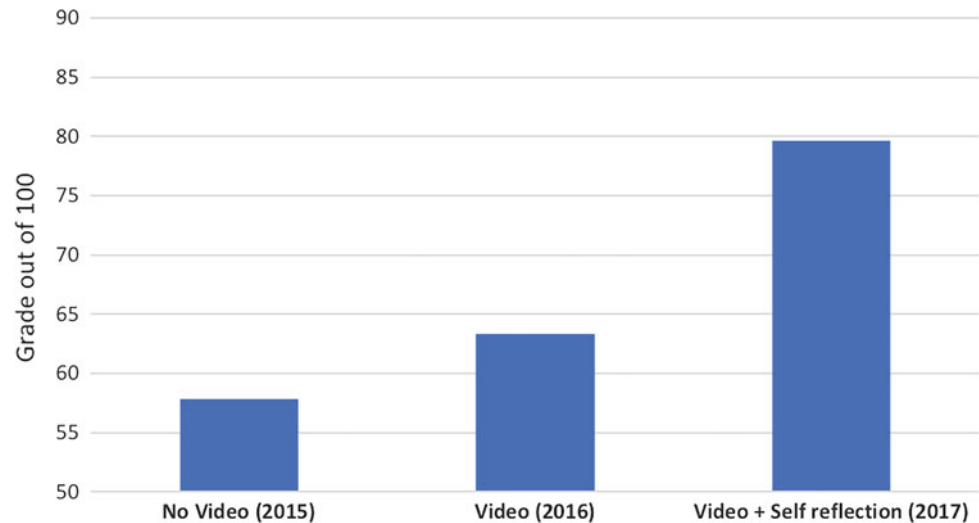


Fig. 2 Students' performance in their averaged final practical exam between the years 2015–2017: 2015 (control), 2016 (introduction of video), 2017 (introduction of video and self-reflection)



self-assessment can motivate self-improvement by helping them to identify their strengths and weaknesses, as well as gain insights on the effects of their behaviors [30].

Although video-based self-reflective assessment is thought to be useful in improving the students' understanding of their clinical skills and the problems that they encounter in clinical practice, it is not always appreciated by the students. Sometimes students do not like the ways in which tutors use reflection and self-assessment to help achieve learning goals, or they feel uncomfortable when they observe their behaviors [32]. Further issues raised regarding the use of these methodologies are that they are very time consuming for the teaching staff, and there are concerns about students' readiness and ability to self-assess [28]. While video-based self-assessment does not suit everyone and must be handled with sensitivity when used, it is recommended to lead to greater personal and professional self-awareness of growth and development. This study reinforces the use of these methodologies to offer students insight regarding their practice and to encourage them to become more conscious about the process of learning, especially regarding the development of transferable skills.

5 Conclusions

Studies suggest that effective communication skills and patient-centered approach learning involve more than the mere acquisition of information, requiring that learners have more active skills-based practice and reflective assessments. The results of this study suggest that the inclusion of the recording of role-play interactions and self-reflection assessments increases the quality of communication skills training for dental students, by enhancing their dentist-patient relationship skills, engagement, satisfaction with evaluation

and the quality of the feedback that can be provided by the facilitators. Further studies are needed to evaluate the efficiency of video-based self-assessment on the performance of other clinical skills and to confirm if these short-term effects can be sustained in the longer term.

Conflict of Interest The authors declare they have no conflict of interests.

References

1. Roter, D.L., Hall, J.A.: Physicians' interviewing styles and medical information obtained from patients. *J. Gen. Intern. Med.* **2**, 325–329 (1987)
2. Beckman, H.B., Frankel, R.M.: The effect of physician behavior on the collection of data. *Ann. Intern. Med.* **101**, 692–696 (1984)
3. Ayn, C., Robinson, L., Nason, A., Lovas, J.: Determining recommendations for improvement of communication skills training in dental education: a scoping review. *J. Dent. Educ.* **81**(4), 479–488 (2017). <https://doi.org/10.21815/JDE.016.003>
4. Ha, J.F., Longnecker, N.: Doctor-patient communication: a review. *Ochsner J* **10**(1), 38–43 (2010)
5. Yoo, M.S., Son, Y.J., Kim, Y.S., Park, J.H.: Video-based self-assessment: Implementation and evaluation in an undergraduate nursing course. *Nurse Educ. Today* **29**, 585–589 (2009)
6. Hannah, A., Millichamp, C.J., Ayers, K.M.S.: A communication skills course for undergraduate dental students. *J. Dent. Educ.* **68** (9), 970–977 (2004)
7. Biro, P.A., Hewson, N.D.: A survey of patients' attitudes towards their dentists. *Aust. Dent. J.* **21**, 388–394 (1976)
8. Corah, N.L., O'Shea, R.M., Bissell, G.D., et al.: The dentist-patient relationship: perceived dentist behaviors that reduce patient anxiety and increase satisfaction. *J. Am. Dent. Assoc.* **116**, 73–76 (1988)
9. Gale, E.N., Carlsson, S.G., Eriksson, A., Jontell, M.: Effects of dentists' behavior on patients' attitudes. *J. Am. Dent. Assoc.* **109**, 444–446 (1984)
10. Mellor, A.C., Milgrom, P.: Dentist' attitudes toward frustrating patient visits: relationship to satisfaction and malpractice complaints. *J. Public Health Dent.* **56**, 6–11 (1996)

11. Rouse, R.A., Hamilton, M.A.: Dentists' technical competence, communication, and personality as predictors of dental patient anxiety. *J. Behav. Med.* **13**(3), 307–319 (1990)
12. Haden, N.K., Hendricson, W.D., Kassebaum, D.K., et al.: Curriculum change in dental education, 2003–09. *J. Dent. Educ.* **74**(5), 539–557 (2010)
13. General Dental Council: Student professionalism and fitness to practise: standards for the dental team—Guidance for students. England, London (2016)
14. American Association of Dental Schools: Curriculum guidelines for behavioral science. *J. Dent. Educ.* **57**(8), 648–657 (1993)
15. Australian Dental Council: Australian dental council professional competencies of the newly qualified dentist. Melbourne, Australia (2016)
16. Yoshida, T., Milgrom, P., Coldwell, S.: How do U.S. and Canadian dental schools teach interpersonal communication skills? *J. Dent. Educ.* **66**, 1281–1287 (2012)
17. McGoldrick, P.M., Pine, C.: A review of teaching of behavioural sciences in the United Kingdom dental undergraduate curriculum. *Br. Dent. J.* **186**, 576–580 (1990)
18. Anderson, J.: *Cognitive Psychology and Its Implication*. Free. Co., New York (1990)
19. Kupst, M.J., Dresser, K., Schulman, J.L., Paul, M.H.: Evaluation of methods to improve communication in the physician-patient relationship. *Am. J. Orthopsychiatry* **45**, 420–429 (1975)
20. Putnam, S.M., Stiles, W.B., Jacob, M.C., James, S.A.: Teaching the medical interview: an intervention study. *J. Gen. Intern. Med.* **3**, 38–47 (1988)
21. Silverman, J., Kurtz, S., Draper, J.: Defining what to teach and learn: an overview of the communication skills curriculum. In: Silverman, J., Kurtz, S., Draper, J. (eds.) *Skills for Communicating with Patients*. Radcliffe Medical Press, Abingdon, UK, pp. 1–16 (1998)
22. Griffith University: Student Experience of Courses (SEC) and Teaching (SET) at: [http://policies.griffith.edu.au/pdf/Student Experience of Courses and Teaching.pdf](http://policies.griffith.edu.au/pdf/Student%20Experience%20of%20Courses%20and%20Teaching.pdf) (2014)
23. Curran, V.R., Casimiro, L., Banfield, V., et al.: Research for Interprofessional Competency-Based Evaluation (RICE). *J. Interprof. Care* **23**(3), 297–300 (2008)
24. Curran, V.R., Hollett, A., Casimiro, L., et al.: Development and validation of the interprofessional collaborator assessment rubric (ICAR). *J. Interprof. Care* **25**, 339–344 (2011)
25. Hayward, M., Curran, V.R., Schulz, H., et al.: Reliability of the interprofessional collaborator assessment rubric (ICAR) in multi source feedback (MSF) with post-graduate medical residents. *BMC Med. Educ.* **14**, 1049 (2014). <https://doi.org/10.1186/s12909-014-0279-9>
26. Dearnley, C.A., Meddings, F.S.: Student self-assessment and its impact on learning—a pilot study. *Nurse Educ. Today* **27**(4), 333–340 (2007)
27. Mazor, K.M., Haley, H.L., Sullivan, K., Quirk, M.E.: The video-based test of communication skills: description, development, and preliminary findings. *Teach. Learn. Med.* **19**(2), 162–167 (2007)
28. Zick, A., Granieri, M., Makoul, G.: First-year medical students' assessment of their own communication skills: a video-based, open-ended approach. *Patient Educ. Couns.* **68**(2), 161–166 (2007)
29. Pinsky, L.E., Wipf, J.E.: A picture is worth a thousand words: practical use of videotape in teaching. *J. Gen. Intern. Med.* **15**(11), 805–810 (2000)
30. Epstein, D.C., Hovancsesk, T.M., Dolan, L.P., et al.: Lights! Camera! Action!: video projects in the classroom. *J. Nurs. Educ.* **42**(12), 558–561 (2003)
31. Travale, I.L.: Computer-assisted instruction for novice nurses in critical care. *J. Contin. Educ. Nurs.* **38**(3), 132–138 (2007)
32. Price, B.: Self-assessment and reflection in nurse education. *Nurs. Stand.* **19**(29), 33–37 (2005)

A Systematic Study of Electronic Structure for Anti-cancer Drug Molecule 5-Fluorouracil Within Various Solvents from First-Principles Calculations

Linh Gia Hoang, Trang Thuy Nguyen, Toan The Nguyen, Tan Le Hoang Doan, and Duc Nguyen Manh

Abstract

5-Fluorouracil (5-FU) has been widely used in chemotherapy treatments of cancer for several decades. Ongoing research investigation is devoted to have a better understanding of its anti-cancer activities and to overcome side effects and drug resistance. In this work, electronic structure of 5-FU molecule in various solvents is investigated from first principles. Our results exhibit that exact exchange contribution to the electron-electron interaction is important to optimize bond angles while correlation term is important for bond lengths. B3LYP/cc-pDVZ is the best basis set for calculation of IR-active vibration. It is found that diffusion functions included into Gaussian wave-function basis sets over-estimate dipole moment of the molecule. At low dielectric constant region, the dipole moment of the 5-FU molecule increases quickly but then reaches saturated value around 5.10 D at dielectric constant higher than 30. There is a correlation between the change of HOMO-LUMO gap and the change of C–C bond length induced by the electrostatic interaction between the molecule and solvents.

Keywords

5-Fluorouracil • Anti-cancer drug • IR spectrum • Electronic structure • First-principles methods • Influences of solvent

1 Introduction

Cancer is a dangerous disease that has a high mortality and is difficult to treat. Common cancer treatments try to remove (surgery) or destroy (radiation therapy) cancer cells as well as prevent them from further growth (chemotherapy). 5-Fluorouracil (5-FU), $C_4H_3FN_2O_2$ is one of the most popular drugs used in chemotherapy treatments for several cancers such as colon, esophageal, stomach, pancreatic, breast and cervical cancer [1]. It is a type of anti-metabolite drugs which both inhibits essential bio-synthetic processes and is incorporated into DNA and RNA to inhibit their normal functions, and hence, inhibits cancer cell division [2]. However, its clinical applications have been greatly limited due to side effects and drug resistance [3–5].

Numerous ongoing researches are devoted to achieve a better controlling of side effects and to overcome drug resistance of 5-FU based drugs in different environments. Understanding behaviors of 5-FU molecule in solvents is an essential step towards these targets because any drug to be delivered and absorbed in human body must be loaded into a carrier material and presented in form of solution. Selecting an appropriate solvent for drug loading, delivery and absorption is of particular importance to control the rates and equilibrium positions of chemical reactions. In this work, electronic behaviors of 5-FU molecule in various solvents were investigated from first principles using Gaussian wave-function basis sets. Our results demonstrate the effects of diffusion functions, polarized functions, correlation contribution and exact exchange contribution to electron-electron interaction in accurately describing the geometrical structure and the dipole moment of the

L. G. Hoang (✉) · T. T. Nguyen · T. T. Nguyen
VNU Key Laboratory on Multiscale Simulation of Complex Systems, VNU University of Science, Vietnam National University - Hanoi, Hanoi, Vietnam
e-mail: gialinhkisa@gmail.com

T. T. Nguyen · T. L. H. Doan
Center for Innovative Materials and Architectures, Vietnam National University - Ho Chi Minh City, Ho Chi Minh City, Vietnam

T. L. H. Doan
Faculty of Chemistry, University of Science, Vietnam National University - Ho Chi Minh City, Ho Chi Minh City, Vietnam

D. Nguyen Manh
CCFE, United Kingdom, Atomic Energy Authority, Abingdon, OX14 3DB, UK

molecule. Electrostatic interaction between 5-FU molecule and solvent strongly affects electron distribution by distorting molecular orbital shapes but does not significantly change its eigenvalue spectrum.

2 Computational Methods

Our calculations were performed with Gaussian 09 package (G09) [6]. Among first principles methods provided by G09, Hartree-Fock self-consistent field (HF-SCF) method includes exact exchange term but does not fully incorporate electron correlation [7]. Conventional density functional theory (DFT) methods consider both exchange and correlation interactions at local density approximation (LDA) or semi-local density approximation—generalized gradient approximation (GGA) [8, 9]. Although LDA and GGA functionals are applicable for all systems from atoms, molecules to solids, they have a moderate accuracy [10]. Higher accuracy for chemical purposes requires more specifically designed functionals. Mixing some SCF-HF exact exchange into a GGA functional to form a hybrid functional is a good way to improve accuracy. Hybrid functional B3LYP which is BLYP—GGA functional with 20% HF exact exchange is designed to produce smaller errors for main-group organic molecules than GGA functionals [11, 12]. In our calculations, both HF-SCF method and DFT method with BLYP and B3LYP functionals were utilized. Wave functions of 5-FU molecule are represented in the basis set of Gaussian-type orbitals of various sizes including 3–21G, 6–31G(*md*, *np*), 6–31 ++G(*md*, *np*) (*m*, *n* = 0, 1, 2, 3) developed by Pople's group [13], cc-pVDZ and Aug-cc-pVDZ developed by Dunning's group [14].

The structure of 5-FU molecule was relaxed until the force on each atom falls below 0.001 eV/Å. The self-consistent electron density is converged until the density matrix difference is below 10^{-6} . The IR active vibrations were calculated in the double-harmonic approximation [15] where molecular vibrations are described as harmonic oscillator corresponding to the classical normal modes of a coupled system of oscillators:

$$M_i \frac{d^2 u_{i\mu}}{dt^2} = - \sum_{j\nu} K_{i\mu,j\nu} u_{j\nu}$$

$$K_{i\mu,j\nu} = \frac{\partial^2 E}{\partial u_{i\mu} \partial u_{j\nu}}$$

and the IR spectroscopic intensities are determined by the dynamical charge tensor of which elements Z_i are first-order geometric derivatives of the molecular electric dipole moment:

$$p_\alpha = \frac{-\partial E}{\partial \varepsilon_\alpha}$$

$$Z_{\alpha,i\mu} = \frac{-\partial^2 E}{\partial \varepsilon_\alpha \partial u_{i\mu}}$$

M_i is the mass of the i th atom and $u_{i\mu}$ is the μ coordinate of the i th atom. $K_{i\mu,j\nu}$ are force constants with i, j from 1 to N (N is the number of atoms in the considered molecule), μ and ν can be x, y or z . E is the total energy of the molecule which is calculated by first principle methods. p_α and ε_α is molecular electric dipole moment and electric field in α direction (α can be x, y or z) respectively. The effects of solvents were considered from statistical aspect using Polarized Continuum Model (PCM) [16]. In these methods, the solvent is described as a homogeneous polarizable medium with a given dielectric constant ε . In our work, we consider several solvents including water $\varepsilon = 78.39$, dimethylsulfoxide $\varepsilon = 46.70$, ethanol $\varepsilon = 32.63$, ethyl acetate $\varepsilon = 6.02$ and dioxane $\varepsilon = 2.21$. The molecule forms a cavity within that medium. The surface of the cavity is the union of interlocking atomic spheres with radii equal to Van de Waals radii of corresponding atoms. The charge distribution of the molecule induces a polarization of the surrounding medium and vice versa. The mutual polarizing between polarizable medium and the molecule is treated self-consistently in G09.

3 Results and Discussion

3.1 Effect of Basis Set and Functional

The information of 5-FU geometrical structure optimized by various methods is compared with experimental data [17]. The deviations of calculated structures from experiment are evaluated in terms of root mean square error (RMSE) shown in Table 1. Additional diffusion functions (in 6–31G ++(*p*,*d*) and aug-cc-pVDZ basis sets) significantly improve bond angles. The bond lengths are significantly under-estimated by HF methods but are over-estimated by BLYP-DFT methods. Hybrid functional methods strongly improve the bond lengths but do not improve the bond angles. This suggests that exact exchange term is important to bond angles while correlation term is important to bond lengths. Additional information supporting this point is that Dunning's correlation consistent basis set slightly improves bond angle relatively to Pople's basis sets. Table 2 summarizes calculated IR-active vibration modes with previous experimental results [18]. Our calculations reproduce all observed IR-active vibration modes. Some predicted IR modes, 3133 and 722 and 610 cm^{-1} , were missed in experimental measurement because of their low activities. The low-frequency

Table 1 Percentage of root mean square errors (RMSEs) of calculated frequencies of IR active modes, bond lengths and bond angles of 5-FU

Basis set	RMS error		
	Frequencies	Bond length	Bond angle
HF 3-21G	6.12	1.33	1.54
HF 6-31G(d)	2.29	1.60	1.40
HF 6-31G(d, p)	2.36	1.61	1.37
BLYP 6-31G(d)	3.45	1.13	1.93
B3LYP 6-31 ++G(d, p)	2.43	0.44	1.61
B3LYP 6-31G(d, p)	2.50	0.36	1.71
B3LYP 6-31G(d)	2.42	0.33	1.73
B3LYP 6-311G(d, p)	1.89	0.28	1.77
B3LYP cc-pVDZ	1.55	0.34	1.67
B3LYP Aug-cc-pVDZ	2.10	0.41	1.58

vibrations (below 430 cm^{-1}) were out of experimental range. The RMSE in Table 1 suggests B3LYP/cc-pVDZ is the best for IR-active vibration calculation.

A benchmark of basis set effect on dipole moment was considered in dioxane solvent because of available experimental value for dipole moment of 5-FU in this solvent

$P_{\text{exp}} = 4.11 \pm 0.05\text{ D}$ [19]. Pople's basis sets are divided into no-diffusion group and diffusion group. For each group, there is a convergence of dipole moment value when the basis set size is increased by increasing numbers of polarized functions (Fig. 1). Additional diffusion functions lead to larger dipole moment values. Once again, the usage of

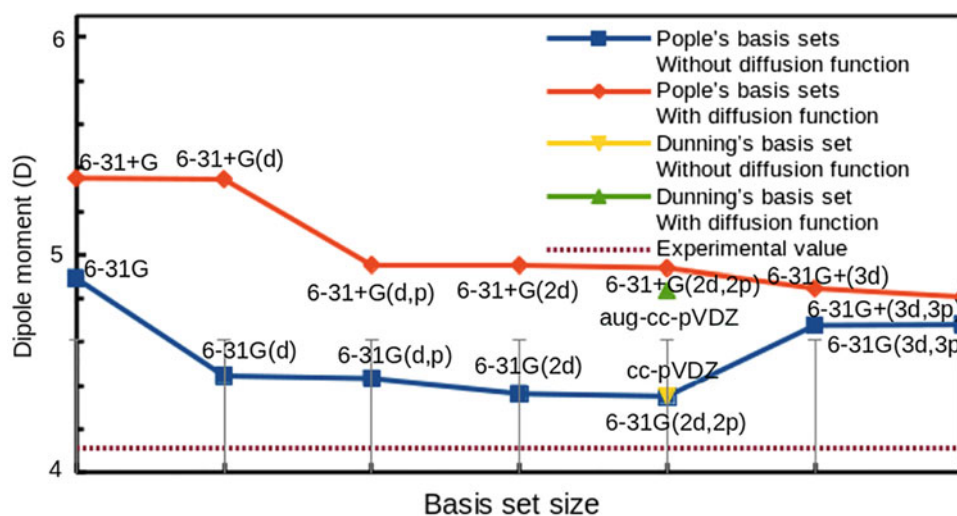
Table 2 A summary of IR-active vibration modes from experimental measurements and first principles calculations

HF	HF	HF	BLYP	B3LYP	B3LYP	B3LYP	B3LYP	B3LYP	B3LYP	B3LYP	Intensity	Exp	
3-21G	6-31G (d)	6-31G (d, p)	6-31G (d)	6-31 ++G (d, p)	6-31G (d, p)	6-31G (d)	6-311G (d, p)	cc-pVDZ	Aug-cc-pVDZ	(cc-pVDZ)			
3463.2	3498.6	3525.7	3501.3	3520.2	3519.0	3498.6	3524.9	3525.0	3526.1	110.0	3480.0	$\nu(\text{N}_1\text{-H}_7)$	
3428.5	3460.0	3485.2	3457.9	3475.0	3475.9	3456.9	3479.6	3476.8	3479.3	69.9	3427.5	$\nu(\text{N}_3\text{-H}_9)$	
3110.9	3088.9	3083.3	3458.9	3476.0	3117.0	3120.9	3113.7	3132.7	3133.9	2.7		$\nu(\text{C}_6\text{-H}_{12})$	
1772.2	1817.5	1825.0	1754.7	1745.4	1773.6	1773.3	1767.8	1780.9	1739.1	539.4	1780.0	$\nu(\text{C}_2=\text{O}_8)$, $\nu(\text{C}_4=\text{O}_{10})$, $\nu(\text{N}_1\text{-H}_7)$	
1762.1	1803.0	1810.0	1712.3	1720.8	1743.8	1742.8	1739.3	1750.0	1716.2	575.8	1746.5	$\nu(\text{C}_4=\text{O}_{10})$, $\nu(\text{C}_2=\text{O}_8)$, $\nu(\text{N}_3\text{-H}_9)$	
1730.1	1727.0	1734.3	1640.1	1657.4	1665.1	1664.8	1661.2	1678.9	1663.3	31.5	1686.5	$\nu(\text{C}_5=\text{C}_6)$, ν ring	
1478.6	1491.1	1495.5	1435.4	1448.0	1448.3	1451.2	1451.5	1460.1	1452.9	47.7	1472.0	$(\text{N}_1\text{-H}_7)$, δ ring	
1425.9	1419.0	1421.3	1362.4	1375.3	1375.1	1379.1	1377.8	1384.6	1378.6	63.0	1400.5	δ ring, $\delta(\text{N}_1\text{-H}_7)$	
1397.1	1401.6	1400.6	1341.7	1351.6	1343.0	1352.5	1361.4	1351.9	1352.3	10.5	1367.0	$\delta(\text{N}_3\text{-H}_9)$, $\delta(\text{N}_1\text{-H}_7)$, δ ring	
1349.4	1343.2	1345.5	1296.2	1303.6	1301.7	1305.5	1301.2	1305.0	1305.2	16.2	1333.5	$\delta(\text{C}_6\text{-H}_{12})$, δ ring, $\delta(\text{N}_1\text{-H}_7)$	
1246.1	1246.2	1251.2	1219.2	1218.8	1234.4	1234.4	1218.6	1238.1	1216.8	229.5	1247.5	$\nu(\text{C}_5\text{-F}_{11})$, ν ring	
1186.0	1188.8	1190.1	1126.0	1146.4	1140.7	1143.7	1138.3	1153.1	1150.5	77.5	1184.0	$\delta(\text{C}_6\text{-H}_{12})$, $\delta(\text{N}_3\text{-H}_9)$, δ ring	
1126.2	1123.4	1123.8	1092.9	1116.8	1115.0	1117.9	1114.7	1123.9	1118.4	23.1	1147.0	$\delta(\text{CCH})$, $\delta(\text{N}_1\text{-H}_7)$, δ ring	

(continued)

Table 2 (continued)

HF	HF	HF	BLYP	B3LYP	B3LYP	B3LYP	B3LYP	B3LYP	B3LYP	B3LYP	Intensity	Exp	
3-21G	6-31G (d)	6-31G (d, p)	6-31G (d)	6-31 + +G (d, p)	6-31G (d, p)	6-31G (d)	6-311G (d, p)	cc-pVDZ	Aug-cc-pVDZ	(cc-pVDZ)			
1024.0	952.8	954.2	922.1	935.1	930.8	933.1	935.8	940.7	938.0	12.6	959.5	$\delta(\text{N}_3\text{-H}_9)$, $\delta(\text{C}_6\text{-H}_{12})$, δ ring	
947.8	925.2	927.8	831.9	863.8	853.4	852.1	861.8	871.3	875.2	26.1	876.5	$\gamma(\text{C}_6\text{-H}_{12})$	
909.0	803.0	806.2	778.4	784.1	785.3	784.9	789.1	788.7	785.9	32.2	806.5	δ ring	
811.7	768.2	771.7	710.8	723.7	718.5	717.8	749.0	750.9	748.8	19.9	757.5	δ ring	
810.8	751.1	753.9	704.4	716.2	716.4	716.3	738.4	733.4	731.8	43.6	749.5	$\gamma(\text{C}_2=\text{O}_8)$, $\gamma(\text{C}_4=\text{O}_{10})$, γ ring	
740.9	718.3	721.1	705.4	717.2	712.1	711.9	715.8	722.2	718.5	10.3		$\gamma(\text{C-N}_3\text{-H})$, γ ring	
713.4	649.7	651.7	648.8	637.3	648.0	648.8	654.5	657.9	665.3	60.5	653.0	$\gamma(\text{N}_3\text{-H}_9)$	
635.2	616.9	619.7	649.8	638.3	603.1	602.7	610.8	609.8	605.9	2.0		δ ring	
616.4	527.7	530.1	524.8	523.3	523.9	522.6	531.9	529.6	547.5	53.2	527.0	$\gamma(\text{N}_1\text{-H}_7)$	
534.7	500.4	504.1	509.2	517.5	515.3	515.0	518.9	519.1	519.6	6.7	532.0	δ ring	
453.2	441.9	443.9	435.0	438.7	436.9	436.6	440.6	439.8	440.2	6.9	451.0	$\delta(\text{C}_5\text{-F}_{11})$, $\delta(\text{C}=\text{O})$, δ ring	
423.4	386.1	388.2	436.0	439.7	372.5	372.0	378.0	378.1	376.3	17.6		$\delta(\text{OCNCO})$, δ ring	
384.8	368.0	369.5	437.0	440.7	362.1	361.8	369.9	375.8	374.8	8.5		$\gamma(\text{C}=\text{C-H})$, γ ring	
383.4	339.9	343.3	438.0	441.7	333.4	331.2	336.8	337.3	336.6	11.4		$\gamma(\text{NC}=\text{CF})$, γ ring	
286.7	293.2	294.7	439.0	442.7	288.1	287.8	292.2	290.2	292.9	0.9		$\delta(\text{OCCF})$, δ ring	
185.6	150.1	151.4	440.0	443.7	146.6	145.7	147.5	143.9	153.9	0.5		$\gamma(\text{C}=\text{O})$, $\gamma(\text{N}_3=\text{H}_9)$, γ ring	
125.6	110.9	111.9	441.0	444.7	113.0	112.3	112.7	111.2	115.8	1.3		$\gamma(\text{C}=\text{O})$, $\gamma(\text{C}_5\text{-F}_{11})$, $\gamma(\text{N}_1\text{-H}_7)$, γ ring	

Fig. 1 The convergence of calculated dipole moment with respect to basis set size

Dunning's correlation consistent basis sets slightly improves the results. Over-estimations of dipole moment of uracil molecule, the non-halogenated original chemical of 5-FU, by MP2(PBE1PBE,CCSD)/aug-cc-pVDZ(aug-cc-pVTZ) were also observed previously [20–22].

3.2 Effects of Solvent

Figure 2b shows the change of dipole moment with respect to dielectric constant of solvent. According to this, at low dielectric constant, the dipole moment of 5-FU molecule increases with respect to solvent dielectric constant. But, then, it reaches saturation value around 5.10 D at dielectric constant higher than 30. It should be noted that large dipole moment of 5-FU is responsible for its hydrophilicity which in turn determine the stability of hydrogen bond. D. V. D. Spoel et al. showed that hydrogen bond between water molecules with larger dipole moments is stable while the barrier of breaking hydrogen bond is lowered down in case of methanol, ethanol and propanol with smaller dipole moments [23]. On the other hand, drug molecules are usually encapsulated with some delivery material to improve their

bioactivity. The dynamics of both the encapsulation and drug release is usually dominated by hydrogen bonding. Hence, a solvent with suitable dielectric constant can help to control the dynamics of those procedure.

The nature of intra-molecular bonds can be derived from electron density deformation which is the difference between molecular electron density and total electron density of isolated atoms shown in Fig. 2a. Strong covalence bonds between C₄–C₅ and C₅–C₆ are demonstrated by a strong increasing of electron density in the regions between these atoms. Less covalence bonds are between C₆–H₁₂, C₂–N₁, C₂–N₃ and C₄–O₁₀ respectively. C₅–F₁₁ and C₂–O₈ bonds are strongly polarized.

Figure 2c shows the evolution of HOMO-LUMO gap with respect to solvent dielectric constant. In all solvents, HOMO and LUMO has bonding and antibonding natural of C₅–C₆ π bond, respectively. HOMO-LUMO gap exhibits a saturated behavior in which it reduces more quickly at low dielectric constant and then reaches saturate value around 5.3760 eV for dielectric constant larger than 30. The saturate reducing of HOMO-LUMO gap can be explained by the saturate increasing of C₅–C₆ bond length which reduces the corresponding bonding-antibonding interaction as shown in

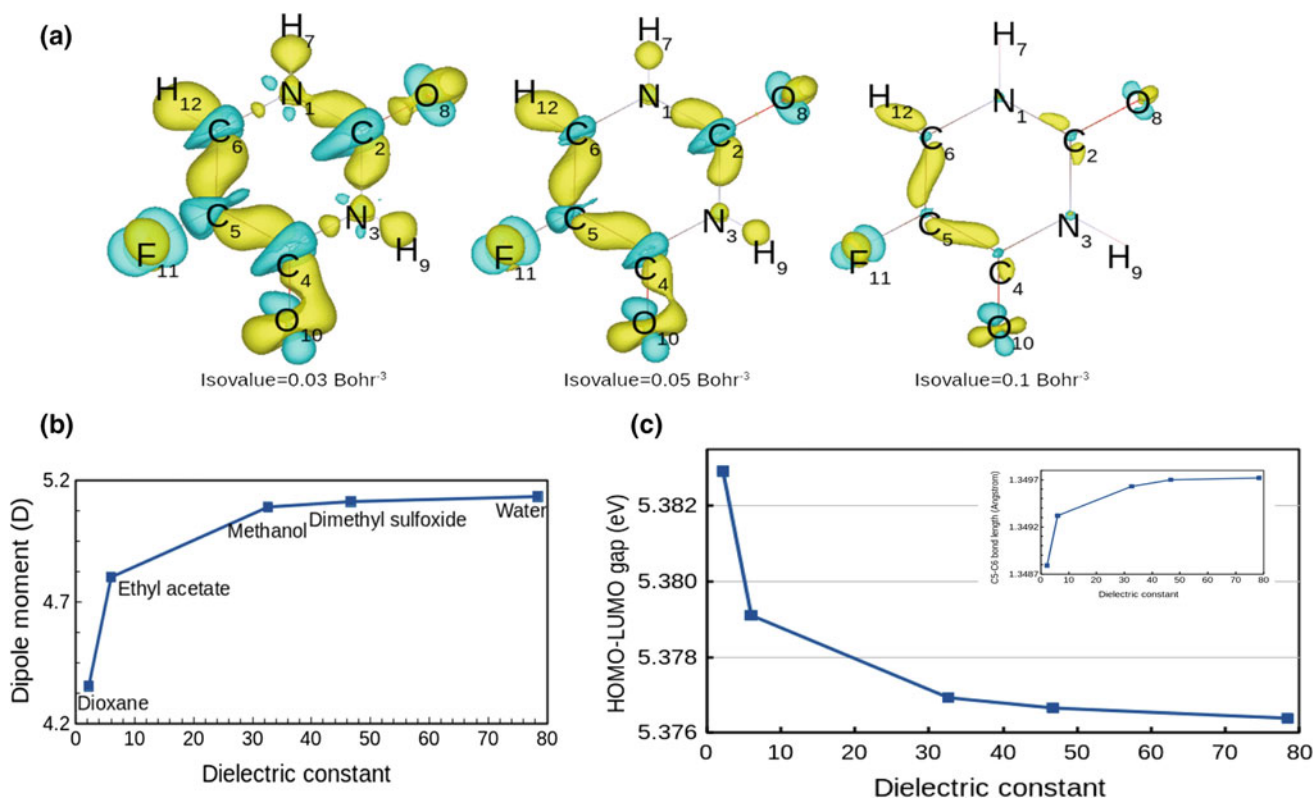


Fig. 2 a Isosurfaces at three absolute values of electron density deformation of 5-FU molecule in dioxane solvent. Yellow and blue, respectively, denote the increase and decrease of electron density when the molecular bonds form. b Change of 5-FU dipole moment with

respect to dielectric constant. c The evolution of band gap with respect to solvent dielectric constant. The inset shows the corresponding change of C₅–C₆ bond length

the inset of Fig. 2c. The reducing of HOMO-LUMO gap corresponds to a red shift in UV-Vis absorption spectrum. This effect is known as “positive solvatochromism” effect in which solvent polarity stabilizes the dipolar first excited state of the molecule [24]. The red shift in case of 5-FU is very weak, $\Delta E \sim 6$ meV due to the insignificant change of C₅–C₆ bond length. However, in framework of PCM method used here, solvents were considered as non-structured continuum and only static dielectric constant was taken into account as macroscopic solvent parameter. For a satisfactory quantitative description, discrete approach which takes into account individual solvents molecules explicitly should be utilized to treat solute-solvent interactions in a more realistic way.

4 Conclusions

In conclusion, exact exchange contribution to electron-electron interaction is important to optimize bond angles while correlation term is important for bond lengths. The deviations of calculated IR spectra from experiment are in consistence with corresponding optimized structures. Diffusion functions over-estimate dipole moment of the molecule. In the framework of PCM, the dipole moment of the 5-FU molecule increases with respect to solvent dielectric constant and reaches saturation value around 5.10 D at dielectric constant as high as more than 30. Electrostatic interaction between the molecule and solvents slightly stabilizes its dipolar first excited state. The solvent-induced changes in HOMO-LUMO gap predicted by PCM model is very small but in accordance with the change of C₅–C₆ bond length. For more satisfactory quantitative description, discrete approach for solvent must be utilized to treat solute-solvent interactions in a more realistic way.

Acknowledgements This work was partially supported by Vietnam National University Ho Chi Minh City under grant number TX-2018-50-01 and Vietnam National University Ha Noi under grant number TXTCN.17.04. **Conflict of Interest** The authors declare that they have no conflict of interest.

References

1. Lexi-Drugs. Lexicomp [Internet]. Hudson, OH: Wolters Kluwer Health, Inc. 1978–2013. 5-fluorouracil; [cited 2018 March]. Available from: <http://online.lexi.com>
2. Longley, D.B., Harkin, D.P., Johnston, P.G.: *Nat. Rev. Cancer* **3**, 330–338 (2003)
3. Rutman, R.J., Cantarow, A., Paschkis, K.E.: *Cancer Res.* **14**, 119–123 (1954)
4. Hulme, T.A., Price, S.L., Tocher, D.A.: *J. Am. Chem. Soc.* **127**, 1116–1117 (2005)
5. Thomas, S.A., Grami, Z., Mehta, S., Patel, K.: *Cancer Cell and Microenvironment* **3**, e1266 (2016)
6. Gaussian 09, Revision E.01, Frisch, M.J., Trucks, G.W., Schlegel, H.B., Scuseria, G.E., Robb, M.A., Cheeseman, J.R., Scalmani, G., Barone, V., Mennucci, B., Petersson, G.A., Nakatsuji, H., Caricato, M., Li, X., Hratchian, H.P., Izmaylov, A.F., Bloino, J., Zheng, G., Sonnenberg, J.L., Hada, M., Ehara, M., Toyota, K., Fukuda, R., Hasegawa, J., Ishida, M., Nakajima, T., Honda, Y., Kitao, O., Nakai, H., Vreven, T., Montgomery, Jr. J.A., Peralta, J. E., Ogliaro, F., Bearpark, M., Heyd, J.J., Brothers, E., Kudin, K. N., Staroverov, V.N., Keith, T., Kobayashi, R., Normand, J., Raghavachari, K., Rendell, A., Burant, J.C., Iyengar, S.S., Tomasi, J., Cossi, M., Rega, N., Millam, J.M., Klene, M., Knox, J.E., Cross, J.B., Bakken, V., Adamo, C., Jaramillo, J., Gomperts, R., Stratmann, R.E., Yazyev, O., Austin, A.J., Cammi, R., Pomelli, C., Ochterski, J.W., Martin, R.L., Morokuma, K., Zakrzewski, V.G., Voth, G.A., Salvador, P., Dannenberg, J.J., Dapprich, S., Daniels, A.D., Farkas, O., Foresman, J. B., Ortiz, J.V., Cioslowski, J., Fox, D.J.: Gaussian, Inc., Wallingford CT (2013)
7. Hasanein, A.A., Evans, M.W.: The hartree–fock self-consistent field method. *Comput. Methods Quantum Chem.* **2**, 39–78 (1996)
8. Parr, R.G., Yang, W. (1994) *Density-functional theory of atoms and molecules.* Oxford University Press, Oxford. ISBN 978-0-19-509276-9
9. Perdew, J.P., Chevary, J.A., Vosko, S.H., Jackson, K.A., Pederson, M.R., Singh, D.J., Fiolhais, C.: *Phys. Rev. B* **46**, 6671—Published 15 September 1992; Erratum *Phys. Rev. B* **48**, 4978 (1993)
10. Elliott, P., Lee, D., Cangi, A., Burke, K.: *Phys. Rev. Lett.* **100**, 256406 (2008)
11. Becker, A.D.: *Phys. Rev. A* **38**, 3098–3100 (1993)
12. Stephens, P.J., Devlin, F.J., Chabalowski, C.F., Frisch, M.J.: *J. Phys. Chem.* **98**, 11623–11627 (1994)
13. Ditchfield, R., Hehre, W.J., Pople, J.A.: *J. Chem. Phys.* **54**(2), 724–728 (1971)
14. Dunning, H.T.: *J. Chem. Phys.* **90**(2), 1007–1023 (1989)
15. Pederson, M.R., Baruah, T., Allen, P.B., Schmidt, C.: *J. Chem. Theory Comp.* **1**(4), 590–596 (2005)
16. Tomasi, J., Mennucci, B., Cammi, R.: *Chem. Rev.* **105**(8), 2999–3094 (2005)
17. Rastogi, V.K., Jain, V., Yadav, R.A., Singh, C., Palafox, M.A.: *J. Raman Spectrosc.* **31**, 595–603 (2000)
18. Dobrowolski, J.C., Rode, J.E., Kołos, R., Jamróz, M.H., Bajdor, K., Mazurek, A.P.: *J. Phys. Chem. A* **109**, 2167–2182 (2005)
19. Kulakowska, I., Geller, M., Lesyng, B., Wierzychowski, K.L.: Dipole moments of 2,4-diketopyrimidines: Part II: Uracil, thymine and their derivatives, *Biochimica et Biophysica Acta (BBA)—Nucleic Acids and Protein Synthesis* **361**, 119–130 (1974)
20. Brown, R.D., Godfrey, P.D., McNaughton, D., Pierlot, A.P.: *J. Am. Chem. Soc.* **110**, 2329 (1988)
21. Millefiori, S., Alparone, A.: *Chem. Phys.* **303**, 27 (2004)
22. Gester, R.M., Bistafa, C., Georg, H.C., Coutinho, K., Canuto, S.: *Theor. Chem. Acc.* **133**, 1424 (2014)
23. van der Spoel, D., van Maaren, P.J., Larsson, P., Timneanu, N.: *J. Phys. Chem. B* **110**, 4393–4398 (2006)
24. Reichardt, C.: *Chem. Rev.* **94**, 2319–2358 (1994)

Author Index

A

Anh, M.N., 225
Anh, Nguyen Thi My, 219
Anh, Pham Thi Tram, 657
An, Le Nguyen My, 283

B

Baaden, Marc, 261
Baidillah, Marlin Ramadhan, 243
Basse, Enobong E., 347
Becce, Michele, 209
Binh, Nguyen Thanh, 455, 493
Bonani, Walter, 147
Bui, Anh The, 567
Bui, Chi-Bao, 407, 685
Bui, Cuc T., 119
Bui, Nam Hoang, 61
Bui, Nghia Hieu, 139
Bui, Ngu, 537
Bui, Quoc Thang, 169

C

Campbell, James, 567
Carre, Matt J., 213
Cass, Anthony E.G., 337
Chau, T.P., 597, 619, 627, 641
Choi, Kyu Yeong, 379

D

Dan, Chu Quang, 3
Dang, Hoang Phuc, 153
Dang, Khiem Tran, 15, 21
Dang, L.V., 489
Dang, Nhi-Thao Ngoc, 143, 175
Dang, Tin T., 31, 43, 81
Darma, Panji Nursetia, 243
Dinh, Anh, 31, 43, 77, 81, 447
Dinh, Dong-Luong, 467
Dinh, Duc Trinh-Minh, 401
Doan, J., 289, 295, 651
Doan, N., 277, 289, 295, 585, 591, 597, 619, 627, 633, 641, 651
Doan, Nghiem, 163
Doan, Tan Le Hoang, 721
Do, H.G., 585
Do, Hung Ngoc, 473

Do, L.D., 591
Dong, Le Thanh, 707
Do, Ngoc Phuc Chau, 677, 681
Do, Ngoc Thuy Linh, 677
Do, Thai M., 67, 95
Do, Thien B.T., 95
Duc, Nguyen Huu, 647
Duong, Cong-Truyen, 247
Duong, Le Binh, 353, 699
Duong, Q.T., 277
Duong ThiThuy, Hang, 499
Duong, Tien Dat, 577
Dwyer-Joyce, Rob, 213

E

Ellison, Peter, 213

F

Fantini, Sergio, 375

G

Gi, Geon, 467
Greenhalgh, Leah, 369
Gwak, Jeonghwan, 379

H

Hai, Nguyen Thanh, 477
Hai, Vu Duy, 3
Hang, Nguyen Thi Diem, 657
Hang, N.T., 43
Hien, Ngo Thi Minh, 219
Hien, Nguyen Mong, 493
Hiep, Nguyen Thi, 283
Hieu, L.C., 225, 489
Higgins, Stuart G., 209
Hoang, Linh Gia, 721
Hoang, Ngoc Lin, 193
Hoang The, Hop, 499
Hoang, Tuan, 323
Ho, Hieu Minh, 319
Ho, H.L., 641
Hollfelder, Florian, 361
Ho, Minh H., 95
Hong, Minh Nguyen, 559

Ho, Thuy Thanh Thi, 605
 Hung, Dao Viet, 3
 Hung, Nguyen Manh, 477
 Hung, Pham Manh, 3
 Hung, Phan Dang, 3
 Huong, Nguyen Thi Minh, 513
 Hutmacher, Dietmar W., 153
 Huynh, Chan-Khon, 301
 Huynh, Dai Phu, 313
 Huynh, Khanh Quoc, 61
 Huynh, Khon, 323, 333, 413
 Huynh, Le Minh, 319
 Huynh, L.T., 641
 Huynh, Minh-Vy, 395
 Huynh, Phat K., 119
 Huynh, Quang Linh, 51, 57, 521
 Huynh, Quoc T., 103
 Huynh, Quyen B., 127
 Huynh, Thi Bich Mai, 693
 Huynh, T.M., 619, 627
 Huynh, T.Q., 597, 619, 627, 633, 641
 Huynh, Trinh Ngoc, 389
 Huy, Tran Thanh, 461

I

Iman, Al Amin Saichul, 243
 Iramina, Keiji, 231
 Ito, Daiyu, 527

J

Jang, Dong Pyo, 27
 Ji, Keven Seung Yong, 567
 Jingshi, Huang, 243

K

Kamada, Yuko, 527
 Khai, Le Quoc, 461, 657
 Khang, Nguyen M., 31
 Khiem, Dang Tran, 11, 115
 Khon, Huynh Chan, 239
 Kien, N.V.T., 81
 Kien, Tran, 657
 Kiet Anh, T., 235
 Kim, In Young, 27
 Kim, Jae Gwan, 379
 Kim, Minhee, 379
 Kim, Sun I., 27
 Kim, Tae-Seong, 467
 Kim, Tae Yeon, 467
 Koishi, M., 235

L

Lao, Thuan Duc, 605, 611
 Le, Chi Hieu, 693
 Le, Cong-Dat, 247
 Le, Dang Cao, 231
 Le, Dan Linh, 389
 Le Dinh, Hung, 567
 Lee, Byong-Taek, 301
 Lee, Eunice, 567
 Lee, Jang Jae, 379

Lee, Jongshill, 27
 Lee, Kun Ho, 379
 Lee, P.P., 571
 Lee, Soo Yeol, 467
 Lee, Walter T., 567
 Lee, W.T., 571
 Legname, Giuseppe, 255
 Le, Hai Thanh, 39
 Le, Hien-Phuong, 143, 175
 Le, Hieu Xuan, 401
 Le Minh, Ky, 567
 Le, Ngoc Hoang, 197
 Le, Ngoc Thuy Trang, 193
 Le, Nhan Thanh, 231
 Le, Phu Duong, 51, 57
 Le, Quang Tri, 169
 Le, Quoc Khai, 521
 Le, Quy Khang, 681
 Le, Thanh-Dong, 333
 Le, Thanh-Xuan, 333
 Le, Thi Duy Hanh, 147
 Le, Thi Vy Tuyet, 169
 Le, Thuong T., 435
 Le, Thuy Ai Huyen, 605, 611
 Le, Toan, 537
 Le, Triet Minh, 543
 Le, Trieu Hai-Nguyen, 543
 Le, Trieu Nguyen Hai, 505
 Le, Trung, 537
 Le, Trung Q., 119, 127, 543, 551
 Le, Trung Quoc, 505
 Le, Tuyet, 159
 Le, Van Cam Thi, 231
 Lewis, Roger, 213
 Le, Xuan-Hieu, 395
 Liaudanskaya, Volha, 147
 Lieu, Hung Chi, 605
 Li, J., 235
 Li, Jianping, 239
 Linh, Huynh Quang, 219, 461, 513, 657
 Linh, T.M., 81
 Linton, Patricia E., 369
 Liu, Shiyang, 163
 Luong, Tin Dai, 139
 Luu, Linh, 551
 Luu, Loc, 77
 Ly, Han, 333
 Ly, Khanh Loan, 203
 Ly, Loan Khanh, 319
 Ly, Minh H., 31

M

Mai, Linh, 473
 Mai, Ngoc Anh, 577
 Mai, Nguyen Thi Kim, 219
 Mai, Si-Nguyen, 413
 Maiti, Raman, 213
 Makhanov, S.S., 489
 Martinez Sanchez, Noe A., 213
 Ma, Zhichao, 341
 Migliaresi, Claudio, 147
 Minh, Doan Binh, 707
 Minh, H.L., 225, 489
 Minh, Vo Hoang Thuc, 219

Morikawa, Shigehiro, 15, 21
 Motta, Antonella, 147
 Munguia, J., 341

N

Nagasaki, Yukio, 185
 Naka, Shigeyuki, 11, 15, 21, 115
 Nam, Nguyen Quoc Duy, 219
 Nam, N.P., 87
 Neville, Anne, 213
 Nghia, Nguyen Thanh, 477
 Ngoc, Pham Phuc, 3
 Ngo, Dat Duc, 483
 Ngo, L.T. Quynh, 585
 Nguyen, An T.L., 109
 Nguyen, Cuu Khoa, 193, 197
 Nguyen, Dai Hai, 189, 193, 197
 Nguyen, Dat Tan, 139, 179
 Nguyen, Diem Huong Tran, 189
 Nguyen, Dien Thanh Giang, 269
 Nguyen, Dong Yen Pham, 189
 Nguyen, D.T., 591
 Nguyen, Duc-Nam, 247
 Nguyen, Hai Ngoc, 231
 Nguyen, Hai Thanh, 483
 Nguyen, Hiep Thi, 139, 143, 175, 203, 307
 Nguyen, Hoang Mai Le, 269
 Nguyen, Hoang-Tuan, 323, 333
 Nguyen, K.T., 571
 Nguyen, Linh Thuy Ba, 301
 Nguyen, Mai Hoang, 473
 Nguyen Manh, Duc, 721
 Nguyen, Minh Nhat, 427
 Nguyen, M.T., 597
 Nguyen, M.T.T., 627
 Nguyen, My Thi Ngoc, 159
 Nguyen, Nam P., 67, 95
 Nguyen, Nga, 567
 Nguyen, Ngoc-Bao-Tran, 395
 Nguyen, Ngoc C., 435
 Nguyen, Ngoc Minh Thinh, 51
 Nguyen, Ngoc Thi-thanh, 307
 Nguyen, Nguyen D., 447
 Nguyen, Nguyen Trong, 513
 Nguyen, Nhung T., 127
 Nguyen, P.H., 627
 Nguyen, Phuong Mai Thi, 611
 Nguyen, Thanh Truc, 319
 Nguyen, Thao-Vi, 407
 Nguyen, Thi Diem Hang, 521
 Nguyen, Thien, 379
 Nguyen, Thien M., 109
 Nguyen, Thi-Hiep, 179, 301, 319
 Nguyen, Thi Hue, 269
 Nguyen, Thi Kim Cuc, 693
 Nguyen, Thi Nga, 269
 Nguyen, Thi Ngoc Mai, 577
 Nguyen, Thi Ngoc Thanh, 269
 Nguyen, Thinh P., 109
 Nguyen, Thi Thu Hoai, 677, 681
 Nguyen Thi, Yen Nhi, 193
 Nguyen, Thuy Ha, 57
 Nguyen, Tien Ngoc-Thuy, 179
 Nguyen, Toan The, 721
 Nguyen, Trang Thuy, 721

Nguyen, Tran Khanh Tran, 51
 Nguyen, Tran Kim Hoang, 57
 Nguyen, Trong Thuc, 677, 681
 Nguyen, Trung, 567
 Nguyen, Tuan-Anh, 663
 NguyenTuan, Khai, 499
 Nguyen, Tuan T., 435
 Nguyen, Uyen D., 103
 Nguyen, V.A., 591
 Nguyen, Van Duy, 693
 Nguyen, Vien Phuc, 483
 Nguyen-Vu, Viet Linh, 313
 Nguyen, Y.L., 109
 Nhan, Vo Thanh, 669
 Nhi, Do Tuyet, 219
 Nhi, Tran T., 31
 Nitta, Norihisa, 15

O

O'Hare, Danny, 337
 Ooga, Masatoshi, 527

P

Packianather, Michael, 693
 Packianather, M.S., 489
 Park, Hye Min, 467
 Park, Jeong Min, 467
 Park, Ki Dong, 189
 Perrault, Cécile M., 213, 323, 333
 Pham, Chi Hoang Linh, 685
 Pham, D.H., 585
 Pham, Gia-Phu, 413
 Pham, Hien Thi-Thu, 39, 61, 383, 401, 421, 427, 531
 Pham, Huy Q., 127
 Pham, Linh Phuong Tran, 189
 Pham, Minh M.N., 421
 Pham-Nguyen, Thuy-Vy, 333
 Pham, Phong, 551
 Pham, Thao, 375
 Pham Thi, Bac Ly, 193
 Pham, Thi Hai Mien, 51, 57
 Pham, Thi Lan Anh, 681
 Pham, Thi-Thu-Hien, 389, 395, 407, 413
 Pham, Thi Tram Anh, 521
 Pham, Tho Tuan Anh, 169
 Pham, Thu Thuy, 693
 Phan, Hai T., 109
 Phan, Hao T., 119
 Phan, Minh Lai-Nhat, 427

Q

Quang, Do Tran, 559
 Quang, Nguyen D., 447
 Quoc, L.H., 225, 489

R

Ramirez-Reivich, Alejandro, 213
 Rashid, Mamun, 369
 Rehbein, G., 715
 Reher, P., 277, 289, 295, 651, 715
 Reher, V., 715

S

Sallis, Philip, 347
 Sassaroli, Angelo, 375
 Seong, Hyejeong, 209
 Sharma, Sanjiv, 337
 Shaw, Kirsty J., 369
 Stevens, Molly M., 209

T

Takei, M., 235
 Takei, Masahiro, 239, 243
 Tang, T.D., 225
 Tan, H.K., 571
 Tani, Soichiro, 11, 115
 Tani, Tohru, 11, 15, 21, 115
 Tan, N.C., 571
 Ta, Vu Thuc Oanh, 663
 Tgavalekos, Kristen, 375
 Thach, Ha, 323
 Thai, D.M., 87
 Thang, Nguyen Ngoc, 219
 Thanh, Nguyen Chi, 455
 Than, Minh H.N., 421
 Thao, P.T.N., 43
 The, Nguyen Huu, 493
 Thi, Men Nguyen, 559
 Thi, Ngoc Tram Nguyen, 197
 Thinh, Tran Quang, 353, 699
 Thuy, Hang Dang, 559
 Thuy, Le Nu Ngoc, 657
 Thuy, Tran Hong, 353, 699
 Tien, Hoang Anh, 647, 669
 Tin, Dang T., 447
 Toi, Vo Van, 283
 Toi, V.V., 87
 To, Minh Quan, 169
 Tong, Uyen, 323
 Tran, An Nhu-Phu, 401
 Tran, Bao Ngoc, 51
 Tran, Binh Q., 103
 Tran, D.N., 597, 619, 627
 Tran Duc, Tan, 499
 Trang, Kien, 473
 Tran, Ha, 159
 Tran, H.T., 585
 Tran, Kiet Anh, 239
 Tran, Le Bao Ha, 169
 Tran, Lien, 567
 Tran, Long Thanh, 383
 Tran, Luan M., 435
 Tran, Nam Minh-phuong, 139, 307
 Tran, Phong A., 153
 Tran, Quang Chung, 577
 Tran, Quynh Ngan, 677
 Tran, Thanh Hoa, 255
 Tran, Thanh Hoang, 693
 Tran, Van-Su, 473
 Trinh, C.H., 619
 Trinh, Ngoc Le Van, 169
 Truc, Nguyen Thanh, 283
 Truc, Tran Thi Thanh, 669
 Trung, Dung Dao, 567
 Trung, Lai Huu Phuong, 3
 Trung, V.T., 225
 Truong, K.N., 585

Truong, L., 277, 289, 295, 651
 Truong, Phuong Kim, 611
 Truong, Tuan Dinh, 531
 Truong, Viet Anh, 401
 Tsai, Yuh-Show, 441
 Tuan, Mai Anh, 353, 699
 Tu, N.H., 225
 Tuyen, Vo Ngoc My, 283
 Tuyet, Vo Thi Hong, 455, 493

U

Ugurluoglu, Y., 341

V

Van Anh, Vo Duong, 219
 Van Binh, Duong, 477
 Van Nguyen, Duong, 499
 Van Pham, Thanh, 499
 Van, Toi V., 119, 127
 Van Toi, Vo, 139, 143, 175
 Van Tran, An, 499
 van Vliet, Liisa D., 361
 Van Vo, Toi, 203, 505, 543
 Van Vu Quan, Trieu, 353, 699
 Viet, T.N., 87
 Vinh, Nguyen Quoc, 11
 Vi, Tran Quoc, 3
 Vo, Anh Thi Ngoc, 505
 Vohra, Priya, 567
 Vo, K.V., 641
 Vo, Minh-Thanh, 473
 Vo, Minh Thuy, 319
 Vong, Long Binh, 185
 Vo, Tan Thanh, 57
 Vo, Thanh Nguyet Nguyen, 189
 Vo, Thi-Phuong-Trinh, 395
 Vo, Toi V., 67, 95, 109
 Vo, Uyen Vy, 197
 Vo, Van Toi, 179, 319, 333, 413
 Vu, Nga Thi-Hang, 61
 Vuong, Bao Quoc, 473
 Vuong, Tuan-Anh, 323

W

Wagner, Rasmus, 213
 Wakayama, Sayaka, 527
 Wakayama, Teruhiko, 527
 Wang, Gui, 163

X

Xuan, Chu Thi, 353, 699

Y

Yamada, Atsushi, 11, 15, 21, 115
 Yanagisawa, Ryota, 243
 Ye, Hua, 301
 Yock, P.G., 571

Z

Zeng, Jia-Huang, 441